

HOT CORROSION AND EROSION BEHAVIOR OF NANOSTRUCTURED AND CONVENTIONAL COATINGS

A THESIS

*Submitted in partial fulfilment of the
requirements for the award of the degree*

of

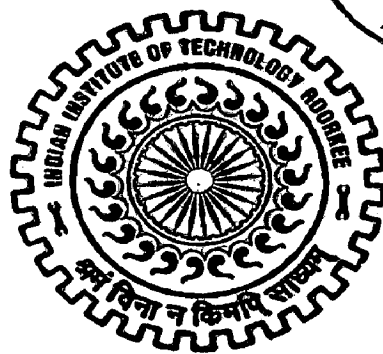
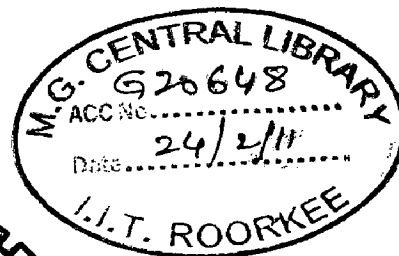
DOCTOR OF PHILOSOPHY

in

METALLURGICAL AND MATERIALS ENGINEERING

by

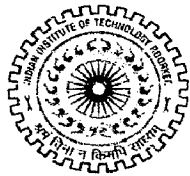
VIKAS CHAWLA



DEPARTMENT OF METALLURGICAL AND MATERIALS ENGINEERING
INDIAN INSTITUTE OF TECHNOLOGY ROORKEE
ROORKEE - 247 667 (INDIA)

AUGUST, 2009

©INDIAN INSTITUTE OF TECHNOLOGY ROORKEE, ROORKEE, 2009
ALL RIGHTS RESERVED



INDIAN INSTITUTE OF TECHNOLOGY ROORKEE


CANDIDATE'S DECLARATION


I hereby certify that the work which is being presented in the thesis entitled "**Hot Corrosion and Erosion Behavior of Nanostructured and Conventional Coatings,**" in partial fulfillment of the requirement for the award of the Degree of Doctor of Philosophy and submitted in the Department of Metallurgical and Materials Engineering of the Indian Institute of Technology Roorkee, Roorkee is an authentic record of my own work carried out during a period from January, 2006 to August, 2009 under the supervision of Dr. D. Puri, Assistant Professor, Dr. Satya Prakash, Professor, Department of Metallurgical and Materials Engineering, Indian Institute of Technology Roorkee, Roorkee, and Dr. Buta Singh Sidhu, Professor and Head, Yadwindra Engineering College, Talwandi Saboo, Bathinda, Punjab.


The matter presented in this thesis has not been submitted by me for the award of any other degree of this or any other Institute.


(VIKAS CHAWLA)

This is to certify that the above statement made by the candidate is correct to the best of our knowledge.


(Satya Prakash)
Supervisor


(Buta Singh Sidhu)
Supervisor


(D. Puri)
Supervisor

Date:- 19.08.09

The Ph.D. Viva-Voice examination of **Mr. Vikas Chawla**, Research Scholar, has been held on _____

Signature of Supervisors

Signature of External Examiner

Materials degradation at high temperatures is a serious problem in several high tech industries. Power plants are one of the major industries which encounter severe corrosion problems resulting in the substantial loss. The problem is becoming more prominent as the plants are getting older. Attempts to increase the efficiency of steam generating plant by raising the final steam temperature above 600°C and the use of gas turbines for the production of cheap electric power have made working conditions more severe for the materials. The boiler tubes used for super-heaters and re-heaters in the steam generating systems are subjected to fireside corrosion, resulting in tube wall thinning and premature failure. Hot corrosion has been identified as a serious problem in high temperature applications such as in boilers, gas turbines, waste incinerations, diesel engines, coal gasification plants, chemical plants and other energy generation systems.

Also, erosion-corrosion by solid particles in gaseous environments at elevated temperatures and hence wastage of alloys, is a serious problem in many industrial processes. Small, solid particles propelled by generally oxidizing gases in various fluid flow patterns constitute the primary operating environments in the combustion regions of energy generating boilers operating on such fossil fuels as coal and various kinds of biomass. High-temperature erosion-corrosion and oxidation of the heat transfer pipes and other structural materials in the coal fired boilers are recognized as being the main cause of downtime at power generating plants, accounting for 50% to 75% of the total arrest time. Maintenance costs for replacing the broken pipes in such installations are also very high and are estimated to be up to 54% of the total production costs. These facts emphasize the need to develop more and more corrosion resistant materials for such applications. Therefore, the boiler steel needs to be protected.

In this regard, it is learnt from the published literature that one possible, practical, reliable and economically viable way to control or prevent the high temperature corrosion and erosion problems of the superheaters and reheaters of the boilers is an application of a thin layer of corrosion resistant coatings having good thermal conductivity. The physical vapour deposition (PVD) and plasma spray (a thermal

spray process) have been reported to be two major coating processing technologies used. In recent years, corrosion performance of nanostructured materials/coatings is a hot topic in the corrosion field. Nanostructured materials indeed behave differently than their microscopic counterparts because their characteristic sizes are smaller than the characteristic length scales of physical phenomenon occurring in bulk materials. In many tribological applications, hard coatings of metal nitrides are now commonly used. In the past years, hard protective TiAlN coatings and AlCrN coatings were widely used for wear resistant properties. Recently these coatings are gaining importance for high temperature wear, corrosion and oxidation resistance applications.

It is important to understand the nature of all types of environmental degradation of metals and alloys as vividly as possible so that preventive measures against metal loss and failure can be economically devised to ensure safety and reliability in the use of metallic components. The present study has been performed to evaluate the behavior of the nanostructured and conventional metal nitride coatings (obtained on the boiler tube steels and a Fe-based superalloy); when exposed to high temperature oxidation in air, molten salt ($\text{Na}_2\text{SO}_4\text{-60\%V}_2\text{O}_5$) environment, in actual degrading conditions prevailing in a coal fired boiler of a thermal plant, erosion in simulated coal-fired boiler environment and simulated marine environment. Three types of boiler steel substrate materials namely "ASTM-SA210-Grade A-1," "ASTM-SA213-T-11" and steel "ASTM-SA213-T-22" and a Fe-based superalloy having Midhani Grade Superfer 800H have been selected for the present study as the substrate materials. The nanostructured thin TiAlN and AlCrN coatings; with thickness around $4\mu\text{m}$, were deposited on the substrates at Oerlikon Balzers Coatings India Limited, Gurgaon, India. The conventional thick TiAl and AlCr coatings were deposited on the substrates by Plasma Spraying. The coating work was carried out at a commercial firm namely Anod Plasma Limited, Kanpur, India. The gas nitriding of the plasma sprayed conventional thick Ti-Al and Al-Cr coatings was done in the lab. The as-coated specimens were characterized by metallography, SEM, AFM, Porosity analysis, EDAX and X-ray mapping. Microhardness, bond strength and Surface roughness have also been measured.

All the coatings were dense, uniform, continuous and adherent. The thickness of coating was in the range of $5.2\text{-}6.3\ \mu\text{m}$, $4.2\text{-}5.5\ \mu\text{m}$, $140\text{-}174\ \mu\text{m}$ and $122\text{-}166\ \mu\text{m}$ for the nanostructured TiAlN, nanostructured AlCrN, conventional TiAlN and conventional AlCrN coatings respectively. The nanostructured thin TiAlN and AlCrN coatings exhibited negligible porosity values for as coated; which were less than 0.5 %. The conventional

TiAlN and AlCrN coatings showed; higher porosity values (1.90-4.30%) for as sprayed conventional Ti-Al and Al-Cr coatings; which after gas nitriding were found to be less than 0.65 %. The grain size (calculated by Scherrer formula from XRD plot) for nanostructured thin TiAlN and AlCrN coatings was less than 22 and 28 nm respectively which was further verified by AFM analysis. A good adhesion of the conventional thick TiAlN and AlCrN coatings was evident from bond test results. Average bond strength of 68.74 MPa and 54.69 MPa was observed in case of conventional TiAlN and AlCrN coatings respectively.

The behavior of uncoated and coated alloys has been studied in the air, molten salt and actual industrial environment. Air and molten salt studies performed in the laboratory furnace for 50 cycles each cycle consisting of 1 hour heating at 900°C followed by 20 minutes cooling. At the end of each cycle the samples were critically examined and the change in weight was recorded. In case of studies under the molten salt, a uniform layer (3-5 mg/cm²) of the mixture of Na₂SO₄-60%V₂O₅ was coated on the samples with the help of camel hair brush by preheating the sample at 250°C. The coated as well as bare alloy specimens were exposed to the platen super-heater zone of the coal fired boiler of Stage-II at Guru Nanak Dev Thermal Plant, Bathinda, Punjab (India). The specimens were exposed to the combustion environment for 10 cycles. Each cycle consisted of 100 hours heating followed by 1 hour cooling at ambient conditions. The temperature was measured at regular intervals during the study and the average temperature was about 900°C with variation of ± 10°C. At the end of each cycle the samples were critically examined regarding the colour, lustre, tendency to spall and adherence of scale and then subjected to weight change measurements. XRD and SEM/EDAX techniques were used to identify the phases obtained and the elemental analysis of the surface scale. These corroded samples were then cut across the cross-sections and mounted to study the cross-sectional details by X-Ray mapping.

Based on the overall weight gain after 50 cycles in air and in an aggressive Na₂SO₄-60%V₂O₅ (molten salt) environment at 900°C temperature, the oxidation resistance of the bare Fe-based alloys studied in the present investigation has been found to be in the following order:

AIR ENVIRONMENT

S.F 800H superalloy > Grade A-1 boiler steel > T-11 boiler steel > T-22 boiler steel

Na₂SO₄-60%V₂O₅ (MOLTEN SALT) ENVIRONMENT

S.F 800H superalloy > T-11 boiler steel > Grade A-1 boiler steel > T-22 boiler steel

The superior oxidation resistance of the Superfer 800H superalloy may be attributed to the development of homogeneous and continuous scale consisting of oxides of Ni and Cr due to higher percentage of Ni and Cr in the Superfer 800H. The higher weight gain and spalling as observed in case of T-11 and T-22 boiler steels may be attributed to the presence of molybdenum in the steels. During initial oxidation; Fe is oxidized and the oxide scale is protective in nature. With progress of oxidation molybdenum becomes enriched at the alloy interface, leading to the formation of an inner layer of molten MoO₃ (m. p. 795°C) which penetrates along the alloy-scale interface. This liquid oxide disrupts and dissolves the protective oxide scale, causing the alloy to suffer catastrophic oxidation. Based on the overall weight gain after 50 cycles in air and in molten salt environment at 900°C temperature, the oxidation resistance of the coating on the Fe-based alloys has been found to be in the following order:

AIR ENVIRONMENT

Substrate ASTM-SA210-Grade A-1 Boiler Steel:

Conventional AlCrN > Conventional TiAlN > Nanost. AlCrN > Nanost. TiAlN > Bare Grade A-1

Substrate ASTM-SA213-T-11 Boiler Steel:

Conventional AlCrN > Conventional TiAlN > Nanost. AlCrN > Nanost. TiAlN > Bare T-11

Substrate ASTM-SA213-T-22 Boiler Steel:

Conventional AlCrN > Nanost. AlCrN > Conventional TiAlN > Bare T-22 > Nanost. TiAlN

Substrate Superfer 800H Superalloy:

Nanost. AlCrN > Nanost. TiAlN > Bare S.F 800H > Conventional TiAlN > Conventional AlCrN

Na₂SO₄-60%V₂O₅ (MOLTEN SALT) ENVIRONMENT

Substrate ASTM-SA210-Grade A-1 Boiler Steel:

Conventional AlCrN > Conventional TiAlN > Nanost. TiAlN > Nanost. AlCrN > Bare Grade A-1

Substrate ASTM-SA213-T-11 Boiler Steel:

Conventional AlCrN > Nanost. AlCrN > Nanost. TiAlN > Conventional TiAlN > Bare T-11

Substrate ASTM-SA213-T-22 Boiler Steel:

Conventional AlCrN > Nanost. TiAlN > Conventional TiAlN > Nanost. AlCrN > Bare T-22

Substrate Superfer 800H Superalloy:

Nanost. AlCrN > Nanost. TiAlN > Conventional TiAlN > Conventional AlCrN > Bare S.F 800H

All the coatings have shown protection to the substrate based on the overall weight gain after 50 cycles in air environment at 900°C temperature except nanostructured TiAlN coated T-22 boiler steel. The nanostructured TiAlN and AlCrN coatings has shown resistance to oxidation to some extent as the overall weight gain is less, but failed to sustain during the course of oxidation study. This might be due to the formation of oxide scale which is composed of a porous oxide mixture of TiO₂ and Al₂O₃, with the domination of TiO₂. The plasma sprayed gas nitride conventional thick coatings i.e. TiAlN and AlCrN when subjected to cyclic oxidation studies at 900°C for 50 cycles developed a protective scale mainly consisting on Al₂O₃ along with some amount of TiO₂ (in case of conventional TiAlN coating) and Cr₂O₃ (conventional AlCrN coating). In case of T-11 and T-22 boiler steels; the conventional TiAlN coating failed to sustain during the course of study. The weight change plots for the uncoated and coated alloys indicated that the oxidation behavior has shown conformance to parabolic rate law. Development of some minor cracks near or along the edges of the coated specimens may be attributed to the thermal shocks due to differences in the heat expansion coefficients of the oxides, coatings and the substrate.

In case of specimens exposed to actual industrial environment; based on the materials depth affected by corrosion or corrosion rate in mils per year (mpy) after 1000 hours of exposure, the corrosion resistance of the bare Fe-based alloys studied in the present investigation has been found to be in the following order:

S.F 800H superalloy > Grade A-1 boiler steel > T-22 boiler steel > T-11 boiler steel

Based on the materials depth effected by corrosion or corrosion rate in mils per year (mpy) after 1000 hours of exposure, the corrosion resistance of the uncoated and coated Fe-based alloys studied in the present investigation has been found to be in the following order:

Substrate ASTM-SA210-Grade A-1 Boiler Steel:

Conventional TiAlN > Conventional AlCrN > Nanost. TiAlN > Bare Grade A-1> Nanost. AlCrN

Substrate ASTM-SA213-T-11 Boiler Steel:

Conventional TiAlN > Conventional AlCrN > Nanost. TiAlN > Nanost. AlCrN > Bare T-11

Substrate ASTM-SA213-T-22 Boiler Steel:

Conventional TiAlN > Conventional AlCrN > Nanost. AlCrN > Conventional TiAlN > Bare T-22

Substrate Superfer 800H Superalloy:

Conventional TiAlN and AlCrN > Nanost. TiAlN > Nanost. AlCrN > Bare S.F 800H

The coated as well as uncoated boiler steels have shown higher corrosion rate as compare to Superfer 800H supeallloy. In case of boiler steels; maximum corrosion rate has been observed in bare T-11 and minimum in case of conventional TiAlN coated Grade A-1 boiler steel. All the coatings have shown resistance to corrosion in terms of corrosion rate when compared with respective bare alloy except nanostructured AlCrN coated Grade A-1. The conventional coatings have shown good resistance to the corrosive environment as the oxygen penetration is limited to very less thickness as compare to the uncoated and nanostructured coated boiler steels. All the coated as well as uncoated boiler steels have shown ash deposition on the surface. Thus final thickness is contributed by scale formation, erosion and ash deposition.

Erosion testing was carried out using a solid particle erosion test rig TR-471-M10 Air Jet Erosion Tester (Ducom Instruments Private Limited, Bangalore, India. The samples were cleaned in acetone, dried, weighed to an accuracy of 1×10^{-5} g using an electronic balance, eroded in the test rig for 3 hours and then weighed again to determine weight loss. In the present study standard alumina 50 micron was used as erodent. The two temperatures were taken for the test, sample temperature 400°C and air/erodent temperature 900°C simulated to service conditions of boiler tubes in which sample temperature and flow gas temperature correspond to the inner and outer temperature of water wall pipes. Erosion resistance was measured in terms of volume loss after the erosion testing. All the specimens subjected to erosion wear were analyzed for the characterization of erosion products. The specimens were analyzed using surface SEM, EDAX and measurement of surface profiles using optical profilometer.

All the uncoated and nanostructured TiAlN and AlCrN coated alloys have shown higher erosion rate at oblique impact (at 30°) than at normal impact (at 90°), which indicate ductile behavior as proposed by Murthy et al. (2001). The nanostructured thin TiAlN and AlCrN coatings were removed by the continuous strikes of the eroding particles on the surface of the coatings in most of the cases. The plasma sprayed conventional TiAlN coatings have successfully protected the substrates. All the conventional thick TiAlN coated alloys have shown higher erosion rate at oblique

impact (at 30°) than at normal impact (at 90°) thus indicating ductile behavior except in case of Grade A-1 boiler steel. The plasma sprayed conventional AlCrN coatings have successfully protected the substrates at both impact angles except in case of T-11 boiler steel. The conventional AlCrN coating gets removed by the continuous strikes of the eroding particles on the surface of the coating in case of T-11 boiler steel at both impact angles. All the conventional thick AlCrN coated alloys have shown higher erosion rate at normal impact (at 90°) than at oblique impact (at 30°) except in case of Superfer 800H superalloy.

In order to evaluate the corrosion behavior of the substrates and coatings in simulated marine environment; linear polarization resistance (LPR) and potentiodynamic polarization tests were conducted in an aerated 3 wt% NaCl solution at room temperature. The initial corrosion current density and LPR (R_p) was measured by LPR test. It can be inferred from the corrosion parameters i.e. corrosion current densities (i_{corr}) obtained in LPR test that all the coatings are protecting the substrates except conventional coatings on T-11 boiler steel and conventional TiAlN coated Superfer 800H superalloy. In case of uncoated alloys; bare T-22 boiler steel has shown maximum corrosion current density ($108.60 \mu\text{A}/\text{cm}^2$) and Superfer 800H has shown best corrosion resistance at initial stage on the basis of corrosion current density ($05.37 \mu\text{A}/\text{cm}^2$) and polarization resistance values obtained in the test. In Potentiodynamic polarization test; the corrosion current densities of the coatings were found much lower than that of the substrate steel except for nanostructured and conventional TiAlN coated Superfer 800H superalloy. Also, the corrosion current densities of the substrate and the coatings were found much lower as compared to the LPR test (at initial stage) results. A protective oxide layer may have formed which has blocked further corrosion. The corrosion product formed may have reduced the passage of the electrolyte to attack the samples, and hence providing protection.

The ASTM B117 Salt Fog test was used to evaluate the performance of the uncoated and nanostructured thin TiAlN and AlCrN coatings. In the B117 test, the samples are exposed to a salt fog generated from a 5% sodium chloride solution with a pH between 6.5 and 7.2 in salt fog testing set up (HSK 1000, Heraeus Votsch, Germany). All the samples were placed in the salt fog chamber for 24 Hrs, 48 Hrs and 72 Hrs. After exposure; samples were monitored and analyzed by using XRD and SEM/EDAX

techniques. The uncoated boiler steels have shown higher weight loss per unit area in all three test conditions i.e. 24 Hrs, 48 Hrs and 72 Hrs tests; as compared to their coated counterparts. The uncoated as well as nanostructured TiAlN and AlCrN coated Superfer 800H superalloy have performed well as these specimens have shown no weight change during exposure for 24 Hrs, 48 Hrs and 72 Hrs to salt fog tests. Both the coatings (nanostructured TiAlN and AlCrN) have shown good protection to the substrate in terms of weight loss per unit area. Also, the weight loss per unit area increases with the duration of the test in case of bare and coated boilers steels. In case of uncoated boiler steel; the T-11 and T-22 have shown higher weight loss than Grade A-1 for 24 Hrs test duration. The bare Grade A-1 boilers steel undergoes higher weight loss during 48 Hrs and 72 Hrs test studies as compared to T-11 and T-22 boiler steels. XRD diffractograms for uncoated boiler steels have also indicated Fe_3O_4 is the main phases present in the oxide scale.

ACKNOWLEDGEMENTS

मेरा मुझ में कुछ नहीं जो कुछ है सब तेरा तेरा तुझ को सौंपते क्या लागे है मेरा.....

The author is highly indebted to the Great and Gracious Almighty God who blessed him with spiritual support and fortitude at each and every stage of this work and humbly dedicates this work to the supreme power of this universe. The author would like to express his reverence and great admiration for his parents Sh. K.L. Chawla and Smt. Ved Chawla who dreamt in a small village about higher education of their children and have always been the guiding force for him.

The author feels a sense of privilege and pleasure to express his sense of gratitude to Dr. Satya Prakash, Professor, Dr. D. Puri, Asst. Prof., Department of Metallurgical and Materials Engineering (MMED), Indian Institute of Technology, Roorkee and Dr. Buta Singh Sidhu, Professor and Head, Yadwindra Engineering College, Talwandi Saboo, Bathinda, Punjab, India for their valuable guidance and untiring efforts throughout the tenure of this work. They have been an inspiring and driving force where targets appeared to be difficult during the course of work. Their timely help, constructive criticism and painstaking efforts made the author capable of compiling the thesis in its present form.

No work can be implemented in isolation and the author is no exception to this rule. He feels a sense of pride in taking this opportunity to express his sincere thanks to the various helping hands during the course of work. He is highly indebted to Dr. S. K. Nath, Head, MMED for his co-operation in extending the necessary facilities and supports during the concluding phase of this work. Author is grateful to Dr. R. D. Agarwal and Dr. Surendra Singh for their valuable suggestions and timely help during the course of this work. Author wishes to record his deep sense of gratitude to Head, Institute Instrumentation Centre (IIC), Indian Institute of Technology Roorkee for extending necessary facilities during the experimental and analysis work.

Again the author is extremely obliged and wishes to owe his sincere thanks to the technical and administrative staff of the MMED, especially to Mr. Rajinder Sharma, Late (Mr). Shamsheer Singh, Mr. Kuldeep Sharma, Mr. Narinder Kumar, Mr. M. Aslam, Mr. T. K. Sharma, Mr. Shakti Gupta, Mr. S. M. Giri, Mr. Kailash Chand, Mr. Naresh and Mr. Balesh Kumar who helped him in all possible ways during the experimental work.

The author is immensely grateful to Mr. R. K. Tandon, Managing Director, Anod Plasma Spray Ltd., Kanpur and Er. Jatinder Dabral, Manager, Oerlikon Balzers Coating India Limited, Gurgaon for extending coating facilities. He owes his sincere thanks to Er. Pardeep Singh, Sr. Xen., for his extended help and support to carry out the experimentation work at Guru Nanak Dev Thermal Plant (GNDTP), Bathinda, Punjab. Special thanks are due to Mr. Gurcharan Singh foreman G.N.D.T.P., Bathinda for his kind co-operation and help during experimentation work.

Author expresses his gratitude to the administration of Lala Lajpat Rai Institute of Engineering and Technology, Moga, Punjab for allowing on study leave to carry out this work at I.I.T Roorkee. The financial support rendered by All India Council of Technical Education (AICTE) New Delhi under National Doctoral Fellowship (NDF) is highly acknowledged. Author wishes to thank friends and colleagues for their encouragement and camaraderie help to keep things in perspective. Thanks are due to Mr. Manish Goyal, Mr. Yashwant Mehta, Mr. Sanjeev Bajaj, Mr. Balwinder Raj, Mr. Santosh Vishwakarma, Mr. Samarjeet Rawat, Mr. Nilesh Sharma, Mr. Subash Kamal, Mr. Pawan Sapra, Mr. Gurbhinder Singh, Mr. Vipin Chawla, Mr. Amit Chawla, Mr. S. K. Panigrahi, Mr. Gurpreet Singh, Mr. Manoj Mittal and Mr. Kuldeep Ranã. Thanks are also due to his colleagues from Lala Lajpat Rai Institute of Engineering and Technology, Moga, Punjab for their co-operation and moral support and his students for their best wishes.

A sense of apology is due to author's sweet daughter Yashita and loving son Neelesh, who probably missed many precious moments of paternal love and care. The wife of author, Mrs. Amita Chawla deserves special thanks and grand appreciation for her persistent moral support and capability to rejuvenate the author during the leaning phases of the work. The author is falling short of words to express gratitude to her for the determination shown to bear extra household responsibilities during the tenure of this work. Author sincerely acknowledges the help extended by his father-in-law Mr. Jagdish Lal and mother-in-law Smt. Janak Dulari in this regard with immense gratitude. Author is highly grateful to his sisters Vandana, Shallu (Gudu) and brothers-in-law Mr. Rajesh Kapoor and Mr. Gaurav Khurana for their continual co-operation during the course of this work. Author would like to thank his brothers Bhupesh and Amit and sisters-in-law Shallu and Usha for their best wishes extended from time to time.

The entire work carried out for this investigation has been presented in to nine chapters:

- Chapter-1 contains the introductory remarks about hot corrosion and erosion problem faced by the various industries and especially in coal fired boilers. The ways to counteract this problem are also briefly discussed.
- Chapter-2 begins with exhaustive survey of literature regarding various aspects and mechanism of hot corrosion and erosion in different degrading environments. Critical review of studies in air, molten salt and energy generation systems has been made. The various aspects for the control of these degradations and more detailed behavior of coatings have also been reviewed.
- Chapter-3 deals with the experimental procedure for the present study. It includes the procedure to obtain the coatings, their characterization, high temperature oxidation studies in air, molten salt environment and in a coal fired boiler of a thermal plant, erosion studies in simulated coal-fired boiler environment and corrosion studies in simulated marine environment.
- Chapter-4 deals with the results and discussion for the bare and coated ASTM-SA210 Grade A-1 boiler steel exposed to different degradation environments.
- Chapter-5 deals with the results and discussion for the bare and coated ASTM-SA213-T-11 boiler steel exposed to different degradation environments.
- Chapter-6 deals with the results and discussion for the bare and coated ASTM-SA213-T-22 boiler steel exposed to different degradation environments.
- Chapter-7 deals with the results and discussion for the bare and coated Superfer 800H superalloy exposed to different degradation environments.
- Chapter-8 It includes comprehensive discussions on the results obtained in present study.
- Chapter-9 major conclusions of the study on the effect of various coatings on their behavior in the above mentioned environments; have been presented.

	Page No.
Abstract	i
Acknowledgements	ix
Preface	xi
List of Figures	xxiv
List of Tables	lxi
List of Patents Filed and Research Publications	lxv
Abbreviations	lxviii
CHAPTER 1 INTRODUCTION	1
CHAPTER 2 LITERATURE REVIEW	7
2.1 HIGH TEMPERATURE PROCESSES AND MATERIALS	7
2.2 HIGH TEMPERATURE OXIDATION	9
2.2.1 Mechanisms of High Temperature Oxidation	11
2.2.2 Oxidation Behavior of Iron-Based Alloys	14
2.2.3 Oxidation Behavior of Superalloys	16
2.3 HOT CORROSION 16	
2.3.1 High Temperature (Type-I) Hot Corrosion (HTHC)	17
2.3.2 Low Temperature (Type-II) Hot Corrosion (LTHC)	18
2.3.3 Hot Corrosion Degradation Sequence	18
2.3.3.1 The Initiation Stage	18
2.3.3.2 The Propagation Stage	20
2.3.4 Chemistry of Salts	20
2.3.4.1 Chemistry and Phase Stability of Na ₂ SO ₄ Salt	20
2.3.4.2 Vanadate Solution Chemistry	21

2.4 FAILURE OF OXIDE SCALE	23
2.5 ELEMENTS AFFECTING HOT CORROSION OF METALS/ALLOY	27
2.6 HOT CORROSION IN THE MOLTEN SALT (Na₂SO₄-V₂O₅) ENVIRONMENT	28
2.7 HOT CORROSION IN ENERGY GENERATION SYSTEMS	32
2.8 COUNTERMEASURES AGAINST HOT CORROSION	35
2.9 MECHANICALLY ASSISTED DEGRADATION OF METALS	37
2.9.1 Solid Particle Erosion	39
2.9.1.1 Factors affecting solid particle erosion at room temperature	41
2.9.1.2 Factors affecting solid particle erosion at elevated temperature	44
2.9.1.3 Solid Particle Erosion of Metals and Alloys	45
2.10 EROSION-CORROSION	48
2.10.1 Erosion-Corrosion of Metals and Alloys	53
2.11 COMBATING EROSION-CORROSION	56
2.12 MARINE CORROSION	58
2.12.1 Marine Atmospheres induced Corrosion	60
2.12.2 Factors affecting Marine Corrosion	67
2.12.3 Countermeasures against Marine Corrosion	69
2.13 PROTECTIVE COATINGS	70
2.14 COATING PROCESSES	73
2.15 THERMAL SPRAYING PROCESS	74
2.16 PLASMA SPRAYING	78
2.16.1 Plasma Spraying-The Process	78
2.17 VAPOR DEPOSITION PROCESSES	81
2.17.1 Physical Vapor Deposition Process	82

2.17.1.1	Sputtering	82
2.17.1.2	Evaporation	84
2.17.1.3	Ion Plating	84
2.17.2	Plasma Assisted Physical Vapor Deposition Process	85
2.17.3	Applications of Plasma Assisted Physical Vapor Deposition Process	86
2.18	SOME STUDIES RELATED TO Ti-AI AND Al-Cr BASED COATINGS	87
2.19	PATENT SEARCH	89
2.20	PROBLEM FORMULATION	89
CHAPTER 3	EXPERIMENTAL TECHNIQUES AND PROCEDURES	98
3.1	SUBSTRATE MATERIALS	98
3.2	DEVELOPMENT OF COATINGS	99
3.2.1	Nanostructured Thin Coatings	99
3.2.1.1	Preparation of Substrate Materials	99
3.2.1.2	Formulation of coatings	101
3.2.2	Conventional Thick Coatings	101
3.2.2.1	Preparation of Substrate Materials	101
3.2.2.1	Feedstock Materials for Coatings	102
3.2.2.2	Formulation of Coatings	104
3.2.2.3	Gas Nitriding	105
3.3	CHARACTERIZATION OF THE COATINGS	106
3.3.1	Specimen preparation	106
3.3.2	Measurement of Coating Thickness	106
3.3.3	Measurement of Porosity	107
3.3.4	Metallographic Studies	107
3.3.5	Measurement of Microhardness	107
3.3.6	Measurement of Surface Roughness	108
3.3.7	Measurement of Bond Strength	108

3.3.8	Atomic Force Microscopy (AFM) Analysis	108
3.3.9	X-Ray Diffraction (XRD) Analysis	109
3.3.10	Scanning Electron Microscopy (SEM) and Energy Dispersive X-ray (EDAX) Analysis	109
3.3.10.1	Surface Morphology/EDAX Analysis	109
3.3.10.2	Cross sectional analysis	110
3.3.10.3	X-ray mapping analysis	110
3.4	HIGH TEMPERATURE OXIDATION AND HOT CORROSION STUDIES	111
3.4.1	Experimental Setup	111
3.4.2	Oxidation Studies in Air	113
3.4.3	Hot Corrosion Studies in Molten Salt (Na_2SO_4 - 60% V_2O_5)	113
3.4.3.1	Coating of Molten Salt	113
3.4.3.2	Hot Corrosion Studies	113
3.4.4	Studies in coal fired Industrial boiler Environment	113
3.5	ANALYSIS OF CORROSION PRODUCTS OF OXIDATION IN AIR, MOLTEN SALTS AND INDUSTRIAL ENVIRONMENT	116
3.5.1	Visual Observation	116
3.5.2	Weight change Studies	116
3.5.3	Evaluation of Corrosion Rate in Terms of Wall Thickness Lost	117
3.5.4	X-ray diffraction (XRD) Analysis	117
3.5.5	SEM/EDAX Analysis	117
3.5.5.1	Surface Morphology	117
3.5.5.2	Cross-Sectional analysis	117
3.5.5.3	X-ray mapping analysis	118
3.6.1	EROSION STUDIES IN SIMULATED COAL-FIRED BOILER ENVIRONMENT	118
3.6.1	Experimental Setup	118
3.6.2	Erosion Studies in an Air Jet Erosion Test Rig	119
3.6.3	Analysis of eroded surfaces	120
3.6.3.1	Visual Observation	121

3.6.3.2	Erosion rate in terms of Volume loss	121
3.6.3.3	SEM/EDAX Analysis	122
3.7	CORROSION STUDIES IN SIMULATED MARINE ENVIRONMENT	122
3.7.1	Linear polarization resistance (LPR) and potentiodynamic polarization tests	122
3.7.2	Salt spray (Fog) testing	124
3.7.2.1	Analysis of corroded specimens	125
3.7.2.1.1	Visual Observation	125
3.7.2.1.2	SEM/EDAX Analysis	125
3.7.2.1.3	X-ray diffraction (XRD) Analysis	125
3.7.2.1.4	Weight loss measurement	125
CHAPTER 4	SUBSTRATE ASTM-SA210 GRADE A-1 BOILER STEEL	126
4.1	CHARACTERIZATION OF COATINGS	126
4.1.1	Results	126
4.1.1.1	Visual observations	126
4.1.1.2	Surface analysis	127
4.1.1.3	Cross-sectional analysis	135
4.1.2	Discussion	140
4.1.3	Conclusions	144
4.2	OXIDATION STUDIES IN AIR	146
4.2.1	Results	146
4.2.1.1	Visual observations	146
4.2.1.2	Weight change measurements	148
4.2.1.3	Surface scale analysis	150
4.2.1.4	Cross-sectional analysis	154
4.2.2	Summary of Results	162
4.2.3	Discussion	162
4.2.4	Conclusions	165

4.3 HOT CORROSION STUDIES IN MOLTEN SALT ENVIRONMENT	166
4.3.1 Results	166
4.3.1.1 Visual observations	166
4.3.1.2 Weight change measurements	168
4.3.1.3 Surface scale analysis	171
4.3.1.4 Cross-sectional analysis	173
4.3.2 Summary of Results	183
4.3.3 Discussion	183
4.3.4 Conclusions	187
4.4 EROSION STUDIES IN SIMULATED COAL-FIRED BOILER ENVIRONMENT	188
4.4.1 Results	188
4.4.1.1 Visual observations	188
4.4.1.2 Erosion rate	190
4.4.1.3 SEM/EDAX Analysis	191
4.4.2 Discussion	196
4.4.3 Conclusions	201
4.5 CORROSION STUDIES IN SIMULATED MARINE ENVIRONMENT	203
4.5.1 Results and Discussion	203
4.5.1.1 Linear polarization resistance (LPR) and potentiodynamic polarization Tests	203
4.5.1.2 Salt spray (Fog) testing	208
4.5.2 Conclusions	217
4.6 EROSION-CORROSION STUDIES IN INDUSTRIAL ENVIRONMENT	219
4.6.1 Results	219
4.6.1.1 Visual observations	219
4.6.1.2 Weight change and sample thickness measurements	221
4.6.1.3 Surface scale analysis	223
4.6.1.4 Cross-sectional analysis	226

4.6.2	Summary of Results	236
4.6.3	Discussion	236
4.6.4	Conclusions	239
CHAPTER 5	SUBSTRATE ASTM-SA213-T-11 BOILER STEEL	241
5.1	CHARACTERISATION OF COATINGS	241
5.1.1	Results	241
5.1.1.1	Visual observations	241
5.1.1.2	Surface analysis	242
5.1.1.3	Cross-sectional analysis	250
5.1.2	Discussion	255
5.1.3	Conclusions	258
5.2	OXIDATION STUDIES IN AIR	259
5.2.1	Results	259
5.2.1.1	Visual observations	259
5.2.1.2	Weight change measurements	261
5.2.1.3	Surface scale analysis	263
5.2.1.4	Cross-sectional analysis	265
5.2.2	Summary of Results	274
5.2.3	Discussion	274
5.2.4	Conclusions	277
5.3	HOT CORROSION STUDIES IN MOLTEN SALT ENVIRONMENT	279
5.3.1	Results	279
5.3.1.1	Visual observations	279
5.3.1.2	Weight change measurements	281
5.3.1.3	Surface scale analysis	284
5.3.1.4	Cross-sectional analysis	287
5.3.2	Summary of Results	295
5.3.3	Discussion	296

5.3.4	Conclusions	299
5.4 EROSION STUDIES IN SIMULATED COAL-FIRED BOILER ENVIRONMENT		301
5.4.1	Results	301
5.4.1.1	Visual observations	301
5.4.1.2	Erosion rate	303
5.4.1.3	SEM/EDAX Analysis	304
5.4.2	Discussion	308
5.4.3	Conclusions	313
5.5 CORROSION STUDIES IN SIMULATED MARINE ENVIRONMENT		314
5.5.1	Results and Discussion	314
5.5.1.1	Linear polarization resistance (LPR) and potentiodynamic polarization tests	314
5.5.1.2	Salt spray (Fog) testing	319
5.5.2	Conclusions	327
5.6 EROSION-CORROSION STUDIES IN INDUSTRIAL ENVIRONMENT		329
5.6.1	Results	329
5.6.1.1	Visual observations	329
5.6.1.2	Weight change and sample thickness measurements	331
5.6.1.3	Surface scale analysis	333
5.6.1.4	Cross-sectional analysis	336
5.6.2	Summary of Results	346
5.6.3	Discussion	347
5.6.4	Conclusions	349
CHAPTER 6	SUBSTRATE ASTM-SA213-T-22 BOILER STEEL	350
6.1 CHARACTERISATION OF COATINGS		350
6.1.1	Results	350
6.1.1.1	Visual observations	350
6.1.1.2	Surface analysis	351

6.1.1.3	Cross-sectional analysis	359
6.1.2	Discussion	364
6.1.3	Conclusions	367
6.2	OXIDATION STUDIES IN AIR	368
6.2.1	Results	368
6.2.1.1	Visual observations	368
6.2.1.2	Weight change measurements	370
6.2.1.3	Surface scale analysis	372
6.2.1.4	Cross-sectional analysis	376
6.2.2	Summary of Results	384
6.2.3	Discussion	385
6.2.4	Conclusions	388
6.3	HOT CORROSION STUDIES IN MOLTEN SALT ENVIRONMENT	389
6.3.1	Results	389
6.3.1.1	Visual observations	389
6.3.1.2	Weight change measurements	391
6.3.1.3	Surface scale analysis	394
6.3.1.4	Cross-sectional analysis	397
6.3.2	Summary of Results	405
6.3.3	Discussion	405
6.3.4	Conclusions	410
6.4	EROSION STUDIES IN SIMULATED COAL-FIRED BOILER ENVIRONMENT	412
6.4.1	Results	412
6.4.1.1	Visual observations	412
6.4.1.2	Erosion rate	414
6.4.1.3	SEM/EDAX Analysis	415
6.4.2	Discussion	420
6.4.3	Conclusions	424

6.5 CORROSION STUDIES IN SIMULATED MARINE ENVIRONMENT	426
6.5.1 Results and Discussion	426
6.5.1.1 Linear polarization resistance (LPR) and potentiodynamic polarization tests	426
6.5.1.2 Salt spray (Fog) testing	431
6.5.2 Conclusions	439
6.6 EROSION-CORROSION STUDIES IN INDUSTRIAL ENVIRONMENT	441
6.6.1 Results	441
6.6.1.1 Visual observations	441
6.6.1.2 Weight change and sample thickness measurements	443
6.6.1.3 Surface scale analysis	445
6.6.1.4 Cross-sectional analysis	448
6.6.2 Summary of Results	458
6.6.3 Discussion	458
6.6.4 Conclusions	461
CHAPTER 7 SUBSTRATE SUPERFER 800H SUPERALLOY	463
7.1 CHARACTERISATION OF COATINGS	463
7.1.1 Results	463
7.1.1.1 Visual observations	463
7.1.1.2 Surface analysis	464
7.1.1.3 Cross-sectional analysis	472
7.1.2 Discussion	477
7.1.3 Conclusions	480
7.2 OXIDATION STUDIES IN AIR	481
7.2.1 Results	481
7.2.1.1 Visual observations	481
7.2.1.2 Weight change measurements	483
7.2.1.3 Surface scale analysis	485

7.2.1.4 Cross-sectional analysis	487
7.2.2 Summary of Results	497
7.2.3 Discussion	498
7.2.4 Conclusions	501
7.3 HOT CORROSION STUDIES IN MOLTEN SALT ENVIRONMENT	503
7.3.1 Results	503
7.3.1.1 Visual observations	503
7.3.1.2 Weight change measurements	505
7.3.1.3 Surface scale analysis	508
7.3.1.4 Cross-sectional analysis	511
7.3.2 Summary of Results	520
7.3.3 Discussion	521
7.3.4 Conclusions	524
7.4 EROSION STUDIES IN SIMULATED COAL-FIRED BOILER ENVIRONMENT	525
7.4.1 Results	525
7.4.1.1 Visual observations	525
7.4.1.2 Erosion rate	527
7.4.1.3 SEM/EDAX Analysis	528
7.4.2 Discussion	532
7.4.3 Conclusions	537
7.5 CORROSION STUDIES IN SIMULATED MARINE ENVIRONMENT	538
7.5.1 Results and Discussion	538
7.5.1.1 Linear polarization resistance (LPR) and potentiodynamic polarization tests	538
7.5.1.2 Salt spray (Fog) testing	542
7.5.2 Conclusions	546
7.6 EROSION-CORROSION STUDIES IN INDUSTRIAL ENVIRONMENT	547
7.6.1 Results	547

7.6.1.1	Visual observations	547
7.6.1.2	Weight change and sample thickness measurements	549
7.6.1.3	Surface scale analysis	551
7.6.1.4	Cross-sectional analysis	554
7.6.2	Summary of Results	564
7.6.3	Discussion	565
7.6.4	Conclusions	567
CHAPTER 8	COMPARATIVE DISCUSSION	568
8.1	OXIDATION STUDIES IN AIR	568
8.2	HOT CORROSION STUDIES IN MOLTEN SALT ENVIRONMENT	571
8.3	EROSION STUDIES IN SIMULATED COAL-FIRED BOILER ENVIRONMENT	573
8.4	CORROSION STUDIES IN SIMULATED MARINE ENVIRONMENT	576
8.4.1	Linear polarization resistance (LPR) and potentiodynamic polarization Tests	576
8.4.2	Salt spray (Fog) testing	579
8.5	EROSION-CORROSION STUDIES IN INDUSTRIAL ENVIRONMENT	582
8.6	EVALUATION OF PERFORMANCE OF VARIOUS SUBSTRATE-COATING COMBINATIONS IN DIFFERENT ENVIRONMENT	586
CHAPTER 9	CONCLUSIONS	589
	SUGGESTIONS FOR FUTURE WORK	597
	APPENDIX	598
	REFERENCES	609

LIST OF FIGURES

Figure No.	Particulars	Page No.
Fig. 2.1	Schematic illustrations of the mechanisms of oxidation at the surface of a metal	11
Fig. 2.2	Mechanisms of oxidation at the surface of a metal (Wagner, 1987)	12
Fig. 2.3	Schematic of the variation with alloy chromium content of the oxidation rate and oxide scale structure, based on isothermal studies at 1000°C in 0.13 atm oxygen (Wright, 1987)	15
Fig. 2.4	Schematic diagram illustrating the conditions that develop during the initiation and the propagation of hot corrosion attack and to identify the factors that determine the time at which the transition from the initiation to the propagation stage occurs	19
Fig. 2.5	Na-Cr-S-O phase diagram for 1200K (Rapp, 1986)	21
Fig. 2.6	Phase stability diagram for Na-V-S-O phase diagram at 900°C (Hwang and Rapp, 1989)	22
Fig. 2.7	Schematic illustration of the growth of chromia scales in (i) adherent oxide scale, in the presence of oxygen active elements and with predominant inward transport of oxygen, and (ii) spalled oxide scale, in the absence of oxygen active elements and with predominant outward transport of chromia through the scale (Kofstad, 1990)	24
Fig. 2.8	Phase Diagram for Na ₂ SO ₄ -V ₂ O ₅ System (Otero et al., 1987)	29
Fig. 2.9	Schematic diagram showing probable hot corrosion mechanism in Na ₂ SO ₄ -60%V ₂ O ₅ after exposure for 50 cycles at 900°C for alloys: (a) Superni 75; (b) Superni 601 (Gitanjaly, 2003)	31
Fig. 2.10	Schematic illustration of coal fired boiler (Khanna, 2002 and Marriott, 1990)	33
Fig. 2.11	Enhanced corrosion of superheater, associated with the formation of a molten deposit on the tube walls (Khanna, 2002)	34

Fig. 2.12	Schematic of erosive wear (Bhushan and Gupta, 1991)	38
Fig. 2.13	Schematic of mechanically assisted degradation of metals by cavitation	39
Fig. 2.14	(a) Schematic diagram showing the influence of impact angle on erosion rate in the case of ductile and brittle materials; (b) variation of erosion rate of steel with particle size at normal impact at different impact velocities; (c) influence of impact angle on erosion rate in the case of spherical and angular particles; (d) influence of flux rate of erodent particles on the erosion rate of a 1018 steel (Sundarajan et al., 1997)	43
Fig. 2.15	Classification of erosion-corrosion according to Kang et al. (1987)	50
Fig. 2.16	Schematic representation of metal erosion (a) & (b); and oxide erosion (c), illustrating the nature of interaction between the oxide scale and the substrate during erosion	51
Fig. 2.17	Schematic representation of: (a) oxidation affected erosion; (b) oxidation controlled erosion by continuous mode; (c) oxidation controlled erosion by spalling	52
Fig. 2.18	Model illustrating the oxide formation during oxidation and erosion-corrosion at 550°C	55
Fig. 2.19	(a) Effect of NaCl concentration on the corrosion rate of iron in aerated room-temperature solutions; (b) Zones of corrosion for steel piling in seawater, and relative loss of metal thickness in each zone (Dexter, 1987)	59
Fig. 2.20	Schematics of two distinct corrosion processes, (a) the corrosion process showing the separation of anodic and cathodic sites; (b) the corrosion process involving two cathodic reactions (Soesmith, 1987)	63
Fig. 2.21	Corrosion tube growth mechanism (Fontana and Greene, 1967 and Liang, 2008)	65
Fig. 2.22	Hypothetical anodic and cathodic polarization behavior for a material exhibiting passive anodic behavior (Davis and Hardbound, 1999)	66
Fig. 2.23	Coating deposition processes (Bhushan and Gupta, 1991)	74
Fig. 2.24	Historical development of thermal spraying equipment, processes, and materials	75

Fig. 2.25	Schematic development of the thermal spray process and mechanism of coating build-up	76
Fig. 2.26	Coating deposition and the oxidation process (Herman, 1988)	77
Fig. 2.27	Schematics for oxidation of particles, in-flight (Deshpande et al., 2006)	78
Fig. 2.28	The plasma spray apparatus (Batchelor et al, 2003)	80
Fig. 2.29	The mechanism of coating deposition (Batchelor et al, 2003)	81
Fig. 2.30	Various PVD processes; (a) Sputtering; (b) Evaporation; (c) Ion Plating (Pierson, 1987)	83
Fig. 3.1	Optical micrographs of substrate alloys; (a) ASTM-SA210 Grade A-1 boiler steel, 200X, (b) ASTM-SA213-T-11 boiler steel, 200X, (c) ASTM-SA-213-T-22 boiler steel, 200X, (d) Superfer 800H superalloy, 200X	99
Fig. 3.2	SEM/EDAX patterns (showing Wt %) for different coating powders; (a) Ti-metal powder, (b) Al-metal powder, (c) Cr-metal powder, (d) Ti-Al (50-50 Wt %) powder, (e) Al-Cr (70-30 Wt %) powder	103
Fig. 3.3	Front and rear views of the set-up used for gas nitriding of the plasma sprayed conventional thick Ti-Al and Al-Cr coatings in the laboratory	105
Fig. 3.4	Experimental set up for high temperature oxidation and hot corrosion studies; (a) Heat Zone inside furnace, (b) Molten salt coating, (c) Silicon tube furnace, (d) Oven for pre heating the specimens, (e) Electronic balance	112
Fig. 3.5	Analysis of fly ash; (a) SEM morphology and (b) EDAX compositional analysis	115
Fig. 3.6	Experimental set-up for erosion-corrosion in simulated coal-fired boiler environment (a) Air Jet Erosion Tester, (b) Interior view of specimen loading chamber	119
Fig. 3.7	Analysis of Alumina (Al_2O_3); (a) SEM morphology and (b) EDAX compositional analysis	121
Fig. 3.8	Experimental set-up for linear polarization resistance (LPR) and potentiodynamic polarization tests (a) Potentiostat, (b) Specimen coated with nail-paint (c) Test cell	123
Fig. 3.9	Experimental set-up for Salt spray (Fog) testing (a) Salt fog testing set up,	124

(b) Salt fog chamber, (c) Interior view of chamber

Fig. 4.1	Surface macrographs for the as coated ASTM-SA210 Grade A-1 boiler steel (a) Nanostructured TiAlN coating, (b) Nanostructured AlCrN coating, (c) Conventional TiAlN coating, (d) Conventional AlCrN coating	127
Fig. 4.2	Optical micrograph (200 X) of the surface of as coated ASTM-SA210 Grade A-1 boiler steel (a) Nanostructured TiAlN coating, (b) Nanostructured AlCrN coating, (c) Conventional TiAlN coating, (d) Conventional AlCrN coating	128
Fig. 4.3	X-Ray Diffraction pattern of as coated ASTM-SA210 Grade A-1 boiler steel (a) Nanostructured TiAlN coating, (b) Nanostructured AlCrN coating, (c) Conventional TiAlN coating, (d) Conventional AlCrN coating	130
Fig. 4.4	2D and 3D AFM images for the as coated ASTM-SA210 Grade A-1 boiler steel (a) & (b) Nanostructured TiAlN coating, (c) & (d) Nanostructured AlCrN coating	131
Fig. 4.5	Microhardness profile across the cross-section for Conventional TiAlN and Conventional AlCrN coating on ASTM-SA210 Grade A-1 boiler steel	132
Fig. 4.6	Fractured surfaces of a Plasma sprayed gas nitrided specimens after ASTM C633 tensile test; (a) Conventional TiAlN coating, (b) Conventional AlCrN coating	132
Fig. 4.7	Surface-scale morphology and EDAX patterns from different spots on as coated ASTM-SA210 Grade A-1 boiler steel (a) Nanostructured TiAlN coating (10000X), (b) Nanostructured AlCrN coating (10000X), (c) Conventional TiAlN coating (200X), (d) Conventional AlCrN coating (200X)	134
Fig. 4.8 (a)	Composition image (SEI) and X-ray mapping of the cross-section of as-coated nanostructured TiAlN coating on ASTM-SA210 Grade A-1 boiler steel	136
Fig. 4.8 (b)	Composition image (SEI) and X-ray mapping of the cross-section of as-coated nanostructured AlCrN coating on ASTM-SA210 Grade A-1 boiler	137
Fig. 4.8 (c)	Composition image (SEI) and X-ray mapping of the cross-section of as-coated conventional TiAlN coating on ASTM-SA210 Gr A-1 boiler steel	138

Fig. 4.8 (d)	Composition image (SEI) and X-ray mapping of the cross-section of as-coated conventional AlCrN coating on ASTM-SA210 Grade A-1 boiler steel	139
Fig. 4.9	Surface macrographs of uncoated and coated ASTM-SA210 Grade A-1 boiler steel after exposure to cyclic oxidation in air at 900°C for 50 cycles : (a) Uncoated Grade A1 boiler steel, (b) Nanostructured TiAlN coating, (c) Nanostructured AlCrN coating, (d) Conventional TiAlN coating, (e) Conventional AlCrN coating	147
Fig. 4.10	Weight gain/area vs time (number of cycles) for the uncoated and coated ASTM SA210 Grade A-1 boiler steel subjected to cyclic oxidation in air at 900°C for 50 cycles	148
Fig. 4.11	Column chart showing cumulative weight gain per unit area for the uncoated and coated ASTM-SA210 Grade A-1 boiler steel subjected to cyclic oxidation in air at 900°C for 50 cycles; (A) Uncoated, (B) Nanostructured TiAlN coating, (C) Nanostructured AlCrN coating, (D) Conventional TiAlN coating, (E) Conventional AlCrN coating	149
Fig. 4.12	Weight gain/area square vs time (number of cycles) for the uncoated and coated ASTM-SA210 Grade A-1 boiler steel subjected to cyclic oxidation in air at 900°C for 50 cycles	150
Fig. 4.13 (a)	X-Ray Diffraction pattern of uncoated and coated ASTM-SA210 Grade A-1 boiler steel exposed to cyclic oxidation in air at 900°C for 50 cycles: (A) Uncoated Grade A-1 boiler steel, (B) Nanostructured TiAlN coating, (C) Nanostructured AlCrN coating	152
Fig. 4.13 (b)	X-Ray Diffraction pattern of uncoated and coated ASTM-SA210 Grade A-1 boiler steel exposed to cyclic oxidation in air at 900°C for 50 cycles: (A) Conventional TiAlN coating, (B) Conventional AlCrN coating	152
Fig. 4.14	Surface-scale morphology and EDAX patterns from different spots on uncoated and coated ASTM-SA210 Grade A1 boiler steel after exposure to cyclic oxidation in air at 900°C for 50 cycles : (a) Uncoated Grade A-1 boiler steel, (b) Nanostructured TiAlN coating, (c) Nanostructured AlCrN coating, (d) Conventional TiAlN coating, (e) Conventional AlCrN coating	153

Fig. 4.15	Oxide scale morphology and variation of elemental composition across the cross-section of the uncoated and coated ASTM-SA210 Grade A-1 boiler steel after exposure to cyclic oxidation in air at 900°C for 50 cycles: (a) Uncoated Grade A1 boiler steel (75 X), (b) Nanostructured TiAlN coating (100 X), (c) Nanostructured AlCrN coating (100 X), (d) Conventional TiAlN coating (250 X), (e) Conventional AlCrN coating (300 X)	155
Fig. 4.16 (a)	Composition image (BSEI) and X-ray mapping of the cross-section of uncoated ASTM-SA210 Grade A-1 boiler steel subjected to cyclic oxidation in air at 900°C for 50 cycles	156
Fig. 4.16 (b)	Composition image (BSEI) and X-ray mapping of the cross Section of Nanostructured TiAlN coated ASTM-SA210 Grade A-1 boiler steel subjected to cyclic oxidation in air at 900°C for 50 cycles	157
Fig. 4.16 (c)	Composition image (BSEI) and X-ray mapping of the crossSection of Nanostructured AlCrN coated ASTM-SA210 Grade A-1 boiler steel subjected to cyclic oxidation in air at 900°C for 50 cycles	158
Fig. 4.16 (d)	Composition image (BSEI) and X-ray mapping of the cross Section of conventional TiAlN coated ASTM-SA210 Grade A-1 boiler steel subjected to cyclic oxidation in air at 900°C for 50 cycles	159
Fig. 4.16 (e)	Composition image (BSEI) and X-ray mapping of the cross-section of conventional AlCrN coated ASTM-SA210 Grade A1 boiler steel subjected to cyclic oxidation in air at 900°C for 50 cycles	160
Fig. 4.17	Surface macrographs of uncoated and coated ASTM-SA210 Grade A-1 boiler steel exposed to molten salt ($\text{Na}_2\text{SO}_4\text{-60\%V}_2\text{O}_5$) environment at 900°C for 50 cycles : (a) Uncoated Grade A1 boiler steel, (b) Nanostructured TiAlN coating, (c) Nanostructured AlCrN coating, (d) Conventional TiAlN coating, (e) Conventional AlCrN coating	167
Fig. 4.18	Weight gain/area vs time (number of cycles) for the uncoated and coated ASTM-SA210 Grade A-1 boiler steel exposed to molten salt ($\text{Na}_2\text{SO}_4\text{-60\%V}_2\text{O}_5$) environment at 900°C for 50 cycles	169
Fig. 4.19	Column chart showing cumulative weight gain per unit area for the	169

	uncoated and coated ASTM-SA210 Grade A-1 boiler steel exposed to molten salt ($\text{Na}_2\text{SO}_4\text{-60\%V}_2\text{O}_5$) environment at 900°C for 50 cycles: (A) Uncoated, (B) Nanostructured TiAlN coating, (C) Nanostructured AlCrN coating, (D) Conventional TiAlN coating, (E) Conventional AlCrN coating	
Fig. 4.20	Weight gain/area square vs time (number of cycles) for the uncoated and coated ASTM-SA210 Grade A-1 boiler steel exposed to molten salt ($\text{Na}_2\text{SO}_4\text{-60\%V}_2\text{O}_5$) environment at 900°C for 50 cycles	170
Fig. 4.21 (a)	X-Ray Diffraction pattern of uncoated and coated ASTM-SA210 Grade A-1 boiler steel exposed to molten salt ($\text{Na}_2\text{SO}_4\text{-60\%V}_2\text{O}_5$) environment at 900°C for 50 cycles: (A) Uncoated Grade A-1 boiler steel, (B) Nanostructured TiAlN coating, (C) Nanostructured AlCrN coating	172
Fig. 4.21 (b)	X-Ray Diffraction pattern of uncoated and coated ASTM-SA210 Grade A-1 boiler steel exposed to molten salt ($\text{Na}_2\text{SO}_4\text{-60\%V}_2\text{O}_5$) environment at 900°C for 50 cycles: (A) Conventional TiAlN coating, (B) Conventional AlCrN coating	172
Fig. 4.22	Surface-scale morphology and EDAX patterns from different spots on uncoated and coated ASTM-SA210 Grade A1 boiler steel exposed to molten salt ($\text{Na}_2\text{SO}_4\text{-60\%V}_2\text{O}_5$) environment at 900°C for 50 cycles: (a) Uncoated Grade A1 boiler steel, (b) Nanostructured TiAlN coating, (c) Nanostructured AlCrN coating, (d) Conventional TiAlN coating, (e) Conventional AlCrN coating	174
Fig. 4.23	Oxide scale morphology and variation of elemental composition across the cross-section of the uncoated and coated ASTM-SA210 Grade A-1 boiler steel exposed to molten salt ($\text{Na}_2\text{SO}_4\text{-60\%V}_2\text{O}_5$) environment at 900°C for 50 cycles: (a) Uncoated Grade A1 boiler steel (70 X), (b) Nanostructured TiAlN coating (71 X), (c) Nanostructured AlCrN coating (55 X), (d) Conventional TiAlN coating (300 X), (e) Conventional AlCrN coating (250 X)	176
Fig. 4.24 (a)	Composition image (BSEI) and X-ray mapping of the cross-section of uncoated ASTM-SA210 Grade A-1 boiler steel exposed to molten salt ($\text{Na}_2\text{SO}_4\text{-60\%V}_2\text{O}_5$) environment at 900°C for 50 cycles	177

Fig. 4.24 (b)	Composition image (BSEI) and X-ray mapping of the cross-section of Nanostructured TiAlN coated ASTM-SA210 Grade A-1 boiler steel exposed to molten salt ($\text{Na}_2\text{SO}_4\text{-60\%V}_2\text{O}_5$) environment at 900°C for 50 cycles	178
Fig. 4.24 (c)	Composition image (BSEI) and X-ray mapping of the cross-section of Nanostructured AlCrN coated ASTM-SA210 Grade A-1 boiler steel exposed to molten salt ($\text{Na}_2\text{SO}_4\text{-60\%V}_2\text{O}_5$) environment at 900°C for 50 cycles	179
Fig. 4.24 (d)	Composition image (BSEI) and X-ray mapping of the cross-section of conventional TiAlN coated ASTM-SA210 Grade A-1 boiler steel exposed to molten salt ($\text{Na}_2\text{SO}_4\text{-60\%V}_2\text{O}_5$) environment at 900°C for 50 cycles	180
Fig. 4.24 (e)	Composition image (BSEI) and X-ray mapping of the cross-section of conventional AlCrN coated ASTM-SA210 Grade A1 boiler steel exposed to molten salt ($\text{Na}_2\text{SO}_4\text{-60\%V}_2\text{O}_5$) environment at 900°C for 50 cycles	181
Fig. 4.25	Surface macrographs of eroded uncoated and coated ASTM-SA210 Grade A-1 boiler steel exposed to high temperature erosion studies in simulated coal-fired boiler environment	189
Fig. 4.26	Column chart showing the Volume wear rate of uncoated and coated ASTM-SA210 Grade A-1 boiler steel eroded at normal and oblique impact: (A) Uncoated Grade A-1 boiler steel, (B) Nanostructured TiAlN coating, (C) Nanostructured AlCrN coating, (D) Conventional TiAlN coating, (E) Conventional AlCrN coating	191
Fig. 4.27	Surface-scale morphology and EDAX patterns from different spots on eroded uncoated and coated ASTM-SA210 Grade A-1 boiler steel exposed to high temperature erosion studies in simulated coal-fired boiler environment at impact angle 90°: (a) Uncoated Grade A1 boiler steel, (b) Nanostructured TiAlN coating, (c) Nanostructured AlCrN coating, (d) Conventional TiAlN coating, (e) Conventional AlCrN coating	193
Fig. 4.28	Surface-scale morphology and EDAX patterns from different spots on eroded uncoated and coated ASTM-SA210 Grade A-1 boiler steel exposed to high temperature erosion studies in simulated coal-fired	195

	boiler environment at impact angle 30°: (a) Uncoated Grade A1 boiler steel, (b) Nanostructured TiAlN coating, (c) Nanostructured AlCrN coating, (d) Conventional TiAlN coating, (e) Conventional AlCrN coating	
Fig. 4.29	Schematic representation of (a) & (b); metal erosion, and (c) oxide erosion illustrating the nature of interaction between the oxide scale and the substrate during erosion	199
Fig. 4.30	Schematic representation of coating fracture dependent on impact angle; (a) Low angle, (b) High angle	200
Fig. 4.31	Potentiodynamic Polarization Curves for uncoated and coated ASTM-SA210 Grade A-1 boiler steel	206
Fig. 4.32	Protective efficiency and Polarization resistance of uncoated and coated ASTM-SA210 Grade A-1 boiler steel: (A) Uncoated Grade A1 boiler steel, (B) Nanostructured TiAlN coating, (C) Nanostructured AlCrN coating, (D) Conventional TiAlN coating, (E) Conventional AlCrN coating	207
Fig. 4.33	Surface macrographs of uncoated and coated ASTM-SA210 Grade A-1 boiler steel subjected to salt-fog testing (5% NaCl) : (A) Uncoated Grade A-1 boiler steel subjected to 24hrs, 48hrs and 72 hrs testing; (B) Nanostructured TiAlN coated Grade A-1 boiler steel subjected to 24hrs, 48hrs and 72 hrs testing; (C) Nanostructured AlCrN coated Grade A-1 boiler steel subjected to 24hrs, 48hrs and 72 hrs testing	209
Fig. 4.34	Surface macrographs of uncoated and coated ASTM-SA210 Grade A-1 boiler steel subjected to salt-fog testing (5% NaCl) for 24 hrs: (a) Uncoated Grade A1 boiler steel (b) Nanostructured TiAlN coating (c) Nanostructured AlCrN coating	210
Fig. 4.35	Surface macrographs of uncoated and coated ASTM-SA210 Grade A1 boiler steel subjected to salt-fog testing (5% NaCl) for 48 hrs: (a) Uncoated Grade A1 boiler steel (b) Nanostructured TiAlN coating (c) Nanostructured AlCrN coating	211
Fig. 4.36	Surface macrographs of uncoated and coated ASTM-SA210 Grade A-1 boiler steel subjected to salt-fog testing (5% NaCl) for 72 hrs: (a) Uncoated Grade A1 boiler steel (b) Nanostructured TiAlN coating (c)	212

Nanostructured AlCrN coating

- Fig. 4.37 (a)** X-Ray Diffraction pattern of uncoated ASTM-SA210 Grade A-1 boiler steel subjected to salt-fog testing (5% NaCl) for 24 Hrs, 48 Hrs and 72 Hrs 213
- Fig. 4.37 (b)** X-Ray Diffraction pattern of coated ASTM-SA210 Grade A-1 boiler steel subjected to salt-fog testing (5% NaCl) for 24 Hrs, 48 Hrs and 72 Hrs: (A) Nanostructured TiAlN coating, (B) Nanostructured AlCrN coating 214
- Fig. 4.38** Column chart showing weight loss per unit area for the uncoated and coated ASTM-SA210 Grade A-1 boiler steel subjected to salt-fog testing (5% NaCl) : (A) Uncoated Grade A-1 boiler steel subjected to 24hrs, 48hrs and 72 hrs testing; (B) Nanostructured TiAlN coated Grade A-1 boiler steel subjected to 24hrs, 48hrs and 72 hrs testing; (C) Nanostructured AlCrN coated Grade A-1 boiler steel subjected to 24hrs, 48hrs and 72 hrs testing 216
- Fig. 4.39** Corrosion evolution of the as-deposited coatings in salt spray test; a: initiation of corrosion micro-crack, b: cracks propagation, c: crack branching, d: formation of corrosion hole 216
- Fig. 4.40** Surface macrographs of uncoated and coated ASTM-SA210 Grade A1 boiler steel exposed to super-heater of the coal fired boiler environment at 900°C for 1000 hours : (a) Uncoated Grade A1 boiler steel, (b) Nanostructured TiAlN coating, (c) Nanostructured AlCrN coating, (d) Conventional TiAlN coating, (e) Conventional AlCrN coating 220
- Fig. 4.41** Weight gain/area vs time for uncoated and coated ASTM-SA210 Grade A-1 boiler steel exposed to super-heater of the coal fired boiler environment at 900°C for 1000 hours 222
- Fig. 4.42** Bar chart indicating overall gain in thickness for uncoated and coated ASTM-SA210 Grade A-1 boiler steel specimens exposed to super-heater of the coal fired boiler environment at 900°C for 1000 hours 222
- Fig. 4.43 (a)** X-Ray Diffraction pattern of uncoated and coated ASTM-SA210 Grade A-1 boiler steel exposed to platen superheater of the coal fired boiler environment at 900°C for 1000 Hrs: (A) Uncoated Grade A-1 boiler steel, (B) Nanostructured TiAlN coating, (C) Nanostructured AlCrN coating 224

Fig. 4.43 (b)	X-Ray Diffraction pattern of coated ASTM-SA210 Grade A-1 boiler steel exposed to platen superheater of the coal fired boiler environment at 900°C for 1000 Hrs: (A) Conventional TiAlN coating, (B) Conventional AlCrN coating	224
Fig. 4.44	Surface-scale morphology and EDAX patterns from different spots on uncoated and coated ASTM-SA210 Grade A-1 boiler steel exposed to platen superheater of the coal fired boiler environment at 900°C for 1000 Hrs: (a) Uncoated Grade A-1 boiler steel, (b) Nanostructured TiAlN coating, (c) Nanostructured AlCrN coating, (d) Conventional TiAlN coating, (e) Conventional AlCrN coating	225
Fig. 4.45	Oxide scale morphology and variation of elemental composition across the cross- section of the bare and coated ASTM-SA210 Grade A-1 boiler steel exposed to platen superheater of the coal fired boiler environment at 900°C for 1000 Hrs: (a) Uncoated Grade A-1 boiler steel (65 X), (b) Nanostructured TiAlN coating (45 X), (c) Nanostructured AlCrN coating (31 X), (d) Conventional TiAlN coating (300 X), (e) Conventional AlCrN coating (260 X)	228
Fig. 4.46	Bar chart indicating the extent of erosion/corrosion for uncoated and coated ASTM-SA210 Grade A1 boiler steel specimens exposed to super-heater of the coal fired boiler environment at 900°C for 1000 hours	229
Fig. 4.47	Corrosion rate in mils per year (mpy) for bare and coated ASTM-SA210 Grade A-1 boiler steel exposed to super-heater of the coal fired boiler environment at 900°C for 1000 hours	230
Fig. 4.48 (a)	Composition image (BSEI) and X-ray mapping of the cross-section of uncoated ASTM-SA210 Grade A1 boiler steel exposed to platen super-heater of the coal fired boiler environment at 900°C for 1000 Hrs	231
Fig. 4.48 (b)	Composition image (BSEI) and X-ray mapping of the cross-section of Nanostructured TiAlN coated ASTM-SA210 Grade A1 boiler steel exposed to platen super-heater of the coal fired boiler environment at 900°C for 1000 Hrs	232
Fig. 4.48 (c)	Composition image (BSEI) and X-ray mapping of the cross-section of	233

Nanostructured AlCrN coated ASTM-SA210 Grade A1 boiler steel exposed to platen super-heater of the coal fired boiler environment at 900°C for 1000 Hrs

Fig. 4.48 (d)	Composition image (BSEI) and X-ray mapping of the cross-section of conventional TiAlN coated ASTM-SA210 Grade A-1 boiler steel exposed to platen super-heater of the coal fired boiler environment at 900°C for 1000 Hrs	234
Fig. 4.48 (e)	Composition image (BSEI) and X-ray mapping of the cross-section of conventional AlCrN coated ASTM-SA210 Grade A-1 boiler steel exposed to platen super-heater of the coal fired boiler environment at 900°C for 1000 Hrs	235
Fig. 5.1	Surface macrographs for the as coated ASTM-SA213-T-11 boiler steel (a) Nanostructured TiAlN coating, (b) Nanostructured AlCrN coating, (c) Conventional TiAlN coating, (d) Conventional AlCrN coating	242
Fig. 5.2	Optical micrograph (200 X) of the surface of as coated ASTM-SA213-T-11 boiler steel (a) Nanostructured TiAlN coating, (b) Nanostructured AlCrN coating, (c) Conventional TiAlN coating, (d) Conventional AlCrN coating	243
Fig. 5.3	Surface-scale morphology and EDAX patterns from different spots on as coated ASTM-SA213-T-11 boiler steel (a) Nanostructured TiAlN coating, (b) Nanostructured AlCrN coating, (c) Conventional TiAlN coating, (d) Conventional AlCrN coating	245
Fig. 5.4	2D and 3D AFM images for the as coated ASTM-SA213-T-11 boiler steel (a) & (b) Nanostructured TiAlN coating, (c) & (d) Nanostructured AlCrN coating	246
Fig. 5.5	Microhardness profile across the cross-section for Conventional TiAlN and Conventional AlCrN coating on ASTM-SA213-T-11 boiler steel	247
Fig. 5.6	Fracture surfaces of a Plasma sprayed gas nitride specimen after ASTM C633 tensile test; (a) Conventional TiAlN coating, (b) Conventional AlCrN coating	247
Fig. 5.7	Surface-scale morphology and EDAX patterns from different spots on as coated ASTM-SA213-T-11 boiler steel (a) Nanostructured TiAlN coating,	249

(b) Nanostructured AlCrN coating, (c) Conventional TiAlN coating, (d) Conventional AlCrN coating

Fig. 5.8 (a)	Composition image (BSEI) and X-ray mapping of the cross-section of as-coated nanostructured TiAlN coating on ASTM-SA213-T-11 boiler steel	251
Fig. 5.8 (b)	Composition image (BSEI) and X-ray mapping of the cross-section of as-coated nanostructured AlCrN coating on ASTM-SA213-T-11 boiler steel	252
Fig. 5.8 (c)	Composition image (SEI) and X-ray mapping of the cross-section of as-coated conventional TiAlN coating on ASTM-SA213-T-11 boiler steel	253
Fig. 5.8 (d)	Composition image (BSEI) and X-ray mapping of the cross-section of as-coated conventional AlCrN coating on ASTM-SA213-T-11 boiler steel	254
Fig. 5.9	Surface macrographs of <u>uncoated and coated</u> ASTM-SA213-T-11 boiler steel after exposure to cyclic oxidation in air at 900°C for 50 cycles : (a) Uncoated T-11 boiler steel, (b) Nanostructured TiAlN coating, (c) Nanostructured AlCrN coating, (d) Conventional TiAlN coating, (e) Conventional AlCrN coating	260
Fig. 5.10	Weight gain/area vs time (number of cycles) for the uncoated and coated ASTM-SA213-T-11 boiler steel subjected to cyclic oxidation in air at 900°C for 50 cycles	261
Fig. 5.11	Column chart showing cumulative weight gain per unit area for the uncoated and coated ASTM-SA213-T-11 boiler steel subjected to cyclic oxidation in air at 900°C for 50 cycles; (A) Uncoated T-11 boiler steel, (B) Nanostructured TiAlN coating, (C) Nanostructured AlCrN coating, (D) Conventional TiAlN coating, (E) Conventional AlCrN coating	262
Fig. 5.12	Weight gain/area square vs time (number of cycles) for the uncoated and coated ASTM-SA213-T-11 boiler steel subjected to cyclic oxidation in air at 900°C for 50 cycles	262
Fig. 5.13 (a)	X-Ray Diffraction pattern of uncoated and coated ASTM-SA213-T-11 boiler steel exposed to cyclic oxidation in air at 900°C for 50 cycle : (A) Uncoated T-11 boiler steel, (B) Nanostructured TiAlN coating, (C) Nanostructured AlCrN coating	264
Fig. 5.13 (b)	X-Ray Diffraction pattern of uncoated and coated ASTM-SA213-T-11	264

boiler steel exposed to cyclic oxidation in air at 900°C for 50 cycles: (A) Conventional TiAlN coating, (B) Conventional AlCrN coating

- Fig. 5.14** Surface-scale morphology and EDAX patterns from different spots on uncoated and coated ASTM-SA213-T-11 boiler steel after exposure to cyclic oxidation in air at 900°C for 50 cycles : (a) Uncoated T-11 boiler steel, (b) Nanostructured TiAlN coating, (c) Nanostructured AlCrN coating, (d) Conventional TiAlN coating, (e) Conventional AlCrN coating 266
- Fig. 5.15** Oxide scale morphology and variation of elemental composition across the cross- section of the uncoated and coated ASTM-SA213-T-11 boiler steel after exposure to cyclic oxidation in air at 900°C for 50 cycles: (a) Uncoated T-11 boiler steel (65 X), (b) Nanostructured TiAlN coating (70 X), (c) Nanostructured AlCrN coating (70 X), (d) Conventional TiAlN coating (140 X), (e) Conventional AlCrN coating (100 X) 266
- Fig. 5.16 (a)** Composition image (BSEI) and X-ray mapping of the cross-section of uncoated ASTM-SA213-T-11 boiler steel subjected to cyclic oxidation in air at 900°C for 50 cycles 269
- Fig. 5.16 (b)** Composition image (SEI) and X-ray mapping of the cross-section of Nanostructured TiAlN coated ASTM-SA213-T-11 boiler steel subjected to cyclic oxidation in air at 900°C for 50 cycles 270
- Fig. 5.16 (c)** Composition image (SEI) and X-ray mapping of the cross-section of Nanostructured AlCrN coated ASTM-SA213-T-11 boiler steel subjected to cyclic oxidation in air at 900°C for 50 cycles 271
- Fig. 5.16 (d)** Composition image (BSEI) and X-ray mapping of the cross-section of conventional TiAlN coated ASTM-SA213-T-11 boiler steel subjected to cyclic oxidation in air at 900°C for 50 cycles 272
- Fig. 5.16 (e)** Composition image (BSEI) and X-ray mapping of the cross-section of conventional AlCrN coated ASTM-SA213-T-11 boiler steel subjected to cyclic oxidation in air at 900°C for 50 cycles 273
- Fig. 5.17** Surface macrographs of uncoated and coated ASTM-SA213-T-11 boiler steel exposed to molten salt (Na_2SO_4 -60% V_2O_5) environment at 900°C for 50 cycles: (a) Uncoated T-11 boiler steel, (b) Nanostructured TiAlN 280

	coating, (c) Nanostructured AlCrN coating, (d) Conventional TiAlN coating, (e) Conventional AlCrN coating	
Fig. 5.18	Weight gain/area vs time (number of cycles) for the uncoated and coated ASTM-SA213-T-11 boiler steel exposed to molten salt (Na_2SO_4 -60% V_2O_5) environment at 900°C for 50 cycles	282
Fig. 5.19	Column chart showing cumulative weight gain per unit area for the uncoated and coated ASTM-SA213-T-11 boiler steel exposed to molten salt (Na_2SO_4 -60% V_2O_5) environment at 900°C for 50 cycles; (A) Bare T-11 boiler steel, (B) Nanostructured TiAlN coating, (C) Nanostructured AlCrN coating, (D) Conventional TiAlN coating, (E) Conventional AlCrN coating	282
Fig. 5.20	Weight gain/area square vs time (number of cycles) for the uncoated and coated ASTM-SA213-T-11 boiler steel exposed to molten salt (Na_2SO_4 -60% V_2O_5) environment at 900°C for 50 cycles	283
Fig. 5.21 (a)	X-Ray Diffraction pattern of uncoated and coated ASTM-SA213-T-11 boiler steel exposed to molten salt (Na_2SO_4 -60% V_2O_5) environment at 900°C for 50 cycles: (A) Uncoated T-11 boiler steel, (B) Nanostructured TiAlN coating, (C) Nanostructured AlCrN coating	285
Fig. 5.21 (b)	X-Ray Diffraction pattern of uncoated and coated ASTM-SA213-T-11 boiler steel exposed to molten salt (Na_2SO_4 -60% V_2O_5) environment at 900°C for 50 cycles: (A) Uncoated T-11 boiler steel, (B) Nanostructured TiAlN coating, (C) Nanostructured AlCrN coating	285
Fig. 5.22	Surface-scale morphology and EDAX patterns from different spots on uncoated and coated ASTM-SA213-T-11 boiler steel exposed to molten salt (Na_2SO_4 -60% V_2O_5) environment at 900°C for 50 cycles: (a) Uncoated T-11 boiler steel, (b) Nanostructured TiAlN coating, (c) Nanostructured AlCrN coating, (d) Conventional TiAlN coating, (e) Conventional AlCrN coating	286
Fig. 5.23	Oxide scale morphology and variation of elemental composition across the cross-section of the uncoated and coated ASTM-SA213-T-11 boiler steel exposed to molten salt (Na_2SO_4 -60% V_2O_5) environment at 900°C for 50 cycles: (a) Uncoated T-11 boiler steel (90 X), (b) Nanostructured	289

	TiAlN coating (70 X), (c) Nanostructured AlCrN coating (161 X), (d) Conventional TiAlN coating (90 X), (e) Conventional AlCrN coating (90 X)	
Fig. 5.24 (a)	Composition image (BSEI) and X-ray mapping of the cross-section of uncoated ASTM-SA213-T-11 boiler steel exposed to molten salt (Na_2SO_4 -60% V_2O_5) environment at 900°C for 50 cycles	290
Fig. 5.24 (b)	Composition image (BSEI) and X-ray mapping of the cross-section of Nanostructured TiAlN coated ASTM-SA213-T-11 boiler steel exposed to molten salt (Na_2SO_4 -60% V_2O_5) environment at 900°C for 50 cycles	291
Fig. 5.24 (c)	Composition image (BSEI) and X-ray mapping of the cross-section of Nanostructured AlCrN coated ASTM-SA213-T-11 boiler steel exposed to molten salt (Na_2SO_4 -60% V_2O_5) environment at 900°C for 50 cycles	292
Fig. 5.24(d)	Composition image (BSEI) and X-ray mapping of the cross-section of conventional TiAlN coated ASTM-SA213-T-11 boiler steel exposed to molten salt (Na_2SO_4 -60% V_2O_5) environment at 900°C for 50 cycles	293
Fig. 5.24 (e)	Composition image (BSEI) and X-ray mapping of the cross-section of conventional AlCrN coated ASTM-SA213-T-11 boiler steel exposed to molten salt (Na_2SO_4 -60% V_2O_5) environment at 900°C for 50 cycles	294
Fig. 5.25	Surface macrographs of eroded uncoated and coated ASTM-SA213-T-11 boiler steel exposed to high temperature erosion studies in simulated coal-fired boiler environment	302
Fig. 5.26	Column chart showing the Volume wear rate of uncoated and coated ASTM-SA213-T-11 boiler steel eroded at normal and oblique impact: (A) Uncoated T-11 boiler steel, (B) Nanostructured TiAlN coating, (C) Nanostructured AlCrN coating, (D) Conventional TiAlN coating, (E) Conventional AlCrN coating	303
Fig. 5.27	Surface-scale morphology and EDAX patterns from different spots on eroded uncoated and coated ASTM-SA213-T-11 boiler steel exposed to high temperature erosion studies in simulated coal-fired boiler environment at impact angle 90°: (a) Uncoated T-11 boiler steel, (b) Nanostructured TiAlN coating, (c) Nanostructured AlCrN coating, (d) Conventional TiAlN coating, (e) Conventional AlCrN coating	305

Fig. 5.28	Surface-scale morphology and EDAX patterns from different spots on eroded uncoated and coated ASTM-SA213-T-11 boiler steel exposed to high temperature erosion studies in simulated coal-fired boiler environment at impact angle 30°: (a) Uncoated T-11 boiler steel, (b) Nanostructured TiAlN coating, (c) Nanostructured AlCrN coating, (d) Conventional TiAlN coating, (e) Conventional AlCrN coating	306
Fig. 5.29	Schematic representation of (a) & (b); metal erosion, and (c) oxide erosion illustrating the nature of interaction between the oxide scale and the substrate during erosion	311
Fig. 5.30	Schematic representation of coating fracture dependent on impact angle; (a) Low angle, (b) High angle	312
Fig. 5.31	Potentiodynamic Polarization Curves for bare and coated ASTM-SA213-T-11 boiler steel	317
Fig. 5.32	Protective efficiency and Polarization resistance of bare and coated T-11 boiler steel: (A) Bare T-11 boiler steel, (B) Nanostructured TiAlN coating, (C) Nanostructured AlCrN coating, (D) Conventional TiAlN coating, (E) Conventional AlCrN coating	317
Fig. 5.33	Surface macrographs of uncoated and coated ASTM-SA213-T-11 boiler steel subjected to salt-fog testing (5% NaCl) : (A) Uncoated T-11 boiler steel subjected to 24hrs, 48hrs and 72 hrs testing; (B) Nanostructured TiAlN coating subjected to 24hrs, 48hrs and 72 hrs testing; (C) Nanostructured AlCrN coating subjected to 24hrs, 48hrs and 72 hrs testing	319
Fig. 5.34	Surface macrographs of uncoated and coated ASTM-SA213-T-11 boiler steel subjected to salt-fog testing (5% NaCl) for 24 hrs: (a) Uncoated ASTM-SA213-T-11 boiler steel (b) Nanostructured TiAlN coating (c) Nanostructured AlCrN coating	321
Fig. 5.35	Surface macrographs of uncoated and coated ASTM-SA213-T-11 boiler steel subjected to salt-fog testing (5% NaCl) for 48 hrs: (a) Uncoated ASTM-SA213-T-11 boiler steel (b) Nanostructured TiAlN coating (c) Nanostructured AlCrN coating	322

Fig. 5.36	Surface macrographs of uncoated and coated ASTM-SA213-T-11 boiler steel subjected to salt-fog testing (5% NaCl) for 72 hrs: (a) Uncoated ASTM-SA213-T-11 boiler steel (b) Nanostructured TiAlN coating (c) Nanostructured AlCrN coating	323
Fig. 5.37	X-Ray Diffraction pattern of uncoated and coated ASTM-SA213-T-11 boiler steel subjected to salt-fog testing (5% NaCl) for 24 Hrs, 48 Hrs and 72 Hrs: (A) Uncoated T-11 boiler steel, (B) Nanostructured TiAlN coating, (C) Nanostructured AlCrN coating	324
Fig. 5.38	Column chart showing weight loss per unit area for the uncoated and coated ASTM-SA213-T-11 boiler steel subjected to salt-fog testing (5% NaCl) : (A) Uncoated T-11 boiler steel subjected to 24hrs, 48hrs and 72 hrs testing; (B) Nanostructured TiAlN coated T-11 boiler steel subjected to 24hrs, 48hrs and 72 hrs testing; (C) Nanostructured AlCrN coated T-11 boiler steel subjected to 24hrs, 48hrs and 72 hrs testing	325
Fig. 5.39	Corrosion evolution of the as-deposited coatings in salt spray test; a: initiation of corrosion micro-crack, b: cracks propagation, c: crack branching, d: formation of corrosion hole	326
Fig. 5.40	Surface macrographs of uncoated and coated ASTM-SA213-T-11 boiler steel exposed to super-heater of the coal fired boiler environment at 900°C for 1000 hours: (a) Uncoated T-11 boiler steel, (b) Nanostructured TiAlN coating, (c) Nanostructured AlCrN coating, (d) Conventional TiAlN coating, (e) Conventional AlCrN coating	330
Fig. 5.41	Weight gain/area vs time for uncoated and coated ASTM-SA213-T-11 boiler steel exposed to super-heater of the coal fired boiler environment at 900°C for 1000 hours	332
Fig. 5.42	Bar chart indicating overall gain in thickness for uncoated and coated ASTM-SA213-T-11 boiler steel specimens exposed to super-heater of the coal fired boiler environment at 900°C for 1000 hours	332
Fig. 5.43 (a)	X-Ray Diffraction pattern of bare and coated ASTM-SA213-T-11 boiler steel exposed to platen superheater of the coal fired boiler environment at 900°C for 1000 Hrs: (A) bare T-11 boiler steel, (B) Nanostructured	334

TiAlN coating, (C) Nanostructured AlCrN coating

- Fig. 5.43 (b)** X-Ray Diffraction pattern of coated ASTM-SA213-T-11 boiler steel exposed to platen superheater of the coal fired boiler environment at 900°C for 1000 Hrs: (A) Conventional TiAlN coating, (B) Conventional AlCrN coating 334
- Fig. 5.44** Surface-scale morphology and EDAX patterns from different spots on uncoated and coated ASTM-SA213-T-11 boiler steel exposed to platen superheater of the coal fired boiler environment at 900°C for 1000 Hrs: (a) Uncoated T-11 boiler steel, (b) Nanostructured TiAlN coating, (c) Nanostructured AlCrN coating, (d) Conventional TiAlN coating, (e) Conventional AlCrN coating 335
- Fig. 5.45** Oxide scale morphology and variation of elemental composition across the cross-section of the uncoated and coated ASTM-SA213-T-11 boiler steel exposed to platen super-heater of the coal fired boiler environment at 900°C for 1000 Hrs: (a) Uncoated T-11 boiler steel (36 X), (b) Nanostructured TiAlN coating (60 X), (c) Nanostructured AlCrN coating (45 X), (d) Conventional TiAlN coating (100 X), (e) Conventional AlCrN coating (60 X) 338
- Fig. 5.46** Bar chart indicating the extent of erosion/corrosion for uncoated and coated ASTM-SA213 T-11 boiler steel specimens exposed to super heater of the coal fired boiler environment at 900°C for 1000 hours 339
- Fig. 5.47** Corrosion rate in mils per year (mpy) for uncoated and coated ASTM-SA213-T-11 boiler steel exposed to super-heater of the coal fired boiler environment at 900°C for 1000 hours 340
- Fig. 5.48 (a)** Composition image (BSEI) and X-ray mapping of the cross-section of uncoated ASTM-SA213-T-11 boiler steel exposed to platen super-heater of the coal fired boiler environment at 900°C for 1000 Hrs 341
- Fig. 5.48 (b)** Composition image (BSEI) and X-ray mapping of the cross-section of Nanostructured TiAlN coated ASTM-SA213-T-11 boiler steel exposed to platen super-heater of the coal fired boiler environment at 900°C for 1000 Hrs 342

Fig. 5.48 (c)	Composition image (BSEI) and X-ray mapping of the cross-section of Nanostructured AlCrN coated ASTM-SA213-T-11 boiler steel exposed to platen super-heater of the coal fired boiler environment at 900°C for 1000 Hrs	343
Fig. 5.48 (d)	Composition image (BSEI) and X-ray mapping of the cross-section of conventional TiAlN coated ASTM-SA213-T-11 boiler steel exposed to platen super-heater of the coal fired boiler environment at 900°C for 1000 Hrs	344
Fig. 5.48 (e)	Composition image (BSEI) and X-ray mapping of the cross-section of conventional AlCrN coated ASTM-SA213-T-11 boiler steel exposed to platen super-heater of the coal fired boiler environment at 900°C for 1000 Hrs	345
Fig. 6.1	Surface macrographs for the as coated ASTM-SA213-T-22 boiler steel (a) Nanostructured TiAlN coating, (b) Nanostructured AlCrN coating, (c) Conventional TiAlN coating, (d) Conventional AlCrN coating	351
Fig. 6.2	Optical micrograph (200 X) of the surface of as coated ASTM-SA213-T-22 boiler steel (a) Nanostructured TiAlN coating, (b) Nanostructured AlCrN coating, (c) Conventional TiAlN coating, (d) Conventional AlCrN coating	352
Fig. 6.3	Surface-scale morphology and EDAX patterns from different spots on as coated ASTM-SA213-T-22 boiler steel (a) Nanostructured TiAlN coating, (b) Nanostructured AlCrN coating, (c) Conventional TiAlN coating, (d) Conventional AlCrN coating	353
Fig. 6.4	2D and 3D AFM images for the as coated ASTM-SA213-T-22 boiler steel (a) & (b) Nanostructured TiAlN coating, (c) & (d) Nanostructured AlCrN coating	354
Fig. 6.5	Microhardness profile across the cross-section for Conventional TiAlN and Conventional AlCrN coating on ASTM-SA213-T-22 boiler steel	356
Fig. 6.6	Fracture surfaces of a Plasma sprayed gas nitride specimen after ASTM C633 tensile test; (a) Conventional TiAlN coating, (b) Conventional AlCrN coating	356
Fig. 6.7	Surface-scale morphology and EDAX patterns from different spots on as	358

coated ASTM-SA213-T-22 boiler steel (a) Nanostructured TiAlN coating (10000 X), (b) Nanostructured AlCrN coating (10000 X), (c) Conventional TiAlN coating (200 X), (d) Conventional AlCrN coating (200 X)

Fig. 6.8 (a)	Composition image (SEI) and X-ray mapping of the cross-section of as-coated nanostructured TiAlN coating on ASTM-SA213-T-22 boiler steel	360
Fig. 6.8 (b)	Composition image (BSEI) and X-ray mapping of the cross-section of as-coated nanostructured AlCrN coating on ASTM-SA213-T-22 boiler steel	361
Fig. 6.8 (c)	Composition image (BSEI) and X-ray mapping of the cross-section of as-coated conventional TiAlN coating on ASTM-SA213-T-22 boiler steel	362
Fig. 6.8 (d)	Composition image (SEI) and X-ray mapping of the cross-section of as-coated conventional AlCrN coating on ASTM-SA213-T-22 boiler steel	363
Fig. 6.9	Surface macrographs of uncoated and coated ASTM-SA213-T-22 boiler steel after exposure to cyclic oxidation in air at 900°C for 50 cycles: (a) Uncoated T-22 boiler steel, (b) Nanostructured TiAlN coating, (c) Nanostructured AlCrN coating, (d) Conventional TiAlN coating, (e) Conventional AlCrN coating	369
Fig. 6.10	Weight gain/area vs time (number of cycles) for the uncoated and coated ASTM-SA213-T-22 boiler steel subjected to cyclic oxidation in air at 900°C for 50 cycles	370
Fig. 6.11	Column chart showing cumulative weight gain per unit area for the uncoated and coated ASTM-SA213-T-22 boiler steel subjected to cyclic oxidation in air at 900°C for 50 cycles: (A) Uncoated T-22 boiler steel, (B) Nanostructured TiAlN coating, (C) Nanostructured AlCrN coating, (D) Conventional TiAlN coating, (E) Conventional AlCrN coating	371
Fig. 6.12	Weight gain/area square vs time (number of cycles) for the uncoated and coated ASTM-SA213-T-22 boiler steel subjected to cyclic oxidation in air at 900°C for 50 cycles	372
Fig. 6.13 (a)	X-Ray Diffraction pattern of uncoated and coated ASTM-SA213-T-22 boiler steel exposed to cyclic oxidation in air at 900°C for 50 cycles: (A) Uncoated T-22 boiler steel, (B) Nanostructured TiAlN coating, (C) Nanostructured AlCrN coating	373

Fig. 6.13 (b)	X-Ray Diffraction pattern of uncoated and coated ASTM-SA213-T-22 boiler steel exposed to cyclic oxidation in air at 900°C for 50 cycles: (A) Conventional TiAlN coating, (B) Conventional AlCrN coating	373
Fig. 6.14	Surface-scale morphology and EDAX patterns from different spots on uncoated and coated ASTM-SA213-T-22 boiler steel after exposure to cyclic oxidation in air at 900°C for 50 cycles : (a) Uncoated T-22 boiler steel, (b) Nanostructured TiAlN coating, (c) Nanostructured AlCrN coating, (d) Conventional TiAlN coating, (e) Conventional AlCrN coating	375
Fig. 6.15	Oxide scale morphology and variation of elemental composition across the cross- section of the uncoated and coated ASTM-SA213-T-22 boiler steel after exposure to cyclic oxidation in air at 900°C for 50 cycles: (a) Uncoated T-22 boiler steel (80 X), (b) Nanostructured TiAlN coating (130 X), (c) Nanostructured AlCrN coating (726 X), (d) Conventional TiAlN coating (150 X), (e) Conventional AlCrN coating (300 X)	378
Fig. 6.16 (a)	Composition image (BSEI) and X-ray mapping of the cross-section of uncoated ASTM-SA213-T-22 boiler steel subjected to cyclic oxidation in air at 900°C for 50 cycles	379
Fig. 6.16 (b)	Composition image (BSEI) and X-ray mapping of the cross-section of Nanostructured TiAlN coated T-22 boiler steel subjected to cyclic oxidation in air at 900°C for 50 cycles	380
Fig. 6.16 (c)	Composition image (BSEI) and X-ray mapping of the cross-section of Nanostructured AlCrN coated T-22 boiler steel subjected to cyclic oxidation in air at 900°C for 50 cycles	381
Fig. 6.16 (d)	Composition image (BSEI) and X-ray mapping of the cross-section of conventional TiAlN coated T-22 boiler steel subjected to cyclic oxidation in air at 900°C for 50 cycles	382
Fig. 6.16 (e)	Composition image (BSEI) and X-ray mapping of the cross-section of conventional AlCrN coated T-22 boiler steel subjected to cyclic oxidation in air at 900°C for 50 cycles	383
Fig. 6.17	Schematic diagram showing probable oxidation mechanism for uncoated T-22 boiler steel exposed to air at 900°C for 50 cycles (Chaterjee et al.,	386

2001 and Singh, Buta, 2003)

- Fig. 6.18** Surface macrographs of uncoated and coated ASTM-SA213-T-22 boiler steel exposed to molten salt (Na_2SO_4 -60% V_2O_5) environment at 900°C for 50 cycles: (a) Uncoated T-22 boiler steel, (b) Nanostructured TiAlN coating, (c) Nanostructured AlCrN coating, (d) Conventional TiAlN coating, (e) Conventional AlCrN coating 390
- Fig. 6.19** Weight gain/area vs time (number of cycles) for the bare and coated ASTM-SA213-T-22 boiler steel exposed to molten salt (Na_2SO_4 -60% V_2O_5) environment at 900°C for 50 cycles 392
- Fig. 6.20** Bar chart showing cumulative weight gain per unit area for the uncoated and coated T-22 boiler steel exposed to molten salt (Na_2SO_4 -60% V_2O_5) environment at 900°C for 50 cycles: (A) bare T-22 boiler steel, (B) Nanostructured TiAlN coating, (C) Nanostructured AlCrN coating, (D) Conventional TiAlN coating, (E) Conventional AlCrN coating 393
- Fig. 6.21** Weight gain/area square vs time (number of cycles) for the uncoated and coated ASTM-SA213-T-22 boiler steel exposed to molten salt (Na_2SO_4 -60% V_2O_5) environment at 900°C for 50 cycles 394
- Fig. 6.22 (a)** X-Ray Diffraction pattern of uncoated and coated ASTM-SA213-T-22 boiler steel exposed to molten salt (Na_2SO_4 -60% V_2O_5) environment at 900°C for 50 cycles: (A) Uncoated T-22 boiler steel, (B) Nanostructured TiAlN coating, (C) Nanostructured AlCrN coating 395
- Fig. 6.22 (b)** X-Ray Diffraction pattern of uncoated and coated ASTM-SA213-T-22 boiler steel exposed to molten salt (Na_2SO_4 -60% V_2O_5) environment at 900°C for 50 cycles: (A) Conventional TiAlN coating, (B) Conventional AlCrN coating 395
- Fig. 6.23** Surface-scale morphology and EDAX patterns from different spots on uncoated and coated T-22 boiler steel exposed to molten salt (Na_2SO_4 -60% V_2O_5) environment at 900°C for 50 cycles: (a) bare T-22 boiler steel, (b) Nanostructured TiAlN coating, (c) Nanostructured AlCrN coating, (d) Conventional TiAlN coating, (e) Conventional AlCrN coating 396

Fig. 6.24	Oxide scale morphology and variation of elemental composition across the cross-section of the uncoated and coated ASTM-SA213-T-22 boiler steel exposed to molten salt (Na_2SO_4 -60% V_2O_5) environment at 900°C for 50 cycles: (a) Uncoated T-22 boiler steel (116 X), (b) Nanostructured TiAlN coating (140 X), (c) Nanostructured AlCrN coating (33 X), (d) Conventional TiAlN coating (100 X), (e) Conventional AlCrN coating (500 X)	398
Fig. 6.25 (a)	Composition image (BSEI) and X-ray mapping of the cross-section of uncoated ASTM-SA213-T-22 boiler steel exposed to molten salt (Na_2SO_4 -60% V_2O_5) environment at 900°C for 50 cycles	399
Fig. 6.25 (b)	Composition image (BSEI) and X-ray mapping of the cross-section of Nanostructured TiAlN coated ASTM-SA213-T-22 boiler steel exposed to molten salt (Na_2SO_4 -60% V_2O_5) environment at 900°C for 50 cycles	401
Fig. 6.25 (c)	Composition image (BSEI) and X-ray mapping of the cross-section of Nanostructured AlCrN coated ASTM-SA213-T-22 boiler steel exposed to molten salt (Na_2SO_4 -60% V_2O_5) environment at 900°C for 50 cycles	402
Fig. 6.25 (d)	Composition image (BSEI) and X-ray mapping of the cross-section of conventional TiAlN coated ASTM-SA213-T-22 boiler steel exposed to molten salt (Na_2SO_4 -60% V_2O_5) environment at 900°C for 50 cycles	403
Fig. 6.25 (e)	Composition image (BSEI) and X-ray mapping of the cross-section of conventional AlCrN coated ASTM-SA213-T-22 boiler steel exposed to molten salt (Na_2SO_4 -60% V_2O_5) environment at 900°C for 50 cycles	404
Fig. 6.26	Surface macrographs of eroded uncoated and coated ASTM-SA213-T-22 boiler steel exposed to high temperature erosion studies in simulated coal-fired boiler environment	413
Fig. 6.27	Column chart showing the Volume wear rate of uncoated and coated ASTM-SA213-T-22 boiler steel eroded at normal and oblique impact: (A) Uncoated T-22 boiler steel, (B) Nanostructured TiAlN coating, (C) Nanostructured AlCrN coating, (D) Conventional TiAlN coating, (E) Conventional AlCrN coating	415
Fig. 6.28	Surface-scale morphology and EDAX patterns from different spots on	417

eroded uncoated and coated ASTM-SA213-T-22 boiler steel exposed to high temperature erosion studies in simulated coal-fired boiler environment at impact angle 90°: (a) Uncoated T-22 boiler steel, (b) Nanostructured TiAlN coating, (c) Nanostructured AlCrN coating, (d) Conventional TiAlN coating, (e) Conventional AlCrN coating

- Fig. 6.29** Surface-scale morphology and EDAX patterns from different spots on eroded uncoated and coated ASTM-SA213-T-22 boiler steel exposed to high temperature erosion studies in simulated coal-fired boiler environment at impact angle 90°: (a) Uncoated T-22 boiler steel, (b) Nanostructured TiAlN coating, (c) Nanostructured AlCrN coating, (d) Conventional TiAlN coating, (e) Conventional AlCrN coating 419
- Fig. 6.30** Schematic representation of (a) & (b); metal erosion, and (c) oxide erosion illustrating the nature of interaction between the oxide scale and the substrate during erosion 422
- Fig. 6.31** Schematic representation of coating fracture dependent on impact angle; (a) Low angle, (b) High angle 424
- Fig. 6.32** Potentiodynamic Polarization Curves for uncoated and coated T-22 boiler steel 429
- Fig. 6.33** Protective efficiency and Polarization resistance of uncoated and coated T-22 boiler steel: (A) Uncoated T-22 boiler steel, (B) Nanostructured TiAlN coating, (C) Nanostructured AlCrN coating, (D) Conventional TiAlN coating, (E) Conventional AlCrN coating 430
- Fig. 6.34** Surface macrographs of uncoated and coated ASTM-SA213-T-22 boiler steel subjected to salt-fog testing (5% NaCl) : (A) Uncoated T-22 boiler steel subjected to 24hrs, 48hrs and 72 hrs testing; (B) Nanostructured TiAlN coating subjected to 24hrs, 48hrs and 72 hrs testing; (C) Nanostructured AlCrN coating subjected to 24hrs, 48hrs and 72 hrs testing 432
- Fig. 6.35** Surface macrographs of uncoated and coated ASTM-SA213-T-22 boiler steel subjected to salt-fog testing (5% NaCl) for 24 hrs: (a) Uncoated ASTM-SA213-T-22 boiler steel (b) Nanostructured TiAlN coating (c) 433

Nanostructured AlCrN coating

- Fig. 6.36** Surface macrographs of uncoated and coated ASTM-SA213-T-22 boiler steel subjected to salt-fog testing (5% NaCl) for 48 hrs: (a) Uncoated ASTM-SA213-T-22 boiler steel (b) Nanostructured TiAlN coating (c) Nanostructured AlCrN coating 434
- Fig. 6.37** Surface macrographs of uncoated and coated ASTM-SA213-T-22 boiler steel subjected to salt-fog testing (5% NaCl) for 72 hrs: (a) Uncoated T-22 boiler steel (b) Nanostructured TiAlN coating (c) Nanostructured AlCrN coating 435
- Fig. 6.38** X-Ray Diffraction pattern of uncoated and coated ASTM-SA213-T-22 boiler steel subjected to salt-fog testing (5% NaCl) for 24 Hrs, 48 Hrs and 72 Hrs: (A) Uncoated T-22 boiler steel, (B) Nanostructured TiAlN coating, (C) Nanostructured AlCrN coating 437
- Fig. 6.39** Column chart showing weight loss per unit area for the uncoated and coated ASTM-SA213-T-22 boiler steel subjected to salt-fog testing (5% NaCl) : (A) Uncoated T-22 boiler steel subjected to 24hrs, 48hrs and 72 hrs testing; (B) Nanostructured TiAlN coated T-22 boiler steel subjected to 24hrs, 48hrs and 72 hrs testing; (C) Nanostructured AlCrN coated T-22 boiler steel subjected to 24hrs, 48hrs and 72 hrs testing 438
- Fig. 6.40** Corrosion evolution of the as-deposited coatings in salt spray test; a: initiation of corrosion micro-crack, b: cracks propagation, c: crack branching, d: formation of corrosion hole 438
- Fig. 6.41** Surface macrographs of uncoated and coated ASTM-SA213-T-22 boiler steel exposed to super-heater of the coal fired boiler environment at 900°C for 1000 hours: (a) Uncoated T-22 boiler steel, (b) Nanostructured TiAlN coating, (c) Nanostructured AlCrN coating, (d) Conventional TiAlN coating, (e) Conventional AlCrN coating 442
- Fig. 6.42** Weight gain/area vs time for uncoated and coated ASTM-SA213-T-22 boiler steel exposed to super-heater of the coal fired boiler environment at 900°C for 1000 hours 444
- Fig. 6.43** Bar chart indicating overall gain in thickness for uncoated and coated 444

ASTM-SA213-T-22 boiler steel specimens exposed to super-heater of the coal fired boiler environment at 900°C for 1000 hours

- Fig. 6.44 (a)** X-Ray Diffraction pattern of uncoated and coated ASTM-SA213-T-22 boiler steel exposed to platen superheater of the coal fired boiler environment at 900°C for 1000 Hrs: (A) Uncoated T-22 boiler steel, (B) Nanostructured TiAlN coating, (C) Nanostructured AlCrN coating 446
- Fig. 6.44 (c)** X-Ray Diffraction pattern of coated ASTM-SA213-T-22 boiler steel exposed to platen superheater of the coal fired boiler environment at 900°C for 1000 Hrs: (A) Conventional TiAlN coating, (B) Conventional AlCrN coating 446
- Fig. 6.45** Surface-scale morphology and EDAX patterns from different spots on uncoated and coated ASTM-SA213-T-22 boiler steel exposed to platen superheater of the coal fired boiler environment at 900°C for 1000 Hrs: (a) Uncoated T-22 boiler steel, (b) Nanostructured TiAlN coating, (c) Nanostructured AlCrN coating, (d) Conventional TiAlN coating, (e) Conventional AlCrN coating 447
- Fig. 6.46** Oxide scale morphology and variation of elemental composition across the cross- section of the uncoated and coated ASTM-SA213-T-22 boiler steel exposed to platen super-heater of the coal fired boiler environment at 900°C for 1000 Hrs: (a) Uncoated T-22 boiler steel (50 X), (b) Nanostructured TiAlN coating (45 X), (c) Nanostructured AlCrN coating (70 X), (d) Conventional TiAlN coating (130 X), (e) Conventional AlCrN coating (82 X) 449
- Fig. 6.47** Bar chart indicating the extent of erosion/corrosion for bare and coated T-22 boiler steel specimens exposed to super-heater of the coal fired boiler environment at 900°C for 1000 hrs 450
- Fig. 6.48** Corrosion rate in mils per year (mpy) for uncoated and coated T-22 boiler steel exposed to super-heater of the coal fired boiler environment at 900°C for 1000 hours: (A) Uncoated T-22 boiler steel, (B) Nanostructured TiAlN coating, (C) Nanostructured AlCrN coating 452
- Fig. 6.49 (a)** Composition image (BSEI) and X-ray mapping of the cross-section of 453

uncoated ASTM-SA213-T-22 boiler steel exposed to platen super-heater of the coal fired boiler environment at 900°C for 1000 Hrs

- Fig. 6.49 (b)** Composition image (BSEI) and X-ray mapping of the cross-section of Nanostructured TiAlN coated ASTM-SA213-T-22 boiler steel exposed to platen super-heater of the coal fired boiler environment at 900°C for 1000 Hrs 454
- Fig. 6.49 (c)** Composition image (BSEI) and X-ray mapping of the cross-section of Nanostructured AlCrN coated ASTM-SA213-T-22 boiler steel exposed to platen super-heater of the coal fired boiler environment at 900°C for 1000 Hrs 455
- Fig. 6.49 (d)** Composition image (BSEI) and X-ray mapping of the cross-section of conventional TiAlN coated ASTM-SA213-T-22 boiler steel exposed to platen super-heater of the coal fired boiler environment at 900°C for 1000 Hrs 456
- Fig. 6.49 (e)** Composition image (BSEI) and X-ray mapping of the cross-section of conventional AlCrN coated ASTM-SA213-T-22 boiler steel exposed to platen super-heater of the coal fired boiler environment at 900°C for 1000 Hrs 457
- Fig. 7.1** Surface macrographs for the as coated Superfer 800H superalloy (a) Nanostructured TiAlN coating, (b) Nanostructured AlCrN coating, (c) Conventional TiAlN coating, (d) Conventional AlCrN coating 464
- Fig. 7.2** Optical micrograph (200 X) of the surface of as coated Superfer 800H superalloy; (a) Nanostructured TiAlN coating, (b) Nanostructured AlCrN coating, (c) Conventional TiAlN coating, (d) Conventional AlCrN coating 465
- Fig. 7.3** Surface-scale morphology and EDAX patterns from different spots on as coated Superfer 800H superalloy (a) Nanostructured TiAlN coating, (b) Nanostructured AlCrN coating, (c) Conventional TiAlN coating, (d) Conventional AlCrN coating 467
- Fig. 7.4** 2D and 3D AFM images for the as coated Superfer 800H superalloy (a) & (b) Nanostructured TiAlN coating, (c) & (d) Nanostructured AlCrN coating 468
- Fig. 7.5** Microhardness profile across the cross-section for Conventional TiAlN 469

and Conventional AlCrN coating on Superfer 800H superalloy

- Fig. 7.6** Fractured surfaces of a Plasma sprayed gas nitrided specimens after ASTM C633 tensile test; (a) Conventional TiAlN coating, (b) Conventional AlCrN coating 469
- Fig. 7.7** Surface-scale morphology and EDAX patterns from different spots on as coated Superfer 800H superalloy (a) Nanostructured TiAlN coating, (b) Nanostructured AlCrN coating, (c) Conventional TiAlN coating, (d) Conventional AlCrN coating 471
- Fig. 7.8 (a)** Composition image (SEI) and X-ray mapping of the cross-section of as-coated nanostructured TiAlN coating on Superfer800H superalloy 473
- Fig. 7.8 (b)** Composition image (BSEI) and X-ray mapping of the cross-section of as-coated nanostructured AlCrN coating on Superfer800H superalloy 474
- Fig. 7.8 (c)** Composition image (BSEI) and X-ray mapping of the cross-section of as-coated conventional TiAlN coating on Superfer800H superalloy 475
- Fig. 7.8 (d)** Composition image (BSEI) and X-ray mapping of the cross-section of as-coated conventional AlCrN coating on Superfer800H superalloy 476
- Fig. 7.9** Surface macrographs of uncoated and coated Superfer 800H superalloy after exposure to cyclic oxidation in air at 900°C for 50 cycles: (a) Uncoated Superfer 800H superalloy, (b) Nanostructured TiAlN coating, (c) Nanostructured AlCrN coating, (d) Conventional TiAlN coating, (e) Conventional AlCrN coating 482
- Fig. 7.10** Weight gain/area vs time (number of cycles) for the uncoated and coated Superfer 800H superalloy subjected to cyclic oxidation in air at 900°C for 50 cycles 483
- Fig. 7.11** Column chart showing cumulative weight gain per unit area for the uncoated and coated Superfer 800H superalloy subjected to cyclic oxidation in air at 900°C for 50 cycles: (A) Uncoated Superfer 800H superalloy, (B) Nanostructured TiAlN coating, (C) Nanostructured AlCrN coating, (D) Conventional TiAlN coating, (E) Conventional AlCrN coating 484
- Fig. 7.12** Weight gain/area square vs time (number of cycles) for the uncoated and coated Superfer 800H superalloy subjected to cyclic oxidation in air 484

at 900°C for 50 cycles

- Fig. 7.13 (a)** X-Ray Diffraction pattern of uncoated and coated Superfer 800H superalloy exposed to cyclic oxidation in air at 900°C for 50 cycles : (A) Uncoated superalloy, (B) Nanostructured TiAlN coating, (C) Nanostructured AlCrN coating 486
- Fig. 7.13 (b)** X-Ray Diffraction pattern of uncoated and coated Superfer 800H superalloy exposed to cyclic oxidation in air at 900°C for 50 cycles: (A) Conventional TiAlN coating, (B) Conventional AlCrN coating 486
- Fig. 7.14** Surface-scale morphology and EDAX patterns from different spots on uncoated and coated Superfer 800H superalloy after exposure to cyclic oxidation in air at 900°C for 50 cycles : (a) Uncoated Superfer 800H superalloy, (b) Nanostructured TiAlN coating, (c) Nanostructured AlCrN coating, (d) Conventional TiAlN coating, (e) Conventional AlCrN coating 488
- Fig. 7.15** Oxide scale morphology and variation of elemental composition across the cross- section of the uncoated and coated Superfer 800H superalloy after exposure to cyclic oxidation in air at 900°C for 50 cycles: (a) Uncoated Superfer 800H superalloy (4000 X), (b) Nanostructured TiAlN coating (4000 X), (c) Nanostructured AlCrN coating (2000 X), (d) Conventional TiAlN coating (500 X), (e) Conventional AlCrN coating (500 X) 490
- Fig. 7.16 (a)** Composition image (BSEI) and X-ray mapping of the cross-section of uncoated Superfer 800H superalloy subjected to cyclic oxidation in air at 900°C for 50 cycles 492
- Fig. 7.16 (b)** Composition image (BSEI) and X-ray mapping of the cross-section of Nanostructured TiAlN coated Superfer 800H superalloy subjected to cyclic oxidation in air at 900°C for 50 cycles 493
- Fig. 7.16 (c)** Composition image (BSEI) and X-ray mapping of the cross-section of Nanostructured AlCrN coated Superfer 800H superalloy subjected to cyclic oxidation in air at 900°C for 50 cycles 494
- Fig. 7.16 (d)** Composition image (BSEI) and X-ray mapping of the cross-section of conventional TiAlN coated Superfer 800H superalloy subjected to cyclic 495

	oxidation in air at 900°C for 50 cycles	
Fig. 7.16 (e)	Composition image (BSEI) and X-ray mapping of the cross-section of conventional AlCrN coated Superfer 800H superalloy subjected to cyclic oxidation in air at 900°C for 50 cycles	496
Fig. 7.17	Schematic diagram showing probable oxidation mechanism for the uncoated superalloy Superfer 800H exposed to air at 900°C for 50 cycles (Singh, Harpreet, 2005)	500
Fig. 7.18	Surface macrographs of uncoated and coated Superfer 800H superalloy exposed to molten salt (Na_2SO_4 -60% V_2O_5) environment at 900°C for 50 cycles: (a) Uncoated Superfer 800H superalloy, (b) Nanostructured TiAlN coating, (c) Nanostructured AlCrN coating, (d) Conventional TiAlN coating, (e) Conventional AlCrN coating	504
Fig. 7.19	Weight gain/area vs time (number of cycles) for the uncoated and coated Superfer 800H superalloy exposed to molten salt (Na_2SO_4 -60% V_2O_5) environment at 900°C for 50 cycles	505
Fig. 7.20	Bar chart showing cumulative weight gain per unit area for the uncoated and coated Superfer 800H superalloy exposed to molten salt (Na_2SO_4 -60% V_2O_5) environment at 900°C for 50 cycles: (A) bare Superfer 800H superalloy, (B) Nanostructured TiAlN coating, (C) Nanostructured AlCrN coating, (D) Conventional TiAlN coating, (E) Conventional AlCrN coating	506
Fig. 7.21	Weight gain/area square vs time (number of cycles) for the uncoated and coated Superfer 800H superalloy exposed to molten salt (Na_2SO_4 -60% V_2O_5) environment at 900°C for 50 cycles	507
Fig. 7.22 (a)	X-Ray Diffraction pattern of uncoated and coated Superfer 800H superalloy exposed to molten salt (Na_2SO_4 -60% V_2O_5) environment at 900°C for 50 cycles: (A) Uncoated superalloy, (B) Nanostructured TiAlN coating, (C) Nanostructured AlCrN coating, (D) Conventional TiAlN coating	509
Fig. 7.22 (b)	X-Ray Diffraction pattern of Conventional AlCrN coated Superfer 800H superalloy exposed to molten salt (Na_2SO_4 -60% V_2O_5) environment at 900°C for 50 cycles	509

Fig. 7.23	Surface-scale morphology and EDAX patterns from different spots on uncoated and coated Superfer 800H superalloy exposed to molten salt (Na_2SO_4 -60% V_2O_5) environment at 900°C for 50 cycles : (a) Uncoated Superfer 800H superalloy, (b) Nanostructured TiAlN coating, (c) Nanostructured AlCrN coating, (d) Conventional TiAlN coating, (e) Conventional AlCrN coating	510
Fig. 7.24	Oxide scale morphology and variation of elemental composition across the cross- section of the uncoated and coated Superfer800H superalloy exposed to molten salt (Na_2SO_4 -60% V_2O_5) environment at 900°C for 50 cycles: (a) Uncoated Superfer800H superalloy (1200X), (b) Nanostructured TiAlN coating (1200 X), (c) Nanostructured AlCrN coating (1700 X), (d) Conventional TiAlN coating (500 X), (e) Conventional AlCrN coating (500 X)	512
Fig. 7.25 (a)	Composition image (BSEI) and X-ray mapping of the cross-section of uncoated Superfer 800H superalloy exposed to molten salt (Na_2SO_4 -60% V_2O_5) environment at 900°C for 50 cycles	515
Fig. 7.25 (b)	Composition image (BSEI) and X-ray mapping of the cross-section of Nanostructured TiAlN coated Superfer 800H superalloy exposed to molten salt (Na_2SO_4 -60% V_2O_5) environment at 900°C for 50 cycles	516
Fig. 7.25 (c)	Composition image (BSEI) and X-ray mapping of the cross-section of Nanostructured AlCrN coated Superfer 800H superalloy exposed to molten salt (Na_2SO_4 -60% V_2O_5) environment at 900°C for 50 cycles	517
Fig. 7.25 (d)	Composition image (BSEI) and X-ray mapping of the cross-section of conventional TiAlN coated Superfer 800H superalloy exposed to molten salt (Na_2SO_4 -60% V_2O_5) environment at 900°C for 50 cycles	518
Fig. 7.25 (e)	Composition image (BSEI) and X-ray mapping of the cross-section of conventional AlCrN coated Superfer 800H superalloy exposed to molten salt (Na_2SO_4 -60% V_2O_5) environment at 900°C for 50 cycles	519
Fig. 7.26	Surface macrographs of eroded uncoated and coated Superfer 800 superalloy exposed to high temperature erosion studies in simulated coal-fired boiler environment	526

Fig. 7.27	Column chart showing the Volume wear rate of uncoated and coated Superfer 800H superalloy eroded at normal and oblique impact: (A) Uncoated Superfer 800H, (B) Nanostructured TiAlN coating, (C) Nanostructured AlCrN coating, (D) Conventional TiAlN coating, (E) Conventional AlCrN coating	527
Fig. 7.28	Surface-scale morphology and EDAX patterns from different spots on eroded uncoated and coated Superfer 800H superalloy exposed to high temperature erosion studies in simulated coal-fired boiler environment at impact angle 90°: (a) Uncoated Superfer 800H, (b) Nanostructured TiAlN coating, (c) Nanostructured AlCrN coating, (d) Conventional TiAlN coating, (e) Conventional AlCrN coating	529
Fig. 7.29	Surface-scale morphology and EDAX patterns from different spots on eroded uncoated and coated Superfer 800H superalloy exposed to high temperature erosion studies in simulated coal-fired boiler environment at impact angle 30°: (a) Uncoated Superfer 800H, (b) Nanostructured TiAlN coating, (c) Nanostructured AlCrN coating, (d) Conventional TiAlN coating, (e) Conventional AlCrN coating	530
Fig. 7.30	Schematic representation of (a) & (b); metal erosion, and (c) oxide erosion illustrating the nature of interaction between the oxide scale and the substrate during erosion	535
Fig. 7.31	Schematic representation of coating fracture dependent on impact angle; (a) Low angle, (b) High angle	536
Fig. 7.32	Potentiodynamic Polarization Curves for uncoated and coated Superfer 800H superalloy	540
Fig. 7.33	Protective efficiency and Polarization resistance of uncoated and coated Superfer 800H superalloy: (A) Uncoated Superfer 800H, (B) Nanostructured TiAlN coating, (C) Nanostructured AlCrN coating, (D) Conventional TiAlN coating, (E) Conventional AlCrN coating	541
Fig. 7.34	Surface macrographs of uncoated and coated Superfer 800H superalloy subjected to salt-fog testing (5% NaCl) : (A) Uncoated T-22 boiler steel subjected to 24hrs, 48hrs and 72 hrs testing; (B) Nanostructured TiAlN	543

coating subjected to 24hrs, 48hrs and 72 hrs testing; (C) Nanostructured AlCrN coating subjected to 24hrs, 48hrs and 72 hrs testing

- Fig. 7.35** Surface macrographs of uncoated and coated Superfer 800H superalloy subjected to salt-fog testing (5% NaCl) for 72 hrs: (a) Uncoated Superfer 800H superalloy (b) Nanostructured TiAlN coating (c) Nanostructured AlCrN coating 544
- Fig. 7.36** X-Ray Diffraction pattern of uncoated and coated Superfer 800H superalloy subjected to salt-fog testing (5% NaCl): : (A) Uncoated Superfer 800H superalloy, (B) Nanostructured TiAlN coating, (C) Nanostructured AlCrN coating 545
- Fig. 7.37** Surface macrographs of uncoated and coated Superfer 800H superalloy exposed to super-heater of the coal fired boiler environment at 900°C for 1000 hours: (a) Uncoated Superfer 800H superalloy, (b) Nanostructured TiAlN coating, (c) Nanostructured AlCrN coating, (d) Conventional TiAlN coating, (e) Conventional AlCrN coating 548
- Fig. 7.38** Weight gain/area vs time for uncoated and coated Superfer 800H superalloy exposed to super-heater of the coal fired boiler environment at 900°C for 1000 hours 549
- Fig. 7.39** Bar chart indicating overall gains/loss in thickness for uncoated and coated Superfer 800H superalloy specimens exposed to super-heater of the coal fired boiler environment at 900°C for 1000 hours: (a) Uncoated Superfer 800H superalloy, (b) Nanostructured TiAlN coating, (c) Nanostructured AlCrN coating, (d) Conventional TiAlN coating, (e) Conventional AlCrN coating 550
- Fig. 7.40 (a)** X-Ray Diffraction pattern of uncoated and coated Superfer 800H superalloy exposed to platen superheater of the coal fired boiler environment at 900°C for 1000 Hrs: (A) Uncoated Superfer 800H superalloy, (B) Nanostructured TiAlN coating, (C) Nanostructured AlCrN coating 552
- Fig. 7.40 (b)** X-Ray Diffraction pattern of coated Superfer 800H superalloy exposed to platen superheater of the coal fired boiler environment at 900°C for 552

Fig. 7.41	<p>1000 Hrs: (A) Conventional TiAlN coating, (B) Conventional AlCrN coating</p> <p>Surface-scale morphology and EDAX patterns from different spots on uncoated and coated Superfer 800H superalloy exposed to platen superheater of the coal fired boiler environment at 900°C for 1000 Hrs :</p> <p>(a) Uncoated Superfer 800H superalloy, (b) Nanostructured TiAlN coating, (c) Nanostructured AlCrN coating, (d) Conventional TiAlN coating, (e) Conventional AlCrN coating</p>	553
Fig. 7.42	<p>Oxide scale morphology and variation of elemental composition across the cross- section of the uncoated and coated Superfer800H superalloy exposed to platen super-heater of the coal fired boiler environment at 900°C for 1000 Hrs: (a) Uncoated Superfer800H superalloy (1600 X), (b) Nanostructured TiAlN coating (1200 X), (c) Nanostructured AlCrN coating (1700 X), (d) Conventional TiAlN coating (800 X), (e) Conventional AlCrN coating (1000 X)</p>	555
Fig. 7.43	<p>Bar chart indicating the extent of erosion/corrosion for uncoated and coated Superfer 800H superalloy specimens exposed to super-heater of the coal fired boiler environment at 900°C for 1000 hours: (a) Uncoated Superfer 800H superalloy, (b) Nanostructured TiAlN coating, (c) Nanostructured AlCrN coating, (d) Conventional TiAlN coating, (e) Conventional AlCrN coating</p>	556
Fig. 7.44	<p>Corrosion rate in mils per year (mpy) for uncoated and coated Superfer 800H superalloy exposed to super-heater of the coal fired boiler environment at 900°C for 1000 hours</p>	557
Fig. 7.45 (a)	<p>Composition image (BSEI) and X-ray mapping of the cross-section of uncoated Superfer 800H superalloy exposed to platen superheater of the coal fired boiler environment at 900°C for 1000 Hrs</p>	559
Fig. 7.45 (b)	<p>Composition image (BSEI) and X-ray mapping of the cross-section of Nanostructured TiAlN coated Superfer 800H superalloy exposed to platen superheater of the coal fired boiler environment at 900°C for 1000 Hrs</p>	560
Fig. 7.45 (c)	<p>Composition image (BSEI) and X-ray mapping of the cross-section of</p>	561

Nanostructured AlCrN coated Superfer 800H superalloy exposed to platen superheater of the coal fired boiler environment at 900°C for 1000 Hrs

- Fig. 7.45 (d)** Composition image (BSEI) and X-ray mapping of the cross-section of conventional TiAlN coated Superfer 800H superalloy exposed to platen superheater of the coal fired boiler environment at 900°C for 1000 Hrs 562
- Fig. 7.45 (e)** Composition image (BSEI) and X-ray mapping of the cross-section of conventional AlCrN coated Superfer 800H superalloy exposed to platen superheater of the coal fired boiler environment at 900°C for 1000 Hrs 563
- Fig. 8.1** Column chart showing cumulative weight gain per unit area (mg/cm^2) for the uncoated and coated alloys' specimens subjected to cyclic oxidation in air at 900°C for 50 cycles; (A) Uncoated, (B) Nanostructured TiAlN coating, (C) Nanostructured AlCrN coating, (D) Conventional TiAlN coating, (E) Conventional AlCrN coating 569
- Fig. 8.2** Column chart showing cumulative weight gain per unit area (mg/cm^2) for the uncoated and coated alloys' specimens exposed to molten salt ($\text{Na}_2\text{SO}_4\text{-60}\%\text{V}_2\text{O}_5$) environment at 900°C for 50 cycles; (A) Uncoated, (B) Nanostructured TiAlN coating, (C) Nanostructured AlCrN coating, (D) Conventional TiAlN coating, (E) Conventional AlCrN coating 571
- Fig. 8.3** Column chart showing the Volume wear rate of uncoated and coated alloys' specimens eroded at normal and oblique impact: (A) Uncoated Alloy, (B) Nanostructured TiAlN coating, (C) Nanostructured AlCrN coating, (D) Conventional TiAlN coating, (E) Conventional AlCrN coating 574
- Fig. 8.4** Column chart showing weight loss per unit area for the uncoated and coated alloys subjected to salt-fog testing (5% NaCl) : (A) Uncoated alloy; (B) Nanostructured TiAlN coating; (C) Nanostructured AlCrN coating 581
- Fig. 8.5** Column chart indicating cumulative weight gain per unit area (mg/cm^2) for the uncoated and coated alloys' specimens exposed to super-heater of the coal fired boiler environment at 900°C for 1000 hours; (A) Uncoated, (B) Nanostructured TiAlN coating, (C) Nanostructured AlCrN coating, (D) Conventional TiAlN coating, (E) Conventional AlCrN coating 582

Fig. 8.6 Column chart indicating the extent of erosion/corrosion for uncoated and coated alloys' specimens exposed to super-heater of the coal fired boiler environment at 900°C for 1000 hours; (A) Uncoated, (B) Nanostructured TiAlN coating, (C) Nanostructured AlCrN coating, (D) Conventional TiAlN coating, (E) Conventional AlCrN coating 584

Fig. 8.7 Column chart indicating corrosion rate (mpy) for the uncoated and coated alloys' specimens exposed to super-heater of the coal fired boiler environment at 900°C for 1000 hours; (A) Uncoated, (B) Nanostructured TiAlN coating, (C) Nanostructured AlCrN coating, (D) Conventional TiAlN coating, (E) Conventional AlCrN coating 585

LIST OF TABLES

Table No.	Particulars	Page No.
Table 2.1	Examples of components subjected to solid particle erosion	40
Table 2.2	Patent search results of topics of interest	90
Table 3.1	Chemical composition (Wt %) and industrial applications of the alloys used	100
Table 3.2	Summary of Nanostructured thin coatings' deposition parameters	102
Table 3.3	Composition, particle size and designation of the coatings powders	104
Table 3.4	Parameters of the argon shrouded plasma spray process	104
Table 3.5	Parameters of the gas nitriding process	106
Table 3.6	Chemical analysis of ash and flue gases inside the boiler	114
Table 3.7	Erosion-Corrosion Test conditions	120
Table 4.1	Microstructural and mechanical properties of nanostructured thin TiAlN and AlCrN coated ASTM-SA210 Grade A-1 boiler steel	129
Table 4.2	Microstructural and mechanical properties of conventional thick TiAlN and AlCrN coated ASTM-SA210 Grade A-1 boiler steel	129
Table 4.3	Parabolic rate constant ' K_p ' values of uncoated and coated ASTM-SA210 Grade A-1 boiler steel subjected to cyclic oxidation in air at 900°C for 50 cycles	151
Table 4.4	Summary of the results obtained for uncoated and coated ASTM-SA210 Grade A-1 boiler steel subjected to cyclic oxidation in air at 900°C for 50 cycles	163
Table 4.5	Parabolic rate constant ' K_p ' values of uncoated and coated ASTM-SA-210 Grade A-1 boiler steel subjected to cyclic oxidation in Na ₂ SO ₄ -60%V ₂ O ₅ (molten salt environment) at 900°C for 50 cycles	170
Table 4.6	Summary of the results obtained for uncoated and coated ASTM-SA-210 Grade A-1 boiler steel subjected to cyclic oxidation in molten salt (Na ₂ SO ₄ -60%V ₂ O ₅) environment at 900°C for 50 cycles	184

Table 4.7	Results of Linear Polarization Resistance Test (LPR) of uncoated and coated ASTM-SA210 Grade A1 boiler steel	204
Table 4.8	Results of Potentiodynamic Polarization Tests of uncoated and coated ASTM-SA210 Grade A-1 boiler steel	205
Table 4.9	Summary of the results obtained for uncoated and coated ASTM-SA210 Grade A-1 boiler steel exposed to super-heater of the coal fired boiler environment at 900°C for 1000 hours	237
Table 5.1	Microstructural and mechanical properties of nanostructured thin TiAlN and AlCrN coated ASTM-SA213-T-11 boiler steel	244
Table 5.2	Microstructural and mechanical properties of conventional thick TiAlN and AlCrN coated ASTM-SA213-T-11 boiler steel	244
Table 5.3	Parabolic rate constant ' K_p ' values of uncoated and coated ASTM-SA213-T-11 boiler steel subjected to cyclic oxidation in air at 900°C for 50 cycles	263
Table 5.4	Summary of the results obtained for uncoated and coated ASTM-SA213-T-11 boiler steel subjected to cyclic oxidation in air at 900°C for 50 cycles	275
Table 5.5	Parabolic rate constant ' K_p ' values of uncoated and coated ASTM-SA213-T-11 boiler steel subjected to cyclic oxidation in Na ₂ SO ₄ -60%V ₂ O ₅ (molten salt) environment at 900°C for 50 cycles	283
Table 5.6	Summary of the results obtained for uncoated and coated ASTM-SA213-T-11 boiler steel subjected to cyclic oxidation in molten salt (Na ₂ SO ₄ -60%V ₂ O ₅) environment at 900°C for 50 cycles	295
Table 5.7	Results of Linear Polarization Resistance Test (LPR) of uncoated and coated ASTM-SA213-T-11 boiler steel	315
Table 5.8	Results of Potentiodynamic Polarization Tests of uncoated and coated ASTM-SA213-T-11 boiler steel	316
Table 5.9	Summary of the results obtained for uncoated and coated ASTM-SA213-T-11 boiler steel exposed to super-heater of the coal fired boiler environment at 900°C for 1000 hours	346
Table 6.1	Microstructural and mechanical properties of nanostructured thin TiAlN and AlCrN coated ASTM-SA213-T-22 boiler steel	353
Table 6.2	Microstructural and mechanical properties of conventional thick TiAlN and AlCrN coated ASTM-SA213-T-22 boiler steel	354

Table 6.3	Parabolic rate constant ' K_p ' values of uncoated and coated ASTM-SA213-T-22 boiler steel subjected to cyclic oxidation in air at 900°C for 50 cycles	372
Table 6.4	Summary of the results obtained for uncoated and coated ASTM-SA213-T-22 boiler steel subjected to cyclic oxidation in air at 900°C for 50 cycles	384
Table 6.5	Parabolic rate constant ' K_p ' values of uncoated and coated ASTM-SA213-T-22 boiler steel subjected to cyclic oxidation in Na ₂ SO ₄ -60%V ₂ O ₅ (molten salt) environment at 900°C for 50 cycles	392
Table 6.6	Summary of the results obtained for uncoated and coated ASTM-SA213-T-22 boiler steel subjected to cyclic oxidation in molten salt (Na ₂ SO ₄ -60%V ₂ O ₅) environment at 900°C for 50 cycles	406
Table 6.7	Results of Linear Polarization Resistance Test (LPR) of uncoated and coated ASTM-SA213-T-22 boiler steel	427
Table 6.8	Results of Potentiodynamic Polarization Tests of uncoated and coated ASTM-SA213-T-22 boiler steel	428
Table 6.9	Summary of the results obtained for uncoated and coated ASTM-SA213-T-22 boiler steel exposed to super-heater of the coal fired boiler environment at 900°C for 1000 hours	459
Table 7.1	Microstructural and mechanical properties of nanostructured thin TiAlN and AlCrN coated Superfer 800H superalloy	460
Table 7.2	Microstructural and mechanical properties of conventional thick TiAlN and AlCrN coated Superfer 800H superalloy	466
Table 7.3	Parabolic rate constant ' K_p ' values of uncoated and coated Superfer800H superalloy subjected to cyclic oxidation in air at 900°C for 50 cycles	485
Table 7.4	Summary of the results obtained for uncoated and coated Superfer 800H superalloy subjected to cyclic oxidation in air at 900°C for 50 cycles	497
Table 7.5	Parabolic rate constant ' K_p ' values of uncoated and coated Superfer 800H superalloy subjected to cyclic oxidation in Na ₂ SO ₄ -60%V ₂ O ₅ molten salt at 900°C for 50 cycles	507
Table 7.6	Summary of the results obtained for uncoated and coated Superfer 800H superalloy subjected to cyclic oxidation in molten salt (Na ₂ SO ₄ -60%V ₂ O ₅) environment at 900°C for 50 cycles	520

Table 7.7	Results of Linear Polarization Resistance Test (LPR) of uncoated and coated Superfer 800H superalloy	539
Table 7.8	Results of Potentiodynamic Polarization Tests of uncoated and coated Superfer 800H superalloy	540
Table 7.9	Summary of the results obtained for uncoated and coated Superfer 800 superalloy exposed to super-heater of the coal fired boiler environment at 900°C for 1000 hours	564
Table 8.1	Results of Linear Polarization Resistance Test (LPR) of bare and coated alloys	578
Table 8.2	Results of Potentiodynamic Polarization Tests of bare and coated alloys	578
Table 8.3 (a)	Performance* of various substrate-coating combinations in different environments	587
Table 8.3 (b)	Performance* of various substrate-coating combinations in different environments	588
Table A-1	Summary of oxidation of Fe, Ni & Co- base alloys in air	598
Table A-2	Summary of oxidation of Fe, Ni & Co- base alloys in Na ₂ SO ₄ , V ₂ O ₅ and Na ₂ SO ₄ - 60% V ₂ O ₅ environments	600
Table A-3	Patent search results for U.S. Patent	604
Table A-4	Thermal expansion coefficients of substrate steels, coatings and oxides	606
Annex. A-5	Certificate of Recognition from Anod Plasma Spray Limited, Kanpur, India	607
Annex. A-6	Certificate of Recognition from GND Thermal Plant, Bathinda, India	608

PATENTS FILED AND RESEARCH PAPERS PUBLISHED/PRESENTED

[A] Patents Filed

Six (06) Patents have been filed through Intellectual Property Rights (IPR) Cell, Indian Institute of Technology Roorkee (I.I.T. Roorkee), Roorkee, India by **Vikas Chawla, S. Prakash, D. Puri and Buta Singh Sidhu.**

[B] Research Papers:

Papers Published:

1. **Vikas Chawla, S. Prakash, Buta Singh, "State of art: Applications of Mechanically Alloyed Nanomaterials: A Review", Materials & Manufacturing Processes, Taylor & Francis Group, Vol: 22, 2007, 469-473.**
2. **Vikas Chawla, D. Puri, S. Prakash, Buta Singh, "Performance of plasma sprayed nanostructured and conventional coatings", Journal of the Australian Ceramic Society, 44[2], 2008, 56-62.**

Papers Communicated:

3. **Vikas Chawla, D. Puri, S. Prakash, Buta Singh, "Hot Corrosion and Erosion problems in coal based power plants in India and possible solutions: a review", Corrosion Science journal.**
4. **Vikas Chawla, D. Puri, S. Prakash, Buta Singh, "Oxidation behavior of nanostructured TiAlN and AlCrN thin coatings on T-22 (ASTM-SA213-T-22) boiler steel", Materials Chemistry and Physics.**
5. **Vikas Chawla, D. Puri, S. Prakash and Buta Singh Sidhu, "Salt Fog Corrosion behavior of nanostructured TiAlN and AlCrN thin coatings on ASTM-SA210 Grade A-1 boiler steel" Materials Chemistry and Physics.**
6. **Vikas Chawla, D. Puri, S. Prakash and Buta Singh Sidhu, "Corrosion behaviour of nanostructured TiAlN and AlCrN coatings on ASTM-SA213-T-11 boiler steel in simulated marine environment" Journal of the Australian Ceramic Society.**

7. **Vikas Chawla, D. Puri, S. Prakash and Buta Singh Sidhu, "Salt fog corrosion behavior of nanostructured TiAlN and AlCrN hard coatings on ASTM-SA213-T-22 boiler steel"** Jordan Journal of Mechanical and Industrial Engineering.
8. **Vikas Chawla, D. Puri, S. Prakash and Buta Singh Sidhu, "Corrosion behaviour of nanostructured TiAlN and AlCrN hard coatings on Superfer 800H superalloy in simulated marine environment"** Journal of Minerals and Materials Characterization and Engineering.
9. **Vikas Chawla, S. Prakash, D. Puri and Buta Singh Sidhu, "Structural characterization and corrosion behavior of nanostructured TiAlN and AlCrN thin coatings in the 3 wt% NaCl solution"** Materials Chemistry and Physics.
10. **Vikas Chawla, D. Puri, S. Prakash, and Buta Singh Sidhu, "Investigation of properties and corrosion behavior of hard TiAlN and AlCrN PVD thin coatings in the 3 wt% NaCl solution"** Journal of the Australian Ceramic Society.
11. **Vikas Chawla, D. Puri, S. Prakash, and Buta Singh Sidhu, "Microstructure and corrosion resistance of PAPVD TiAlN and AlCrN thin coatings on ASTM-SA213-T-22 steel"** Jordan Journal of Mechanical and Industrial Engineering.
12. **Vikas Chawla, D. Puri, S. Prakash and Buta Singh Sidhu, "Characterization and comparison of corrosion behavior of nanostructured TiAlN and AlCrN coatings"** Journal of Minerals and Materials Characterization and Engineering.

[C] Papers in Conferences

International Conferences:

13. **Vikas Chawla, D. Puri, S. Prakash, Buta Singh, "Plasma Sprayed Coatings with Nanostructured materials: A Review"**, International Conference and Exhibition, "Materials and Austceram", organized by the Australian Ceramic society and Materials Australia, 4th -6th July, 2007, Sydney, Australia.
14. **Vikas Chawla, D. Puri, S. Prakash, Buta Singh, Manoj Singla, "State of art: Hot Corrosion"**, Global Conference on "Production & Industrial Engineering (CPIE-2007)", organized by Dr. B.R. Ambedkar National Institute of Technology, Jalandhar, Punjab, 22-24th March, 2007.
15. **Vikas Chawla, D. Puri, S. Prakash, Buta Singh, "Plasma Sprayed Coatings for**

protection against Hot Corrosion”, International Conference on “Advances in Mechanical Engineering (AME 2006)”, organized by Baba Banda Singh Bahadur College of Engineering, Fatehgarh Sahib, Punjab, 1-3rd December, 2006.

16. **Vikas Chawla, D.Puri, S.Prakash and Buta Singh, “Nanomaterials: a Review”, International Conference on “Advances in Mechanical Engineering (AME 2006)”, organized by Baba Banda Singh Bahadur College of Engineering, Fatehgarh Sahib, Punjab, 1-3rd December, 2006.**

17. **Vikas Chawla, Buta Singh, S. Prakash, “Applications of Mechanical Alloyed Nanomaterials”, International Conference organized by Metallurgy Department, Indian Institute of Technology Kharagpur, 3-5th February, 2006.**

National Conferences:

18. **Vikas Chawla, D. Puri, S. Prakash, Buta Singh and Manoj Singla, “A survey of the studies on hard TiAlN and AlCrN coatings”, National Conference on advances in materials and manufacturing technology (AMMT-2007), organized by mechanical engineering department, Punjab Engineering College, Chandigarh on 21-22 September, 2007.**

19. **Vikas Chawla, D.Puri, S.Prakash, and Buta Singh, “How to get nanostructured materials”, National Conference on “Advancement & Futuristic Trends in Mechanical & Materials Engineering”, organized by G.Z.S. College of Engineering & Technology, Bathinda, Punjab, 13-14th October 2006.**

20. **Vikas Chawla, D.Puri, S. Prakash, Buta Singh and Manoj Singla, “ Corrosion in Thermal Power Plants and Preventive Measures: a review”, National Conference on “Advancement & Futuristic Trends in Mechanical & Materials Engineering”, organized by G.Z.S. College of Engineering & Technology, Bathinda, Punjab, 13-14th October 2006.**

[D] Recognition of Work From Industries

1. Anod Plasma Spray Ltd., Kanpur, India (Annexure A.5)
2. Guru Nanak Dev Thermal Plant (GNDTP), Bathinda, India (Annexure A.6)

ABBREVIATIONS

AFM	Atomic Force Microscopy
BSEI	Back Scattered Electron Image
CLA	Centre Line Average Method
EDAX	Energy Dispersive X-ray Analysis
SEM	Scanning Electron Microscopy
GrA1	SA-210-Grade A-1 Boiler Steel
hr	Hour
i_{corr}	Corrosion Current Density
K_p	Parabolic rate constant
l/min	Litre per Minute
LPR	Linear Polarization Resistance
m.p.	Melting Point
min	Minute
mpy	Mils per year
P (%)	Protective Efficiency
RCS	Rapid Coating System
R_p	Linear Polarization Resistance
S.F800H	Superfer 800H Superalloy
T-11	SA-213-T11 Boiler Steel
T-22	SA-213-T22 Boiler Steel
Wt%	Weight percentage
Wt. Gain	Weight Gain
XRD	X-ray Diffraction

Chapter 1

INTRODUCTION

Corrosion is the destruction or deterioration of a material over time due to its reaction with environment to form oxides or sulphides, or other metallic compounds, generally considered to be ores, as material's compositional elements have a natural tendency to return to their most thermodynamically stable state. It is said that corrosion never stops. Corrosion is both costly and dangerous. Corrosion causes plant shut downs, waste of valuable resources, loss or contamination of products, reduction in efficiency and costly maintenance. In USA, the loss due to corrosion is around 4 per cent of GDP. In India, the corrosion losses will be around Rs. 1 lakh crore per annum. Around 80 per cent of the unscheduled shutdowns and breakdowns in industries are due to corrosion and process fouling. Out of the total loss due to corrosion, 25 per cent of loss can be easily saved with pro-active approach and protecting the system by applying protective coatings (Madhu Chittora, 2008). Apart from monetary costs it diminishes our natural resources. From human safety point of view, corrosion is considered more disastrous, as premature failure of bridges, structures or operating equipments can result in human injury or even loss of life.

Metals and alloys get oxidized when they are heated to elevated temperatures in air or highly oxidizing environments, such as a combustion gas with excess of air or oxygen. They often rely on the oxidation reaction to develop a protective oxide scale to resist corrosion attack, such as sulphidation, carburisation, ash/salt deposit corrosion etc. That is why oxidation is considered to be the most important high-temperature corrosion reaction. Further the rate of oxidation for metals and alloys increases with increasing temperature (Lai, 1990). Hot corrosion is the degradation of materials caused by the presence of a deposit of salt or ash in a general sense. In a more restricted sense, hot corrosion is the degradation of metals and alloys owing to oxidation process, which are affected by a liquid salt deposit. Eliaz et al. (2002) have defined the hot corrosion as an accelerated corrosion, resulting from the presence of salt contaminants such as Na_2SO_4 , NaCl , and V_2O_5 that combine to form molten deposits, which damage the protective

surface oxides. In hot corrosion, metals and alloys are subject to degradation at much higher rates than in gaseous oxidation, with a porous, non-protective oxide scale formed at their surface, and sulphides in the substrate.

Hot corrosion was first recognized as a serious problem in 1940s in connection with the degradation of fireside boiler tubes in coal-fired steam generating plants. Since then the problem has been observed in boilers, internal combustion engines, gas turbines, fluidized bed combustion and industrial waste incinerators (Khanna and Jha, 1998). Hot corrosion became a topic of importance and popular interest in the late 60s as gas turbine engines of military aircraft suffered severe corrosion during the operation over sea water in the Vietnam War. Metallographic inspection of failed parts often showed presence of sulphides of nickel and chromium, so the mechanism was initially called as “sulphidation” (Rapp, 1986 and 2002).

Hot corrosion is one of the serious problems for high temperature application, such as aircraft, marine, utility, industrial and land-base gas turbines, boilers, oil refinery furnace and engines. The use of wide range of fuels from natural gas, kerosene, diesel oils, residual oils and gaseous fuels coupled with increased operating temperatures cause hot corrosion (Nicholls, 2002). Higher corrosion rates have occurred due to molten salt deposits even when bio-fuel fired boiler has been operated with steam temperature of 530°C (Salmenoja et al., 1996). On the other hand, in order to meet the demand for more electricity, the operating temperature and pressure of pulverized coal-fired boilers have to be increased (Blum, 1997). As the lower steam temperatures drastically decrease the efficiency of electricity production. The combination of such high-temperatures with contaminants of environment and low grade fuels necessitate special attentions to the phenomenon of hot corrosion.

In energy generation processes the mechanism of hot corrosion is dependent on the formation of a liquid phase that is predominantly Na_2SO_4 or K_2SO_4 . The sulphur released from the coal, forms SO_2 with a minor amount of SO_3 and reacts with the volatilised alkalis to form Na_2SO_4 vapour, which then condenses together with fly ash on the super-heater and reheater tubes in the boiler. Such a liquid phase dissolves the chromium oxide in the protective coating, which allows the base metal to react with sulphate ions to form sulphide ions and non-protective oxides (Natesan, 1976 and Rapp et al., 1981). Due to depletion of high-grade fuels and for economic reasons use

of residual fuel oil in these systems is well known. The damage by hot corrosion is likely to increase by the use of these low quality fuels and higher temperature to increase the efficiency of boilers. According to Khanna (2002) and Marriott (1990) the hot corrosion plays an important role in determining the life of boiler components.

Also, erosion-corrosion by solid particles in gaseous environments at elevated temperatures and hence wastage of alloys, is a serious problem in many industrial processes (Stack et al., 1993 and Stack et al., 1995). Erosion-corrosion of materials occurs in environments as diverse as catalytic cracking systems in oil and gas separation, combined-cycle coal conversion systems such as pressurized fluidized bed combustion, and on the turbine blades of jet engines where erosive component may be caused by the ingestion of particulate material or the accumulation of such material as a result of the corrosion process (Stack et al., 1993). Small, solid particles propelled by generally oxidizing gases in various fluid flow patterns constitute the primary operating environments in the combustion regions of energy generating boilers operating on such fossil fuels as coal and various kinds of biomass (Levy, 1993). Unacceptable levels of surface degradation of metal containment walls and heat exchanger tubing by a combined erosion-corrosion mechanism have been experienced in some boilers, particularly fluidized bed combustors (FBC). The extent of such degradation has varied considerably, both between different boilers and within the same boiler operating on different feedstocks (Levy, 1993).

Coal gasification systems operate at temperature of up to 2000 F (1093°C) and at a pressure of up to 100 atm depending on the specific process and the product, coal gas generates the greatest problems (Rapp and Goto, 1981). The coal used in Indian power stations has large amounts of ash (about 50%), which contain abrasive mineral species such as hard quartz (up to 15%), which increase the erosion propensity of coal (Stringer, 1997 and Wells et al., 2005). Coal contains a wide variety of minerals, but it is generally acknowledged that only those minerals that are harder than steel contribute significantly to the abrasive and erosive behavior of the coal particles (Wells et al., 2005). The vast technical literature available is evidence that corrosion and deposits on the fireside of boiler surfaces or in gas turbines represent important problems (Landry et al., 1959). Erosive, high-temperature wear of heat exchanger tubes and other structural materials in coal-fired boilers has become a key material issue in the design and

operation of thermal power plants and is recognized as being one of the main causes of downtime in these installations, which could account for 50–75% of their total arrest time (Hidalgo et al., 2001A and Hidalgo et al., 2001B). Maintenance costs for replacing broken tubes in the same installations are also very high, and can be estimated at up to 54% of the total production costs (Hidalgo et al., 2001B).

High-temperature oxidation and erosion caused by the impact of fly ashes and unburnt carbon particles are the main problems to solve in these applications, especially in those regions where the component surface temperature is above 873 K. Therefore, the development of wear and high-temperature oxidation protection systems in industrial boilers is a very important topic from both engineering and an economic perspective (Hidalgo et al., 2001A and Hidalgo et al., 2001B). A number of countermeasures are currently in use or under investigation to combat different types of corrosion. While selecting a particular corrosion control strategy it is always emphasized that the protection system must be practical, reliable and economically viable. So far as the high-temperature oxidation and erosion problem of metals and alloys is concerned, it may be tackled by controlling the process parameters, use of inhibitors, designing a suitable industrial alloy, protective coatings and superficially applied oxides as per requirements in the given environment.

Controlling the various process parameters (air/fuel ratio, temperature, pressure etc.) of the boiler and gas turbine is useful to some extent to combat corrosion, but these parameters can be controlled only within certain limits. There are numerous inhibitors commercially available that are intended to reduce the severity of oil ash corrosion, particularly Mg and Mn-based inhibitors, which have proven to be effective (Paul and Seeley, 1991). Investigations in the area of inhibitors like MgO, CeO₂, CaO, MnO₂, etc. have already been done in the department and the decrease in the extent of hot corrosion in the most aggressive environment of Na₂SO₄-60%V₂O₅ at 900⁰C has been achieved. But the major problem being faced is how to inject these inhibitors along with the fuel in the combustion chamber in actual industrial environment (Tiwari and Prakash, 1998 and Gitanjaly et al., 2002).

Material selection, preparation and fabrication are therefore of paramount importance for the efficient functioning of the system components. Present materials being capable of resisting erosive and corrosive environments are highly alloyed, and

thus expensive. In search for cost-effective solutions for erosion-corrosion problems, the effective method of erosion-corrosion prevention is to coat the alloy with a protective layer, which has been used in the current investigation. This is the preferred approach and various coatings like thermal sprayed coatings have become attractive (Uusitalo et al., 2002). Modern design philosophy is based on the use of a substrate to provide the necessary mechanical strength properties and a thin coating to inhibit oxidation and other corrosive degradation processes (Ananthapadmanabhan et al., 1991). It is now generally accepted practice to apply coatings to components in fossil fuel energy generation processes to provide thermal insulation, corrosion and wear resistance and in chemical process plants or boilers to protect the surface of structural steels against surface degradation processes such as wear, oxidation, corrosion and erosion (Wang et al., 1992).

Coating technology is one of the more rapidly growing technologies in the field of materials (Chawla et al., 2007B). Recent studies show that 80% of the total cost for the protection of metals is related to coating applications (Fedrizzi et al., 2004). Coatings provide a way of extending the limits of the use of the materials at the upper end of performance capabilities, by allowing the mechanical properties of the substrate materials to be maintained while protecting against wear, oxidation and corrosion (Singh et al., 2005). According to DeMasi-Marcin and Gupta (1994), physical vapor deposition (PVD) and plasma spray (a thermal spray process) have been reported to be two major coating processing technologies which are used worldwide. The PVD processes have been particularly successful in improving mechanical properties such as wear, friction, and hardness (Pierson, 1987). Their use as corrosion-resistant coatings is also becoming widespread. Among the thermal spray coating processes, plasma spraying is reported to be versatile technology that has been successful as a reliable cost-effective solution for many industrial problems (Fauchais et al., 1997).

In recent years, corrosion performance of nanostructured materials/coatings is a hot topic in corrosion field. As reported by Chawla et al. (2008), in the past decade, attractive properties associated with a nanostructure have been documented for bulk materials, where most of the research in the field of nanomaterials has been focused. Nanostructured materials indeed behave differently than their microscopic counterparts because their characteristic sizes are smaller than the characteristic length scales of

physical phenomenon occurring in bulk materials (Chawla et al., 2007A). In many tribological applications, hard coatings of metal nitrides are now commonly used (Bertrand. et al., 2000). The major properties required for such coatings are hardness and wear resistance. However, because of severe operating conditions, there is a need to combine mechanical features with corrosion resistance properties. In the past years, hard protective TiAlN coatings and AlCrN coatings were widely used for wear resistant properties. Recently these coatings are gaining importance for high temperature wear, corrosion and oxidation resistance applications (Kalss et al., 2006, Fujita, 2005).

It is important to understand the nature of all types of environmental degradation of metals and alloys as vividly as possible so that preventive measures against metal loss and failure can be economically devised to ensure safety and reliability in the use of metallic components (Sidhu and Prakash, 2006). Uusitalo et al. (2003) has also suggested that there is a need to investigate the high temperature corrosion behavior of thermal spray coated materials in different aggressive environments. Mostly Cr and Al are added to enhance the oxidation resistance of alloys. Besides the oxidation resistance at high temperature, the resistance to pitting corrosion at normal temperature is another important performance of these materials (Liu et al., 2007). In many applications, the coated parts are frequently exposed to an aggressive working environment, for instance a Cl⁻ containing corrosive medium which has strong effects in promoting localized corrosion, particularly in marine environment (Jehn and Baumgartner, 1992). The chloride-rich seawater is a harsh environment that can attack the materials by causing pitting and crevice corrosion (Dobrzanski et al., 2007).

Little work has been published on high temperature erosion/corrosion behavior of nanostructured and conventional hard metal nitride coatings to the best of knowledge of the author. The present study has been performed to evaluate the behavior of the nanostructured and conventional metal nitride coatings when exposed to high temperature oxidation in air, molten salt (Na₂SO₄-60%V₂O₅) environment, in actual degrading conditions prevailing in a coal fired boiler of a thermal plant, high temperature solid particle erosion and simulated marine environment. Behavior of these coatings under different degrading environments once evaluated will be helpful in choosing the suitable coating for the given environment.

Chapter 2

LITERATURE REVIEW

Literature review relevant to the research has been divided into four phases. First phase contains a comprehensive review of the existing literature on high temperature oxidation, hot corrosion, erosion-corrosion and marine environment corrosion along with existing characteristics and mechanisms. In the second phase, critical review regarding the protective coatings and coating deposition processes have been described. The existing related patents have been reviewed in the third phase of this chapter. The third phase is related to the problem formulation, scope and objectives of the present research work.

2.1 HIGH TEMPERATURE PROCESSES AND MATERIALS

The attainment of high temperatures has been important in the development of civilization for many countries (Khanna, 2002). In order to meet the demand for more electricity, the operating temperature and pressure of pulverized coal-fired boilers have to be increased (Blum, 1997). As the lower steam temperatures drastically decrease the efficiency of electricity production. Thus, structural materials in many front-line high technology areas have to operate under extreme conditions of temperature, pressure and corrosive environment (Ananthapadmanabhan et al., 1991). Materials degradation at high temperatures is a serious problem in several high tech industries. Gas turbines in aircraft, fossil fueled power plants, refineries, petrochemical industries and heating elements for high temperature furnaces are some examples where corrosion limits the use or reduces the life of these components, considerably affecting the efficiency (Khanna, 2002).

World-wide, the majority of electricity is generated in coal-fired thermal power plants, in which the coal is burned to boil water (Stringer, 1997). Coal is a complex and relatively dirty fuel that contains varying amount of sulfur and a substantial fraction of non combustible mineral constituents, commonly called ash (Natesan, 1997). The coal used in Indian power stations has large amounts of ash (about 50%), which contain abrasive mineral species such as hard quartz (up to 15%), which increase the erosion propensity of coal

(Krishnamoorthy, 1993). The vast technical literature available is evidence that corrosion and deposits on the fireside of boiler tube surfaces or in gas turbines represent important problems.

An increasing demand for more electricity, reduced plant emissions and greater efficiency is forcing power plants to increase the steam temperature and pressure of the boilers. Ultra-supercritical steam conditions greater than 31 MPa and 600°C have been adopted and the thermal efficiency up to 45% have been obtained for the pulverized coal-fired boilers. Efforts are being made to further improve the efficiency of the boilers. Therefore, superheater and re-heater materials which have high creep rupture strength and high corrosion resistance at temperatures of about 750°C and above are required (Blum, 1997; Evans et al., 2004).

Alloys that are used for structural components at higher temperatures in corrosive environments are generally austenitic and ferritic stainless steels and superalloys based on nickel, iron, and cobalt. Superalloys serve in a wide variety of environments where oxygen, sulphur, sodium, vanadium, halogens, and nitrogen are the aggressive reactive species most frequently encountered (Stroosnijder et al., 1994). Iron- and nickel- base superalloys are the commercial alloys commonly used for the high temperature applications. The superior mechanical performance and good corrosion resistance of the superalloys, especially the nickel-base superalloys at high temperature make them favourites as base materials for hot components (such as blades or vanes) in industrial gas turbines and other energy conversion systems. The presence of sufficient amount of aluminum and chromium concentrations permit the selective oxidation of chromium and aluminum in the nickel base superalloy enable them to act as alumina and chromia scale former.

Several very important engineering systems operating at high-temperatures (650-1100°C) involve contact of metallic or ceramic materials with the gaseous combustion products or other oxidizing gases containing inorganic impurities, e.g. steam generators, incinerators, gas turbines, and numerous petrochemical process vessels. As the gases are cooled, fused salt deposits are formed on the hardware (Rapp, 1990). Metals and alloys may experience accelerated oxidation when their surfaces are coated by a thin film of fused salt in

an oxidizing gas. This mode of attack is called hot corrosion. High temperature degradation is one of the main failure modes of hot-section components in the gas turbines. Erosive, high-temperature wear of heat exchanger tubes and other structural materials in coal-fired boilers has become a key material issue in the design and operation of thermal power plants and is recognized as being one of the main causes of downtime in these installations, which could account for 50–75% of their total arrest time (Hidalgo et al., 2001A and Hidalgo et al., 2001B). Maintenance costs for replacing broken tubes in the same installations are also very high, and can be estimated at up to 54% of the total production costs (Hidalgo et al., 2001B).

High temperature oxidation and erosion by the impact of fly ashes and unburned carbon particles are the main problems to be solved in these applications. Therefore, the development of wear and high temperature oxidation protection systems in industrial boilers is a very important topic from both engineering and an economic perspective (Hidalgo, 2001A). Material selection, preparation and fabrication are therefore of paramount importance for the efficient functioning of the system components. Modern design philosophy is based on the use of a substrate to provide the necessary mechanical strength properties and a thin coating to inhibit oxidation and other corrosive degradation processes (Ananthapadmanabhan et al., 1991). So, it is now generally accepted practice to apply coatings to components in fossil fuel energy generation processes to provide thermal insulation, corrosion and wear resistance and in chemical process plants or boilers to protect the surface of structural steels against these surface degradation processes (Wang et al., 1992).

2.2 HIGH TEMPERATURE OXIDATION

Almost all the metals are found in nature in the form of an oxide, sulfide, or some other metal compound. Thus all the metals that are derived from ores, when exposed to air at room temperature, form surface compounds, which may be oxides or other compounds, depending upon the contamination in air (Budinski , 1979 & Khanna, 2002). It takes from a few hours to a few days to form this oxide layer on the surface, depending upon the type of

environment. The rate of the reaction of oxide formation increases many folds, if the sample is exposed to the same atmosphere but at a temperature much higher than the room temperature.

An oxidation reaction between the oxygen gas (O_2) and a metal (M) can be written as:



In the simplest form, oxidation of metal appears as the addition of oxygen to the metal surface. However, the oxidation behavior of metals depends upon various factors and the reaction mechanism involved may prove to be complex (Khanna, 2002).

Thermodynamically, an oxide is likely to form on a metal surface when the oxygen potential in the environment is greater than the oxygen partial pressure in equilibrium with the oxide (Kofstad, 1966). The oxide layer growth may depend upon the accessibility of the metal surface to the oxidizing gas, or on the diffusion of ions or/and electrons (Grainger, 1989). The initial step in the metal-oxygen reaction involves the adsorption of gas on the metal surface. As the reaction proceeds, oxygen may dissolve in the metal, resulting in the formation of oxide layer or separate oxide nuclei on the metal surface (Kofstad, 1966).

If the compound formed on the surface is volatile or continually falls off, the corrosion or oxidation will proceed rapidly, the metal is consumed continuously and the material ultimately fails (Grainger, 1989). However, if the compound formed on the surface of metal is adherent to the surface, it can give protection by acting as a barrier that separates the metal from the gas. Further oxidation may proceed only through a solid-state diffusion of the reactants through the film (Kofstad, 1966). The metal ions and /or oxygen may penetrate across the barrier layer and combine chemically to form new oxide at the scale/gas or scale/metal interface (Stott, 1998). In the first case, Fig.2.1 (A), metal ions and electrons diffuses faster than oxygen ions, which causes the oxide to grow at the outer surface. This mechanism is seen in iron, copper, chromium and cobalt. In the second, Fig.2.1 (B), oxygen ions and electron diffuses through the existing oxide layer faster than metal ions. This causes the oxide layer to grow at the metal/oxide interface, a situation seen in titanium and zirconium (Grainger, 1989).

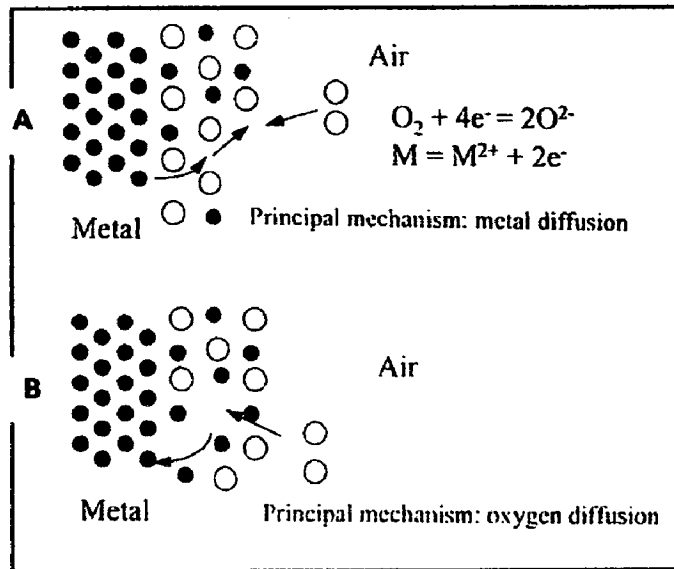


Fig: 2.1 Schematic illustrations of the mechanisms of oxidation at the surface of a metal (Grainger et al, 1989)

2.2.1 Mechanisms of High Temperature Oxidation

In actual practice, alloys, rather than pure metals are used in various high temperature applications. The oxidation behavior of metals is generally modified by the alloying addition to renders them suitable for a particular high temperature application (Khanna, 2002). The rate of oxidation at high temperature depends on the oxide layer that forms on the surface of metal (Chawla et al., 2007C).

Wagner has explained the oxidation behavior for an A-B alloy that is forming both AO and BO oxides (Samuel, 1987). When oxides of metals form, their relative position and distribution depends on the thermodynamic properties of the oxides and the alloy, the diffusion processes and reaction mechanisms. The first situation involves immiscible oxides with the more stable oxide growing slowly. With both AO and BO stable but with rapid growth of AO and slow growth of BO, the more stable BO may nucleate first, but gradually becomes over-whelmed and surrounded by fast-growing AO. Figure 2.2 (a) and (b) illustrate the situation.

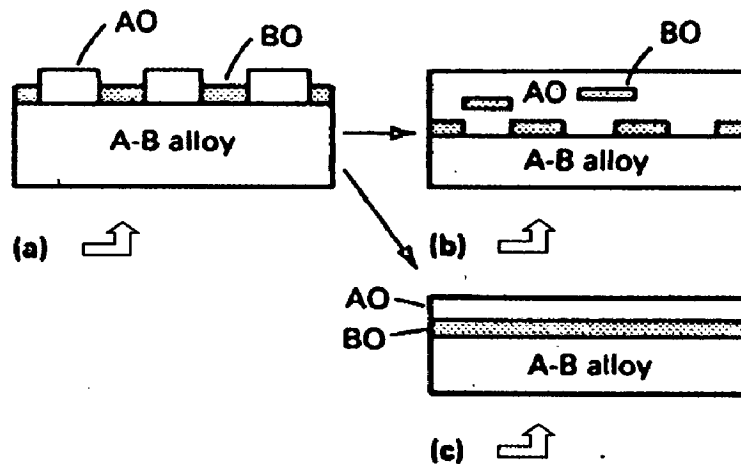
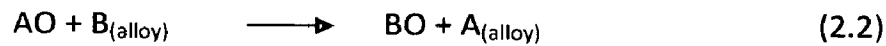


Fig: 2.2 Mechanisms of oxidation at the surface of a metal (Samuel, 1987)

If diffusion in the alloy is rapid, the oxidation proceeds to form an *AO* scale with *BO* islands scattered through it. However, if diffusion in the alloy is slow, the metal becomes depleted of *A* near the metal/oxide interface, while the growth of *BO* continues until it forms a complete layer, undercutting the *AO* (Fig. 2.2 c). Pockets of *AO* at the metal/oxide interface will gradually be eliminated by the displacement reaction:



Because *BO* is thermodynamically more stable than *AO*, this reaction continues even if the oxygen supply is cut off. The second situation involves two oxides that are partially miscible. For alloys rich in *A*, an *AO* scale will form with some *B* ions dissolved sub-stitutionally in the *AO* structure. For alloys rich in *B*, a *BO* layer first forms. If *B* ions diffuse through the scale faster than '*A*' ions, the concentration of *A* ultimately builds up in the scale close to the metal/oxide interface. An *AO* layer then forms underneath the *BO*. On the other hand, if *A* ions diffuses through the original *BO* scale more quickly than *B* ions, the *AO* layer eventually forms on top of the *BO* layer. In addition, if '*A*' ions diffuse rapidly through *BO* and *B* ions diffuse rapidly through *AO*, alternate layers of *BO/AO/BO/AO* may even form. Further, the spinels, which are double oxides of a metal with +2 valence and a metal with +3 valence, having the general formula $MO.Me_2O_3$ and also having the crystal structure of the mineral spinel ($MgO-Al_2O_3$), may form.

The establishment of oxide layer on an alloy takes place by nucleation and growth process (Stott, 1998). Small impinging nuclei of all the thermodynamically stable oxides develop on the surface of the component, when it is exposed to an oxygen rich gas. These initial nuclei of oxide coalesce rapidly to give a complete layer. During this initial or transient stage, the rate of oxidation is rapid; all the elements in the alloy oxidize and the amounts of the various oxides in the layer are approximately proportional to the concentration of the elements in the alloy. Once the transient oxide layer has been established, it continues to grow following diffusion of metal ions to the scale/gas interface or oxygen to the scale/alloy interface.

Further, from the standpoint of oxidation of engineering alloys, the parabolic law is of great importance. As per this law, the oxide growth occurs with a continuing decreasing oxidation rate (Khanna, 2002). This is represented as:

$$x^2 = K_p t \quad (2.3)$$

Where x is the scale thickness in dimensions of length, t is the time and K_p the parabolic growth rate constant in dimensions of length²/time. Most of the metals and engineering alloys follow parabolic kinetics at elevated temperature. However, minor deviations from the parabolic behavior are often observed (Doychak, 1995). According to Smialek (2001) the most of the oxide scales have a very fine grain size, often submicron during the first few hours of oxidation. Since bulk diffusion in many stoichiometric oxides is relatively slow, short-circuit processes such as grain boundary diffusion have a considerable effect on the net growth rate and may cause deviations from true parabolic kinetics. In addition to scale growth kinetics, scale adhesion in cyclic exposures also must be considered for continuous protection to prevent rapid metal consumption upon re-oxidation.

Li et al. (2003) have reported that although considerable insights has been accumulated on mechanisms of high temperature oxidation, from both engineering and more fundamental studies, reaction mechanisms are often not fully understood. Oxidation at high temperature involves the oxidation of selective elements, formation of oxide scales and internal oxidation (Hussain et al., 1994). The phenomenon is too complex to be understood in simple terms of diffusion processes. Authors further said that knowledge of

reaction kinetics and the nature of the surface scales formed during oxidation are important for assessing the degradation characteristics of materials in high temperature applications.

Plenty of literature is available on high temperature oxidation of metals and alloys, which is not possible to review in a sensible manner in such a short space. As an alternative it is proposed to overview the high temperature phenomenon in context with some current studies conducted by various researchers in the field, which may form basis for the formulation of the problem.

2.2.2 Oxidation Behavior of Iron-Based Alloys

Carbon steel is probably the most widely used engineering material. It is extensively used for high temperature application in power plants, chemical, and petrochemical industries, oil refining and in many other industries (Khanna, 2002). Boiler tubes in power plants, reactors vessels in process industries, heat treating fixtures and exhaust train piping are examples of a few components made out of mild steel. The oxidation behavior of mild steels is very similar to that of iron. Carbon steel have negligible oxidation in air up to temperatures of about 250-300°C. Oxidation attack is less than about 20 mg/cm² up to 450°C. Above this temperature, the oxidation rate increases rapidly especially above 600°C. High Strength Low Alloy steels which contain minor additions of alloying elements, such as manganese, silicon, chromium and nickel have lower oxidation rate.

Wright (1987) reported alloys intended for high temperature applications are designed to have the capability of forming protective oxide scale. Figure 2.3 schematically represents the oxidation rate of iron-chromium alloys (1000°C, in 0.13 atm oxygen) and depicts the types of oxide scale associated with various alloy types. A useful concept in assessing the potential high-temperature oxidation behavior of an alloy is that of the reservoir of scale-forming element contained by the alloy in excess of the minimum level (around 20 wt% for iron-chromium alloys at 1000°C, according to Fig.2.3). The more likely the service conditions are to cause repeated loss of the protective oxide scale, the greater the reservoir of scale-forming element required in the alloy for continued protection.

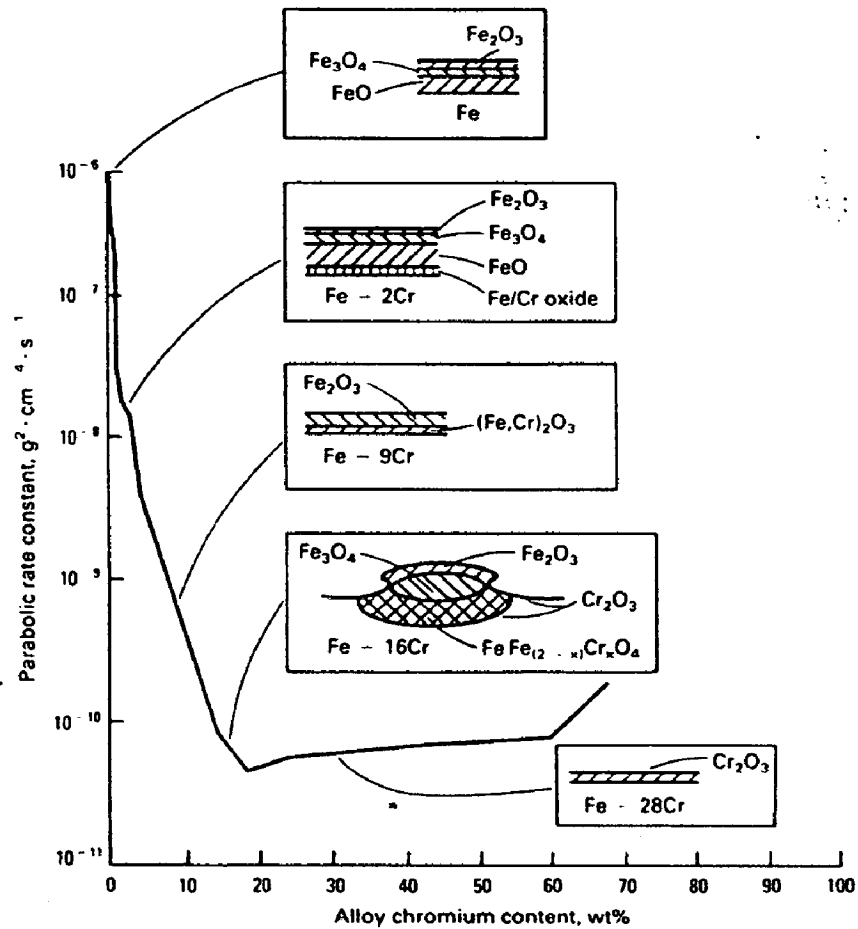


Fig.2.3 Schematic of the variation with alloy chromium content of the oxidation rate and oxide scale structure, based on isothermal studies at 1000°C in 0.13 atm oxygen (Wright, 1987)

Chromium-molybdenum steels are considered to be a better choice for moderate temperature applications. The presence of Mo enhances creep strength at these temperatures, while chromium helps in forming a chromium-rich scale which protects the steel from further oxidation. In case of stainless steel (containing more than 12% Cr), corrosion resistance is imparted by the formation of a protective chromia layer on the surface.

Some of the high temperature oxidation studies conducted by various investigators in air on iron-based alloys are summarized in Appendix A.1.

2.2.3 Oxidation Behavior of Superalloys

Superalloys have been developed for gas turbine engines, which require both superior high temperature strength and strong oxidation resistance (Khanna, 2002). Applications of some of these alloys have now been extended to other industries such as heat treating, chemical processing, petrochemical, oil refining and power generation.

The superalloys have been developed to achieve oxidation resistance by utilizing the concept of selective oxidation. The selective oxidation approach to obtain oxidation resistance in superalloys consists of oxidizing essentially only one element in the superalloy and relying upon this element's oxide for protection. For effective protection, it is anticipated that the oxide should cover the whole surface of the alloy and it must be an oxide through which the diffusion of the reactants takes place at comparatively slow rate. Nickel-, cobalt- and iron-base superalloys make use of the selective oxidation of the aluminum or chromium to develop oxidation resistance (Pettit and Meier, 1985). Further, Pettit and Meier (1985) have reported that the selective oxidation processes are affected by a number of factors such as alloy composition, alloy surface conditions, gas environment and cracking of the oxide scale. Cyclic oxidation conditions whereby the oxide scales crack and spall, as well as certain phases present in the superalloys, both affect the capability to selectively oxidize aluminum or chromium in the superalloys. Some of the high temperature oxidation studies conducted by various investigators in air on Ni, Co and Fe-based superalloys are summarized in Appendix A.1.

2.3 HOT CORROSION

According to Eliaz et al. (2002) and Khanna et al. (1998) hot corrosion is accelerated corrosion of materials at high temperatures, resulting from the presence of salt contaminants such as Na_2SO_4 , NaCl and V_2O_5 that combine to form molten deposits, which damage the protective surface oxides. It is also called deposit corrosion, as the salts first deposit on the surface and then change to liquid melt, either of their own or by forming complex mixtures of salts (Khanna, 2002).

Hot corrosion is observed in boilers, incinerators, diesel engines, mufflers of internal combustion engines and gas turbines. During the combustion stage in heat engines, particularly in gas turbines, sodium and sulphur impurities present either in fuel or in combustion air, react to form sodium sulphate (Na_2SO_4). If the concentration of the sulphate exceeds the saturation vapour pressure at the operating metal temperature for turbine blades and vanes (700-1100°C), then the deposition of the Na_2SO_4 will occur on the surface of these components (Khanna et al., 1998). At higher temperatures the deposits of Na_2SO_4 are molten (m.p.=884°C) and can cause accelerated attack of the Ni, Fe and Co- base superalloys.

Hot corrosion is often divided into two forms of attacks: Type-I (High temperature hot corrosion) and Type-II (Low temperature hot corrosion), as reported by Eliaz et al. (2002) and Khanna et al. (1998). Various parameters may affect the development of these two forms, including alloy composition and thermo-mechanical condition, contaminant composition and flux rate, temperature and temperature cycles, gas composition and velocity, and erosion processes (Eliaz et al., 2002 and Pettit et al., 1987).

2.3.1 High Temperature (Type-I) Hot Corrosion (HTHC)

Type I hot corrosion is observed mainly within the temperature range 850-950°C, when the salt deposit on the metal or alloy is in liquid state (Khanna, 2002, Hancock, 1987, Wright, 1987 and Eliaz et al., 2002). Type-I hot corrosion involves the transport of sulphur from a sulphatic deposit (generally Na_2SO_4) across a preformed oxide into the metallic material with the formation of the most stable sulphides. The dominant salt in Type-I hot corrosion is Na_2SO_4 due to its high thermodynamic stability. Other impurities present either in the fuel or in the air, such as vanadium, phosphorous, lead, and chlorides, can combine with Na_2SO_4 to form compounds with lower melting points, thus broadening the range of attack. For example, Na_2SO_4 (M.P. 884°C) when combined with V_2O_5 (M.P. 670°C), a eutectic is formed with a melting point of 550°C, thus providing a very aggressing environment (Tiwari, 1997). The macroscopic appearance of HTHC is characterized in many cases by severe peeling of the metal and by significant color changes. For instance, greenish tone appears

on the surface of metals and alloys due to the formation of NiO in the area of accelerated attack. Microscopically, the morphology of Type-I is characterized by a sulphidised and depleted region beneath the porous, non-protective, scale. The reaction products frequently exhibit oxide precipitates dispersed in the salt film (Rapp, 1986).

2.3.2 Low Temperature (Type-II) Hot Corrosion (LTHC)

Type-II hot corrosion usually occurs well below the melting point of Na_2SO_4 . The reaction product morphology is characterized by a non-uniform attack in the form of pits, with only little sulphide formation close to the alloy/scale interface and little depletion of Cr or Al in the alloy substrate (Rapp and Zhang, 1994). This form of hot corrosion is observed mainly within the temperature range 650-800°C (Eliaz et al., 2002). Wright (1987) reported that a high partial pressure of SO_3 in the gaseous phase is required in the low temperature hot corrosion reactions to occur, in contrary to High temperature hot corrosion. The localized nature of attack is related to localized failure of the scale as a result of thermal cycling, erosion, or chemical reactions. Microscopic sulphidation or chromium depletion is not generally observed in Type-II hot corrosion (Hancock, 1987; Meier, 1989; Driver et al., 1981; Santorelli et al., 1989).

2.3.3 Hot Corrosion Degradation Sequence

The hot corrosion degradation of superalloys usually involves two distinct stages of attack (Pettit and Meier, 1985; Pettit and Giggins, 1987), namely, an initiation (incubation) stage and propagation stage. Such conditions are depicted schematically in Fig.2.4.

2.3.3.1 The Initiation Stage

No alloy is immune to hot corrosion attack indefinitely although there are some alloy compositions that require a long initiation times before the hot corrosion process moves from the initiation stage to the propagation stage. During the initiation stage of hot corrosion, superalloys are being degraded at rates similar to those that would have prevailed in the absence of the deposits. Elements in the alloy are oxidized and electrons

are transferred from metallic atoms to the reducible substances in the deposit. Consequently, the reaction product barrier that forms beneath the deposit on the alloy surface usually exhibits primarily those features resulting from the gas–alloy reaction (Pettit and Giggins, 1987). Numerous factors affect the time at which the hot corrosion process moves from the initiation stage into the propagation stage as shown in Fig. 2.4.

HOT CORROSION CHRONOLOGY

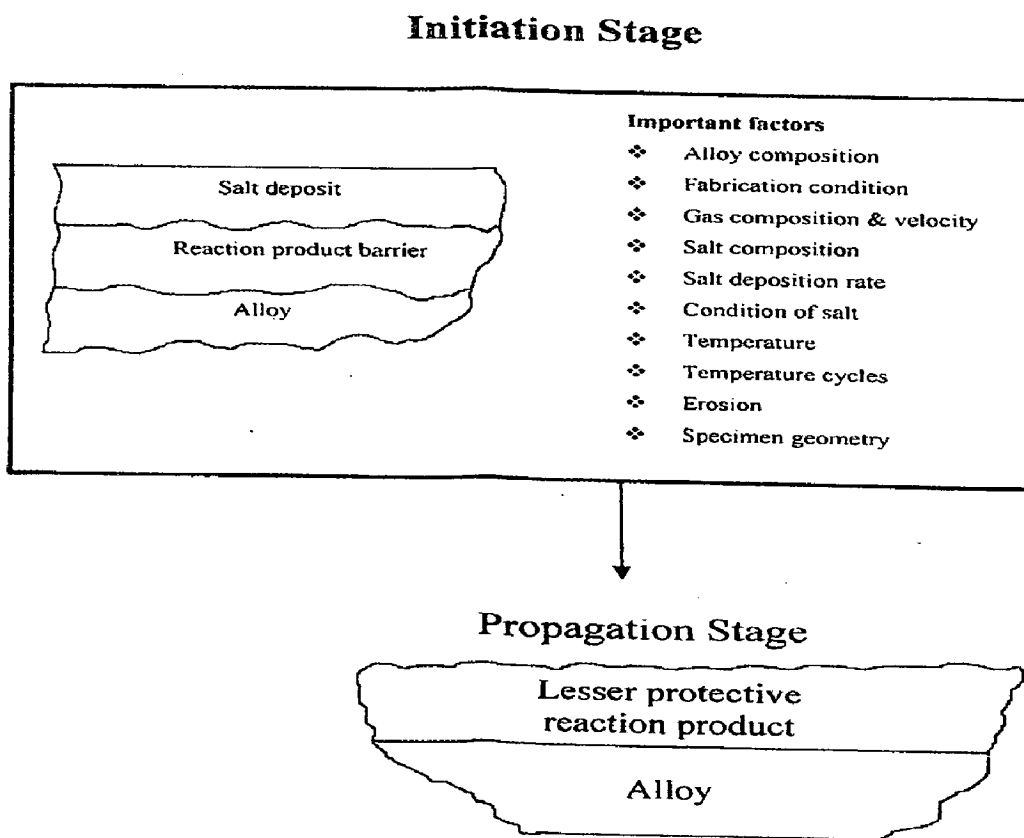


Fig. 2.4 Schematic diagram illustrating the conditions that develop during the initiation and the propagation of hot corrosion attack and to identify the factors that determine the time at which the transition from the initiation to the propagation stage occurs (Pettit and Meier, 1985).

These factors also play the dominant role in determining the type of reaction product that is formed in the propagation stage. This fact is responsible for variety of hot corrosion processes that have been observed when superalloys are exposed to different environments (Pettit and Meier, 1985).

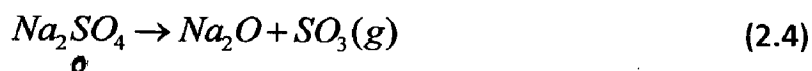
2.3.3.2 The Propagation Stage

The propagation stage of the hot corrosion sequence is the stage for which the superalloy must be removed from service since this stage always has much larger corrosion rates than for the same superalloy in the initiation stage (Pettit and Meier, 1985 and Pettit and Giggins, 1987). Since superalloys always contain elements that have high affinities for oxygen, an oxygen gradient is established across the deposit. Hence, an important effect of the deposit is to separate the superalloy from the gas environment. This situation usually results in a lower oxygen activity over the surface of the alloy than what would have been established in the absence of a deposit (Pettit and Meier, 1984; Pettit and Giggin, 1987).

2.3.4 Chemistry of Salts

2.3.4.1 Chemistry and Phase Stability of Na₂SO₄ Salt

Rapp (1986 and 2002) described that oxyanion melts of alkali nitrates, carbonates, hydroxides and sulphates exhibit an acid base character whereby the acid components may be considered as NO₂(g), CO₂(g), H₂O(g) or SO₃(g) respectively. Although the use of the Lux-Flood selection of NO₃⁻, CO₃²⁻, OH⁻ and SO₄²⁻ as the basic components is common for such fused salts, the oxide ion can be alternatively chosen as the Lewis base in common for all of these salts (Rapp, 1986 and 2002). For a melt of pure Na₂SO₄ (m.p. 884°C), there exists the equilibrium as given below:



According to Rapp (1986), in examining the expected stability of the protective oxide Cr₂O₃, with respect to dissolution either as acidic solutes such as Cr₂(SO₄)₃ or as basic solutes such as Na₂CrO₄ or NaCrO₂, the phase stability diagram for the Cr-S-O system can be superimposed on that for Na-S-O, as shown in Fig. 2.5. The two abscissa scales at the

bottom and top of figure provide alternate parameters for melt basicity (or acidity). Under no conditions is the metal chromium stable in contact with Na_2SO_4 at 1200 K (927°C) (Rapp, 1986).

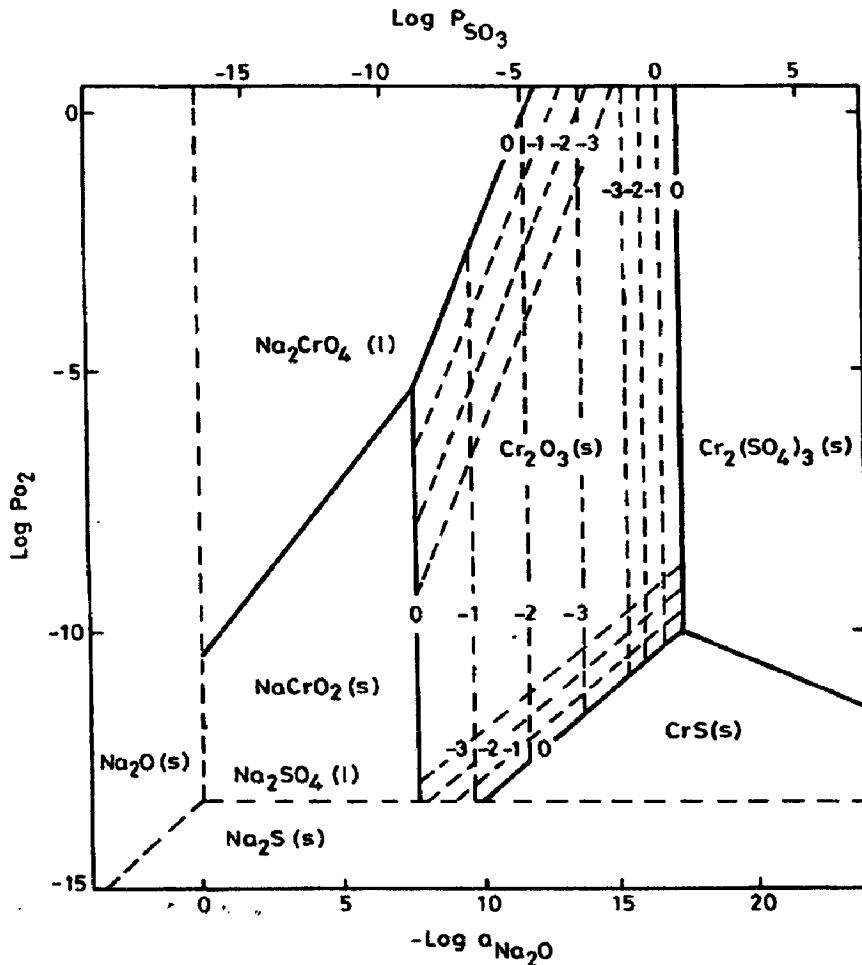


Fig. 2.5 Na-Cr-S-O phase diagram for 1200K (Rapp, 1986)

2.3.4.2 Vanadate Solution Chemistry

As reported by Hwang and Rapp (1989) vanadium is unique, in that it forms a low-melting oxide V_2O_5 . This low melting temperature (670°C under 1 atm of oxygen) results from the peculiar crystal structure of the compound in which vanadium is 5-coordinated with oxygen and in which there occur four different vanadium-oxygen bond lengths (Suito and Gaskell, 1971). Rapp and Goto (1981) have suggested that the presence of such multivalent metal ions in a fused salt deposit could greatly accelerate the hot corrosion rate either by counter diffusion

of the multivalent cations or else by electron hopping, which would provide the fast transport of charge through the salt film.

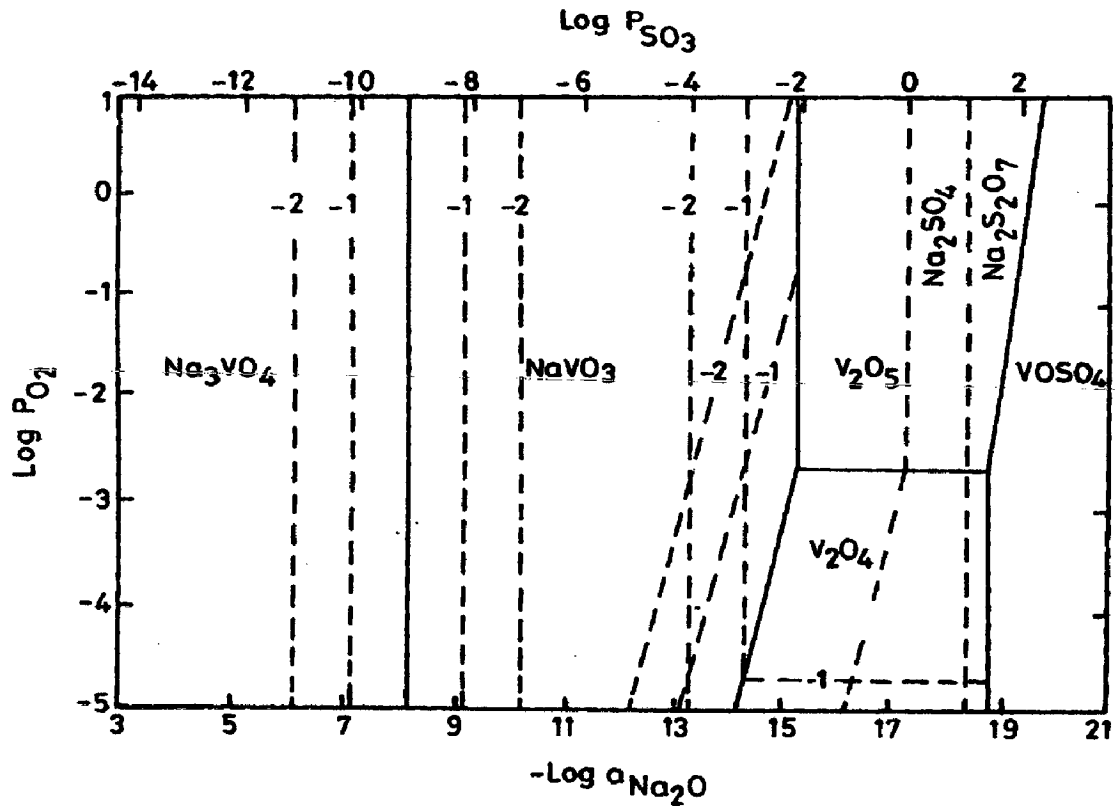
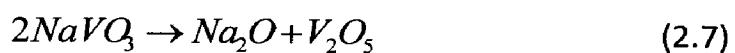
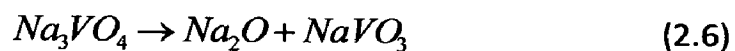
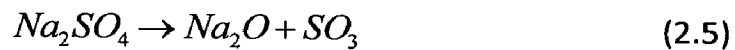


Fig. 2.6 Phase stability diagram for Na-V-S-O phase diagram at 900°C (Hwang and Rapp, 1989)

The phase stability diagram for the Na-V-S-O system at 900°C reported by Hwang and Rapp (1989) has been shown in Fig. 2.6. The dashed lines present the isoactivity lines for the vanadate species in the salt solution. They determined the dependence of the equilibrium concentrations of various vanadate solutes in the sodium sulphate-vanadate solutions on the melt basicity by considering following equilibrium reactions:



The equilibrium concentration of each vanadium compound varies continuously with melt basicity. Na_3VO_4 is the dominant component in the melt at basicity less than 8.2 and V_2O_5 is dominant at basicity greater than 16.3. For basicities between 8.2 and 16.3, NaVO_3 is the most important vanadium solute (Hwang and Rapp, 1989).

2.4 FAILURE OF OXIDE SCALE

The process of oxidation involves nucleation, growth and finally, the formation of a protective oxide scale on the surface (Khanna, 2002). It has been observed from the literature review, that there are varieties of conditions which can be considered for hot corrosion degradation of the materials. Researchers have proposed number of mechanisms for this type of degradation such as failure of oxide scale, sulphidation-oxidation, oxide solubility, and effect of vanadium (Goebel and Pettit, 1970A; Goebel and Pettit, 1970B; Beltran and Shores, 1972; Rapp and Goto, 1981; Pettit and Meier, 1985; Rapp, 1986; Stringer, 1987; Baxter and Natesan, 1989; Otsuka and Rapp, 1990; Zhang et al., 1993; Eliaz et al., 2002). According to Wright (1987), the desired characteristics for a protective oxide scale are: High temperature stability (highly negative Gibbs free energy of formation), low vapor pressure so that the oxide forms as a solid and does not evaporate into the atmosphere, Pilling-Bedworth ratio (PBR, which is defined as the ratio of the molar volume of metal to the molar volume of the oxide formed on it), greater than 1.0 so that the oxide completely covers the metal surface, low coefficient of diffusion of reactants species so that the scale has a slow growth rate, high melting temperature and good adherence to the metal surface.

Mechanical failure and sulphur penetration (or sulphide formation) are the two primary modes of breakdown of protective oxide scales (Baxter and Natesan, 1989). The mechanical failure is mainly due to stress build-up in the oxide and at the scale-metal interface that causes cracking and delamination of oxide scales or the failure may result from erosion or erosion-corrosion. Kofstad (1990) has explained the development of adherent and spalled scale by diffusion processes with the help of a neat sketch shown in Fig. 2.7, which illustrate the growth of chromia scales in the presence or absence of oxygen

active elements. In many cases, the scale formed is very smooth and adherent (Fig. 2.7.i) and does not spall at all while in other cases the spallation starts at the very early stages of oxidation (Fig. 2.7.ii) and continues with intermediate rebuilding of the scale (Khanna, 2002).

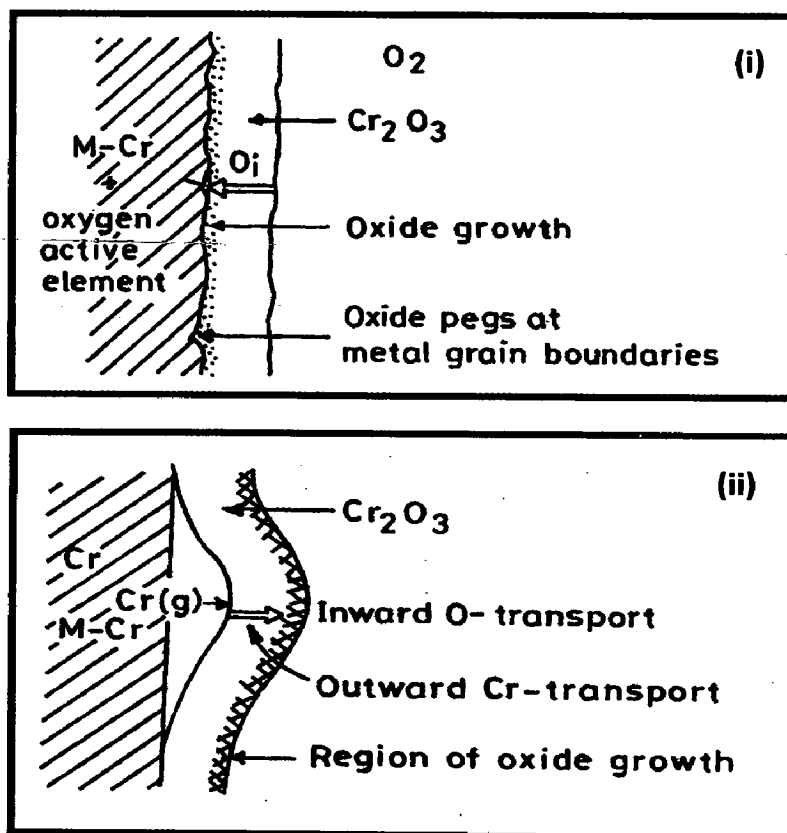


Fig. 2.7 Schematic illustration of the growth of chromia scales in (i) adherent oxide scale, in the presence of oxygen active elements and with predominant inward transport of oxygen, and (ii) spalled oxide scale, in the absence of oxygen active elements and with predominant outward transport of chromia through the scale (Kofstad, 1990)

The main reason for scale spallation is the stress generation in the oxide during its growth. The stress generation depends upon whether the oxide is growing by inward movement of oxygen ions or outward movement of metal ions (Kofstad, 1990). Figure 2.7 illustrate the growth of chromia scales in the presence or absence of oxygen active

elements. When inward oxygen diffusion predominates, oxide formation takes place at the scale-alloy interface, reducing void or cavity formation and thereby increased scale adhesion is achieved. If the voids or cavity move and precipitate at the oxide metal interface, it become the initiation point for the scale spallation (Khanna, 2002).

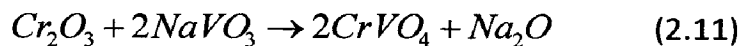
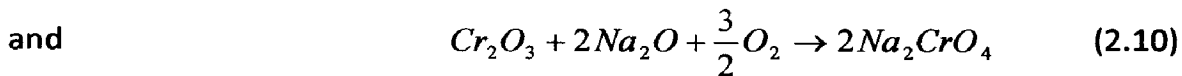
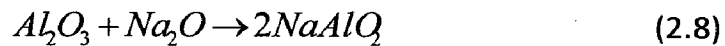
Nucleation and growth of base-metal sulphides at the scale-gas interface are initiated by the penetration of sulphur into the oxide scale. The penetration of sulphur into the oxide can be either through solute diffusion along oxide grain boundaries (short-circuit diffusion) (Atkinson, 1988) or gas molecular transport via physical defects (pores or cracks) (Singh and Birks, 1979). The presence of sulphur in the oxide and at the scale-metal interface increases the outward flux of cations which form sulphides on the oxide surface (Singh and Birks, 1979). Stott et al. (1984) proposed that sulphur-containing species, penetrating through localized short-circuit paths in the oxide, develop sulphide ducts from the scale–metal interface to the scale–gas interface. The sulphide ducts provide easier diffusion paths for the base-metal ions through the oxide to the surface, and eventually allow more rapid growth of sulphide nodules above the oxide. However, Natesan (1985) reported that no transport of sulphur into the oxide, or sulphide duct formation was necessary to form massive mixed iron and chromium sulphides at the oxide–gas interface. Based on the experimental results of sulphidation–oxidation of Incoloy 800, author reported that adsorption of sulphur by the oxide scale accelerates the transport of cations such as Fe and Ni from the substrate to the gas/scale interface and if the sulphur partial pressure in the gas is above that needed for base-metal sulphidation, the transported cations react with sulphur to form sulphides as an outer scale, external to the preformed chromium oxide layer.

Most industrial applications of high temperature materials involve temperature fluctuation. Khanna (2002) reported that the metal usually has a higher coefficient of expansion than the oxide and on cooling induces a compressive stress in the oxide. The greater the disparity between expansion coefficients, the less adherent the oxide becomes during cooling. The imposition of thermal cycling during oxidation leads to enhanced oxidation due to oxide failure, either by decohesion or cracking, and the consequent

exposure of the metal to the oxidant. However, long soaking times at a high temperature between cooling schedules should improve the adhesion of the scale by allowing stress relief at the high temperatures; hence increase its protective potential.

Rapp and Zhang (1994) opined that upon contacting a fused salt, metals and alloy components are oxidized to form thin scales whose protectiveness depends upon the stability of the oxide in the salt. Rapp and Goto (1981) proposed that protective scales on alloy become non-protective when the solubility gradients of the protective oxides in the molten deposit are negative, since continuous dissolution and re-precipitation of oxide is then possible. On the basis of oxide solubilities measurement in molten Na_2SO_4 as a function of the acidity of the salt, authors suggested that a negative gradient of the solubility of the protective oxide in the salt film at the oxide/salt interface should lead to oxide dissolution at this interface and to precipitation of a non-protective oxide away from the interface, where the solubility is lower. Fluxing arises in this case only because of the local variation of sodium oxide activity and/or oxygen partial pressure across the salt film, without any necessity of sulphide-forming reaction. This mechanism can explain a self-sustaining process of dissolution of the protective oxide to maintain an accelerated corrosion attack (Stringer, 1987).

Hwang and Rapp (1989) have reported the solubilities of Al_2O_3 and Cr_2O_3 in a fused Na_2SO_4 -30 mole % NaVO_3 salt solution as follows:



It has been reported that the vanadate ions greatly increase the acidic solubilities of Al_2O_3 and Cr_2O_3 over a wide range of melt basicity.

2.5 ELEMENTS AFFECTING HOT CORROSION OF METALS/ALLOY

The alloying elements, presence of S and Cl⁻ in the deposit and the temperature play important roles in hot corrosion (Khanna et al., 1998). The resistance of superalloy (and other materials) against hot corrosion is directly related to the chemical composition of the alloy and its thermo-chemical history (Eliaz et al., 2002). Unfortunately, many alloying elements have an adverse effect on the mechanical properties of the superalloy at high temperatures and on its resistance to hot corrosion. The elements such as tungsten, vanadium and molybdenum are excellent in improving the mechanical properties, but their presence makes the alloy highly susceptible to hot corrosion (Stringer, 1987 and Otsuka et al., 1990A). Chromium is the most effective alloying element for improving the hot corrosion resistance of materials (Otsuka et al., 1990B). The effect of other alloying elements on the hot corrosion resistance of superalloys has been reported as well. Otsuka et al. (1990B) have suggested that cerium, lanthanum, zirconium, yttrium and scandium significantly increase the resistance because of improvement of adhesion between the alloy and the protective oxide.

Sulphur-induced hot corrosion is generally known as sulphidation (Khanna et al., 1998 and Wright, 1987). Sulphidation is a specific form of hot corrosion but the attack does not always take place via sulphidation. At high temperatures a substantial amount of sulphide phases may be found beneath the molten deposits. As these sulphides begin to oxidize, the resulting phases are not protective because of SO₂ evolution (Khanna et al., 1998).

The presence of chlorine may also affect the hot corrosion of alloys. Cl₂ concentrations in the ppm range may increase the propensity of oxide scales (e.g. Al₂O₃ and Cr₂O₃) on alloys to crack and spall (Khanna et al., 1998). Further, large concentrations of chloride in the deposit causes rapid removal of Al and Cr from alloys by the formation of volatile metal chlorides in the low oxygen pressure regions. The chloride-induced effect is significant between 700 and 1000°C. Temperature is an extremely important factor. The onset temperature of catastrophic attack, "threshold temperature" generally occurs near the melting point of the salt or salt mixture. As temperature is increased further, the rate of

diffusion-controlled processes increases and reaches a maximum at about 980°C for most alloys.

2.6 HOT CORROSION IN THE MOLTEN SALT ($\text{Na}_2\text{SO}_4\text{-V}_2\text{O}_5$) ENVIRONMENT

Tiwari and Prakash (1996 and 1997) and Tiwari (1997) have reported hot corrosion studies on some industrial superalloys in temperature range 700-900°C in the environments comprising of pure Na_2SO_4 , $\text{Na}_2\text{SO}_4\text{-15}\%\text{V}_2\text{O}_5$ and $\text{Na}_2\text{SO}_4\text{-60}\%\text{V}_2\text{O}_5$. Very high corrosion rates were observed in the environment having $\text{Na}_2\text{SO}_4\text{-60}\%\text{V}_2\text{O}_5$ composition. Tiwari et al (1997) further revealed that in $\text{Na}_2\text{SO}_4\text{-60}\%\text{V}_2\text{O}_5$ melt, the degradation was due to the cracking of the protective scale under the influence of the fluxing action of the melt for both Fe-base alloy Superfer 800H and Co- base alloy Superco 605. The enhanced degradation was reported to be due to the presence of tungsten in form of $\text{Na}_2\text{WO}_4\text{-WO}_3$ compound. Authors concluded that the Co-base alloy has inferior corrosion resistance than the Ni-base alloy in $\text{Na}_2\text{SO}_4\text{-60}\%\text{V}_2\text{O}_5$ environment at 900°C.

Otero et al. (1987) investigated the hot corrosion behavior of IN657 (46.5 Cr, 1.32 Nb, bal-Ni) at 635°C in a molten salt environment of 60:40 $\text{V}_2\text{O}_5\text{:Na}_2\text{SO}_4$ (Mol%). They characterized the morphology and chemical compositions of the corrosion products and found that the presence of sulphur and its oxidized compounds favour the formation of isolated lobes with radial morphology. These lobes had great permeability which facilitated the access of oxygen; therefore the protective character of the scale was reduced. They reported that the presence of vanadium and its oxidized products generate compounds with aciculate morphology, which is not very much covering and reduces the protective character of the scale. The equilibrium diagram for varying composition of Na_2SO_4 is shown in Fig. 2.8 and the mixture of $\text{Na}_2\text{SO}_4\text{-60}\%\text{V}_2\text{O}_5$ is seen to have the lowest eutectic temperature.

Molten sulphate-vanadate deposits, resulting from the condensation of combustion products of residual fuels, are extremely corrosive to high-temperature materials in the combustion systems (Natesan, 1976). Luthra and Spacil (1982) carried out a thermochemical analysis of deposits in gas turbines for liquid fuels containing Na, S and V. Authors observed

that the predominant species in the salt deposits formed on the gas turbine surfaces were Na_2SO_4 , V_2O_5 and $\text{Na}_2\text{V}_2\text{O}_6$. This environment is also pertinent to the boilers.

Kolta et al (1972) studied the kinetics of the reactions between Na_2SO_4 (X) and V_2O_5 (Y) and revealed that the rate of reaction depended both on the temperature (600-1300°C) and the molar ratios of X: Y. Authors further found that with increase in the reaction period (>30 min.), there was decrease in reaction rate which finally reached to zero order.

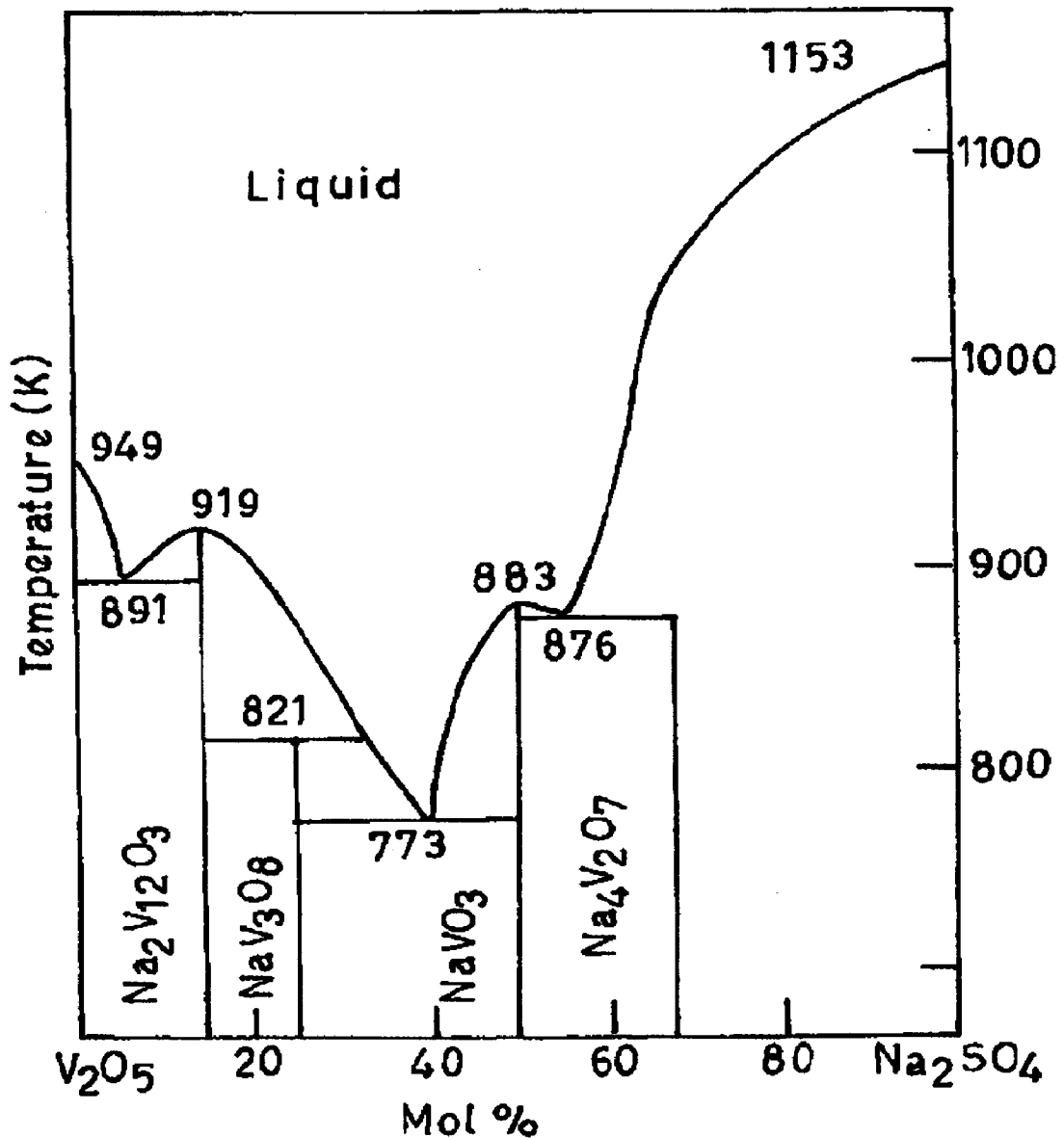


Fig. 2.8 Phase Diagram for Na_2SO_4 - V_2O_5 System (Otero et al., 1987)

This decrease in the reaction rate has been attributed to the formation of vanadosulphate complexes such as $(\text{NaV}_3\text{O}_8)_2 \cdot \text{Na}_2\text{SO}_4$ and $(\text{NaVO}_3)_2 \cdot \text{Na}_2\text{SO}_4$ which get decomposed at higher temperatures giving the meta- and pyro-vanadates respectively. Barbooti et al. (1988) revealed that sodium vanadyl vanadate ($\text{Na}_2\text{O} \cdot \text{V}_2\text{O}_4 \cdot 5\text{V}_2\text{O}_5$), which melts at a relatively low temperature 550°C , is found to be the most common salt deposit on boiler superheaters.

Almeraya et al. (1998A) carried out electrochemical studies of hot corrosion of steel AISI-SA-213-TP-347H in 80 wt% V_2O_5 + 20 wt% Na_2SO_4 at 540°C – 680°C and reported the corrosion rate values of around 0.58-7.14 mm/year. Increase in corrosion was observed with time. However the corrosion potential was observed to be decreasing with increase in temperature from 540 to 680°C . Almeraya et al. (1998 B) further conducted similar studies on type 347H stainless steel under similar environment and temperature range, and revealed the fact that with change in temperature from 540 to 680°C the corrosion potential decreased.

Cuevas-Arteaga et al (2001) used both LPR (Linear Polarisation Resistance) and weight loss techniques during hot corrosion study on alloy 800 in Na_2SO_4 -20% V_2O_5 , and reported slightly higher corrosion rate at 900°C than at 700°C . In both the techniques, corrosion rates increased in the beginning of the experiment but decreased later on until steady values reached. Sidhu (2003) studied the hot corrosion behavior of boiler tube steels namely ASTM-SA210 Grade A-1, ASTM-SA213-T-11 and ASTM-SA213-T-22 in air and molten salt environments of Na_2SO_4 -60% V_2O_5 at 900°C . Authors found that all the steels show less resistance in the molten salt environment than in air. Authors reported that the presence of vanadium, sodium and sulphur reported to accelerates the rate of corrosion of boiler steels in the molten salt environment.

Gitanjaly (2003) has conducted hot corrosion studies on some Ni-, Fe- and Co-based superalloys in an environment of Na_2SO_4 +60% V_2O_5 at 900°C . Whilst the observed corrosion rate was significant in all the superalloys, Ni-base superalloy Superni 75 showed lowest rate of corrosion and the Co-base superalloy Superco-605 the highest. Better corrosion resistance of Ni-base superalloys was attributed to the presence of refractory nickel

vanadate $\text{Ni}(\text{VO}_3)_2$ which acted as a diffusion barrier for the oxidising species and a Cr_2O_3 band. The proposed hot corrosion mechanisms of this study for the superalloys Superni 75 and Superni 601 have been schematically shown in Fig. 2.9. Some of the hot corrosion studies conducted by various investigators in molten salt environment on iron, nickel and cobalt-based alloys are summarized in Appendix A.2.

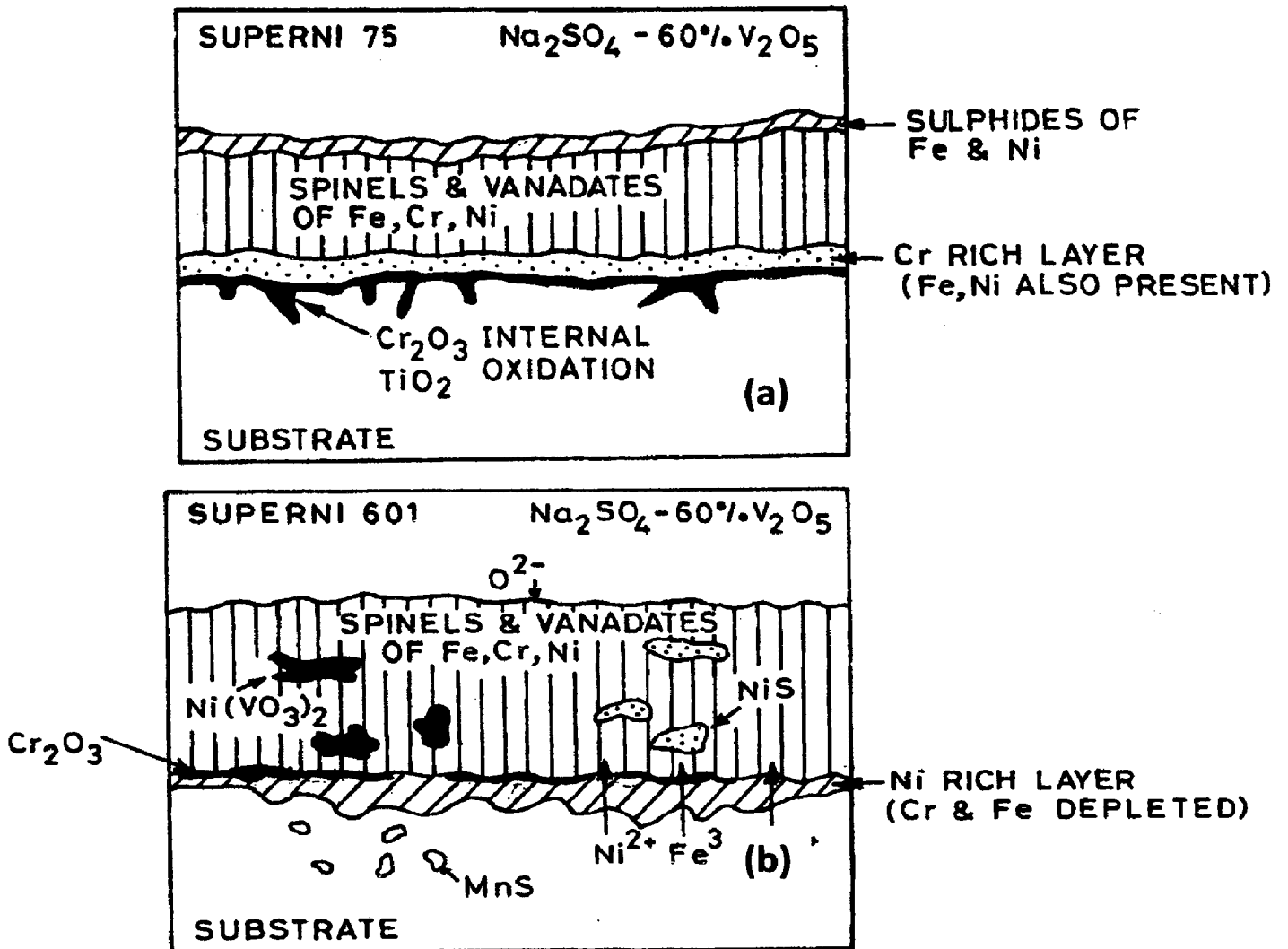


Fig. 2.9 Schematic diagram showing probable hot corrosion mechanism in $\text{Na}_2\text{SO}_4 - 60\% \text{V}_2\text{O}_5$ after exposure for 50 cycles at 900°C for alloys: (a) Superni 75; (b) Superni 601 (Gitanjaly, 2003)

2.7 HOT CORROSION IN ENERGY GENERATION SYSTEMS

The availability of electrical power and the development of millions of devices that use it have made electricity the energy of choice in contemporary industrial societies. It is estimated that in the United States approximately 70% of the electricity is produced in fossil power plants, 15% in nuclear power plants, 12% in hydraulic power plants and the remainder from other types of sources (Viswanathan, 1989). The fuels used in fossil-fired plants are natural gas, petroleum and coal. Natural gas is generally extremely pure and does not constitute a corrosion threat, unless firing is substoichiometric for reducing NO_x emission (Jaffee, 1987). Petroleum fuels can be corrosive to boilers if contain vanadium oxides or alkali sulfates, both of which are highly corrosive to metals in the combustion chamber or hot gas passages. However, coal contains impurities such as sulfur, chlorides and alkali metals, which are extremely corrosive.

Metallic components in coal based energy generation systems are exposed to severe corrosive atmospheres and high temperatures. The corrosive nature of the gaseous environments which contain oxygen, sulphur and carbon may cause rapid material degradation and result in the premature failure of components (Danyluk and Park, 1979, Chawla et al. 2006, and Wang, 1988). The phenomenon of accelerated corrosion at high-temperatures occurs due to the deposition of ashes during combustion processes. Ashes usually have high concentrations of compounds of vanadium, sodium and sulphur, mainly as Na₂SO₄-V₂O₅ complex and sodium-vanadates mixtures. These impurities are also present in residual oils used as fuel (Harada and Kawamura, 1980; Harada et al., 1981; Wong-Moreno and Salgado, 1995). Some mixtures of these compounds have melting points (480 to 510°C) lower than the metallic surface temperatures and turn into liquid state which increases the corrosion rates (Cuevas-Arteaga et al., 2004).

According to Khanna (2002) and Marriott (1990) the hot corrosion plays an important role in determining the life of boiler components. A schematic of a coal-fired boiler showing as two main parts susceptible to hot corrosion is presented in Fig.2.10. Water wall fireside corrosion occurs mainly due to reducing (substoichiometric) conditions caused by incompletely combustion of coal particles and molten salt attack. Reducing conditions lower

the melting point of deposited salt and increase its ability to dissolve the normal oxide scales. Further, local disruption of the normal oxide film on the wall tubes through fluxing by molten salt can lead to accelerated oxidation or oxidation-sulphidation.

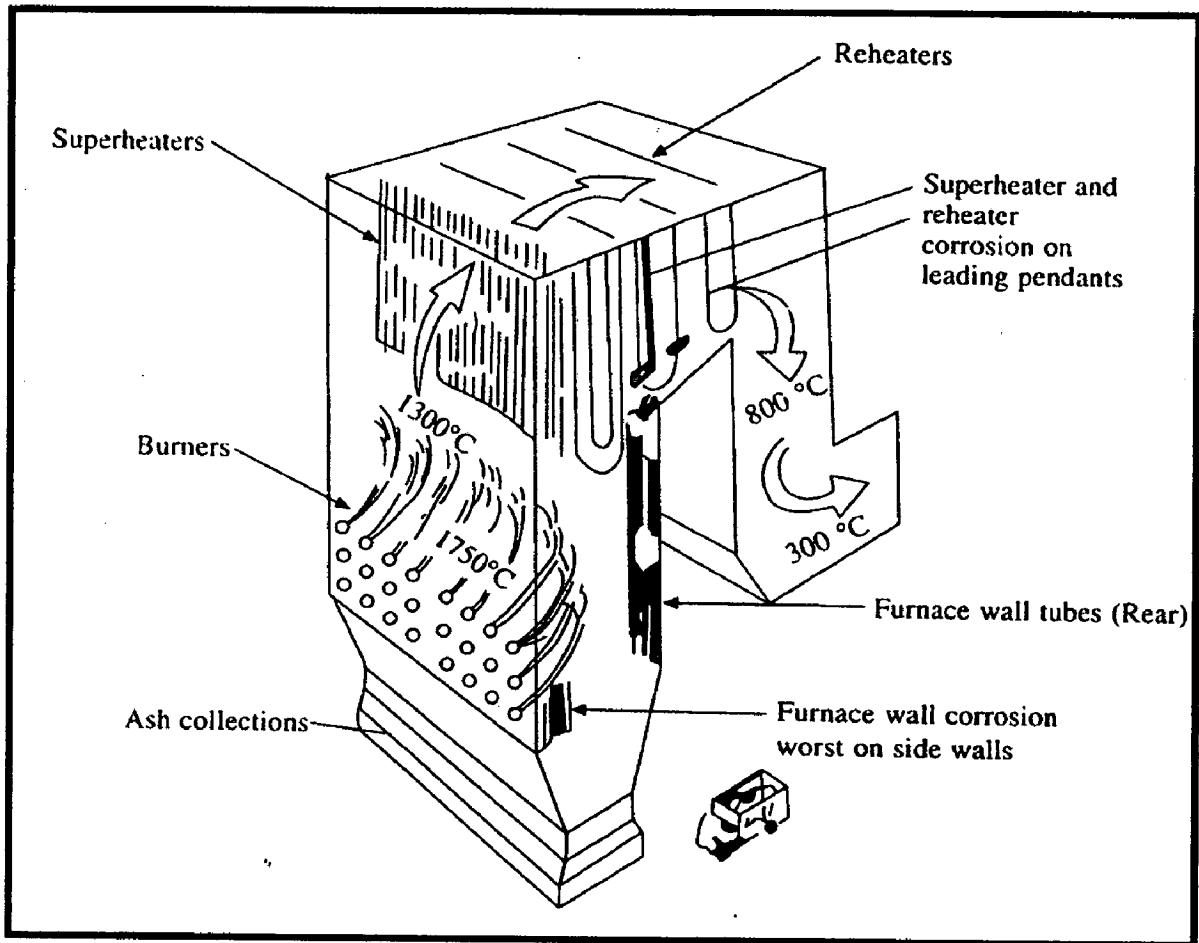
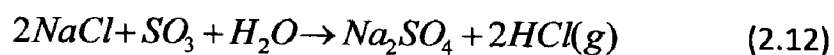


Fig. 2.10 Schematic illustration of coal fired boiler (Khanna, 2002 and Marriott, 1990)

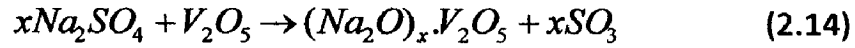
As suggested by Khanna et al. (1998), the sulphur present in coal and fuel oils yields SO_2 on combustion which is partially oxidised to SO_3 . The NaCl (either as impurities in the fuel or in the air) reacts with SO_3 and water vapours at combustion temperatures to yield Na_2SO_4 as below:



At lower temperatures Na_2SO_4 can further react with SO_3 to form sodium pyrosulphate, $\text{Na}_2\text{S}_2\text{O}_7$ with melting point (m. p.) of 401°C:



Small amounts of vanadium may be present in fuel oils, which on combustion forms V_2O_5 . This may further react with Na_2SO_4 to form low melting sodium vanadates, which are highly corrosive.



Thus metals and alloys in combustion gases are exposed to various corrosives such as O_2 , SO_2/SO_3 , molten salts, e.g. Na_2SO_4 or sulphate mixtures, sodium vanadates, $NaCl$ (Khanna et al., 1998). The fireside corrosion of superheaters in coal-fired boilers has restricted lower steam temperatures (Khanna, 2002). The enhanced corrosion of the superheater tubes is generally associated with the deposition of ash along with molten salts on the tube walls as illustrated in Fig.2.11.

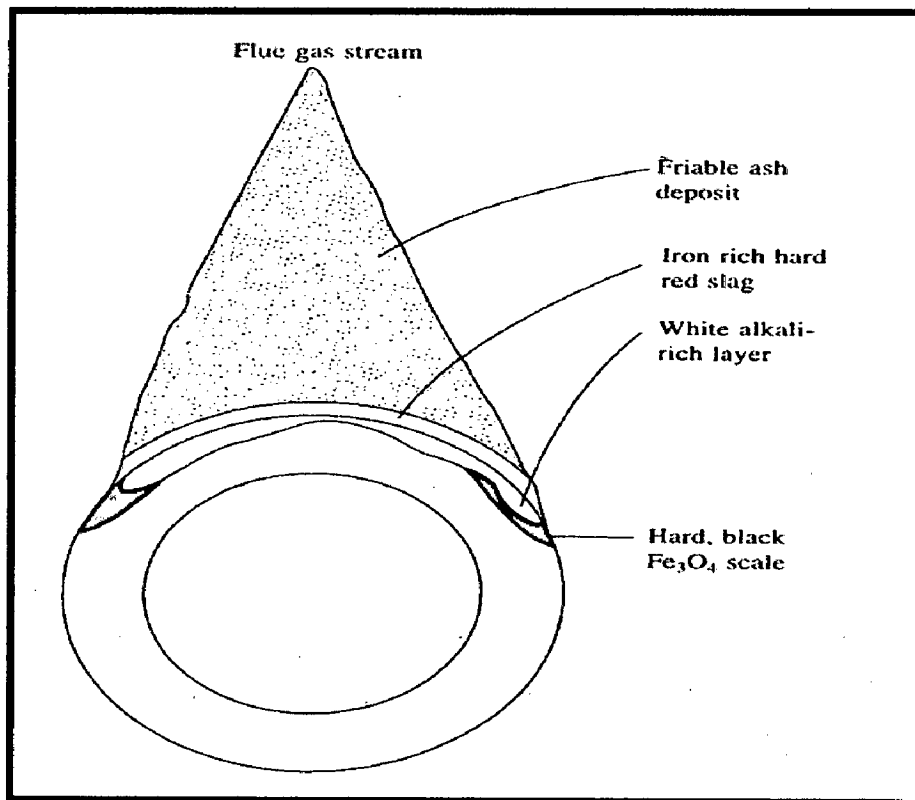


Fig. 2.11 Enhanced corrosion of superheater, associated with the formation of a molten deposit on the tube walls (Khanna, 2002)

Moujahid (1987) observed severe ash corrosion, mechanical deformation and cracks on the cast iron chains of moving grate used for air burning of coal. Liquid coal ash at 1300°C, strongly acidic, dissolves the basic spinel layers which formed on the chains at elevated temperature. The fused ash embeds coal particles and also reduces the thermal efficiency of the equipment. Drastic enhancement in ash corrosion rate has been attributed to the mechanical damages.

2.8 COUNTERMEASURES AGAINST HOT CORROSION

Fuels with sulphur and other impurities cause hot corrosion which significantly reduces the life of components (Sharma, 1996). Corrosion and its associated losses cannot be eliminated completely. However, 25 to 30% of annual corrosion related costs could be saved with development and use of better corrosion control technologies (Koch et al., 2002; Priyantha et al., 2003).

Various time-proven methods for preventing and controlling corrosion depend on the specific material to be protected, environmental concerns such as soil resistivity, humidity and exposure to saltwater or industrial environments, the type of product to be processed or transported and many other factors (Koch et al., 2002). Preventive measures against metal losses and failures due to corrosion should be economically devised to ensure safety and reliability in the use of metallic components (Chatterjee et al., 2001).

Corresponding to the variety of corrosive environments numbers of countermeasures have been developed to avoid excessive material damage. Heath et al. (1997) grouped the countermeasures into following categories:

1. **Alloy selection:** A large number of Fe, Ni- and Co-based alloys exist today especially designed for good resistance to oxidation, sulphidation or corrosion by ash/salt deposits.
2. **Design aspect:** Improve temperature distribution (avoid hot spots), avoid excessive deposition of ash and slags by use of soot blower, rapping, screens etc.
3. **Chemical additives:** Neutralisation of corrosive components in the flue gases by injecting additives such as limestone and dolomite.

4. **Shielding:** SiC tiles in waste incinerations, other type of refractory linings
5. **Coatings:** Different coating techniques are applied to protect the critical surface areas from corrosive gases, including co-extrusion, chromising, weld overlay and thermal spray coatings.

Choice of substrate metal is usually governed by cost, weight and general physical, mechanical or fabrication properties and these factors normally dictate a very limited number of possible materials none of which may be ideal in resisting the corrosive environment which will be encountered in service. In general alloying elements which can improve the hot corrosion resistance of materials such as Cr, Al, etc., often have a negative effect on the mechanical properties in high temperature environments and are expensive (Wu and Okuyama, 1996). As reported by Goebel et al. (1973) and Sims (1987), the corrosion control in highly aggressive applications requires careful selection of materials. Nickel-based superalloys have good mechanical properties and superior corrosion resistance at higher temperatures and are used as base materials for many hot components. However, the hot corrosion is inevitable when these alloys are used at higher temperatures for longer periods of time in an extreme environment.

Inhibitors and fuel additives have been used with varying success to prevent oil ash corrosion. Because of its effectiveness and relatively low cost the most common fuel additives are based upon MgO (Paul and Seeley, 1991). Further the MgO, CaO, ZnSO₄, PbO and SnO₂ based inhibitors are reported to be effective to decrease the extent of hot corrosion pertaining to molten salt environment (Na₂SO₄-60%V₂O₅) for iron-, nickel- and cobalt-based superalloys by Gitanjaly and Prakash (1999), Gitanjaly et al. (2002) and Gitanjaly (2003). However, these inhibitors have shown only limited success due to solubility and/or thermal stability problems in high-temperature, concentrated salt solutions such as in chemical heat pumps (Priyantha et al., 2003).

Increasingly greater demand imposed on materials makes it more difficult or, at the current stage of development, even impossible to combine the different properties required in one single material (Chawla et al., 2006C). Therefore, a composite system of a base material providing the necessary mechanical strength with a protective surface layer

different in structure and/or chemical composition and supplied by a surface treatment can be an optimum choice in combining material properties. Although protective surface treatments are widely used at low temperature, the use of these at elevated temperature is more recent (Chawla et al., 2005). Current high temperature applications are limited largely to the aerospace industry. An enormous challenge exists now to develop and apply these techniques to other high temperature applications (Stroosnijder et al, 1994 and Li et al, 2003).

Wang and Luer (1994) have reported the use of coatings to protect the heat exchanger tubes of fluidized bed combustor from erosion-corrosion problems and Hocking (1993) has also suggested the use of corrosion resistance alloys as coatings to protect substrate alloys having good mechanical properties. Hidalgo et. al. (1997, 1998, 1999 and 2000) have further discussed the use of plasma sprayed thin anti wear and anti oxidation coatings to take care of the high temperature erosion and corrosion problems in energy generation systems. The effective method of hot corrosion prevention is to coat the alloy with a protective layer, which has been used in the current investigation. This is the preferred approach, even when relatively hot corrosion-resistant alloys are used (Eliaz et al., 2002).

2.9 MECHANICALLY ASSISTED DEGRADATION OF METALS

Mechanically assisted degradation of metals is defined as the degradation that involves both corrosion and a wear or fatigue mechanism. Five such forms of degradation are: erosion, fretting, fretting fatigue, cavitation and water drop impingement and corrosion fatigue. Erosion is the removal of material from a surface by high velocity fluids containing solid particles, or small drops of liquid or gas (Bhushan and Gupta, 1991) as shown in Fig. 2.12. According to ASTM standard G76-04, erosion is the progressive loss of original material from a solid surface due to mechanical interaction between that surface and a fluid, a multi-component fluid, or impinging liquid or solid particles. Erosion is a serious problem in many engineering systems, including steam and jet turbines, pipelines and

valves used in slurry transportation of matter and fluidized bed combustion systems (Kosel, 1992).

Cavitation damage is caused by the formation and collapse of vapor bubbles in a liquid near a metal surface (Fig.2.13). Cavitation damage occurs in hydraulic turbines, ship propellers, pump impellers, and other surfaces where high-velocity liquid flow and pressure changes are encountered (Fontana and Greene, 1967). Fretting describes corrosion occurring at contact areas between materials under load subjected to vibration and slip. It appears as pits or grooves in the metal surrounded by corrosion products. Corrosion fatigue is defined as the reduction of fatigue resistance due to the presence of a corrosive medium (Fontana and Greene, 1967).

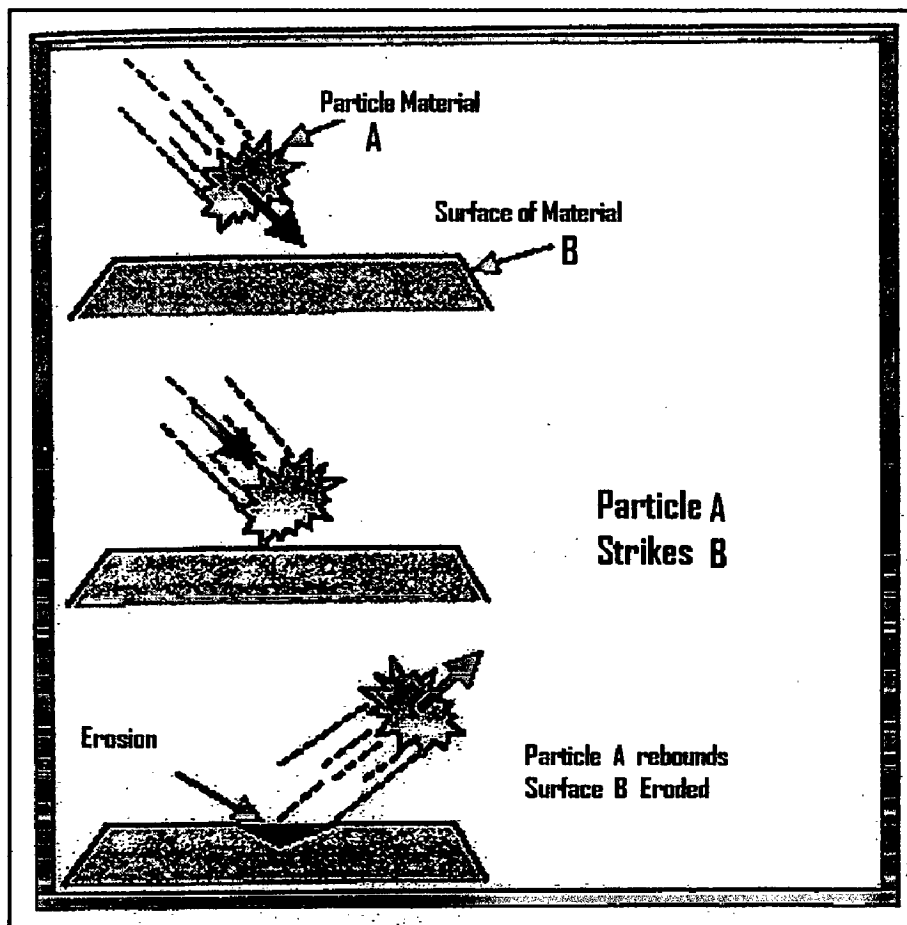


Fig. 2.12 Schematic of erosive wear (Bhushan and Gupta, 1991)

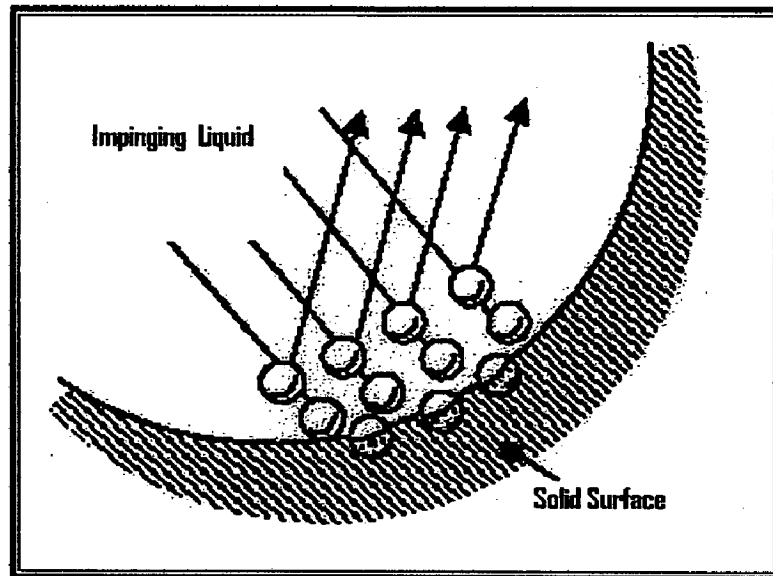


Fig. 2.13 Schematic of mechanically assisted degradation of metals by cavitation (Bhushan and Gupta, 1991)

2.9.1 Solid Particle Erosion

Solid particle erosion (or erosive wear) is the removal of material from component surfaces due to successive impact of hard particles travelling at substantial velocities (Sundarajan et al., 1997). The solid particle erosion is different from the other forms of erosion like liquid impact erosion, slurry erosion, cavitation erosion and fretting. Material removal due to solid particle erosion is a consequence of a series of essentially independent but similar impact events. Thus, the contact between the hard particles and the component surface is of a very short duration. From this point of view the erosion is completely different from the other closely related processes like sliding wear, abrasion, grinding and machining wherein the contact between the tool/abrasive and the target/work-piece is continuous. Degradation of materials due to solid particle erosion, either at room temperature or elevated temperature, is encountered in a large variety of engineering industries as illustrated in Table: 2.1.

Kosel (1992) and Zhang et al. (2000) have reported that the solid particle erosion is a serious problem in many engineering systems, including steam and jet turbines, pipelines and valves carrying particulate matter, sand erosion of helicopter blades and ingestion of sand and erosion of jet engine blades and vanes. According to one of the estimate reported by Stein et al. (1999) solid particle erosion costs US \$150 million a year in term of lost efficiency, forced outage and repair costs. At the same time, the erosion process has been used to advantage in a number of situations like sand blasting of casting, shot peening of rotating components, cutting of hard and brittle materials by abrasive jets and rock drilling (Sundarajan et al., 1997). Solid particles transported in gas or liquid flows cause severe damage on industrial components and lead to expensive repair and part replacement (Mishra et al., 2006A and Mishra et al., 2006B). Thus, the technological and commercial significance of erosion cannot be overlooked.

Table: 2.1 Examples of components subjected to solid particle erosion (Sundarajan et al., 1997)

System	Components
Chemical Plant	Transport tubes carrying abrasive materials in an air stream
Fluidized bed combustor	Boiler heat exchanger tubes in bed tubes, tube banks and expander turbine
Hydraulic mining machinery	Pumps and valves
Coal gasification	Turbine, lock hopper valves
Coal liquification	Valve to throttle the flow of product steam
Propellent system	Rocket motors trail nozzle, gun barrel
Aircraft engines	Compressor and turbine blades
Helicopter engine	Rotor and gas turbine blades

2.9.1.1 Factors affecting solid particle erosion at room temperature

The factors affecting solid particle erosion are: (i) impact velocity, (ii) Impact angle, (iii) particle shape and size, (iv) hardness of erodent, (v) flux rate of erodent particles, (vi) various strengthening mechanisms and (vii) temperature.

- (i) Impact velocity of the erodent particle has the most dramatic effect on the erosion rate. The erosion rate of a material (E) is usually defined as the ratio of weight loss suffered by the eroding material to the weight of the erodent particles causing the loss. The velocity dependence of erosion rate is characterized by the velocity exponent " p " is given by:

$$E = E_0 V^p \quad (2.15)$$

Where E_0 is a constant and V is impact velocity. In the case of metallic materials, Sundararajan and Shewmon (1983) have reported a mean value of 2.55 for " p " for erosion under normal impact. Roy et al. (1994) have reported the values for " p " in case of ceramics and polymer matrix composites as around 3 and 5 respectively. Further Sundarajan et al. (1997) have reported that the velocity exponent is also influenced by other parameters such as impact angle, particle size.

- (ii) Impact angle is defined as the angle between the target material and the trajectory of the erodent. Dependence of erosion rate on the impact angle is largely determined by the nature of target materials. There is a dramatic difference between ductile and brittle materials when the weight loss in erosion is measured as a function of the impact angle. As reported by Bhushan and Gupta (1991), brittle erosion deals with the material removal due to crack formation whereas ductile erosion occurs due to extrusion of microplatelets of the base material from craters, which then flattened and fractured. The erosion rate of ductile materials (like metals and alloys) is maximum at intermediate impact angles (15° , 30°) as shown in Fig. 2.14 (a), whereas the maximum erosion

rate of a brittle materials (like glass) is usually obtained at normal impact angle i.e. at 90° (Sundarajan et al., 1997). This occurs because ductile materials are capable of absorbing the large amount of energy produced by the impacting particles without fracture and brittle materials are capable of withstanding large amount of shear stress (Bhushan and Gupta, 1991). In general, ductile material fail in shear before tension and brittle materials fails in tension before shear. Wensink and Elwensoek (2002) reported that when brittle material i.e. ceramic-type material or oxide scales on metals is impacted by a hard sharp particle, the contact area is formed. After the impact, the plastic deformation leads to large tensile stresses that result in lateral cracks causing the material removal.

- (iii) Particle size is an important variable which influence the erosion behavior (Sundarajan et al., 1997). Further, authors reported that the erosion rate increases with an increase in particle size up to a limiting size (50 to 100 μm) beyond which erosion rate becomes independent of particle size (Fig.2.14. b). Similar observations have also been made by Zhou and Bahadur (1989) and Levy (1989).
- (iv) Several investigators have studied the influence of particle shape on the erosion rate. Levy and Chik (1983) and Brown et al. (1983) observed significantly higher erosion rates in many metallic materials when eroded with angular particles rather than spherical particles. Maximum erosion rate was observed in Cu and Cu based alloys at normal impact angles when a non-friable, spherical steel shot was used as the erodent (Reddy and Sundararajan, 1986). Their observation is presented in Fig.2.14 (c). When an angular SiC is used as the erodent, the same Cu and Cu alloys exhibited a ductile response with regard to erosion behavior. Thus, as the angularity of the erodent particle increases, the erosion rate increases and in addition, the erosion rate-impact angle behavior shifts more towards a ductile response.
- (v) The flux rate of erodent particles usually does not have a significant influence on the erosion rate of metallic materials (Sundarajan et al., 1997). However, at very

high flux rate, due to interference with other particles and also with the rebounding particles, the erosion rate decreases. The above mentioned interference effect due to particle rebounding have been modelled by Anand et al. (1987) and reported that the erosion rate should decrease exponentially with an increase in the flux rate (Fig.2.14. d).

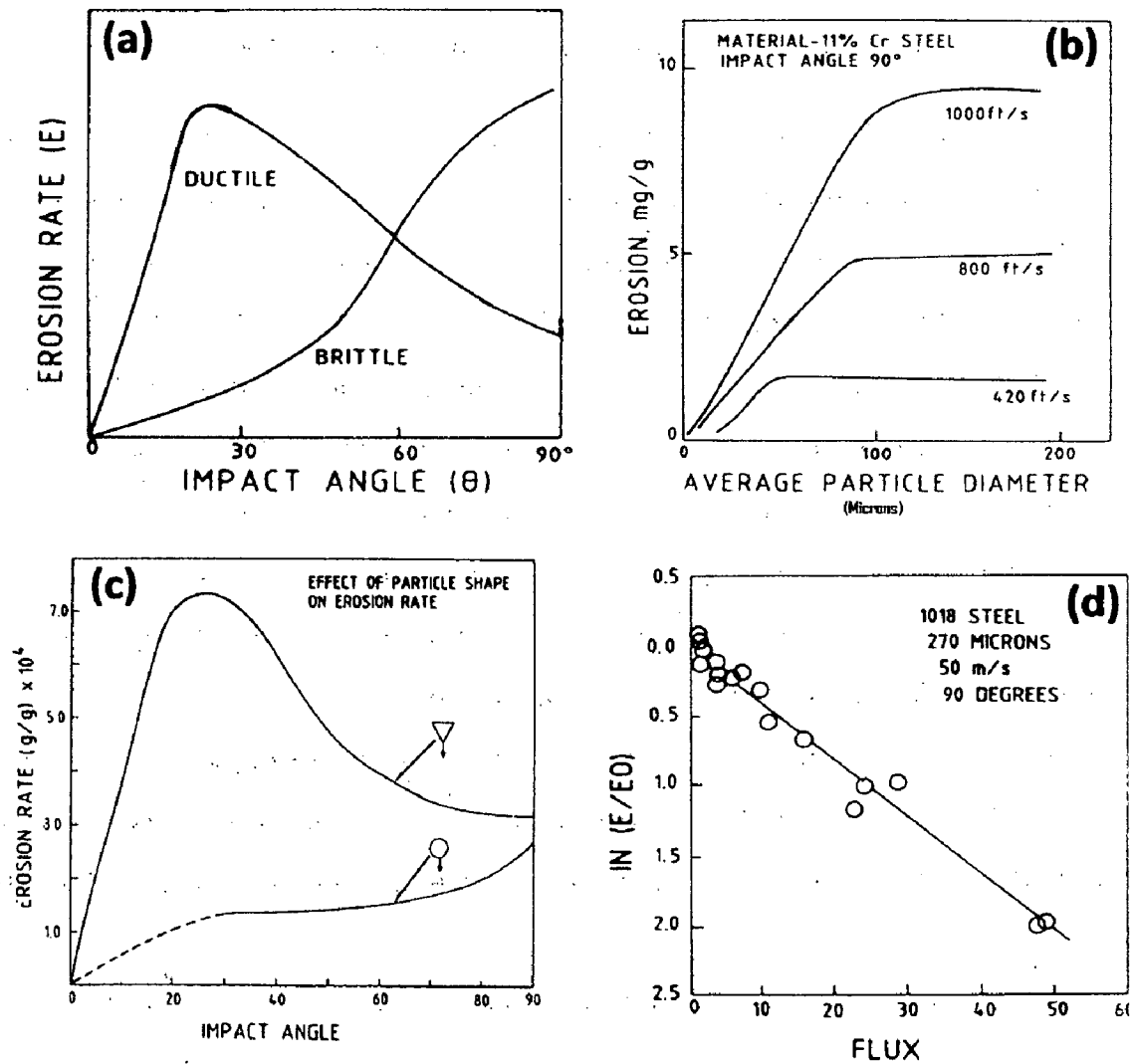


Fig. 2.14 (a) Schematic diagram showing the influence of impact angle on erosion rate in the case of ductile and brittle materials; (b) variation of erosion rate of steel with particle size at normal impact at different impact velocities; (c) influence of impact angle on erosion rate in the case of spherical and angular particles; (d) influence of flux rate of erodent particles on the erosion rate of a 1018 steel (Sundarajan et al., 1997)

- (vi) Sundarajan et al. (1997) have reported the effect of the various strengthening mechanisms on the erosion rate of single phase metals and alloys. None of the strengthening mechanisms like, cold work, grain size hardening and solid solution strengthening available for single phase materials are effective in improving the erosion resistance of the eroding material. Even in multiphase alloys, though the various strengthening mechanisms result in a substantial improvement in material strength, the erosion rate changes only marginally.

2.9.1.2 Factors affecting solid particle erosion at elevated temperature

- (i) Sundarajan et al. (1997) have classified the temperature dependence of erosion rate under three groups. In the first group, the erosion rate initially decreases with increasing temperature, reaches a minimum and then starts increasing with increasing temperature. Materials such as 5Cr-0.5Mo, 17-4PH, 410SS, Alloy 800, Ti-6Al-4V and tungsten, belongs to this group. The second group comprises metals like Ta, lead and alloys like 310SS, 1018 steel, 1100 aluminum (normal impact) which exhibit a temperature independent erosion rate up to a critical temperature followed by an increasing erosion rate with increase in temperature. The group third materials show an ever increasing erosion rate with increasing temperature. Inco 600, carbon steel, 12Cr-1Mo-V steel and 2.25 Cr-1Mo steel, lead and 2024 Al are some of the typical examples of this group.
- (ii) Most of the metallic materials irrespective of temperature of erosion, exhibit a ductile behavior, i.e. a maximum erosion rate at oblique impact angles (10° to 30°).
- (iii) The value of velocity exponent (p) covers a wide range from 0.9 to 2.88 (Sundarajan et al., 1997). The velocity exponent decreases with an increase in erosion test temperature for 304 SS to values as low as 0.9 at low impact velocities. At relatively higher impact velocities, " p " appears to lie in the range 2 to 3.

- (iv) Tabakoff and vital (1983) carried out erosion tests on Inco 600 alloy using quartz particles in the size range of 70 μm to 800 μm . Authors observed that the erosion rate increased marginally with the increase of particle size. In case of 9Cr-1Mo steel, the rate of erosion increases with an increase in particle size, when the steel is eroded at 650°C temperature and also for a 1018 steel eroded at 450°C (Levy et al., 1986, 1989).
- (v) The data available on the influence of particle shape on elevated temperature erosion is very limited. Levy et al. (1986, 1989) investigated the erosion rate of a number of Cr containing steels at 850°C with angular SiC and spherical Al₂O₃ as erodent particles. The erosion rate is considerably higher when SiC is used as the erodent.
- (vi) As reported by Sundarajan et al. (1997), the influence of eroding material properties on the erosion behavior of metallic materials at elevated temperatures has been investigated only to a very little extent. The fact that the various strengthening mechanisms in relation to erosion at room temperature becomes less important or even unimportant at elevated temperatures. At one extreme, if the elevated temperature erosion data pertaining only to high impact velocities and/or with the angular SiC as the erodent is considered, the analysis becomes simpler because the metal erosion is the dominant regime under such conditions. In the case of elevated temperature erosion tests conducted at low velocities and using rounded Al₂O₃ as the erodent, the oxidation effect becomes important. In the case of steels having Cr < 10%, thick Fe₂O₃ scales, very much prone to spalling, formed during erosion leading to high erosion rates. In contrast, in the case of steels having Cr > 10%, segmented and thin Cr₂O₃ + spinel scales formed during erosion, leading to low erosion rate (Sundarajan et al., 1997).

2.9.1.3 Solid Particle Erosion of Metals and Alloys

The solid particle erosion behavior of various metals and alloys at elevated temperatures depends on whether the tests are conducted below or above about T_m , where T_m is the melting point of the erodent material (Singh and Sundararajan, 1990). It was reported that at test temperatures below about $0.35 T_m$ or at higher temperatures with an inert atmosphere, the erosion behaviors of ductile materials appear to be deformation controlled at room temperature. Further, it has been suggested that at higher temperature due allowance should be made for the alteration of mechanical behavior of the eroding material as caused by recovery and recrystallization. In these regimes authors observed from the erosion data that dependence of erosion rate with respect to velocity and impact angle at elevated temperature was similar to that obtained at room temperature. It has further been demonstrated that the mechanism of erosion under such conditions is identical to that obtained at room temperature. Beyond a test temperature of about $0.35T_m$, the oxidation of the eroding material becomes important and thus the nature of the interaction between erosion and oxidation becomes relevant and should be necessarily incorporated in the erosion model.

Hansen (1979) compared the erosion rates of alloys, ceramics and cermets. Author proposed that the order of material rankings would change with any of the change in variables such as velocity, particle type or size, and angle of impingement. Erosion tests using $27 \mu\text{m Al}_2\text{O}_3$ particles at normal incidence and 170 m/s at 20°C and 700°C in nitrogen has been performed. The tests were also conducted with a gas-jet erosion apparatus in which particles are fed from a hopper into a nozzle where they mix and are accelerated by a flowing gas stream (ASTM G76). Author normalized the erosion rates by defining the relative erosion factor (REF) as specimen volume loss divided by that of a stranded material, Stellite 6B. It has been concluded that REFs of most of the metals were similar at 20°C and 700°C, typically within a range of 20%. Tabakoff (1995) studied the high temperature erosion resistance of nickel-based MAR-M246 and cobalt-based X-40 superalloys in an erosion wind tunnel (high temperature), which simulates the operating conditions of steam and gas turbines. These superalloys showed maximum erosion rates at 45° impingement

angle. Further, both alloys showed good erosion resistance to turbo-machinery exposed to high temperatures and velocities.

Chinnadurai and Bahadur (1995) investigated the erosion mechanisms and effect of temperature (240°C to 800°C) on two heat resistant superalloys, Haynes-188 and Waspaloy at the impingement velocity of 50m/s. Authors have shown flake formation and ploughing as two types of erosion mechanisms. According to them flake formation occurs when the surface undergoes plastic deformation because of the repeated impacts of erodent particles. These impacts produce a fine layered structure. The extremities of these layers are severely work hardened and so develop radial cracks. Successive particle impacts break these outer layers thereby causing the erosive loss of material. Flakes are formed during impacts predominantly at high impingement angles and low operating temperatures. It has been reported that in a ploughing process, erodent particles penetrate the surface and travel a short distance thereby tearing the substrate and removing the material. Ploughing occurs predominantly at high operating temperatures. It was concluded that the surface eroded in the 24-200°C temperature range exhibited predominantly the flake appearance while those eroded in the 500 to 800°C range had more of the ploughing effect.

Shanov et al. (1997) investigated the erosion behavior of a nickel-based superalloy Waspaloy. Waspaloy behaved as a ductile material because the maximum erosion was between 30° to 45° impact angle. They also found that the sample temperature has a significant effect on the material erosion rate. Further it has been inferred that the erosion resistance of the Waspaloy decreases at elevated temperatures and were proportional to the particle impact velocity. Tabakoff (1999A, 1999B) also investigated the erosion behavior of INCO 718, Waspaloy, INCO 738 and MAR-246. The effects of the impact angle, particle velocity and temperature on the erosion rate of these superalloys had been experimentally investigated and it was established that these superalloys exhibit ductile erosion pattern and the erosion rate was found to be strongly dependent on the particle velocity. It has been concluded that the alloy INCO 718 wears less at elevated temperatures, while the Waspaloy deterioration is enhanced by raising the temperature.

Yang et al. (2008) have reported the erosion performance of mild steel for boiler tube at temperature from 300 to 800°C. The study was performed with alumina grit at velocity of 12 m/s as erosive particles at two impingement angles 30° and 90°. The erosion rate of the mild steel increased with the increase of the test temperature at the erosion angles of both 30° and 90°. The erosion rate at 800°C was 4 times higher than that at 300°C at an erosion angle 30° and 7 times higher in case of erosion angle 90°.

Sidhu et al. (2007A) studied the solid particle erosion behavior of boiler tube steels Grade A-1, T-11 and T-22 at 250°C temperature using silica sand as erodent. The tests were conducted with particle flow velocity 26 m/s at impact angles 30° and 90°. All the boiler steels have shown relatively higher erosion rate in the early cycles of the study, followed by steady state erosion rate with increase in the duration of study. The variation in the erosion rate was more during the incubation period (up to 4-5 cycles) and thereafter variation reduces because of smooth surface. The T-22 boiler steel has shown marginally higher erosion rate than T-11 steel at both impact angles. The erosion resistance of Grade A-1 was found to be minimum.

2.10 EROSION-CORROSION

Erosion-corrosion by solid particles in gaseous environments at elevated temperatures and hence wastage of alloys, is a serious problem in many industrial processes (Stack et al., 1993 and Stack et al., 1995). Erosion-corrosion of materials occurs in environments such as catalytic cracking systems in oil and gas separation, combined-cycle coal conversion systems such as pressurized fluidized bed combustion, and on the turbine blades of jet engines where erosive component may be caused by the ingestion of particulate material or the accumulation of such material as a result of the corrosion process (Stack et al., 1993). The reason for the extensive research in this area is that a synergy is observed between erosion and corrosion; this means essentially that the degradation can be greater than the sum of the processes operating separately. However, in other cases, the formation of a corrosion product can inhibit erosion; i.e. the erosion rate can be less than in the absence of corrosion. These contrary observations mean that models

developed for solid particle erosion and corrosion in the absence of erosion do not adequately describe many erosion-corrosion processes; hence this is the reason why erosion-corrosion interactions in oxidizing gases have received much attention in recent years (Stack et al., 1993). Numerous investigators have tried to identify the various possible mechanisms for interaction between erosion and corrosion. Such interactions were first described in terms of regimes by Hogmark and his co-workers (Stack et al., 1995).

Hogmark and his co-workers (Stack et al., 1995) identified six different mechanisms of erosion and corrosion interaction ranging from 'erosion-dominated' behavior where erosion of the alloy substrate predominates to 'corrosion-dominated' behavior where degradation due to corrosion is significantly greater than that due to erosion. In the later regime, erosion is considered to be negligible compared to corrosion. The intermediate regimes where corrosion alternately accelerates or inhibits erosion have received much attention from investigators working in the area. These intermediate regimes have been further sub-divided because the transition points can define whether erosion-corrosion rates can increase or decrease as a function of variables such as temperature.

Natesan and Liu (1989) divided the mechanisms of corrosion and erosion into two regimes on the basis of the kinetic energies of the impacting particles. According to them, when the kinetic energy is low, erosion behavior exhibits brittle erosion mechanism characterized by a maximum erosion rate under normal impact condition and a velocity exponent more than 3.0. When the kinetic energy is high, erosion behavior is ductile, i.e. maximum erosion rate occurs at oblique impact angles and the velocity exponent lies in the range of 2-2.5.

Kang and Birks (1987) have reported that four regimes existed, based on erosion-oxidation studies of pure metals (Fig 2.15). Such regimes were termed as: (i) erosion of metal, (ii) oxidation-affected erosion, (iii) erosion-enhanced oxidation, and (iv) oxide erosion. Sundararajan (1990) proposed five different modes of interaction between erosion and oxidation. Authors defined erosion-corrosion regimes as:

- (i) Metal erosion
- (ii) Oxidation-affected erosion

- (iii) Oxide erosion
 - (a) Oxidation-controlled erosion (spalling)
 - (b) Oxidation-controlled erosion (continuous)

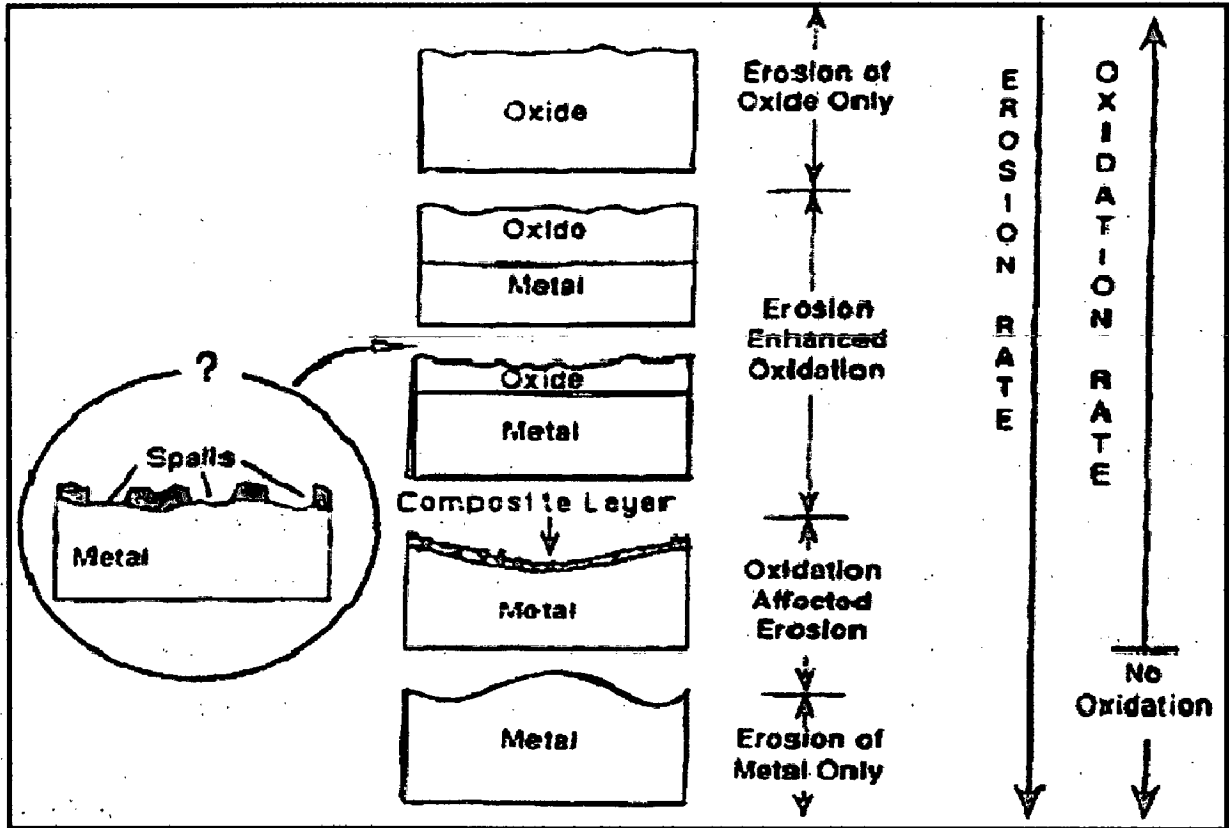


Fig. 2.15 Classification of erosion-corrosion according to Kang et al. (1987)

A number of parameters were introduced for predicting the conditions under which each of these regimes will operate. According to his model if steady state thickness of the oxide scale is smaller than the critical thickness of the oxide scale, three modes of interaction between erosion and oxidation are possible. In the first case, which applies either when there is no oxide scale or when the depth of deformation is much higher than the thickness of the oxide scale, metal erosion becomes important (presented in Figs 2.16.a and 2.16.b). In the second case, when the depth of deformation is smaller than the steady state thickness of the oxide scale, erosion of the oxide scale takes place as illustrated in Fig. 2.16 (c). When the depth of deformation is comparable to the steady state thickness of the

oxide, a regime known as oxidation affected erosion becomes dominant. In this case, erodent actually deforms the substrate along with the oxide scale as shown in Fig. 2.17 (a), leading to the formation of either a composite layer containing oxide and metal loss takes place from the composite layer. The erosion response of this layer depends on the oxide content of the layer. The oxidation controlled mode becomes operative when the steady state thickness of the oxide scale is more than the critical thickness of the oxide scale; the oxidation controlled mode becomes operative. Depending on the extent of growth of the oxide scale during the time interval between two successive impacts at the same site, two different modes can be envisaged. If the scale attains its critical thickness in between two successive impacts, oxidation controlled erosion (continuous) as shown in Fig. 2.17 (b), will be the operating mechanism. Otherwise, oxidation controlled erosion (spalling) becomes important (Fig. 2.17.c).

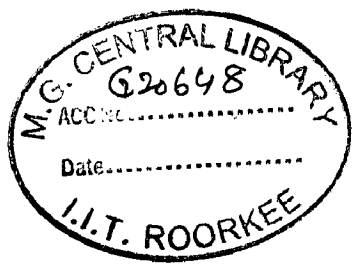
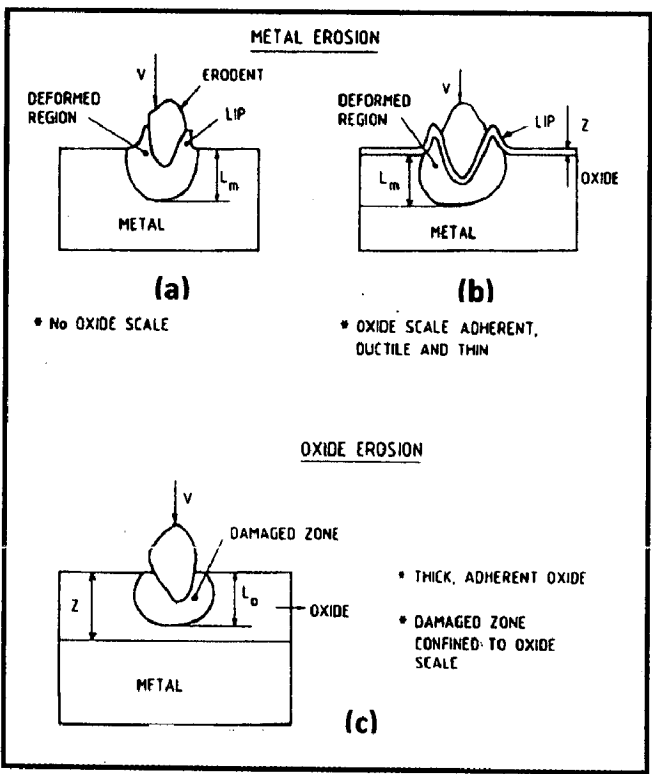


Fig. 2.16 Schematic representation of metal erosion (a) & (b); and oxide erosion (c), illustrating the nature of interaction between the oxide scale and the substrate during erosion (Sundararajan, 1990)

The vast technical literature available is evidence that corrosion and deposits on the fireside of boiler surfaces or in gas turbines represent important problems. When a comparison is made between the amount of ash collected in a boiler or a gas turbine, in the form of deposits, and the total amount of ash released during combustion, the conclusion is clear that most of the ash passes through the unit (Landry et al., 1959). For particles to collect on boiler surfaces or blade surfaces, they must first be brought close to the surface itself and be of the proper size. This can be ascribed to physical phenomenon involving the reaction of particles to the forces to which they are subjected within the stream of gases passing near the surfaces. A particle may hit and then rebound from the surface. If it hits or rubs the surface with sufficient force, erosion will result. On the other hand, if the particle is captured physically or chemically by the surface, a deposit is initiated whose growth appears aerodynamically inevitable. Because of high temperatures, reactions can then take place between the various particles deposited, and also with the gases passing nearby, particularly SO_3 and SO_2 . The resulting compounds may then react, by diffusion, with the metal structure on which they are attached and cause corrosion, which is known as Hot Corrosion (Landry et al., 1959).

Wang (1995) studied the erosion-corrosion behavior of two steels (AISI 1018 low carbon steel and Type 304 stainless steel) by fly ash from a biomass-fired boiler. The tests were carried out at 450°C and at room temperature, with particle velocities of 30 m/s for 5hr duration and at impact angles 30° and 90° . The major mechanism of material wastage was erosion simulated corrosion and corrosion accelerated erosion. Author has further added that the material wastage tested at room temperature for all the materials tested were much lower than those tested at 450°C .

Link et al. (1998) have studied the erosion-corrosion behavior of pure nickel, Ni-20Cr and Ni-30Cr alloys at 700°C and 800°C temperature. The exposures were made using normal impact of an air stream loaded with $20\mu\text{m}$ alumina. The erodent flowed at the rate of 400 mg per min and the velocities used were 75 m/s and 125 m/s. The reaction kinetics was measured discontinuously by interrupting the exposure and measuring weight loss.

Authors proposed that, under erosion-corrosion, the erosive stream prevents the formation of a continuous layer of chromia by removing the oxide faster than it can spread laterally. The specimen is said to be in a state of erosion-maintained transient oxidation. This mechanism implies that it would be difficult for protective scales to form in the presence of erosion and the oxidation behavior of an alloy cannot be used as a guide to its resistance to erosion-corrosion.

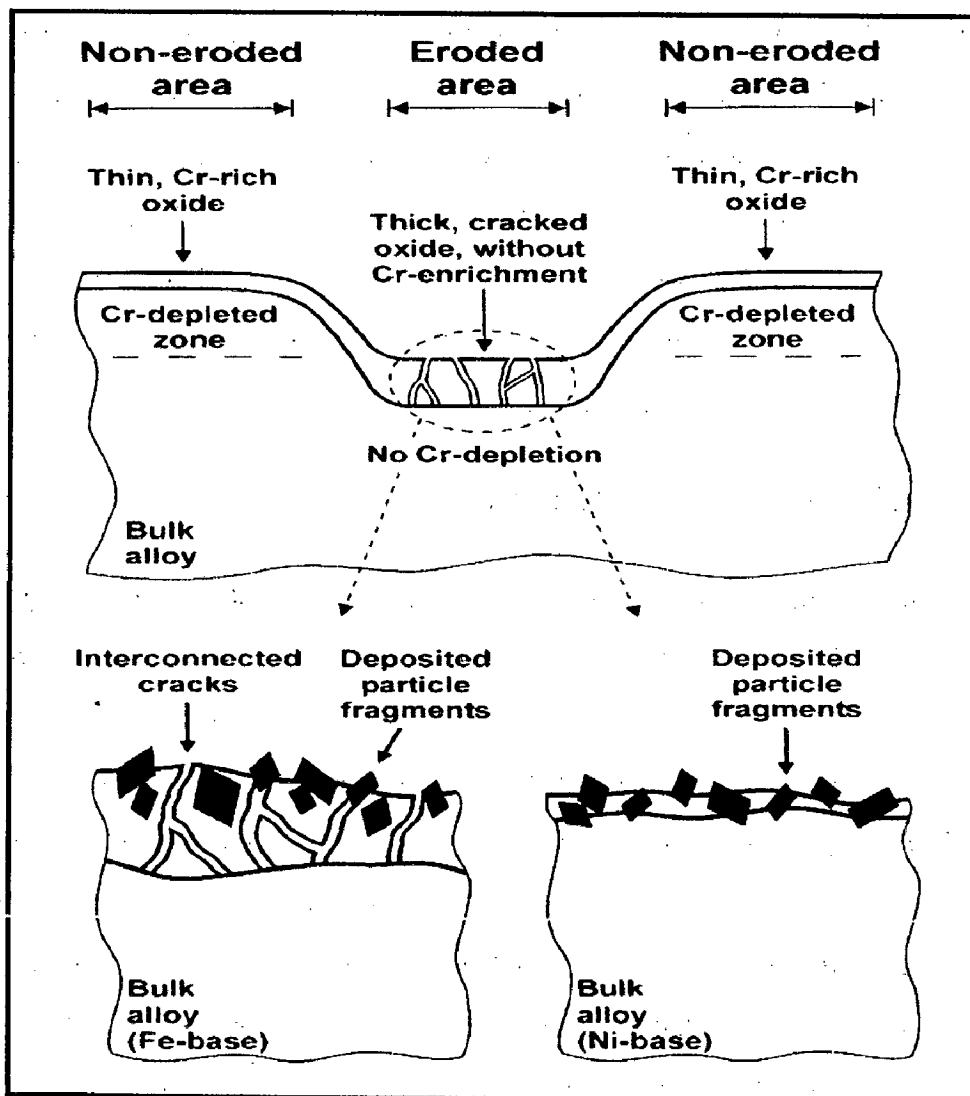


Fig. 2.18 Model illustrating the oxide formation during oxidation and erosion-corrosion at 550°C (Norling and Olefjord, 2003)

Norling and Olefjord (2003) have investigated the erosion-corrosion behavior of four steels (Fe_{2.25}Cr₁Mo, Fe₉Cr₁Mo, AISI 304, 353MA) and one Ni-based superalloy (Inconel 625). The alloys were exposed in a test rig at 550°C in air for 1 day, 1 and 3 weeks. The alumina erodent particle velocity was 1.2m/s. The erosion-corrosion rates for some of the materials were observed in the same order of magnitude as in a real FBC plant. The alloy showing the lowest wastage rate was 353 MA (maximum Cr content). The erosion-corrosion rate of the Ni-based alloy Inconel 625 was considerably high. Authors concluded that the alloy composition affects the wastage rate considerably. The uppermost erosion-corrosion resistance is obtained from the alloy containing the highest Cr-concentration. It has been suggested that the eroding particles cause crack formation in the oxide layer through which oxygen or other oxidizing gases are transported towards the metal. Figure 2.18 summarizes the oxide formation and cracking of the oxide for the higher alloyed Fe- and Ni-based alloys via a model. The strong oxide forming elements (Cr and Mn) are enriched in the thin oxide formed on the surface of the non-eroded areas.

2.11 COMBATING EROSION-CORROSION

Erosive, high-temperature wear of heat exchanger tubes and other structural materials in coal-fired boilers has become a key material issue in the design and operation of thermal power plants and is recognized as being one of the main causes of downtime in these installations, which could account for 50–75% of their total arrest time (Hidalgo et al., 2001A and 2001B). High-temperature oxidation and erosion caused by the impact of fly ashes and unburnt carbon particles are the main problems to solve in these applications, especially in those regions where the component surface temperature is above 873 K. Therefore, the development of wear and high-temperature oxidation protection systems in industrial boilers is a very important topic from both engineering and an economic perspective (Hidalgo et al., 2001A and 2001B). Preventive measures against metal losses and failures due to erosion-corrosion should be economically devised to ensure safety and reliability in the use of metallic components (Chatterjee et al., 2001).

As suggested by Fontana and Greene (1967), five methods of prevention or minimization of damage due to erosion-corrosion are used. These can be grouped into following categories:

1. **Better materials:** The reasons for using better materials which give better performance are obvious. A large number of Fe, Ni- and Co-based alloys exist today especially designed for good resistance to oxidation, erosion- corrosion by ash/salt deposits, but are expensive.
2. **Design:** Erosion-corrosion can be reduced through better design. Design involves change in shape, or geometry i.e. misalignment from one pipe section to the next can cause erosion-corrosion in both flanged and welded joint. Good design implies proper construction and workmanship.
3. **Alteration of the environment:** De-aeration and the addition of inhibitors are effective methods, but in many cases these are not sufficiently economical for minimizing erosion-corrosion damage. Temperature is the worst enemy in erosion-corrosion, which should be reduced. But this will reduce the efficiency of the plant.
4. **Cathodic protection:** This help to reduce attack, but it has not found widespread use for erosion-corrosion due to complexity of the process.
5. **Coatings:** Different coating techniques are applied to protect the critical surface areas from corrosive gases, including co-extrusion, chromising, weld overlay and thermal spray coatings.

Present materials being capable of resisting erosive and corrosive environments are highly alloyed, and thus expensive. In search for cost-effective solutions for erosion-corrosion problems, the effective method of erosion-corrosion prevention is to coat the alloy with a protective layer, which has been used in the current investigation. This is the preferred approach and various coatings like thermal sprayed coatings have become attractive (Uusitalo et al., 2002). Increasingly greater demand imposed on materials makes it more difficult or, at the current stage of development, even impossible to combine the different properties required in one single material (Chawla et al., 2006C). Therefore, a

composite system of a base material providing the necessary mechanical strength with a protective surface layer different in structure and/or chemical composition and supplied by a surface treatment can be an optimum choice in combining material properties.

As reported by Wang and Luer (1994), the use of coatings to protect the heat exchanger tubes of fluidized bed combustor from erosion-corrosion problems. Hocking (1993) has also suggested the use of corrosion resistance alloys as coatings to protect substrate alloys having good mechanical properties. Hidalgo et al. (1997, 1998, 1999 and 2000) have further discussed the use of plasma sprayed thin anti wear and anti oxidation coatings to take care of the high temperature erosion and corrosion problems in energy generation systems. Recent studies show that 80% of the total costs for the protection of metals are related to coating applications. Organic coatings cover a large part of this percentage, but also metallic ones have a relatively big market. In fact, metallic coatings possess, together with good corrosion resistance, good aesthetics, brightness, and interesting mechanical properties such as hardness and wear resistance (Fedrizzi et al., 2004).

2.12 MARINE CORROSION

Marine corrosion includes the deterioration of structures and vessels immersed in seawater, the corrosion of machinery and piping systems that use seawater for cooling and other industrial purposes, and corrosion in marine atmosphere (Heidersbach, 1987). Hossain et al. (2009) have reported that deterioration of the built infrastructure due to marine salts in coastal regions has been, for many years, a significant and ongoing problem. Marine salts adversely affect the durability of the infrastructure and reduce its service life. Although salt water is generally considered to be a corrosive environment, it is not widely understood how corrosive salt water is in comparison to other environments, such as fresh water (Dexter, 1987). Figure 2.19 (a) shows the corrosion rate of iron in aqueous sodium chloride (NaCl) solutions of various concentrations. The maximum corrosion rate occurs near 3.5% NaCl-the approximate salt concentration of seawater. Dobrzanski et al. (2007)

also reported that the chloride-rich seawater is a harsh environment that can attack the materials by causing pitting and crevice corrosion.

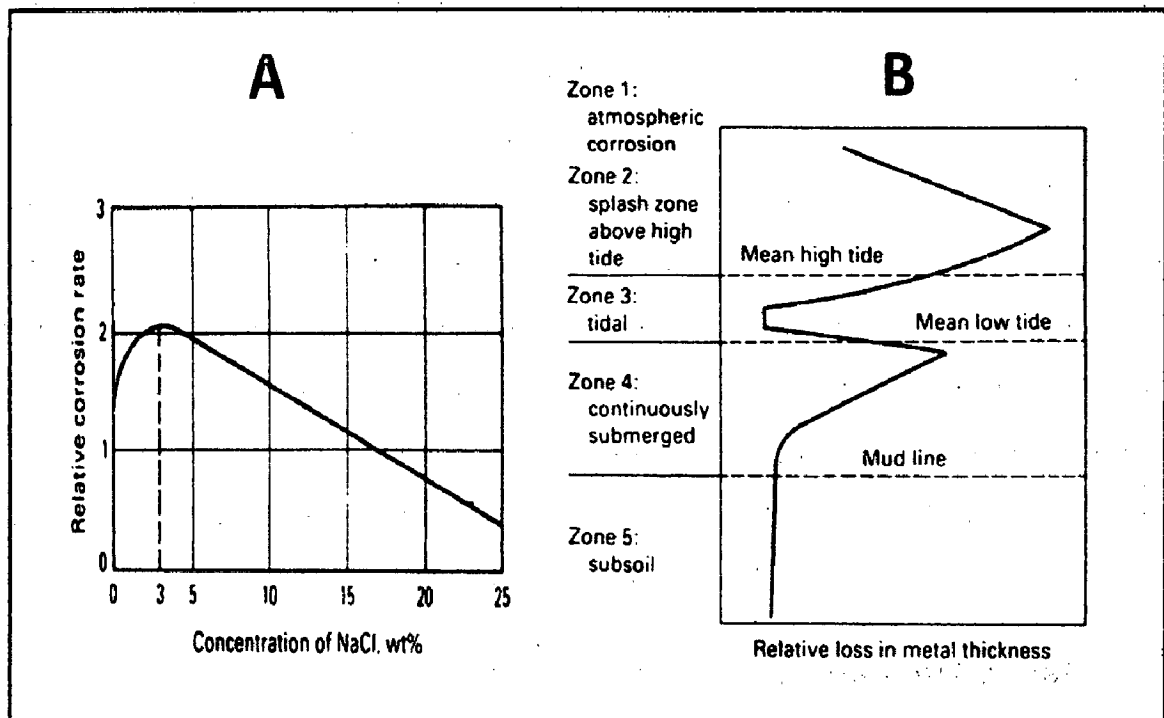


Fig. 2.19 (a) Effect of NaCl concentration on the corrosion rate of iron in aerated room-temperature solutions; (b) Zones of corrosion for steel piling in seawater, and relative loss of metal thickness in each zone (Dexter, 1987)

According to Dexter (1987), the general marine environment includes a great diversity of sub-environments, such as full strength open ocean water, coastal seawater, brackish and estuarine waters, bottom sediments and marine atmospheres. Exposure of structural materials to these environments can be continuous or intermittent, depending on the application. Structures in shallow coastal or estuarine waters are often exposed simultaneously to five zones of corrosion. Beginning with the marine atmosphere, the structure then passes to down through the splash, tidal, continuously submerged (for subtidal), and subsoil (or mud) zone. Figure 2.19 (b) illustrate the relative corrosion rate often experienced on a steel structure passing through all of these zones.

The sea spray, composed primarily of sea water along with particles naturally generated by the action of wind on the seawater surface, introduces ionic species into the

atmosphere, principally chlorides and sulfates (Hossain et al., 2009). The air containing sea spray causes accumulative deposition of ions on the external surface of the materials operating in marine environments, that penetrates the interior of the material through ionic diffusion causing its degeneration. Such environments are extremely dangerous as salt can penetrate and crystallize inside the material, causing deterioration of the material. The atmospheric sulfate and chloride pollutants can enhance conductivity of the wet film on the metal surface, leading to the metal deterioration process (Sahoo and Balasubramaniam, 2008 and Corvo et al., 1995). Chloride ions present in sea aerosol can be considered as a natural pollutant. Chloride ions serve as the catalyzer in accelerating the corrosion process. Further it has been reported that the plain carbon steel is subjected to more severe corrosion attack in a marine environment than in urban and rural media. According to Dobrzanski et al. (2007), resistance to pitting and crevice corrosion is very important if the material is to be used in chloride-containing environments.

2.12.1 Marine Atmospheres induced Corrosion

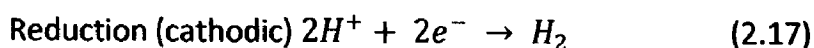
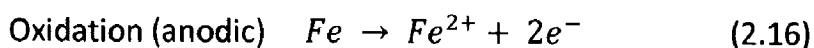
The marine or marine-industrial type environment is generally considered to be most aggressive environment (Griffin, 1987). The marine atmospheric corrosion includes atmospheric corrosion (Zone 1, Fig. 2.19b) and the splash zone above high tide (Zone 2, Fig. 2.19b). For carbon steels in marine exposure, the maximum corrosion rate occurs in the splash zone, in which the alloy is wet almost continually with well-aerated seawater. Griffin (1987) has reported that the annual cost of corrosion in the United States has been estimated at \$167 billion. A reasonable fraction of this amount is the result of atmospheric corrosion. The buildings, automobiles, bridges, storage tanks, ships, and other items that must be coated, repaired, or replaced represents only some of the problem areas of corrosion to the U.S. economy.

Bao et al. (2008) have explained the importance of corrosion induced by marine atmosphere. According to authors, MCrAlY (M = Ni and/or Co) overlay coatings are widely utilized on blades and other high-temperature components in gas turbine engines because of their excellent high-temperature oxidation and hot corrosion resistance, both as

standalone coatings and as bondcoats for thermal barrier coating systems (TBCs). The main function of MCrAlY coatings is on high-temperature protection. Naturally, most research on MCrAlY coatings was on their oxidation and hot corrosion properties at high temperature. However, a distinct fact is that those hot section components especially for airfoils, covered with MCrAlY coatings, will “relax” if they are exposed to ambient temperature for a long period of time during service. Pitting corrosion of compressor blades occurs when moisture-containing salts are collected on. These corrosion pits could cause detrimental consequence, such as penetrative corrosion, and fatigue cracking, etc. (Swadzba et al., 1993). Surprisingly, it seems no research works have been conducted on the behavior of this type of corrosion occurring in MCrAlY coatings on turbine blades. Therefore, it is meaningful to investigate the ambient environmental corrosion behavior and mechanism of the materials as is done in present work by evaluating the corrosion behavior of substrate and coatings in accelerating mode, i.e., by salt spray tests and electrochemical methods.

Corrosion of metals in aqueous environments (marine environment containing moisture and salt, aqueous solutions, atmospheric air, natural waters and man-made solutions) is almost always electrochemical in nature (Merek, 1987). It occurs when two or more electrochemical reactions take place on a metal surface. As a result, some of the elements of the metal or alloy change from a metallic state into a nonmetallic state. The products of corrosion may be dissolved species or solid corrosion products; in either case, the energy of the system is lowered as the metal converts to a lower-energy form (Merek, 1987 and Chawla et al., 2006). Rusting of steel is the best known example of conversion of a metal (iron) into a nonmetallic corrosion products (rust).

For metals, corrosion to occur, an oxidation reaction (generally a metal dissolution or oxide formation) and a cathodic reduction (such as proton or oxygen reduction) must proceed simultaneously. For example, the corrosion of iron in acid solutions is expressed as follows (Fontana and Greene, 1967):

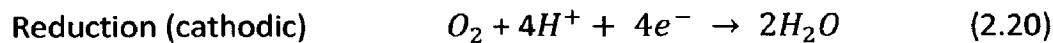
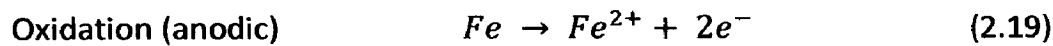


Overall reaction

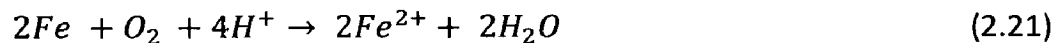


An oxidation reaction or anodic reaction (Eq. 2.16) and reduction or cathodic reactions (Eq. 2.17) are partial reactions-both must occur simultaneously and at the same rate of the metal surface. If this was not true, the metal would spontaneously become electrical charged, which is clearly impossible. This leads to one of the most important basic principles of corrosion: during metallic corrosion, the rate of oxidation equals the rate of reduction in terms of electron production and consumption. Now, when iron is immersed in water or seawater which is exposed to atmosphere i.e. a solution containing dissolved oxygen.

The following expressions are used:



Overall reaction



The reaction for the metal dissolution ($M \rightarrow M^{n+}$) driven by the cathodic reaction $O \rightarrow R$, is:



Where M is a metal, O is oxygen or another oxidizing agent, n+ is the multiple of charge, and R is the reduced species or reduction. The corrosion process has been written as two separate reactions occurring at two distinct sites on the same surface. Figure 2.20 (a) shows these two processes spatially separated for clarity. Whether or not these are actually separated or occur at the same point on the surface does not affect the above principle of charge conservation (Fontana and Greene, 1967).

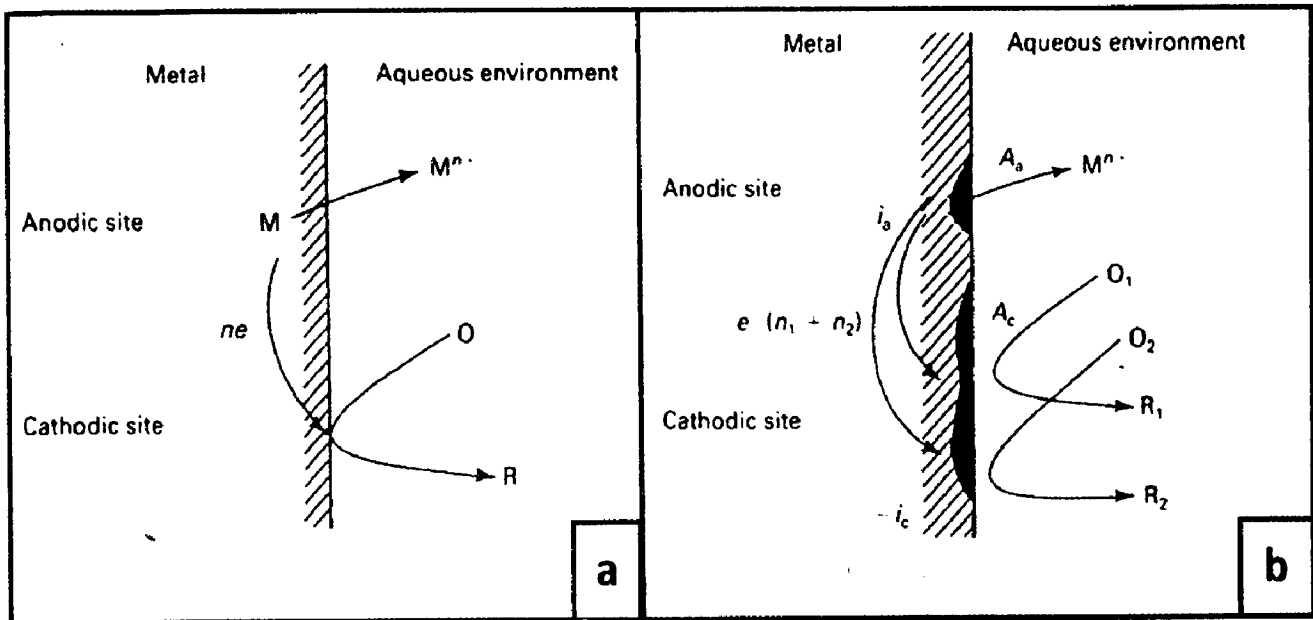


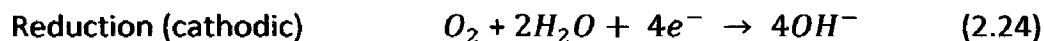
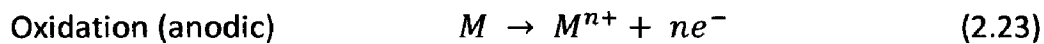
Fig. 2.20 Schematics of two distinct corrosion processes, (a) the corrosion process showing the separation of anodic and cathodic sites; (b) the corrosion process involving two cathodic reactions (Soesmith, 1987)

The corroding metal is equivalent to a short-circuited energy-producing cell in which the energy is dissipated during the consumption of cathodic reagent and the formation of corrosion product (Fig. 2.20.a). Because electrons are liberated by the anodic reaction and consumed by the cathodic reaction, corrosion can be expressed in terms of electrochemical current. Expressing the mass balance requirement in electrochemical terms, it can be stated that the total current flowing into the cathodic reaction must be equal and opposite in sign to, the current flowing out of anodic reaction (Fig. 2.20 b).

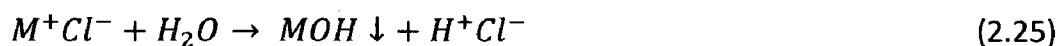
The rate of an electrochemical reaction is limited by various physical and chemical factors (Fontana and Greene, 1967). Hence, an electrochemical reaction is said to be polarized or retarded by these environmental factors. Polarization can be divided into two different types, activation polarization and concentration polarization. Activation polarization refers to an electrochemical process which is controlled by the reaction sequence at the metal-electrolyte interface. Concentration polarization refers to electrochemical reactions which are controlled by the diffusion in the electrolyte. Another phenomenon which is

associated with electrochemical reactions, which has fascinated scientists and engineers for over 120 years, is metallic passivity. It refers to the loss of chemical reactivity experienced by certain metals and alloys under particular environmental conditions (Davis and Hardbound, 1999). That is, certain metal and alloys become essentially inert and act as if they were noble metals. The metals most susceptible to this kind of behavior are the common engineering and structural materials, including iron, nickel, silicon, chromium, titanium, and alloys containing these elements.

A corrosion pit is a unique type of anodic reaction (Fontana and Greene, 1967, Davis and Hardbound, 1999 and Liang, 2008). It is an autocatalytic process. That is, the corrosion processes within a pit produce conditions which are both stimulating and necessary for the continuing activity of the pit. Consider a metal 'M' is being pitted by an aerated NaCl solution. Rapid dissolution occurs within the pit, while oxygen reduction takes place on adjacent surfaces. This process is self-stimulating and self-propagating.



The rapid dissolution of metal within the pit tends to produce an excess of positive charge in this area, resulting in the migration of chloride ions to maintain electro-neutrality. Thus, in the pit there is a high concentration of MCl and, as a result of hydrolysis (Eq. 2.25), a high concentration of hydrogen ions. Both hydrogen and chloride stimulate the dissolution of most metals and alloys, and the entire process accelerates with time (Liang, 2008). The metal chloride and water will react as:



Since the solubility of oxygen is virtually zero in concentrated solutions, no oxygen reduction occurs within a pit. The cathodic oxygen reduction on the surfaces adjacent to pits tends to suppress corrosion. In a sense, pits cathodically protect the rest of the metal surface (Fontana and Greene, 1967).

Liang (2008) and Fontana and Greene (1967) have explained the corrosion tube growth mechanism. At the interface between the pit and the adjacent surface, iron hydroxide forms due to interaction between the OH^- produced by the cathodic reaction and the pit-corrosion producer. This is further oxidized by the dissolved oxygen in the solution to $\text{Fe}(\text{OH})_3$, Fe_3O_4 , Fe_2O_3 , and other oxides. This 'rust' rim grows in the form of a tube as shown in Fig. 2.21. Electrochemical tests methods primarily focus on the control and measurement of the fundamental properties of electrochemical reactions (Davis and Hardbound, 1999). The electrochemical potential is equivalent to the driving force for reactions and it determines the reactions that can occur at the anode and cathode in an electrochemical cell. The current is equivalent to the reaction rate in an operating corrosion cell.

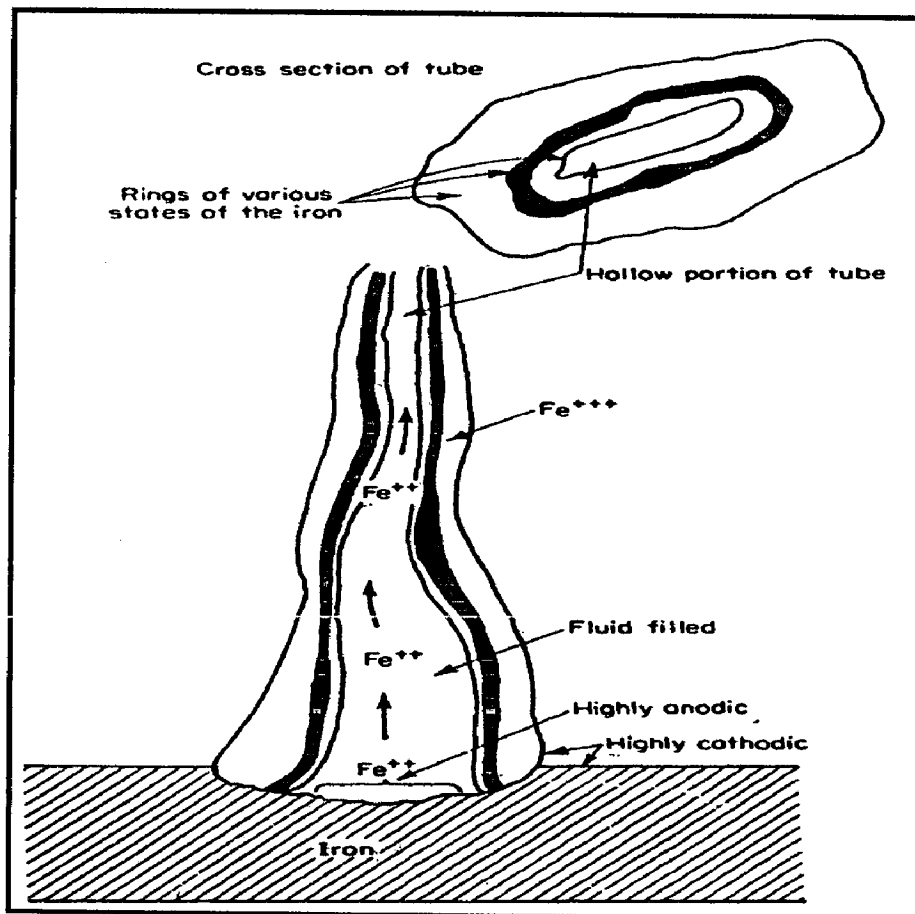


Fig. 2.21 Corrosion tube growth mechanism (Fontana and Greene, 1967 and Liang, 2008)

The greater the current, the greater is the corrosion rate. Scully (1987) reported that pitting and crevice corrosion are usually associated with the breakdown of passivity. The anodic electrochemical behavior of a passive alloy in deaerated acid is schematically shown in Fig. 2.22. The characteristics of this diagram will aid in determining the resistance of an alloy to localized attack. Tests for evaluating the susceptibility of a material to pitting and crevice corrosion include potentiodynamic tests, galvanostatic tests, tribo-ellipsometric methods, pit-propagation rate curves, and electrochemical noise measurements (Scully, 1987).

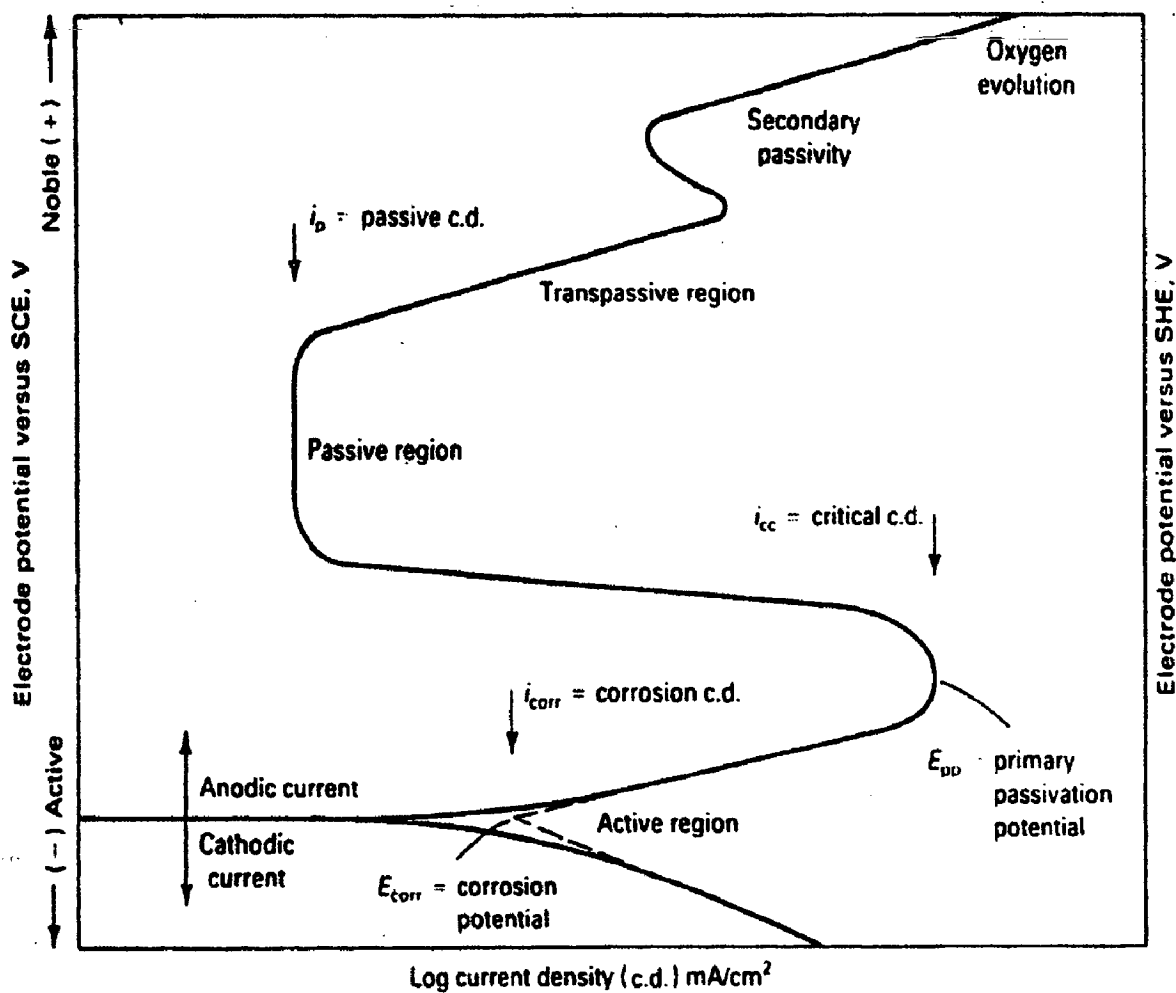


Fig. 2.22 Hypothetical anodic and cathodic polarization behavior for a material exhibiting passive anodic behavior (Davis and Hardbound, 1999)

2.12.2 Factors affecting Marine Corrosion

According to Griffin (1987), a variety of factors affect the atmospheric corrosion behavior of materials. These include moisture, temperature, winds, airborne contaminants, alloy content, location, and biological organisms.

- 1. Moisture:** For corrosion to occur by an electrochemical process there must be an electrolyte present. An electrolyte is a solution that will allow a current to pass through it by the diffusion of anions (negatively charged ions) and cations (positively charged ions). Water that contains ions is a very good electrolyte. Therefore, the amount and availability of moisture present is an important factor in atmosphere corrosion. One of the measures of the effects of moisture is the time of wetness. The corrosion rate increases as the time of wetness increases. The corrosion products and contaminants have also effect on relative humidity. When the sulfur dioxide level increases, there is a corresponding increase in the overall corrosion rate. However, the severity o the marine environment is related to the salt content of the sea spray or dew that contacts the material surface, which is usually more corrosive than rainfall.
- 2. Airborne Contaminants:** The second most important factor in atmospheric corrosion is the contaminants found in air. These can be man-made or natural, such as airborne moisture carrying salt from the sea or sulfur dioxide put into the atmosphere by a coal-burning utility plant. The important contaminants are chlorides, sulfur dioxide, carbon dioxide, nitrogen dioxide and hard dust particles. The maximum corrosion rate is related to the maximum chloride in the atmosphere. The chlorides of calcium and magnesium have a tendency to form liquid films on metal surfaces. The presence of SO_2 in the atmosphere increases the thickness of the electrolyte film and increasing the aggressiveness of the environment whereas the presence of CO_2 lessens the effect of SO_2 .
- 3. Location:** The height above the ground and the distance from the sea are both important. In the splash zone, the corrosion rate is highest slightly above mean high tide. This zone would not only have high chloride content, but would also be

alternately wet and dry. As the height above the sea increases, the corrosion rate decreases because the specimen is not wet as often.

4. **Temperature:** The relative humidity, the dew point, the time of wetness and the kinetics of the corrosion are affected by the temperature. For atmospheric corrosion, there are three distinct patterns with increasing temperature over the range of 20 to 40°C: corrosion rate increases for iron, decreases for zinc and remains constant for copper.
5. **Metallurgical Variables:** As a class, the stainless steel alloys are more susceptible to damage by pitting corrosion than are any other group of metals and alloys (Fontana and Greene, 1967). Surface finish often has a marked effect on pitting resistance. Pitting and localized corrosion are less likely to occur on polished than on etched or ground surfaces. The selection of a particular alloy composition can make a significant difference in the corrosion rate of a material. The significance of chromium (Cr) as an alloying element for atmospheric corrosion conditions classified as moderate and severe marine. Above 12 wt% Cr, the atmospheric corrosion becomes negligible; lower Cr levels result in a rapid increase in the corrosion rate.
6. **Sunlight:** it influences the degree of wetness and affects the performance of coatings and plastics.
7. **Wind:** The direction and velocity of the wind affect the rate of accumulation of particles on metal surfaces. Also, wind disperses the airborne contaminants and pollutants. A marine site may be made even more aggressive by the prevailing winds bringing industrial pollutants, particularly SO₂, to the marine site.
8. **Time:** For many materials, there is decrease in corrosion rate as time increases. This decrease is associated with the formation of protective corrosion layer.
9. **Exposure Time:** One of the difficulties with marine atmospheric corrosion testing is the length of time required for the tests. For steels, a reasonable estimate of long-term corrosion performance can be made from short-term data. This is not always the case; any short-term result must be used very cautiously and it is always best to have long-term test data available.

2.12.3 Countermeasures against Marine Corrosion

Corresponding to the variety of corrosive environments is the number of countermeasures that have been developed to avoid excessive material damage in marine atmosphere. These can be:

1. **Better materials:** The reasons for using better materials which give better performance are obvious. The selection of a particular alloy composition can make a significant difference in the corrosion rate of a material. The significance of chromium (Cr) as an alloying element for atmospheric corrosion conditions classified as moderate and severe marine. Above 12 wt% Cr, the atmospheric corrosion becomes negligible; lower Cr levels result in a rapid increase in the corrosion rate (Griffin, 1987).
2. **Cathodic protection:** Cathodic protection is an electrochemical means of corrosion control that is widely used in the marine environment (Heidersbach et al., 1987). It can be defined as a technique of reducing or eliminating the corrosion rate of a metal by making it the cathode of an electrochemical cell and passing sufficient current through it to reduce its corrosion rate. Two types of cathodic protection systems are commonly used in marine applications: impressed-current (active) systems and sacrificial anode (passive) systems.
3. **Organic Coatings:** Smart and Heidersbach (1987) reported that organic coatings are the principal means of corrosion control for the hulls and topsides of ships and for the splash zones on permanent offshore structures. Organic coatings include primers (inhibitive primers, zinc-rich primers), top coats, chlorinated rubber coatings and epoxies.
4. **Metallic Coatings:** According to Montemarano and Shaw (1987), effective protection from the marine environment can be provided by metallic coatings, which include thermal spray, galvanizing, and for certain applications, electroplating. In general, metallic coatings are two to three times more expensive than their traditional

organic counterparts; therefore the use is usually justified for longer service life and reduced maintenance.

2.13 PROTECTIVE COATINGS

In a wide variety of applications, materials have to operate under severe conditions such as erosion, corrosion and oxidation at higher temperature in hostile chemical environments. Therefore, surface modification of these components is necessary to protect them against various types of degradation (Pawlowski, 1995). Coating technology is one of the more rapidly growing technologies in the field of surface modifications of materials (Chawla et al., 2007B). A coating can be defined as a layer of material, formed naturally or synthetically or deposited artificially on the surface of an object made of another material, with the aim of obtaining required technical or decorative properties (Burakowski and Wierzchon, 1999). There are three main kinds of compositions barriers: Inert or essentially inert, inhibitive and sacrificial. Various combinations of these types are found in coating systems designed to use some or all of the several protective advantages provided. It must be remembered that there is no such thing as a “perfect” coating in a practical sense so none of these types or any combination can be expected to give perfect protections (Hamner, 1977).

Coatings provide a way of extending the limits of use of materials at the upper end of their performance capabilities, by allowing the mechanical properties of the substrate materials to be maintained while protecting them against wear or corrosion (Sidky and Hocking, 1999). In the last few decades, development of protective coatings has become an active area in the field of materials engineering (Wang and Chen, 2003). As summarized by Heath et al. (1997); the main advantages of coatings as follows:

- Very high flexibility concerning alloy selection and optimization for specific resistance to corrosion environments and particle abrasion/erosion. Surface properties can be separated from required mechanical properties of the structural component.

- Coating systems (multi-layered or functionally graded) can be used, combining, for example, good adhesion with optimized corrosion and erosion behavior.
- Unique alloys and microstructures can be obtained with thermal spraying which are not possible with a wrought material. These include continuously graded composites and corrosion resistant amorphous phases.
- Costs of a coating solution are normally significantly lower than those of a highly alloyed bulk material; thermal spray coatings are especially interesting for their cost/performance ratio.
- Thermal spray coatings additionally offer the possibility of on-site application and repair of components, given a sufficient accessibility for the sprayer and his equipment. However, thermal spraying in the workshop is preferred, whenever possible, to achieve optimum results.

The demand for higher performance and increased efficiency has resulted in the progressive increase in the temperatures of operation of turbines. This has been accompanied by the development of single crystal blade technology, more advanced corrosion-resistant coatings and complex cooling techniques (Stott et al, 1994; Conner and Connor, 1994). The development of modern coal fired power generation systems with higher thermal efficiency requires the use of construction materials of higher strength and with improved resistance to the aggressive service atmospheres. These requirements can be fulfilled by protective coatings (Nickel et al., 2002).

Protective surface treatments are widely used at low temperature, but the use of these at elevated temperature is more recent. High-temperature applications are limited largely to the aerospace industry. An enormous challenge exists to develop and apply these techniques to other high-temperature applications (Stroosnijder et al., 1994). Though superalloys have been designed for high temperature applications, however, protective coatings are applied to enhance their life for use in corrosive environments as they are not able to meet the requirement of high-temperature strength and high-temperature corrosion resistance simultaneously (Liu et al., 2001).

Nanostructured protective coatings composed of crystalline/amorphous nanophase mixture have recently attracted increasing interests in fundamental research and industrial applications, because of the possibilities of synthesizing a surface protection layer with unique physical-chemical properties that are often not attained in the bulk materials (Pei et al., 2005). Nanostructured materials as a new class of engineering materials with enhanced properties and structural length scale between 1 and 100 nm (Chawla et al., 2006A). Nanostructured materials indeed behave differently than their microscopic counterparts because their characteristic sizes are smaller than the characteristic length scales of physical phenomena occurring in bulk materials (Chawla et al., 2007A). In recent years; it has been found that nanocrystalline coatings produced by the magnetron sputtering technique had shown superior oxidation corrosion resistance compared with that of conventional polycrystalline alloys (Liu et al., 2007).

Corrosion performance of nanostructured materials/coatings is a hot topic in corrosion field. As reported by Chawla et al. (2008), in the past decade, attractive properties associated with a nanostructure have been documented for bulk materials, where most of the research in the field of nanomaterials has been focused. Nanostructured materials indeed behave differently than their microscopic counterparts because their characteristic sizes are smaller than the characteristic length scales of physical phenomenon occurring in bulk materials (Chawla et al., 2007A). In many tribological applications, hard coatings of metal nitrides are now commonly used (Bertrand et al., 2000). The major properties required for such coatings are hardness and wear resistance. However, because of severe operating conditions, there is a need to combine mechanical features with corrosion resistance properties. In the past years, hard protective TiAlN coatings and AlCrN coatings were widely used for wear resistant properties. Recently these coatings are gaining importance for high temperature wear, corrosion and oxidation resistance applications (Kalss et al., 2006, Fujita, 2005).

The development of a truly satisfactory coating that meets all of the requirements is a difficult task. Accordingly, compromises are often made, depending on the specific application of the coated material in a particular environment. Moreover, because of

coating-environment and coating-substrate reactions, the structures of the actual protective coating systems are complex.

2.14 COATING PROCESSES

There are many coating deposition techniques available, and choosing the best process depends on the functional requirements, adaptability of the coating material to the technique intended, level of adhesion required, (size, shape, and metallurgy of the substrate), and availability and cost of the equipment. The commonly employed coating (both diffusion and overlay) deposition techniques have been enlisted in Fig. 2.23 (Bhushan and Gupta, 1991). These techniques are divided into metallic and non-metallic categories.

From a production point of view, three methods are in current use, these being chemical vapour deposition (CVD) from a pack, physical vapour deposition (PVD) and thermal spraying (metal spraying). A serious drawback of the pack process is the inclusion of pack particles in the coating which can lead to coating failure (Nicoll, 1984). Moreover, disadvantage of the CVD process is that, because it is a non-line-of-site technique, proper masking and tooling become design considerations and an expense (DeMasi-Marcin and Gupta, 1994). Moreover, according to DeMasi-Marcin and Gupta (1994), although the PVD method is a complex process, especially in case of deposition of M-Cr-Al-Y type coatings as the vaporization pressures of each of the elements of interest must be considered for producing controlled alloy chemistry, yet physical vapor deposition and plasma spray (a thermal spray process) have been reported to be two major coating processing technologies which are used worldwide. The PVD processes have been particularly successful in improving mechanical properties such as wear, friction, and hardness (Pierson, 1987). Their use as corrosion-resistant coatings is also becoming widespread. One of the advantages of thermal spraying is the fact that the molten or partly molten coating material droplets are deposited on to a substrate material without melting and only slight heating of the substrate occurs.

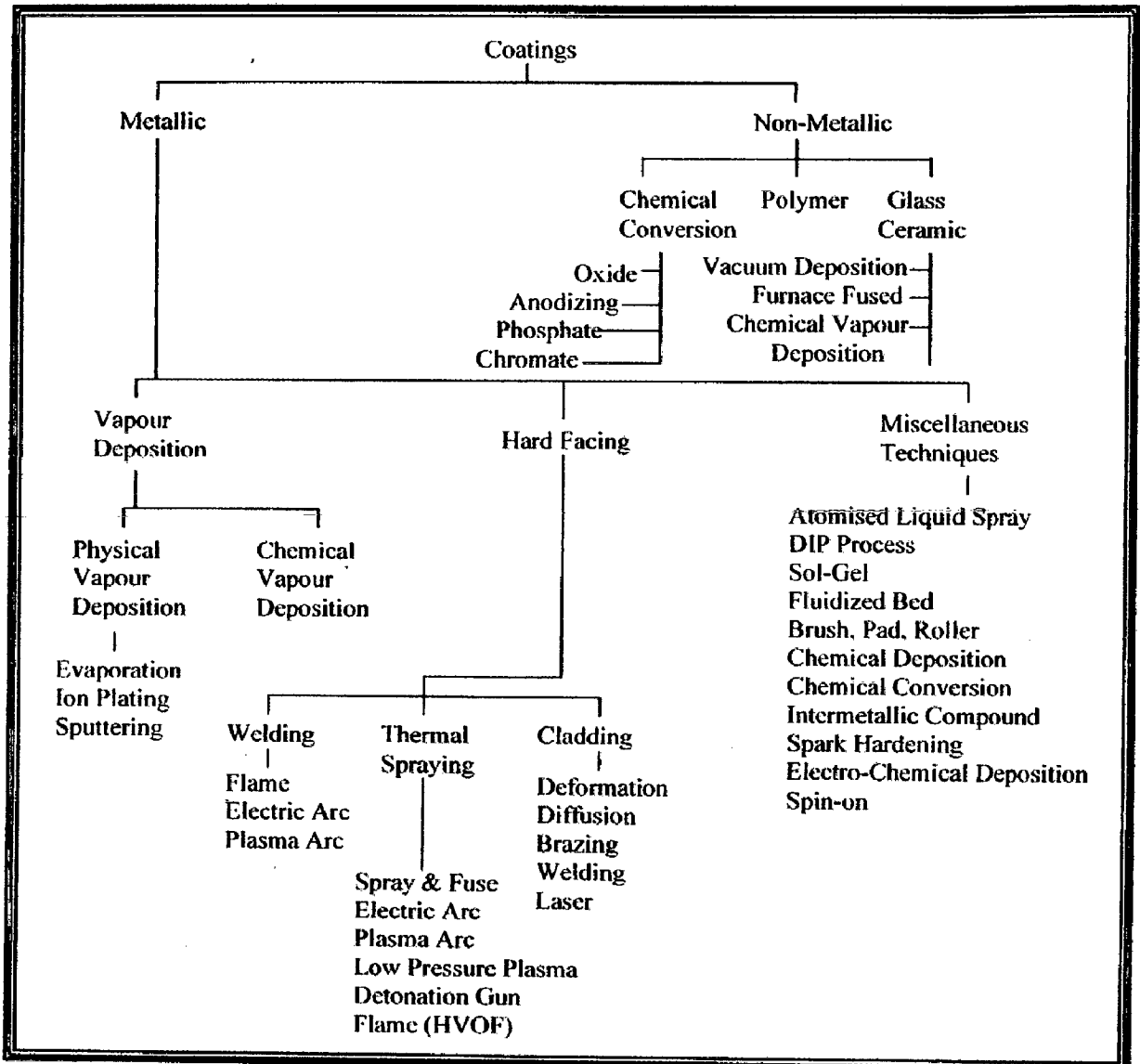


Fig. 2.23 Coating deposition processes (Bhushan and Gupta, 1991)

2.15 THERMAL SPRAYING PROCESS

The earliest records for thermal spraying are patents by the Swiss engineer M.U. Schoop, originating in the early 1900s (Bunshah, 2001). At first lead and tin wires were melted in a welding torch by the energy of an acetylene/oxygen flame. The brilliant idea of using fine atomized metallic particles for production of coatings came to Schoop after

watching his son playing with his toy cannon. Mr. Schoop observed that the hot lead shots that were projected out of the cannon, stuck to almost any surface, the result of which gave him the idea that if metal could be melted and projected in a spray-like manner, then a surface could be built up with that material. The wire-arc spraying process was patented around 1908 by Mr. Schoop, making the deposition of more, and various metals possible (Bunshah, 2001). The technology continued, but expanded in the 70s (Fig. 2.24) due to development of the thermal plasmas and the increasing demand of high-temperature and wear resistant materials and coating systems (Knotek, 2001). Most thermal spray processes require abrasive blasting or a bond coat to optimize the coating adhesion (Budinski, 1998).

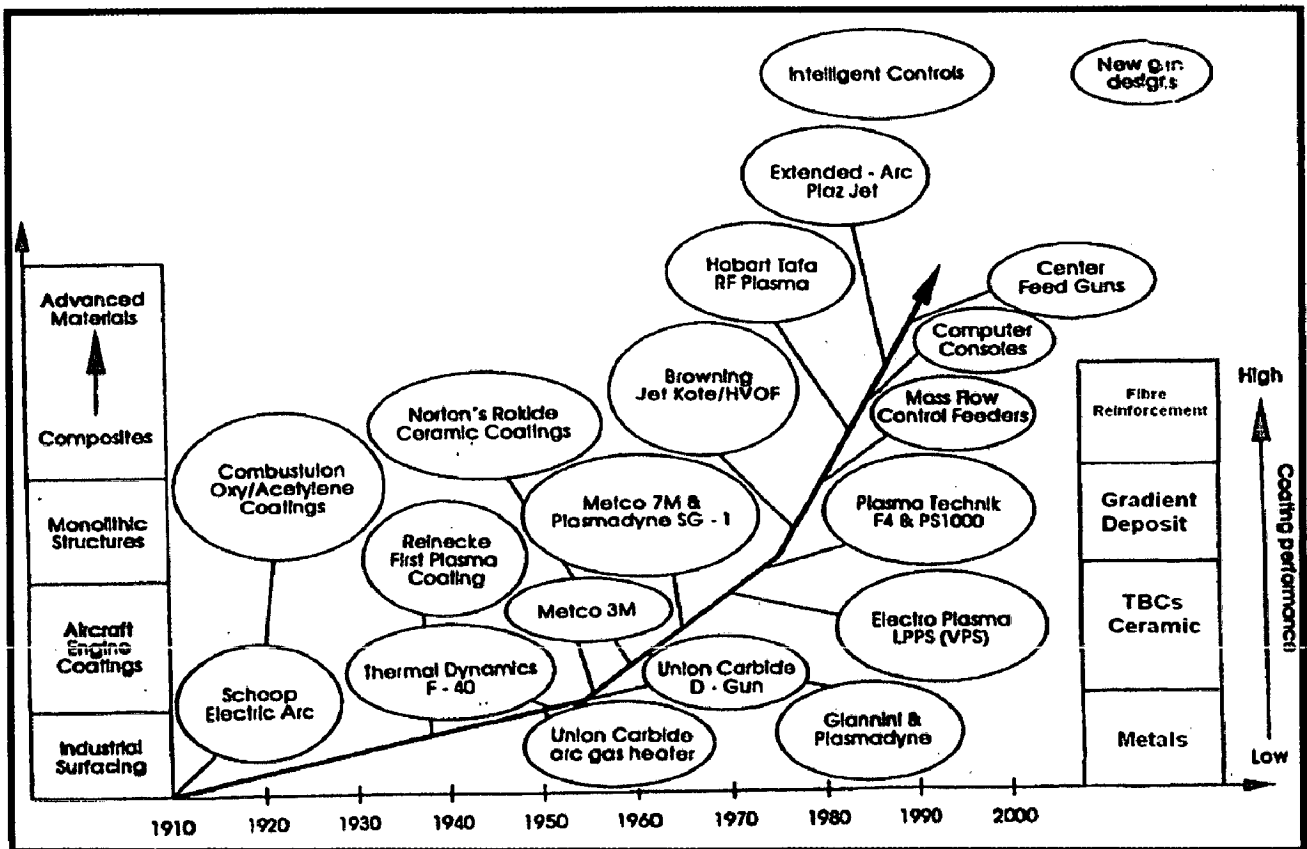


Fig. 2.24 Historical development of thermal spraying equipment, processes, and materials (Bunshah, 2001)

Thermal spraying is a generic coating technique whereby droplets of molten or partially-molten material are generated and projected at a surface to form a coating. The droplets undergo little interaction with the substrate, merely adhering to the roughened surface through physical means to form an “overlay” coating. Generally, any material which does not decompose, vaporize, sublime, or dissociate on heating, can be thermally sprayed. Materials ranging from polymers to metals, cermets and ceramics are routinely sprayed. In the generalized thermal spray process, the coating material in rod, wire or powder form is fed into a high temperature heat source, where it is heated close to, or in excess of its melting temperature. A high velocity accelerating gas or combustion gas stream accelerates the droplets of material to the substrate, where they impact and spread across the surface to form a “splat”, Fig. 2.25 (Matthews, 2004).

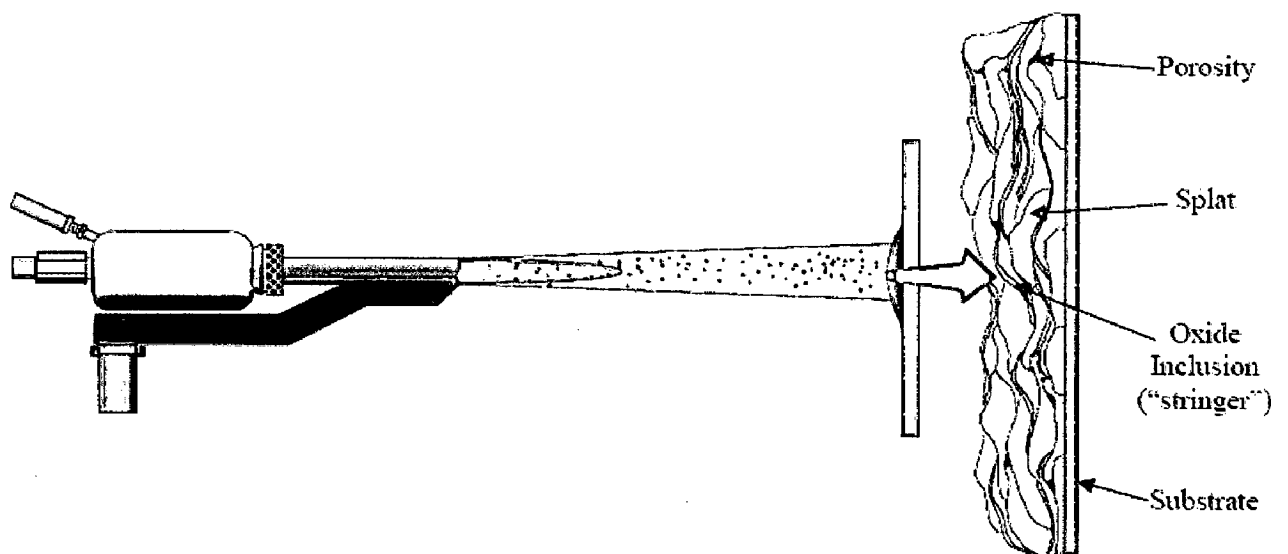


Fig.2.25 Schematic development of the thermal spray process and mechanism of coating build-up (Matthews, 2004)

The thermal spray coating process should start as soon as possible after the surface preparation is completed, since the prepared surface is very active and oxidation, recontamination, etc., should be avoided. The oxidation time during thermal spray coating is short (Fig.2.26) typically less than 0.01 s, and can occur in either the solid or molten state. The oxidation of coatings is not always harmful, it is equally important to control and

understand the different aspects of oxidation of coatings; therefore, it is important to find an optimum level for oxidation of coatings (Herman, 1988; Korpiola and Vuoristo, 1996; Nerz et al., 1992). The Thermal spray processes that have been used to deposit the coatings for the protection against the high-temperature corrosion are enlisted below, summarized by Heath et al. (1997):

- Flame spraying with a powder or wire
- Electric arc wire spraying
- Plasma spraying
- Spray and fuse
- High Velocity Oxy-fuel (HVOF) spraying
- Detonation Gun

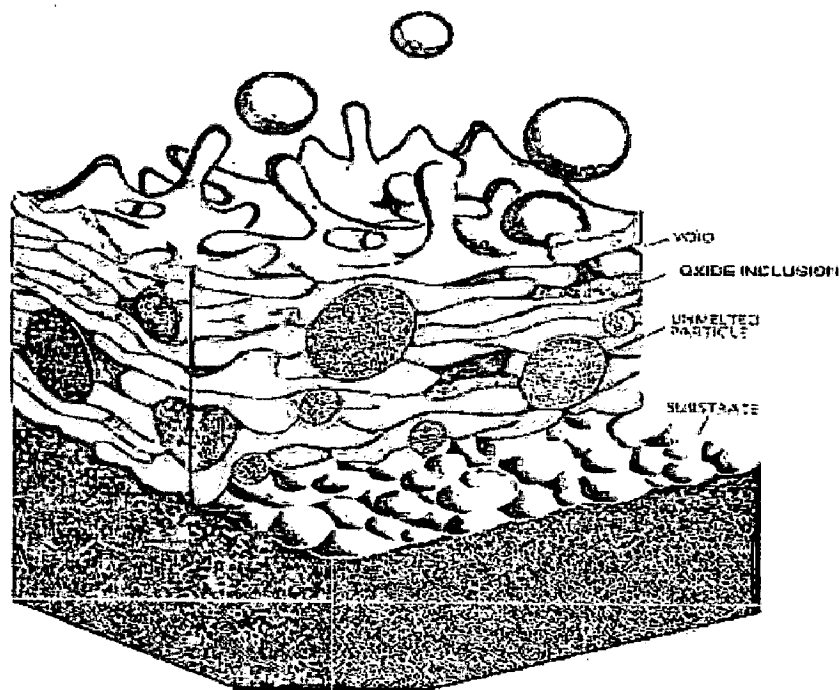


Fig.2.26 Coating deposition and the oxidation process (Herman, 1988)

During in-flight oxidation, a layer of oxide is formed on the molten particle due to chemical reactions between the surface of the liquid phase and oxygen or due to diffusion of oxygen into the liquid (Deshpande et al., 2006). The turbulent mixing of the liquid part of the powder particle during its flight destroys the surface layer of oxides and causes the

oxides to be distributed more uniformly through the bulk volume of the particle. However, when temperature of the particle starts dropping during later part of the flight, these oxides tend to solidify and a thin oxide shell would form around the droplet (Fig.2.27).

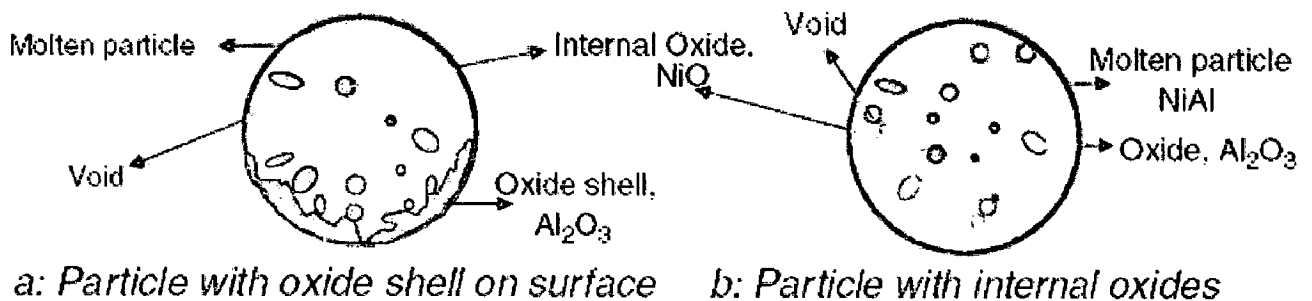


Fig. 2.27 Schematics for oxidation of particles, in-flight (Deshpande et al., 2006)

A variety of engineering problems have been solved using thermal spraying applications. Thermal spray coatings are being increasingly and successfully used for a broad variety of high temperature corrosion applications (Heath et al., 1997). The use of thermal spraying ranges across many manufacturing processes, from the automotive (Nakagawa et al., 1994) to the space exploration industry (Nicoll, 1994). Among the thermal spray coating processes, plasma spraying is reported to be versatile technology that has been successful as a reliable cost-effective solution for many industrial problems (Fauchais et al., 1997).

2.16 PLASMA SPRAYING

Plasma spraying is the most flexible/versatile thermal spray process with respect to the sprayed materials. The high temperatures of plasma spray processes permit the deposition of coatings for applications in areas of liquid and high temperature corrosion and wear protection and also special applications for thermal, electrical, and biomedical purposes (Bunshah, 2001).

Plasma techniques are capable of producing thick coatings films more than 100 μm at high production rates with no degradation of the mechanical properties of the alloy substrate (Yoshida, 1993). Among other key features of plasma spraying are formation of

microstructures with fine, noncolumnar and equiaxed grains, ability to produce homogeneous coatings that do not change in composition with thickness (length of deposition time), ability to process materials in virtually any environment (e.g., air, reduced-pressure inert gas, high pressure, under water) (National Materials Advisory Board, 1996).

Plasma spraying is gaining importance in many critical areas of application, which include corrosion, temperature and abrasion resistant coatings and production of monolithic and near net shape shapes. The plasma spray also finds application in reclamation of worn or corroded components, production of aerospace and nuclear power components. A new application of plasma spraying is in producing hydroxyapatite coatings onto the stems of orthopaedic endoprostheses (Batchelor et al, 2003). High temperature superconductive materials have also been deposited by the plasma spray process (Pfender, 1988). It enables a whole range of materials including metals and alloys to be plasma sprayed on to a great variety of substrate types and geometries (Modi et al., 1986 and Wu and Okuyama, 1996).

2.16.1 Plasma Spraying-The Process

A plasma torch or gun consists of a water cooled copper anode and a thoriated (2 wt%) tungsten cathode as shown in Fig. 2.28. A gas, usually argon or nitrogen or a mixture of these with hydrogen or helium flows around the cathode and exits through the anode nozzle. A dc arc is maintained between the electrodes and plasma of ions and atoms emerges at a temperature of 6,000-12,000°C at a distance of 1 cm from the nozzle, decreasing rapidly to 3000°C at a distance of 10 cm from the nozzle. The point of entry of the powder into the plasma jet is usually in the diverging portion of the nozzle or sometimes the powder is fed externally. Plasma gas velocities with most conventional torches are subsonic. Near the nozzle, the gas velocity is 200-600 ms⁻¹ but the particle velocity is only 20 ms⁻¹. However the particle acceleration (due to gas frictional forces) is 100000 gf so that 18 µm particles reach a maximum velocity of 275 ms⁻¹ at a distance of 6 cm from the nozzle (Sidky and Hocking, 1999).

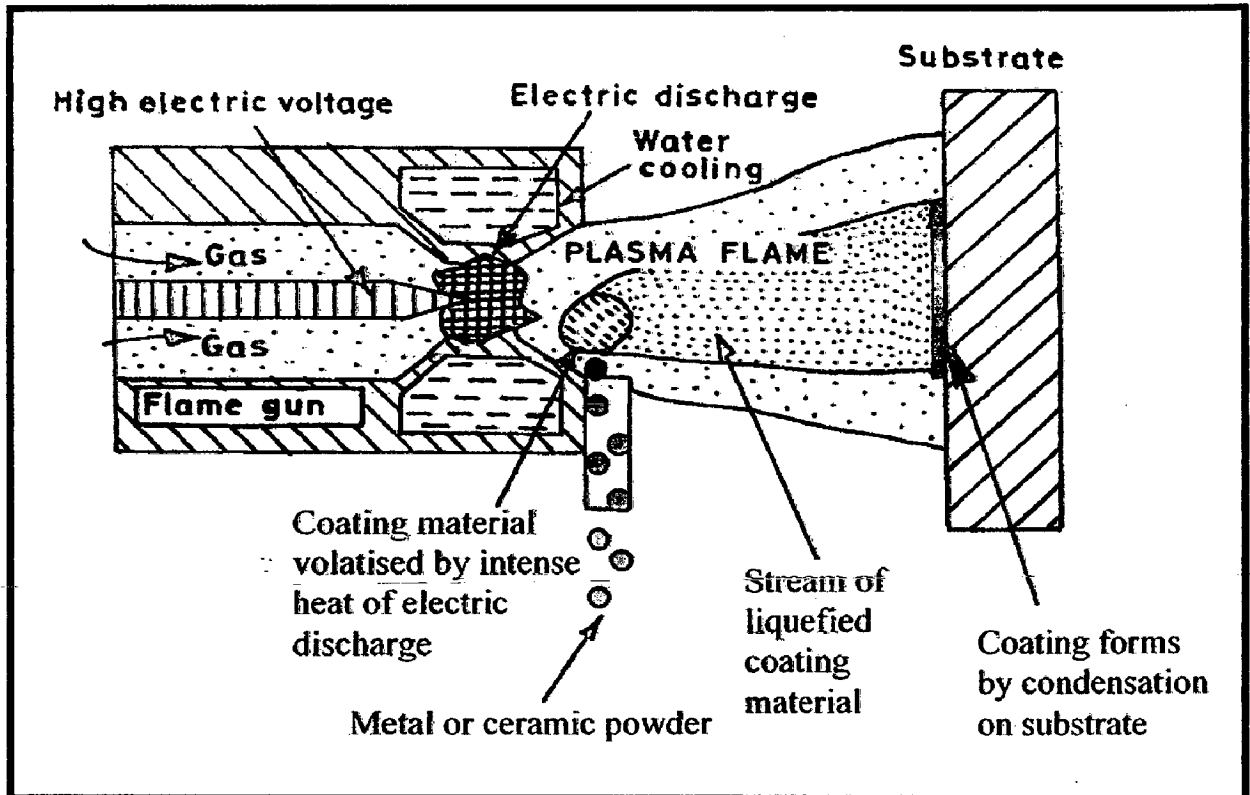


Fig. 2.28 The plasma spray apparatus (Batchelor et al, 2003)

The very high temperature generated in plasma spray process melts even the most refractory particles. Further, Plasma spraying operates at high energy levels; the power consumption of a typical coating unit is approximately 50 kW with an electric current of several hundred amperes flowing in the plasma arc (Batchelor et al., 2003). The high impingement speeds of the molten particles during spraying are intended to ensure that the molten droplets disintegrate on contact instead of remaining as discrete droplets, this process is known as splat formation.

The structure of the plasma sprayed coatings can be envisaged as a series of interlocking splats (Batchelor et al., 2003). The splats have columnar or equi-axed structures with grain sizes between 50 and 200 nm. However this fine structure is altered by grain size effect, large volume fraction of internal interfaces, voids, pores and so on (Fauchais, 2004). Upon impact on the substrate, the liquid particles will flatten and freeze. The freezing time of small particles (about 30 μm) is in the range 10^{-7} to 10^{-6} s. During this time between 50 and 100 particles impinge per square meter.

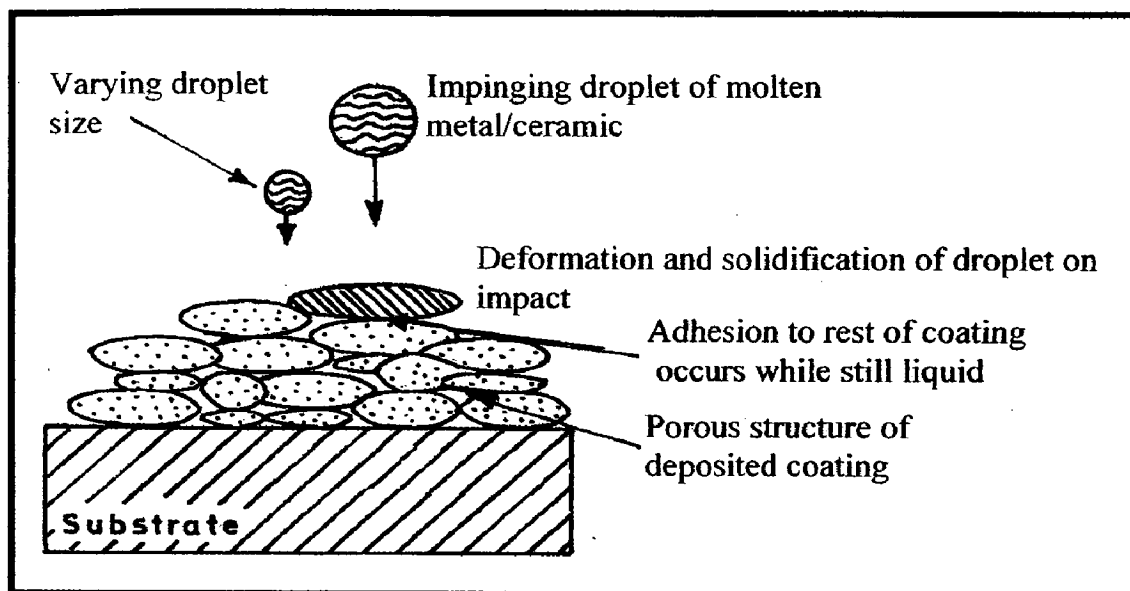


Fig. 2.29 The mechanism of coating deposition (Batchelor et al., 2003)

As a consequence, the freezing of a particle is completely isolated, i.e. it is not affected by other particles. The coatings built up particle by particle and each particle is frozen before the next particle arrives (Fig. 2.29). This results in a layered structured (lamellae) coating (Pfender, 1988). The plasma spray is often done in closed chamber filled with inert gas, to prevent the escape of any polluting or toxic debris from the process and to suppress the oxidation of the metal powder during the plasma spraying.

2.17 VAPOR DEPOSITION PROCESSES

Vapor deposited coatings modify the surface properties of materials. They are widely used and have been particularly successful in improving such mechanical properties as wear, friction, and hardness in cutting applications (Pierson, 1987). Vapour deposition processes can be divided into two types, (a) physical deposition (PVD) and (b) chemical vapour deposition (CVD), which in turn comprise various subcategories (Bunshah, 2001). PVD processes involve the creation of material vapors, (by evaporation, sputtering, ion plating) and subsequent condensation onto a substrate to form the film. CVD processes are

generally defined as the deposition of a solid material from the vapor phase onto a (usually) heated substrate as a result of chemical reactions.

According to Schneider et al. (2000), historically the first sputtering experiments were reported by Grove in 1852, early reports on evaporation were made by Faraday in 1857, and the first arc deposition was patented by Edison in 1892. The PVD (physical vapour deposition) techniques are widely used nowadays for improvement of the mechanical and other properties, of a broad range of engineering materials. The application of PVD techniques ranges over a wide variety of applications from decorative, to high temperature superconducting films (Bunshah, 2001). The thickness of these deposits can vary from angstroms to millimeters.

2.17.1 Physical Vapor Deposition Process

According to Randhawa (1991), all deposition processes involve three major steps for the formation of a thin film on a substrate: (1) creation of a flux of condensable species (neutral atoms and ions); (2) transport of the species created thus from source to substrate; (3) film growth on the substrate. The basic PVD processes fall into three general categories: (a) Sputtering, (b) Evaporation, and (c) Ion Plating.

2.17.1.1 Sputtering

Sputtering is the basic PVD process. In this process, the species for condensation are created by the positive ions of an inert gas bombarding the source, which is called the target, and thus generating atoms-ions of the target material by momentum transfer. The sputtering rate is thus dependent on the power input to the target, *i.e.* the cathode voltage and current for sputtering. In reactive sputtering, however, one must consider target poisoning effects (Randhawa, 1991). Further, the sputtering rate is also dependent on the plasma in the vicinity of the target surface. Figure 2.30 (a) shows a schematic of the sputtering process. In most cases, the inert or noble gas is argon. Argon has higher mass than other noble gases, such as neon or helium, and is easier to ionize (Pierson, 1987). Higher mass gives a higher sputtering yield, especially if the mass of the bombarding

particle is of the same order of magnitude or is greater than that of the target atom. Other gases, such as oxygen or nitrogen may be used, but these may react chemically with the target.

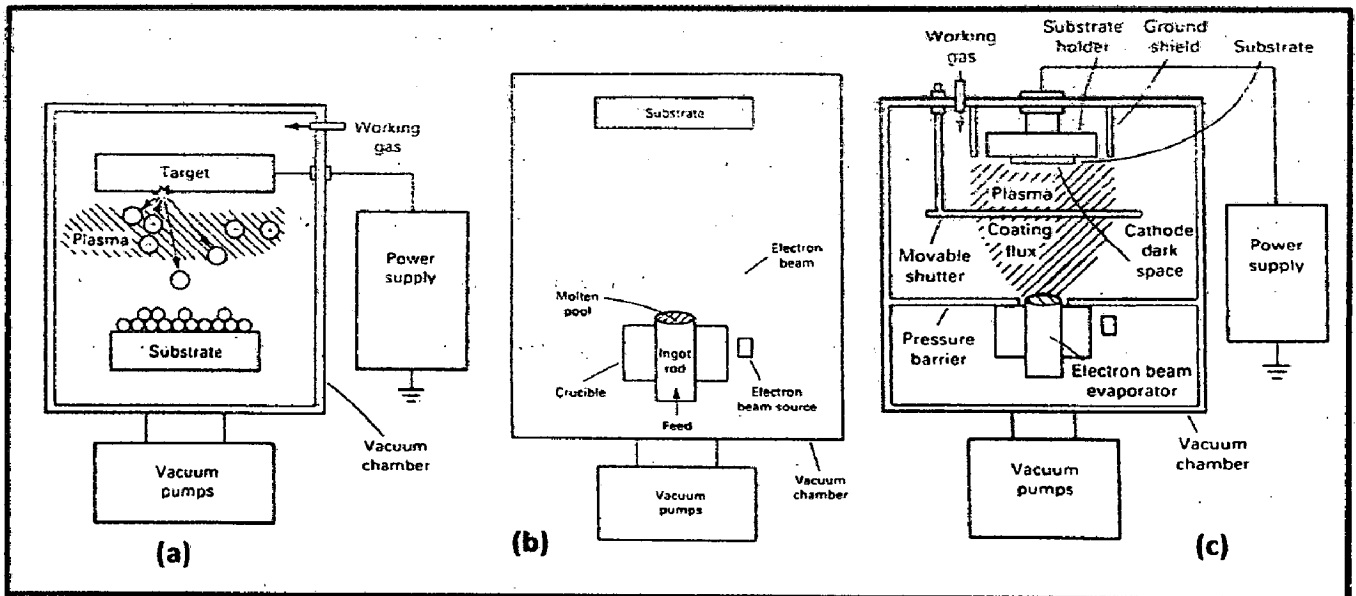


Fig. 2.30 Various PVD processes; (a) Sputtering; (b) Evaporation; (c) Ion Plating (Pierson, 1987)

The sputtering process begins when an electric discharge is produced and the argon becomes ionized. The low pressure electric discharge is known as glow discharge, and the ionized gas is termed plasma (Bunshah, 2001). The target (the source of coating material) is negatively biased and therefore attracts the positively charged argon ions, which are accelerated in glow discharge. This attraction of the ions to the target (also called bombardment) causes the target to sputter, which means that material is dislodged from the target surface because of momentum energy exchange.

Sputtering developed very rapidly in the 1970s in the semiconductor industry, in which the technique is essential for mass production. Sputtering is making rapid inroads in such corrosion applications as high-chromium alloy coatings on the turbine blades and many other new applications that require high-quality coatings with good adhesion.

2.17.1.2 Evaporation

Evaporation was the first PVD process used on an industrial basis for aluminum metallization of plastics and glass for decorative purposes (Pierson, 1987). Originally the most widely used process; evaporation has now been overtaken by sputtering.

In the case of an evaporation process, the condensable species are created by physical heating of the source material (Randhawa, 1991). This is achieved by resistance heating, electron beam heating, arc evaporation, induction heating or flash evaporation methods. The evaporation rate varies directly with the vapor pressure of the source material which in turn depends on the surface temperature of the source material. Figure 2.30 (b) shows a schematic of the evaporation process. Practically all metals can be evaporated, making evaporation a universal process with regard to metals.

2.17.1.3 Ion Plating

Ion Plating is actually a hybrid concept based on the evaporation (or sputtering) mechanism coupled with a glow discharge (Fig. 2.30.c). There are three possible deposition systems: resistance evaporation, electron beam evaporation and sputtering. All three systems generate plasma by a glow discharge, thus imparting a large increase in the energy of the deposition species. According to Mattox (2000), ion plating is an atomistic vacuum coating process in which the deposition film is continuously or periodically bombarded by energetic atomic-sized inert or reactive particles that can affect the growth and properties of the film.

It is generally accepted that plasma plays the same part as high temperature in improving the adhesion and increasing the reactivity of the coating. The simplest forms of ion plating are ion nitriding and ion carburizing, in which nitrogen or carbon ions are obtained from the ionization of nitrogen or a hydrocarbon. The deposited species in ion plating have higher energy than those of evaporation or sputtering processes: this result in improved adhesion as well as a deposit with improved structure and fewer imperfections (Pierson, 1987). On the negative side, the equipment is more complicated and therefore more expensive than either evaporation or sputtering equipment.

2.17.2 Plasma Assisted Physical Vapor Deposition Process

Plasma assisted physical vapor deposition (PAPVD) involves the condensation of vapor created from a solid source, in the presence of a glow discharge or plasma (Schneider et al., 2000). Typical PAPVD processes are evaporative ion plating; reactive sputtering and some plasma/ion beam based and/or assisted deposition techniques. State of the art PAPVD processes allow the deposition of metals, alloys, ceramic and polymer thin films onto a wide range of substrate materials. The original PAPVD system was patented by Berghaus in 1938, but until the 1960s the potential of the process was not recognized when Mattox coined the term 'ion plating' and led the research into ion plating of metallic films (Schneider et al., 2000). By the early 1980s evaporation systems were in widespread use for the production of ceramic coatings, especially for cutting tools, most notably by the Balzers' company. The reactions of importance in the plasma-assisted PVD processes are ionization, dissociation, electron impact excitations and the ion energies involved (Randhawa, 1991).

The plasma-assisted ion plating process involves ion bombardment of the substrate prior to deposition for substrate cleaning and during deposition to modify film properties (Randhawa, 1991). Plasma-assisted ion plating is commonly applied for metal films, oxides, nitrides, carbides, carbonitrides, alloy films and multicomponent materials. Plasma-assisted sputtering in which the depositing species are ejected from the target surface as a result of the momentum transfer from the bombarding ions of the plasma and condense on suitably placed substrates, constitutes one of the oldest applications of plasmas in material processing (Randhawa, 1991). Inert gas plasmas (usually argon) at low pressures typically in the range 1-70 mTorr are generally used.

In Activated reactive evaporation (ARE), a plasma discharge is sustained in a flux of evaporated material and a reactive gas. The dissociation and ionization which are induced in the low pressure (1-35mTorr) reactive gas promotes reactivity on the surface of the growing film. ARE is used for depositing metal oxides, carbides, nitrides and carbonitrides. According to Randhawa (1991), the plasma-assisted processes discussed above involve creation of depositing species of metal or alloys or dissociated gas atoms or vapors in the presence of discharge plasmas. The major role of plasma in this case is twofold: (1) to activate the

reactions between evaporating metal species and reactive gas to enhance the formation of compound films; (2) to modify the growth kinetics and hence structure-morphology and thus physical properties of the deposit.

2.17.3 Applications of Plasma Assisted Physical Vapor Deposition Process

Plasma-assisted deposition processes are used in a wide variety of applications. The widespread applications of plasma-assisted PVD techniques have been in the area of perishable cutting tools, decorative coating of jewelry, watch cases and bands, eye glass frames, corrosion applications, optical applications etc. The performance of cutting and forming tools can be significantly improved by applying a thin film of refractory metal nitride or carbide. Since the commercialization of physical vapor deposited (PVD) TiN coatings in early 1980s, transition metal nitrides based hard coatings have been successfully used for the materials protection particularly to improve cutting tools lifetime (Budinski, 1998). This type of coating, however, suffered severe oxidation at the temperatures 550 or 600°C (He et al., 2001). A possible solution was found in consideration to the fact that both TiN and TiAlN have the same crystallographic structure (fcc), and therefore addition of Al atoms to the TiN matrix in the 1990s. At high temperature exposures, a very dense and strongly adhesive Al₂O₃ film is observed because of diffusion of Al atoms to the surface, which stops further oxidation (He et al., 2001). Since the addition of aluminum increases the oxidation resistance of Ti-N coatings, a similar effect on the oxidation resistance of Cr-N coatings should be expected (Priyantha et al., 2003). It has been reported that the hardness, oxidation resistance and the tribological properties improve with increasing Al-content up to 70-75% in the AlCrN coatings as long as fcc-structure is predominant. For higher aluminum content, hcp-structure starts to form and thus the oxidation resistance deteriorates (Stein et al., 1999).

There are many environments in which parts and components come into contact with chemical fluids which may be corrosive (Bunshah, 2001A). TiN films are found to be highly resistant to chemical attack from concentrated acids or other such corrosive chemicals. However, the choice of substrate used can aggravate these problems. If the

substrate has a lot of free iron or nickel, it is found that galvanic corrosion tends to dominate the situation. In such cases, CrN films were found to be more effective. CrN films are also found to be very effective in controlling the wear and corrosion in automobile bearings. A variety of surgical tools and instruments (Randhawa, 1991) are being coated with wear resistant and corrosion-resistant coatings. The coatings primarily being used are TiN and CrN. The coated instruments not only provide improved life but also are more compatible with the chemicals used for sterilization and storage.

2.18 SOME STUDIES RELATED TO Ti-Al AND Al-Cr BASED COATINGS

In the last decades, transition metal nitrides have been studied intensively due to their superior mechanical properties and are widely used today (Man et al., 2004). Quesada et al. have reported that coating materials with the widest applications to improve mechanical and tribological properties are those composed by titanium like TiN, TiC, TiCN and TiAlN (Quesada et al., 2006). These ceramic materials exhibit important characteristics like high hardness, low friction coefficient and wear resistance among others. It is well known that TiN, the most widely used material for hard coatings, however quickly oxidizes at temperatures near 550°C, resulting in fast wear of the hard coating in cases where the matching processes involve higher temperature. As a possible solution to this problem, Al atoms have been added to the TiN material taking into account that both TiN and TiAlN have the same crystallographic structure (fcc). In high temperature applications, a very dense and strongly adhesive Al₂O₃ film is observed because of diffusion of Al atoms to the surface, which stops further oxidation. It was demonstrated that the hardness increases with Al content until a certain point. A wide variety of microstructures can be obtained by varying the Al content and deposition parameters.

Endrino et al. (2007) have reported that chromium nitride coatings oxidize due to the outward diffusion of chromium and the formation of chromium oxide surface layers. Oxidation studies have shown the superior oxidation resistance of the ternary Al_xCr_{1-x}N as compared to Al_xTi_{1-x}N. This makes wear resistant Al_xCr_{1-x}N coatings better candidates for many specific applications. Recently, a number of studies have been performed on the

impact of aluminum content on the hardness and oxidation resistance of Al–Cr–N coatings. It has been reported that the hardness, oxidation resistance and the tribological properties improve with increasing Al-content up to 70–75% in the AlCrN coatings as long as the fcc-structure is predominant. For higher aluminum content hcp-structure starts to form and the oxidation resistance deteriorates. In the hcp case the oxidation rate is almost tripled compared to the fcc-AlCrN.

Kalss et al. (2006) have studied some Ti and Al based coating and reported that the TiAl-based nitrides such as TiAlN and AlTiN were stable against oxidation up to temperatures about 800°C. The coating with best oxidation resistance was AlCrN. Even at 1100°C only a thin layer of about 150nm in thickness could be observed. These coatings exhibit good thermal conductivity and better wear resistance. Sugehis et al. (2006) have studied corrosion performance of duplex treatments based on plasma nitriding and PAPVD TiAlN coatings. The plasma nitrided substrates were coated commercially with BALINIT FUTURA NANO (TiAlN) coatings (Balzers, Inc., USA). The nanograined TiAlN coating has shown better results than that of conventional counterpart.

Thermal spray coating of titanium (Ti) by plasma spraying in the air is predominantly comprised of Ti oxide and nitride, as Ti is an active metal to react easily with ambient gases containing oxygen and nitrogen while spraying (Adachi and Nakata, 2007). The sprayed Ti coating contains so many cracks and pores internally, which cause to decrease the adhesive strength and the corrosion protections properties (Adachi and Nakata, 2007). They have reported that the adhesive strength of the coating was improved by filling cracks and pores of the Ti compounds layers with the Al phase to form a dense microstructure, and also by hardening the Ti compounds and Al phase with the oxygen and nitrogen contained in the coating. Further, they have reported that the sprayed Ti-50 mass% Al coatings had higher adhesive strength than the other coatings sprayed and had the maximum value. Since the addition of aluminum increases the oxidation resistance of Ti-N coatings, a similar effect on the oxidation resistance of Cr-N coatings is expected (Spain et al., 2005). Conclusively, Adachi and Nakata (2007) have reported that the formation of the Ti–Al sprayed coating on the substrate would proceed as follows. At first, the compounds of Ti oxide and nitride in

the fused particles would be solidified almost as soon as adhering to the substrate, as the melting points of TiO and TiN are 2023 K and 3223 K, respectively, which are much higher than that of Al, 933 K. Then, cracks and pores between the Ti compound layers would be filled with the melting Al particles, and the coating finally became solidified as a whole.

2.19 PATENT SEARCH

After reviewing the literature critically, the patent search has been done on some related topics of interest. Table.2.2 shows the search results for some topics regarding World Intellectual Property Organization; European Patent Office website; U.S. Patent Database. The U.S Database has shown 02 (Reported in Appendix A.3) patents for “Nitrided Ti-Al and Al-Cr based coatings high temperature applications”; and “Protective Ti-Al and Al-Cr based nitrided coatings” along with 50 patents (Reported in Appendix A.3) for “Development of hot corrosion oxidation resistant coatings”. The World Intellectual Property Organization and European Patent Office website have shown zero patents on the topics listed in Table.2.2.



2.20 PROBLEM FORMULATION

2.20.1 Scope

Materials degradation at high temperatures is a serious problem in several high tech industries. Power plants are one of the major industries which encounter severe corrosion problems resulting in the substantial loss. The problem is becoming more prominent as the plants are getting older. Attempts to increase the efficiency of steam generating plant by raising the final steam temperature above 600°C and the use of gas turbines for the production of cheap electric power have made working conditions more severe for the materials (Thilakan et al., 1967). The boiler tubes used for super-heaters and re-heaters in the steam generating systems are subjected to fireside corrosion, resulting in tube wall thinning and premature failure. Hot corrosion has been identified as a serious problem in

high temperature applications such as in boilers, gas turbines, waste incinerations, diesel engines, coal gasification plants, chemical plants and other energy generation systems.

Table: 2.2 Patent search results of topics of interest

Sr. No.	TOPIC	WORLD INTELLECTUAL PROPERTY ORGANIZATION 	 Europäisches Patentamt European Patent Office Office européen des brevets	U.S. PATENT
01	NITRIDED AND Ti-Al AND Al-Cr AND BASED AND COATINGS AND HIGH AND TEMPERATURE AND APPLICATIONS	0 records	0 records	02 patents
02	DEVELOPMENT AND OF AND Ti-Al AND Al-Cr AND BASED AND NITRIDED AND COATINGS AND FOR AND BOILER AND APPLICATIONS	0 records	0 records	0 records
03	DEVELOPMENT AND OF AND HOT AND CORROSION AND OXIDATION AND RESISTANT AND COATINGS	0 records	0 records	50 patents
04	PROTECTIVE AND Ti-Al AND Al-Cr AND BASED AND NITRIDED AND COATINGS	0 records	0 records	02 patents

Hot corrosion is induced by the impurities such as Na, V, S etc. present in the coal or in the fuel oil used for combustion in the mentioned applications. In some situations, these impurities may be inhaled from the working environment, for instance NaCl in marine atmospheres. There is a general agreement that condensed alkali metal salts notably, Na_2SO_4 , are a prerequisite to hot corrosion (Beltran and Shores, 1972). Coal is an attractive

fuel owing to its low price linked to its worldwide availability and due to the future shortage of other fossil fuel reserves such as oil and gas (Sidhu et al., 2006D). Also, due to high cost of removing the impurities, the use of this low grade fuel is usually justified. Combustion of coal generates very corrosive media particularly near the superheater tubes of the boilers (Weulersse-Mouturat et al., 2004). These are the major areas where critical high-temperature fireside corrosion problems are encountered, particularly on the leading tubes in a bank. The corrosion has been attributed to the fluxing action of the molten salt on the oxide scales formed over the tubes, leading to a rapid localized corrosion, accompanied by the sulphidation (Beltran and Shores, 1972).

High-temperature erosion-corrosion and oxidation of the heat transfer pipes and other structural materials in the coal fired boilers are recognized as being the main cause of downtime at power generating plants, accounting for 50% to 75% of the total arrest time (Cutler, 1978). Erosion-corrosion of materials occurs in environments as diverse as catalytic cracking systems in oil and gas separation, combined-cycle coal conversion systems such as pressurized fluidized bed combustion, and on the turbine blades of jet engines where erosive component may be caused by the ingestion of particulate material or the accumulation of such material as a result of the corrosion process (Stack et al., 1993). Maintenance costs for replacing the broken pipes in such installations are also very high and are estimated to be up to 54% of the total production costs (Chandler and Quigley, 1986).

In case study of a coal fired boiler of a power plant in north western region of India, Prakash et al (2001) have reported that out of 89 failures occurring in one year duration, 50 failures were found to be due to hot corrosion and erosion by ash. These facts emphasize the need to develop more and more corrosion resistant materials for such applications. Therefore, the boiler steel needs to be protected. It is important to understand the nature of all types of environmental degradation of metals and alloys as vividly as possible so that preventive measures against metal loss and failure can be economically devised to ensure safety and reliability in the use of metallic components (Sidhu and Prakash, 2006A).

Fe and Ni-based superalloys are extensively used in turbine blades of industrial gas turbines and jet engines. Mostly Cr and Al are added in superalloys to enhance the oxidation resistance. Besides the oxidation resistance of superalloys at high temperature, the resistance to pitting corrosion at normal temperature is another important performance of these materials (Liu et al., 2007). The chloride-rich seawater is a harsh environment that can attack the materials by causing pitting and crevice corrosion (Dobrzanski et al., 2007). Surprisingly, it seems no research works have been conducted on the behavior of this type of corrosion occurring in high temperature corrosion resistant coatings. Therefore, it is meaningful to investigate the ambient environmental corrosion behavior and mechanism of the materials as is done in present work by evaluating the corrosion behavior of substrate and coatings in simulated marine environment.

It has been learnt from the literature that high temperature corrosion and erosion problems needs to be arrested through some other preventive means; prominent among them being controlling process parameters, use of inhibitors, application of protective coatings etc. as there lies little scope in improvement of the combustion environments. In Indian context, this is even more relevant as the Indian coal is found to have high ash content (Sharma, 1996). Further, the use of inhibitors is not easily viable due to practical implications in injecting these inhibitors along with the fuel in the combustion chamber in an actual industrial environment (Tiwari and Prakash, 1998 and Gitanjaly et al., 2002). In this regard, it is further learnt from the published literature that one possible, practical, reliable and economically viable way to control or prevent the high temperature corrosion and erosion problems of the superheaters and reheaters of the boilers is an application of a thin layer of corrosion resistant coatings having good thermal conductivity.

Due to the continuously rising cost of the bulk materials as well as increased material requirements, the coating techniques have been given more importance in the recent times. Therefore, the use of protective overlay coatings has been identified as a potential area for the present research. Porosity, stress generation and interlayer separation between the different deposited layers are the prominent parameters to be considered for selecting a particular process for deposition of the corrosion resistant

coating as they are the preferential corrosion paths where the corrosion species can penetrate through the coating to reach the substrate and may cause rapid corrosion attack. The easiness, economy and convenience of operations are the other major factors that must be considered for applying the coatings to industrial installations.

The physical vapour deposition (PVD) and plasma spray (a thermal spray process) have been reported to be two major coating processing technologies used worldwide (DeMasi-Marcin and Gupta, 1994). Thermal spray has emerged as an important tool of increasingly sophisticated surface engineering technology. It is one of the many methods of applying overlay coatings for applications ranging from protection of materials in harsh environments, to dimensional restoration of worn machine elements (Yamada et al, 2002). Among the thermal spray coating processes, plasma spraying is reported to be versatile technology that has been successful as a reliable cost-effective solution for many industrial problems (Fauchais et al, 1997). In recent years, corrosion performance of nanostructured materials/coatings is a hot topic in corrosion field. As reported by Chawla et al. (2008), in the past decade, attractive properties associated with a nanostructure have been documented for bulk materials, where most of the research in the field of nanomaterials has been focused. Nanostructured materials indeed behave differently than their microscopic counterparts because their characteristic sizes are smaller than the characteristic length scales of physical phenomenon occurring in bulk materials (Chawla et al., 2007A). In many tribological applications, hard coatings of metal nitrides are now commonly used (Bertrand et al., 2000). The major properties required for such coatings are hardness and wear resistance. However, because of severe operating conditions, there is a need to combine mechanical features with corrosion resistance properties. In the past years, hard protective TiAlN coatings and AlCrN coatings were widely used for wear resistant properties. Recently these coatings are gaining importance for high temperature wear, corrosion and oxidation resistance applications (Kals et al., 2006; Fujita, 2005).

Recent reports emphasized that the understanding of the degradation and failure mechanisms of high-temperature coatings in the field need to be improved, particularly with respect to the effects of engine operation and environment on the coating

performance e.g., thermal cycling (National Materials Advisory Board, 1996). In general, the reaction behavior of protective coatings in environments of their use and their interactions with the substrate during high-temperature performance is not well understood (Chatterjee et al, 2001). Uusitalo et al (2003) has also suggested that there is a need to investigate the high temperature corrosion behavior of thermal spray coated materials in different aggressive environments.

In an earlier work conducted by Buta Singh (2003) in our department, laser remelting of the plasma sprayed coatings was attempted to eliminate the porosity of the coatings. However, he observed that these laser remelted coatings showed slightly inferior hot corrosion resistance in molten salt environment as compared to the as coated samples. This behavior was attributed to the presence of vertical cracks in the laser remelted samples after exposure to hot corrosion, through which the oxidizing environment could reach the substrate steels. Harpreet Singh (2005) has studied oxidation behavior of plasma sprayed NiCrAlY, Ni-20Cr, Stellite-6 and Ni₃Al coatings on Ni- and Fe-based superalloys and in all the cases, NiCrAlY was used as a bond coat. He reported that NiCrAlY coating on Fe-based superalloy has provided the best protection in both air and molten salt environment. Sidhu T.S., (2006C) has studied the hot corrosion behavior of HVOF sprayed coatings in the laboratory as well as in actual industrial boiler environment and concluded that Ni-20Cr coating provided highest protection; whereas, satellite-6 coating provided the least resistance to molten salt environment in the laboratory. In case of industrial environment, he reported that Ni-20Cr showed a better resistance and the least resistance was observed in case of Cr₃C₂-NiCr coatings. He further explained that the high chromium content in Cr₃C₂-NiCr coating resulted in the formation of thick network of chromium oxide around the nickel rich splats and responsible for spallation and disintegration of the coating due to the difference in coefficient of thermal expansion of oxide scale, the coating and the substrate.

Little work has been published on high temperature erosion/corrosion behavior of nanostructured and conventional hard metal nitride coatings to the best of knowledge of the author. The present study has been performed to evaluate the behavior of the nanostructured and conventional metal nitride coatings when exposed to high temperature

oxidation in air, molten salt (Na_2SO_4 -60% V_2O_5) environment, in actual degrading conditions prevailing in a coal fired boiler of a thermal plant, high temperature solid particle erosion and simulated marine environment. Three types of boiler steel substrate materials namely “ASTM-SA210-Grade A1,” “ASTM-SA213-T-11” and steel “ASTM-SA213-T-22” and a Fe-based superalloy having Midhani Grade Superfer 800H have been selected for the present study as the substrate materials. Boiler steels were procured in the tube form from the mentioned thermal power plant and the superalloy was procured in form of rolled sheets from Mishra Dhatu Nigam Ltd, Hyderabad (India). The boiler steels are used as boiler tube materials in some of the power plants in Northern India. The selected superalloy is widely used for steam boilers, furnace equipment, heat exchangers and piping in the chemical industry, reformers and baffle plates/tubes in fertilizer plants. Behavior of these coatings under different degrading environments once evaluated will be helpful in choosing the suitable coating for the given environment.

2.20.2 Objective

1. The objective of the present research work is aimed at studying the behavior of the nanostructured and conventional metal nitride coatings when exposed to high temperature oxidation in air, molten salt (Na_2SO_4 -60% V_2O_5) environment, in actual degrading conditions prevailing in a coal fired boiler of a thermal plant, high temperature solid particle erosion and simulated marine environment. The conventional thick (by plasma spraying and gas nitrided) and nanostructured thin (by physical vapor deposition process) TiAlN and AlCrN coatings have been developed on boiler steels i.e. Grade A-1, T-11 and T-22 and a superalloy Superfer 800H.
2. To compare the oxidation and hot corrosion performance of the coated with bare alloys and assess its suitability for using it in the boiler super-heaters and re-heaters, and for other future hot section components to be used in similar corrosive environments.
3. To understand and propose mechanisms for the high-temperature corrosion of the uncoated and coated alloys, wherever possible. As far as the testing in air

environment is concerned, the study could also provide useful information regarding the adhesion of the coatings and the spalling tendency of their oxide scales apart from air oxidation behavior of the coatings.

4. In order to establish the behavior of these coatings and bare alloys in the actual working conditions in which they may be used, the coatings are investigated in the operational environment of the coal fired boiler at Guru Nanak Dev Thermal Plant, Bathinda, Punjab, India.
5. In both the laboratory as well in industrial environments, the experiments are planned to conduct under cyclic conditions as it provides the severest conditions for testing and represents the actual industrial environment where breakdown and shutdown occur frequently.
6. The conventional thick and nanostructured thin TiAlN and AlCrN coatings; after high temperature air oxidation and hot corrosion studies were characterized by the techniques such as XRD, SEM/EDAX and X-ray mapping to render an insight into the corrosion mechanisms based on the morphology of the corroded products formed on the coated alloys. The similar characterizations studies were performed for the corroded uncoated alloys.
7. To compare the high temperature erosion behavior of coated and uncoated alloys. The erosion studies were carried out using a high temperature air-jet erosion test rig at a velocity of 35 ms^{-1} and impingement angles of 30° and 90° . The tests were carried out at high temperatures. The two temperatures were taken for the test, sample temperature 400°C and air/erodent temperature 900°C simulated to service conditions of boiler tubes in which sample temperature and flow gas temperature correspond to the inner and outer temperature of water wall pipes. The alumina particles of average size $50 \mu\text{m}$ were used as erodent.
8. Erosion rates in terms of volumetric loss (mm^3/g) for different uncoated and coated alloys are compared. The eroded samples were analyzed with SEM/EDAX and optical profilometer. The erosion rate data for each coated alloy has been plotted along with

uncoated alloy in order to assess the coating performance. Efforts have been made to understand the mode of erosion.

9. In order to evaluate the corrosion behavior of the substrates and coatings in simulated marine environment; by electrochemical methods i.e. linear polarization resistance (LPR) and potentiodynamic polarization tests in an aerated 3.0 wt% NaCl solution at room temperature; and salt spray (Fog) tests. The LPR and potentiodynamic polarization tests were carried out using EG&G PAR model 273A potentiostat. The ASTM B117 Salt Fog test was used to evaluate the performance of the specimens.
10. The initial corrosion current density and LPR (R_p) was measured by LPR test. Potentiodynamic polarization curves of the substrate and each film and the corrosion parameters were compared. In case of salt fog tested coated and uncoated specimens after exposure were monitored and analyzed by using XRD, weight change measurement and SEM/EDAX techniques.
11. To summarize the important contributions made in the present work on Nanostructured and conventional metal nitride coatings on selected boiler steels and a superalloy and highlight the scope for future work in the high temperature corrosion of coatings.

Chapter 3

EXPERIMENTAL TECHNIQUES AND PROCEDURES

This chapter presents the experimental techniques and procedures employed for deposition and characterization of coatings. A detailed description of high temperature oxidation studies in air and in molten salt environments, erosion-corrosion in simulated coal-fired environment, corrosion studies in simulated marine environment and erosion-corrosion studies in an actual industrial environment; of coated and bare alloys is given in this chapter. The procedures for analyzing the corrosion products are discussed. The specifications of the equipments used are furnished.

3.1 SUBSTRATE MATERIALS

Selection of candidate material for the study has been made after consultation with Guru Nanak Dev Thermal Plant, Bathinda (India) and Mishra Dhatu Nigham Ltd, Hyderabad (India). Three types of boiler steel substrate materials (low carbon steel) namely "ASTM-SA210-Grade A-1 (Grade A-1)," 1Cr-0.5Mo steel "ASTM-SA213-T-11 (Grade T-11)" and 2.25Cr-1Mo steel "ASTM-SA213-T-22(Grade T-22)" and a Fe-based superalloy having Midhani Grade Superfer 800H have been selected for the present study as the substrate materials. The boiler steels are used as boiler tube materials in some of the power plants in Northern India. Grade A-1 has a wide range of applications in boilers, especially in the construction of their water walls. When the service conditions are stringent from the point of temperature and pressure other two types of steel (Grade T-11 and T-22) are being employed. The selected superalloy is widely used for steam boilers, furnace equipment and piping in the chemical industry, baffle plates/tubes in fertilizer plants. Boiler steels were procured in the tube form from the above mentioned thermal power plant and the superalloy was procured in the form of rolled sheets from Mishra Dhatu Nigham Ltd, Hyderabad (India). The actual chemical composition of these alloys has been determined with the help of Optical Emission Spectrometer (Thermo Jarrel Ash, TJA181/81, U.S.A); which is reported in Table 3.1 along with nominal chemical composition. Figure 3.1 shows the

optical micrographs (X 200) of the substrates using Zeiss Axiovert 200 MAT Inverted Optical microscope.

3.2 DEVELOPMENT OF COATINGS

3.2.1 Nanostructured Thin Coatings

3.2.1.1 Preparation of Substrate Materials

Specimens with dimensions of approximately 20mm X 15mm X 5mm were cut from the alloy tubes (in case of boiler steels) and rolled sheet (in case of superalloy). The specimens were polished using emery papers of 220, 400, 600 grit sizes and subsequently on 1/0, 2/0, 3/0 and 4/0 grades and then mirror polished using cloth polishing wheel machine with $1\mu\text{m}$ lavigated alumina powder suspension. The specimens were prepared manually and all care was taken to avoid any structural changes in the specimens.

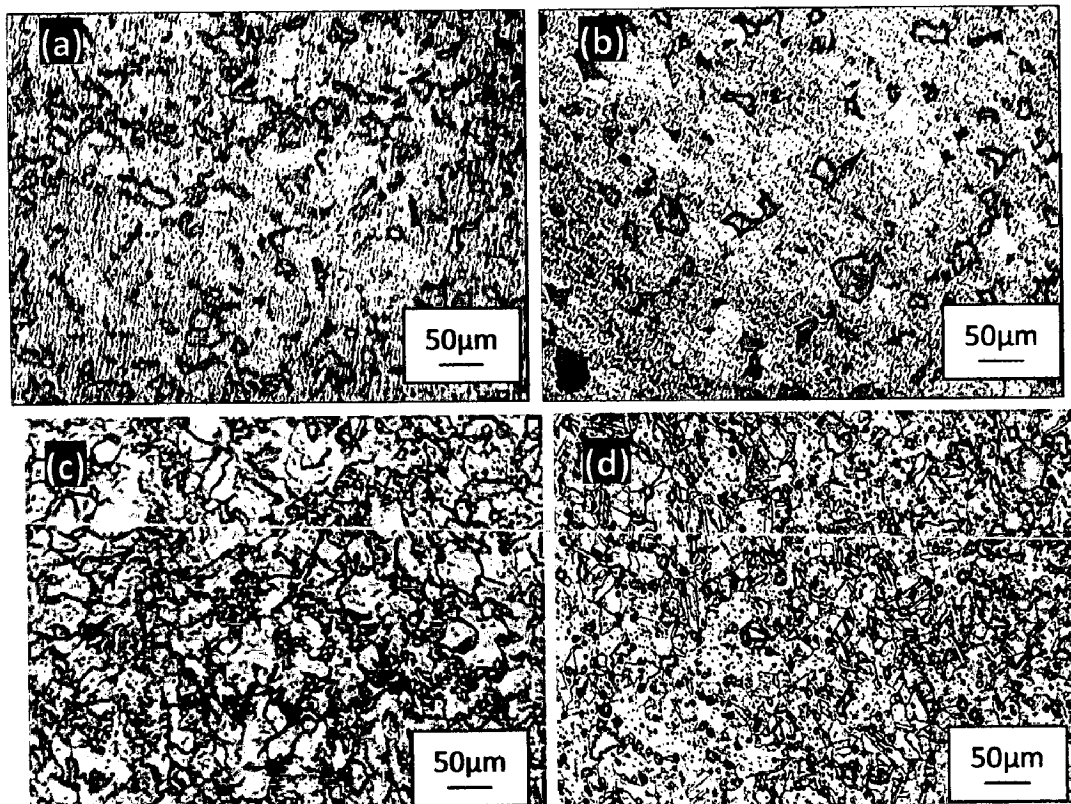


Fig. 3.1 Optical micrographs of substrate alloys; (a) ASTM-SA210 Grade A-1 boiler steel, 200X, (b) ASTM-SA213-T-11 boiler steel, 200X, (c) ASTM-SA-213-T-22 boiler steel, 200X, (d) Superfer 800H superalloy, 200X

Table 3.1: Chemical composition (Wt %) and industrial applications of the alloys used

Alloy Grade ↓	Elements ⇔	C	Mn	Si	S	P	Cr	Mo	Ni	Ti	Al	Fe	Recommended Applications (Manufacturer's Catalogue)
ASTM- SA210 Grade A1	Nominal	0.27	0.93	0.1	0.058	0.048	-	-	-	-	-	Bal.	Boiler parts specially in the construction of water walls
	Actual	0.2768	0.6725	0.1725	0.00517	0.0093	-	-	-	-	-	Bal.	
ASTM- SA213-T-11	Nominal	0.15	0.3-0.6	0.5-1	0.03	0.03	1-1.5	0.44-0.65	-	-	-	Bal.	Boiler parts where service conditions are stringent from the point of temperature and pressure
	Actual	0.16183	0.44101	0.28212	0.00507	0.01330	0.9114	0.5125	-	-	-	Bal.	
ASTM- SA213-T-22	Nominal	0.15	0.3-0.6	0.5	0.03	0.03	1.9-2.6	0.87-1.13	-	-	-	Bal.	Boiler parts where service conditions are stringent from the point of temperature and pressure
	Actual	0.16587	0.35597	0.11598	0.00153	0.02026	2.6460	0.90275	-	-	-	Bal.	
Superfer 800H	Nominal	0.10	1.0	0.6	-	-	19.5	-	30.8	0.44	0.34	Bal.	Steam boilers. Furnace equipment, heat exchanger and piping in chemical industry, reformer, baffle plates/tubes in fertilizers plants
	Actual	0.1	1.5	1.0	-	-	21	-	32	0.3	0.3	Bal.	

3.2.1.2 Formulation of coatings

The nanostructured thin TiAlN and AlCrN coatings; with a thickness around 4 μ m, were deposited on the substrates at Oerlikon Balzers Coatings India Limited, Gurgaon, India. A front-loading *Balzer's rapid coating system (RCS) machine (make Oerlikon Balzers, Swiss)* was used for the deposition of the coatings. The machine is equipped with 6 cathodic arc sources. In case of nanostructured thin TiAlN coatings; two of the six sources were used to deposit a thin, 0.3 μ m thick TiN sub-layer to improve adhesion of coating. The remaining four sources were employed to deposit the main layer of the coatings, which was obtained using customized sintered targets. Whereas in case of nanostructured thin AlCrN coating; all the six targets sources were employed to deposit the main layer of the coatings. The Oerlikon Balzers Coatings India Limited, Gurgaon, India has optimized the coating parameters for all the substrates. The compositions of the targets used, coating thickness and the summary of the process parameters are presented in Table 3.2. For all coatings; argon (Ar) and pure nitrogen atmosphere was used during deposition. Prior to deposition all the substrates were cleaned in two steps: firstly with Ultrasonic Pre-Cleaner (make Imeco, Pune, India) and secondly with Ultrasonic Cleaning Machine with 9 Tanks including hot air dryer (make Oerlikon Balzers Ltd. India) for 1.5 Hrs.

3.2.2 Conventional Thick Coatings

3.2.2.1 Preparation of Substrate Materials

Specimens with dimensions of approximately 20mm X 15mm X 5mm were cut from the alloy sheets. The specimens were polished using emery papers of 220, 400, 600 grit sizes and subsequently on 1/0, 2/0, 3/0 and 4/0 grades. These substrates are then grit blasted with alumina powders (Grit 45) prior to the deposition of the coatings by Plasma Spraying (a thermal spray process), for developing better adhesion between the substrates and the coatings. The specimens were prepared manually and all care was taken to avoid any structural changes in the specimens.

Table 3.2: Summary of Nanostructured thin coatings' deposition parameters

Coating Parameters	Nanostructured TiAlN	Nanostructured AlCrN
Machine used	Standard balzers rapid coating system (RCS) machine	Standard balzers rapid coating system (RCS) machine
Make	Oerlikon Balzers, Swiss	Oerlikon Balzers, Swiss
Targets composition	Ti, Ti ₅₀ Al ₅₀	Al ₇₀ Cr ₃₀
Number of targets	Ti (02), Ti ₅₀ Al ₅₀ (04)	Al ₇₀ Cr ₃₀ (06)
Targets power	3.5KW	3.5KW
Reactive gas	Nitrogen	Nitrogen
Deposition Pressure	3.5 Pa	3.5 Pa
Substrate Bias Voltage	-40V to -170V	-40V to -170V
Coating Thickness	4 $\mu\text{m} \pm 1 \mu\text{m}$	4 $\mu\text{m} \pm 1 \mu\text{m}$

3.2.2.1 Feedstock Materials for Coatings

Two types of coating powders namely Ti-50Al (50 Ti-50 Al Wt %) and Al-30Cr (70 Al-30 Cr Wt %) were chosen for plasma spray deposition on the four types of substrates. These powders were prepared in laboratory ball mill for 8 hrs to form a uniform mixture from three types of commercially available alloy powders namely Titanium powder with minimum assay 98.0 % (Art.6322) supplied by Loba Chemie, Mumbai, India, Aluminum powder with minimum assay 90.0 % and size 200 mesh (Art. 37064) and Chromium powder with minimum assay 99.0 % and size 60 mesh (Art. 36054) supplied by S.D. Fine Chemical Limited, Mumbai, India. SEM (Scanning Electron Microscopy) micrographs along with EDAX (Energy Dispersive X-Ray Analysis) reveal the morphology of coating powders as shown in Fig. 3.2. The chemical composition and particle size of the coating powders are reported in Table 3.3. It may be mentioned here that these coating powders have been selected for depositing the coatings on the substrates as the characterization and high temperature corrosion studies of these coated substrates are scarce in the literature.

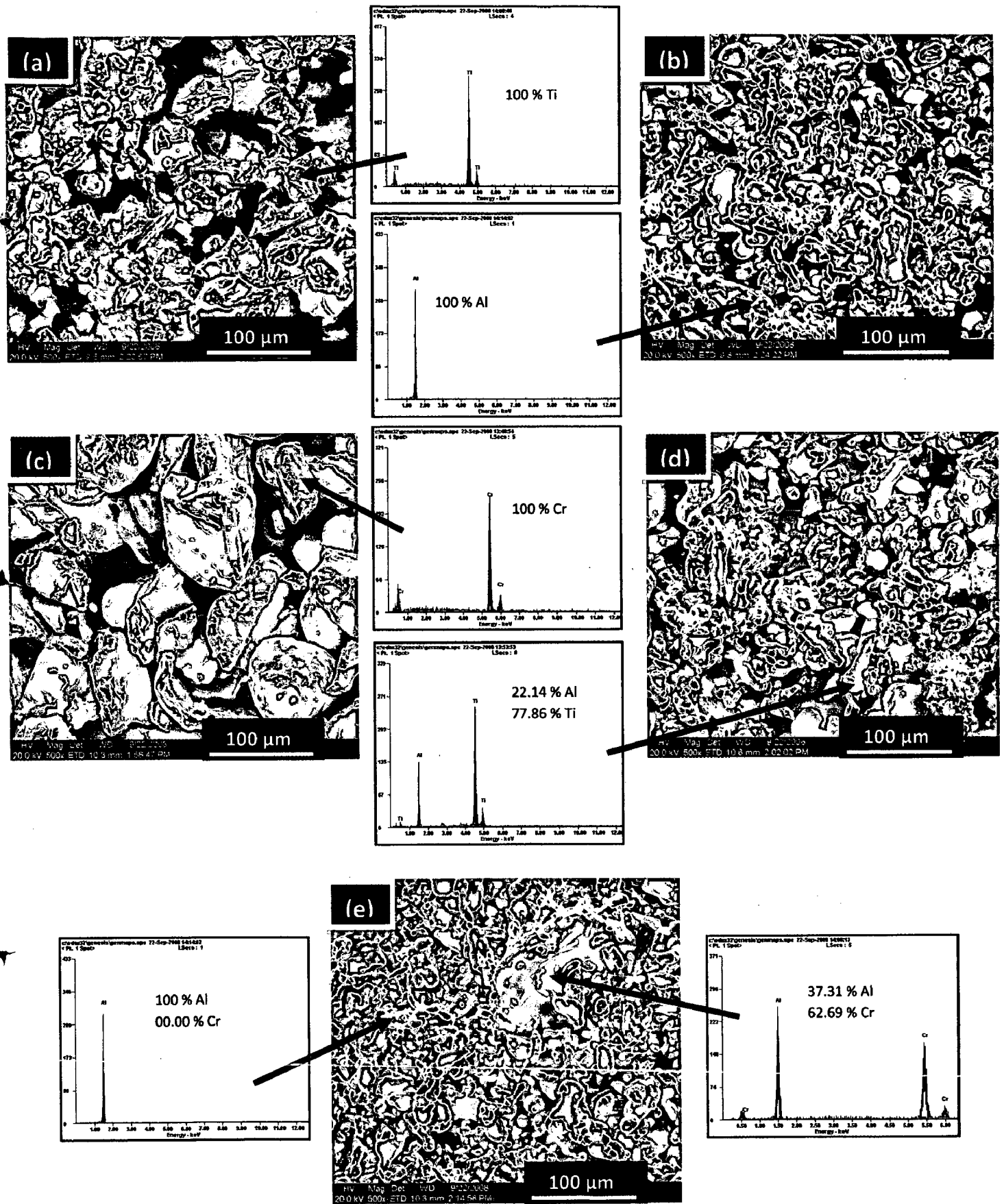


Fig. 3.2

SEM/EDAX patterns (showing Wt %) for different coating powders; (a) Ti-metal powder, (b) Al-metal powder, (c) Cr-metal powder, (d) Ti-Al (50-50 Wt %) powder, (e) Al-Cr (70-30 Wt %) powder

Table 3.3: Composition, particle size and designation of the coatings powders

Coating Powder	Composition (Wt %)	Particle Size (μm)
Ti-50 Al	50 % Ti and 50 % Al	05-55 μm
Al-30 Cr	70 % Al and 30 % Cr	05-90 μm

3.2.2.2 Formulation of Coatings

The coating work was carried out a commercial firm namely Anod Plasma Limited, Kanpur, India. They used 40 kW Miller Thermal (USA) plasma spray apparatus to apply the coatings. Argon was used as powder carrying and shielding gas. Standard spray parameters were designed by the above firm for depositing the coatings in the present work. All the process parameters were kept constant throughout the coating process while spraying distance was maintained in a narrow range of 90-110 mm. The process parameters for the shrouded plasma spray process employed for applying the coatings are summarized in Table 3.4.

Table 3.4: Parameters of the argon shrouded plasma spray process

Arc Current (A)	750
Arc Voltage (V)	45
Powder Feed Rate (rev/min)	5.2
Spraying Distance (mm)	90-110
Plasma Arc Gas (Argon) Pressure	58 psi
Powder Gas Pressure	60 psi
AVX Gas Pressure	10 psi

3.2.2.3 Gas Nitriding

Gas nitriding is a case hardening process whereby nitrogen is introduced into the surface of an alloy by holding it at a suitable temperature in contact with a nitrogenous gas i.e. nitrogen or ammonia. After reviewing the literature critically; it was decided to do the gas nitriding of the plasma sprayed conventional thick Ti-Al and Al-Cr coatings in the lab. The apparatus used for the gas nitriding process is shown in Fig.3.3; which consist of a long steel tube placed in a silicon tube furnace. In the front view (Fig.3.3), the steel tube is connected to the nitrogen cylinder for nitrogen supply and in the rear view; the outlet of the nitrogen gas is through water for slow and constant discharge rate. The gas nitriding parameters were optimized after conducting several trials on plasma sprayed coated specimens. The process parameters employed for the gas nitriding are as summarized in Table.3.5.

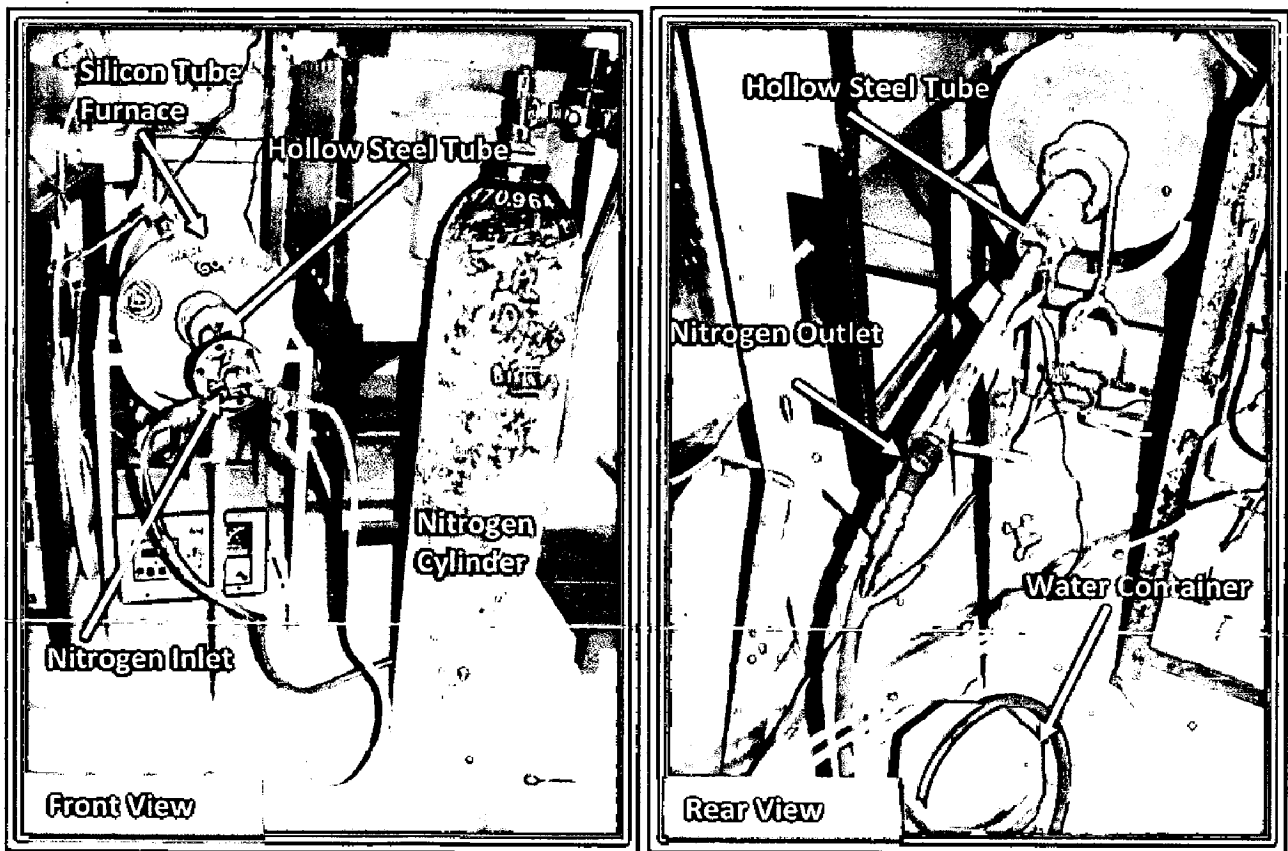


Fig. 3.3 Front and rear views of the set-up used for gas nitriding of the plasma sprayed conventional thick Ti-Al and Al-Cr coatings in the laboratory

Table 3.5: Parameters of the gas nitriding process

Temperature	650 °C	
Duration	3 hrs	For Ti-Al coating
	5 hrs	For Al-Cr coating
Discharge Rate of nitrogen	0.3 l/min	

3.3 CHARACTERIZATION OF THE COATINGS

3.3.1 Specimen preparation

The as-coated specimens were cut with a diamond cutter (Buehler's Precision Diamond Saw, Model ISOMET 1000, made in USA) across its cross-section and subsequently hot mounted in Buehler's transoptic powder (20-3400-080). Subsequently, the mounted specimens were polished manually using emery papers of 220, 400, 600 grit sizes and subsequently on 1/0, 2/0, 3/0 and 4/0 grades. Finally, the specimens were mirror polished on a cloth polishing wheel machine with 0.05 μm alumina powder suspension. The specimens were washed thoroughly with flowing water, and dried in hot air to remove any moisture.

3.3.2 Measurement of Coating Thickness

The thickness of the coatings was monitored during the coating processes. In case of plasma sprayed conventional thick coatings; the thickness was monitored with a Minitest-2000 thin film thickness gauge (made in Germany, precision $\pm 1 \mu\text{m}$). Efforts were made to obtain the coatings with uniform thickness. The thickness of some of the as-coated specimens (nanostructured as well as conventional coatings) were further verified by cutting along the cross-section and mounted (as explained in Section 3.3.1). A Field emission scanning electron microscope (FE-SEM)(FEI Quanta 200F, Made in Czech Republic) was used to obtain the back scattered electron (BSE) images. The average coating thickness measured from the BSE images at different locations is reported in Chapter 4, 5, 6 and 7 of the present study.

3.3.3 Measurement of Porosity

Porosity of the coatings was measured with an image analyser using Zeiss Axiovert 200 MAT inverted optical microscope, fitted with imaging software Zeiss Axiovision Release 4.1, (Germany) software, which was developed based on ASTM B276. The magnification was chosen such that the coating microstructure image covers the screen and allows the resolution of the voids that contributes notably to the total porosity area percentage. The process of selecting the appropriate range of light grey contrast spots was carried out methodically by stereographic imaging to ensure that only voids were selected. The analysis using image processing software determines the pore area size in the view field by converting the pore areas (grey-level areas) into a background color such as red while the rest of the microstructure remains in its original color. The area of one feature is numerically related to the total area of the picture, as the program counts the number of one color type pixels (red) and sets that as a ratio of the total number of pixels in the picture (total area). About twenty (20) separate locations were selected to avoid the overlap between two locations and determine the area percent porosity and the values are reported in Chapter 4, 5, 6 and 7 of the present study.

3.3.4 Metallographic Studies

The as-coated specimens were prepared as explained in Section 3.3.1 for metallographic studies. Specimens were then examined under Zeiss Axiovert 200 MAT Inverted Optical Microscope interfaced with imaging software Zeiss AxioVision Release 4.1 to obtain surface microstructures of the coatings. The surface as well as cross-sectional microstructures of the specimens is discussed in Chapter 4, 5, 6 and 7 of the present study.

3.3.5 Measurement of Microhardness

For obtaining microhardness of the gas nitrided plasma sprayed coatings, the specimens were cut, mounted and polished as explained in section 3.3.1. The microhardness of the as sprayed coatings was measured by using Miniload 2 Microhardness Tester (Leitz, Germany) fitted with a Vickers pyramidal diamond indenter. A 15 g (147.1mN) load was applied

to the indenter for penetration of as sprayed coatings. Hardness value was calculated from the relation $Hv = 1854.4 \times \frac{F}{d^2}$ where 'F' is the load in grams and 'd' is the diameter of the indenter in micrometer. Each reported value of the microhardness is the average value of five measurements. These microhardness values are plotted as a function of distance from the coating/substrate interface and incorporated in Chapter 4, 5, 6 and 7 of the present study.

3.3.6 Measurement of Surface Roughness

The surface roughness (Ra) values of the gas nitrided plasma sprayed as coated specimens were measured using Surface Roughness Tester (Mitutoyo SJ-201, Japan). Each reported value of surface roughness (Ra) is the mean of five observations taken at different locations. The centre line average (CLA) method was used to obtain the Ra values.

3.3.7 Measurement of Bond Strength

The bond strength of the gas nitrided plasma sprayed coatings was tested using the ASTM standard C633-01. This test method covers the determination of the degree of adhesion (bonding strength) of a coating to a substrate or the cohesion strength of the coating in a tension normal to the surface. The test consists of coating one face of a substrate fixture, bonding this coating to the face of a loading fixture, and subjecting this assembly of coating and fixtures to a tensile load normal to the plane of the coating. A data acquisition system has continuously recorded the tensile load exerted by the machine. It is adapted particularly for testing coatings applied by thermal spray, which is defined to include the combustion flame, plasma arc, two wire arc, high-velocity oxygen fuel and detonation processes for spraying feedstock, which may be in the form of , wire, rod or powder. A total of three specimens were tested and average value of the bond strength is reported in Chapter 4, 5, 6 and 7 of the present study.

3.3.8 Atomic Force Microscopy (AFM) Analysis

The surface morphology (2D and 3D) of the nanostructured thin as coated specimens; was characterized by Atomic Force Microscope (AFM) (Model: NTEGRA, NT-

MDT, Ireland). Also, the surface roughness and particle size were calculated which are reported Chapter 4, 5, 6 and 7 of the present study.

3.3.9 X-Ray Diffraction (XRD) Analysis

XRD analysis was carried out for the as coated specimens to identify the various phases present on their surfaces. The X-ray diffraction patterns were obtained by a Bruker AXS D-8 Advance Diffractometer (Germany) with $\text{CuK}\alpha$ radiation and nickel filter at 30 mA under a voltage of 40 kV. The specimens were scanned with a scanning speed of $2^\circ/\text{min}$ in 2θ range of 20° to 120° and the intensities were recorded. Assuming height of the most prominent peak as 100%, the relative intensities were calculated for all the peaks. The diffractometer interfaced with Bruker DIFFRAC^{plus} X-Ray diffraction software provides 'd' values directly on the diffraction pattern. These 'd' values were then used for identification of various phases with the help of JCPDS data cards. The grain size of the nanostructured thin coatings was estimated from Scherrer formula (Cullity, 1970) as follows:

$$D = 0.9 \lambda / B \cos\theta$$

Where λ , B and θ are the X-ray wavelength (1.54056 Å), Bragg diffraction angle and line width at half maximum, respectively. The grain size values of the nanostructured thin coatings are presented in Chapter 4, 5, 6 and 7 of the present study.

3.3.10 Scanning Electron Microscopy (SEM) and Energy Dispersive X-ray (EDAX) Analysis

3.3.10.1 Surface Morphology/EDAX Analysis

The surface morphologies of the coating powders and as coated specimens were studied with the help of a Field Emission Scanning Electron Microscope (FEI Quanta 200F, Made in Czech Republic) fitted with EDAX Genesis software attachment; with an aim to understand the morphology of the coating powders and to identify inclusions, un-melted, partially melted particles and pores in the as sprayed coatings. The EDAX genesis software indicates the elemental compositions (weight %) present at point/area of interest. Although

the composition correspond to selected points on the as-sprayed surfaces it is useful to understand the formation of desired compositions in the coatings. SEM/EDAX analysis of the as coated specimens is reported in Chapter 4, 5, 6 and 7 of the present study.

3.3.10.2 Cross sectional analysis

The sample was prepared as explained in the section 3.3.1. The analysis was carried out using a Field Emission Scanning Electron Microscope (FEI Quanta 200F, Made in Czech Republic) fitted with EDAX Genesis software attachment. The back scattered electron images were taken and the EDAX analysis was performed across the cross section to ascertain elemental composition (weight %) at different points as well as to identify the presence of various elements along the cross-section of the coatings.

3.3.10.3 X-ray mapping analysis

To obtain cross-sectional analysis of the different elements present in the coatings, the specimens were cut along the cross-section, mounted and polished in accordance with the procedure already discussed in section 3.3.1. X-ray mapping analysis of the samples was done on field emission scanning electron microscope (FEI, Quanta 200F Company) for image acquisition entailed a backscattered electron image (BSEI) and secondary electron image (SEI) mode. An accelerating voltage of 20-25 kV, a working distance of 9–10 mm, and an image size of 1024*884 pixels were used for getting quality images. Energy Dispersive X-ray Analysis (EDAX) and X-ray mapping were employed while imaging on FE-SEM was carried out to obtain elemental composition at different areas of the coating and surface morphology of the coatings, respectively. The specimen were silver pasted between samples and the stub in order to have conductivity, thereafter, gold coated to facilitate elemental X-ray mapping analysis of the different elements present across the coating. The selected area has three regions i.e. substrate, coating and some epoxy region. X-ray mappings were obtained for all the elements of the substrate and the coatings, but only those mappings are reported which indicates the presence of some element.

3.4 HIGH TEMPERATURE OXIDATION AND HOT CORROSION STUDIES

3.4.1 Experimental Setup

Oxidation and hot corrosion studies were conducted at 900°C in a laboratory silicon carbide tube furnace (make Digitech, India) as shown in Fig.3.4 (a & c). The furnace was calibrated to an accuracy of $\pm 5^\circ\text{C}$ using Platinum/Platinum-13% Rhodium thermocouple fitted with a temperature indicator of Electromek (Model-1551 P), India. The bare as well as the coated specimens were polished down to 1 μm alumina wheel cloth polishing to obtain similar condition of reaction before being subjected to corrosion run. The physical dimensions of the specimens were then recorded carefully with Sylvac digital vernier caliper (Swiss make, resolution 0.01) to evaluate their surface areas. Subsequently, the specimens were washed properly with acetone and dried in hot air to remove the moisture. During experimentation, the prepared specimen was kept in an alumina boat and the weight of boat and specimen was measured. The alumina boats used for the studies were pre-heated at a constant temperature of 1200°C for 12 hours and it was assumed that their weight would remain constant during the course of high temperature cyclic oxidation/corrosion study. Then, the boat containing the specimen was inserted into hot zone of the furnace maintained at a temperature of 900°C. The weight of the boat loaded with the specimen was measured after each cycle during the corrosion run, the spalled scale if any was also considered during the weight change measurements. Holding time in the furnace was one hour in still air followed by cooling at the ambient temperature for 20 minutes. Following this, weight of the boat along with specimen was measured and this constituted one cycle of the oxidation study. Electronic Balance Model CB-120 (Contech, Mumbai, India) having a sensitivity of 10^{-3} g was used to conduct the weight change studies (Fig.3.4.e). The specimens were subjected to visual observations carefully after the end of each cycle with respect to color or any other physical aspect of the oxide scales being formed. All oxidation and hot corrosion studies were carried out for 50 cycles. The reproducibility in the experiments was established by repeating hot corrosion experiments for three cases.

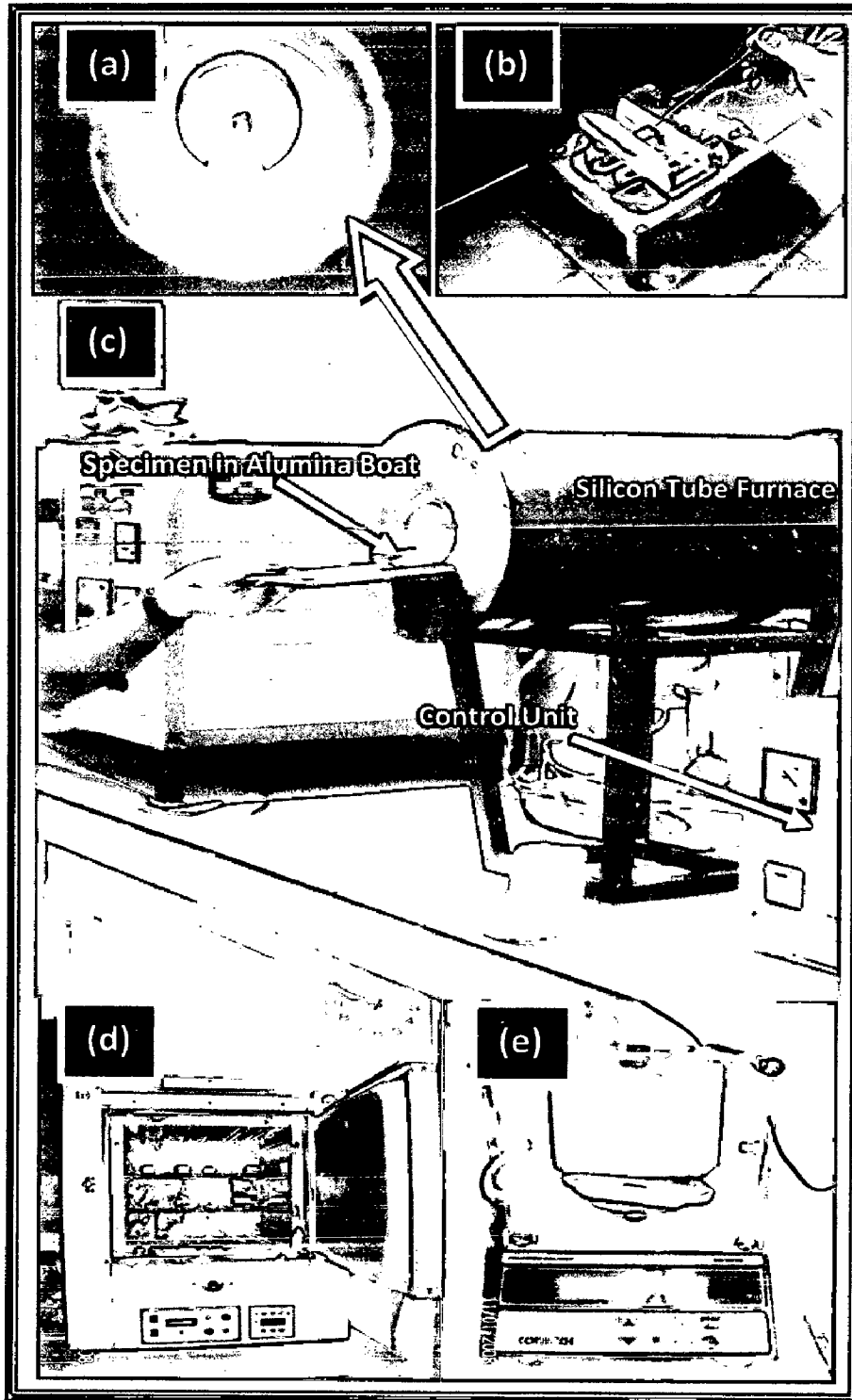


Fig. 3.4 Experimental set up for high temperature oxidation and hot corrosion studies; (a) Heat Zone inside furnace, (b) Molten salt coating, (c) Silicon tube furnace, (d) Oven for pre heating the specimens, (e) Electronic balance

3.4.2 Oxidation Studies in Air

The oxidation tests at 900°C were performed on all four bare alloys (mirror polished) as well as coated alloys in laboratory silicon tube furnace (Fig.3.3) up to 50 cycles as discussed in section 3.4.1.

3.4.3 Hot Corrosion Studies in Molten Salt (Na_2SO_4 - 60% V_2O_5)

3.4.3.1 Coating of Molten Salt

The as coated as well as bare specimens (mirror polished) were prepared for studies as discussed in section 3.4.1. The specimens were then heated in an oven up to 250°C and a salt mixture of Na_2SO_4 -60% V_2O_5 dissolved in distilled water was coated on all the six surfaces of the warm polished specimens with the help of a camel hair brush (Fig.3.4.b). The salt Na_2SO_4 was obtained from S.D. Fine-chem Limited (Art. 40223), Mumbai and V_2O_5 was obtained from Loba Chemie Pvt. Ltd (Art. 6470), Mumbai. Amount of the salt coating was kept in the range of 3.0 -5.0 mg/cm². The salt coated specimens as well as the alumina boats were then dried in the oven (Fig.3.4.d) for 3 hours at 100°C and weighed before being exposed to hot corrosion tests.

3.4.3.2 Hot Corrosion Studies

The bare as well as coated specimens after application of salt coating were subjected to hot corrosion in the laboratory furnace at 900°C for 50 cycles as discussed in section 3.4.1.

3.4.4 Studies in coal fired Industrial boiler Environment

The coated as well as bare alloy specimens were exposed to the platen super-heater zone of the coal fired boiler of Stage-II at Guru Nanak Dev Thermal Plant, Bathinda, Punjab (India). This zone was selected for the present study as many breakdowns occurred in this power plant due to hot corrosion degradation of the platen super-heater tubes of the coal fired boilers. A hole of 1.2 mm diameter was drilled in all the specimens to hang them in the boiler for experimentation. The coated as well as bare specimens

were polished down to 1 μ m alumina on a cloth polishing wheel machine to obtain similar conditions of reaction on the surface of all the specimens. The physical dimensions of the specimens were measured with a Sylvac digital vernier caliper (Swiss make, resolution 0.01), to evaluate their surface areas.

Table 3.6: Chemical analysis of ash and flue gases inside the boiler

Ash		Flue Gases	
Constituent	Wt. %age	(Volumetric flow, 231 m ³ /sec)	
Silica	54.70	Constituent	Value relative to flue gases
Fe ₂ O ₃	5.18	SO _x	236 mg/m ³
Al ₂ O ₃ - Fe ₂ O ₃ /Al ₂ O ₃	29.56	NO _x	1004 μ g/m ³
Calcium oxide	1.48	CO ₂	12%
Magnesium oxide	1.45	O ₂	7%
SO ₃	0.23	40% excess air was supplied to the boiler for the combustion of coal.	
Na ₂ O	0.34		
K ₂ O	1.35		
Ignition loss	4.31		

To measure the thickness during experimentations, the average thickness of each specimen (average of 10 measurements) was measured using Sylvac micrometer screw gauge (Swiss make, resolution 0.001), before exposing them to the boiler environment. The coated as well as bare specimens were then hanged with the help of a stainless steel wire through the soot blower dummy points at 27 m height from the base of the boiler. The specimens were exposed to the combustion environment for 10 cycles. Each cycle consisted of 100 hours heating followed by 1 hour cooling at ambient conditions. The temperature was measured at regular intervals during the study and the average temperature was about 900°C with variation of $\pm 10^\circ\text{C}$.

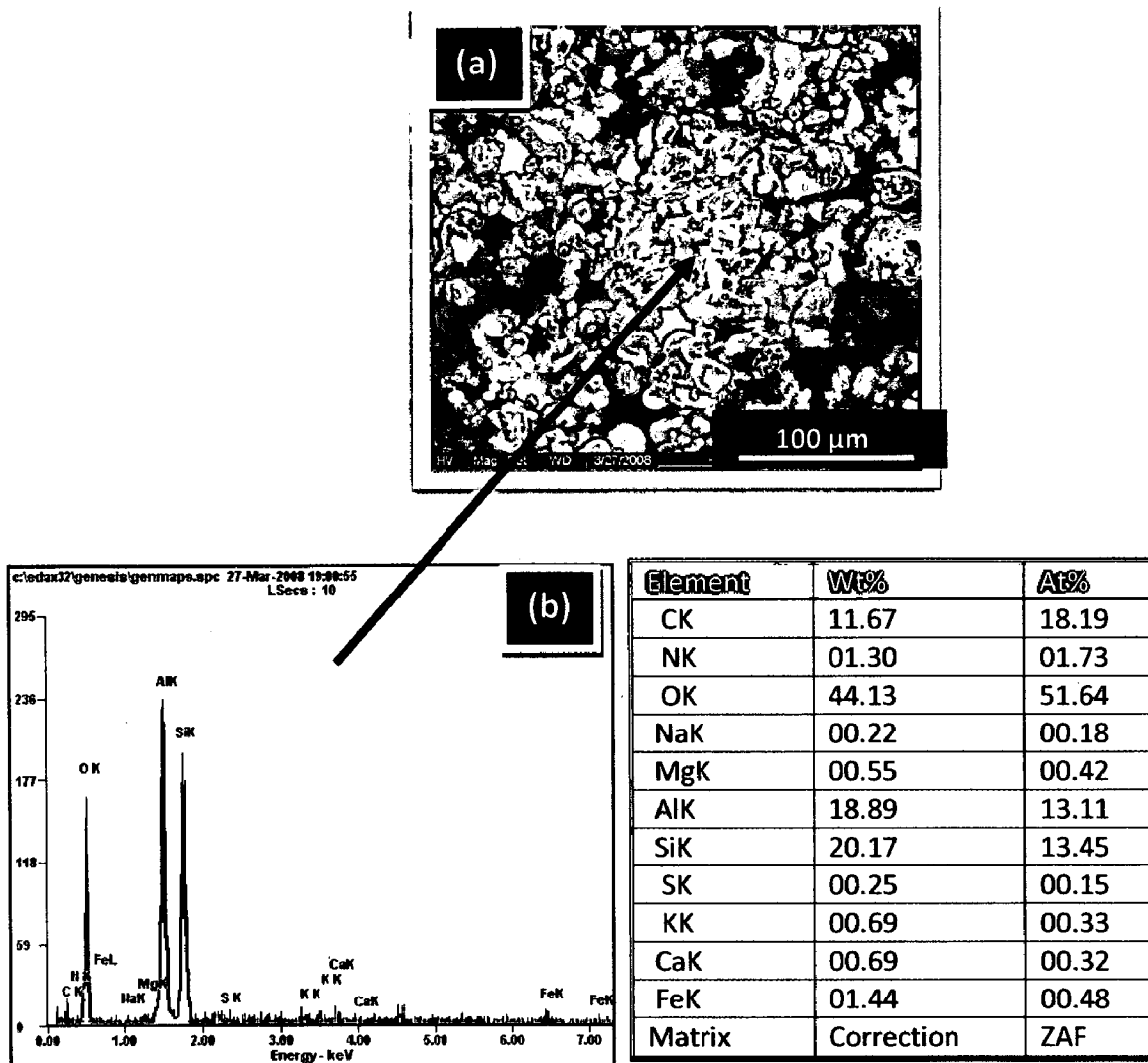


Fig. 3.5 Analysis of fly ash; (a) SEM morphology and (b) EDAX compositional analysis

After the end of each cycle, the specimens were visually observed for any change in the surface texture, further it has been washed by acetone and weight of the specimens were measured subsequently using an Electronic Balance Model CB-120 (Contech, Mumbai, India, and sensitivity 10^{-3} g). The chemical analysis of the flue gas and ash present inside the boiler is given in Table 3.6. The SEM/EDAX analysis of the fly ash is shown in Fig. 3.5. After the end of each cycle, the specimens were subjected to careful visual observation for any change in the surface.

3.5.5.3 X-ray mapping analysis

X-ray mapping analysis of the oxidized and corroded samples was done on field emission scanning electron microscope (FEI, Quanta 200F Company) as described in section 3.3.10.3. The selected area has three regions i.e. substrate, scale and some epoxy region. X-ray mappings were obtained for all the elements of the substrate and the scale, but only those mappings are reported which indicates the presence of some element.

3.6 EROSION STUDIES IN SIMULATED COAL-FIRED BOILER ENVIRONMENT

3.6.1 Experimental Setup

Erosion testing was carried out using a solid particle erosion test rig TR-471-M10 Air Jet Erosion Tester (Ducom Instruments Private Limited, Bangalore, India) capable of conducting tests at room temperature as well as high temperature shown in Fig.3.6. The rig consisted of an air compressor, erodent feeding system, mixing chamber, furnace unit, specimen holder, nozzle, erodent collection chamber, pneumatic control box and electrical control box. The test method utilizes a repeated impact erosion approach involving a small nozzle delivering a stream of gas containing abrasive particles which impacts the surface of a test specimen.

Dry compressed air was mixed with the erodent particles, which were fed at a constant rate from hopper through erodent feeding system in the mixing chamber and then accelerated by passing the mixture through a converging nozzle made of inconel material of 4 mm diameter. These accelerated particles impacted the specimen kept in the furnace unit consisting of specimen heater and air heater. The specimen could be held at various angles with respect to the impacting particles using an adjustable sample holder. The discharge rate of the particles could be controlled by varying the frequency of motor speed in the erodent feeding system. The erodent feeding system consists of a hopper which allows erodent to fall under gravity through throat on a wheel which is rotated by a motor through timer belt. Motor speed determines the extent of discharge. The impact velocities of the particles could be varied by varying the pressure of the compressed air.

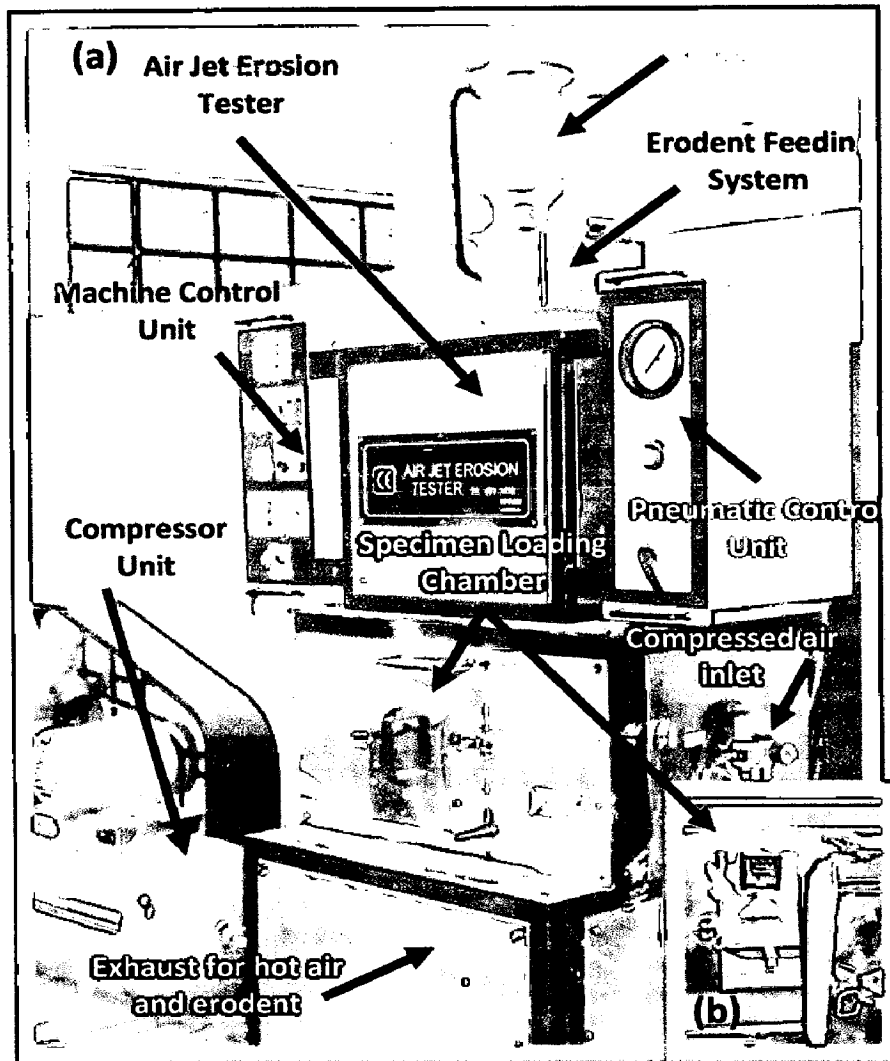


Fig. 3.6 Experimental set-up for erosion-corrosion in simulated coal-fired boiler environment (a) Air Jet Erosion Tester, (b) Interior view of specimen loading chamber

3.6.2 Erosion Studies in an Air Jet Erosion Test Rig

The studies were performed for uncoated as well as coated specimens for the purpose of comparison. The erosion test conditions utilized in the present study are listed in Table 3.7. A standard test procedure was employed for each erosion test. The uncoated as well as the coated specimens were polished down to 1 μ m alumina wheel cloth polishing to obtain similar condition on all the samples before being subjected to erosion run. The samples were cleaned in acetone, dried, weighed to an accuracy of 1×10^{-5} g using an electronic balance, eroded in the test rig for 3 hours and then weighed again to determine weight loss. In the present study

standard alumina 50 micron (supplied with Erosion Test Rig by Ducom Instruments Private Limited, Bangalore, India) was used as erodent (Fig. 3.7).

The two temperatures were taken for the test (Table 3.7), sample temperature 400°C and air/erodent temperature 900°C simulated to service conditions of boiler tubes in which sample temperature and flow gas temperature correspond to the inner and outer temperature of water wall pipes. In general, Erosion resistance is measured using weight loss technique by measuring the weights before and after the test. But at high temperature, weight change measurements leads to flawed results due to oxidation of samples. In order to overcome the limitations of the weight change technique, a different technique was used for the present investigation. Erosion resistance was measured in terms of volume loss after the erosion testing.

Table 3.7 Erosion-Corrosion Test conditions

Erodent material	Alumina (Irregular shape)
Erodent Specifications	50 micron Al ₂ O ₃
Particle velocity (m/s)	35m/s
Erodent feed rate (g/min)	2 gm/min
Impact angle (°)	30, 90
Test temperature	Sample Temperature 400°C and Air Temperature 900°C
Nozzle diameter (mm)	4
Test time (Hrs)	3 Hours

3.6.3 Analysis of eroded surfaces

All the specimens subjected to erosion wear were analyzed for the characterization of erosion products. The specimens were analyzed using surface SEM, EDAX and measurement of surface profiles using optical profilometer.

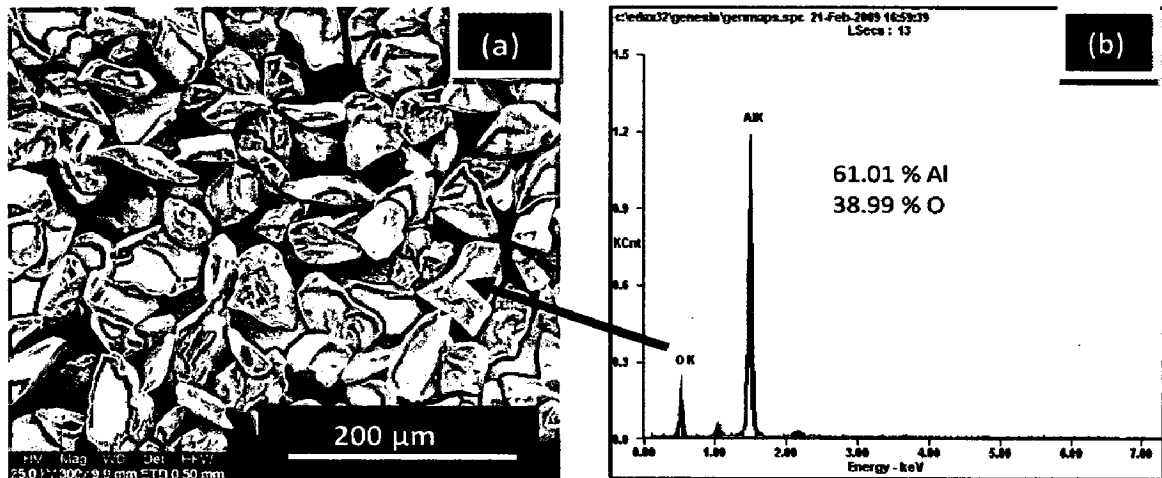


Fig. 3.7 Analysis of Alumina (Al₂O₃); (a) SEM morphology and (b) EDAX compositional analysis

3.6.3.1 Visual Observation

For the specimens eroded in laboratory test rig, visual examination was made after the completion of erosion cycles and the macrographs of the eroded specimens were taken.

3.6.3.2 Erosion rate in terms of Volume loss

The volume loss occurred after erosion testing was measured by using non contact optical profilometry. The method was used to evaluate surface characteristics, such as erosion volume loss and depth, surface topography. Veeco Optical Profilometer (NT 1100, USA make) was used. This method characterizes and quantifies critical dimensions (such as area and volume of the damaged erosion wear scars), and topographical features. It has three-dimensional profiling capability with excellent precision and accuracy. The shape of a surface can be displayed by a computer-generated map developed from digital data derived from a three-dimensional interferogram of the surface.

The erosion depth was measured at six random locations to obtain the average erosion depth of an eroded scar on an eroded specimen. At each location (including eroded

and uneroded area) surface profiles were taken. The intact/unaffected surface (uneroded area) was used as a reference plane for the erosion depth measurement. At each erosion scar, six contour maps were obtained. The maximum erosion depth was obtained by measuring a step height between a nominal surface and a zero level of the bottom wear surface of the erosion scar in a cross-sectional profile of each contour map. Then, the mean value of the six maximum erosion depths was determined and defined as the mean erosion depth. The erosion scar area was measured using Image analysis software (Image J 1.41). Thus, the erosion wear volume loss can be calculated. The histograms illustrating the erosion rates in terms of volume loss (mm^3/g) have been plotted to compare erosion rates of different uncoated alloys and coated alloys and have been discussed in Chapters 4, 5, 6 and 7.

3.6.3.3 SEM/EDAX Analysis

Surface SEM analysis of the eroded samples was conducted using Field emission scanning electron microscope (FEI Company, Quanta 200F) with EDAX attachment as explained in section 3.3.10.1. EDAX analysis at few points of interest was taken which are presented in Chapters 4, 5, 6 and 7.

3.7 CORROSION STUDIES IN SIMULATED MARINE ENVIRONMENT

3.7.1 Linear polarization resistance (LPR) and potentiodynamic polarization tests

In order to evaluate the corrosion behavior of the substrates and coatings in simulated marine environment; linear polarization resistance (LPR) and potentiodynamic polarization tests were conducted in an aerated 3 wt% NaCl solution at room temperature. The electrolyte employed was prepared with NaCl analytical grade reagent with minimum assay 99.9 % supplied by Qualigens Fine Chemicals, Mumbai, India and deionised water. The LPR and potentiodynamic polarization tests were carried out using EG&G PAR model 273A potentiostat as shown in Fig.3.8. The test cell used was having the provisions in the form of circular openings of different sizes to permit the introduction of the two high purity graphite counter electrodes, the working electrode (test specimen) and the Luggin probe

capillary tube, which housed the saturated calomel reference electrode (SCE). The tip of the Luggin probe capillary was placed near the sample. The exposed surface area of all specimens was 1 cm^2 and the remaining portion except the exposed area was painted with good quality nail-polish in order to prevent the initiation of corrosion. Before the electrochemical measurements, samples were allowed to stabilize at their open circuit potential for 30 min.

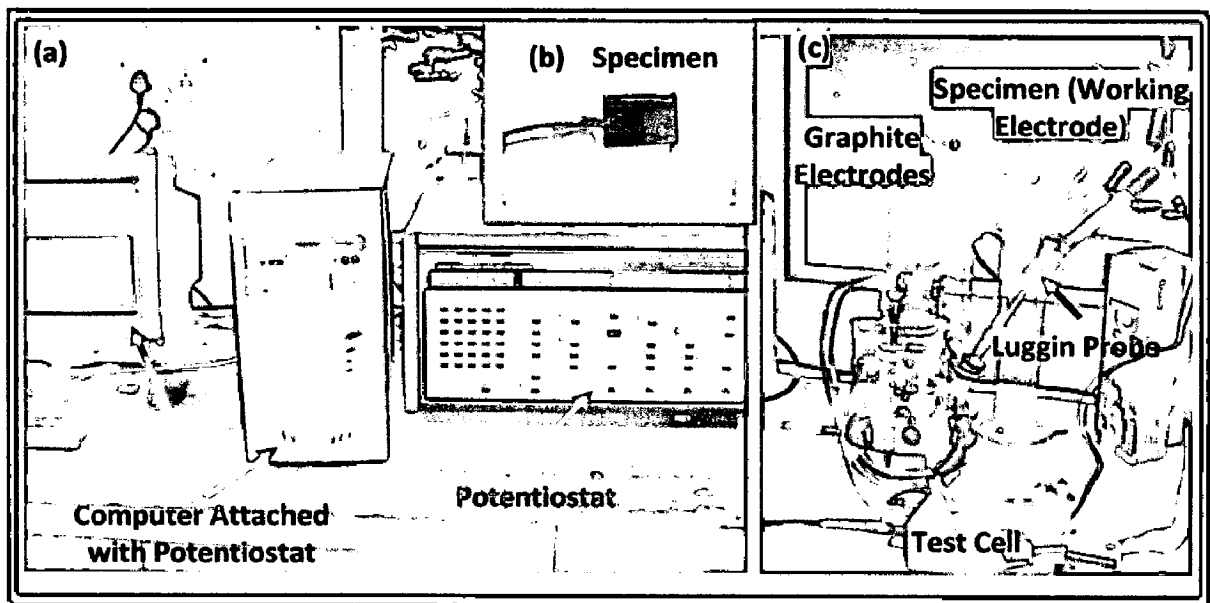


Fig. 3.8 Experimental set-up for linear polarization resistance (LPR) and potentiodynamic polarization tests (a) Potentiostat, (b) Specimen coated with nail-paint (c) Test cell

The initial corrosion current density and LPR (R_p) was measured by LPR test. The primary reason was that linear polarization scans were conducted in very small potential range (-20mV to $+20\text{mV}$ vs Open Circuit Potential), which does not damage the surface of the sample, unlike potentiodynamic polarization scans, which require scanning over a longer potential range (Sahoo and Balasubramaniam, 2007). Potentiodynamic polarization measurements were carried out starting from $-250 \text{ mV}_{\text{OCP}}$ to $1600 \text{ mV}_{\text{SCE}}$ with a scan rate of 0.5 mV/s . The potentiodynamic polarization plots were interpreted using SoftcorrTM III

Chapter 4

SUBSTRATE ASTM-SA210 GRADE A-1 BOILER STEEL

This chapter deals with the results and discussion for the bare and coated ASTM-SA210 Grade A-1 boiler steel exposed to different degradation environments. It includes the characterization of the nanostructured and conventional TiAlN and AlCrN coatings on Grade A-1 boiler steel and their behavior when exposed to high temperature oxidation studies in air, molten salt ($\text{Na}_2\text{SO}_4\text{-60}\%\text{V}_2\text{O}_5$) environment and in a coal fired boiler of a thermal plant, erosion studies in simulated coal-fired boiler environment and corrosion studies in simulated marine environment.

4.1 CHARACTERIZATION OF COATINGS

The present work has been focused to characterize the conventional thick (by plasma spraying and gas nitrided) and nanostructured thin (by physical vapor deposition process) TiAlN and AlCrN coatings developed on ASTM-SA210 Grade A-1 boiler steel.

4.1.1 Results

4.1.1.1 Visual observations

The nanostructured thin (by Physical Vapor Deposition process) and conventional thick (by Plasma Spraying and Gas Nitriding) TiAlN and AlCrN coatings have been formulated successfully on ASTM-SA210 Grade A-1 boiler steel. The macrographs of as-coated Grade A-1 boiler steel are shown in Fig.4.1. It can be observed from the macrographs; the nanostructured thin TiAlN coating is violet grey in color and nanostructured thin AlCrN coating is light grey in color. Visual observations indicate; the surface of nanostructured coatings is smooth whereas the surface of conventional thick coatings is rough. The color of the thick coatings appeared as grey with some bluish shining. Also, Optical micrographs of the nanostructured and conventional coatings are shown in Fig.4.2. The nanostructured coatings (Fig.4.2.a & b) have uniform microstructure. It is evident from the microstructure

that the coatings contain some pores and inclusions. In case of conventional thick coatings (Fig.4.2.c & d); the massive microstructure can be observed with irregularly shaped grains.

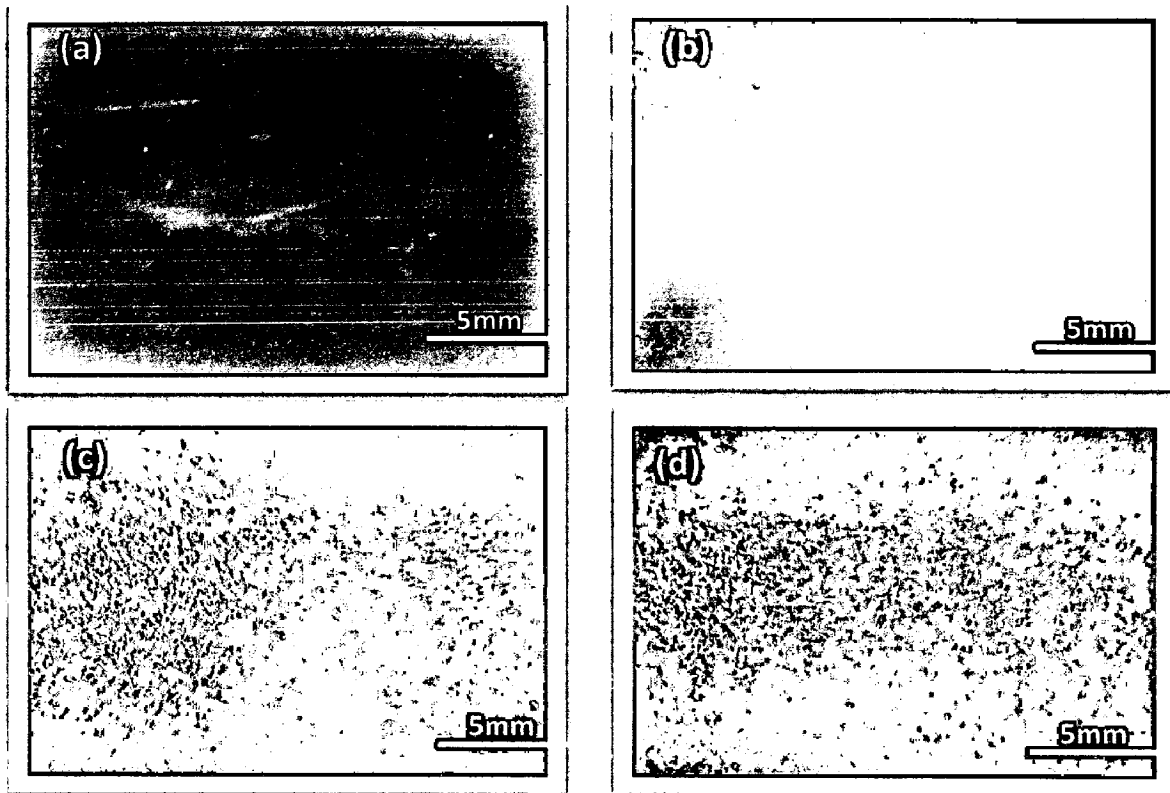


Fig. 4.1 Surface macrographs for the as coated ASTM-SA210 Grade A-1 boiler steel (a) Nanostructured TiAlN coating, (b) Nanostructured AlCrN coating, (c) Conventional TiAlN coating, (d) Conventional AlCrN coating

4.1.1.2 Surface analysis

4.1.1.2.1 X-ray diffraction analysis (XRD)

XRD diffractograms for nanostructured and conventional TiAlN and AlCrN coated Grade A-1 boiler steel are depicted in Fig.4.3 on reduced scale. As indicated by the diffractograms in Fig.4.3; TiN and AlN are the main phases present in the nanostructured thin TiAlN coating. Further, in case of nanostructured AlCrN coating, the prominent phases are CrN and AlN. The grain size of the nanostructured thin coatings was estimated from

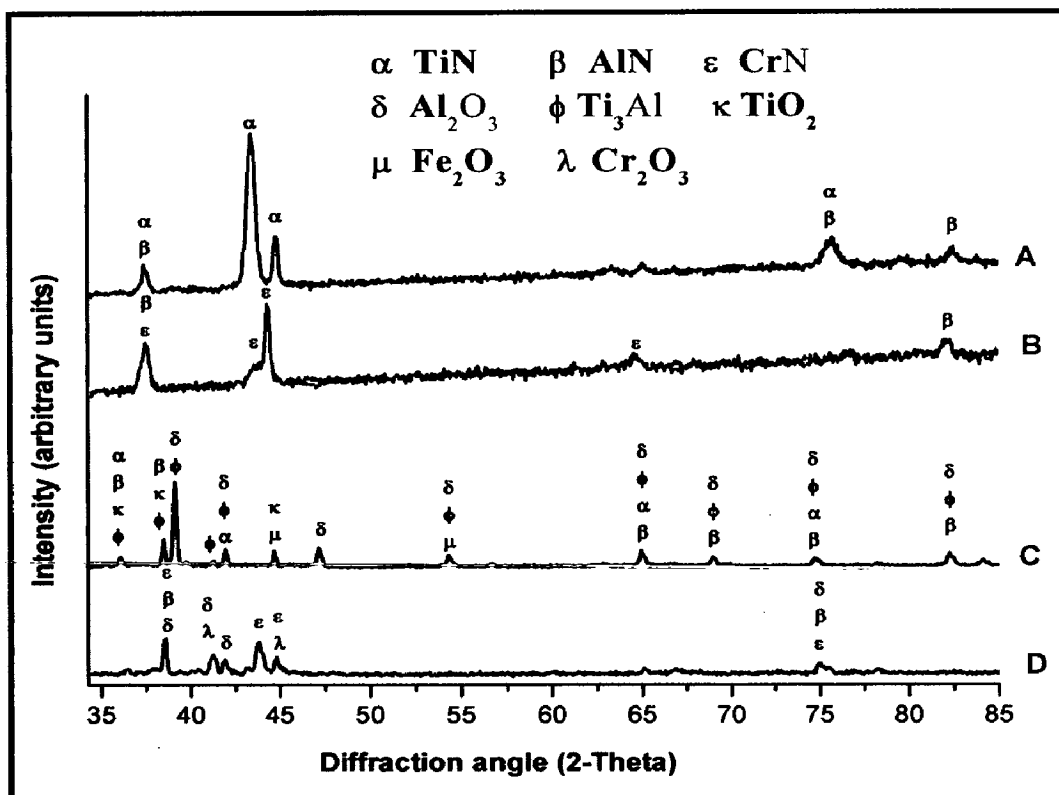


Fig. 4.3 X-Ray Diffraction pattern of as coated ASTM-SA210 Grade A-1 boiler steel (a) Nanostructured TiAlN coating, (b) Nanostructured AlCrN coating, (c) Conventional TiAlN coating, (d) Conventional AlCrN coating

4.1.1.2.3 AFM analysis of the as deposited nanostructured thin coatings

The surface topography of the nanostructured thin TiAlN and AlCrN coatings was studied using Atomic Force Microscope (AFM: NT-MDT: NTEGRA Model) in semi contact mode. Figure 4.4 shows the AFM surface morphology (2D and 3D) of the nanostructured thin TiAlN and AlCrN coatings deposited on Grade A-1 boiler steel. The difference in the morphology between the two coatings can be inferred by comparing the 2D images in Fig. 4.4 (a) and (c); however a clearer comparison of the coatings could be afforded by viewing 3D images in Fig. 4.4 (b) and (d). As the axis scale indicates the overall roughness of the nanostructured TiAlN coating (Fig. 4.4.b) is less than that of AlCrN coating (Fig. 4.4.d). The surface roughness and particle size in the coatings as analyzed by AFM analysis; reported in

4.1.1.2.5 Evaluation of microhardness and bond strength of the conventional coatings

The microhardness of the coatings has been measured along the cross-section of the conventional thick TiAlN and AlCrN coated Grade A-1 boiler steel. Figure 4.5 shows the microhardness profiles along the cross-section of the coatings as a function of distance from the coating-substrate interface. The critical hardness values of the substrate Grade A-1 boiler steel was found to be in the range 200-250 Hv. From the microhardness profiles (Fig.4.5) it is obvious that the conventional TiAlN coating has shown maximum microhardness of the order of 900-950 Hv. The conventional thick AlCrN coating has shown microhardness of the order of 600-700 Hv.

The bond strength of the conventional thick TiAlN and AlCrN coatings was measured on three specimens as per ASTM standard C633-01. The coatings failed at the substrate-coating interface while remaining attached to the adhesive (Fig.4.6). Average bond strength of 68.74 MPa and 54.69 MPa was observed in case of conventional TiAlN and AlCrN coatings respectively (Table.4.2).

4.1.1.2.6 Surface morphology of coatings

SEM micrographs along with EDAX point analysis reveal the surface morphology of the nanostructured and conventional TiAlN and AlCrN coated Grade A-1 boiler steel; are shown in Fig.4.7. Micrograph (Fig.4.7.a) for nanostructured thin TiAlN coating at higher magnification (10000 X) indicates grey matrix with some black and white contrast regions. Dense structure with lower porosity is observed in the coating microstructure and also it is free from cracks. EDAX analysis at point 1 and point 2 in Fig.4.7 indicates the presence of Ti, Al and N with negligible amount of Fe. The black colored areas revealed the higher amount of Ti and less concentration of Al as compared to the white contrast region. In case of nanostructured thin AlCrN coated Grade A-1 boiler steel, the SEM micrograph indicates dense grey colored coating with tiny dark grey particles dispersed in the matrix. EDAX point analysis (Point 3 and 4 in Fig.4.7) shows, the coating is rich in Al, Cr and N along with small amount of Fe and oxygen (Fig.4.7.b).

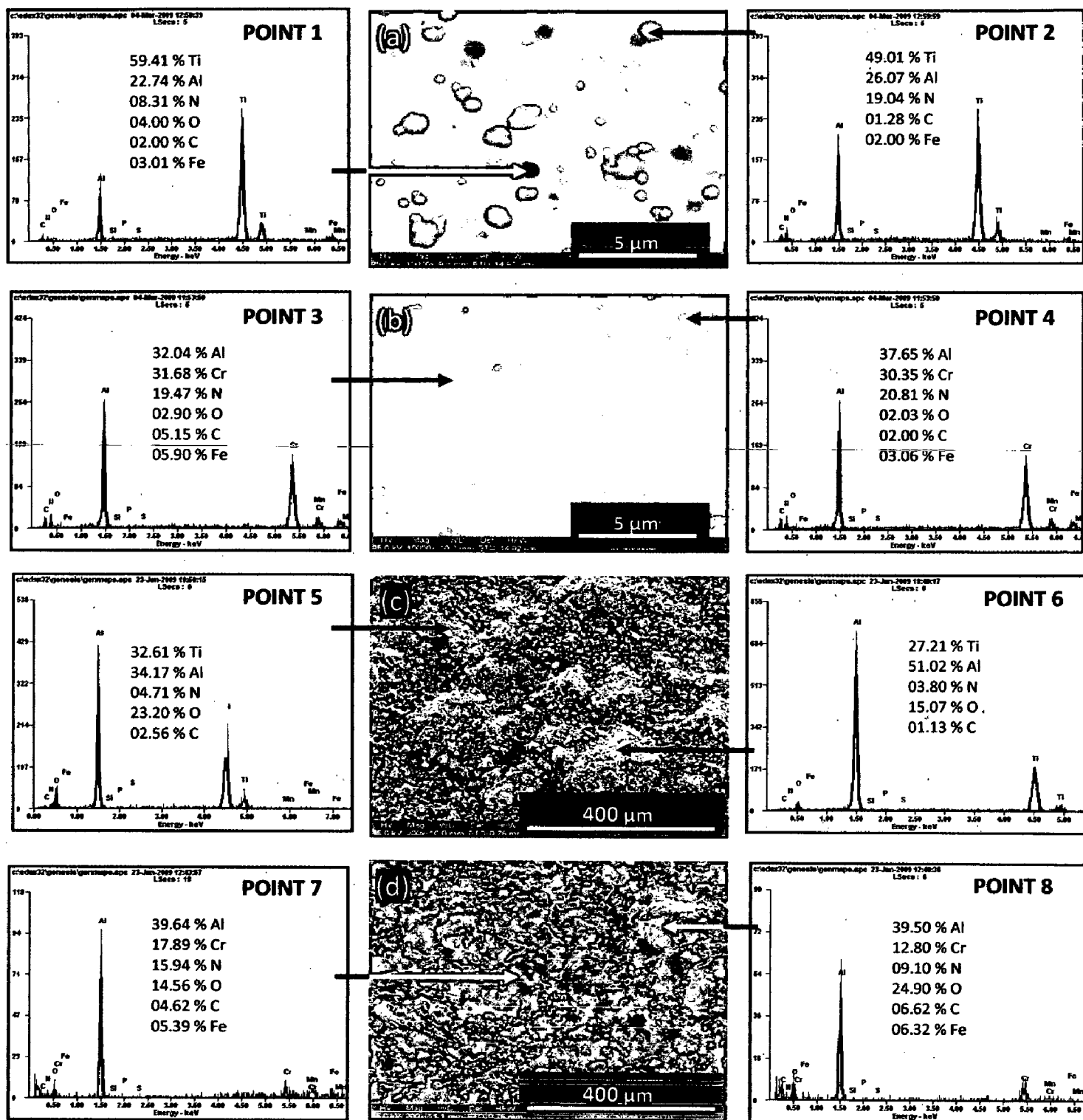


Fig. 4.7 Surface-scale morphology and EDAX patterns from different spots on as coated ASTM-SA210 Grade A-1 boiler steel (a) Nanostructured TiAlN coating, (b) Nanostructured AlCrN coating, (c) Conventional TiAlN coating, (d) Conventional AlCrN coating

The micrographs in case of conventional plasma sprayed gas nitride TiAlN and AlCrN coatings are shown in Fig.4.7(c and d). In general microscopic features indicate that the conventional coatings are homogeneous, massive and free from cracks. Presence of some oxide stringers as well as open pores has been noticed in general in the conventional coatings. The EDAX point analysis (Point 5 and 6 in Fig.4.7); in case of conventional TiAlN coating indicates the higher concentration of Ti and Al in the coating along with some amount of N and oxygen. The presence of Al and Cr along with N and oxygen is revealed by EDAX analysis in case of conventional AlCrN coating (Point 7 and 8 in Fig.4.7).

4.1.1.3 Cross-sectional analysis

4.1.1.3.1 Coating thickness

The as-coated samples were cut across the cross section using Buehler Isomet 1000 precision saw and mounted in transoptic mounting resin and subsequently mirror polished to obtain scanning electron back scattered micrographs and X-ray mapping of different elements for coated Grade A-1 boiler steel. The coating thickness values were measured from SEM back scattered micrographs as shown in Fig.4.8; and average coating thickness is reported in Table.4.2. The measured average coating thickness values for nanostructured thin and conventional thick TiAlN and AlCrN coatings are 6.1, 4.2, 172 and 166 respectively.

4.1.1.3.2 X-Ray mapping

BSEI and X-ray mapping analysis for nanostructured and conventional TiAlN and AlCrN coated Grade A-1 boiler steel is shown in Fig. 4.8. The BSEI and X-ray mapping analysis of the nanostructured TiAlN coated Grade A-1 boiler steel is presented in Fig. 4.8.(a). The X-ray mapping indicates presence of Al and Ti along with small amount of N in the coating and no diffusion of Fe from the substrate has been observed. In case of nanostructured thin AlCrN coated Grade A-1 boiler steel; the BSEI and X-ray mapping are shown in Fig. 4.8.(b).

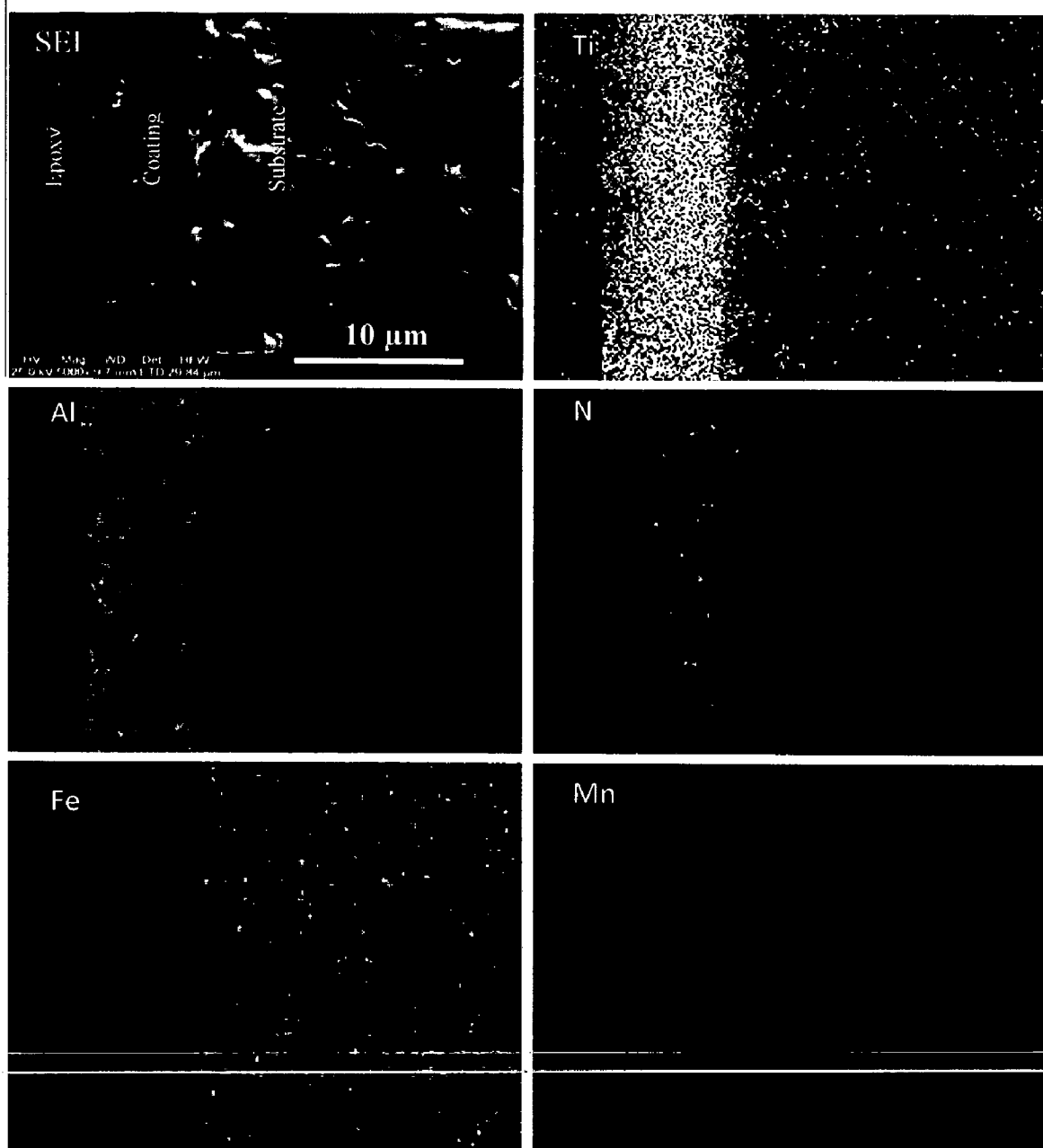


Fig. 4.8 (a) Composition image (SEI) and X-ray mapping of the cross-section of as-coated nanostructured TiAlN coating on ASTM-SA210 Grade A-1 boiler steel

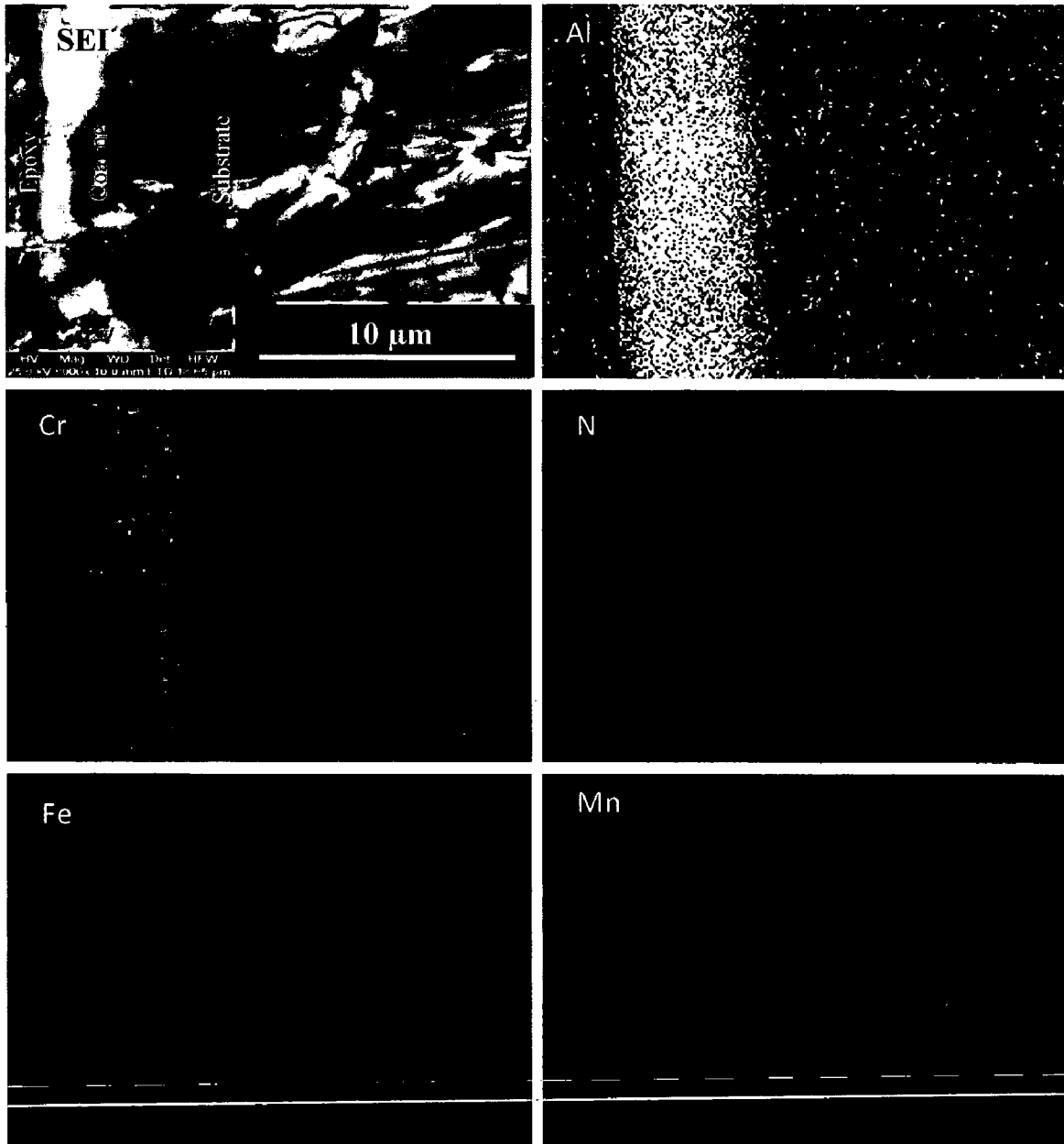


Fig. 4.8 (b) Composition image (SEI) and X-ray mapping of the cross-section of as-coated nanostructured AlCrN coating on ASTM-SA210 Grade A-1 boiler steel

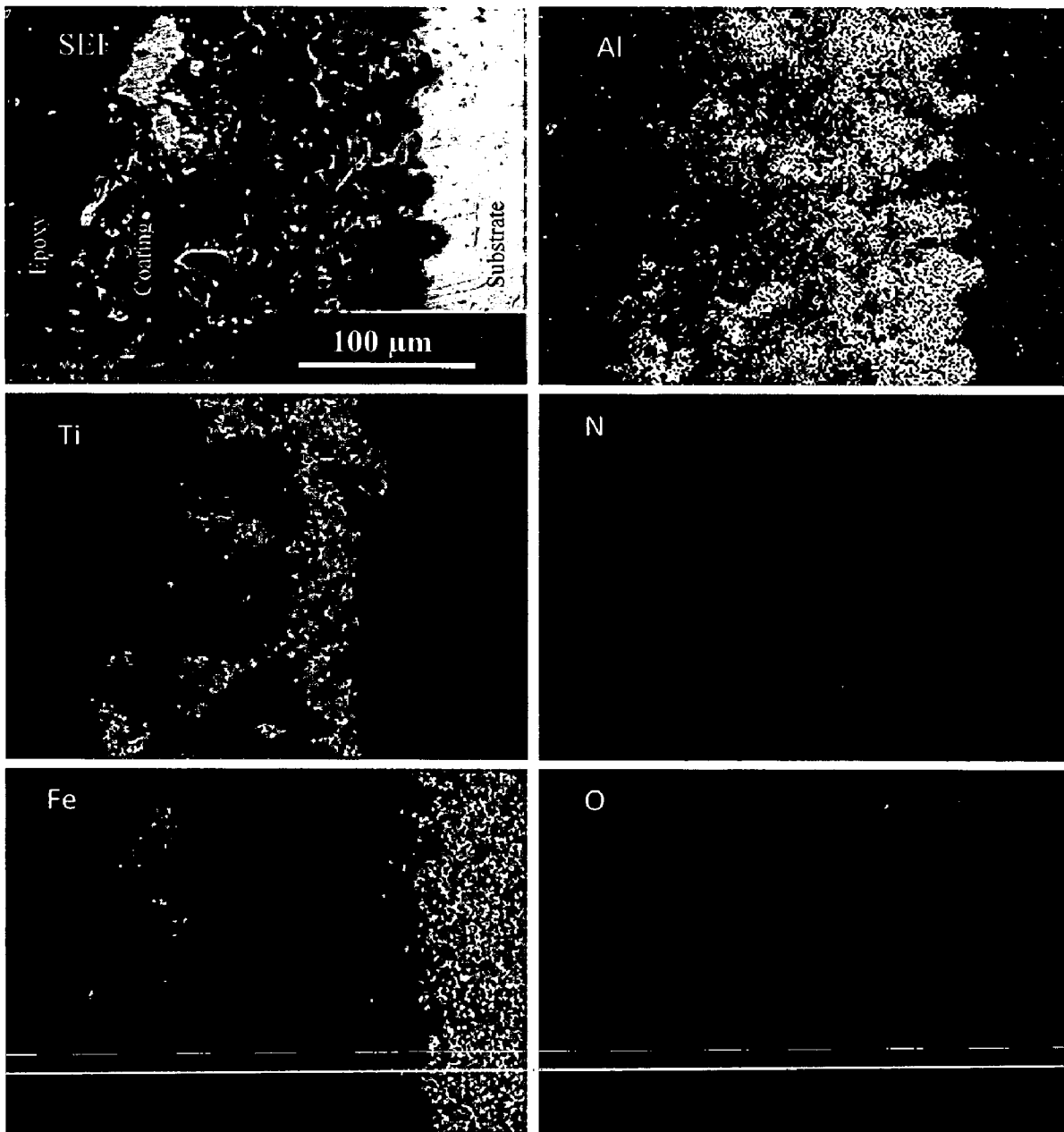


Fig. 4.8 (c) Composition image (SEI) and X-ray mapping of the cross-section of as-coated conventional TiAlN coating on ASTM-SA210 Grade A-1 boiler steel

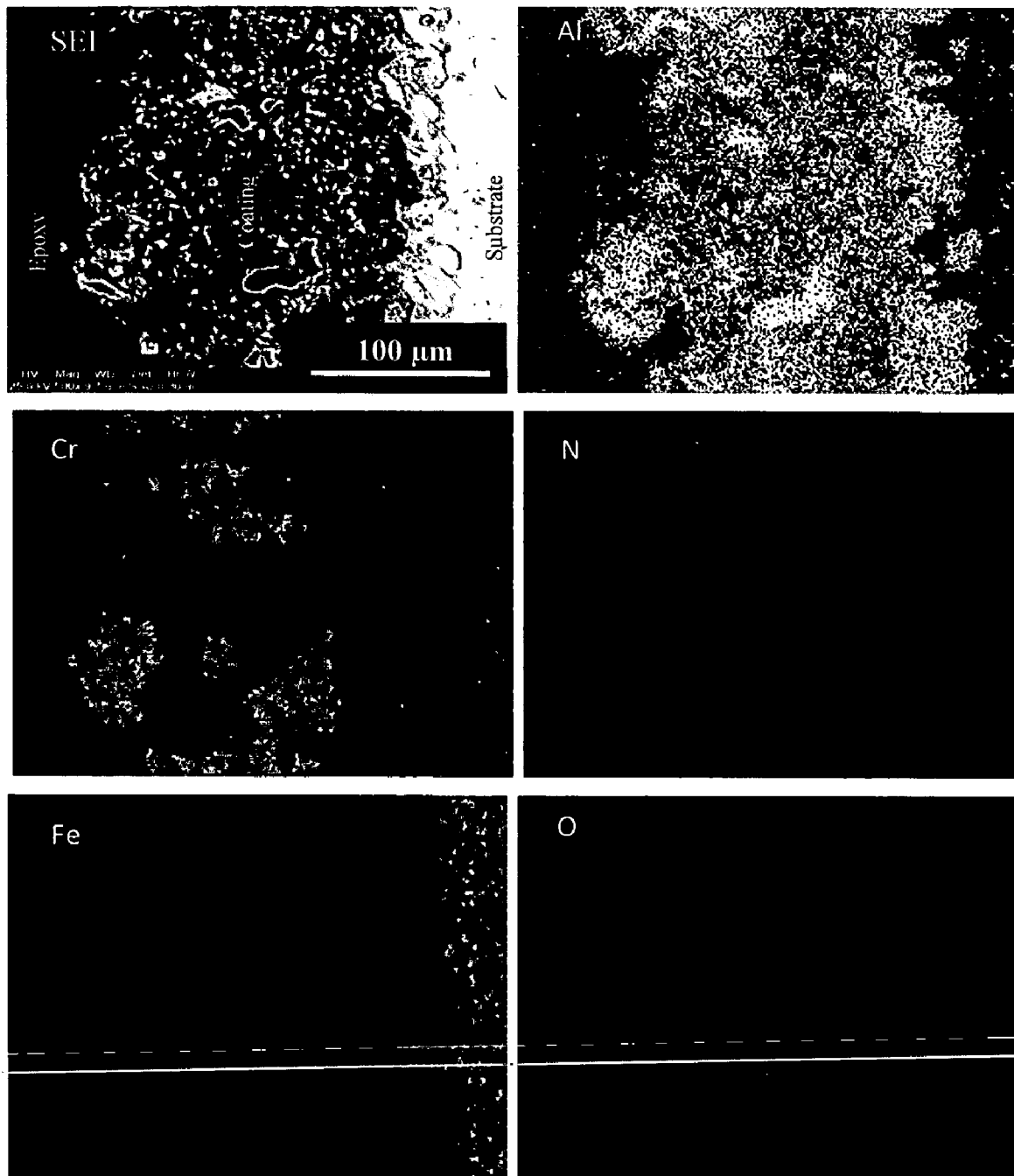


Fig. 4.8 (d) Composition image (SEI) and X-ray mapping of the cross-section of as-coated conventional AlCrN coating on ASTM-SA210 Grade A-1 boiler steel

The X-ray mapping indicates the presence of Al and Cr along with some concentration of N in the coating; and no diffusion of Fe and other elements from the substrate have been observed. In case of conventional thick TiAlN coated Grade A-1 boiler steel, Fig.4.8.(c), Al and Ti rich coating along with negligible amount of N and O; has been observed. The diffusion of Fe from the substrate has taken place as indicated by X-ray mapping analysis. Figure.4.8.(d) depicts the BSEI and X-ray mapping in case of conventional AlCrN coated Grade A-1 boiler steel. The coating is rich in Al and Cr with negligible presence of N and O. The X-ray mapping analysis indicates the presence of thin horizontal bands of Al and O in the coating.

4.1.2 Discussion

The nanostructured thin TiAlN and AlCrN coatings on ASTM-SA210 Grade A-1 boiler steel were obtained using a front-loading Balzer's rapid coating system (RCS) machine at Oerlikon Balzers Ltd. Gurgaon (India). In case of conventional thick TiAlN and AlCrN coatings; the plasma spray coatings were obtained at Anod Plasma Ltd. Kanpur (India) using a 40 kW Miller Thermal Plasma Spray apparatus. The compositions of the targets used and the summary of the process parameters are presented in detail in chapter 3. The coating thickness was measured along the cross-section for some of the randomly selected samples and reported in Table 4.1 and 4.2. The coatings thickness was observed to be 6.1 and 4.2 μm in case of nanostructured TiAlN and AlCrN coatings respectively. The self-disintegration of thicker coatings usually restricts the thickness of the coatings (Sidhu et al, 2004). In case of conventional thick coatings; it was possible to obtain a thickness in range of 150-200 μm for Ti-Al and Al-Cr coatings. After coating deposition process; the gas nitriding was done in lab in order to obtain hard metal nitride coatings. The coating thickness was measured along the cross-section for some randomly selected samples and reported in Table 4.2. The coatings thickness was observed as 172 and 166 μm in case of conventional thick TiAlN and AlCrN coatings respectively.

The surface appearance of nanostructured TiAlN coating was violet grey in color and light grey in case of nanostructured AlCrN coating (Fig.4.1). In case of conventional thick

coatings: the surface appearance of conventional TiAlN and AlCrN coatings was grey with some bluish shining (Fig.4.1). The surface of conventional thick coatings was rough. As inferred from optical micrographs (Fig.4.2 a & b) that the nanostructured coatings were dense with uniform microstructure. It is evident from the microstructure that the coatings contain some pores and inclusions. In case of conventional thick coatings (Fig.4.2.c & d); the massive microstructure could be observed with irregularly shaped grains.

The negligible porosity values for as coated nanostructured thin TiAlN and AlCrN coatings were observed; which were less than 0.5 % (Table 4.1). The measured porosity values of plasma sprayed and gas nitrided coatings are reported in Table 4.2. The measured values of porosity (2.00-4.30%) for as sprayed conventional Ti-Al and Al-Cr coatings are almost in close agreement with the findings of Chen et al. (1993), Erickson et al. (1998), Hidalgo et al. (1998 and 1999), Singh (2003) and Sidhu et al. (2004 and 2005A) for thermal plasma sprayed coatings. Further, the porosity values found to be less than 0.6% after gas nitriding, which may be because of elimination of microstructural in-homogeneities by filling of pores and voids by nitrogen during gas nitriding.

The phases identified by XRD analysis (Fig.4.3) for nanostructured thin TiAlN coating are TiN and AlN. The phases analyzed are also in agreement with that reported by Yoo et al. (2008), Falub et al. (2007) and Man et al. (2004). The prominent phases in case of nanostructured AlCrN coating are CrN and AlN which are in agreement with the findings of Reiter et al. (2005) and Endrino et al. (2006). Further, the main phases identified for the conventional thick TiAlN coating are Al₂O₃, TiN, Ti₃Al, AlN and small peaks of TiO₂ and Fe₂O₃. The phases identified in case of conventional thick AlCrN coating are CrN, AlN, and Al₂O₃ with minor peaks of Cr₂O₃. The presence of metal nitride phases indicates that the gas nitriding process has successfully produced the desired coatings. Further, the phases analyzed are also in agreement with that reported by Adachi and Nakata (2007).

The grain size (Table.4.1) of the nanostructured thin coatings was estimated from Scherrer formula (Cullity, 1970) as follows:

$$D = 0.9 \lambda / B \cos\theta \quad (4.1)$$

Where λ , B and θ are the X-ray wavelength (1.54056 Å), Bragg diffraction angle and line width at half maximum, respectively. The calculated grain size for nanostructured thin TiAlN and AlCrN coatings was 16 and 26 nm respectively. The grain size in case of nanostructured coatings was further verified by AFM analysis and reported in Table 4.1. The nanostructured thin TiAlN coating had shown smaller particle size (18 nm) as compared to nanostructured thin AlCrN coating (28 nm). The particle size determined by AFM analysis is in good agreement with the results obtained from Scherrer formula.

The surface roughness was also measured with AFM analysis and reported in Table 4.1. As the axis scale indicates the overall roughness of the nanostructured TiAlN coating (Fig. 4.4.b) is less than that of AlCrN coating (Fig. 4.4.d). The surface roughness in case of nanostructured TiAlN coating was observed 3.75 nm and 6.10 nm in case of nanostructured AlCrN coating (Table.4.1). The coating surface was very rough in case of conventional thick TiAlN and AlCrN coatings due to the presence of unmelted/partially melted particles and the roughness was found to be in the range of 10.35-15.13 μm and 11.84-15.23 μm respectively. The centre line average (CLA) method was used to obtain the R_a values.

Hardness is the most frequently quoted mechanical property of the coatings (Tucker, 1994). The observed microhardness values (Fig.4.5) for the conventional coatings are within the range of microhardness values reported for plasma coatings by Adachi and Nakata (2007), Vuoristo et al. (1994), Chen and Hutchings (1998) and Westergard et al.(1998). Microhardness plots indicate some increase in the microhardness of substrate steel at the substrate coating interface. The hardening of the substrates as observed in the current study might have occurred due to the high speed impact of the coating particles during plasma spray deposition similar to the findings of Singh (2003), Hidalgo et al. (1997, 1998, 1999 and 2000) and Sidhu et al. (2004 and 2005B). The observed non-uniformity in the hardness values along the thickness of the coatings may be due to the microstructural changes along the cross section of the coatings (Staia et al., 2001). Moreover, the microhardness and other properties of the thermal spray coatings are anisotropic because of typical splat structure and directional solidification (Tucker, 1994).

The bond strength of the conventional thick TiAlN and AlCrN coatings was measured on three specimens as per ASTM standard C633-01. The coatings failed at the substrate-coating interface while remaining attached to the adhesive (Fig.4.6). Average bond strength of 68.74 MPa and 54.69 MPa was observed in case of conventional TiAlN and AlCrN coatings respectively. The bond strength in case of conventional TiAlN coatings (68.74 MPa) is almost in good agreement with the results reported by Adachi and Nakata (2007).

SEM micrographs along with EDAX point analysis reveal the surface morphology of the nanostructured and conventional TiAlN and AlCrN coated ASTM-SA210 Grade A-1 boiler steel; are shown in Fig.4.7. Surface EDAX analysis supported the results obtained by XRD (Fig.4.3) and X-ray mapping analysis (Fig.4.8) in all the coatings. The presence of Ti, Al and N with negligible amount of Fe (in nanostructured TiAlN coating), Al, Cr and N along with small amount of Fe and oxygen (in nanostructured TiAlN coating), the higher concentration of Ti and Al in the coating along with some amount of N and oxygen (in conventional TiAlN coating) and Al and Cr along with N and oxygen (in conventional AlCrN coating); is revealed by surface EDAX analysis (Fig.4.7). Also, the XRD analysis indicates the presence of the oxide phases in the coatings i.e. Al_2O_3 , TiO_2 and Fe_2O_3 in case of conventional TiAlN coating and the presence of Al_2O_3 and Cr_2O_3 in case of conventional AlCrN coatings. The oxides may form due to the in-flight oxidation during spraying process and/or preexisting in the feed material (Bluni and Mardar, 1996). The latter reason for the oxides formation in the structure of coatings under study looks to be more relevant as the chances of in-flight oxidation are meager in case of the shrouded plasma spraying. Deshpande et al. (2006) proposed that, during in-flight oxidation, a layer of oxide is formed on the molten particle due to chemical reactions between the surface of the liquid phase and oxygen or due to diffusion of oxygen into the liquid. The turbulent mixing of the liquid part of the powder particle during its flight destroys the surface layer of oxides and causes the oxides to be distributed more uniformly through the bulk volume of the particle. However, when temperature of the particle starts dropping during later part of the flight, these oxides tend to solidify and a thin oxide shell would form around the droplet. The oxidation time during thermal spray coating is short typically less than 0.01 s, and can occur in either the solid or molten state. The oxidation of

coatings is not always harmful, it is equally important to control and understand the different aspects of oxidation of coatings; therefore, it is important to find an optimum level for oxidation of coatings (Herman, 1988; Korpiola and Vuoristo, 1996; Nerz et al., 1992). The diffusion of Fe from the substrate to the coating (in conventional coatings) was identified by XRD and X-ray-mapping analysis. This type of diffusion of the base metal component into the coating has also been observed by Wang et al. (2001).

4.1.3 Conclusions

The nanostructured thin TiAlN and AlCrN coatings (by physical vapour deposition process) and conventional thick TiAlN and AlCrN coatings (by plasma spraying followed by gas nitriding process) were successfully deposited on ASTM-SA210 Grade A-1 boiler steel. The coatings were characterized for microstructural features and hardness in present work. The following observations were made based on the present study:

1. The nanostructured thin TiAlN and AlCrN coatings exhibited negligible porosity values; which were less than 0.5 %. The conventional TiAlN and AlCrN coatings showed; higher porosity values (2.00-4.30%) for as sprayed conventional Ti-Al and Al-Cr coatings which has been found to be less than 0.6 % after gas nitriding.
2. The phases identified by XRD analysis for nanostructured thin TiAlN coating are TiN and AlN. Further, in case of nanostructured AlCrN coating, the prominent phases are CrN and AlN. The main phases identified (by XRD analysis) for the conventional thick TiAlN coating were Al₂O₃, TiN, Ti₃Al, AlN along with small peaks of TiO₂ and Fe₂O₃. The phases identified in case of conventional thick AlCrN coating were CrN, AlN, and Al₂O₃ with minor peaks of Cr₂O₃.
3. The grain size (calculated by Scherrer formula from XRD plot) for nanostructured thin TiAlN and AlCrN coatings was 16 and 26 nm respectively. The particle size determined by AFM analysis is in good agreement with the results obtained from Scherrer formula.

4. The surface roughness in case of nanostructured TiAlN coating was observed 3.75 nm and 6.10 nm in case of nanostructured AlCrN coating. The coating surface was very rough in case of conventional thick TiAlN and AlCrN coatings.
5. The average bond strength of 68.74 MPa and 54.69 MPa Psi was observed in case of conventional TiAlN and AlCrN coatings respectively.

4.2 OXIDATION STUDIES IN AIR

The present work has been focused to compare the cyclic oxidation behavior of conventional thick (by plasma spraying and gas nitrided) and nanostructured thin (by physical vapor deposition process) TiAlN and AlCrN coatings on ASTM-SA210 Grade A-1 boiler steel, in air environment, at 900°C for 50 cycles. The kinetics of the cyclic oxidation of coated as well as uncoated specimens was determined using the weight change studies. After the oxidation studies, the exposed specimens were analyzed by XRD, SEM-EDAX analysis and elemental X-ray mapping. The detailed experimental procedure is explained in chapter 3.

4.2.1 Results

4.2.1.1 Visual observations

The macrographs for uncoated and coated ASTM-SA210 Grade A-1 boiler steel subjected to cyclic oxidation in air at 900°C for 50 cycles are shown in Fig.4.9. For the uncoated Grade A-1 boiler steel, a grey colored scale appeared on the surface right from the 2nd cycle. This bare steel showed spalling of scale and scale starts falling in the boat after 3rd cycle. Some metallic sound was also observed during cooling for some cycles. At the end of cyclic study; a blackish grey colored scale with cracks was observed (Fig.4.9.a).

In case of nanostructured thin TiAlN coated Grade A-1 boiler steel, color of the oxide scale at the end of the study was observed to be grey with some whitish grey areas on the surface, as shown in Fig.4.9 (b). Grey color spots were observed after 13th cycle. Subsequently, cracks were developed in the scale and spalling was observed after 30th cycle. Whereas nanostructured thin AlCrN coated Grade A-1 boiler steel has shown the formation of smooth scale with the presence of very fine cracks, when subjected to cyclic oxidation in air at 900°C for 50 cycles, as shown in Fig.4.9 (c). Golden and ink blue reflections were observed in the scale, after the completion of 2nd cycle, which turned to dark grey subsequently. The oxide scale at the end of cyclic study has shown very fine cracks on the surface. Some amount of superficial spalling was noticed at the end of 3rd cycle in case of

conventional thick TiAlN coated Grade A-1 boiler steel, which may be due to the loosely bond particles on the surface of the coating. A visual observation of (Fig.4.9.d), showed the formation of very light grey color in the middle of the sample along with dark grey sides after 6th cycle.

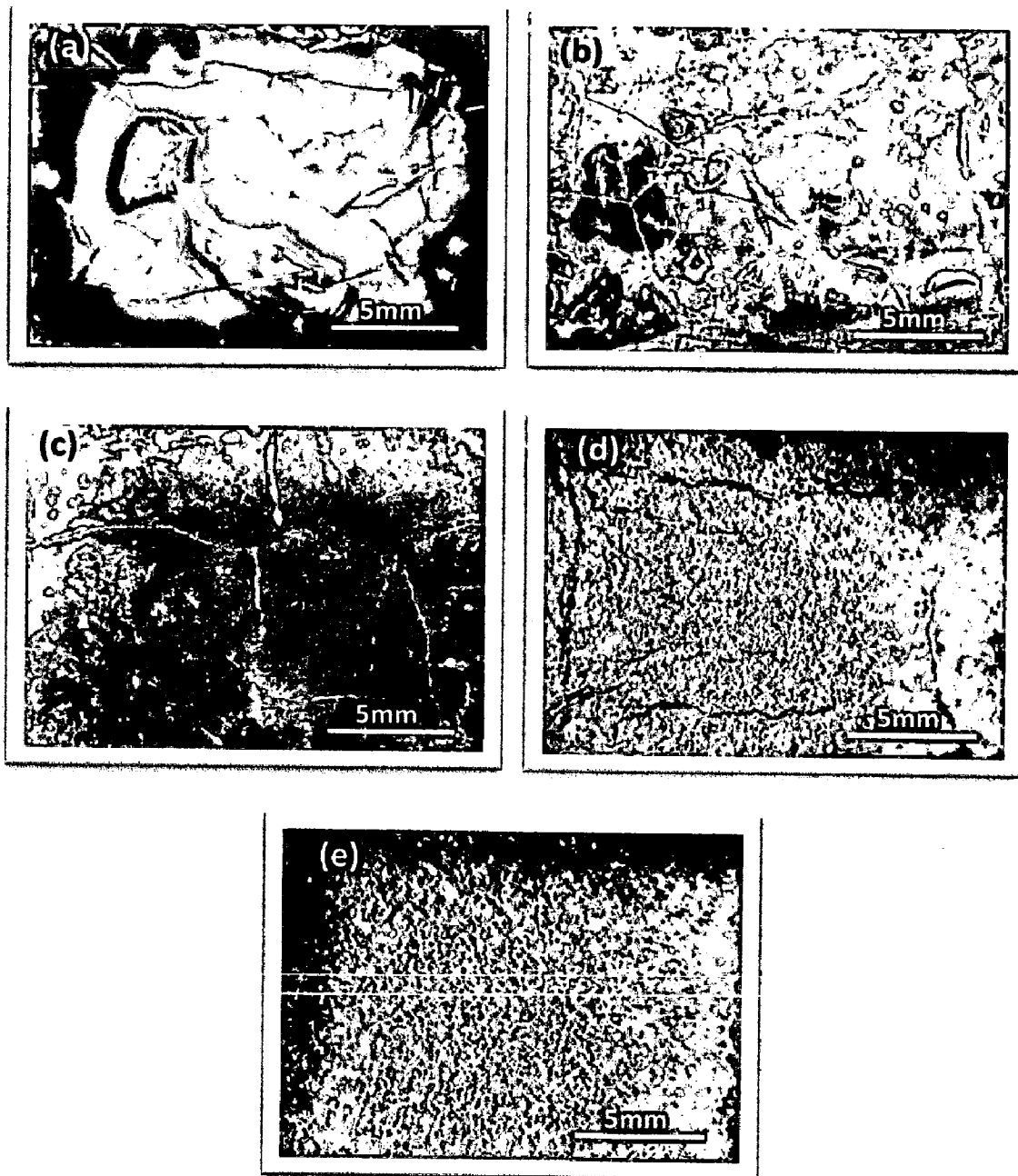


Fig. 4.9 Surface macrographs of uncoated and coated ASTM-SA210 Grade A-1 boiler steel after exposure to cyclic oxidation in air at 900°C for 50 cycles : (a) Uncoated Grade A-1 boiler steel, (b) Nanostructured TiAlN coating, (c) Nanostructured AlCrN coating, (d) Conventional TiAlN coating, (e) Conventional AlCrN coating

After 46th cycle, four brownish grey lines have been observed on the surface as shown in Fig.4.9 (d) and rest of the surface appearance was observed as whitish grey. The scale was smooth and adherent to the substrate. In case of conventional thick AlCrN coated Grade A-1 boiler steel, color of the oxide scale was bluish grey after 4th cycle, which turned to whitish grey in the middle along with brownish grey corners at the end of the cyclic study (Fig.4.9.e). The scale was found to be adherent and smooth.

4.2.1.2 Weight change measurements

Weight gain per unit area (mg/cm^2) versus time (number of cycles plot) for coated and bare ASTM-SA210 Grade A-1 boiler steel subjected to cyclic oxidation in air at 900°C for 50 cycles, is presented in Fig.4.10. It can be inferred from the plots that the uncoated and nanostructured thin coated Grade A-1 boiler steels have shown high rate of oxidation as compared to conventional thick coatings. The plots for all samples shows higher weight gain at initial cycles followed by gradual weight gain.

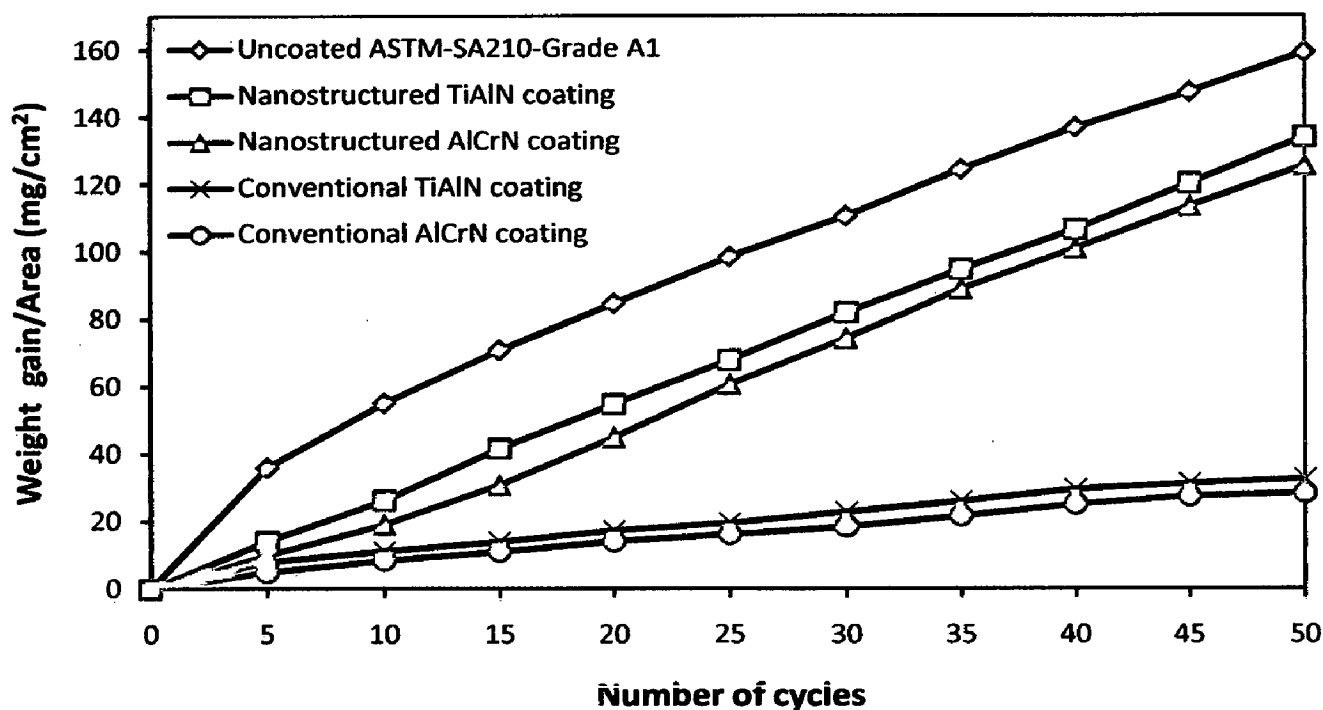


Fig. 4.10 Weight gain/area vs time (number of cycles) for the uncoated and coated ASTM SA210 Grade A-1 boiler steel subjected to cyclic oxidation in air at 900°C for 50 cycles

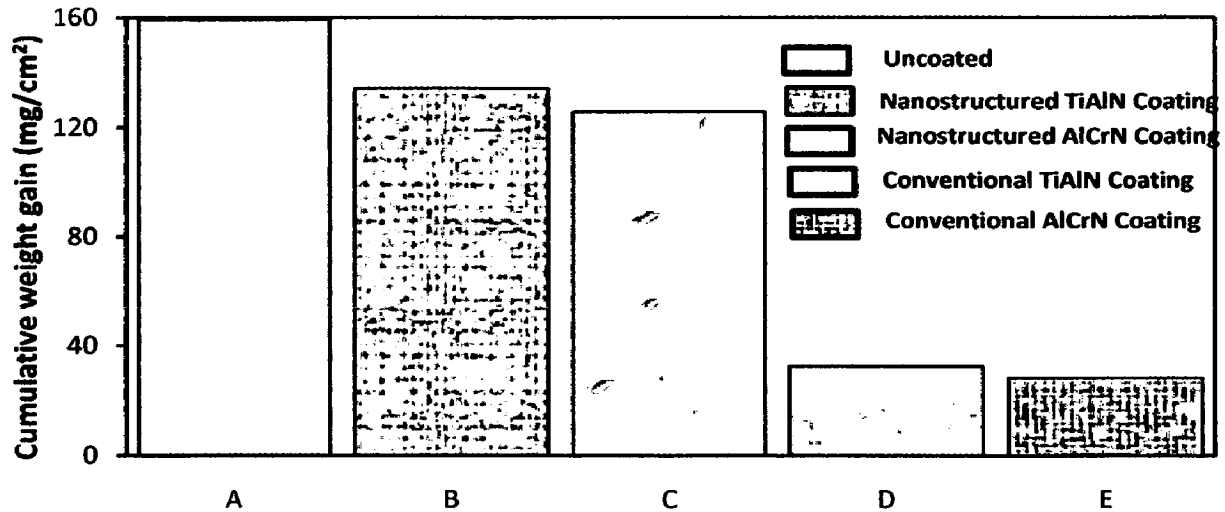


Fig. 4.11 Column chart showing cumulative weight gain per unit area for the uncoated and coated ASTM-SA210 Grade A-1 boiler steel subjected to cyclic oxidation in air at 900°C for 50 cycles; (A) Uncoated, (B) Nanostructured TiAlN coating, (C) Nanostructured AlCrN coating, (D) Conventional TiAlN coating, (E) Conventional AlCrN coating

The conventional thick coatings have shown full protection to the substrate steel as the weight gain becomes almost constant after 5th cycle, as shown in Fig.4.10. The thin nanostructured coatings have provided the protection to the substrate to some extent, as the weight gain rate is less than that of uncoated Grade A-1 boiler steel, which has shown highest rate of oxidation. The cumulative weight gain per unit area for the coated and uncoated Grade A-1 boiler steel subjected to cyclic oxidation in air at 900°C for 50 cycles is shown in Fig. 4.11. Further, the overall weight gain is highest in case of uncoated Grade A-1 boiler steel and is lowest in case of conventional thick AlCrN coated steel (17% of weight gain in case of uncoated Grade A-1 boiler steel). In Fig.4.12, the $(\text{weight gain/area})^2$ versus number of cycles plot are shown for all the cases to ascertain conformance with the parabolic rate law. The coated and uncoated Grade A-1 boiler steel followed the parabolic rate law as evident from the Fig.4.12. The parabolic rate constant K_p was calculated by a linear least-square algorithm to a function in the form of $(W/A)^2 = K_p t$, where W/A is the weight gain per unit surface area (mg/cm^2) and 't' indicates the number of cycles representing the time of exposure. The parabolic rate constants for the bare and coated

Grade A-1 boiler steel calculated on the basis of 50 cycle's exposure data are shown in Table.4.3. It is inferred that the 'K_p' values for the coated Grade A-1 boiler steel were less than the bare boiler steel.

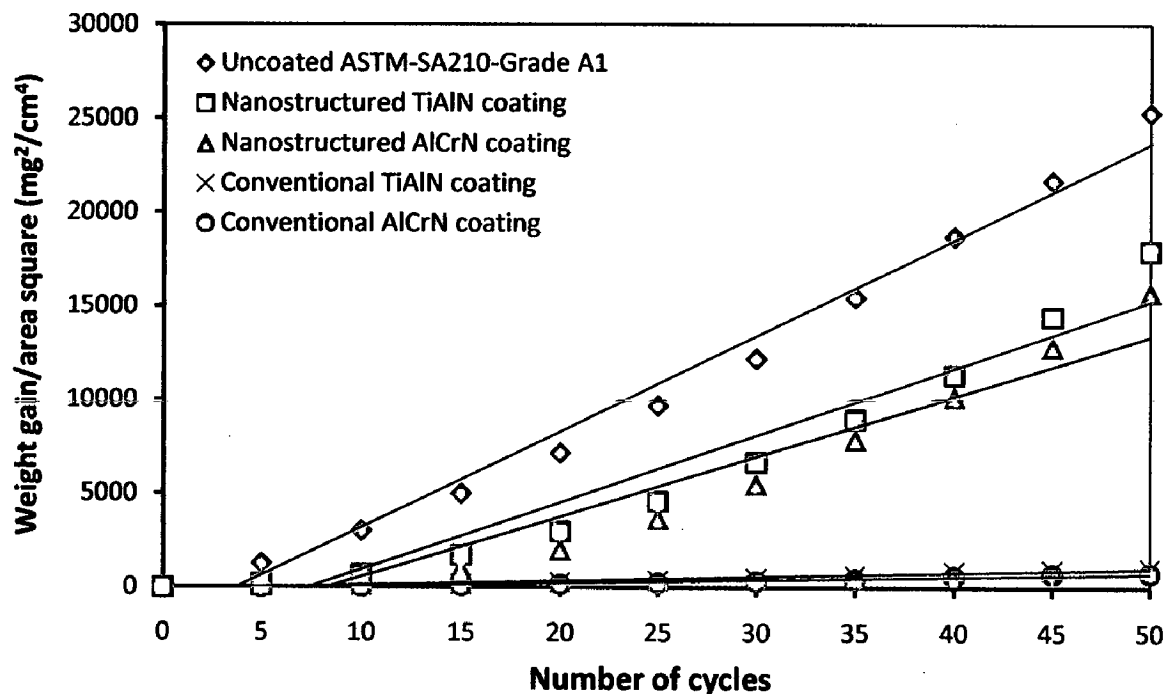


Fig. 4.12 Weight gain/area square vs time (number of cycles) for the uncoated and coated ASTM-SA210 Grade A-1 boiler steel subjected to cyclic oxidation in air at 900°C for 50 cycles

4.2.1.3 Surface scale analysis

4.2.1.3.1 X-ray diffraction analysis (XRD)

XRD diffractograms for coated and uncoated ASTM-SA210 Grade A-1 boiler steel subjected to cyclic oxidation in air at 900 °C for 50 cycles are depicted in Fig.4.13 on reduced scale. As indicated by the diffractograms in Fig.4.13 (a), Fe₂O₃ is the main phases present in the oxide scale of uncoated and nanostructured thin TiAlN and AlCrN coated Grade A-1 boiler steel. In nanostructured TiAlN coating, minor phase such as Al₂O₃ has been observed, whereas in case of nanostructured AlCrN coating, Cr₂O₃ along with Al₂O₃ have been observed (Fig.4.13.a). Further, the main phases identified for the conventional thick

TiAlN coating are Al₂O₃, Ti, Ti₃Al, Al and TiO₂ (Fig.4.13.b). The surface oxides on conventional thick AlCrN coating were, Cr₂O₃, Al₂O₃ and Fe₂O₃ (Fig.4.13.b).

Table 4.3 Parabolic rate constant ' K_p ' values of uncoated and coated ASTM-SA210 Grade A-1 boiler steel subjected to cyclic oxidation in air at 900°C for 50 cycles

Substrate / Coating	$K_p \times 10^{-08} \text{ gm}^2 \text{ cm}^{-4} \text{ s}^{-1}$
Uncoated Grade A-1 boiler steel	14.211
Nanostructured TiAlN coating	09.963
Nanostructured AlCrN coating	08.933
Conventional TiAlN coating	00.626
Conventional AlCrN coating	00.474

4.2.1.3.2 Surface scale morphology

SEM micrographs along with EDAX point analysis reveals the surface morphology of the coated and uncoated Grade A-1 boiler steel subjected to cyclic oxidation in air at 900 °C for 50 cycles are shown in Fig.4.14. Micrograph (shown in Fig.4.14 .a) for uncoated Grade A-1 boiler steel indicates a scale containing distorted grains. EDAX analysis at point 1 and point 2 in Fig.4.14 indicates the formation of mainly iron oxide. The SEM micrograph of oxidized nanostructured thin TiAlN coatings is shown in Fig.4.14 (b). The developed surface scale appears like vertical needles (Point 4) grown on matrix (Point 3). EDAX analysis of the scale revealed the presence of Fe (52.86 %) and O (38.88 %) as the main elements in needles and Fe (93.04 %) and minor amount of oxygen in the matrix along with very small amount of Al and Ti. In case of nanostructured thin AlCrN coated Grade A-1 boiler steel; the SEM micrograph indicates the needles like pattern. EDAX point analysis shows the top scale rich in Fe and O. The small amount of Mn, Al, N, Cr, and C are also present.

Fig

The surface scale developed on conventional thick TiAlN coated Grade A-1 steel is massive and without any cracks, with white contrast (Point 7) and grey contrast regions (Point 8). EDAX analysis indicates the presence of Ti, Al and O as the main phases along with very small amount of Fe. The white contrast region as indicated by Point 7 in Fig.4.14 depicts the presence of lesser Al (37.17 %) and more Ti (12.02 %) as compared to the dark contrast region which indicates Al (42.31 %) along with Ti (01.61 %). A homogeneous and continuous surface scale is developed on conventional thick AlCrN coated Grade A1 boiler steel, which has Al, Cr and O as main elements (Fig.4.14.e). The white contrast region (Point 9) indicates more Cr (17.39) and less Al (50.99 %) and O (30.02 %) as compared to the dark region (Point 10).

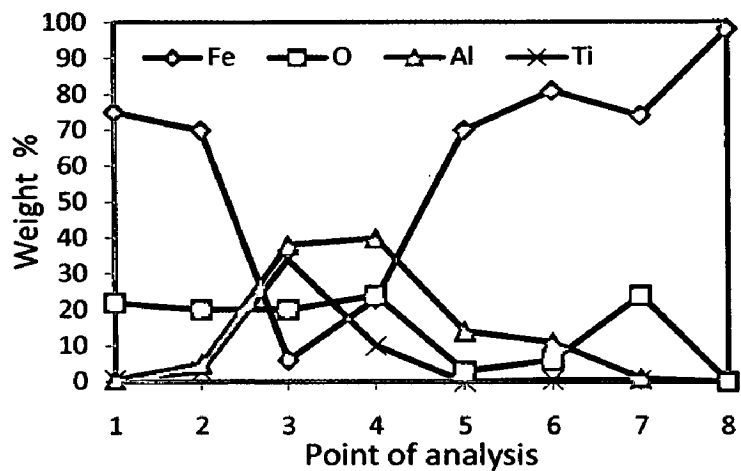
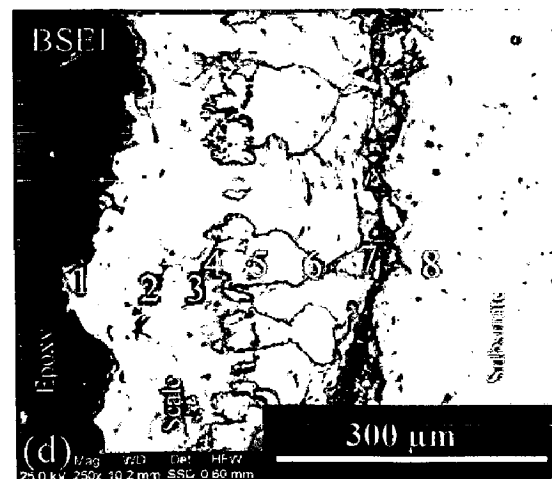
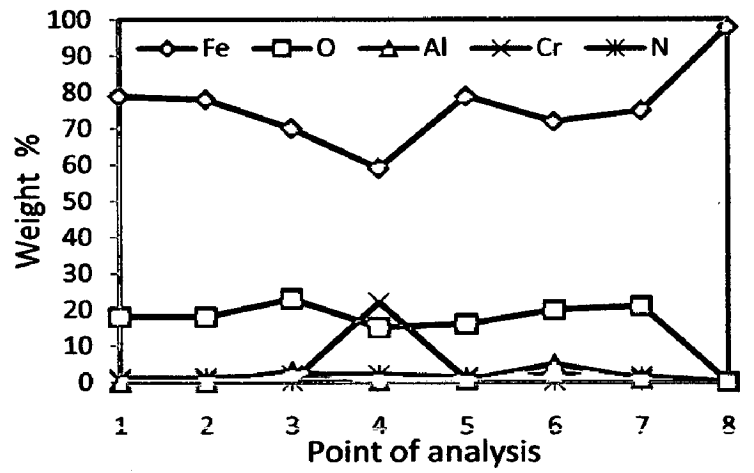
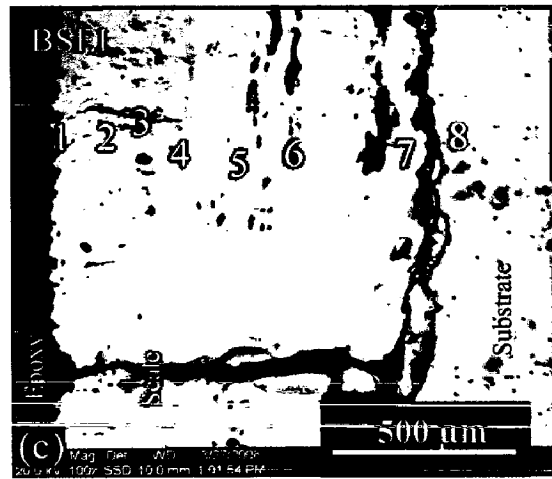
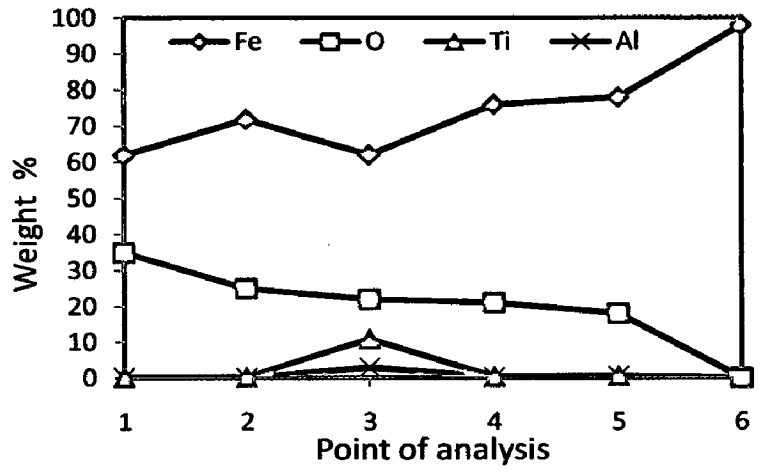
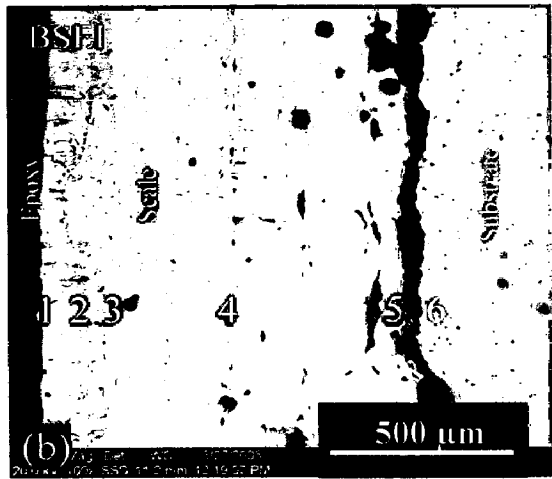
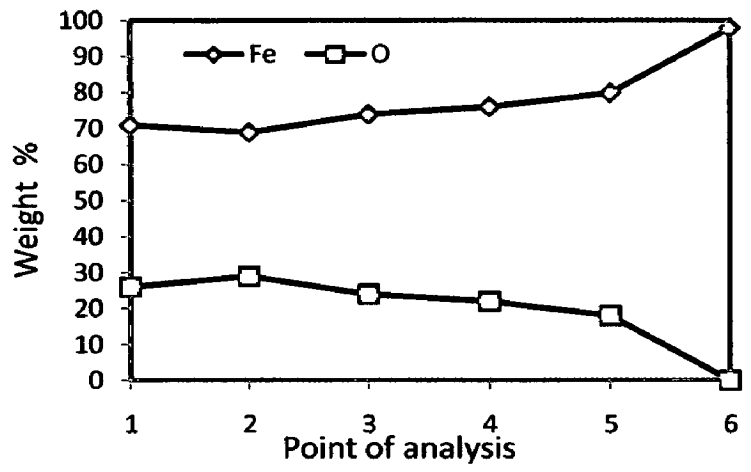
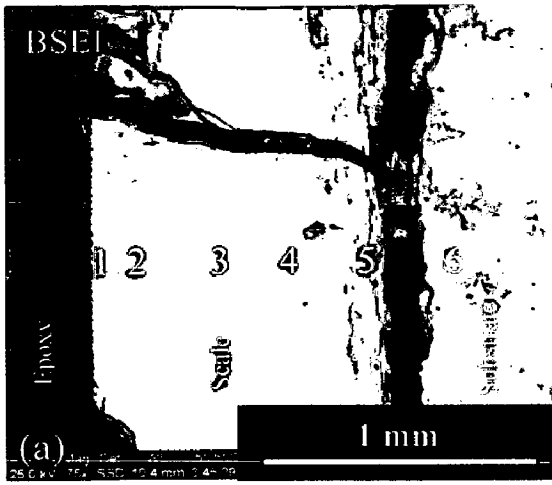
4.2.1.4 Cross-sectional analysis

4.2.1.4.1 Scale thickness

The oxidized samples were cut across the cross section using Buehler Isomet 1000 precision saw and mounted in transoptic mounting resin and subsequently mirror polished to obtain scanning electron back scattered micrographs and X-ray mapping of different elements for coated and uncoated Grade A-1 boiler steel. The scale thickness values were measured from SEM back scattered micrographs as shown in Fig.4.15. Very thick scale is observed in case of uncoated Grade A-1 boiler steel, which is around 5.23 times thicker than the scale measured for conventional thick AlCrN coated Grade A-1 boiler steel. The measured average scale thickness values for uncoated Grade A-1, nanostructured thin TiAlN, nanostructured thin AlCrN, conventional thick TiAlN and conventional thick AlCrN coatings are 1100, 978, 934, 272 and 210 μm respectively.

4.2.1.4.2 Cross-sectional scale morphology

Back Scattered Electron Image (BSEI) micrograph and elemental variation across the cross-section for coated and uncoated Grade A-1 boiler steel subjected to cyclic oxidation in air at 900°C for 50 cycles are shown in Fig.4.15.



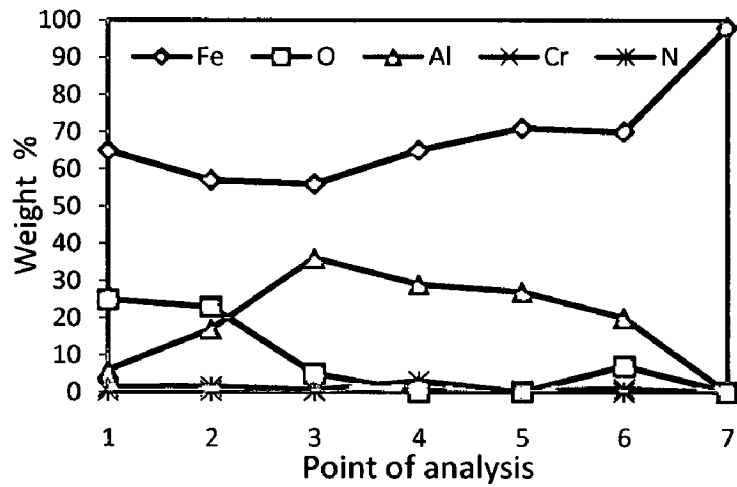
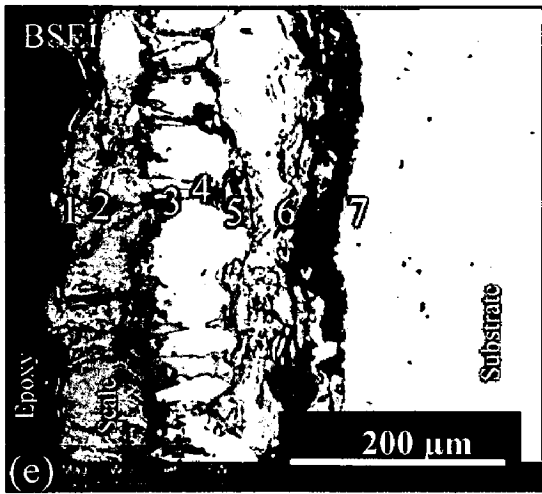


Fig. 4.15 Oxide scale morphology and variation of elemental composition across the cross-section of the uncoated and coated ASTM-SA210 Grade A1 boiler steel after exposure to cyclic oxidation in air at 900°C for 50 cycles: (a) Uncoated Grade A1 boiler steel (75 X), (b) Nanostructured TiAlN coating (100 X), (c) Nanostructured AlCrN coating (100 X), (d) Conventional TiAlN coating (250 X), (e) Conventional AlCrN coating (300 X)

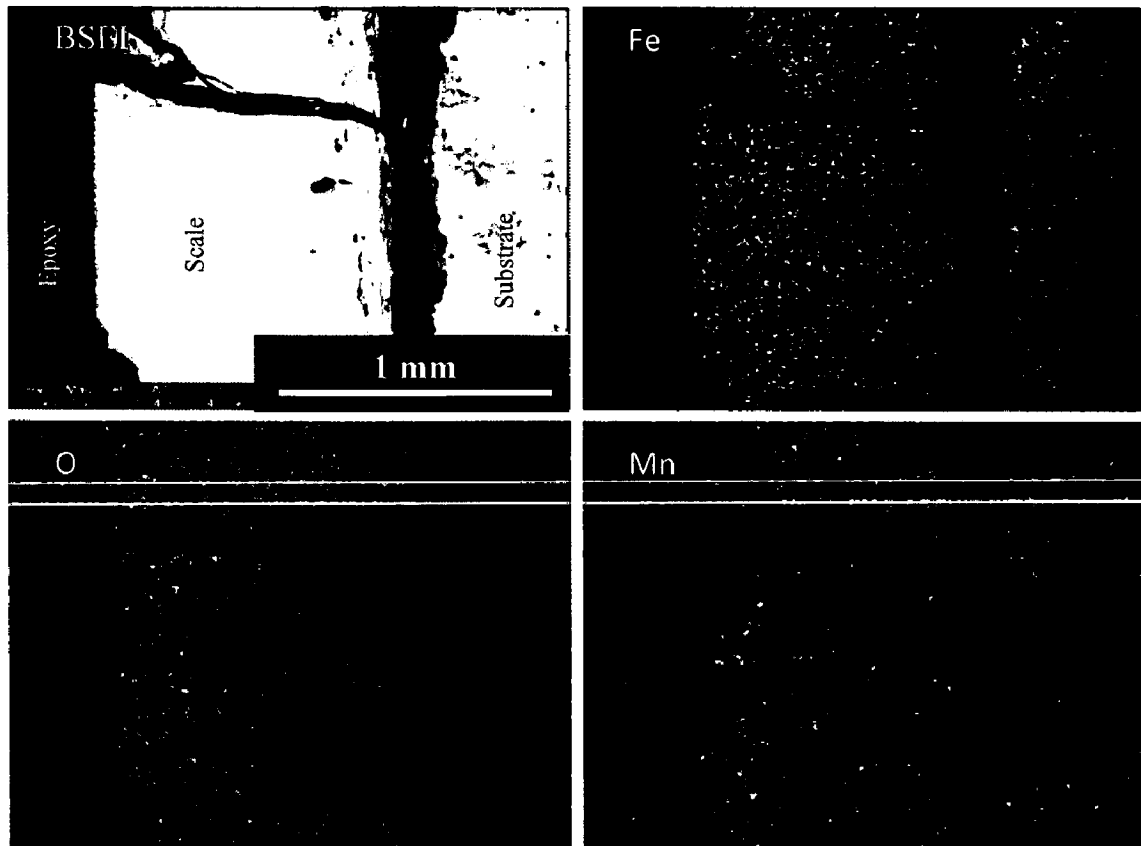


Fig. 4.16 (a) Composition image (BSEI) and X-ray mapping of the cross-section of uncoated ASTM-SA210 Grade A-1 boiler steel subjected to cyclic oxidation in air at 900°C for 50 cycles

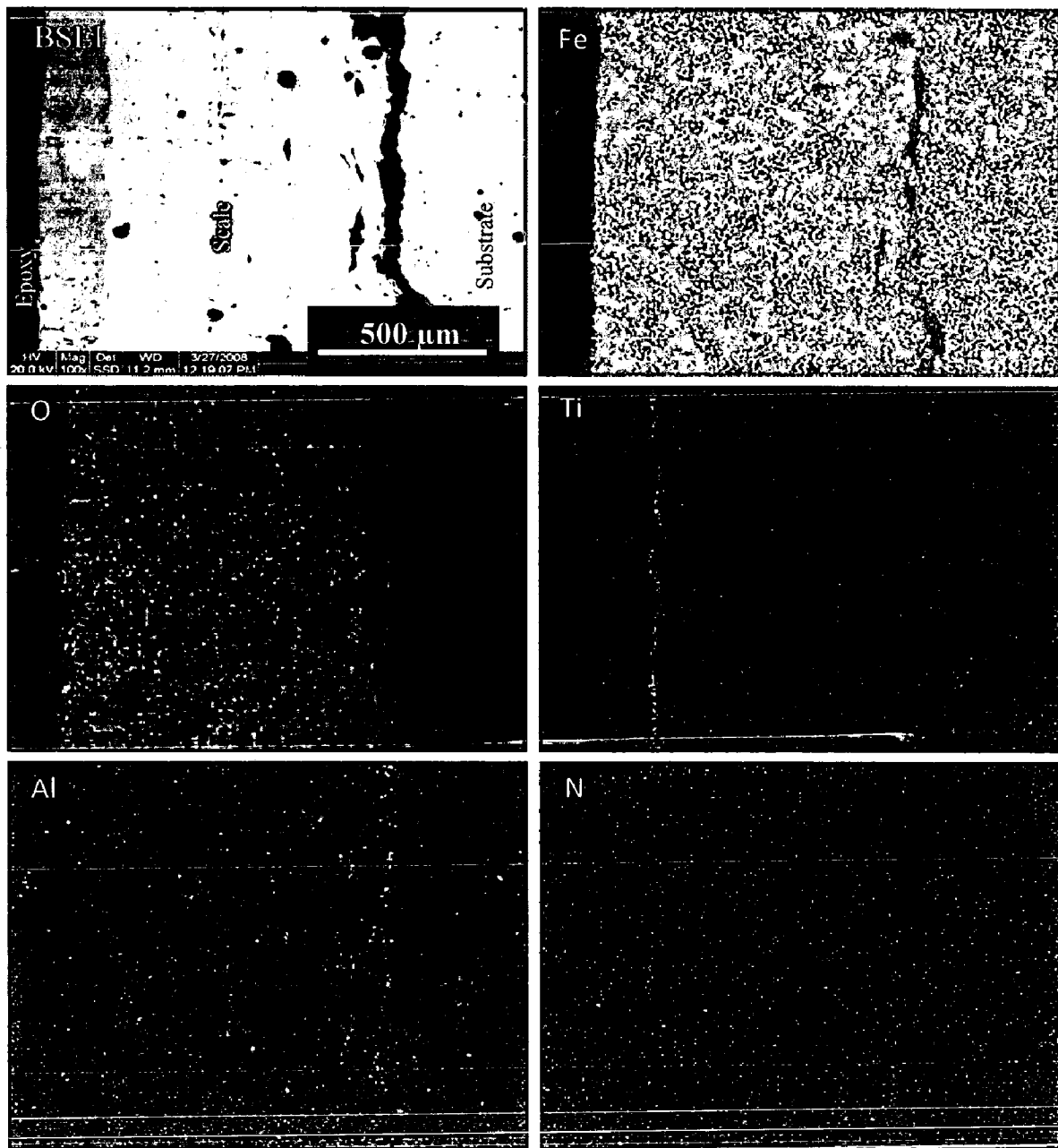


Fig. 4.16 (b) Composition image (BSEI) and X-ray mapping of the cross-section of Nanostructured TiAlN coated ASTM-SA210 Grade A-1 boiler steel subjected to cyclic oxidation in air at 900°C for 50 cycles

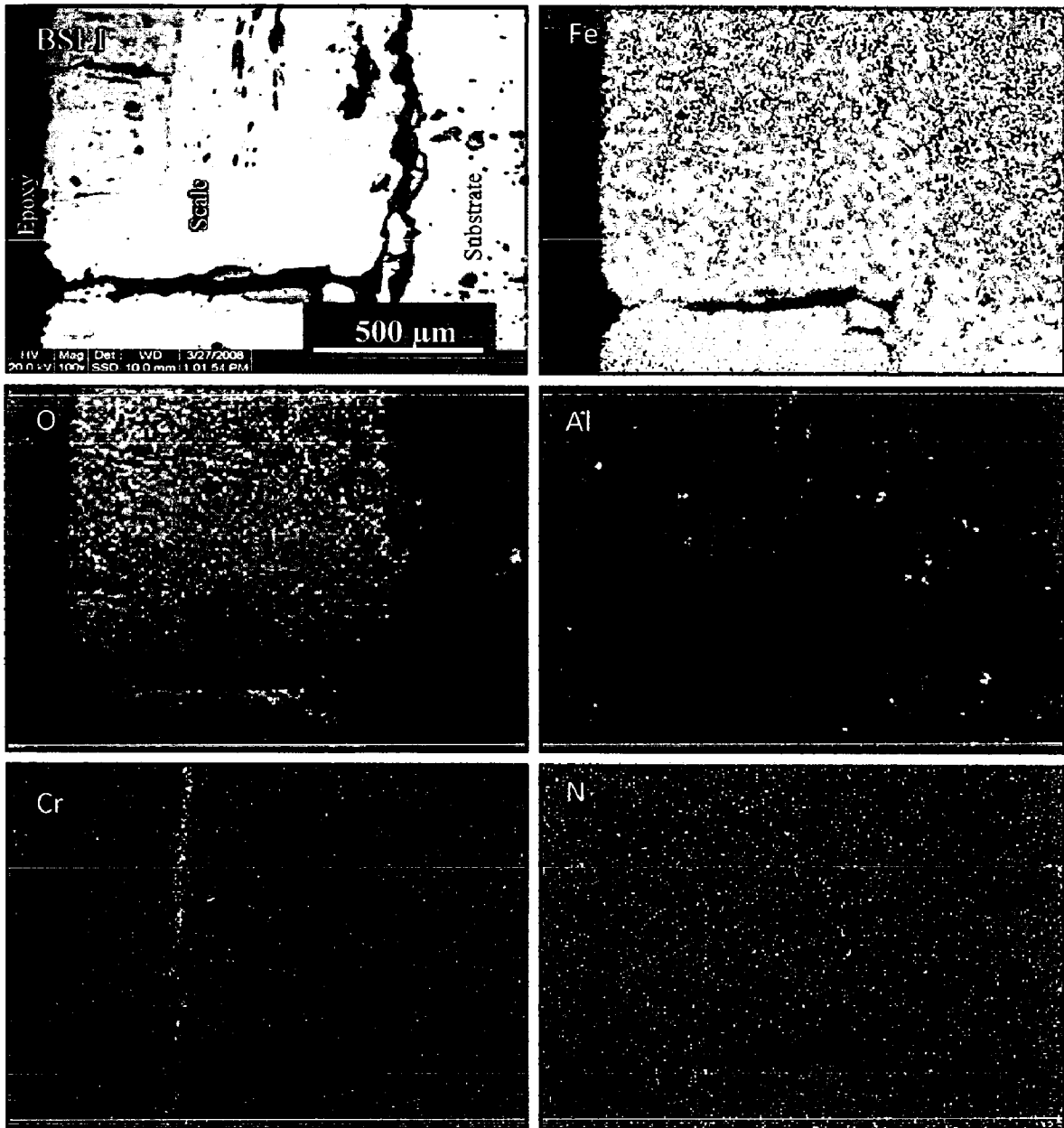


Fig. 4.16 (c) Composition image (BSEI) and X-ray mapping of the cross-section of Nanostructured AlCrN coated ASTM-SA210 Grade A-1 boiler steel subjected to cyclic oxidation in air at 900°C for 50 cycles

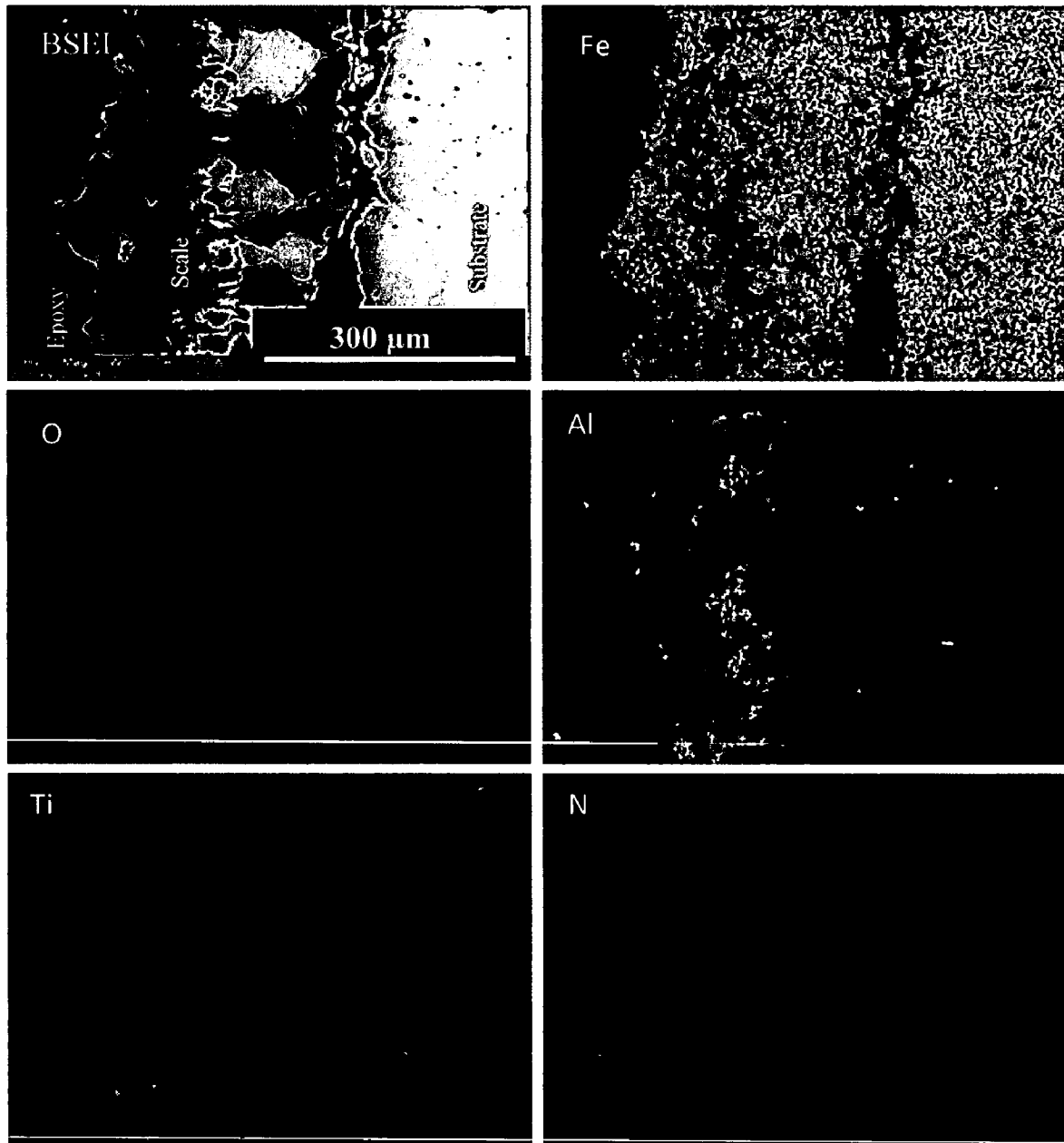


Fig. 4.16 (d) Composition image (BSEI) and X-ray mapping of the cross-section of conventional TiAlN coated ASTM-SA210 Grade A-1 boiler steel subjected to cyclic oxidation in air at 900°C for 50 cycles

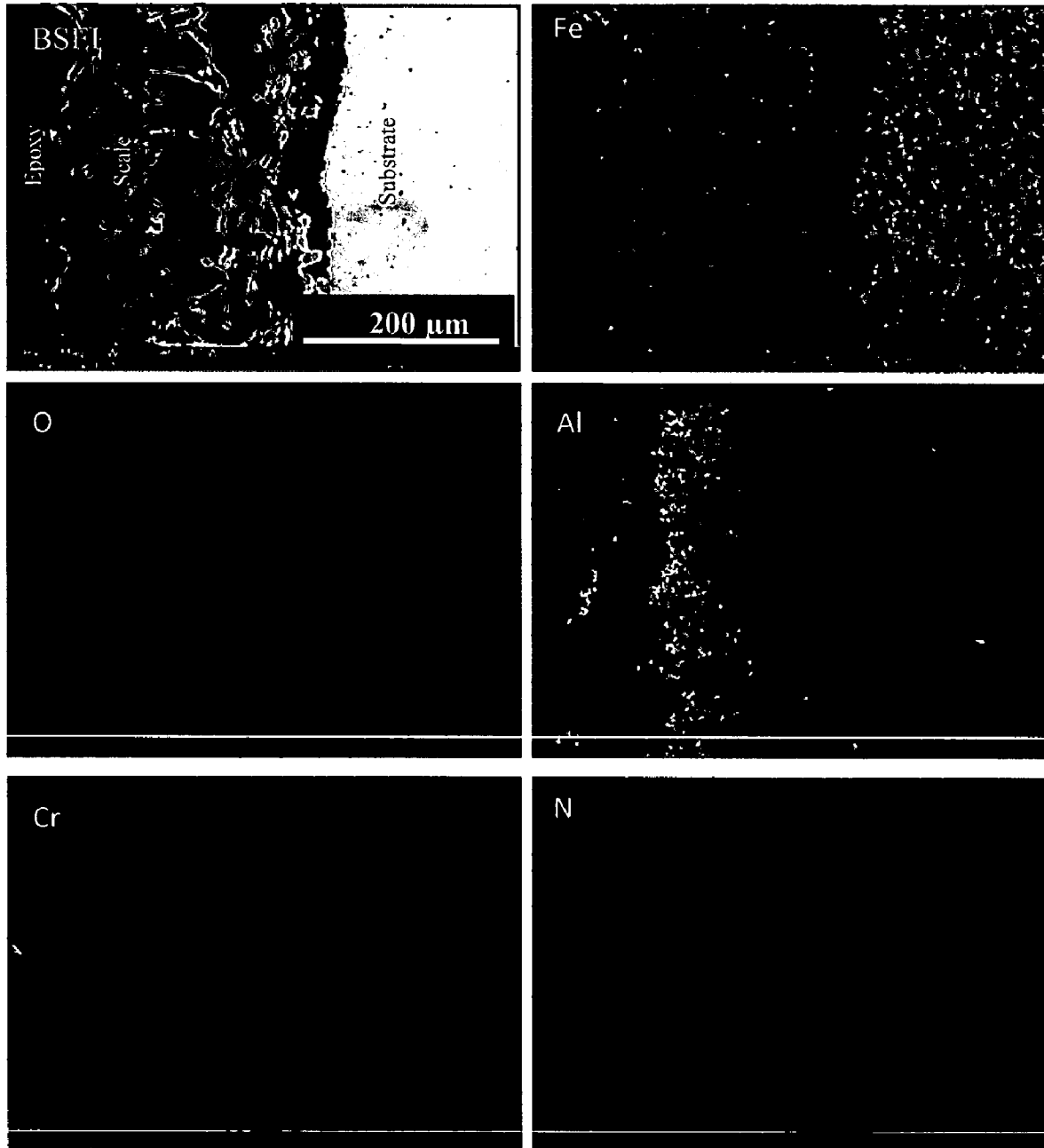


Fig. 4.16 (e) Composition image (BSEI) and X-ray mapping of the cross-section of conventional AlCrN coated ASTM-SA210 Grade A1 boiler steel subjected to cyclic oxidation in air at 900°C for 50 cycles

The SEM micrograph in case of uncoated Grade A-1 boiler steel shows thick scale (Fig.4.15.a). The scale is fragile and indicating cracking. EDAX analysis reveals the presence of iron and oxygen throughout the scale. The existence of significant amount of oxygen and iron indicates the possibility of Fe_2O_3 in the oxide scale. BSEI micrograph and elemental variation depicted in Fig.4.15 (b), for the exposed cross-section of nanostructured thin TiAlN coated Grade A-1 boiler steel shows the thick, continuous and adherent scale. The EDAX analysis reveals the presence of Fe, Ti, Al and oxygen throughout the scale. Point 3 (Fig.4.15.b) in the micrograph depicts the good percentage of Ti and Al along with Fe and oxygen. A thick and adherent oxide scale can be seen in case of nanostructured AlCrN coated Grade A1 boiler steel (Fig.4.15.c).The scale is indicating cracking. The EDAX point analysis indicates the presence of Fe and oxygen throughout the scale along with minor amounts of Cr and Al at point 4 and 6 (Fig.4.15.c).

In case of conventional TiAlN coated Grade A-1 boiler steel, the scale is non uniform, thin and adherent as depicted in Fig.4.15 (d). The EDAX point analysis indicates the presence of Fe, O, Ti and Al throughout the scale with variable amounts. A location at point 3 and 4 in Fig.4.15 (d) shows higher percentage of Al and Ti with negligible percentage of Fe, whereas at point 2, 5, 6 and 7, the percentage amount of Fe is more. The conventional thick AlCrN coated Grade A-1 boiler steel (Fig.4.15.e) indicates continuous, thin and adherent scale. EDAX point analysis shows the presence of Fe and Al throughout the scale. The top scale shows higher percentage of Fe and O along with good amount of Al (point 1 and 2 in Fig.4.15.e). In the subscale region as indicated by points 3, 4, 5 and 6, the scale is rich in Fe and Al with negligible amount of O, Cr and N.

4.2.1.4.3 X-Ray mapping

X-ray mappings for a part of oxide scale of uncoated and coated Grade A-1 boiler steel oxidized in air at 900°C for 50 cycles are shown in Fig. 4.16. In case of uncoated Grade A-1 boiler steel, the scale mainly contains iron and oxygen with some amount of manganese, as indicated by X-ray mapping. The X-ray mapping analysis of the scale formed on nanostructured TiAlN coated Grade A-1 boiler steel is presented in Fig. 4.16 (b). The X-

ray mapping indicates presence of oxygen and iron throughout the scale with a thin irregular band of Ti in the scale. In case of nanostructured thin AlCrN coated Grade A-1 boiler steel; the BSEI and X-ray mapping are shown in Fig. 4.16 (c). The X-ray mapping indicates the presence of iron and oxygen throughout the scale. A thin irregular band of Al and Cr is also present. In case of conventional thick TiAlN coated Grade A-1 boiler steel, Fig.4.16 (d); Al and Ti rich splats are clearly seen along with Fe and oxygen. Ti is present in the upper scale along with Fe and O. The bright regions of Al are overlapping with O and in some regions of Al, oxygen is completely absent. Figure 4.16 (e) depicts the X-ray mapping in case of conventional AlCrN coated Grade A-1 boiler steel. The Al is present in the sub scale region along with Fe, where O is completely missing. The upper scale is rich in Fe and Oxygen.

4.2.2 Summary of Results

Results obtained after exposure of uncoated and coated ASTM-SA210 Grade A-1 boiler steel to cyclic oxidation in air at 900°C for 50 cycles are summarized in Table.4.4.

4.2.3 Discussion

The weight change plots (Fig.4.10) for the uncoated and coated Grade A-1 boiler steel indicated that the oxidation behavior has shown conformance to parabolic rate law. The parabolic kinetic behavior is due to the diffusion controlled mechanism operating at 900°C under cyclic conditions (Mahesh et al., 2008). Small deviation from the parabolic rate law might be due to the cyclic scale growth. The higher weight gain during the first few cycles might be attributed to the rapid formation of oxides at the splat boundaries and within the open pores due to the penetration of the oxidizing species, further the subsequent increase in weight gain is gradual (Singh H et al., 2007). The parabolic rate constant for the uncoated Grade A-1 boiler steel is found to be greater than all the coatings.

It is well known that the performance of thermal sprayed coatings in high temperature corrosive environment depends upon the several factors such as porosity, inclusions, oxides and size and shape of the splat microstructures (Dent et al., 1999).

Table 4.4 Summary of the results obtained for uncoated and coated ASTM-SA210 Grade A-1 boiler steel subjected to cyclic oxidation in air at 900°C for 50 cycles

Coating	Cumulative Weight gain (mg/cm ²)	Parabolic rate constant ($K_p \times 10^{-08}$ gm ² cm ⁻⁴ s ⁻¹)	XRD phases	Remarks
Uncoated Grade-A-1 boiler steel	159.17	14.211	Fe ₂ O ₃	A grey colored scale with spalling tendency appeared on the surface right from the 2 nd cycle. Some metallic sound was also observed during cooling for some cycles. At the end uniform scale with cracks and blackish grey color surface appearance was observed
Nanostructured TiAlN coating	134.15	09.963	Fe ₂ O ₃ and Al ₂ O ₃	Color of the oxide scale at the end of the study was observed to be grey with some whitish grey areas on the surface. Grey color spots were observed after 13 th cycle. Subsequently, cracks were developed in the scale and spalling was observed after 30 th cycle.
Nanostructured AlCrN coating	125.62	08.933	Fe ₂ O ₃ , Al ₂ O ₃ and Cr ₂ O ₃	Golden and ink blue reflections were observed in the scale, after the completion of 2 nd cycle, which turned to dark grey subsequently. The oxide scale at the end of cyclic study was smooth with very fine cracks on the surface.
Conventional TiAlN Coating	32.65	00.626	Al ₂ O ₃ , Ti, Ti ₃ Al, Al and TiO ₂	At the end; four brownish grey lines have been observed on the whitish grey surface. Some amount of superficial spalling was noticed at the end of 3 rd cycle. The scale was smooth and adherent to the substrate.
Conventional AlCrN coating	28.32	00.474	Cr ₂ O ₃ , Al ₂ O ₃ and Fe ₂ O ₃	Color of the oxide scale was bluish grey after 4 th cycle, which turned to whitish grey in the middle along with brownish grey corners at the end of the cyclic study. The scale was found to be adherent and smooth.

In case of conventional thick coatings, after rapid weight gain during initial cycles the coatings subsequently becomes dense and movement of oxidizing species to the inner portion of the coating gets slowed down once the oxides are formed at places of porosity and splat boundaries. This would relatively minimize the weight gain and results in the steady state oxidation behavior with the prolonged exposure time. It is evident from XRD (Fig.4.13) results of the oxidized conventional thick coated Grade A-1 boiler steel that Al_2O_3 as the main phase along TiO_2 (in case of conventional TiAlN coating) and Cr_2O_3 (conventional AlCrN coating), which are further supported by EDAX (Fig.4.14. d & e) and X-ray mapping (Fig.4.16.d & e) analysis (which shows some locations where Al and O co-exists). For conventional thick AlCrN coating: The existence of Fe_2O_3 on the surface indicates the diffusion of Fe from the substrate during oxidation at temperature of 900°C .

The oxidation rate (total weight gain values after 50 cycles) of the coated and uncoated Grade A-1 boiler steel follows the sequence as given below:

Uncoated Gr A1 > Nanostructured TiAlN > Nanostructured AlCrN > Conventional TiAlN > Conventional AlCrN

During cyclic testing, cracks and spalling of oxide scale (Fig.4.15.a & c) might be attributed to the different values of thermal coefficients for the coating, scale and the substrate as reported by Sidhu et al. (2003), Singh et al. (2004), Evans et al. (2001), Wang et al. (2002) and Niranatlumpong et al (2000). Though these cracks the corrosive environment can quickly reach the base metal and cut its way under the coating to result in adhesion loss and spalling, whereas some elements may diffuse outwards through these cracks to form oxides or spinels (Singh H et al., 2004). The presence of Fe and oxygen (Fig.4.16.) in the top of the scale is believed to be due to the diffusion of iron through the pores and cracks that appeared in the coating during the course of oxidation studies (Singh Buta et al., 2003).

The nanostructured coatings has shown resistance to oxidation to some extent as the overall weight gain is less than as compared to the uncoated Grade A-1 boiler steel, but failed to provide full protection to the substrate. This might be due to the difference in thermal expansion co-efficient as explained above. However, the parabolic rate constant value (Table 4.3) for nanostructured coatings is quite less than that of uncoated Grade A-1

boiler steel. In case of nanostructured TiAlN coating, Fe_2O_3 is the main phase present in the scale as indicated by the XRD (Fig.4.13.b), EDAX (Fig. 4.14.b) and X-ray mapping (Fig.4.16.b) analysis. The surface morphology (Fig.4.14.c), XRD (Fig 4.13.c) and X-ray mapping (Fig.4.16.c) analysis in case of nanostructured AlCrN coating, indicates the presence of Fe_2O_3 as the main phase along with a thin band of Cr, which might be the reason for lesser oxidation rate as compared to the uncoated Grade A-1 boiler steel. In the present investigation it has been observed that conventional thick TiAlN and AlCrN coatings can provide a very good oxidation resistance at high temperature although these hard coatings are traditionally specified for wear and erosion applications.

4.2.4 Conclusions

The high temperature oxidation behavior of uncoated and coated ASTM-SA210 Grade A-1 boiler steel have been investigated in air at 900°C for 50 cycles. The following conclusions are made:

1. The plasma sprayed gas nitride conventional thick coatings i.e. TiAlN and AlCrN when subjected to cyclic oxidation at 900°C for 50 cycles developed a protective scale mainly consisting on Al_2O_3 along with some amount of TiO_2 (in case of conventional TiAlN coating) and Cr_2O_3 (in case of conventional AlCrN coating) and the oxide scale formed is adherent to the substrate.
2. The nanostructured TiAlN and AlCrN coatings has shown resistance to oxidation to some extent as the overall weight gain is less as compared to the uncoated Grade A-1 boiler steel, but failed to provide full protection to the substrate.
3. The oxidation rate (total weight gain values after 50 cycles) of the coated and uncoated Grade A1 boiler steel follows the sequence as given below:
Uncoated Grade A-1 > Nanostructured TiAlN > Nanostructured AlCrN > Conventional TiAlN > Conventional AlCrN
4. In case of uncoated Grade A-1 boiler steel, the weight gain is highest. The conventional thick TiAlN and AlCrN coatings can provide a very good corrosion resistance at high temperature applications.

4.3 HOT CORROSION STUDIES IN MOLTEN SALT ENVIRONMENT

There is no reported study on cyclic high temperature corrosion behavior of nanostructured thin and conventional thick TiAlN and AlCrN hard coatings in molten salt environment. Therefore, the present research work has been focused to investigate and compare the hot corrosion behavior of conventional thick (by plasma spraying and gas nitrided) and nanostructured thin (by physical vapor deposition process) TiAlN and AlCrN coatings on ASTM-SA210 Grade A-1 boiler steel, in an aggressive environment of Na₂SO₄-60%V₂O₅ molten salt at 900°C under cyclic conditions. XRD, SEM/EDAX and X-ray mapping techniques have been used to characterize the corrosion products. The detailed experimental procedure is reported in chapter 3.

4.3.1 Results

4.3.1.1 Visual observations

The macrographs for uncoated and coated ASTM-SA210 Grade A-1 boiler steel subjected to cyclic oxidation in Na₂SO₄-60%V₂O₅ molten salt at 900°C for 50 cycles are shown in Fig.4.17. For the uncoated Grade A-1 boiler steel, a light grey colored scale appeared on the surface right from the 2nd cycle. After 16th cycle dark grey color spots appeared on the surface with hairline cracks. This bare steel showed severe spalling of the oxide scale after 25th cycle and scale starts falling in the boat. Some metallic sound was also observed during cooling for some cycles. At the end of cyclic study, uniform scale with severe cracks and blackish grey color surface appearance in the middle with light grey color along the sides was observed which can be seen in Fig.4.17 (a).

In case of nanostructured thin TiAlN coating, color of the oxide scale at the end of the study was observed to be grey with some whitish grey areas on the surface, as shown in Fig.4.17 (b). Hairline cracks were observed after 16th cycle. Subsequently, few very fine cracks were developed in the scale and spalling was observed. The nanostructured thin AlCrN coated Grade A-1 boiler steel has shown the formation of grey colored scale with severe spalling and visible cracks over the whole area as shown in Fig.4.17(c).

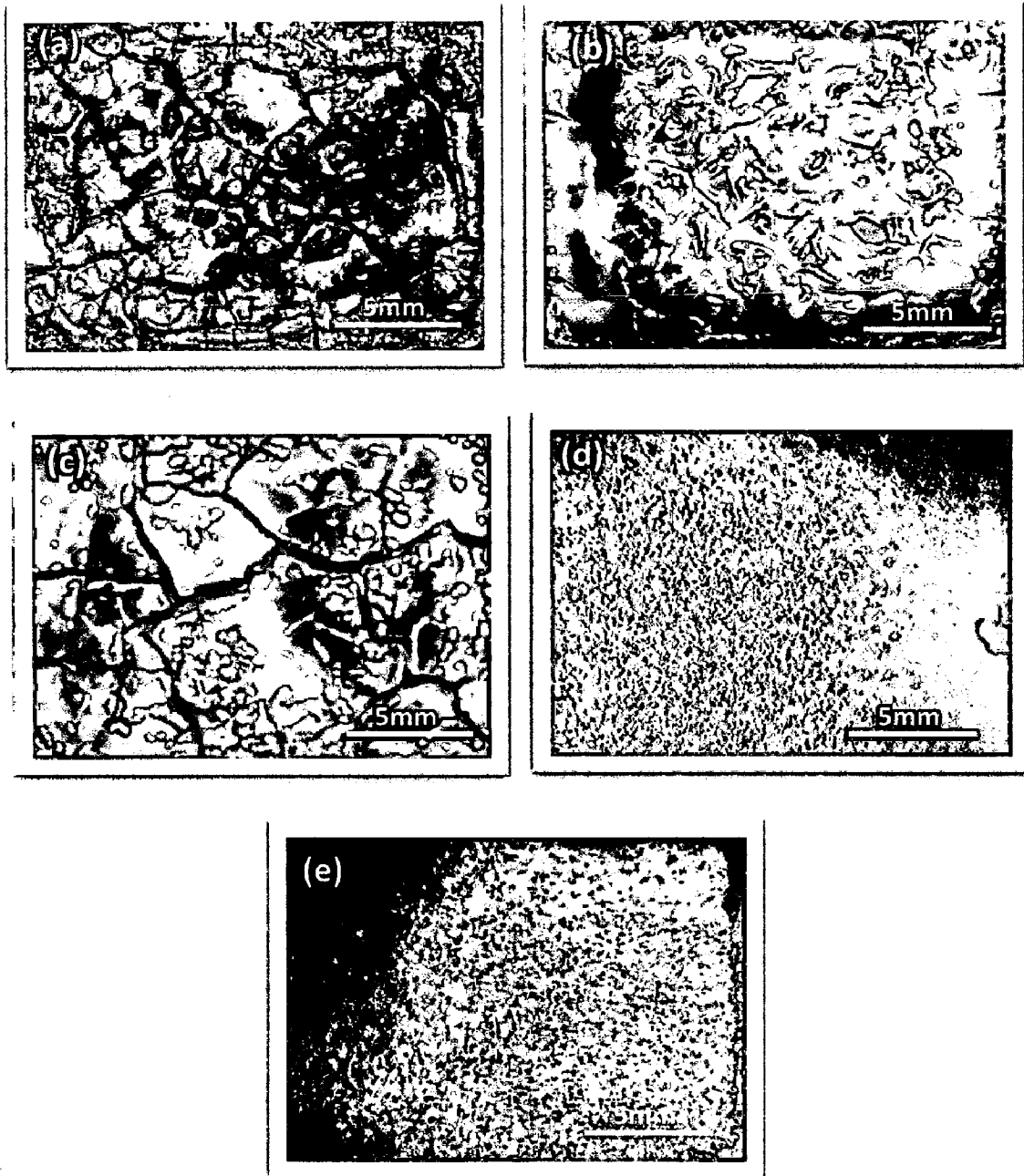


Fig. 4.17 Surface macrographs of uncoated and coated ASTM-SA210 Grade A-1 boiler steel exposed to molten salt ($\text{Na}_2\text{SO}_4\text{-60\%V}_2\text{O}_5$) environment at 900°C for 50 cycles : (a) Uncoated Grade A-1 boiler steel, (b) Nanostructured TiAlN coating, (c) Nanostructured AlCrN coating, (d) Conventional TiAlN coating, (e) Conventional AlCrN coating

Dark grey spots were observed in the scale, after the completion of 9th cycle, these turned to light and dark grey subsequently. Fine hairline cracks were observed after 17th cycle which turn into severe cracking after 33rd cycle and continued to 50th cycle. A visual observation of conventional thick TiAlN coated Grade A-1 boiler steel (Fig.4.17.d), showed the formation of brownish grey color in the middle of the sample along with dark grey sides at the end of the study. Some amount of superficial spalling was noticed at the end of 5th cycle, which may be due to the loosely bond particles on the surface of the coating. The scale was smooth and adherent to the substrate. In case of conventional thick AlCrN coated Grade A-1 boiler steel, color of the oxide scale was whitish grey at the end of the study (Fig.4.17.e). The scale was found to be adherent and smooth and no sign of spalling was observed at any stage during the course of the study.

4.3.1.2 Weight change measurements

Weight gain per unit area (mg/cm^2) versus time expressed in number of cycles plot for coated and bare ASTM-SA210 Grade A-1 boiler steel subjected to cyclic oxidation in Na_2SO_4 -60% V_2O_5 (molten salt environment) at 900°C for 50 cycles, is presented in Fig. 4.18. It can be inferred from the plots that the uncoated and nanostructured thin coated Grade A-1 boiler steels have shown high rate of oxidation as compared to conventional thick coatings. The plots for conventional thick samples shows relatively higher weight gain at initial cycles followed by gradual weight gain. The conventional thick coatings have shown protection to the substrate steel as the weight gain becomes almost constant after 5th cycle. The thin nanostructured TiAlN coating has provided the protection to the substrate to some extent, as the weight gain rate is slightly lower than that of uncoated Grade A-1 boiler steel. The nanostructured AlCrN thin coating has provided no protection to the substrate steel as the weight gain rate is almost same as in case of uncoated Grade A-1 boiler steel.

The cumulative weight gain per unit area for the coated and bare Grade A-1 boiler steel subjected to cyclic oxidation in Na_2SO_4 -60% V_2O_5 (molten salt environment) at 900°C for 50 cycles is shown in Fig.4.19.

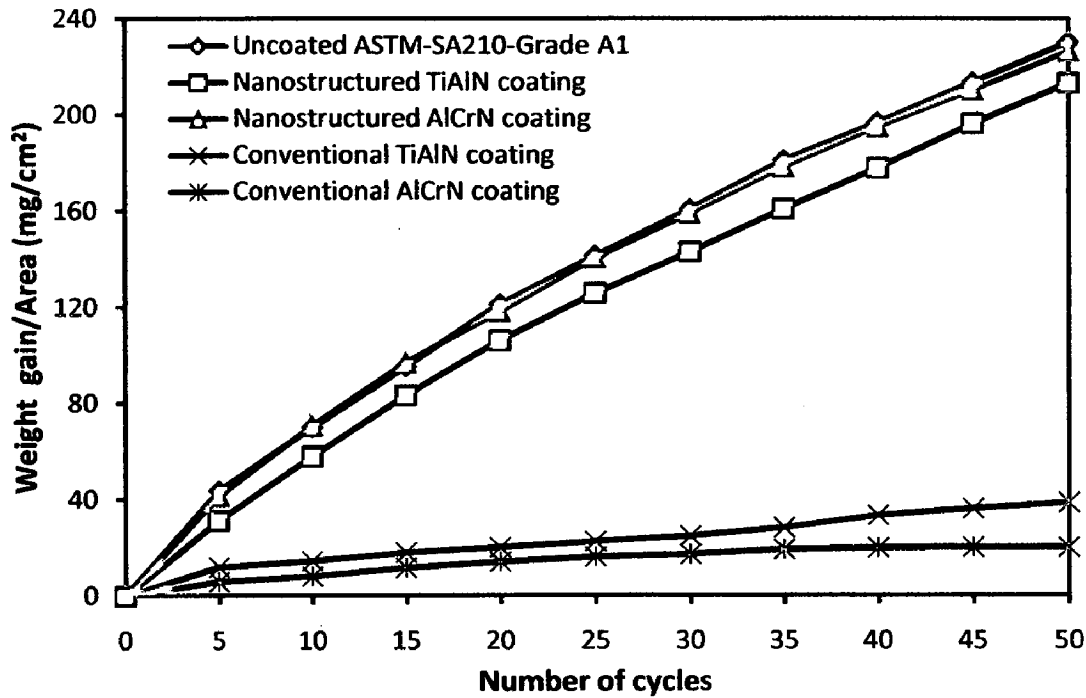


Fig. 4.18 Weight gain/area vs time (number of cycles) for the uncoated and coated ASTM-SA210 Grade A-1 boiler steel exposed to molten salt ($\text{Na}_2\text{SO}_4\text{-60}\%\text{V}_2\text{O}_5$) environment at 900°C for 50 cycles

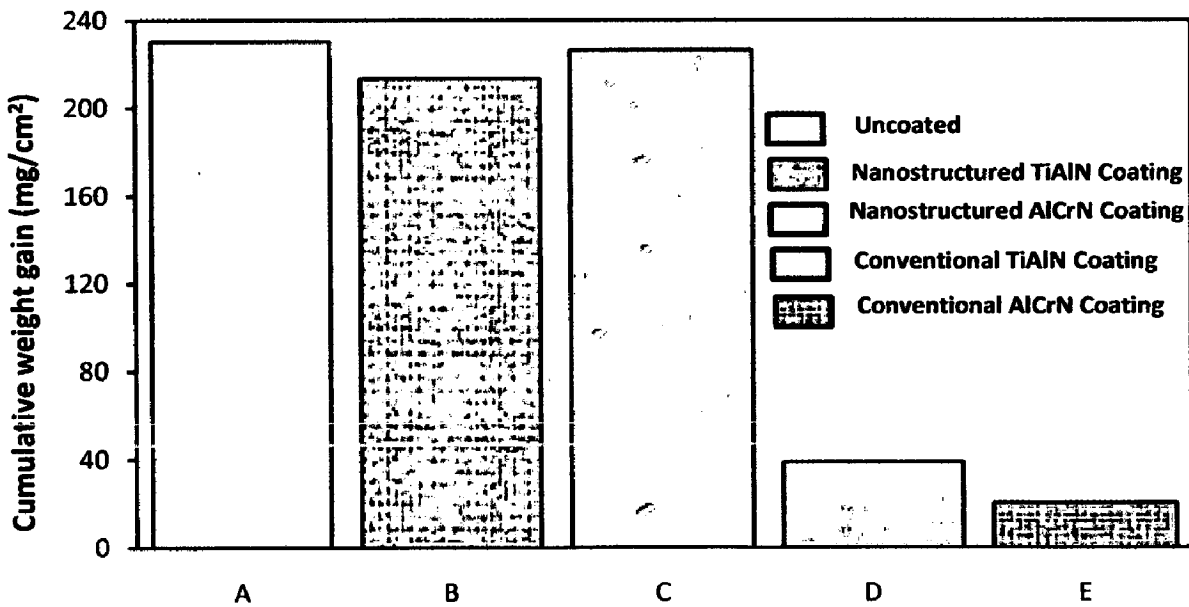


Fig. 4.19 Column chart showing cumulative weight gain per unit area for the uncoated and coated ASTM-SA210 Grade A-1 boiler steel exposed to molten salt ($\text{Na}_2\text{SO}_4\text{-60}\%\text{V}_2\text{O}_5$) environment at 900°C for 50 cycles: (A) Uncoated, (B) Nanostructured TiAlN coating, (C) Nanostructured AlCrN coating, (D) Conventional TiAlN coating, (E) Conventional AlCrN coating

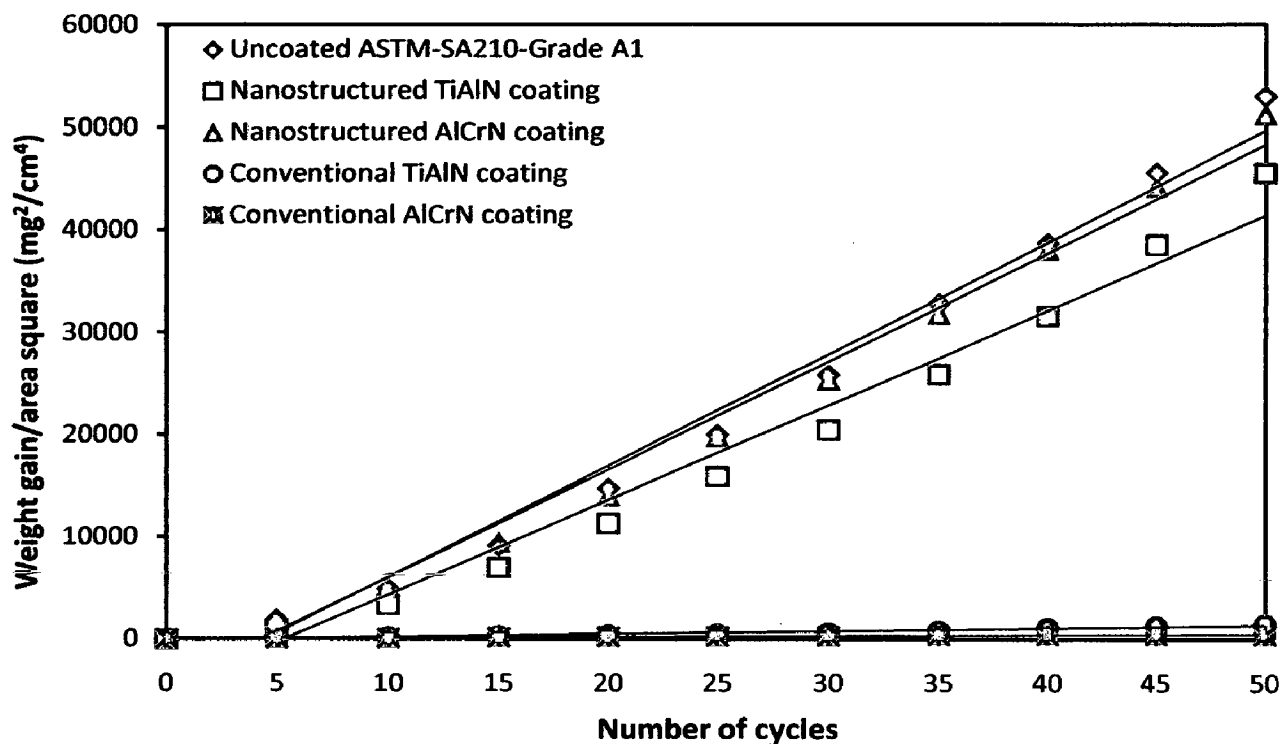


Fig. 4.20 Weight gain/area square vs time (number of cycles) for the uncoated and coated ASTM-SA210 Grade A-1 boiler steel exposed to molten salt (Na_2SO_4 -60% V_2O_5) environment at 900°C for 50 cycles

Table 4.5: Parabolic rate constant ' K_p ' values of uncoated and coated ASTM-SA-210 Grade A-1 boiler steel subjected to cyclic oxidation in Na_2SO_4 -60% V_2O_5 (molten salt environment) at 900°C for 50 cycles

Substrate / Coating	$K_p \times 10^{-08} \text{ gm}^2 \text{ cm}^{-4} \text{ s}^{-1}$
Uncoated Grade A1 boiler steel	30.27
Nanostructured TiAlN coating	29.36
Nanostructured AlCrN coating	25.75
Conventional TiAlN coating	00.25
Conventional AlCrN coating	00.81

As evident from Fig.4.19; the overall weight gain is highest in case of uncoated Grade A-1 boiler steel and is lowest in case of conventional thick AlCrN coated steel. The weight gain in case of conventional AlCrN coated Grade A-1 boiler steel is only 08 % of weight gain in case of uncoated Grade A-1 boiler steel and in case of conventional TiAlN coating, the weight gain is 16 % of the weight gain in case of uncoated boiler steel.

In Fig.4.20; the $(\text{weight gain/area})^2$ versus number of cycles plot are shown for all the cases to ascertain conformance with the parabolic rate law. All the coated and uncoated ASTM-SA210 Grade A-1 boiler steel followed the parabolic rate law as evident from the Fig.4.20. The parabolic rate constant K_p was calculated by a linear least-square algorithm to a function in the form of $(W/A)^2 = K_p t$, where W/A is the weight gain per unit surface area (mg/cm^2) and 't' indicates the number of cycles representing the time of exposure. The parabolic rate constants for the bare and coated Grade A-1 boiler steel calculated on the basis of 50 cycle's exposure data are shown in Table.4.5. The ' K_p ' values for the coated Grade A-1 boiler steel are less than the bare boiler steel.

4.3.1.3 Surface scale analysis

4.3.1.3.1 X-ray diffraction analysis (XRD)

XRD diffractograms for coated and uncoated ASTM-SA210 Grade A-1 boiler steel subjected to cyclic oxidation in $\text{Na}_2\text{SO}_4\text{-60\%V}_2\text{O}_5$ (molten salt environment) at 900°C for 50 cycles are depicted in Fig.4.21 (a and b) on reduced scale. As indicated by the diffractograms Fe_2O_3 is the main phases present in the oxide scale of uncoated and nanostructured thin TiAlN and AlCrN coated Grade A-1 boiler steels (Fig.4.21.a). In nanostructured TiAlN coating, minor phase such as Al_2O_3 has been observed, whereas in case of nanostructured AlCrN coating, Cr_2O_3 has been observed. Further, the main phases identified for the conventional thick TiAlN coating are Al_2O_3 , Ti_3Al , Al, TiO_2 and Fe_2O_3 (Fig.4.21.b). The surface oxides on conventional thick AlCrN coating were Al_2O_3 and Cr_2O_3 (Fig.4.21.b).

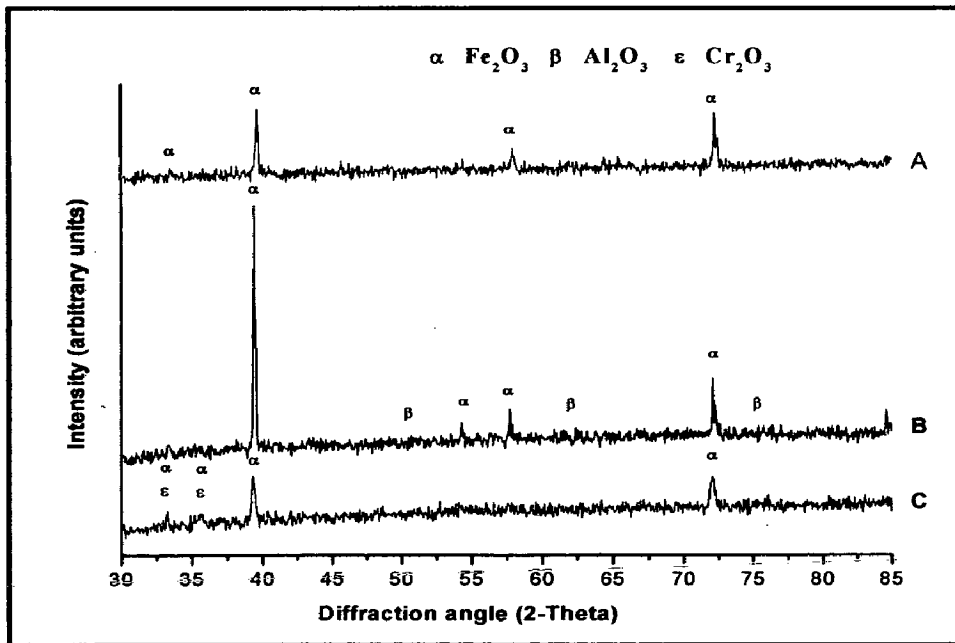


Fig. 4.21 (a) X-Ray Diffraction pattern of uncoated and coated ASTM-SA210 Grade A-1 boiler steel exposed to molten salt ($\text{Na}_2\text{SO}_4\text{-60\%V}_2\text{O}_5$) environment at 900°C for 50 cycles: (A) Uncoated Grade A-1 boiler steel, (B) Nanostructured TiAlN coating, (C) Nanostructured AlCrN coating

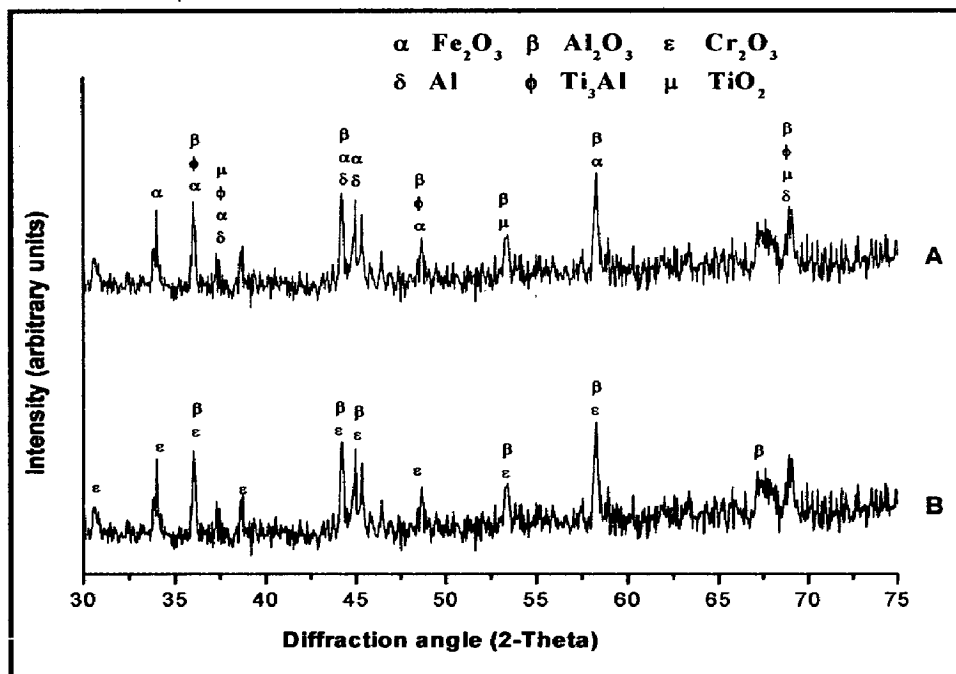


Fig. 4.21 (b) X-Ray Diffraction pattern of uncoated and coated ASTM-SA210 Grade A-1 boiler steel exposed to molten salt ($\text{Na}_2\text{SO}_4\text{-60\%V}_2\text{O}_5$) environment at 900°C for 50 cycles: (A) Conventional TiAlN coating, (B) Conventional AlCrN coating

4.3.1.3.2 Surface scale morphology

SEM micrographs along with EDAX point analysis reveals the surface morphology of the coated and uncoated Grade A-1 boiler steel subjected to cyclic oxidation in Na_2SO_4 -60% V_2O_5 (molten salt environment) at 900°C for 50 cycles are shown in Fig.4.22. Micrograph (shown in Fig.4.22.a) for uncoated Grade A-1 boiler steel indicates a scale developed which appears like needles grown on matrix containing distorted grains. EDAX analysis at point 1 and point 2 on Fig.4.22 indicates the formation of mainly iron oxide.

The SEM micrograph of oxidized nanostructured thin TiAlN coatings is shown in Fig.4.22 (b). The surface scale containing distorted grains. EDAX analysis of the scale revealed the presence of Fe and O as the main elements along with very small amount of Al and Ti. In case of nanostructured thin AlCrN coated Grade A-1 boiler steel, EDAX point analysis shows, the top scale is rich in Fe and O. The small amount of Al, Na, Cr, and C are also present. The surface scale developed on conventional thick TiAlN coated Grade A-1 steel is massive and without any cracks, with white contrast regions. EDAX analysis indicates the presence of Ti, Al and O as the main phases along with very small amount of Fe. The white contrast region as indicated by Point 7 on Fig.4.22 depicts the presence of lesser Al (23.76 %) and more Ti (16.01 %) as compared to the grey contrast region which indicates Al (45.48 %) along with Ti (02.09 %). A homogeneous and continuous surface scale is developed on conventional thick AlCrN coated Grade A-1 boiler steel. EDAX point analysis shows Al (47.84%), Cr (9.34%) and O (37.18%) as the main elements in the scale (Fig.4.22.e) along with very small amount of Fe, Na and V.

4.3.1.4 Cross-sectional analysis

4.3.1.4.1 Scale thickness

The oxidized samples were cut across the cross section using Buehler Isomet 1000 precision saw and mounted in transoptic mounting resin and subsequently mirror polished to obtain scanning electron back scattered micrographs and X-ray mapping of different elements for coated and uncoated Grade A-1 boiler steel.

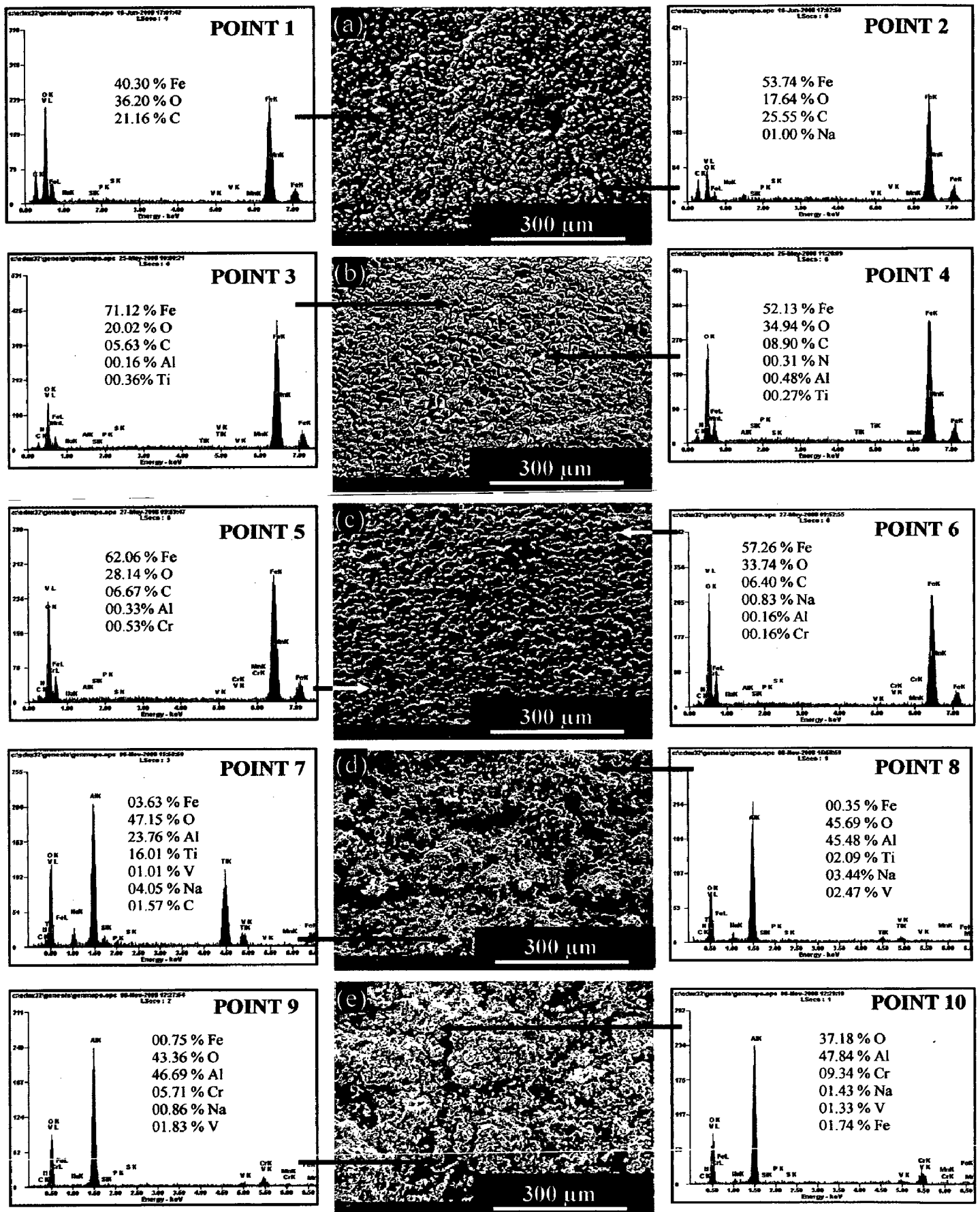


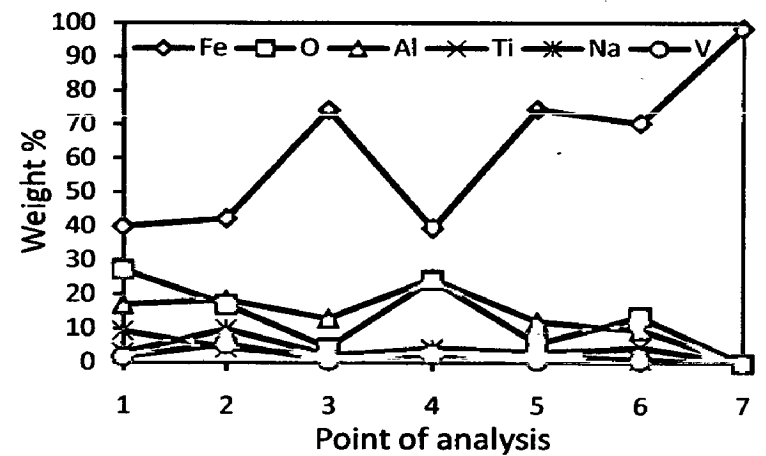
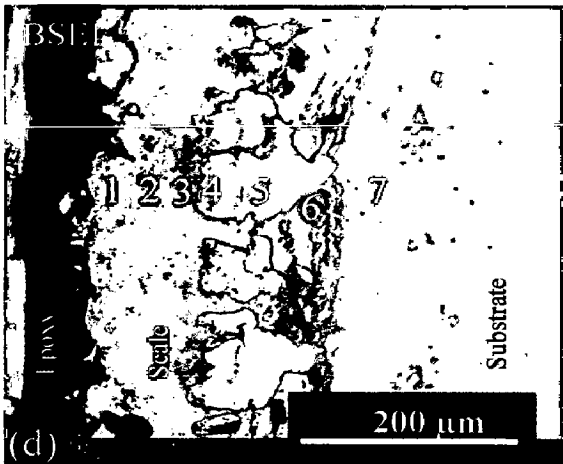
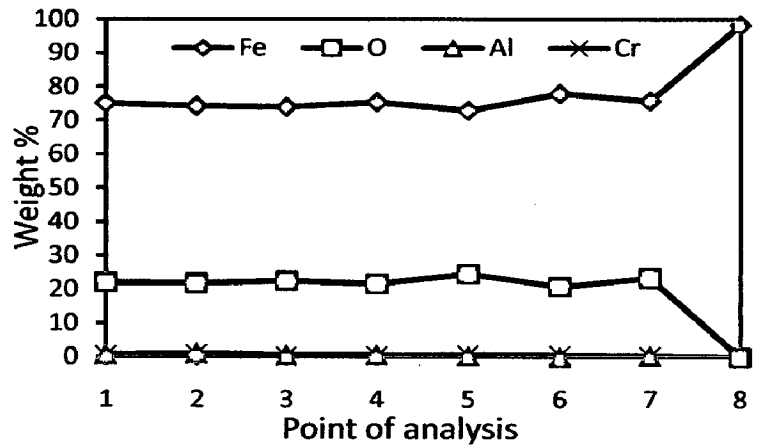
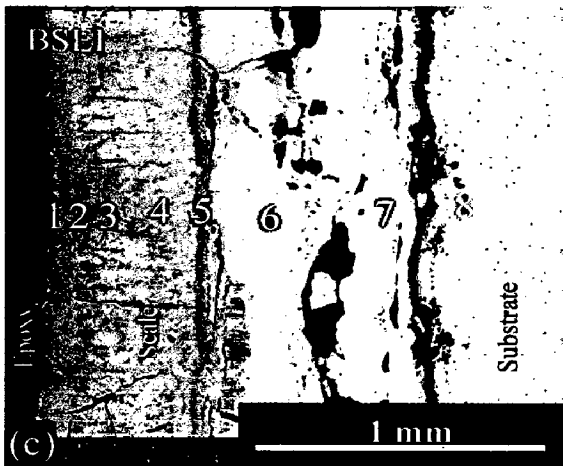
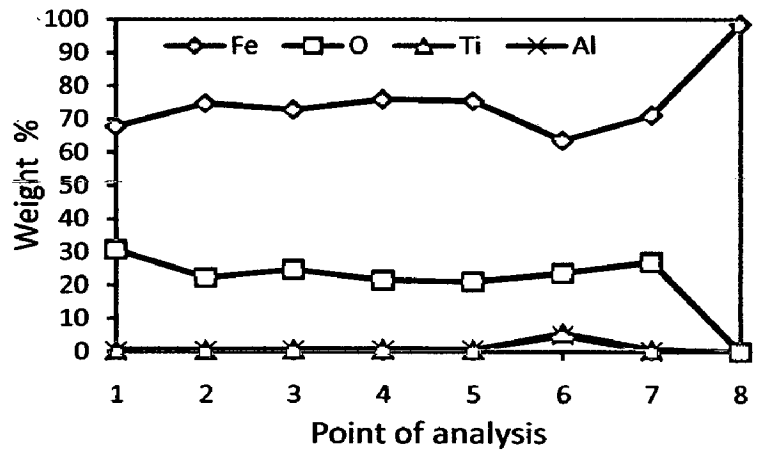
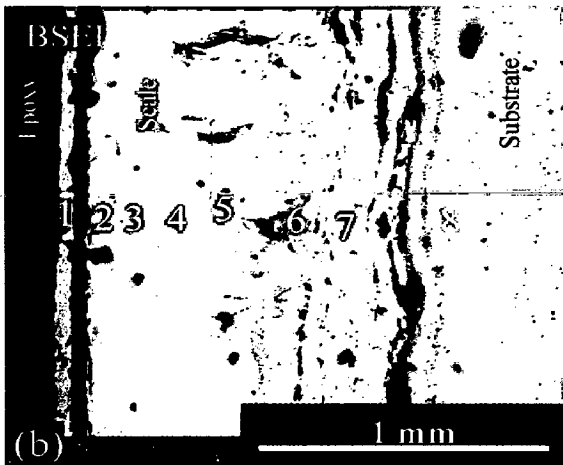
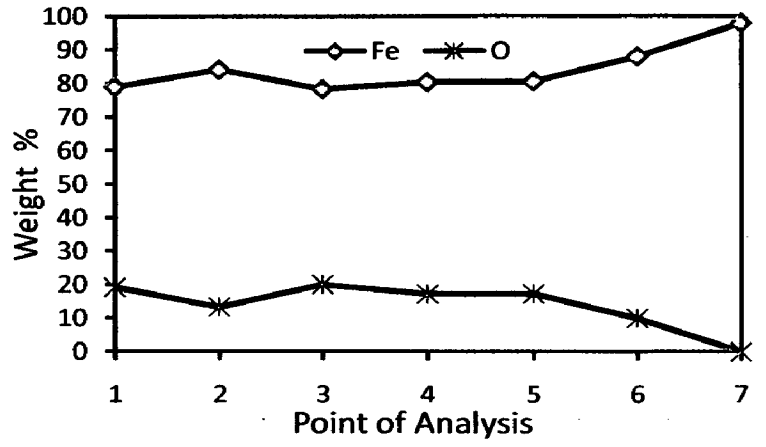
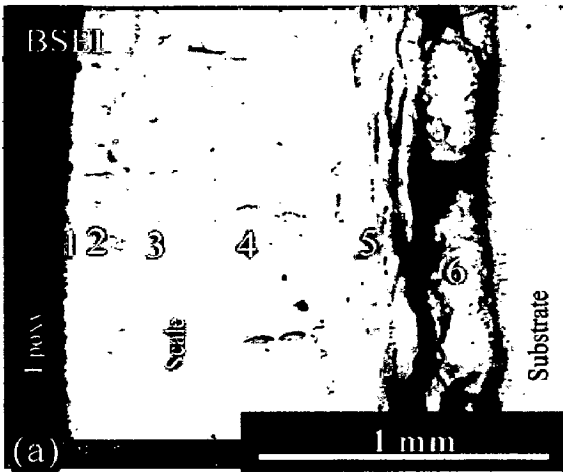
Fig. 4.22 Surface-scale morphology and EDAX patterns from different spots on uncoated and coated ASTM-SA210 Grade A-1 boiler steel exposed to molten salt (Na_2SO_4 -60% V_2O_5) environment at 900°C for 50 cycles: (a) Uncoated Grade A1 boiler steel, (b) Nanostructured TiAlN coating, (c) Nanostructured AlCrN coating, (d) Conventional TiAlN coating, (e) Conventional AlCrN coating

The scale thickness values were measured from SEM back scattered micrographs as shown in Fig.4.23. Very thick scale is observed in case of uncoated Grade A-1 boiler steel, which is around 10.13 times thicker than the scale measured for conventional thick AlCrN coated Grade A-1 boiler steel. The measured average scale thickness values for uncoated Grade A-1, nanostructured thin TiAlN, nanostructured thin AlCrN, conventional thick TiAlN and conventional thick AlCrN coatings are 1480, 1205, 1294, 282 and 146 μm respectively. The conventional coatings have shown good resistance to the corrosive environment as the oxygen penetration is limited to very less thickness as compared to the uncoated and nanostructured coated Grade A-1 boiler steel.

4.3.1.4.2 Cross-sectional scale morphology

Back Scattered Electron Image (BSEI) micrograph and elemental variation across the cross-section for coated and uncoated ASTM-SA210 Grade A-1 boiler steel subjected to cyclic oxidation in Na_2SO_4 -60% V_2O_5 molten salt at 900°C for 50 cycles are shown in Fig.4.23. The SEM micrograph in case of uncoated Grade A-1 boiler steel shows thick scale as shown in Fig. 4.23 (a). Also, the scale is fragile and indicating cracking. The scale is not adherent to the substrate and showing tendency to get away from the substrate. EDAX analysis reveals the presence of iron and oxygen throughout the scale. The existence of significant amount of oxygen indicates the possibility Fe_2O_3 in the oxide scale.

BSEI micrograph and elemental variation depicted in Fig.4.23 (b), for the exposed cross-section of nanostructured thin TiAlN coated Grade A-1 boiler steel shows the thick, continuous and adherent scale. The EDAX analysis reveals the presence of Fe, and O throughout the scale. A location at point 6 (Fig.4.23.b) in the micrograph depicts the good percentage of Ti and Al along with Fe and oxygen. A thick and adherent oxide scale can be seen in case of nanostructured AlCrN coated Grade A-1 boiler steel (Fig.4.23.c).The scale is showing fine cracks at some locations. The EDAX point analysis indicates the presence of Fe and O throughout the scale.



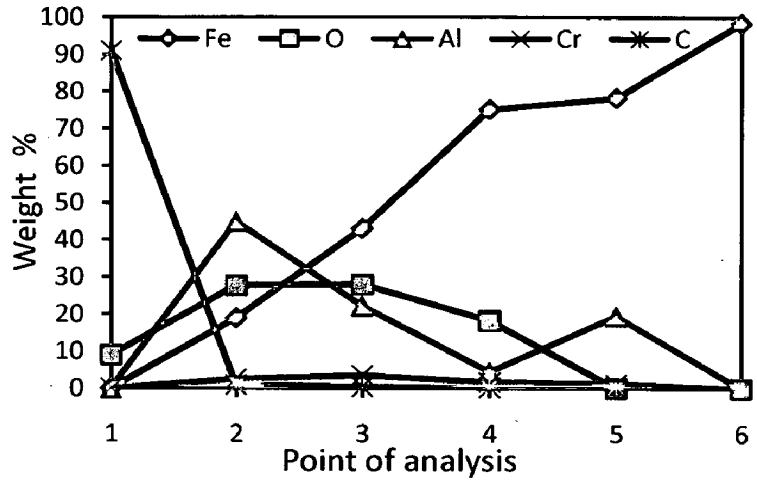
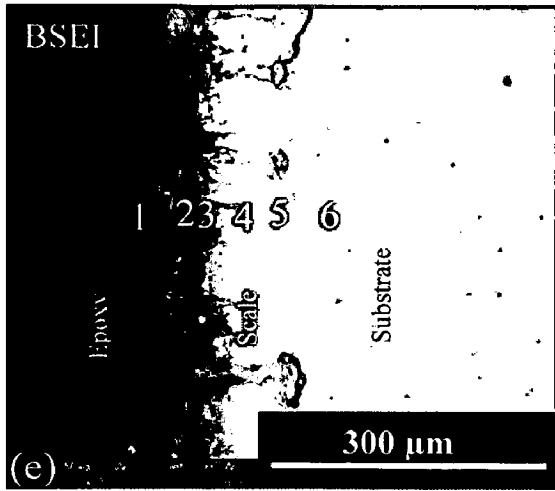


Fig. 4.23 Oxide scale morphology and variation of elemental composition across the cross-section of the uncoated and coated ASTM-SA210 Grade A-1 boiler steel exposed to molten salt ($\text{Na}_2\text{SO}_4\text{-60}\%\text{V}_2\text{O}_5$) environment at 900°C for 50 cycles: (a) Uncoated Grade A1 boiler steel (70 X), (b) Nanostructured TiAlN coating (71 X), (c) Nanostructured AlCrN coating (55 X), (d) Conventional TiAlN coating (300 X), (e) Conventional AlCrN coating (250 X)

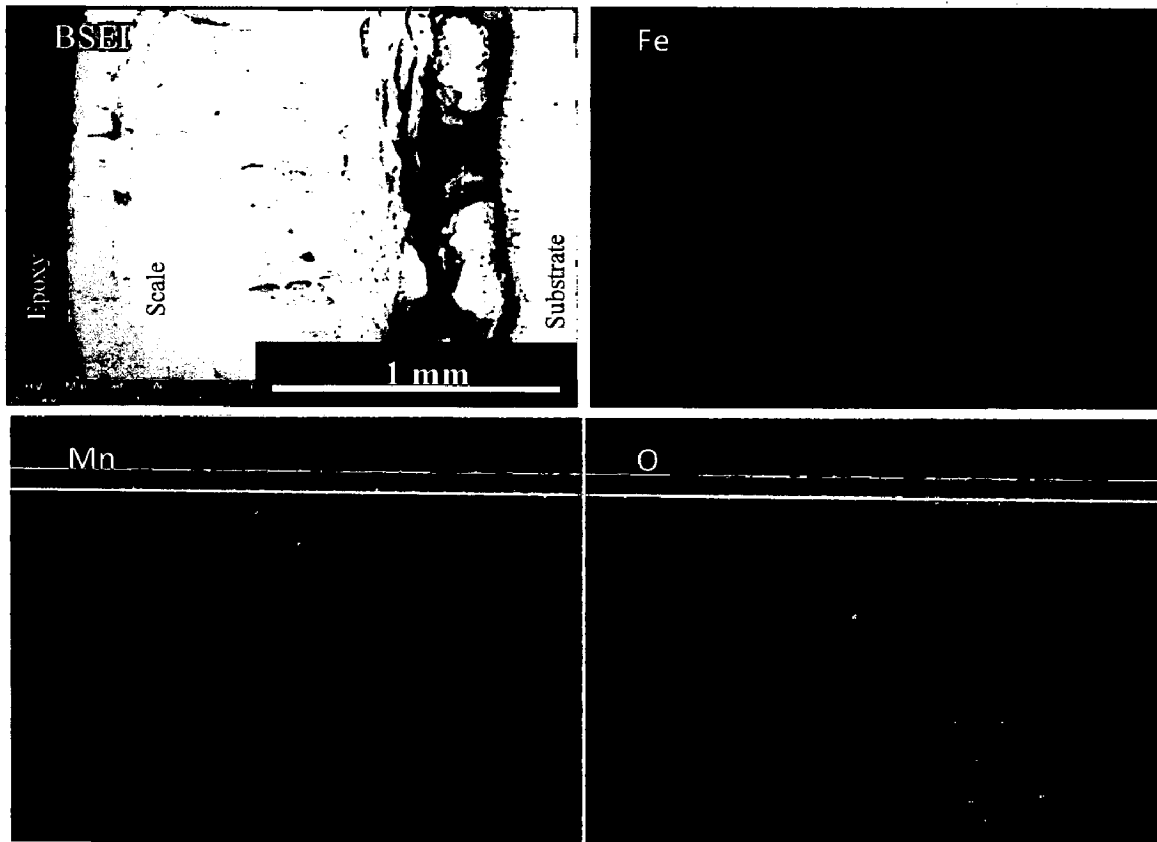


Fig. 4.24 (a) Composition image (BSEI) and X-ray mapping of the cross-section of uncoated ASTM-SA210 Grade A-1 boiler steel exposed to molten salt ($\text{Na}_2\text{SO}_4\text{-60}\%\text{V}_2\text{O}_5$) environment at 900°C for 50 cycles

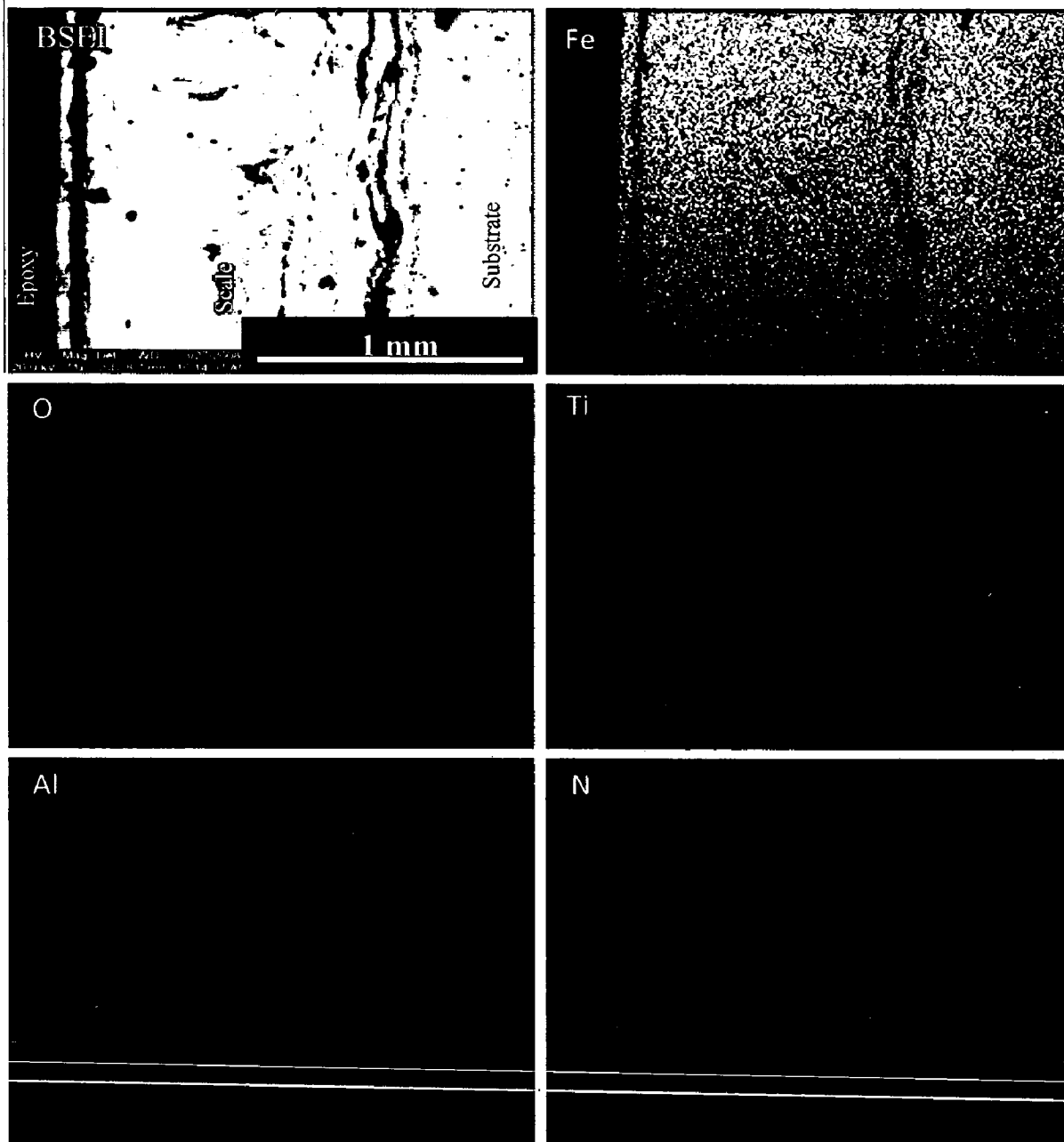


Fig. 4.24 (b) Composition image (BSEI) and X-ray mapping of the cross-section of Nanostructured TiAlN coated ASTM-SA210 Grade A-1 boiler steel exposed to molten salt (Na_2SO_4 -60% V_2O_5) environment at 900°C for 50 cycles

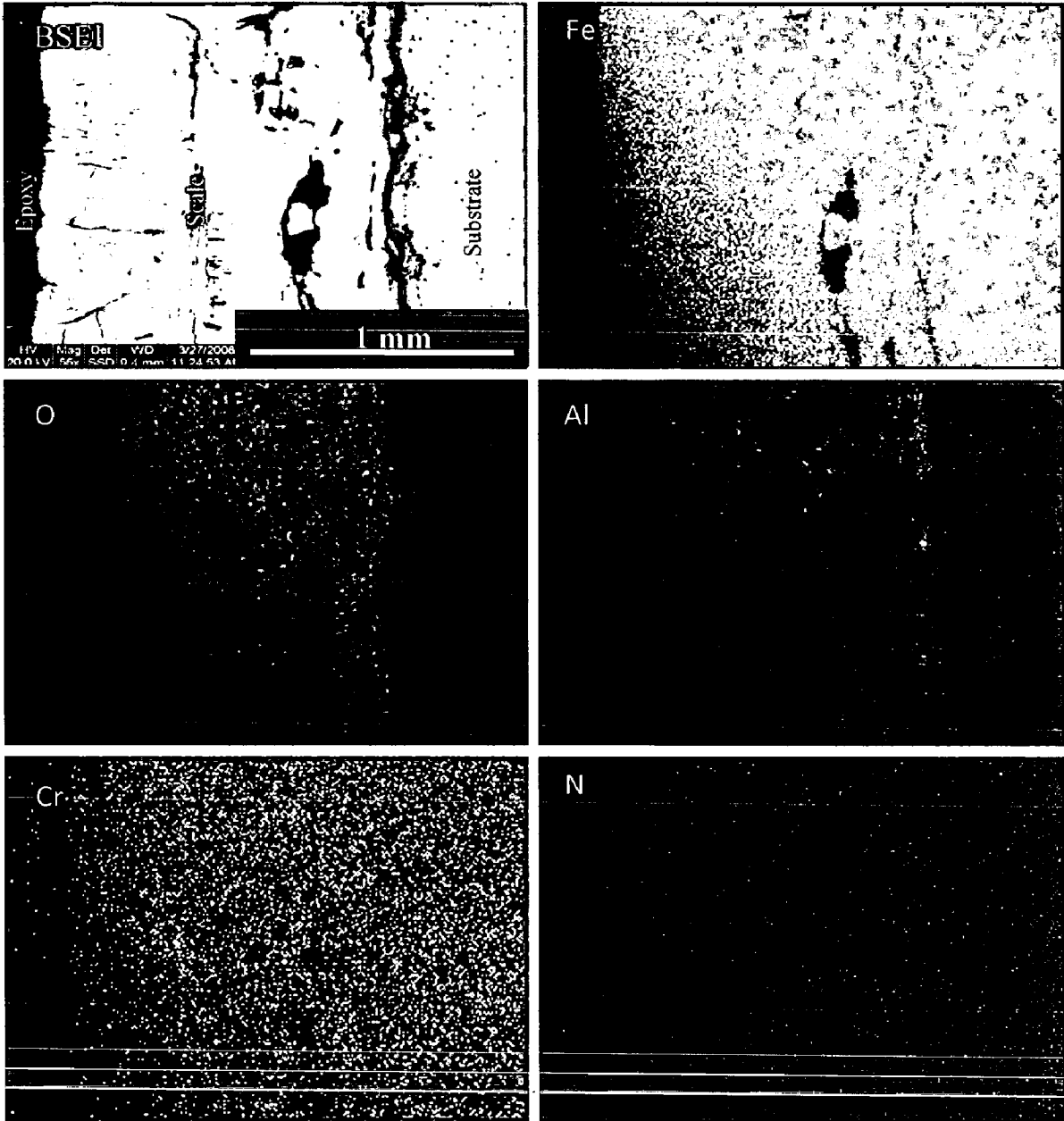


Fig. 4.24 (c) Composition image (BSEI) and X-ray mapping of the cross-section of Nanostructured AlCrN coated ASTM-SA210 Grade A-1 boiler steel exposed to molten salt (Na_2SO_4 -60% V_2O_5) environment at 900°C for 50 cycles

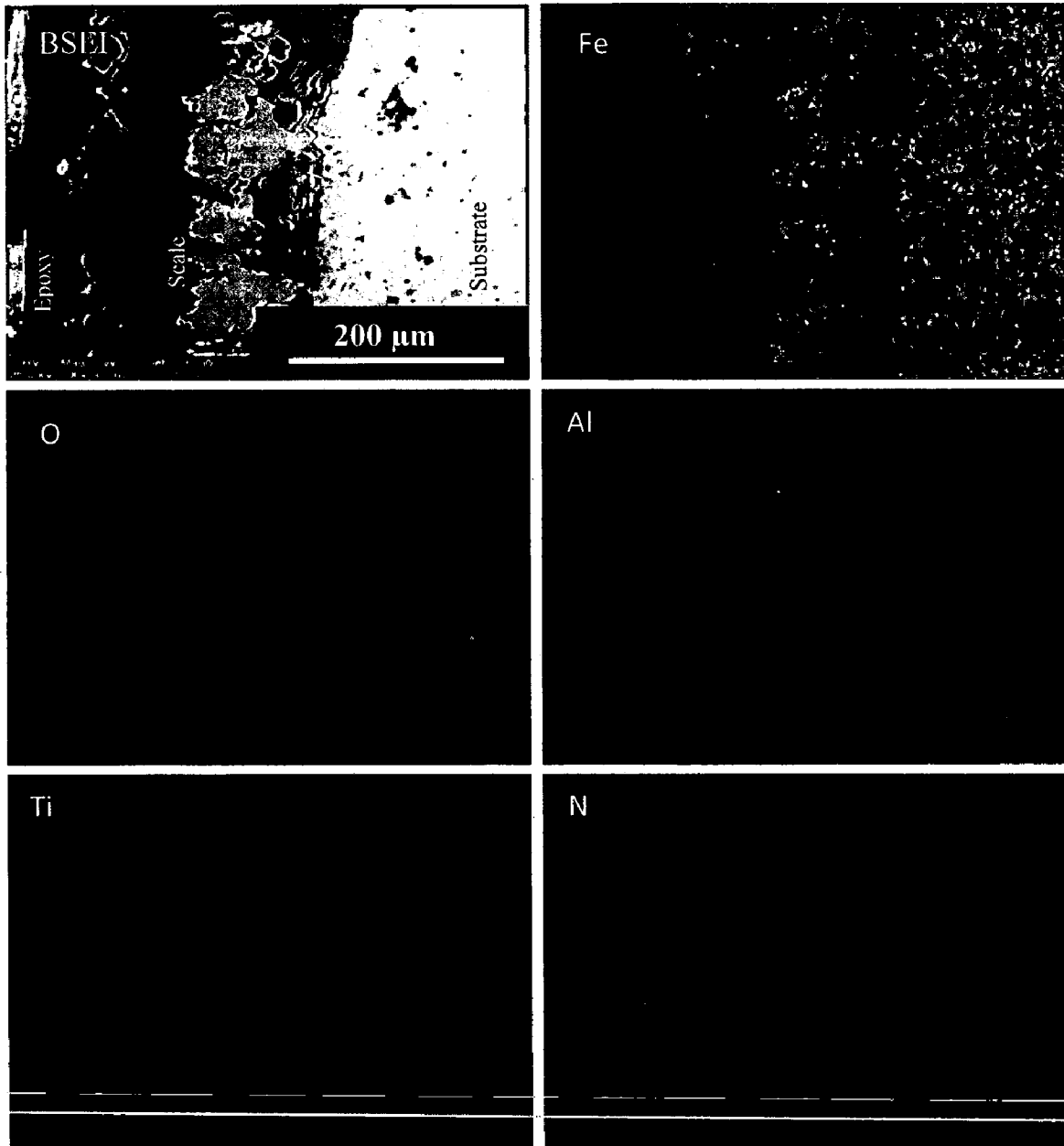


Fig. 4.24 (d) Composition image (BSEI) and X-ray mapping of the cross-section of conventional TiAlN coated ASTM-SA210 Grade A-1 boiler steel exposed to molten salt (Na_2SO_4 -60% V_2O_5) environment at 900°C for 50 cycles

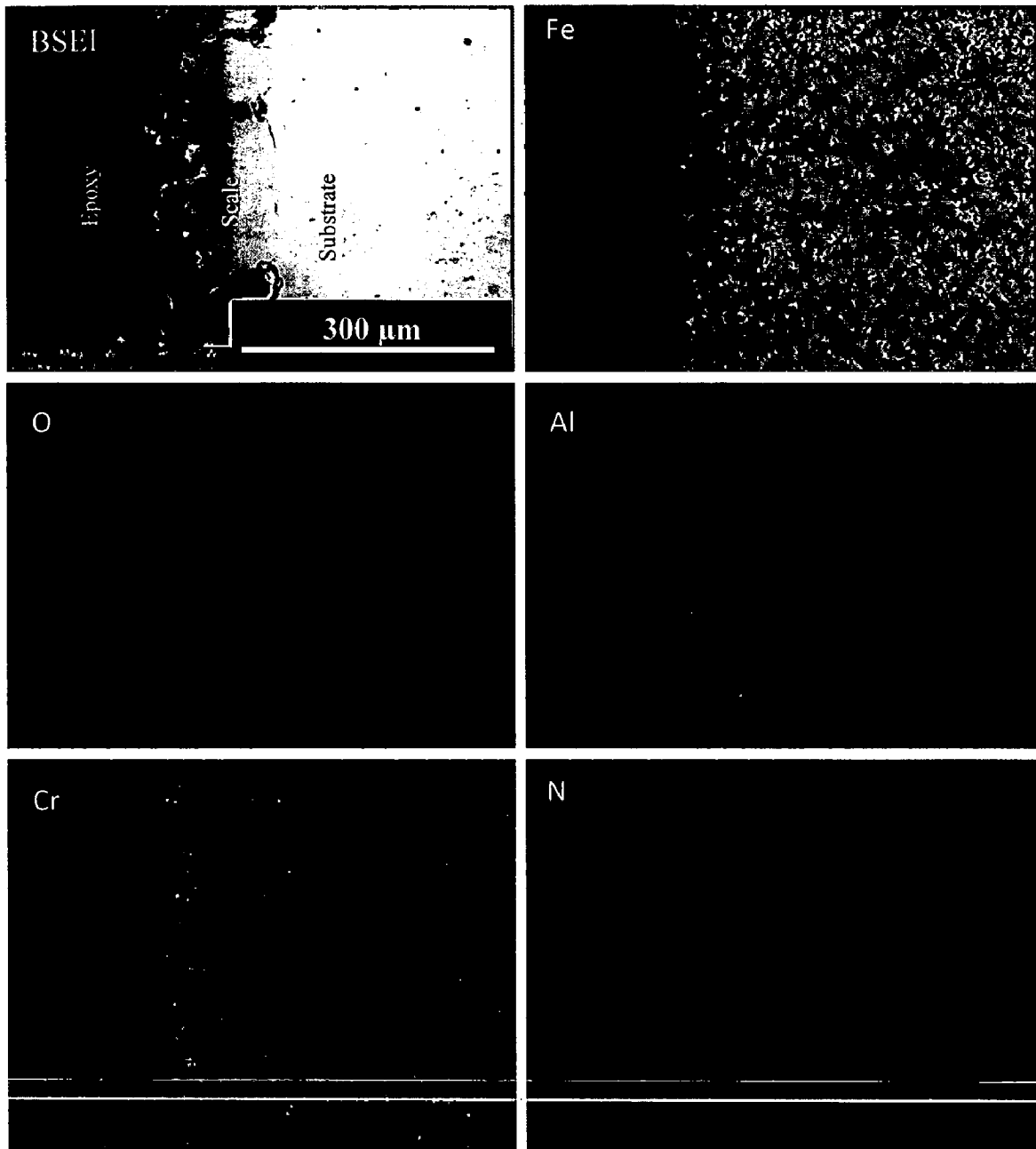


Fig. 4.24 (e) Composition image (BSEI) and X-ray mapping of the cross-section of conventional AlCrN coated ASTM-SA210 Grade A1 boiler steel exposed to molten salt (Na_2SO_4 -60% V_2O_5) environment at 900°C for 50 cycles

In case of conventional TiAlN coated Garde A-1 boiler steel, the scale is non uniform, thin and adherent as depicted in Fig.4.23 (d). The EDAX point analysis indicates the presence of Fe, O, Ti and Al throughout the scale with variable amounts. A location at point 4 in Fig.4.23 (d) shows higher percentage of Al along with Fe and O. The amount of Ti in the top scale is higher (Point 1) which decreases subsequently towards the substrate. In the top scale Na and V are also present as revealed from the cross-section micrograph (Fig.4.23.d). The conventional thick AlCrN coated Grade A-1 boiler steel (Fig.4.23.e) indicates continuous, thin and adherent scale. EDAX point analysis shows the presence of Al, O and Fe throughout the scale. The top scale shows higher percentage of Al and O along with good amount of Fe (point 2 in Fig.4.23.e). In the subscale region as indicated by points 3, 4, 5 and 6, the amount of Fe is increasing and of Al and O is decreasing as we move towards the substrate/scale interface. The presence of Cr in the top scale is indicated by the EDAX point analysis at point 3 in Fig.4.23 (e).

4.3.1.4.3 X-Ray mapping

X-ray mappings for a part of oxide scale of uncoated and coated ASTM-SA210 Grade A-1 boiler steel oxidized in Na_2SO_4 -60% V_2O_5 (molten salt environment) at 900 °C for 50 cycles are shown in Fig. 4.24. In case of uncoated Grade A-1 boiler steel, the micrograph (Fig.4.24.a) indicates a dense scale, which mainly contains iron and oxygen with some amount of manganese, as indicated by X-ray mapping. The X-ray mapping analysis of the scale formed on nanostructured TiAlN coated Grade A-1 boiler steel is presented in Fig. 4.24 (b). The X-ray mapping indicates presence of oxygen and iron throughout the scale with a thin band of Al in the top scale. In case of nanostructured thin AlCrN coated Grade A-1 boiler steel; the BSEI and X-ray mapping are shown in Fig. 4.24 (c). The X-ray mapping indicates the presence of iron and oxygen throughout the scale. A very small percentage of Al is indicated at the scale/substrate interface.

In case of conventional thick TiAlN coated Grade A-1 boiler steel, Fig.4.24 (d); Al and Ti rich bands are clearly seen along with Fe and oxygen. Titanium (Ti) is present in the upper scale along with Fe and O. The bright regions of Al are overlapping with O and in some

regions of Al, oxygen is completely absent. Figure 4.24 (e) depicts the X-ray mapping in case of conventional AlCrN coated Grade A-1 boiler steel. The thick band of Al is present in the top scale region. The upper scale is rich in Al with a thin band of O and Cr. The oxygen fails to break the thick Al band and thus present in the top scale as a very thin band along with some Cr. A few horizontal strings of O can be seen in the X-ray mapping, where O gets succeeded in entering to the scale. The oxygen is not present in the substrate. So, we can say the conventional thick AlCrN coating has provided the full protection to the Grade A-1 boiler steel in the corrosive environment.

4.3.2 Summary of Results

Results obtained after exposure of uncoated and coated ASTM-SA210 Grade A-1 boiler steel to cyclic oxidation in Na_2SO_4 -60% V_2O_5 (molten salt environment) at 900°C for 50 cycles are summarized in Table.4.6.

4.3.3 Discussion

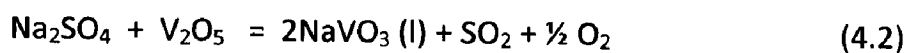
The non protective conditions can be immediately inferred from the BSEI image of the corroded bare Grade A-1 boiler steel; where the scale has detached from the substrate and cracked (Fig.4.23.a). Further the formation of Fe_2O_3 in the spalled scale (Fig.4.21) has also been reported to be non-protective by Das et al. (2002) during their hot corrosion study on Fe_3Al -based iron aluminides in Na_2SO_4 atmosphere. Formation of only iron oxide in the given molten salt environment is further supported by Holt and Kofstad (1989) where authors reported that in the high temperature region having $\text{O}_2 + 4\% \text{SO}_2/\text{SO}_3$ {where $\text{Fe}_2(\text{SO}_4)_3$ is formed on the surface}, the reaction mechanism is essentially that of the oxidation of iron in oxygen and the scale consists of $\text{Fe}_{1-y}\text{O}/\text{Fe}_3\text{O}_4/\text{Fe}_2\text{O}_3$. The XRD analysis (Fig.4.21) of the nanostructured coatings after hot corrosion studies in Na_2SO_4 -60% V_2O_5 (molten salt environment) at 900°C indicates the presence of Fe_2O_3 in the top scale, which is further supported by EDAX analysis (Fig.4.22).

Table 4.6 Summary of the results obtained for uncoated and coated ASTM-SA-210 Grade A-1 boiler steel subjected to cyclic oxidation in molten salt (Na_2SO_4 -60% V_2O_5) environment at 900°C for 50 cycles

Coating	Cumulative Weight gain (mg/cm^2)	Parabolic rate constant ($K_p \times 10^{-08} \text{ gm}^2\text{cm}^{-4}\text{s}^{-1}$)	XRD phases	Remarks
Uncoated Grade-A-1 boiler steel	230.26	30.27	Fe_2O_3	A grey colored scale appeared on the surface right from the 2 nd cycle. After 16 th cycle, dark grey colored spots appeared on the surface with hairline cracks. Severe spalling of scale after the 25 th cycle, and scale starts falling in the boat. At the end of cyclic study, uniform scale with severe cracks and blackish grey color surface appearance in the middle with light grey color along the sides; was observed.
Nanostructured TiAlN coating	213.40	29.36	Fe_2O_3 and Al_2O_3	Color of the oxide scale at the end of the study was observed to be grey with some whitish grey areas on the surface. Hairline cracks were observed after 16 th cycle. Subsequently, few very fine cracks were developed in the scale and spalling was observed.
Nanostructured AlCrN coating	226.44	25.75	Fe_2O_3 , and Cr_2O_3	Dark grey spots were observed on the surface after the completion of 9 th cycle, which turned to light and dark grey spots subsequently. After 17 th cycle, fine hairline cracks were observed which turn into severe cracking after 33 rd cycle and continued to 50 th cycle.
Conventional TiAlN Coating	38.73	00.25	Al_2O_3 , Ti_3Al , Al , TiO_2 and Fe_2O_3	The smooth and adherent oxide scale was brownish grey color in the middle of the sample along with dark grey sides
Conventional AlCrN coating	20.11	00.81	Al_2O_3 and Cr_2O_3	The whitish grey oxide scale was found to be adherent and smooth and no sign of spalling was observed at any stage during the course of the study.

Due to the formation of Fe₂O₃ in the scale as major phase (which is reported to be non-protective oxide scale) these coatings have shown higher weight gain (Fig.4.19) and offer very less protection to the substrate as compared to the conventional coatings. In case of conventional TiAlN and AlCrN coatings, the protective oxides of aluminum and chromium have been detected by XRD analysis (Fig.4.21). The results are further supported by EDAX of surface (Fig.4.22.d and e) and cross-section (Fig.4.23. d and e). Due to which these two coatings have performed brilliantly and provided the full protection to the substrate boiler steel, as it is obvious from the weight change plot (Fig.4.18). During cyclic testing, cracks in the oxide scale (Fig.4.17.a & c) and spalling of the uncoated and nanostructured coatings might be attributed to the different values of thermal coefficients for the coating, scale and the substrate as reported by Sidhu et al. (2003), Singh et al. (2004), Evans et al. (2001), Wang et al. (2002) and Niranatlumpong et al (2000). Though these cracks the corrosive environment can quickly reach the base metal and cut its way under the coating to result in adhesion loss and spalling, whereas some elements may diffuse outwards through these cracks to form oxides or spinels (Singh H et al., 2004). The presence of Fe and oxygen (Fig.4.24.a, b and c) in the top of the scale of the bare and nanostructured thin coated Grade-A-1 boiler steel is believed to be due to the diffusion of iron through the pores and cracks that appeared in the coating during the course of oxidation studies (Singh B et al., 2003).

The weight change plots (Fig. 4.18 and 4.20) indicate that the oxidation behavior of the specimens has shown conformance to parabolic rate law. The parabolic kinetic behavior is due to the diffusion controlled mechanism operating at 900°C under cyclic conditions (Mahesh et al., 2008). Small deviation from the parabolic rate law might be due to the cyclic scale growth. The rapid increase in the weight gain during the initial period of exposure to Na₂SO₄-60%V₂O₅ (molten salt environment) at 900°C may be due to the rapid diffusion of oxygen through the molten salt layer. Kolta et al. (1972) proposed that in the temperature range of 900°C, the Na₂SO₄ and V₂O₅ will combine to form NaVO₃ (having a melting point of 610°C) as follows:



This NaVO_3 acts as a catalyst and also serves as an oxygen carrier to the base alloy through the open pores present on the surface, which will lead to the rapid oxidation of the base elements of the substrate to form a protective oxide scale. Hence, an increase in the weight gain of the alloys occurs in the early stages of the hot corrosion. During the subsequent cycles, the formations of oxides have blocked the diffusion of corrosive species by covering the pores and the splat boundaries. The rapid increase in the weight gain during the initial period was also reported by Sidhu et al (2006E), Harpreet Singh et al.(2005), Tiwari and Prakash (1997) and Ul-amid (2003) during studies on the hot corrosion of alloys.

The parabolic rate constant for the uncoated and nanostructured thin coated Grade-A1 boiler steel is found to be nearly equal, which is higher than that of conventional thick coatings (Table.4.5). Both conventional thick TiAlN and AlCrN coatings have been found successful in reducing the overall weight gain of bare Grade-A1 boiler steel. The oxidation rate (total weight gain values after 50 cycles) of the coated and uncoated Grade-A1 boiler steel follows the sequence as given below:

Uncoated Gr A1 > Nanostructured AlCrN > Nanostructured TiAlN > Conventional TiAlN > Conventional AlCrN

In case of nanostructured TiAlN and AlCrN coatings, Fe_2O_3 is the main phase present in the scale as indicated by the XRD (Fig.4.21), EDAX (Fig. 4.22.b and c) and X-ray mapping (Fig. 4.24.b and c) analysis. The coatings has shown resistance to oxidation to some extent as the overall weight gain is less than as compared to the uncoated Grade-A1 boiler steel, but failed to provide full protection to the substrate which may be due to the difference in thermal expansion coefficient. In case of, plasma sprayed gas nitride conventional thick coatings i.e. TiAlN and AlCrN when subjected to cyclic oxidation in Na_2SO_4 -60% V_2O_5 molten salt at 900°C develops a scale mainly consisting on aluminum oxide and chromium oxide, which are supported by XRD (Fig.4.21), EDAX (Fig.4.23.d and e) and X-ray mapping analysis (Fig.4.24.d and e). These oxides are very protective as reported by Ul-Hamid (2003) and Sundarajan et al. (2004A). A thick band of Al is protecting the substrate from the environment as shown by X-ray mapping analysis (Fig.4.24.d and e). It can be mentioned based on the present investigation that conventional thick TiAlN and AlCrN coatings can

provide a very good oxidation resistance in Na_2SO_4 -60% V_2O_5 molten salt environment at high temperature although these hard coatings are traditionally specified for wear and erosion applications.

4.3.4 Conclusions

The high temperature oxidation behaviors of uncoated and coated ASTM-SA210 Grade A-1 boiler steel have been investigated in Na_2SO_4 -60% V_2O_5 molten salt at 900°C for 50 cycles. The behavior of nanostructured TiAlN and AlCrN coatings were compared with conventional counterparts and the following conclusions are made:

1. The plasma sprayed gas nitride conventional thick coatings i.e. TiAlN and AlCrN have developed a protective scale mainly consisting on aluminum oxide and chromium oxide.
2. The nanostructured TiAlN and AlCrN coatings has shown resistance to oxidation only up to some extent as the overall weight gain is less than as compared to the uncoated Grade A-1 boiler steel.
3. The oxidation rate (total weight gain values after 50 cycles) of the coated and uncoated Grade A-1 boiler steel follows the sequence as given below:
Uncoated Grade A-1 > Nanostructured AlCrN > Nanostructured TiAlN > Conventional TiAlN > Conventional AlCrN
4. In case of uncoated Grade-A1 boiler steel, the weight gain is highest with thickest scale. Some cracks are also observed in case of bare and nanostructured thin AlCrN coated boiler steel.
5. The conventional thick TiAlN and AlCrN coatings can provide a very good oxidation resistance in Na_2SO_4 -60% V_2O_5 (molten salt environment) at high temperature to Grade A-1 boiler steel substrate.
6. The oxide scale formed is adherent to the substrate in all coatings. But in case of bare Grade-A-1 boiler steel, the scale is found to be detached from the substrate after hot corrosion studies.

4.4 EROSION STUDIES IN SIMULATED COAL-FIRED BOILER ENVIRONMENT

The present work has been focused to compare the high temperature erosion behavior of conventional thick (by plasma spraying and gas nitrided) and nanostructured thin (by physical vapor deposition process) TiAlN and AlCrN coatings on ASTM-SA210 Grade A-1 boiler steel. The erosion studies were carried out using a high temperature air-jet erosion test rig at a velocity of 35 ms^{-1} and impingement angles of 30° and 90° . The tests were carried out at high temperatures. The two temperatures were taken for the test, sample temperature 400°C and air/erodent temperature 900°C simulated to service conditions of boiler tubes in which sample temperature and flow gas temperature correspond to the inner and outer temperature of water wall pipes. The alumina particles of average size $50 \mu\text{m}$ were used as erodent. Erosion rates in terms of volumetric loss (mm^3/g) for different uncoated and coated alloys are compared. The eroded samples were analyzed with SEM/EDX and optical profilometer. The erosion rate data for each coated alloy has been plotted along with uncoated alloy in order to assess the coating performance. Efforts have been made to understand the mode of erosion.

4.4.1 Results

4.4.1.1 Visual observations

The macrographs for uncoated and coated ASTM-SA210 Grade A-1 boiler steel subjected to erosion studies in simulated coal-fired boiler environment are shown in Fig.4.25. The effect of corrosion along with the erosion was observed. The shape of the scar (developed by constant strike of erodent) is circular in case of normal impact (at 90°) and elliptical in case of oblique impact (at 30°) of erodent. The uncoated Grade A-1 boiler steel shows a thin scale. The erosion seems to clean the scale off the surface in the eroded/corroded region. The impact of erodent removes the scale down to the substrate-scale interface. Away from this eroded region a thin layer of scale was observed on the surface and the eroded/corroded region showed rust colored discoloration (Fig.4.25.a).

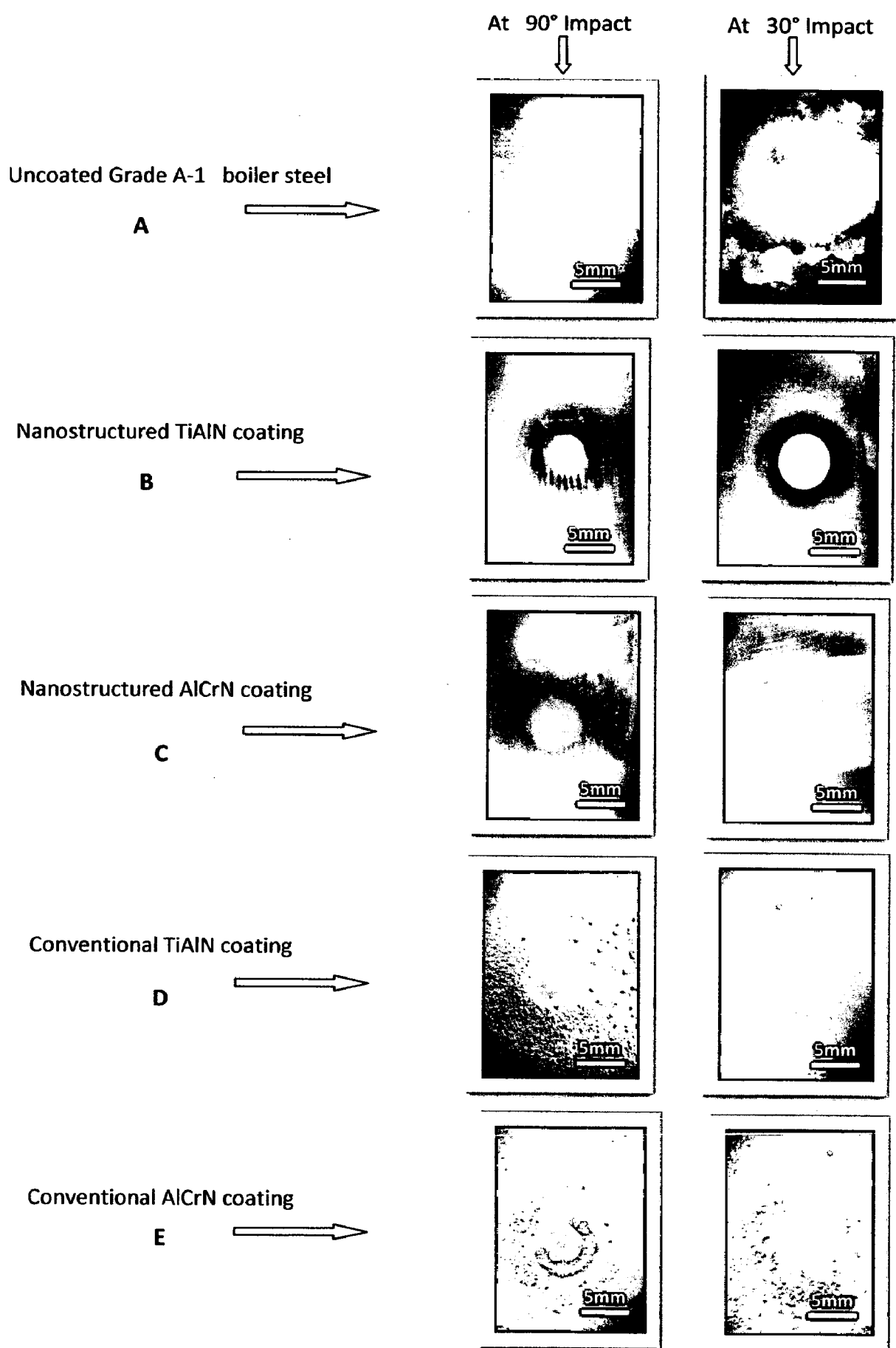


Fig. 4.25 Surface macrographs of eroded uncoated and coated ASTM-SA210 Grade A-1 boiler steel exposed to high temperature erosion studies in simulated coal-fired boiler environment

The nanostructured TiAlN coated Grade A-1 boiler steel showed clear marks of erosion as shown in Fig.4.25 (b). The color of the coated specimen changed from violet-grey to whitish at scar and blackish blue ring around the scar. The macrograph in case of eroded nanostructured AlCrN coating are shown in Fig.4.25 (c). The color of the scars was observed as light grey surrounded by dark colored ring. A visual observation of conventional thick TiAlN and AlCrN coated Grade A-1 boiler steel (Fig.4.25.d and e), showed the formation of dark grey colored scar surrounded by a light colored ring. Also, the un-eroded area around the scars appeared as rough surface.

4.4.1.2 Erosion rate

The erosion loss has been calculated by volume change method. The volume loss occurred after erosion testing was measured by using non contact optical profilometry as explained in chapter 3. The erosion depth was measured at six random locations to obtain the average erosion depth of an eroded scar. At each location (including eroded and un-eroded area) surface profiles were taken.

The erosion rate for uncoated and coated ASTM-SA210 Grade A-1 boiler steel at an impact velocity of 35 ms^{-1} and impingement angle of 30° and 90° when substrate temperature was 400°C and surrounding air at 900°C ; is shown in Fig. 4.26. The volume erosion rate for uncoated Grade A-1, nanostructured thin TiAlN, nanostructured thin AlCrN, conventional thick TiAlN and conventional thick AlCrN coatings; is 0.2955×10^{-3} , 0.03758×10^{-3} , 0.03078×10^{-3} , 2.073×10^{-3} and $3.12 \times 10^{-3} \text{ mm}^3/\text{gm}$ respectively at 90° impact angle. While at 30° impact, the volume erosion rate for uncoated Grade A-1, nanostructured thin TiAlN, nanostructured thin AlCrN, conventional thick TiAlN and conventional thick AlCrN coatings; is 0.494×10^{-3} , 0.0553×10^{-3} , 0.0392×10^{-3} , 1.898×10^{-3} and $2.557 \times 10^{-3} \text{ mm}^3/\text{gm}$ respectively.

From the graph, it can be inferred that the erosion rate of the uncoated Grade A-1 boiler steel eroded at oblique impact i.e. at 30° impingement angle is more as compared to erosion rate at 90° impact thus showing the typical behavior of ductile materials. The similar behavior was observed in case of the nanostructured thin TiAlN and AlCrN hard coatings with

negligible overall volume erosion loss (Fig.4.26). In case of the conventional thick TiAlN and AlCrN coated Grade A-1 boiler steel; the erosion rate at normal impact i.e. at 90° impingement angle is more as compared to erosion rate at 30° impact thus showing the typical behavior of brittle materials.

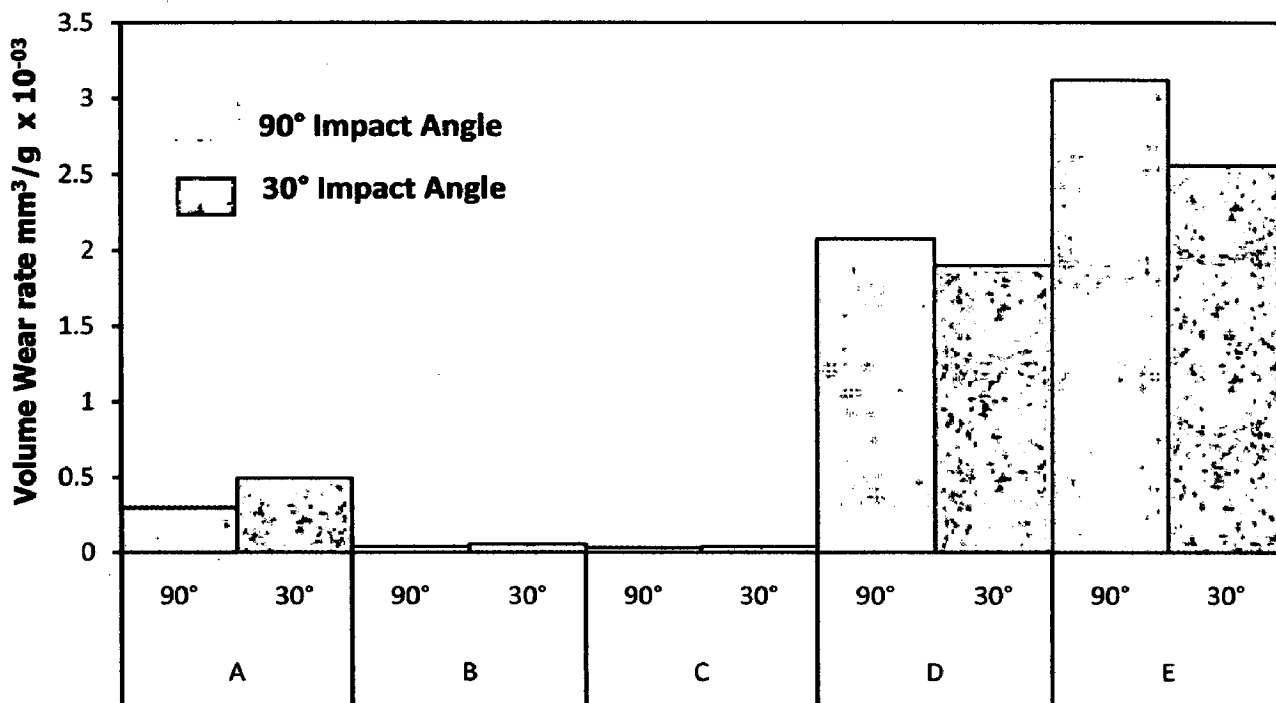


Fig. 4.26 Column chart showing the Volume wear rate of uncoated and coated ASTM-SA210 Grade A-1 boiler steel eroded at normal and oblique impact: (A) Uncoated Grade A-1 boiler steel, (B) Nanostructured TiAlN coating, (C) Nanostructured AlCrN coating, (D) Conventional TiAlN coating, (E) Conventional AlCrN coating

4.4.1.3 SEM/EDAX Analysis

SEM micrographs along with EDAX point analysis reveals the surface morphology of the uncoated and coated ASTM-SA210 Grade A-1 boiler steel subjected to erosion studies in simulated coal-fired boiler environment when substrate temperature was 400°C and surrounding air at 900°C; are shown in Fig. 4.27 and 4.28. The SEM observations were made on the eroded surface of all the uncoated and coated Grade A-1 boiler steel specimens at both the impact angles i.e. at 90° and 30°. Scanning electron microscopy

(SEM) revealed various erosion mechanisms like metal removal, oxide chipping, fracture and spalling within the oxide/coating layer and at the scale/metal interface etc. The micrographs have revealed fracture at the surfaces with impressions of formation of craters with crack network.

Micrographs (Fig.4.27) for the eroded surfaces of uncoated and coated Grade A-1 boiler steel at 90° impact angle, clearly indicates the formation of crater, oxide fracture and removal, coating fracture and retained erodent. It can be observed from the micrographs of the eroded surface of the uncoated boiler steel (Fig.4.27.a) that the erodent particles deform the exposed surface by ploughing and introducing the craters in the matrix by displacing material to the side. EDAX analysis revealed the presence of Fe, Al and O as the main elements on the eroded area, which indicates the formation of iron oxide due to oxidation and presence of retained erodent i.e. alumina. In case of nanostructured TiAlN coating (Fig.4.27.b); the micrograph revealed shallow impact craters. EDAX analysis indicates the presence of Fe, Al and O as the main elements along with some amount of Ti, Mn and Si. This is the indication that the nanostructured coating is severely damaged and fractured when the eroding particle strikes the surface of a coating at 90°; and hence failed to protect the substrate. Further, in case of nanostructured AlCrN coating; the signs of coatings removal and retained erodent have been observed (Fig. 4.27.c). EDAX analysis shows the presence of Al and Cr along with N as the main elements (which are main elements of coating) along with some amount of iron and oxygen. The erodent impacts causes cracking and fracture of some part of the coating, but fails to remove the coating completely.

The micrograph of the conventional TiAlN coating (Fig.4.27.d) revealed the oxide fracture and removal at various locations. When the eroding particle strikes the surface of the coating at 90° the material is severely damaged and fractured as shown in Fig. 4.27 (d). EDAX analysis shows the presence of Al, Ti and O as the main elements along with very less amount of Fe and C; indicating that the coating is still there after three hours continuous erodent impacts at an impact velocity of 35 ms⁻¹ and impingement angle of 90° when substrate temperature was 400°C and surrounding air at 900°C.

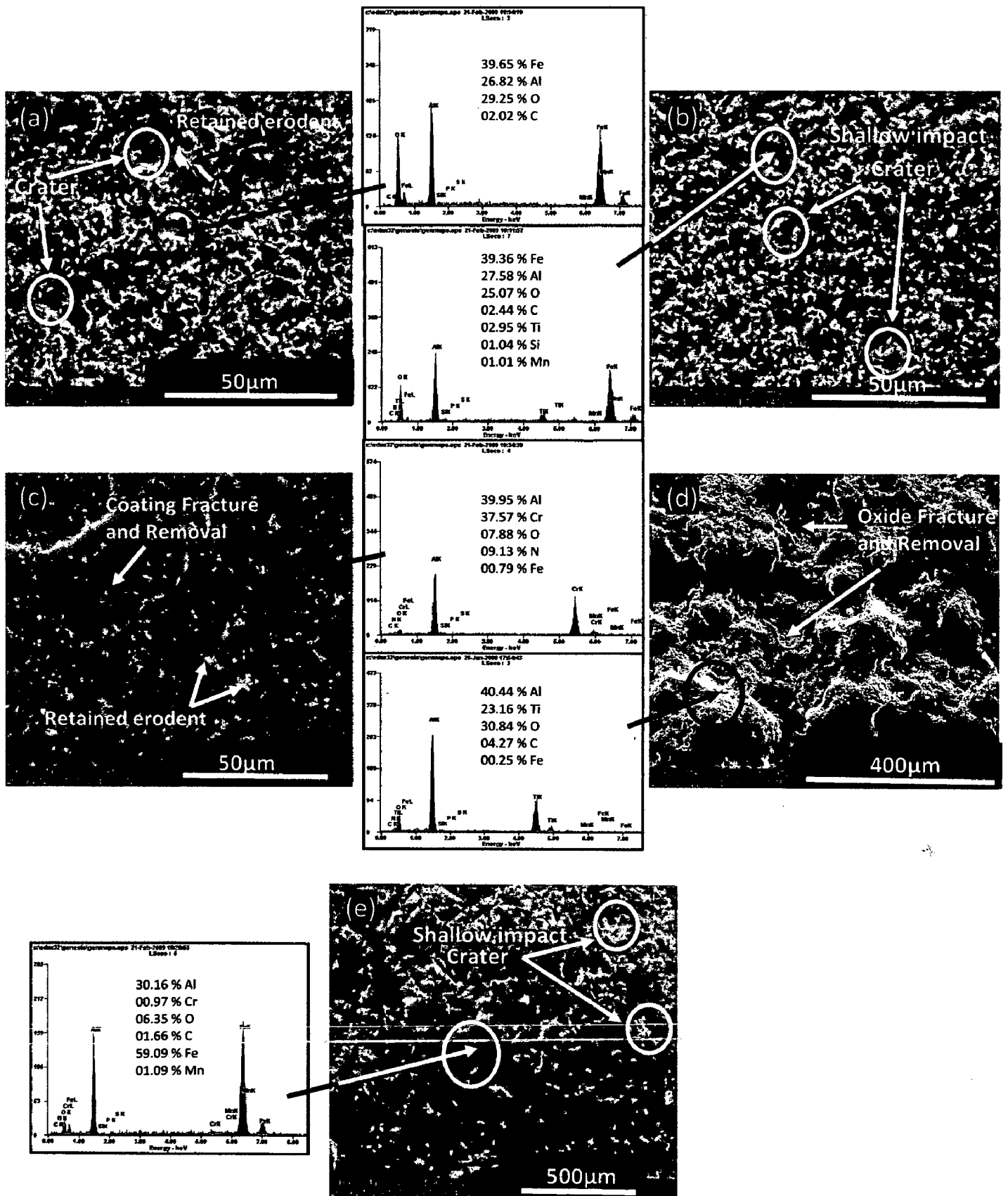


Fig. 4.27 Surface-scale morphology and EDAX patterns from different spots on eroded uncoated and coated ASTM-SA210 Grade A-1 boiler steel exposed to high temperature erosion studies in simulated coal-fired boiler environment at impact angle 90°: (a) Uncoated Grade A1 boiler steel, (b) Nanostructured TiAlN coating, (c) Nanostructured AlCrN coating, (d) Conventional TiAlN coating, (e) Conventional AlCrN coating

The coating has successfully protected the substrate. Further in case of conventional AlCrN coating, the erodent particle impacts have severely damaged the coating by causing cracking and fracture (Fig. 4.27.e). EDAX analysis revealed the presence of Al and Fe as the main elements with small amount of O, Mn and C; indicating that the coating has failed to protect the substrate and hence exposed the substrate.

In case of 30° impact, Micrographs (Fig.4.28) for the eroded surfaces of uncoated and coated Grade A-1 boiler steel clearly indicates presence of retained erodent, the formation of wider and shallow crater, crack propagation, oxide fracture and removal and coating fracture. In case of uncoated boiler steel; the micrographs (Fig.4.28.a) revealed the severe deformation at the surface resulting in formation of craters with minor cracks. EDAX analysis revealed the presence of Fe, Al and O as the main elements on the eroded area, which indicates the formation of iron oxide due to oxidation and presence of retained erodent i.e. alumina. Micrograph in case of nanostructured TiAlN coating (Fig.4.28.b); revealed shallow impact craters with minor cracks. EDAX analysis indicates the presence of Fe, Al and O as the main elements along with some amount of Ti and C. It can be inferred that the nanostructured TiAlN coating gets severely damaged and fractured when the eroding particle strikes the surface of a coating at 30° and failed to protect substrate. Further, in case of nanostructured AlCrN coating; the signs of crater and crack propagation have been observed (Fig. 4.28.c). EDAX analysis shows the presence of Al and Fe along with some amount of O, Cr, Mn and C. The erodent impacts causes cracking and fracture of the coating, and removed the coating completely thus exposing the substrate. The micrograph of the conventional TiAlN coating (Fig.4.28.d) revealed the oxide fracture and removal at various locations along with craters. When the eroding particle strikes the surface of the coating at 30° the material is severely damaged and fractured (Fig. 4.28.d). EDAX analysis shows the presence of Al, Ti and O as the main elements along with very less amount of Fe and C. It can be inferred that the coating is still there after three hours continuous erodent impacts at an impact velocity of 35 ms⁻¹ and impingement angle of 30° when substrate temperature was 400°C and surrounding air at 900°C.

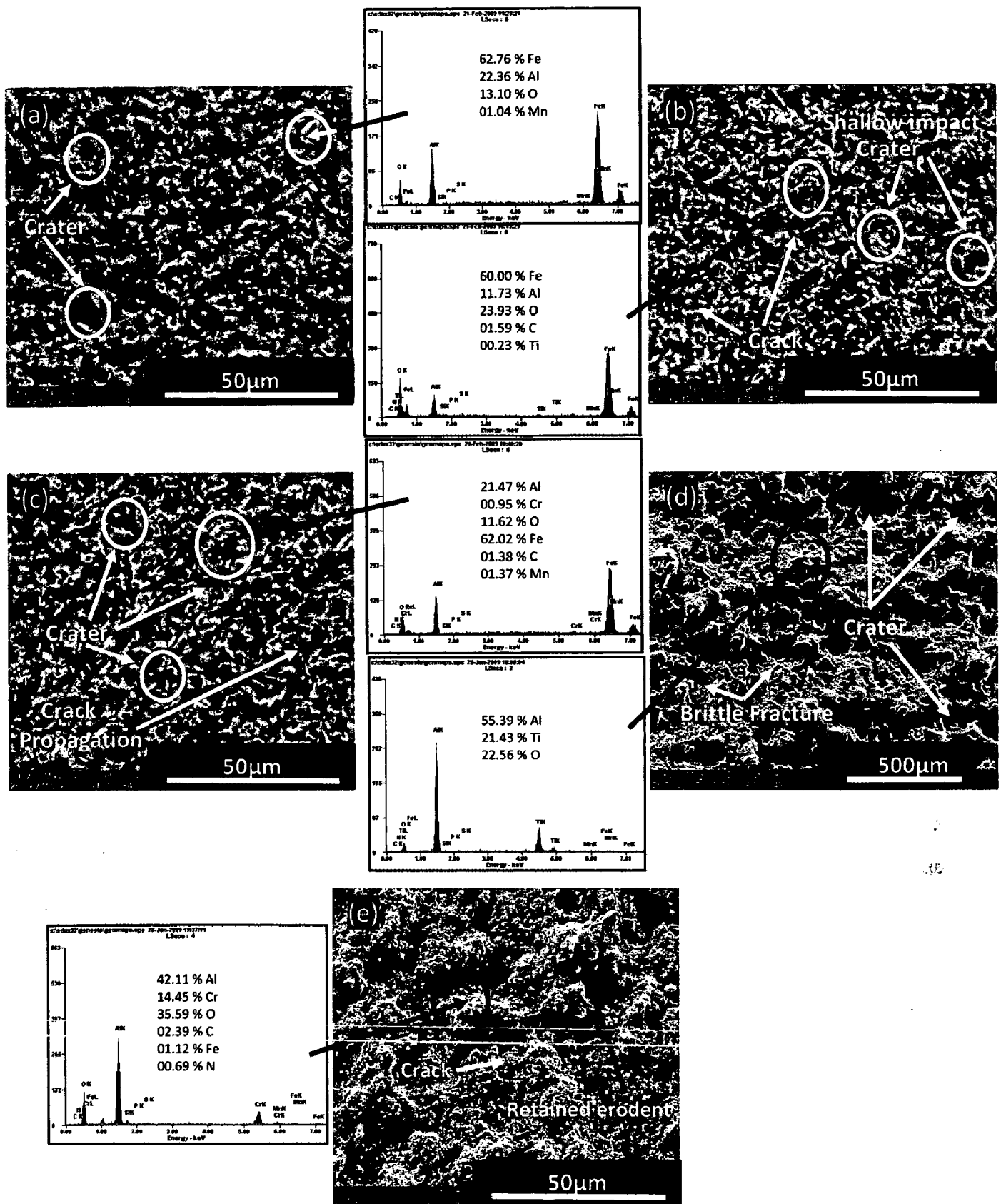


Fig. 4.28 Surface-scale morphology and EDAX patterns from different spots on eroded uncoated and coated ASTM-SA210 Grade A-1 boiler steel exposed to high temperature erosion studies in simulated coal-fired boiler environment at impact angle 30°: (a) Uncoated Grade A1 boiler steel, (b) Nanostructured TiAlN coating, (c) Nanostructured AlCrN coating, (d) Conventional TiAlN coating, (e) Conventional AlCrN coating

The coating has successfully protected the substrate. Further in case of conventional AlCrN coating, the erodent particle impacts have severely damaged the coating by causing cracking and fracture (Fig. 4.28.e). EDAX analysis revealed the presence of Al, Cr and O as the main elements with small amount of Fe and N; indicating that the coating has successfully protected the substrate.

4.4.2 Discussion

In erosion testing, the material is eroded by continuous impact of erodent particles; the erosion starts at the centre first, and then proceeds towards the edges of the samples. The shape of developed scar depends on the angle of impact. When erodent strikes the surface at an impact angle of 90° , material is eroded creating a circular depression; while at a 30° impact angle, material is eroded forming an elliptical shape depression. The erosion rate for uncoated and coated Grade A-1 boiler steel at an impact velocity of 35 ms^{-1} and impingement angle of 30° and 90° when substrate temperature was 400°C and surrounding air at 900°C ; is shown in Fig.4.26. The volume erosion rate for uncoated Grade A-1, nanostructured thin TiAlN, nanostructured thin AlCrN, conventional thick TiAlN and conventional thick AlCrN coatings; is 0.2955×10^{-3} , 0.03758×10^{-3} , 0.03078×10^{-3} , 2.073×10^{-3} and $3.12 \times 10^{-3} \text{ mm}^3/\text{gm}$ respectively at 90° impact angle. Based on the present data the erosion rates for 90° impact angle can be arranged in the following order:

Conventional AlCrN > Conventional TiAlN > Uncoated steel > Nanostructured TiAlN > Nanostructured AlCrN

It can be inferred from the above data that the relative erosion resistance of conventional thick AlCrN coating is least among the uncoated and coated Grade A-1 boiler steel specimens. Further, the SEM/EDAX analysis (Fig.4.27) indicates that in case of nanostructured AlCrN, conventional thick TiAlN coated Grade A-1 boiler steel; the coating is still there after three hours continuous erodent impacts at an impact velocity of 35 ms^{-1} and impingement angle of 90° when substrate temperature was 400°C and surrounding air at 900°C . These coatings have successfully protected the substrate. The nanostructured thin TiAlN and conventional AlCrN hard coatings were removed

completely by the continuous strikes of the eroding particles on the surface of the coating at 90° (Fig.4.27).

While at 30° impact; the volume erosion rate for uncoated Grade A-1, nanostructured thin TiAlN, nanostructured thin AlCrN, conventional thick TiAlN and conventional thick AlCrN coatings; is 0.494×10^{-3} , 0.0553×10^{-3} , 0.0392×10^{-3} , 1.898×10^{-3} and 2.557×10^{-3} mm³/gm respectively.

Based on the present data the erosion rates for 30° impact angle can be arranged in the following order:

Conventional AlCrN > Conventional TiAlN > Uncoated steel > Nanostructured TiAlN > Nanostructured AlCrN

It can be inferred from the above data that the relative erosion resistance of conventional thick AlCrN coating is least among the uncoated and coated Grade A-1 boiler steel specimens. The erosion resistance sequence for the uncoated and coated Grade A-1 boiler steel is independent of the impact angle in this case. Further, the FE-SEM/EDAX analysis (Fig.4.28) indicates that in case of conventional thick TiAlN and AlCrN coated Grade A-1 boiler steel; the coating is still there after three hours continuous erodent impacts at an impact velocity of 35 ms⁻¹ and impingement angle of 30° when substrate temperature was 400°C and surrounding air at 900°C. These coatings have successfully protected the substrate. The nanostructured TiAlN and AlCrN coatings were removed completely by the continuous strikes of the eroding particles on the surface of the coating at 30° (Fig.4.28).

The solid particle erosion rate of the uncoated and nanostructured thin TiAlN and AlCrN coated Grade A-1 boiler steel as shown in Fig.4.26 indicated that maximum erosion took place at 30° impact angle, which indicate ductile behavior as proposed by Murthy et al. (2001). Authors suggested that the material subjected to erosion initially undergoes plastic deformation and is later removed by subsequent impacts of the erodent on the surface. The ploughing occurs by the impact of the erodent particles and lips or ridges are formed at the bank of the craters. These lips are fractured or removed with further erosion. At low erosion temperatures, at high impact velocities and feed rates, there is no oxide scale. Even if there is any oxide scale, it will be very thin and it will be able to

deform in the same manner as that of the substrate target. The works of Shida and Fujikawa (1985), Singh and Sundararajan (1990) Levy et al., (1986) can be considered elevated temperature erosion of metals with minimum or negligible oxidation. Under such circumstances, erosion takes place from the metallic surface and this mechanism of erosion is called metal erosion. Most of the metallic materials, irrespective of temperature of erosion, exhibit a ductile behavior, i.e. a maximum erosion rate at oblique impact angles (Tabakoff W and Vittal, 1983). The erosion behavior in this regime is similar to the ambient temperature erosion behavior of metallic materials. The erosion response in the metal erosion regime is ductile as described by Bellman and Lavy (1981). Authors suggested that the creation of platelet-like edges by impact extrusion protrude outward over adjacent material and the loss of these platelets appears to be responsible for the mass loss. Authors have further explained that repeated deformation of craters and forming of new craters is common and some platelets are extruded several times before getting knocked off.

Sundararajan and Roy (1997) proposed a model of metal erosion and oxide erosion. According to his model if steady state thickness of the oxide scale is smaller than the critical thickness of the oxide scale, three modes of interaction between erosion and oxidation are possible. In the first case, which applies either when there is no oxide scale or when the depth of deformation is much higher than the thickness of the oxide scale (as in the case of uncoated and nanostructured thin coated Grade A-1 boiler steel in present case), metal erosion becomes important (presented in Figs 4.29. a and b). In the second case, when the depth of deformation is smaller than the steady state thickness of the oxide scale, erosion of the oxide scale takes place as illustrated in Fig. 4.29 (c).

The solid particle erosion rate of the conventional thick TiAlN and AlCrN coated Grade A-1 boiler steel as shown in Fig.4.26 indicated that maximum erosion took place at 90° impact angle, which indicate brittle behavior of the conventional coatings. As metal nitride coatings are hard and brittle in nature so erosion of brittle materials is identified as a complex mechanism in which different stages like tribochemical reaction, microfracture etc. operate. In case of brittle materials; loss in solid particle erosion occurs predominantly through the formation and interaction of a subsurface micro crack network (Guessasma et al., 2006). Authors further suggested that the material removal is related to the formation

and propagation of cracks. The cracks develop on the surface when the surface stresses reach a critical value to initiate microcracking. When these cracks propagate and intersect with the surface, material is lost. Hence for a brittle material the erosion resistance is a function of its resistance to crack. Also, erosion in plasma sprayed coatings has been attributed to the failure of individual splat boundaries (Ramm et al., 1993). In the present investigation, the conventional coatings showed brittle erosion morphology as indicated by their cracked and chipped surfaces (Fig.4.27 and 4.28).

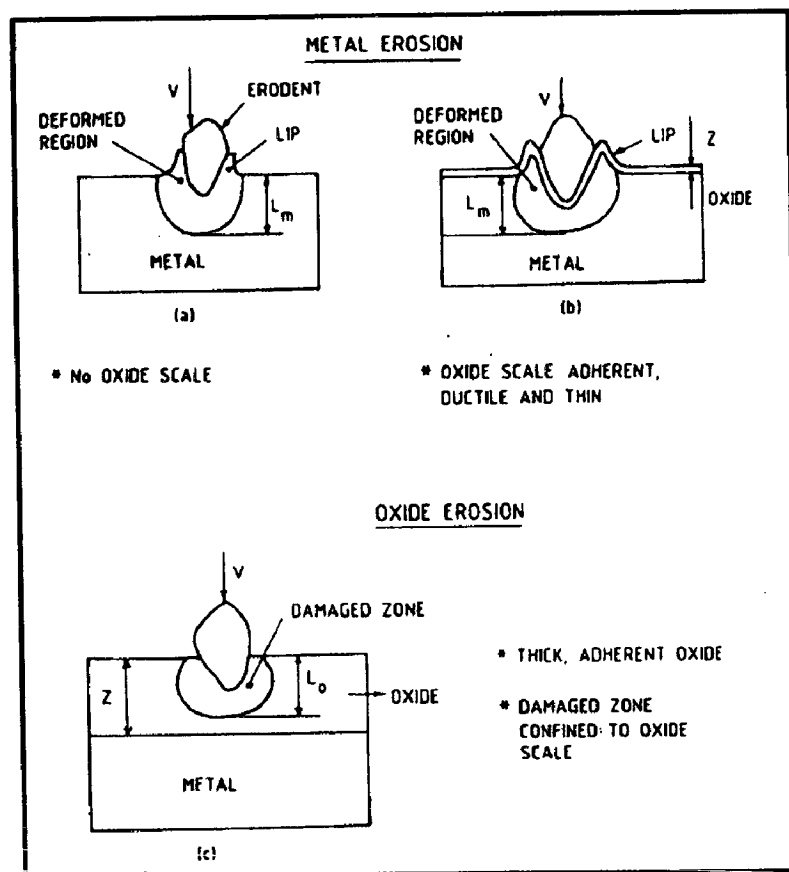


Fig. 4.29 Schematic representation of (a) & (b); metal erosion, and (c) oxide erosion illustrating the nature of interaction between the oxide scale and the substrate during erosion (Sundararajan and Roy 1997)

Under continual impacting of particles, the radial and lateral cracks were developed, and then fractured and loosened pieces were chipped off. Finally, many small voids and pits formed. Similar observations have been reported by Habib et al., (2006) and Branco et al., (2004). Also, at relatively higher temperatures and lower particle feed rates and impact

velocity, the oxide scale that forms during erosion is brittle and non-adherent. In such cases, the oxide scale gets removed after it attains a critical thickness. The erosion behavior in this regime exhibits a brittle erosion response.

So in conventional thick TiAlN and AlCrN coatings; the erosion rate was high at normal impact and low at oblique impact. The difference in erosion rates for shallow and normal impact angles can be attributed to the different material removal mechanisms in these two cases. At low angle impact, the kinetic energy of the erodent particles contributes mainly to the ploughing mechanism and very little to normal repeated impact. The ploughing mechanism is associated with the plastic smearing and cutting of the materials, while the repeated impact mechanism is responsible for initiating and propagating the grain boundary microcracks. Conventional metal nitride coatings have high hardness, and thus they are not easily plastically deformed. Hence the material removal rate is low. At high angle impact, the kinetic energy of the impinging particles contributes mainly to repeated impact. Brittle nature of the materials allows the cracks readily to propagate to form crack networks. The subsequent impacts will easily remove the surface material via the ejection of the upper layer grains.

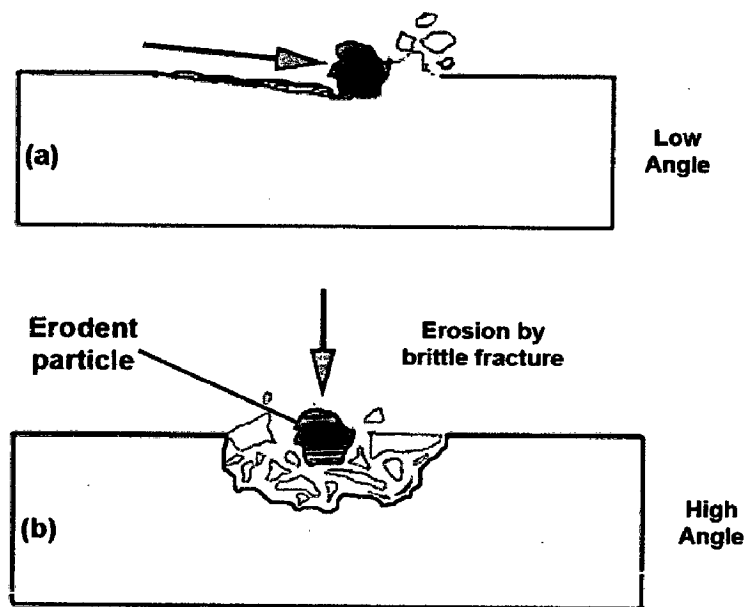


Fig. 4.30 Schematic representation of coating fracture dependent on impact angle; (a) Low angle, (b) High angle

Hence the material removal rate is high. Figure 4.30 shows schematically the fracture of coatings dependent on impact angle. It is shown schematically how an impinging solid particle can damage coating surfaces. From the present study, it can be inferred that that in case of conventional thick coatings; the erosion rates of alloys were greatest at 90° impact angle, which is the characteristic erosion behavior of brittle materials. The solid particle erosion rate of the uncoated and nanostructured thin TiAlN and AlCrN coated Grade A-1 boiler steel as shown in Fig.4.26 indicated that maximum erosion took place at 30° impact angle, which indicate ductile behavior.

4.4.3 Conclusions

The erosion behavior of conventional thick (by plasma spraying and gas nitrided) and nanostructured thin (by physical vapor deposition process) TiAlN and AlCrN coatings on Grade A-1 boiler steel in simulated coal-fired boiler environment has been analyzed. The following conclusions are made:

1. The erosion rates for 90° impact angle can be arranged in the following order:

Conventional AlCrN > Conventional TiAlN > Uncoated steel > Nanostructured TiAlN > Nanostructured AlCrN

The relative erosion resistance of conventional thick AlCrN coating is least among the uncoated and coated Grade A-1 boiler steel specimens.

2. The nanostructured AlCrN, conventional thick TiAlN coatings have successfully protected the substrate at 90° impact. The nanostructured thin TiAlN and conventional AlCrN hard coatings were removed completely by the continuous strikes of the eroding particles on the surface of the coating at 90° impact.
3. At 30° impact, the volume erosion rate can be arranged in the following order:

Conventional AlCrN > Conventional TiAlN > Uncoated steel > Nanostructured TiAlN > Nanostructured AlCrN

The relative erosion resistance of conventional thick AlCrN coating is least among the uncoated and coated Grade A-1 boiler steel specimens.

4. The conventional thick TiAlN and AlCrN coatings have successfully protected the substrate. The nanostructured TiAlN and AlCrN coatings were removed completely by the continuous strikes of the eroding particles on the surface of the coating at 30° impact.
5. From the present study, it can be inferred that that in case of conventional thick coatings; the erosion rates of alloys were greatest at 90° impact angle, which is the characteristic erosion behavior of brittle materials. The solid particle erosion rate of the uncoated and nanostructured thin TiAlN and AlCrN coated Grade A-1 boiler steel is higher at 30° impact angle, which indicate ductile behavior.

4.5 CORROSION STUDIES IN SIMULATED MARINE ENVIRONMENT

The research works on the corrosion behavior of high temperature corrosion resistant coatings in marine environments is scarce in the literature. Therefore, it is meaningful to investigate the ambient environmental corrosion behavior and mechanism of the materials as is done in present work by evaluating the corrosion behavior of substrate and coatings in simulated marine environment. Therefore, the present work has been focused to compare the corrosion behavior of conventional thick (by plasma spraying and gas nitrided) and nanostructured thin (by physical vapor deposition process) TiAlN and AlCrN coatings on ASTM-SA210 Grade A-1 boiler steel, by electrochemical methods i.e. linear polarization resistance (LPR) and potentiodynamic polarization tests in an aerated 3.0 wt% NaCl solution at room temperature; and salt spray (Fog) tests. The detailed experimental procedure is explained in chapter 3.

4.5.1 Results and Discussion

4.5.1.1 Linear polarization resistance (LPR) and potentiodynamic polarization tests

Linear polarization resistance (LPR) and potentiodynamic polarization tests were conducted in an aerated 3 wt% NaCl solution at room temperature in order to evaluate the corrosion behavior of the substrate and coatings. The initial corrosion current density and LPR (R_p) was measured by LPR test. The linear polarization scans are conducted in very small potential range (-20mV to + 20mV vs Open Circuit Potential), which does not damage the surface of the sample. Whereas the potentiodynamic polarization scans require scanning over a longer potential range (Sahoo and Balasubramaniam 2007).

The corrosion parameters obtained in LPR test are shown in Table 4.7. The corrosion current densities of all the coatings were found much lower than that of the substrate. The uncoated Grade A-1 boiler steel has shown maximum current density i.e. $22.40 \mu\text{A}/\text{cm}^2$. The nanostructured thin TiAlN coating at initial stage has performed very well and showed best corrosion resistance in terms of corrosion current density and polarization resistance. The

corrosion protection is provided by all the coatings at initial stage as indicated by the LPR test results in terms of corrosion current density and polarization resistance (Table 4.7). Potentiodynamic polarization curves of the substrate and each film are shown in Fig.4.31 and the corrosion parameters in Table 4.8. The corrosion current density and the corrosion potential were obtained by the intersection of the extrapolation of anodic and cathodic Tafel curves. The corrosion current densities of the coatings were found much lower than that of the substrate steel. The corrosion current densities of the substrate and the coatings were found much lower as compared to the LPR test (at initial stage) results. A protective oxide layer may have formed which has blocked further corrosion. The corrosion product formed may have reduced the passage of the electrolyte to attack the samples, and hence providing protection.

The corrosion rate (i_{corr}) of the specimens was obtained using the Stern-Geary equation(Eq.4.3).

$$i_{corr} = \frac{1}{2.303} \times \frac{\beta_a \beta_c}{R_p \times (\beta_a + \beta_c)} = \frac{Z}{R_p} \quad (4.3)$$

Where β_a = anodic Tafel slope, β_c = cathodic Tafel slope, R_p = polarization resistance and, Z is a function of the Tafel slopes.

Table 4.7 Results of Linear Polarization Resistance Test (LPR) of uncoated and coated ASTM-SA210 Grade A1 boiler steel

Substrate / Coating	E_{corr} (mV)	i_{corr} ($\mu\text{A}/\text{cm}^2$)	β_a (V/decade)	β_c (V/decade)	R_p ($\text{k}\Omega\text{-cm}^2$)
Uncoated Grade A-1 boiler steel	-589.2	22.40	0.1	0.1	0.969
Nanostructured TiAlN coating	-448.7	01.92	0.1	0.1	11.27
Nanostructured AlCrN coating	-537.6	09.42	0.1	0.1	02.30
Conventional TiAlN coating	-667.5	12.87	0.1	0.1	01.68
Conventional AlCrN coating	-567.3	03.77	0.1	0.1	05.75

In potentiodynamic polarization tests the nanostructured thin TiAlN coating has performed very well and showed best corrosion resistance as evident from corrosion current density and polarization resistance values reported in Table 4.8. The conventional thick TiAlN and AlCrN coatings have shown performance comparable to nanostructured TiAlN coating in terms of corrosion current density and polarization resistance. The corrosion current densities are 2.071 and 1.308 $\mu\text{A}/\text{cm}^2$ for conventional TiAlN and AlCrN coatings respectively, which are very less as compared to the corrosion current density in case of uncoated ASTM-SA210 Grade A-1 boiler steel (9.498 $\mu\text{A}/\text{cm}^2$).

From polarization test results, the protective efficiency, P_i (%) of the coatings can be calculated by Eq. (4.4):

$$P_i (\%) = \left[1 - \left(\frac{i_{\text{corr}}}{i_{\text{corr}}^0} \right) \right] \times 100 \quad (4.4)$$

Where i_{corr} and i_{corr}^0 indicate the corrosion current density of the film and substrate, respectively [Yoo et al., 2008]. Figure 4.32 shows the variation in protective efficiency and polarization resistance of uncoated and coated ASTM-SA210 Grade A-1 boiler steel subjected potentiodynamic polarization test.

Table 4.8 Results of Potentiodynamic Polarization Tests of uncoated and coated ASTM-SA210 Grade A-1 boiler steel

Substrate / Coating	E_{corr} (mV)	i_{corr} ($\mu\text{A}/\text{cm}^2$)	β_a (V/decade)	β_c (V/decade)	R_p ($\text{k}\Omega\text{-cm}^2$)	P_i (%)	F (%)
Uncoated Grade A1	-606.0	9.498	0.0759	0.3089	02.78	--	--
Nanostructured TiAlN	-405.6	0.676	0.0642	0.2136	40.38	92.87	0.015
Nanostructured AlCrN	-442.1	5.982	0.0735	0.3790	04.46	37.01	0.432
Conventional TiAlN	-872.4	2.071	0.1593	146.5×10^{18}	33.33	78.19	0.371
Conventional AlCrN	-562.9	1.308	0.1517	0.2520	31.43	86.22	2.390

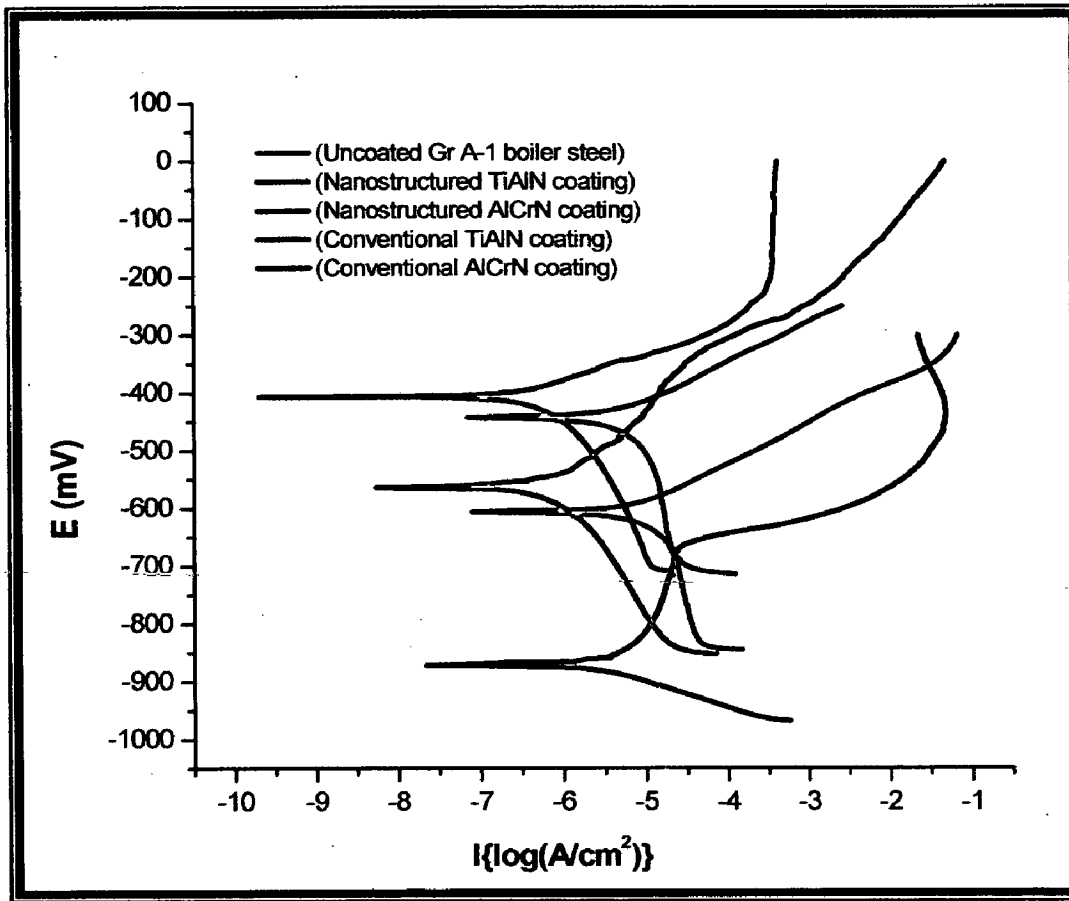


Fig. 4.31 Potentiodynamic Polarization Curves for uncoated and coated ASTM-SA210 Grade A-1 boiler steel

The nanostructured thin TiAlN coating showed the highest protective efficiency of 92.87 % caused by lowest corrosion current density of $0.676\mu\text{A}/\text{cm}^2$. The observed protection by the nanostructured TiAlN and AlCrN coatings in an aerated 3 wt.% NaCl solution at room temperature, are almost in agreement with the findings of Yoo et al. (2008) and Xing-zhao et al. (2008). The conventional thick TiAlN and AlCrN coatings have also shown protection to the substrate with protective efficiency 78.19 % and 86.22 % respectively.

For further justification the porosity values has also been measured quantitatively by the electrochemical methods [Yoo et al., 2008] according to Eq. (4.5) and reported in Table 4.8.

$$F (\%) = \left[\frac{R_{pm}}{R_p} \times 10^{-|\Delta E_{corr}/\beta_a|} \right] \times 100 \quad (4.5)$$

Where ΔE_{corr} the corrosion potential difference between the substrate and coating layer, R_p the polarization resistance of the coating-substrate system, β_a the anodic Tafel constant of substrate, R_{pm} is the polarization resistance of the substrate and F represent porosity. The porosity measurement of the coatings is presented in Table 4.8.

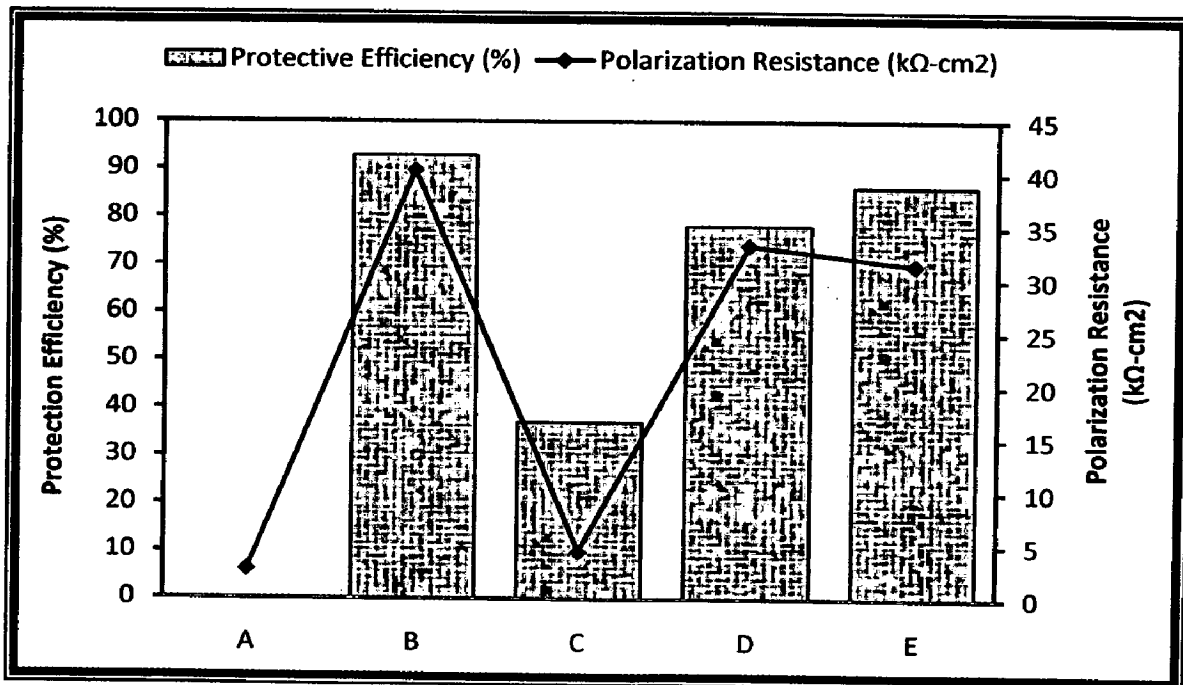


Fig. 4.32 Protective efficiency and Polarization resistance of uncoated and coated ASTM-SA210 Grade A-1 boiler steel: (A) Uncoated Grade A1 boiler steel, (B) Nanostructured TiAlN coating, (C) Nanostructured AlCrN coating, (D) Conventional TiAlN coating, (E) Conventional AlCrN coating

The nanostructured TiAlN film has shown minimum porosity of 0.015% and conventional AlCrN has shown maximum 2.39% porosity value. In case of nanostructured AlCrN and conventional TiAlN coatings, the porosity measurement by electrochemical test

analysis and with image analyser, having software Dewinter Materials Plus 1.01 based on ASTM B276, is having closer results. The difference in the measured porosity by these two methods in case of nanostructured TiAlN and conventional AlCrN coatings may be because that image analysis (IA) measures both open as well as closed porosity and cannot distinguish between the two, whereas electrochemical test is able to assess pore connectivity in a coating that exists due to the interlamellar pores and intralamellar cracks (Deshpande et al., 2004). The porosity also affects the corrosion current density, as more is the connected porosity the higher is the corrosion current.

4.5.1.2 Salt spray (Fog) testing

The ASTM B117 Salt Fog test was used to evaluate the performance of the uncoated and nanostructured thin TiAlN and AlCrN coated ASTM-SA210 Grade A-1 boiler steel. The salt fog test is an accelerated corrosion test by which samples exposed to the same conditions can be compared. In the B117 test, the samples are exposed to a salt fog generated from a 5% sodium chloride solution with a pH between 6.5 and 7.2. All the samples were placed in the salt fog chamber for 24 Hrs, 48 Hrs and 72 Hrs. Photographs were taken before and subsequent to exposure to document the surface conditions. Initial weight and dimensions were also measured. After exposure; samples were monitored and analyzed by using XRD and SEM/EDAX techniques. Then all the samples were cleaned in running water not warmer than 38°C to remove salt deposits from the surface and then immediately dried with compressed air.

The macro morphologies of the uncoated and nanostructured thin TiAlN and AlCrN coated Grade A-1 boiler steel exposed to salt fog test for 24 Hrs, 48 Hrs and 72 Hrs; are depicted in Fig.4.33. The uncoated Grade A-1 boiler steel suffered severe corrosion in all the three test conditions i.e. 24 Hrs, 48 Hrs and 72 Hrs (Fig. 4.33.A). The brownish colored corrosion product on the surface of the samples and corrosion pits are visible. The nanostructured coated samples have shown resistance to the corrosion as compared to the uncoated Grade A-1 boiler steel. The nanostructured TiAlN coatings have shown negligible corrosion products in case of 24 Hrs study, but for 48 Hrs and 72 Hrs studies, some

corrosion products formation has been observed (Fig. 4.33.B). In case of nanostructured AlCrN coating, the surface of the samples was no longer uniform as before the test in case of salt fog testing for 48 Hrs and 72 Hrs (Fig. 4.33.C). Some corrosion products can also be seen in case of the sample exposed to the salt mist corrosion for 24 Hrs.

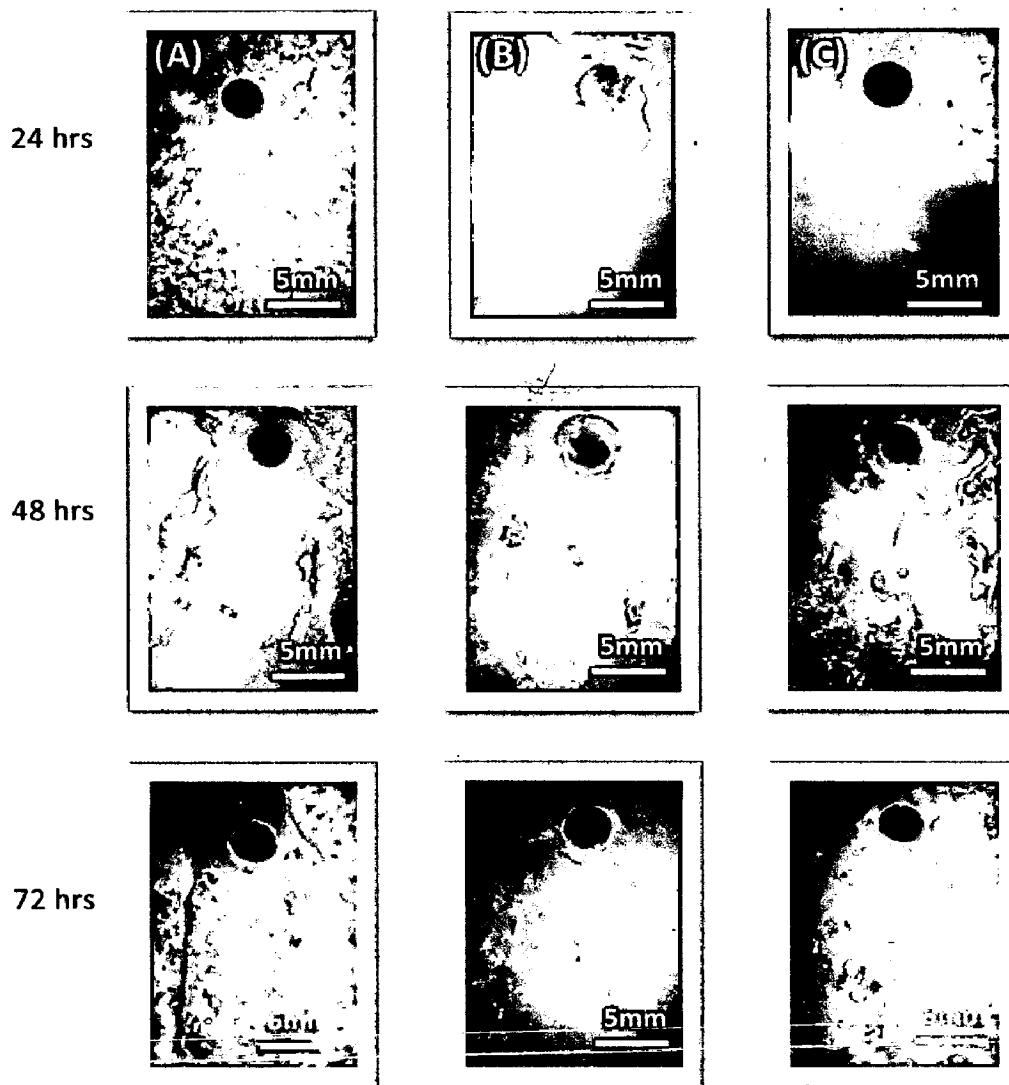


Fig. 4.33 Surface macrographs of uncoated and coated ASTM-SA210 Grade A-1 boiler steel subjected to salt-fog testing (5% NaCl) : (A) Uncoated Grade A-1 boiler steel subjected to 24hrs, 48hrs and 72 hrs testing; (B) Nanostructured TiAlN coated Grade A-1 boiler steel subjected to 24hrs, 48hrs and 72 hrs testing; (C) Nanostructured AlCrN coated Grade A-1 boiler steel subjected to 24hrs, 48hrs and 72 hrs testing

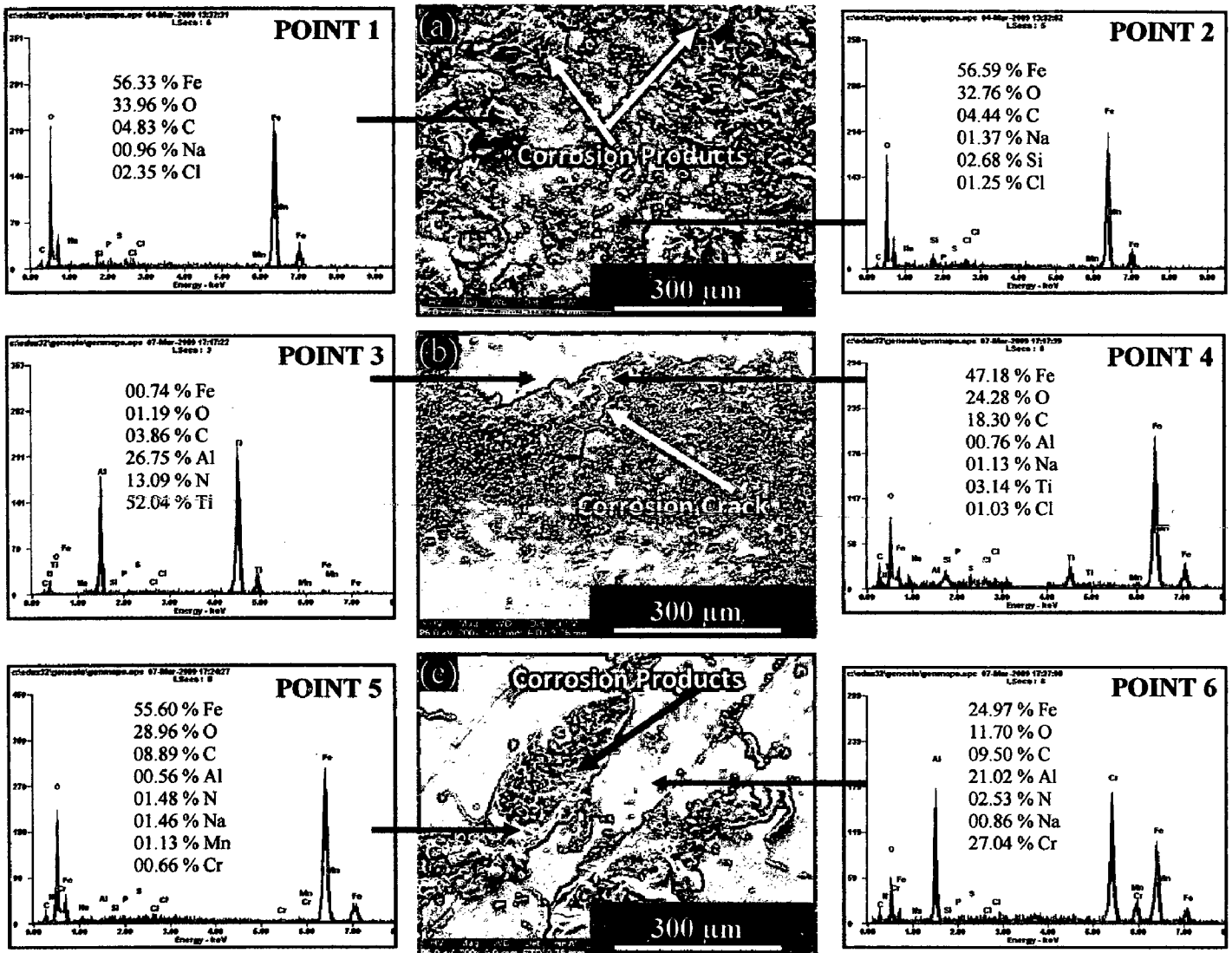


Fig. 4.34 Surface macrographs of uncoated and coated ASTM-SA210 Grade A-1 boiler steel subjected to salt-fog testing (5% NaCl) for 24 hrs: (a) Uncoated Grade A1 boiler steel (b) Nanostructured TiAlN coating (c) Nanostructured AlCrN coating

Figure 4.34 shows the surface SEM images of uncoated and nanostructured TiAlN and AlCrN coated Grade A-1 boiler exposed to salt fog test for 24 Hrs. Figure 4.34 (a) reveals; massive corrosion products accumulated on the surface of uncoated boiler steel. The EDAX analysis at some locations points out the presence of iron and oxygen on the corroded surface (Point 1 and 2 in Fig. 4.34). In case of nanostructured TiAlN coating; corrosion cracks were also observed on the surface (Fig. 4.34.b).

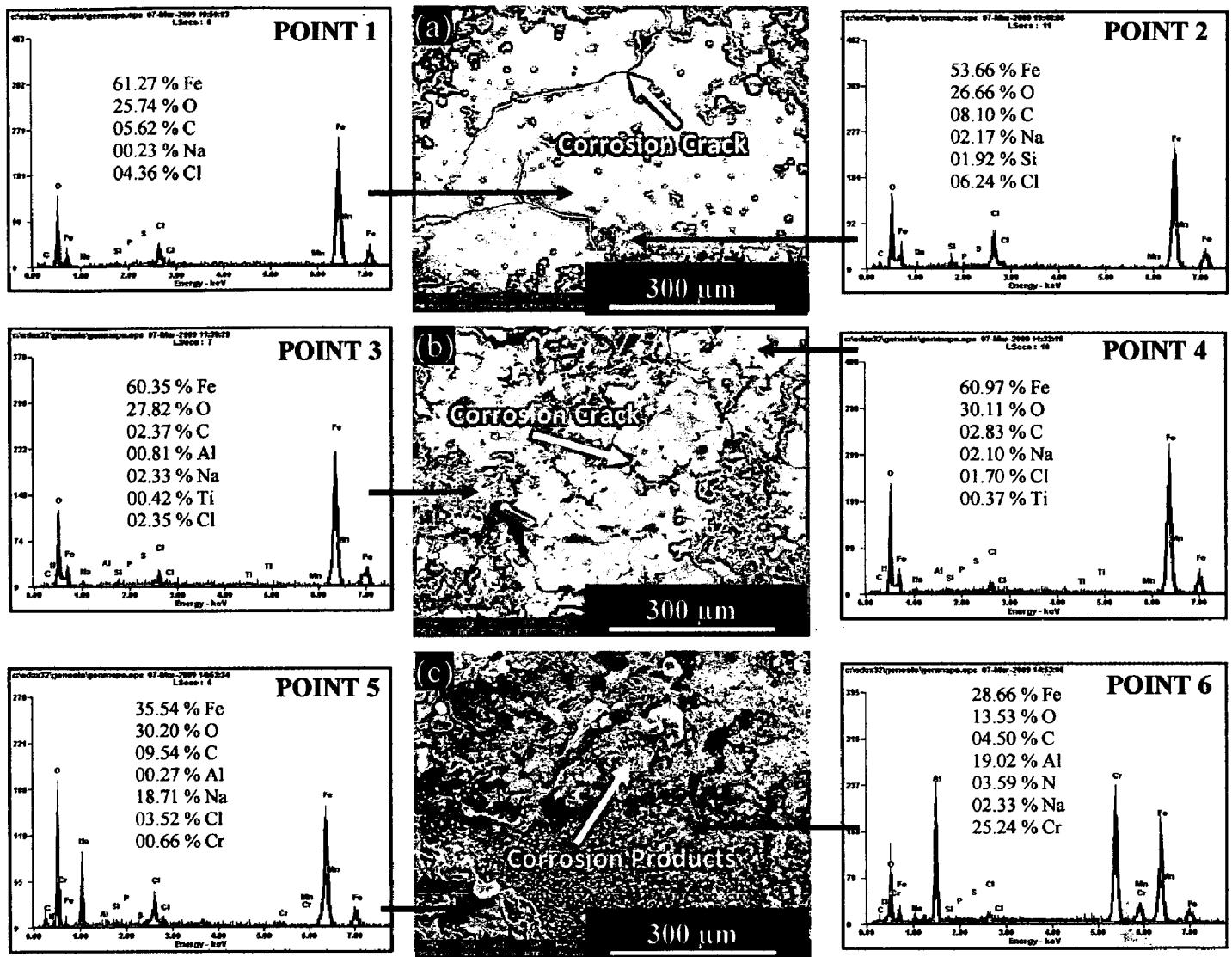


Fig. 4.35 Surface macrographs of uncoated and coated ASTM-SA210 Grade A1 boiler steel subjected to salt-fog testing (5% NaCl) for 48 hrs: (a) Uncoated Grade A1 boiler steel (b) Nanostructured TiAlN coating (c) Nanostructured AlCrN coating

The EDAX point analysis (Point 4 on Fig. 4.34) reveals the presence of Fe and O as the main elements in the corrosion products with negligible amount of Al and Ti. The un-corroded un-reacted surface (Point 3) is rich in Ti, Al and N with negligible amount of Fe and oxygen. Figure 4.34 (c) shows the SEM image of the nanostructured AlCrN coating. The corrosion products were composed of Fe and O with negligible amount of AL, Cr, N and Mn (Point 5 in Fig. 4.34). Figure 4.35 shows the surface SEM images of uncoated and nanostructured TiAlN and AlCrN coated Grade A-1 boiler steel exposed to salt fog test for 48 Hrs.

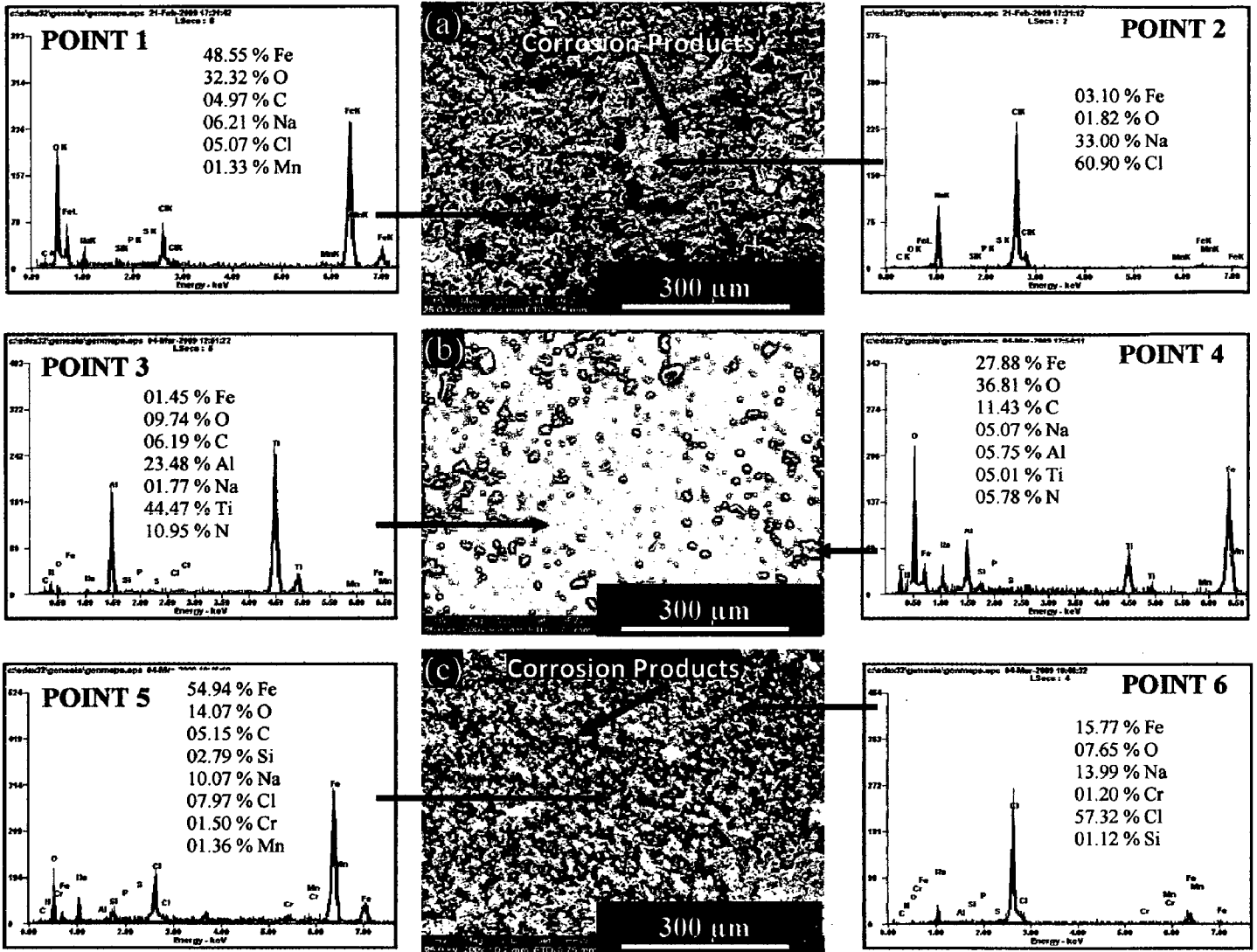


Fig. 4.36 Surface macrographs of uncoated and coated ASTM-SA210 Grade A-1 boiler steel subjected to salt-fog testing (5% NaCl) for 72 hrs: (a) Uncoated Grade A1 boiler steel (b) Nanostructured TiAlN coating (c) Nanostructured AlCrN coating

The uncoated Grade A-1 boiler steel has shown severe corrosion with corrosion cracks and corrosion products on the surface. The EDAX analysis shows the presence of Fe and O as the main elements along with some Mn, Cl and Na. As can be seen in Fig. 4.35 (b and c), corrosion cracks were observed on the surface of as-deposited nanostructured TiAlN and AlCrN coatings after salt spray tests. Massive corrosion products were accumulated around the corrosion crevice.

Obviously, severer corrosion would proceed in the as-deposited nanostructured thin coatings through the cracks, and cause coating cracking and fracture damage in the subsequent service at elevated temperatures. EDAX analysis (Point 3 and 4 on Fig. 4.35) of nanostructured TiAlN coating indicates the presence of Fe and O. The corrosion products in case of nanostructured AlCrN coating were found rich in iron and oxygen with some amount of Al, Cr and Mn. The EDAX point analysis at point 6 in Fig.4.35; reveals the presence of Al, Cr and Fe as the main element with less amount of oxygen. The surface SEM images of uncoated and nanostructured TiAlN and AlCrN coated Grade A-1 boiler steel exposed to salt fog test for 72 Hrs; are shown in Fig.4.36. Massive corrosion products were accumulated on the surface in case of uncoated and nanostructured AlCrN coated Grade A-1 boiler steel after salt fog tests. EDAX analysis (Fig.4.36) shows the corrosion products were composed of mainly Fe and O in all test samples.

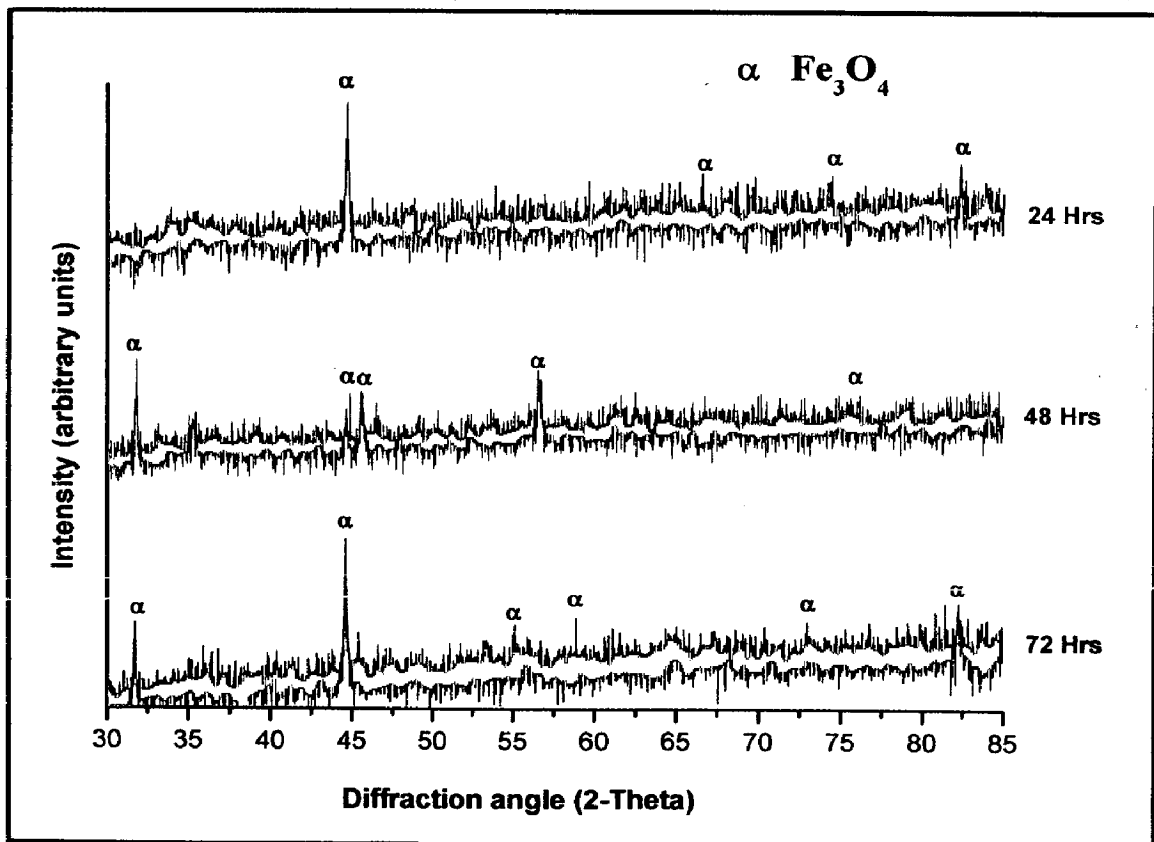


Fig. 4.37 (a) X-Ray Diffraction pattern of uncoated ASTM-SA210 Grade A-1 boiler steel subjected to salt-fog testing (5% NaCl) for 24 Hrs, 48 Hrs and 72 Hrs

XRD diffractograms for coated and uncoated ASTM-SA210 Grade A-1 boiler steel subjected to salt fog tests for 24 Hrs, 48 Hrs and 72 Hr; are depicted in Fig.4.37 on reduced scale. As indicated by the diffractograms in Fig.4.37 (a), Fe_3O_4 is the main phases present in the oxide scale of uncoated Grade A-1 boiler steel. In nanostructured TiAlN coating, AlN, TiN and Fe_3O_4 are the main phases revealed with minor phases i.e. TiO_2 and Al_2O_3 (Fig. 4.37.b). Further, the main phases identified for the nanostructured AlCrN coating are CrN, AlN along with Al_2O_3 , Cr_2O_3 and Fe_3O_4 . The formation of Fe_3O_4 in the scale of corroded specimens in salt spray tests is found to be in agreement with the results reported by Panda, Bijayani et al. (2008) and Vera et al (2009).

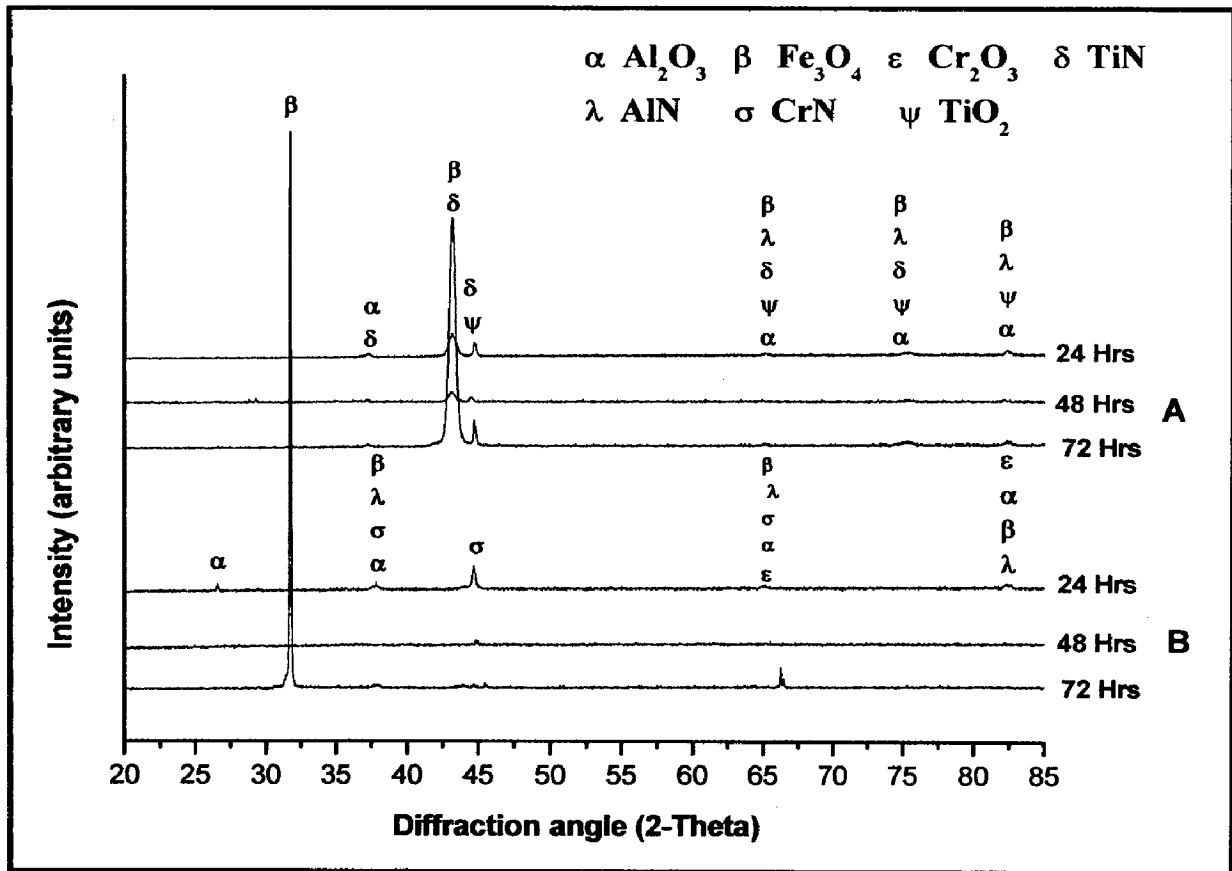


Fig. 4.37 (b) X-Ray Diffraction pattern of coated ASTM-SA210 Grade A-1 boiler steel subjected to salt-fog testing (5% NaCl) for 24 Hrs, 48 Hrs and 72 Hrs: (A) Nanostructured TiAlN coating, (B) Nanostructured AlCrN coating

The weight loss measurements were carried out for the uncoated and nanostructured thin TiAlN and AlCrN coated Grade A-1 boiler steel exposed to the salt fog tests for 24 Hrs, 48 Hrs and 72 Hrs. Fig. 4.38, depicts the column chart showing the weight loss per unit area for the uncoated and coated Grade A-1 boiler steel. It can be inferred from the plots that the uncoated Grade A-1 boiler steel has shown maximum weight loss per unit area in all three test conditions i.e. 24 Hrs, 48 Hrs and 72 Hrs tests; as compared to the coated counterparts. Both the coatings have shown good protection to the substrate in terms of weight loss per unit area.

As can be seen in Fig.4.38 for uncoated and coated Grade A-1 boiler steel; the weight loss per unit area increases with the duration of the test. The weight loss per unit area in case of nanostructured thin TiAlN coating is less as compared to the nanostructured AlCrN coating and uncoated boiler steel in all test conditions. It can be mentioned based on the present investigation that nanostructured thin TiAlN and AlCrN coatings can provide a very good corrosion resistance when exposed to the simulated marine environment i.e. salt fog test. Salt spray corrosion is an electrochemical reaction process (Bao et al., 2007). Generally, the corrosion resistance is influenced significantly by several factors, such as compositions, internal microstructure, and especially the surface condition.

The proposed corrosion mechanism of the coated specimen is as explained in Fig.4.39; which is similar to the one reported by Bao et al., (2007). Micro-cracks got initiated by residual stress during deposition of coatings. The micro-cracks would be corroded easily and the solution would infiltrate into loose corrosion products and reach crack tip to sustain the internal corrosion, followed by crack propagation (Fig. 4.39 b and c). This process obeys the rules of crevice corrosion. Acidity in the cracks increased significantly as neutralisation was not easily obtained by exchanging solution between inside and outside the cracks. An ascending acidity accelerates the corrosion attack and results in an unfavourable inner structure. When the acid solution flows across pores, corrosion will take place and enlarge a pore to a corrosion hole.

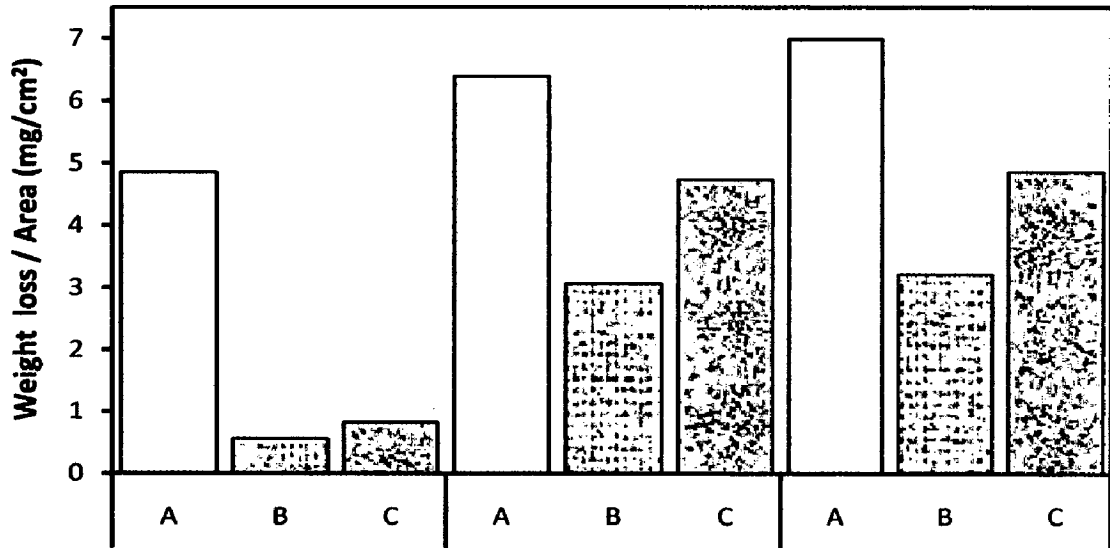


Fig. 4.38 Column chart showing weight loss per unit area for the uncoated and coated ASTM-SA210 Grade A-1 boiler steel subjected to salt-fog testing (5% NaCl) : (A) Uncoated Grade A-1 boiler steel subjected to 24hrs, 48hrs and 72 hrs testing; (B) Nanostructured TiAlN coated Grade A-1 boiler steel subjected to 24hrs, 48hrs and 72 hrs testing; (C) Nanostructured AlCrN coated Grade A-1 boiler steel subjected to 24hrs, 48hrs and 72 hrs testing

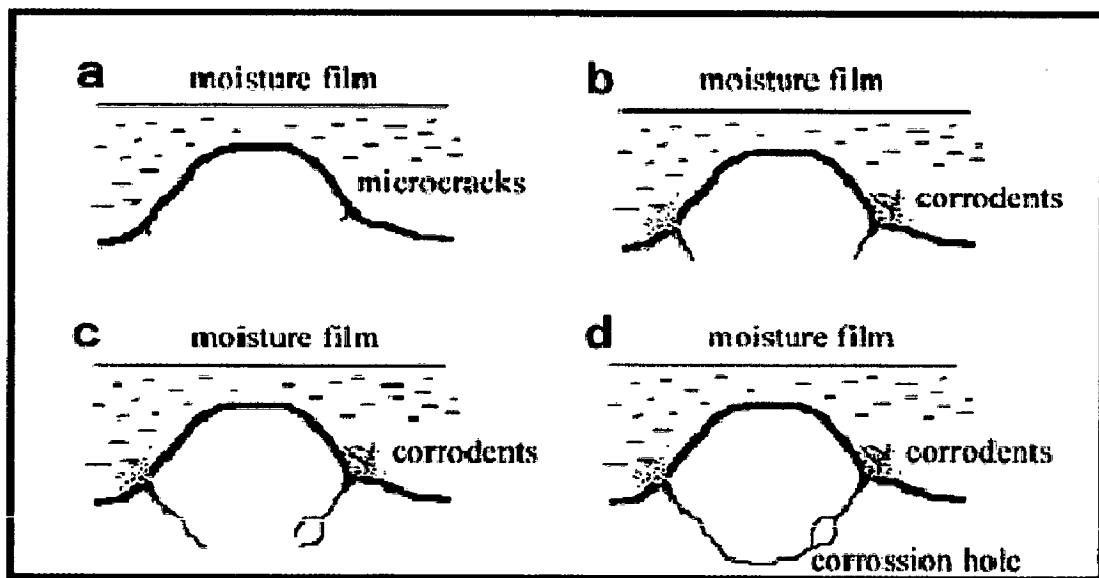


Fig. 4.39 Corrosion evolution of the as-deposited coatings in salt spray test; a: initiation of corrosion micro-crack, b: cracks propagation, c: crack branching, d: formation of corrosion hole (Bao et al., 2007)

4.5.2 Conclusions

The corrosion behavior of conventional thick (by plasma spraying and gas nitrided) and nanostructured thin (by physical vapor deposition process) TiAlN and AlCrN coatings on ASTM-SA210 Grade A-1 boiler steel, has been analyzed by electrochemical methods i.e. linear polarization resistance (LPR) and potentiodynamic polarization tests in an aerated 3.0 wt% NaCl solution at room temperature; and salt spray (Fog) tests (5.0 wt% NaCl). The following conclusions are made:

1. In Linear polarization resistance (LPR) test, the corrosion current densities of all the coatings were found much lower than that of the substrate. The corrosion resistance of the coatings and substrate followed the sequence:
Nanostructured TiAlN > Conventional AlCrN > Nanostructured AlCrN > Conventional TiAlN > Substrate
2. The corrosion protection is provided by all the coatings at initial stage as indicated by the LPR test results in terms of corrosion current density and polarization resistance. The uncoated Grade A-1 boiler steel has shown maximum corrosion current density and minimum in case of nanostructured thin TiAlN coating.
3. In Potentiodynamic Polarization test, the corrosion current densities of the films were found much lower than that of the substrate steel. All the coatings have performed well in 3 wt. % NaCl solution in comparison to the substrate steel.
4. The corrosion current densities of the substrate and the coatings in Potentiodynamic Polarization test were found much lower as compared to the LPR test (at initial stage) results. This may be due to the formation of protective oxide layer which has blocked the passage of the electrolyte to attack the samples. The corrosion resistance of the coatings and substrate followed the sequence:
Nanostructured TiAlN > Conventional AlCrN > Conventional TiAlN > Nanostructured AlCrN > Substrate

5. The measured protective efficiency for nanostructured thin TiAlN, nanostructured thin AlCrN, conventional thick TiAlN and conventional thick AlCrN coatings is 92.87%, 37.01%, 78.19% and 86.22% respectively.
6. The porosity values has also been measured quantitatively by the electrochemical methods for nanostructured thin TiAlN, nanostructured thin AlCrN, conventional thick TiAlN and conventional thick AlCrN coatings, which are 0.015%,0.432%, 0.371% and 2.39% respectively.
7. In salt spray tests; the uncoated Grade A-1 boiler steel suffered severe corrosion in all three test conditions i.e. 24 Hrs, 48 Hrs and 72 Hrs. The nanostructured coated samples have shown resistance to the corrosion as compared to the uncoated Grade A-1 boiler steel.
8. The weight loss per unit area increases with the duration of the test. The weight loss per unit area in case of nanosructured thin TiAlN coating is less than as compared to the nanostructured AlCrN coating and uncoated boiler steel in all test conditions.
9. The nanostructured thin TiAlN and AlCrN coatings can provide a very good corrosion resistance when exposed to the simulated marine environment i.e. salt fog test.

4.6 EROSION-CORROSION STUDIES IN INDUSTRIAL ENVIRONMENT

After conducting the various experiments on uncoated and coated ASTM-SA210 Grade A-1 boiler steel in lab, the present research work has been focused to investigate and compare the high temperature corrosion and erosion behavior of conventional thick (by plasma spraying and gas nitrided) and nanostructured thin (by physical vapor deposition process) TiAlN and AlCrN coatings on Grade A-1 boiler steel, in actual industrial environment of coal fired boiler. The uncoated and coated specimens were exposed to low temperature super-heater zone of the coal fired boiler of Guru Nanak Dev Thermal Power Plant, Bathinda, Punjab, India. The specimens were hanged in the platen super-heater of coal fired boiler for 10 cycles, each cycle consisting of 100 hours exposure followed by 1 hour cooling at ambient temperature at gas temperature 900°C. The detailed experimental procedure is explained in chapter 3.

4.6.1 Results

4.6.1.1 Visual observations

The macrographs for uncoated and coated ASTM-SA210 Grade A-1 boiler steel exposed to super-heater of the coal fired boiler environment at 900°C for 1000 hours are shown in Fig.4.40. For the uncoated Grade A-1 boiler steel, a dark black grey colored scale appeared on the surface right from the 1st cycle. Ash deposition has started just after the 1st cycle and the sample showed spalling and gets welded with the wire with which it was hanged in the boiler environment. After every cycle; the samples were washed with acetone in order to remove ash deposited before weight measurement. Erosion was also observed after 2nd cycle at some spots on the surface of the sample. Ash deposition, erosion and severe spalling in case of bare Grade A-1 boiler steel continued to last cycle. At the end of cyclic study; ash deposition on fragile scale and blackish brown color surface appearance in the middle with whitish grey color along the sides was observed which can be seen in Fig.4.40 (a). In case of nanostructured thin TiAlN coated Grade A-1 boiler steel, color of the oxide scale at the end of the study was observed to be blackish grey with some visible cracks and ash deposited surface, as shown in Fig.4.40 (b): Ash deposition has started just

after the 1st cycle and the sample showed spalling and gets welded with the wire with which it was hanged in the boiler environment. Ash deposition, erosion and severe spalling were observed throughout the cyclic study.

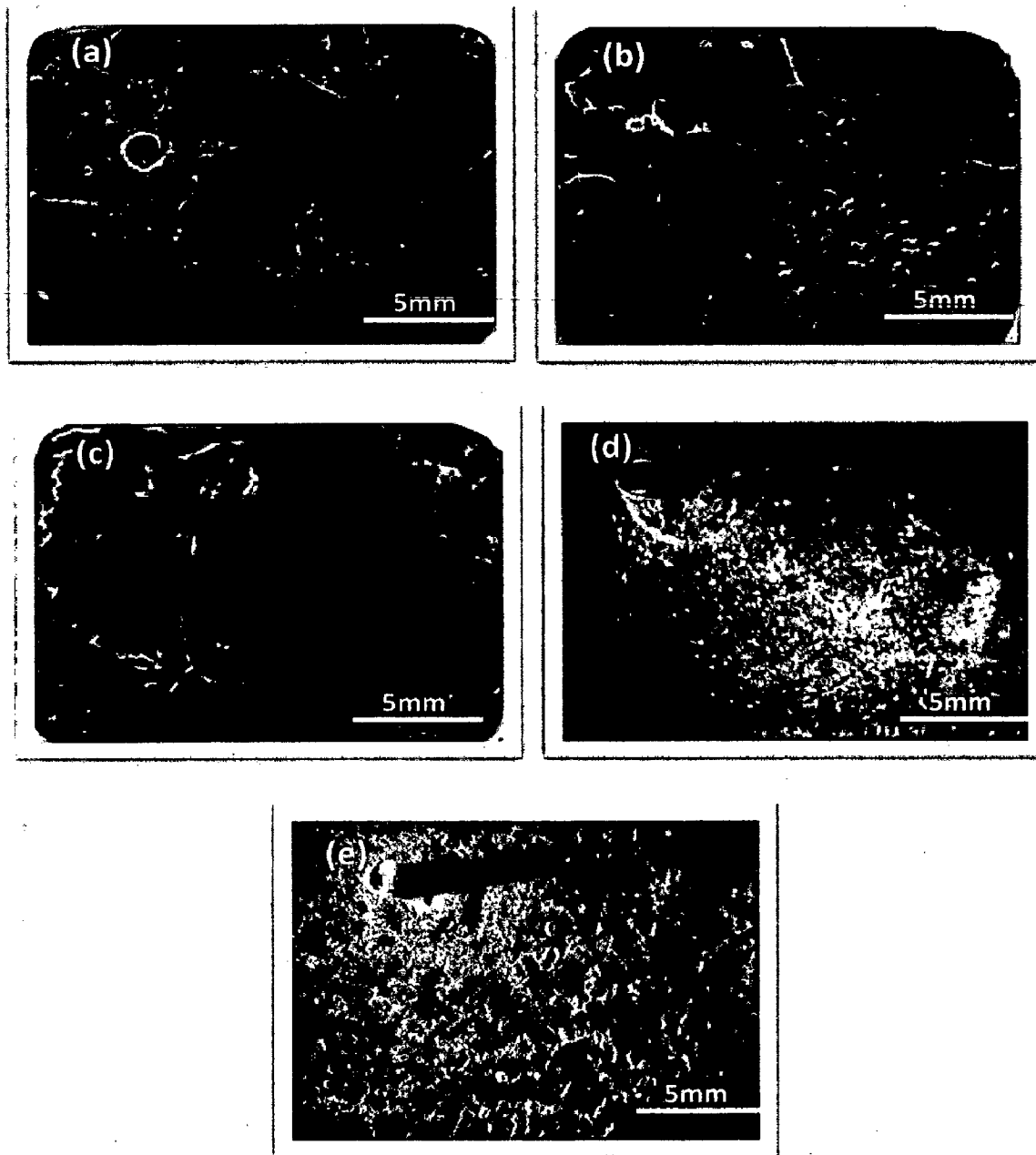


Fig. 4.40 Surface macrographs of uncoated and coated ASTM-SA210 Grade A-1 boiler steel exposed to super-heater of the coal fired boiler environment at 900°C for 1000 hours : (a) Uncoated Grade A-1 boiler steel, (b) Nanostructured TiAlN coating, (c) Nanostructured AlCrN coating, (d) Conventional TiAlN coating, (e) Conventional AlCrN coating

The nanostructured thin AlCrN coated Grade A-1 boiler steel has shown the formation of dark blackish grey colored scale with severe spalling and visible hairline cracks over the whole area, as shown in Fig.4.40 (c). After 1st cycle, golden spots were seen on the surface with ash deposition and no sign of spalling and thermal expansion of the material. The scale shows spalling after 3rd cycle and the sample gets welded to the wire. The ash deposition, erosion and spalling continue till the end.

A visual observation of conventional thick TiAlN coated Grade A-1 boiler steel (Fig.4.40.d), showed the formation of bluish grey colored ash deposited scale at the end of the study. The scale was rough and adherent to the substrate. The sample gets welded to the wire after 4th cycle and no spalling was observed afterwards. The rough scale may be due to the erosion. In case of conventional thick AlCrN coated Grade A-1 boiler steel, color of the ash deposited oxide scale was dark grey with some whitish areas at the end of the study. The scale was found to be adherent. No spalling was observed till 4th cycle after which the sample gets welded to the wire and showed spalling and signs of erosion (Fig. 4.40.e).

4.6.1.2 Weight change and sample thickness measurements

Weight gain per unit area (mg/cm^2) versus time expressed in number of cycles plot for coated and bare Grade A-1 boiler steel exposed to super-heater of the coal fired boiler environment at 900°C for 1000 hours; is presented in Fig. 4.41. However weight change data could not be of much use for predicting the corrosion behavior because of suspected spalling and ash deposition on the specimens. Although the specimens were washed with acetone after every cycle before weight measurement in order to remove ash deposited yet it was difficult to remove the ash completely. Hence extent of corrosion could only be monitored by measuring the thickness of the un-reacted sample after the total exposure of 1000 hrs i.e. measuring scale thickness in cross-sectional view. It can be inferred from the plots (Fig.4.41) that the uncoated and nanostructured thin coated Grade A-1 boiler steels have shown high weight gain as compared to the conventional thick coatings.

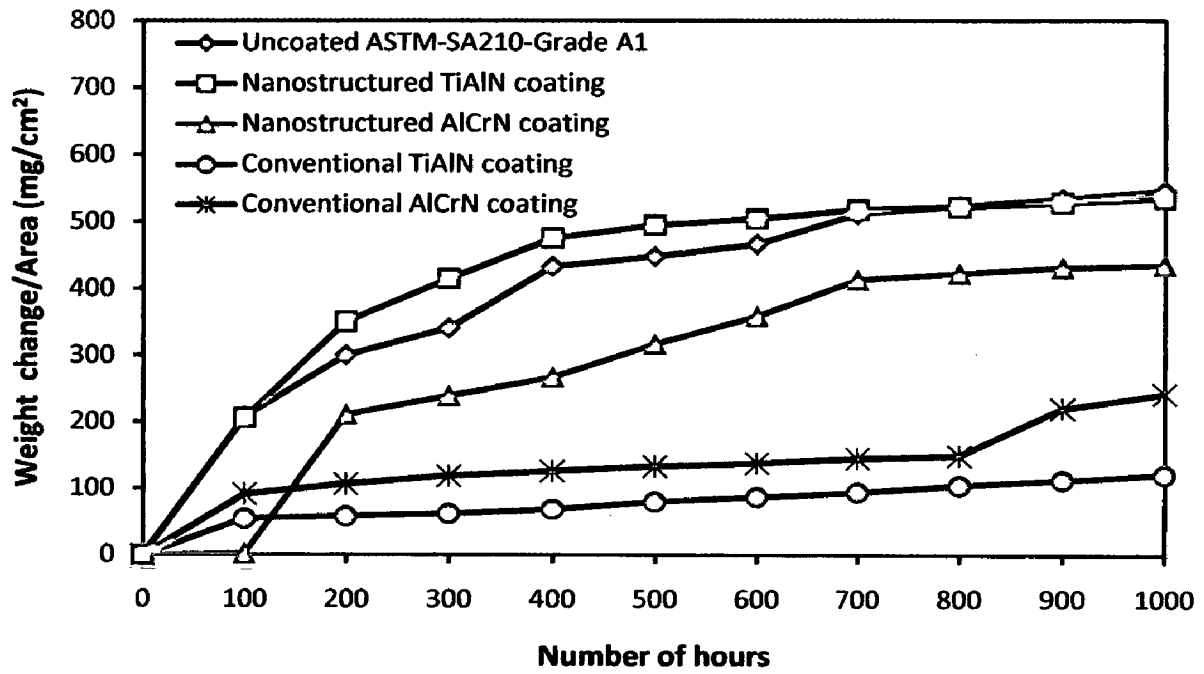


Fig. 4.41 Weight gain/area vs time for uncoated and coated ASTM-SA210 Grade A-1 boiler steel exposed to super-heater of the coal fired boiler environment at 900°C for 1000 hours

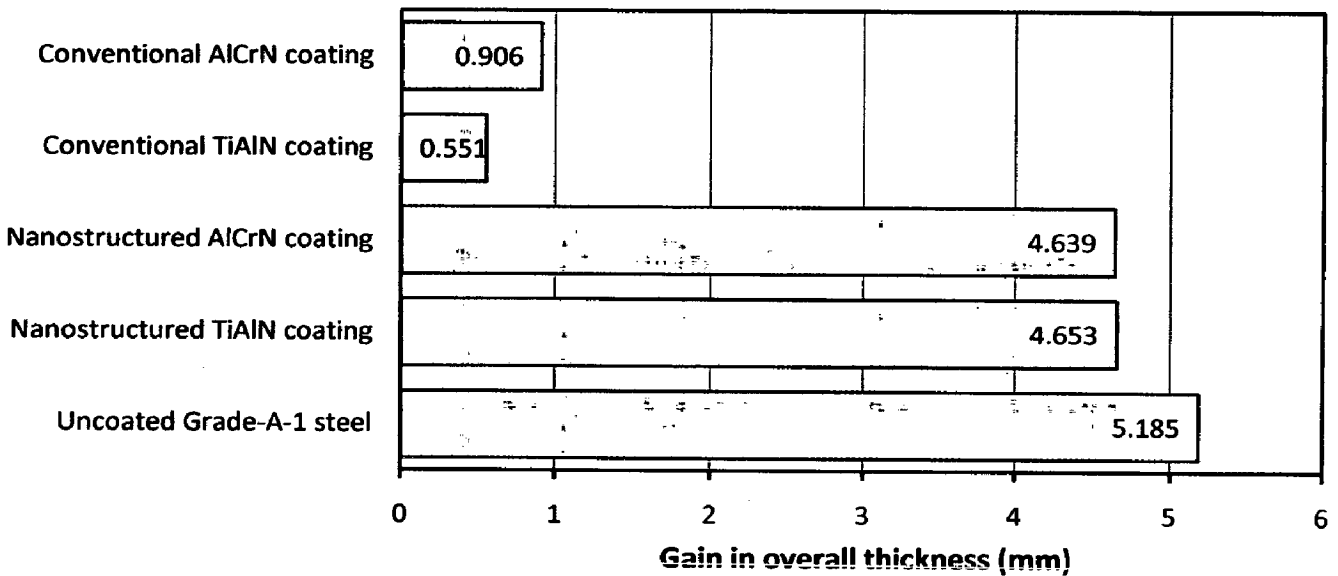


Fig. 4.42 Bar chart indicating overall gain in thickness for uncoated and coated ASTM-SA210 Grade A-1 boiler steel specimens exposed to super-heater of the coal fired boiler environment at 900°C for 1000 hours

The conventional AlCrN coating has shown gradual erosion-corrosion rate after initial cycles and again higher rate after 8th cycle where as the weight gain in case of conventional TiAlN coating is gradual after 1st cycle. The thin nanostructured AlCrN coating has shown weight gain rate less than that of uncoated Grade-A1 boiler steel whereas it is more in case of nanostructured TiAlN coating (Fig.4.41). Bar chart (Fig.4.42) indicates the overall gain/loss in the thickness (in mm) of the specimen. All the coatings and bare Grade A-1 boiler steel have shown increase in overall thickness after erosion-corrosion for 1000 hrs. The thickness of the specimens was measured before and after the erosion-corrosion test and average of ten values has been used to calculate the thickness gain/loss. The measured average gain in overall specimen thickness values for uncoated Grade A-1, nanostructured thin TiAlN, nanostructured thin AlCrN, conventional thick TiAlN and conventional thick AlCrN coatings are 5.185, 4.653, 4.639, 0.551 and 0.906 mm respectively.

4.6.1.3 Surface scale analysis

4.6.1.3.1 X-ray diffraction analysis (XRD)

XRD diffractograms for coated and uncoated ASTM-SA210 Grade A-1 boiler steel exposed to super-heater of the coal fired boiler environment at 900°C for 1000 hours; are depicted in Fig.4.43 (a and b) on reduced scale. As indicated by the diffractograms in Fig.4.43, Fe₂O₃, Al₂O₃ and SiO₂ are the main phases present in the oxide scale of coated and uncoated Grade A-1 boiler steel. In case of conventional thick TiAlN coating; addition to the above mentioned phases Ti₃Al is also present in the oxide scale.

4.6.1.3.2 Surface scale morphology

SEM micrographs along with EDAX point analysis reveals the surface morphology of the coated and uncoated ASTM-SA210 Grade A-1 boiler steel exposed to super-heater of the coal fired boiler environment at 900°C for 1000 hours; are shown in Fig.4.44. Micrograph (Fig.4.44.a) for uncoated Grade A-1 boiler steel indicates a scale developed dark grey and white regions.

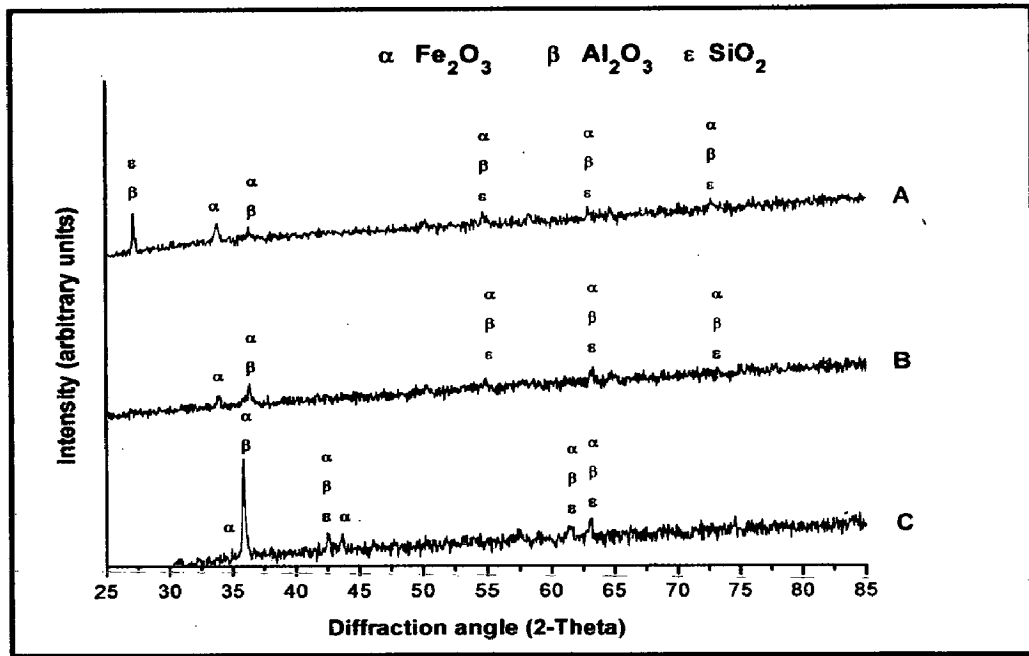


Fig. 4.43 (a) X-Ray Diffraction pattern of uncoated and coated ASTM-SA210 Grade A-1 boiler steel exposed to platen superheater of the coal fired boiler environment at 900°C for 1000 Hrs: (A) Uncoated Grade A-1 boiler steel, (B) Nanostructured TiAlN coating, (C) Nanostructured AlCrN coating

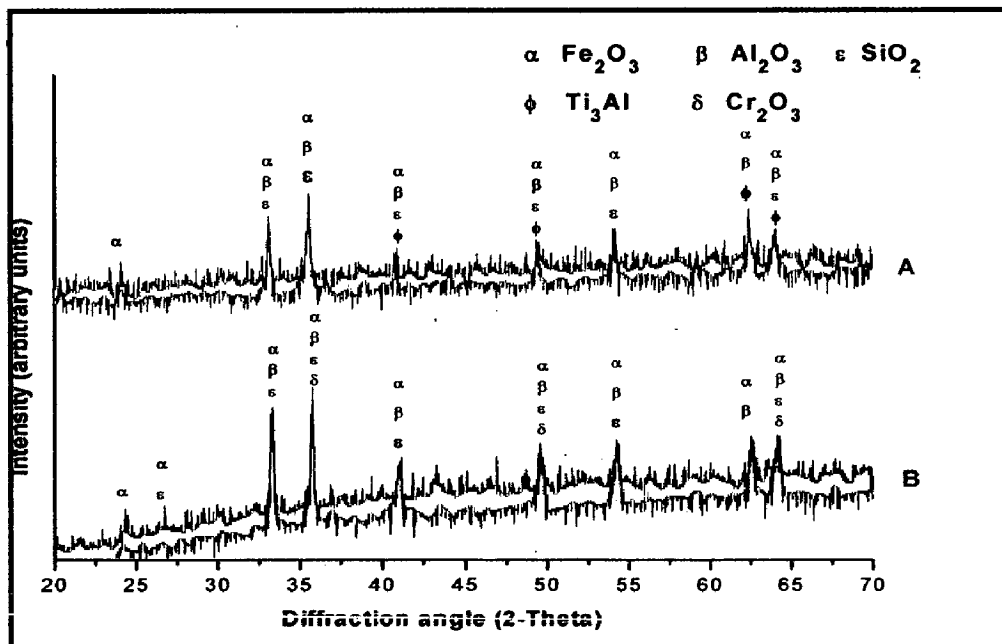


Fig. 4.43 (b) X-Ray Diffraction pattern of coated ASTM-SA210 Grade A-1 boiler steel exposed to platen superheater of the coal fired boiler environment at 900°C for 1000 Hrs: (A) Conventional TiAlN coating, (B) Conventional AlCrN coating

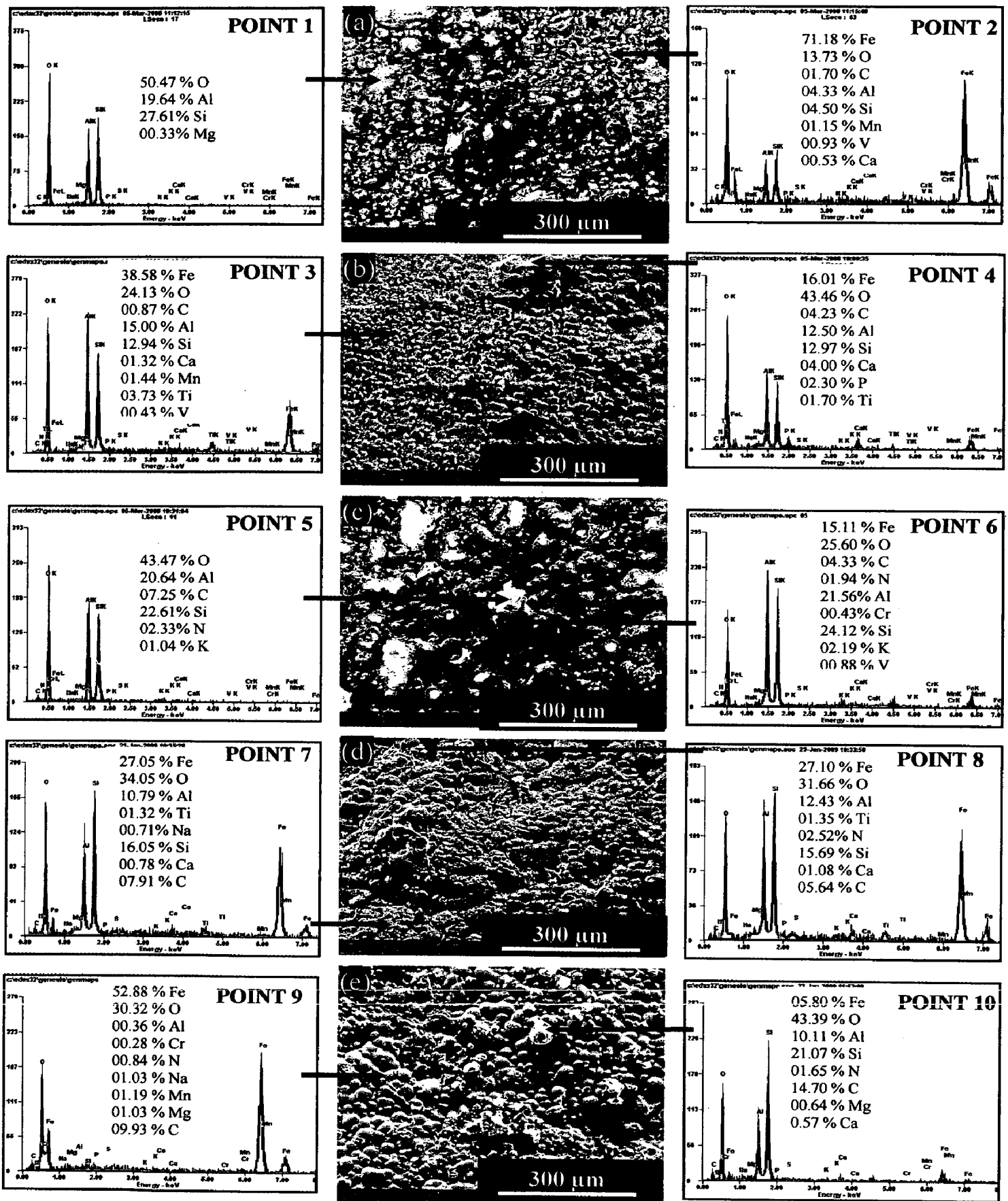


Fig. 4.44 Surface-scale morphology and EDAX patterns from different spots on uncoated and coated ASTM-SA210 Grade A-1 boiler steel exposed to platen superheater of the coal fired boiler environment at 900°C for 1000 Hrs: (a) Uncoated Grade A-1 boiler steel, (b) Nanostructured TiAlN coating, (c) Nanostructured AlCrN coating, (d) Conventional TiAlN coating, (e) Conventional AlCrN coating

EDAX analysis at point 1 on Fig.4.44 (white region) indicates the presence of Al, O and Si with no iron, which may be the ash. The dark grey region (Point 2) mainly consists of Fe and O with minor amounts of Al and Si. The SEM micrograph of oxidized nanostructured thin TiAlN coatings is shown in Fig.4.44 (b). The surface scale containing distorted grains. EDAX analysis (Point 3 and 4) of the scale revealed the presence of Fe, O, Al and Si as the main elements along small amount of Ti, P and Ca. In case of nanostructured thin AlCrN coated Grade A-1 boiler steel, the scale consists of white and dark grey regions. EDAX point analysis at point 5 (white region) shows the presence of Al, Si and O along with K, C and N with no iron, whereas the dark grey region (Point 6) shows higher amount of Al, O, Si and Fe along with small amount of K, V and Cr.

The surface scale developed on conventional thick TiAlN coated Grade A-1 steel is massive and without any cracks. EDAX analysis indicates the presence of Si, Al, Fe and O as the main phases along with very small amount of Ti and Ca. A spalled surface scale is developed on conventional thick AlCrN coated Grade A-1 boiler steel. EDAX point analysis at point 10 (white region) shows Al (10.11%), Si (21.07%) and O (43.39%) as the main elements in the scale (Fig.4.44.e) along with very small amount of Fe, C and Ca whereas the matrix is rich in Fe (52.88 %), O (30.32 %) with negligible Al and Si.

4.6.1.4 Cross-sectional analysis

4.6.1.4.1 Cross-sectional scale morphology

Back Scattered Electron Image (BSEI) micrograph and elemental variation across the cross-section for coated and uncoated Grade A-1 boiler steel exposed to super-heater of the coal fired boiler environment at 900°C for 1000 hours; are shown in Fig.4.45. The SEM micrograph (Fig.4.45.a) in case of uncoated Grade A-1 boiler steel shows thick scale. Also, the scale is fragile and indicating cracking. EDAX analysis reveals the presence of iron and oxygen throughout the scale. The existence of significant amount of oxygen points out the possibility of Fe₂O₃ in the oxide scale.

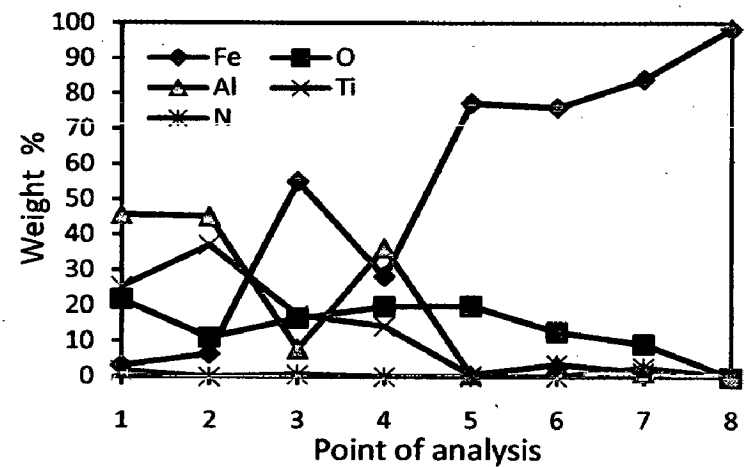
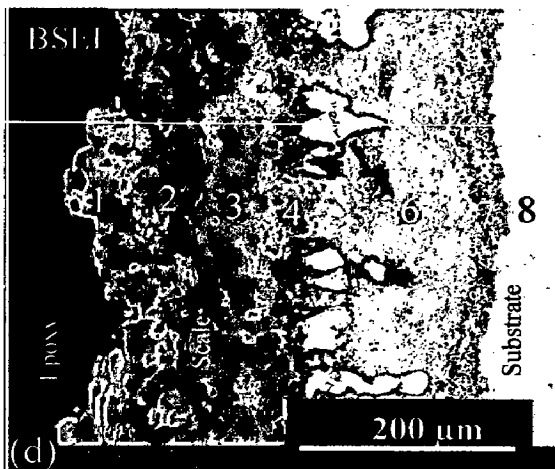
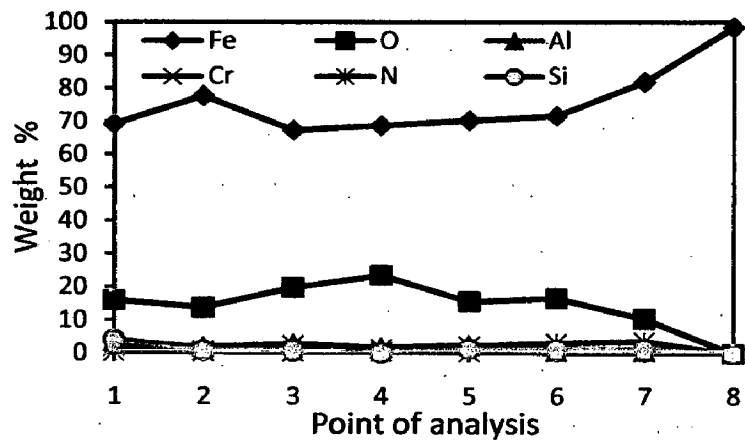
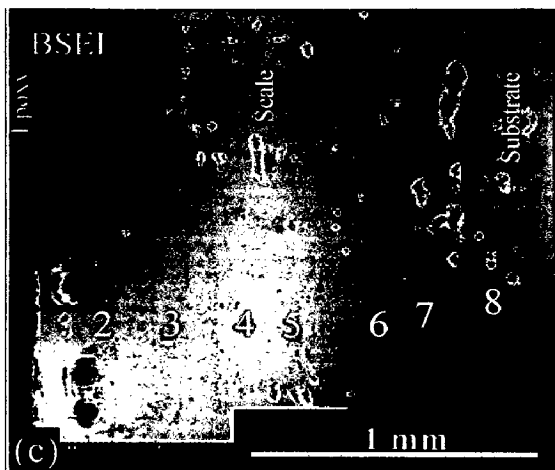
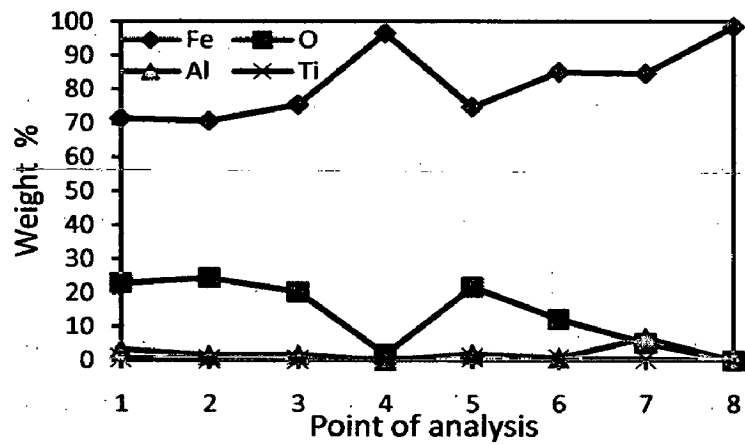
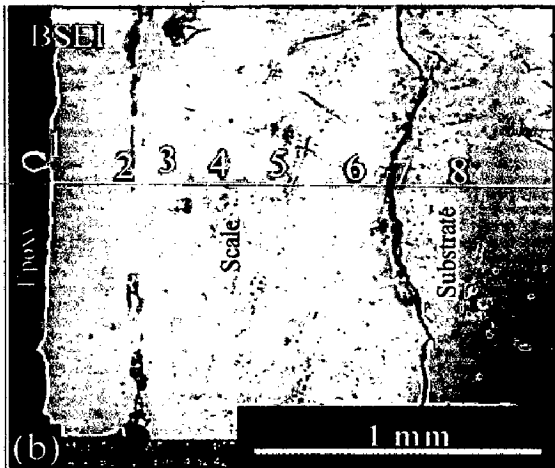
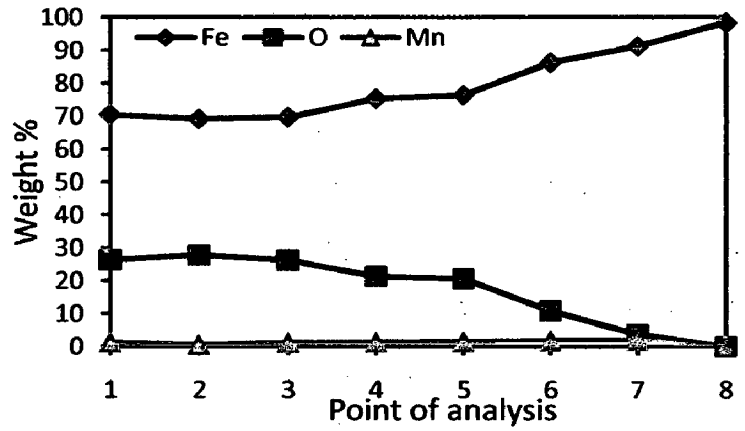
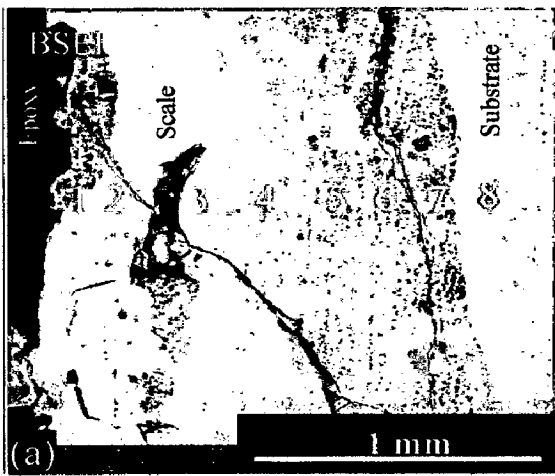
BSEI micrograph and elemental variation depicted in Fig.4.45 (b), for the cross-section of nanostructured thin TiAlN coated Grade A-1 boiler steel shows the thick,

continuous and adherent scale. The scale is showing fine cracks at some locations. The EDAX analysis reveals the presence of Fe, and O throughout the scale. A location at point 7 (Fig.4.45.b) in the micrograph depicts the good percentage of Al along with Fe and oxygen. A thick and adherent oxide scale can be seen in case of nanostructured AlCrN coated Grade A-1 boiler steel (Fig.4.45.c). The EDAX point analysis indicates the presence of Fe and O throughout the scale.

In case of conventional TiAlN coated Grade A-1 boiler steel, the scale is non uniform, thin and adherent as depicted in Fig.4.45 (d). The EDAX point analysis indicates the presence of Fe, O, Ti and Al throughout the scale with variable amounts. The amount of Ti and Al in the top scale is higher (Point 1 and 2) which decreases subsequently after point 5 as we move towards the substrate. The conventional thick AlCrN coated Grade A-1 boiler steel (Fig.4.45.e) indicates uniform, thin and adherent scale. EDAX point analysis shows the presence of Al, O and Fe throughout the scale. The top scale shows higher percentage of Al and O where the concentration of Fe decrease (point 2 and 3 on Fig.4.45.e). This trend is also visible at point 5; where Al increases and Fe decreases.

4.6.1.4.2 Scale thickness

The oxidized samples were cut across the cross section using Buehler Isomet 1000 precision saw and mounted in transoptic mounting resin and subsequently mirror polished to obtain scanning electron back scattered micrographs and X-ray mapping of different elements for coated and uncoated Grade A-1 boiler steel. The scale thickness values were measured from SEM back scattered micrographs as shown in Fig.4.45. The extent of erosion-corrosion in terms of scale/coating thickness (in microns) and corrosion rate in mils per year (mpy) for coated and uncoated Grade A-1 boiler steel exposed to super-heater of the coal fired boiler environment at 900°C for 1000 hours; are shown in Fig.4.46 and 4.47 respectively. Very thick scale is observed in case of uncoated and nanostructured coated Grade A-1 boiler steel.



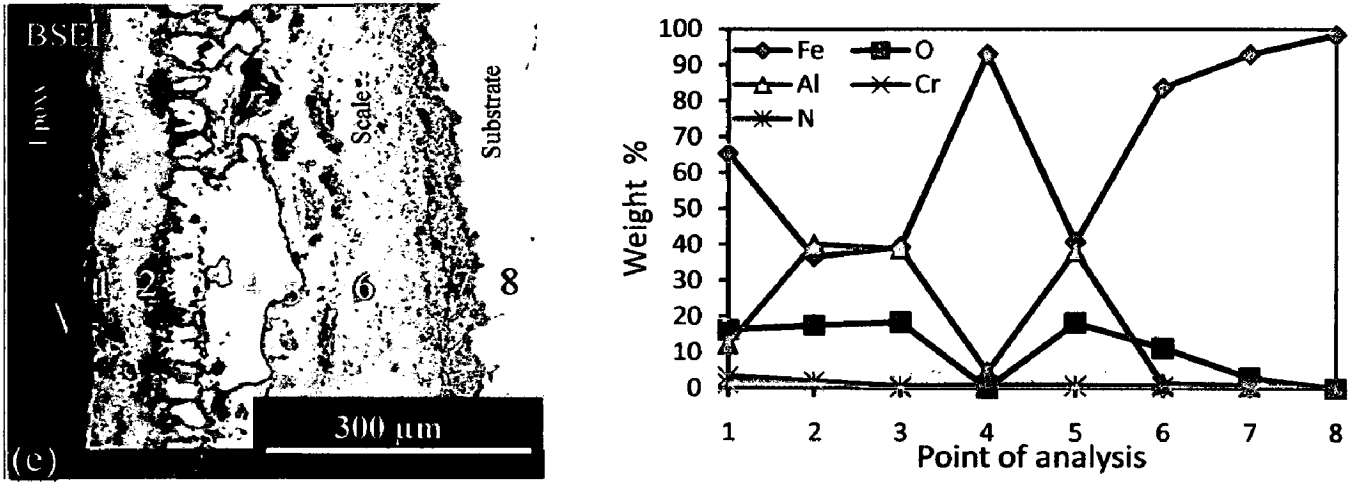


Fig. 4.45 Oxide scale morphology and variation of elemental composition across the cross-section of the uncoated and coated ASTM-SA210 Grade A-1 boiler steel exposed to platen superheater of the coal fired boiler environment at 900°C for 1000 Hrs: (a) Uncoated Grade A-1 boiler steel (65 X), (b) Nanostructured TiAlN coating (45 X), (c) Nanostructured AlCrN coating (31 X), (d) Conventional TiAlN coating (300 X), (e) Conventional AlCrN coating (260 X)

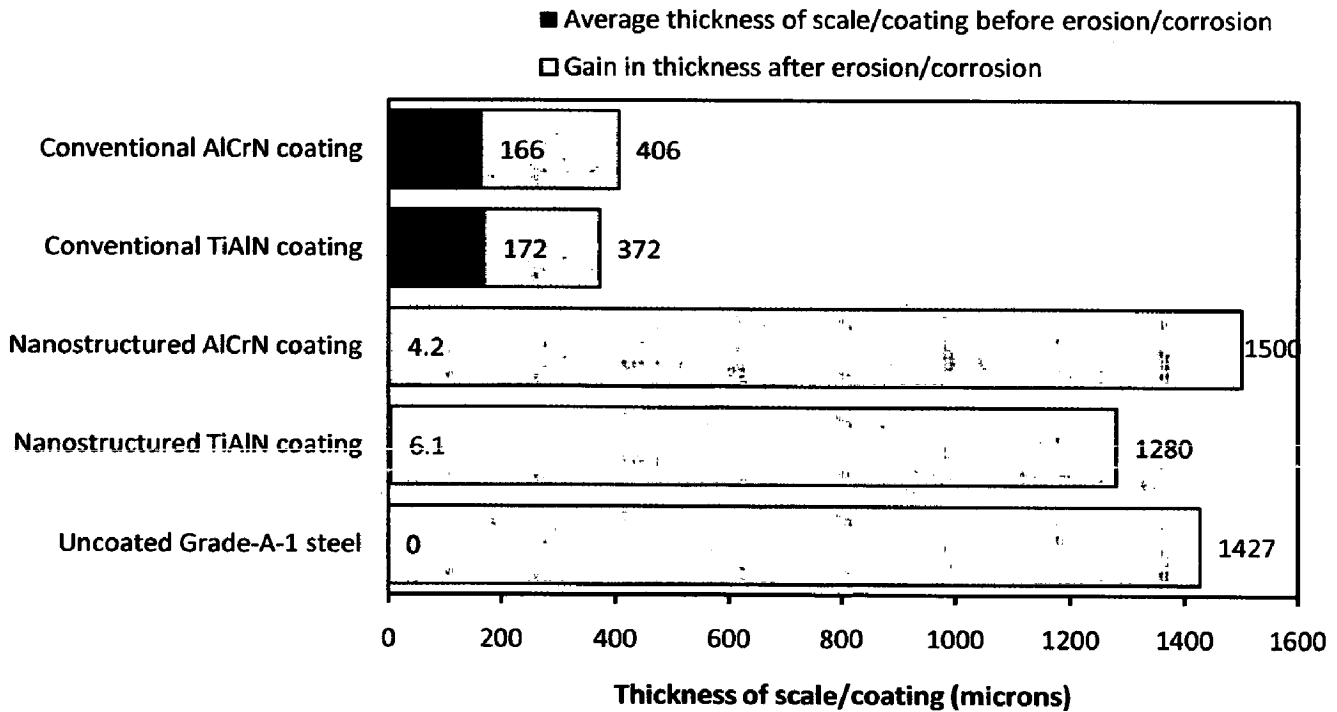


Fig. 4.46 Bar chart indicating the extent of erosion/corrosion for uncoated and coated ASTM-SA210 Grade A-1 boiler steel specimens exposed to super-heater of the coal fired boiler environment at 900°C for 1000 hours

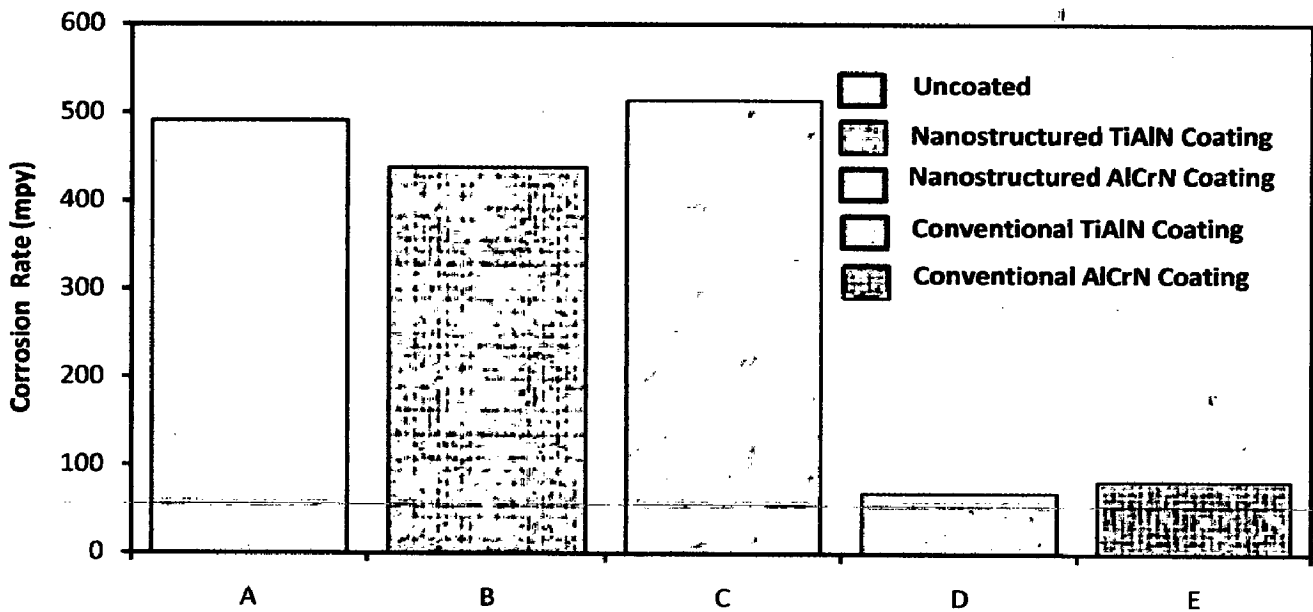


Fig. 4.47 Corrosion rate in mils per year (mpy) for uncoated and coated ASTM-SA210 Grade A-1 boiler steel exposed to super-heater of the coal fired boiler environment at 900°C for 1000 hours: (A) Uncoated Grade A-1 boiler steel, (B) Nanostructured TiAlN coating, (C) Nanostructured AlCrN coating, (D) Conventional TiAlN coating, (E) Conventional AlCrN coating

The measured corrosion rate for uncoated Grade A-1, nanostructured thin TiAlN, nanostructured thin AlCrN, conventional thick TiAlN and conventional thick AlCrN coatings are 491, 438, 513, 68 and 82 mpy respectively. The conventional coatings have shown good resistance to the corrosive environment as the oxygen penetration is limited to very less thickness as compared to the uncoated and nanostructured coated Grade A-1 boiler steel (Fig.4.46 and 4.47).

4.6.1.4.3 X-Ray mapping

X-ray mappings for a part of oxide scale of uncoated and coated Grade A-1 boiler steel exposed to super-heater of the coal fired boiler environment at 900°C for 1000 hours; are shown in Fig. 4.48.

In case of conventional thick TiAlN coated Grade A-1 boiler steel, Fig.4.48 (d), Al and Ti rich thick bands are clearly seen along with Fe and oxygen. Ti is present in the upper scale along with Fe and O. Figure (4.48.e) depicts the X-ray mapping in case of conventional AlCrN coated Grade A-1 boiler steel. The thick band of Al is present in the top scale region. The upper scale is rich in Al with O and Fe. A thin band of Al and O can be seen in the top scale where Fe is completely missing.

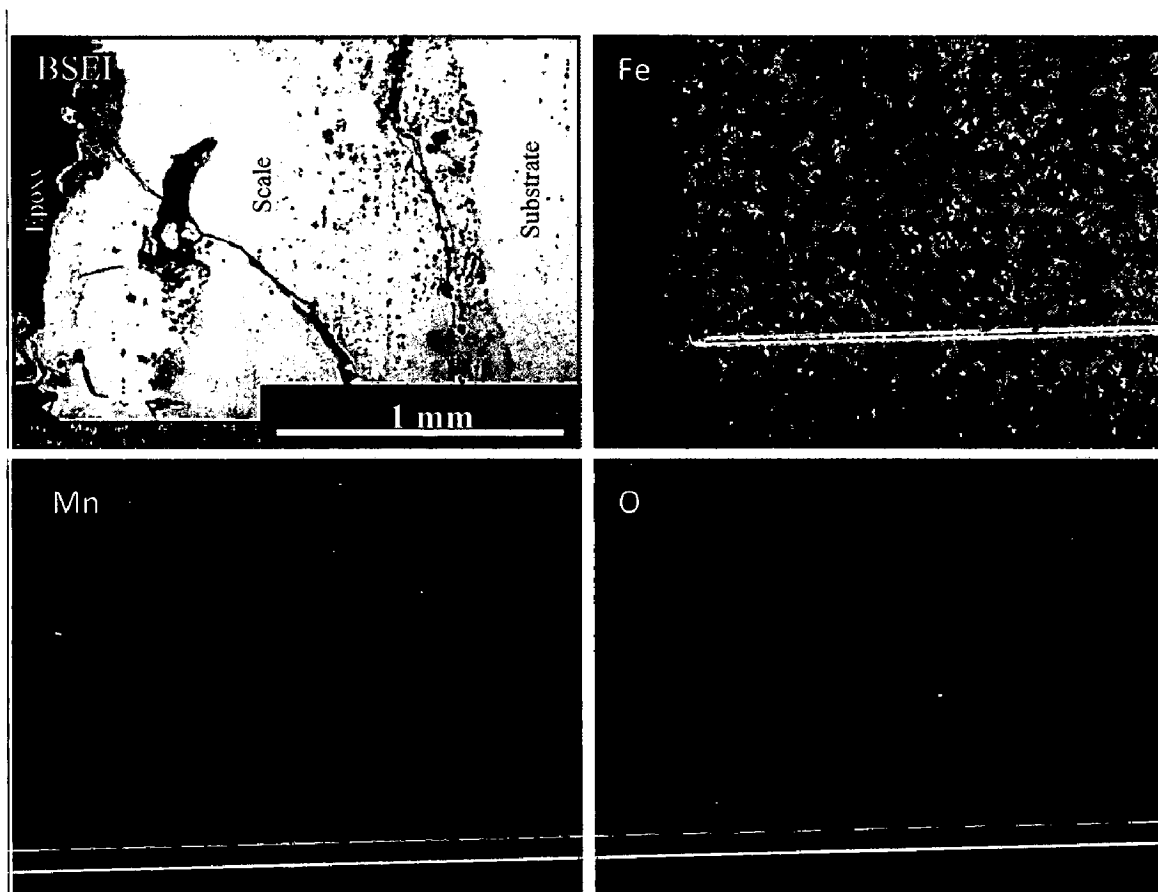


Fig. 4.48 (a) Composition image (BSEI) and X-ray mapping of the cross-section of uncoated ASTM-SA210 Grade A-1 boiler steel exposed to platen super-heater of the coal fired boiler environment at 900°C for 1000 Hrs

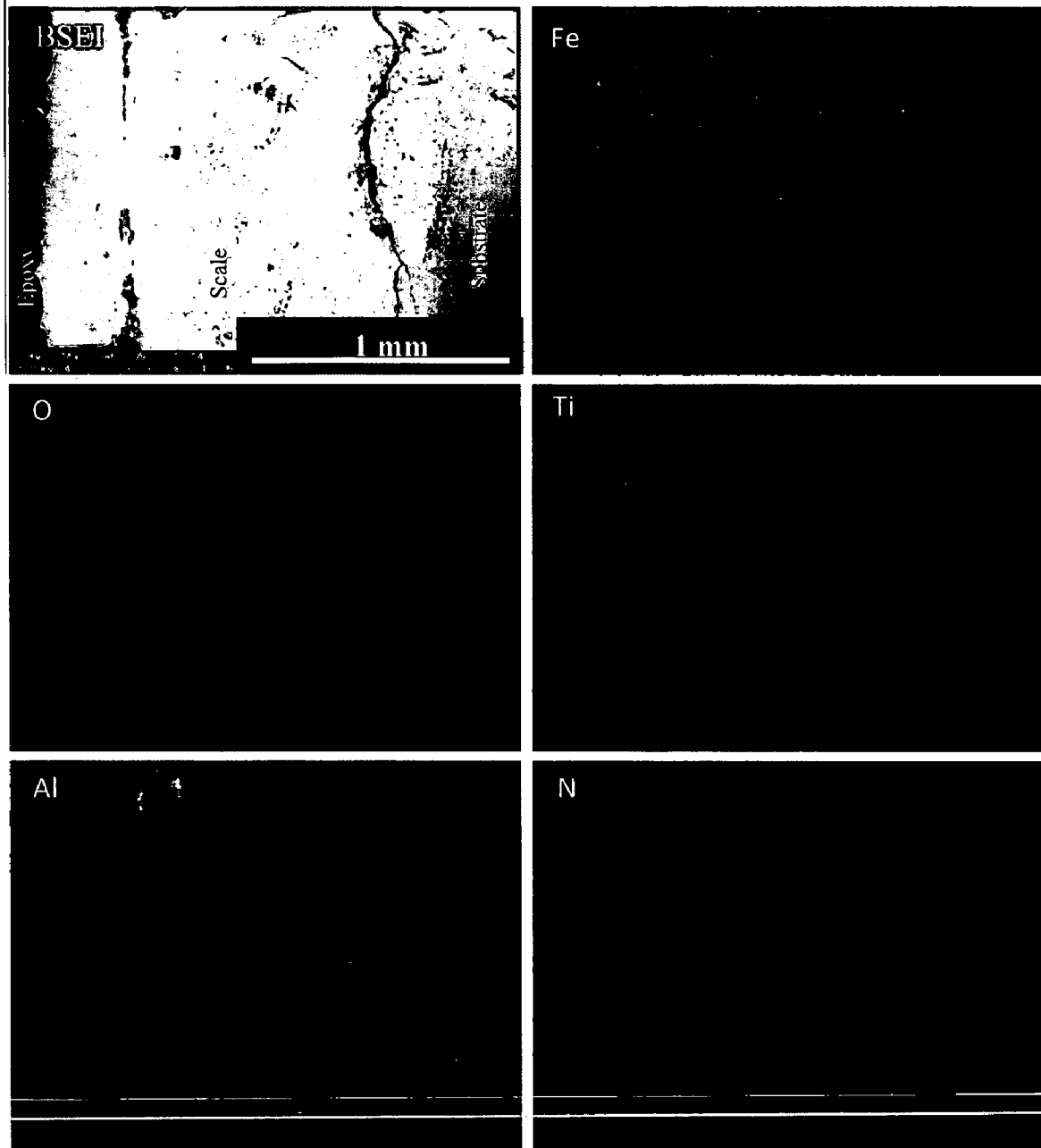


Fig. 4.48 (b) Composition image (BSEI) and X-ray mapping of the cross-section of Nanostructured TiAlN coated ASTM-SA210 Grade A-1 boiler steel exposed to platen super-heater of the coal fired boiler environment at 900°C for 1000 Hrs

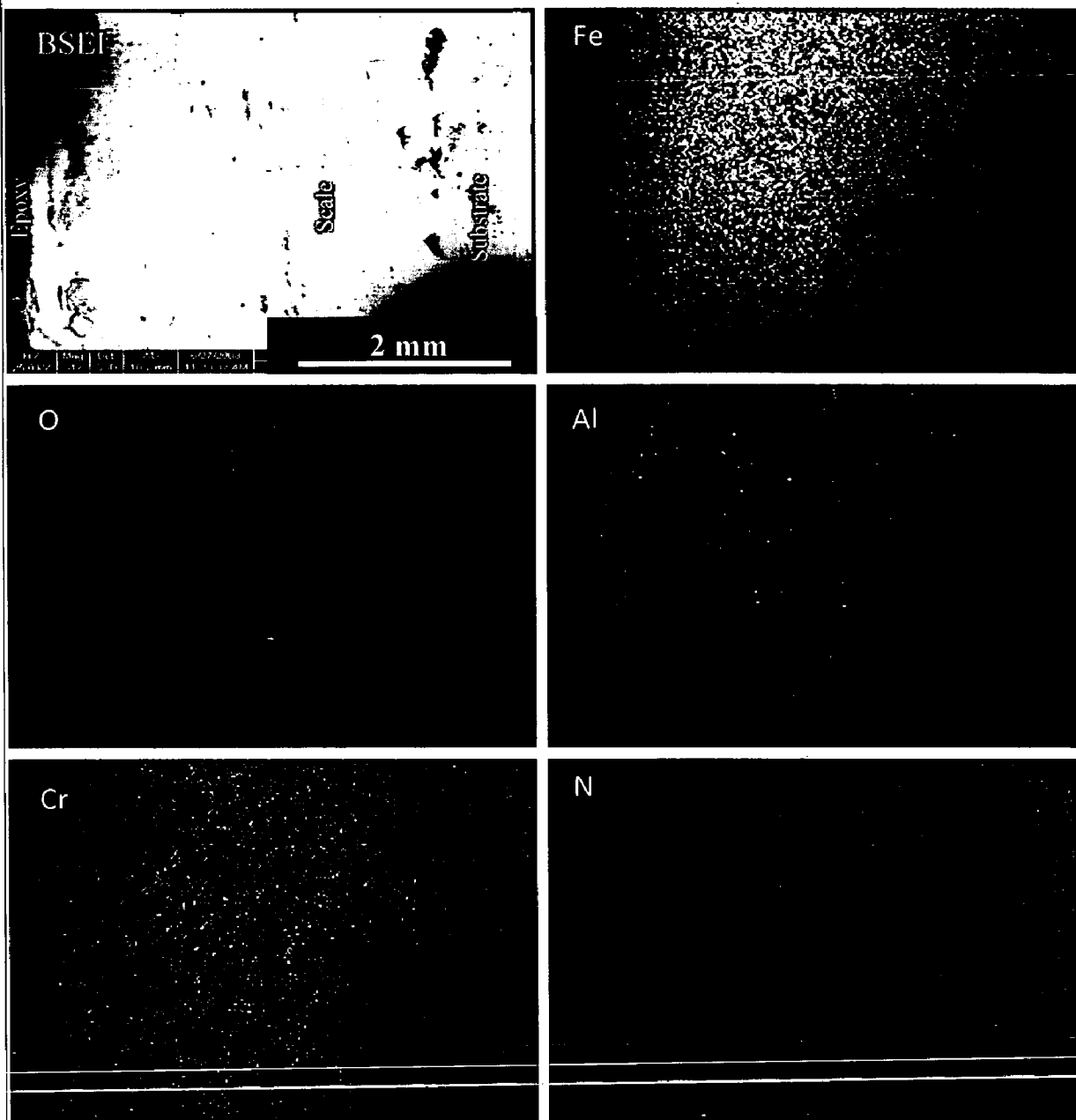


Fig. 4.48 (c) Composition image (BSEI) and X-ray mapping of the cross-section of Nanostructured AlCrN coated ASTM-SA210 Grade A-1 boiler steel exposed to platen super-heater of the coal fired boiler environment at 900°C for 1000 Hrs

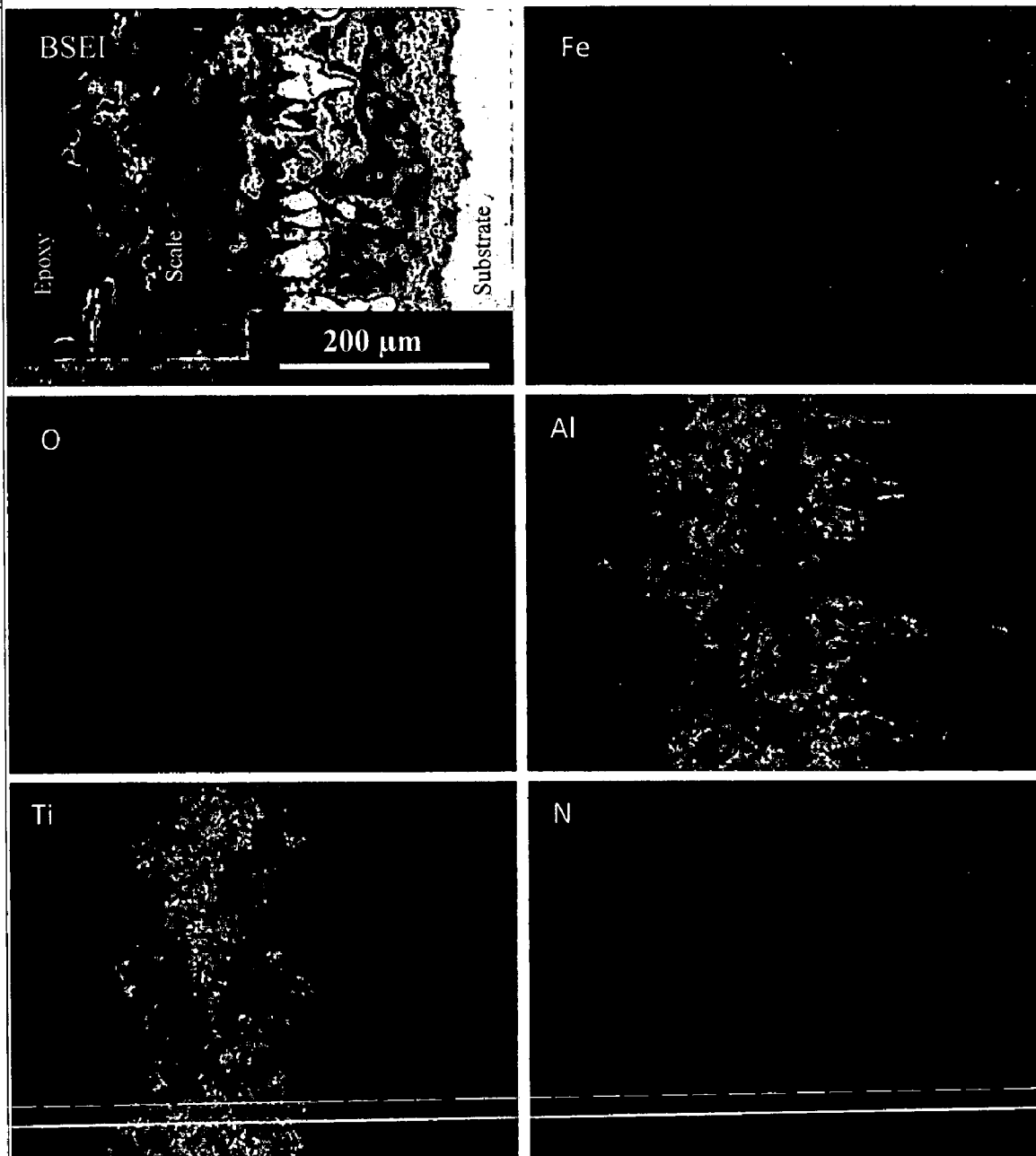


Fig. 4.48 (d) Composition image (BSEI) and X-ray mapping of the cross-section of conventional TiAlN coated ASTM-SA210 Grade A-1 boiler steel exposed to platen super-heater of the coal fired boiler environment at 900°C for 1000 Hrs

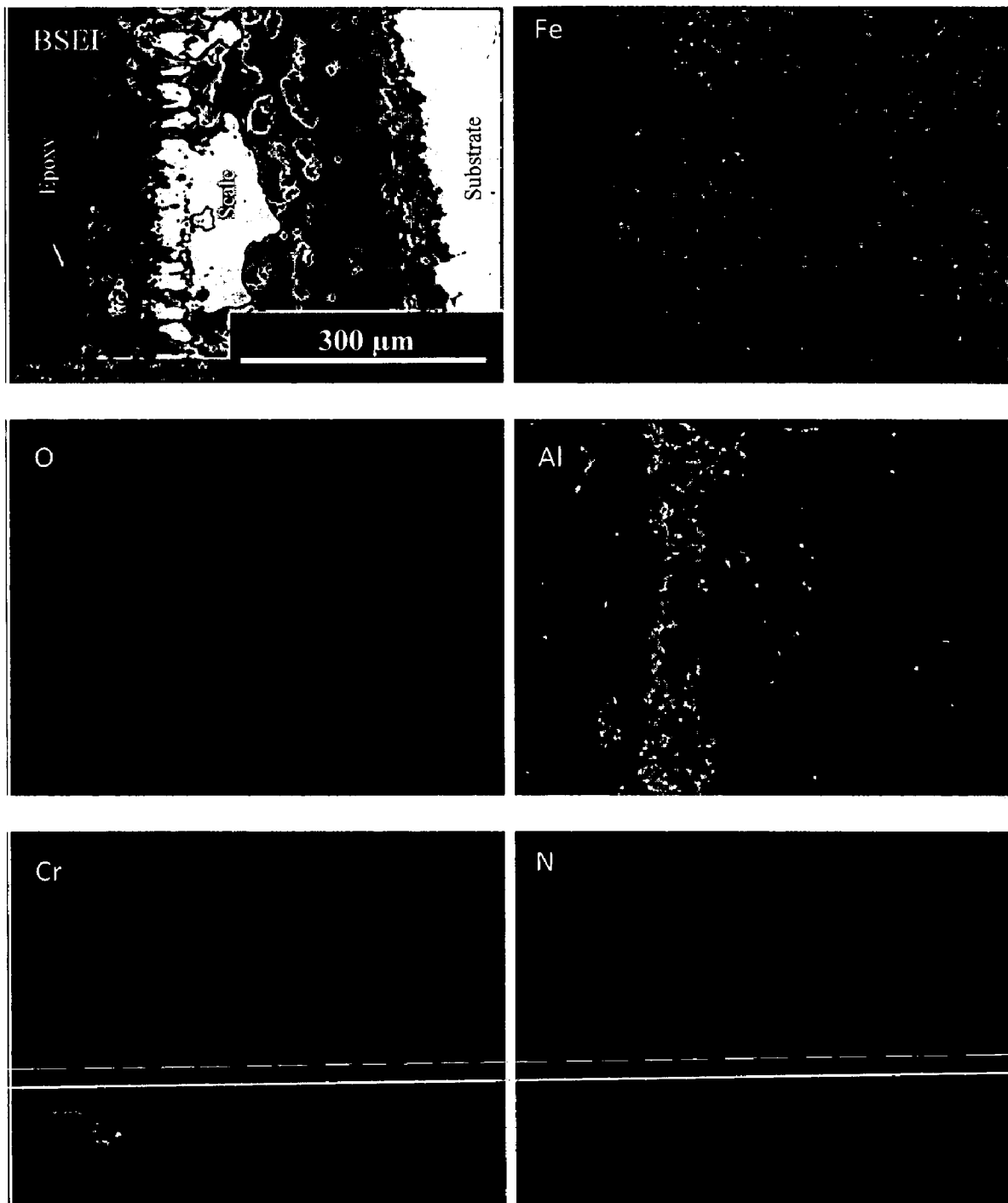


Fig.4.48 (e) Composition image (BSEI) and X-ray mapping of the cross-section of conventional AlCrN coated ASTM-SA210 Grade A-1 boiler steel exposed to platen super-heater of the coal fired boiler environment at 900°C for 1000 Hrs

In case of uncoated Grade A-1 boiler steel, the micrograph (Fig.4.48.a) indicates a dense scale, which mainly contains iron and oxygen with some amount of manganese, as indicated by X-ray mapping. The X-ray mapping analysis of the scale formed on nanostructured TiAlN coated Grade A-1 boiler steel is presented in Fig. 4.48.b. The X-ray mapping indicates presence of oxygen and iron throughout the scale with a thin band of Al in the sub-scale. In case of nanostructured thin AlCrN coated Grade A-1 boiler steel; the BSEI and X-ray mapping are shown in Fig. 4.48.c. The X-ray mapping indicates the presence of iron and oxygen throughout the scale.

4.6.2 Summary of Results

Results obtained after 1000 hrs of exposure of uncoated and coated Grade A-1 boiler steel to super-heater of the coal fired boiler environment at 900°C are summarized in Table 4.9.

4.6.3 Discussion

Fragile scale with tendency to spall has been observed for the uncoated Grade A-1 boiler steel used in present investigation (Fig.4.40). The higher weight gain (Fig.4.41) of uncoated and nanostructured thin TiAlN and AlCrN coated Grade-A-1 boiler steel than conventional thick might be attributed to spallation of the oxide scale in the actual environment of the coal fired boiler and fluxing action of the molten salt along with erosion of oxide scale. The most common deposit found on boiler super heaters is sodium vanadyl vanadate, $\text{Na}_2\text{O} \cdot \text{V}_2\text{O}_4 \cdot 5\text{V}_2\text{O}_5$, which melts at a relatively low temperature, 550°C, above the melting point, this ash material corrodes metals by long-term contact (Sidhu and Prakash, 2006). The accumulation of low melting-point salts from flue-gas on the fire side surface of boiler tubes induces hot corrosion and is considered a root cause for the severe wastage of tube materials used for super heaters and reheaters in “advanced” steam-generating system (Sidhu et al, 2005). The interaction of ash (Na_2O , K_2O etc.) with the boiler gas (SO_2 , SO_3 , O_2 etc.) results in the formation of alkali sulphates (K_2SO_4 , Na_2SO_4).

Table 4.9 Summary of the results obtained for uncoated and coated ASTM-SA210 Grade A-1 boiler steel exposed to super-heater of the coal fired boiler environment at 900°C for 1000 hours

Coating	Weight gain mg/cm ²	Extent of Corrosion (mm)	Corrosion Rate (mpy)	XRD phases	Remarks
Uncoated Grade-A-1 boiler steel	546.58	1.427	491.2	Fe ₂ O ₃ , Al ₂ O ₃ and SiO ₂	Ash deposited scale with severe spalling and blackish brown colored surface appearance. Ash deposition, erosion and severe spalling continued to last cycle.
Nanostructured TiAlN coating	535.36	1.280	438.0	Fe ₂ O ₃ , Al ₂ O ₃ and SiO ₂	Color of the oxide scale at the end of the study was observed to be blackish grey with some visible cracks and ash deposited surface. Erosion and ash deposition continued till end of the study.
Nanostructured AlCrN coating	435.50	1.500	513.8	Fe ₂ O ₃ , Al ₂ O ₃ and SiO ₂	The formation of dark blackish grey colored scale with severe spalling and visible hairline cracks was observed at the end. The ash deposition, erosion and spalling continue till the end.
Conventional TiAlN Coating	121.31	0.372	68.94	Fe ₂ O ₃ , Al ₂ O ₃ , SiO ₂ and Ti ₃ Al	Bluish grey colored ash deposited scale at the end of the study. The scale was rough and adherent to the substrate.
Conventional AlCrN coating	242.67	0.406	82.69	Fe ₂ O ₃ , Al ₂ O ₃ and SiO ₂	Color of the ash deposited oxide scale was dark grey with some whitish areas at the end. The scale was found to be adherent. No spalling was observed till 4 th cycle after which the sample showed spalling and signs of erosion.

These alkali sulphates react with iron oxides (present in the scale or in the ash itself), in presence of SO_3 in the gas, to form alkali-ion trisulphates $(\text{Na}, \text{K})_3\text{Fe}(\text{SO}_4)_3$, these alkali-iron trisulphates are molten at the operating temperature of the boiler due to their low melting temperatures: 624°C for $\text{Na}_3\text{Fe}(\text{SO}_4)_3$, 618°C for $\text{K}_3\text{Fe}(\text{SO}_4)_3$ and 552°C for the mixed compound $(\text{Na}, \text{K})_3\text{Fe}(\text{SO}_4)_3$ (Srivastava et al, 1997; Weulersse-Mouturat et al., 2004). These molten compounds can flux the scale or react with the alloy to form internal sulphides. Therefore, the alkali-iron trisulphides are responsible for the degradation of super-heater in the coal-fired plants.

Conventional thick TiAlN and AlCrN coatings have been found successful in reducing the overall weight gain of bare Grade A-1 boiler steel. The higher weight gain during the first few cycles might be attributed to the rapid formation of oxides at the splat boundaries and within the open pores due to the penetration of the oxidizing species, further the subsequent increase in weight is gradual (Singh H et al., 2007). There is continuous formation of thin oxide scale with subsequent depletion by spallation and erosion under cyclic test conditions. The top surface may contains inclusions, which leads to vertical cracks through which the corrosive species might have penetrated along the crack and between the metallic layers. The cracks and oxide layer have propagated parallel to the top surface. During cyclic testing, cracks in the oxide scale and spalling of the uncoated and coated Grade A-1 boiler steel might be attributed to the different values of thermal coefficients for the coating, scale and the substrate as reported by Sidhu et al. (2003), Singh et al. (2004), Evans et al. (2001), Wang et al. (2002) and Niranatlumpong et al (2000).

The presence of Fe and oxygen (Fig.4.45) in the top of the scale of the uncoated and coated Grade-A-1 boiler steel is believed to be due to the diffusion of iron through the pores and cracks that appeared in the coating during the course of oxidation studies (Singh Buta et al., 2003). The phases revealed by XRD diffractograms are found to be in agreement with those reported by Longa-Nova et al (1996), Calvarin et al (2000) and Nickel et al (2002). In case of conventional thick TiAlN coating; addition to the above mentioned phases Ti_3Al is also present in the oxide scale (Fig.4.43). Formation of hematite (Fe_2O_3) as revealed by the X-ray diffractograms might be due to the reaction of iron with

oxygen since iron is the main constituent of boiler steel. Formation of such type of oxides has also been analyzed by Prakash et al (2001) and Srikanth et al (2003) during the failure analysis of superheater tubes caused by fireside corrosion. The formation of Al_2O_3 and SiO_2 might be due to the deposition of ash on the eroded-corroded tubes. The higher amount of Al and Si is found in the ash. The presence of such phases in slag has also been reported by John (1986) in his study on slag, gas and deposit thermochemistry in a coal gasifier and the possibility for formation of such phase in ash constituents during combustion has further been reported by Nelson et al (1959). Absence of sulphide formation as indicated by the XRD analysis is further supported by the findings of Crossley et al (1948). They reported that the presence of fly ash particles rich in magnetite reduced the concentration of SO_3 in the boiler system fired by mechanical stokers.

It can be mentioned based on the present investigation that conventional thick TiAlN and AlCrN coatings can provide erosion-corrosion resistance when exposed to super-heater of the coal fired boiler environment at 900°C . It is well supported by corrosion rate plot (Fig.4.47) as the corrosion rate is very less in case of conventional thick coatings as compared to the uncoated and nanostructured coated Grade A-1 boiler steel. These results are well supported by EDAX (Fig.4.44) and X-ray mapping analysis (Fig.4.48). The resistance offered by conventional thick TiAlN and AlCrN coatings to the erosion-corrosion in boiler environment may be due to the presence of a thick band of Al along with oxygen; as shown by X-ray mapping analysis (Fig.4.48.d and e).

4.6.4 Conclusions

The high temperature erosion-corrosion behaviors of uncoated and coated ASTM-SA210 Grade A-1 boiler steel have been investigated in super-heater of the coal fired boiler environment at 900°C for 1000 hours (10 cycles). The behavior of nanostructured TiAlN and AlCrN coatings were compared with their conventional counterparts and the following conclusions are made:

1. The plasma sprayed gas nitride conventional thick coatings i.e. TiAlN and AlCrN have developed a protective scale mainly consisting on aluminum oxide.

2. All the coated as well as uncoated boiler steels have shown ash deposition on the surface. Thus final thickness is contributed by scale formation, erosion and ash deposition.
3. The corrosion rate for the uncoated and coated Grade A-1 boiler steel specimens exposed to the super-heater of the coal fired boiler environment at 900°C follows the sequence:
Nanostructured AlCrN > Uncoated Grade A-1 > Nanostructured TiAlN > Conventional AlCrN > Conventional TiAlN
4. The nanostructured TiAlN and AlCrN coatings has shown resistance to erosion-corrosion to some extent as the overall weight gain and thickness are less than as compared to the uncoated Grade A-1 boiler steel, but failed to provide full protection to the substrate.
5. Thick TiAlN and AlCrN coatings can provide good erosion-corrosion resistance when exposed to super-heater of the coal fired boiler environment at 900°C.
6. The oxide scale formed is adherent to the substrate in all coatings. But in case of uncoated and nanostructured coated Grade-A-1 boiler steel, the scale is found to be fragile with some cracks.

SUBSTRATE ASTM-SA213-T-11 BOILER STEEL

This chapter deals with the results and discussion for the bare and coated ASTM-SA213-T-11 boiler steel exposed to different degradation environments. It includes the characterization of the nanostructured and conventional TiAlN and AlCrN coatings on T-11 boiler steel and their behavior when exposed to high temperature oxidation studies in air, molten salt (Na_2SO_4 -60% V_2O_5) environment and in a coal fired boiler of a thermal plant, erosion studies in simulated coal-fired boiler environment and corrosion studies in simulated marine environment.

5.1 CHARACTERISATION OF COATINGS

Little work has been published on high temperature corrosion behavior of nanostructured and conventional hard metal nitride coatings to the best of the knowledge of the author. Therefore, these coatings were developed on the ASTM-SA213-T-11 boiler steel and their behavior was studied when exposed to high temperature oxidation in air, molten salt environment, industrial environment, high temperature solid particle erosion and simulated marine environment. In the present section the conventional thick (by plasma spraying and gas nitrided) and nanostructured thin (by physical vapor deposition process) TiAlN and AlCrN coatings developed on ASTM-SA213-T-11 boiler steel have been characterized.

5.1.1 Results

5.1.1.1 Visual observations

The nanostructured thin (by Physical Vapor Deposition process) and conventional thick (by Plasma Spraying and Gas Nitriding) TiAlN and AlCrN coatings have been formulated successfully on ASTM-SA213-T-11 boiler steel. The macrographs of as-coated T-11 boiler steel are shown in Fig.5.1. As observed from the macrographs the nanostructured thin TiAlN coating is violet grey in color and nanostructured thin AlCrN coating is light grey in color. Visual observations indicate; the surface of nanostructured

coatings is smooth whereas the surface of conventional thick coatings is rough. The color of the thick coatings appeared as dark grey. Also, Optical micrographs of the nanostructured and conventional coatings are shown in Fig. 5.2. The nanostructured coatings (Fig.5.2.a & b) have uniform microstructure. It is evident from the microstructure that the coatings contain some pores and inclusions. In case of conventional thick coatings (Fig. 5.2.c & d); the massive microstructure can be observed with irregularly shaped grains.

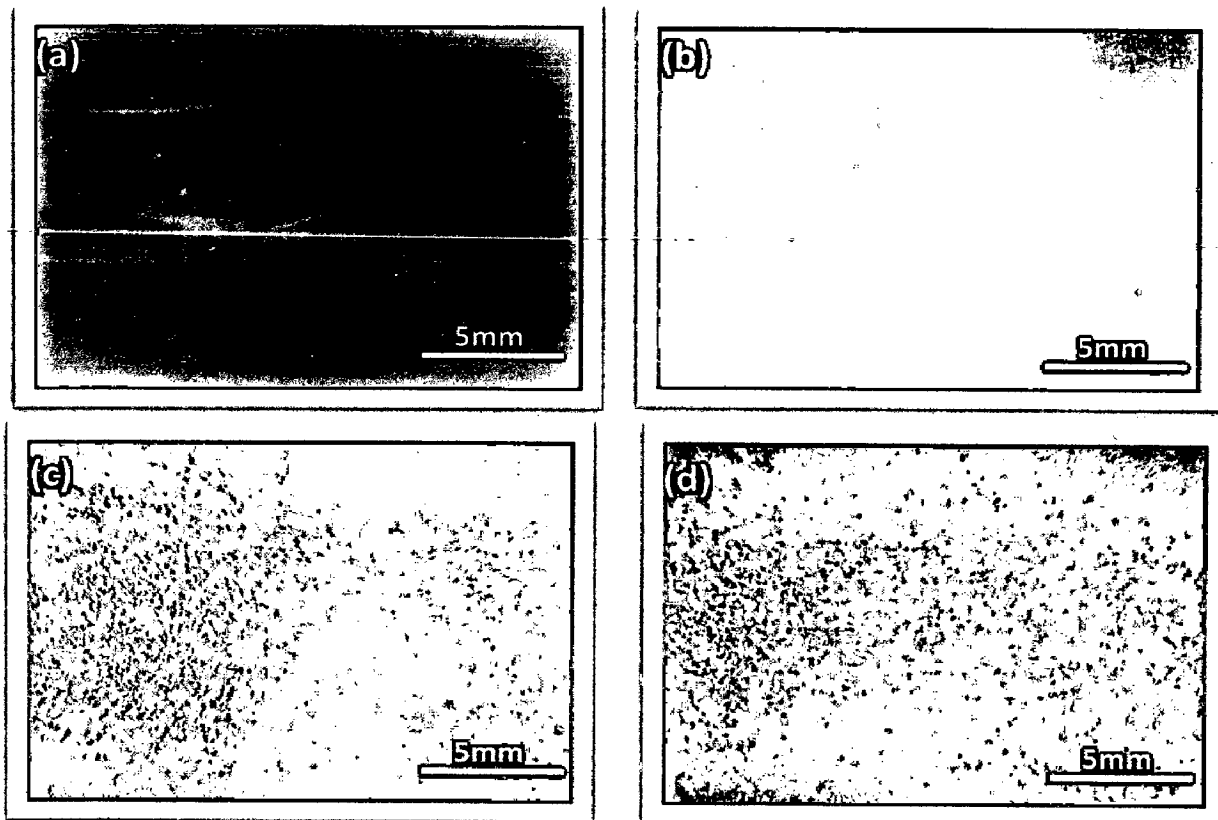


Fig. 5.1 Surface macrographs for the as coated ASTM-SA213-T-11 boiler steel (a) Nanostructured TiAlN coating, (b) Nanostructured AlCrN coating, (c) Conventional TiAlN coating, (d) Conventional AlCrN coating

5.1.1.2 Surface analysis

5.1.1.2.1 X-ray diffraction analysis (XRD)

XRD diffractograms for nanostructured and conventional TiAlN and AlCrN coated T-11 boiler steel are depicted in Fig.5.3 on reduced scale. TiN and AlN are the main phases identified in the nanostructured thin TiAlN coating. Further, in case of

nanostructured AlCrN coating, the prominent phases are CrN and AlN. The grain size of the nanostructured thin coatings was estimated from Scherrer formula (as explained in Chapter 3); which is reported in Table.5.1. The calculated grain size for nanostructured thin TiAlN and AlCrN coatings is 15 and 21 nm respectively. Further, the main phases identified for the conventional thick TiAlN coating are Al₂O₃, TiN, Ti₃Al, AlN and TiO₂. The phases identified in case of conventional thick AlCrN coating are CrN, AlN, and Al₂O₃ with minor peaks of Cr₂O₃.

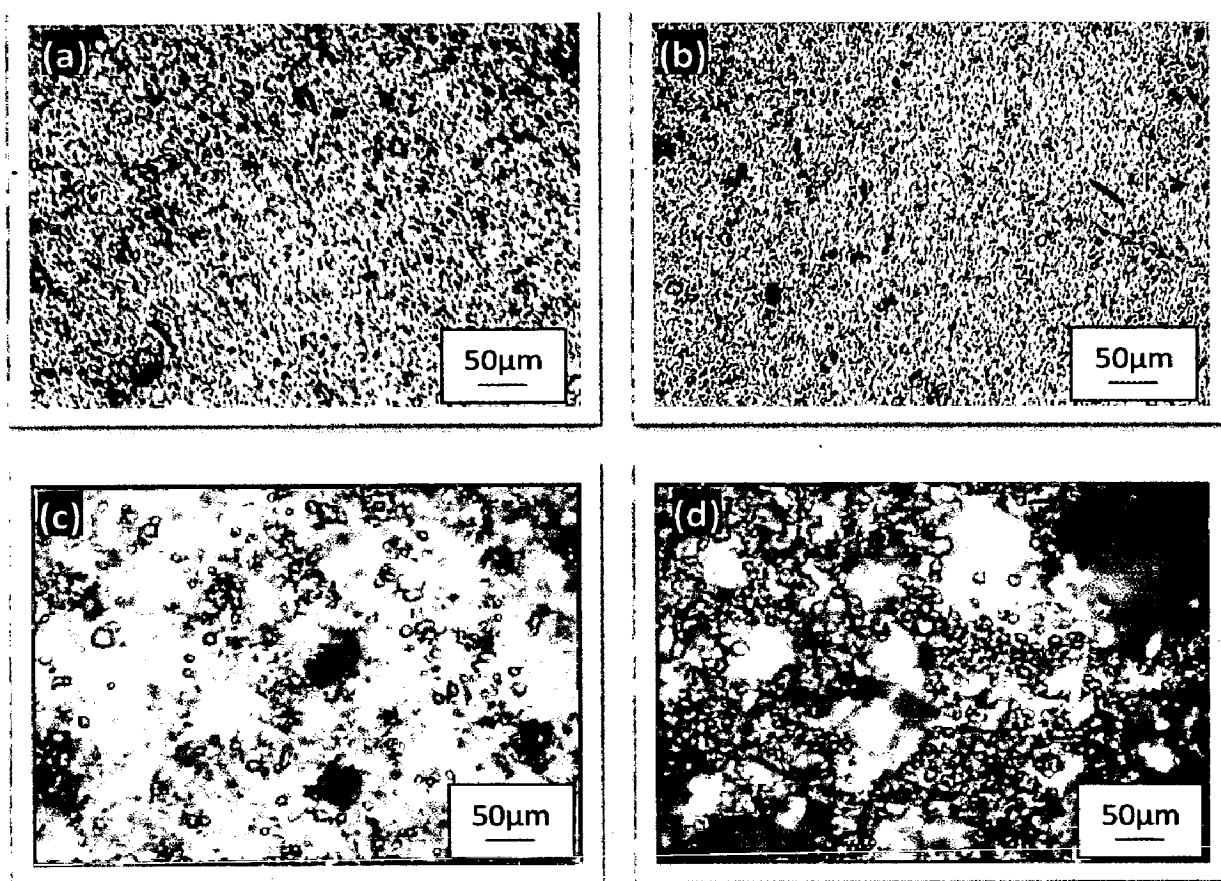


Fig. 5.2 Optical micrograph (200 X) of the surface of as coated ASTM-SA213-T-11 boiler steel (a) Nanostructured TiAlN coating, (b) Nanostructured AlCrN coating, (c) Conventional TiAlN coating, (d) Conventional AlCrN coating

5.1.1.2.2 Porosity analysis

The porosity analysis is of prime importance in high temperature corrosion studies. The dense coatings are supposed to provide very good corrosion resistance as

compared to porous coatings. The porosity measurements were made by PMP3 inverted metallurgical microscope with stereographic imaging and subsequently the porosity was evaluated with the help of software as explained in chapter 3. The porosity of nanostructured thin TiAlN and AlCrN coatings was found below 0.4 % (Table.5.1). In case of conventional thick coatings; the porosity of as sprayed Ti-Al (2.60-4.00 %) and Al-Cr (2.50-4.10 %) coatings was also evaluated; which is reported in Table.5.2. A considerable decrease in the porosity had been observed after gas nitriding and it was found to be less than 0.6 % (Table.5.2).

Table 5.1 Microstructural and mechanical properties of nanostructured thin TiAlN and AlCrN coated ASTM-SA213-T-11 boiler steel

Coating	Surface Roughness (nm)	Particle Size (nm)		Coating Thickness (μm)	Porosity (% age)	Coating Color
		Scherrer Formula	AFM Analysis			
Nanostructured TiAlN Coating	03.69	15	14	5.2	< 0.4	violet-grey
Nanostructured AlCrN Coating	05.18	21	20	5.5	< 0.4	light-grey

Table 5.2 Microstructural and mechanical properties of conventional thick TiAlN and AlCrN coated ASTM-SA213-T-11 boiler steel

Coating	Surface Roughness (μm)	Coating Thickness (μm)	Porosity (% age)		Bond Strength (MPa)	Coating Color
			As Sprayed	After Gas Nitriding		
Conventional TiAlN Coating	7.36-14.31	174	2.60-4.00	< 0.6	68.74	Bluish-grey
Conventional AlCrN Coating	12.20-15.45	122	2.50-4.10	< 0.6	54.69	Bluish-grey

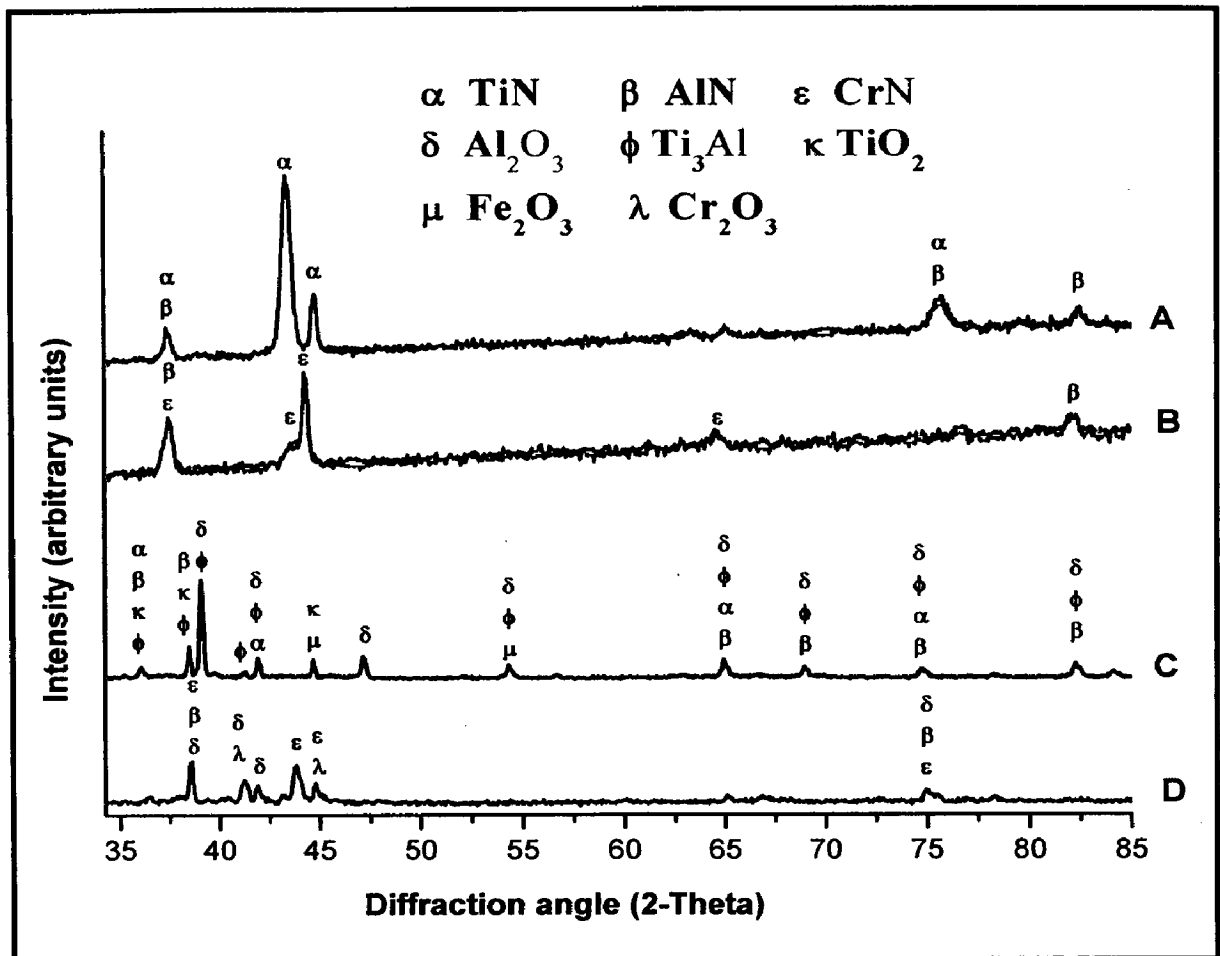


Fig. 5.3 Surface-scale morphology and EDAX patterns from different spots on as coated ASTM-SA213-T-11 boiler steel (a) Nanostructured TiAlN coating, (b) Nanostructured AlCrN coating, (c) Conventional TiAlN coating, (d) Conventional AlCrN coating

5.1.1.2.3 AFM analysis of the as deposited nanostructured thin coatings

The surface topography of the nanostructured thin TiAlN and AlCrN coatings was studied using Atomic Force Microscope (AFM NT-MDT: NTEGRA Model) in semi contact mode. Figure 5.4 shows the AFM surface morphology (2D and 3D) of the nanostructured thin TiAlN and AlCrN coatings deposited on T-11 boiler steel. The difference in the morphology between the two coatings can be inferred by comparing the 2D images in Fig. 5.4 (a) and (c); however a clearer comparison of the coatings could be afforded by viewing 3D images in Fig. 5.4 (b) and (d). As the axis scale indicates the overall roughness of the nanostructured TiAlN coating (Fig. 5.4.b) is less than that of AlCrN coating

(Fig.5.4.d). The surface roughness and particle size in the coatings was also provided by AFM analysis; which are reported in Table.5.1. The surface roughness in case of nanostructured TiAlN coating was observed 3.69 nm and 5.18 nm in case of nanostructured AlCrN coating (Table.5.1). The nanostructured thin TiAlN coating had shown lesser particle size (14 nm) as compared to nanostructured thin AlCrN coating (20 nm).

5.1.1.2.4 Surface roughness (R_a) values of the conventional thick coatings

The coating surface was very rough in case of conventional thick TiAlN and AlCrN coatings due to the presence of unmelted/partially melted particles and the roughness was found to be in the range of 07.36-14.31 μm and 12.20-15.45 μm respectively. The centre line average (CLA) method was used to obtain the R_a values.

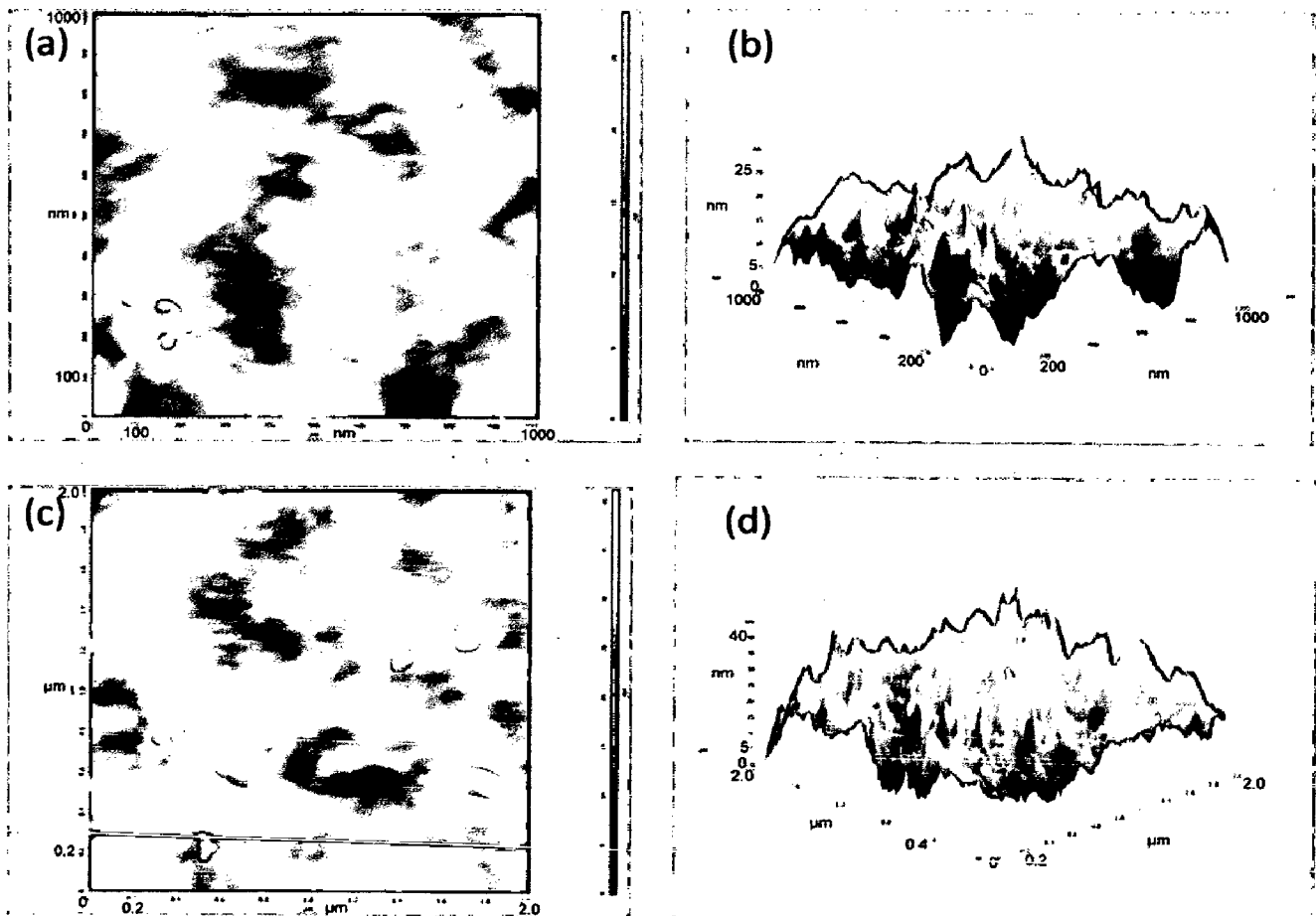


Fig. 5.4 2D and 3D AFM images for the as coated ASTM-SA213-T-11 boiler steel (a) & (b) Nanostructured TiAlN coating, (c) & (d) Nanostructured AlCrN coating

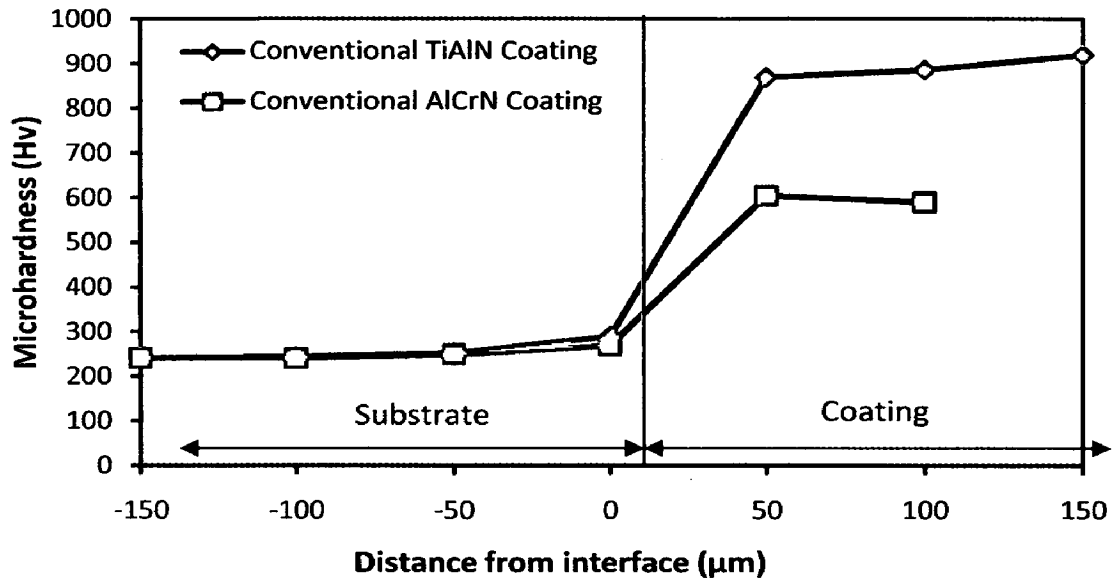


Fig. 5.5 Microhardness profile across the cross-section for Conventional TiAlN and Conventional AlCrN coating on ASTM-SA213-T-11 boiler steel

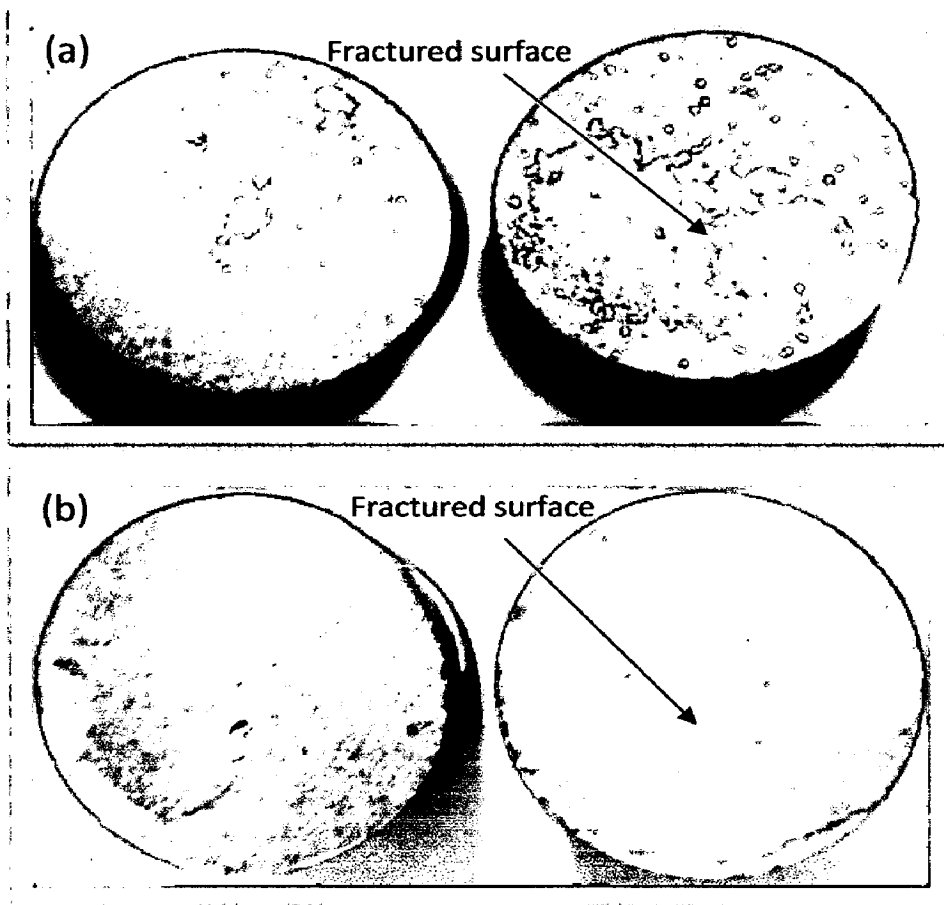


Fig. 5.6 Fracture surfaces of a Plasma sprayed gas nitride specimen after ASTM C633 tensile test; (a) Conventional TiAlN coating, (b) Conventional AlCrN coating

5.1.1.2.5 Evaluation of microhardness and bond strength of conventional coatings

The hardness of the coatings has been measured along the cross-section of the conventional thick TiAlN and AlCrN coated T-11 boiler steel. Figure 5.5 shows the microhardness profiles along the cross-section of the coatings as a function of distance from the coating-substrate interface. The critical microhardness value of the substrate T-11 boiler steel was found to be in the range 200-300 Hv. From the microhardness profiles (Fig.5.5) it is obvious that the conventional TiAlN coating has shown maximum microhardness of the order of 900-1000 Hv. The conventional thick AlCrN coating has shown microhardness of the order of 650-700 Hv.

The bond strength of the conventional thick TiAlN and AlCrN coatings was measured on three specimens as per ASTM standard C633-01. The coatings failed at the substrate-coating interface while remaining attached to the adhesive (Fig.5.6). Average bond strength of 68.74 MPa and 54.69 MPa was observed in case of conventional TiAlN and AlCrN coatings respectively (Table.5.2).

5.1.1.2.6 Surface morphology of coatings

SEM micrographs along with EDAX point analysis reveal the surface morphology of the nanostructured and conventional TiAlN and AlCrN coated T-11 boiler steel; are shown in Fig.5.7. Micrograph (Fig.5.7.a) for nanostructured thin TiAlN coating at higher magnification (10000 X) indicates grey matrix with some black and white contrast regions. Dense structure with lower porosity is observed in the coating microstructure and also it is free from cracks. EDAX analysis at point 1 and point 2 on Fig.5.7 indicates the presence of Ti, Al and N with negligible amount of O and Fe. The black colored areas revealed the higher amount of Ti and less concentration of Al as compared to the white contrast region. In case of nanostructured thin AlCrN coated T-11 boiler steel, the SEM micrograph indicates dense grey colored coating with tiny dark grey particles dispersed in the matrix. EDAX point analysis (Point 3 and 4 on Fig.5.7) shows, the coating is rich in Al, Cr and N along with small amount of Fe and oxygen (Fig.5.7.b). The micrographs in case of conventional plasma sprayed gas nitride TiAlN and AlCrN coatings are shown in Fig.5.7(c and d). In general microscopic features indicate that the conventional coatings are homogeneous and massive, free from cracks.

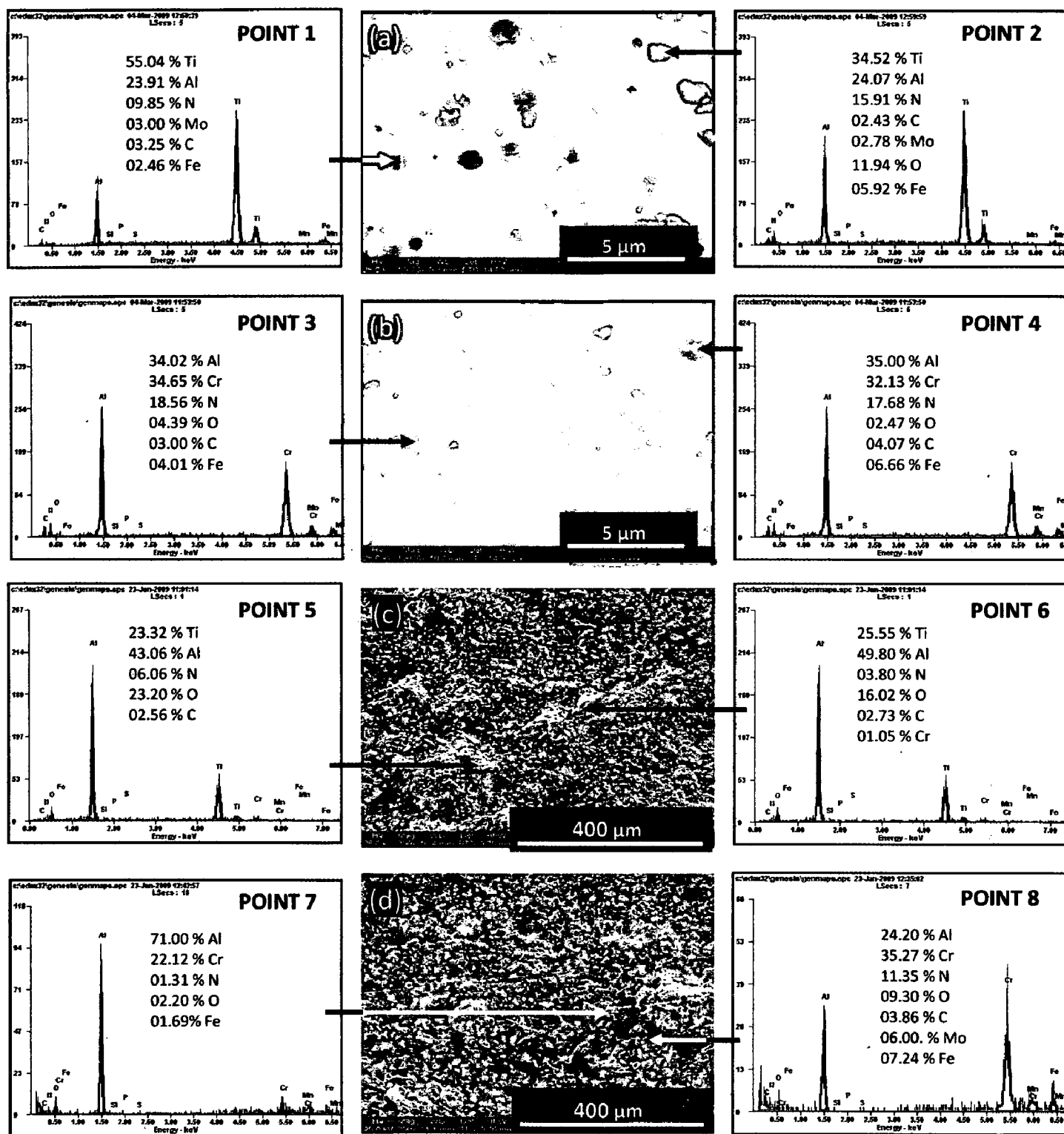


Fig. 5.7 Surface-scale morphology and EDAX patterns from different spots on as coated ASTM-SA213-T-11 boiler steel (a) Nanostructured TiAlN coating, (b) Nanostructured AlCrN coating, (c) Conventional TiAlN coating, (d) Conventional AlCrN coating

Presence of some oxide stringers as well as open pores has been noticed in general in the conventional coatings. The EDAX point analysis (Point 5 and 6 on Fig.5.7); in case of conventional TiAlN coating indicates the higher concentration of Ti and Al in the coating along with N and oxygen. The presence of Al and Cr along with N and oxygen is revealed by EDAX analysis in case of conventional AlCrN coating (Point 7 and 8 in Fig.5.7).

5.1.1.3 Cross-sectional analysis

5.1.1.3.1 Coating thickness

The as-coated samples were cut across the cross section using Buehler Isomet 1000 precision saw and mounted in transoptic mounting resin and subsequently mirror polished to obtain scanning electron back scattered micrographs and X-ray mapping of different elements for coated ~~cross section~~ T-11 boiler steel. The coating thickness values were measured from SEM back scattered micrographs as shown in Fig.5.8; and average coating thickness is reported in Table.5.2. The measured average coating thickness values for nanostructured thin and conventional thick TiAlN and AlCrN coatings are 5.2, 5.5, 174 and 122 μm respectively.

5.1.1.3.2 X-Ray mapping

BSEI and X-ray mapping analysis for nanostructured and conventional TiAlN and AlCrN coated T-11 boiler steel is shown in Fig. 5.8. The X-ray mapping indicates presence of Al and Ti along with small amount of N in the nanostructured TiAlN coating (Fig. 5.8.a). In case of nanostructured thin AlCrN coated T-11 boiler steel; the BSEI and X-ray mapping are shown in Fig. 5.8 (b). The X-ray mapping indicates the presence of Al and Cr along with some concentration of N in the coating. In case of conventional thick TiAlN coated T-11 boiler steel, Fig.5.8 (c), Al and Ti rich coating along with negligible amount of N and O; has been observed. The diffusion of Fe from the substrate has taken place as indicated by X-ray mapping analysis. Figure.5.8 (d) depicts the BSEI and X-ray mapping in case of conventional AlCrN coated T-11 boiler steel. The coating is rich in Al and Cr with negligible presence of N and O. The X-ray mapping analysis indicates the presence of Fe in the coating.

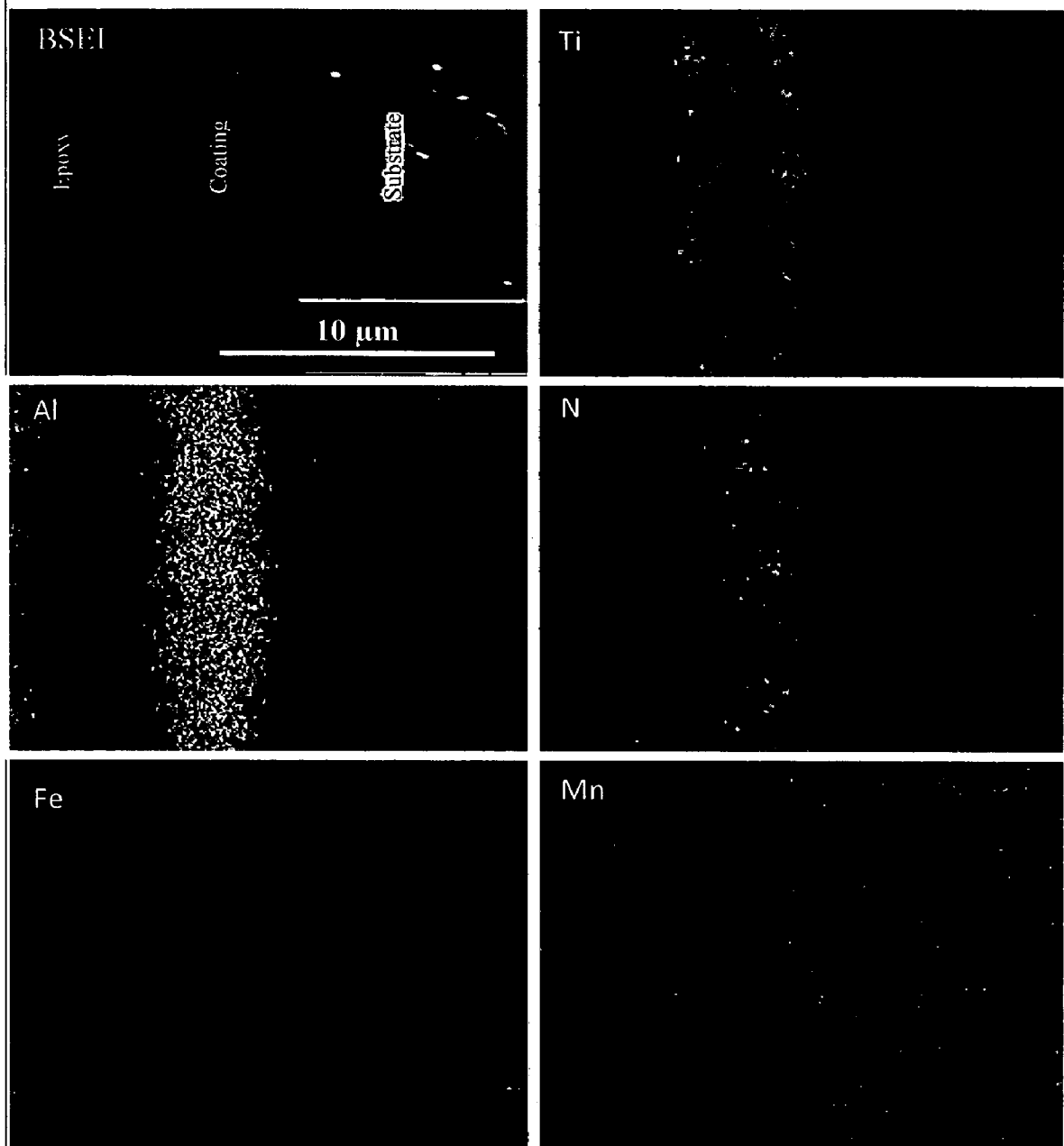


Fig. 5.8 (a) Composition image (BSEI) and X-ray mapping of the cross-section of as-coated nanostructured TiAlN coating on ASTM-SA213-T-11 boiler steel

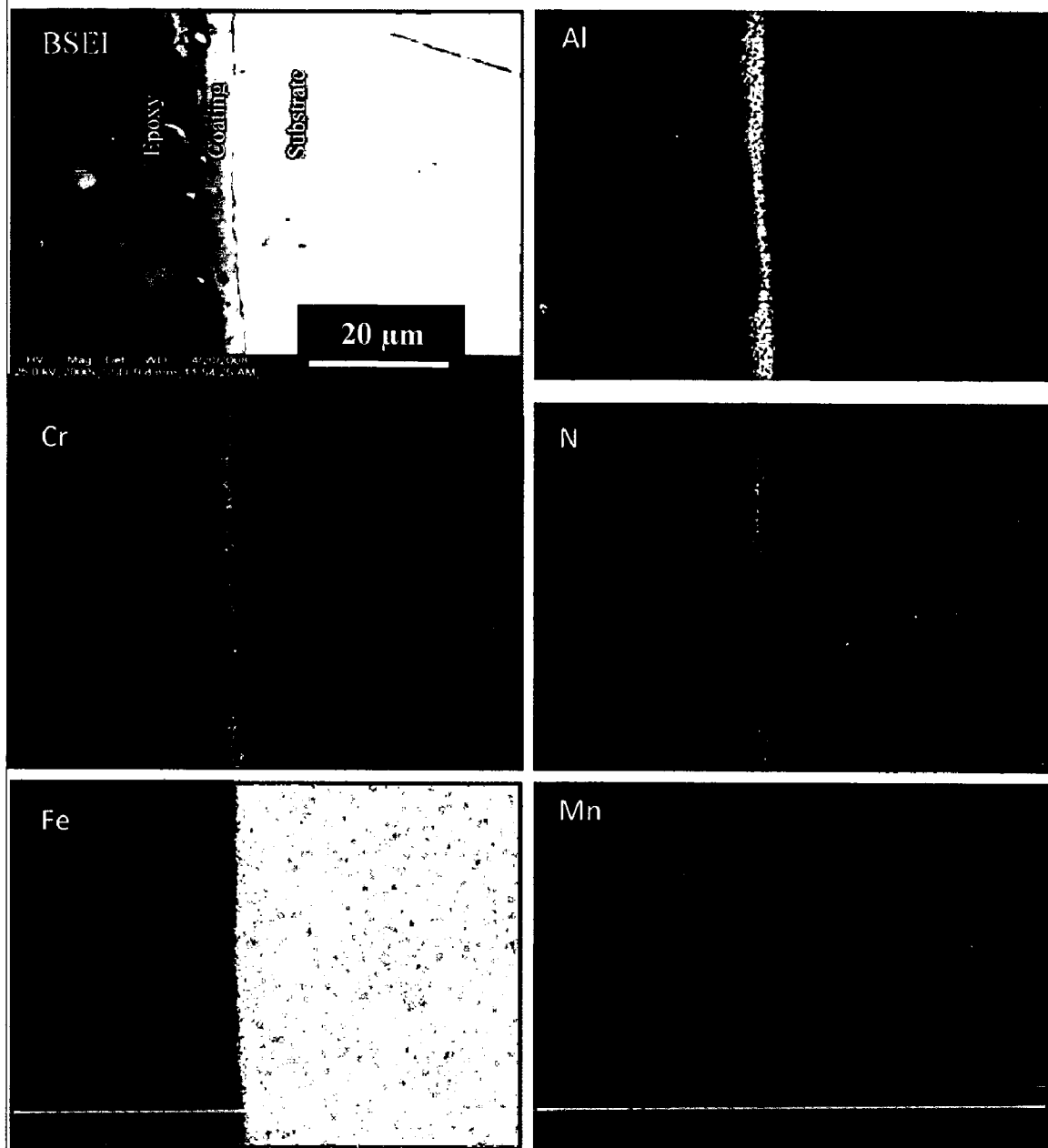


Fig. 5.8 (b) Composition image (BSEI) and X-ray mapping of the cross-section of as-coated nanostructured AlCrN coating on ASTM-SA213-T-11 boiler steel

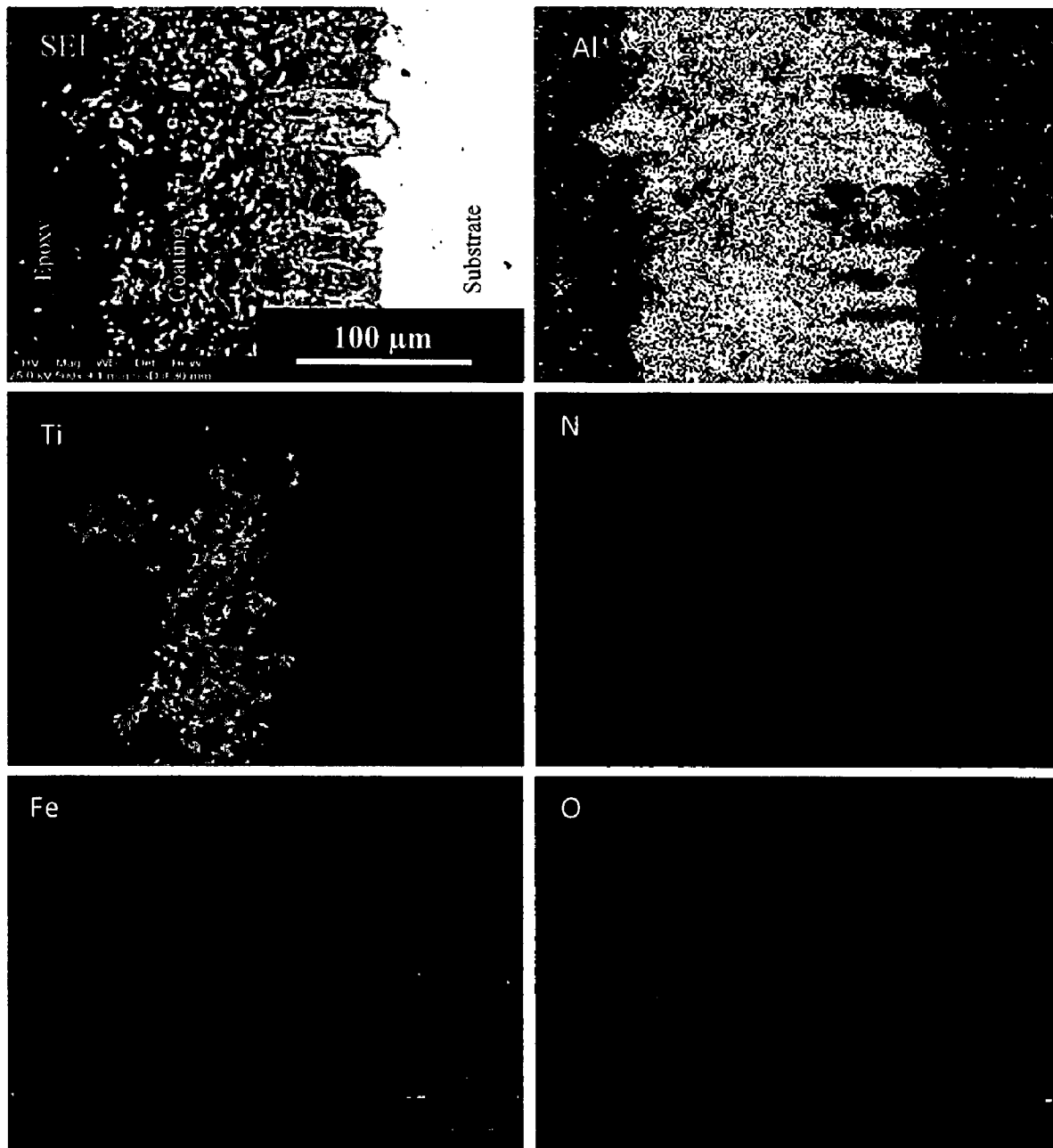


Fig. 5.8 (c) Composition image (SEI) and X-ray mapping of the cross-section of as-coated conventional TiAlN coating on ASTM-SA213-T-11 boiler steel

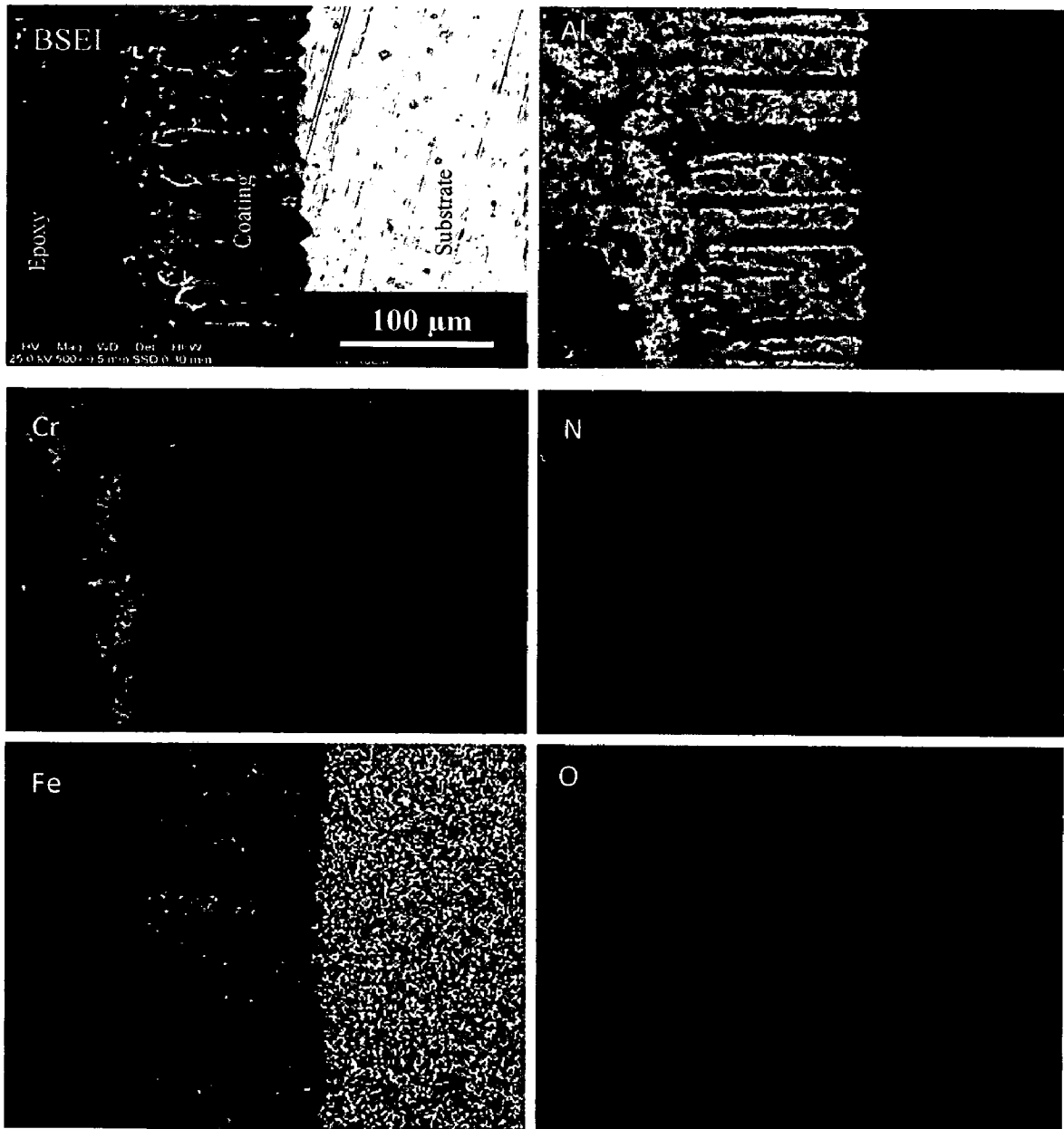


Fig. 5.8 (d) Composition image (BSEI) and X-ray mapping of the cross-section of as-coated conventional AlCrN coating on ASTM-SA213-T-11 boiler steel

5.1.2 Discussion

The nanostructured thin TiAlN and AlCrN coatings on ASTM-SA213-T-11 boiler steel were obtained using a front-loading Balzer's rapid coating system (RCS) machine at Oerlikon Balzers Ltd. Gurgaon (India). In case of conventional thick TiAlN and AlCrN coatings; the plasma spray coatings were obtained at Anod Plasma Ltd. Kanpur (India) using a 40 kW Miller Thermal Plasma Spray apparatus. The surface appearance of nanostructured TiAlN coating was violet grey in color and light grey in case of nanostructured AlCrN coating (Fig.5.1). In case of conventional thick coatings: the surface appearance of conventional TiAlN and AlCrN coatings was grey with some bluish shining (Fig.5.1). The surface of conventional thick coatings was rough. As inferred from optical micrographs (Fig.5.2 a & b) that the nanostructured coatings were dense with uniform microstructure. It is evident from the microstructure that the coatings contain some pores and inclusions. In case of conventional thick coatings (Fig.5.2.c & d); the massive microstructure could be observed with irregularly shaped grains.

The phases identified by XRD analysis (Fig.5.3) for nanostructured thin TiAlN coating are TiN and AlN. The phases analyzed are also in agreement with that reported by Yoo et al. (2008), Falub et al. (2007) and Man et al. (2004). The prominent phases in case of nanostructured AlCrN coating are CrN and AlN which are in agreement with the findings of Reiter et al. (2005) and Endrino et al. (2006). Further, the main phases identified for the conventional thick TiAlN coating are Al₂O₃, TiN, Ti₃Al, AlN and small peaks of TiO₂ and Fe₂O₃. The phases identified in case of conventional thick AlCrN coating are CrN, AlN, and Al₂O₃ with minor peaks of Cr₂O₃. The presence of metal nitride phases indicates that the gas nitriding process has successfully produced the desired coatings. Further, the phases analyzed are also in agreement with that reported by Adachi and Nakata (2007).

The grain size (Table.5.1) of the nanostructured thin coatings was estimated from Scherrer formula (Cullity, 1970) and further verified by AFM analysis (reported in Table 5.1). The particle size determined by AFM analysis is in good agreement with the results obtained from Scherrer formula. The nanostructured thin TiAlN coating had shown smaller particle size (15 nm) as compared to nanostructured thin AlCrN coating (21 nm).

The coating thickness was measured along the cross-section for some of the randomly selected samples and reported in Table 5.1 and 5.2. The coatings thickness was

observed to be 5.2 and 5.5 μm in case of nanostructured TiAlN and AlCrN coatings respectively. The self-disintegration of thicker coatings usually restricts the thickness of the coatings (Sidhu et al., 2004). In case of conventional thick coatings; it was possible to obtain a thickness in range of 150-200 μm for Ti-Al and Al-Cr coatings. After coating deposition process; the gas nitriding was done in lab in order to obtain hard metal nitride coatings. The coating thickness was measured along the cross-section for some randomly selected samples and reported in Table 5.2. The coatings thickness was observed as 174 and 122 μm in case of conventional thick TiAlN and AlCrN coatings respectively.

The surface roughness was also measured with AFM analysis and reported in Table 5.1. As the axis scale indicates the overall roughness of the nanostructured TiAlN coating (Fig.5.4.b) is less than that of AlCrN coating (Fig.5.4.d). The coating surface was very rough in case of conventional thick TiAlN and AlCrN coatings due to the presence of unmelted/partially melted particles. The negligible porosity values for as coated nanostructured thin TiAlN and AlCrN coatings were observed; which were less than 0.4 % (Table.5.1). The measured porosity values of plasma sprayed and gas nitrided coatings are reported in Table 5.2. The measured values of porosity (2.50-4.10%) for as sprayed conventional Ti-Al and Al-Cr coatings are almost in close agreement with the findings of Chen et al (1993), Erickson et al (1998), Hidalgo et al (1998 and 1999), Singh (2003) and Sidhu et al (2004 and 2005) for thermal plasma sprayed coatings. Further, the porosity values found to be less than 0.6% after gas nitriding, which may be because of elimination of microstructural in-homogeneities by filling of pores and voids by nitrogen during gas nitriding.

Hardness is the most frequently quoted mechanical property of the coatings (Tucker, 1994). The observed microhardness values (Fig.5.5) for the conventional coatings are within the range of microhardness values reported for plasma coatings by Adachi and Nakata (2007), Vuoristo et al. (1994), Chen and Hutchings (1998) and Westergard et al. (1998). Microhardness plots indicate some increase in the microhardness of substrate steel at the substrate coating interface. The hardening of the substrates as observed in the current study might have occurred due to the high speed impact of the coating particles during plasma spray deposition similar to the findings of Singh (2003), Hidalgo et al. (1997, 1998, 1999 and 2000) and Sidhu et al. (2004 and 2005). The observed non-uniformity in the hardness values along the thickness of the coatings may be due to the

microstructural changes along the cross section of the coatings (Staia et al., 2001). Moreover, the microhardness and other properties of the thermal spray coatings are anisotropic because of typical splat structure and directional solidification (Tucker, 1994). The bond strength of the conventional thick TiAlN and AlCrN coatings was measured on three specimens as per ASTM standard C633-01. The coatings failed at the substrate-coating interface while remaining attached to the adhesive (Fig.5.6). Average bond strength of 68.74 MPa and 54.69 MPa was observed in case of conventional TiAlN and AlCrN coatings respectively. The bond strength in case of conventional TiAlN coatings (68.74 MPa) is almost in good agreement with the results reported by Adachi and Nakata (2007).

Surface EDAX analysis supported the results obtained by XRD (Fig.5.3) and X-ray mapping analysis (Fig.5.8) in all the coatings. The presence of Ti, Al and N with negligible amount of Fe (in nanostructured TiAlN coating), Al, Cr and N along with small amount of Fe and oxygen (in nanostructured TiAlN coating), the higher concentration of Ti and Al in the coating along with some amount of N and oxygen (in conventional TiAlN coating) and Al and Cr along with N and oxygen (in conventional AlCrN coating); is revealed by surface EDAX analysis (Fig.5.7). Also, the XRD analysis indicates the presence of the oxide phases in the coatings i.e. Al_2O_3 , TiO_2 and Fe_2O_3 in case of conventional TiAlN coating and the presence of Al_2O_3 and Cr_2O_3 in case of conventional AlCrN coatings. The oxides may form due to the in-flight oxidation during spraying process and/or preexisting in the feed material (Bluni and Mardar, 1996). The latter reason for the oxides formation in the structure of coatings under study looks to be more relevant as the chances of in-flight oxidation are meager in case of the shrouded plasma spraying. Deshpande et al. (2006) proposed that, during in-flight oxidation, a layer of oxide is formed on the molten particle due to chemical reactions between the surface of the liquid phase and oxygen or due to diffusion of oxygen into the liquid. The turbulent mixing of the liquid part of the powder particle during its flight destroys the surface layer of oxides and causes the oxides to be distributed more uniformly through the bulk volume of the particle. However, when temperature of the particle starts dropping during later part of the flight, these oxides tend to solidify and a thin oxide shell would form around the droplet. The oxidation time during thermal spray coating is short typically less than 0.01 s, and can occur in either the solid or molten state. The oxidation of coatings is not always

harmful, it is equally important to control and understand the different aspects of oxidation of coatings; therefore, it is important to find an optimum level for oxidation of coatings (Herman, 1988; Korpiola and Vuoristo, 1996; Nerz et al., 1992).

5.1.3 Conclusions

The nanostructured thin TiAlN and AlCrN coatings (by physical vapour deposition process at Oerlikon Balzers Ltd. Gurgaon, India) and conventional thick TiAlN and AlCrN coatings (by plasma spraying process at Anod Plasma Ltd. Kanpur, India; followed by gas nitriding process) were successfully deposited on ASTM-SA213-T-11 boiler steel. The coatings were characterized for microstructural features and hardness in present work. The following observations were made based on the present study:

1. The nanostructured thin TiAlN and AlCrN coatings exhibited negligible porosity values for as coated (0.4 %). The conventional TiAlN and AlCrN coatings showed; higher porosity values (2.50-4.10 %) for as sprayed conventional Ti-Al and Al-Cr coatings which after gas nitriding were found to be less than 0.6 %.
2. The presence of metal nitride phases as identified by XRD analysis; indicates that the gas nitriding process has successfully produced the desired coatings.
3. The grain size of the nanostructured thin coatings was estimated from Scherrer formula and further verified by AFM analysis. The particle size determined by AFM analysis is in good agreement with the results obtained from Scherrer formula. The nanostructured thin TiAlN coating had shown smaller particle size (15 nm) as compared to nanostructured thin AlCrN coating (21 nm).
4. The surface roughness of nanostructured TiAlN coating was observed to be 3.69 nm and 5.18 nm for nanostructured AlCrN coating. The coating surface was very rough in case of conventional thick TiAlN and AlCrN coatings.
5. A good adhesion of the conventional thick TiAlN and AlCrN coatings was evident from bond test results. Average bond strength of 68.74 MPa and 54.69 MPa Psi was observed in case of conventional TiAlN and AlCrN coatings respectively.

5.2 OXIDATION STUDIES IN AIR

The present work has been focused to compare the cyclic oxidation behavior of conventional thick (by plasma spraying and gas nitrided) and nanostructured thin (by physical vapor deposition process) TiAlN and AlCrN coatings on ASTM-SA213-T-11 boiler steel, in air environment, at 900°C for 50 cycles. The kinetics of the cyclic oxidation of coated as well as uncoated specimens was determined using the weight change studies. After the oxidation studies, the exposed specimens were analyzed by XRD, SEM-EDAX analysis and elemental X-ray mapping. The detailed experimental procedure is explained in chapter 3.

5.2.1 Results

5.2.1.1 Visual observations

The macrographs for uncoated and coated ASTM-SA213-T-11 boiler steel subjected to cyclic oxidation in air at 900°C for 50 cycles are shown in Fig.5.9. For the uncoated T-11 boiler steel, a grey colored scale appeared on the surface right from the 2nd cycle. This bare steel showed spalling of scale from the 2nd cycle onward. Some metallic sound was also observed during cooling after 6th cycle which continued till 50th cycle. At the end of cyclic study, uniform scale with cracks and blackish grey color surface appearance, was observed which can be seen in Fig.5.9 (a).

In case of nanostructured thin TiAlN coated T-11 boiler steel, color of the oxide scale at the end of the study was observed to be brownish grey with severe cracking on the surface, as shown in Fig.5.9 (b). After 4th cycle, the scale starts falling in the boat and grey color spots were seen. Rapid spalling of scale was observed after 10th cycle. The nanostructured thin AlCrN coated T-11 boiler steel has shown the formation of smooth scale with the presence of very fine cracks, when subjected to cyclic oxidation in air at 900 °C for 50 cycles, as shown in Fig.5.9 (c). Golden and ink blue reflections were observed in the scale, after the completion of 2nd cycle, which turned to dark grey subsequently. The oxide scale at the end of cyclic study has shown very fine cracks on the surface.

A visual observation of conventional thick TiAlN coated T-11 boiler steel (Fig.5.9.d), showed the formation of light grey color in the middle of the sample along

with bluish grey sides after 6th cycle. After 11th cycle, severe spalling was observed and a very fine layer of coating gets separated from the substrate and fallen in the boat. At the end of 50 cycles, dark grey sides along with brownish spots at some locations have been observed on the surface as shown in Fig.5.9 (d) and rest of the surface appearance was observed as whitish grey.

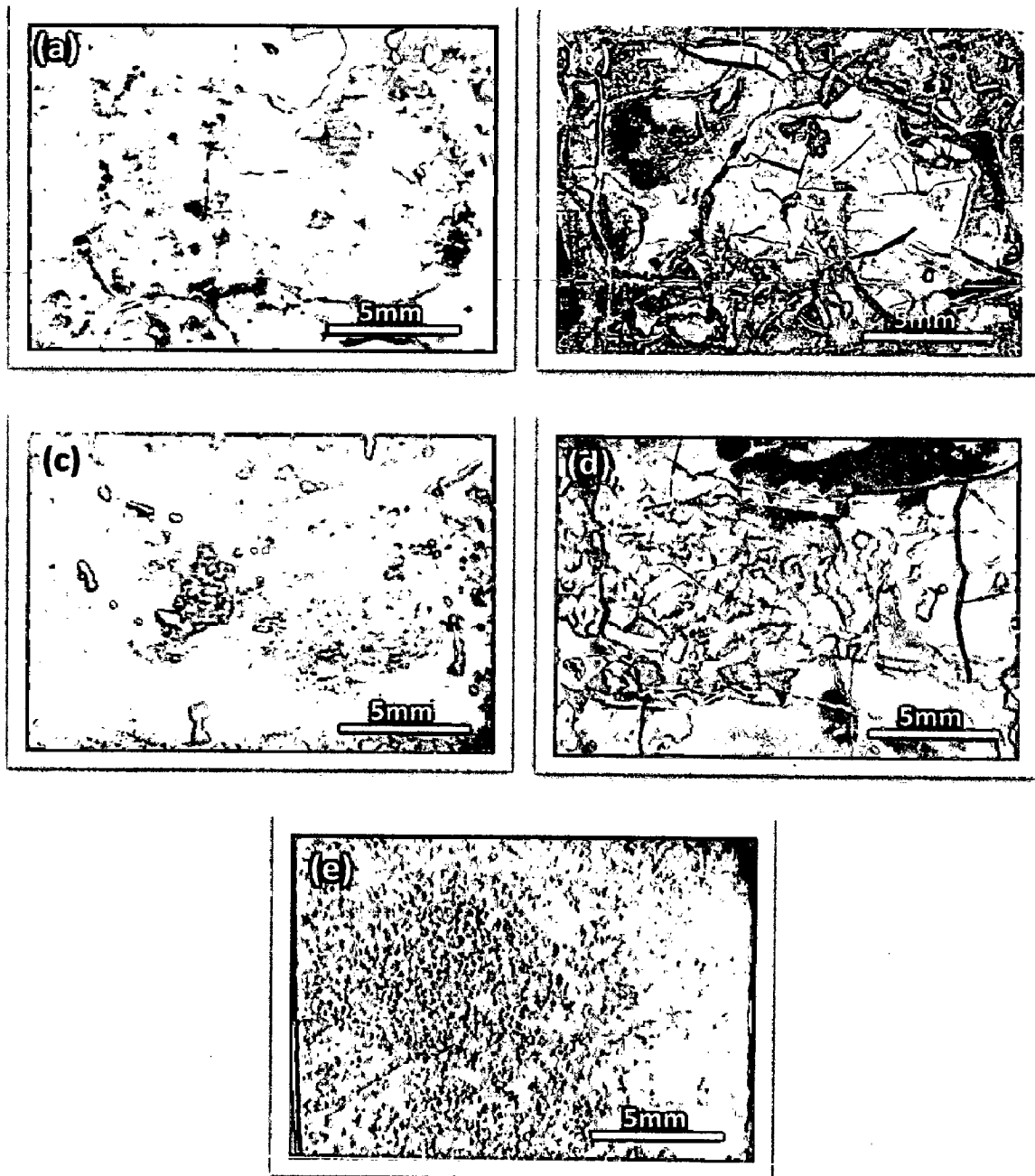


Fig. 5.9 Surface macrographs of uncoated and coated ASTM-SA213-T-11 boiler steel after exposure to cyclic oxidation in air at 900°C for 50 cycles : (a) Uncoated T-11 boiler steel, (b) Nanostructured TiAlN coating, (c) Nanostructured AlCrN coating, (d) Conventional TiAlN coating, (e) Conventional AlCrN coating

In case of conventional thick AlCrN coated T-11 boiler steel, color of the oxide scale was bluish grey after 4th cycle, which turned to whitish grey at the end of the cyclic study (Fig.5.9.e). Some amount of superficial spalling was noticed at the end of 3rd cycle, which may be due to the loosely bond particles on the surface of the coating. The scale was found to be adherent and smooth with a very fine hair line crack.

5.2.1.2 Weight change measurements

Weight gain per unit area (mg/cm^2) versus time expressed in number of cycles plot for coated and bare T-11 boiler steel subjected to cyclic oxidation in air at 900°C for 50 cycles, is presented in Fig.5.10. The plots for all samples shows higher weight gain at initial cycles followed by gradual weight gain. It can be inferred from the plots that the uncoated T-11 boiler steels have shown high rate of oxidation as compared to the coatings. The cumulative weight gain per unit area for the coated and uncoated T-11 boiler steel subjected to cyclic oxidation in air at 900°C for 50 cycles is shown in Fig.5.11. Further, the overall weight gain is highest in case of uncoated T-11 boiler steel and is lowest in case of conventional thick AlCrN coated steel, which is 67% of the weight gain in case of uncoated T-11 boiler steel. Figure 5.12 shows $(\text{weight gain}/\text{area})^2$ versus number of cycles for all the cases to ascertain conformance with the parabolic rate law.

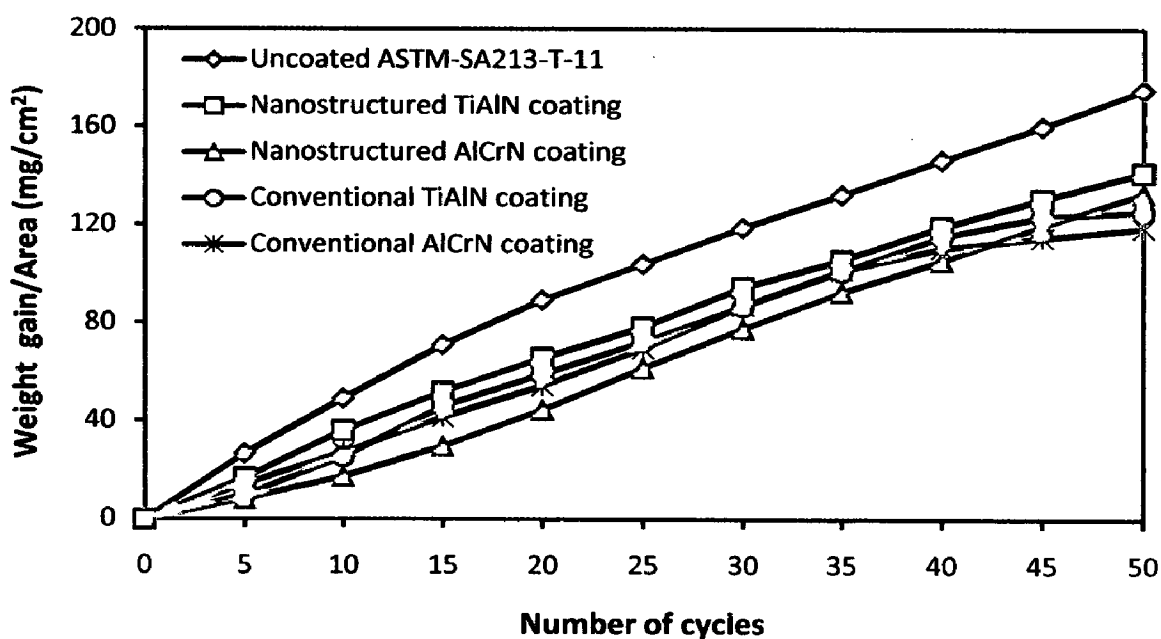


Fig. 5.10 Weight gain/area vs time (number of cycles) for the uncoated and coated ASTM-SA213-T-11 boiler steel subjected to cyclic oxidation in air at 900°C for 50 cycles

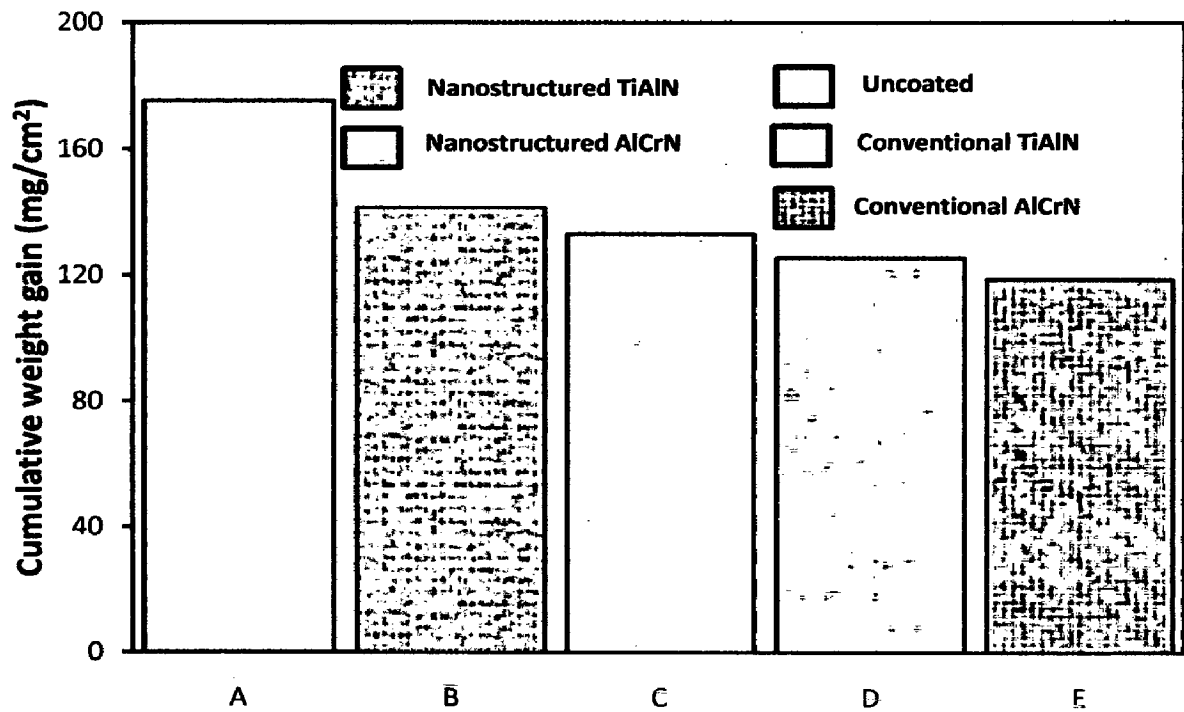


Fig. 5.11 Column chart showing cumulative weight gain per unit area for the uncoated and coated ASTM-SA213-T-11 boiler steel subjected to cyclic oxidation in air at 900°C for 50 cycles; (A) Uncoated T-11 boiler steel, (B) Nanostructured TiAlN coating, (C) Nanostructured AlCrN coating, (D) Conventional TiAlN coating, (E) Conventional AlCrN coating

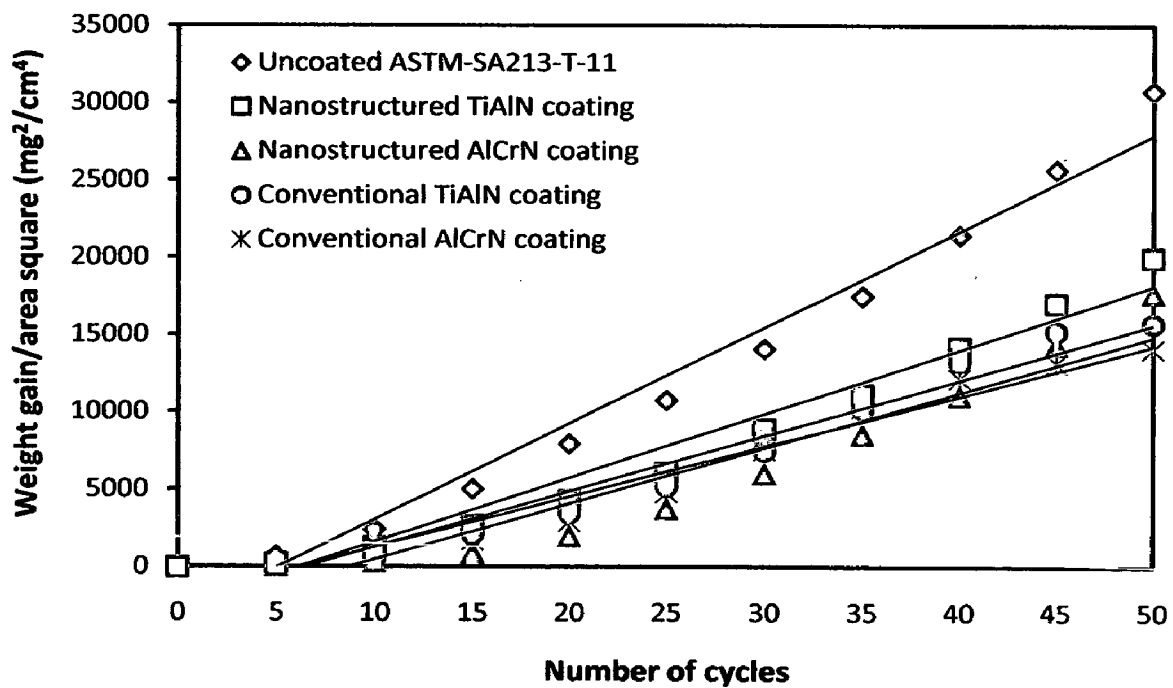


Fig. 5.12 Weight gain/area square vs time (number of cycles) for the uncoated and coated ASTM-SA213-T-11 boiler steel subjected to cyclic oxidation in air at 900°C for 50 cycles

All the coated and uncoated T-11 boiler steels followed the parabolic rate law as evident from the Fig.5.12. The parabolic rate constant K_p was calculated by a linear least-square algorithm to a function in the form of $(W/A)^2 = K_p t$, where W/A is the weight gain per unit surface area (mg/cm^2) and 't' indicates the number of cycles representing the time of exposure. The parabolic rate constants for the bare and coated T-11 boiler steel calculated on the basis of 50 cycle's exposure data are shown in Table.5.3. It is inferred that the ' K_p ' values for the coated T-11 boiler steel were less than bare boiler steel.

Table 5.3 Parabolic rate constant ' K_p ' values of uncoated and coated ASTM-SA213-T-11 boiler steel subjected to cyclic oxidation in air at 900°C for 50 cycles

Substrate / Coating	$K_p \times 10^{-08} \text{ gm}^2 \text{ cm}^{-4} \text{ s}^{-1}$
Uncoated T-11 boiler steel	17.26
Nanostructured TiAlN coating	11.49
Nanostructured AlCrN coating	09.97
Conventional TiAlN coating	09.97
Conventional AlCrN coating	09.01

5.2.1.3 Surface scale analysis

5.2.1.3.1 X-ray diffraction analysis (XRD)

XRD diffractograms for coated and uncoated ASTM-SA213-T-11 boiler steel subjected to cyclic oxidation in air at 900 °C for 50 cycles are depicted in Fig.5.13 (a and b) on reduced scale. As indicated by the diffractograms Fe_2O_3 is the main phases present in the oxide scale of uncoated and nanostructured thin TiAlN and AlCrN coated T-11 boiler steel along with small amount of Cr_2O_3 for uncoated and nanostructured thin AlCrN coated T-11 boiler steel. Further, the main phases identified for the conventional thick TiAlN coating are Fe_2O_3 , Al_2O_3 , Ti_3Al and Al. The oxide phase found in case of conventional thick AlCrN coating was Al_2O_3 .

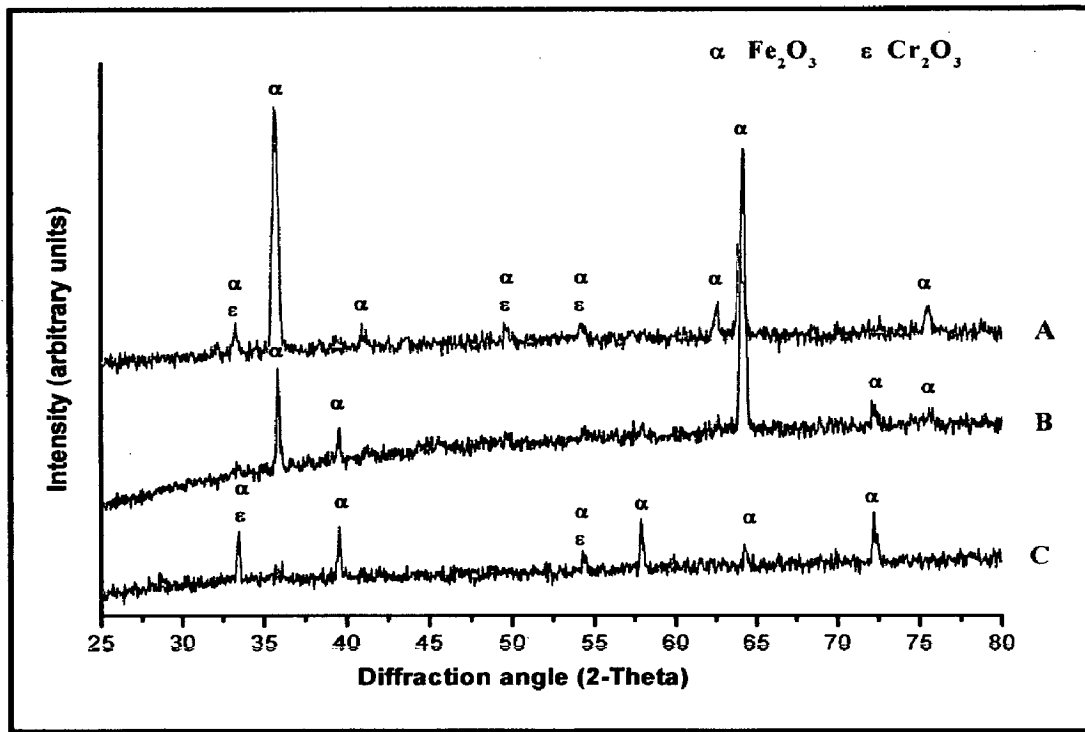


Fig. 5.13 (a) X-Ray Diffraction pattern of uncoated and coated ASTM-SA213-T-11 boiler steel exposed to cyclic oxidation in air at 900°C for 50 cycle : (A) Uncoated T-11 boiler steel, (B) Nanostructured TiAlN coating, (C) Nanostructured AlCrN coating

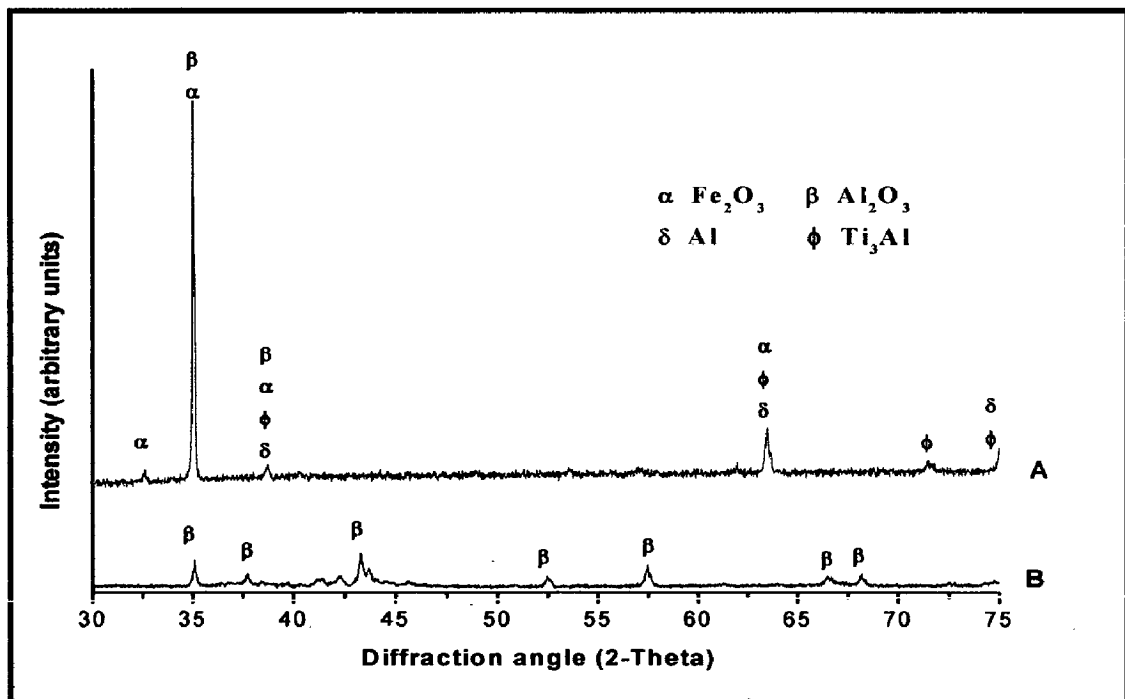


Fig. 5.13 (b) X-Ray Diffraction pattern of uncoated and coated ASTM-SA213-T-11 boiler steel exposed to cyclic oxidation in air at 900°C for 50 cycles: (A) Conventional TiAlN coating, (B) Conventional AlCrN coating

5.2.1.3.2 Surface scale morphology

SEM micrographs along with EDAX point analysis reveals the surface morphology of the coated and uncoated ASTM-SA213-T-11 boiler steel subjected to cyclic oxidation in air at 900°C for 50 cycles are shown in Fig.5.14. The oxide scale for uncoated T-11 boiler steel indicates the dominance of Fe and O (Fig.5.14.a). A small amount of Mo and Mn are also found in the scale. The SEM micrograph of oxidized nanostructured thin TiAlN coatings is shown in Fig.5.14 (b). EDAX analysis of the scale revealed the presence of Fe (54.31%) and O (26.73%) as the main elements in the matrix along with small amount of Mo and Mn (Point 4 on Fig.5.14). The dark region as indicated by point 3 on Fig.5.14 depicts the presence of Fe (80.72%) as main element present with very small amount of O (04.72%). In case of nanostructured thin AlCrN coated T-11 boiler steel, the SEM micrograph indicates the needles like pattern. EDAX point analysis shows, the top scale is rich in Fe, O and Mo.

The surface scale developed on conventional thick TiAlN coated T-11 steel is with white contrast (Point 7) and grey contrast regions (Point 8). EDAX analysis at point 7 indicates the presence of Ti, Al and O as the main phases along with very small amount of Fe, whereas the dark region (Point 8 in Fig.5.14) indicates Fe (73.73%) and Mo (13.57%) as the main elements. A homogeneous and continuous surface scale is developed on conventional thick AlCrN coated T-11 boiler steel, which has Al, Cr and O as the main elements (Fig.5.14.e).

5.2.1.4 Cross-sectional analysis

5.2.1.4.1 Scale thickness

The oxidized samples were cut across the cross section, mounted and subsequently mirror polished to obtain scanning electron back scattered micrographs and X-ray mapping of different elements for coated and uncoated T-11 boiler steel. The scale thickness values were measured from SEM back scattered micrographs as shown in Fig.5.15. Very thick scale is observed in case of uncoated T-11 boiler steel. The measured average scale thickness values for uncoated T-11 boiler steel, nanostructured thin TiAlN, nanostructured thin AlCrN, conventional thick TiAlN and conventional thick AlCrN coatings are 1266, 992, 968, 671 and 1000 μm respectively.

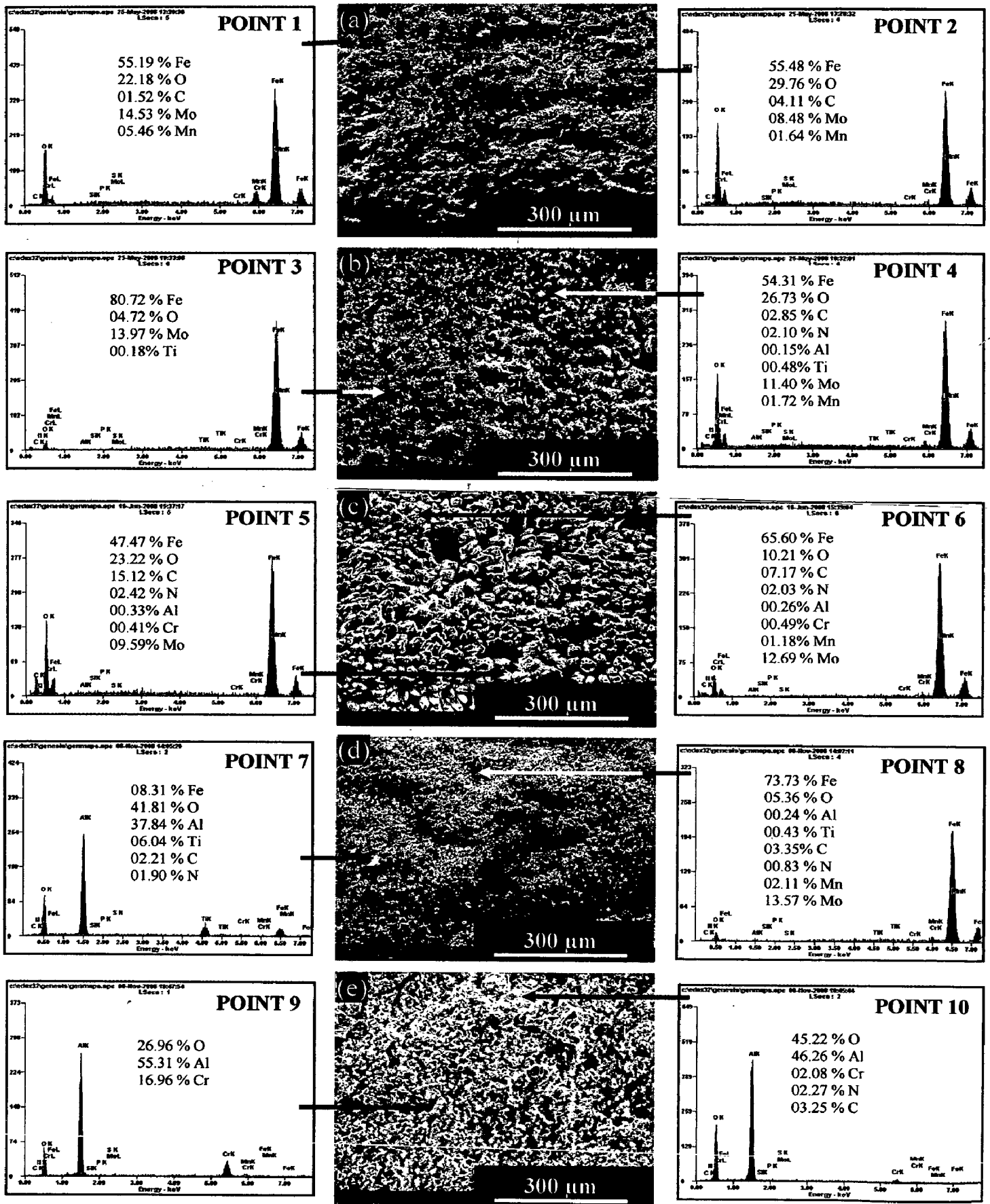


Fig. 5.14 Surface-scale morphology and EDAX patterns from different spots on uncoated and coated ASTM-SA213-T-11 boiler steel after exposure to cyclic oxidation in air at 900°C for 50 cycles : (a) Uncoated T-11 boiler steel, (b) Nanostructured TiAlN coating, (c) Nanostructured AlCrN coating, (d) Conventional TiAlN coating, (e) Conventional AlCrN coating

5.2.1.4.2 Cross-sectional scale morphology

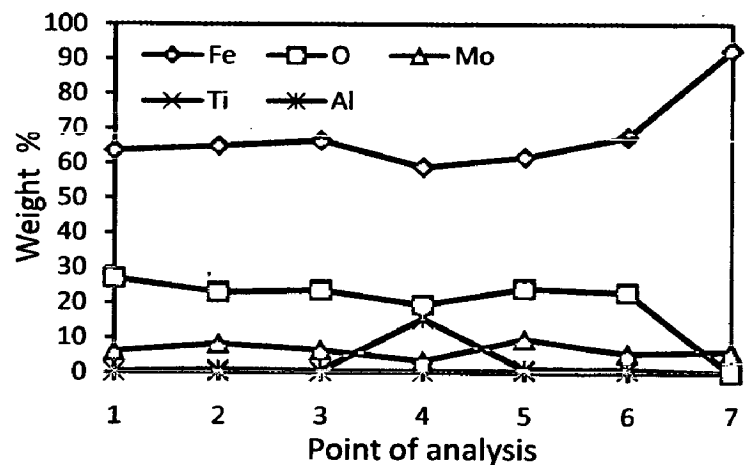
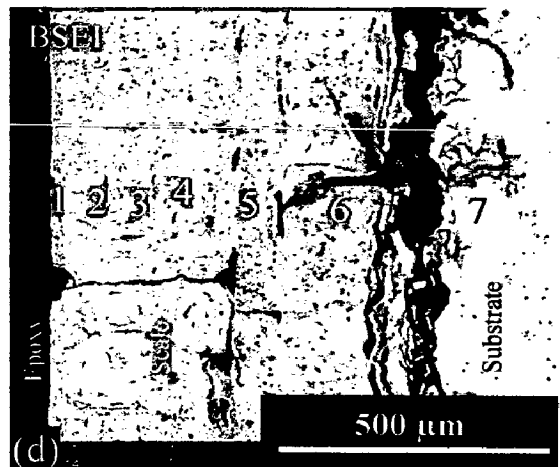
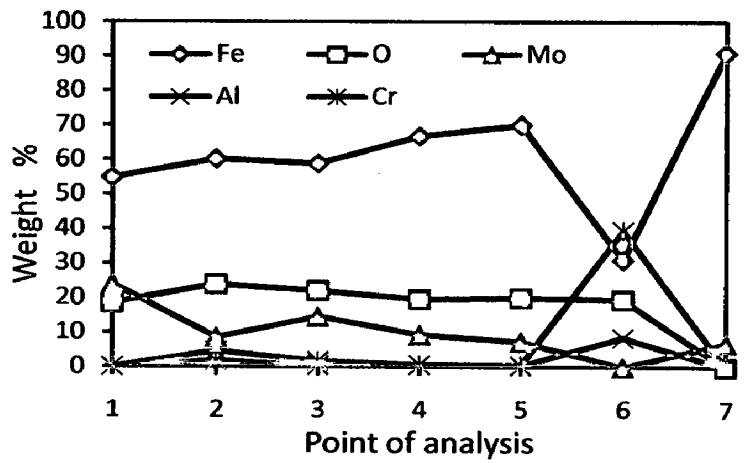
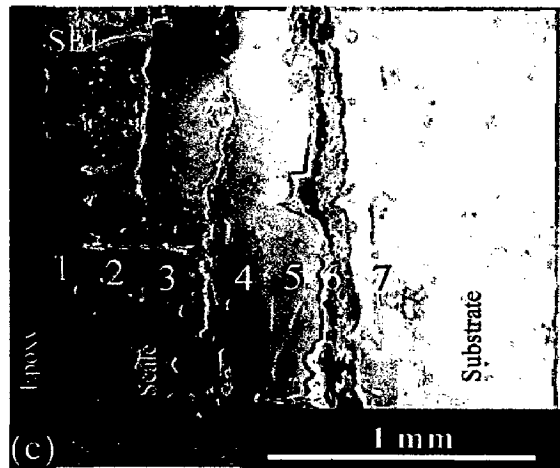
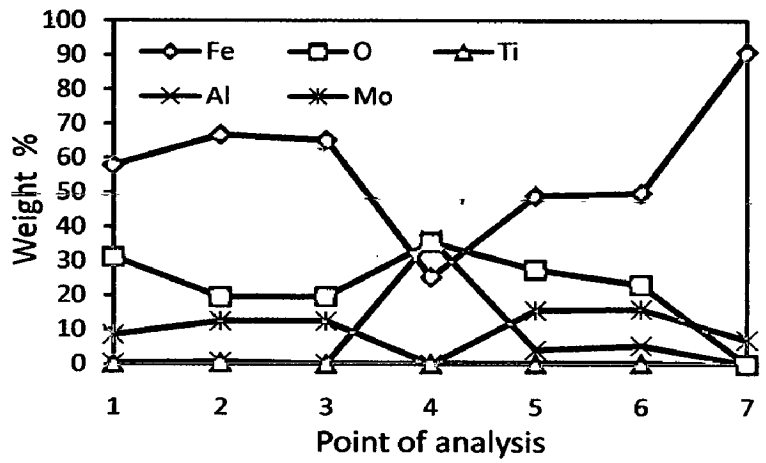
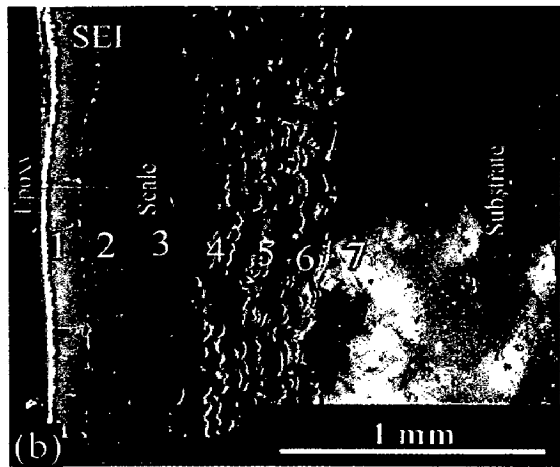
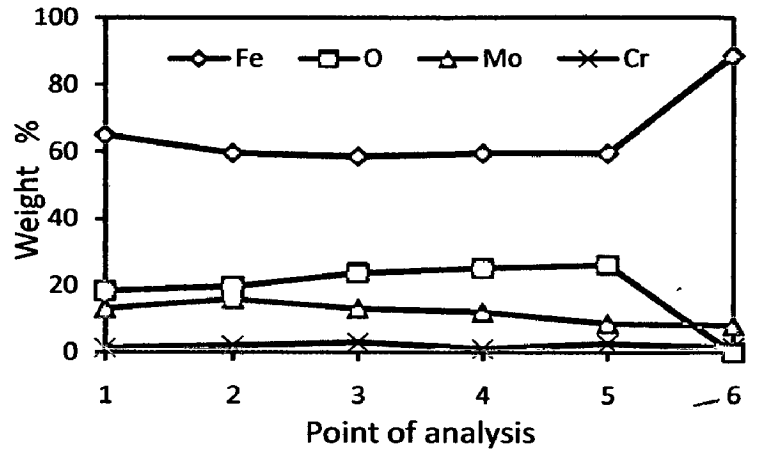
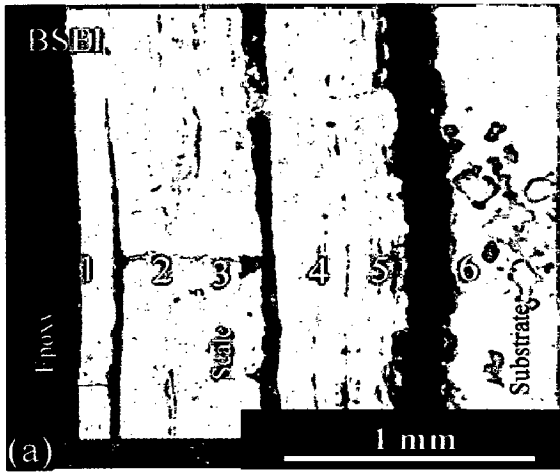
Back Scattered Electron Image (BSEI) micrograph and elemental variation across the cross-section for coated and uncoated ASTM-SA213-T-11 boiler steel subjected to cyclic oxidation in air at 900°C for 50 cycles are shown in Fig.5.15. The SEM micrograph in case of uncoated T-11 boiler steel shows thick scale as shown in Fig. 5.15 (a). Also, the scale is fragile and indicating cracking. EDAX analysis reveals the presence of iron and oxygen throughout the scale. The existence of significant amount of oxygen points out the possibility of Fe_2O_3 in the oxide scale.

BSEI micrograph and elemental variation depicted in Fig.5.15 (b), for the exposed cross-section of nanostructured thin TiAlN coated T-11 boiler steel shows the thick, continuous and adherent scale. The EDAX analysis reveals the presence of Fe, Mo, Al and oxygen throughout the scale. A location at point 4 (Fig.5.15.b) in the micrograph depicts the good percentage of Al and O along with small amount of Fe. A thick and adherent oxide scale can be seen in case of nanostructured AlCrN coated T-11 boiler steel (Fig.5.15.c). The scale is indicating cracking. The EDAX point analysis indicates the presence of Fe, Mo, Al, Cr and oxygen in the oxide scale. At point 6 i.e. interface of substrate and scale, a good percentage of Cr, Al and O is present.

In case of conventional TiAlN coated T-11 boiler steel, the scale is uniform and adherent as depicted in Fig.5.15 (d), but with cracks. The EDAX point analysis indicates the presence of Fe, O, and Mo throughout the scale with variable amounts. A location at point 4 shows good percentage of Al with O and Fe. The conventional thick AlCrN coated T-11 boiler steel (Fig.5.15.e) indicates continuous, thick and adherent scale. EDAX point analysis shows the presence of Fe, Mo and O throughout the scale. The top scale shows higher percentage of Fe and O along with good amount of Al (point 1 and 2 in Fig.5.15.e). In the subscale region the percentage of Al decreased to zero.

5.2.1.4.3 X-Ray mapping

X-ray mappings for a part of oxide scale of uncoated and coated ASTM-SA213-T-11 boiler steel oxidized in air at 900 °C for 50 cycles are shown in Fig. 5.16. In case of uncoated T-11 boiler steel, the micrograph (Fig.5.16.a) indicates a dense scale, which mainly contains iron and oxygen with some amount of Cr as indicated by X-ray mapping.



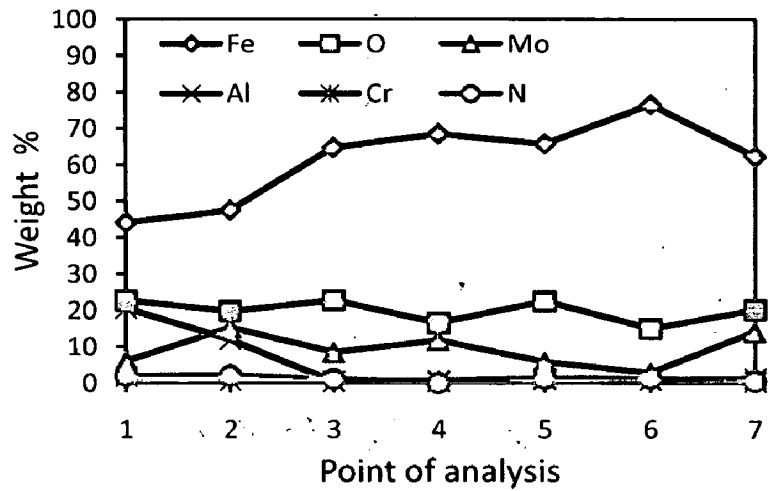
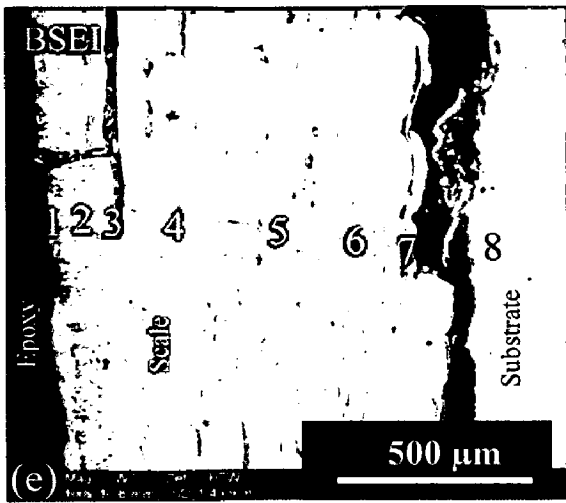


Fig. 5.15 Oxide scale morphology and variation of elemental composition across the cross-section of the uncoated and coated ASTM-SA213-T-11 boiler steel after exposure to cyclic oxidation in air at 900°C for 50 cycles: (a) Uncoated T-11 boiler steel (65 X), (b) Nanostructured TiAlN coating (70 X), (c) Nanostructured AlCrN coating (70 X), (d) Conventional TiAlN coating (140 X), (e) Conventional AlCrN coating (100 X)

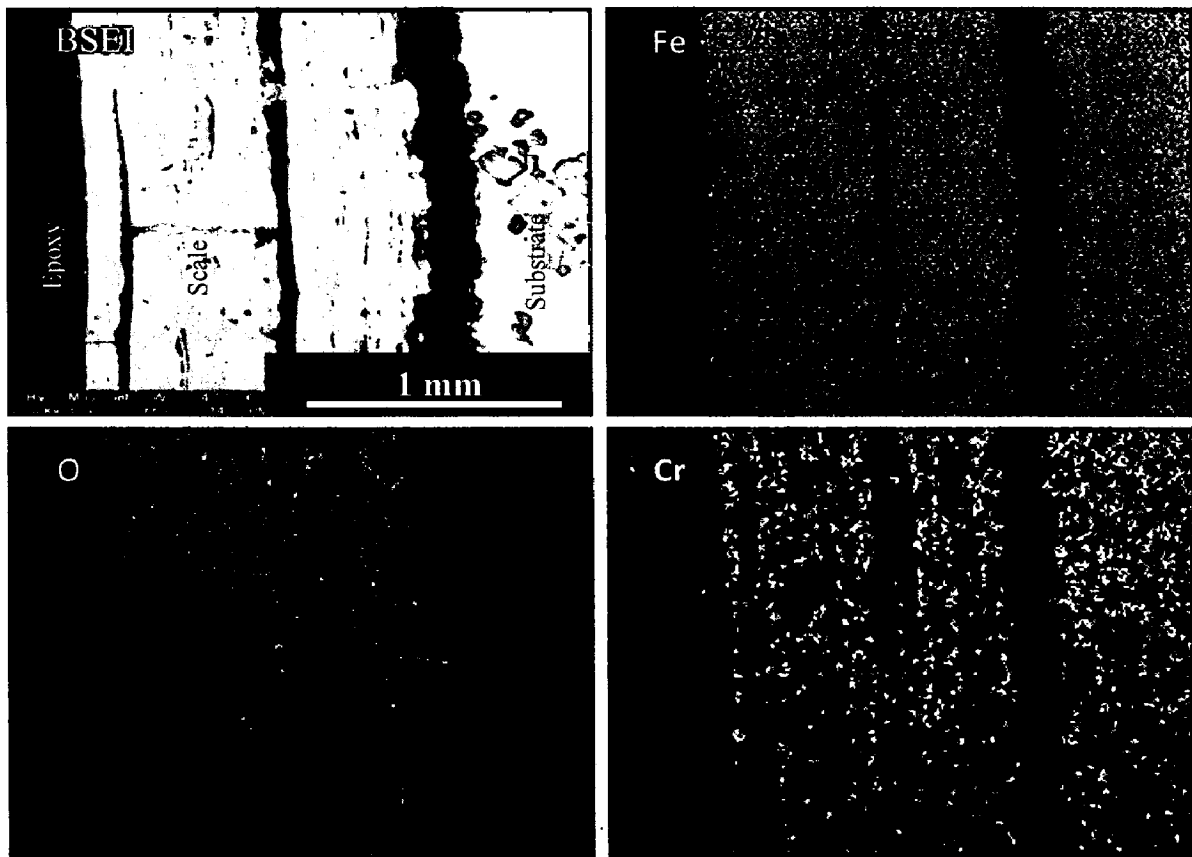


Fig. 5.16 (a) Composition image (BSEI) and X-ray mapping of the cross-section of uncoated ASTM-SA213-T-11 boiler steel subjected to cyclic oxidation in air at 900°C for 50 cycles

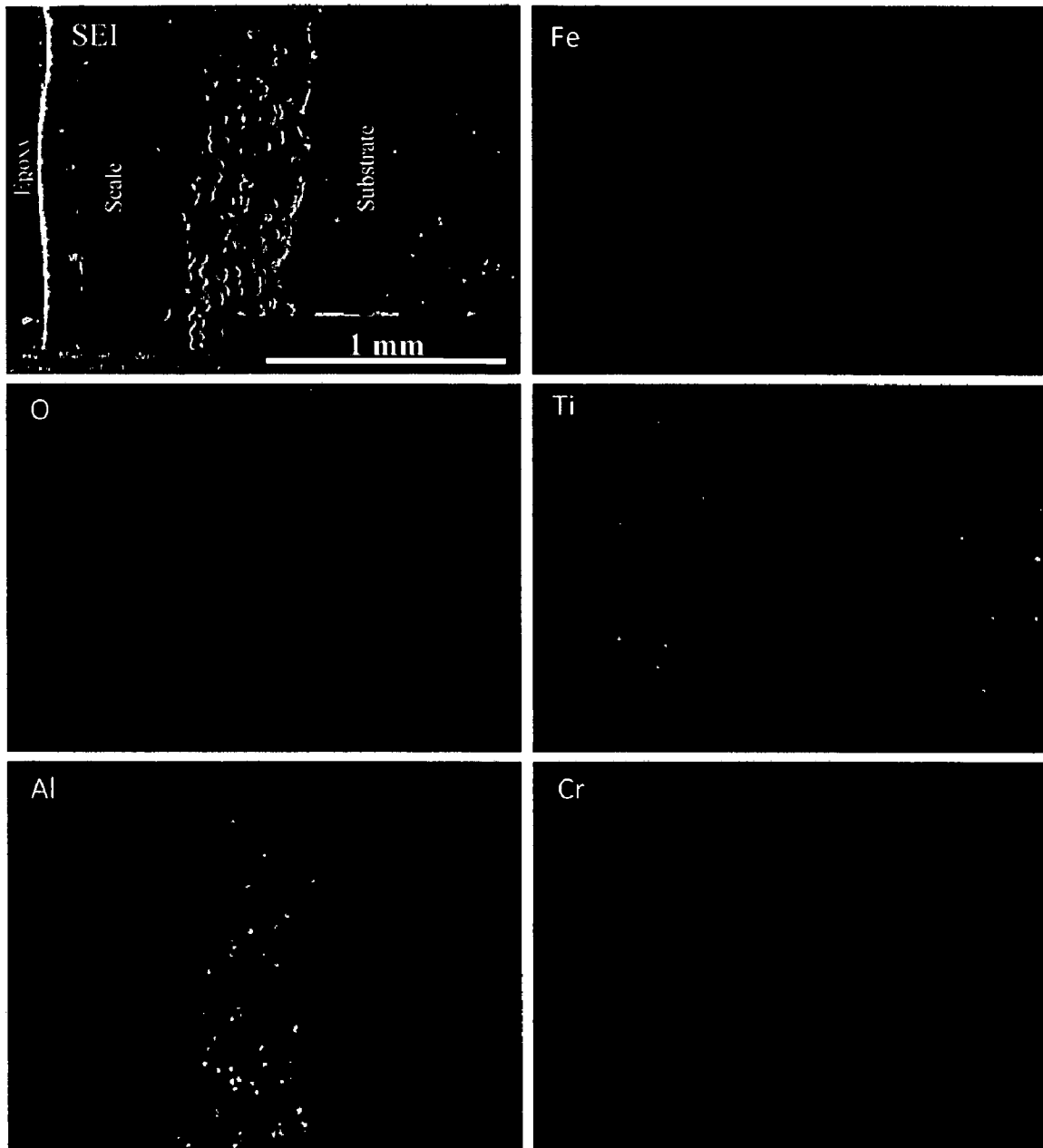


Fig. 5.16 (b) Composition image (SEI) and X-ray mapping of the cross-section of Nanostructured TiAlN coated ASTM-SA213-T-11 boiler steel subjected to cyclic oxidation in air at 900°C for 50 cycles

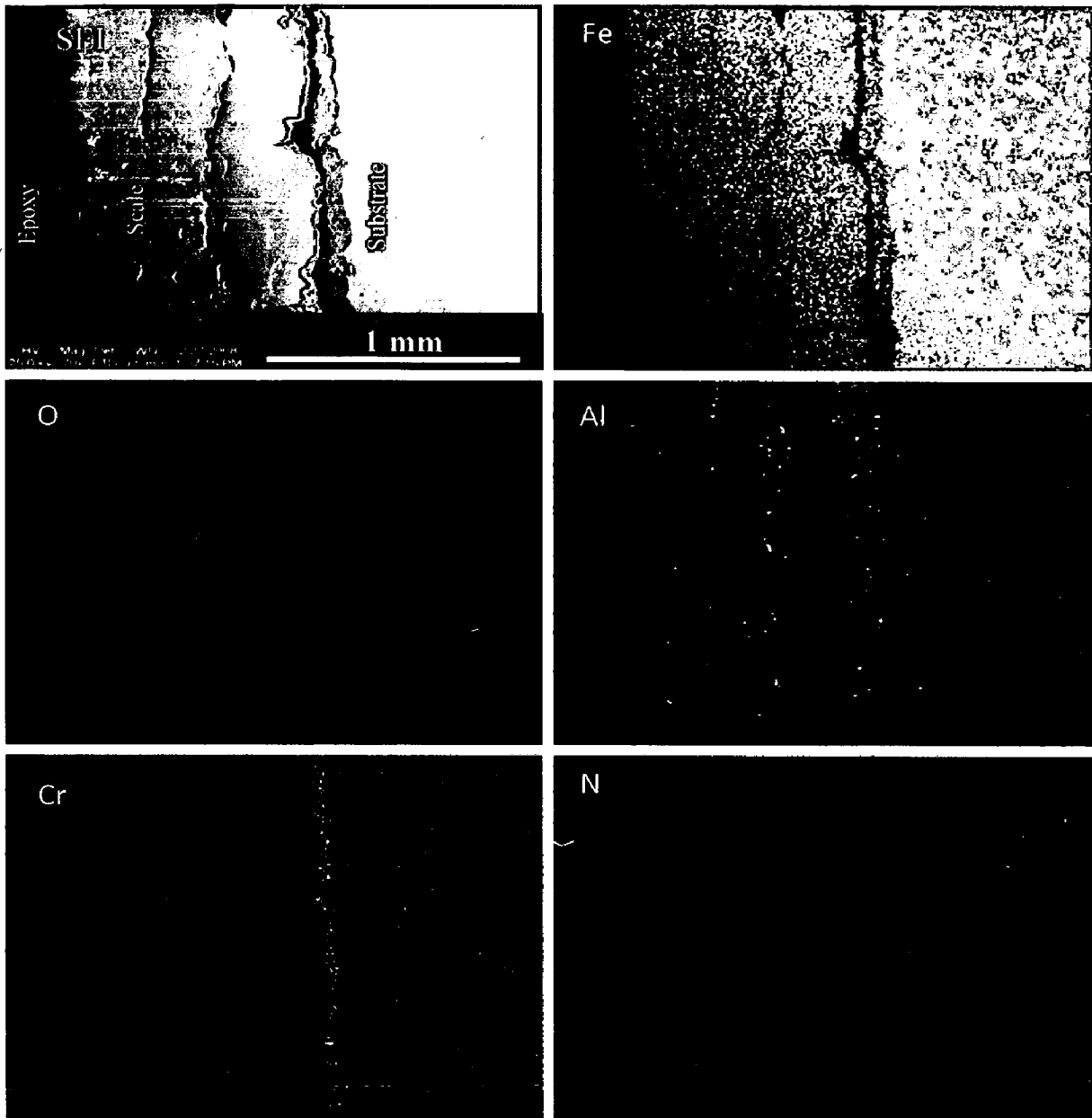


Fig. 5.16 (c) Composition image (SEI) and X-ray mapping of the cross-section of Nanostructured AlCrN coated ASTM-SA213-T-11 boiler steel subjected to cyclic oxidation in air at 900°C for 50 cycles

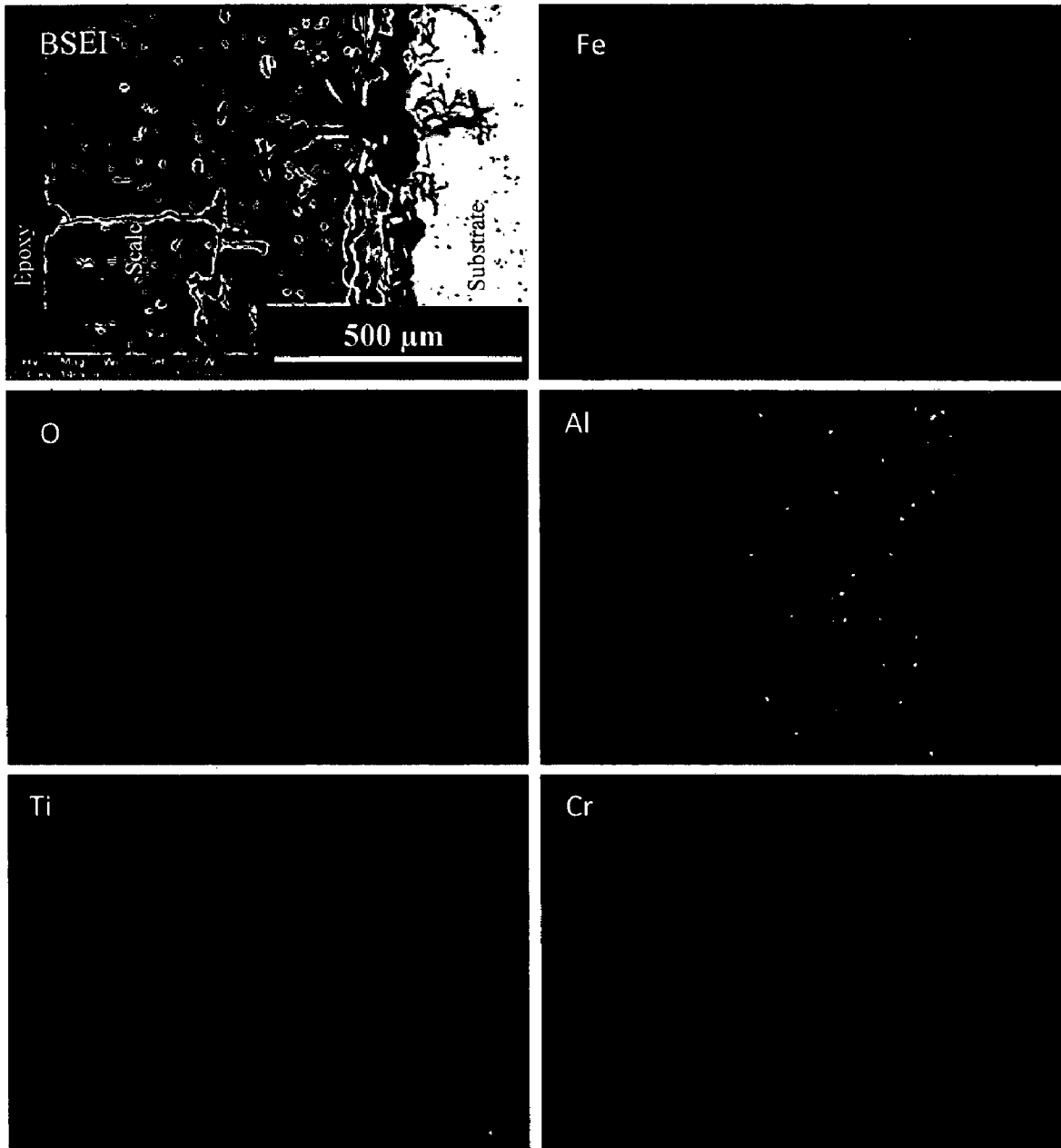


Fig. 5.16 (d) Composition image (BSEI) and X-ray mapping of the cross-section of conventional TiAlN coated ASTM-SA213-T-11 boiler steel subjected to cyclic oxidation in air at 900°C for 50 cycles

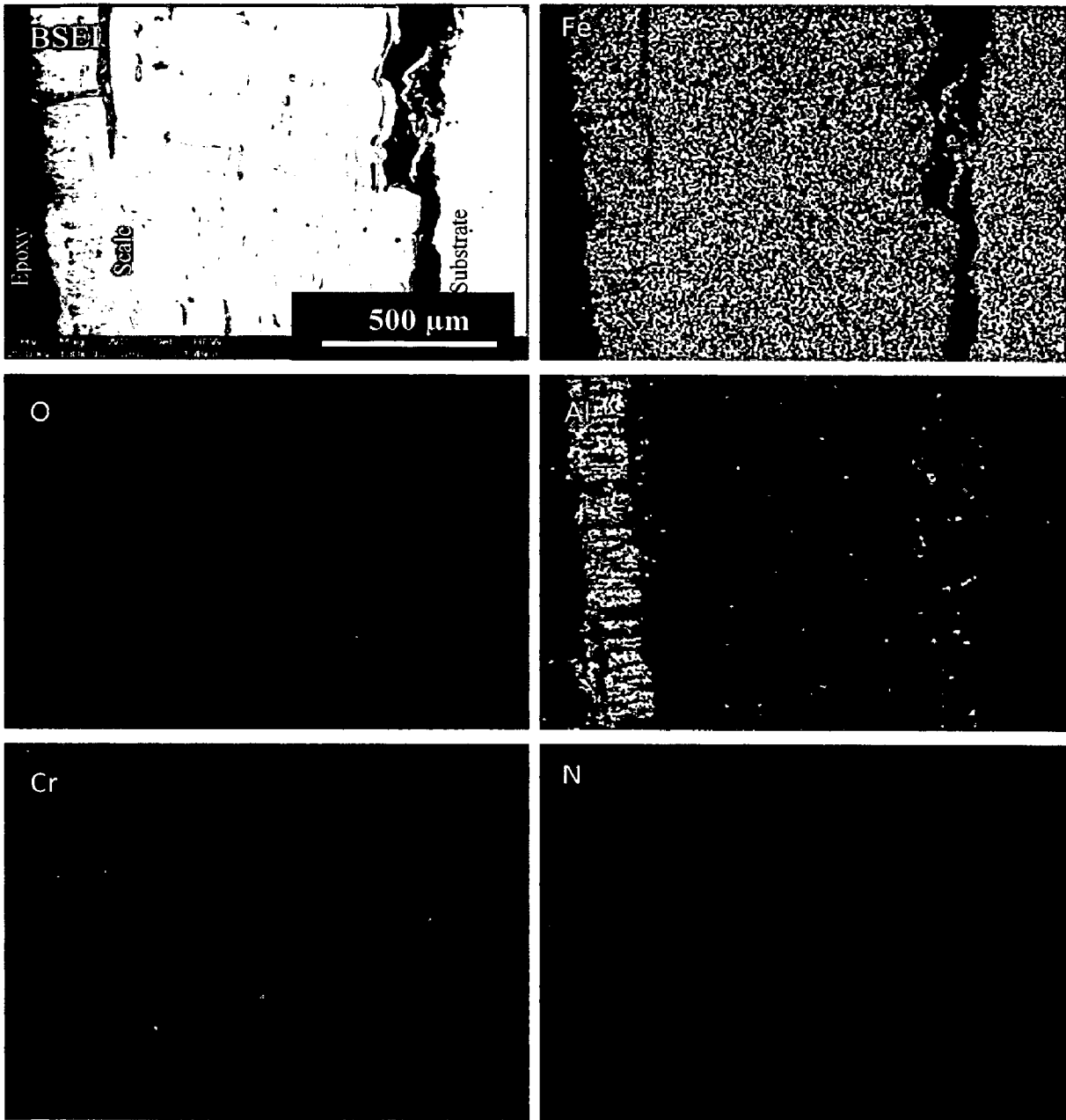


Fig. 5.16 (e) Composition image (BSEI) and X-ray mapping of the cross-section of conventional AlCrN coated ASTM-SA213-T-11 boiler steel subjected to cyclic oxidation in air at 900°C for 50 cycles

Figure 5.16 (b), shows X-ray mapping analysis of the scale formed on nanostructured TiAlN coated T-11 boiler steel. The X-ray mapping indicates presence of oxygen and iron throughout the scale with a thick regular band of Al at scale substrate interface. In case of nanostructured thin AlCrN coated T-11 boiler steel subjected to cyclic oxidation in air, the BSEI and X-ray mapping are shown in Fig. 5.16 (c). The X-ray mapping indicates the presence of iron and oxygen throughout the scale. A thin irregular band of Cr is present at the interface. In case of conventional thick TiAlN coated T-11 boiler steel, Fig.5.16 (d), Fe and O are present throughout the scale. Fig.8.e, depicts the X-ray mapping in case of conventional AlCrN coated T-11 boiler steel. Thick band of Al is present in the top scale region along with Fe and O and the sub scale is rich in Fe and O.

5.2.2 Summary of Results

Results obtained after exposure of uncoated and coated ASTM-SA213-T-11 boiler steel to cyclic oxidation in air at 900°C for 50 cycles are summarized in Table.5.4.

5.2.3 Discussion

During cyclic testing, cracks in the oxide scale (Fig.5.15.a, c & d) and spalling of the uncoated, nanostructured AlCrN and conventional TiAlN coatings might be attributed to the different values of thermal expansion coefficients for the coating, scale and the substrate as reported by Sidhu et al. (2003), Singh H et al. (2004), Evans et al. (2001), Wang et al. (2002) and Niranatlumpong et al (2000). Further Niranatlumpong et al. (2000) opined that spallation could be initiated by the rapid growth of void-like defects lying adjacent to coating protuberances, at which tensile radial stress developed during cooling as a result of the thermal contraction mismatch between the oxide and coating is maximum. The formation of cracks in the coating originates from stresses developed in the deposit or at the coating-base metal interface (Heath et al., 1997). Though these cracks the corrosive environment can quickly reach the base metal and cut its way under the coating to result in adhesion loss and spalling, whereas some elements may diffuse outwards through these cracks to form oxides or spinels (Singh H et al., 2004). This may be the reason for severe spalling and hence failure of conventional TiAlN coating which results falling of a thin layer of scale in the boat just after 11th cycle.

Table 5.4 Summary of the results obtained for uncoated and coated ASTM-SA213-T-11 boiler steel subjected to cyclic oxidation in air at 900°C for 50 cycles

Coating	Cumulative Weight gain (mg/cm ²)	Parabolic rate constant ($K_p \times 10^{-08}$ gm ² cm ⁻⁴ s ⁻¹)	XRD phases	Remarks
Uncoated T-11 boiler steel	175.37	17.26	Fe ₂ O ₃	A grey colored scale with spalling tendency appeared on the surface right from the 2 nd cycle. Some metallic sound was also observed during cooling for after 6 th cycles. At the end uniform scale with cracks and blackish grey color surface appearance was observed
Nanostructured TiAlN coating	141.49	11.49	Fe ₂ O ₃	Color of the oxide scale at the end of the study was observed to be brownish grey with severe cracking on the surface. After 4 th cycle, the scale starts falling in the boat and grey color spots were seen. The coating gets destroyed and scale starts falling rapidly in the boat after 10 th cycle.
Nanostructured AlCrN coating	133.10	09.97	Fe ₂ O ₃ , and Cr ₂ O ₃	Golden and ink blue reflections were observed in the scale, after the completion of 2 nd cycle, which turned to dark grey subsequently. The oxide scale at the end of cyclic study was smooth with very fine cracks on the surface.
Conventional TiAlN Coating	125.51	09.97	Fe ₂ O ₃ , Al ₂ O ₃ , Ti ₃ Al and Al	After 11 th cycle, severe spalling was observed and a very fine layer of coating gets separated from the substrate and fallen in the boat. At the end of 50 cycles, dark grey sides along with brownish spots at some locations have been observed on the whitish grey surface.
Conventional AlCrN coating	118.78	09.01	Al ₂ O ₃	Color of the oxide scale was bluish grey after 4 th cycle, which turned to whitish grey at the end of the cyclic study. The scale was found to be adherent and smooth with a very fine hair line crack.

The presence of Fe, Mo and oxygen (Fig.5.15) in the top of the scale, is believed to be due to the diffusion of iron and molybdenum through the pores and cracks that appeared in the coating during the course of oxidation studies (Singh Buta et al., 2003). Sever spalling and inferior oxidation resistance of nanostructured and conventional TiAlN coatings may be as opined by Xing-zhao Ding et al. (2008). According to them, in an oxidation or corrosive environment Ti element often forms a porous non-protective oxide scale, which limits the oxidation and corrosion resistance of titanium-based coatings. Kazuhisa Fujita (2005) has reported that the oxide scale of binary TiAl alloy is composed of a porous oxide mixture of TiO_2 and Al_2O_3 , which has dominated by TiO_2 . This might be the reason for rapid increase in oxidation rate of TiAlN coatings after 16th cycle (Fig. 5.10). Kalss et al. (2006) have also reported the formation of oxidized layer of thickness of about 350nm for TiAlN coating at 900°C. Due to high temperature the segregation of titanium and aluminum atoms is probable. Evidently, high temperature oxidation involved diffusion of aluminum atoms to the surface to form a thin aluminum oxide top layer while the remaining titanium under layered formed titanium dioxide. At 950°C, the whole coating was decomposed and pure titanium dioxide was formed (Kalss et al., 2006), which is supported by Man et al. (2004).

The weight change plots (Fig.5.10) for the uncoated and coated T-11 boiler steel indicated that the oxidation behavior has shown conformance to parabolic rate law. The parabolic kinetic behavior is due to the diffusion controlled mechanism operating at 900°C under cyclic conditions (Mahesh et al., 2008). Small deviation from the parabolic rate law might be due to the cyclic scale growth. The higher weight gain during the first few cycles might be attributed to the rapid formation of oxides at the splat boundaries and within the open pores due to the penetration of the oxidizing species, further the subsequent increase in weight gain is gradual (Singh H et al., 2007). The parabolic rate constant for the uncoated T-11 boiler steel is found to be greater than all the coatings.

Conventional thick AlCrN coatings have been found successful in reducing the overall weight gain of bare T-11 boiler steel. It is evident form XRD (Fig.5.13) results of the oxidized conventional thick AlCrN coated T-11 boiler steel that Al_2O_3 as the main phase which has further been supported by EDAX (Fig.5.14. e) and X-ray mapping (Fig.5.16. e) analysis.

The oxidation rate (total weight gain values after 50 cycles) of the coated and uncoated T-11 boiler steel follows the sequence as given below:

Bare T-11 > Nanostructured TiAlN > Nanostructured AlCrN > Conventional TiAlN > Conventional AlCrN

The parabolic rate constant (K_p) values for the coated T-11 boiler steel were less than that of bare boiler steel. It is nearly half in case of coated steel (Table.5.3). Thus, the coated T-11 boiler steels have shown lower rate of oxidation than bare boiler steel. The presence of some percentage of chromium in the subscale as revealed by the X-ray mapping analysis (Fig.5.16) across the cross-section of bare T-11 steel is in accordance with the findings of Sadique et al. (2000). The authors have reported that Fe-Cr alloys in oxygen at higher temperature (950-1050⁰C) form spinel ($FeCr_2O_4$) and Cr_2O_3 on the inner side and Fe_2O_3 on the outer side of the scale. This can also be attributed to depletion of iron due to oxidation to form the upper scale thereby leaving chromium rich pockets those further get oxidized to form iron chromium spinel.

In case of nanostructured TiAlN and AlCrN coatings, Fe_2O_3 is the main phase present in the scale as indicated by the XRD (Fig.5.13. b & c), EDAX (Fig. 5.14. b & c) and X-ray mapping (Fig.5.16. b & c) analysis along with a thick band of Al and thin band of Cr at the interface of scale and substrate, respectively. The nanostructured coatings has shown resistance to oxidation to some extent as the overall weight gain is less than as compared to the uncoated T-11 boiler steel, but failed to provide full protection to the substrate. This might be due to the difference in thermal expansion co-efficient as explained above.

5.2.4 Conclusions

The high temperature oxidation behaviors of uncoated and coated ASTM-SA213-T-11 boiler steel have been investigated in air at 900°C for 50 cycles. The behavior of nanostructured TiAlN and AlCrN coatings were compared with their conventional counterparts and the following conclusions are made:

1. The plasma sprayed conventional thick coatings AlCrN when subjected to cyclic oxidation at 900°C for 50 cycles developed a protective scale mainly consisting on Al_2O_3 .

2. The conventional TiAlN coating failed as of severe spalling just after 11th cycle, which may be initiated by the rapid growth of void-like defects lying adjacent to coating protuberances, at which tensile radial stress developed during cooling as a result of the thermal contraction mismatch between the oxide and coating is maximum.
3. The nanostructured TiAlN and AlCrN coatings has shown resistance to oxidation to some extent as the overall weight gain is less than as compared to the uncoated T-11 boiler steel, but failed to provide full protection to the substrate.
4. The oxidation rate (total weight gain values after 50 cycles) of the coated and uncoated T-11 boiler steel follows the sequence as given below:
Uncoated T-11 > Nanostructured TiAlN > Nanostructured AlCrN > Conventional TiAlN > Conventional AlCrN
5. In case of uncoated T-11 boiler steel, the weight gain is highest with thickest scale. The parabolic rate constant in case of coatings is very less as compared to the bare steel.
6. Sever spalling and inferior oxidation resistance of nanostructured and conventional TiAlN coatings may due to the reason as in an oxidation or corrosive environment Ti element often forms a porous non-protective oxide scale, which limits the oxidation and corrosion resistance of titanium-based coatings.
7. The oxide scale formed is adherent to the substrate in all cases.

5.3 HOT CORROSION STUDIES IN MOLTEN SALT ENVIRONMENT

The present research work has been focused to investigate and compare the hot corrosion behavior of conventional thick (by plasma spraying and gas nitrided) and nanostructured thin (by physical vapor deposition process) TiAlN and AlCrN coatings on ASTM-SA213-T-11 boiler steel, in an aggressive environment of Na₂SO₄-60%V₂O₅ (molten salt) at 900°C under cyclic conditions. Long-term exposure of the coatings in the aggressive high temperature environment with the characterization of the failure mechanisms is essential for estimating the protection capability of the coatings (Uusitalo et al., 2003). X-ray diffraction (XRD), scanning electron microscopy/energy-dispersive analysis (SEM/EDAX) and X-ray mapping techniques have been used to characterize corrosion products after hot corrosion at 900°C. The detailed experimental procedure is reported in chapter 3.

5.3.1 Results

5.3.1.1 Visual observations

The macrographs for uncoated and coated ASTM-SA213-T-11 boiler steel subjected to cyclic oxidation in Na₂SO₄-60%V₂O₅ (molten salt) environment at 900°C for 50 cycles are shown in Fig.5.17. For the uncoated T-11 boiler steel, a grey colored scale appeared on the surface right from the 3rd cycle. This bare steel showed spalling of scale just after the 5th cycle. After 16th cycle fine cracks were observed which grow further and after 29th cycle the scale starts falling in the boat. Some metallic sound was also observed during cooling after 4th cycle which continued till 50th cycle. At the end of cyclic study, uniform scale with cracks and dark grey color surface appearance, was observed which can be seen in Fig.5.17. (a).

In case of nanostructured thin TiAlN coated T-11 boiler steel, color of the oxide scale at the end of the study was observed to be brownish grey, as shown in Fig.5.17 (b). After 8th cycle, some dark and light grey spots were observed on the surface. Spalling was observed after 10th cycle and after 26th cycle the surface becomes rough and the scale remains adherent to the substrate till 50th cycle. The nanostructured thin AlCrN coated T-11 boiler steel has shown the formation of smooth scale with the presence of

very fine cracks, as shown in Fig.5.17 (c). Some hairline cracks were observed after 9th cycle which continued till 50th cycle. After 35th cycle some scale fall in the boat. The surface appearance after 37th cycle was light grey at middle area of the sample with dark grey sides, which turns to blackish grey after 50th cycle.

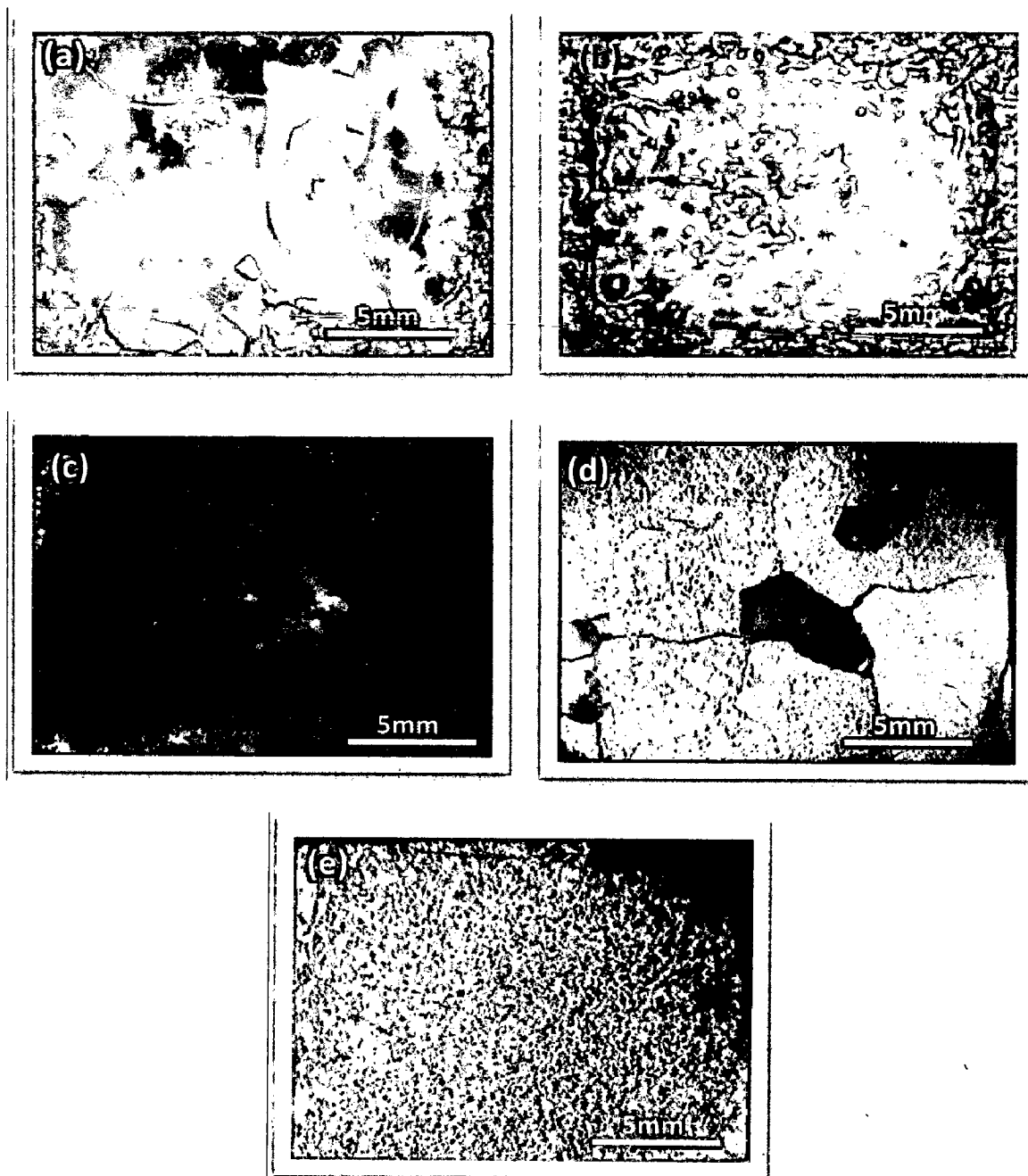


Fig. 5.17 Surface macrographs of uncoated and coated ASTM-SA213-T-11 boiler steel exposed to molten salt ($\text{Na}_2\text{SO}_4\text{-60\%V}_2\text{O}_5$) environment at 900°C for 50 cycles: (a) Uncoated T-11 boiler steel, (b) Nanostructured TiAlN coating, (c) Nanostructured AlCrN coating, (d) Conventional TiAlN coating, (e) Conventional AlCrN coating

A visual observation of conventional thick TiAlN coated T-11 boiler steel (Fig.5.17.d), showed no sign of spalling in the initial cycles. After 16th cycle hairline cracks were observed along the edges but the scale is adherent to the substrate till 20th cycle. A very small layer of scale gets detached from the sample and falls in the boat after 21st cycle. After 39th cycle more strips of scale starts falling in the boat. At the end of the study, a brownish grey layer of scale is visible on the surface along with some cracks and some darks grey areas from where the scale gets detached from the substrate (Fig.5.17.d). In case of conventional thick AlCrN coated T-11 boiler steel, color of the oxide scale was whitish grey after 4th cycle, which continued during the course of the study (Fig.5.17.e). A very small amount of superficial spalling was noticed at the end of 3rd cycle, which may be due to the loosely bond particles on the surface of the coating. The scale was found to be adherent and smooth.

5.3.1.2 Weight change measurements

Weight gain per unit area (mg/cm^2) versus time expressed in number of cycles plot for coated and bare T-11 boiler steel subjected to cyclic oxidation in Na_2SO_4 -60% V_2O_5 (molten salt) environment at 900°C for 50 cycles, is presented in Fig.5.18. The plots for all samples shows higher weight gain at initial cycles followed by gradual weight gain. It can be inferred from the plots that the uncoated T-11 boiler steels have showed high rate of oxidation as compared to the coatings. After 16th cycle, the conventional TiAlN coating has shown increase in oxidation rate which further increases after 21st cycle as shown in Fig.5.18.

The cumulative weight gain per unit area for the coated and uncoated T-11 boiler steel subjected to cyclic oxidation in Na_2SO_4 -60% V_2O_5 (molten salt) environment at 900°C for 50 cycles is shown in Fig.5.19. Further, the overall weight gain is highest in case of uncoated T-11 boiler steel and is lowest in case of conventional thick AlCrN coated steel, which is 50% of the weight gain in case of uncoated T-11 boiler steel. Both conventional and nanostructured AlCrN coatings have performed well and shown less weight gain as compared to the conventional and nanostructured TiAlN coatings as shown in Fig.5.19.

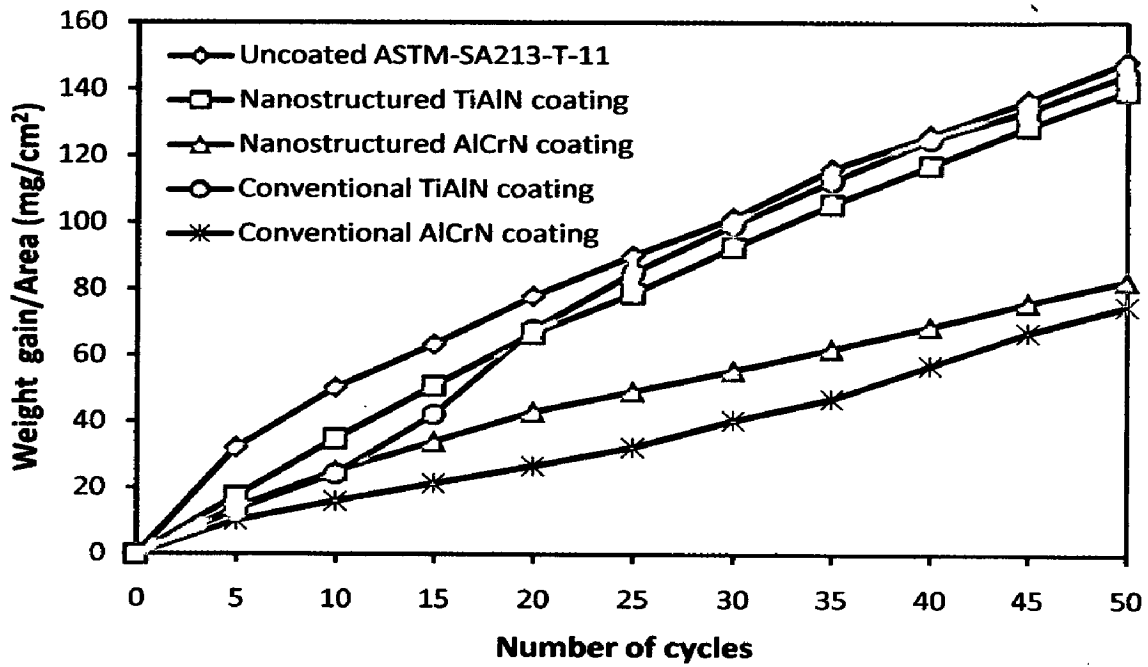


Fig. 5.18 Weight gain/area vs time (number of cycles) for the uncoated and coated ASTM-SA213-T-11 boiler steel exposed to molten salt ($\text{Na}_2\text{SO}_4\text{-60}\%\text{V}_2\text{O}_5$) environment at 900°C for 50 cycles

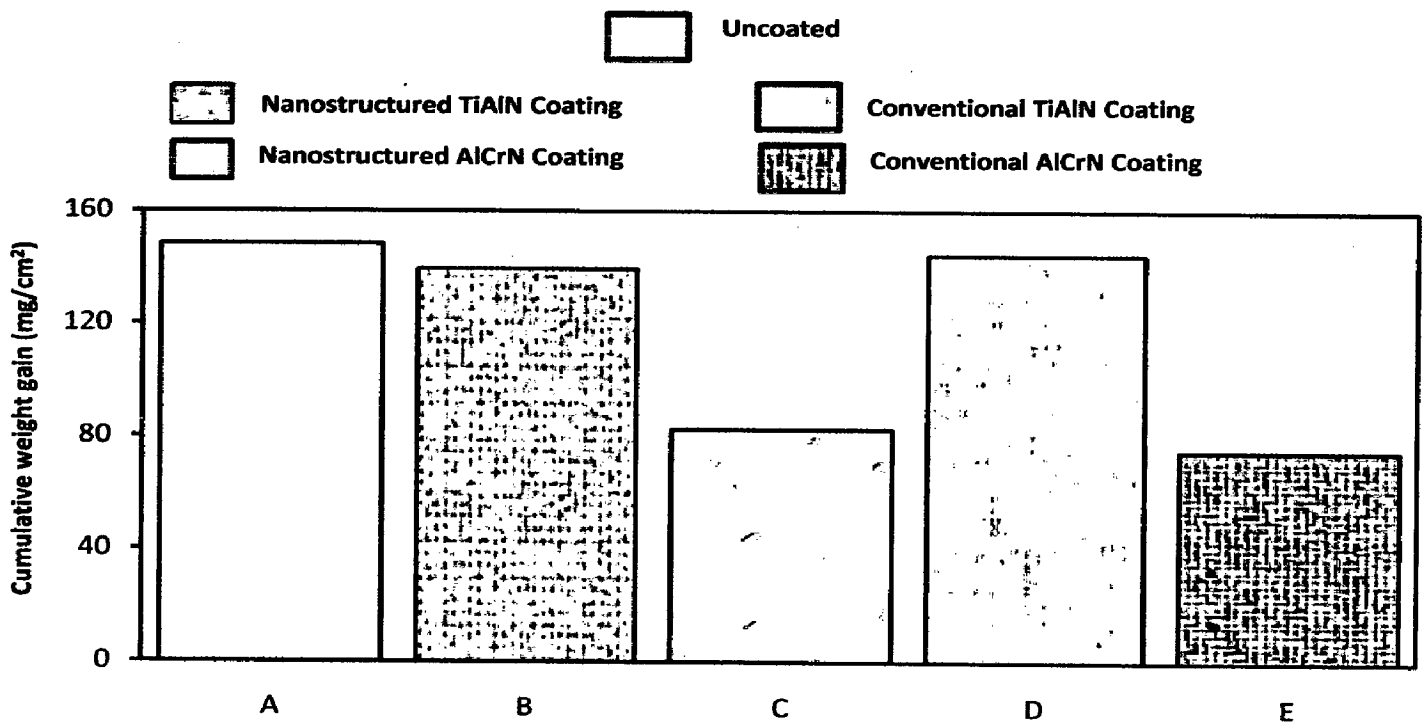


Fig. 5.19 Column chart showing cumulative weight gain per unit area for the uncoated and coated ASTM-SA213-T-11 boiler steel exposed to molten salt ($\text{Na}_2\text{SO}_4\text{-60}\%\text{V}_2\text{O}_5$) environment at 900°C for 50 cycles; (A) Bare T-11 boiler steel, (B) Nanostructured TiAlN coating, (C) Nanostructured AlCrN coating, (D) Conventional TiAlN coating, (E) Conventional AlCrN coating

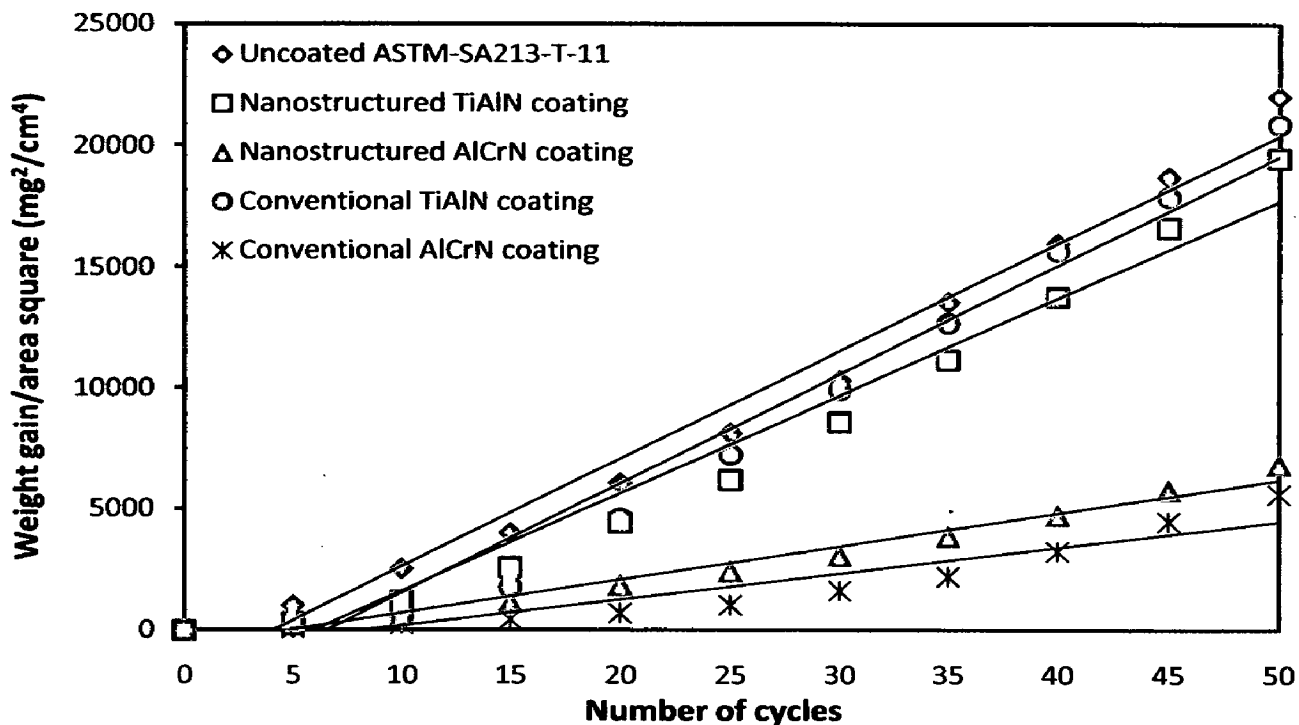


Fig. 5.20 Weight gain/area square vs time (number of cycles) for the uncoated and coated ASTM-SA213-T-11 boiler steel exposed to molten salt (Na_2SO_4 -60% V_2O_5) environment at 900°C for 50 cycles

Table 5.5 Parabolic rate constant ' K_p ' values of uncoated and coated ASTM-SA213-T-11 boiler steel subjected to cyclic oxidation in Na_2SO_4 -60% V_2O_5 (molten salt) environment at 900°C for 50 cycles

Substrate / Coating	$K_p \times 10^{-08} \text{ gm}^2\text{cm}^{-4}\text{s}^{-1}$
Uncoated T-11 boiler steel	12.33
Nanostructured TiAlN coating	11.11
Nanostructured AlCrN coating	03.80
Conventional TiAlN coating	12.49
Conventional AlCrN coating	02.98

Figure 5.20 shows the $(\text{weight gain/area})^2$ versus number of cycles plot for all the cases to ascertain conformance with the parabolic rate law. All the coated and uncoated T-11 boiler steel followed the parabolic rate law as evident from the Fig.5.20. The parabolic rate constant K_p was calculated by a linear least-square algorithm to a function in the form of $(W/A)^2 = K_p t$, where W/A is the weight gain per unit surface area (mg/cm^2) and 't' indicates the number of cycles representing the time of exposure. The parabolic rate constants for the bare and coated T-11 boiler steel calculated on the basis of 50 cycle's exposure data are shown in Table.5.5. It is inferred that the ' K_p ' values for the nanostructured and conventional AlCrN coated T-11 boiler steel were less than that of bare, nanostructured and conventional TiAlN coated T-11 boiler steel.

5.3.1.3 Surface scale analysis

5.3.1.3.1 X-ray diffraction analysis (XRD)

XRD diffractograms for coated and uncoated ASTM-SA213-T-11 boiler steel subjected to cyclic oxidation in Na_2SO_4 -60% V_2O_5 (molten salt) environment at 900°C for 50 cycles are depicted in Fig.5.21 (a and b) on reduced scale. As indicated by the diffractograms Fe_2O_3 is the main phases present in the oxide scale of uncoated and nanostructured thin TiAlN and AlCrN coated T-11 boiler steel along with small amount of Cr_2O_3 for uncoated and nanostructured thin TiAlN coating and weak peaks of Al_2O_3 and Cr_2O_3 in case of nanostructured AlCrN coating. Further, the main phases identified for the conventional thick TiAlN coating are Fe_2O_3 , Al_2O_3 , Ti_3Al and TiO_2 . The oxide phases found in case of conventional thick AlCrN coating were Fe_2O_3 , Cr_2O_3 and Al_2O_3 .

5.3.1.3.2 Surface scale morphology

SEM micrographs along with EDAX point analysis reveals the surface morphology of the coated and uncoated ASTM-SA213-T-11 boiler steel subjected to cyclic oxidation in Na_2SO_4 -60% V_2O_5 (molten salt) environment at 900°C for 50 cycles are shown in Fig.5.22. The oxide scale for uncoated T-11 boiler steel indicates the dominance of Fe and O (Fig.5.22 .a) along with small amount of Mo and C. The surface scale shows distorted grains like microstructure. The SEM micrograph of oxidized nanostructured thin TiAlN coatings is shown in Fig.5.22 (b).

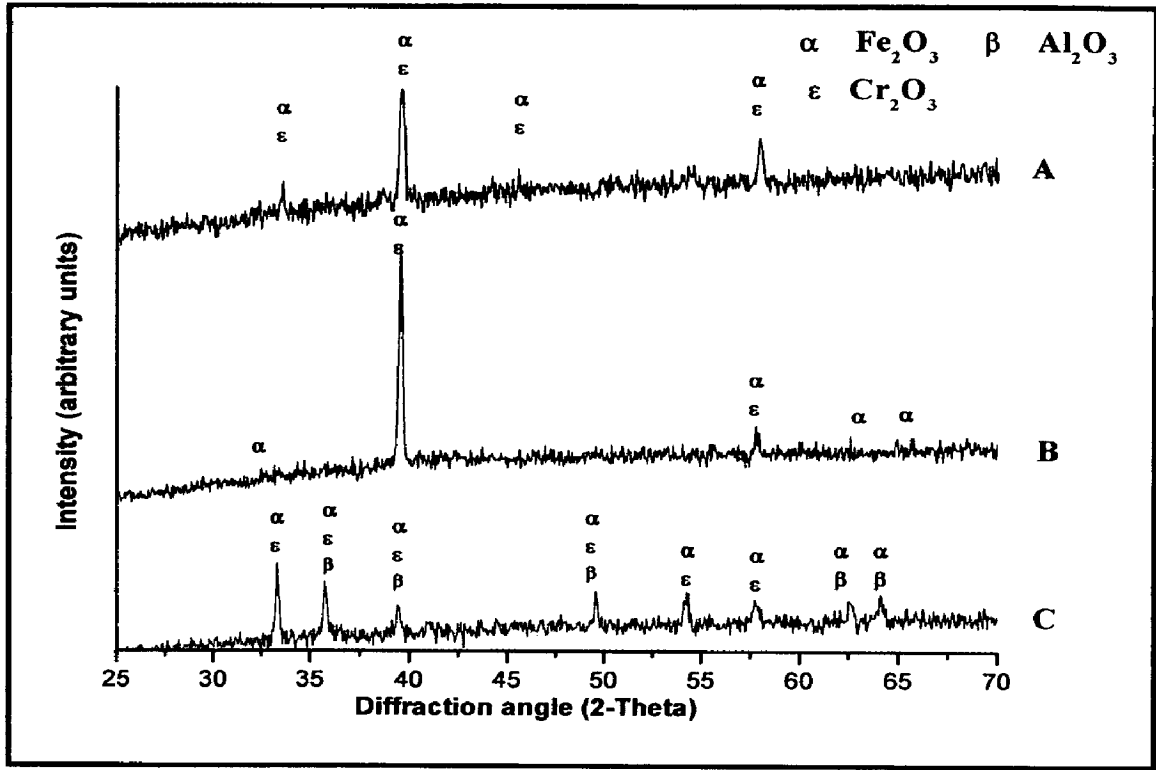


Fig. 5.21 (a) X-Ray Diffraction pattern of uncoated and coated ASTM-SA213-T-11 boiler steel exposed to molten salt (Na_2SO_4 -60% V_2O_5) environment at 900°C for 50 cycles: (A) Uncoated T-11 boiler steel, (B) Nanostructured TiAlN coating, (C) Nanostructured AlCrN coating

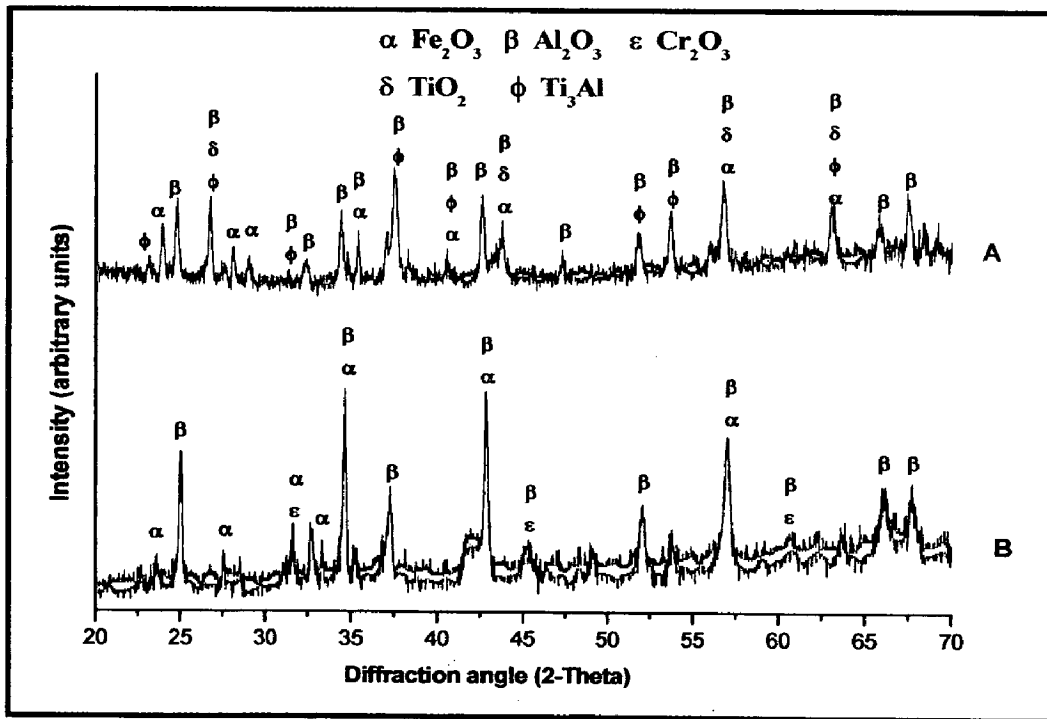


Fig. 5.21 (b) X-Ray Diffraction pattern of uncoated and coated ASTM-SA213-T-11 boiler steel exposed to molten salt (Na_2SO_4 -60% V_2O_5) environment at 900°C for 50 cycles: (A) Conventional TiAlN coating, (B) Conventional AlCrN coating

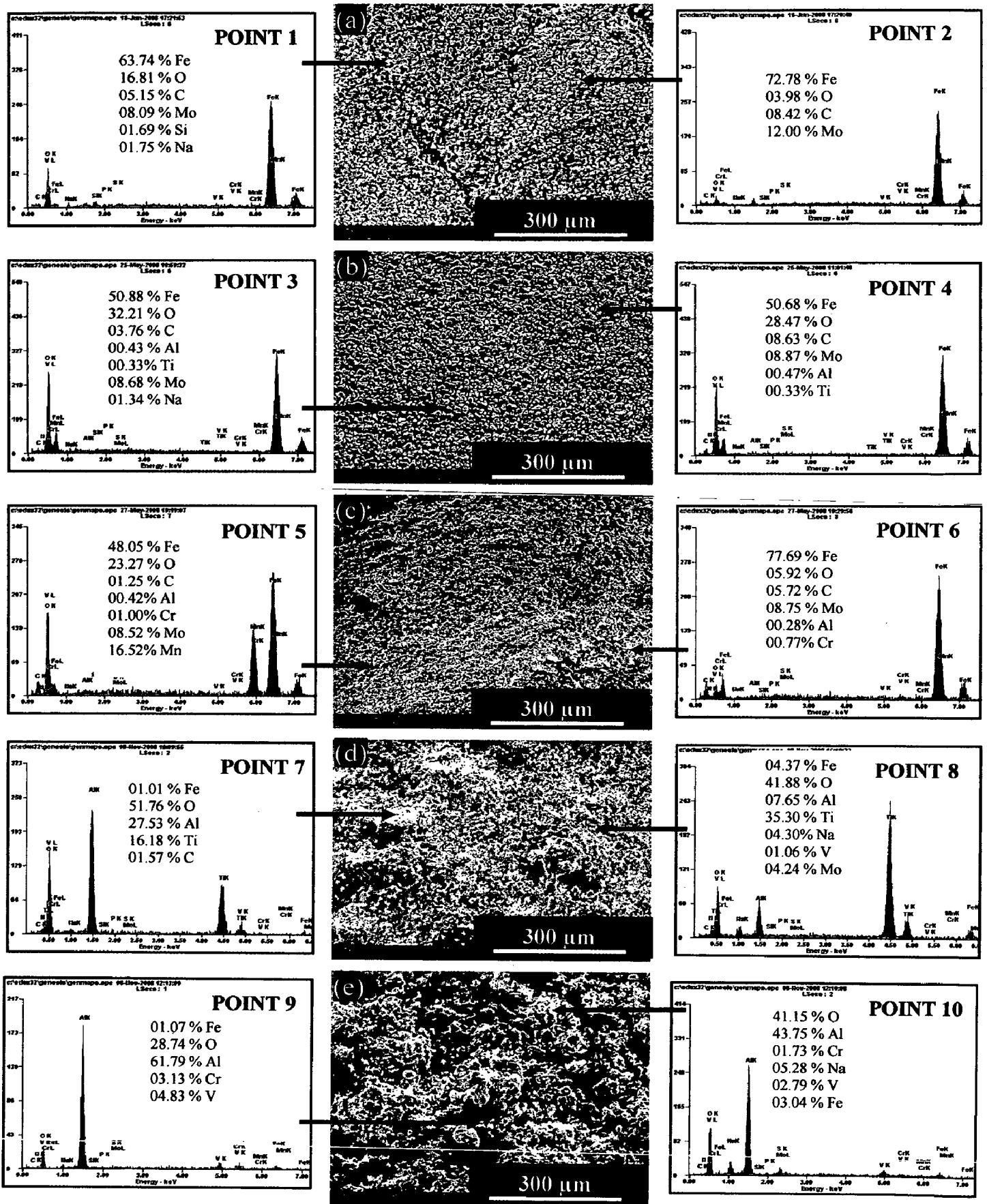


Fig. 5.22 Surface-scale morphology and EDAX patterns from different spots on uncoated and coated ASTM-SA213-T-11 boiler steel exposed to molten salt (Na_2SO_4 -60% V_2O_5) environment at 900°C for 50 cycles: (a) Uncoated T-11 boiler steel, (b) Nanostructured TiAlN coating, (c) Nanostructured AlCrN coating, (d) Conventional TiAlN coating, (e) Conventional AlCrN coating

EDAX analysis of the scale revealed the presence of Fe (50.68 %) and O (28.47 %) as the main elements in the matrix along with small amount of Mo, Na and C (Point 4 on Fig.5.22). In case of nanostructured thin AlCrN coated T-11 boiler steel, the SEM micrograph indicates the porous material like pattern. EDAX point analysis shows, the top scale is rich in Fe, O, Mn and Mo. The region indicated by point 5 (dark grey) in Fig.5.22, is showing more O and less Fe as compared to the region indicated by point 6 (whitish grey). The surface scale developed on conventional thick TiAlN coated T-11 steel is having white contrast (Point 7) and grey contrast regions (Point 8). EDAX analysis at point 7 indicates the presence of Ti (16.18%), Al (27.53%) and O (51.76%) as the main phases along with very small amount of Fe (01.01%), whereas the dark region (Point 8 in Fig.5.22) indicates Ti (35.30 %) and O (41.88 %) as the main elements with small amounts of Al (7.65%), Fe (4.37%), Mo (4.24%), Na (4.30%) and V (1.06%). A homogeneous and continuous surface scale is developed on conventional thick AlCrN coated T-11 boiler steel, which has Al (61.79%) and O (28.74%) as main elements (Fig.5.22.e) along with small amounts of Cr, Na, V and Fe.

5.3.1.4 Cross-sectional analysis

5.3.1.4.1 Scale thickness

The oxidized samples were cut across the cross section using Buehler Isomet 1000 precision saw and mounted in transoptic mounting resin and subsequently mirror polished to obtain scanning electron back scattered micrographs and X-ray mapping of different elements for coated and uncoated ASTM-SA213-T-11 boiler steel. The scale thickness values were measured from SEM back scattered micrographs as shown in Fig.5.23. Very thick scale is observed in case of conventional and nanostructured TiAlN coated T-11 boiler steel. The measured average scale thickness values for uncoated T-11 boiler steel, nanostructured thin TiAlN, nanostructured thin AlCrN, conventional thick TiAlN and conventional thick AlCrN coatings are 886, 1093, 578, 1190 and 650 μm respectively.

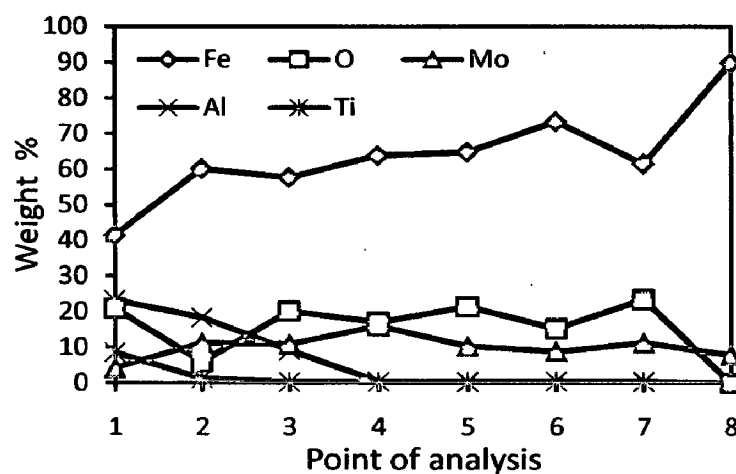
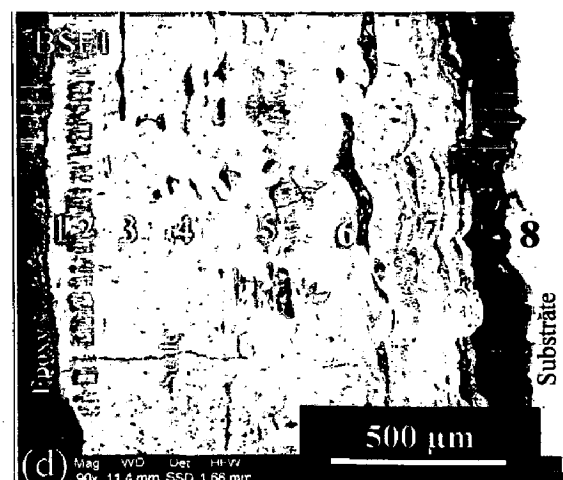
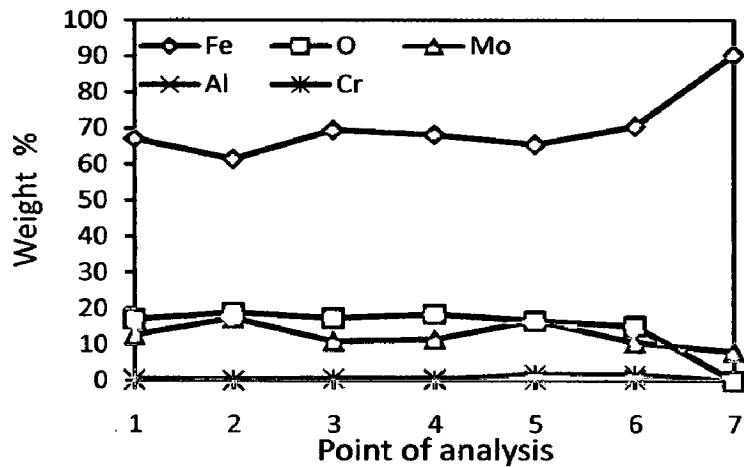
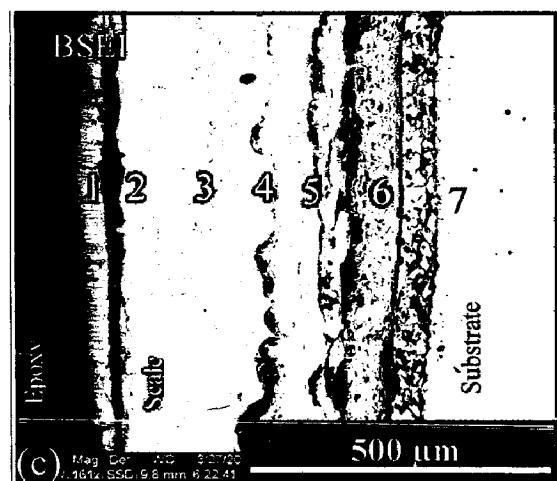
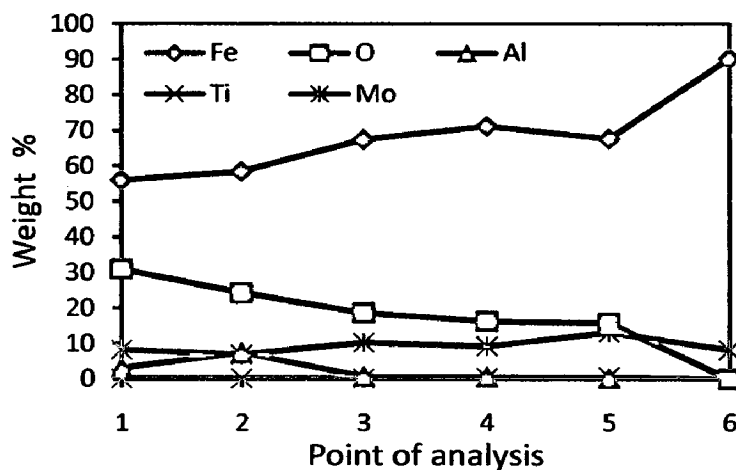
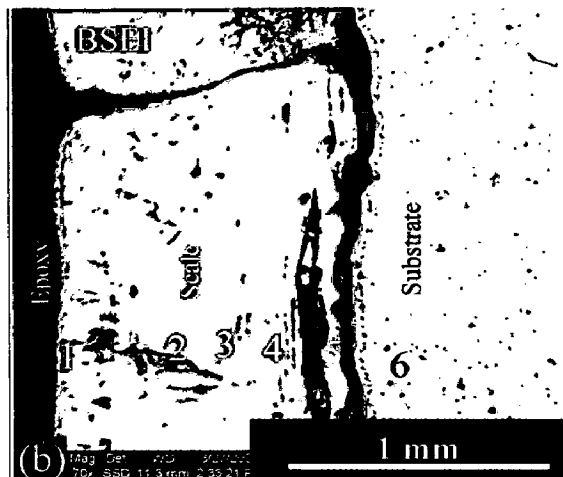
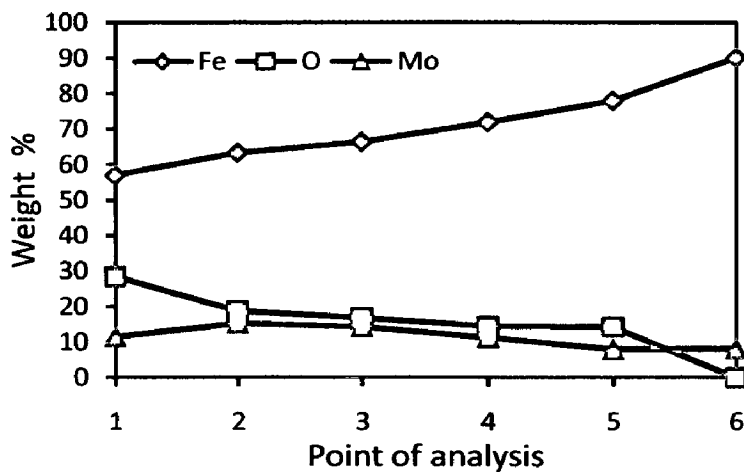
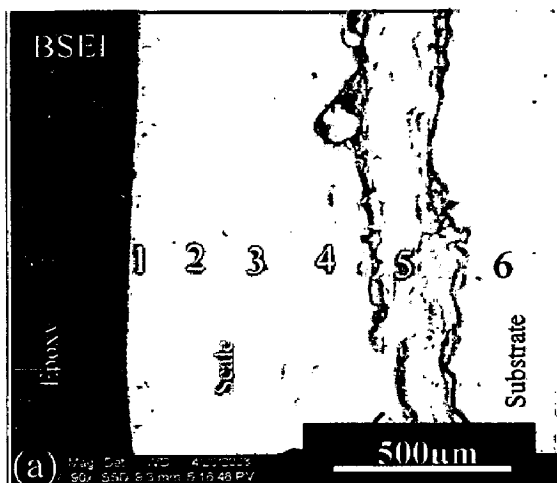
5.3.1.4.2 Cross-sectional scale morphology

Back Scattered Electron Image (BSEI) micrograph and elemental variation across the cross-section for coated and uncoated ASTM-SA213-T-11 boiler steel subjected to cyclic oxidation in Na_2SO_4 -60% V_2O_5 (molten salt) environment at 900°C for 50 cycles are shown in Fig.5.23. The SEM micrograph in case of uncoated T-11 boiler steel shows thick scale as shown in Fig. 5.23 (a). EDAX analysis reveals the presence of iron molybdenum and oxygen throughout the scale. The existence of significant amount of oxygen points out the possibility Fe_2O_3 in the oxide scale. BSEI micrograph and elemental variation depicted in Fig.5.23 (b), for the exposed cross-section of nanostructured thin TiAlN coated T-11 boiler steel shows the thick and continuous scale. Also, the scale is fragile and indicating cracking in the direction perpendicular to the surface. The EDAX analysis reveals the presence of Fe, Mo and oxygen throughout the scale. A location at point 2 (Fig.5.23.b) in the micrograph depicts the good percentage of Al and O. A thick and adherent oxide scale can be seen in case of nanostructured AlCrN coated T-11 boiler steel (Fig.5.23.c). The scale is indicating cracking along the surface. The EDAX point analysis indicates the presence of Fe, Mo and oxygen in the oxide scale.

In case of conventional TiAlN coated T-11 boiler steel, the scale is uniform and adherent as depicted in Fig.5.23 (d), but with cracks. The EDAX point analysis indicates the presence of Fe, O, and Mo throughout the scale with variable amounts. The top scale is rich in Al and Ti. A location at points 1 and 2 shows good percentage of Ti, Al with O and Fe. The conventional thick AlCrN coated T-11 boiler steel (Fig.5.23.e) indicates continuous, thick and adherent scale. EDAX point analysis shows the presence of Fe, Al, Mo and O throughout the scale. The top scale shows higher percentage of Fe and O along with good amount of Al (point 1, 2 and 3 in Fig.5.23.e). In the subscale region the Al is completely absent.

5.3.1.4.3 X-Ray mapping

X-ray mappings for a part of oxide scale of uncoated and coated ASTM-SA213-T-11 boiler steel oxidized in Na_2SO_4 -60% V_2O_5 (molten salt) environment at 900°C for 50 cycles are shown in Fig. 5.24.



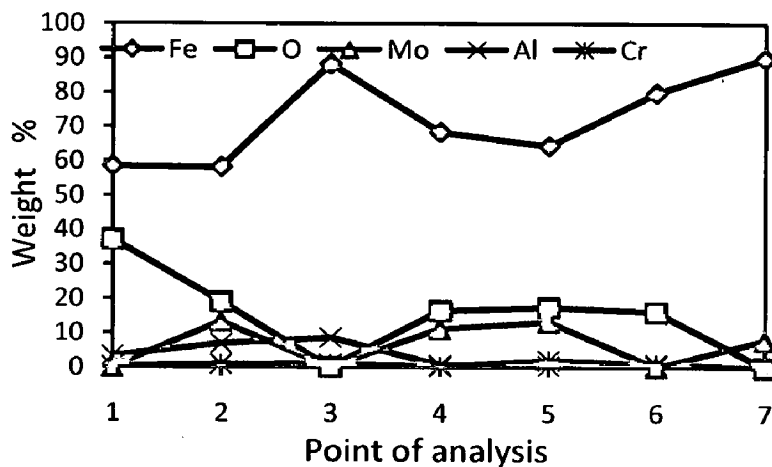
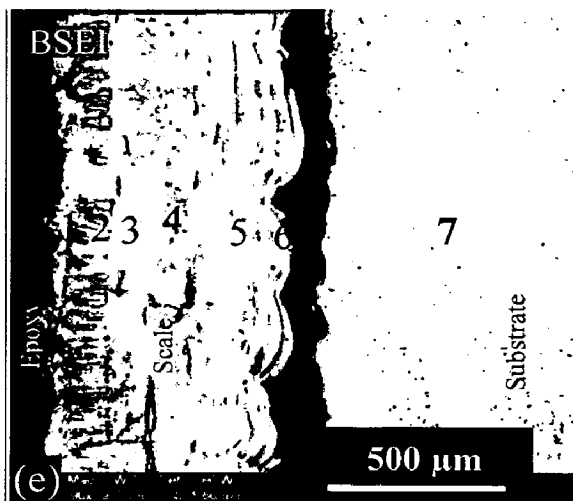


Fig. 5.23 Oxide scale morphology and variation of elemental composition across the cross-section of the uncoated and coated ASTM-SA213-T-11 boiler steel exposed to molten salt ($\text{Na}_2\text{SO}_4\text{-60\%V}_2\text{O}_5$) environment at 900°C for 50 cycles: (a) Uncoated T-11 boiler steel (90 X), (b) Nanostructured TiAlN coating (70 X), (c) Nanostructured AlCrN coating (161 X), (d) Conventional TiAlN coating (90 X), (e) Conventional AlCrN coating (90 X)

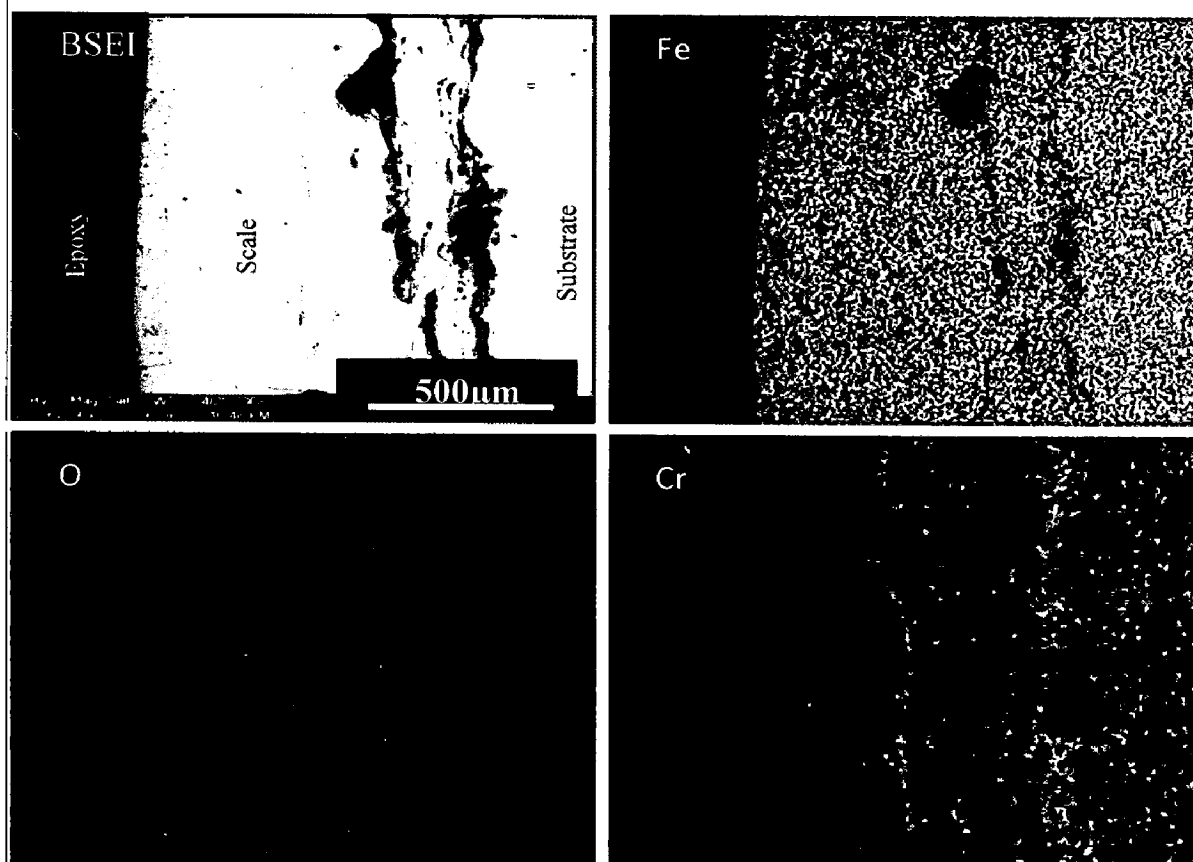


Fig. 5.24 (a) Composition image (BSEI) and X-ray mapping of the cross-section of uncoated ASTM-SA213-T-11 boiler steel exposed to molten salt ($\text{Na}_2\text{SO}_4\text{-60\%V}_2\text{O}_5$) environment at 900°C for 50 cycles

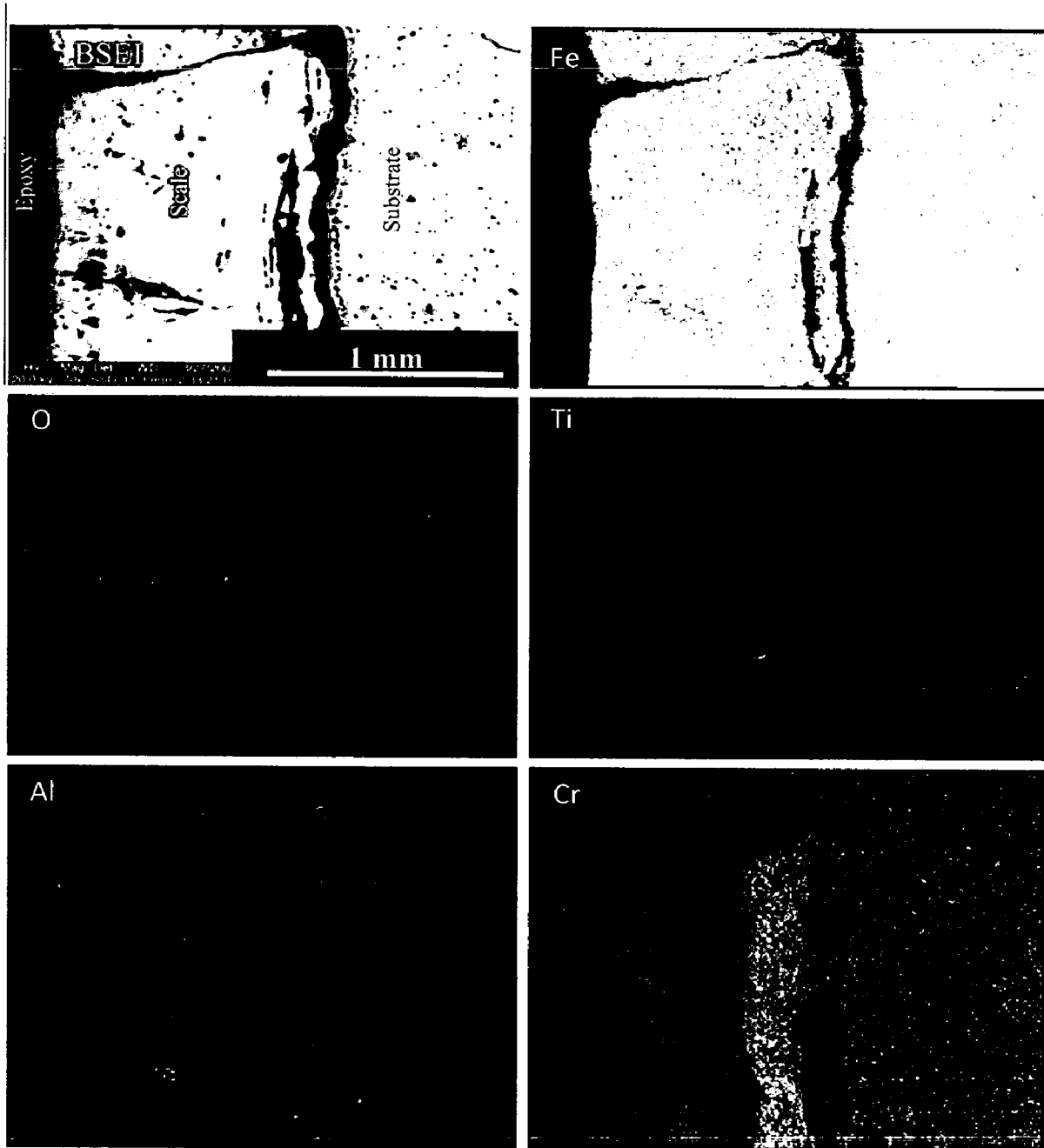


Fig. 5.24 (b) Composition image (BSEI) and X-ray mapping of the cross-section of Nanostructured TiAlN coated ASTM-SA213-T-11 boiler steel exposed to molten salt (Na_2SO_4 -60% V_2O_5) environment at 900°C for 50 cycles

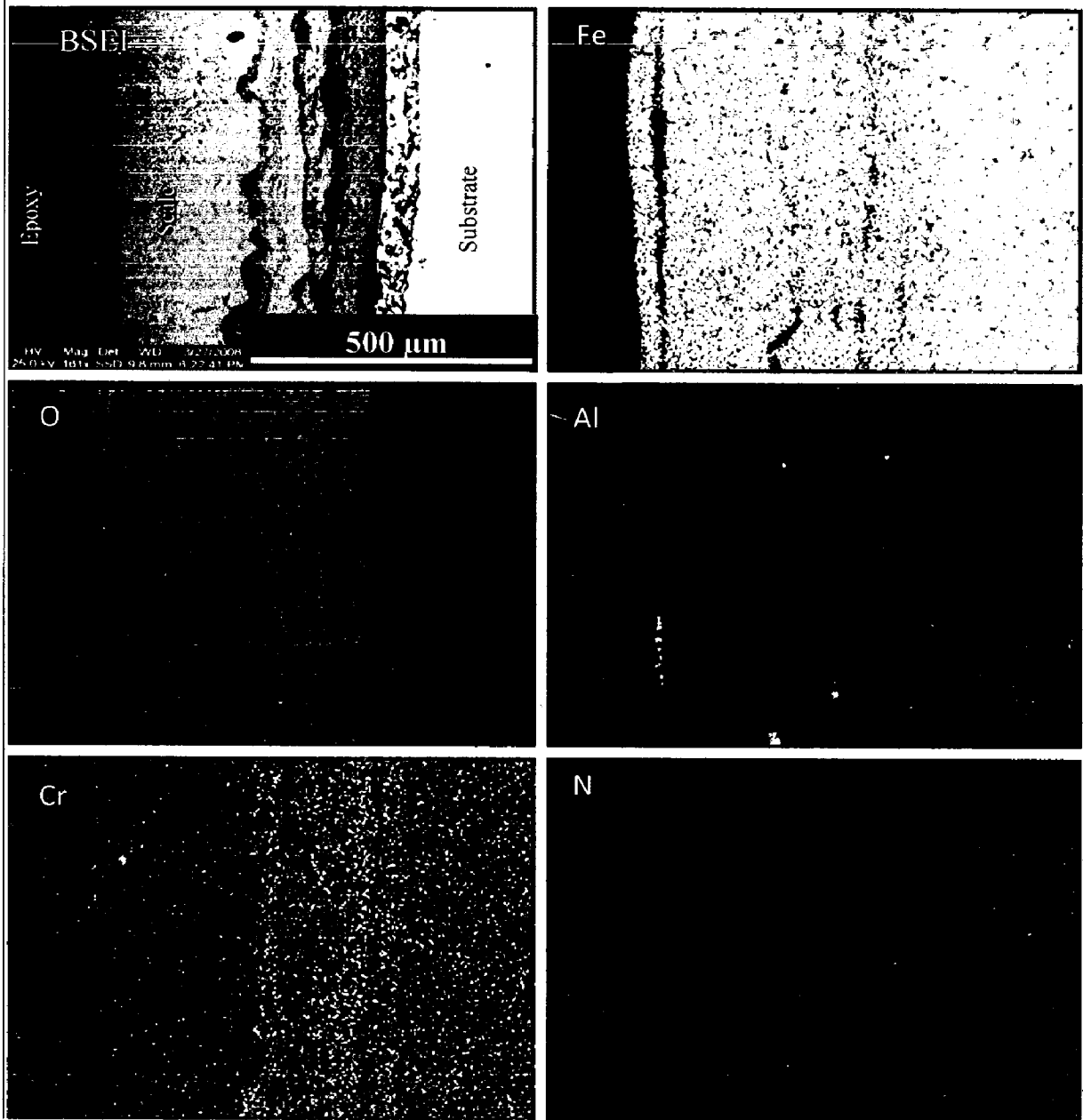


Fig. 5.24 (c) Composition image (BSEI) and X-ray mapping of the cross-section of Nanostructured AlCrN coated ASTM-SA213-T-11 boiler steel exposed to molten salt (Na_2SO_4 -60% V_2O_5) environment at 900°C for 50 cycles

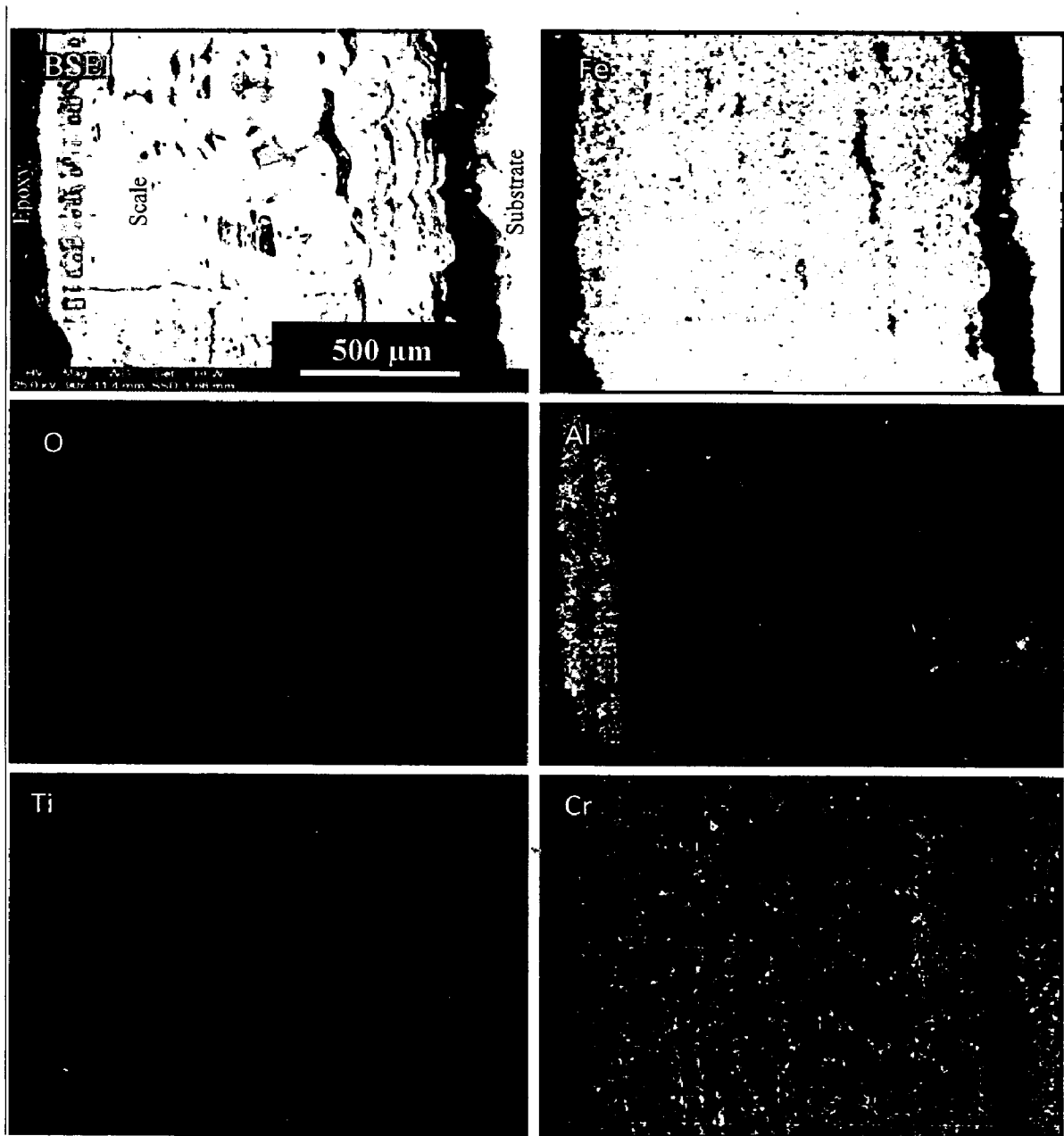


Fig. 5.24 (d) Composition image (BSEI) and X-ray mapping of the cross-section of conventional TiAlN coated ASTM-SA213-T-11 boiler steel exposed to molten salt (Na_2SO_4 -60% V_2O_5) environment at 900°C for 50 cycles

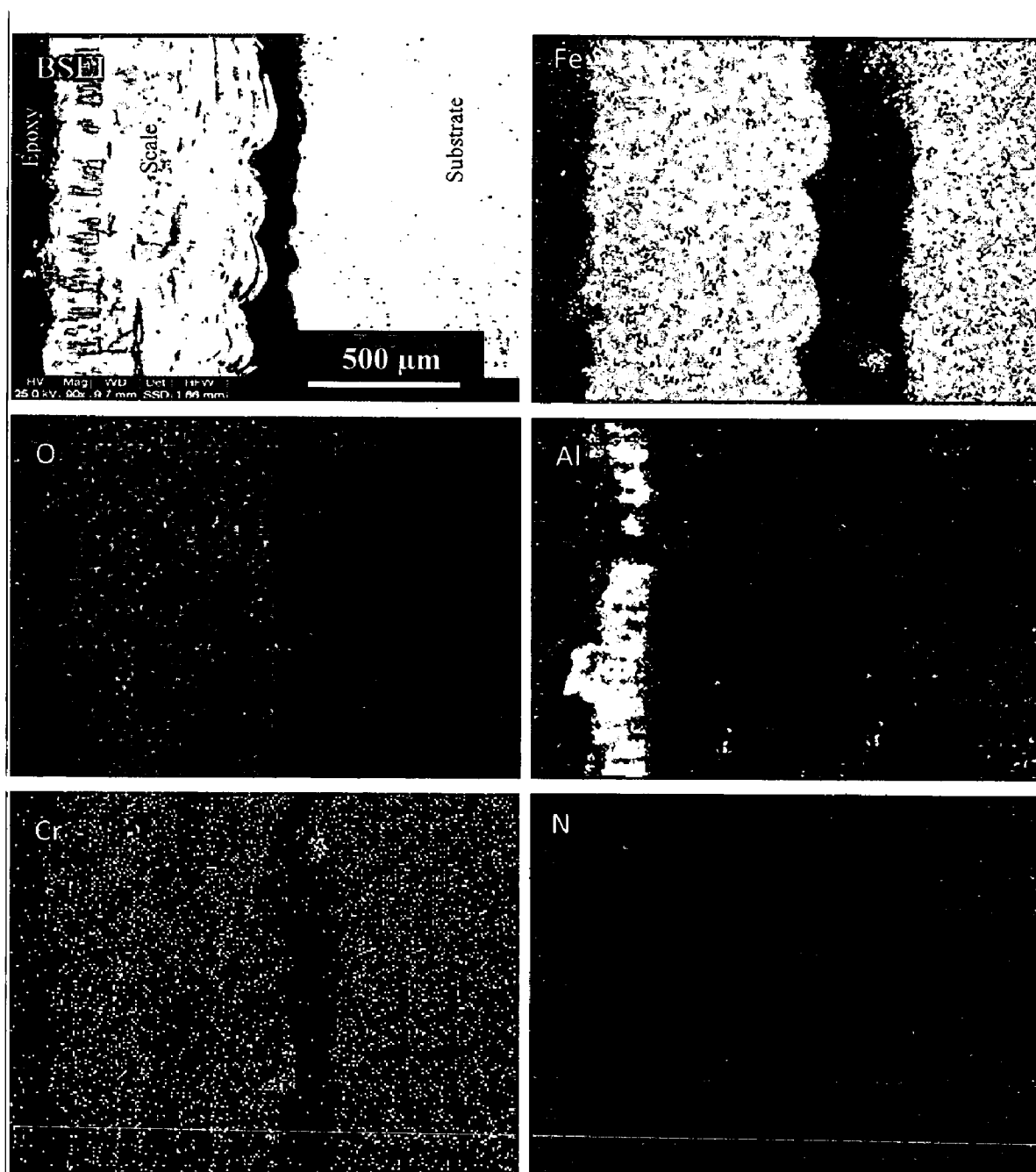


Fig. 5.24 (e) Composition image (BSEI) and X-ray mapping of the cross-section of conventional AlCrN coated ASTM-SA213-T-11 boiler steel exposed to molten salt (Na_2SO_4 -60% V_2O_5) environment at 900°C for 50 cycles

Table 5.6 Summary of the results obtained for uncoated and coated ASTM-SA213-T-11 boiler steel subjected to cyclic oxidation in molten salt (Na_2SO_4 -60% V_2O_5) environment at 900°C for 50 cycles

Coating	Cumulative Weight gain (mg/cm^2)	Parabolic rate constant ($K_p \times 10^{-08} \text{ gm}^2\text{cm}^{-4}\text{s}^{-1}$)	XRD phases	Remarks
Uncoated T-11 boiler steel	148.42	12.33	Fe_2O_3	A grey colored scale appeared on the surface right from the 3 rd cycle. This bare steel showed spalling of scale just after the 5 th cycle. After 16 th cycle fine cracks were observed which grow further and after 29 th cycle the scale starts falling in the boat. At the end of cyclic study, uniform scale with cracks and dark grey color surface appearance, was observed
Nanostructured TiAlN coating	139.59	11.11	Fe_2O_3 and Cr_2O_3	Color of the oxide scale at the end of the study was observed to be light brownish grey. Spalling was observed after 10 th cycle and after 26 th cycle the surface becomes rough and the scale remains adherent to the substrate till 50 th cycle.
Nanostructured AlCrN coating	82.70	03.80	Fe_2O_3 , Al_2O_3 and Cr_2O_3	Smooth scale with the presence of very fine cracks. The surface appearance after 37 th cycle was light grey at middle area of the sample with dark grey sides, which turns to blackish grey after 50 th cycle.
Conventional TiAlN Coating	144.51	12.49	Fe_2O_3 , Al_2O_3 , Ti_3Al and TiO_2	No signs of spalling in the initial cycles. After 16 th cycle hairline cracks were observed along the edges but the scale is adherent to the substrate till 20 th cycle. A very small layer of scale gets detached from the sample and falls in the boat after 21 st cycle. At the end of the study, a brownish grey layer of scale is visible on the surface along with some cracks.
Conventional AlCrN coating	74.98	02.98	Fe_2O_3 , Cr_2O_3 and Al_2O_3	Color of the oxide scale was whitish grey after 4 th cycle, which continued during the course of the study. A very small amount of superficial spalling was noticed at the end of 3 rd cycle, which may be due to the loosely bond particles on the surface of the coating. The scale was found to be adherent and smooth.

In case of uncoated T-11 boiler steel, the micrograph (Fig.5.24.a) indicates a dense scale, which mainly contains iron and oxygen with some amount of chromium, as indicated by X-ray mapping. Figure 5.24 (b), shows X-ray mapping analysis of the scale formed on nanostructured TiAlN coated T-11 boiler steel. The X-ray mapping indicates presence of oxygen and iron throughout the scale with some pockets of Al in the scale and at the interface of scale and substrate. Also, a thin band of Ti and Cr is visible. In case of nanostructured thin AlCrN coated T-11 boiler steel, the BSEI and X-ray mapping are shown in Fig. 5.24 (c). The X-ray mapping indicates the presence of iron and oxygen throughout the scale. A thin irregular band of Al is present in the top scale. Thin bands of Cr can be seen near the scale/substrate interface. In case of conventional thick TiAlN coated T-11 boiler steel, Fig.5.24 (d), Fe and O are present throughout the scale. But, the top scale is rich in Al and Ti, as a thick band of these elements can be seen in top scale. Fig.5.24 (e), depicts the X-ray mapping in case of conventional AlCrN coated T-11 boiler steel. Thick band of Al is present in the top scale region along with Fe and O. The sub scale is rich in Fe and O with some pockets of Cr.

5.3.2 Summary of Results

Results obtained after exposure of uncoated and coated ASTM-SA213-T-11 boiler steel to cyclic oxidation in Na_2SO_4 -60% V_2O_5 (molten salt) environment at 900°C for 50 cycles are summarized in Table.5.6.

5.3.3 Discussion

The surface macrographs of bare and coated ASTM-SA213-T-11 boiler steel subjected to cyclic oxidation in Na_2SO_4 -60% V_2O_5 (molten salt) environment at 900°C for 50 cycles are shown in Fig.5.17. It is observed from the macrographs that the oxide scale was intact with the coating and marginal spalling was observed from the surface in case of nanostructured and conventional AlCrN coatings (Fig.5.17.c and e). But, in case of nanostructured and conventional TiAlN coated T-11 boiler steel, severe spalling was observed (Fig.5.17.b and d).

The appearance of cracks/peeling off in the coatings during hot corrosion studies may be attributed to the different values of thermal expansion coefficients for the coating, scale and the substrate as reported by Sidhu et al. (2003), Singh H et al.

(2004), Evans et al. (2001), Wang et al. (2002) and Niranatlumpong et al. (2000). Further Niranatlumpong et al. (2000) opined that spallation could be initiated by the rapid growth of void-like defects lying adjacent to coating protuberances, at which tensile radial stress developed during cooling as a result of the thermal contraction mismatch between the oxide and coating is maximum. The formation of cracks in the coating originates from stresses developed in the deposit or at the coating-base metal interface (Heath et al., 1997). Though these cracks the corrosive environment can quickly reach the base metal and cut its way under the coating to result in adhesion loss and spalling, whereas some elements may diffuse outwards through these cracks to form oxides or spinels (Singh H et al., 2004) as revealed by XRD and EDAX analysis. Also as reported by Chatterjee et al. (2001), during initial oxidation iron is oxidized and the oxide scale is protective in nature. With progress of oxidation Mo becomes enriched at the alloy interface, leading to the formation of an inner layer of molten MoO_3 (m. p. 795°C) which penetrates along the alloy-scale interface. This liquid oxide disrupts and dissolves the protective oxide scale, causing the alloy to suffer catastrophic oxidation (Lai, 1990). This may be the reasons for severe spalling and hence failure of nanostructured and conventional TiAlN coating.

The weight change plots (Fig.5.18) for the uncoated and coated T-11 boiler steel indicated that the oxidation behavior has shown conformance to parabolic rate law. The parabolic kinetic behavior is due to the diffusion controlled mechanism operating at 900°C under cyclic conditions (Mahesh et al., 2008). Small deviation from the parabolic rate law might be due to the cyclic scale growth. The rapid increase in the weight gain during the initial period of exposure to Na_2SO_4 -60% V_2O_5 (molten salt) environment at 900°C may be due to the rapid diffusion of oxygen through the molten salt layer. Kolta et al. (1972) proposed that in the temperature range of 900°C , the Na_2SO_4 and V_2O_5 will combine to form NaVO_3 having a melting point of 610°C . This NaVO_3 acts as a catalyst and also serves as an oxygen carrier to the base alloy through the open pores present on the surface, which will lead to the rapid oxidation of the base elements of the substrate to form a protective oxide scale. Hence, an increase in the weight gain of the alloys occurs in the early stages of the hot corrosion. There may be simultaneous dissolution of Cr_2O_3 in the molten salt due to the reaction (Seiersten and Kofstad, 1987; Swaminathan et al., 1993):



During the subsequent cycles, the formations of oxides have blocked the diffusion of corrosive species by covering the pores and the splat boundaries. The rapid increase in the weight gain during the initial period was also reported by Sidhu et al. (2006B), Harpreet Singh et al. (2005), Tiwari and Prakash (1997) and Ul-amid (2003) during studies on the hot corrosion of alloys.

The surface XRD analysis (Fig.5.21) indicated the formation of Fe_2O_3 as the main constituent of the top scale in case of bare, nanostructured and conventional TiAlN and nanostructured AlCrN coated boiler steel. The formation of Fe_2O_3 has also been observed by Shi (1993) for the oxidation of iron by Na_2SO_4 at 750°C and by Tiwari and Prakash (1996) during hot corrosion of Iron-base superalloy in the Na_2SO_4 -60% V_2O_5 environment at 900°C . Weak intensity peaks of Cr_2O_3 in the scale of T-11 steel may due to the presence of some amount of chromium in the alloy steel. The presence of some percentage of chromium in the subscale as revealed by the X-ray mapping analysis (Fig.5.24) across the cross-section for T-11 steel is in accordance with the findings of Sadique et al. (2000). The authors have reported that Fe-Cr alloys in oxygen at higher temperature (950 - 1050°C) form spinel (FeCr_2O_4) and Cr_2O_3 on the inner side and Fe_2O_3 on the outer side of the scale. This can also be attributed to depletion of iron due to oxidation to form the upper scale thereby leaving chromium rich pockets those further get oxidized to form iron chromium spinel.

Conventional thick and nanostructured thin AlCrN coatings have been found successful in reducing the overall weight gain of bare T-11 boiler steel. It is evident from XRD (Fig.5.21) results of the oxidized conventional thick and nanostructured thin AlCrN coated T-11 boiler steel that Al_2O_3 as the main phase which are further supported by EDAX (Fig.5.22) and X-ray mapping (Fig.5.24) analysis. A thick band of Al in the top scale (Fig.5.24.e) is observed in case of conventional AlCrN coating, which may have acted as a barrier to the environment. The oxidation rate (total weight gain values after 50 cycles) of the coated and uncoated T-11 boiler steel follows the sequence as given below:

Bare T-11 > Conventional TiAlN > Nanostructured TiAlN > Nanostructured AlCrN > Conventional AlCrN

The nanostructured TiAlN coating has shown resistance to oxidation to some extent as the overall weight gain is less than as compared to the uncoated T-11 boiler steel. The conventional thick TiAlN coatings has shown protection up to 16th cycle as observed in weight gain plot (Fig.5.18) supported by visual observations, but it fails to provide the protection to the substrate till 50th cycle. Inferior oxidation resistance of TiAlN coating may be as opined by Ding et al. (2008); in an oxidation or corrosive environment Ti element often forms a porous non-protective oxide scale, which limits the oxidation and corrosion resistance of titanium-based coatings. Fujita (2005) has further reported that the oxide scale of binary TiAl alloy is composed of a porous oxide mixture of TiO₂ and Al₂O₃, which has dominated by TiO₂. This might be the reason for rapid increase in oxidation rate of TiAlN coatings after 16th cycle (Fig. 5.18). Kalss et al. (2006) have reported, at 900°C an oxidized layer of thickness of about 350nm for TiAlN coating was measured. Due to high temperature the segregation of titanium and aluminum atoms is probable. Evidently, high temperature oxidation involved diffusion of aluminum atoms to the surface to form a thin aluminum oxide top layer while the remaining titanium under layered formed titanium dioxide. At 950°C, the whole coating was decomposed and pure titanium dioxide was formed (Kalss et al., 2006), which is supported by Man et al. (2004).

5.3.4 Conclusions

The high temperature oxidation behaviors of uncoated and coated ASTM-SA213-T-11 boiler steel have been investigated in Na₂SO₄-60%V₂O₅ (molten salt) environment at 900°C for 50 cycles. The behavior of nanostructured TiAlN and AlCrN coatings were compared with their conventional counterparts and the following conclusions are made:

1. The plasma sprayed gas nitride conventional thick AlCrN coating when subjected to cyclic oxidation in Na₂SO₄-60%V₂O₅ molten salt at 900°C for 50 cycles developed a protective scale mainly consisting on aluminum oxide and chromium oxide.
2. The oxidation rate of the coated and uncoated T-11 boiler steel follows the sequence as given below:

Bare T-11 > Conventional TiAlN > Nanostructured TiAlN > Nanostructured AlCrN > Conventional AlCrN

- 3. The nanostructured thin AlCrN coatings has shown resistance to oxidation as the overall weight gain is less than as compared to the uncoated T-11 boiler steel.**
- 4. In case of uncoated T-11 boiler steel, the weight gain is highest with thickest scale. Some cracks are also observed in case of bare, nanostructured thin and conventional thick TiAlN coated boiler steel.**
- 5. Nanostructured thin and conventional thick AlCrN coatings can provide a good oxidation resistance in Na_2SO_4 -60% V_2O_5 molten salt environment at high temperature.**
- 6. The oxide scale formed is adherent to the substrate in all coatings. But in case of bare nanostructured thin and conventional thick TiAlN coated boiler steel, the scale is found to be detached from the substrate after hot corrosion studies.**
- 7. The appearance of cracks/peeling off in the coatings during hot corrosion studies may be attributed to the different values of thermal expansion coefficients for the coating, substrate steels and oxides formed.**

5.4 EROSION STUDIES IN SIMULATED COAL-FIRED BOILER ENVIRONMENT

The present work has been focused to compare the high temperature erosion behavior of conventional thick (by plasma spraying and gas nitrided) and nanostructured thin (by physical vapor deposition process) TiAlN and AlCrN coatings on ASTM-SA213-T-11 boiler steel. The erosion studies were carried out using a high temperature air-jet erosion test rig at a velocity of 35 ms^{-1} and impingement angles of 30° and 90° . The tests were carried out at high temperatures. The two temperatures were taken for the test, sample temperature 400°C and air/erodent temperature 900°C simulated to service conditions of boiler tubes in which sample temperature and flow gas temperature correspond to the inner and outer temperature of water wall pipes. The alumina particles of average size $50 \mu\text{m}$ were used as erodent. Erosion rates in terms of volumetric loss (mm^3/g) for different uncoated and coated alloys are compared. The eroded samples were analyzed with SEM/EDX and optical profilometer. The erosion rate data for each coated alloy has been plotted along with uncoated alloy in order to assess the coating performance. Efforts have been made to understand the mode of erosion.

5.4.1 Results

5.4.1.1 Visual observations

The macrographs for uncoated and coated ASTM-SA213-T-11 boiler steel subjected to erosion studies in simulated coal-fired boiler environment are shown in Fig.5.25. The effect of corrosion along with the erosion was observed. The shape of the scar (developed by constant strike of erodent) is circular in case of normal impact (at 90°) and elliptical in case of oblique impact (at 30°) of erodent. The uncoated T-11 boiler steel shows a thin scale. The erosion seems to clean the scale off the surface in the eroded/corroded region. The impact of erodent removes the scale down to the substrate-scale interface. Away from this eroded region a thin layer of scale was observed on the surface and the eroded/corroded region showed rust colored discoloration (Fig.5.25.a). The nanostructured TiAlN coated T-11 boiler steel showed marks of erosion as shown in Fig.5.25 (b). The color of the coated specimen changed from violet-grey to whitish at scar and blackish blue ring around the scar.

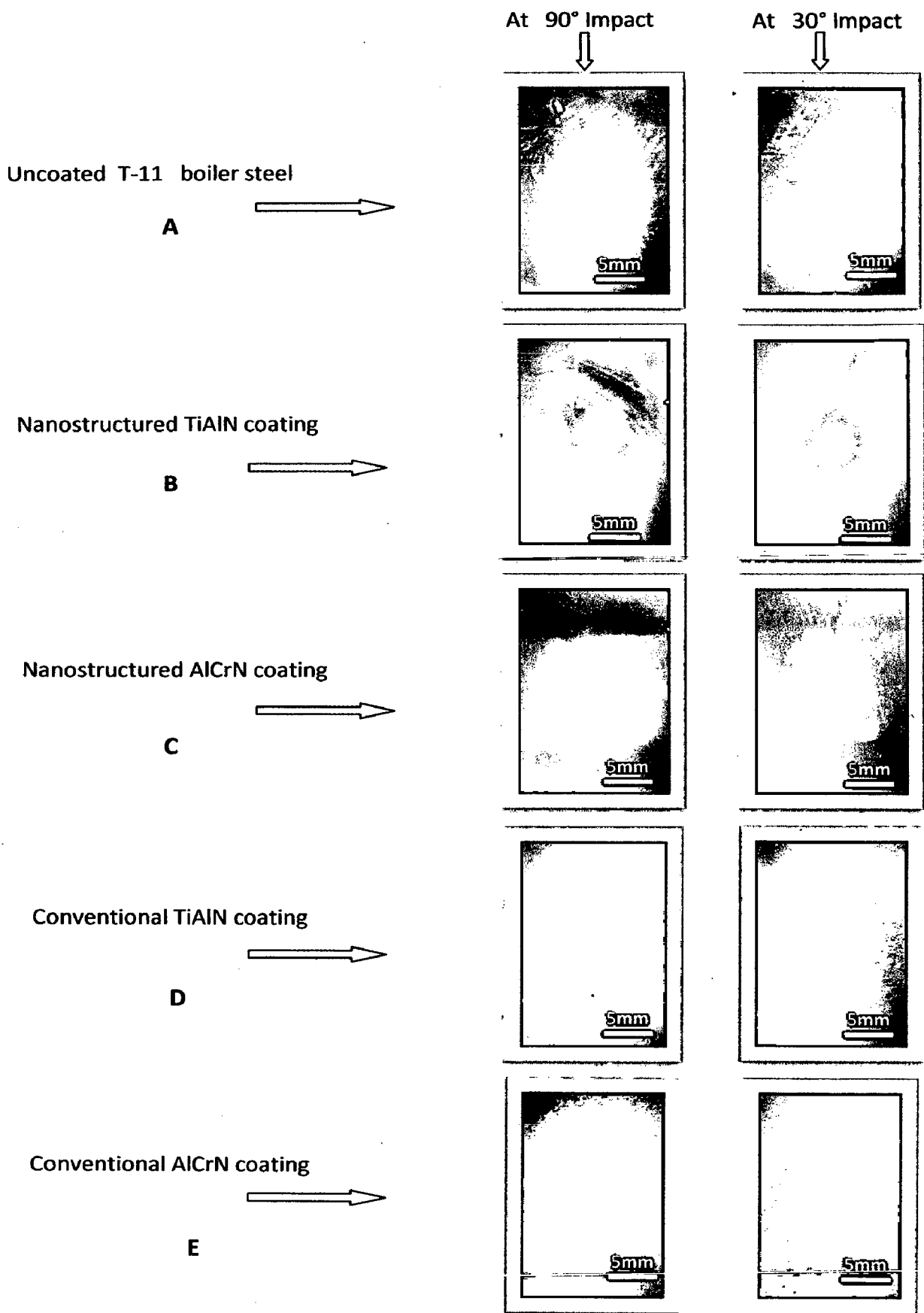


Fig. 5.25 Surface macrographs of eroded uncoated and coated ASTM-SA213-T-11 boiler steel exposed to high temperature erosion studies in simulated coal-fired boiler environment

The macrograph in case of eroded nanostructured AlCrN coating are shown in Fig.5.25 (c). The color of the scars was observed as light grey surrounded by dark colored ring. A visual observation of conventional thick TiAlN and AlCrN coated T-11 boiler steel (Fig.5.25.d and e), showed the formation of dark grey colored scar surrounded by a light colored ring. Also, the un-eroded area around the scars appeared as rough surface.

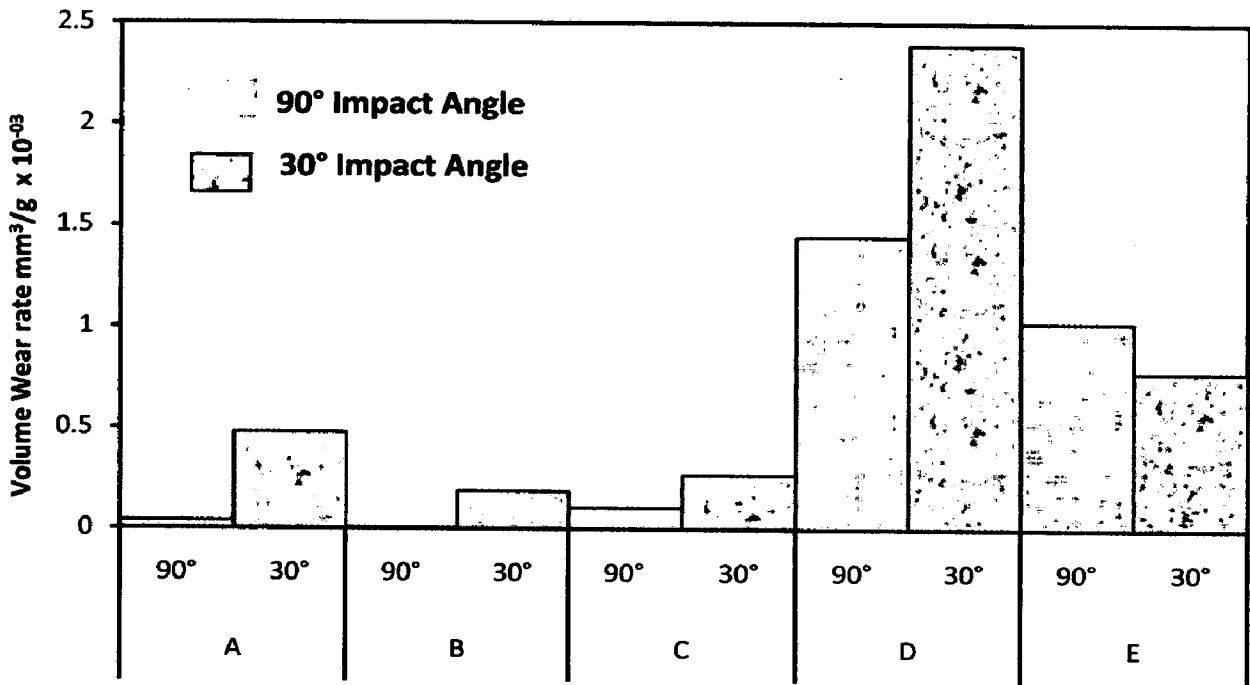


Fig. 5.26 Column chart showing the Volume wear rate of uncoated and coated ASTM-SA213-T-11 boiler steel eroded at normal and oblique impact: (A) Uncoated T-11 boiler steel, (B) Nanostructured TiAlN coating, (C) Nanostructured AlCrN coating, (D) Conventional TiAlN coating, (E) Conventional AlCrN coating

5.4.1.2 Erosion rate

The erosion loss has been calculated by volume change method. The volume loss occurred after erosion testing was measured by using non contact optical profilometry as explained in chapter 3. The erosion rate for uncoated and coated T-11 boiler steel at an impact velocity of 35 ms⁻¹ and impingement angle of 30° and 90° when substrate temperature was 400°C and surrounding air at 900°C; is shown in Fig.5.26. The volume erosion rate for uncoated T-11, nanostructured thin TiAlN, nanostructured thin AlCrN, conventional thick TiAlN and conventional thick AlCrN coatings; is 0.0387 x10⁻³,

0.00432 $\times 10^{-3}$, 0.105 $\times 10^{-3}$, 1.444 $\times 10^{-3}$ and 1.02325 $\times 10^{-3}$ mm³/gm respectively at 90° impact angle. While at 30° impact, the volume erosion rate for uncoated T-11, nanostructured thin TiAlN, nanostructured thin AlCrN, conventional thick TiAlN and conventional thick AlCrN coatings; is 0.4762 $\times 10^{-3}$, 0.1850 $\times 10^{-3}$, 0.2670 $\times 10^{-3}$, 2.3987 $\times 10^{-3}$ and 0.7767 $\times 10^{-3}$ mm³/gm respectively.

From the graph, it can be inferred that the erosion rate of the uncoated T-11 boiler steel eroded at oblique impact i.e. at 30° impingement angle is more as compared to erosion rate at 90° impact thus showing the typical behavior of ductile materials. The similar behavior was observed in case of the nanostructured thin TiAlN, AlCrN and conventional thick TiAlN coatings (Fig.5.26). In case of the conventional thick AlCrN coated T-11 boiler steel; the erosion rate at normal impact i.e. at 90° impingement angle is more as compared to erosion rate at 30° impact thus showing the typical behavior of brittle materials. Also, the overall volume erosion rate in case of conventional AlCrN coating is less as compared to conventional thick TiAlN coating.

5.4.1.3 SEM/EDAX Analysis

SEM micrographs along with EDAX point analysis reveals the surface morphology of the uncoated and coated T-11 boiler steel subjected to erosion studies in simulated coal-fired boiler environment when substrate temperature was 400°C and surrounding air at 900°C; are shown in Fig. 5.27 and 5.28. The SEM observations were made on the eroded surface of all the uncoated and coated T-11 boiler steel specimens at both the impact angles i.e. at 90° and 30°. Scanning electron microscopy (SEM) revealed various erosion mechanisms like metal removal, oxide chipping, fracture and spalling within the oxide/coating layer and at the scale/metal interface etc. The micrographs have revealed fracture at the surfaces with impressions of formation of craters with crack network.

Micrographs (Fig.5.27) for the eroded surfaces of uncoated and coated T-11 boiler steel at 90° impact angle, clearly indicates the formation of crater, impact zone, oxide fracture and removal, coating fracture and retained erodent. It can be observed from the micrographs of the eroded surface of the uncoated boiler steel (Fig.5.27.a) that the erodent particles deform the exposed surface by ploughing and introducing the craters in the matrix by displacing material to the side.

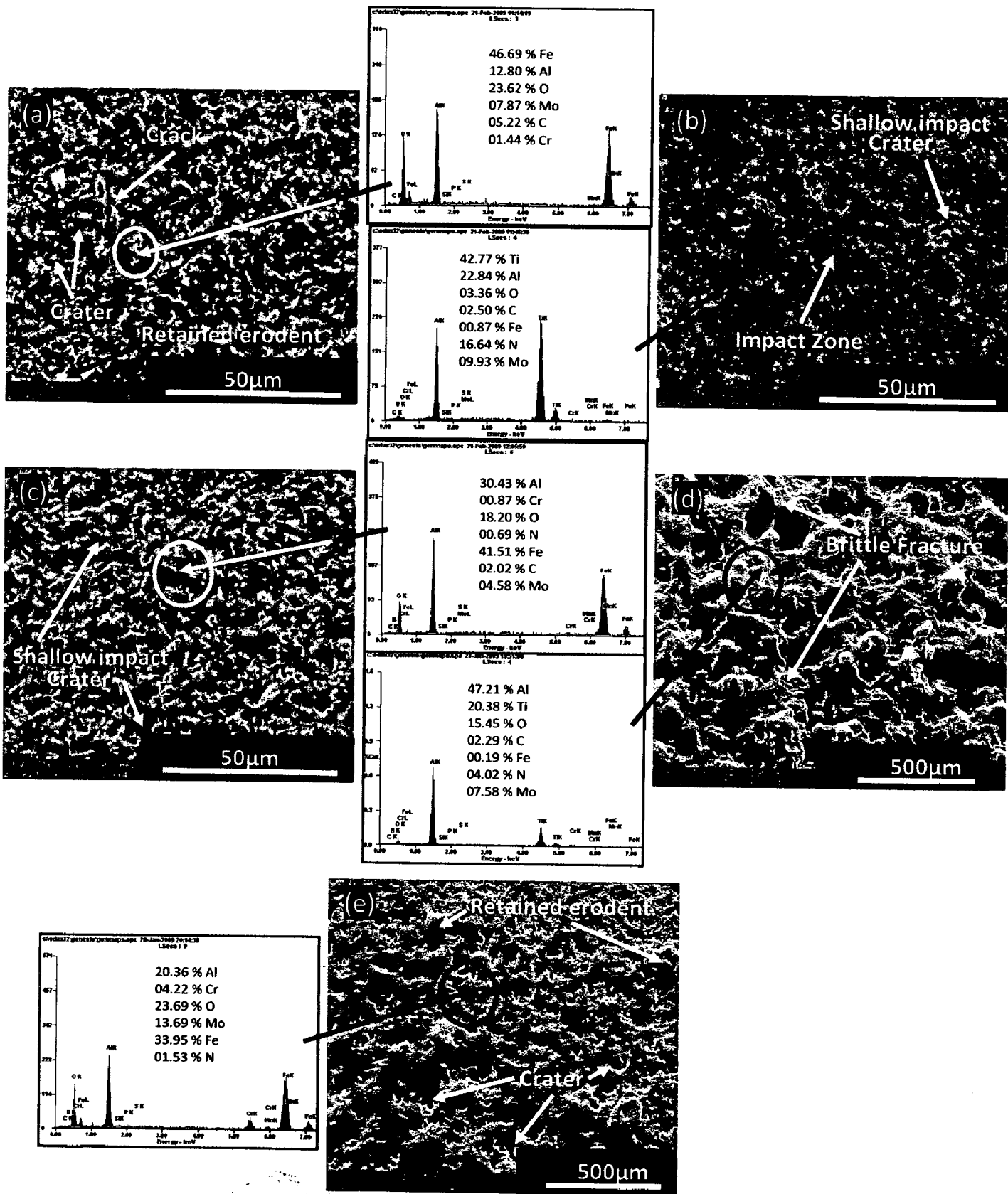


Fig. 5.27 Surface-scale morphology and EDAX patterns from different spots on eroded uncoated and coated ASTM-SA213-T-11 boiler steel exposed to high temperature erosion studies in simulated coal-fired boiler environment at impact angle 90°: (a) Uncoated T-11 boiler steel, (b) Nanostructured TiAlN coating, (c) Nanostructured AlCrN coating, (d) Conventional TiAlN coating, (e) Conventional AlCrN coating

formation of craters with minor cracks. EDAX analysis revealed the presence of Fe, Al and O as the main elements on the eroded area, which indicates the formation of iron oxide due to oxidation and presence of retained erodent i.e. alumina. Micrograph in case of nanostructured TiAlN and AlCrN coatings (Fig.5.28.b and c); revealed shallow impact craters with retained erodent. EDAX analysis indicates the presence of Fe, Al and O as the main elements along with some amount of Cr, Ti and C. It can be inferred that the nanostructured coatings gets severely damaged and fractured when the eroding particle strikes the surface of a coating at 30° and failed to protect substrate.

The micrograph of the conventional TiAlN coating (Fig.5.28.d) revealed the oxide fracture and removal at various locations along with craters. When the eroding particle strikes the surface of the coating at 30° the material is severely damaged and fractured as shown in Fig.5.28 (d). EDAX analysis shows the presence of Al, Ti and O as the main elements along with very less amount of Fe and C. It can be inferred that the coating is still there after three hours continuous erodent impacts at an impact velocity of 35 ms⁻¹ and impingement angle of 30° when substrate temperature was 400°C and surrounding air at 900°C. The coating has successfully protected the substrate. Further in case of conventional AlCrN coating, the erodent particle impacts have severely damaged the coating by causing cracking and fracture. The impact zone is wider (Fig.5.28.e) which may be caused by the continuous subsequent impacts of erodent particles. Also, the signs of splat debonding and craters can be observed in micrograph. EDAX analysis revealed the presence of Al and Fe as the main elements with small amount of O, Mn and C; indicating that the coating has failed to protect the substrate and hence exposed the substrate.

5.4.2 Discussion

In erosion testing, the material is eroded by continuous impact of erodent particles; the erosion starts at the centre first, and then proceeds towards the edges of the samples. The shape of developed scar depends on the angle of impact. When erodent strikes the surface at an impact angle of 90°, material is eroded creating a circular depression; while at a 30° impact angle, material is eroded forming an elliptical shape depression. The erosion rate for uncoated and coated T-11 boiler steel at an impact velocity of 35 ms⁻¹ and impingement angle of 30° and 90° when substrate

temperature was 400°C and surrounding air at 900°C; is shown in Fig.5.26. The volume erosion rate for uncoated T-11, nanostructured thin TiAlN, nanostructured thin AlCrN, conventional thick TiAlN and conventional thick AlCrN coatings; is 0.0387×10^{-3} , 0.00432×10^{-3} , 0.105×10^{-3} , 1.444×10^{-3} and 1.02325×10^{-3} mm³/gm respectively at 90° impact angle. Based on the present data the erosion rates for 90° impact angle can be arranged in the following order:

Conventional TiAlN > Conventional AlCrN > Nanostructured AlCrN > Bare T-11 > Nanostructured TiAlN

It can be inferred from the above data that the relative erosion resistance of conventional thick TiAlN coating is least among the uncoated and coated T-11 boiler steel specimens. Further, the SEM/EDAX analysis (Fig.5.27) indicates that in case of nanostructured and conventional TiAlN coated T-11 boiler steel; the coating is still there after three hours continuous erodent impacts at an impact velocity of 35 ms⁻¹ and impingement angle of 90° when substrate temperature was 400°C and surrounding air at 900°C. These coatings have successfully protected the substrate. The nanostructured and conventional AlCrN hard coatings were removed by the continuous strikes of the eroding particles on the surface of the coating at 90° (Fig.5.27).

While at 30° impact, the volume erosion rate for uncoated T-11, nanostructured thin TiAlN, nanostructured thin AlCrN, conventional thick TiAlN and conventional thick AlCrN coatings; is 0.4762×10^{-3} , 0.1850×10^{-3} , 0.2670×10^{-3} , 2.3987×10^{-3} and 0.7767×10^{-3} mm³/gm respectively. Based on the present data the erosion rates for 30° impact angle can be arranged in the following order:

Conventional TiAlN > Conventional AlCrN > Bare T-11 > Nanostructured AlCrN > Nanostructured TiAlN

It can be inferred from the above data that the relative erosion resistance of conventional thick TiAlN coating is least among the uncoated and coated T-11 boiler steel specimens. The erosion resistance sequence for the conventional coatings is independent of the impact angle in this case. Further, the SEM/EDAX analysis (Fig.5.28) indicates that in case of conventional thick TiAlN coated T-11 boiler steel; the coating is still there after three hours continuous erodent impacts at an impact velocity of 35 ms⁻¹ and impingement angle of 30° when substrate temperature was 400°C and surrounding air at 900°C. This coating has successfully protected the substrate. The

nanostructured TiAlN and AlCrN and conventional AlCrN coatings were removed by the continuous strikes of the eroding particles on the surface of the coating at 30° (Fig.5.28).

The solid particle erosion rate of the uncoated and nanostructured thin TiAlN and AlCrN coated T-11 boiler steel as shown in Fig.5.26 indicated that maximum erosion took place at 30° impact angle, which indicate ductile behavior as proposed by Murthy et al (2001). Authors suggested that the material subjected to erosion initially undergoes plastic deformation and is later removed by subsequent impacts of the erodent on the surface. The ploughing occurs by the impact of the erodent particles and lips or ridges are formed at the bank of the craters. These lips are fractured or removed with further erosion. At low erosion temperatures, at high impact velocities and feed rates, there is no oxide scale. Even if there is any oxide scale, it will be very thin and it will be able to deform in the same manner as that of the substrate target. The works of Shida and Fujikawa (1985), Singh and Sundararajan (1990) Levy et al., (1986) can be considered elevated temperature erosion of metals with minimum or negligible oxidation. Under such circumstances, erosion takes place from the metallic surface and this mechanism of erosion is called metal erosion. Most of the metallic materials, irrespective of temperature of erosion, exhibit a ductile behavior, i.e. a maximum erosion rate at oblique impact angles (Tabakoff W and Vittal, 1983). The erosion behavior in this regime is similar to the ambient temperature erosion behavior of metallic materials. The erosion response in the metal erosion regime is ductile as described by Bellman and Lavy (1981). Authors suggested that the creation of platelet-like edges by impact extrusion protrude outward over adjacent material and the loss of these platelets appears to be responsible for the mass loss. Authors have further explained that repeated deformation of craters and forming of new craters is common and some platelets are extruded several times before getting knocked off.

Sundararajan and Roy (1997) proposed a model of metal erosion and oxide erosion. According to his model if steady state thickness of the oxide scale is smaller than the critical thickness of the oxide scale, three modes of interaction between erosion and oxidation are possible. In the first case, which applies either when there is no oxide scale or when the depth of deformation is much higher than the thickness of the oxide scale (as in the case of uncoated and nanostructured thin coated T-11 boiler

steel in present case), metal erosion becomes important (presented in Figs 5.29.a and b). In the second case, when the depth of deformation is smaller than the steady state thickness of the oxide scale, erosion of the oxide scale takes place as illustrated in Fig. 5.29 (c).

The solid particle erosion rate of the conventional thick TiAlN coated T-11 boiler steel as shown in Fig.5.26 indicated that maximum erosion took place at 30° impact angle, which indicate ductile behavior of the conventional coatings. The solid particle erosion rate of the conventional thick AlCrN coated T-11 boiler steel as shown in Fig.5.26 indicated that maximum erosion took place at 90° impact angle, which indicate brittle behavior of the conventional coatings. In case of brittle materials; loss in solid particle erosion occurs predominantly through the formation and interaction of a subsurface micro crack network (Guessasma et al., 2006).

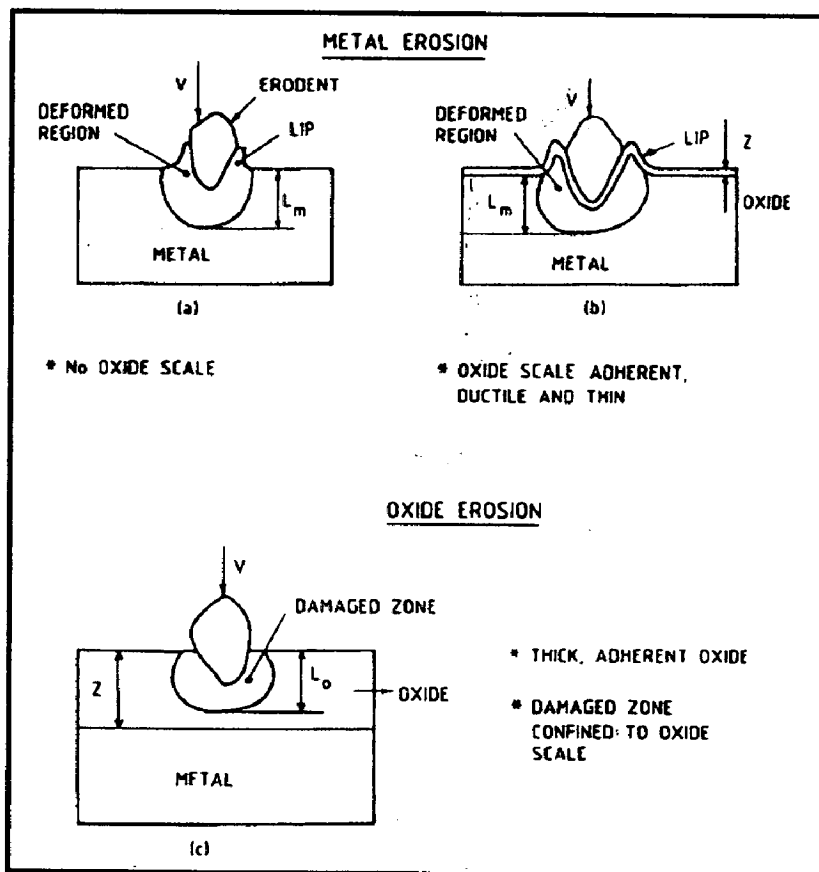


Fig. 5.29 Schematic representation of (a) & (b); metal erosion, and (c) oxide erosion illustrating the nature of interaction between the oxide scale and the substrate during erosion (Sundararajan and Roy, 1997)

So in conventional thick AlCrN coatings; the erosion rate was high at normal impact and low at oblique impact. Whereas in case of conventional thick TiAlN coating; the erosion rate was high at oblique impact and low at normal impact. The difference in erosion rates for shallow and normal impact angles can be attributed to the different material removal mechanisms in these two cases. At low angle impact, the kinetic energy of the erodent particles contributes mainly to the ploughing mechanism and very little to normal repeated impact. The ploughing mechanism is associated with the plastic smearing and cutting of the materials, while the repeated impact mechanism is responsible for initiating and propagating the grain boundary microcracks. Brittle materials are not easily plastically deformed. Hence the material removal rate is low in case of brittle materials and higher in case of ductile materials. At high angle impact, the kinetic energy of the impinging particles contributes mainly to repeated impact.

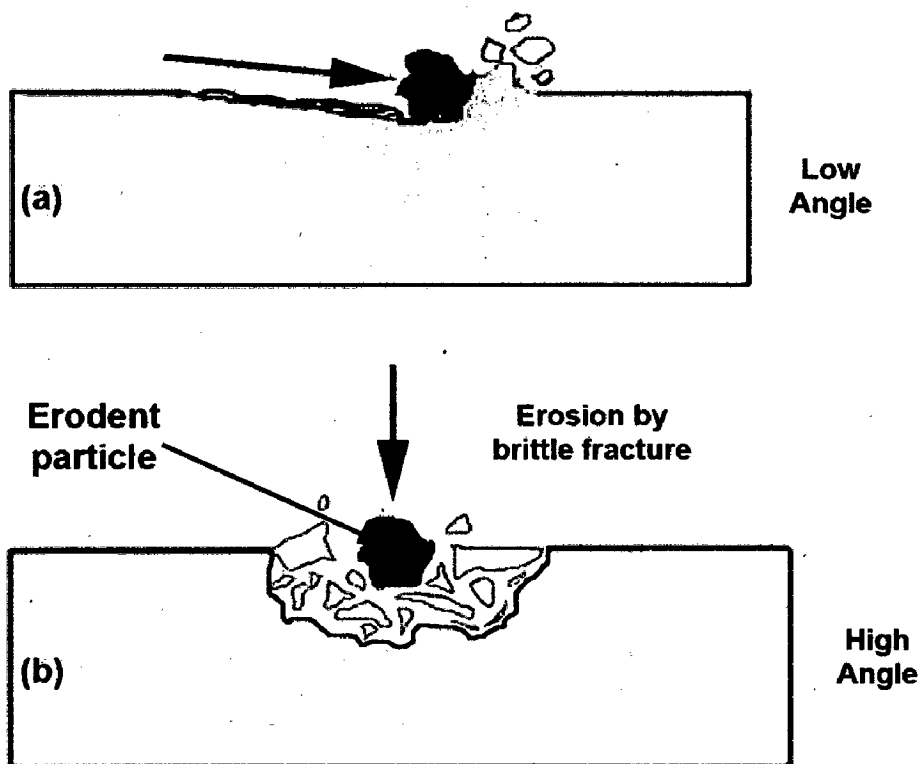


Fig. 5.30 Schematic representation of coating fracture dependent on impact angle; (a) Low angle, (b) High angle

Brittle nature of the materials allows the cracks readily to propagate to form crack networks. The subsequent impacts will easily remove the surface material via the ejection of the upper layer grains. Hence the material removal rate is high in brittle materials. Figure 5.30 shows schematically the fracture of coatings dependent on impact angle. It is shown schematically how an impinging solid particle can damage coating surfaces.

5.4.3 Conclusions

The erosion behavior of conventional thick (by plasma spraying and gas nitrided) and nanostructured thin (by physical vapor deposition process) TiAlN and AlCrN coatings on ASTM-SA213-T-11 boiler steel at an impact velocity of 35 ms^{-1} and impingement angle of 90° and 30° when substrate temperature was 400°C and surrounding air at 900°C ; has been analyzed. The following conclusions are made:

1. The erosion rates for 90° impact angle can be arranged in the following order:
Conventional TiAlN > Conventional AlCrN > Nanostructured AlCrN > Bare T-11 > Nanostructured TiAlN
2. The nanostructured and conventional TiAlN coatings have successfully protected the substrate at 90° impact.
3. At 30° impact, the volume erosion rate can be arranged in the following order:
Conventional TiAlN > Conventional AlCrN > Bare T-11 > Nanostructured AlCrN > Nanostructured TiAlN
4. The conventional thick TiAlN coating has successfully protected the substrate. The conventional AlCrN, nanostructured TiAlN and AlCrN coatings were removed by the continuous strikes of the eroding particles on the surface of the coating at 30° impact.
5. In case of conventional thick AlCrN coating; the erosion rate was more at 90° impact angle, which is the characteristic erosion behavior of brittle materials. The solid particle erosion rate of the uncoated, conventional thick TiAlN and nanostructured thin TiAlN and AlCrN coated T-11 boiler steel was maximum at 30° impact angle, which indicate ductile behavior.

5.5 CORROSION STUDIES IN SIMULATED MARINE ENVIRONMENT

The research works on the corrosion behavior of high temperature corrosion resistant coatings in marine environments is scarce in the literature. Therefore, it is meaningful to investigate the ambient environmental corrosion behavior and mechanism of the materials as is done in present work by evaluating the corrosion behavior of substrate and coatings in simulated marine environment. Therefore, the present work has been focused to compare the corrosion behavior of conventional thick (by plasma spraying and gas nitrided) and nanostructured thin (by physical vapor deposition process) TiAlN and AlCrN coatings on ASTM-SA213-T-11 boiler steel, by electrochemical methods i.e. linear polarization resistance (LPR) and potentiodynamic polarization tests in an aerated 3.0 wt% NaCl solution at room temperature; and salt spray (Fog) tests. The detailed experimental procedure is explained in chapter 3.

5.5.1 Results and Discussion

5.5.1.1 Linear polarization resistance (LPR) and potentiodynamic polarization tests

Linear polarization resistance (LPR) and potentiodynamic polarization tests were conducted in an aerated 3 wt% NaCl solution at room temperature in order to evaluate the corrosion behavior of the substrate and coatings. The initial corrosion current density and LPR (R_p) was measured by LPR test. The linear polarization scans are conducted in very small potential range (-20mV to + 20mV vs Open Circuit Potential), which does not damage the surface of the sample. Whereas the potentiodynamic polarization scans require scanning over a longer potential range (Sahoo and Balasubramaniam, 2007).

The corrosion parameters obtained in LPR test are shown in Table 5.7. The corrosion current density in case of nanostructured thin coatings was found much lower than that of the substrate. The conventional thick coatings have shown higher corrosion current density as compared to the substrate and nanostructured coatings, which may be due to the open pores and voids in the coating. The conventional thick AlCrN coating has shown maximum current density i.e. $51.89 \mu\text{A}/\text{cm}^2$. The nanostructured thin TiAlN coating has performed very well and showed best corrosion resistance on the basis of

corrosion current density and polarization resistance. The corrosion protection is provided by the nanostructured thin coatings at initial stage as indicated by the LPR test results in terms of corrosion current density and polarization resistance (Table.5.7).

Potentiodynamic polarization curves of the substrate and each film are shown in Fig.5.31 and the corrosion parameters in Table 5.8. The corrosion current density and the corrosion potential were obtained by the intersection of the extrapolation of anodic and cathodic Tafel curves. The corrosion current densities of the coatings were found much lower than that of the substrate steel. The corrosion current densities of the substrate and the coatings were found much lower as compared to the LPR test (at initial stage) results also. A protective oxide layer may have formed which has blocked further corrosion. The corrosion product formed may have reduced the passage of the electrolyte to attack the samples, and hence providing protection.

Table 5.7 Results of Linear Polarization Resistance Test (LPR) of uncoated and coated ASTM-SA213-T-11 boiler steel

Substrate / Coating	E_{corr} (mV)	i_{corr} ($\mu\text{A}/\text{cm}^2$)	β_a (V/decade)	β_c (V/decade)	R_p ($\text{k}\Omega\text{-cm}^2$)
Uncoated T-11 boiler steel	-601.1	12.54	0.1	0.1	01.73
Nanostructured TiAlN coating	-536.6	03.99	0.1	0.1	05.43
Nanostructured AlCrN coating	-540.1	08.99	0.1	0.1	02.44
Conventional TiAlN coating	-740.1	43.63	0.1	0.1	00.49
Conventional AlCrN coating	-740.1	51.89	0.1	0.1	00.41

The corrosion rate (i_{corr}) of the specimens was obtained using the Stern-Geary equation (Eq.5.2).

$$i_{corr} = \frac{1}{2.303} \times \frac{\beta_a \beta_c}{R_p \times (\beta_a + \beta_c)} = \frac{Z}{R_p} \quad (5.2)$$

Where β_a = anodic Tafel slope, β_c = cathodic Tafel slope, R_p = polarization resistance and, Z is a function of the Tafel slopes.

In potentiodynamic polarization tests the conventional thick TiAlN coating has indicated best corrosion resistance as evident from corrosion current density and polarization resistance values reported in Table.5.8. The nanostructured thin TiAlN and AlCrN coatings have shown performance comparable to conventional thick TiAlN coating in terms of corrosion current density and polarization resistance. The measured corrosion current density for uncoated ASTM-SA213-T-11 boiler steel , nanostructured thin TiAlN, nanostructured thin AlCrN, conventional thick TiAlN and conventional thick AlCrN coatings is 8.085, 1.268, 0.315, 0.059 and 6.641 $\mu\text{A}/\text{cm}^2$ respectively.

Thus all the coatings have shown protection to the bare T-11 boiler steel in 3 wt. % NaCl solution.

From polarization test results, the protective efficiency, P_i (%) of the coatings can be calculated by Eq. (5.3):

$$P_i (\%) = \left[1 - \left(\frac{i_{corr}}{i_{corr}^0} \right) \right] \times 100 \quad (5.3)$$

Where i_{corr} and i_{corr}^0 indicate the corrosion current density of the film and substrate, respectively [Yoo et al., 2008].

Table 5.8 Results of Potentiodynamic Polarization Tests of uncoated and coated ASTM-SA213-T-11 boiler steel

Substrate / Coating	E_{corr} (mV)	i_{corr} ($\mu\text{A}/\text{cm}^2$)	β_a (V/decade)	β_c (V/decade)	R_p ($\text{k}\Omega\text{-cm}^2$)	P_i (%)	F (%)
Uncoated T-11 boiler steel	-567.6	08.085	0.0689	0.2771	23.95	--	--
Nanostructured TiAlN	-441.0	01.268	0.1220	0.2140	33.73	84.31	01.05
Nanostructured AlCrN	-410.3	00.315	0.2150	0.2390	64.77	96.10	00.19
Conventional TiAlN	-882.1	00.059	0.0506	0.0520	187.78	99.20	0.0003
Conventional AlCrN	-894.9	06.641	0.1232	0.0660	02.80	17.86	0.0153

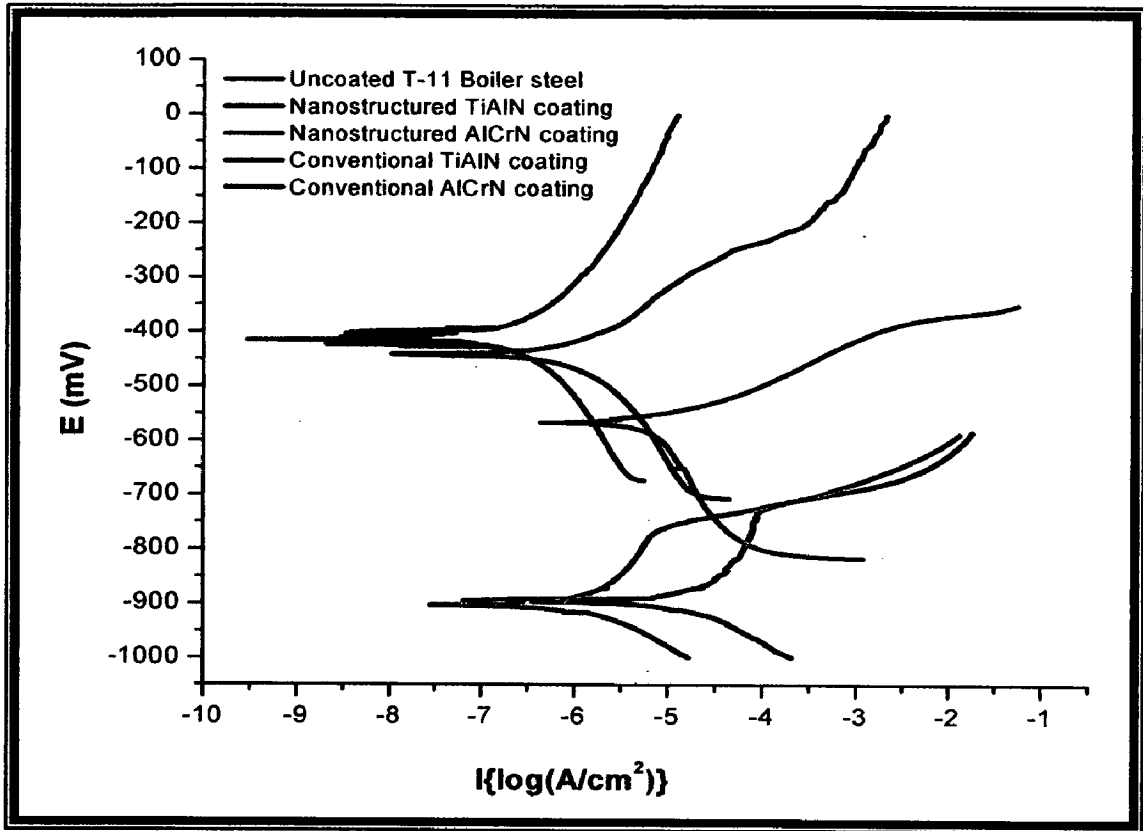


Fig. 5.31 Potentiodynamic Polarization Curves for uncoated and coated ASTM-SA213-T-11 boiler steel

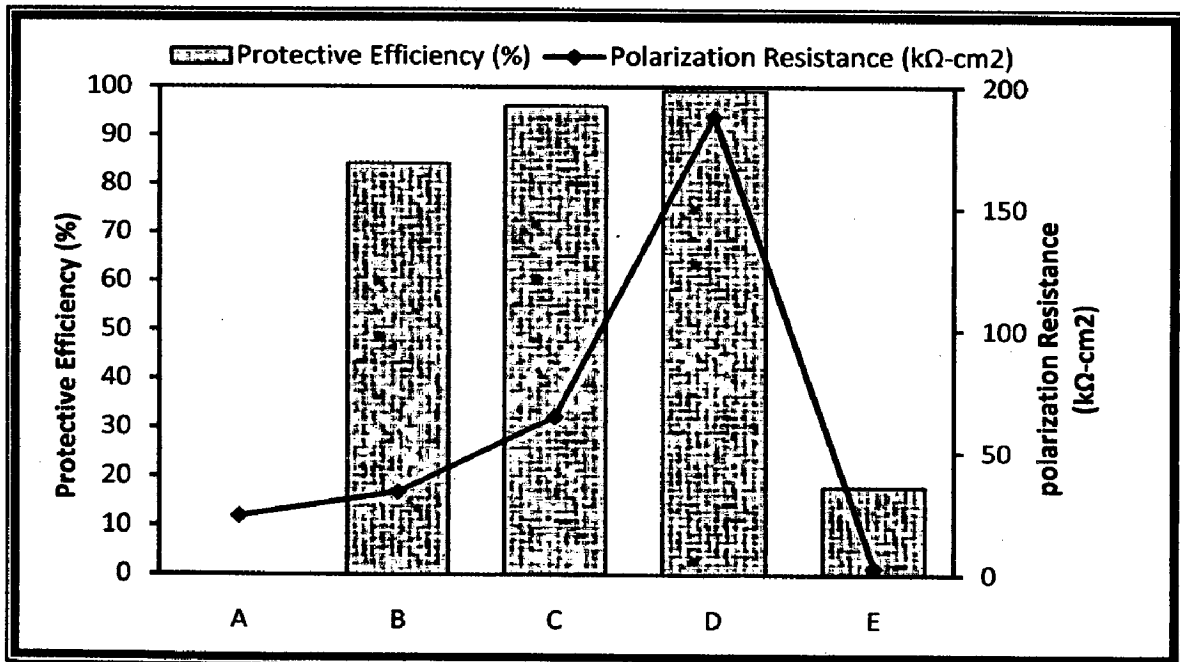


Fig. 5.32 Protective efficiency and Polarization resistance of uncoated and coated ASTM-SA213T-11 boiler steel: (A) Uncoated T-11 boiler steel, (B) Nanostructured TiAlN coating, (C) Nanostructured AlCrN coating, (D) Conventional TiAlN coating, (E) Conventional AlCrN coating

Figure 5.32 shows the variation in protective efficiency and polarization resistance of uncoated and coated T-11 boiler steel subjected potentiodynamic polarization test. The conventional thick TiAlN coating showed the highest protective efficiency of 99.20 % caused by lowest corrosion current density of $0.059 \mu\text{A}/\text{cm}^2$. The nanostructured thin TiAlN and AlCrN coatings have shown protective efficiency 84.31% and 96.10% respectively. The observed protection by the nanostructured TiAlN and AlCrN coatings in an aerated 3 wt.% NaCl solution at room temperature, are almost in agreement with the findings of Yoo et al. (2008) and Xing-zhao et al. (2008). The conventional thick AlCrN coatings have also shown protection to the substrate but with protective efficiency 17.86 %.

For further justification the porosity values has also been measured quantitatively by the electrochemical methods (Yoo et al., 2008) according to Eq. (5.4) and reported in Table.5.8.

$$F (\%) = \left[\frac{R_{pm}}{R_p} \times 10^{-|\Delta E_{\text{corr}}/\beta_a|} \right] \times 100 \quad (5.4)$$

Where ΔE_{corr} the corrosion potential difference between the substrate and coating layer, R_p the polarization resistance of the coating-substrate system, β_a the anodic Tafel constant of substrate, R_{pm} is the polarization resistance of the substrate and F represent porosity. The porosity measurement of the coatings is presented in Table 5.8. The conventional thick TiAlN film has shown minimum porosity of 0.0003% and nanostructured thin TiAlN has shown maximum 1.05% porosity value. The porosity measurement by electrochemical test analysis and with image analyser, having software Dewinter Materials Plus 1.01 based on ASTM B276, are having different results. The difference in the measured porosity by these two methods in case of nanostructured TiAlN and conventional AlCrN coatings may be because that image analysis (IA) measures both open as well as closed porosity and cannot distinguish between the two, whereas electrochemical test is able to assess pore connectivity in a coating that exists due to the interlamellar pores and intralamellar cracks (Deshpande et al., 2004). The porosity also affects the corrosion current density, as more is the connected porosity the higher is the corrosion current.

5.5.1.2 Salt spray (Fog) testing

The ASTM B117 Salt Fog test was used to evaluate the performance of the uncoated and nanostructured thin TiAlN and AlCrN coated ASTM-SA213-T-11 boiler steel. The salt fog test is an accelerated corrosion test by which samples exposed to the same conditions can be compared. In the B117 test, the samples are exposed to a salt fog generated from a 5% sodium chloride solution with a pH between 6.5 and 7.2. All the samples were placed in the salt fog chamber for 24 Hrs, 48 Hrs and 72 Hrs.

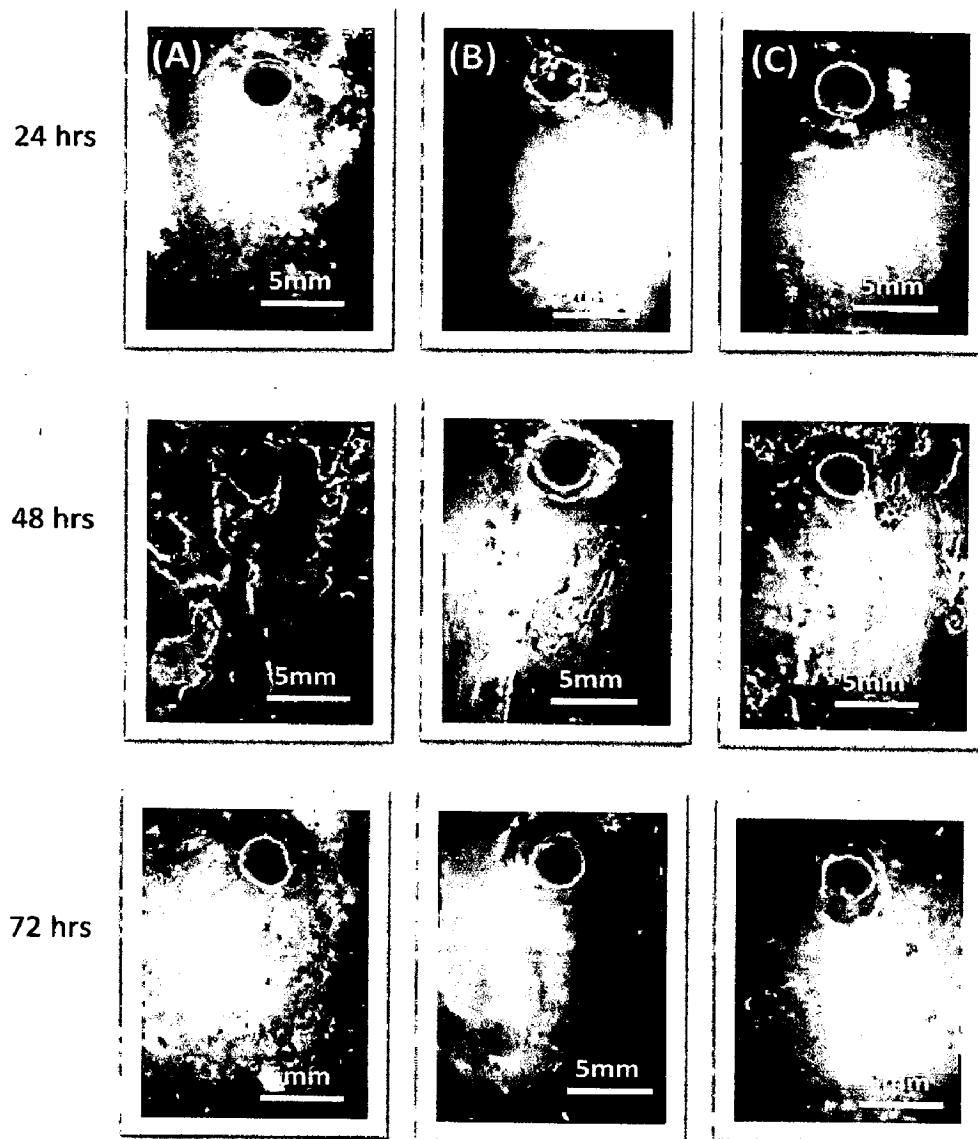


Fig. 5.33 Surface macrographs of uncoated and coated ASTM-SA213-T-11 boiler steel subjected to salt-fog testing (5% NaCl) : (A) Uncoated T-11 boiler steel subjected to 24hrs, 48hrs and 72 hrs testing; (B) Nanostructured TiAlN coating subjected to 24hrs, 48hrs and 72 hrs testing; (C) Nanostructured AlCrN coating subjected to 24hrs, 48hrs and 72 hrs testing

Photographs were taken before and subsequent to exposure to document the surface conditions. Initial weight and dimensions were measured. After exposure; samples were monitored and analyzed by using XRD and SEM/EDAX techniques. The macro morphologies of the uncoated and nanostructured thin TiAlN and AlCrN coated T-11 boiler steel exposed to salt fog test for 24 Hrs, 48 Hrs and 72 Hrs; are depicted in Fig.5.33. The uncoated T-11 boiler steel suffered severe corrosion in all three test conditions i.e. 24 Hrs, 48 Hrs and 72 Hrs (Fig.5.33.A). The brownish colored corrosion product on the surface of the samples and corrosion pits are visible. The nanostructured coated samples have shown resistance to the corrosion as compared to the uncoated T-11 boiler steel. The nanostructured TiAlN coatings have shown negligible corrosion products in case of 24 Hrs study, but for 48 Hrs and 72 Hrs studies, these have also shown the formation of some corrosion products (Fig.5.33.B). In case of nanostructured AlCrN coating, the surface of the samples was no longer uniform as before the test in case of salt fog testing for 48 Hrs and 72 Hrs (Fig.5.33.C). Some corrosion products can also be seen in case of the sample exposed to the salt mist corrosion for 24 Hrs.

Figure 5.34 shows the surface SEM images of uncoated and nanostructured TiAlN and AlCrN coated T-11 boiler exposed to salt fog test for 24 Hrs. As can be seen in Fig.5.34 (a), massive corrosion products were accumulated on the surface of uncoated boiler steel. The EDAX analysis at some locations indicates the presence of iron and oxygen on the corroded surface (Point 1 and 2 on Fig.5.34). In case of nanostructured TiAlN coating; very less corrosion products are visible (Fig.5.34.b). The EDAX analysis (Point 3 and 4 on Fig.5.34) revealed the presence of Ti and Al as the main elements with small amount of Fe, N, Mo and O. Fig.5.34 (c) shows the SEM image of the nanostructured AlCrN coating.

The surface is rich in Al, Cr along with N and negligible amount of Fe and O; as revealed by EDAX analysis (Point 5 and 6 on Fig.5.34). Figure 5.35 shows the surface SEM images of uncoated and nanostructured TiAlN and AlCrN coated T-11 boiler steel exposed to salt fog test for 48 Hrs. The uncoated T-11 boiler steel has shown severe corrosion as shown in Fig.5.35 (a). Corrosion cracks and corrosion products can be seen on the surface. The EDAX analysis shows the presence of Fe and O as the main elements along with some Mo, Cl and Na.

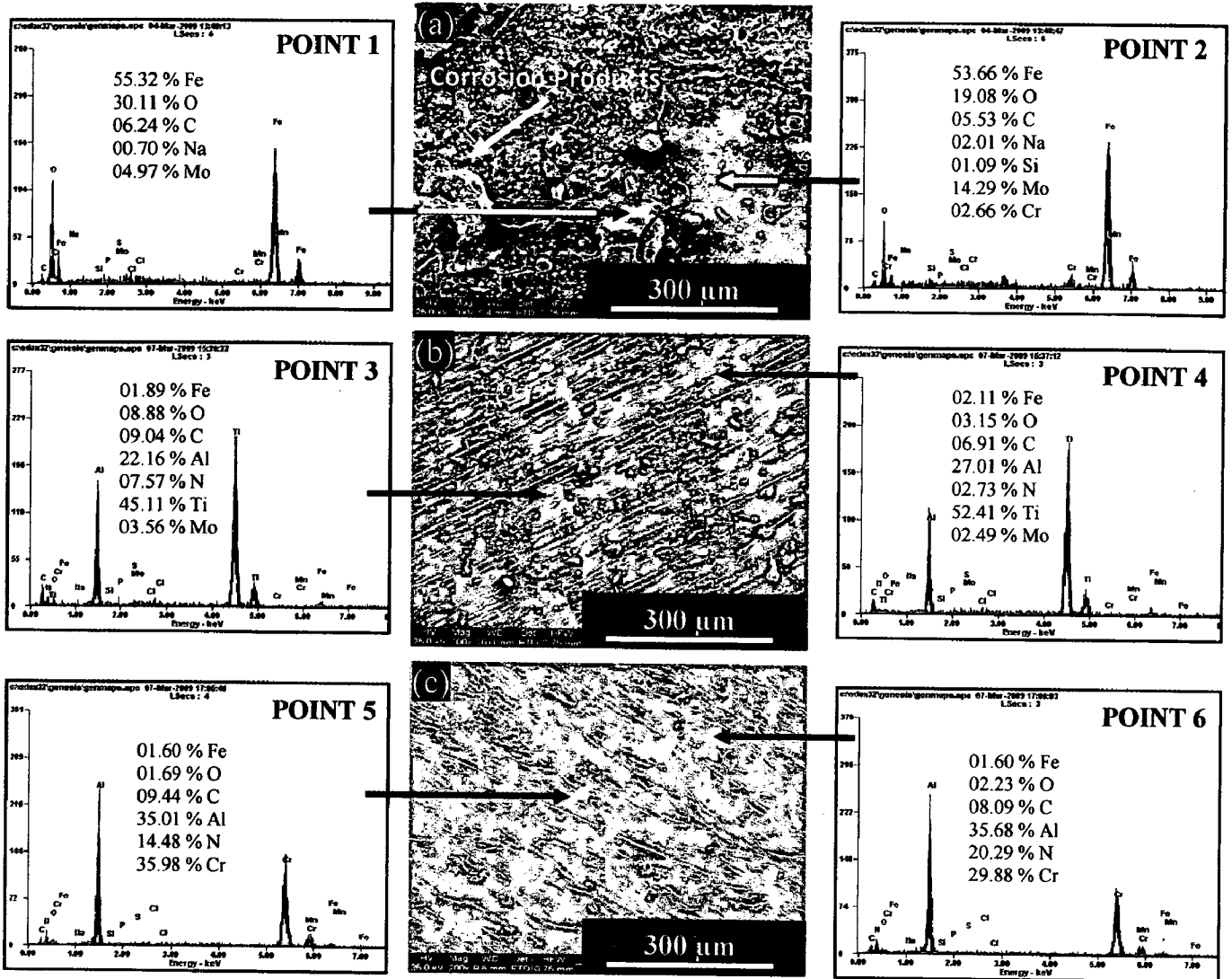


Fig. 5.34 Surface macrographs of uncoated and coated ASTM-SA213-T-11 boiler steel subjected to salt-fog testing (5% NaCl) for 24 hrs: (a) Uncoated ASTM-SA213-T-11 boiler steel (b) Nanostructured TiAlN coating (c) Nanostructured AlCrN coating

As can be seen in Fig.5.35 (b & c), corrosion cracks were observed on the surface of as-deposited nanostructured TiAlN and AlCrN coatings after salt spray tests. Massive corrosion products were accumulated around the corrosion crevice. Obviously, severer corrosion would proceed in the as-deposited nanostructured thin coatings through the cracks, and cause coating cracking and fracture damage in the subsequent service at elevated temperatures. EDAX analysis (Point 3 and 4) in case of nanostructured TiAlN coating indicates the products were composed of Fe and O.

XRD diffractograms for coated and uncoated T-11 boiler steel subjected to salt fog tests for 24 Hrs, 48 Hrs and 72 Hr; are depicted in Fig.5.37 on reduced scale. As indicated by the diffractograms; Fe_3O_4 and with some minor peaks of Cr_2O_3 are the main phases present in the oxide scale of uncoated T-11 boiler steel. In nanostructured TiAlN coating, AlN, TiN and Fe_3O_4 are the main phases revealed with minor phases i.e. TiO_2 and Al_2O_3 .

Further, the main phases identified for the nanostructured AlCrN coating are CrN, AlN along with Al_2O_3 , Cr_2O_3 and Fe_3O_4 . The formation of Fe_3O_4 in the scale of corroded specimens in salt spray tests is found to be in agreement with those reported by Panda, Bijayani et al. (2008) and Vera et al. (2009).

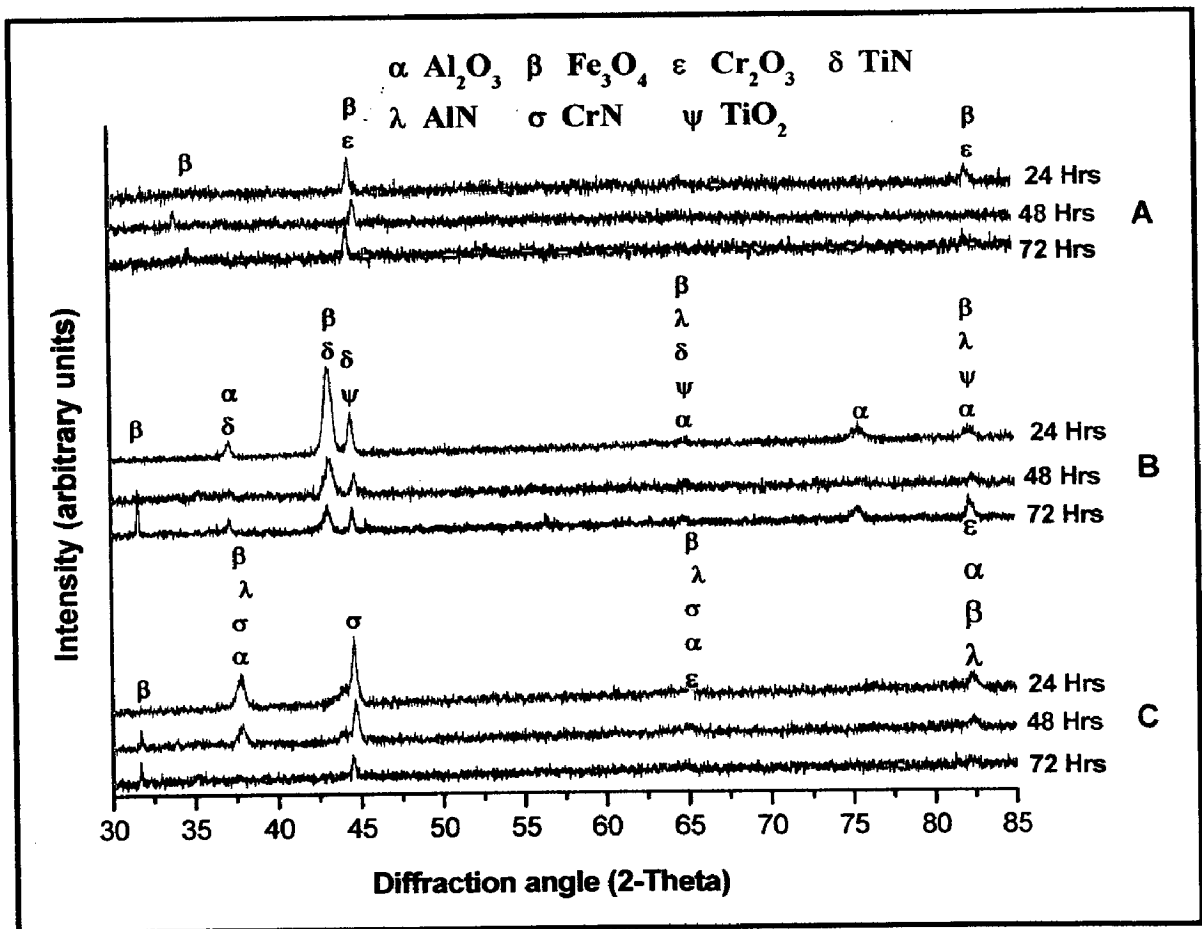


Fig. 5.37 X-Ray Diffraction pattern of uncoated and coated ASTM-SA213-T-11 boiler steel subjected to salt-fog testing (5% NaCl) for 24 Hrs, 48 Hrs and 72 Hrs: (A) Uncoated T-11 boiler steel, (B) Nanostructured TiAlN coating, (C) Nanostructured AlCrN coating

The weight loss measurements were carried out for the uncoated and nanostructured thin TiAlN and AlCrN coated T-11 boiler steel exposed to the salt fog tests for 24 Hrs, 48 Hrs and 72 Hrs. Fig. 5.38, depicts the column chart showing the weight loss per unit area for the uncoated and coated T-11 boiler steel. It can be inferred from the plots that the uncoated T-11 boiler steel has shown maximum weight loss per unit area in all three test conditions i.e. 24 Hrs, 48 Hrs and 72 Hrs tests; as compared to the coated counterparts. Both the coatings have shown good protection to the substrate in terms of weight loss per unit area. As can be seen in Fig.5.38 for uncoated and coated T-11 boiler steel; the weight loss per unit area increases with the duration of the test. The weight loss per unit area in case of nanostructured thin TiAlN coating is less than as compared to the nanostructured AlCrN coating and uncoated boiler steel in all test conditions. It can be mentioned based on the present investigation that nanostructured thin TiAlN and AlCrN coatings can provide a very good corrosion resistance when exposed to the simulated marine environment i.e. salt fog test.

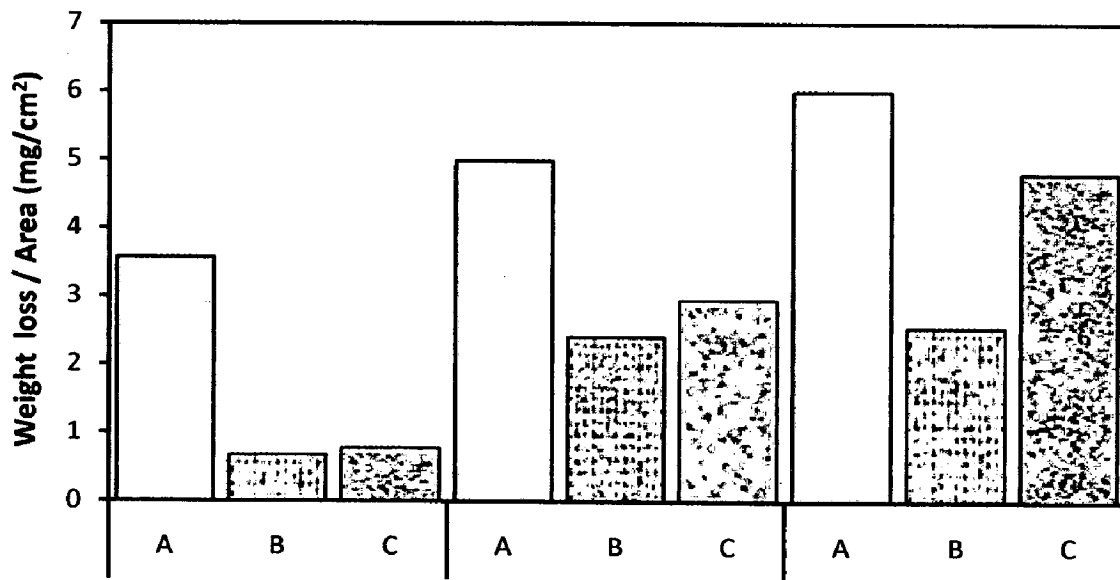


Fig. 5.38 Column chart showing weight loss per unit area for the uncoated and coated ASTM-SA213-T-11 boiler steel subjected to salt-fog testing (5% NaCl): (A) Uncoated T-11 boiler steel subjected to 24hrs, 48hrs and 72 hrs testing; (B) Nanostructured TiAlN coated T-11 boiler steel subjected to 24hrs, 48hrs and 72 hrs testing; (C) Nanostructured AlCrN coated T-11 boiler steel subjected to 24hrs, 48hrs and 72 hrs testing

Salt spray corrosion is an electrochemical reaction process (Bao et al., 2007). Generally, the corrosion resistance is influenced significantly by several factors, such as compositions, internal microstructure, and especially the surface condition. The proposed corrosion mechanism of the coated specimen is as explained in Fig.5.39; which is similar to the one reported by Bao et al., (2007). Micro-cracks got initiated by residual stress during deposition of coatings. The micro-cracks would be corroded easily and the solution would infiltrate into loose corrosion products and reach crack tip to sustain the internal corrosion, followed by crack propagation (Fig. 5.39 b and c). This process obeys the rules of crevice corrosion. Acidity in the cracks increased significantly as neutralization was not easily obtained by exchanging solution between inside and outside the cracks. An ascending acidity accelerates the corrosion attack and results in an unfavorable inner structure. When the acid solution flows across pores, corrosion will take place and enlarge a pore to a corrosion hole.

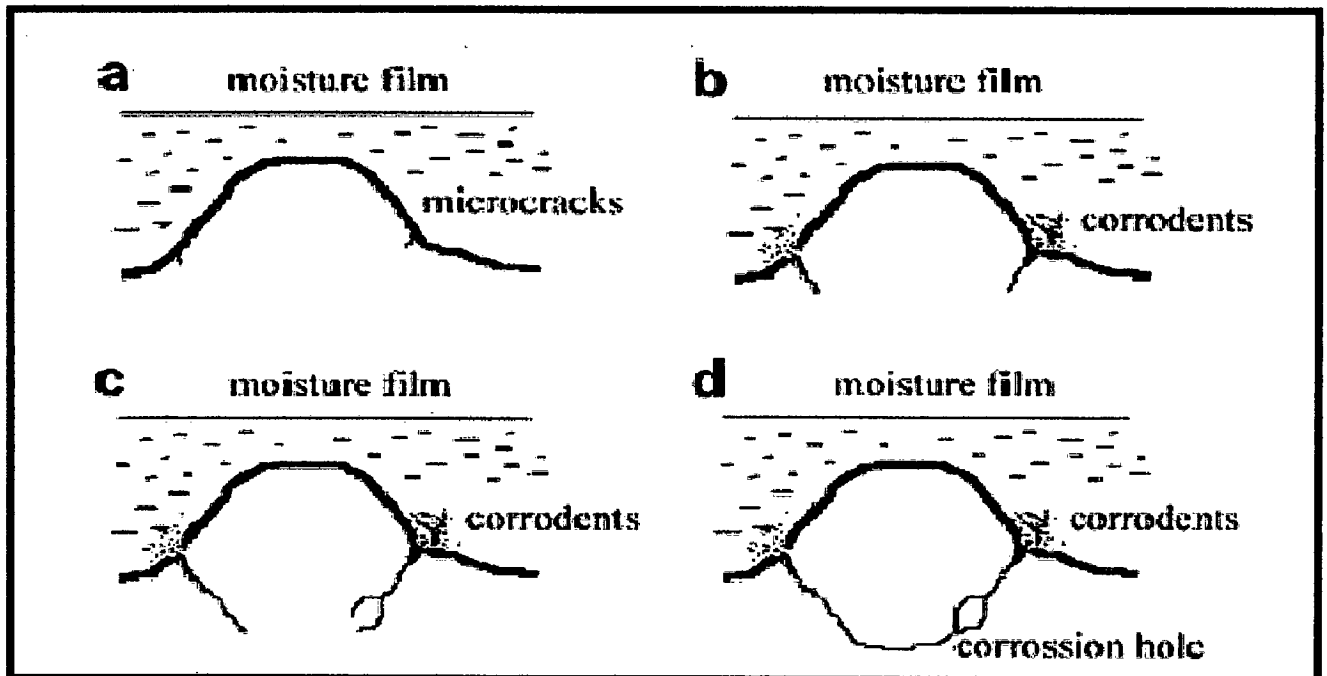


Fig. 5.39 Corrosion evolution of the as-deposited coatings in salt spray test; a: initiation of corrosion micro-crack, b: cracks propagation, c: crack branching, d: formation of corrosion hole (Bao et al., 2007)

5.5.2 Conclusions

The corrosion behavior of uncoated and coated ASTM-SA213-T-11 boiler steel have been investigated by electrochemical methods i.e. linear polarization resistance (LPR) and potentiodynamic polarization tests in an aerated 3.0 wt% NaCl solution at room temperature; and salt spray (Fog) tests. The behavior of nanostructured TiAlN and AlCrN coatings were compared with their conventional counterparts and the following conclusions are made:

1. In Linear polarization resistance (LPR) test, the corrosion current densities of nanostructured thin coatings were found much lower than that of the substrate, whereas the conventional thick coatings have shown higher current densities. The corrosion resistance of the coatings and substrate followed the sequence:
Nanostructured TiAlN > Nanostructured AlCrN > Bare T-11 > Conventional TiAlN > Conventional AlCrN
2. The corrosion protection is provided by the nanostructured thin coatings at initial stage as indicated by the LPR test results in terms of corrosion current density and polarization resistance. The conventional thick AlCrN coating has shown maximum corrosion current density.
3. In Potentiodynamic Polarization test, the corrosion current densities of the coatings were found much lower than that of the substrate steel. All the coatings have shown protection to the substrate T-11 boiler steel in 3 wt. % NaCl solution.
4. The corrosion current densities of the substrate and the coatings in Potentiodynamic Polarization test were found much lower as compared to the LPR test (at initial stage) results. The corrosion resistance of the coatings and substrate followed the sequence:
Conventional TiAlN > Nanostructured AlCrN > Nanostructured TiAlN > Conventional AlCrN > Bare T-11
5. The measured protective efficiency for nanostructured thin TiAlN, nanostructured thin AlCrN, conventional thick TiAlN and conventional thick AlCrN coatings is 84.31%, 96.10%, 99.20% and 17.86% respectively.

6. The porosity values has also been measured quantitatively by the electrochemical methods for nanostructured thin TiAlN, nanostructured thin AlCrN, conventional thick TiAlN and conventional thick AlCrN coatings, which are 1.05%, 0.19%, 0.0003% and 0.0159% respectively.
7. In salt spray tests; the uncoated T-11 boiler steel suffered severe corrosion in all three test conditions i.e. 24 Hrs, 48 Hrs and 72 Hrs. The nanostructured coated samples have shown resistance to the corrosion as compared to the uncoated T-11 boiler steel.
8. It can be inferred from the weight loss per unit area plots that the uncoated T-11 boiler steel has shown maximum weight loss per unit area in all three test conditions i.e. 24 Hrs, 48 Hrs and 72 Hrs tests; as compared to the coated counterparts.
9. The weight loss per unit area in case of nanostructured thin TiAlN coating is less than as compared to the nanostructured AlCrN coating and uncoated boiler steel in all test conditions.
10. It can be mentioned based on the present investigation that nanostructured thin TiAlN and AlCrN coatings can provide resistance to corrosion when exposed to the simulated marine environment i.e. salt fog test.

5.6 EROSION-CORROSION STUDIES IN INDUSTRIAL ENVIRONMENT

After conducting the various experiments on uncoated and coated ASTM-SA213-T-11 boiler steel in lab; the present research work has been focused to investigate and compare the high temperature corrosion and erosion behavior of conventional thick (by plasma spraying and gas nitrided) and nanostructured thin (by physical vapor deposition process) TiAlN and AlCrN coatings on T-11 boiler steel, in actual industrial environment of coal fired boiler. The uncoated and coated specimens were exposed to low temperature super-heater zone of the coal fired boiler of Guru Nanak Dev Thermal Power Plant, Bathinda, Punjab, India. The specimens were hanged in the platen super-heater of coal fired boiler where the gas temperature was around $900^{\circ}\text{C} \pm 10^{\circ}\text{C}$. Hot corrosion experiments were performed for 10 cycles, each cycle consisting of 100 hours exposure followed by 1 hour cooling at ambient temperature. The detailed experimental procedure is explained in chapter 3.

5.6.1 Results

5.6.1.1 Visual observations

The macrographs for uncoated and coated ASTM-SA213-T-11 boiler steel exposed to super-heater of the coal fired boiler environment at 900°C for 1000 hours are shown in Fig.5.40. For the uncoated T-11 boiler steel, a dark black grey colored scale appeared on the surface right from the 1st cycle. Ash deposition has started just after the 1st cycle and the sample showed spalling and gets welded used to hang these samples in the boiler environment. After every cycle; the samples were washed with acetone in order to remove ash deposited before weight measurement. Erosion was also observed after 2nd cycle on one of the edges. Ash deposition, erosion and severe spalling in case of bare T-11 boiler steel continued to last cycle. At the end of cyclic study, ash deposited with fragile scale indicating severe spalling and dark grey colored surface appearance in the middle with brownish colored scale along the sides was observed which can be seen in Fig.5.40 (a).

In case of nanostructured thin TiAlN coated T-11 boiler steel, color of the oxide scale at the end of the study was observed to be blackish grey with some brownish

colored areas from where the top scale gets spalled, as shown in Fig.5.40 (b). Ash deposition has started just after the 1st cycle and the sample showed golden shine after 2st cycle and no sign of spalling was observed till 3rd cycle.

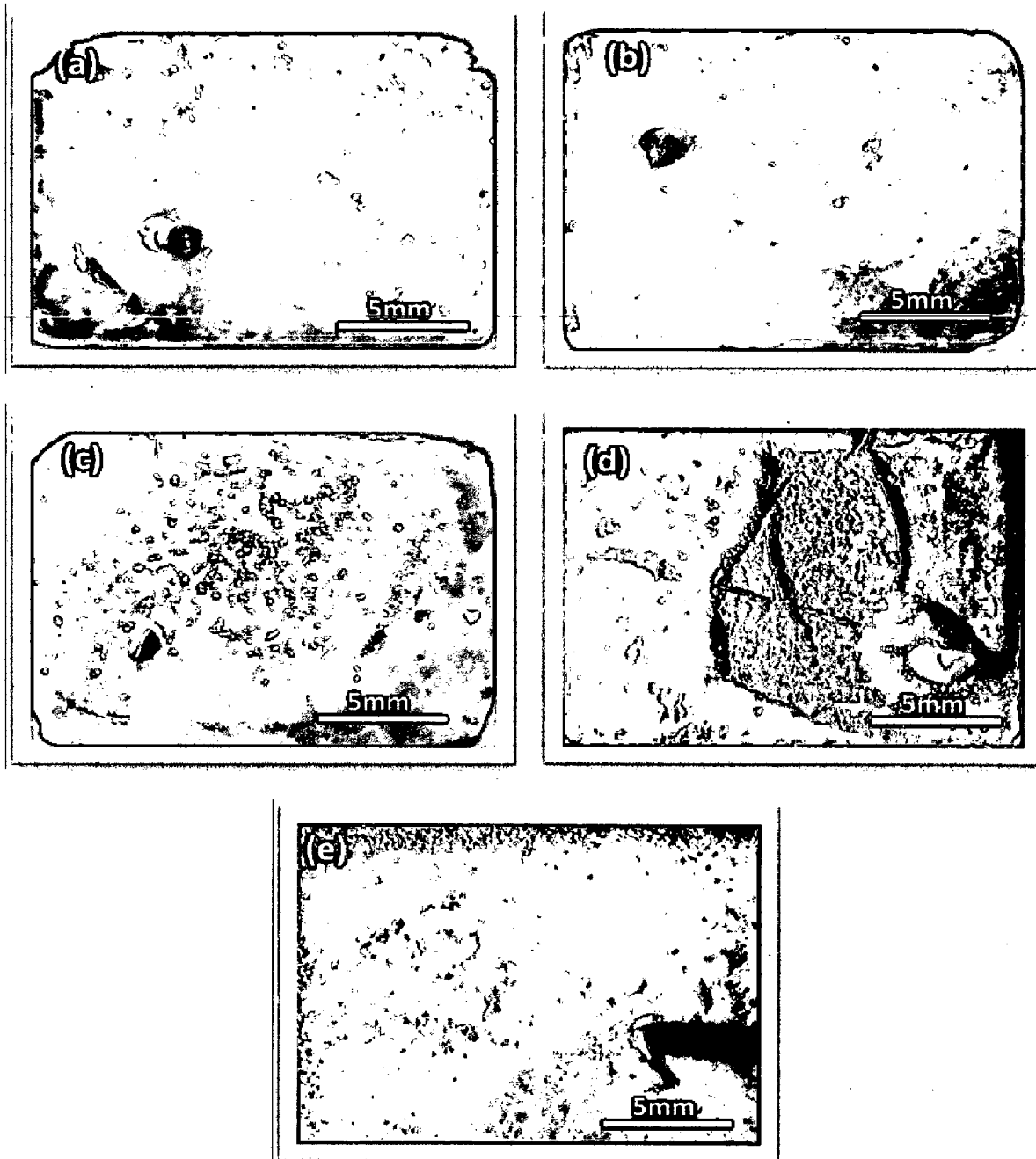


Fig. 5.40 Surface macrographs of uncoated and coated ASTM-SA213-T-11 boiler steel exposed to super-heater of the coal fired boiler environment at 900°C for 1000 hours: (a) Uncoated T-11 boiler steel, (b) Nanostructured TiAlN coating, (c) Nanostructured AlCrN coating, (d) Conventional TiAlN coating, (e) Conventional AlCrN coating

After 3rd cycle spalling of the specimen was observed and it gets welded with the wire with which it was hanged in the boiler environment. Ash deposition, erosion and spalling continued up to last cycle. The nanostructured thin AlCrN coated T-11 boiler steel has shown the formation of dark blackish grey colored scale with severe spalling and visible hairline cracks over the whole area, as shown in Fig.5.40 (c). After 1st cycle, dark black colored scale was seen on the surface with ash deposition and no sign of spalling and thermal expansion of the material. The scale shows spalling after 3rd cycle and the sample gets welded to the wire. During 6th cycle; some scale at two corners gets broken and fallen in the boiler. The ash deposition, erosion and spalling continue till the end.

A visual observation of conventional thick TiAlN coated T-11 boiler steel (Fig.5.40.d), showed the formation of blackish grey colored scale on half portion and whitish grey colored scale on the remaining area; at the end of the cyclic study. The scale was rough and adherent to the substrate. The sample gets welded to the wire after 3rd cycle and fine cracks were seen on the surface. After 4th cycle a thin chip of the scale gets removed from the middle surface and fallen in the boiler. In case of conventional thick AlCrN coated T-11 boiler steel, color of the ash deposited oxide scale was dark grey with some whitish areas at the end of the study (Fig.5.40.e). The scale was found to be adherent. No spalling was observed till 5th cycle after which the sample gets welded to the wire and showed spalling and signs of erosion.

5.6.1.2 Weight change and sample thickness measurements

Weight gain per unit area (mg/cm^2) versus time expressed in number of cycles plot for coated and bare T-11 boiler steel exposed to super-heater of the coal fired boiler environment at 900°C for 1000 hours; is presented in Fig.5.41. However weight change data could not be of much use for predicting the corrosion behavior because of suspected spalling and ash deposition on the specimens. Although the specimens were washed with acetone after every cycle before weight measurement in order to remove ash deposited yet it was difficult to remove the ash completely. Hence extent of corrosion could only be monitored by measuring the thickness of the un-reacted sample after the total exposure of 1000 hrs i.e. measuring scale thickness in cross-sectional view.

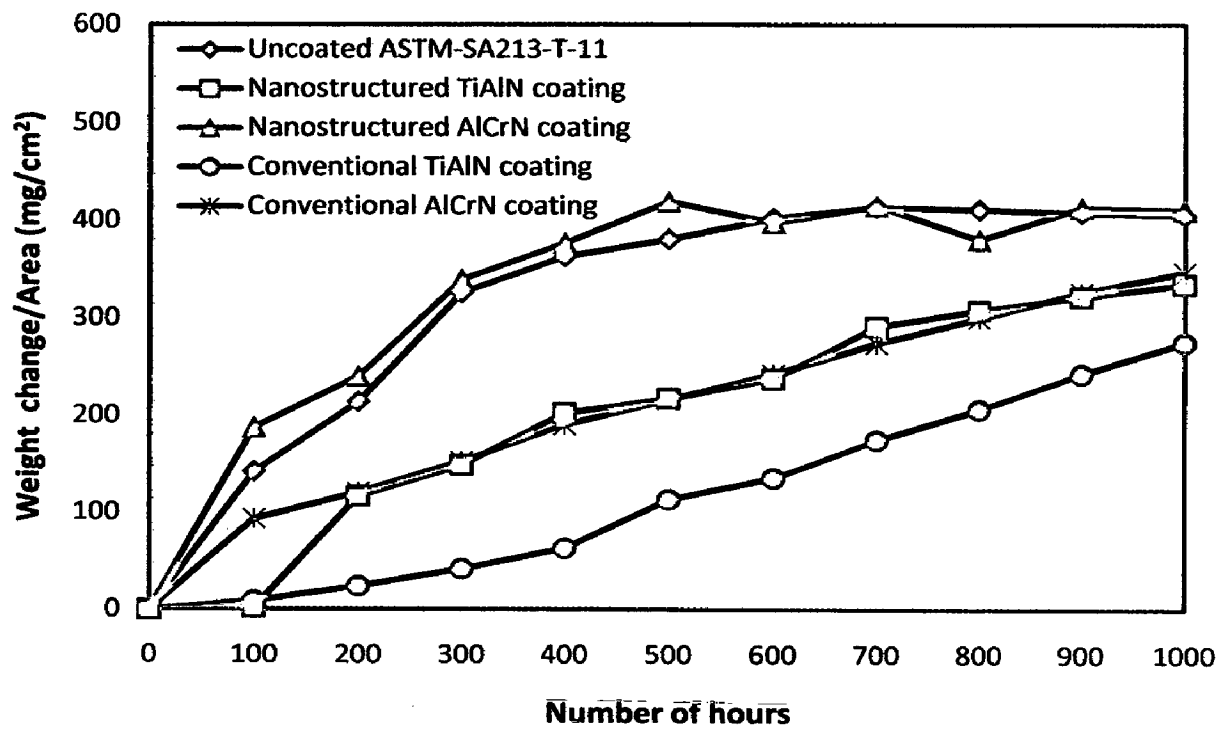


Fig. 5.41 Weight gain/area vs time for uncoated and coated ASTM-SA213-T-11 boiler steel exposed to super-heater of the coal fired boiler environment at 900°C for 1000 hours

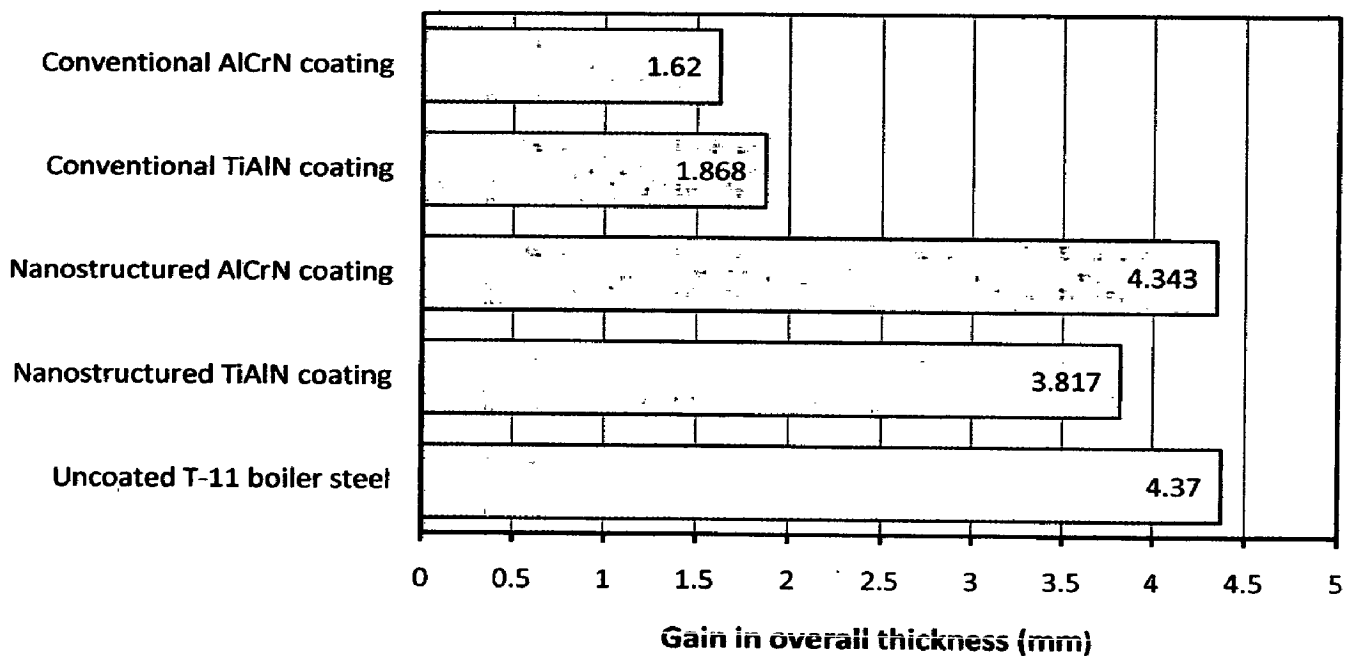


Fig. 5.42 Bar chart indicating overall gain in thickness for uncoated and coated ASTM-SA213-T-11 boiler steel specimens exposed to super-heater of the coal fired boiler environment at 900°C for 1000 hours

It can be inferred from the plots (Fig.5.41) that the uncoated and nanostructured thin AlCrN coated T-11 boiler steels have shown high weight gain as compared to the conventional thick and nanostructured TiAlN coatings. The conventional TiAlN coating has shown minimum erosion-corrosion rate and weight gain. The weight gain in case of nanostructured TiAlN and conventional AlCrN coatings is higher than that of conventional TiAlN coating and less than that of uncoated and nanostructured AlCrN coated T-11 boiler steel (Fig.5.41).

Bar chart in Fig.5.42 indicates the overall gain/loss in the thickness (in mm) of the specimen. Bar chart (Fig.5.42) indicates the overall gain/loss in the thickness (in mm) of the specimen. All the coatings and bare T-11 boiler steel have shown increase in overall thickness after erosion-corrosion for 1000 hrs. The thickness of the specimens was measured before and after the erosion-corrosion test and average of ten values has been used to calculate the thickness gain/loss. The measured average gain in overall specimen thickness values for uncoated T-11, nanostructured thin TiAlN, nanostructured thin AlCrN, conventional thick TiAlN and conventional thick AlCrN coatings are 4.370, 3.8170, 4.343, 1.868 and 1.620 mm respectively.

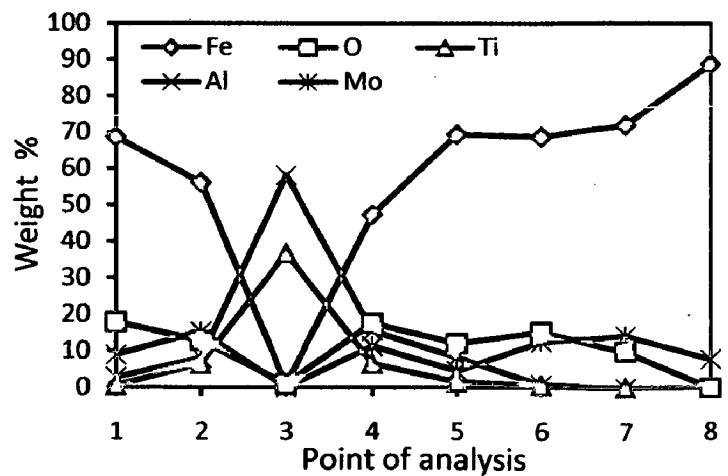
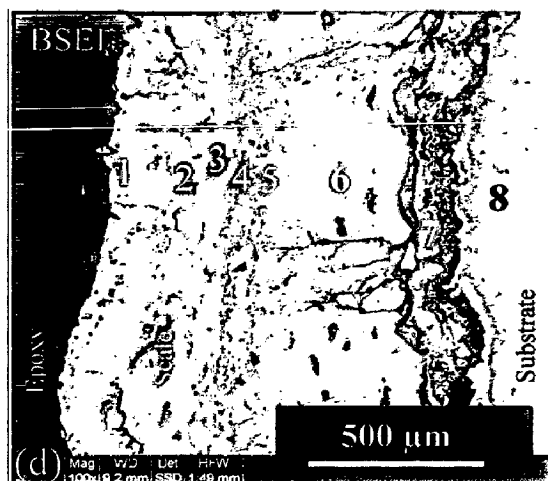
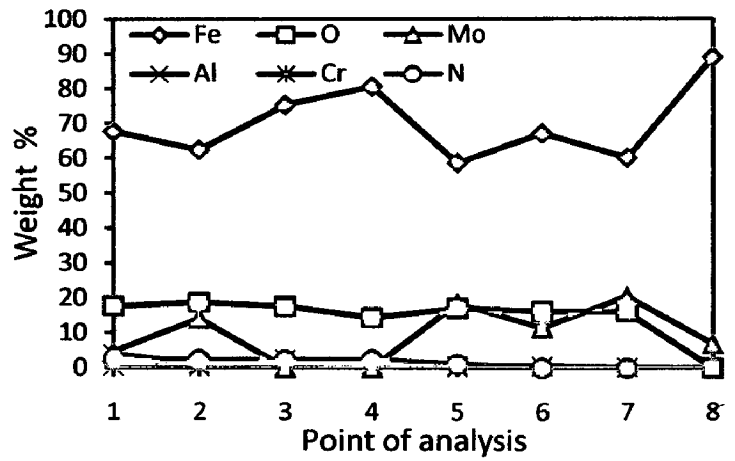
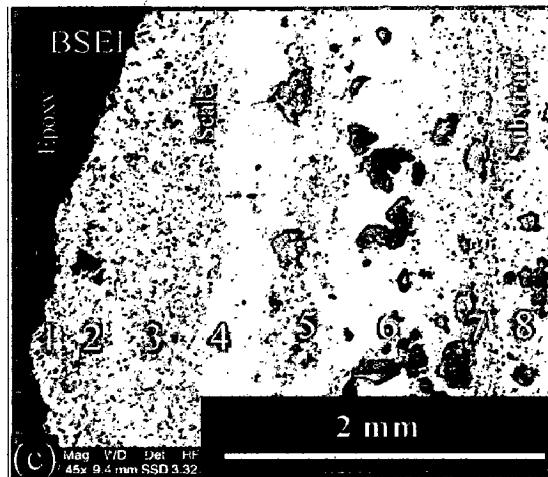
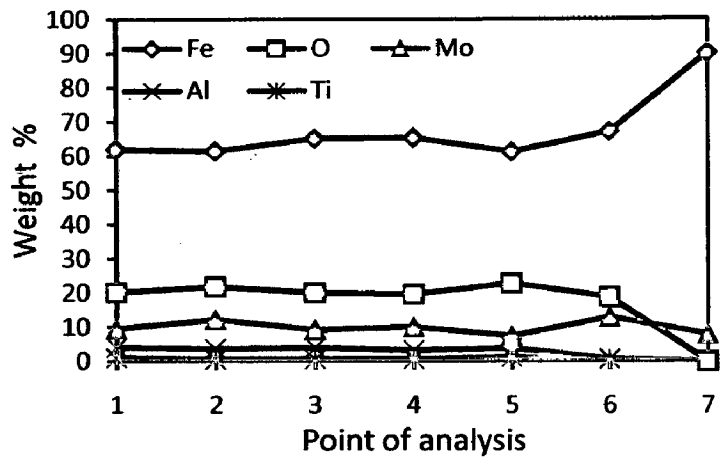
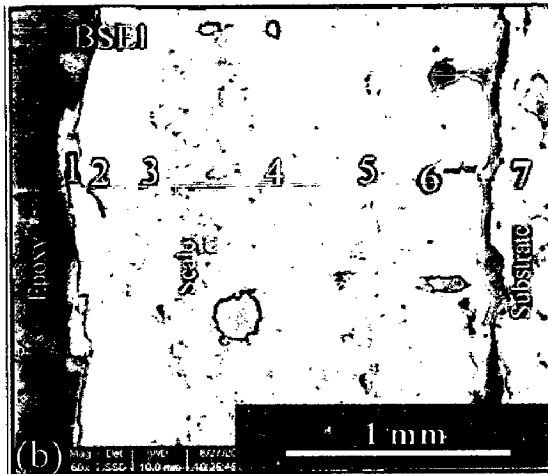
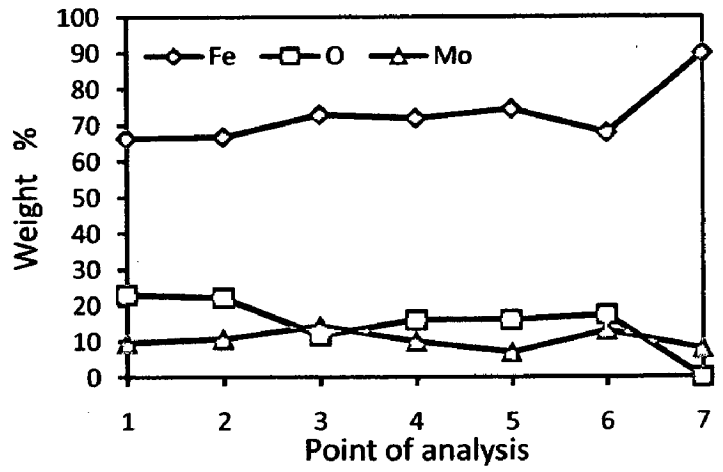
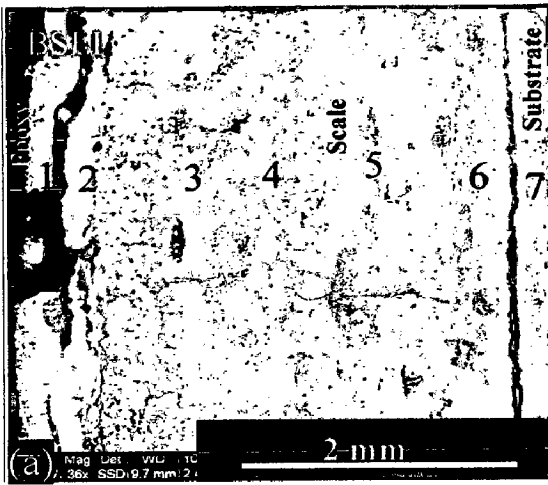
5.6.1.3 Surface scale analysis

5.6.1.3.1 X-ray diffraction analysis (XRD)

XRD diffractograms for coated and uncoated T-11 boiler steel exposed to super-heater of the coal fired boiler environment at 900°C for 1000 hours; are depicted in Fig.5.43 on reduced scale. As indicated by the diffractograms in Fig.5.43, Fe_2O_3 , Al_2O_3 and SiO_2 are the main phases present in the oxide scale of coated and uncoated T-11 boiler steel. In case of conventional thick TiAlN coating; addition to the above mentioned phases Ti_3Al is also present in the oxide scale (Fig.5.43).

5.6.1.3.2 Surface scale morphology

SEM micrographs along with EDAX point analysis reveals the surface morphology of the coated and uncoated T-11 boiler steel exposed to super-heater of the coal fired boiler environment at 900°C for 1000 hours; are shown in Fig.5.44.



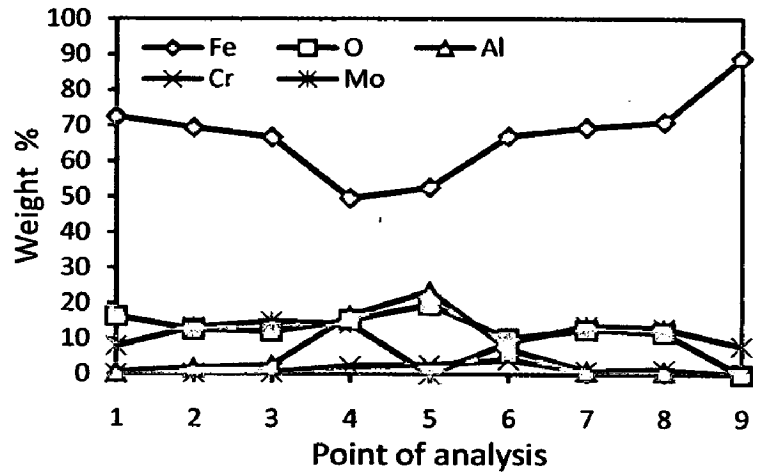
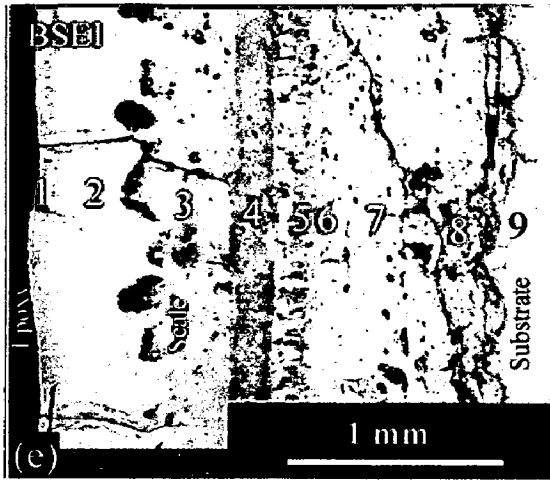


Fig. 5.45 Oxide scale morphology and variation of elemental composition across the cross-section of the uncoated and coated ASTM-SA213-T-11 boiler steel exposed to platen super-heater of the coal fired boiler environment at 900°C for 1000 Hrs: (a) Uncoated T-11 boiler steel (36 X), (b) Nanostructured TiAlN coating (60 X), (c) Nanostructured AlCrN coating (45 X), (d) Conventional TiAlN coating (100 X), (e) Conventional AlCrN coating (60 X)

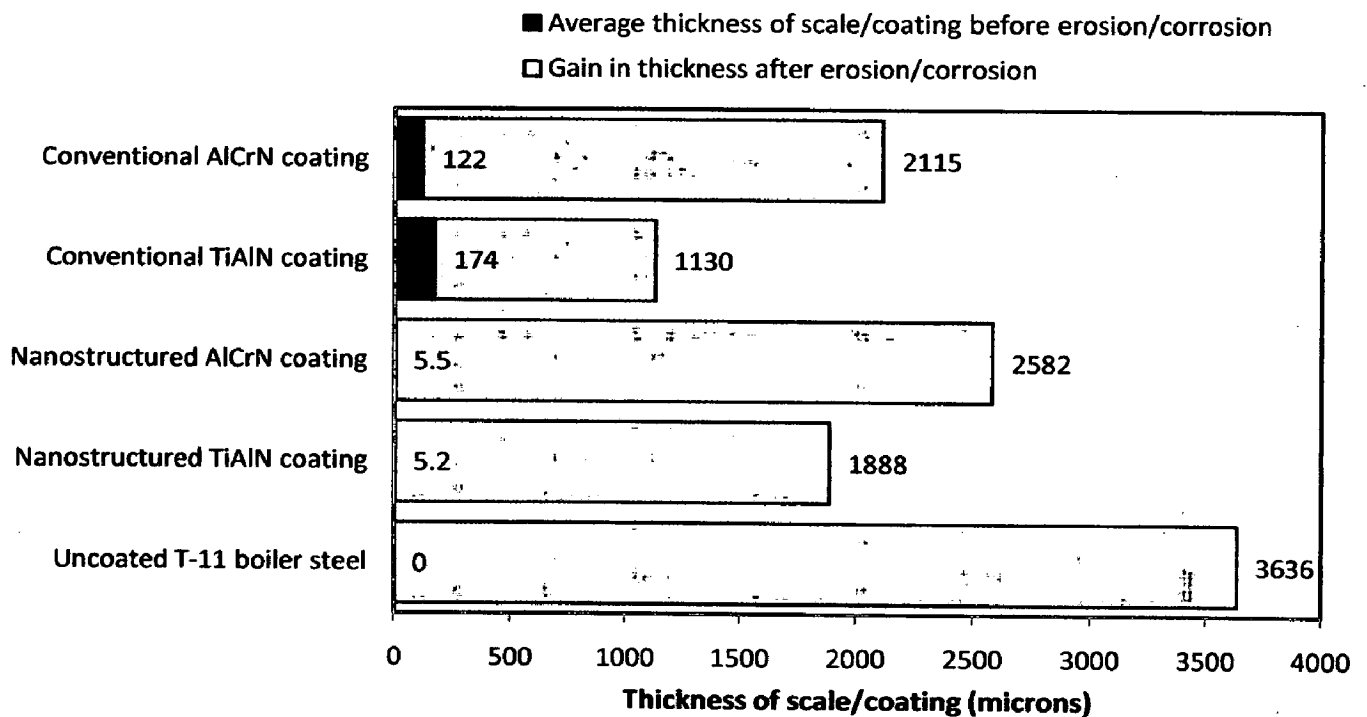


Fig. 5.46 Bar chart indicating the extent of erosion/corrosion for uncoated and coated ASTM-SA213-T-11 boiler steel specimens exposed to super-heater of the coal fired boiler environment at 900°C for 1000 hours

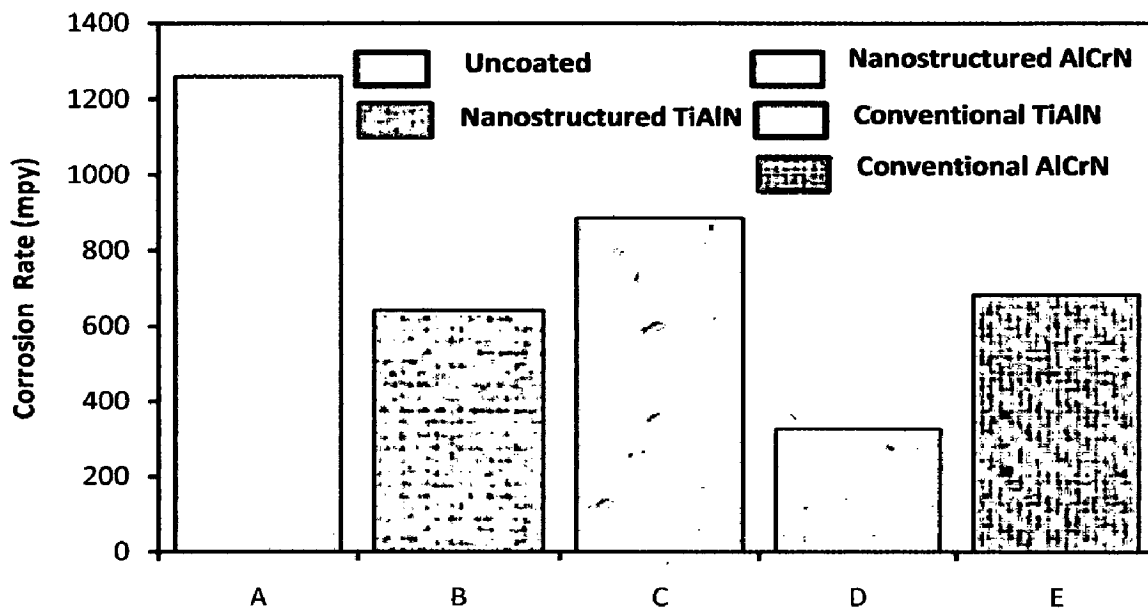


Fig. 5.47 Corrosion rate in mils per year (mpy) for uncoated and coated ASTM-SA213-T-11 boiler steel exposed to super-heater of the coal fired boiler environment at 900°C for 1000 hours: (A) Uncoated T-11 boiler steel, (B) Nanostructured TiAlN coating, (C) Nanostructured AlCrN coating, (D) Conventional TiAlN coating, (E) Conventional AlCrN coating

5.6.1.4.3 X-Ray mapping

X-ray mappings for a part of oxide scale of uncoated and coated ASTM-SA213-T-11 boiler steel exposed to super-heater of the coal fired boiler environment at 900°C for 1000 hours; are shown in Fig. 5.48. In case of uncoated T-11 boiler steel, the micrograph (Fig.5.48.a) indicates a dense scale, which mainly contains iron and oxygen with a thick band of Cr near scale/substrate interface, as indicated by X-ray mapping.

The X-ray mapping analysis of the scale formed on nanostructured TiAlN coated T-11 boiler steel is presented in Fig. 5.48 (b). The X-ray mapping indicates presence of oxygen and iron throughout the scale with a small amount of Al in the top scale. In case of nanostructured thin AlCrN coated T-11 boiler steel; the BSEI and X-ray mapping are shown in Fig. 5.48 (c). The X-ray mapping indicates the presence of iron and oxygen throughout the scale. In case of conventional thick TiAlN coated T-11 boiler steel, Fig.5.48 (d), Al and Ti rich thick bands are clearly seen along with Fe and oxygen in the sub-scale region. Figure 5.48 (e) depicts the X-ray mapping in case of conventional AlCrN coated T-11 boiler steel. The thick band of Al is present in the sub-scale region. The upper scale is rich in Fe and O.

It can be inferred from the plots (Fig.5.41) that the uncoated and nanostructured thin AlCrN coated T-11 boiler steels have shown high weight gain as compared to the conventional thick and nanostructured TiAlN coatings. The conventional TiAlN coating has shown minimum erosion-corrosion rate and weight gain. The weight gain in case of nanostructured TiAlN and conventional AlCrN coatings is higher than that of conventional TiAlN coating and less than that of uncoated and nanostructured AlCrN coated T-11 boiler steel (Fig.5.41).

Bar chart in Fig.5.42 indicates the overall gain/loss in the thickness (in mm) of the specimen. Bar chart (Fig.5.42) indicates the overall gain/loss in the thickness (in mm) of the specimen. All the coatings and bare T-11 boiler steel have shown increase in overall thickness after erosion-corrosion for 1000 hrs. The thickness of the specimens was measured before and after the erosion-corrosion test and average of ten values has been used to calculate the thickness gain/loss. The measured average gain in overall specimen thickness values for uncoated T-11, nanostructured thin TiAlN, nanostructured thin AlCrN, conventional thick TiAlN and conventional thick AlCrN coatings are 4.370, 3.8170, 4.343, 1.868 and 1.620 mm respectively.

5.6.1.3 Surface scale analysis

5.6.1.3.1 X-ray diffraction analysis (XRD)

XRD diffractograms for coated and uncoated T-11 boiler steel exposed to super-heater of the coal fired boiler environment at 900°C for 1000 hours; are depicted in Fig.5.43 on reduced scale. As indicated by the diffractograms in Fig.5.43, Fe_2O_3 , Al_2O_3 and SiO_2 are the main phases present in the oxide scale of coated and uncoated T-11 boiler steel. In case of conventional thick TiAlN coating; addition to the above mentioned phases Ti_3Al is also present in the oxide scale (Fig.5.43).

5.6.1.3.2 Surface scale morphology

SEM micrographs along with EDAX point analysis reveals the surface morphology of the coated and uncoated T-11 boiler steel exposed to super-heater of the coal fired boiler environment at 900°C for 1000 hours; are shown in Fig.5.44.

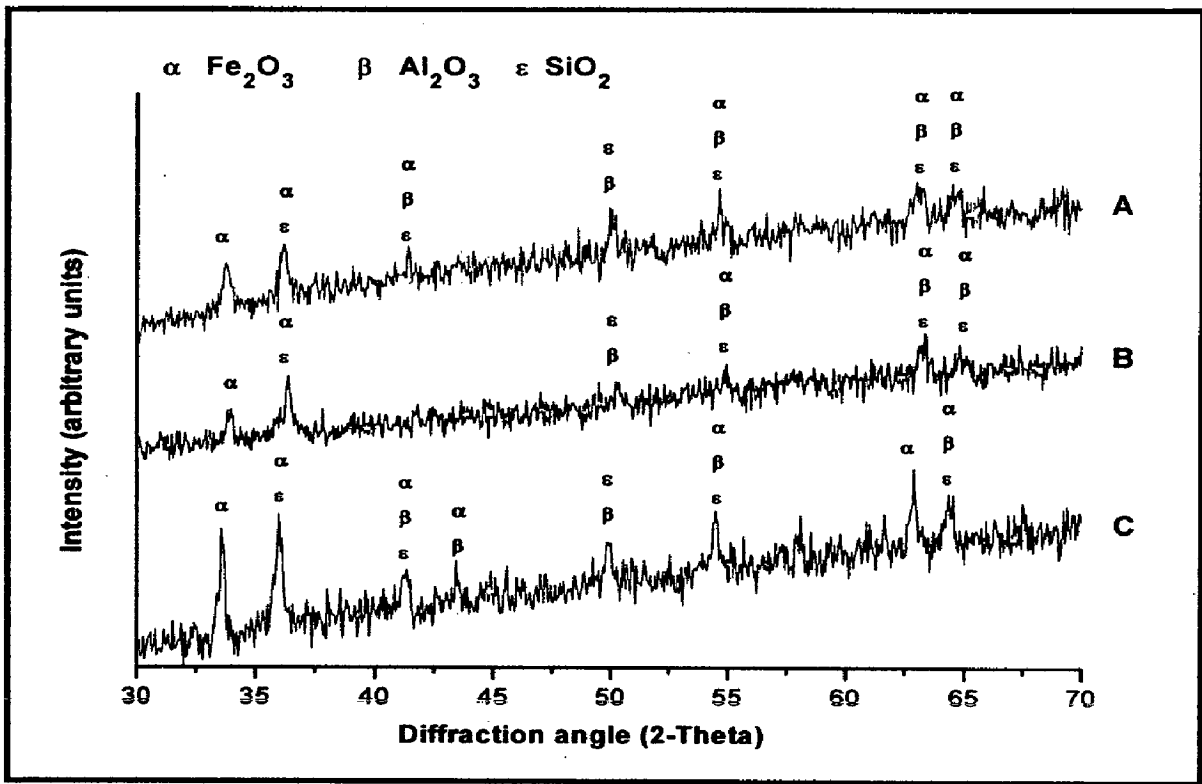


Fig. 5.43 (a) X-Ray Diffraction pattern of uncoated and coated ASTM-SA213-T-11 boiler steel exposed to platen superheater of the coal fired boiler environment at 900°C for 1000 Hrs: (A) Uncoated T-11 boiler steel, (B) Nanostructured TiAlN coating, (C) Nanostructured AlCrN coating

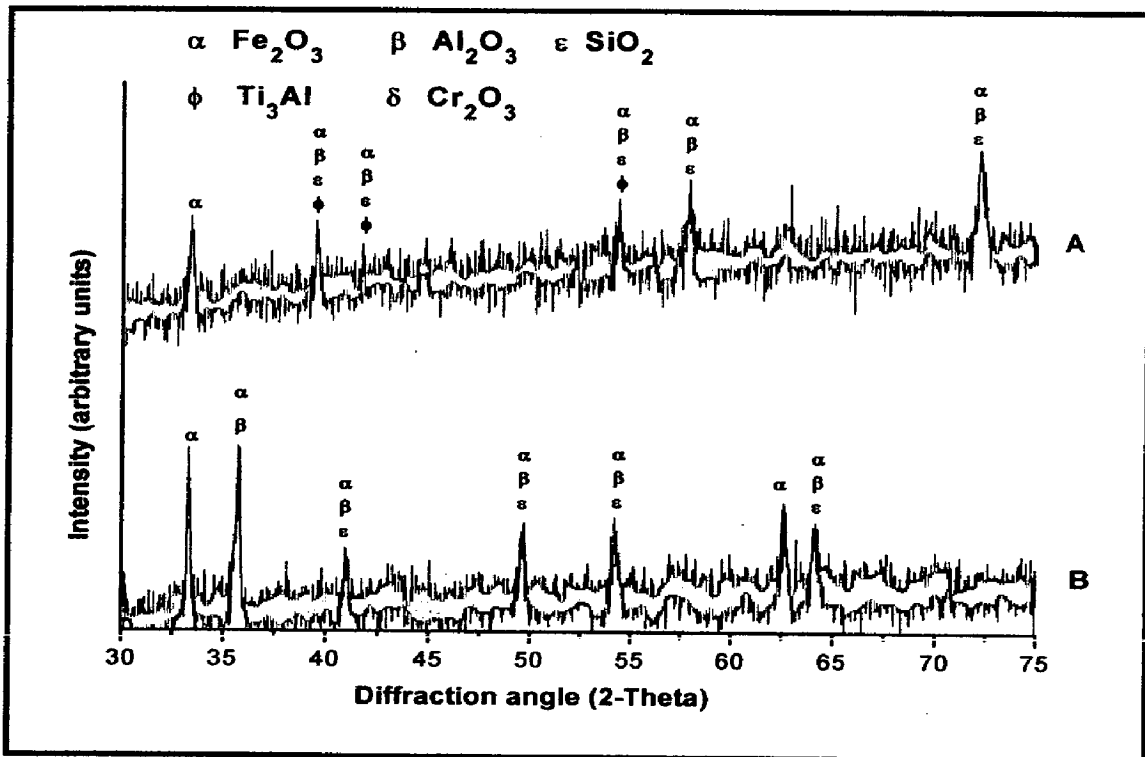


Fig. 5.43 (b) X-Ray Diffraction pattern of coated ASTM-SA213-T-11 boiler steel exposed to platen superheater of the coal fired boiler environment at 900°C for 1000 Hrs: (A) Conventional TiAlN coating, (B) Conventional AlCrN coating

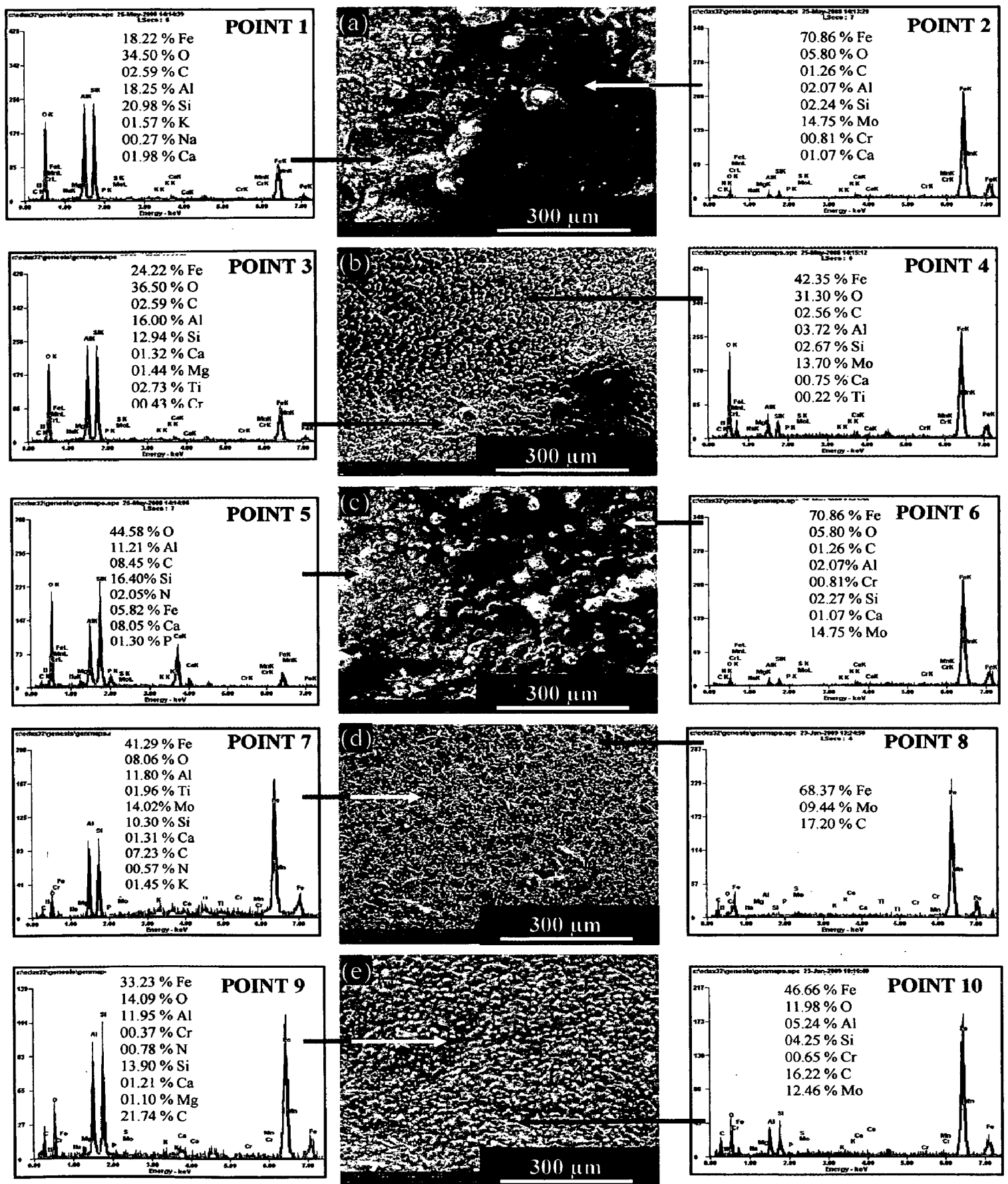


Fig. 5.44 Surface-scale morphology and EDAX patterns from different spots on uncoated and coated ASTM-SA213-T-11 boiler steel exposed to platen superheater of the coal fired boiler environment at 900°C for 1000 Hrs: (a) Uncoated T-11 boiler steel, (b) Nanostructured TiAlN coating, (c) Nanostructured AlCrN coating, (d) Conventional TiAlN coating, (e) Conventional AlCrN coating

Micrograph (shown in Fig.5.44.a) for uncoated T-11 boiler steel indicates the scale developed with blackish grey and white regions. Also the surface shows the signs of erosion. EDAX analysis at point 1 on Fig.5.44 (white region) indicates the presence of Al, O and Si alongwith iron, which may be the ash. The blackish grey region (Point 2) mainly consists of Fe and O with minor amounts of Al and Si. The SEM micrograph of oxidized nanostructured thin TiAlN coatings is shown in Fig.5.44 (b). The surface scale shows as if vertical needles developed on a matrix. EDAX analysis (Point 3 and 4) of the scale revealed the presence of Fe, O, Al and Si as the main elements along small amount of Ti, Cr and Mo. In case of nanostructured thin AlCrN coated T-11 boiler steel, the scale consists of white and dark grey regions. EDAX point analysis at point 5 (white region) shows the presence of Al, Si and O along with P, Ca and N with small amount of iron, whereas the dark grey region (Point 6) shows maximum concentration of Fe along with small amount of Al, Si, Cr and Ca with Mo.

The surface scale developed on conventional thick TiAlN coated T-11 steel is like small white needles dispersed in a matrix. The white needles (Point 7 in Fig.5.44) have shown higher percentage of Al, Si, O, Ti, Mo and less concentration of Fe as compared to the matrix (Point 8). A spalled surface scale is developed on conventional thick AlCrN coated T-11 boiler steel. EDAX point analysis reveals the presence of Fe, Al, O, Si along with small amount of Ca, Mo, Mg, Cr and Carbon.

5.6.1.4 Cross-sectional analysis

5.6.1.4.1 Cross-sectional scale morphology

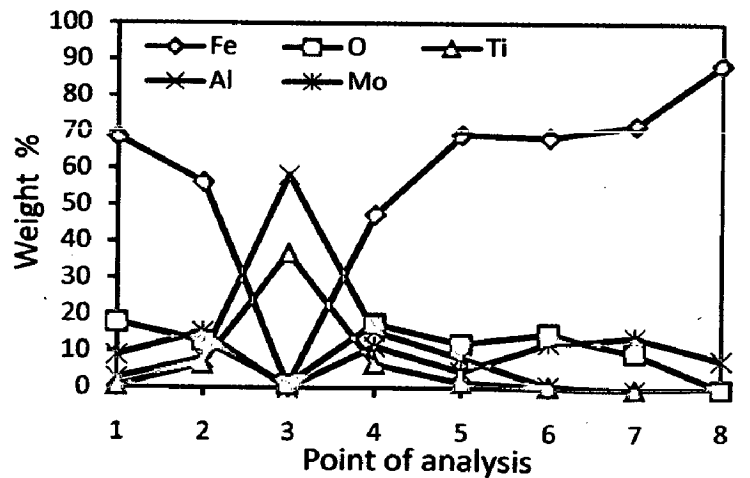
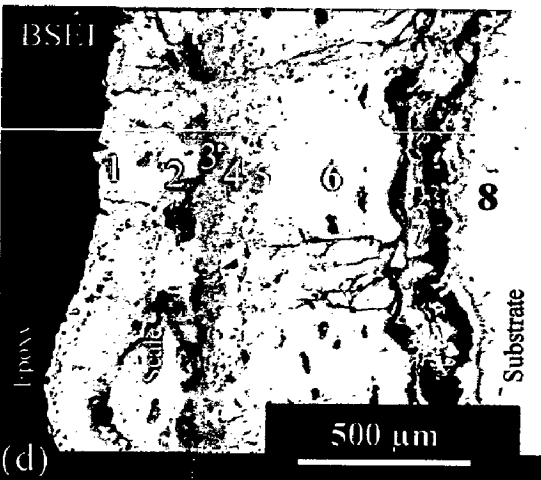
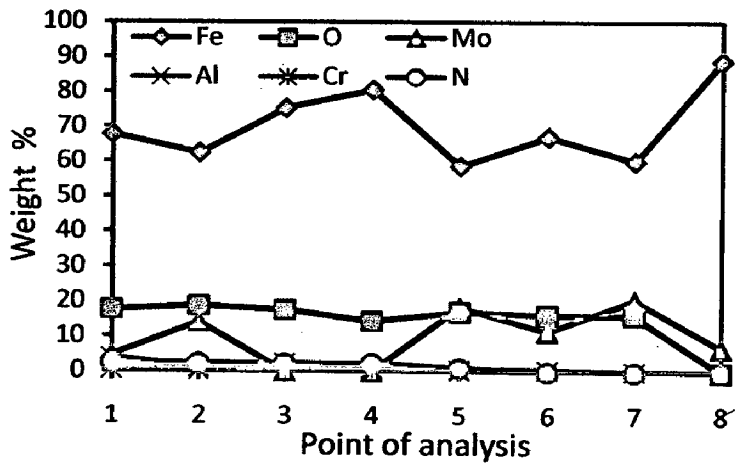
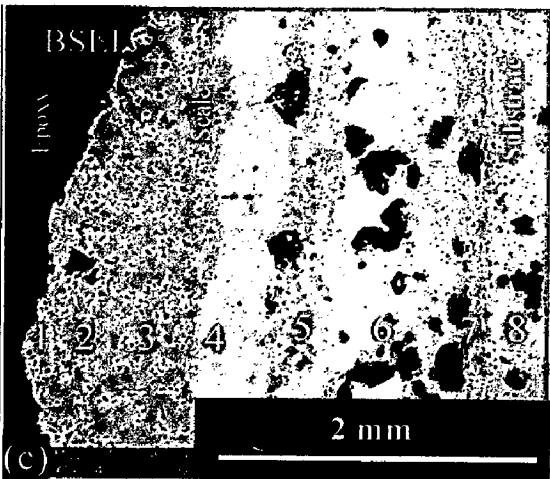
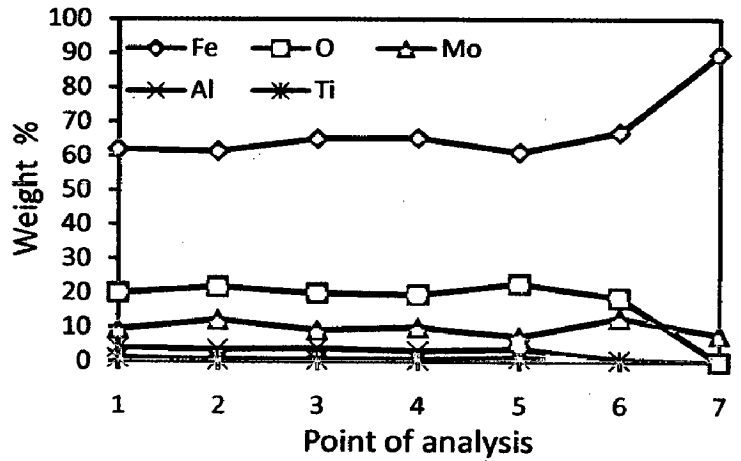
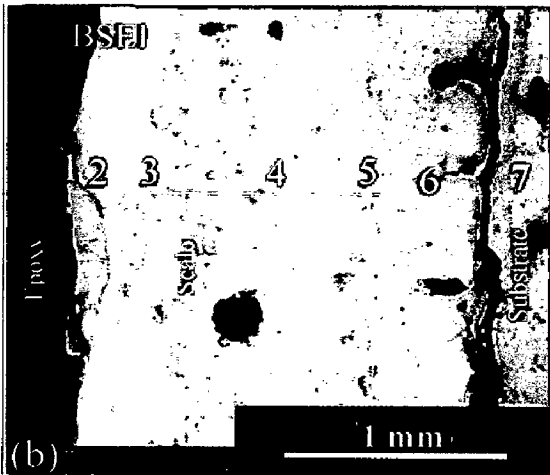
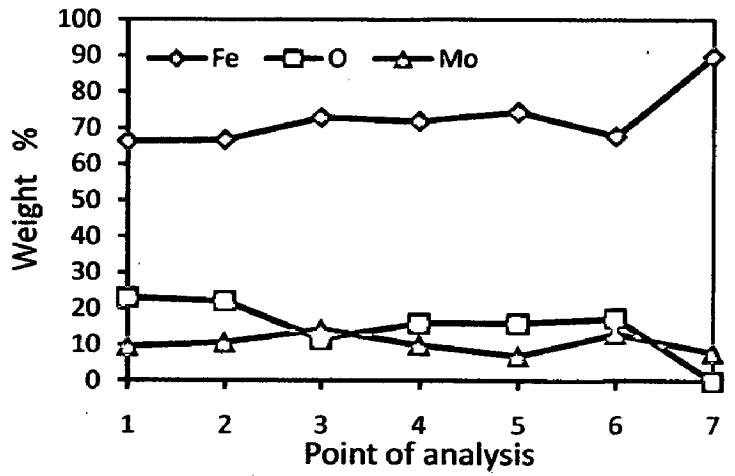
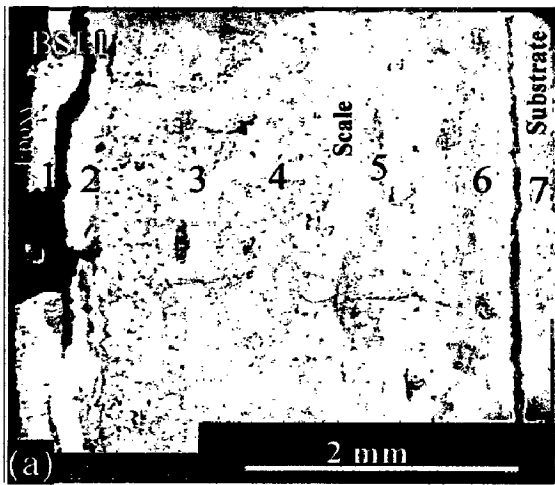
Back Scattered Electron Image (BSEI) micrograph and elemental variation across the cross-section for coated and uncoated T-11 boiler steel exposed to super-heater of the coal fired boiler environment at 900°C for 1000 hours; are shown in Fig.5.45. The SEM micrograph (Fig.5.45.a) in case of uncoated T-11 boiler steel shows thick scale. The scale is fragile and indicating cracking. EDAX analysis reveals the presence of Fe, Mo and O throughout the scale. The existence of significant amount of oxygen points out the possibility Fe_2O_3 in the oxide scale. BSEI micrograph and elemental variation depicted in Fig.5.45 (b), for the exposed cross-section of nanostructured thin TiAlN coated T-11 boiler steel shows the thick, continuous and adherent scale. The scale is showing fine cracks at some locations.

The EDAX analysis reveals the presence of Fe, Mo and O throughout the scale along with very small amount of Al throughout the scale. A thick and adherent oxide scale can be seen in case of nanostructured AlCrN coated T-11 boiler steel (Fig.5.45.c). The EDAX point analysis indicates the presence of Fe, Mo and O throughout the scale with variable amount. In case of conventional TiAlN coated T-11 boiler steel, the scale is non-uniform, thin and adherent as depicted in Fig.5.45 (d). The EDAX point analysis indicates the presence of Fe, O, Mo, Ti and Al throughout the scale with variable amounts. The amount of Ti and Al in the top scale is higher (Point 1 and 2) which decreases subsequently after point 6 towards the substrate. The concentration of Ti and Al is maximum at point 3 where Fe, Mo and O are completely absent. The conventional thick AlCrN coated T-11 boiler steel (Fig.5.45.e) indicates uniform, thin and adherent scale. EDAX point analysis shows the presence of Fe, O and Mo throughout the scale. The top scale is rich in Fe and O with some amount of Al, Cr and Mo. The sub scale has shown higher concentration of Al and Cr (Point 4, 5 and 6 on Fig.5.45.e).

5.6.1.4.2 Scale thickness

The oxidized samples were cut across the cross section using Buehler Isomet 1000 precision saw and mounted in transoptic mounting resin and subsequently mirror polished to obtain scanning electron back scattered micrographs and X-ray mapping of different elements for coated and uncoated T-11 boiler steel. The scale thickness values were measured from SEM back scattered micrographs as shown in Fig.5.45. The extent of erosion-corrosion in terms of scale/coating thickness (in microns) and corrosion rate in mils per year (mpy) for coated and uncoated T-11 boiler steel exposed to super-heater of the coal fired boiler environment at 900°C for 1000 hours; are shown in Fig.5.46 and 5.47 respectively.

Very thick scale is observed in case of uncoated and nanostructured coated T-11 boiler steel. The measured corrosion rate (mpy) for uncoated T-11, nanostructured thin TiAlN, nanostructured thin AlCrN, conventional thick TiAlN and conventional thick AlCrN coatings are 1260, 641, 886, 327 and 683 mpy respectively. The nanostructured and conventional coatings have shown good resistance to the corrosive environment as the oxygen penetration is limited to very less thickness as compared to the uncoated T-11 boiler steel (Fig.5.46 and 5.47).



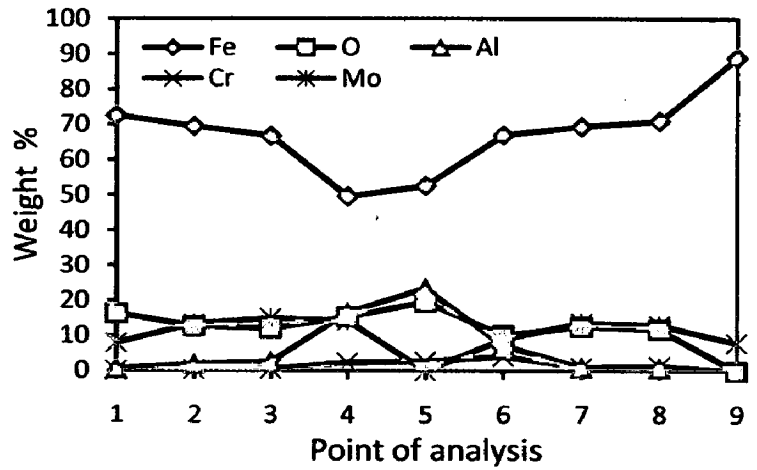
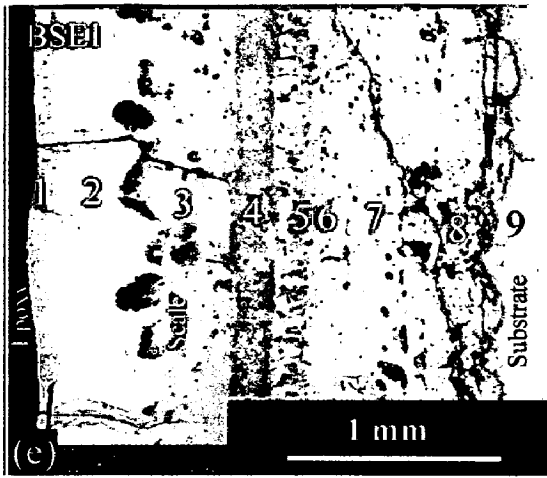


Fig. 5.45 Oxide scale morphology and variation of elemental composition across the cross-section of the uncoated and coated ASTM-SA213-T-11 boiler steel exposed to platen super-heater of the coal fired boiler environment at 900°C for 1000 Hrs: (a) Uncoated T-11 boiler steel (36 X), (b) Nanostructured TiAlN coating (60 X), (c) Nanostructured AlCrN coating (45 X), (d) Conventional TiAlN coating (100 X), (e) Conventional AlCrN coating (60 X)

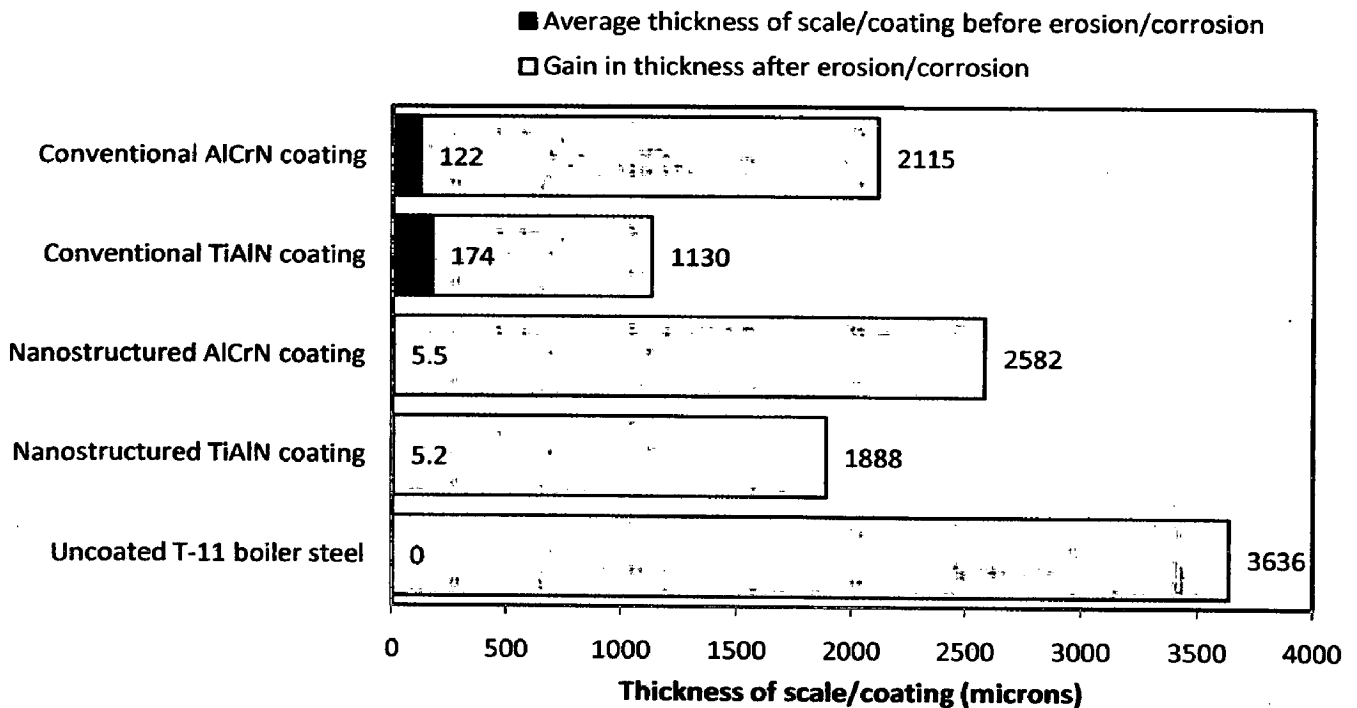


Fig. 5.46 Bar chart indicating the extent of erosion/corrosion for uncoated and coated ASTM-SA213-T-11 boiler steel specimens exposed to super-heater of the coal fired boiler environment at 900°C for 1000 hours

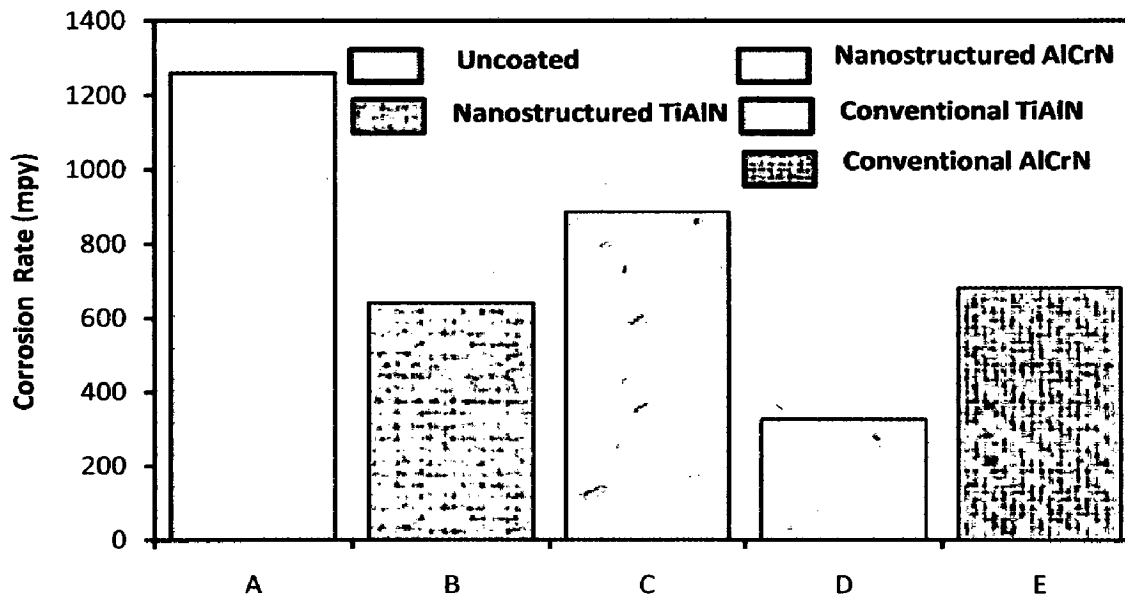


Fig. 5.47 Corrosion rate in mils per year (mpy) for uncoated and coated ASTM-SA213-T-11 boiler steel exposed to super-heater of the coal fired boiler environment at 900°C for 1000 hours: (A) Uncoated T-11 boiler steel, (B) Nanostructured TiAlN coating, (C) Nanostructured AlCrN coating, (D) Conventional TiAlN coating, (E) Conventional AlCrN coating

5.6.1.4.3 X-Ray mapping

X-ray mappings for a part of oxide scale of uncoated and coated ASTM-SA213-T-11 boiler steel exposed to super-heater of the coal fired boiler environment at 900°C for 1000 hours; are shown in Fig. 5.48. In case of uncoated T-11 boiler steel, the micrograph (Fig.5.48.a) indicates a dense scale, which mainly contains iron and oxygen with a thick band of Cr near scale/substrate interface, as indicated by X-ray mapping.

The X-ray mapping analysis of the scale formed on nanostructured TiAlN coated T-11 boiler steel is presented in Fig. 5.48 (b). The X-ray mapping indicates presence of oxygen and iron throughout the scale with a small amount of Al in the top scale. In case of nanostructured thin AlCrN coated T-11 boiler steel; the BSEI and X-ray mapping are shown in Fig. 5.48 (c). The X-ray mapping indicates the presence of iron and oxygen throughout the scale. In case of conventional thick TiAlN coated T-11 boiler steel, Fig.5.48 (d), Al and Ti rich thick bands are clearly seen along with Fe and oxygen in the sub-scale region. Figure 5.48 (e) depicts the X-ray mapping in case of conventional AlCrN coated T-11 boiler steel. The thick band of Al is present in the sub-scale region. The upper scale is rich in Fe and O.

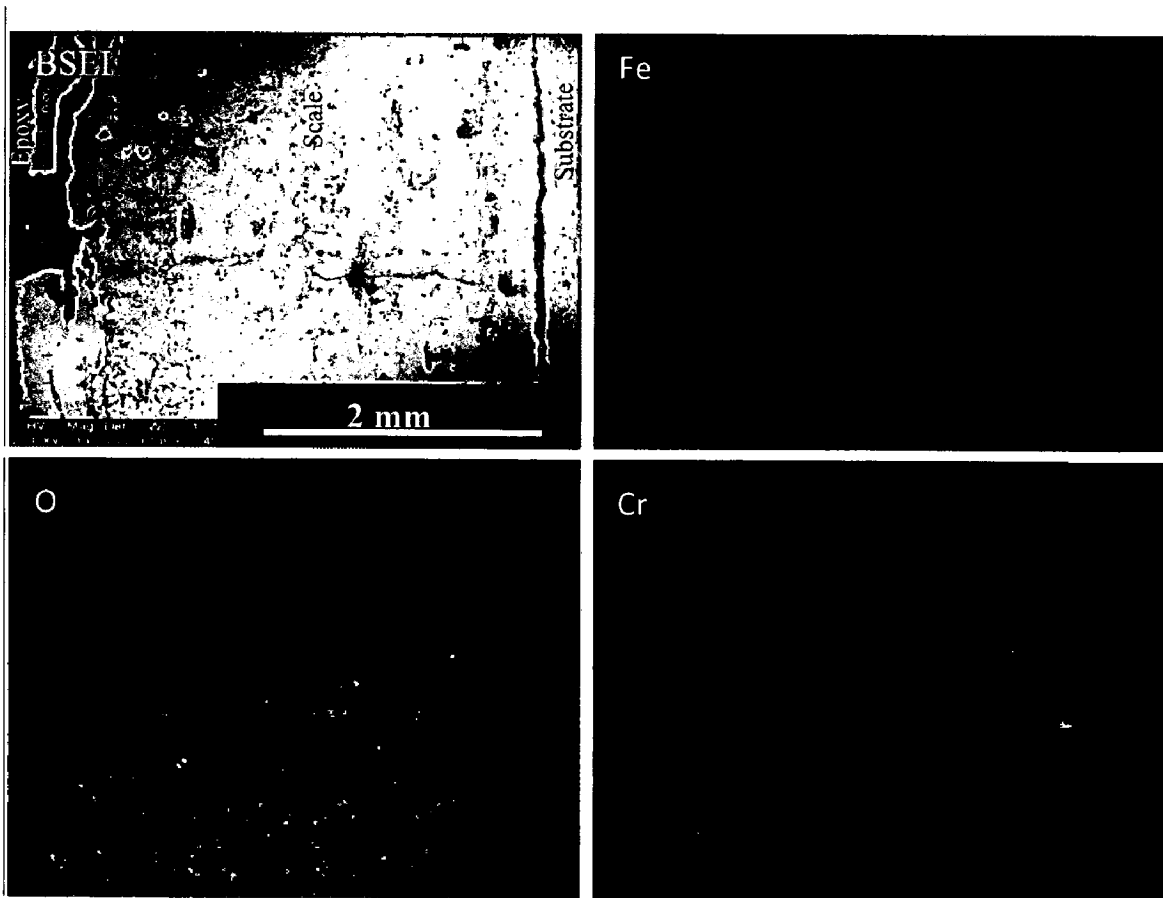


Fig. 5.48 (a) Composition image (BSEI) and X-ray mapping of the cross-section of uncoated ASTM-SA213-T-11 boiler steel exposed to platen super-heater of the coal fired boiler environment at 900°C for 1000 Hrs

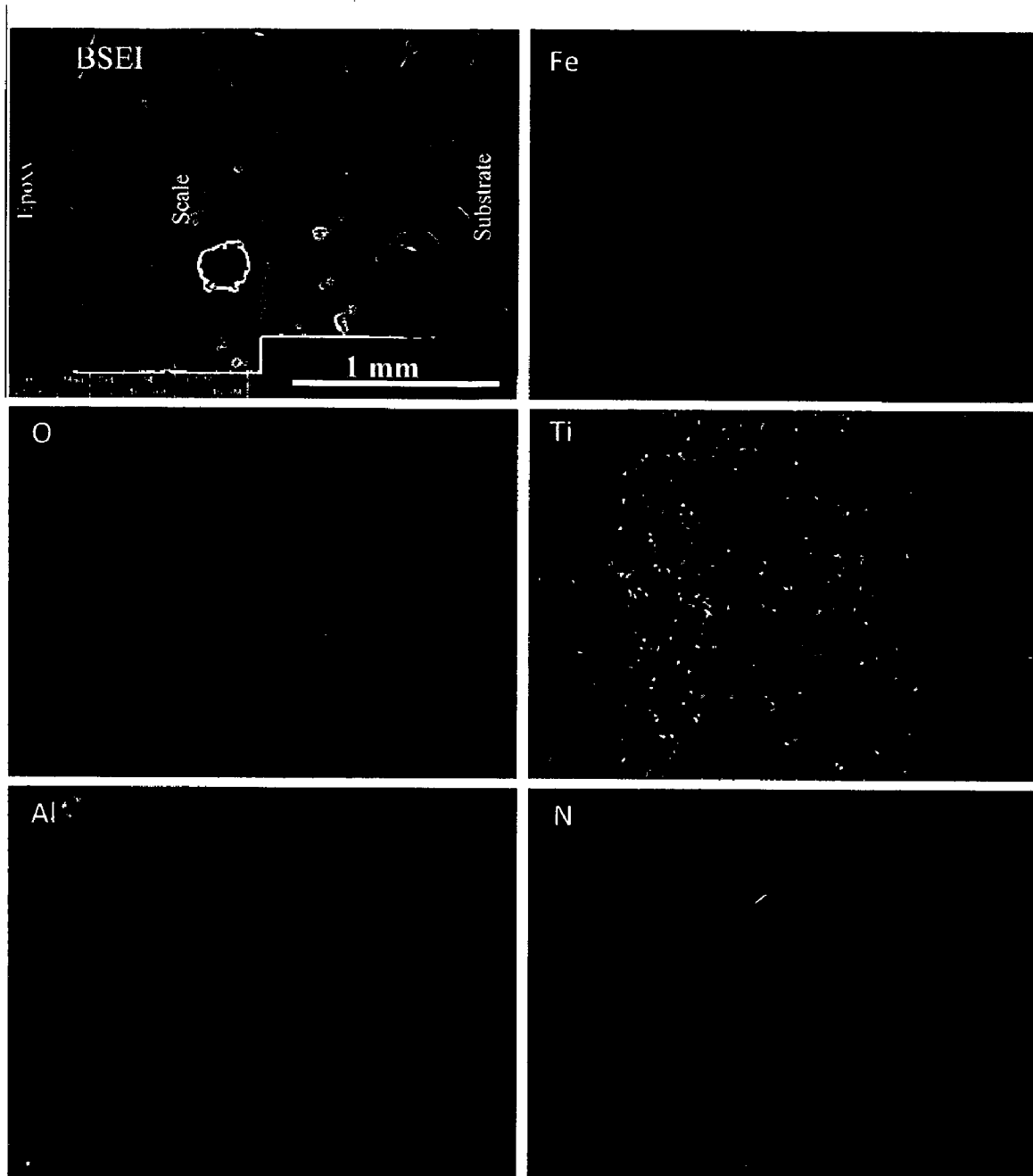


Fig. 5.48 (b) Composition image (BSEI) and X-ray mapping of the cross-section of Nanostructured TiAlN coated ASTM-SA213-T-11 boiler steel exposed to platen super-heater of the coal fired boiler environment at 900°C for 1000 Hrs

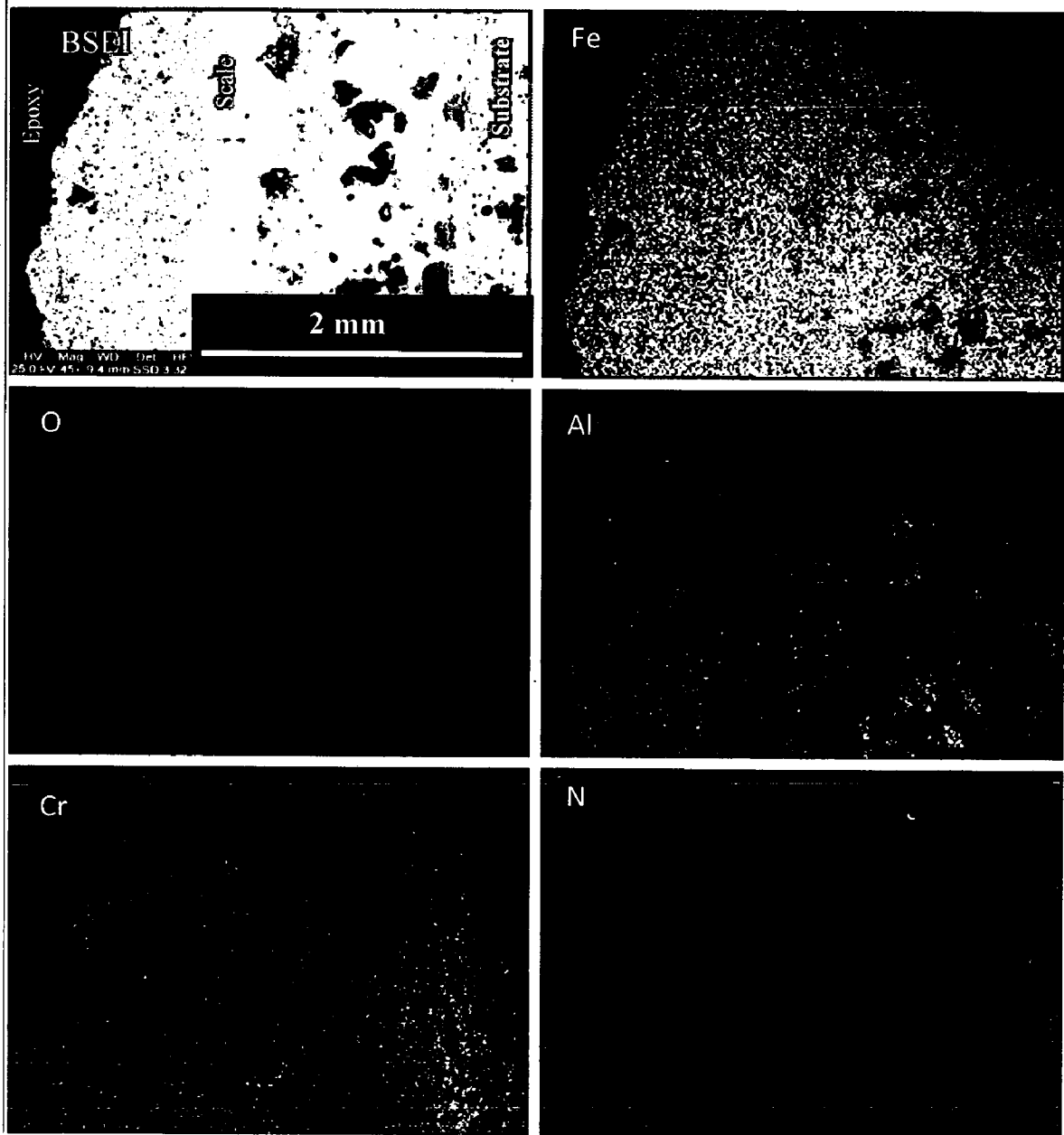


Fig. 5.48 (c) Composition image (BSEI) and X-ray mapping of the cross-section of Nanostructured AlCrN coated ASTM-SA213-T-11 boiler steel exposed to platen super-heater of the coal fired boiler environment at 900°C for 1000 Hrs

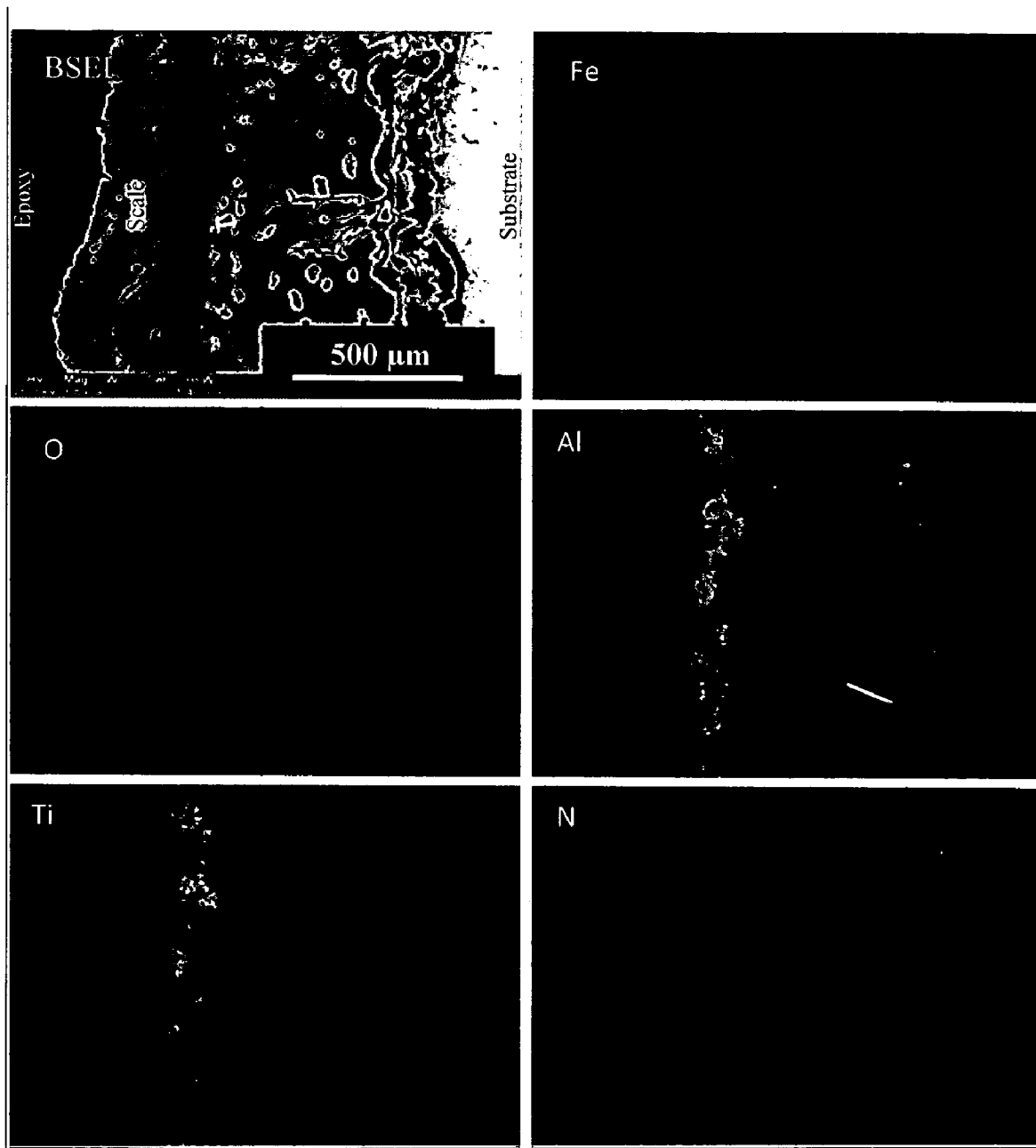


Fig. 5.48 (d) Composition image (BSEI) and X-ray mapping of the cross-section of conventional TiAlN coated ASTM-SA213-T-11 boiler steel exposed to platen super-heater of the coal fired boiler environment at 900°C for 1000 Hrs

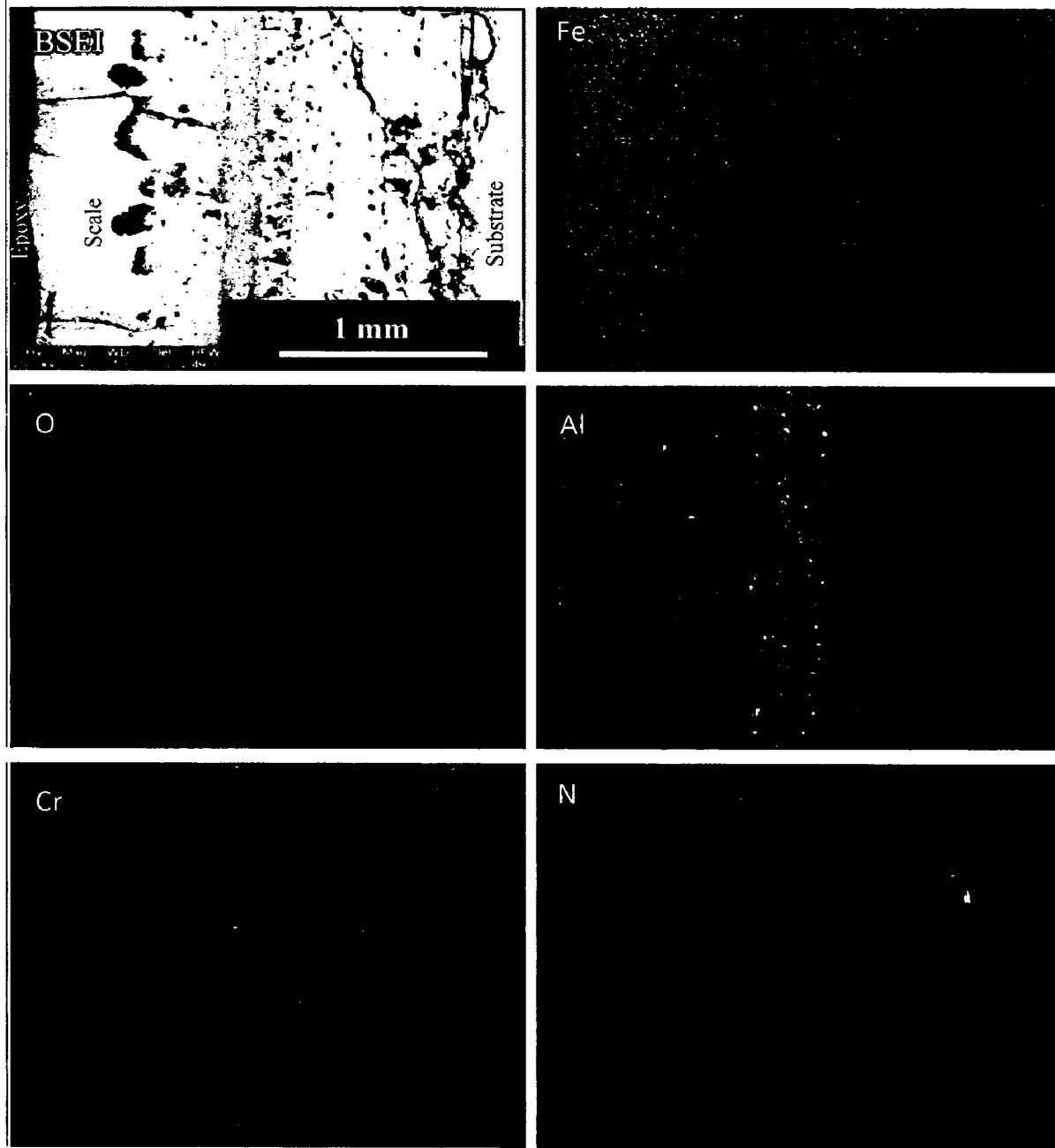


Fig. 5.48 (e) Composition image (BSEI) and X-ray mapping of the cross-section of conventional AlCrN coated ASTM-SA213-T-11 boiler steel exposed to platen super-heater of the coal fired boiler environment at 900°C for 1000 Hrs

5.6.2 Summary of Results

Results obtained after 1000 hrs of exposure of uncoated and coated ASTM-SA213-T-11 boiler steel to super-heater of the coal fired boiler environment at 900°C are summarized in Table.5.9.

Table 5.9 Summary of the results obtained for uncoated and coated ASTM-SA213-T-11 boiler steel exposed to super-heater of the coal fired boiler environment at 900°C for 1000 hours

Coating	Weight gain mg/cm ²	Extent of Corrosion (mm)	Corrosion Rate (mpy)	XRD phases	Remarks
Uncoated T-11 boiler steel	405.53	3.636	1260.0	Fe ₂ O ₃ , Al ₂ O ₃ and SiO ₂	Ash deposited scale with severe spalling and dark grey colored surface appearance in the middle with brownish colored scale along the sides. Ash deposition, erosion and severe spalling continued to last cycle.
Nanostructured TiAlN coating	335.01	1.888	641.2	Fe ₂ O ₃ , Al ₂ O ₃ and SiO ₂	Color of the oxide scale at the end of the study was blackish grey with some brownish colored areas from which scale gets removed and regenerated. Erosion and ash deposition continued till end of the study.
Nanostructured AlCrN coating	410.89	2.582	886.3	Fe ₂ O ₃ , Al ₂ O ₃ and SiO ₂	The formation of dark blackish grey colored scale with severe spalling and visible hairline cracks was observed at the end. The ash deposition, erosion and spalling continue till the end.
Conventional TiAlN Coating	274.94	1.130	327.6	Fe ₂ O ₃ , Al ₂ O ₃ , SiO ₂ and Ti ₃ Al	The formation of blackish grey colored scale on half portion and whitish grey colored scale on the remaining area; at the end of the study. The scale was rough and adherent to the substrate.
Conventional AlCrN coating	347.56	2.115	683.2	Fe ₂ O ₃ , Al ₂ O ₃ and SiO ₂	Color of the ash deposited oxide scale was dark grey with some whitish areas at the end. The scale was found to be adherent. No spalling was observed till 5 th cycle after which the sample showed spalling and signs of erosion.

5.6.3 Discussion

The combustion of coal generates very corrosive media particularly near the superheater tubes (Weulersse-Mouturat et al., 2004). A dynamic surface layer consisting of a mechanical mixture of particles from the boiler gases and oxide scale growing from the base metal is formed on boiler tubes (Sidhu et al., 2006F). The accommodation of these low melting-point salts from the flue-gas on the fire side surface of boiler tubes induces hot corrosion and is considered a root cause for the severe wastage of tube materials used for superheaters and reheaters in “advanced” steam-generating systems (Sidhu et al., 2006G). Sulphides have not been generally identified in the scale of samples tested in the coal fired boiler environment; which is similar to the finding of Crossley et al. (1948). The fly ash particles rich in magnetite reduce the concentration of SO_3 in the boiler environment.

Fragile scale with tendency to spall has been observed for the uncoated and nanostructured thin TiAlN and AlCrN coated T-11 boiler steel used in present investigation (Fig.5.40).The ash deposition, erosion and tendency to spall continued till the end of the study. In case of nanostructured and conventional TiAlN coatings; the scale gets removed and regenerated at some locations. It may be due to the erosion as the coal used in Indian power stations has large amounts of ash (about 50%), which contain abrasive mineral species such as hard quartz (up to 15%) which increase the erosion propensity of coal (Krishnamoorthy, and Seetharamu, 1989). In case of conventional AlCrN coatings; no spalling was observed till 5th cycle. The surface of scale is rough in case of conventional thick coatings.

The presence of Fe and oxygen (Fig.5.45.) in the top of the scale of the coated T-11 boiler steel is believed to be due to the diffusion of iron through the pores and cracks that appeared in the coating during the course of oxidation studies (Singh Buta , 2003). As indicated by the XRD diffractograms in Fig.5.43; Fe_2O_3 , Al_2O_3 and SiO_2 are the main phases present in the oxide scale of coated and uncoated T-11 boiler steel. The phases revealed by XRD diffractograms are found to be in agreement with those reported by Longa-Nova et al. (1996), Calvarin et al. (2000) and Nickel et al. (2002). In case of conventional thick TiAlN coating; addition to the above mentioned phases Ti_3Al is also present in the oxide scale (Fig.5.43). Formation of hematite (Fe_2O_3) as revealed by the X-ray diffractograms (Fig.5.43) might be due to the reaction of iron with oxygen since iron is

the main constituent of boiler steel. Formation of such type of oxides has also been analyzed by Prakash et al. (2001) and Srikanth et al. (2003) during the failure analysis of superheater tubes caused by fireside corrosion. The formation of Al_2O_3 and SiO_2 might be due to the deposition of ash on the eroded-corroded tubes. The higher amount of Al and Si is found in the ash. The presence of such phases in slag has also been reported by John (1986) during study on slag, gas and deposit thermochemistry in a coal gasifier and the possibility for formation of such phase in ash constituents during combustion has further been reported by Nelson et al. (1959).

The higher weight gain (which is the net result of erosion and oxidation) is observed in case of uncoated and nanostructured thin AlCrN coated T-11 boiler steel as compared to the nanostructured TiAlN and conventional thick coatings; exposed to super-heater of the coal fired boiler environment at 900°C for 1000 hours (Fig.5.41). It might be attributed to spallation of the oxide scale in the actual environment of the coal fired boiler and fluxing action of the molten salt along with erosion of oxide scale. There is continuous formation of thin oxide scale with subsequent depletion by spallation and erosion under cyclic test conditions. The top surface may contains inclusions, which leads to vertical cracks through which the corrosive species might have penetrated along the crack and between the metallic layers. The cracks and oxide layer have propagated parallel to the top surface. During cyclic testing, cracks in the oxide scale and spalling of the uncoated and coated T-11 boiler steel might be attributed to the different values of thermal expansion coefficients for the coating, scale and the substrate as reported by Sidhu et al. (2003), Singh H et al. (2004), Evans et al. (2001), Wang et al. (2002) and Niranatlumpong et al (2000).

Both conventional thick coatings and nanostructured thin TiAlN coating have been found successful in reducing the overall weight gain of T-11 boiler steel. However weight change data could not be of much use for predicting the corrosion behavior because of suspected spalling and ash deposition on the specimens. Thus, the extent of erosion-corrosion in terms of scale/coating thickness (in microns) and corrosion rate in mils per year (mpy) for coated and uncoated T-11 boiler steel exposed to super-heater of the coal fired boiler environment at 900°C for 1000 hours; are shown in Fig.5.46 and 5.47 respectively. All the coatings have shown lower corrosion rate as compared to bare T-11 boiler steel. It is well supported by corrosion rate plot (Fig.5.47). The

nanostructured and conventional coatings have shown good resistance to the corrosive environment as the oxygen penetration is limited to very less thickness as compared to the uncoated T-11 boiler steel (Fig.5.46 and 5.47). These results are well supported by EDAX (Fig.5.44) and X-ray mapping analysis (Fig.5.48). The resistance offered by conventional thick TiAlN and AlCrN coatings to the erosion-corrosion in boiler environment may be due to the presence of a thick band of Al along with oxygen in the sub-scale region; as shown by X-ray mapping analysis (Fig.5.48.d and e). In case of nanostructured thin TiAlN coating, the presence of Al band in the top scale may be the reason for its better performance as compared to the nanostructured AlCrN coating and uncoated T-11 boiler steel (Fig.5.48.b).

5.6.4 Conclusions

The high temperature erosion-corrosion behaviors of uncoated and coated ASTM-SA213-T-11 boiler steel have been investigated in super-heater of the coal fired boiler environment at 900°C for 1000 hours (10 cycles). The following conclusions are made:

1. The plasma sprayed gas nitride conventional thick coatings i.e. TiAlN and AlCrN have developed a protective scale mainly consisting of aluminum oxide.
2. All the coated as well as uncoated boiler steels have shown ash deposition on the surface. Thus final thickness is contributed by scale formation, erosion and ash deposition.
3. The corrosion rate in mpy for the uncoated and coated T-11 boiler steel specimens exposed to the super-heater of the coal fired boiler environment at 900°C follows the sequence:
Uncoated T-11 > Nanostructured AlCrN > Conventional TiAlN > Nanostructured AlCrN > Conventional TiAlN
4. The nanostructured TiAlN and AlCrN coatings has shown resistance to erosion-corrosion to some extent as the overall weight gain and thickness are less than as compared to the uncoated T-11 boiler steel. The oxide scale formed is adherent to the substrate in all coatings. But in case of uncoated and nanostructured coated T-11 boiler steel, the scale is found to be fragile with some cracks.

Chapter 6

SUBSTRATE ASTM-SA213-T-22 BOILER STEEL

This chapter deals with the results and discussion for the bare and coated ASTM-SA213-T-22 boiler steel exposed to different degradation environments. It includes the characterization of the nanostructured and conventional TiAlN and AlCrN coatings on T-22 boiler steel and their behavior when exposed to high temperature oxidation studies in air, molten salt ($\text{Na}_2\text{SO}_4\text{-60\%V}_2\text{O}_5$) environment and in a coal fired boiler of a thermal plant, erosion studies in simulated coal-fired boiler environment and corrosion studies in simulated marine environment.

6.1 CHARACTERISATION OF COATINGS

Little work has been published on high temperature corrosion behavior of nanostructured and conventional hard metal nitride coatings to the best of the knowledge of the author. Therefore, these coatings were developed on the ASTM-SA213-T-22 boiler steel and their behavior was studied when exposed to high temperature oxidation in air, molten salt environment, industrial environment, high temperature solid particle erosion and simulated marine environment. In the present section the conventional thick (by plasma spraying and gas nitrided) and nanostructured thin (by physical vapor deposition process) TiAlN and AlCrN coatings developed on T-22 boiler steel have been characterized.

6.1.1 Results

6.1.1.1 Visual observations

The macrographs of as-coated T-22 boiler steel are shown in Fig.6.1. The nanostructured thin TiAlN coating is violet grey in color and nanostructured thin AlCrN coating is light grey in color (Fig. 6.1). Visual observations indicate; the surface of nanostructured coatings is smooth whereas the surface of conventional thick coatings is rough. The color of the thick coatings appeared as dark grey. Also, Optical micrographs of the nanostructured and conventional coatings are shown in Fig.6.2.

The nanostructured coatings (Fig.6.2.a and b) have uniform microstructure having some pores and inclusions. In case of conventional thick coatings (Fig.6.2.c and d); the massive microstructure can be observed with irregularly shaped grains.

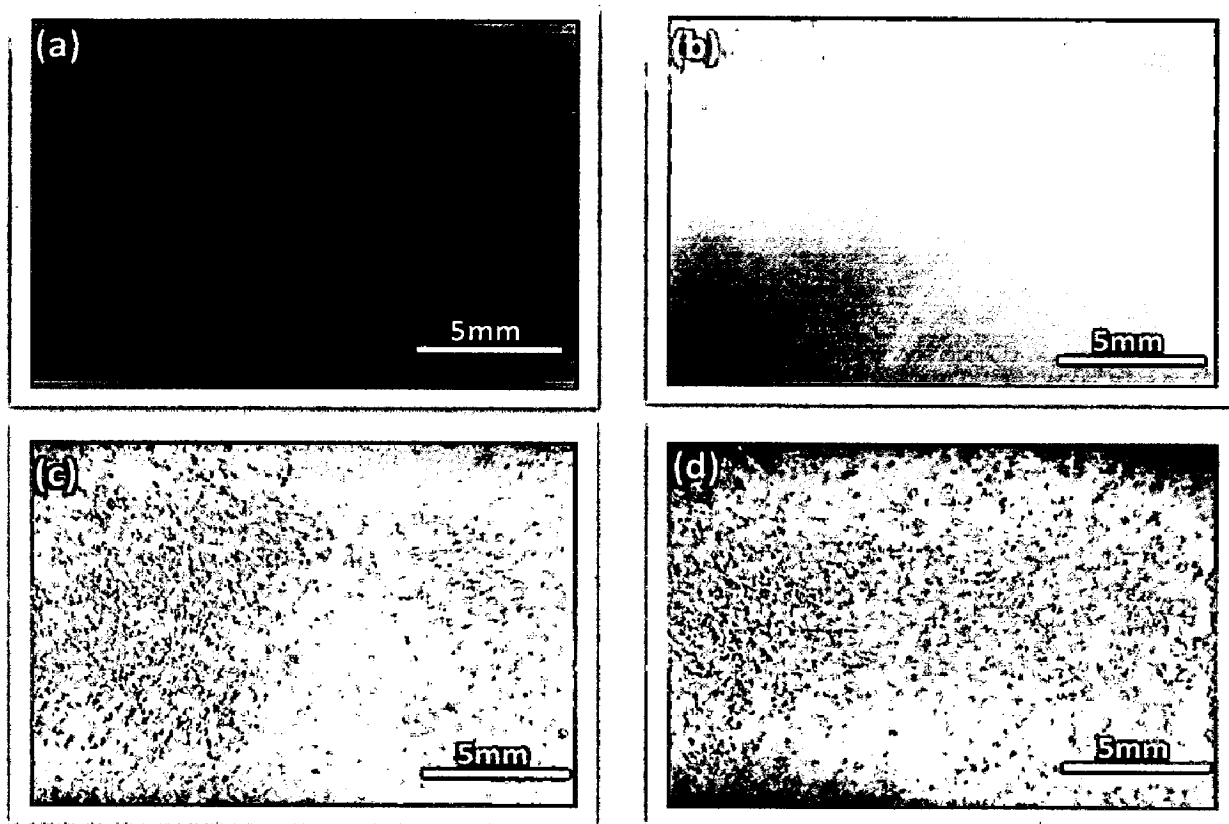


Fig. 6.1 Surface macrographs for the as coated ASTM-SA213-T-22 boiler steel (a) Nanostructured TiAlN coating, (b) Nanostructured AlCrN coating, (c) Conventional TiAlN coating, (d) Conventional AlCrN coating

6.1.1.2 Surface analysis

6.1.1.2.1 X-ray diffraction analysis (XRD)

XRD diffractograms for nanostructured and conventional TiAlN and AlCrN coated ASTM-SA213-T-22 boiler steel are depicted in Fig.6.3 on reduced scale. As indicated by the diffractograms in Fig.6.3; TiN and AlN are the main phases present in the nanostructured thin TiAlN coating. Further, in case of nanostructured AlCrN coating, the prominent phases are CrN and AlN. The grain size of the nanostructured thin coatings was estimated from Scherrer formula and reported in Table.6.1. The calculated grain

size for nanostructured thin TiAlN and AlCrN coatings is 18 and 25 nm respectively. Further, the main phases identified for the conventional thick TiAlN coating are Al₂O₃, TiN, Ti₃Al, AlN and TiO₂. The phases identified in case of conventional thick AlCrN coating are CrN, AlN, and Al₂O₃ with minor peaks of Cr₂O₃.

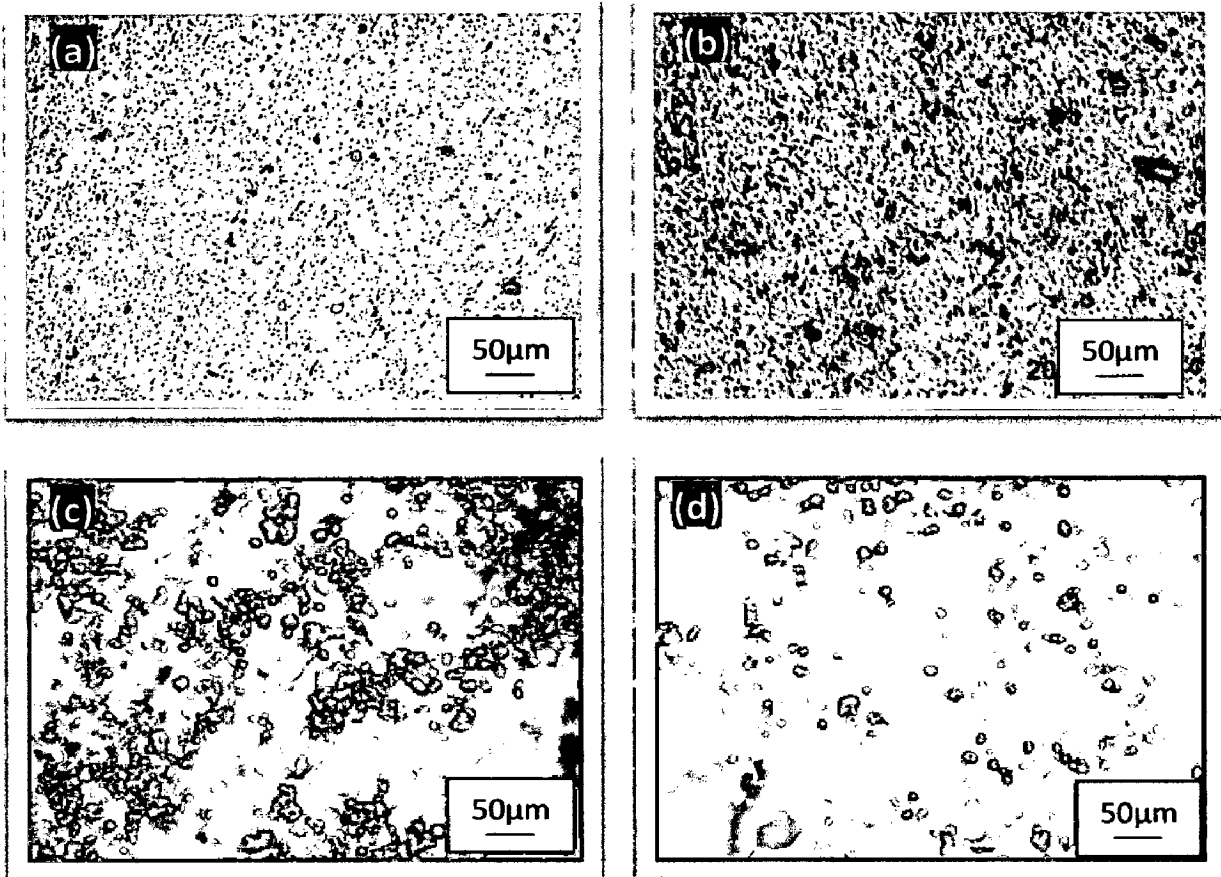


Fig. 6.2 Optical micrograph (200 X) of the surface of as coated ASTM-SA213-T-22 boiler steel (a) Nanostructured TiAlN coating, (b) Nanostructured AlCrN coating, (c) Conventional TiAlN coating, (d) Conventional AlCrN coating

6.1.1.2.2 Porosity analysis

The porosity analysis is of prime importance in high temperature corrosion studies. The dense coatings are supposed to provide very good corrosion resistance as compared to porous coatings. The porosity measurements were made by PMP3 inverted metallurgical microscope with stereographic. The porosity of nanostructured thin TiAlN and AlCrN coatings was found below 0.45 % (Table.6.1). In case of conventional thick coatings; the porosity of as sprayed Ti-Al (1.00-4.00 %) and Al-Cr (2.50-4.10 %) coatings was also evaluated; which is reported in Table.6.2. A considerable decrease in the

porosity had been observed after gas nitriding and it was found to be less than 0.6 % (Table.6.2).

Table 6.1 Microstructural and mechanical properties of nanostructured thin TiAlN and AlCrN coated ASTM-SA213-T-22 boiler steel

Coating	Surface Roughness (nm)	Particle Size (nm)		Coating Thickness (μm)	Porosity (% age)	Coating Color
		Scherrer Formula	AFM Analysis			
Nanostructured TiAlN Coating	04.52	18	22	6.3	< 0.45	violet-grey
Nanostructured AlCrN Coating	06.19	25	27	4.2	< 0.45	light-grey

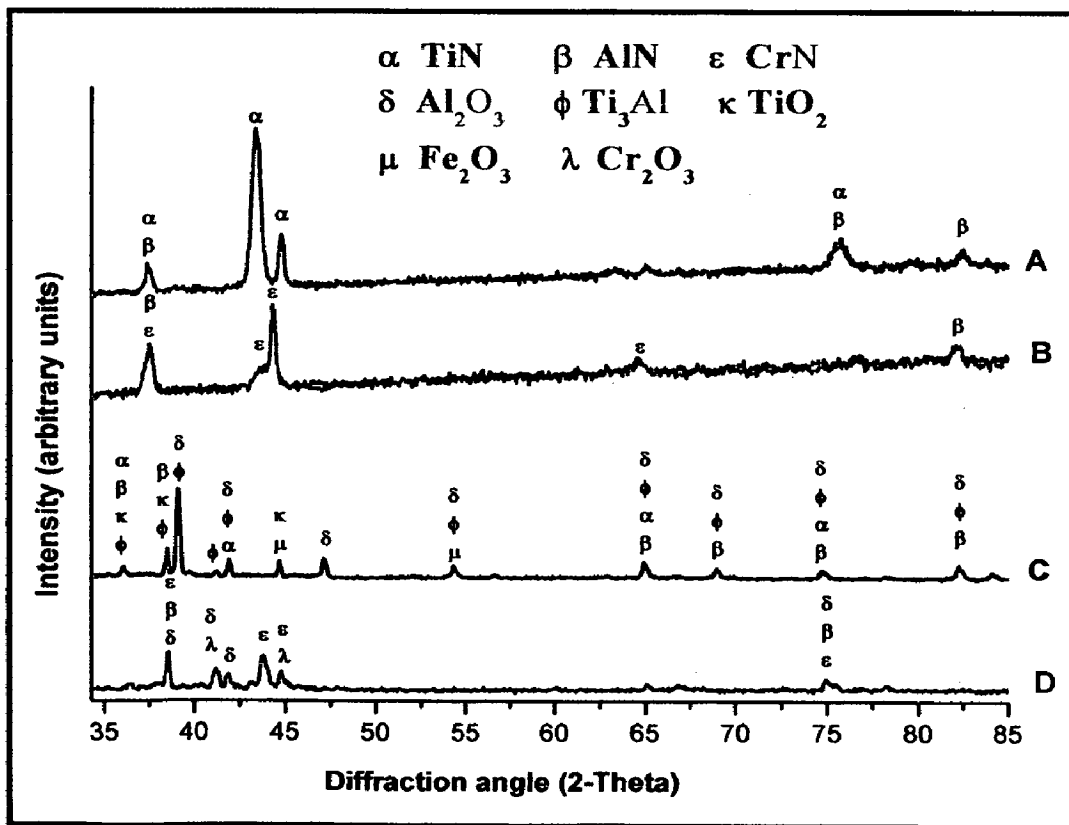


Fig. 6.3 Surface-scale morphology and EDAX patterns from different spots on as coated ASTM-SA213-T-22 boiler steel (a) Nanostructured TiAlN coating, (b) Nanostructured AlCrN coating, (c) Conventional TiAlN coating, (d) Conventional AlCrN coating

Table 6.2 Microstructural and mechanical properties of conventional thick TiAlN and AlCrN coated ASTM-SA213-T-22 boiler steel

Coating	Surface Roughness (μm)	Coating Thickness (μm)	Porosity (% age)		Bond Strength (MPa)	Coating Color
			<i>As Sprayed</i>	<i>After Gas Nitriding</i>		
Conventional TiAlN Coating	13.10-16.12	170	1.00-4.00	< 0.6	68.74	light-grey
Conventional AlCrN Coating	10.63-15.60	142	2.50-4.10	< 0.6	54.69	Bluish-grey

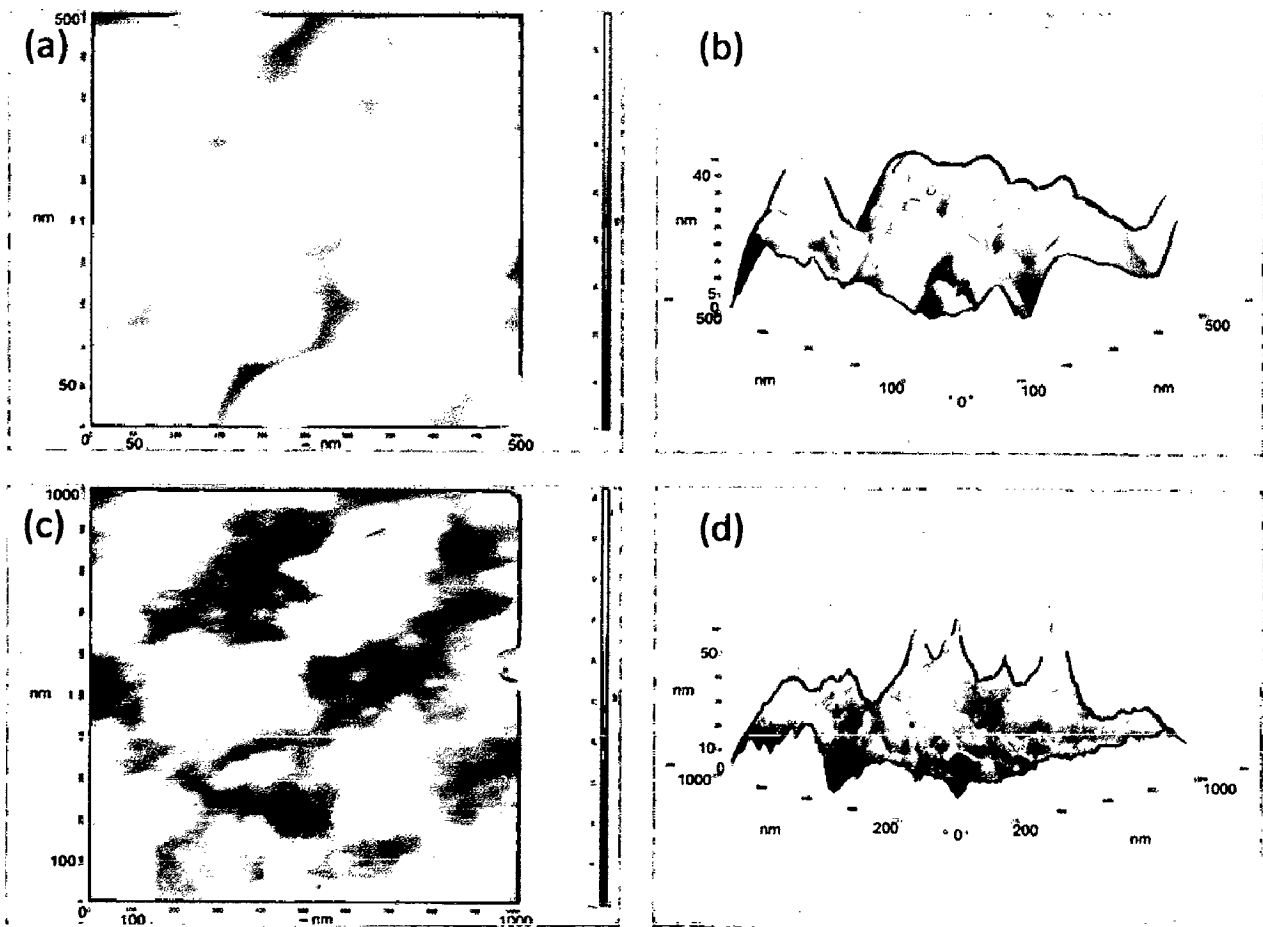


Fig. 6.4 2D and 3D AFM images for the as coated ASTM-SA213-T-22 boiler steel (a) & (b) Nanostructured TiAlN coating, (c) & (d) Nanostructured AlCrN coating

6.1.1.2.3 AFM analysis of the as deposited nanostructured thin coatings

The surface topography of the nanostructured thin TiAlN and AlCrN coatings was studied using Atomic Force Microscope (NT-MDT: NTEGRA Model) in semi contact mode. Figure 6.4 shows the AFM surface morphology (2D and 3D) of the nanostructured thin TiAlN and AlCrN coatings deposited on T-22 boiler steel. The difference in the morphology between the two coatings can be inferred by comparing the 2D images in Fig. 6.4 (a) and (c); however a comparison of the coatings could be made by viewing 3D images in Fig. 6.4 (b) and (d). As the axis scale indicates the overall roughness of the nanostructured TiAlN coating (Fig. 6.4.b) is less than that of AlCrN coating (Fig.6.4.d). The surface roughness and particle size in the coatings was also provided by AFM analysis; which are reported in Table.6.1. The surface roughness in case of nanostructured TiAlN coating was observed 04.52 nm and 06.19 nm in case of nanostructured AlCrN coating (Table.6.1). The nanostructured thin TiAlN coating had shown lesser particle size (22 nm) as compared to nanostructured thin AlCrN coating (27 nm).

6.1.1.2.4 Surface roughness (R_a) values of the conventional thick coatings

The coating surface was very rough in case of conventional thick TiAlN and AlCrN coatings due to the presence of unmelted/partially melted particles and the roughness was found to be in the range of 13.10-16.12 μm and 10.63-15.60 μm respectively.

6.1.1.2.5 Evaluation of microhardness and bond strength of conventional coatings

The hardness of the coatings has been measured along the cross-section of the conventional thick TiAlN and AlCrN coated T-22 boiler steel. Figure 6.5 shows the microhardness profiles along the cross-section of the coatings as a function of distance from the coating-substrate interface. The critical microhardness value of the substrate T-22 boiler steel was found to be in the range 250-300 Hv. From the microhardness profiles (Fig.6.5) it is obvious that the conventional TiAlN coating has shown maximum microhardness of the order of 800-900 Hv. The conventional thick AlCrN coating has shown microhardness of the order of 600-700 Hv.

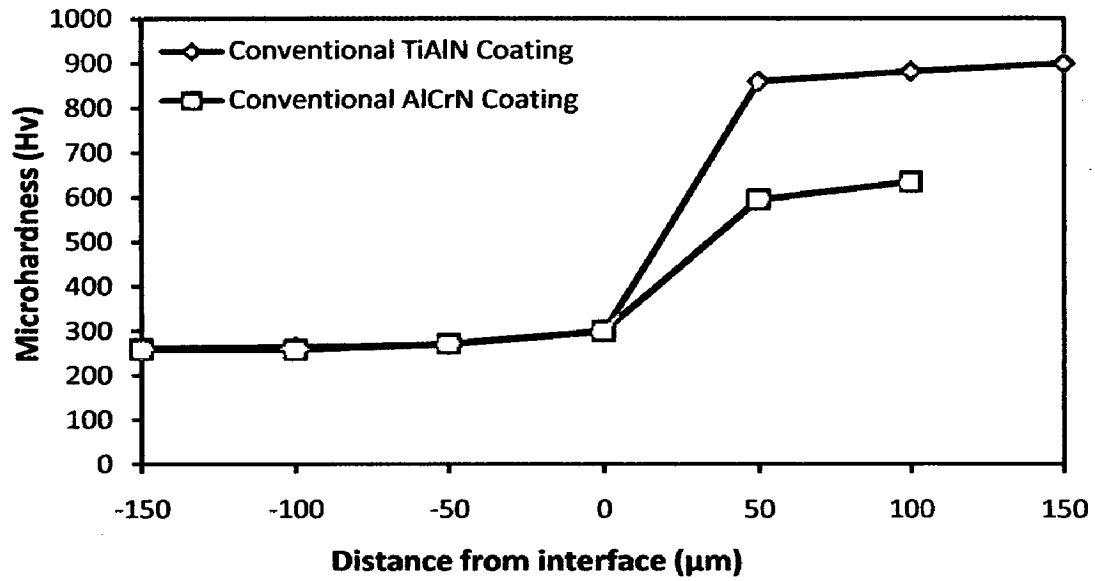


Fig. 6.5 Microhardness profile across the cross-section for Conventional TiAlN and Conventional AlCrN coating on ASTM-SA213-T-22 boiler steel

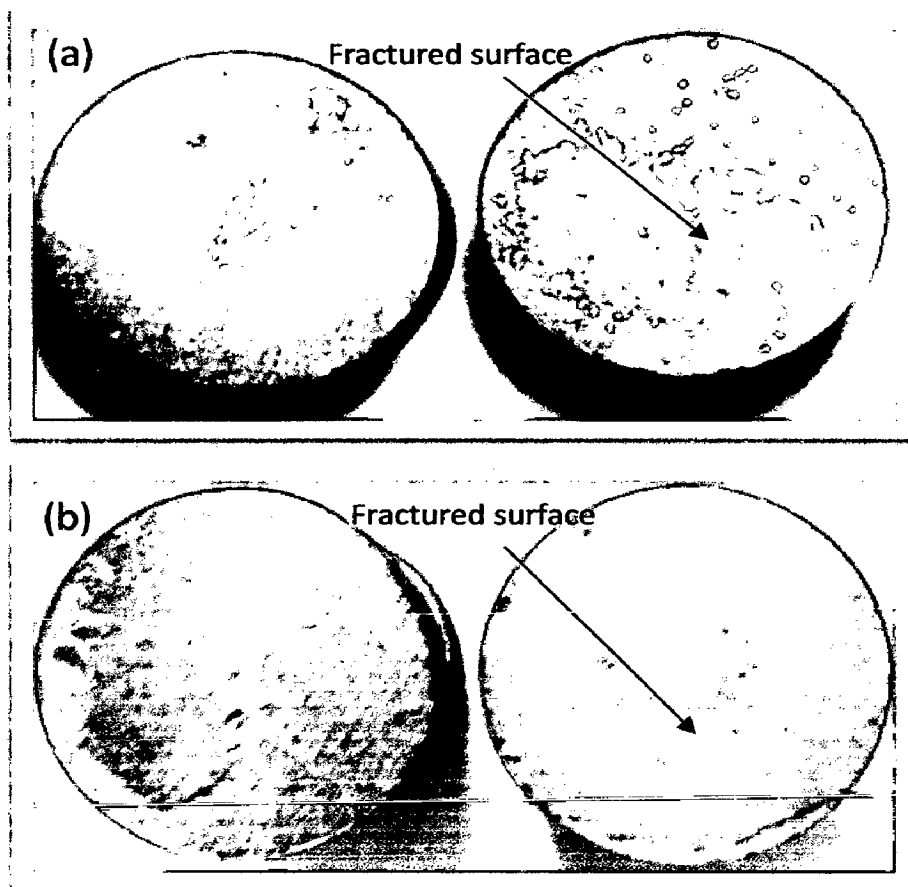


Fig. 6.6 Fracture surfaces of a Plasma sprayed gas nitride specimen after ASTM C633 tensile test; (a) Conventional TiAlN coating, (b) Conventional AlCrN coating

The bond strength of the conventional thick TiAlN and AlCrN coatings was measured on three specimens as per ASTM standard C633-01. The coatings failed at the substrate-coating interface while remaining attached to the adhesive (Fig.6.6). Average bond strength of 68.74 MPa and 54.69 MPa was observed in case of conventional TiAlN and AlCrN coatings respectively (Table.6.2).

6.1.1.2.6 Surface morphology of coatings

SEM micrographs along with EDS spectrum reveal the surface morphology of the nanostructured and conventional TiAlN and AlCrN coated ASTM-SA213-T-22 boiler steel; are shown in Fig.6.7. Micrograph (Fig.6.7.a) for nanostructured thin TiAlN coating at high magnification (10000 X) indicates grey matrix with some black and white contrast regions. Dense structure with lower porosity is observed in the coating microstructure and also it is free from cracks. EDAX analysis at point 1 and point 2 in Fig.6.7 indicates the presence of Ti, Al and N with negligible amount of Mo, O and Fe. The black colored areas contain higher amount of Ti and less concentration of Al as compared to the white contrast region. In case of nanostructured thin AlCrN coated T-22 boiler steel, the SEM micrograph indicates dense grey colored coating with tiny dark grey particles dispersed in the matrix. EDAX point analysis (Point 3 and 4 in Fig.6.7) shows, the coating is rich in Al, Cr and N along with small amount of Mo, Fe and oxygen (Fig.6.7.b). The micrographs in case of conventional plasma sprayed gas nitride TiAlN and AlCrN coatings are shown in Fig.6.7(c and d). In general microscopic features indicate that the conventional coatings are homogeneous and massive, free from cracks. Presence of some oxide stringers as well as open pores has been noticed in general in the conventional coatings. The EDAX point analysis (Point 5 and 6 on Fig.6.7); in case of conventional TiAlN coating indicates the higher concentration of Ti and Al in the coating along with N and oxygen. The presence of Al and Cr along with N and oxygen is revealed by EDAX analysis in case of conventional AlCrN coating (Point 7 and 8 on Fig.6.7).

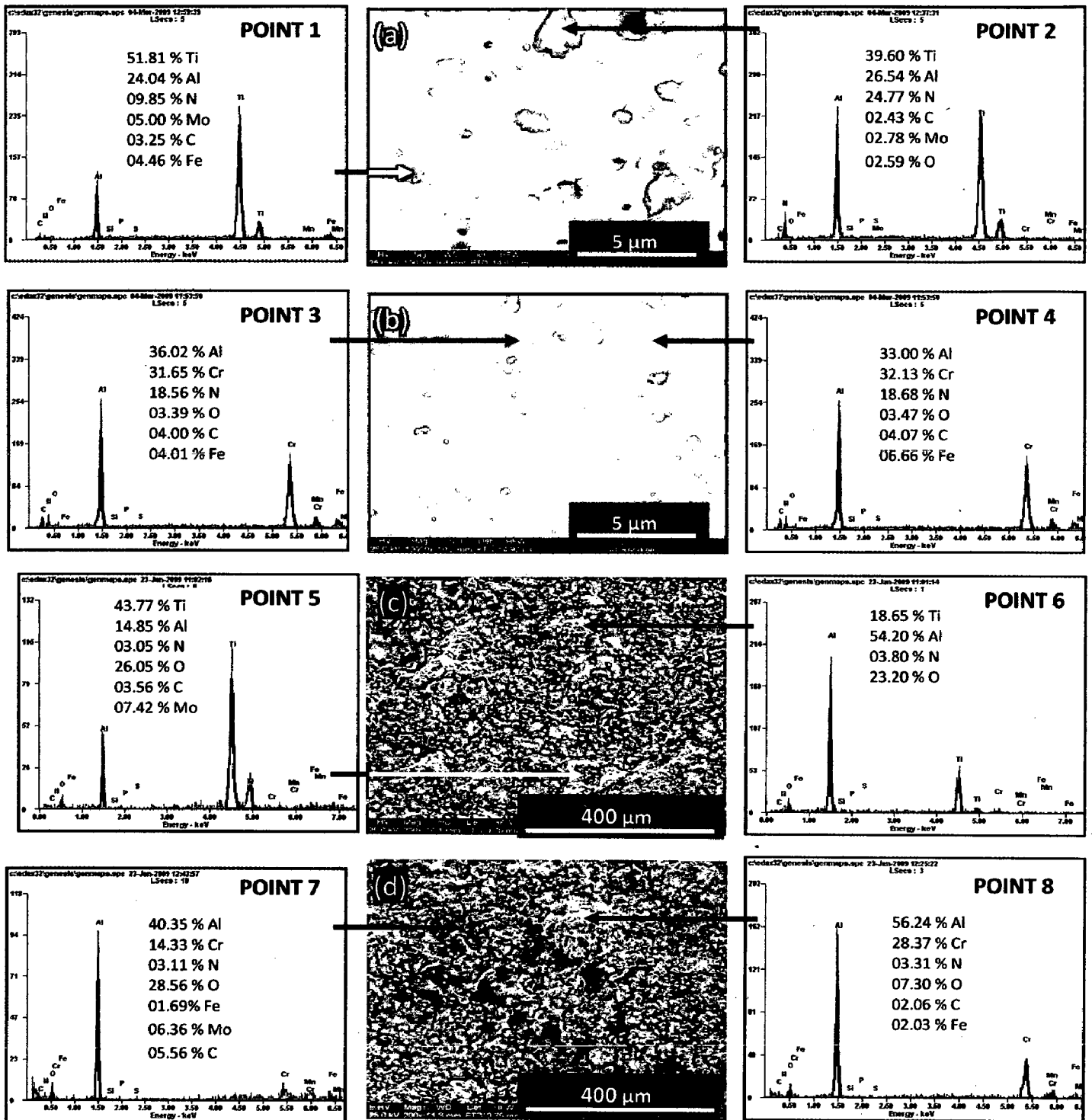


Fig. 6.7 Surface-scale morphology and EDAX patterns from different spots on as coated ASTM-SA213-T-22 boiler steel (a) Nanostructured TiAlN coating (10000 X), (b) Nanostructured AlCrN coating (10000 X), (c) Conventional TiAlN coating (200 X), (d) Conventional AlCrN coating (200 X)

6.1.1.3 Cross-sectional analysis

6.1.1.3.1 Coating thickness

The as-coated samples were cut across the cross section using Buehler Isomet 1000 precision saw and mounted in transoptic mounting resin and subsequently mirror polished to obtain scanning electron back scattered micrographs and X-ray mapping of different elements for coated T-22 boiler steel. The coating thickness values were measured from SEM back scattered micrographs as shown in Fig.6.8; and the average coating thickness is reported in Table.6.2. The measured average coating thickness values for nanostructured thin and conventional thick TiAlN and AlCrN coatings are 6.3, 4.2, 170 and 142 μm respectively.

6.1.1.3.2 X-Ray mapping

BSEI and X-ray mapping analysis for nanostructured and conventional TiAlN and AlCrN coated ASTM-SA213-T-22 boiler steel is shown in Fig. 6.8. The BSEI and X-ray mapping analysis of the nanostructured TiAlN coated T-22 boiler steel is presented in Fig.6.8 (a). The X-ray mapping indicates presence of Al and Ti along with small amount of N in the coating and no diffusion of Fe from the substrate has been observed. In case of nanostructured thin AlCrN coated T-22 boiler steel; the BSEI and X-ray mapping are shown in Fig. 6.8.b. The X-ray mapping indicates the presence of Al and Cr along with some concentration of N in the coating. In case of conventional thick TiAlN coated T-22 boiler steel, Fig.6.8 (c), Al and Ti rich coating along with negligible amount of N and O; has been observed. Minor diffusion of Fe from the substrate has taken place as indicated by X-ray mapping analysis. Figure.6.8 (e) depicts the BSEI and X-ray mapping in case of conventional AlCrN coated T-22 boiler steel. The coating is rich in Al and Cr with some presence of N and O. The X-ray mapping analysis indicates the presence of Fe in the coating; which may have diffused from the substrate.

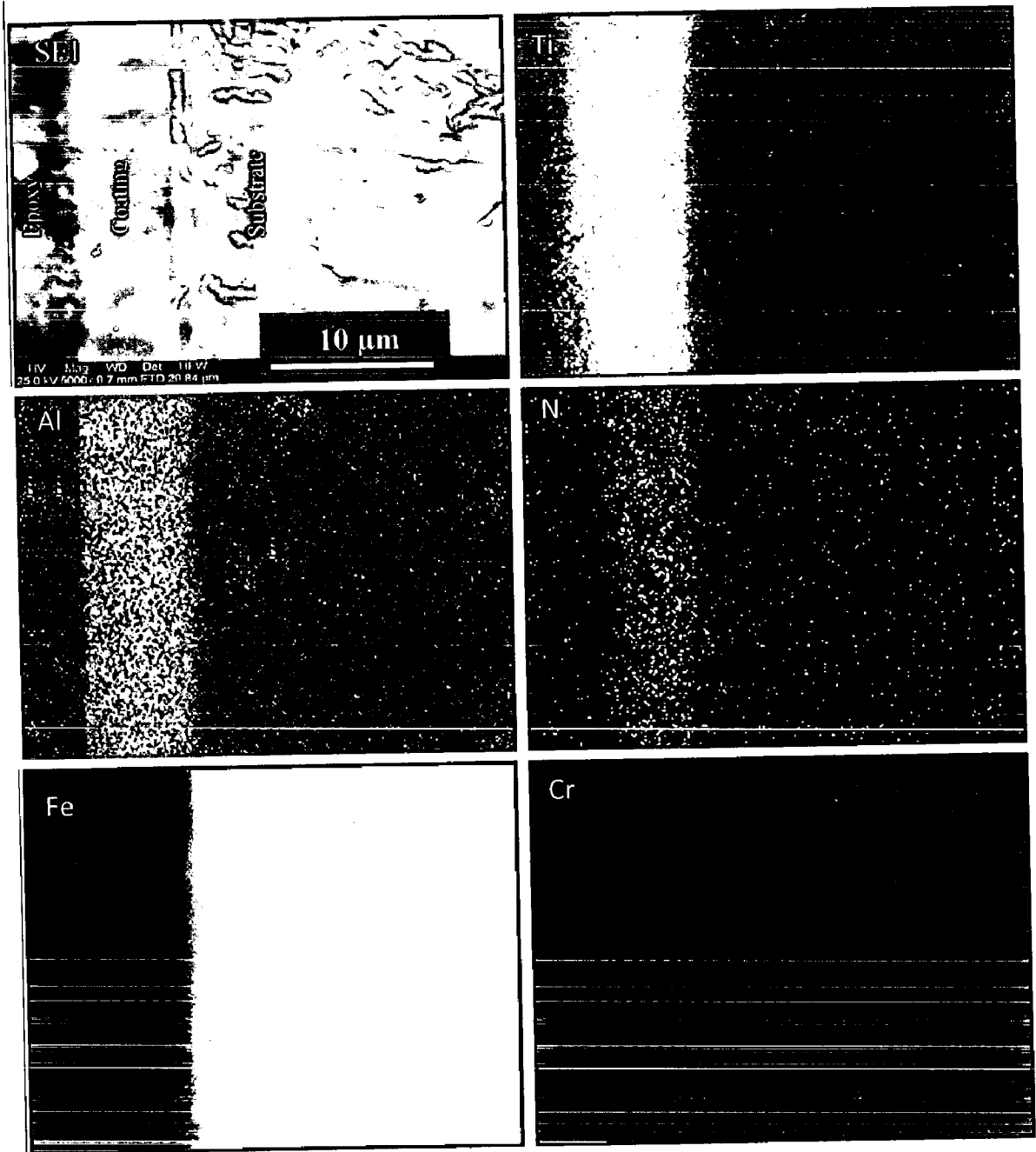


Fig. 6.8 (a) Composition image (SEI) and X-ray mapping of the cross-section of as-coated nanostructured TiAlN coating on ASTM-SA213-T-22 boiler steel

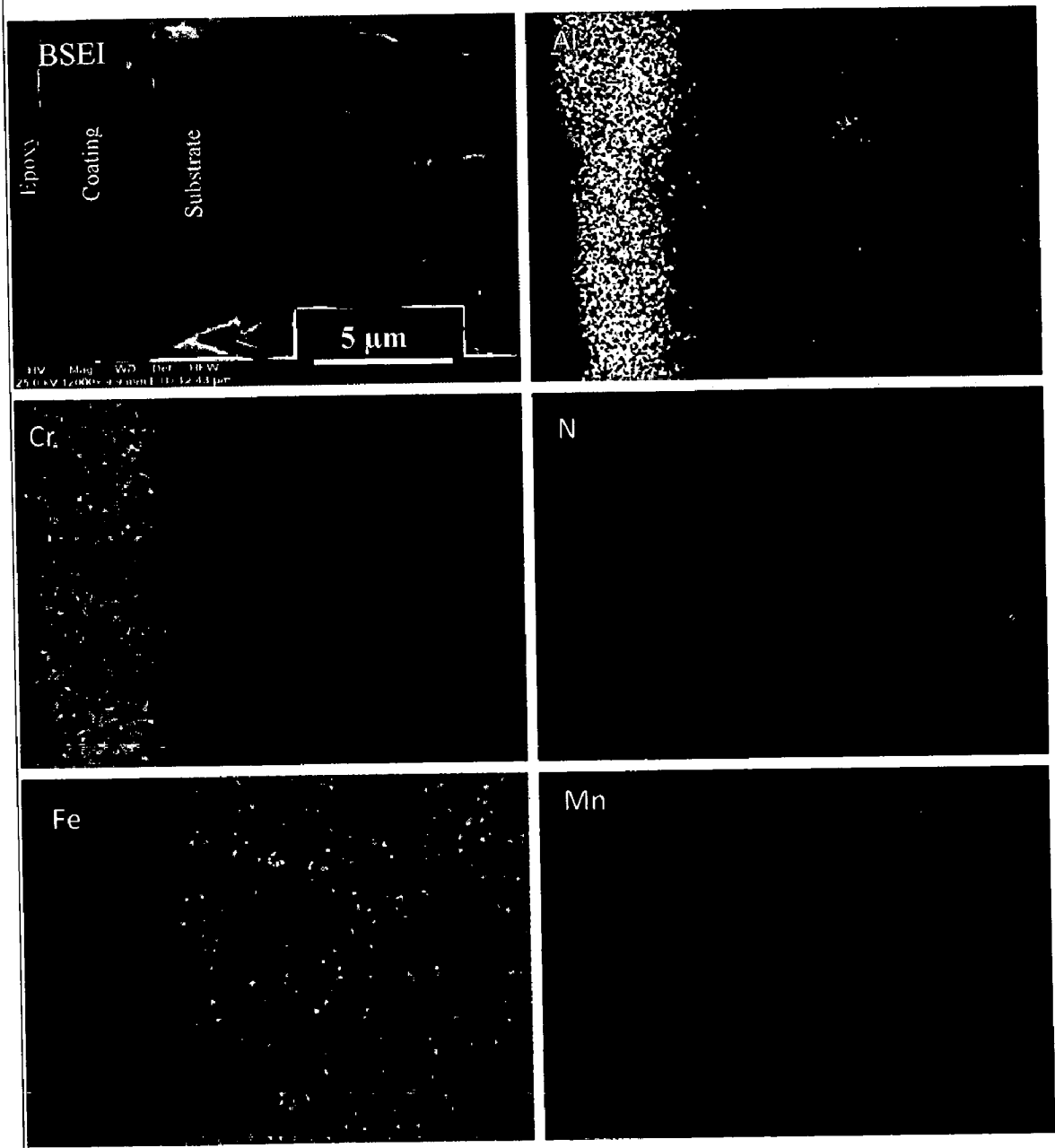


Fig. 6.8 (b) Composition image (BSEI) and X-ray mapping of the cross-section of as-coated nanostructured AlCrN coating on ASTM-SA213-T-22 boiler steel

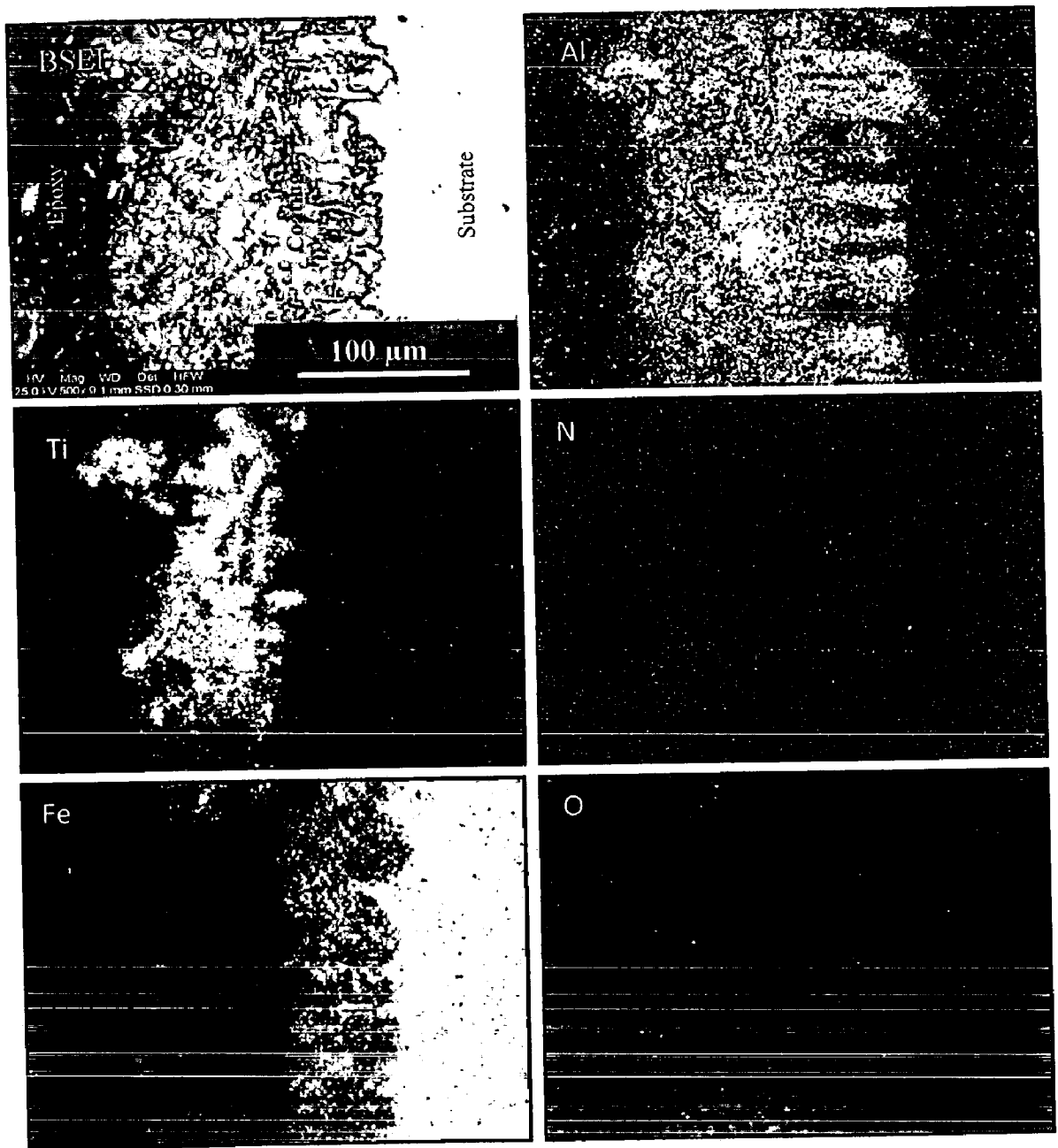


Fig. 6.8 (c) Composition image (BSEI) and X-ray mapping of the cross-section of as-coated conventional TiAlN coating on ASTM-SA213-T-22 boiler steel

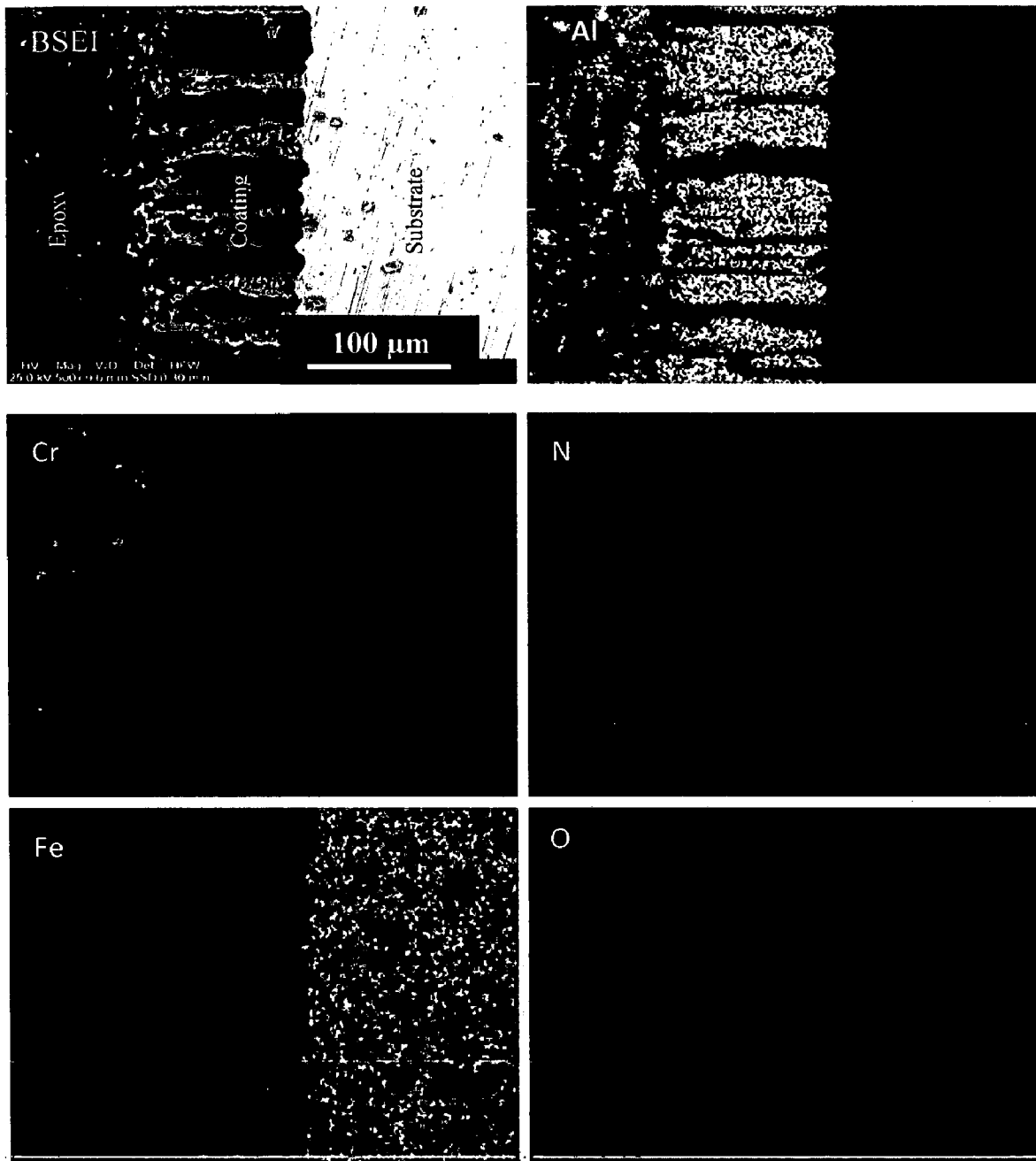


Fig. 6.8 (d) Composition image (SEI) and X-ray mapping of the cross-section of as-coated conventional AlCrN coating on ASTM-SA213-T-22 boiler steel

6.1.2 Discussion

The nanostructured thin TiAlN and AlCrN coatings on ASTM-SA213-T-22 boiler steel were obtained using a front-loading Balzer's rapid coating system (RCS) machine at Oerlikon Balzers Ltd. Gurgaon (India). In case of conventional thick TiAlN and AlCrN coatings; the plasma spray coatings were obtained at Anod Plasma Ltd. Kanpur (India) using a 40 kW Miller Thermal Plasma Spray apparatus. The surface appearance of nanostructured TiAlN coating was violet grey in color and light grey in case of nanostructured AlCrN coating (Fig.6.1). In case of conventional thick coatings: the surface appearance of conventional TiAlN and AlCrN coatings was grey with some bluish shining (Fig.6.1). The surface of conventional thick coatings was rough. As inferred from optical micrographs (Fig.6.2 a & b) that the nanostructured coatings were dense with uniform microstructure. It is evident from the microstructure that the coatings contain some pores and inclusions. In case of conventional thick coatings (Fig.6.2.c & d); the massive microstructure could be observed with irregularly shaped grains.

The phases identified by XRD analysis (Fig.6.3) for nanostructured thin TiAlN coating are TiN and AlN. The phases analyzed are also in agreement with that reported by Yoo et al. (2008), Falub et al. (2007) and Man et al. (2004). The prominent phases in case of nanostructured AlCrN coating are CrN and AlN which are in agreement with the findings of Reiter et al. (2005) and Endrino et al. (2006). Further, the main phases identified for the conventional thick TiAlN coating are Al_2O_3 , TiN, Ti_3Al , AlN and small peaks of TiO_2 and Fe_2O_3 . The phases identified in case of conventional thick AlCrN coating are CrN, AlN, and Al_2O_3 with minor peaks of Cr_2O_3 . The presence of metal nitride phases indicates that the gas nitriding process has successfully produced the desired coatings. Further, the phases analyzed are also in agreement with that reported by Adachi and Nakata (2007).

The grain size (Table.6.1) of the nanostructured thin coatings was estimated from Scherrer formula (Cullity, 1970) and further verified by AFM analysis (reported in Table 6.1). The particle size determined by AFM analysis is in good agreement with the results obtained from Scherrer formula. The nanostructured thin TiAlN coating had shown smaller particle size (22 nm) as compared to nanostructured thin AlCrN coating (27 nm).

The coating thickness was measured along the cross-section for some of the randomly selected samples and reported in Table 6.1 and 6.2. The coatings thickness was

observed to be 6.3 and 4.2 μm in case of nanostructured TiAlN and AlCrN coatings respectively. The self-disintegration of thicker coatings usually restricts the thickness of the coatings (Sidhu et al., 2004). In case of conventional thick coatings; it was possible to obtain a thickness in range of 150-200 μm for Ti-Al and Al-Cr coatings. After coating deposition process; the gas nitriding was done in lab in order to obtain hard metal nitride coatings. The coating thickness was measured along the cross-section for some randomly selected samples and reported in Table 6.2. The coatings thickness was observed as 170 and 142 μm in case of conventional thick TiAlN and AlCrN coatings respectively.

The surface roughness was also measured with AFM analysis and reported in Table 6.1. As the axis scale indicates the overall roughness of the nanostructured TiAlN coating (Fig.6.4.b) is less than that of AlCrN coating (Fig.6.4.d). The coating surface was very rough in case of conventional thick TiAlN and AlCrN coatings due to the presence of unmelted/partially melted particles. The negligible porosity values for as coated nanostructured thin TiAlN and AlCrN coatings were observed; which were less than 0.45 % (Table.6.1). The measured porosity values of plasma sprayed and gas nitrided coatings are reported in Table 6.2. The measured values of porosity (1.00 - 4.10 %) for as sprayed conventional Ti-Al and Al-Cr coatings are almost in close agreement with the findings of Chen et al. (1993), Erickson et al. (1998), Hidalgo et al. (1998 and 1999), Singh (2003) and Sidhu et al. (2004 and 2005) for thermal plasma sprayed coatings. Further, the porosity values found to be less than 0.6% after gas nitriding, which may be because of elimination of microstructural in-homogeneities by filling of pores and voids by nitrogen during gas nitriding.

Hardness is the most frequently quoted mechanical property of the coatings (Tucker, 1994). The observed microhardness values (Fig.6.5) for the conventional coatings are within the range of microhardness values reported for plasma coatings by Adachi and Nakata (2007), Vuoristo et al. (1994), Chen and Hutchings (1998) and Westergard et al. (1998). Microhardness plots indicate some increase in the microhardness of substrate steel at the substrate coating interface. The hardening of the substrates as observed in the current study might have occurred due to the high speed impact of the coating particles during plasma spray deposition similar to the findings of Singh (2003), Hidalgo et al. (1997, 1998, 1999 and 2000) and Sidhu et al. (2004 and 2005). The observed non-uniformity in the hardness values along the thickness of the coatings may be due to the

microstructural changes along the cross section of the coatings (Staia et al., 2001). Moreover, the microhardness and other properties of the thermal spray coatings are anisotropic because of typical splat structure and directional solidification (Tucker, 1994). The bond strength of the conventional thick TiAlN and AlCrN coatings was measured on three specimens as per ASTM standard C633-01. The coatings failed at the substrate-coating interface while remaining attached to the adhesive (Fig.6.6). Average bond strength of 68.74 MPa and 54.69 MPa was observed in case of conventional TiAlN and AlCrN coatings respectively. The bond strength in case of conventional TiAlN coatings (68.74 MPa) is almost in good agreement with the results reported by Adachi and Nakata (2007).

Surface EDAX analysis supported the results obtained by XRD (Fig.6.3) and X-ray mapping analysis (Fig.6.8) in all the coatings. The presence of Ti, Al and N with negligible amount of Fe (in nanostructured TiAlN coating), Al, Cr and N along with small amount of Fe and oxygen (in nanostructured TiAlN coating), the higher concentration of Ti and Al in the coating along with some amount of N and oxygen (in conventional TiAlN coating) and Al and Cr along with N and oxygen (in conventional AlCrN coating); is revealed by surface EDAX analysis (Fig.6.7). Also, the XRD analysis indicates the presence of the oxide phases in the coatings i.e. Al_2O_3 , TiO_2 and Fe_2O_3 in case of conventional TiAlN coating and the presence of Al_2O_3 and Cr_2O_3 in case of conventional AlCrN coatings. The oxides may form due to the in-flight oxidation during spraying process and/or preexisting in the feed material (Bluni and Mardar, 1996). The latter reason for the oxides formation in the structure of coatings under study looks to be more relevant as the chances of in-flight oxidation are meager in case of the shrouded plasma spraying. Deshpande et al. (2006) proposed that, during in-flight oxidation, a layer of oxide is formed on the molten particle due to chemical reactions between the surface of the liquid phase and oxygen or due to diffusion of oxygen into the liquid. The turbulent mixing of the liquid part of the powder particle during its flight destroys the surface layer of oxides and causes the oxides to be distributed more uniformly through the bulk volume of the particle. However, when temperature of the particle starts dropping during later part of the flight, these oxides tend to solidify and a thin oxide shell would form around the droplet. The oxidation time during thermal spray coating is short typically less than 0.01 s, and can occur in either the solid or molten state. The oxidation of coatings is not always

harmful, it is equally important to control and understand the different aspects of oxidation of coatings; therefore, it is important to find an optimum level for oxidation of coatings (Herman, 1988; Korpiola and Vuoristo, 1996; Nerz et al., 1992).

6.1.3 Conclusions

The nanostructured thin TiAlN and AlCrN coatings (by physical vapour deposition process at Oerlikon Balzers Ltd. Gurgaon, India) and conventional thick TiAlN and AlCrN coatings (by plasma spraying process at Anod Plasma Ltd. Kanpur, India; followed by gas nitriding process) were successfully deposited on ASTM-SA213-T-22 boiler steel. The coatings were characterized for microstructural features and hardness in present work. The following observations were made based on the present study:

1. The nanostructured thin TiAlN and AlCrN coatings exhibited negligible porosity values for as coated; which were less than 0.45 %. The conventional TiAlN and AlCrN coatings showed; higher porosity values (1.00-4.10 %) for as sprayed conventional Ti-Al and Al-Cr coatings which after gas nitriding were found to be less than 0.6 %.
2. The presence of metal nitride phases as identified by XRD analysis indicates that the gas nitriding process has successfully produced the desired coatings.
3. The grain size of the nanostructured thin coatings was estimated from Scherrer formula and further verified by AFM analysis. The particle size determined by AFM analysis is in good agreement with the results obtained from Scherrer formula. The nanostructured thin TiAlN coating had shown smaller particle size (22 nm) as compared to nanostructured thin AlCrN coating (27 nm).
4. The surface roughness of nanostructured TiAlN coating was observed to be 4.52 nm and 6.19 nm for nanostructured AlCrN coating. The coating surface was very rough in case of conventional thick TiAlN and AlCrN coatings.
5. A good adhesion of the conventional thick TiAlN and AlCrN coatings was evident from bond test results. Average bond strength of 68.74 MPa and 54.69 MPa Psi was observed in case of conventional TiAlN and AlCrN coatings respectively.

6.2 OXIDATION STUDIES IN AIR

Some power plants in India are using ASTM-SA213-T-22 as boiler tubes material due to its performance in stringent service conditions of pressure and temperature. The metallic components in fuel-conversion or power generating units, invariably, subjected to thermal cycling or thermal fluctuation under the actual service conditions, which lead to failure of the protective Cr_2O_3 and Al_2O_3 layers (Mitra et al., 1993). Therefore, the present work has been focused to compare the cyclic oxidation behavior of conventional thick (by plasma spraying and gas nitrided) and nanostructured thin (by physical vapor deposition process) TiAlN and AlCrN coatings on ASTM-SA213-T-22 boiler steel at 900°C.

6.2.1 Results

6.2.1.1 Visual observations

The macrographs for uncoated and coated ASTM-SA213-T-22 boiler steel subjected to cyclic oxidation in air at 900°C for 50 cycles are shown in Fig.6.9. For the uncoated T-22 boiler steel, a grey colored scale appeared on the surface right from the 1st cycle. The surface appearance of the scale turned to brownish grey tone which remained till the end of 50th cycle. This bare steel showed spalling of scale just after the 5th cycle, which continued till the end of 50 cycles. At the end of cyclic study, irregular and fragile scale was observed with deep cracks and blackish grey color (with brownish grey appearance at some places) surface appearance, which can also be seen in Fig.6.9 (a).

Color of the oxide scale at the end of the study was observed to be grey with some blackish grey areas on the surface, in case of nanostructured thin TiAlN coated T-22 boiler steel (Fig.6.9 .b). The color of the scale after 2nd cycle was observed as whitish brown which changes to grey with golden and black spots at few areas after subsequent cycles. After 20th cycle severe swelling and peeling of the oxide scale was observed. Some of the scale was seen getting detached from the surface of the nanostructured TiAlN coated T-22 boiler steel. The nanostructured thin AlCrN coated T-22 boiler steel has shown the formation of smooth scale without the presence of cracks, when subjected to cyclic oxidation in air at 900°C for 50 cycles. Color of the oxide scale at the end of the study was observed to be dark grey, as shown in Fig.6.9 (c). The scale was

lustrous without any tendency to spall. Golden and ink blue reflections were observed in the scale, after the completion of 2nd cycle, which turned to dark grey subsequently. A visual observation of conventional thick TiAlN coated T-22 boiler steel showed the formation of light grey color in the middle of the sample along with bluish grey sides after 2nd cycle. After 21st cycle, a small portion of scale at corner falls in the boat. Severe spalling was observed after 29th cycle.

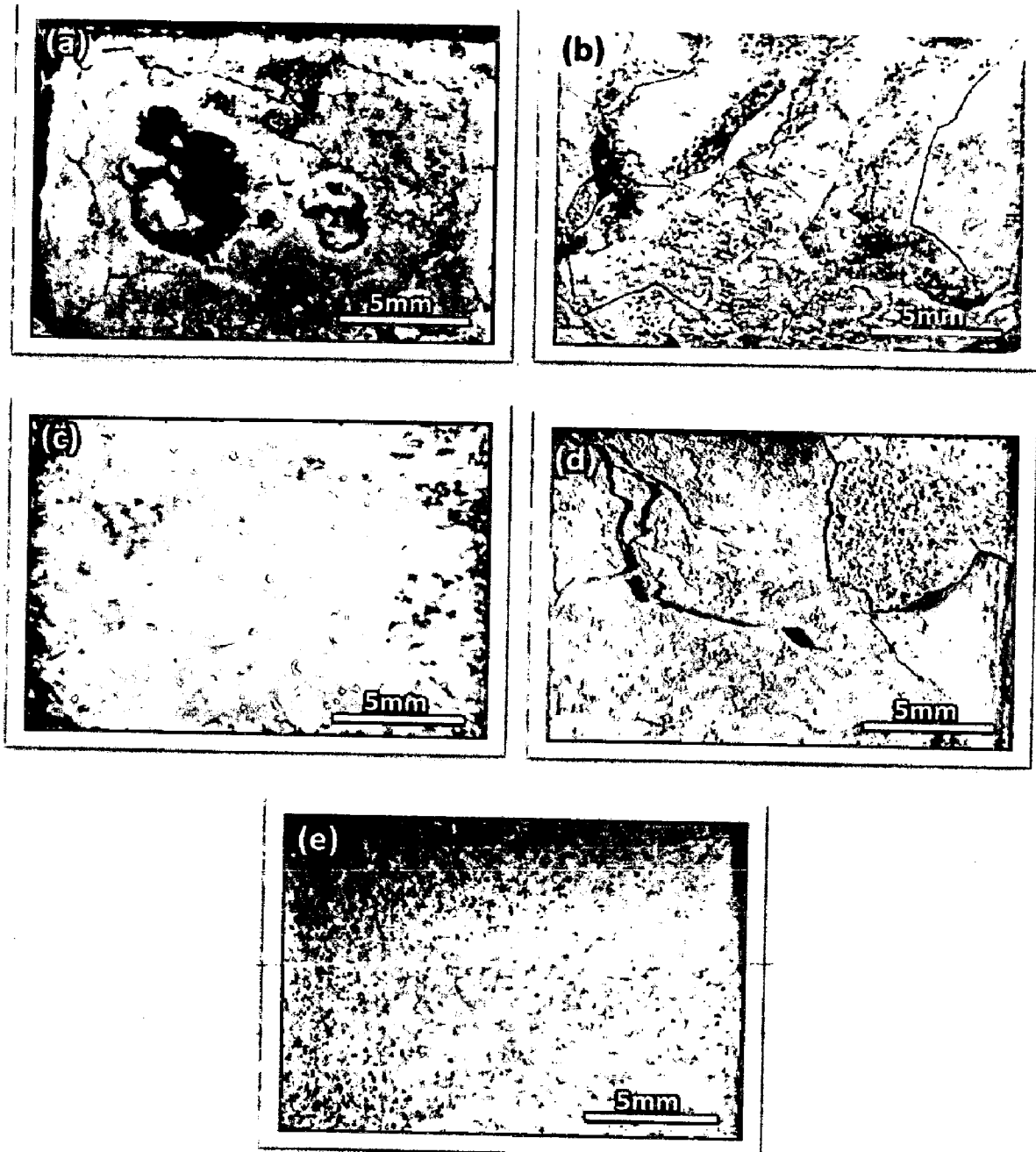


Fig. 6.9 Surface macrographs of uncoated and coated ASTM-SA213-T-22 boiler steel after exposure to cyclic oxidation in air at 900°C for 50 cycles: (a) Uncoated T-22 boiler steel, (b) Nanostructured TiAlN coating, (c) Nanostructured AlCrN coating, (d) Conventional TiAlN coating, (e) Conventional AlCrN coating

At the end of 50 cycles, whitish grey colored scale (with cracks) was observed as shown in Fig.6.9 (d). In case of conventional thick AlCrN coated T-22 boiler steel, the surface becomes rough after first cycle and dark blue line was observed at one of the edges (Fig.6.9.e). After 9th cycle, bluish dots were seen on the surface which remains up to end. At the end of the study, the scale was found to be adherent with light grey surface appearance.

6.2.1.2 Weight change measurements

Weight gain per unit area (mg/cm^2) versus time expressed in number of cycles plot for coated and bare T-22 boiler steel subjected to cyclic oxidation in air at 900°C for 50 cycles, is presented in Fig. 6.10. The plots for all samples shows higher weight gain at initial cycles followed by gradual weight gain. It can be inferred from the plots that the uncoated and nanostructured thin TiAlN coated T-22 boiler steels have shown initially high rate of oxidation as compared to other coatings, followed by a nearly constant rate. After 20th cycle, the oxidation rate in case of nanostructured thin TiAlN coated sample increased abruptly up to the 50th cycle. The cumulative weight gain per unit area for the coated and uncoated T-22 boiler steel subjected to cyclic oxidation in air at 900°C for 50 cycles is shown in Fig. 6.11.

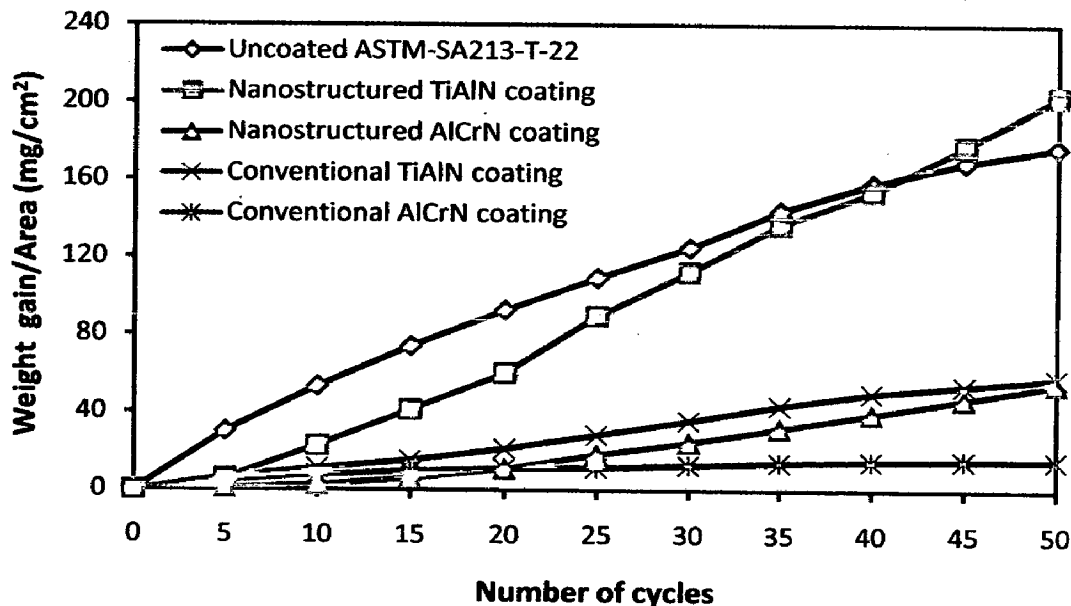


Fig. 6.10 Weight gain/area vs time (number of cycles) for the uncoated and coated ASTM-SA213-T-22 boiler steel subjected to cyclic oxidation in air at 900°C for 50 cycles

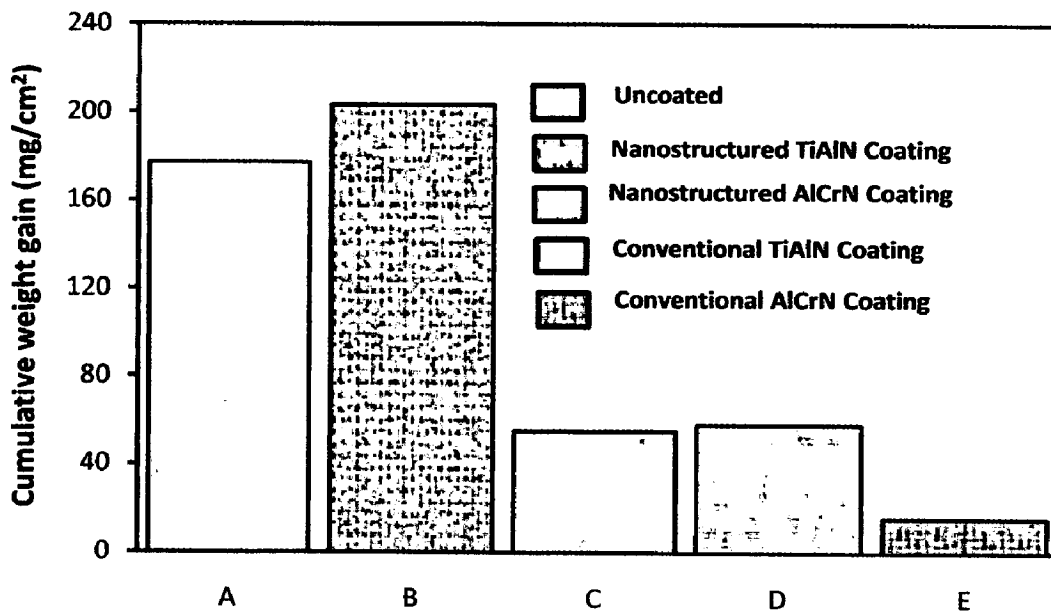


Fig. 6.11 Column chart showing cumulative weight gain per unit area for the uncoated and coated ASTM-SA213-T-22 boiler steel subjected to cyclic oxidation in air at 900°C for 50 cycles: (A) Uncoated T-22 boiler steel, (B) Nanostructured TiAlN coating, (C) Nanostructured AlCrN coating, (D) Conventional TiAlN coating, (E) Conventional AlCrN coating

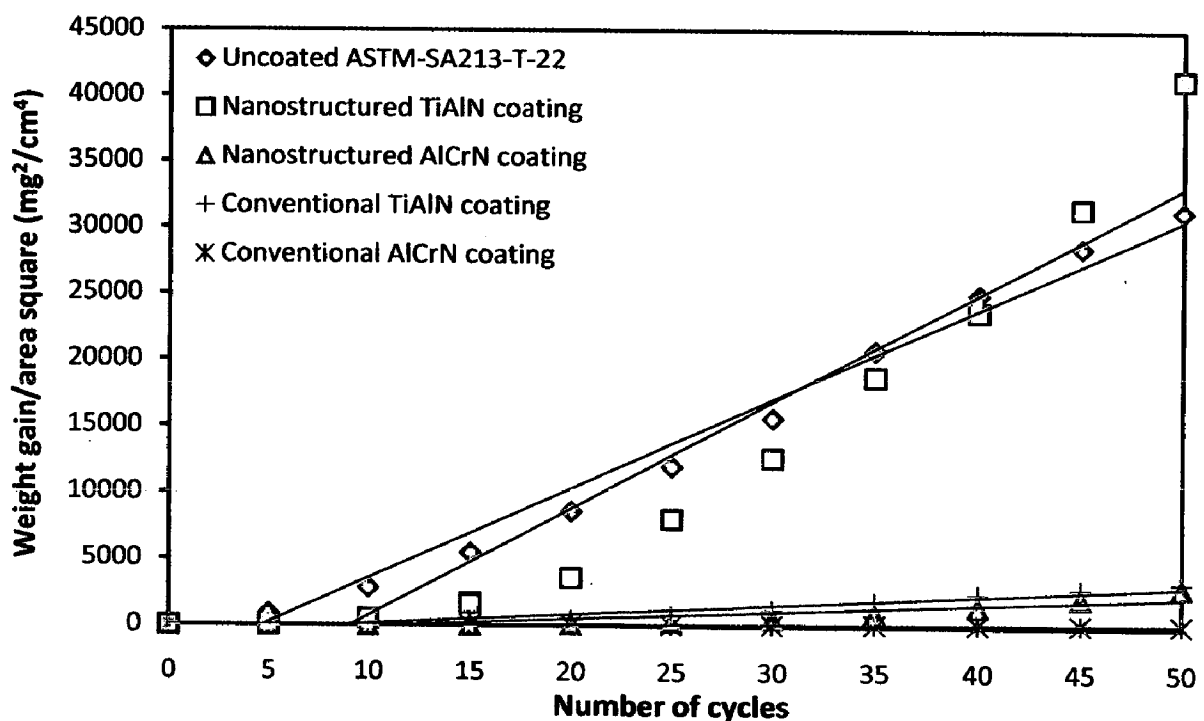


Fig. 6.12 Weight gain/area square vs time (number of cycles) for the uncoated and coated ASTM-SA213-T-22 boiler steel subjected to cyclic oxidation in air at 900°C for 50 cycles

Further, the overall weight gain is highest in case of uncoated T-22 boiler steel and is lowest in case of conventional thick AlCrN coated steel, which is 08.87% of the weight gain in case of uncoated T-22 boiler steel. Figure 6.12 shows the $(\text{weight gain/area})^2$ versus number of cycles plot for all the cases to ascertain conformance with the parabolic rate law. All the coated and uncoated T-22 boiler steel followed the parabolic rate law as evident from the Fig.6.12. The parabolic rate constant K_p was calculated by a linear least-square algorithm to a function in the form of $(W/A)^2 = K_p t$, where W/A is the weight gain per unit surface area (mg/cm^2) and 't' indicates the number of cycles representing the time of exposure. The parabolic rate constants for the bare and coated T-22 boiler steel calculated on the basis of 50 cycle's exposure data are shown in Table.1. The ' K_p ' value for the uncoated and nanostructured thin TiAlN coated T-22 boiler steel is higher than in case of other coatings.

Table 6.3 Parabolic rate constant ' K_p ' values of uncoated and coated ASTM-SA213-T-22 boiler steel subjected to cyclic oxidation in air at 900°C for 50 cycles

Substrate / Coating	$K_p \times 10^{-08} \text{ gm}^2\text{cm}^{-4}\text{s}^{-1}$
Uncoated T-22 boiler steel	18.80
Nanostructured TiAlN coating	22.52
Nanostructured AlCrN coating	01.57
Conventional TiAlN coating	02.01
Conventional AlCrN coating	00.14

6.2.1.3 Surface scale analysis

6.2.1.3.1 X-ray diffraction analysis (XRD)

XRD diffractograms for coated and uncoated T-22 boiler steel subjected to cyclic oxidation in air at 900°C for 50 cycles are depicted in Fig.6.13 (a and b) on reduced scale.

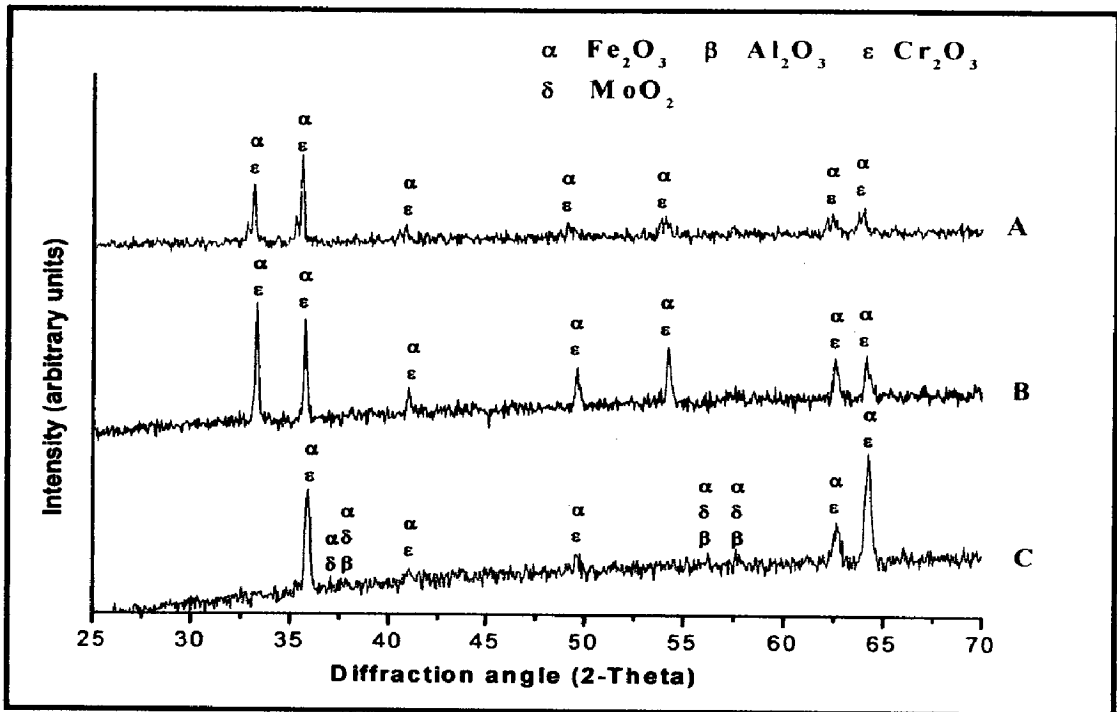


Fig. 6.13 (a) X-Ray Diffraction pattern of uncoated and coated ASTM-SA213-T-22 boiler steel exposed to cyclic oxidation in air at 900°C for 50 cycles: (A) Uncoated T-22 boiler steel, (B) Nanostructured TiAlN coating, (C) Nanostructured AlCrN coating

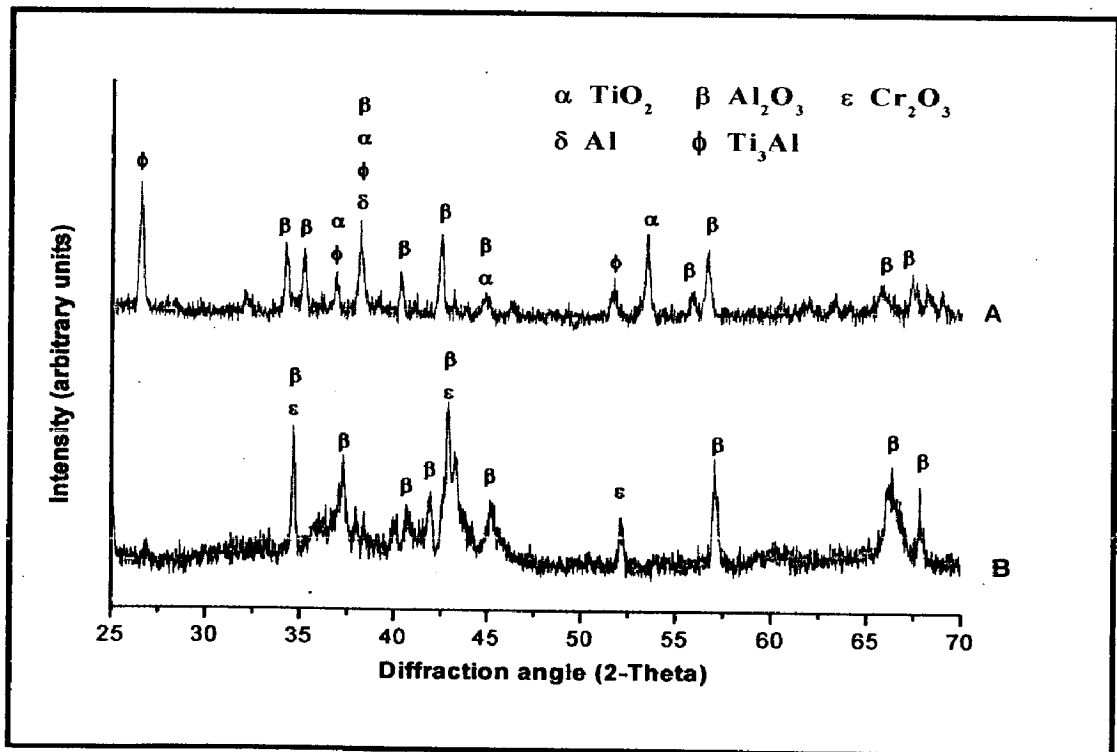
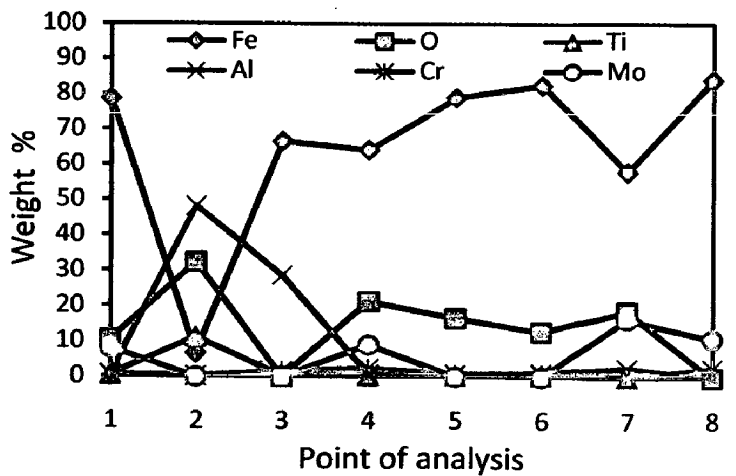
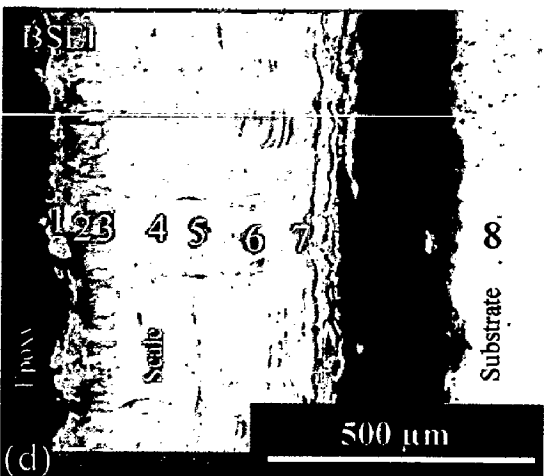
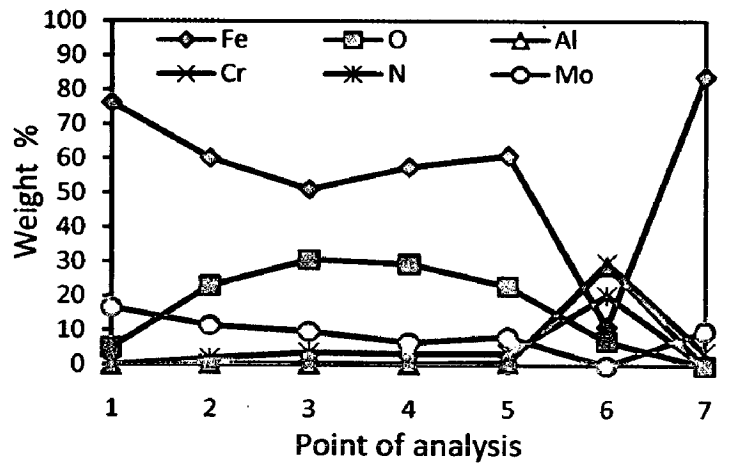
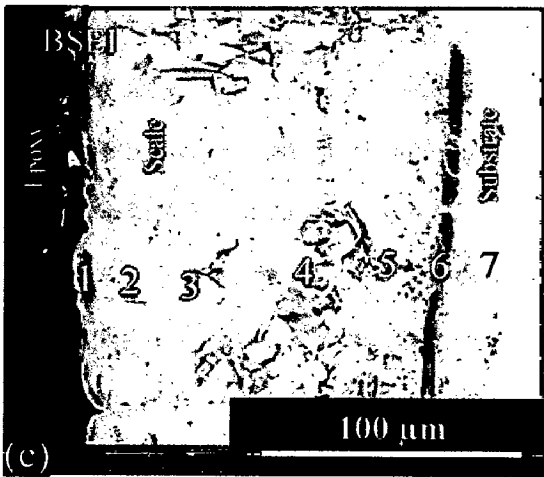
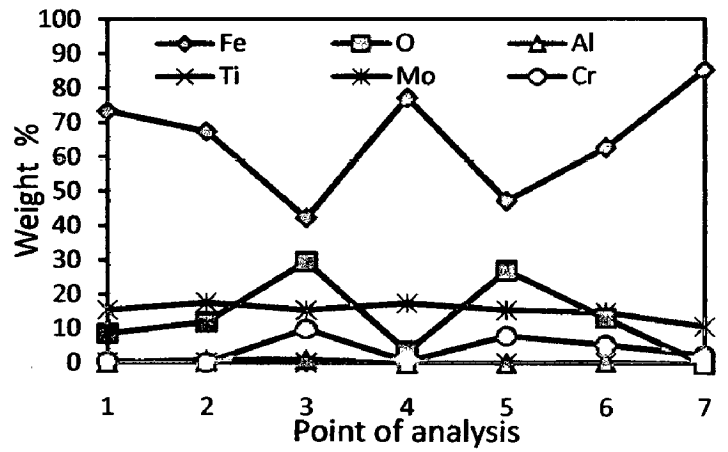
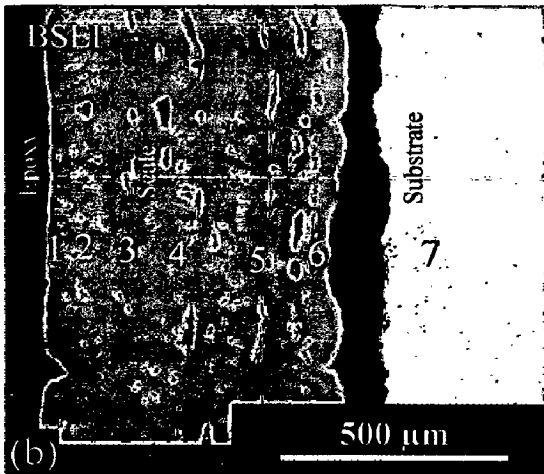
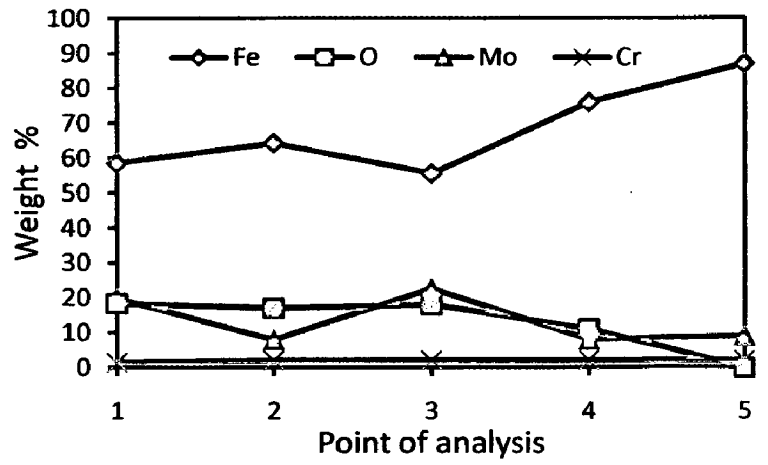
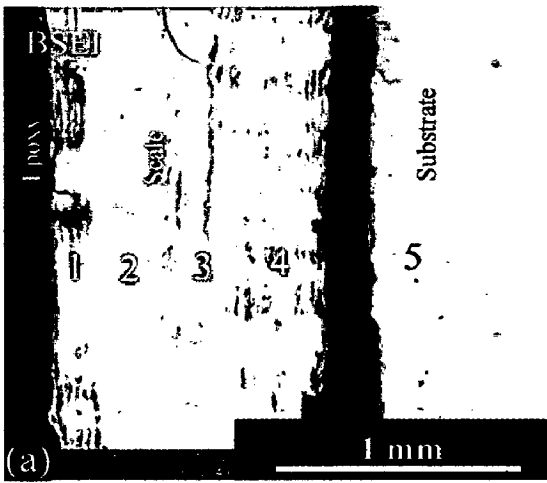


Fig. 6.13 (b) X-Ray Diffraction pattern of uncoated and coated ASTM-SA213-T-22 boiler steel exposed to cyclic oxidation in air at 900°C for 50 cycles: (A) Conventional TiAlN coating, (B) Conventional AlCrN coating



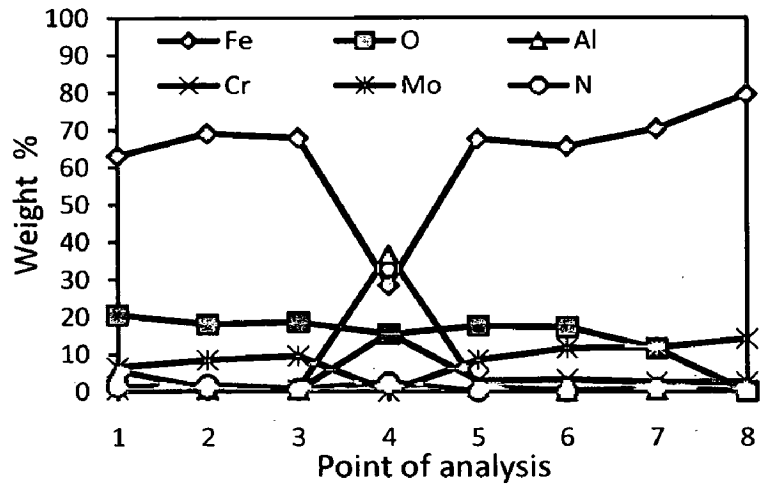
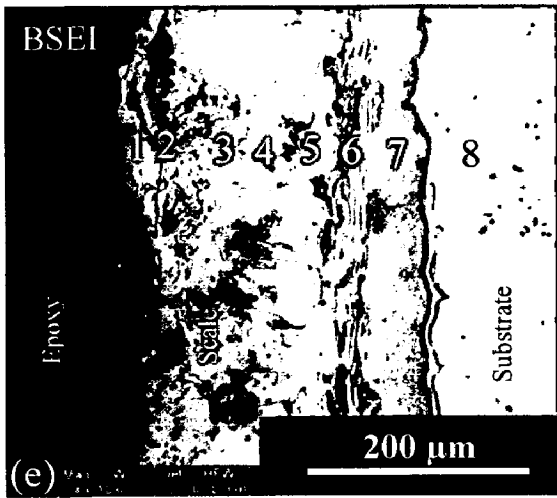


Fig. 6.15 Oxide scale morphology and variation of elemental composition across the cross-section of the uncoated and coated ASTM-SA213-T-22 boiler steel after exposure to cyclic oxidation in air at 900°C for 50 cycles: (a) Uncoated T-22 boiler steel (80 X), (b) Nanostructured TiAlN coating (130 X), (c) Nanostructured AlCrN coating (726 X), (d) Conventional TiAlN coating (150 X), (e) Conventional AlCrN coating (300 X)

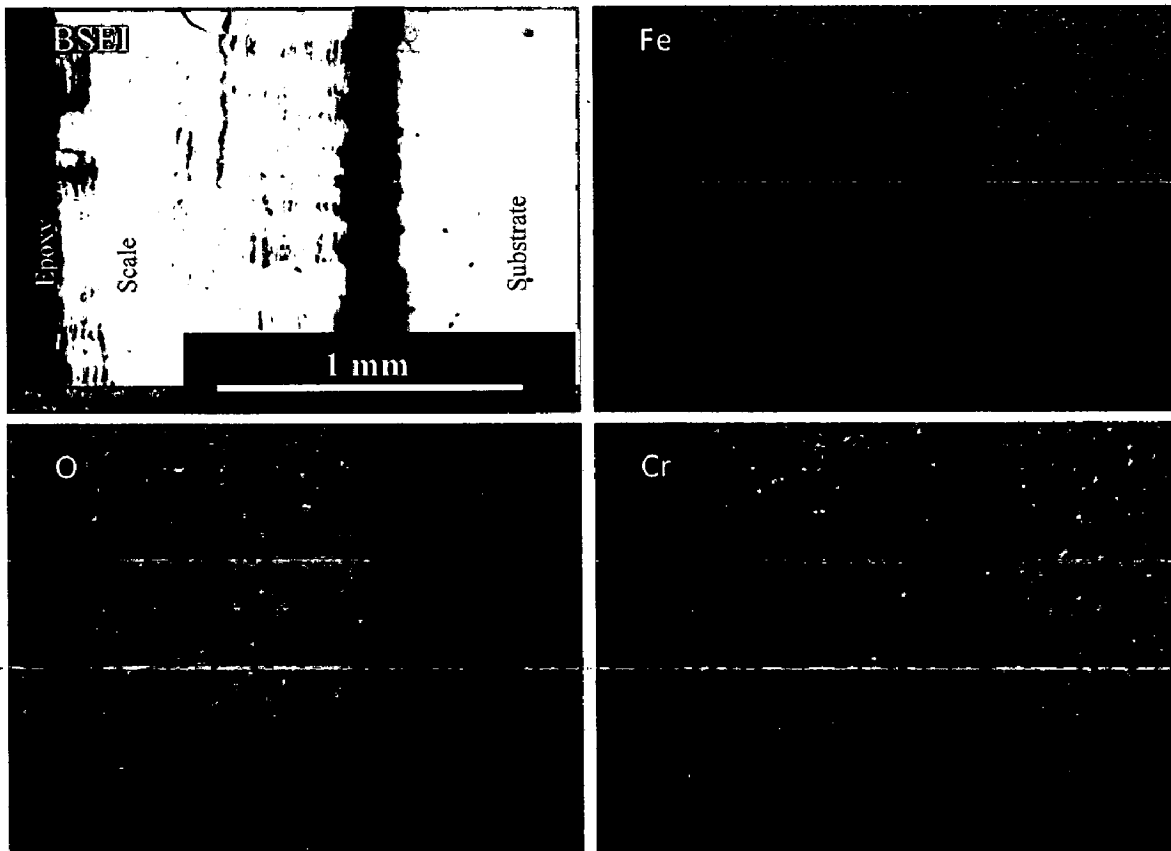


Fig. 6.16 (a) Composition image (BSEI) and X-ray mapping of the cross-section of uncoated ASTM-SA213-T-22 boiler steel subjected to cyclic oxidation in air at 900°C for 50 cycles

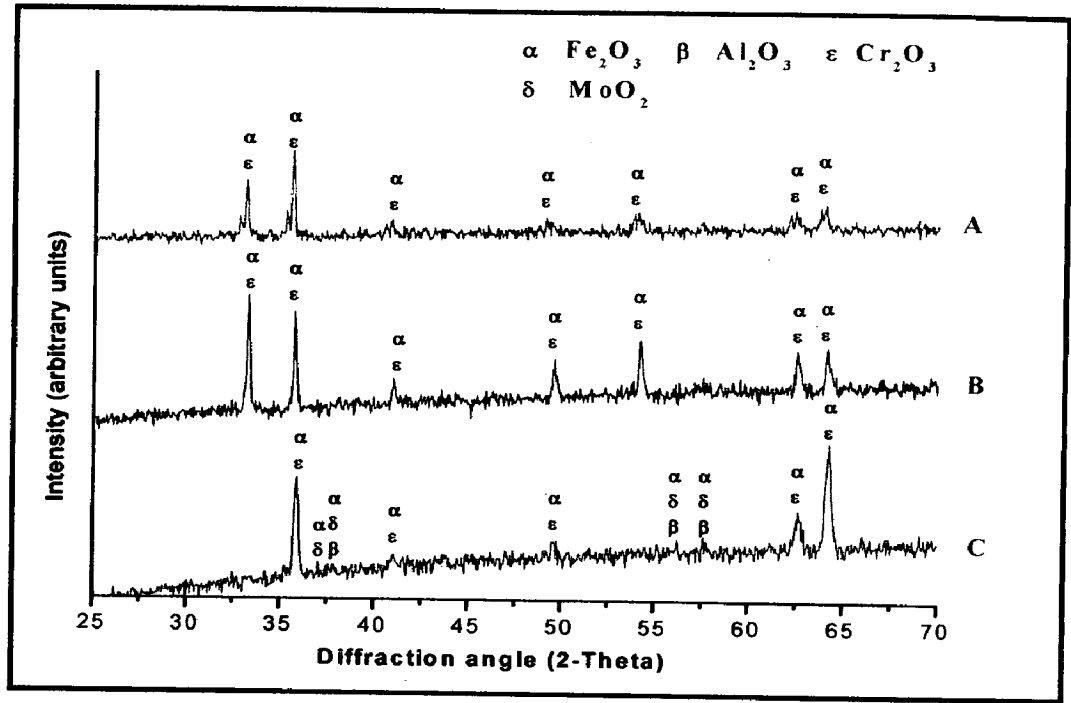


Fig. 6.13 (a) X-Ray Diffraction pattern of uncoated and coated ASTM-SA213-T-22 boiler steel exposed to cyclic oxidation in air at 900°C for 50 cycles: (A) Uncoated T-22 boiler steel, (B) Nanostructured TiAlN coating, (C) Nanostructured AlCrN coating

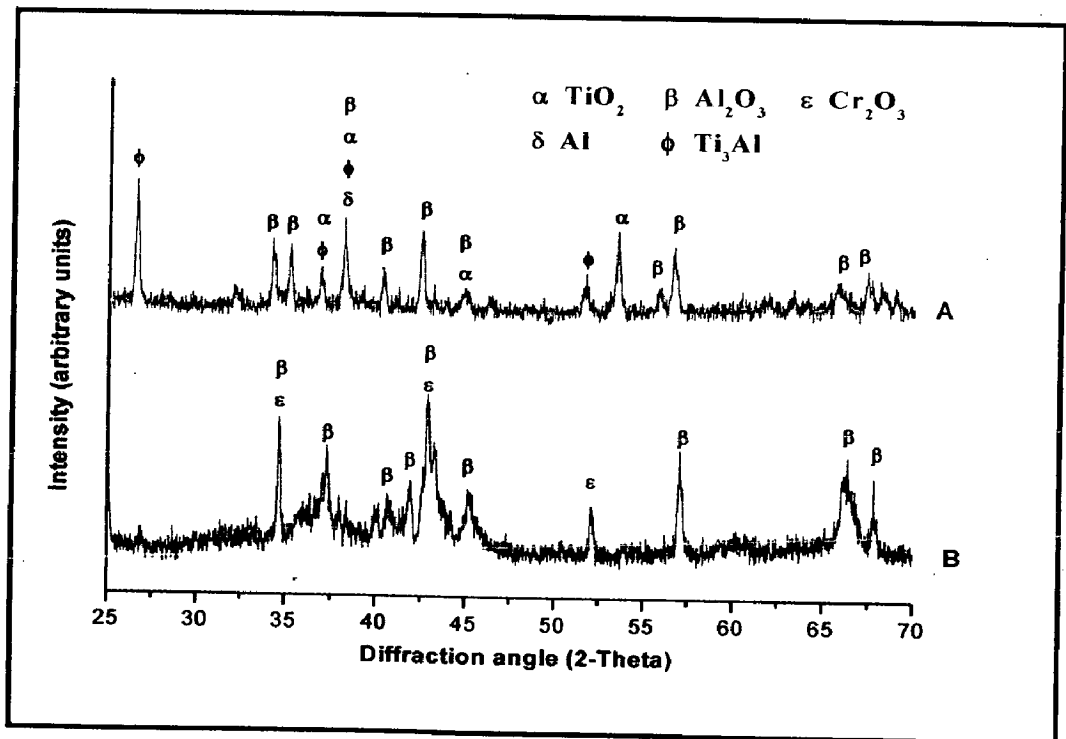
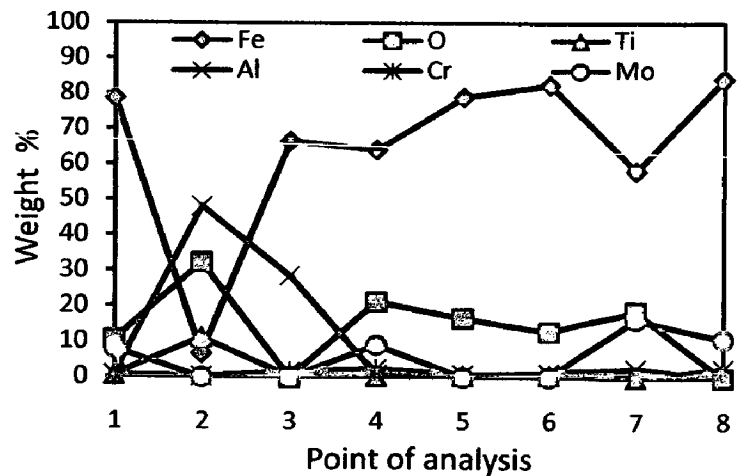
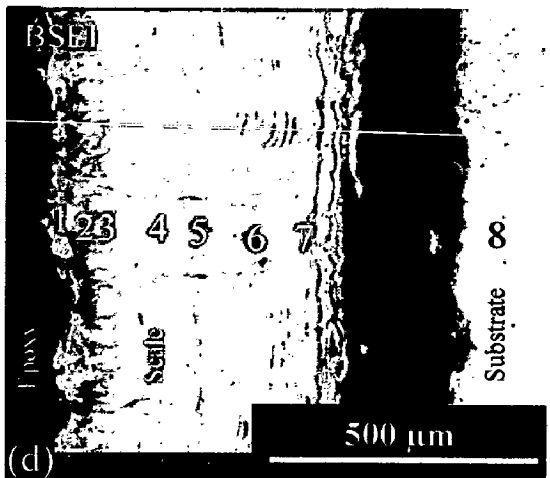
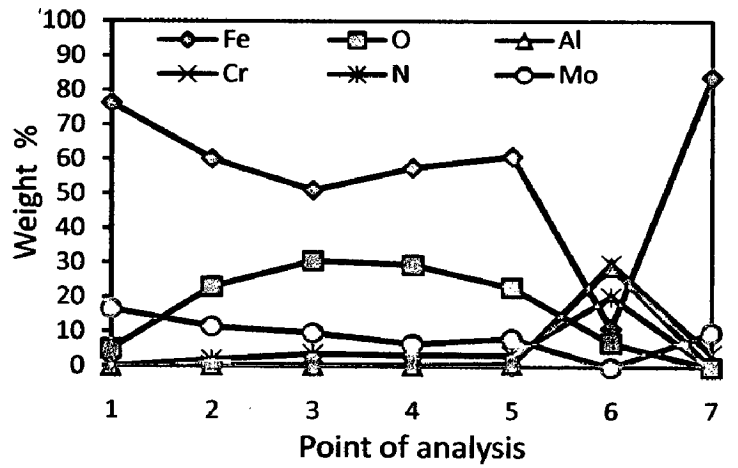
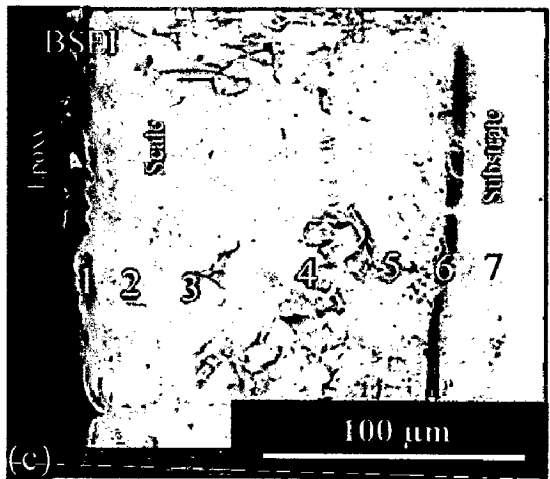
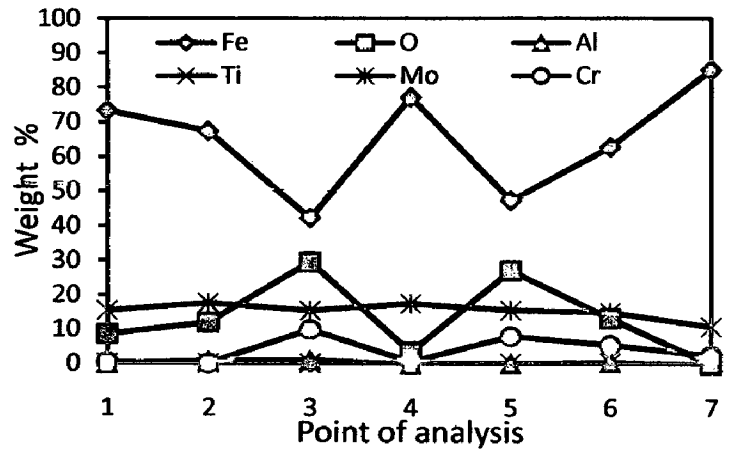
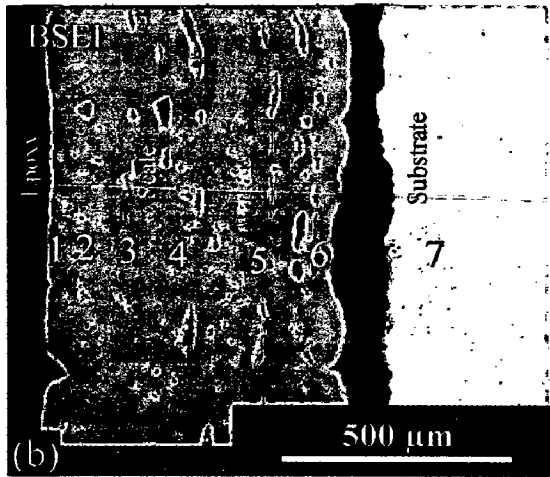
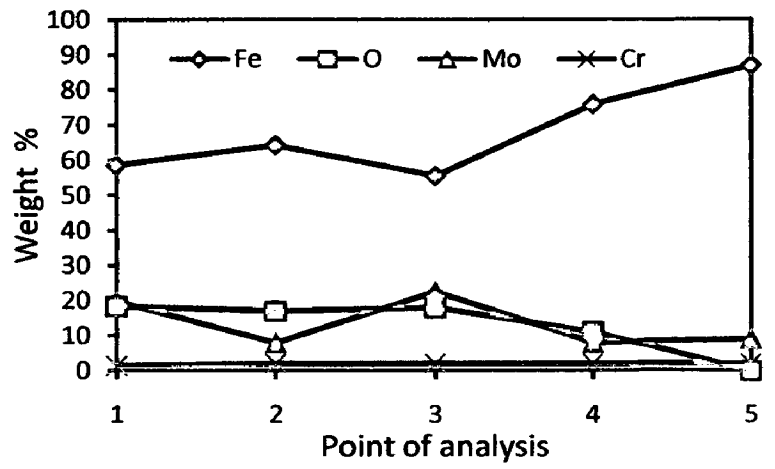
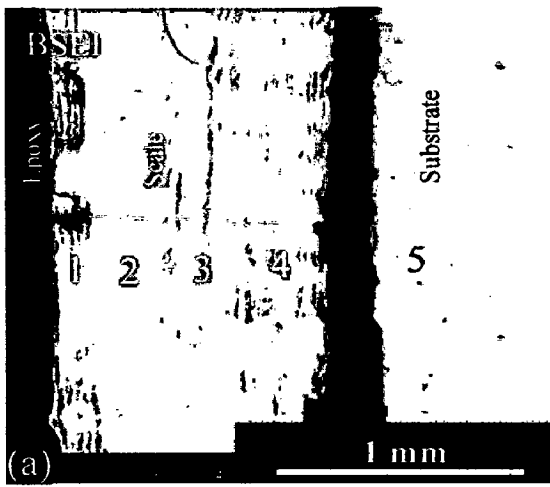


Fig. 6.13 (b) X-Ray Diffraction pattern of uncoated and coated ASTM-SA213-T-22 boiler steel exposed to cyclic oxidation in air at 900°C for 50 cycles: (A) Conventional TiAlN coating, (B) Conventional AlCrN coating



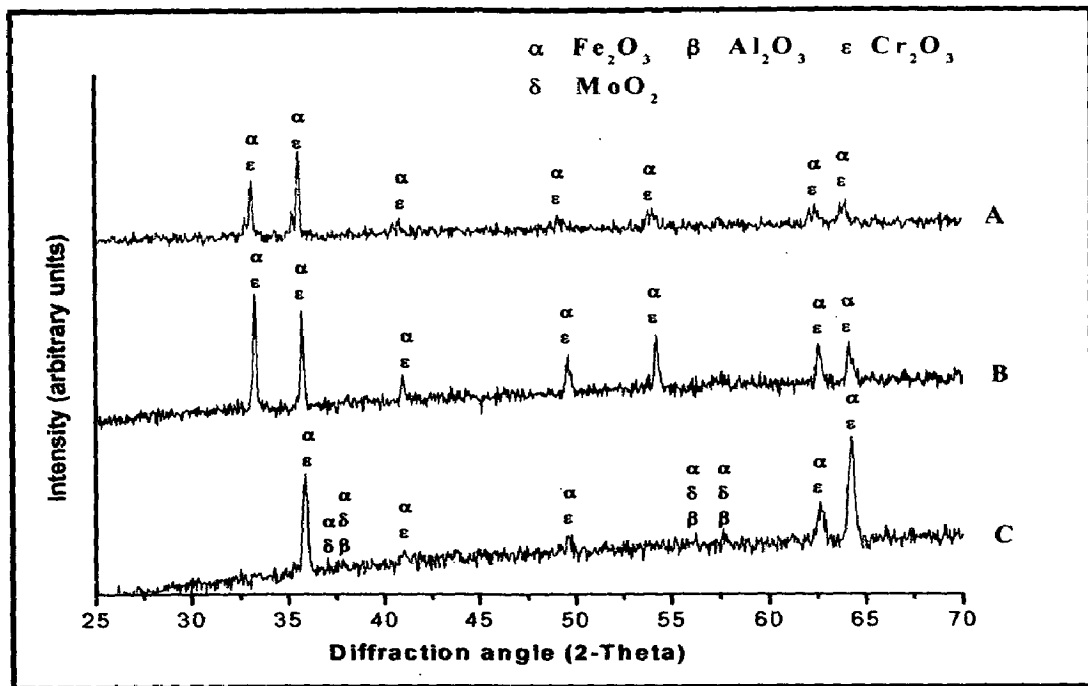


Fig. 6.13 (a) X-Ray Diffraction pattern of uncoated and coated ASTM-SA213-T-22 boiler steel exposed to cyclic oxidation in air at 900°C for 50 cycles: (A) Uncoated T-22 boiler steel, (B) Nanostructured TiAlN coating, (C) Nanostructured AlCrN coating

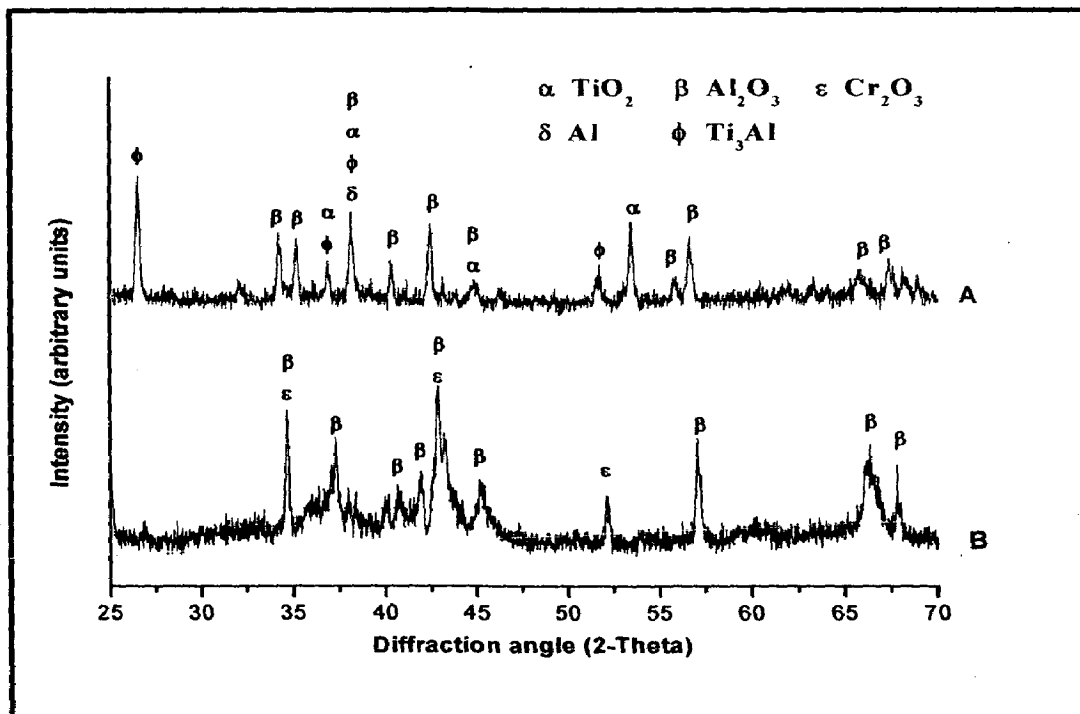


Fig. 6.13 (b) X-Ray Diffraction pattern of uncoated and coated ASTM-SA213-T-22 boiler steel exposed to cyclic oxidation in air at 900°C for 50 cycles: (A) Conventional TiAlN coating, (B) Conventional AlCrN coating

As indicated by the diffractograms in Fig.6.13, Fe_2O_3 is the main phases present in the oxide scale of uncoated and nanostructured thin TiAlN and AlCrN coated T-22 boiler steel along with small amount of Cr_2O_3 . Weak peaks of Al_2O_3 and MoO_2 are found in case of nanostructured thin AlCrN coating. Further, the main phases identified for the conventional thick TiAlN coating are Al_2O_3 , Ti_2O_3 , Ti_3Al and Al. The oxide phases found in case of conventional thick AlCrN coating are Al_2O_3 and Cr_2O_3 .

6.2.1.3.2 Surface scale morphology

SEM micrographs along with EDAX point analysis reveals the surface morphology of the coated and uncoated T-22 boiler steel subjected to cyclic oxidation in air at 900°C for 50 cycles are shown in Fig.6.14. The oxide scale for uncoated T-22 boiler steel indicates the dominance of Fe and O (Fig.6.14 .a). A small amount of Mo and Cr are also found in the scale.

SEM micrograph of oxidized nanostructured thin TiAlN coatings is shown in Fig.6.14 (b). The oxide scale is mainly consisting of dark grey matrix (Point 3) and white needles dispersed in matrix on some locations (Point 4). The top scale is rich in Fe, Mo, O, and Mn as analyzed by EDAX analysis. The small amount of Al, Ti, Cr, C, Si, and P are also present. In case of nanostructured thin AlCrN coated T-22 boiler steel, the SEM micrograph indicates the dense dimples like surface appearance (Point 6 on Fig. 6.14. c). The EDAX point analysis shows, the top scale is rich in Fe, Mo and O. The small amount of Mn, Al, N, Cr and C are also present.

The surface scale developed on conventional thick TiAlN coated T-22 steel is with white contrast (Point 8) and few black contrast regions (Point 7). EDAX analysis at point 7 indicates the presence of Ti, Al and O as the main phases along with very small amount of Fe, whereas the dark region (Point 8 on Fig.6.14) indicates more amount of Ti (26.60 %) and less Al (40.57 %) as compared to the white region. A homogeneous and continuous surface scale is developed on conventional thick AlCrN coated T-22 boiler steel, which has Al, Cr and O as the main elements (Fig.6.14.e).

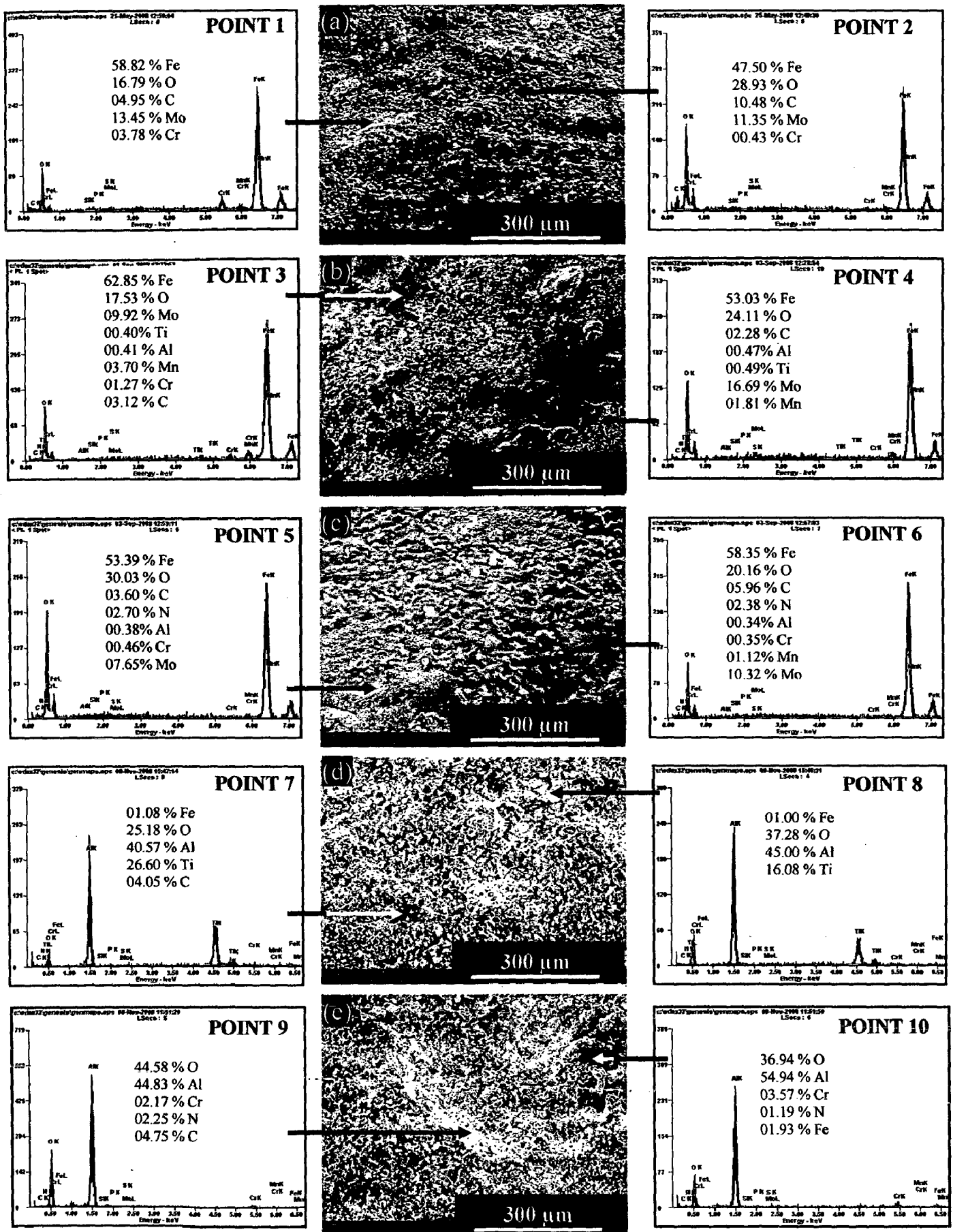


Fig. 6.14 Surface-scale morphology and EDAX patterns from different spots on uncoated and coated ASTM-SA213-T-22 boiler steel after exposure to cyclic oxidation in air at 900°C for 50 cycles : (a) Uncoated T-22 boiler steel, (b) Nanostructured TiAlN coating, (c) Nanostructured AlCrN coating, (d) Conventional TiAlN coating, (e) Conventional AlCrN coating

6.2.1.4 Cross-sectional analysis

6.2.1.4.1 Scale thickness

The oxidized samples were cut across the cross section using Buehler Isomet 1000 precision saw and mounted in transoptic mounting resin and subsequently mirror polished to obtain scanning electron back scattered micrographs and X-ray mapping of different elements for coated and uncoated T-22 boiler steel. The scale thickness values were measured from SEM back scattered micrographs as shown in Fig.6.15. Very thick scale is observed in case of uncoated T-22 boiler steel. The measured average scale thickness values for uncoated T-22 boiler steel, nanostructured thin TiAlN, nanostructured thin AlCrN, conventional thick TiAlN and conventional thick AlCrN coatings are 1150, 666, 137, 545 and 276 μm respectively.

6.2.1.4.2 Cross-sectional scale morphology

Back Scattered Electron Image (BSEI) micrograph and elemental variation across the cross-section for coated and uncoated T-22 boiler steel subjected to cyclic oxidation in air at 900°C for 50 cycles are shown in Fig.6.15. The SEM micrograph in case of uncoated T-22 boiler steel shows thick scale as shown in Fig. 6.15 (a). EDAX analysis reveals the presence of iron, oxygen and molybdenum throughout the scale. The existence of significant amount of oxygen points out the possibility Fe_2O_3 in the oxide scale. BSEI micrograph and elemental variation depicted in Fig.6.15 (b), for the exposed cross-section of nanostructured thin TiAlN coated T-22 boiler steel shows the thick and continuous scale. The EDAX analysis reveals the presence of Fe, Mo, Cr and oxygen throughout the scale. Presence of comparatively higher amount of Cr at points 3, 5 and 6 (Fig.6.15.b) indicates the possibility of Cr_2O_3 in the scale.

A thick and adherent oxide scale can be seen in case of nanostructured AlCrN coated T-22 boiler steel (Fig.6.15.c). The presence of oxygen at the scale substrate interface may be due to the in flight oxidation of coating or oxygen might have penetrated during initial cycles of oxidation run along the intersplat boundaries. The EDAX analysis indicates the presence of Fe, Mo and oxygen throughout the scale. The outer portion of the scale is rich in Fe, Mo and oxygen. Thin band of AlCrN coating (point 6) is seen between substrate and scale. This thin band at scale substrate interface (dark

grey line) mainly contains Al, Cr, N and traces of Fe, Mo and oxygen (point 6). At some points thin film has gaps.

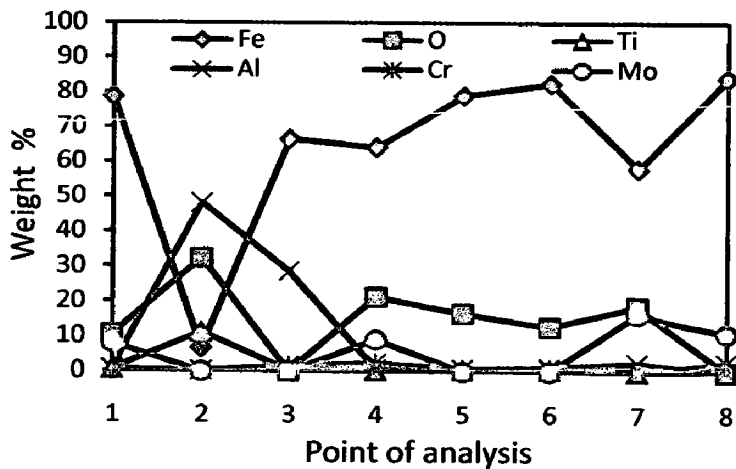
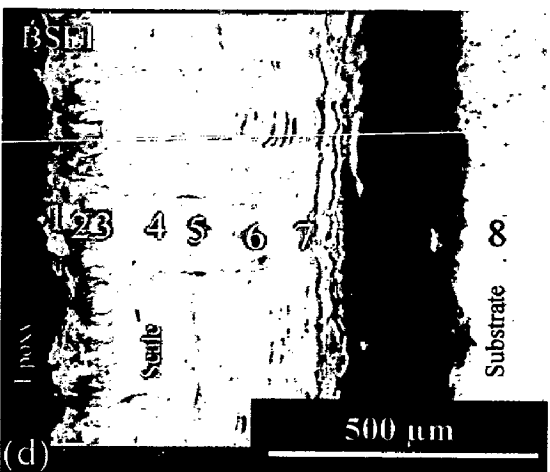
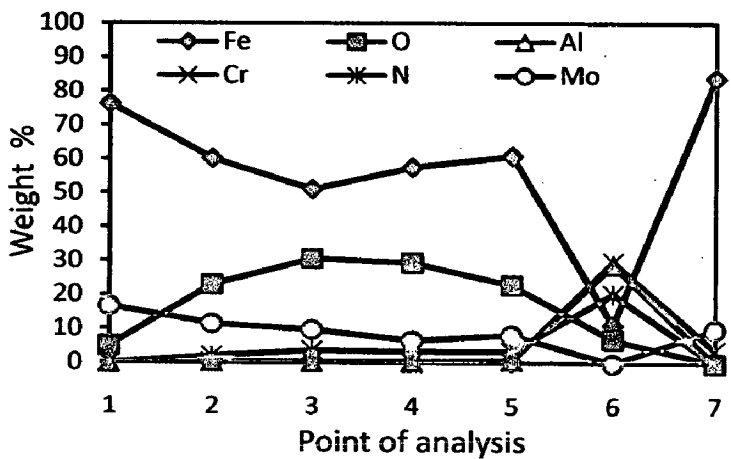
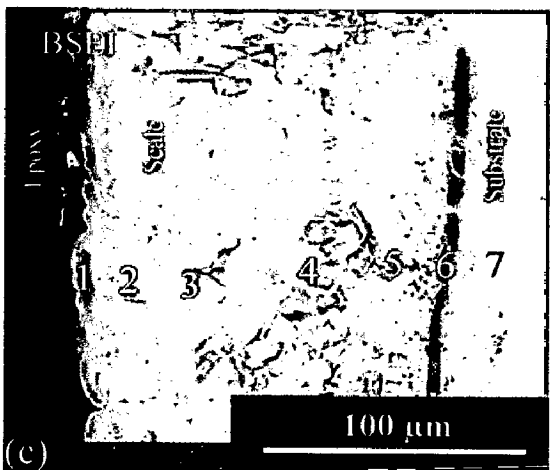
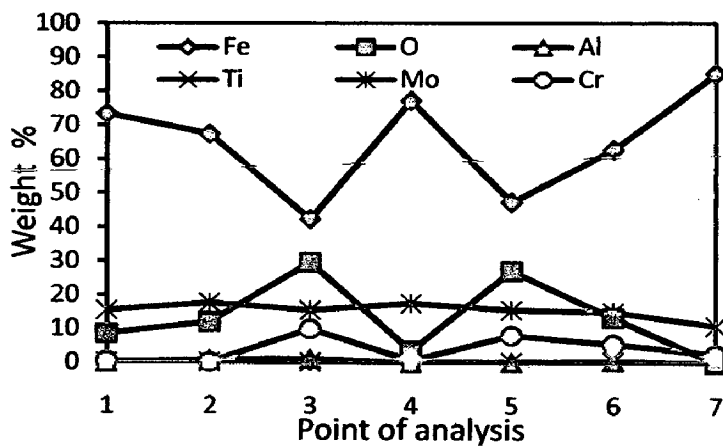
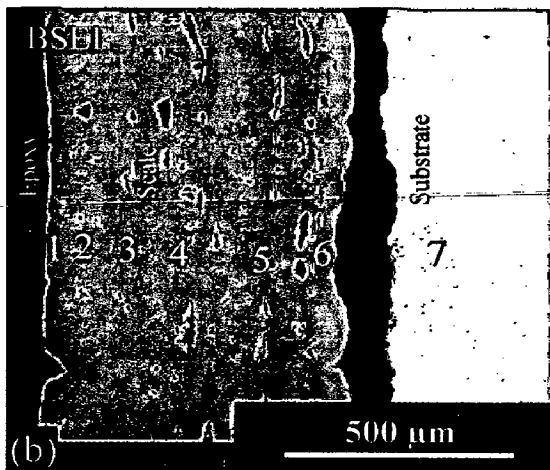
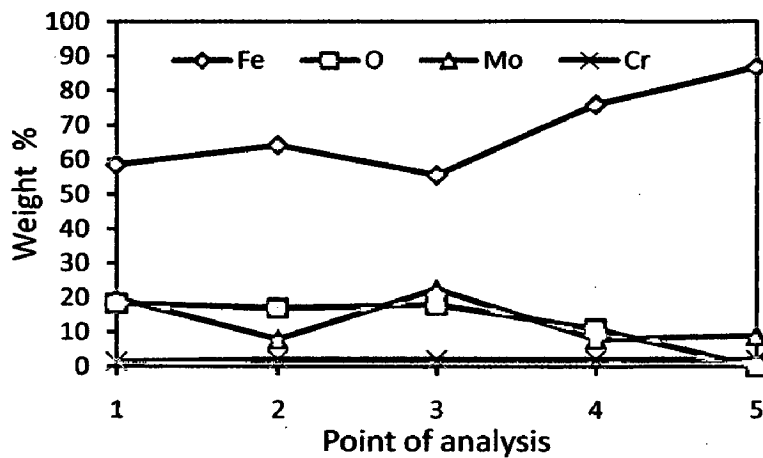
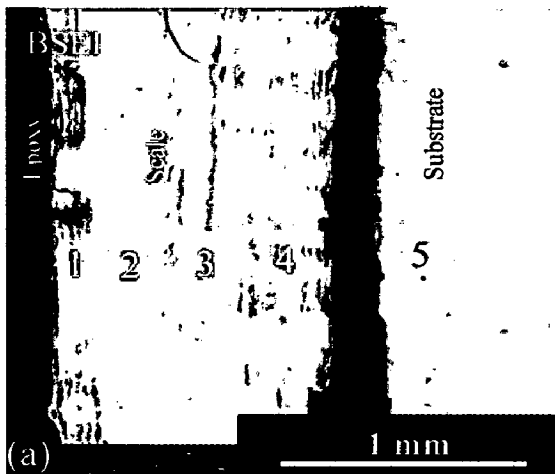
In case of conventional TiAlN coated T-22 boiler steel, the scale is uniform and adherent as depicted in Fig.6.15 (d). The EDAX point analysis indicates the presence of Fe, O, Al, Ti and Mo in the scale with variable amounts. The top scale is rich in Ti and Al along with O (Point 1, 2 and 3 on Fig.6.15.d). The conventional thick AlCrN coated T-22 boiler steel (Fig.6.15.e) indicates continuous, thick and adherent scale. EDAX point analysis shows the presence of Fe, Al, Cr, Mo and O throughout the scale. A location at points 4 (Fig.6.15.e) in the micrograph depicts the abrupt increase in percentage of Al and Cr with decrease in the percentage of Fe and Mo.

6.2.1.4.3 X-Ray mapping

X-ray mappings for a part of oxide scale of uncoated and coated T-22 boiler steel oxidized in air at 900 °C for 50 cycles are shown in Fig. 6.16. In case of uncoated T-22 boiler steel, the micrograph (Fig.6.16.a) indicates a dense scale, which mainly contains iron and oxygen with some amount of chromium.

Figure 6.16(b), shows X-ray mapping analysis of the scale formed on nanostructured TiAlN coated T-22 boiler steel. The BSEI image indicates the formation of a dense scale which has detached from the surface. The X-ray mapping also indicates thin irregular Cr bands parallel to each other in the scale. In case of nanostructured thin AlCrN coated T-22 boiler steel subjected to cyclic oxidation in air, the BSEI and X-ray mapping are shown in Fig. 6.16 (c). The scale formed is dense and adherent to the substrate without any crack in the scale or at substrate-scale interface. The X-ray mapping indicates the presence of iron and oxygen throughout the scale. A thin band of Al, Cr and N is also indicated by X-ray mapping at scale substrate interface, where iron and oxygen are completely absent.

In case of conventional thick TiAlN coated T-22 boiler steel, Fig.6.16 (d), Fe and O are present throughout the scale. Thick band of Al is present in the top scale region along with Ti. The sub scale is rich in Fe and O. Fig.6.16 (e), depicts the X-ray mapping in case of conventional AlCrN coated T-22 boiler steel. Thick band of Al is present in the top scale region along with Cr. The sub scale is rich in Fe.



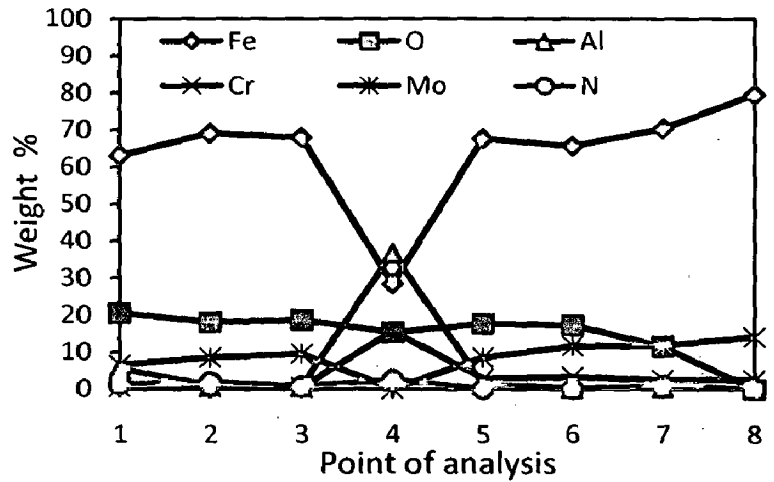
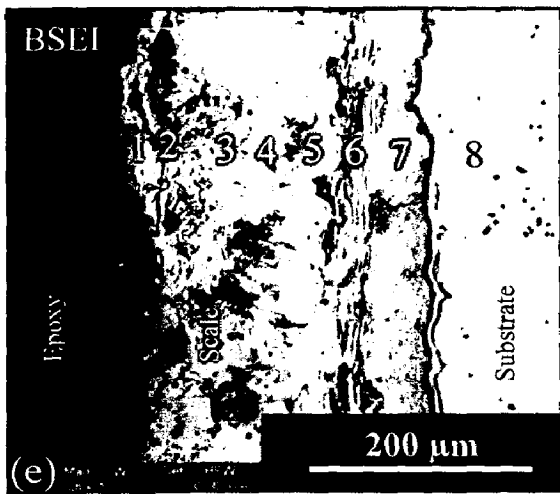


Fig. 6.15 Oxide scale morphology and variation of elemental composition across the cross-section of the uncoated and coated ASTM-SA213-T-22 boiler steel after exposure to cyclic oxidation in air at 900°C for 50 cycles: (a) Uncoated T-22 boiler steel (80 X), (b) Nanostructured TiAlN coating (130 X), (c) Nanostructured AlCrN coating (726 X), (d) Conventional TiAlN coating (150 X), (e) Conventional AlCrN coating (300 X)

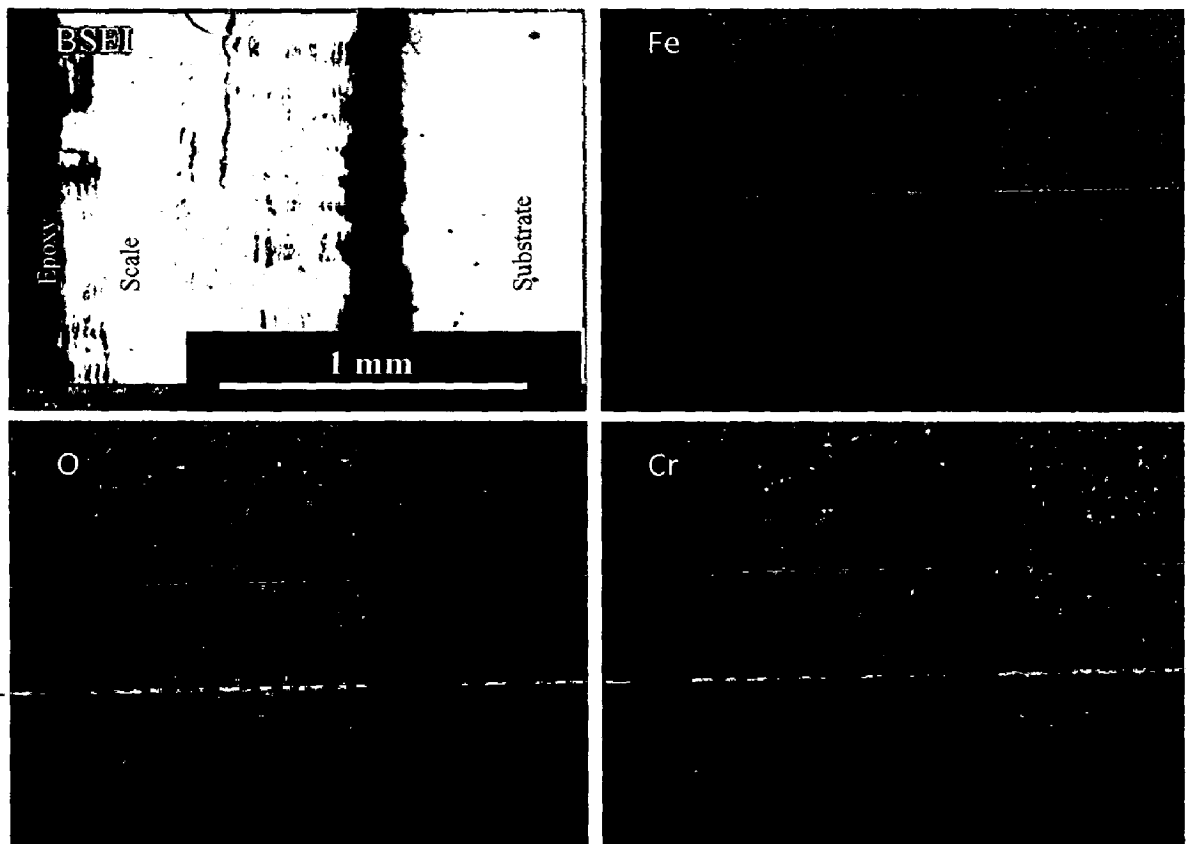


Fig. 6.16 (a) Composition image (BSEI) and X-ray mapping of the cross-section of uncoated ASTM-SA213-T-22 boiler steel subjected to cyclic oxidation in air at 900°C for 50 cycles

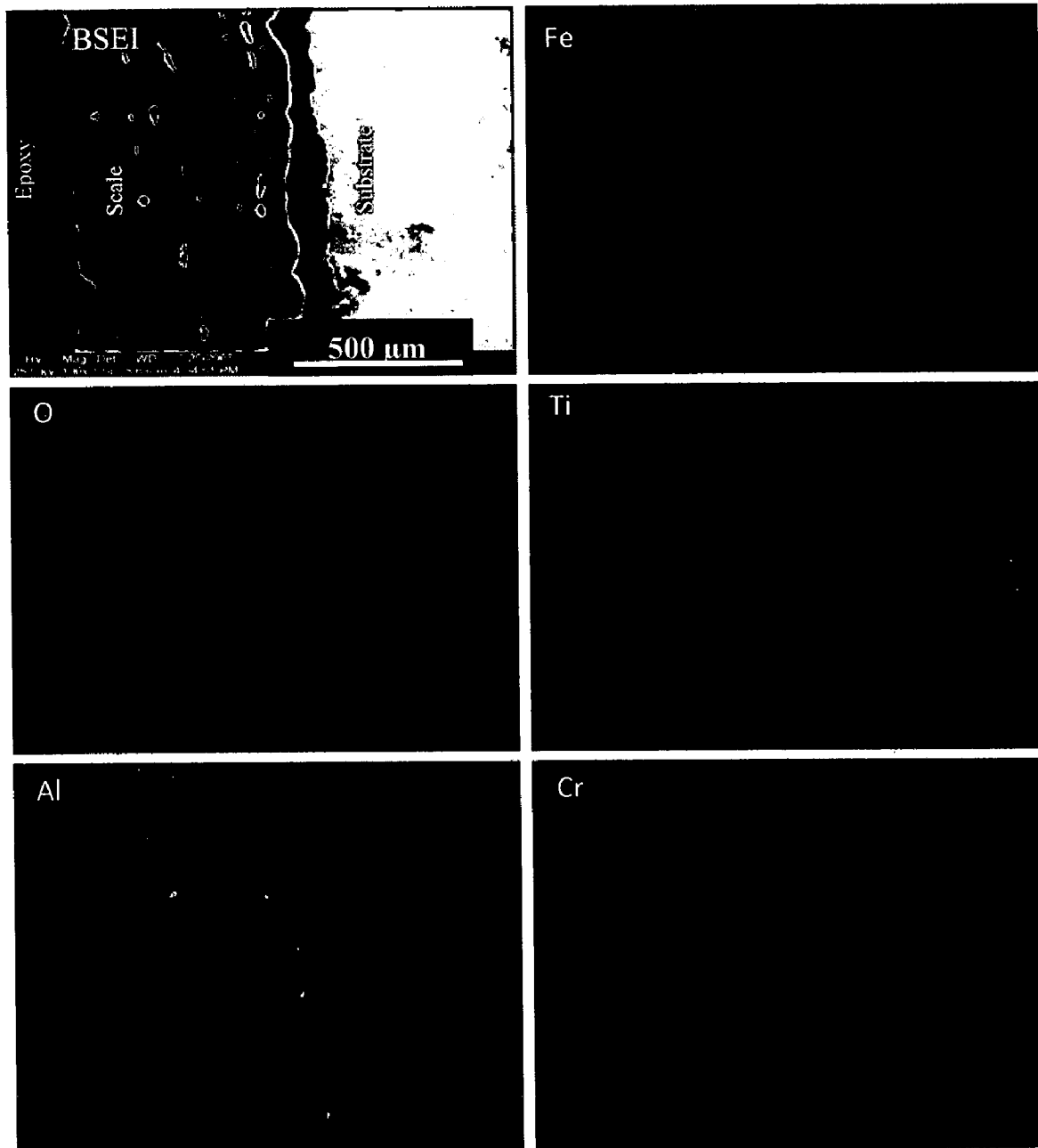


Fig. 6.16 (b) Composition image (BSEI) and X-ray mapping of the cross-section of Nanostructured TiAlN coated ASTM-SA213-T-22 boiler steel subjected to cyclic oxidation in air at 900°C for 50 cycles

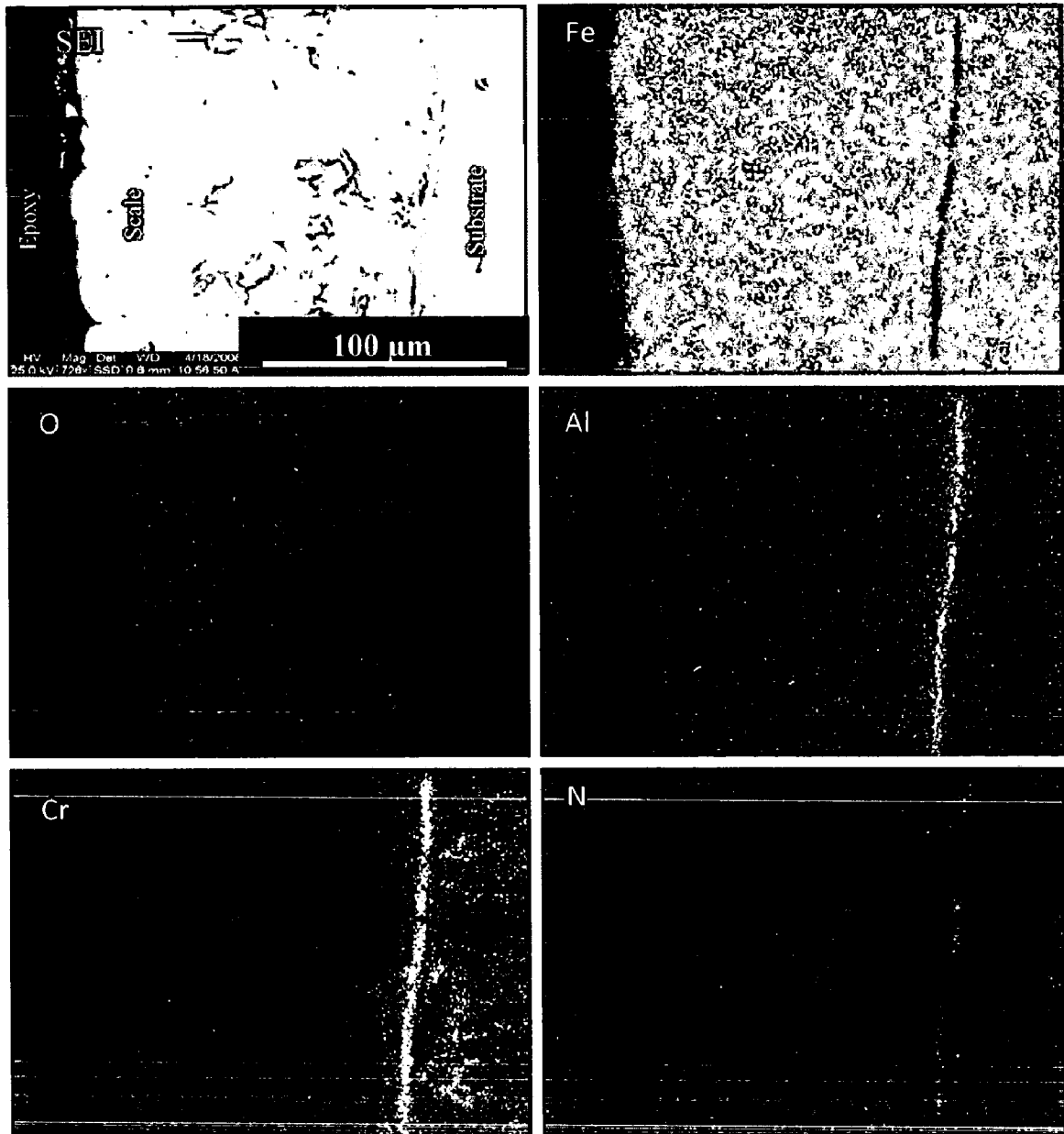


Fig. 6.16 (c) Composition image (BSEI) and X-ray mapping of the cross-section of Nanostructured AlCrN coated ASTM-SA213-T-22 boiler steel subjected to cyclic oxidation in air at 900°C for 50 cycles

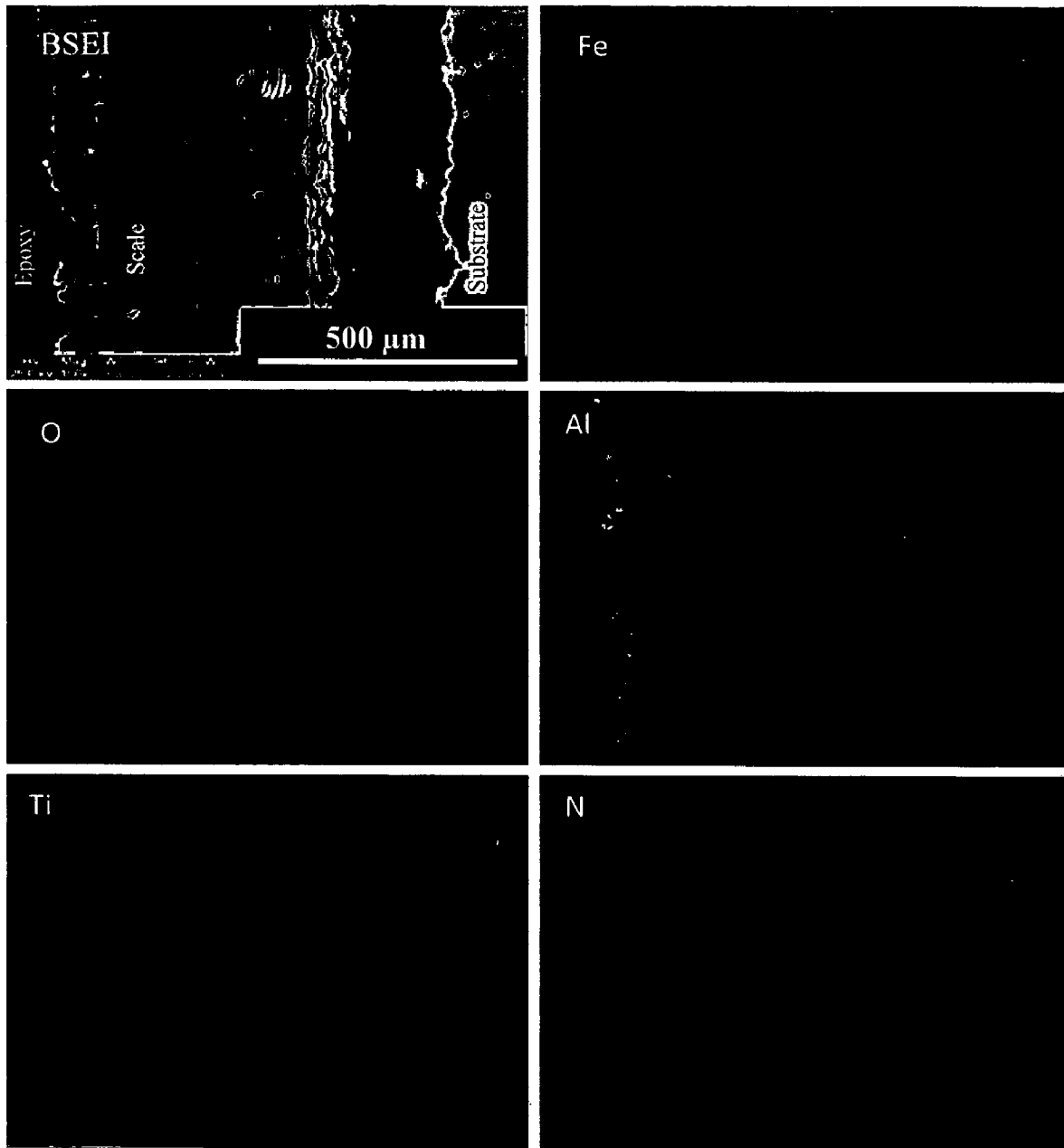


Fig. 6.16 (d) Composition image (BSEI) and X-ray mapping of the cross-section of conventional TiAlN coated ASTM-SA213-T-22 boiler steel subjected to cyclic oxidation in air at 900°C for 50 cycles

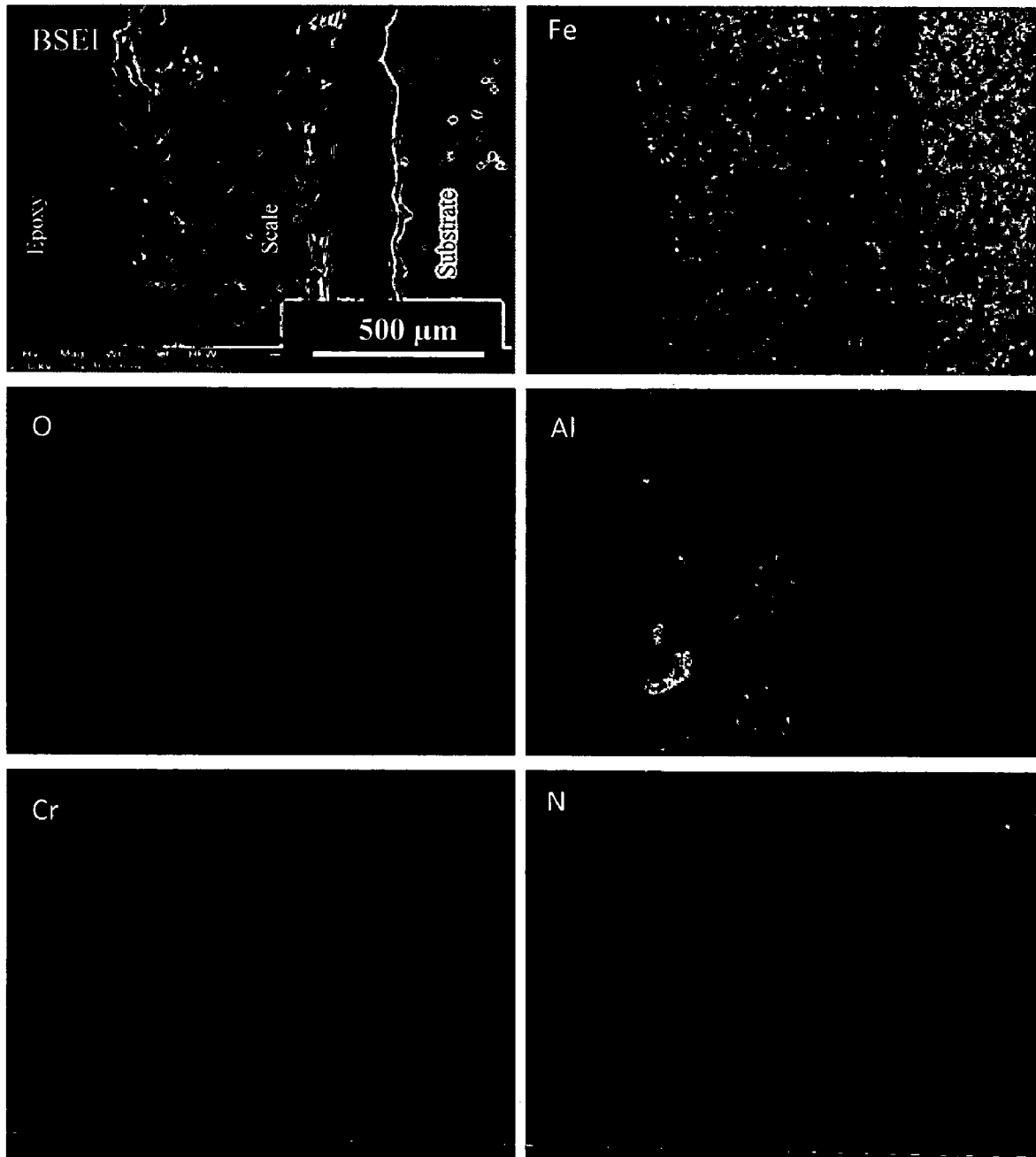


Fig. 6.16 (e) Composition image (BSEI) and X-ray mapping of the cross-section of conventional AlCrN coated ASTM-SA213-T-22 boiler steel subjected to cyclic oxidation in air at 900°C for 50 cycles

6.2.2 Summary of Results

Results obtained after exposure of uncoated and coated ASTM-SA213-T-22 boiler steel to cyclic oxidation in air at 900°C for 50 cycles are summarized in Table.6.4.

Table 6.4 Summary of the results obtained for uncoated and coated ASTM-SA213-T-22 boiler steel subjected to cyclic oxidation in air at 900°C for 50 cycles

Coating	Cumulative Weight gain (mg/cm ²)	Parabolic rate constant ($K_p \times 10^{-08}$ gm ² cm ⁻⁴ s ⁻¹)	XRD phases	Remarks
Uncoated T-22 boiler steel	177.24	18.80	Fe ₂ O ₃ and Cr ₂ O ₃	A grey colored scale appeared on the surface right from the 1 st cycle. Spalling was observed during the course of the study. At the end of the cyclic study, irregular and fragile scale was observed with deep cracks and blackish grey color surface appearance.
Nanostructured TiAlN coating	203.39	22.52	Fe ₂ O ₃ and Cr ₂ O ₃	Color of the oxide scale at the end of the study was observed to be grey with some blackish grey areas on the surface. After 20 th cycle severe swelling and peeling of the oxide scale was observed. Some of the scale was seen getting detached from the surface.
Nanostructured AlCrN coating	55.27	01.57	Fe ₂ O ₃ , Cr ₂ O ₃ , Al ₂ O ₃ and MoO ₂	Golden and ink blue reflections were observed in the scale, after the completion of 2 nd cycle, which turned to dark grey subsequently. The scale was found to be lustrous, with no tendency to spall. The oxide scale at the end of cyclic study was smooth.
Conventional TiAlN Coating	58.21	02.01	Al ₂ O ₃ , Ti ₂ O ₃ , Ti ₃ Al and Al	The formation of very light grey color in the middle of the sample along with bluish grey sides after 2 nd cycle. After 21 st cycle, a small portion of scale at corner falls in the boat. Severe spalling was observed after 29 th cycle. At the end of 50 cycles, whitish grey colored scale (with cracks) was observed.
Conventional AlCrN coating	15.73	00.14	Al ₂ O ₃ and Cr ₂ O ₃	The surface becomes rough after first cycle and dark blue line was observed at one of the edges. After 9 th cycle, bluish dots were seen on the surface which remains up to end. At the end of the study, the scale was found to be adherent with light grey surface appearance.

6.2.3 Discussion

The weight change plots (Fig.6.10) for the uncoated and coated ASTM-SA213-T-22 boiler steel indicated that the oxidation behavior has shown conformance to parabolic rate law. The parabolic kinetic behavior is due to the diffusion controlled mechanism operating at 900°C under cyclic conditions (Mahesh et al., 2008). Small deviation from the parabolic rate law might be due to the cyclic scale growth. The higher weight gain during the first few cycles might be attributed to the rapid formation of oxides at the splat boundaries and within the open pores due to the penetration of the oxidizing species, further the subsequent increase in weight is gradual (Singh H et al., 2007). The parabolic rate constant for the nanostructured thin TiAlN coated T-22 boiler steel is found to be greater than the uncoated and other coatings.

Conventional thick and nanostructured AlCrN and conventional TiAlN coatings have been found successful in reducing the overall weight gain of bare T-22 boiler steel by 92%, 69% and 68% respectively. The oxidation rate (total weight gain values after 50 cycles) of the coated and uncoated T-22 boiler steel boiler steel follows the sequence as given below:

Nanostructured TiAlN > Bare T-22 > Conventional TiAlN > Nanostructured AlCrN > Conventional AlCrN

The spalling as observed in case of T-22 steels may be attributed to the presence of molybdenum in the steels. Chatterjee et al. (2001) have suggested that during initial oxidation Fe is oxidized and the oxide scale is protective in nature. With progress of oxidation Mo becomes enriched at the alloy scale interface, leading to the formation of an inner layer of molten MoO_3 (m. p. 795°C) which penetrates along the alloy-scale interface. This liquid oxide disrupts and dissolves the protective oxide scale, causing the alloy to suffer catastrophic oxidation (Lai, 1990). Chaterjee et al. (2001) has further suggested that molybdenum is noble than the other alloying elements; MoO_3 will reduce to a lower oxide of molybdenum or even to molybdenum. Simultaneously MoO_3 may exert dissolving action on other oxides, such as Fe_2O_3 and Cr_2O_3 and this fluxing may further get accelerated by the enthalpy of formation of Fe_2O_3 and Cr_2O_3 which tends to increase in the temperature at the alloy-scale interface. The proposed mechanism of

attack is explained in Fig.6.17 which is identical to the one reported by Chaterjee et al. (2001) and Singh, Buta (2003).

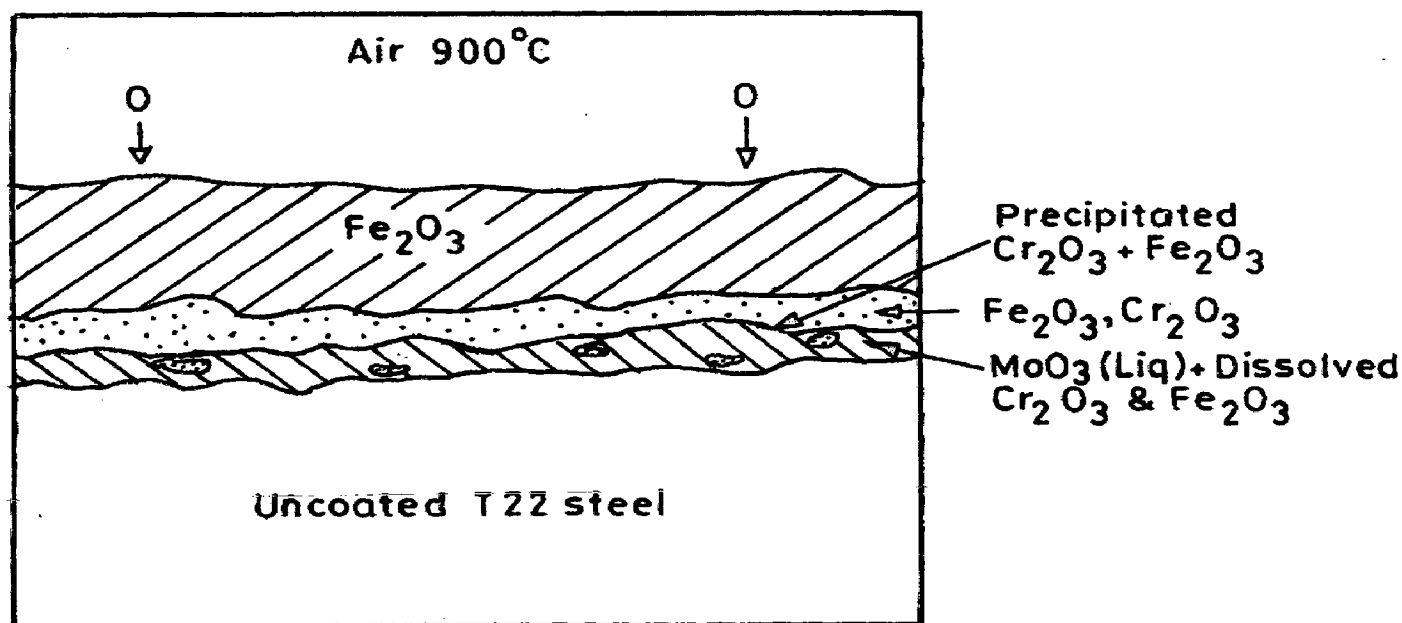


Fig. 6.17 Schematic diagram showing probable oxidation mechanism for bare T-22 boiler steel exposed to air at 900°C for 50 cycles (Chaterjee et al., 2001 and Singh, Buta, 2003)

During cyclic testing, cracks in the oxide scale (Fig.6.15.a & b) and spalling of the uncoated, nanostructured TiAlN and conventional TiAlN coatings might be attributed to the different values of thermal expansion coefficients for the coating, scale and the substrate as reported by Sidhu et al. (2003), Singh H et al. (2004), Evans et al. (2001), Wang et al. (2002) and Niranatlumpong et al. (2000). The formation of cracks in the coating originates from stresses developed in the deposit or at the coating-base metal interface (Heath et al., 1997). Through these cracks the corrosive environment can quickly reach the base metal and cut its way under the coating to result in adhesion loss and spalling, whereas some elements may diffuse outwards through these cracks to form oxides or spinels (Singh et al., 2004). This may be the reason for severe spalling and hence failure of nanostructured and conventional TiAlN coating which results falling of a thin layer of scale in the boat just after 29th cycle. The presence of Fe, Mo and oxygen (Fig.6.15) in the top of the scale, is believed to be due to the diffusion of iron and

molybdenum through the pores and cracks that appeared in the coating during the course of oxidation studies (Singh Buta, 2003).

Inferior oxidation resistance of nanostructured thin and conventional thick TiAlN coating may be as opined by Ding et al. (2008). Accordingly in an oxidation or corrosive environment Ti element often forms a porous non-protective oxide scale, which limits the oxidation and corrosion resistance of titanium-based coatings. This has further been reported by Fujita (2005) that the oxide scale of binary TiAl alloy is composed of a porous oxide mixture of TiO_2 and Al_2O_3 , which has dominated by TiO_2 . This might be the reason for rapid increase in oxidation rate of nanostructured thin TiAlN coatings after 20th cycle (Fig. 6.10). Kalss et al. (2006) have measured at 900°C an oxidized layer of thickness of about 350 nm for TiAlN coating. Due to high temperature the segregation of titanium and aluminum atoms is probable. Evidently, high temperature oxidation involved diffusion of aluminum atoms to the surface to form a thin aluminum oxide top layer while the remaining titanium under layered formed titanium dioxide.

In case of nanostructured thin TiAlN coating, the presence of Fe_2O_3 in the upper layer of the scale is followed by a subscale in which Fe_2O_3 and Cr_2O_3 are present, as indicated by the XRD (Fig.6.13), SEM-EDAX (Fig. 6.14.b) and X-ray mapping (Fig. 6.16.b). the presence of Cr in the subscale along with oxygen and iron. This can be attributed to the depletion of iron due to oxidation to form the upper scale, thereby leaving chromium-rich pockets those have further oxidized to form parallel and irregular chromium oxide bands. These bands of chromium oxide may have prevented the deep penetration of the environment, as the scale thickness is less in case of oxidized nanostructured thin TiAlN coated T-22 boiler steel than that of uncoated boiler steel.

It is well known that the performance of thermal sprayed coatings in high temperature corrosive environment depends upon the several factors such as porosity, inclusions, oxides and size and shape of the splat microstructures as reported in the literature (Dent et al., 1999). It is evident from XRD (Fig.6.13) results of the oxidized conventional thick AlCrN coated T-22 boiler steel that Al_2O_3 as the main phase which are further supported by EDAX (Fig.6.14.e) and X-ray mapping (Fig.6.16.e) analysis. Therefore, the conventional thick AlCrN coating has been found successful in reducing the overall weight gain of bare T-22 boiler steel by 92%.

6.2.4 Conclusions

The high temperature oxidation behaviors of uncoated and coated ASTM-SA213-T-22 boiler steel have been investigated in air at 900°C for 50 cycles. The behavior of nanostructured TiAlN and AlCrN coatings were compared with their conventional counterparts and the following conclusions are made:

1. The plasma sprayed conventional thick AlCrN coatings when subjected to cyclic oxidation at 900 °C for 50 cycles developed a protective scale mainly consisting of Al₂O₃ and provided the good resistance against oxidation.
2. The nanostructured AlCrN coating has provided good resistance against oxidation in air at 900°C for 50 cycles and provided the necessary protection to the base metal. The AlCrN coating has sustained during the course of oxidation study.
3. The conventional TiAlN coating failed as of severe spalling after 29th cycle, which may be initiated by the rapid growth of void-like defects lying adjacent to coating protuberances.
4. The oxidation rate (total weight gain values after 50 cycles) of the coated and uncoated T-22 boiler steel follows the sequence as given below:
Nanostructured TiAlN > Uncoated T-22 > Conventional TiAlN > Nanostructured AlCrN > Conventional AlCrN
5. In case of nanostructured thin TiAlN coating, the weight gain is highest, whereas thickest scale was observed in case of bare T-22 boiler steel.
6. The difference in thermal expansion coefficients between oxides, coating and base steel perhaps led to the cracking of the oxide scale and coatings. The internal oxidation has been observed in all cases.

6.3 HOT CORROSION STUDIES IN MOLTEN SALT ENVIRONMENT

the present research work has been focused to investigate and compare the hot corrosion behavior of conventional thick (by plasma spraying and gas nitrided) and nanostructured thin (by physical vapor deposition process) TiAlN and AlCrN coatings on ASTM-SA213-T-22 boiler steel, in an aggressive environment of Na_2SO_4 -60% V_2O_5 molten salt at 900°C under cyclic conditions. The hot corrosion environment, Na_2SO_4 -60% V_2O_5 has been selected in the present investigation because it simulates the conditions of the molten sulfate-vandate deposits resulting from the condensation of combustion products of low-grade fuels (Sidhu et al., 2007). These low melting compounds react and dissolve the protective oxides formed on the components of boilers. X-ray diffraction (XRD), scanning electron microscopy/energy-dispersive analysis (SEM/EDAX) and X-ray mapping techniques have been used to characterize corrosion products after hot corrosion at 900°C.

6.3.1 Results

6.3.1.1 Visual observations

The macrographs for uncoated and coated ASTM-SA213-T-22 boiler steel subjected to cyclic oxidation in Na_2SO_4 -60% V_2O_5 (molten salt) environment at 900°C for 50 cycles are shown in Fig.6.18. For the uncoated T-22 boiler steel, a grey colored scale appeared on the surface right from the 1st cycle. This bare steel showed spalling of scale just after the 5th cycle, which continued till the end of 50 cycles. At the end of cyclic study, irregular and fragile scale was observed with deep cracks and blackish grey color surface appearance, which can be seen in Fig.6.18 (a).

Color of the oxide scale at the end of the study was observed to be blackish grey from the middle portion of the sample with light grey sides, in case of nanostructured thin TiAlN coated T-22 boiler steel (Fig.6.18.b). The dark and light grey spots at some locations were observed after 16th cycle. After 25th cycle hairline cracks were observed in the oxide scale. The scale remains adherent to the substrate during the course of the study. The nanostructured thin AlCrN coated T-22 boiler steel has shown the formation of fragile scale with cracks, when subjected to cyclic oxidation in Na_2SO_4 -60% V_2O_5 molten salt at 900°C for 50 cycles. Color of the oxide scale at the end of the study was

observed to be dark grey, as shown in Fig.6.18 (c). The scale starts falling in the boat just after 3rd cycle and this trend continued till 50th cycle. New layers of scale were forming and falling in the boat.

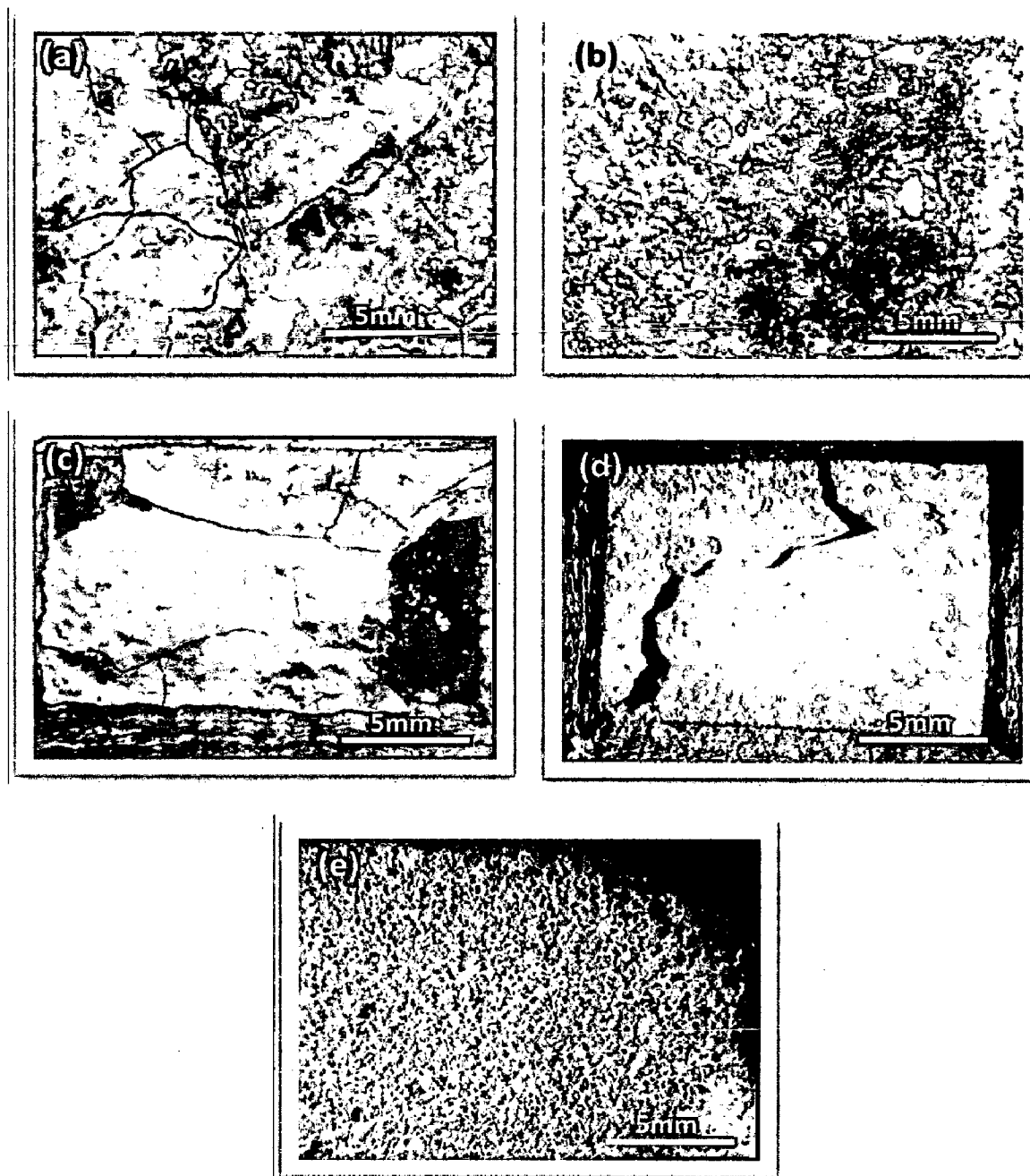


Fig. 6.18 Surface macrographs of uncoated and coated ASTM-SA213-T-22 boiler steel exposed to molten salt (Na_2SO_4 -60% V_2O_5) environment at 900°C for 50 cycles: (a) Uncoated T-22 boiler steel, (b) Nanostructured TiAlN coating, (c) Nanostructured AlCrN coating, (d) Conventional TiAlN coating, (e) Conventional AlCrN coating

The conventional thick TiAlN coated T-22 boiler steel has shown surprising behavior during hot corrosion studies. There was no sign of spalling till 20th cycle and the weight change rate was gradual. After 21st cycle, the scale formed on the upper surface of the specimen shows severe spalling and it gets separated from the substrate and fall in the boat, whereas the lower surface of the sample which is in touch with the boat wall shows no sign of spalling and the scale is adherent to the substrate. This trend continued till 50th cycle and results in loss of metal thickness at high rate on the top surface of the sample. The color of the scale observed at the end was dark grey with severe cracking on the top surface of the sample as shown in Fig.6.18 (d). In case of conventional thick AlCrN coated T-22 boiler steel, the surface becomes rough after first cycle. During the study no spalling and cracking was observed. At the end of the study, the scale was found to be adherent with light grey surface appearance (Fig.6.18.e).

6.3.1.2 Weight change measurements

Weight gain per unit area (mg/cm^2) versus time expressed in number of cycles plot for coated and bare T-22 boiler steel subjected to cyclic oxidation in Na_2SO_4 -60% V_2O_5 (molten salt) environment at 900°C for 50 cycles, is presented in Fig. 6.19. The plots for all samples shows higher weight gain at initial cycles followed by gradual weight gain except in case of conventional TiAlN coating which has shown abrupt increase in oxidation rate after 21st cycle. The cumulative weight gain per unit area for the coated and uncoated T-22 boiler steel subjected to cyclic oxidation in Na_2SO_4 -60% V_2O_5 (molten salt) environment at 900°C for 50 cycles is shown in Fig. 6.20. The overall weight gain is highest ($348.5 \text{ mg}/\text{cm}^2$) in case of uncoated T-22 boiler steel and is lowest in case of conventional thick AlCrN coated ($28.16 \text{ mg}/\text{cm}^2$) steel, which is 08.07% of the weight gain in case of uncoated T-22 boiler steel. Further, the final weight gain in case of nanostructured TiAlN, nanostructured AlCrN and conventional TiAlN coatings is 73.36, 345.05 and $212.77 \text{ mg}/\text{cm}^2$ respectively.

Figure 6.21 shows the $(\text{weight gain}/\text{area})^2$ versus number of cycles plot for all the cases to ascertain conformance with the parabolic rate law. All the coated and uncoated ASTM-SA213-T-22 boiler steel followed the parabolic rate law as evident from the Fig.6.21. The parabolic rate constant K_p was calculated by a linear least-square algorithm

to a function in the form of $(W/A)^2 = K_p t$, where W/A is the weight gain per unit surface area (mg/cm^2) and 't' indicates the number of cycles representing the time of exposure. The parabolic rate constants for the bare and coated T-22 boiler steel calculated on the basis of 50 cycle's exposure data are shown in Table.6.5. The ' K_p ' value for the uncoated and nanostructured thin TiAlN coated T-22 boiler steel is higher than in case of other coatings.

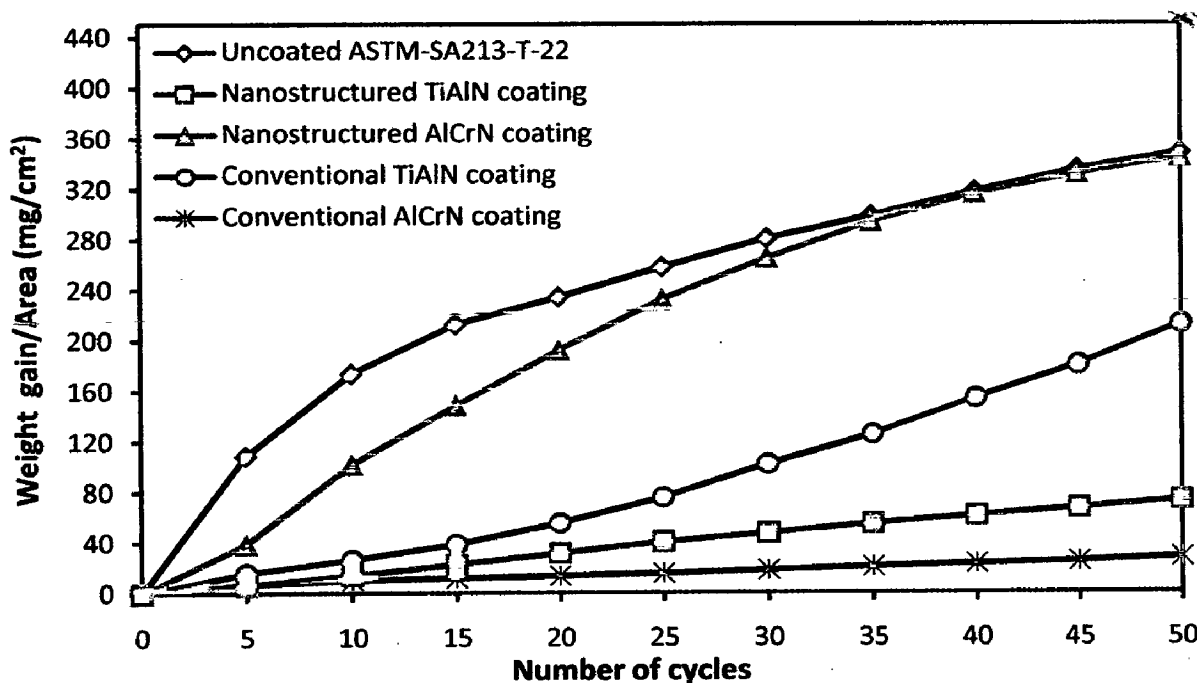


Fig. 6.19 Weight gain/area vs time (number of cycles) for the uncoated and coated ASTM-SA213-T-22 boiler steel exposed to molten salt (Na_2SO_4 -60% V_2O_5) environment at 900°C for 50 cycles

Table 6.5 Parabolic rate constant ' K_p ' values of uncoated and coated ASTM-SA213-T-22 boiler steel subjected to cyclic oxidation in Na_2SO_4 -60% V_2O_5 (molten salt) environment at 900°C for 50 cycles

Substrate / Coating	$K_p \times 10^{-08} \text{ gm}^2 \text{ cm}^{-4} \text{ s}^{-1}$
Uncoated T-22 boiler steel	67.36
Nanostructured TiAlN coating	03.10
Nanostructured AlCrN coating	73.72
Conventional TiAlN coating	23.26
Conventional AlCrN coating	00.41

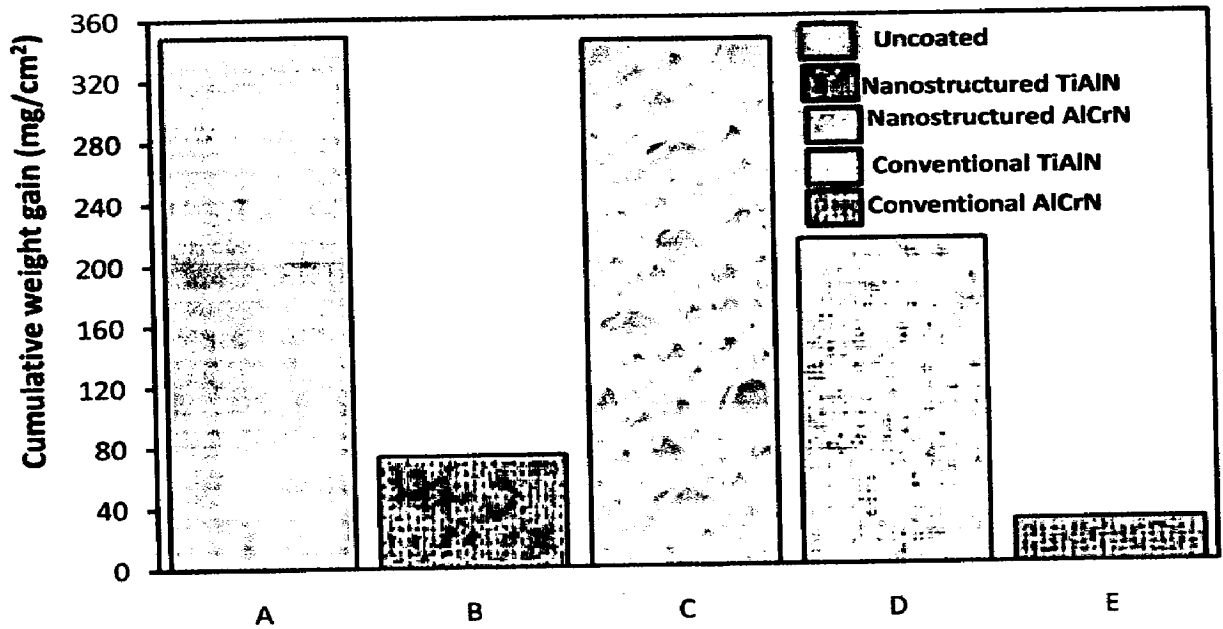


Fig. 6.20 Bar chart showing cumulative weight gain per unit area for the uncoated and coated ASTM-SA213-T-22 boiler steel exposed to molten salt ($\text{Na}_2\text{SO}_4\text{-60}\%\text{V}_2\text{O}_5$) environment at 900°C for 50 cycles: (A) Uncoated T-22 boiler steel, (B) Nanostructured TiAlN coating, (C) Nanostructured AlCrN coating, (D) Conventional TiAlN coating, (E) Conventional AlCrN coating

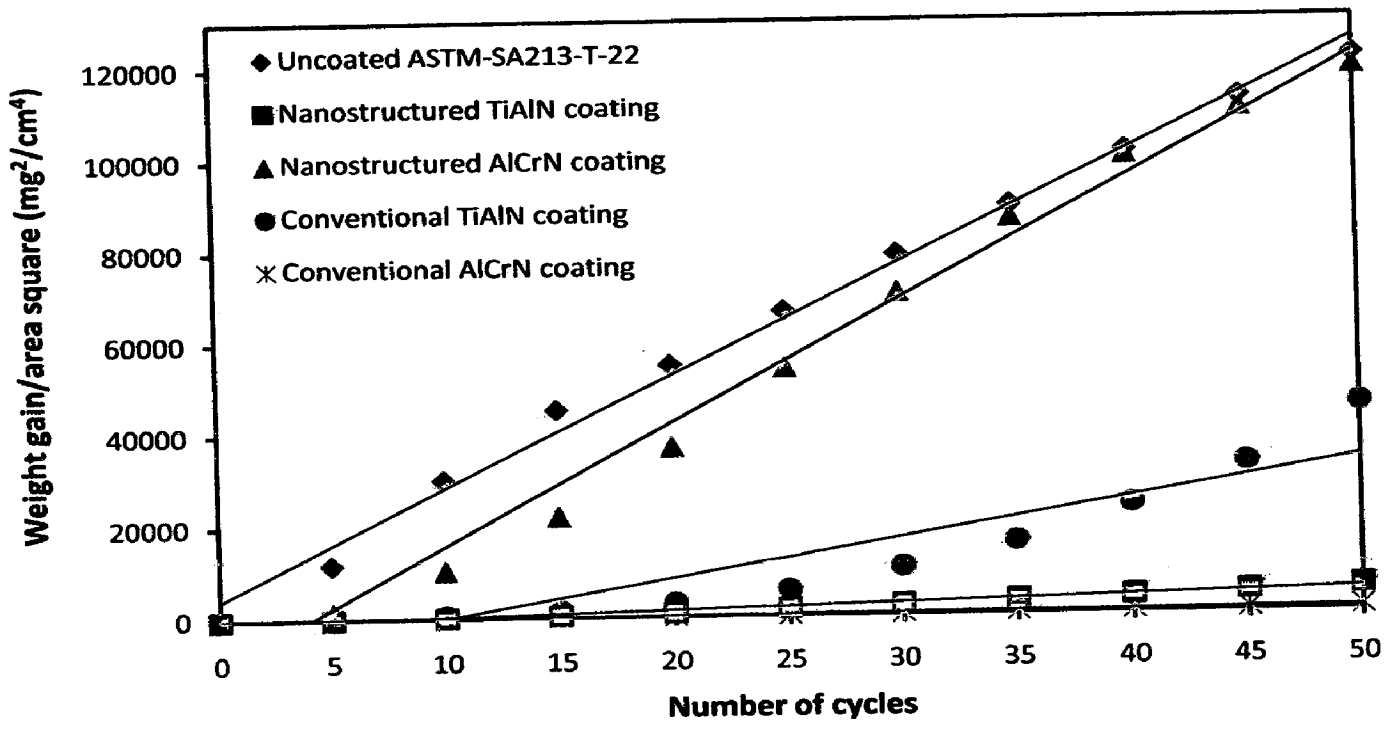


Fig. 6.21 Weight gain/area square vs time (number of cycles) for the uncoated and coated ASTM-SA213-T-22 boiler steel exposed to molten salt ($\text{Na}_2\text{SO}_4\text{-60}\%\text{V}_2\text{O}_5$) environment at 900°C for 50 cycles

6.3.1.3 Surface scale analysis

6.3.1.3.1 X-ray diffraction analysis (XRD)

XRD diffractograms for coated and uncoated ASTM-SA213-T-22 boiler steel subjected to cyclic oxidation in Na_2SO_4 -60% V_2O_5 (molten salt) environment at 900°C for 50 cycles are depicted in Fig.6.22 (a and b) on reduced scale. As indicated by the diffractograms Fe_2O_3 and Cr_2O_3 are the main phases present in the oxide scale of uncoated, conventional TiAlN and nanostructured thin TiAlN and AlCrN coated T-22 boiler steel. Also, weak peaks of Al_2O_3 are found in case of nanostructured thin TiAlN coating. Further, the oxide phases found in case of conventional thick AlCrN coating are Al_2O_3 and Cr_2O_3 .

6.3.1.3.2 Surface scale morphology

SEM micrographs along with EDAX point analysis reveals the surface morphology of the coated and uncoated ASTM-SA213-T-22 boiler steel subjected to cyclic oxidation in Na_2SO_4 -60% V_2O_5 (molten salt) environment at 900 °C for 50 cycles are shown in Fig.6.23: The oxide scale for uncoated T-22 boiler steel indicates the dominance of Fe and O (Fig.6.23.a). A small amount of Mo, Mn and Cr are also observed in the scale. The surface scale shows distorted and spalled grains like microstructure. The grains are of dark grey color (point 1) and boundaries are whitish in appearance (point 2).

The SEM micrograph of oxidized nanostructured thin TiAlN coatings is shown in Fig.6.23 (b). The oxide scale is mainly consisting of dark grey matrix (Point 4) and white needles dispersed in a matrix (Point 3) structure. EDAX analysis shows, the top scale rich in Fe and O with small amounts of Mo, Al, Ti, N, V, Na and Mn. As revealed by the EDAX analysis; matrix contains more amount of iron, whereas the needles like region contains higher amount of oxygen. In case of nanostructured thin AlCrN coated T-22 boiler steel, the SEM micrograph indicates distorted and spalled grains like microstructure as shown in Fig.6.23 (c). The EDAX point analysis shows the top scale rich in Fe, Mo and O. The small amount of Cr, Mn, Al, and Si are also present. The whitish region (point 6 on Fig.6.23.c) shows more amount of oxygen as compared to the dark grey area (point 5 on Fig.6.23.c).

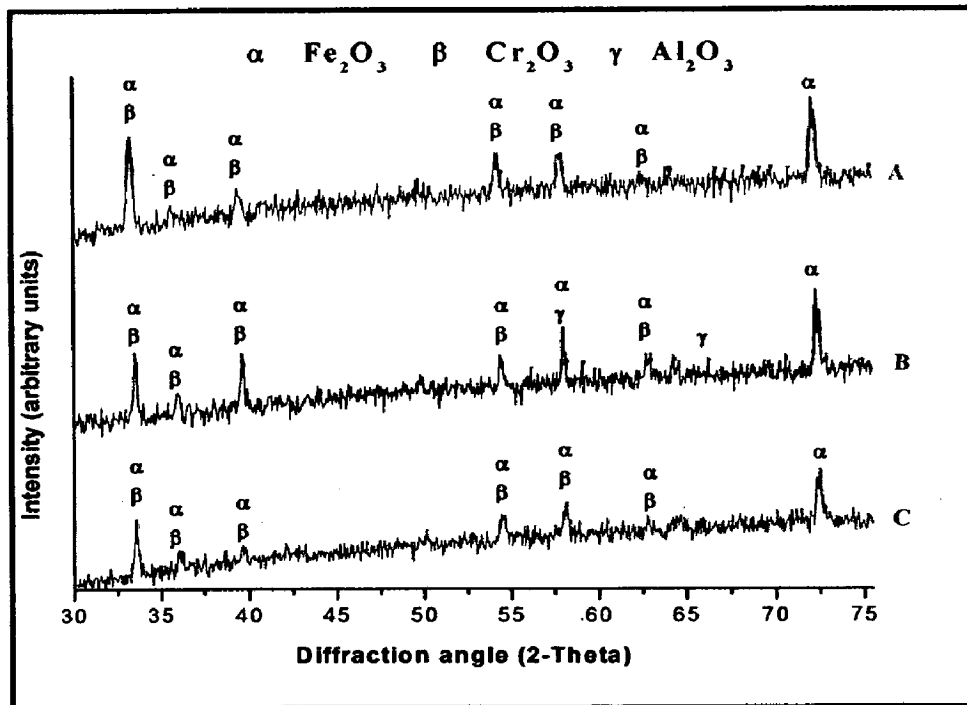


Fig. 6.22 (a) X-Ray Diffraction pattern of uncoated and coated ASTM-SA213-T-22 boiler steel exposed to molten salt (Na_2SO_4 -60% V_2O_5) environment at 900°C for 50 cycles: (A) Uncoated T-22 boiler steel, (B) Nanostructured TiAlN coating, (C) Nanostructured AlCrN coating

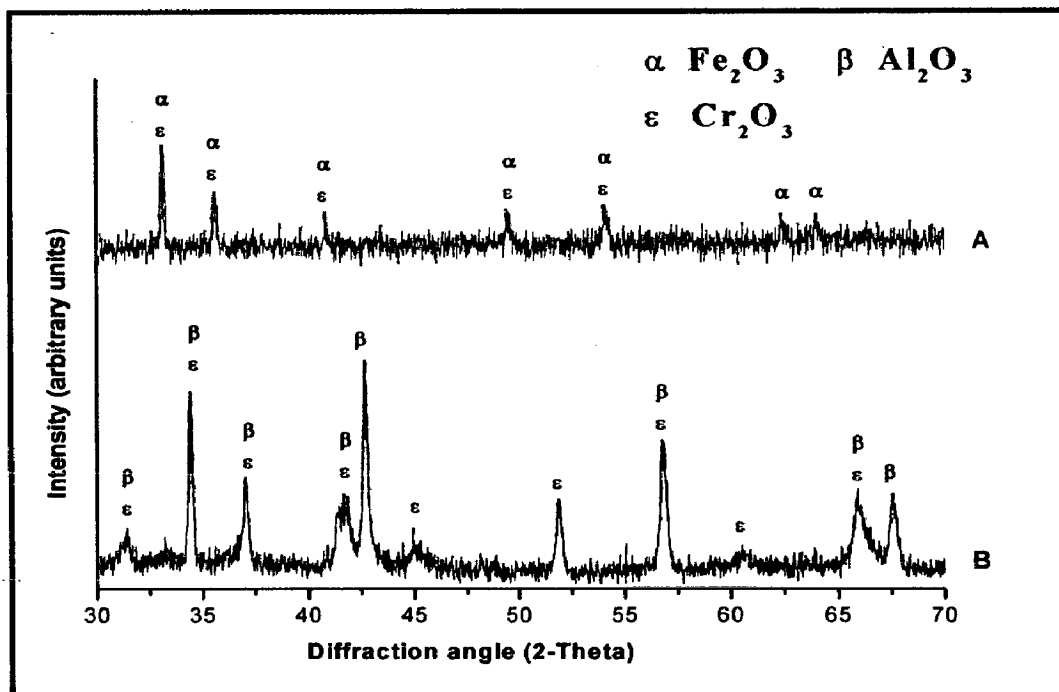


Fig. 6.22 (b) X-Ray Diffraction pattern of uncoated and coated ASTM-SA213-T-22 boiler steel exposed to molten salt (Na_2SO_4 -60% V_2O_5) environment at 900°C for 50 cycles: (A) Conventional TiAlN coating, (B) Conventional AlCrN coating

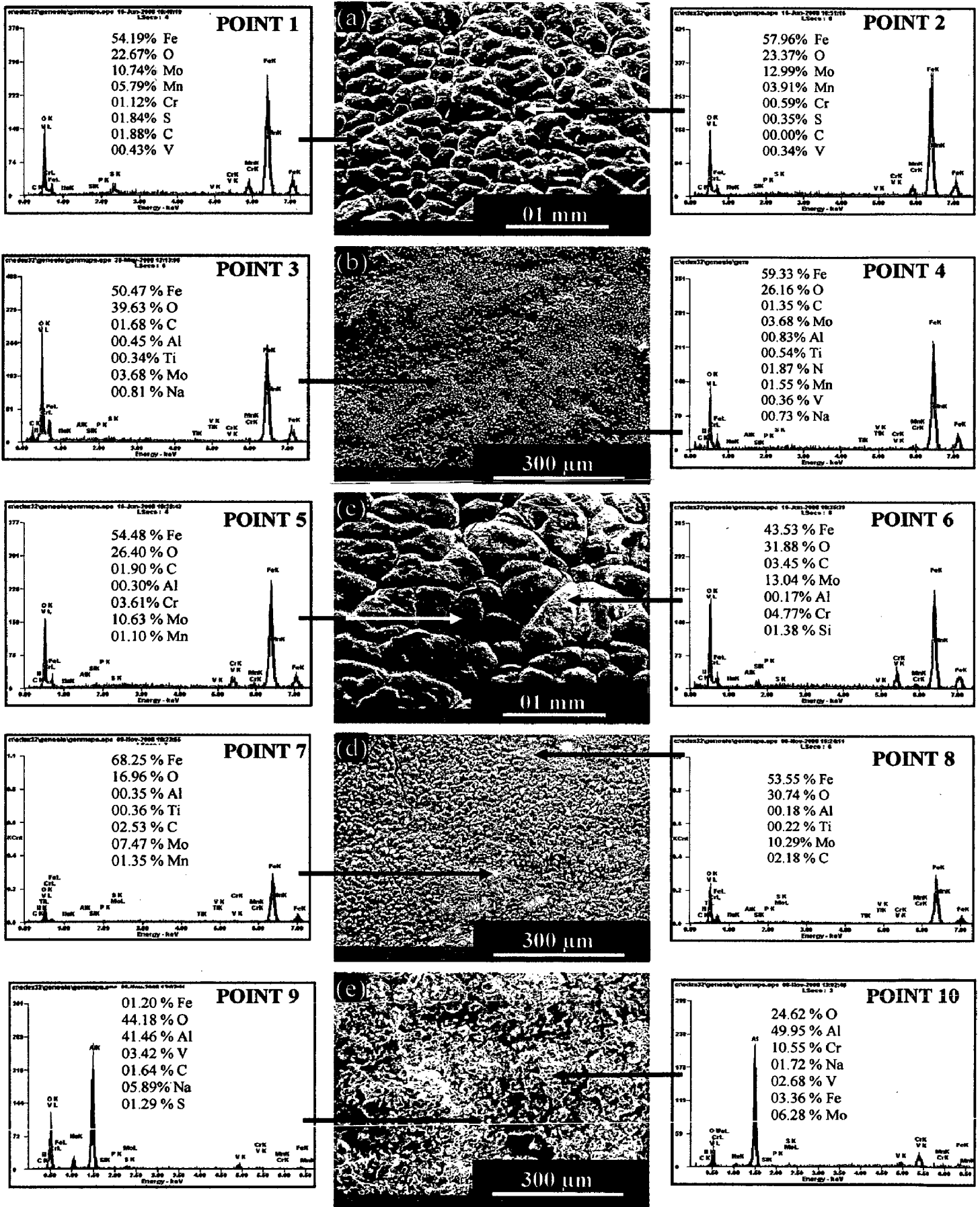


Fig. 6.23 Surface-scale morphology and EDAX patterns from different spots on uncoated and coated ASTM-SA213-T-22 boiler steel exposed to molten salt (Na_2SO_4 -60% V_2O_5) environment at 900°C for 50 cycles: (a) Uncoated T-22 boiler steel, (b) Nanostructured TiAlN coating, (c) Nanostructured AlCrN coating, (d) Conventional TiAlN coating, (e) Conventional AlCrN coating

The surface scale developed on conventional thick TiAlN coated T-22 steel indicates the dominance of Fe and O (Fig.6.23 .d). A small amount of Mo and Mn are also observed in the scale. A homogeneous and continuous surface scale is developed on conventional thick AlCrN coated T-22 boiler steel as shown in Fig.6.23 (e). The EDAX point analysis shows, the top scale is rich in Al and O with good amount of Cr. The point analysis at point 10 (whitish region) in Fig.6.23 (e) shows more amount of Al and Cr and less amount of oxygen as compared to the analysis at point 9 (grey contrast region).

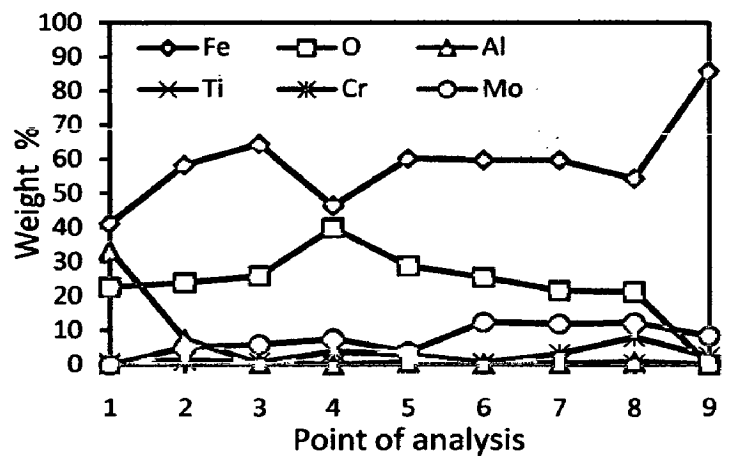
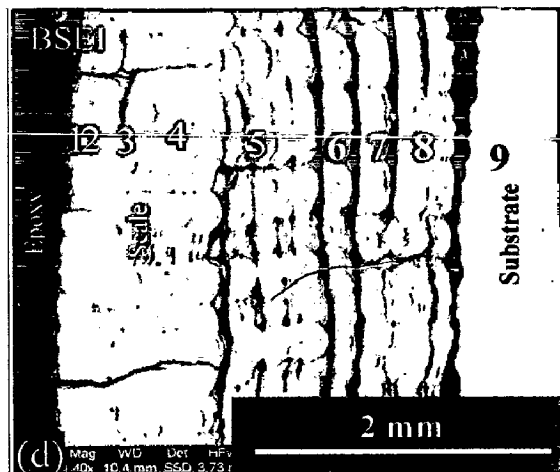
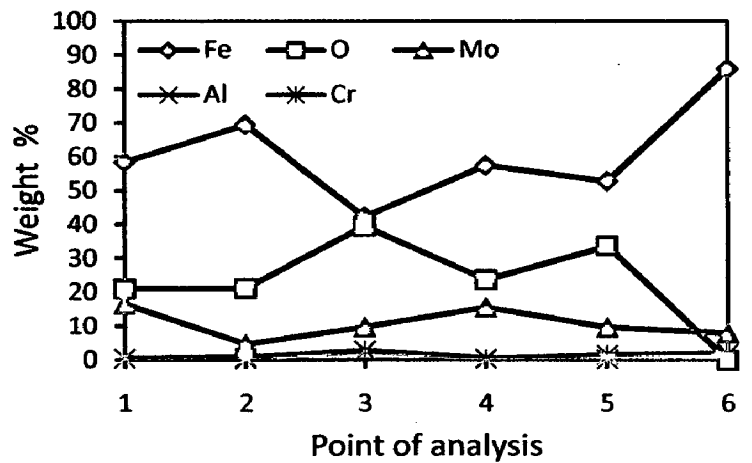
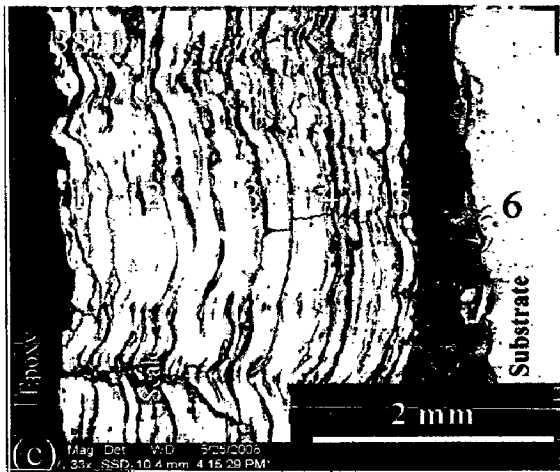
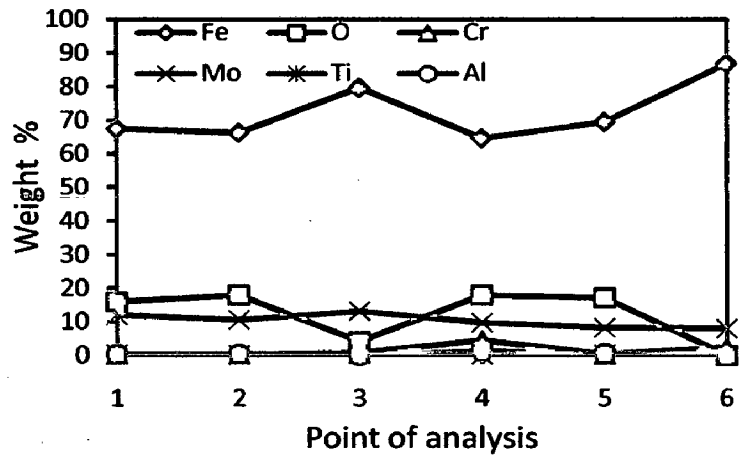
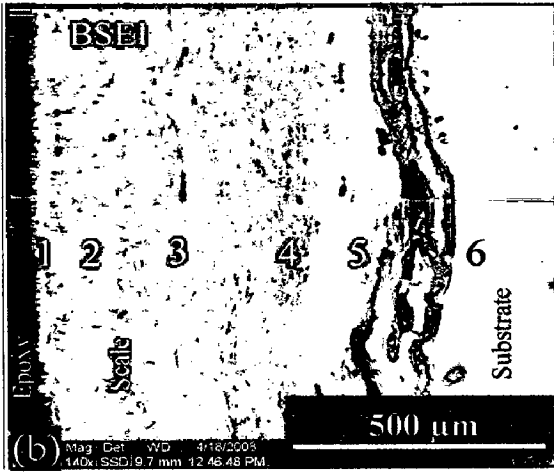
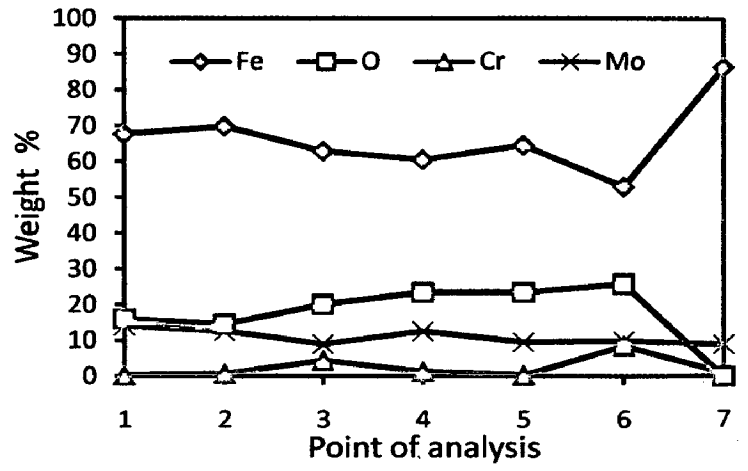
6.3.1.4 Cross-sectional analysis

6.3.1.4.1 Scale thickness

The oxidized samples were cut across the cross section using Buehler Isomet 1000 precision saw and mounted in transoptic mounting resin and subsequently mirror polished to obtain scanning electron back scattered micrographs and X-ray mapping of different elements for coated and uncoated ASTM-SA213-T-22 boiler steel. The scale thickness values were measured from SEM back scattered micrographs as shown in Fig.6.24. Very thick scale is observed in case of nanostructured AlCrN and conventional thick TiAlN coated T-22 boiler steel. The measured average scale thickness values for uncoated T-22 boiler steel, nanostructured thin TiAlN, nanostructured thin AlCrN, conventional thick TiAlN and conventional thick AlCrN coatings are 895, 738, 2900, 2575 and 110 μm respectively.

6.3.1.4.2 Cross-sectional scale morphology

Back Scattered Electron Image (BSEI) micrograph and elemental variation across the cross-section for coated and uncoated ASTM-SA213-T-22 boiler steel subjected to cyclic oxidation in Na_2SO_4 -60% V_2O_5 (molten salt) environment at 900°C for 50 cycles are shown in Fig.6.24. The SEM micrograph in case of uncoated T-22 boiler steel shows uniform thick scale as shown in Fig. 6.24 (a). The EDAX analysis reveals the presence of iron, oxygen and molybdenum throughout the scale along Cr at some points (points 3 and 6 on Fig.6.24.a). The existence of significant amount of oxygen points out the possibility Fe_2O_3 in the oxide scale.



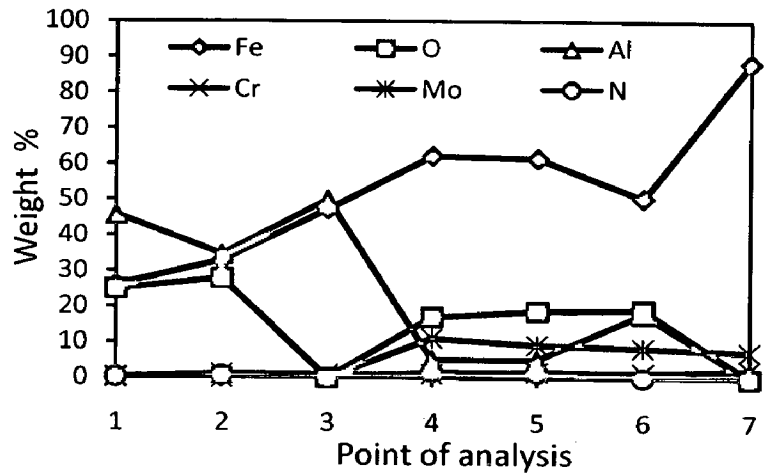
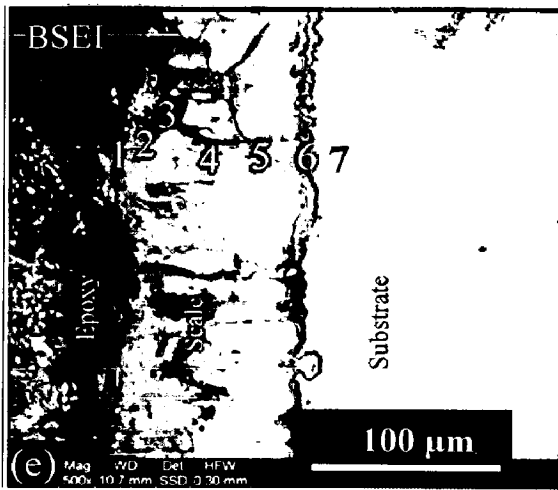


Fig. 6.24 Oxide scale morphology and variation of elemental composition across the cross-section of the uncoated and coated ASTM-SA213-T-22 boiler steel exposed to molten salt ($\text{Na}_2\text{SO}_4\text{-60}\%\text{V}_2\text{O}_5$) environment at 900°C for 50 cycles: (a) Uncoated T-22 boiler steel (116 X), (b) Nanostructured TiAlN coating (140 X), (c) Nanostructured AlCrN coating (33 X), (d) Conventional TiAlN coating (100 X), (e) Conventional AlCrN coating (500 X)

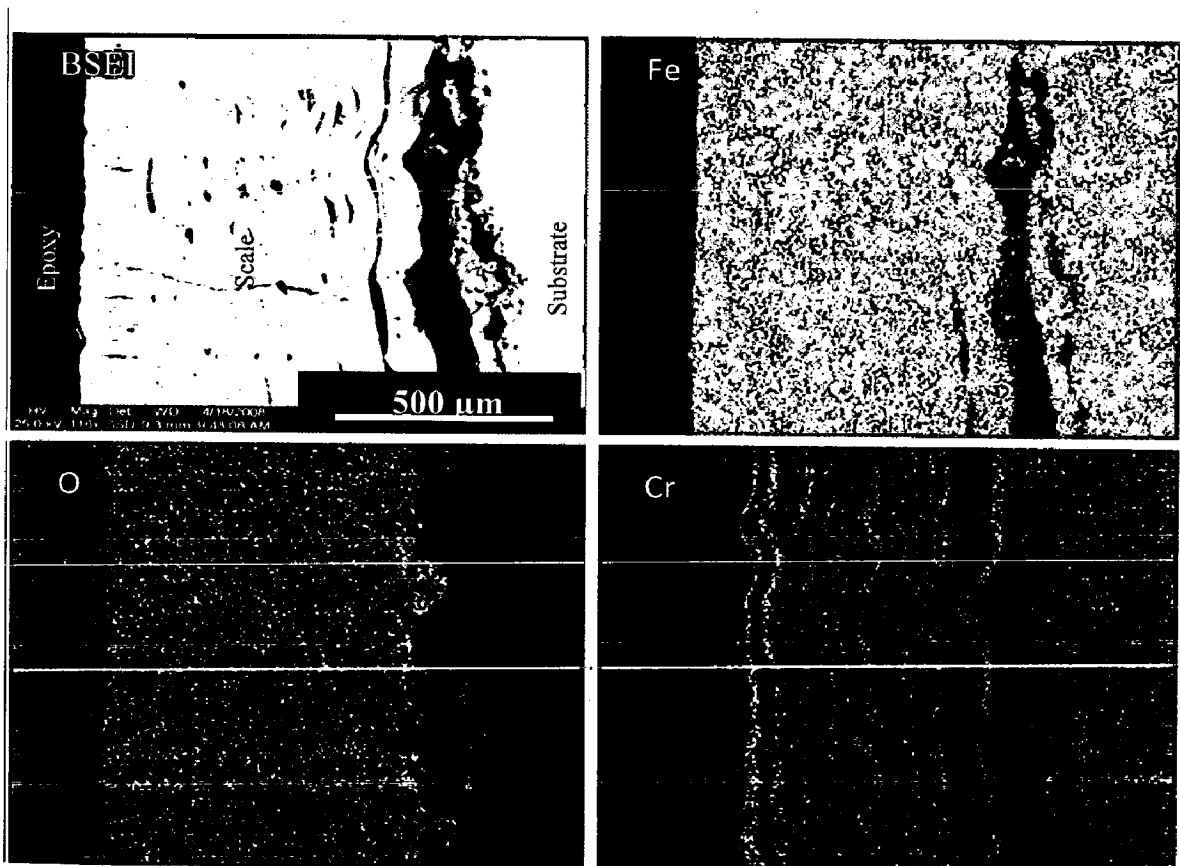


Fig. 6.25 (a) Composition image (BSEI) and X-ray mapping of the cross-section of uncoated ASTM-SA213-T-22 boiler steel exposed to molten salt ($\text{Na}_2\text{SO}_4\text{-60}\%\text{V}_2\text{O}_5$) environment at 900°C for 50 cycles

Also, the points where Cr content is more shows less Fe and more oxygen as compared to the other points. This is showing the possibility of Cr_2O_3 in the scale. BSEI micrograph and elemental variation depicted in Fig.6.24 (b), for the exposed cross-section of nanostructured thin TiAlN coated T-22 boiler steel shows the thick, continuous and adherent scale. The EDAX analysis reveals the presence of Fe, Mo and oxygen throughout the scale. A location at points 4 (Fig.6.24.b) in the micrograph depicts the increase in percentage of Cr with decrease in percentage of Fe and Mo. A thick and fragile oxide scale can be seen in case of nanostructured AlCrN coated T-22 boiler steel (Fig.6.24.c). The scale is showing cracking. The EDAX point analysis indicates the presence of Fe, Mo and oxygen in the oxide scale along with good amount of Cr at some points (points 3 in Fig.6.24.a).

In case of conventional TiAlN coated T-22 boiler steel, the scale is fragile and showing severe cracking along the surface as depicted in Fig.6.24 (d). The EDAX point analysis indicates the presence of Fe, O and Mo in the scale with variable amounts. The top scale is rich in Al along with O and Fe (Point 1 in Fig.6.24.d). The conventional thick AlCrN coated T-22 boiler steel (Fig.6.24.e) indicates continuous, thin and adherent scale. EDAX point analysis shows the presence of Fe, Al, and O throughout the scale. The concentration of Al is more in the top scale as shown by analysis at point 1, 2, 3 and then at the scale/substrate interface i.e. point 6 in Fig.6.24 (e).

6.3.1.4.3 X-Ray mapping

X-ray mappings for a part of oxide scale of uncoated and coated ASTM-SA213-T-22 boiler steel oxidized in Na_2SO_4 -60% V_2O_5 (molten salt) environment at 900 °C for 50 cycles are shown in Fig. 6.25. In case of uncoated T-22 boiler steel, the micrograph (Fig.6.25.a) indicates a dense scale, which mainly contains iron and oxygen with some amount of chromium. Presence of thin bands of Cr in the scale indicates the rich and Cr depleted regions.

Figure 6.25 (b), shows X-ray mapping analysis of the scale formed on nanostructured TiAlN coated T-22 boiler steel. The BSEI image and X-ray mapping shows the formation of a dense scale consisting mainly of iron, oxygen and chromium.

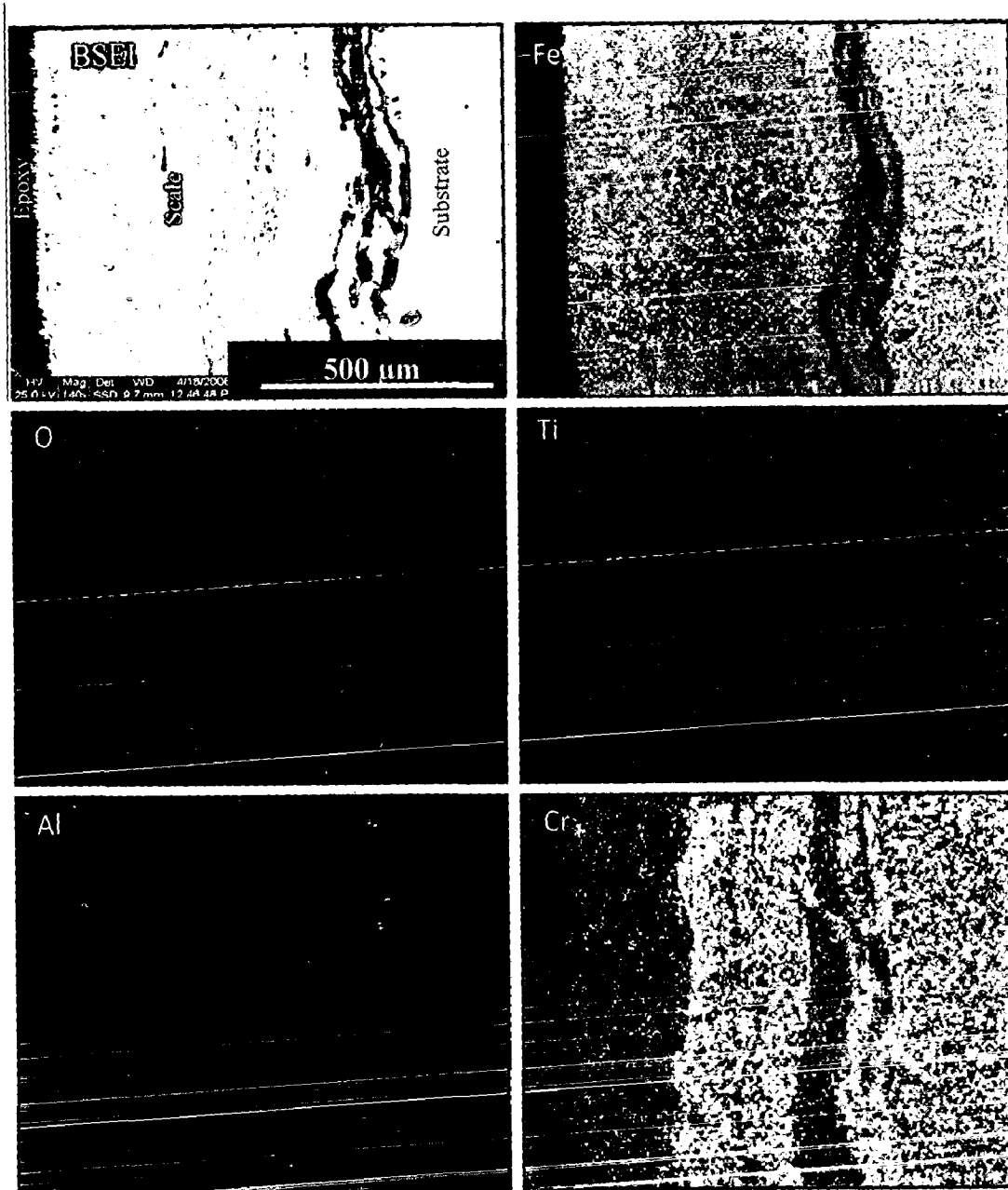


Fig. 6.25 (b) Composition image (BSEI) and X-ray mapping of the cross-section of Nanostructured TiAlN coated ASTM-SA213-T-22 boiler steel exposed to molten salt (Na_2SO_4 -60% V_2O_5) environment at 900°C for 50 cycles

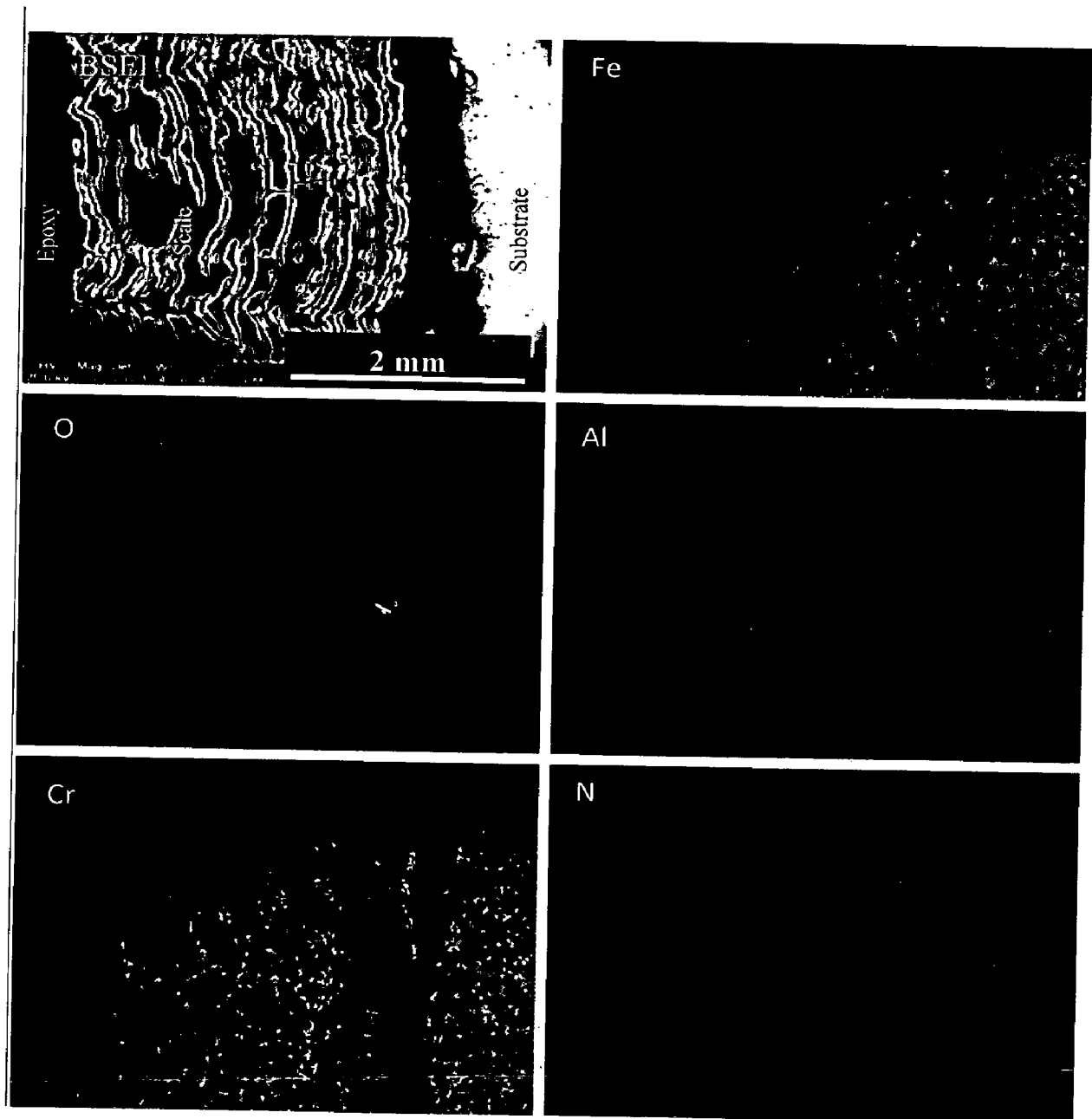


Fig. 6.25 (c) Composition image (BSEI) and X-ray mapping of the cross-section of Nanostructured AlCrN coated ASTM-SA213-T-22 boiler steel exposed to molten salt (Na_2SO_4 -60% V_2O_5) environment at 900°C for 50 cycles

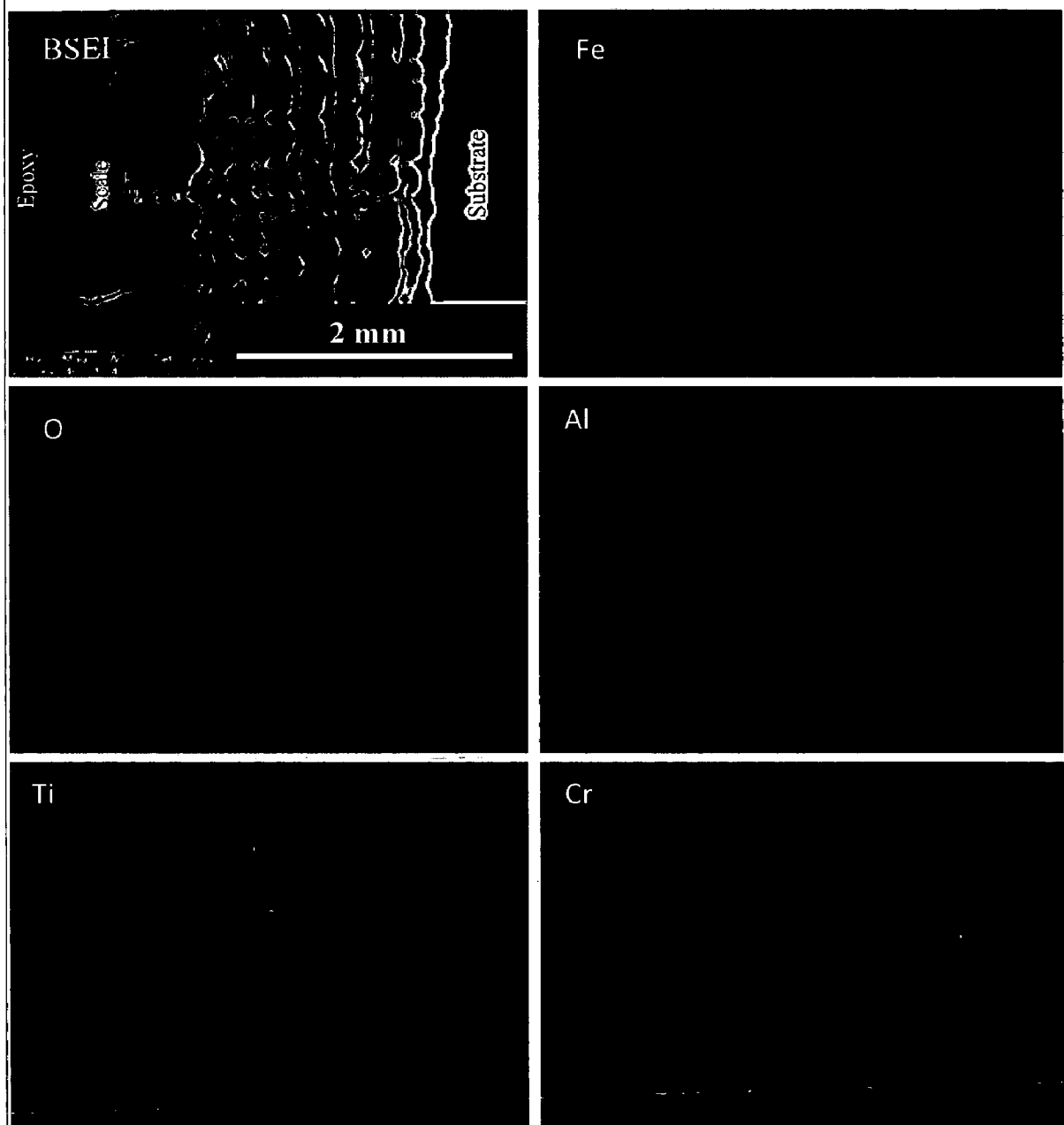


Fig.6.25 (d) Composition image (BSEI) and X-ray mapping of the cross-section of conventional TiAlN coated ASTM-SA213-T-22 boiler steel exposed to molten salt (Na_2SO_4 -60% V_2O_5) environment at 900°C for 50 cycles

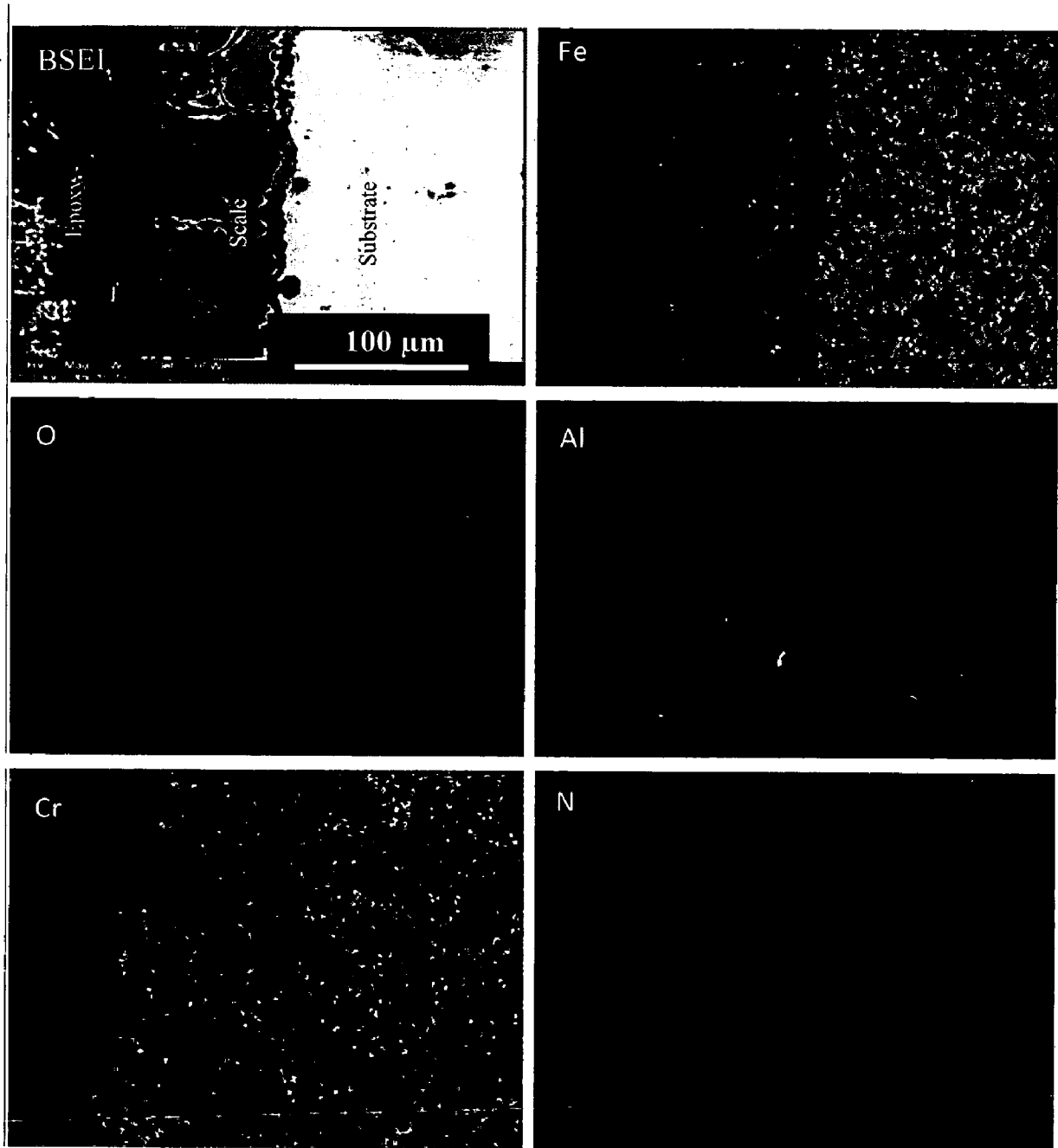


Fig. 6.25 (e) Composition image (BSEI) and X-ray mapping of the cross-section of conventional AlCrN coated ASTM-SA213-T-22 boiler steel exposed to molten salt (Na_2SO_4 -60% V_2O_5) environment at 900°C for 50 cycles

The X-ray mapping also indicates thick bands of Cr parallel to each other, near the scale/substrate interface. In case of nanostructured thin AlCrN coated T-22 boiler, the BSEI and X-ray mapping are shown in Fig. 6.25 (c). The scale formed is fragile. The X-ray mapping indicates the presence of iron and oxygen throughout the scale. Few parallel thin bands of Al and Cr can be seen at some locations, where iron is completely absent. In case of conventional thick TiAlN coated T-22 boiler steel, Fig.6.25 (d), Fe and O are present throughout the scale. A thin band of Al is present in the top scale. The sub scale is rich in Fe and O along with some amount of Cr in the sub scale region. Fig.6.25 (e), depicts the X-ray mapping in case of conventional AlCrN coated T-22 boiler steel. Thick band of aluminum is present in the top scale region along with iron. As revealed from the X-ray mapping results, the oxygen fails to enter in the substrate region. The conventional AlCrN coating is fully protective and not allowing the environment to enter in the substrate.

6.3.2 Summary of Results

Results obtained after exposure of uncoated and coated ASTM-SA213-T-22 boiler steel to cyclic oxidation in Na_2SO_4 -60% V_2O_5 (molten salt) environment at 900°C for 50 cycles are summarized in Table.6.5.

6.3.3 Discussion

The bare, nanostructured AlCrN and conventional TiAlN coated T-22 boiler steel showed accelerated corrosion in Na_2SO_4 -60% V_2O_5 (molten salt) environment at 900°C and weight gain was relatively higher as compared to the other two coatings (Fig.6.19 and 6.20). The weight gain graph (Fig.6.19) for all samples shows higher weight gain at initial cycles followed by gradual weight gain except in case of conventional TiAlN coating, which has shown abrupt increase in oxidation rate after 21st cycle. The weight change plots for the uncoated and coated T-22 boiler steel has shown conformance to parabolic rate law. The parabolic behavior is due to the diffusion controlled mechanism operating at 900°C under cyclic conditions (Mahesh et al., 2008). Small deviation from the parabolic rate law might be due to the cyclic scale growth.

Table 6.6 Summary of the results obtained for uncoated and coated ASTM-SA213-T-22 boiler steel subjected to cyclic oxidation in molten salt (Na_2SO_4 -60% V_2O_5) environment at 900°C for 50 cycles

Coating	Cumulative Weight gain (mg/cm^2)	Parabolic rate constant ($K_p \times 10^{-08} \text{ gm}^2\text{cm}^{-4}\text{s}^{-1}$)	XRD phases	Remarks
Uncoated T-22 boiler steel	348.55	67.36	Fe_2O_3 and Cr_2O_3	A grey colored scale appeared on the surface right from the 1 st cycle. This bare steel showed spalling of scale just after the 5 th cycle, which continued till the end of 50 cycles. At the end of cyclic study, irregular and fragile scale was observed with deep cracks and blackish grey color surface appearance
Nanostructured TiAlN coating	73.36	03.10	Fe_2O_3 , Cr_2O_3 and Al_2O_3	Color of the oxide scale at the end of the study was observed to be blackish grey middle portion of the sample with light grey sides. The scale remains adherent to the substrate during the course of the study.
Nanostructured AlCrN coating	345.05	73.72	Fe_2O_3 , and Cr_2O_3	Color of the oxide scale at the end of the study was observed to be dark grey. The scale starts falling in the boat just after 3 rd cycle and this trend continued till 50 th cycle. New layers of scale were forming and falling in the boat.
Conventional TiAlN Coating	212.77	23.26	Fe_2O_3 , and Cr_2O_3	There was no sign of spalling till 20 th cycle and the weight change rate was gradual. After 21 st cycle, the scale formed on the upper surface of the specimen shows severe spalling and it gets separated from the substrate and fall in the boat, whereas the lower surface of the sample which is in touch with the boat wall shows no sign of spalling and the scale is adherent to the substrate. This trend continued till 50 th cycle.
Conventional AlCrN coating	28.16	00.41	Al_2O_3 and Cr_2O_3	The surface becomes rough after first cycle. During the study no spalling and cracking was observed. At the end of the study, the scale was found to be adherent with light grey surface appearance.

The higher weight gain during the first few cycles might be attributed to the rapid formation of oxides at the splat boundaries and within the open pores due to the penetration of the oxidizing species. Once the oxides are formed at places of porosity and splat boundaries, the coating becomes dense and the diffusion of oxidizing species to the internal portions of the coatings gets slowed down and the growth of the oxides becomes limited mainly to the surface of the specimens. This, in turn, will make the weight gain and hence the oxidation rate steady with the further progress of exposure time (Singh et al., 2007 and Sidhu et al., 2006).

The rapid increase in the weight gain during the initial period of exposure to Na₂SO₄-60%V₂O₅ (molten salt) environment at 900°C can also be attributed to the possible formation of NaVO₃. Kolta et al. (1972) proposed that at temperature range of 900°C, the Na₂SO₄ and V₂O₅ will combine to form NaVO₃, as represented by eq.(6.1) having a melting point of 610°C.



This NaVO₃ acts as a catalyst and also serves as an oxygen carrier to the base alloy through the open pores present on the surface, which will lead to the rapid oxidation of the base elements of the substrate to form a protective oxide scale. There may be simultaneous dissolution of protective oxide Cr₂O₃ in the molten salt due to the reaction (Seiersten and Kofstad, 1987; Swaminathan et al., 1993):



The Na₂CrO₄ gets evaporated as a gas (Fryburg et al., 1984 and Guo et al., 2006). The rapid increase in the weight gain during the initial period was also reported by Sidhu et al. (2006), Harpreet Singh et al.(2005), Tiwari and Prakash (1997) and Ul-amid (2003) during studies on the hot corrosion of alloys.

Conventional thick AlCrN and nanostructured TiAlN coatings have been found successful in reducing the overall weight gain of bare T-22 boiler steel. The parabolic rate constant (K_p) was obtained from the slope of the linear regression fitted line (cumulative weight gain/area)² versus number of cycles (Table.6.4). The parabolic rate constant for the uncoated and nanostructured AlCrN coatings is found to be higher than the conventional AlCrN, conventional and nanostructured TiAlN coatings. The oxidation

rate (total weight gain values after 50 cycles) of the coated and uncoated T-22 boiler steel boiler steel follows the sequence as given below:

Bare T-22 > Nanostructured AlCrN > Conventional TiAlN > Nanostructured TiAlN > Conventional AlCrN

The surface XRD analysis (Fig.6.22) indicated the formation of Fe_2O_3 as the main constituent of the top scale along with weak peaks of Cr_2O_3 in case of bare, nanostructured and conventional TiAlN and nanostructured AlCrN coated boiler steel. The formation of Fe_2O_3 has also been observed by Shi (1993) for the oxidation of iron by Na_2SO_4 at 750°C and by Tiwari and Prakash (1996) during hot corrosion of Iron-base superalloy in the Na_2SO_4 -60% V_2O_5 (molten salt) environment at 900°C . Weak intensity peaks of Cr_2O_3 in the scale of T-22 steel may be due to the presence of some amount of chromium in the alloy steel. The presence of some percentage of chromium in the subscale as revealed by the X-ray mapping analysis (Fig.6.25) across the cross-section for T-22 steel is in accordance with the findings of Sadique et al. (2000). The authors have reported that Fe-Cr alloys in oxygen at higher temperature (950 - 1050°C) form spinel (FeCr_2O_4) and Cr_2O_3 on the inner side and Fe_2O_3 on the outer side of the scale. This can also be attributed to depletion of iron due to oxidation to form the upper scale thereby leaving chromium rich pockets those further get oxidized to form iron chromium spinel. XRD analysis (Fig.6.22) revealed the presence of protective Cr_2O_3 and Al_2O_3 oxides in case of conventional AlCrN coating, which are further supported by EDAX analysis of surface (Fig.6.23.e) and cross-section (Fig.6.24.e) and X-ray mapping (Fig.6.25.e) analysis. This may be the reason of excellent performance of conventional AlCrN coating in Na_2SO_4 -60% V_2O_5 (molten salt) environment at 900°C .

The severe spalling and cracking as observed in case of bare, nanostructured AlCrN and conventional TiAlN coated T-22 steels may be attributed to the presence of molybdenum in the steels. Chatterjee et al. (2001) have suggested that during initial hours oxidation Fe oxidizes and the oxide scale is protective in nature. With progress of oxidation Mo becomes enriched at the alloy scale interface, leading to the formation of an inner layer of molten MoO_3 (m. p. 795°C). MoO_3 might have further reacted with Na_2SO_4 as per the following reaction resulting in the formation of low temperature melting phase Na_2MoO_4 .



This might have led to the acidic fluxing of the protective oxide scale. This liquid oxide disrupts and dissolves the protective oxide scale, causing the alloy to suffer catastrophic oxidation (Lai, 1990). Identical results have been reported by Peters et al. (1976), Fryburg et al. (1982), Pettit and Meier (1984) and Misra (1986). The severe spalling of scale identical to the present study for similar type of steel i.e. T-22 type of steel during hot corrosion in medium BTU coal gasifier environment has also been reported by Wang (1988) where more than 70% of the scale got spalled during testing. Further Misra (1986) reported the spalling of thick external porous scale which spalled off completely on cooling during corrosion experiments at 900°C and 950°C.

Accelerated corrosion observed in the present study in case of bare, nanostructured AlCrN and conventional TiAlN coated T-22 boiler steel up to the end of exposure may be in accordance with the findings of Misra (1986). The author reported that higher the concentration of Mo, the sooner the melt would attain the MoO₃ activity necessary for the formation of solid NiMoO₄ and this would cause a decrease in the length of the period of accelerated corrosion. Lower percentage of Mo (0.87-1.13%) in the concerned alloy for the present study might have increased the period of accelerating corrosion up to the end of 50 cycles. Probably this factor is responsible for the higher weight gain for bare, nanostructured AlCrN and conventional TiAlN coated T-22 boiler steel.

During cyclic testing, severe cracking in the oxide scale (Fig.6.18.d and Fig.6.24.d) of the conventional TiAlN coatings might be attributed to the different values of thermal expansion coefficients for the coating, scale and the substrate as reported by Sidhu et al. (2003), Singh et al. (2004), Evans et al. (2001), Wang et al. (2002) and Niranatlumpong et al (2000). The formation of cracks in the coating originates from stresses developed in the deposit or at the coating-base metal interface (Heath et al., 1997). Also, inferior oxidation resistance of conventional thick TiAlN coating may be as opined by Ding et al. (2008). In an oxidation or corrosive environment Ti element often forms a porous non-protective oxide scale, which limits the oxidation and corrosion resistance of titanium-based coatings. This has further been reported by Fujita (2005), where authors have

reported that the oxide scale of binary TiAl alloy is composed of a porous oxide mixture of TiO_2 and Al_2O_3 , which has dominated by TiO_2 .

In case of nanostructured thin TiAlN coating, the Fe_2O_3 in the top layer and Fe_2O_3 and Cr_2O_3 in the subscale analyzed by the XRD (Fig.6.22), SEM-EDAX (Fig. 6.23.b) and X-ray mapping (Fig. 6.25.b). Figure 6.25 (b) indicated the presence of a thick band of Cr in the subscale along with oxygen and iron. This can be attributed to the depletion of iron due to oxidation to form the upper scale, thereby leaving chromium-rich pockets those have further oxidized to form a regular chromium oxide bands. This band of chromium oxide may have prevented the deep penetration of the reacting environment, as the scale thickness is less in case of oxidized nanostructured thin TiAlN coated T-22 boiler steel than that of uncoated boiler steel. It can be mentioned based on the present investigation that conventional thick AlCrN and nanostructured TiAlN coatings can provide a very good oxidation resistance in Na_2SO_4 -60% V_2O_5 molten salt environment at high temperature.

6.3.4 Conclusions

The high temperature oxidation behaviors of uncoated and coated ASTM-SA213-T-22 boiler steel have been investigated in Na_2SO_4 -60% V_2O_5 molten salt at 900 °C for 50 cycles. The behavior of nanostructured TiAlN and AlCrN coatings were compared with their conventional counterparts and the following conclusions are made:

1. The oxidation rate (total weight gain values after 50 cycles) of the coated and uncoated T-22 boiler steel follows the sequence as given below:
Uncoated T-22 > Nanostructured AlCrN > Conventional TiAlN > Nanostructured TiAlN > Conventional AlCrN
2. The plasma sprayed gas nitride conventional thick AlCrN coating developed a protective scale mainly consisting of aluminum oxide and chromium oxide.
3. The nanostructured thin TiAlN coatings has shown resistance to oxidation as the overall weight gain is less than as compared to the uncoated T-22 boiler steel.
4. In case of uncoated T-22 boiler steel, the weight gain is highest with thickest scale. Severe spalling and cracking is also observed in case of bare, nanostructured thin AlCrN and conventional thick TiAlN coated boiler steel.

5. The nanostructured thin TiAlN and conventional thick AlCrN coatings can provide a good oxidation resistance in Na_2SO_4 -60% V_2O_5 molten salt environment at high temperature.
6. The oxide scale formed is adherent to the substrate in nanostructured thin TiAlN and conventional thick AlCrN coated ASTM-SA213-T-22 boiler steel. But in case of bare nanostructured thin AlCrN and conventional thick TiAlN coated boiler steel, the scale is found to be detached from the substrate after hot corrosion studies.
7. The appearance of cracks/peeling off in the coatings during hot corrosion studies may be attributed to the different values of thermal expansion coefficients for the coating, substrate steel and oxides.

6.4 EROSION STUDIES IN SIMULATED COAL-FIRED BOILER ENVIRONMENT

The present work has been focused to compare the high temperature erosion behavior of conventional thick (by plasma spraying and gas nitrided) and nanostructured thin (by physical vapor deposition process) TiAlN and AlCrN coatings on ASTM-SA213-T-22 boiler steel. The erosion studies were carried out using a high temperature air-jet erosion test rig at a velocity of 35 ms^{-1} and impingement angles of 30° and 90° . The tests were carried out at high temperatures. The two temperatures were taken for the test, sample temperature 400°C and air/erodent temperature 900°C simulated to service conditions of boiler tubes in which sample temperature and flow gas temperature correspond to the inner and outer temperature of water wall pipes. The alumina particles of average size $50 \mu\text{m}$ were used as erodent. Erosion rates in terms of volumetric loss (mm^3/g) for different uncoated and coated alloys are compared. The eroded samples were analyzed with SEM/EDX and optical profilometer. The erosion rate data for each coated alloy has been plotted along with uncoated alloy in order to assess the coating performance. Efforts have been made to understand the mode of erosion.

6.4.1 Results

6.4.1.1 Visual observations

The macrographs for uncoated and coated ASTM-SA213-T-22 boiler steel subjected to erosion studies in simulated coal-fired boiler environment are shown in Fig.6.26. The effect of corrosion along with the erosion was observed. The shape of the scar (developed by constant strike of erodent) is circular in case of normal impact (at 90°) and elliptical in case of oblique impact (at 30°) of erodent. The uncoated T-22 boiler steel shows a thin scale. The erosion seems to clean the scale off the surface in the eroded/corroded region. The impact of erodent removes the scale down to the substrate-scale interface. Away from this eroded region a thin layer of scale was observed on the surface and the eroded/corroded region showed rust colored discoloration (Fig.6.26.a). The nanostructured TiAlN coated T-22 boiler steel showed marks of erosion as shown in Fig.6.26 (b). The color of the coated specimen changed from violet-grey to carbon black at scar and blackish blue ring around the scar. The macrograph in case of eroded nanostructured AlCrN coating are shown in Fig.6.26 (c).

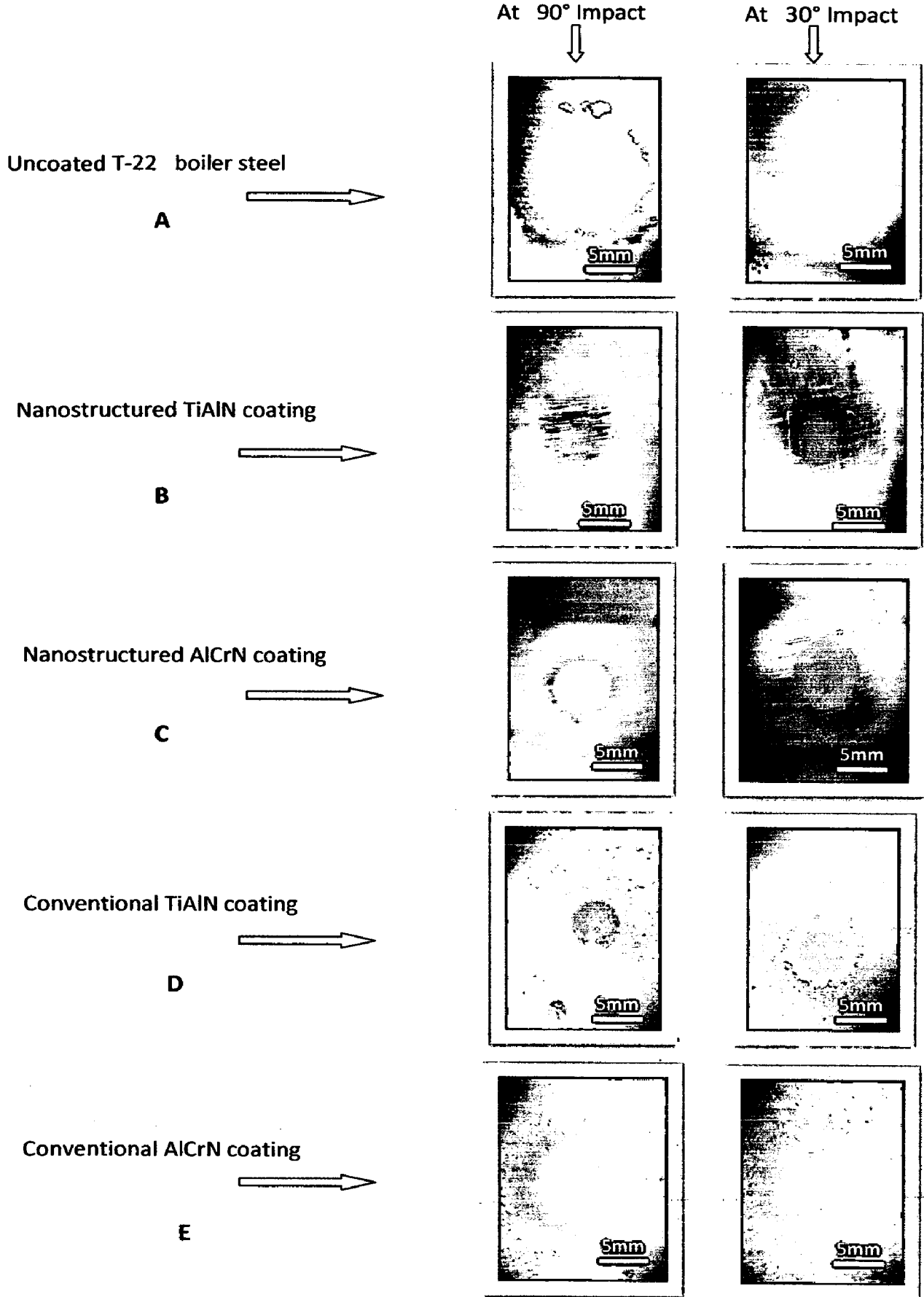


Fig. 6.26 Surface macrographs of eroded uncoated and coated ASTM-SA213-T-22 boiler steel exposed to high temperature erosion studies in simulated coal-fired boiler environment

The color of the scars was observed as light grey surrounded by dark colored ring. A visual observation of conventional thick TiAlN and AlCrN coated T-22 boiler steel (Fig.6.26.d and e), showed the formation of dark grey colored scar surrounded by a light colored ring. Also, the un-eroded area around the scars appeared as rough surface.

6.4.1.2 Erosion rate

The erosion loss has been calculated by volume change method. The volume loss occurred after erosion testing was measured by using non contact optical profilometry as explained in chapter 3. The erosion depth was measured at six random locations to obtain the average erosion depth of an eroded scar. At each location (including eroded and un-eroded area) surface profiles were taken.

The erosion rate for uncoated and coated T-22 boiler steel at an impact velocity of 35 ms^{-1} and impingement angle of 30° and 90° when substrate temperature was 400°C and surrounding air at 900°C ; is shown in Fig. 6.27. The volume erosion rate for uncoated T-22, nanostructured thin TiAlN, nanostructured thin AlCrN, conventional thick TiAlN and conventional thick AlCrN coatings; is 0.38425×10^{-3} , 0.03544×10^{-3} , 0.0819×10^{-3} , 2.135×10^{-3} and $2.0287 \times 10^{-3} \text{ mm}^3/\text{gm}$ respectively at 90° impact angle. While at 30° impact, the volume erosion rate for uncoated T-22, nanostructured thin TiAlN, nanostructured thin AlCrN, conventional thick TiAlN and conventional thick AlCrN coatings; is 0.4196×10^{-3} , 0.0691×10^{-3} , 0.0956×10^{-3} , 3.01725×10^{-3} and $1.636 \times 10^{-3} \text{ mm}^3/\text{gm}$ respectively.

From the graph, it can be inferred that the erosion rate of the uncoated T-22 boiler steel eroded at oblique impact i.e. at 30° impingement angle is slightly more as compared to erosion rate at 90° impact. Also, in case of conventional TiAlN and nanostructured coatings; the erosion rate is higher at oblique impact than at normal impact thus showing the typical behavior of ductile materials. The overall volume erosion rate is negligible in case of nanostructured coatings when compared with the uncoated boiler steel and conventional coatings. The volume erosion rate in case of conventional AlCrN coating is higher at normal impact. The overall volume erosion rate in case of conventional AlCrN coating is less as compared to conventional thick TiAlN coating.

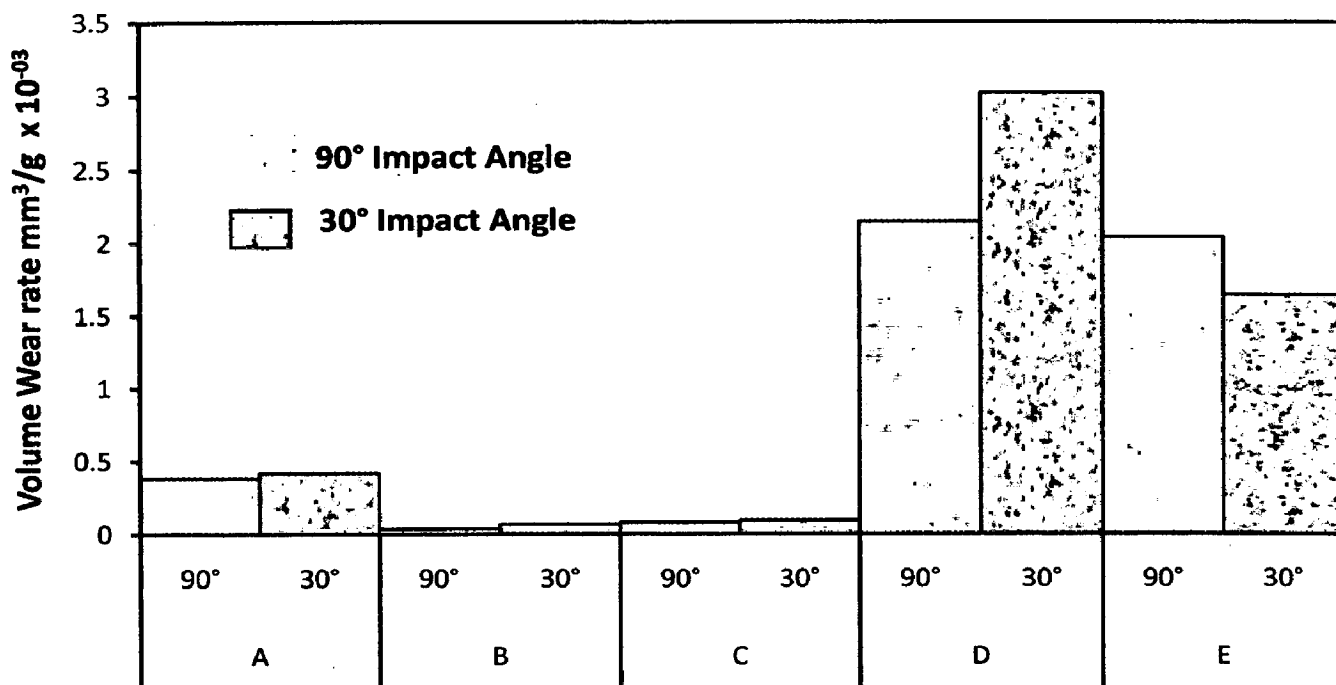


Fig. 6.27 Column chart showing the Volume wear rate of uncoated and coated ASTM-SA213-T-22 boiler steel eroded at normal and oblique impact: (A) Uncoated T-22 boiler steel, (B) Nanostructured TiAlN coating, (C) Nanostructured AlCrN coating, (D) Conventional TiAlN coating, (E) Conventional AlCrN coating

6.4.1.3 SEM/EDAX Analysis

SEM micrographs along with EDAX point analysis reveals the surface morphology of the uncoated and coated T-22 boiler steel subjected to erosion studies in simulated coal-fired boiler environment when substrate temperature was 400°C and surrounding air at 900°C; are shown in Fig. 6.28 and 6.29. The SEM observations were made on the eroded surface of all the uncoated and coated T-22 boiler steel specimens at both the impact angles i.e. at 90° and 30°. Scanning electron microscopy (SEM) revealed various erosion mechanisms like metal removal, oxide chipping, fracture and spalling within the oxide/coating layer and at the scale/metal interface etc. The micrographs have revealed fracture at the surfaces with impressions of formation of craters with crack network.

Micrographs (Fig.6.28) for the eroded surfaces of uncoated and coated T-22 boiler steel at 90° impact angle, clearly indicates the formation of crater, impact zone,

oxide fracture and removal, coating fracture and retained erodent. It can be observed from the micrographs of the eroded surface of the uncoated boiler steel (Fig.6.28.a) that the erodent particles deform the exposed surface by ploughing and introducing the craters in the matrix by displacing material to the side. EDAX analysis revealed the presence of Fe, Al, Mo and O as the main elements on the eroded area, which indicates the formation of iron oxide due to oxidation and presence of retained erodent i.e. alumina. In case of nanostructured TiAlN coating (Fig.6.28.b); the micrograph revealed retained erodent, shallow impact craters with wider impact zone. EDAX analysis shows the presence of Ti and Al along with N as the main elements (which are main elements of coating) along with very less amount of Mo, Fe and O. The erodent impacts causes shallow craters but fails to remove the coating completely. The coating has shown full protection to the substrate when eroded at an impact velocity of 35 ms^{-1} and impingement angle of 90° under simulated coal-fired boiler environment. Further, in case of nanostructured AlCrN coating; the signs of coating removal and shallow impact crater have been observed (Fig. 6.28.c). EDAX analysis shows the presence of Al and Fe along with O as the main elements along with very less amount of chromium. The erodent impacts causes cracking and fracture of the coating and thus removed the coating completely.

The micrograph of the conventional TiAlN coating (Fig.6.28.d) revealed the signs of brittle fracture and removal of oxide layer at various locations. When the eroding particle strikes the surface of the coating at 90° the material is severely damaged and fractured as shown in Fig. 6.28 (d). EDAX analysis shows the presence of Al, Ti and O as the main elements along with very less amount of Fe, Cr and Mo; indicating that the coating is still there after three hours continuous erodent impacts at an impact velocity of 35 ms^{-1} and impingement angle of 90° when substrate temperature was 400°C and surrounding air at 900°C . The coating has successfully protected the substrate. Further in case of conventional AlCrN coating, the erodent particle impacts have severely damaged the coating by causing cracking and fracture. EDAX analysis revealed the presence of Al, O and Fe as the main elements with small amount of Mo and Cr; indicating that the coating has failed to protect the substrate and hence exposed the substrate (Fig.6.28.e).

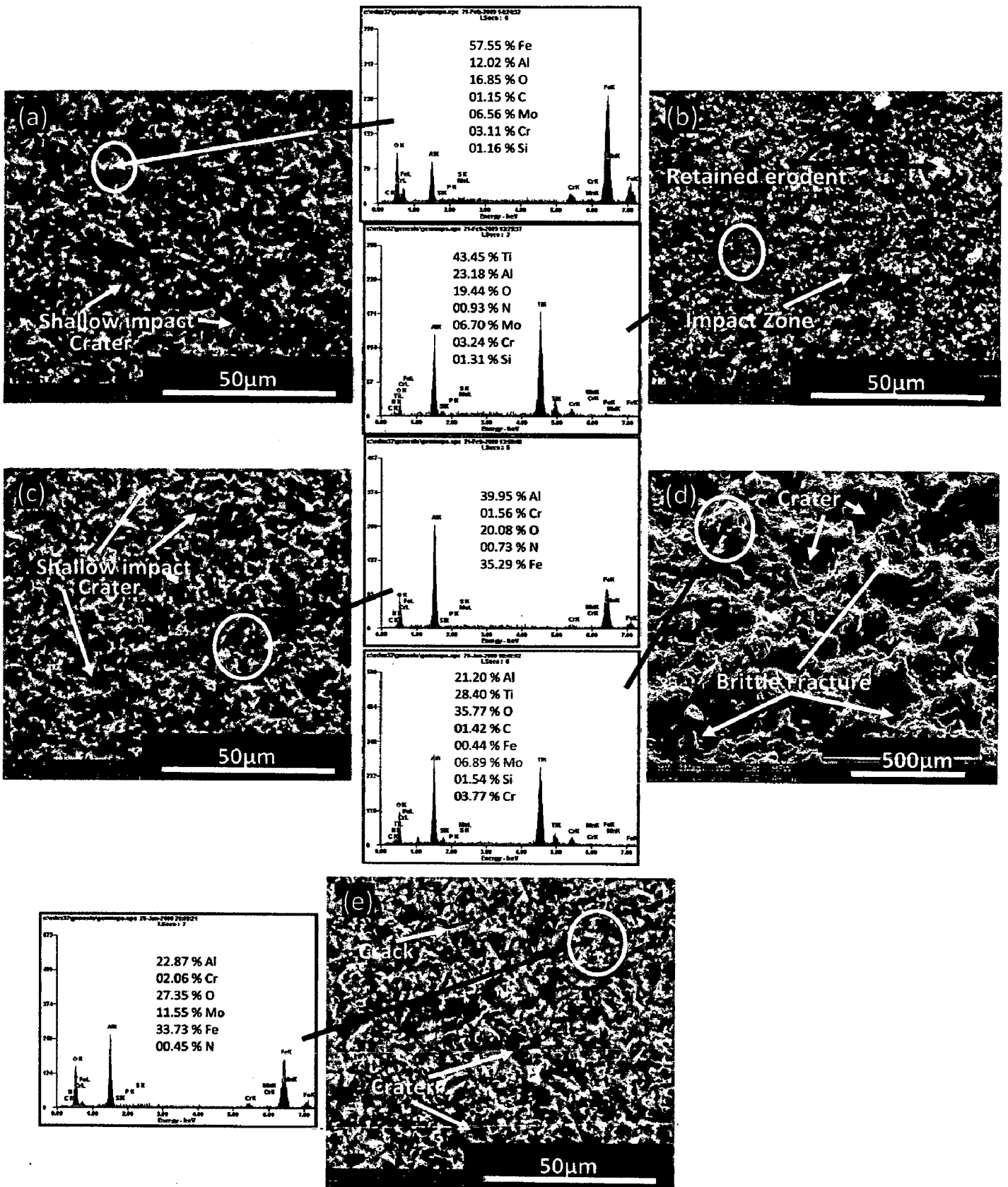


Fig. 6.28 Surface-scale morphology and EDAX patterns from different spots on eroded uncoated and coated ASTM-SA213-T-22 boiler steel exposed to high temperature erosion studies in simulated coal-fired boiler environment at impact angle 90°: (a) Uncoated T-22 boiler steel, (b) Nanostructured TiAlN coating, (c) Nanostructured AlCrN coating, (d) Conventional TiAlN coating, (e) Conventional AlCrN coating

In case of 30° impact, Micrographs (Fig.6.29) for the eroded surfaces of uncoated and coated T-22 boiler steel clearly indicates presence of retained erodent, the formation of wider and shallow crater, crack propagation, oxide fracture and removal and coating fracture. In case of uncoated boiler steel; the micrographs (Fig.6.29.a) revealed the severe deformation at the surface resulting in formation of craters with minor cracks. EDAX analysis revealed the presence of Fe, Al and O as the main elements on the eroded area, which indicates the formation of iron oxide due to oxidation and presence of retained erodent i.e. alumina. In case of nanostructured TiAlN coating (Fig.6.29.b); the micrograph revealed retained erodent, shallow impact craters with wider impact zone. EDAX analysis shows the presence of Ti and Al along with N as the main elements (which are main elements of coating) along with very less amount of Mo, Fe and O. The erodent impacts causes shallow craters but fails to remove the coating completely. The coating has shown full protection to the substrate eroded under simulated coal-fired boiler environment. Micrograph in case of nanostructured AlCrN coatings (Fig.6.29.c); revealed shallow impact craters with retained erodent. EDAX analysis indicates the presence of Fe, Al and O as the main elements along with some amount of Cr, N and Mo. It can be inferred that the nanostructured AlCrN coating gets severely damaged and fractured when the eroding particle strikes the surface of a coating at 30° and failed to protect substrate.

The micrograph of the conventional TiAlN coating (Fig.6.29.d) revealed the oxide fracture and removal at various locations along with craters. When the eroding particle strikes the surface of the coating at 30° the material is severely damaged and fractured as shown in Fig. 6.29 (d). EDAX analysis shows the presence of Al, Ti and O as the main elements along with very less amount of Fe, Mo and Cr. Further in case of conventional AlCrN coating, the erodent particle impacts have severely damaged the coating by causing cracking and fracture. EDAX analysis revealed the presence of Al and Cr as the main elements with small amount of O, N and C; indicating that the coating has shown protection to the substrate (Fig.6.29.e). It can be inferred that the conventional TiAlN and AlCrN coatings were still there after three hours continuous erodent impacts at an impact velocity of 35 ms⁻¹ and impingement angle of 30° when substrate temperature was 400°C and surrounding air at 900°C. These coatings have successfully protected the substrate.

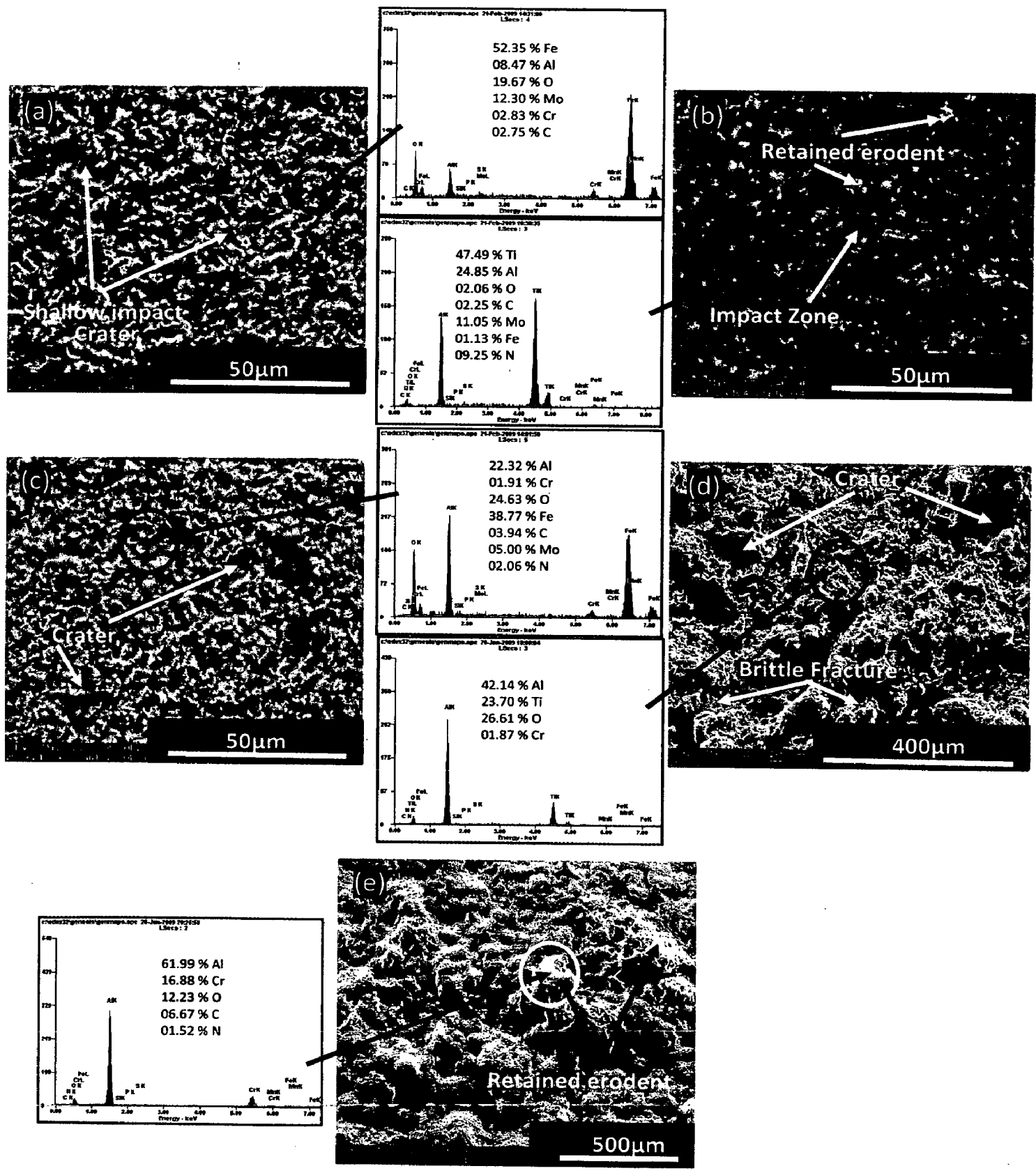


Fig. 6.29 Surface-scale morphology and EDAX patterns from different spots on eroded uncoated and coated ASTM-SA213-T-22 boiler steel exposed to high temperature erosion studies in simulated coal-fired boiler environment at impact angle 30°: (a) Uncoated T-22 boiler steel, (b) Nanostructured TiAlN coating, (c) Nanostructured AlCrN coating, (d) Conventional TiAlN coating, (e) Conventional AlCrN coating

6.4.2 Discussion

In erosion testing, the material is eroded by continuous impact of erodent particles; the erosion starts at the centre first, and then proceeds towards the edges of the samples. The shape of developed scar depends on the angle of impact. When erodent strikes the surface at an impact angle of 90° , material is eroded creating a circular depression; while at a 30° impact angle, material is eroded forming an elliptical shape depression. The erosion rate for uncoated and coated T-22 boiler steel at an impact velocity of 35 ms^{-1} and impingement angle of 30° and 90° when substrate temperature was 400°C and surrounding air at 900°C ; is shown in Fig. 6.27. The volume erosion rate for uncoated T-22, nanostructured thin TiAlN, nanostructured thin AlCrN, conventional thick TiAlN and conventional thick AlCrN coatings; is 0.38425×10^{-3} , 0.03544×10^{-3} , 0.0819×10^{-3} , 2.135×10^{-3} and $2.0287 \times 10^{-3} \text{ mm}^3/\text{gm}$ respectively at 90° impact angle. Based on the present data the erosion rates for 90° impact angle can be arranged in the following order:

Conventional TiAlN > Conventional AlCrN > Bare T-22 > Nanostructured AlCrN > Nanostructured TiAlN

It can be inferred from the above data that the relative erosion resistance of conventional thick TiAlN coating is least among the uncoated and coated T-22 boiler steel specimens. Further, the SEM/EDAX analysis (Fig.6.28) indicates that in case of nanostructured and conventional TiAlN coated T-22 boiler steel; the coating is still there after three hours continuous erodent impacts at an impact velocity of 35 ms^{-1} and impingement angle of 90° when substrate temperature was 400°C and surrounding air at 900°C . These coatings have successfully protected the substrate. The nanostructured and conventional AlCrN hard coatings were removed by the continuous strikes of the eroding particles on the surface of the coating at 90° (Fig.6.28).

While at 30° impact, the volume erosion rate for uncoated T-22, nanostructured thin TiAlN, nanostructured thin AlCrN, conventional thick TiAlN and conventional thick AlCrN coatings; is 0.4196×10^{-3} , 0.0691×10^{-3} , 0.0426×10^{-3} , 3.01725×10^{-3} and $1.636 \times 10^{-3} \text{ mm}^3/\text{gm}$ respectively. Based on the present data the erosion rates for 30° impact angle can be arranged in the following order:

Conventional TiAlN > Conventional AlCrN > Bare T-22 > Nanostructured AlCrN > Nanostructured TiAlN

It can be inferred from the above data that the relative erosion resistance of conventional thick TiAlN coating is least among the uncoated and coated T-22 boiler steel specimens. The erosion resistance sequence for the conventional coatings is independent of the impact angle in this case. Further, the SEM/EDAX analysis (Fig.6.29) indicates that in case of conventional and nanostructured TiAlN and conventional AlCrN coated T-22 boiler steel; the coating is still there after three hours continuous erodent impacts at an impact velocity of 35 ms^{-1} and impingement angle of 30° when substrate temperature was 400°C and surrounding air at 900°C . These coatings have successfully protected the substrate. The nanostructured AlCrN coating was removed by the continuous strikes of the eroding particles on the surface of the coating at 30° (Fig.6.29).

The solid particle erosion rate of the uncoated and nanostructured thin TiAlN and AlCrN coated T-22 boiler steel as shown in Fig.6.27 indicated that maximum erosion took place at 30° impact angle, which indicate ductile behavior as proposed by Murthy et al (2001). Authors suggested that the material subjected to erosion initially undergoes plastic deformation and is later removed by subsequent impacts of the erodent on the surface. The ploughing occurs by the impact of the erodent particles and lips or ridges are formed at the bank of the craters. These lips are fractured or removed with further erosion. At low erosion temperatures, at high impact velocities and feed rates, there is no oxide scale. Even if there is any oxide scale, it will be very thin and it will be able to deform in the same manner as that of the substrate target. The works of Shida and Fujikawa (1985), Singh and Sundararajan (1990) Levy et al., (1986) can be considered elevated temperature erosion of metals with minimum or negligible oxidation. Under such circumstances, erosion takes place from the metallic surface and this mechanism of erosion is called metal erosion. Most of the metallic materials, irrespective of temperature of erosion, exhibit a ductile behavior, i.e. a maximum erosion rate at oblique impact angles (Tabakoff and Vittal, 1983). The erosion behavior in this regime is similar to the ambient temperature erosion behavior of metallic materials. The erosion response in the metal erosion regime is ductile as described by Bellman and Lavy (1981). Authors suggested that the creation of platelet-like edges by impact extrusion protrude outward over adjacent material and the loss of these platelets appears to be responsible for the mass loss. Authors have further explained that

repeated deformation of craters and forming of new craters is common and some platelets are extruded several times before getting knocked off.

Sundararajan and Roy (1997) proposed a model of metal erosion and oxide erosion. According to his model if steady state thickness of the oxide scale is smaller than the critical thickness of the oxide scale, three modes of interaction between erosion and oxidation are possible. In the first case, which applies either when there is no oxide scale or when the depth of deformation is much higher than the thickness of the oxide scale (as in the case of uncoated and nanostructured thin coated T-22 boiler steel in present case), metal erosion becomes important (presented in Figs 6.30. a & b). In the second case, when the depth of deformation is smaller than the steady state thickness of the oxide scale, erosion of the oxide scale takes place as illustrated in Fig. 6.30 (c).

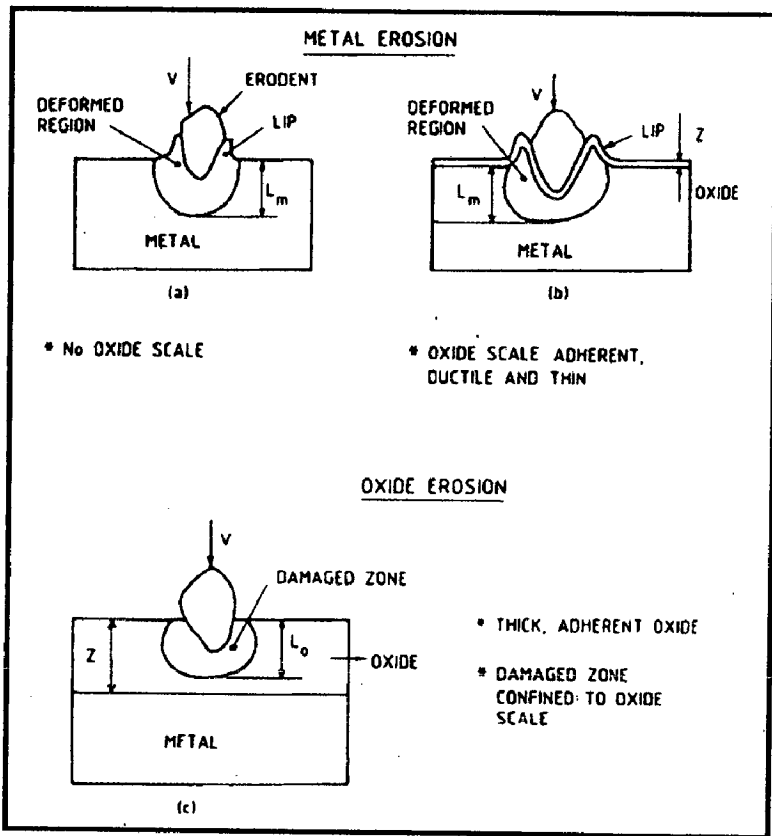


Fig. 6.30 Schematic representation of (a) & (b); metal erosion, and (c) oxide erosion illustrating the nature of interaction between the oxide scale and the substrate during erosion (Sundararajan and Roy 1997)

The solid particle erosion rate of the conventional thick TiAlN coated T-22 boiler steel as shown in Fig.6.27 indicated that maximum erosion took place at 30° impact angle, which indicate ductile behavior of the conventional coatings. The solid particle erosion rate of the conventional thick AlCrN coated T-22 boiler steel as shown in Fig.6.27 indicated that maximum erosion took place at 90° impact angle, which indicate brittle behavior of the conventional coatings. In case of brittle materials; loss in solid particle erosion occurs predominantly through the formation and interaction of a subsurface micro crack network (Guessasma et al., 2006). So in conventional thick AlCrN coatings; the erosion rate was high at normal impact and low at oblique impact. Whereas in case of conventional thick TiAlN coating; the erosion rate was high at oblique impact and low at normal impact.

The difference in erosion rates for shallow and normal impact angles can be attributed to the different material removal mechanisms in these two cases. At low angle impact, the kinetic energy of the erodent particles contributes mainly to the ploughing mechanism and very little to normal repeated impact. The ploughing mechanism is associated with the plastic smearing and cutting of the materials, while the repeated impact mechanism is responsible for initiating and propagating the grain boundary microcracks. Brittle materials are not easily plastically deformed. Hence the material removal rate is low in case of brittle materials and higher in case of ductile materials. At high angle impact, the kinetic energy of the impinging particles contributes mainly to repeated impact. Brittle nature of the materials allows the cracks readily to propagate to form crack networks. The subsequent impacts will easily remove the surface material via the ejection of the upper layer grains. Hence the material removal rate is high in brittle materials. Figure 6.31 shows schematically the fracture of coatings dependent on impact angle. It is shown schematically how an impinging solid particle can damage coating surfaces.

From the present study, it can be inferred that that in case of conventional thick AlCrN coating; the erosion rate of alloys was more at 90° impact angle, which is the characteristic erosion behavior of brittle materials. The solid particle erosion rate of the uncoated, conventional thick TiAlN and nanostructured thin TiAlN and AlCrN coated T-22 boiler steel as shown in Fig.6.27 indicated that maximum erosion took place at 30° impact angle, which indicate ductile behavior.

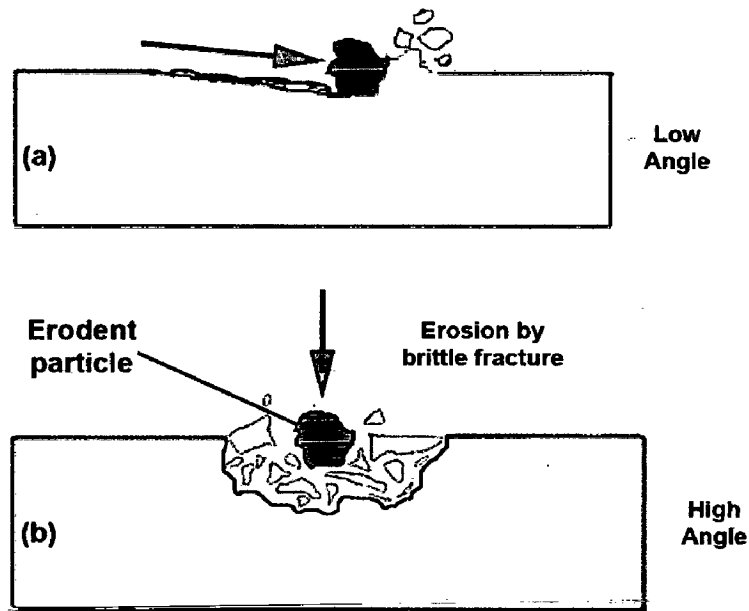


Fig. 6.31 Schematic representation of coating fracture dependent on impact angle; (a) Low angle, (b) High angle

6.4.3 Conclusions

The erosion behavior of conventional thick (by plasma spraying and gas nitrided) and nanostructured thin (by physical vapor deposition process) TiAlN and AlCrN coatings on ASTM-SA213-T-22 boiler steel at an impact velocity of 35 ms^{-1} and impingement angle of 90° and 30° when substrate temperature was 400°C and surrounding air at 900°C ; has been analyzed. The following conclusions are made:

1. The erosion rates for 90° impact angle can be arranged in the following order:
Conventional TiAlN > Conventional AlCrN > Bare T-22 > Nanostructured AlCrN > Nanostructured TiAlN
2. The nanostructured and conventional TiAlN coatings have successfully protected the substrate at 90° impact. The nanostructured and conventional AlCrN hard coatings were removed by the continuous strikes of the eroding particles on the surface of the coating at 90° impact.

3. At 30° impact, the volume erosion rate can be arranged in the following order:
Conventional TiAlN > Conventional AlCrN > Bare T-22 > Nanostructured AlCrN > Nanostructured TiAlN
4. The conventional and nanostructured TiAlN and conventional AlCrN coatings have successfully protected the substrate. The nanostructured AlCrN coating was removed by the continuous strikes of the eroding particles on the surface of the coating at 30° impact.
5. In case of conventional thick AlCrN coating; the erosion rate was more at 90° impact angle, which is the characteristic erosion behavior of brittle materials. The solid particle erosion rate of the uncoated, conventional thick TiAlN and nanostructured thin TiAlN and AlCrN coated T-22 boiler steel was maximum at 30° impact angle, which indicate ductile behavior.

Where β_a = anodic Tafel slope, β_c = cathodic Tafel slope, R_p = polarization resistance and, Z is a function of the Tafel slopes.

In potentiodynamic polarization tests the nanostructured AlCrN coating showed good corrosion resistance as evident from corrosion current density ($0.87 \mu\text{A}/\text{cm}^2$) and polarization resistance ($27.39 \text{ k}\Omega\text{-cm}^2$) values reported in Table.6.7. All the coatings have performed well in 3 wt. % NaCl solution when compared to the behavior of the substrate steel. The measured corrosion current density for uncoated T-22 boiler steel, nanostructured thin TiAlN, nanostructured thin AlCrN, conventional thick TiAlN and AlCrN coatings is 17.02, 4.72, 0.87, 8.97 and $3.93 \mu\text{A}/\text{cm}^2$ respectively.

From polarization test results, the protective efficiency, P_i (%) of the coatings can be calculated by Eq. (6.5):

$$P_i (\%) = \left[1 - \left(\frac{i_{corr}}{i_{corr}^o} \right) \right] \times 100 \quad (6.5)$$

Where i_{corr} and i_{corr}^o indicate the corrosion current density of the coating and substrate, respectively (Yoo et al., 2008).

Table 6.8 Results of Potentiodynamic Polarization Tests of uncoated and coated ASTM-SA213-T-22 boiler steel

Substrate / Coating	E_{corr} (mV)	i_{corr} ($\mu\text{A}/\text{cm}^2$)	β_a (V/decade)	β_c (V/decade)	R_p ($\text{k}\Omega\text{-cm}^2$)	P_i (%)	F (%)
Uncoated T-22 boiler steel	-540.2	17.02	0.0632	1.180	01.53	--	--
Nanostructured TiAlN	-457.4	04.72	0.0902	0.398	06.76	72.26	01.100
Nanostructured AlCrN	-436.6	00.87	0.0806	0.172	27.39	94.88	00.280
Conventional TiAlN	-551.7	08.97	0.2000	0.149	04.13	47.27	02.430
Conventional AlCrN	-849.9	3.93	0.1430	0.098	06.42	76.87	0.0003

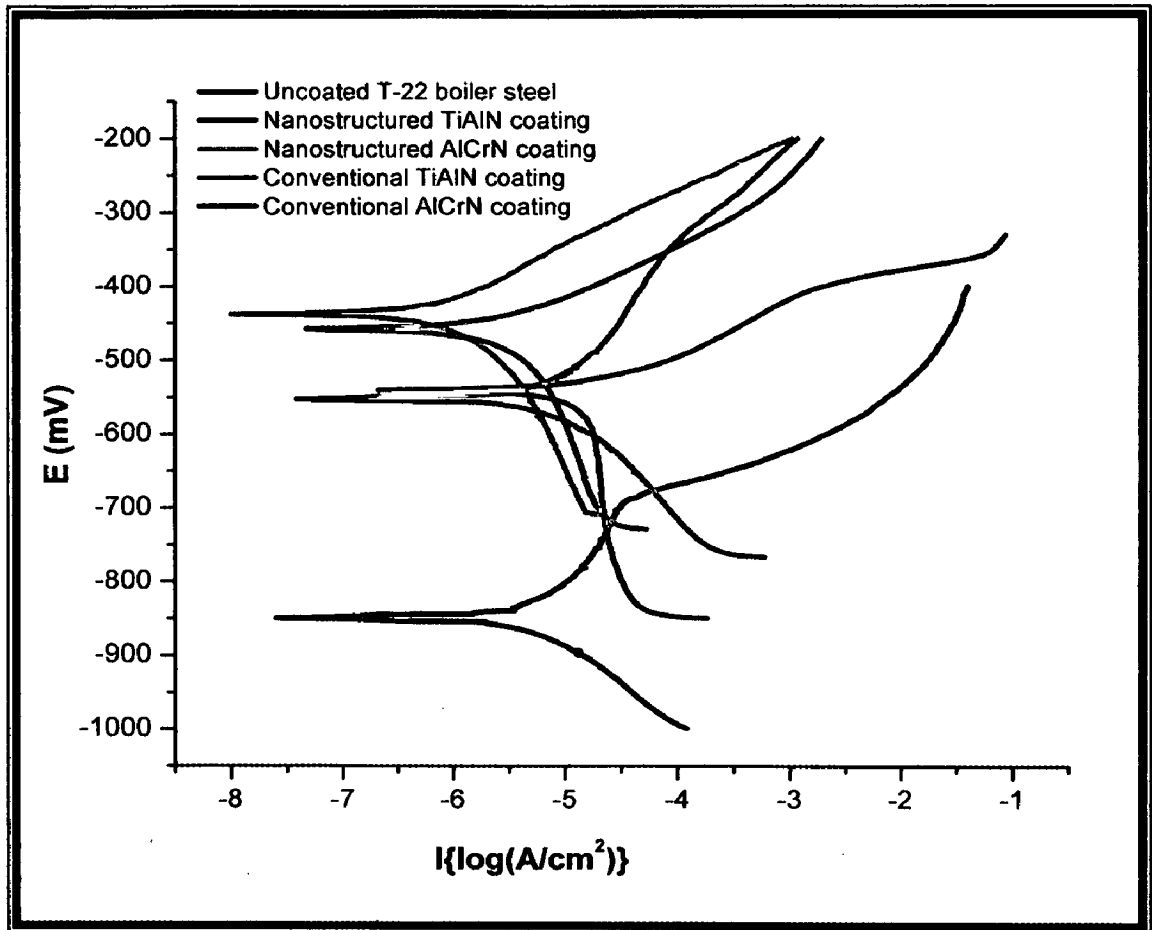


Fig. 6.32 Potentiodynamic Polarization Curves for uncoated and coated ASTM-SA213-T-22 boiler steel

Figure 6.33 shows the variation in protective efficiency and polarization resistance of uncoated and coated T-22 boiler steel subjected potentiodynamic polarization test. The nanostructured thin AlCrN coating showed the highest protective efficiency of 94.88% with lowest corrosion current density of $0.059 \mu A/cm^2$. The nanostructured TiAlN, conventional thick TiAlN and AlCrN coatings have shown protective efficiency 72.29%, 47.27% and 76.87% respectively. The observed protection by the nanostructured TiAlN and AlCrN coatings in an aerated 3 wt.% NaCl solution at room temperature, are almost in agreement with the findings of Yoo et al. (2008) and Xing-zhao et al. (2008).

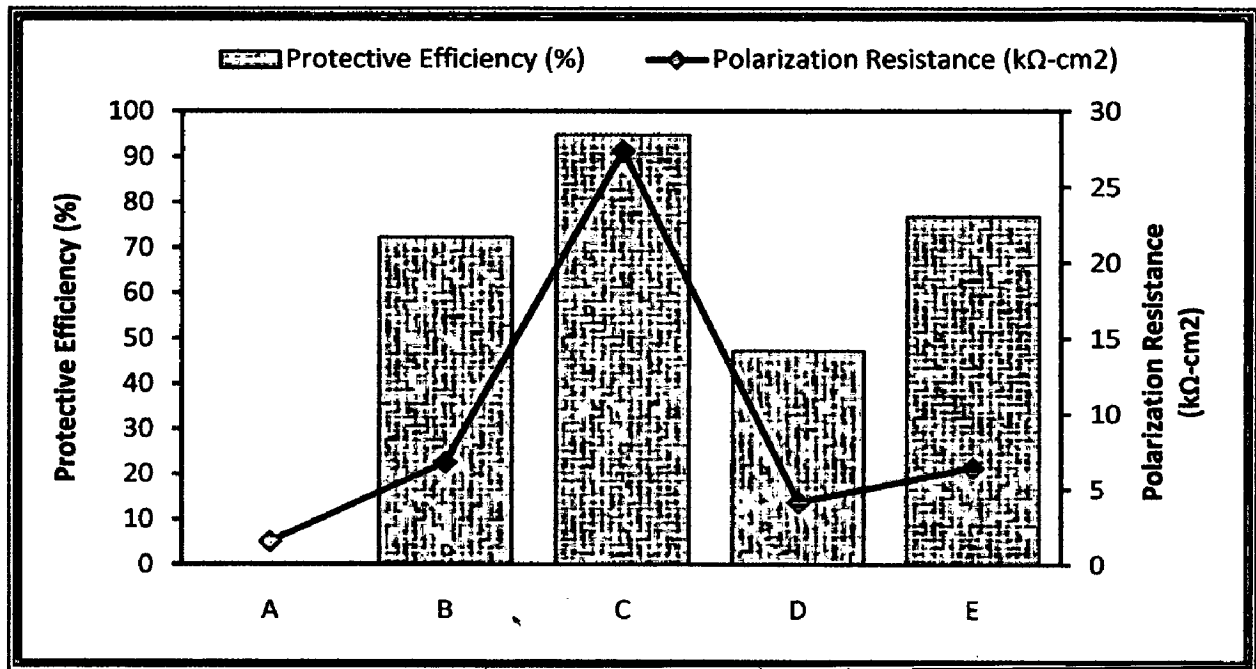


Fig. 6.33 Protective efficiency and Polarization resistance of uncoated and coated ASTM-SA213T-22 boiler steel: (A) Uncoated T-22 boiler steel, (B) Nanostructured TiAlN coating, (C) Nanostructured AlCrN coating, (D) Conventional TiAlN coating, (E) Conventional AlCrN coating

For further justification the porosity values has also been measured quantitatively by the electrochemical methods [Yoo et al., 2008] according to Eq. (6.6) and reported in Table.6.8:

$$F (\%) = \left[\frac{R_{pm}}{R_p} \times 10^{-|\Delta E_{corr}/\beta_a|} \right] \times 100 \quad (6.6)$$

Where ΔE_{corr} the corrosion potential difference between the substrate and coating layer, R_p the polarization resistance of the coating-substrate system, β_a the anodic Tafel constant of substrate, R_{pm} is the polarization resistance of the substrate and F represent porosity.

The porosity measurement of the coatings is presented in Table 6.8. The conventional thick AlCrN coating has shown minimum porosity of 0.0003% and conventional thick TiAlN has shown maximum porosity (2.43%). The porosity measurement by electrochemical test analysis and with image analyser, having software Dewinter Materials Plus 1.01 based on ASTM B276, are having different results. The difference in the measured porosity by these two methods in case of nanostructured

TiAlN and conventional AlCrN coatings may be because that image analysis (IA) measures both open as well as closed porosity and cannot distinguish between the two, whereas electrochemical test is able to assess pore connectivity in a coating that exists due to the interlamellar pores and intralamellar cracks (Deshpande et al., 2004). The porosity also affects the corrosion current density, as more is the connected porosity the higher is the corrosion current.

6.5.1.2 Salt spray (Fog) testing

The ASTM B117 Salt Fog test was used to evaluate the performance of the uncoated and nanostructured thin TiAlN and AlCrN coated ASTM-SA213-T-11 boiler steel. The salt fog test is an accelerated corrosion test by which samples exposed to the same conditions can be compared. In the B117 test, the samples are exposed to a salt fog generated from a 5% sodium chloride solution with a pH between 6.5 and 7.2. All the samples were placed in the salt fog chamber for 24 Hrs, 48 Hrs and 72 Hrs. Photographs were taken before and subsequent to exposure to document the surface conditions. Initial weight and dimensions were measured. After exposure; samples were monitored and analyzed by using XRD and SEM/EDAX techniques. Then all the samples were cleaned in running water not warmer than 38°C to remove salt deposits from the surface and then immediately dried with compressed air.

The macro morphologies of the uncoated and nanostructured thin TiAlN and AlCrN coated T-22 boiler steel exposed to salt fog test for 24 Hrs, 48 Hrs and 72 Hrs; are depicted in Fig.6.34. The uncoated T-22 boiler steel suffered severe corrosion in all three test conditions i.e. 24 Hrs, 48 Hrs and 72 Hrs (Fig.6.34.A). The brownish colored corrosion product on the surface of the samples and corrosion pits are visible. The nanostructured coated samples have shown resistance to the corrosion as compared to the uncoated T-22 boiler steel. The nanostructured TiAlN coatings have shown negligible corrosion products in case of 24 Hrs study, but for 48 Hrs and 72 Hrs studies, these have shown the formation of some corrosion products (Fig.6.34.B). In case of nanostructured AlCrN coating, some corrosion products can be seen on the surface in all the three test durations but still very less as compared to the uncoated T-22 boiler steel.

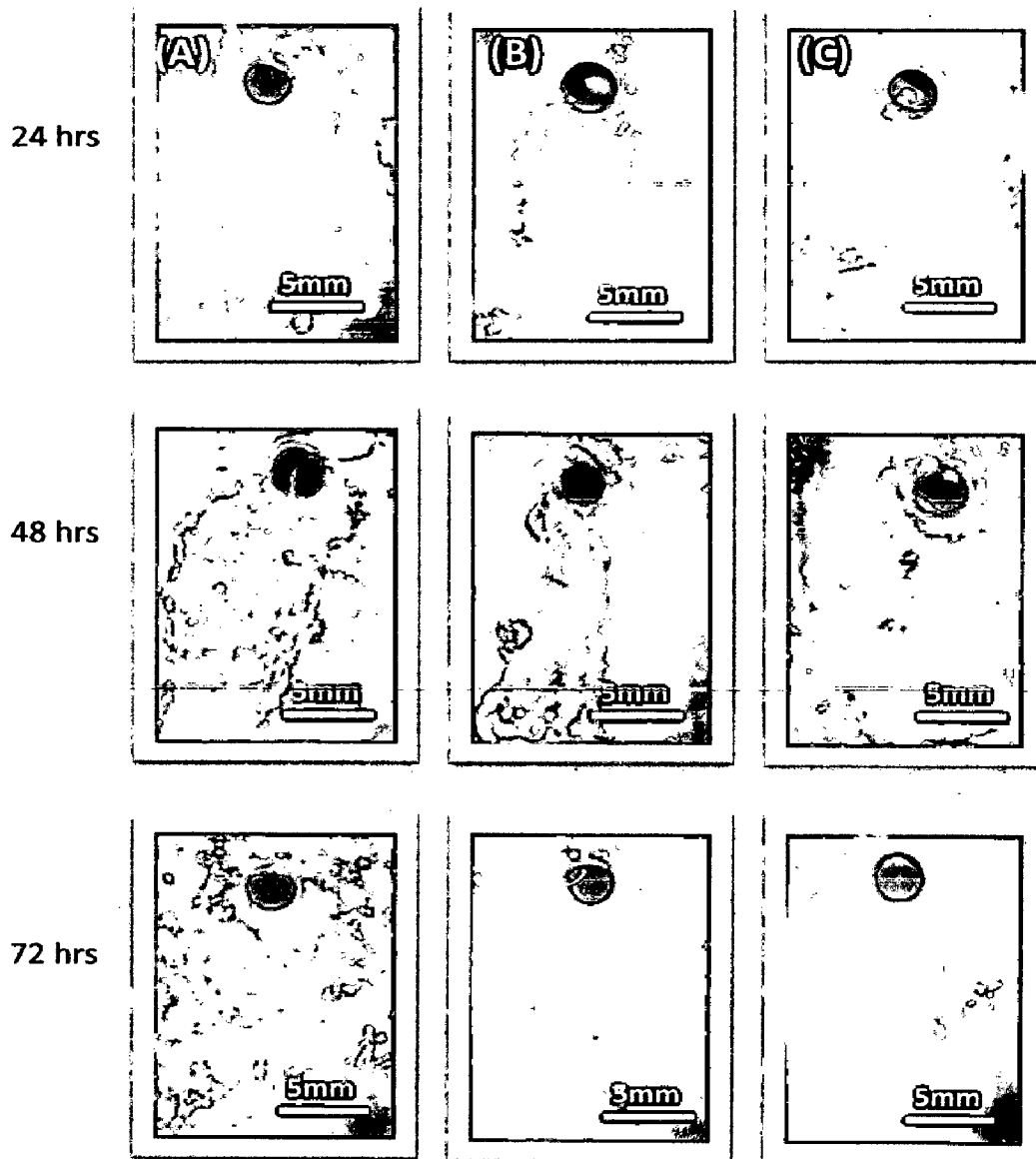


Fig. 6.34 Surface macrographs of uncoated and coated ASTM-SA213-T-22 boiler steel subjected to salt-fog testing (5% NaCl): (A) Uncoated T-22 boiler steel subjected to 24hrs, 48hrs and 72 hrs testing; (B) Nanostructured TiAlN coating subjected to 24hrs, 48hrs and 72 hrs testing; (C) Nanostructured AlCrN coating subjected to 24hrs, 48hrs and 72 hrs testing

Figure 6.35 shows the surface SEM images with EDAX point analysis of uncoated and nanostructured TiAlN and AlCrN coated T-22 boiler steel exposed to salt fog test for 24 Hrs. As can be seen in Fig.6.35 (a), massive corrosion products were accumulated on the surface of uncoated T-22 boiler steel. The EDAX analysis at some locations of interest points out the presence of iron and oxygen on the corroded surface (Point 1 and 2 on Fig.6.35).

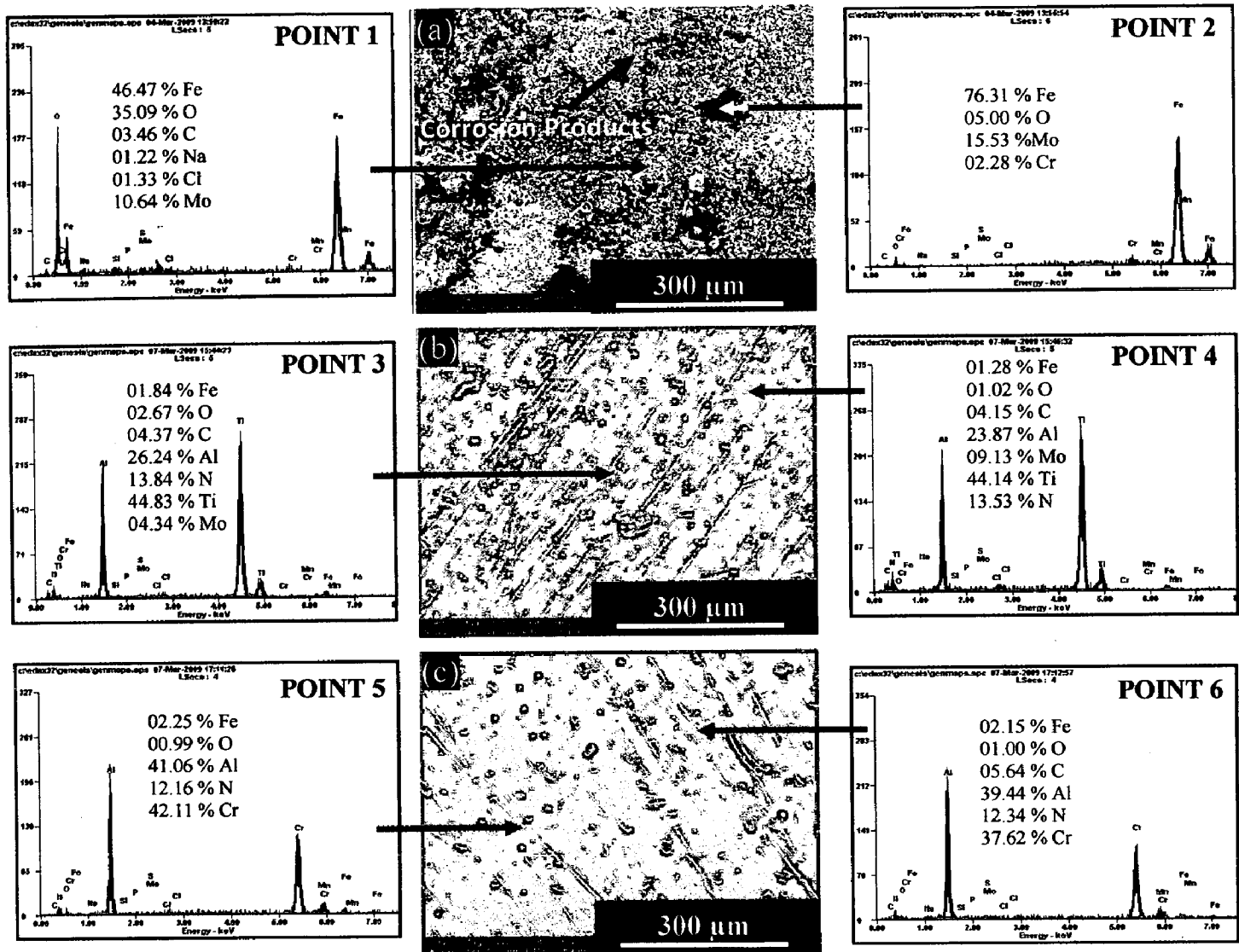


Fig. 6.35 Surface macrographs of uncoated and coated ASTM-SA213-T-22 boiler steel subjected to salt-fog testing (5% NaCl) for 24 hrs: (a) Uncoated ASTM-SA213-T-22 boiler steel (b) Nanostructured TiAlN coating (c) Nanostructured AlCrN coating

In case of nanostructured thin TiAlN and AlCrN coatings; no corrosion products were visible (Fig.6.35.b and c). The EDAX point analysis (Point 3 to 6 in Fig.6.35) revealed the presence of the coating elements with negligible presence of Fe and O. So, in case of 24 Hrs test conditions; the nanostructured thin coatings have performed well and protected the substrate material.

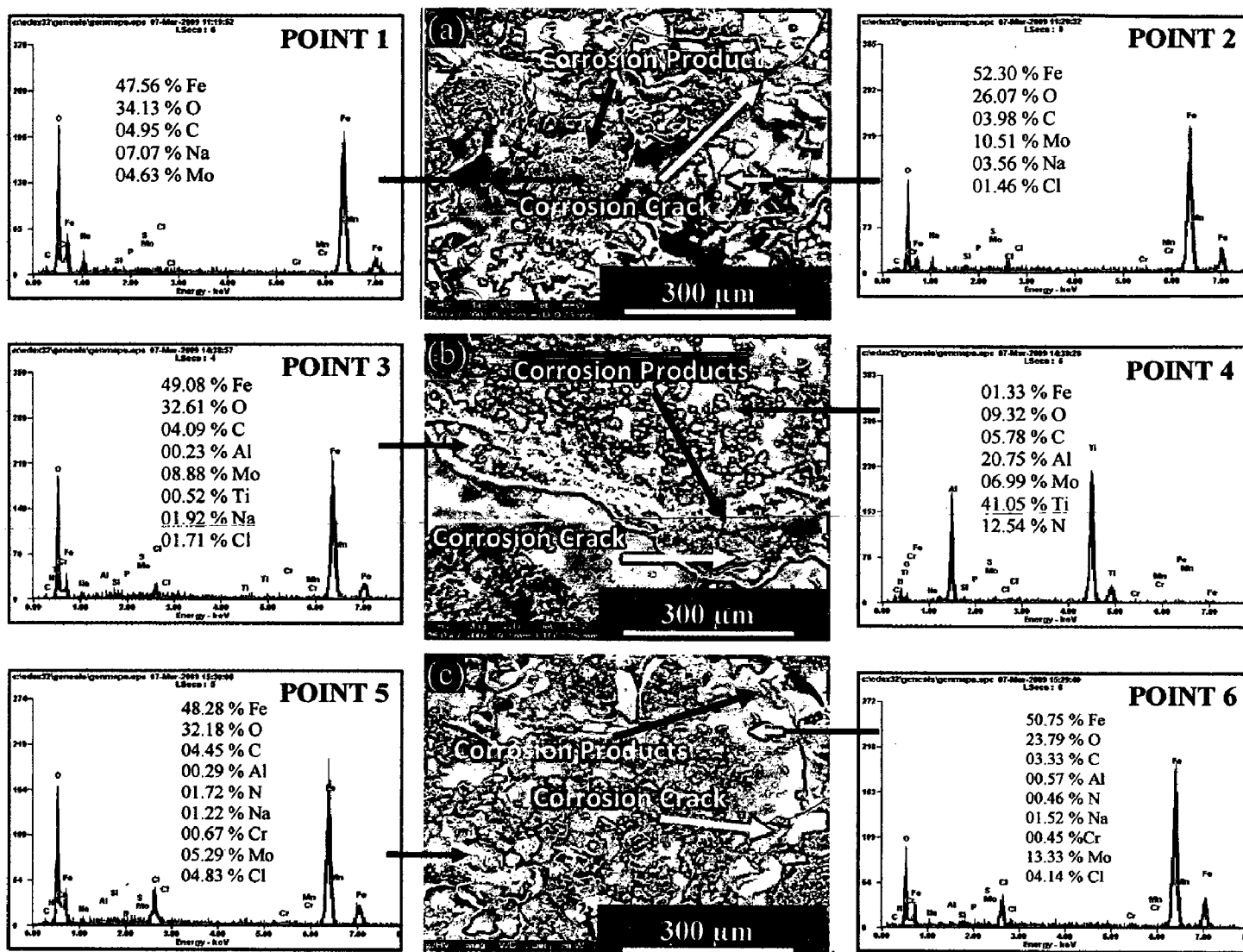


Fig. 6.36 Surface macrographs of uncoated and coated ASTM-SA213-T-22 boiler steel subjected to salt-fog testing (5% NaCl) for 48 hrs: (a) Uncoated ASTM-SA213-T-22 boiler steel (b) Nanostructured TiAlN coating (c) Nanostructured AlCrN coating

Figure 6.36 shows the surface SEM images of uncoated and nanostructured TiAlN and AlCrN coated T-22 boiler steel exposed to salt fog test for 48 Hrs. The uncoated T-22 boiler steel has shown severe corrosion as shown in Fig.6.36 (a). Corrosion cracks and corrosion products can be seen on the surface. The EDAX analysis shows the presence of Fe and O as the main elements along with some Mn, Cl and Na. As can be seen in Fig.6.36 (b and c), the as-deposited nanostructured TiAlN and AlCrN coatings were cracked after salt spray tests.

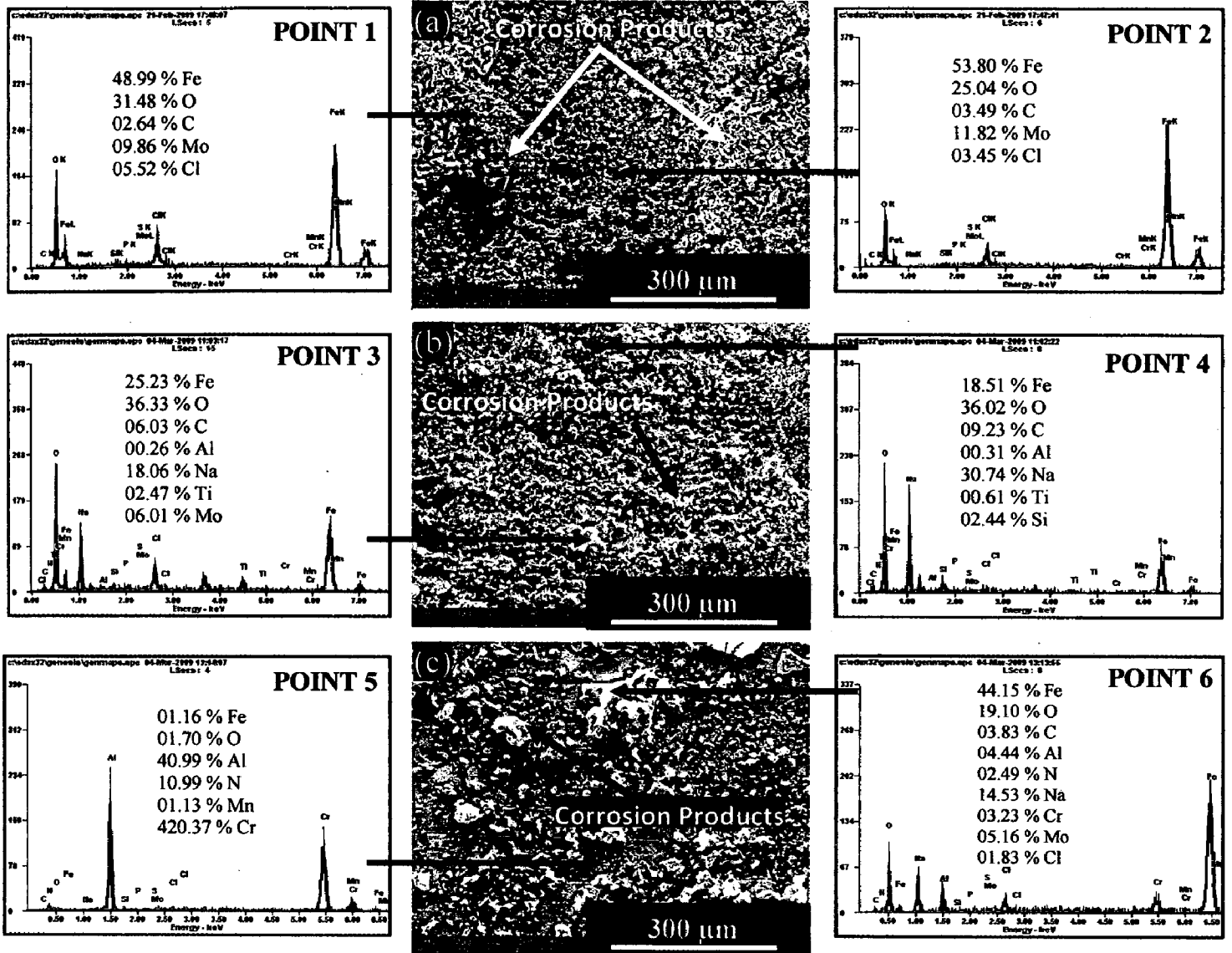


Fig. 6.37 Surface macrographs of uncoated and coated ASTM-SA213-T-22 boiler steel subjected to salt-fog testing (5% NaCl) for 72 hrs: (a) Uncoated T-22 boiler steel (b) Nanostructured TiAlN coating (c) Nanostructured AlCrN coating

Massive corrosion products were accumulated around the corrosion crevice. Obviously, severe corrosion would proceed in the as-deposited nanostructured thin coatings through the cracks, and cause coating cracking and fracture damage in the subsequent service at elevated temperatures. EDAX analysis (Point 3 and 4 on Fig.6.36) in case of nanostructured TiAlN coating indicates the products were composed of Fe and O.

The corrosion products in case of nanostructured AlCrN coating were found rich in iron and oxygen with some amount of Al, Cr and Mn (Point 3 and 4 on Fig.6.36). The surface SEM images of uncoated and nanostructured TiAlN and AlCrN coated T-22 boiler exposed to salt fog test for 72 Hrs; are shown in Fig.6.37. Massive corrosion products were accumulated on the surface in case of uncoated T-22 boiler steel after salt fog tests. EDAX analysis (Point 3 and 4 on Fig.6.37) in case of nanostructured TiAlN coating indicates the products composed of Fe and O. In case of nanostructured thin AlCrN coating; EDAX point analysis (Point 5 on Fig.6.37) revealed the presence of Al and Cr as the main element in the un-corroded area of the surface and Fe and O rich corrosion products (Point 6 on Fig.6.37).

XRD diffractograms for coated and uncoated T-22 boiler steel subjected to salt fog tests for 24 Hrs, 48 Hrs and 72 Hr; are depicted in Fig.6.38 on reduced scale. As indicated by the diffractograms in Fig.6.38, Fe_3O_4 and with some minor peaks of Cr_2O_3 are the main phases present in the oxide scale of uncoated T-22 boiler steel. In nanostructured TiAlN coating, AlN, TiN and Fe_3O_4 are the main phases revealed with minor phases i.e. TiO_2 and Al_2O_3 . Further, the main phases identified for the nanostructured AlCrN coating are CrN, AlN along with Al_2O_3 , Cr_2O_3 and Fe_3O_4 . The formation of Fe_3O_4 in the scale of corroded specimens in salt spray tests is found to be in agreement with those reported by Bijayani et al. (2008) and Vera et al. (2009).

The weight loss measurements were carried out for the uncoated and nanostructured thin TiAlN and AlCrN coated T-22 boiler steel exposed to the salt fog tests for 24 Hrs, 48 Hrs and 72 Hrs. Fig. 6.39, depicts the column chart showing the weight loss per unit area for the uncoated and coated T-22 boiler steel. It can be inferred from the plots that the uncoated T-22 boiler steel has shown maximum weight loss per unit area in all the three test durations i.e. 24 Hrs, 48 Hrs and 72 Hrs tests; as compared to the coated counterparts. Both the coatings have shown good protection to the substrate in terms of weight loss per unit area. As can be seen in Fig.6.39 for uncoated and coated T-22 boiler steel; the weight loss per unit area increases with the duration of the test. The weight loss per unit area in case of nanostructured thin TiAlN coating is less than as compared to the nanostructured AlCrN coating and uncoated boiler steel in all test conditions.

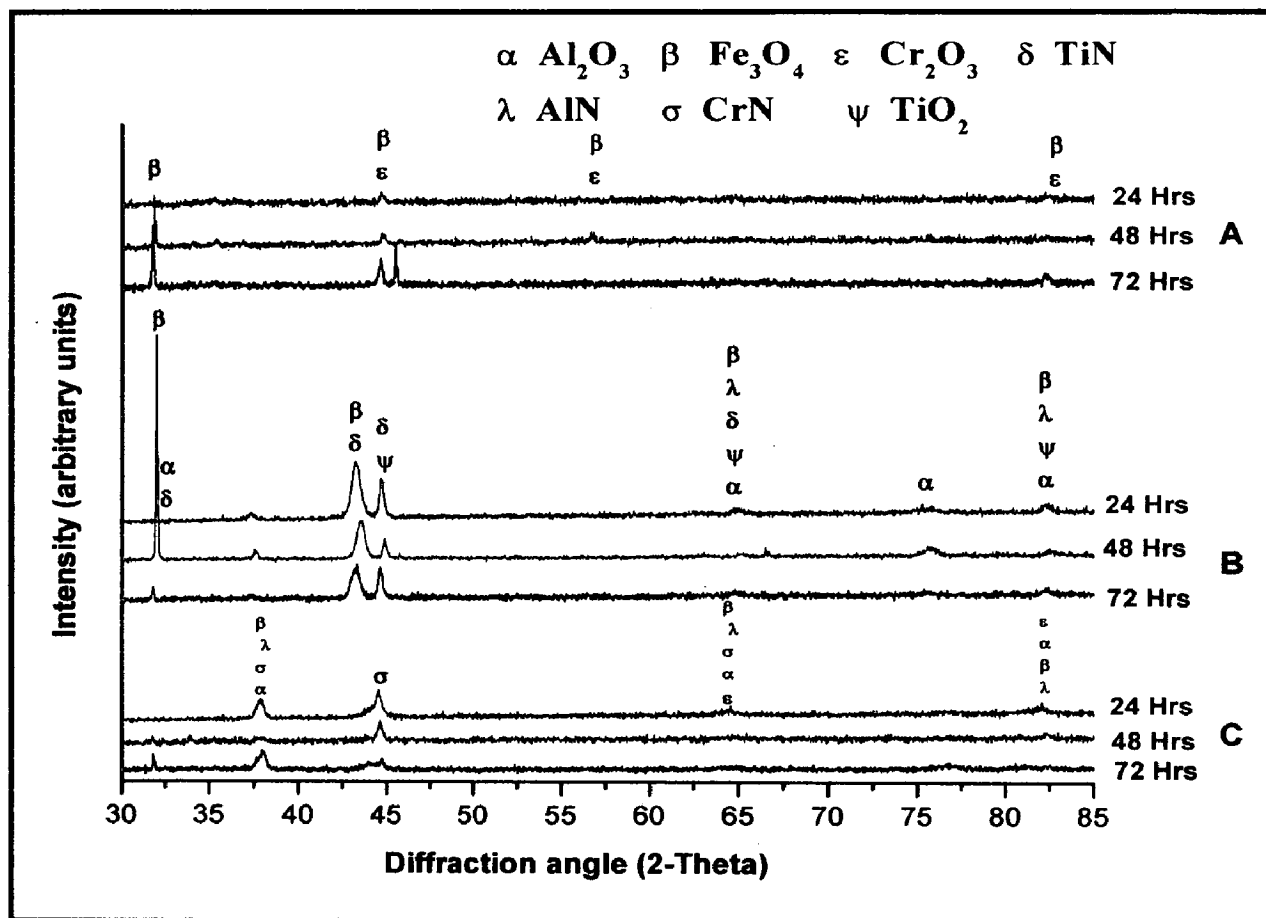


Fig. 6.38 X-Ray Diffraction pattern of uncoated and coated ASTM-SA213-T-22 boiler steel subjected to salt-fog testing (5% NaCl) for 24 Hrs, 48 Hrs and 72 Hrs: (A) Uncoated T-22 boiler steel, (B) Nanostructured TiAlN coating, (C) Nanostructured AlCrN coating

It can be mentioned based on the present investigation that nanostructured thin TiAlN and AlCrN coatings can provide a very good corrosion resistance when exposed to the simulated marine environment i.e. salt fog test.

Salt spray corrosion is an electrochemical reaction process (Bao, et al., 2007). Generally, the corrosion resistance is influenced significantly by several factors, such as compositions, internal microstructure, and especially the surface condition. The proposed corrosion mechanism of the coated specimen is as explained in Fig.6.40; which is similar to the one reported by Bao et al. (2007). Micro-cracks got initiated by residual stress during deposition of coatings. The micro-cracks would be corroded easily and the solution would infiltrate into loose corrosion products and reach crack tip to sustain the internal corrosion, followed by crack propagation (Fig. 6.40 b and c).

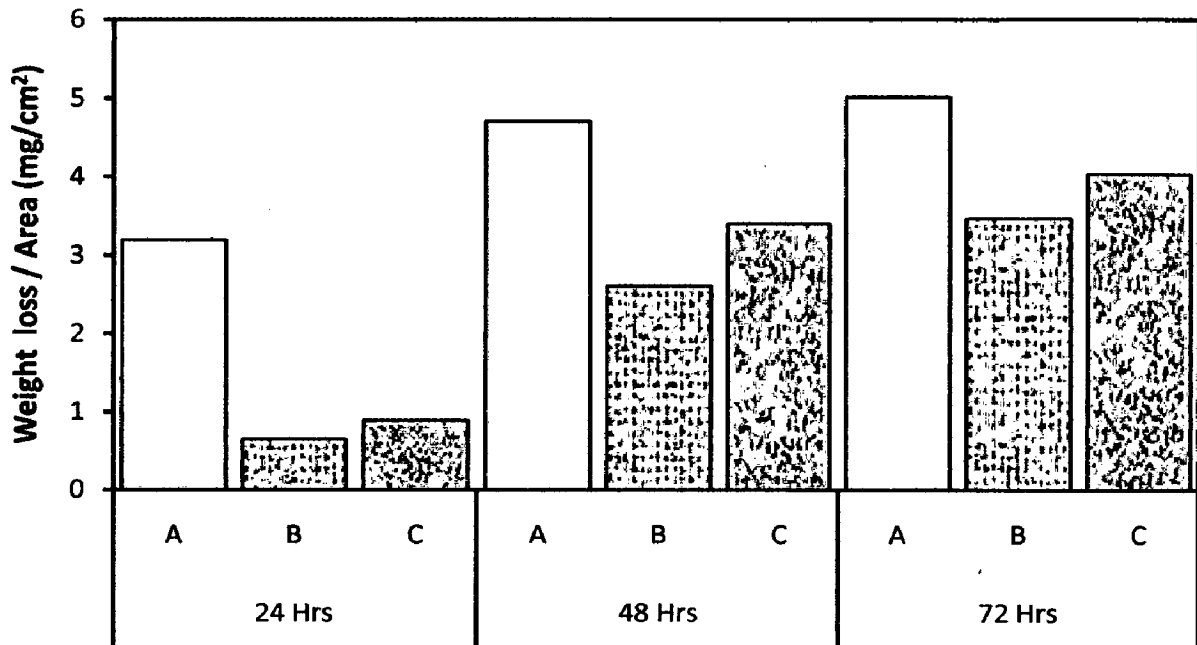


Fig. 6.39 Column chart showing weight loss per unit area for the uncoated and coated ASTM-SA213-T-22 boiler steel subjected to salt-fog testing (5% NaCl) : (A) Uncoated T-22 boiler steel subjected to 24hrs, 48hrs and 72 hrs testing; (B) Nanostructured TiAlN coated T-22 boiler steel subjected to 24hrs, 48hrs and 72 hrs testing; (C) Nanostructured AlCrN coated T-22 boiler steel subjected to 24hrs, 48hrs and 72 hrs testing

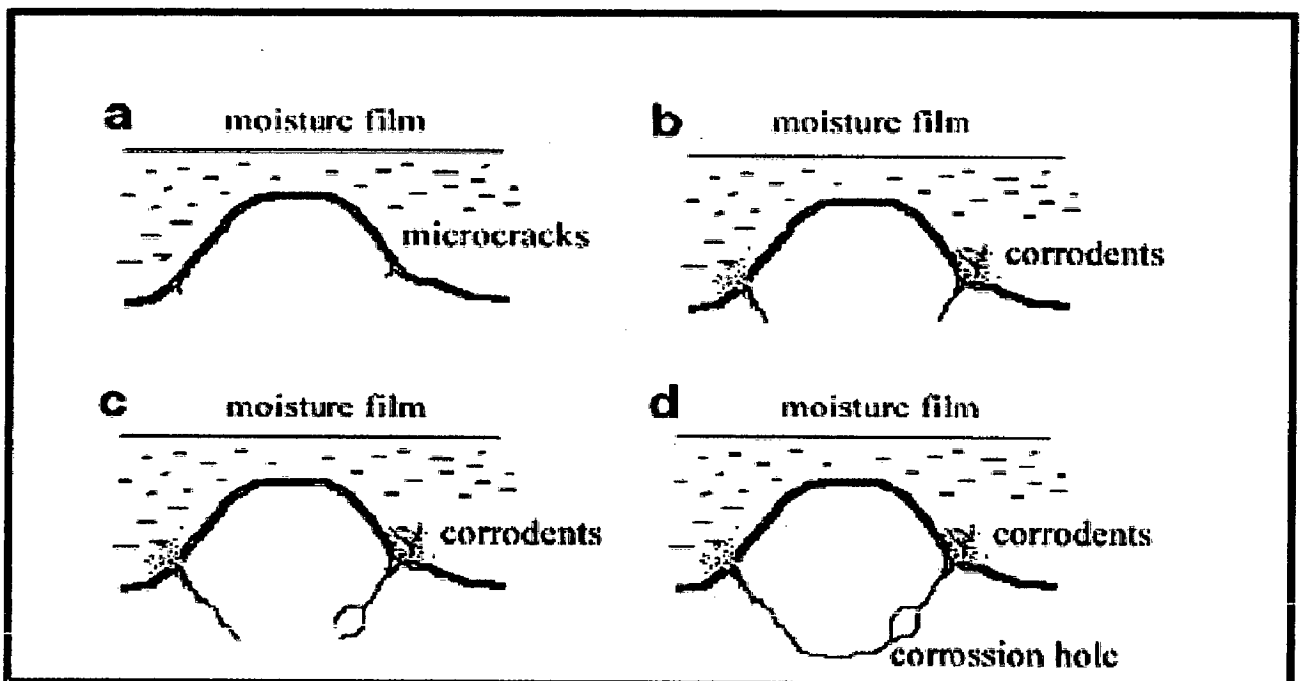


Fig. 6.40 Corrosion evolution of the as-deposited coatings in salt spray test; a: initiation of corrosion micro-crack, b: cracks propagation, c: crack branching, d: formation of corrosion hole (Bao et al., 2007)

This process obeys the rules of crevice corrosion. Acidity in the cracks increased significantly as neutralization was not easily obtained by exchanging solution between inside and outside the cracks. An ascending acidity accelerates the corrosion attack and results in an unfavourable inner structure. When the acid solution flows across pores, corrosion will take place and enlarge a pore to a corrosion hole.

6.5.2 Conclusions

The corrosion behavior of conventional thick (by plasma spraying and gas nitrided) and nanostructured thin (by physical vapor deposition process) TiAlN and AlCrN coatings on ASTM-SA213-T-22 boiler steel, has been analyzed by electrochemical methods i.e. linear polarization resistance (LPR) and potentiodynamic polarization tests in an aerated 3.0 wt% NaCl solution at room temperature; and salt spray (Fog) tests (5.0 wt% NaCl). The following conclusions are made:

1. In Linear polarization resistance (LPR) test, the corrosion current densities of all the coatings were found much lower than that of the substrate. The corrosion resistance of the coatings and substrate followed the sequence:
Nanostructured TiAlN > Nanostructured AlCrN > Conventional TiAlN > Conventional AlCrN > Substrate
2. In Potentiodynamic Polarization test, the corrosion current densities of the coatings were found lower than that of the substrate steel. All the coatings have performed well in 3 wt. % NaCl solution when compared to the behavior of substrate steel.
3. The corrosion current densities of the substrate and the coatings in Potentiodynamic Polarization test were found much lower as compared to the LPR test (at initial stage) results. The corrosion resistance of the coatings and substrate followed the sequence:
Nanostructured AlCrN > Conventional AlCrN > Nanostructured TiAlN > Conventional TiAlN > Substrate
4. The measured protective efficiency for nanostructured thin TiAlN, nanostructured thin AlCrN, conventional thick TiAlN and conventional thick AlCrN coatings is 72.26%, 94.88%, 47.27% and 76.87% respectively.

5. The porosity values measured for nanostructured thin TiAlN, nanostructured thin AlCrN, conventional thick TiAlN and conventional thick AlCrN coatings, which are 1.05%, 0.19%, 0.0003% and 0.0159% respectively.
6. In salt spray tests; the uncoated T-22 boiler steel suffered severe corrosion in all three test conditions i.e. 24 Hrs, 48 Hrs and 72 Hrs. The nanostructured coated samples have shown resistance to the corrosion as compared to the uncoated T-22 boiler steel.
7. The weight loss per unit area increases with the duration of the test. The weight loss per unit area in case of nanostructured thin TiAlN coating is less than as compared to the nanostructured AlCrN coating and uncoated boiler steel in all test conditions.
8. It can be mentioned based on the present investigation that nanostructured thin TiAlN and AlCrN coatings can provide good corrosion resistance when exposed to the simulated marine environment i.e. salt fog test.

6.6 EROSION-CORROSION STUDIES IN INDUSTRIAL ENVIRONMENT

After conducting the various experiments on uncoated and coated ASTM-SA213-T-22 boiler steel in lab; the present research work has been focused to investigate and compare the high temperature corrosion and erosion behavior of conventional thick (by plasma spraying and gas nitrided) and nanostructured thin (by physical vapor deposition process) TiAlN and AlCrN coatings on T-22 boiler steel, in actual industrial environment of coal fired boiler. The uncoated and coated specimens were exposed to low temperature super-heater zone of the coal fired boiler of Guru Nanak Dev Thermal Power Plant, Bathinda, Punjab, India. The specimens were hanged in the platen super-heater of coal fired boiler where the gas temperature was around $900^{\circ}\text{C} \pm 10^{\circ}\text{C}$. Hot corrosion experiments were performed for 10 cycles, each cycle consisting of 100 hours exposure followed by 1 hour cooling at ambient temperature. The detailed experimental procedure is explained in chapter 3.

6.6.1 Results

6.6.1.1 Visual observations

The macrographs for bare and coated ASTM-SA213-T-22 boiler steel exposed to super-heater of the coal fired boiler environment at 900°C for 1000 hours are shown in Fig.6.41. For the uncoated T-22 boiler steel, a dark grey colored fragile scale appeared on the surface right from the 1st cycle. Ash deposition has also been started after the 1st cycle and the sample showed spalling and gets welded with the wire with which it was hanged in the boiler environment. After every cycle; the samples were washed with acetone in order to remove ash deposited before weight measurement. Erosion was also observed after 2nd cycle along the edges. Ash deposition, erosion and severe spalling in case of bare T-22 boiler steel continue to the last cycle. At the end of cyclic study, ash deposited fragile scale with severe spalling and dark grey colored surface appearance and visible cracks; was observed which can be also seen in Fig.6.41 (a).

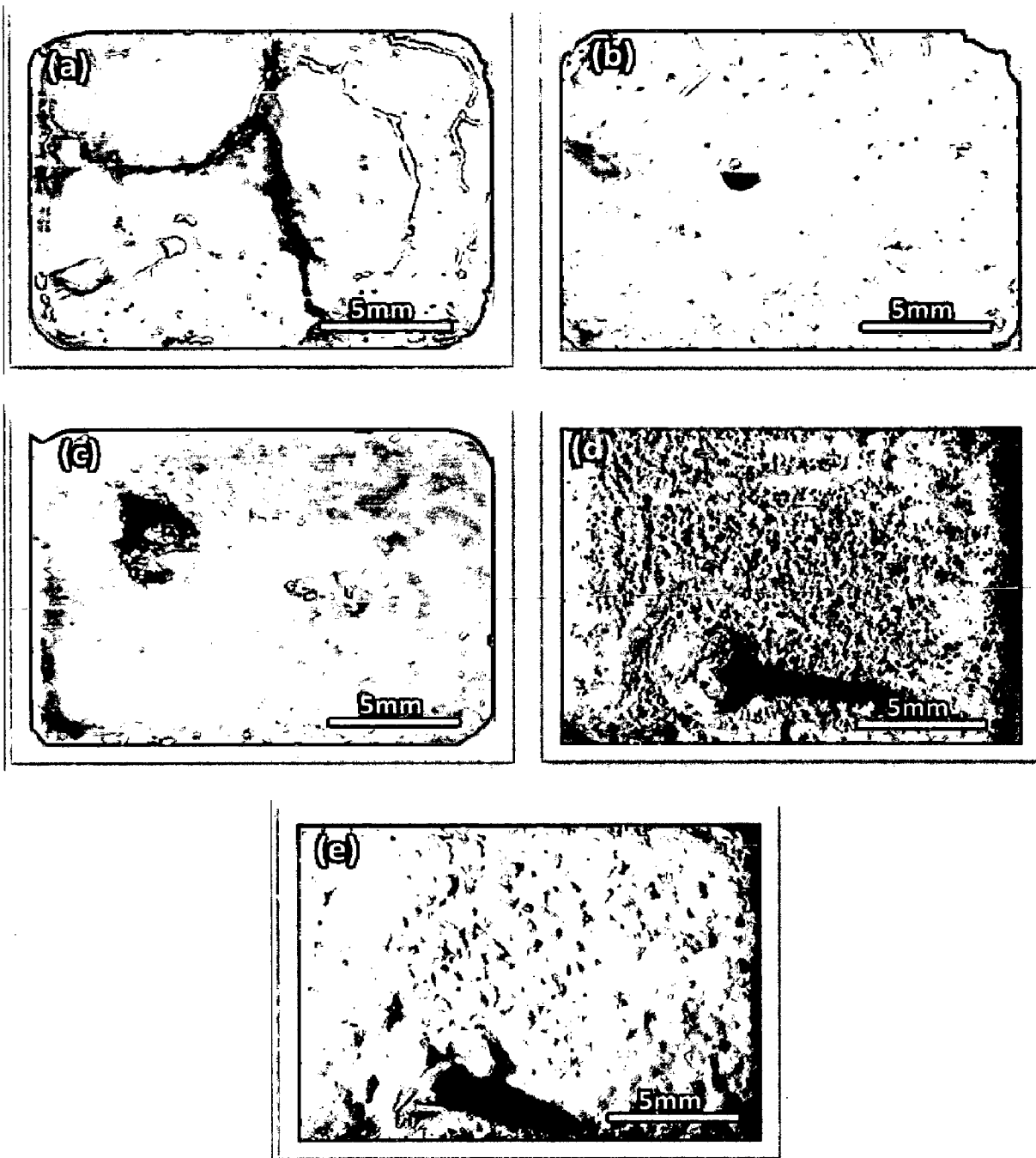


Fig. 6.41 Surface macrographs of uncoated and coated ASTM-SA213-T-22 boiler steel exposed to super-heater of the coal fired boiler environment at 900°C for 1000 hours: (a) Uncoated T-22 boiler steel, (b) Nanostructured TiAlN coating, (c) Nanostructured AlCrN coating, (d) Conventional TiAlN coating, (e) Conventional AlCrN coating

In case of nanostructured thin TiAlN coated T-22 boiler steel, color of the oxide scale at the end of the study was observed to be brownish grey as shown in Fig.6.41 (b). Ash deposition has started after the 1st cycle and the sample showed spalling and it gets welded with the wire with which it was hanged in the boiler environment. During 3rd

cycle some scale at one of the corners gets broken and fallen in the boiler. Ash deposition, erosion and spalling continued to last cycle. The nanostructured thin AlCrN coated T-22 boiler steel has shown the formation of dark blackish grey colored scale with some brownish colored spots as shown in Fig.6.41 (c). After 1st cycle, grey colored scale with some golden spots was seen on the surface with ash deposition without any sign of spalling. The scale shows spalling during 3rd cycle and the sample gets welded to the wire. During 6th cycle; some scale at one of the corners gets broken and fallen in the boiler. The ash deposition, erosion and spalling continue till the end.

A visual observation of conventional thick TiAlN coated T-22 boiler steel (Fig.6.41.d), showed the formation of light grey colored scale at the end of the study. The scale was rough and adherent to the substrate. The sample gets welded to the wire after 3rd cycle. In case of conventional thick AlCrN coated T-22 boiler steel, color of the ash deposited oxide scale was dark grey with some signs of a spalled area at the end of the study (Fig.6.41.e). The scale was found to be adherent. No spalling was observed till 4th cycle after which the sample gets welded to the wire and showed spalling and signs of erosion.

6.6.1.2 Weight change and sample thickness measurements

Weight gain per unit area (mg/cm^2) versus time expressed in number of cycles plot for coated and bare ASTM-SA213-T-22 boiler steel exposed to super-heater of the coal fired boiler environment at 900°C for 1000 hours; is presented in Fig. 6.42. However weight change data could not be of much use for predicting the corrosion behavior because of suspected spalling and ash deposition on the specimens. Although the specimens were washed with acetone after every cycle before weight measurement in order to remove ash deposited yet it was difficult to remove the ash completely. Hence extent of corrosion could only be monitored by measuring the thickness of the unreacted sample after the total exposure of 1000 hrs i.e. measuring scale thickness in cross-sectional view.

It can be inferred from the plots (Fig.6.42) that the uncoated and nanostructured thin TiAlN coated T-22 boiler steels have shown high weight gain as compared to the conventional thick and nanostructured AlCrN coatings.

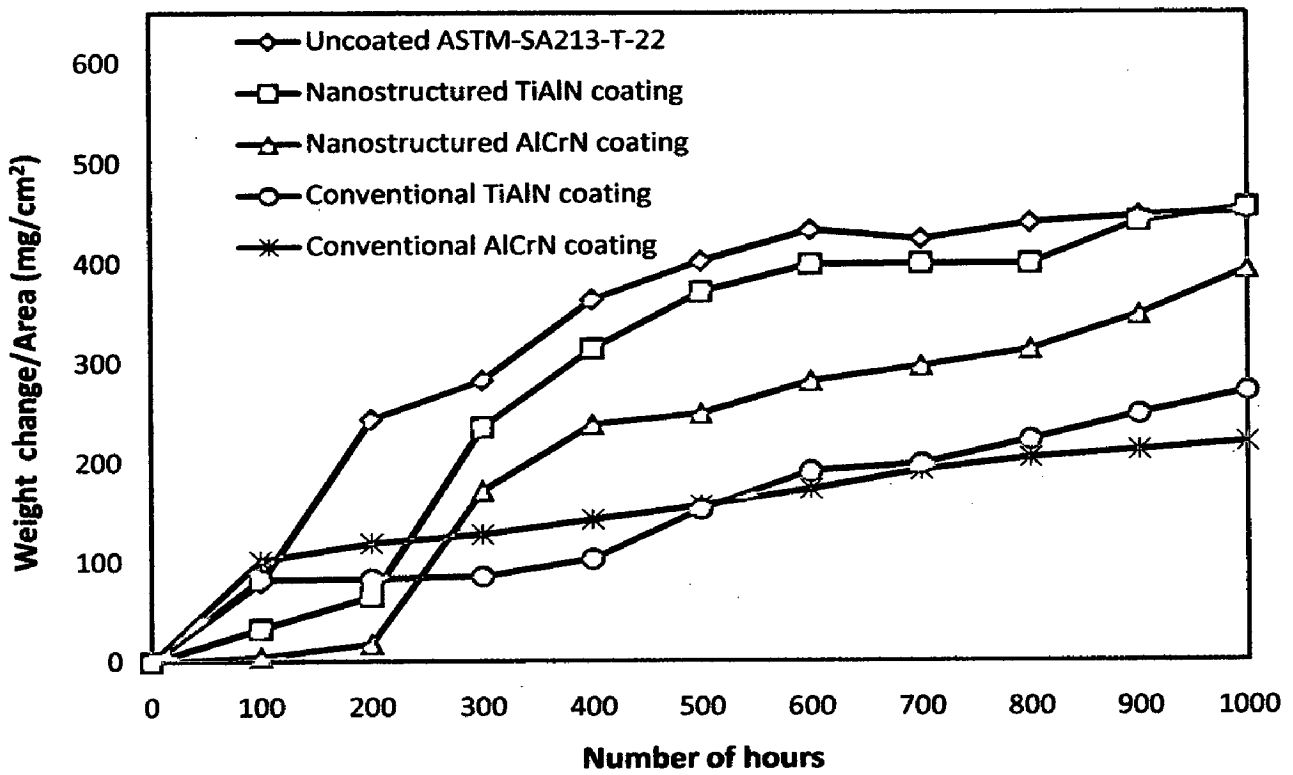


Fig. 6.42 Weight gain/area vs time for uncoated and coated ASTM-SA213-T-22 boiler steel exposed to super-heater of the coal fired boiler environment at 900°C for 1000 hours

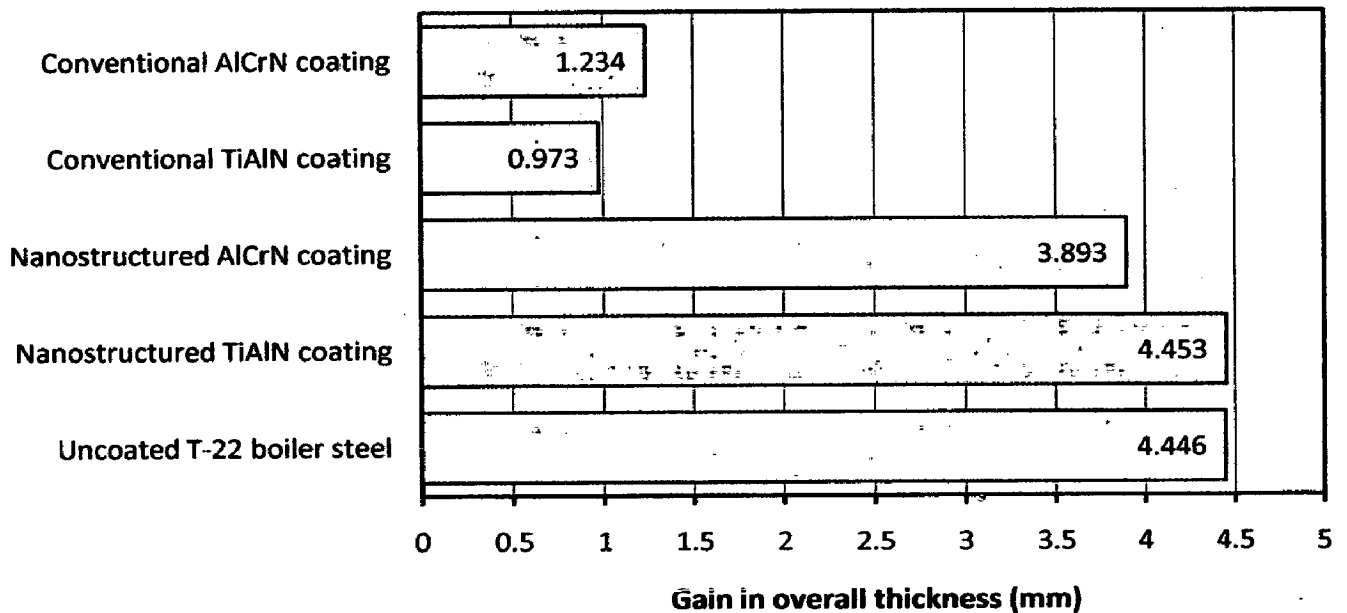


Fig. 6.43 Bar chart indicating overall gain in thickness for uncoated and coated ASTM-SA213-T-22 boiler steel specimens exposed to super-heater of the coal fired boiler environment at 900°C for 1000 hours

The erosion-corrosion rate in case of nanostructured coatings was very less during first two cycle and then increases rapidly during 3rd cycle and followed by gradual increase in erosion-corrosion rate. In case of conventional coatings; the initial erosion-corrosion rate is high during initial cycle which becomes gradual in the subsequent cycles. The conventional coatings have shown much less weight gain as compared to the uncoated T-22 boiler steel. The nanostructured coatings have shown gain in weight in between the gain in case of uncoated and conventional coatings (Fig.6.42). The conventional AlCrN coating has shown minimum erosion-corrosion rate and weight gain.

Bar chart in Fig.6.43 indicates the overall gain/loss in the thickness (in mm) of the specimen. All the coatings and bare T-22 boiler steel have shown increase in overall thickness after erosion-corrosion for 1000 hrs. The thickness of the specimens was measured before and after the erosion-corrosion test and average of ten values has been used to calculate the thickness gain/loss. The measured average gain in overall specimen thickness values for uncoated T-22, nanostructured thin TiAlN, nanostructured thin AlCrN, conventional thick TiAlN and AlCrN coatings are 4.446, 4.453, 3.893, 0.973 and 1.234 mm respectively.

6.6.1.3 Surface scale analysis

6.6.1.3.1 X-ray diffraction analysis (XRD)

XRD diffractograms for coated and uncoated ASTM-SA213-T-22 boiler steel exposed to super-heater of the coal fired boiler environment at 900°C for 1000 hours; are depicted in Fig.6.44 (a and b) on reduced scale. As indicated by the diffractograms Fe₂O₃, Al₂O₃ and SiO₂ are the main phases present in the oxide scale of coated and uncoated T-22 boiler steel. In case of conventional thick AlCrN coating; the presence of SiO₂ is not observed in the oxide scale (Fig.6.44).

6.6.1.3.2 Surface scale morphology

SEM micrographs along with EDAX point analysis reveals the surface morphology of the coated and uncoated ASTM-SA213-T-22 boiler steel exposed to super-heater of the coal fired boiler environment at 900°C for 1000 hours; are shown in Fig.6.45.

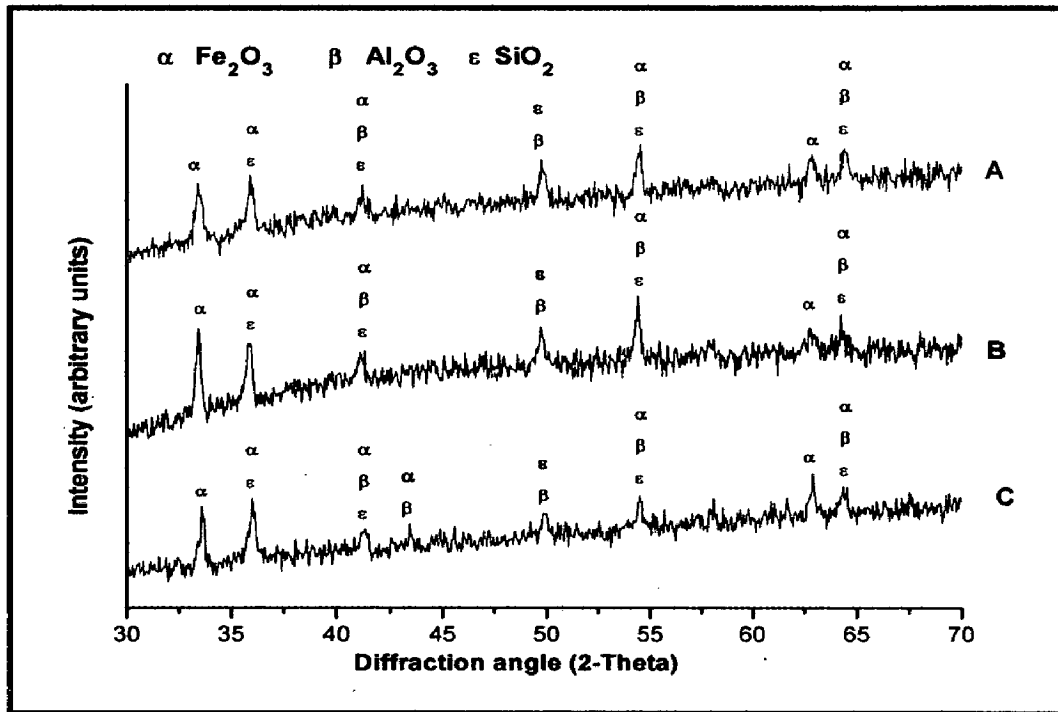


Fig. 6.44 (a) X-Ray Diffraction pattern of uncoated and coated ASTM-SA213-T-22 boiler steel exposed to platen superheater of the coal fired boiler environment at 900°C for 1000 Hrs: (A) Uncoated T-22 boiler steel, (B) Nanostructured TiAlN coating, (C) Nanostructured AlCrN coating

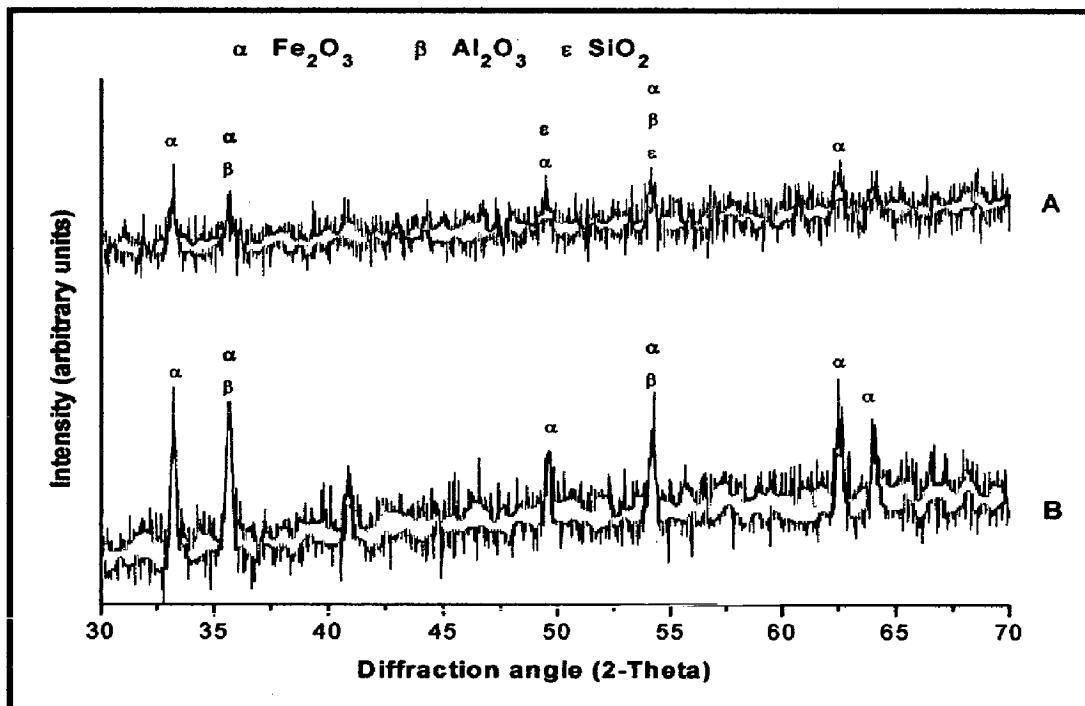


Fig. 6.44 (b) X-Ray Diffraction pattern of coated ASTM-SA213-T-22 boiler steel exposed to platen superheater of the coal fired boiler environment at 900°C for 1000 Hrs: (A) Conventional TiAlN coating, (B) Conventional AlCrN coating

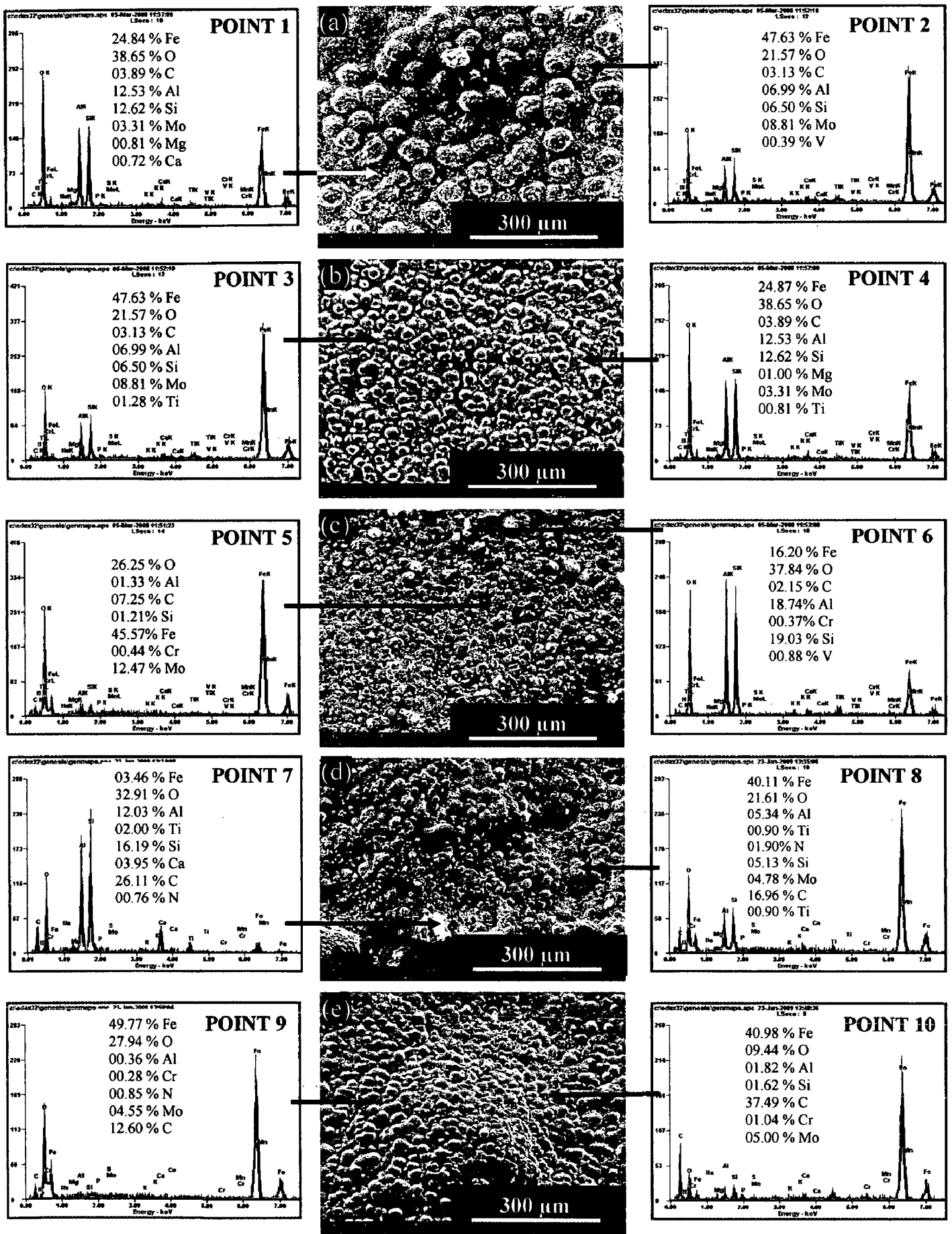


Fig. 6.45 Surface-scale morphology and EDAX patterns from different spots on uncoated and coated ASTM-SA213-T-22 boiler steel exposed to platen superheater of the coal fired boiler environment at 900°C for 1000 Hrs: (a) Uncoated T-22 boiler steel, (b) Nanostructured TiAlN coating, (c) Nanostructured AlCrN coating, (d) Conventional TiAlN coating, (e) Conventional AlCrN coating

Very thick scale is observed in case of uncoated and nanostructured coated T-22 boiler steel. The measured corrosion rate (mpy) for uncoated T-22, nanostructured thin TiAlN, nanostructured thin AlCrN, conventional thick TiAlN and conventional thick AlCrN coatings are 911, 775, 508, 208 and 447 mpy respectively. The coatings have shown good resistance to the corrosive environment in terms of corrosion rate (Fig.6.48). The extent of erosion-corrosion is least in case of conventional TiAlN coating.

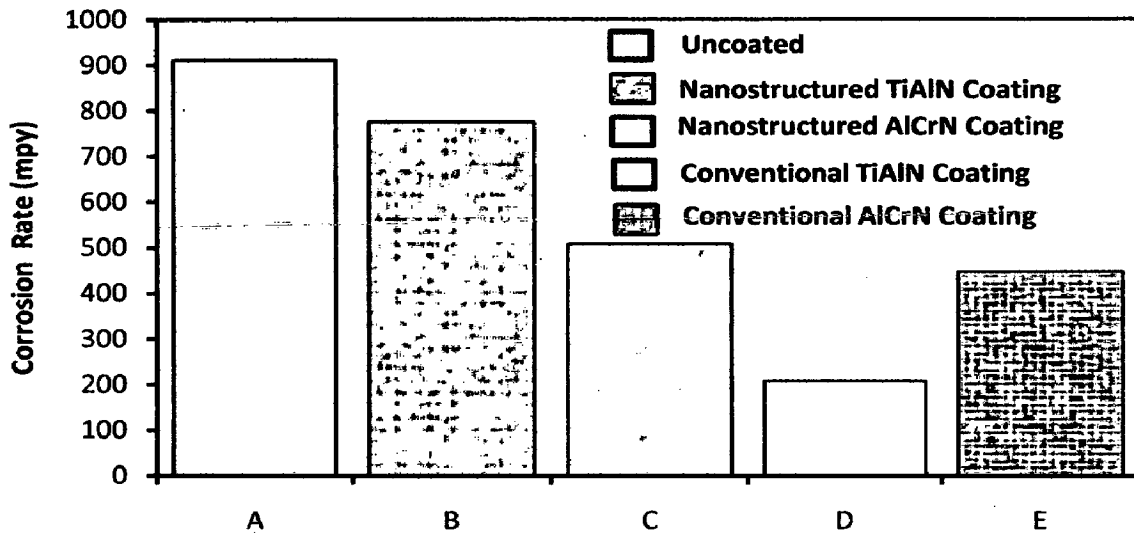


Fig. 6.48 Corrosion rate in mils per year (mpy) for uncoated and coated ASTM-SA213-T-22 boiler steel exposed to super-heater of the coal fired boiler environment at 900°C for 1000 hours: (A) Uncoated T-22 boiler steel, (B) Nanostructured TiAlN coating, (C) Nanostructured AlCrN coating, (D) Conventional TiAlN coating, (E) Conventional AlCrN coating

6.6.1.4.3 X-Ray mapping

X-ray mappings for a part of oxide scale of uncoated and coated ASTM-SA213-T-22 boiler steel exposed to super-heater of the coal fired boiler environment at 900°C for 1000 hours; are shown in Fig. 6.49. In case of uncoated T-22 boiler steel, the micrograph (Fig.6.49.a) indicates a dense scale, which mainly contains iron and oxygen with a thick band of Cr near scale/substrate interface, as indicated by X-ray mapping. The X-ray mapping analysis of the scale formed on nanostructured TiAlN coated T-22 boiler steel is presented in Fig. 6.49 (b).

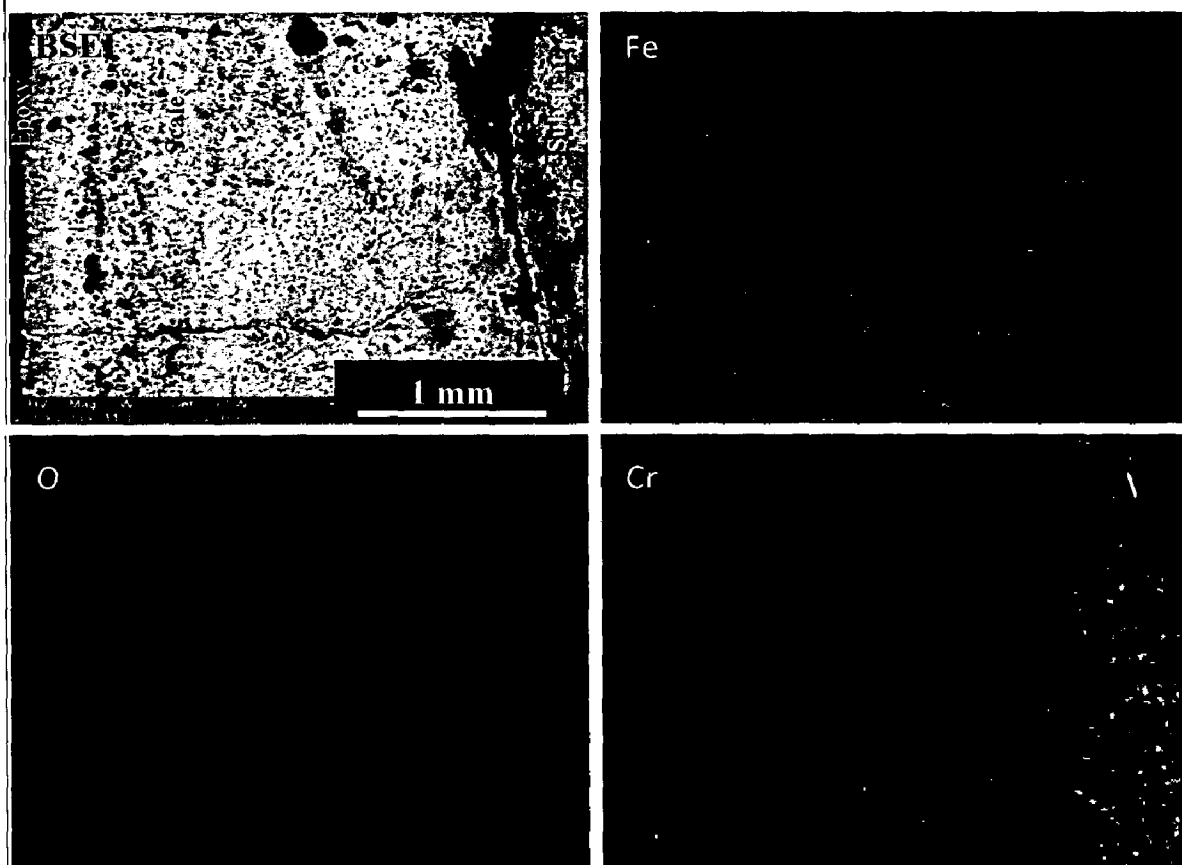


Fig. 6.49 (a) Composition image (BSEI) and X-ray mapping of the cross-section of uncoated ASTM-SA213-T-22 boiler steel exposed to platen super-heater of the coal fired boiler environment at 900°C for 1000 Hrs

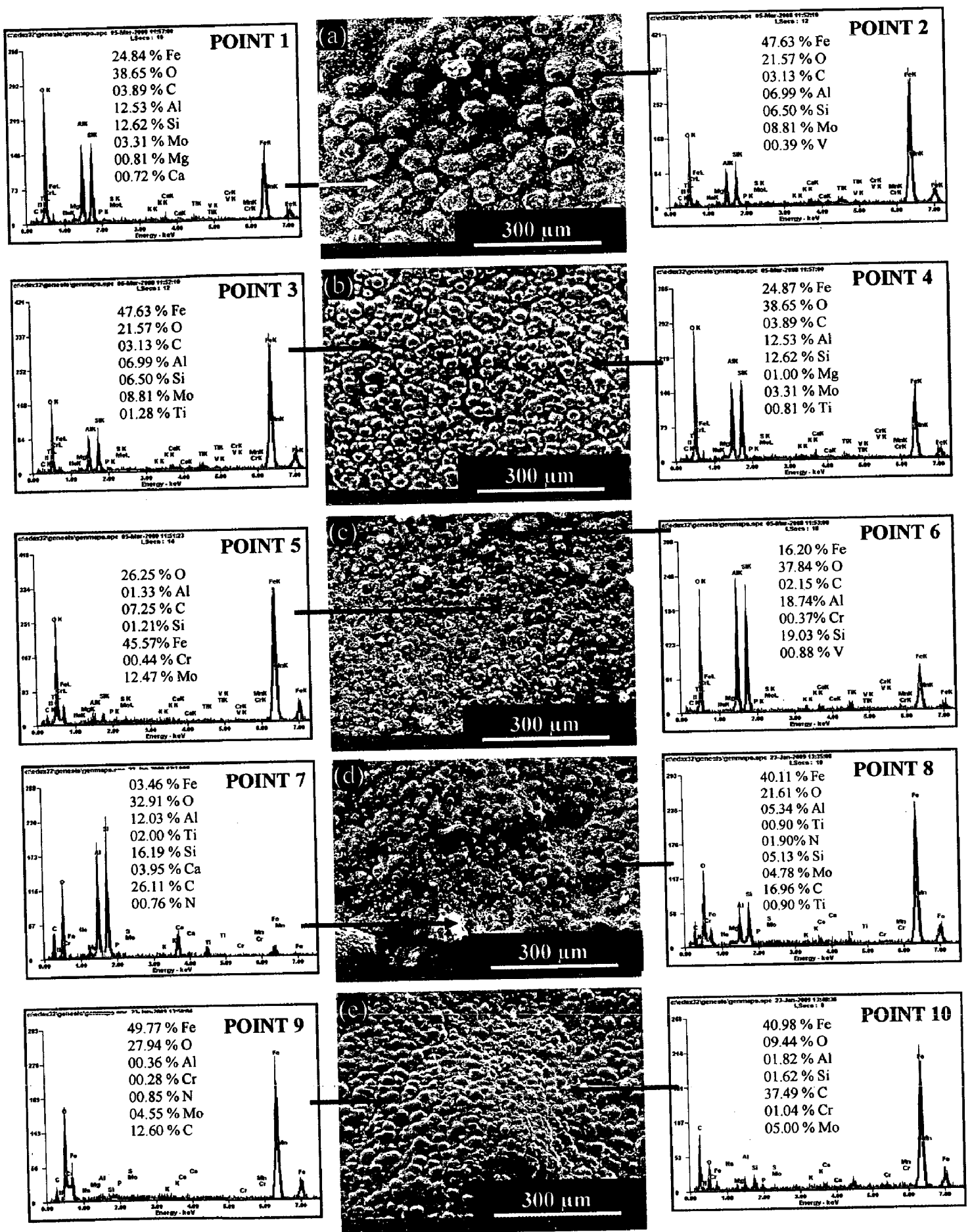


Fig. 6.45 Surface-scale morphology and EDAX patterns from different spots on uncoated and coated ASTM-SA213-T-22 boiler steel exposed to platen superheater of the coal fired boiler environment at 900°C for 1000 Hrs: (a) Uncoated T-22 boiler steel, (b) Nanostructured TiAlN coating, (c) Nanostructured AlCrN coating, (d) Conventional TiAlN coating, (e) Conventional AlCrN coating

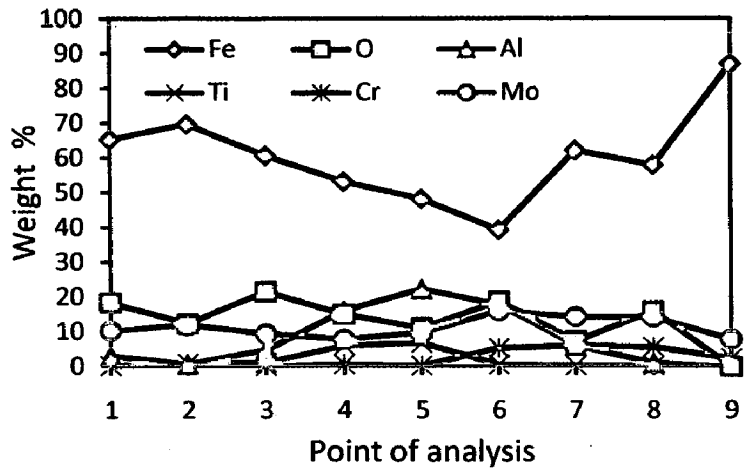
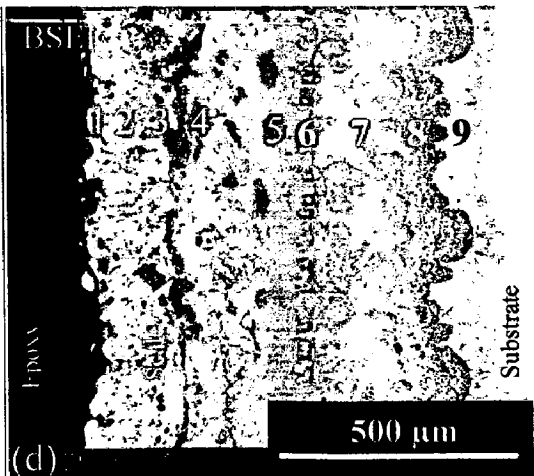
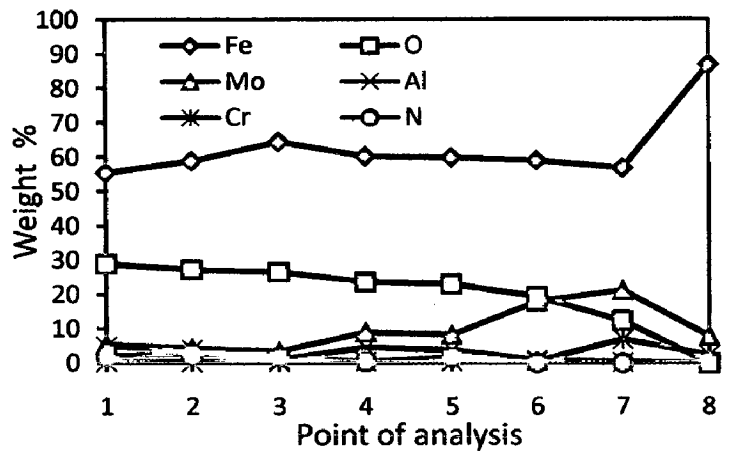
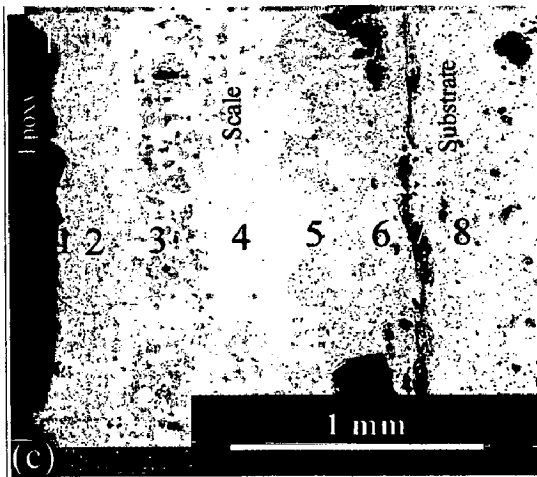
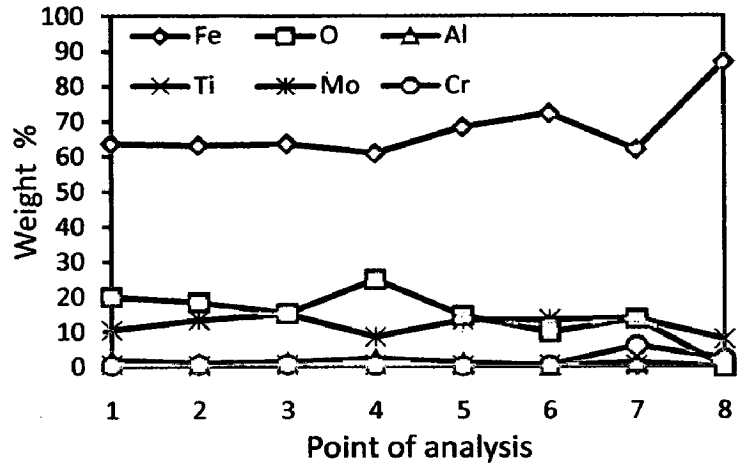
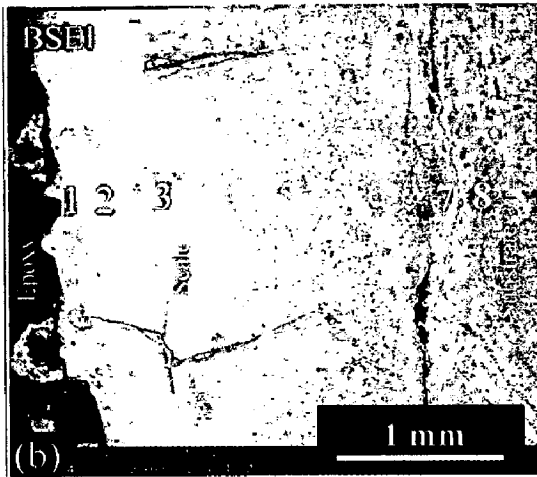
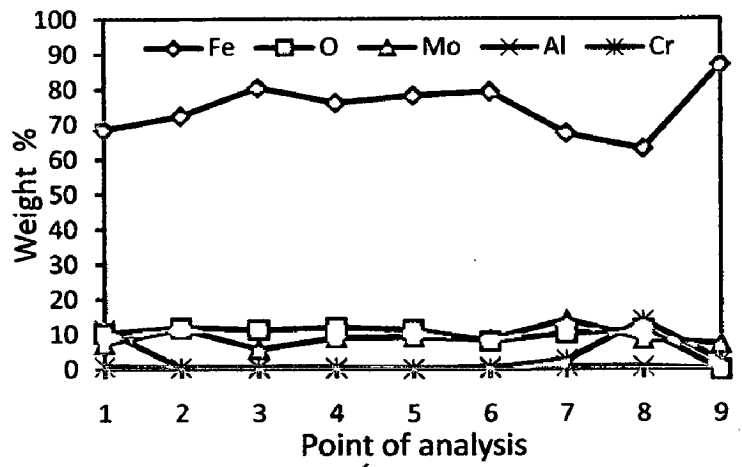
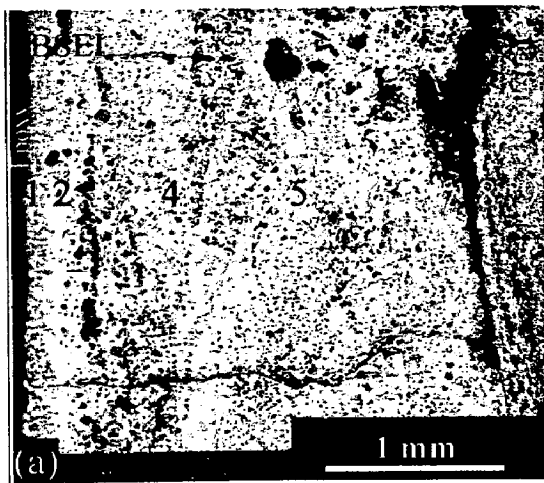
Micrograph (shown in Fig.6.45.a) for uncoated T-22 boiler steel shows the top scale appearance like round tiny particles (Point 2) developed in a matrix (Point 1). EDAX analysis reveal the presence of Fe, O, Al and Si along with small amount of Ca, Mo and V. The matrix shows higher percentage of O, Al and Si and less concentration of Fe as compared to the tiny particles. The SEM micrograph of oxidized nanostructured thin TiAlN coatings is shown in Fig.6.45 (b). The top scale is similar to that of the uncoated T-22 boiler steel. EDAX analysis (Point 3 and 4) of the scale revealed the presence of Fe, O, Al and Si as the main elements along with small amount of Ti, Cr, Mg and Mo. In case of nanostructured thin AlCrN coated T-22 boiler steel, the scale consists of dark grey distorted grains (Fig.6.45.c) along with some white contrast spots (Point 6). EDAX point analysis at point 6 shows the presence of Al, Si and O along with V and Cr with small amount of iron, whereas the dark grey region (Point 5) shows maximum concentration of Fe along with small amount of Al, Si, Cr and Mo.

The surface scale developed on conventional thick TiAlN coated T-22 steel appears like the surface scale in case of nanostructured thin TiAlN coating. The white contrast regions (Fig.6.45.d) have shown higher percentage of Al, Si, O, Ti, C and less concentration of Fe as compared to the matrix (Point 8). A spalled surface scale is developed on conventional thick AlCrN coated T-22 boiler steel. The top scale is rich in Fe, O along with Al, Cr, C and Mo (Fig.6.45.e).

6.6.1.4 Cross-sectional analysis

6.6.1.4.1 Cross-sectional scale morphology

Back Scattered Electron Image (BSEI) micrograph and elemental variation across the cross-section for coated and uncoated ASTM-SA213-T-22 boiler steel exposed to super-heater of the coal fired boiler environment at 900°C for 1000 hours; are shown in Fig.6.46. The SEM micrograph (Fig.6.46.a) in case of uncoated T-22 boiler steel shows thick scale. Also, the scale is fragile and indicating cracking. EDAX analysis reveals the presence of Fe, Mo and O throughout the scale along with some amount of Cr and Al. In the top scale Al is present as indicated by EDAX analysis at point 1 in Fig.6.46 (a). Also, amount of Cr is higher at point 8 near scale/substrate interface. The existence of significant amount of iron and oxygen points out the possibility Fe₂O₃ in the oxide scale.



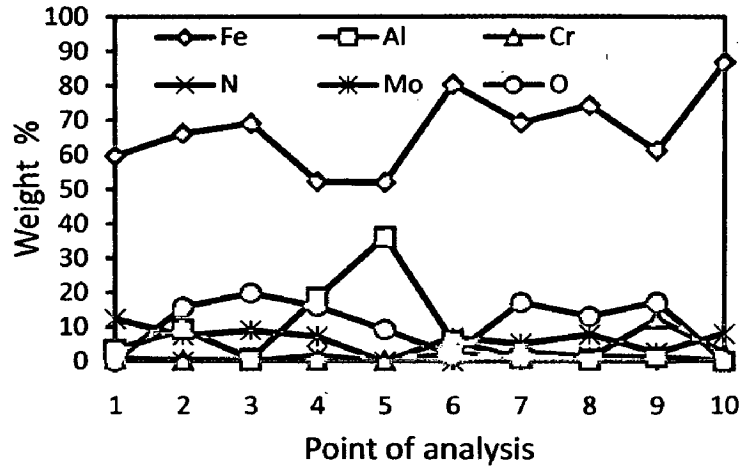
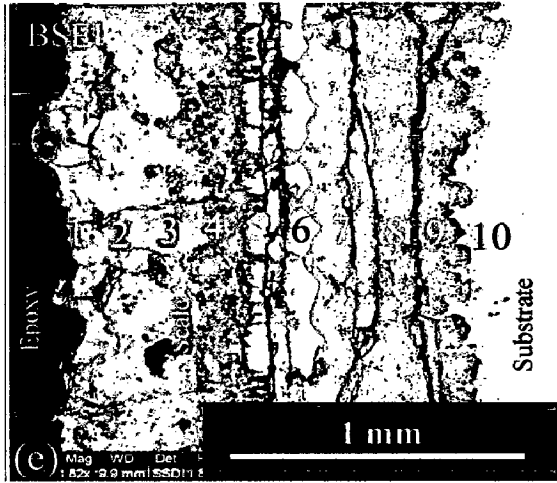


Fig. 6.46 Oxide scale morphology and variation of elemental composition across the cross-section of the uncoated and coated ASTM-SA213-T-22 boiler steel exposed to platen super-heater of the coal fired boiler environment at 900°C for 1000 Hrs: (a) Uncoated T-22 boiler steel (50 X), (b) Nanostructured TiAlN coating (45 X), (c) Nanostructured AlCrN coating (70 X), (d) Conventional TiAlN coating (130 X), (e) Conventional AlCrN coating (82 X)

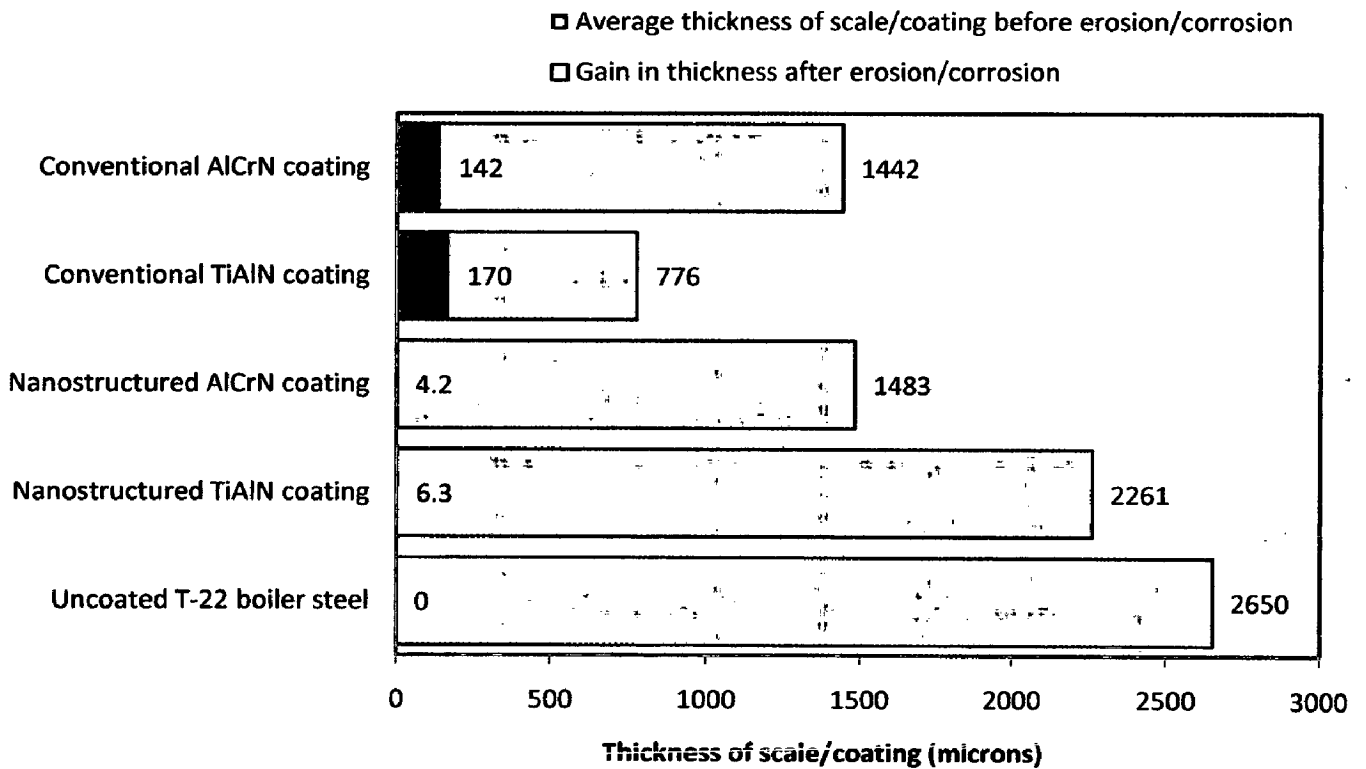


Fig. 6.47 Bar chart indicating the extent of erosion/corrosion for uncoated and coated ASTM-SA213-T-22 boiler steel specimens exposed to super-heater of the coal fired boiler environment at 900°C for 1000 hours

BSEI micrograph and elemental variation depicted in Fig.6.46 (b), for the exposed cross-section of nanostructured thin TiAlN coated T-22 boiler steel shows the thick, continuous and adherent scale. The EDAX analysis reveals the presence of Fe, Mo and O throughout the scale along with very small amount of Cr. At scale/substrate interface; higher concentration of Cr is observed. A thick and adherent oxide scale can be seen in case of nanostructured AlCrN coated T-22 boiler steel (Fig.6.46.c). The EDAX point analysis indicates the presence of Fe, Mo and O throughout the scale with variable amounts of Al and Cr. The top scale is rich in Fe, O and Al as shown by point 1, 2 and 3 in Fig.6.46 (c). Also, in the sub-scale region and at scale substrate interface the concentration of Al and Cr is higher (point 4 and 7).

In case of conventional TiAlN coated T-22 boiler steel, the scale is uniform, thin and adherent as depicted in Fig.6.46 (d). The EDAX point analysis indicates the presence of Fe, O, Cr, Mo, Ti and Al throughout the scale with variable amounts. The amount of Ti and Al in the sub-scale region is higher (Fig.6.46.d). The top scale is rich in Fe, O and Mo (Point 1, 2 and 3). The concentration of Cr is found more near the scale-substrate region (Fig.6.46.d). The conventional thick AlCrN coated T-22 boiler steel (Fig.6.46.e) indicates uniform, thin and adherent scale. EDAX point analysis shows the presence of Al, Fe, O and Mo throughout the scale. The top scale is rich in Al, Fe and O with some amount of Mo. The sub scale has shown higher concentration of Al as indicated by points 4, 5 and 6 in Fig.6.46 (e).

6.6.1.4.2 Scale thickness

The oxidized samples were cut across the cross section using Buehler Isomet 1000 precision saw and mounted in transoptic mounting resin and subsequently mirror polished to obtain scanning electron back scattered micrographs and X-ray mapping of different elements for coated and uncoated T-22 boiler steel. The scale thickness values were measured from SEM back scattered micrographs as shown in Fig.6.46. The extent of erosion-corrosion in terms of scale/coating thickness (in microns) and corrosion rate in mils per year (mpy) for coated and bare T-22 boiler steel exposed to super-heater of the coal fired boiler environment at 900°C for 1000 hours; are shown in Fig.6.47 and 6.48 respectively.

Very thick scale is observed in case of uncoated and nanostructured coated T-22 boiler steel. The measured corrosion rate (mpy) for uncoated T-22, nanostructured thin TiAlN, nanostructured thin AlCrN, conventional thick TiAlN and conventional thick AlCrN coatings are 911, 775, 508, 208 and 447 mpy respectively. The coatings have shown good resistance to the corrosive environment in terms of corrosion rate (Fig.6.48). The extent of erosion-corrosion is least in case of conventional TiAlN coating.

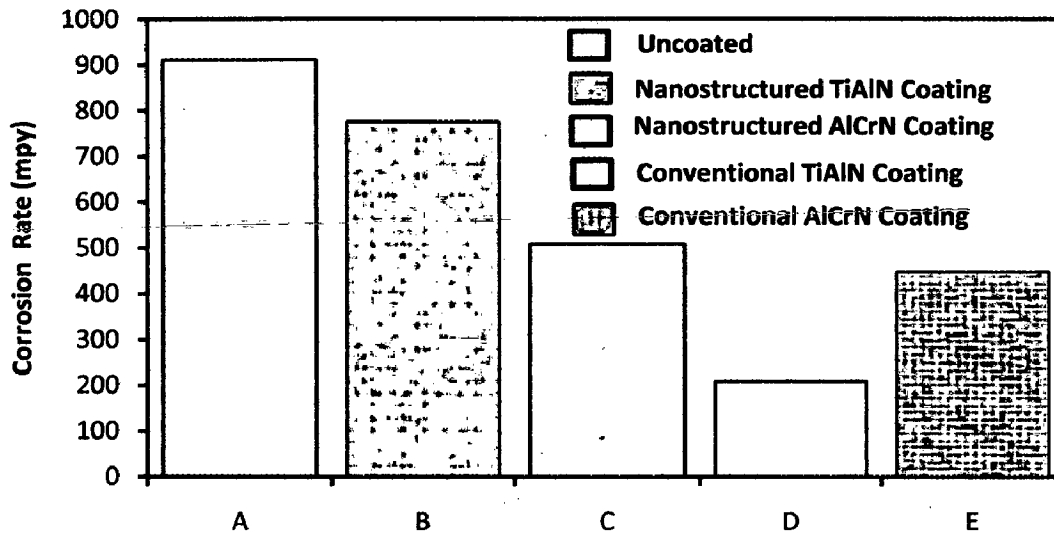


Fig. 6.48 Corrosion rate in mils per year (mpy) for uncoated and coated ASTM-SA213-T-22 boiler steel exposed to super-heater of the coal fired boiler environment at 900°C for 1000 hours: (A) Uncoated T-22 boiler steel, (B) Nanostructured TiAlN coating, (C) Nanostructured AlCrN coating, (D) Conventional TiAlN coating, (E) Conventional AlCrN coating

6.6.1.4.3 X-Ray mapping

X-ray mappings for a part of oxide scale of uncoated and coated ASTM-SA213-T-22 boiler steel exposed to super-heater of the coal fired boiler environment at 900°C for 1000 hours; are shown in Fig. 6.49. In case of uncoated T-22 boiler steel, the micrograph (Fig.6.49.a) indicates a dense scale, which mainly contains iron and oxygen with a thick band of Cr near scale/substrate interface, as indicated by X-ray mapping. The X-ray mapping analysis of the scale formed on nanostructured TiAlN coated T-22 boiler steel is presented in Fig. 6.49 (b).

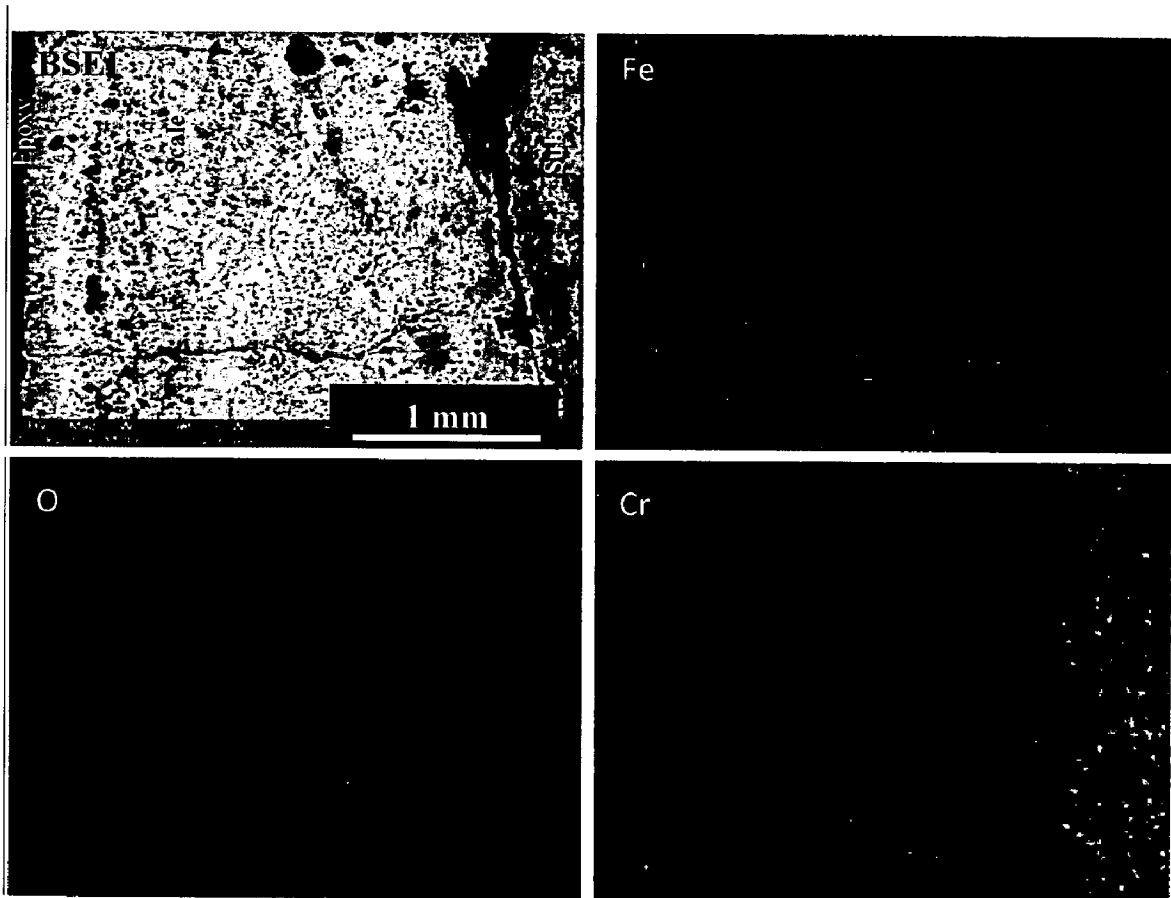


Fig. 6.49 (a) Composition image (BSEI) and X-ray mapping of the cross-section of uncoated ASTM-SA213-T-22 boiler steel exposed to platen super-heater of the coal fired boiler environment at 900°C for 1000 Hrs

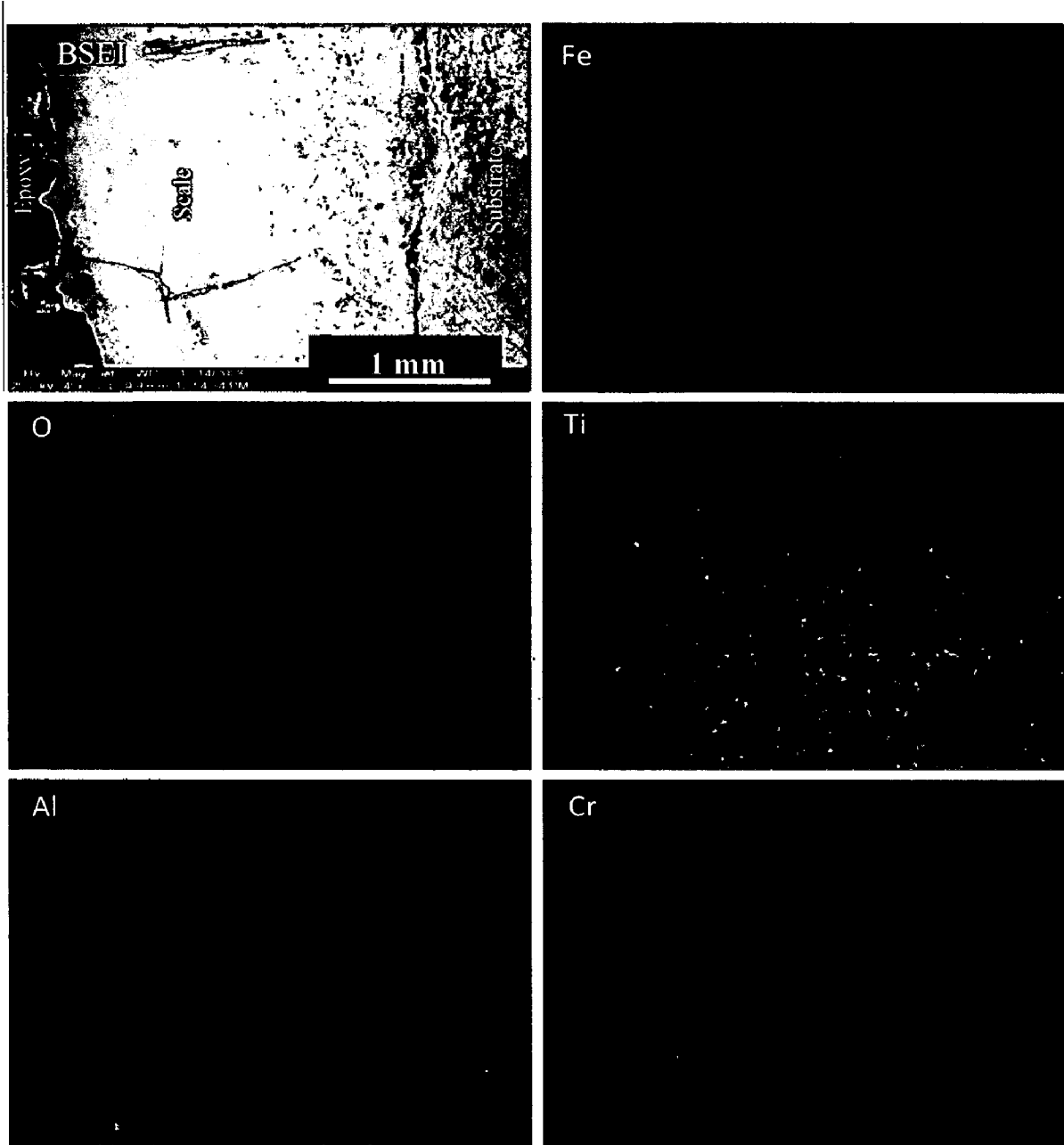


Fig. 6.49 (b) Composition image (BSEI) and X-ray mapping of the cross-section of Nanostructured TiAlN coated ASTM-SA213-T-22 boiler steel exposed to platen super-heater of the coal fired boiler environment at 900°C for 1000 Hrs

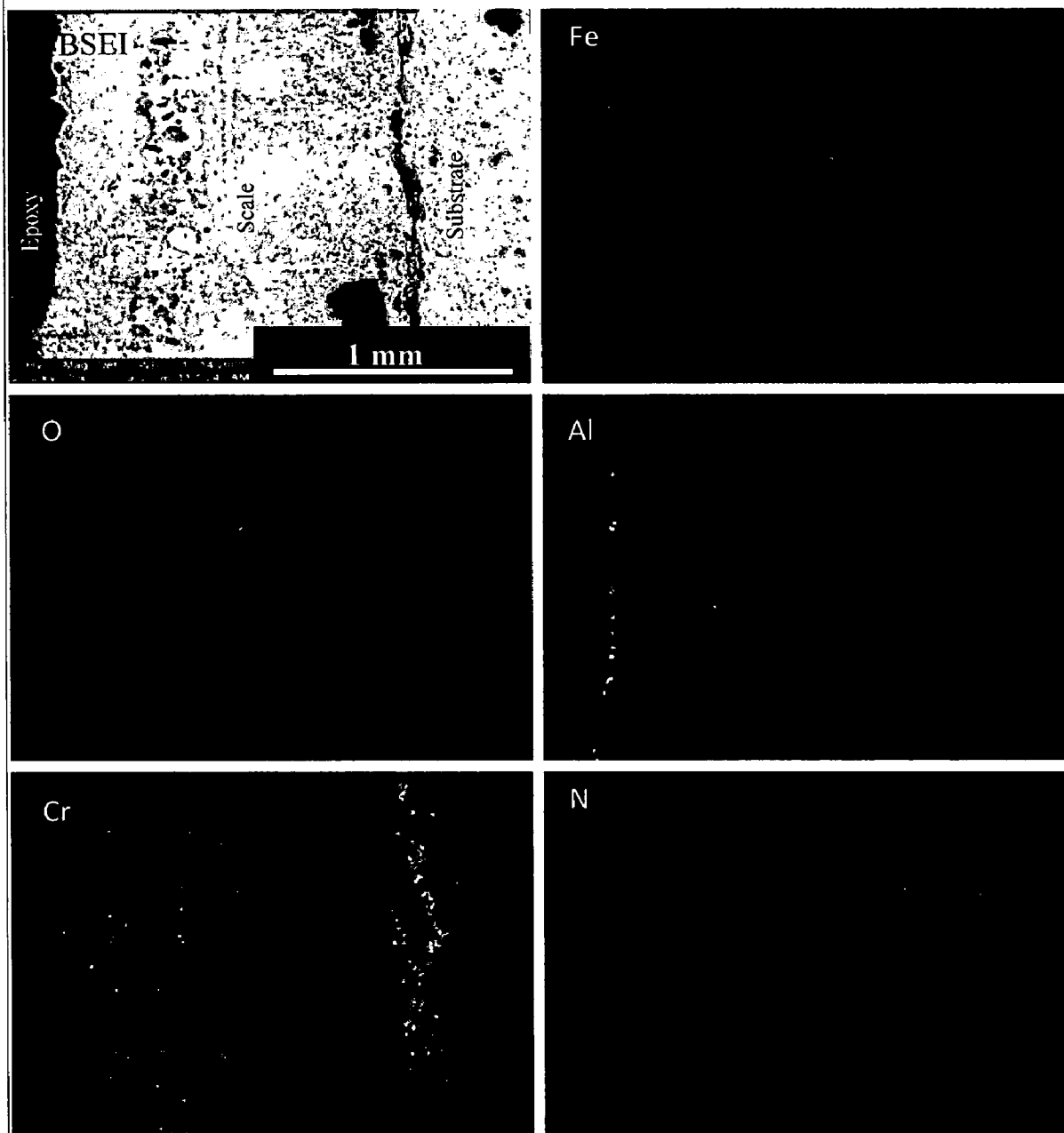


Fig. 6.49 (c) Composition image (BSEI) and X-ray mapping of the cross-section of Nanostructured AlCrN coated ASTM-SA213-T-22 boiler steel exposed to platen super-heater of the coal fired boiler environment at 900°C for 1000 Hrs

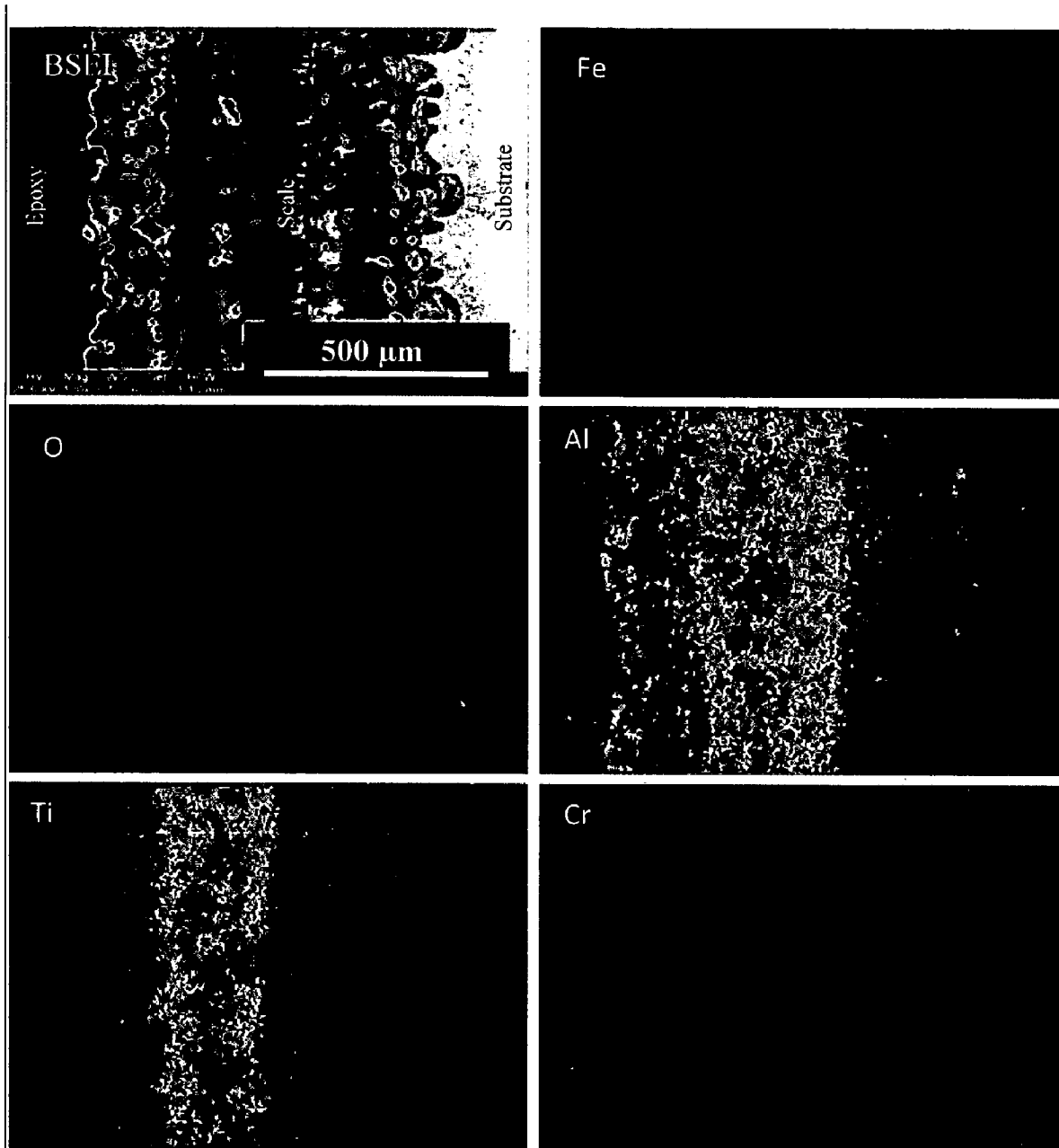


Fig. 6.49 (d) Composition image (BSEI) and X-ray mapping of the cross-section of conventional TiAlN coated ASTM-SA213-T-22 boiler steel exposed to platen super-heater of the coal fired boiler environment at 900°C for 1000 Hrs

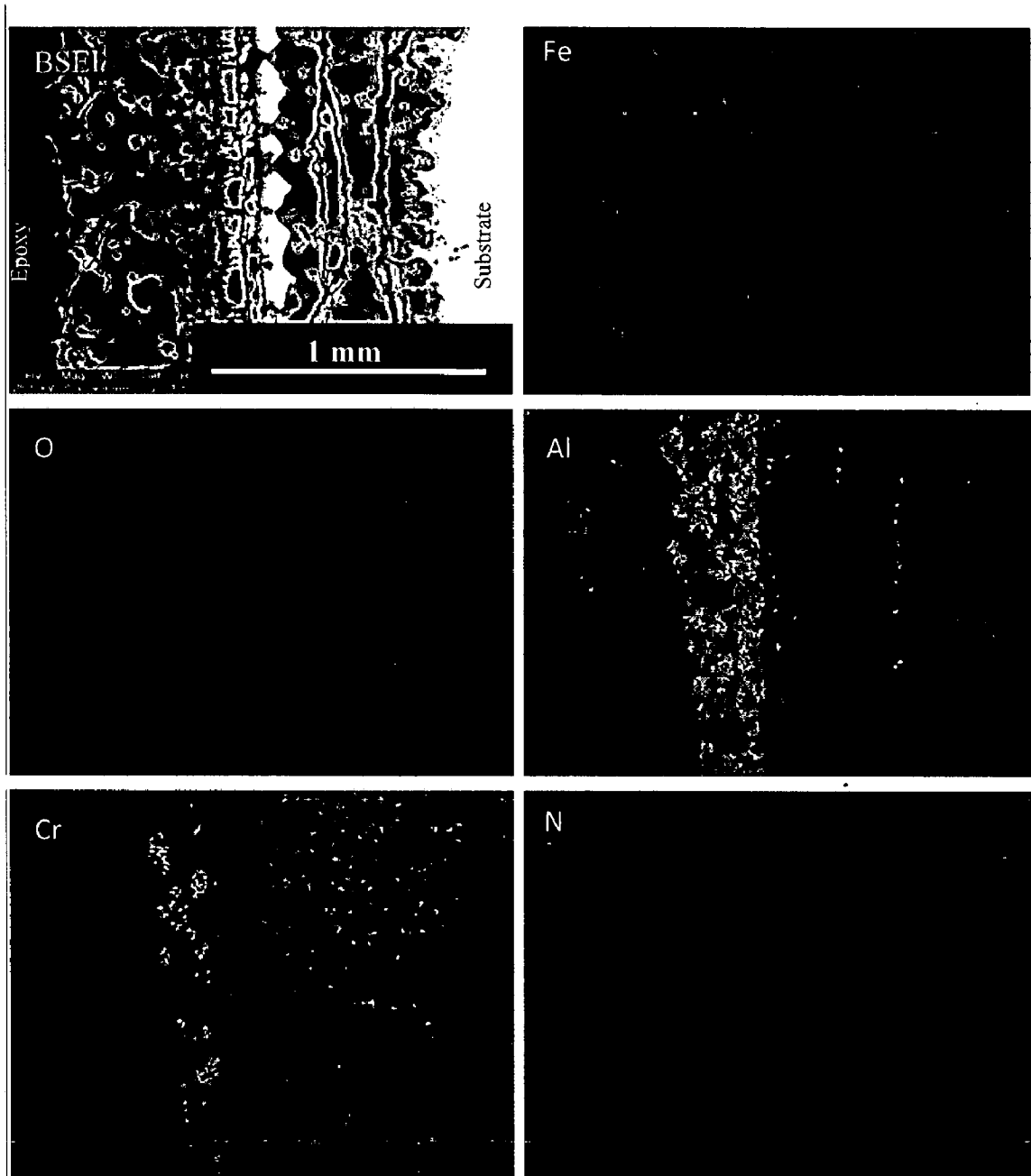


Fig. 6.49 (e) Composition image (BSEI) and X-ray mapping of the cross-section of conventional AlCrN coated ASTM-SA213-T-22 boiler steel exposed to platen super-heater of the coal fired boiler environment at 900°C for 1000 Hrs

The X-ray mapping indicates presence of oxygen and iron throughout the scale with a thin band of Al in the top scale and a thin band of Cr near scale-substrate interface. In case of nanostructured thin AlCrN coated T-22 boiler steel; the BSEI and X-ray mapping are shown in Fig. 6.49 (c). The X-ray mapping indicates the presence of iron and oxygen throughout the scale along with a very thin band of Al in top scale and a thick band of Cr near scale-substrate interface. In case of conventional thick TiAlN coated T-22 boiler steel, Fig.6.49 (d), Al and Ti rich thick bands are clearly seen along with Fe and oxygen in the sub-scale region along with a thick band of Cr near scale-substrate interface. Figure 6.49 (e) depicts the BSEI and X-ray mapping in case of conventional AlCrN coated T-22 boiler steel. The thick band of Al and Cr is present in the sub-scale region. The upper scale is rich in Fe and O.

6.6.2 Summary of Results

Results obtained after 1000 hrs of exposure for uncoated and coated ASTM-SA213-T-22 boiler steel to super-heater of the coal fired boiler environment at 900°C are summarized in Table.6.9.

6.6.3 Discussion

Fragile scale with tendency to spall has been observed for the uncoated and nanostructured thin TiAlN and AlCrN coated T-22 boiler steel used in present investigation (Fig.6.41). The ash deposition, erosion and tendency to spall continued till the end of the study. During cyclic testing, cracks in the oxide scale and spalling of the uncoated and coated T-22 boiler steel might be attributed to the different values of thermal expansion coefficients for the coating, scale and the substrate as reported by Sidhu et al. (2003), Singh et al. (2004), Evans et al. (2001), Wang et al. (2002) and Niranatlumpong et al (2000). The ash deposition, erosion and tendency to spall continued till the end of the study. Also, the scale gets removed and regenerated at some locations. It may be due to the erosion as the coal used in Indian power stations has large amounts of ash (about 50%), which contain abrasive mineral species such as hard quartz (up to 15%) which increase the erosion propensity of coal (Krishnamoorthy and Seetharamu, 1989).

Table 6.9

Summary of the results obtained for uncoated and coated ASTM-SA213-T-22 boiler steel exposed to super-heater of the coal fired boiler environment at 900°C for 1000 hours

Coating	Weight gain mg/cm ²	Extent of Corrosion (mm)	Corrosion Rate (mpy)	XRD phases	Remarks
Uncoated T-22 boiler steel	451.71	2.650	911.04	Fe ₂ O ₃ , Al ₂ O ₃ and SiO ₂	Ash deposited scale with severe spalling and dark grey colored surface appearance. Ash deposition, erosion and severe spalling continued till last cycle.
Nanostructured TiAlN coating	455.80	2.261	775.2	Fe ₂ O ₃ , Al ₂ O ₃ and SiO ₂	Color of the oxide scale at the end of the study was brownish grey with some lines as marks of erosion. Erosion and ash deposition continued till end of the study.
Nanostructured AlCrN coating	393.80	1.483	508.08	Fe ₂ O ₃ , Al ₂ O ₃ and SiO ₂	The formation of dark blackish grey colored scale with some brownish colored areas at the end. The ash deposition, erosion and spalling continue till the end.
Conventional TiAlN Coating	271.86	0.776	208.5	Fe ₂ O ₃ , Al ₂ O ₃ and SiO ₂	The formation of light grey colored scale at the end of the study. The scale was rough and adherent to the substrate.
Conventional AlCrN coating	220.69	1.442	447.6	Fe ₂ O ₃ , Al ₂ O ₃ and SiO ₂	Color of the ash deposited oxide scale was dark grey at the end. The scale was found to be adherent. No spalling was observed till 4 th cycle after which the sample gets welded to the wire and showed spalling and signs of erosion.

In case of conventional coatings; no spalling was observed during initial cycles of study. The surface of scale is rough in case of conventional thick coatings. As indicated by the diffractograms in Fig.6.44, Fe_2O_3 , Al_2O_3 and SiO_2 are the main phases present in the oxide scale of coated and uncoated T-22 boiler steel. The phases revealed by XRD diffractograms are found to be in agreement with those reported by Longa-Nova et al. (1996), Calvarin et al. (2000) and Nickel et al. (2002). The presence of Fe and oxygen (Fig.4.46) in the top of the scale of the coated T-22 boiler steel is believed to be due to the diffusion of iron through the pores and cracks that appeared in the coating during the course of oxidation studies (Singh Buta, 2003). Also, formation of hematite (Fe_2O_3) as revealed by the X-ray diffractograms (Fig.6.44) has also been analyzed by Prakash et al. (2001) and Srikanth et al. (2003) during the failure analysis of superheater tubes caused by fireside corrosion. The formation of Al_2O_3 and SiO_2 might be due to the deposition of ash on the eroded-corroded tubes. The higher amount of Al and Si is found in the ash. The presence of such phases in slag has also been reported by John (1986) and Nelson et al. (1959). Sulphides have not been generally identified in the scale of samples tested in the coal fired boiler environment; which is similar to the finding of Crossley et al. (1948). The fly ash particles rich in magnetite reduce the concentration of SO_3 in the boiler environment.

The higher weight gain (which is the net result of erosion and oxidation) is observed in case of uncoated and nanostructured thin TiAlN coated T-22 boiler steel as compared to the nanostructured AlCrN and conventional thick coatings; exposed to super-heater of the coal fired boiler environment at 900°C for 1000 hours (Fig.6.42). It might be attributed to spallation of the oxide scale in the actual environment of the coal fired boiler and fluxing action of the molten salt along with erosion of oxide scale. There is continuous formation of thin oxide scale with subsequent depletion by spallation and erosion under cyclic test conditions. The top surface may contains inclusions, which leads to vertical cracks through which the corrosive species might have penetrated along the crack and between the metallic layers. Both conventional thick coatings and nanostructured thin AlCrN coating have been found successful in reducing the overall weight gain of T-22 boiler steel. However weight change data could not be of much use for predicting the corrosion behavior because of suspected spalling and ash deposition

on the specimens. Thus, the extent of erosion-corrosion in terms of scale/coating thickness (in microns) and corrosion rate in mils per year (mpy) for coated and uncoated T-22 boiler steel exposed to super-heater of the coal fired boiler environment at 900°C for 1000 hours; are shown in Fig.6.47 and 6.48 respectively. All the coatings have shown lower corrosion rate as compared to bare T-22 boiler steel (Fig.6.48).

The nanostructured and conventional coatings have shown good resistance to the corrosive environment as the oxygen penetration is limited to very less thickness as compared to the uncoated T-22 boiler steel (Fig.6.47 and 6.48). These results are well supported by EDAX (Fig.6.45) and X-ray mapping analysis (Fig.6.49). The corrosion rate (mpy) for uncoated T-22, nanostructured thin TiAlN, nanostructured thin AlCrN, conventional thick TiAlN and conventional thick AlCrN coatings follows the following sequence:

Bare T-22 > Nanostructured TiAlN coating > Nanostructured AlCrN coating > Conventional AlCrN coating > Conventional TiAlN coating

The nanostructured and conventional coatings have shown good resistance to the corrosive environment in terms of corrosion rate (Fig.6.48) in mpy and the oxygen penetration is also limited to very less thickness as compared to the uncoated T-22 boiler steel (Fig.6.47). The extent of erosion-corrosion is least in case of conventional TiAlN coating. In case of nanostructured thin AlCrN coating, the presence of Al band in the top scale may be the reason for its better performance as compared to the nanostructured TiAlN coating and uncoated T-22 boiler steel (Fig.6.49.b). The resistance offered by conventional thick TiAlN and AlCrN coatings to the erosion-corrosion in boiler environment may be due to the presence of a thick band of Al and Cr (in case of conventional AlCrN coating), Ti and Al (in case of conventional TiAlN coating) along with oxygen in the sub-scale region; as shown by X-ray mapping analysis (Fig.6.49.d and e). The X-ray mapping analysis shows the presence of Cr in the sub-scale region of all the uncoated and coated T-22 boiler steel (Fig.6.49). The presence of chromium in the inner scale has also been reported by Sadique et al. (2000).

6.6.4 Conclusions

The high temperature erosion-corrosion behaviors of uncoated and coated ASTM-SA213-T-22 boiler steel have been investigated in super-heater of the coal fired boiler environment at 900°C for 1000 hours (10 cycles). The behavior of nanostructured TiAlN and AlCrN coatings were compared with conventional counterparts and the following conclusions are made:

1. The plasma sprayed gas nitride conventional thick coatings i.e. TiAlN and AlCrN have developed a protective scale mainly consisting on aluminum oxide.
2. The nanostructured TiAlN and AlCrN coatings have shown resistance to erosion-corrosion to some extent as compared to the uncoated T-22 boiler steel.
3. The corrosion rate (mpy) for uncoated T-22, nanostructured thin TiAlN, nanostructured thin AlCrN, conventional thick TiAlN and conventional thick AlCrN coatings follows the following sequence:
Bare T-22 > Nanostructured TiAlN coating > Nanostructured AlCrN coating > Conventional AlCrN coating > Conventional TiAlN coating
4. All the coated as well as uncoated boiler steels have shown ash deposition on the surface. Thus final thickness is contributed by scale formation, erosion and ash deposition.
5. The oxide scale formed is adherent to the substrate in all coatings. But in case of uncoated and nanostructured coated T-22 boiler steel, the scale is found to be fragile with some cracks.

Chapter 7

SUBSTRATE SUPERFER 800H SUPERALLOY

This chapter deals with the results and discussion for the bare and coated Superfer 800H Fe-based superalloy exposed to different degradation environments. It includes the characterization of the nanostructured and conventional TiAlN and AlCrN coatings on Superfer 800H superalloy and their behavior when exposed to high temperature oxidation studies in air, molten salt ($\text{Na}_2\text{SO}_4\text{-60\%V}_2\text{O}_5$) environment and in a coal fired boiler of a thermal plant, erosion studies in simulated coal-fired boiler environment and corrosion studies in simulated marine environment.

7.1 CHARACTERISATION OF COATINGS

Little work has been published on high temperature corrosion behavior of nanostructured and conventional hard metal nitride coatings to the best of the knowledge of the author. Therefore, these coatings were developed on the Superfer 800H superalloy and their behavior was studied when exposed to high temperature oxidation in air, molten salt environment, industrial environment, high temperature solid particle erosion and simulated marine environment. In the present section the conventional thick (by plasma spraying and gas nitrided) and nanostructured thin (by physical vapor deposition process) TiAlN and AlCrN coatings developed on superalloy have been characterized.

7.1.1 Results

7.1.1.1 Visual observations

The macrographs of as-coated Superfer 800H superalloy are shown in Fig.7.1. The nanostructured thin TiAlN coating is violet grey in color and nanostructured thin AlCrN coating is light grey in color (Fig.7.1). Visual observations indicate; the surface of nanostructured coatings is smooth whereas the surface of conventional thick coatings is rough. The color of the thick coatings appeared as dark grey. Also, Optical micrographs of the nanostructured and conventional coatings are shown in Fig.7.2. The

nanostructured coatings (Fig.7.2.a and b) have uniform microstructure having some pores and inclusions. In case of conventional thick coatings (Fig.7.2.c and d); the massive microstructure can be observed with irregularly shaped grains.

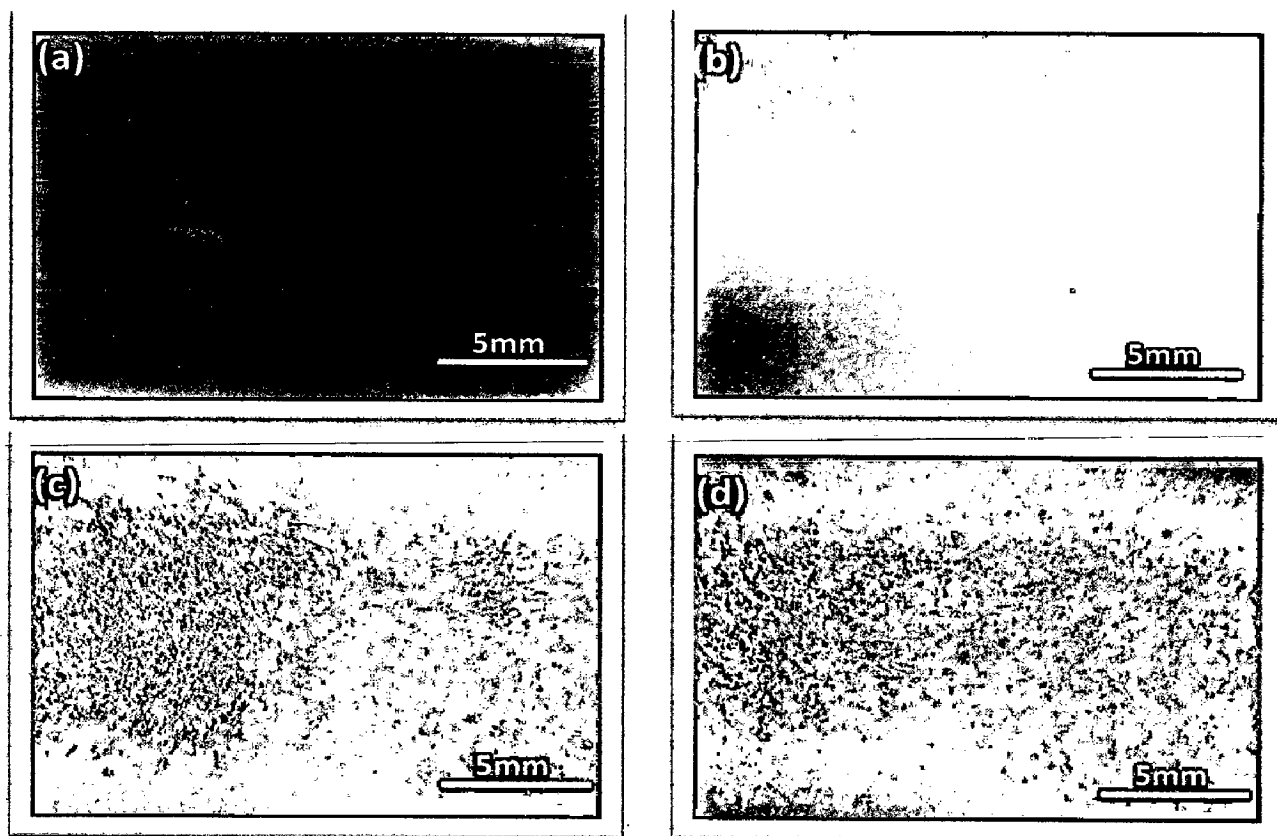


Fig. 7.1 Surface macrographs for the as coated Superfer 800H superalloy (a) Nanostructured TiAlN coating, (b) Nanostructured AlCrN coating, (c) Conventional TiAlN coating, (d) Conventional AlCrN coating

7.1.1.2 Surface analysis

7.1.1.2.1 X-ray diffraction analysis (XRD)

XRD diffractograms for nanostructured and conventional TiAlN and AlCrN coated superalloy are depicted in Fig.7.3 on reduced scale. As indicated by the diffractograms in Fig.7.3; TiN and AlN are the main phases present in the nanostructured thin TiAlN coating. Further, in case of nanostructured AlCrN coating, the prominent phases are CrN and AlN. The grain size of the nanostructured thin coatings was estimated from Scherrer formula; which is reported in Table.7.1. The calculated grain size for nanostructured thin

TiAlN and AlCrN coatings is 09 and 22 nm respectively. Further, the main phases identified for the conventional thick TiAlN coating are Al_2O_3 , TiN, Ti_3Al , AlN and small peaks of TiO_2 . The phases identified in case of conventional thick AlCrN coating are CrN, AlN, and Al_2O_3 with minor peaks of Cr_2O_3 .

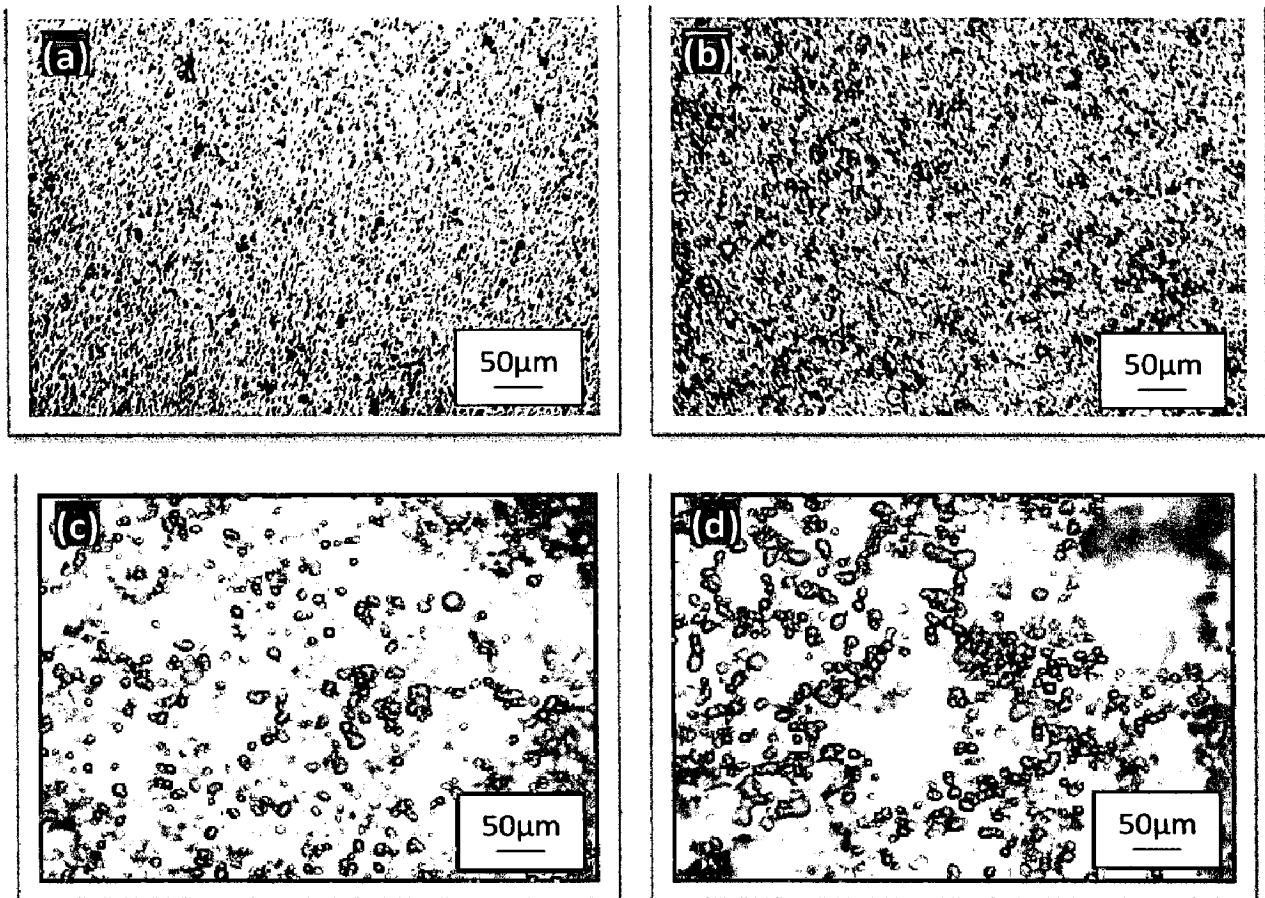


Fig. 7.2 Optical micrograph (200 X) of the surface of as coated Superfer 800H superalloy; (a) Nanostructured TiAlN coating, (b) Nanostructured AlCrN coating, (c) Conventional TiAlN coating, (d) Conventional AlCrN coating

7.1.1.2.2 Porosity analysis

The porosity analysis is of prime importance in high temperature corrosion studies. The dense coatings are supposed to provide very good corrosion resistance as compared to porous coatings. The porosity measurements were made by PMP3 inverted metallurgical microscope with stereographic imaging. The porosity of nanostructured

thin TiAlN and AlCrN coatings was found below 0.5 % (Table.7.1). In case of conventional thick coatings; the porosity of as sprayed Ti-Al (1.90-4.20 %) and Al-Cr (2.0-4.10 %) coatings was also evaluated; which is reported in Table.7.2. A considerable decrease in the porosity had been observed after gas nitriding and it was found to be less than 0.65 % (Table.7.2).

Table 7.1 Microstructural and mechanical properties of nanostructured thin TiAlN and AlCrN coated Superfer 800H superalloy

Coating	Surface Roughness (nm)	Particle Size (nm)		Coating Thickness (μm)	Porosity (% age)	Coating Color
		Scherrer Formula	AFM Analysis			
Nanostructured TiAlN Coating	02.62	09	10	6.3	< 0.35	violet-grey
Nanostructured AlCrN Coating	05.99	22	25	4.4	< 0.5	light-grey

Table 7.2 Microstructural and mechanical properties of conventional thick TiAlN and AlCrN coated Superfer 800H superalloy

Coating	Surface Roughness (μm)	Coating Thickness (μm)	Porosity (% age)		Bond Strength (MPa)	Coating Color
			As Sprayed	After Gas Nitriding		
Conventional TiAlN Coating	10.01-12.48	140	1.90-4.20	< 0.65	68.74	dark-grey
Conventional AlCrN Coating	08.93-11.11	126	2.00-4.10	< 0.60	54.69	Bluish-grey

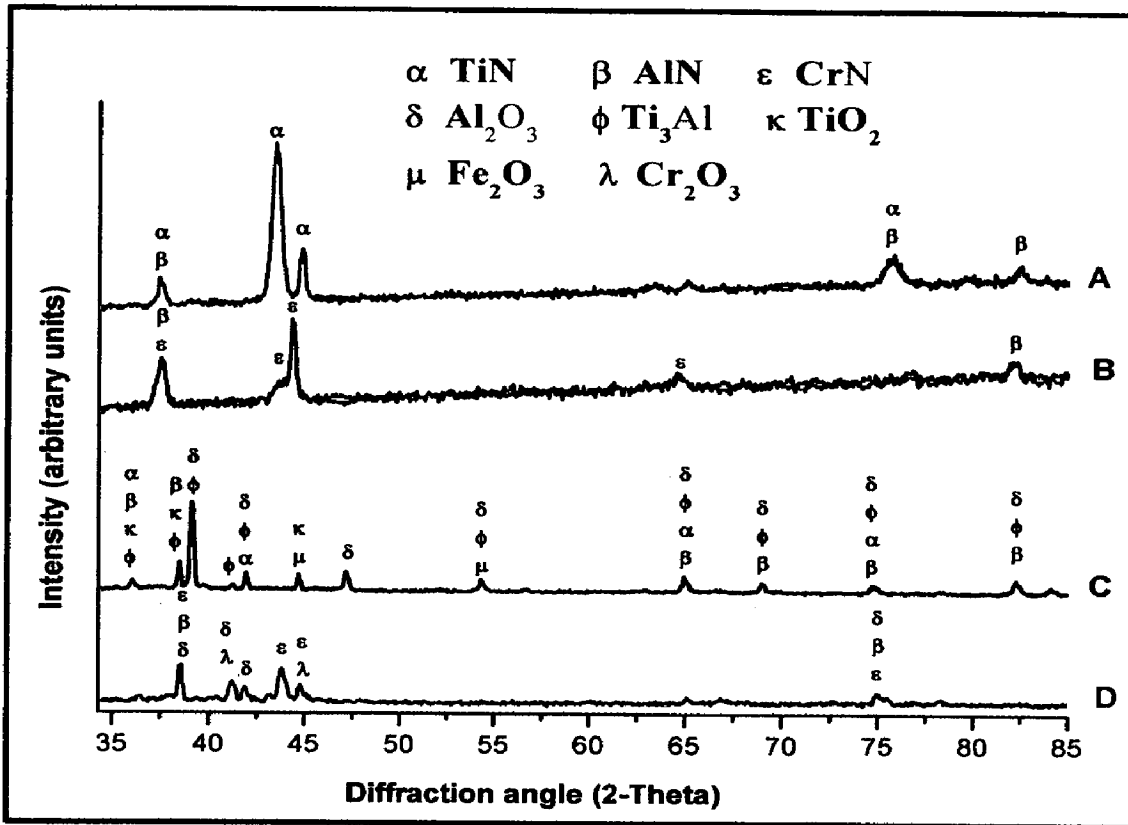


Fig. 7.3 Surface-scale morphology and EDAX patterns from different spots on as coated Superfer 800H superalloy (a) Nanostructured TiAlN coating, (b) Nanostructured AlCrN coating, (c) Conventional TiAlN coating, (d) Conventional AlCrN coating

7.1.1.2.3 AFM analysis of the as deposited nanostructured thin coatings

The surface topography of the nanostructured thin TiAlN and AlCrN coatings was studied using Atomic Force Microscope (AFM: NT-MDT: NTEGRA Model) in semi contact mode. Figure 7.4 shows the AFM surface morphology (2D and 3D) of the nanostructured thin TiAlN and AlCrN coatings deposited on superalloy. The difference in the morphology between the two coatings can be inferred by comparing the 2D images in Fig. 7.4 (a) and (c); however a clearer comparison of the coatings could be afforded by viewing 3D images in Fig. 7.4 (b) and (d). As the axis scale indicates the overall roughness of the nanostructured TiAlN coating (Fig. 7.4.b) is less than that of AlCrN coating (Fig. 7.4.d). The surface roughness and particle size in the coatings as analyzed by AFM analysis; reported in Table.7.1. The surface roughness in case of nanostructured TiAlN coating

was observed to be 5.62 nm and 5.99 nm in case of nanostructured AlCrN coating (Table.7.1). The nanostructured thin TiAlN coating had shown lesser particle size (10 nm) as compared to nanostructured thin AlCrN coating (25 nm).

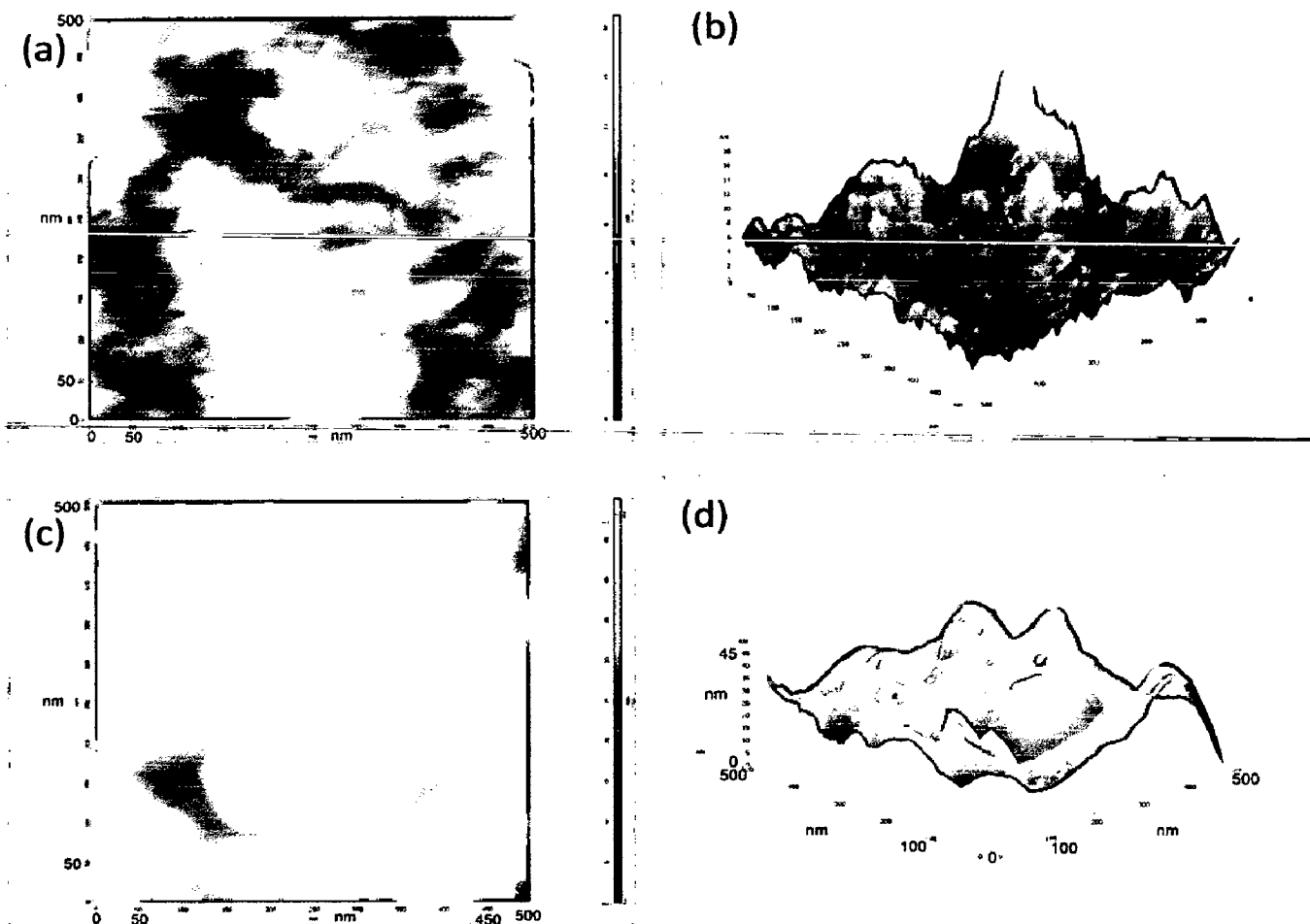


Fig. 7.4 2D and 3D AFM images for the as coated Superfer 800H superalloy (a) & (b) Nanostructured TiAlN coating, (c) & (d) Nanostructured AlCrN coating

7.1.1.2.4 Surface roughness (R_a) values of the conventional thick coatings

The coating surface was very rough in case of conventional thick TiAlN and AlCrN coatings due to the presence of melted/partially melted particles and the roughness was found to be in the range of 10.35-15.13 μm and 11.84-15.23 μm respectively. The centre line average (CLA) method was used to obtain the R_a values.

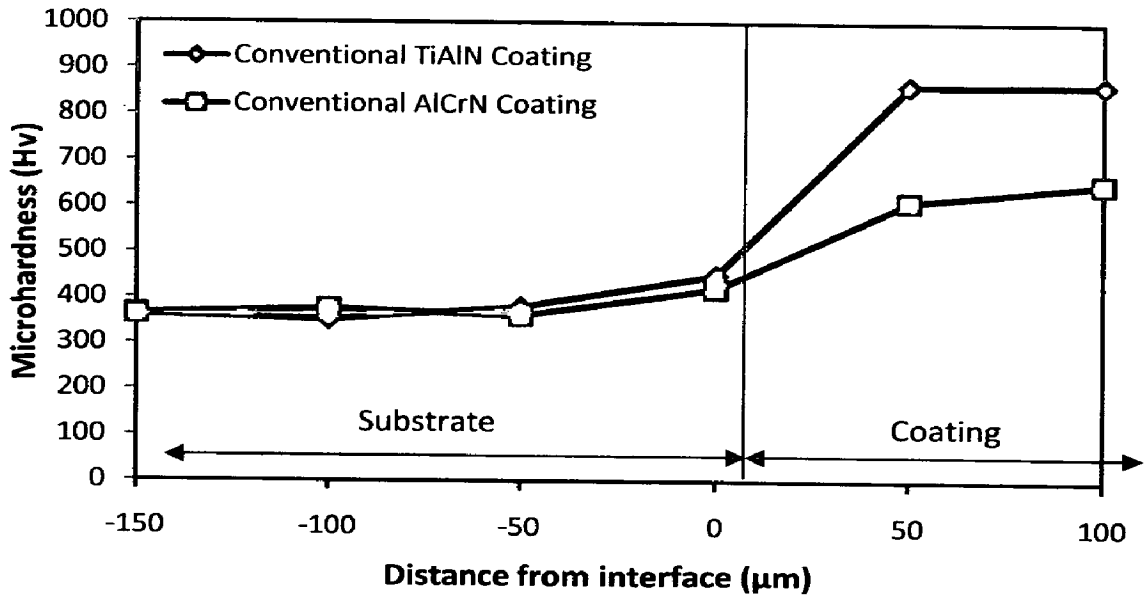


Fig. 7.5 Microhardness profile across the cross-section for Conventional TiAlN and Conventional AlCrN coating on Superfer 800H superalloy

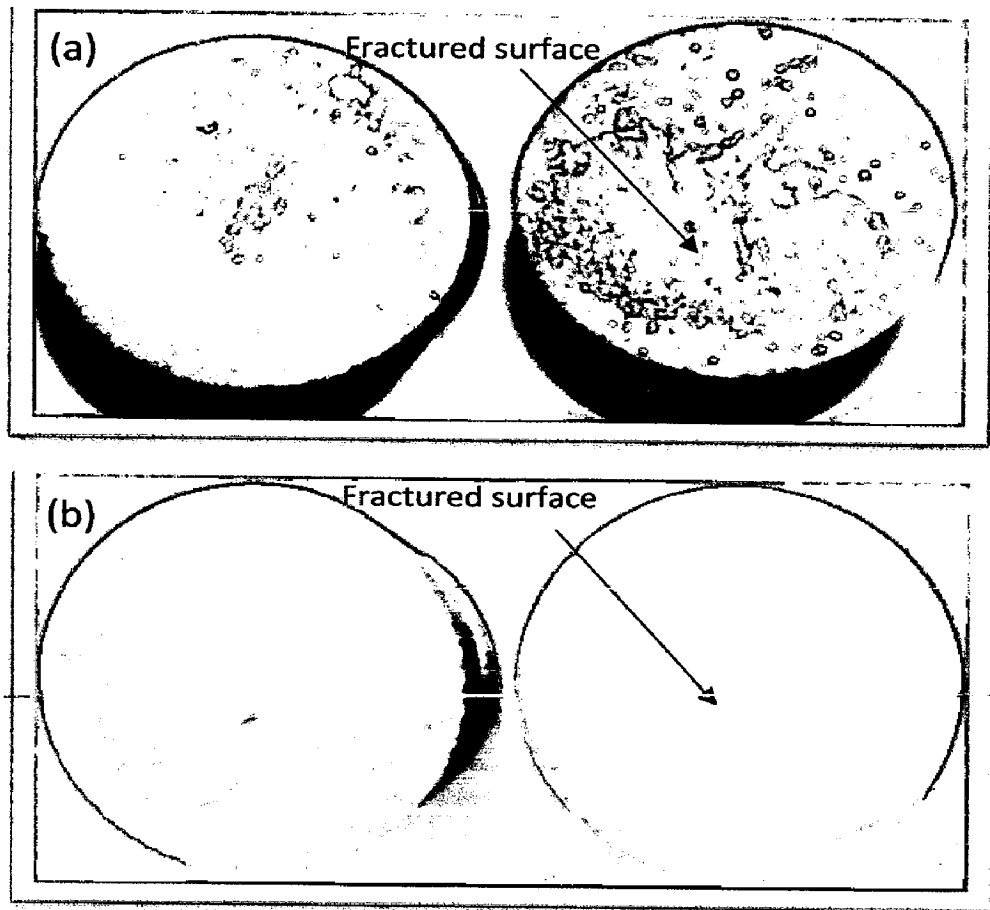


Fig. 7.6 Fractured surfaces of a Plasma sprayed gas nitrated specimens after ASTM C633 tensile test; (a) Conventional TiAlN coating, (b) Conventional AlCrN coating

7.1.1.2.5 Evaluation of microhardness and bond strength of conventional coatings

The microhardness of the coatings has been measured along the cross-section of the conventional thick TiAlN and AlCrN coated Superfer 800H superalloy. Figure 7.5 shows the microhardness profiles along the cross-section of the coatings as a function of distance from the coating-substrate interface. The critical microhardness value of the substrate Superfer 800H superalloy was found to be in the range 300-400 Hv. From the microhardness profiles (Fig.7.5) it is obvious that the conventional TiAlN coating has shown maximum microhardness of the order of 900-950 Hv. The conventional thick AlCrN coating has shown microhardness of the order of 600-650 Hv.

The bond strength of the conventional thick TiAlN and AlCrN coatings was measured on three specimens as per ASTM standard C633-01. The coatings failed at the substrate-coating interface while remaining attached to the adhesive (Fig.7.6). Average bond strength of 68.74 MPa and 54.69 MPa was observed in case of conventional TiAlN and AlCrN coatings respectively (Table.7.2).

7.1.1.2.6 Surface morphology of coatings

SEM micrographs along with EDAX point analysis reveal the surface morphology of the nanostructured and conventional TiAlN and AlCrN coated Superfer 800H superalloy; are shown in Fig.7.7. Micrograph (Fig.7.7.a) for nanostructured thin TiAlN coating at higher magnification (10000 X) indicates grey matrix with some black and white contrast regions. Dense structure with lower porosity is observed in the coating microstructure and also it is free from cracks. EDAX analysis at point 1 and point 2 on Fig.7.7 indicates the presence of Ti, Al and N with negligible amount of O and Fe. The black colored areas revealed the higher amount of Ti and less concentration of Al as compared to the white contrast region. In case of nanostructured thin AlCrN coated superalloy; the SEM micrograph indicates dense grey colored coating with tiny dark grey particles dispersed in the matrix. EDAX point analysis (Point 3 and 4) shows, the coating is rich in Al, Cr and N along with small amount of Fe and oxygen (Fig.7.7.b). The micrographs in case of conventional plasma sprayed gas nitride TiAlN and AlCrN coatings are shown in Fig.7.7 (c and d). In general microscopic features indicate that the conventional coatings are homogeneous and massive, free from cracks.

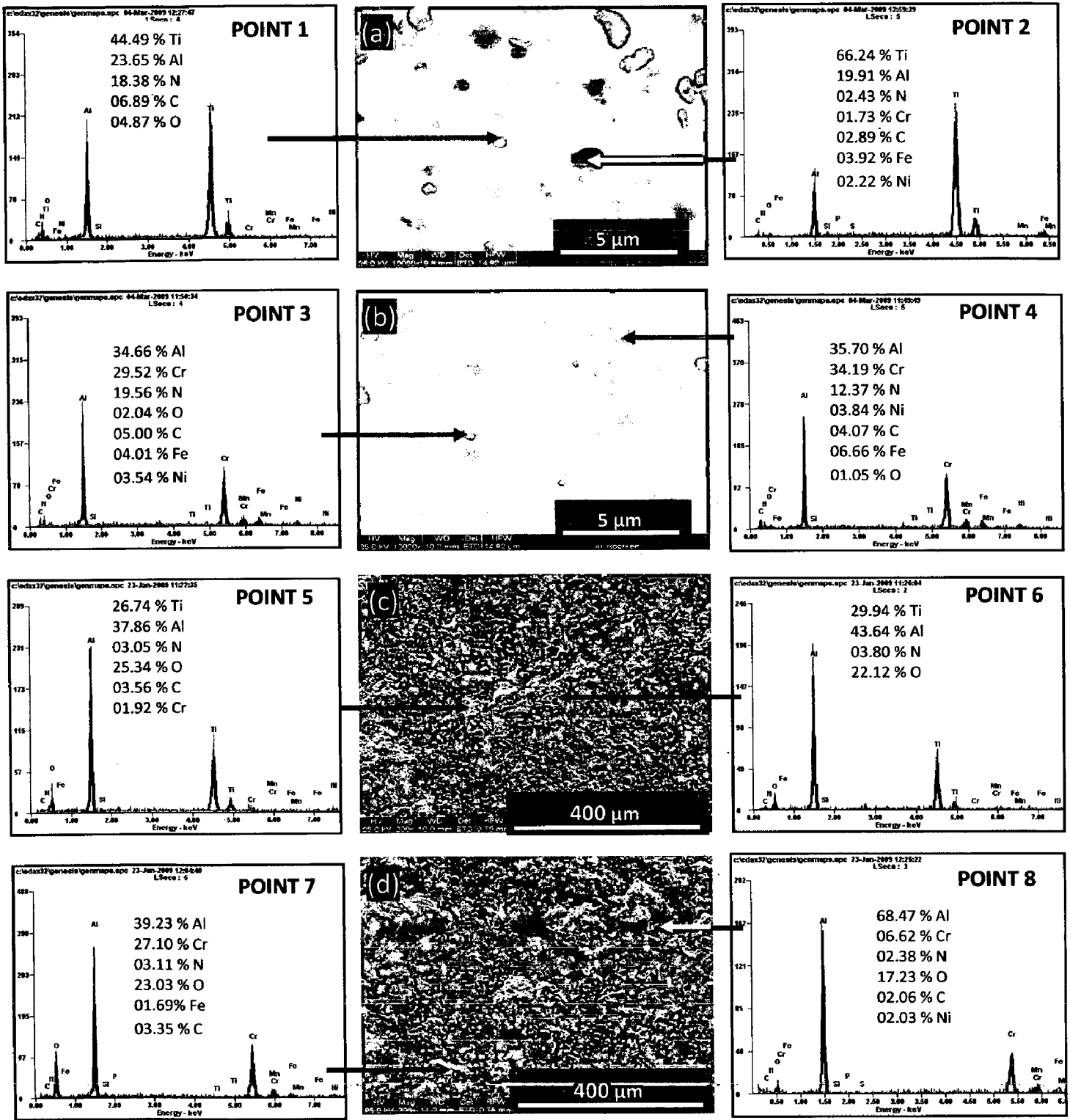


Fig. 7.7 Surface-scale morphology and EDAX patterns from different spots on as coated Superfer 800H superalloy (a) Nanostructured TiAlN coating, (b) Nanostructured AlCrN coating, (c) Conventional TiAlN coating, (d) Conventional AlCrN coating

The EDAX point analysis (Point 5 and 6 in Fig.7.7); in case of conventional TiAlN coating indicates the higher concentration of Ti and Al in the coating along with N and oxygen. The presence of Al and Cr along with N and oxygen revealed by EDAX analysis in case of conventional AlCrN coating (Fig.7.7.d); the white contrast region (Point 7) shows higher concentration of Cr as compared to the dark region (Point 8).

7.1.1.3 Cross-sectional analysis

7.1.1.3.1 Coating thickness

The as-coated samples were cut across the cross section using Buehler Isomet 1000 precision saw and mounted in transoptic mounting resin and subsequently mirror polished to obtain scanning electron back scattered micrographs and X-ray mapping of different elements for coated and uncoated Superfer 800H superalloy. The coating thickness values were measured from SEM back scattered micrographs as shown in Fig.7.8 and average coating thickness is reported in Table.7.2. The measured average coating thickness values for nanostructured thin and conventional thick TiAlN and AlCrN coatings are 6.3, 4.4, 140 and 126 μm respectively.

7.1.1.3.2 X-Ray mapping

BSEI and X-ray mapping analysis for nanostructured and conventional TiAlN and AlCrN coated superalloy is shown in Fig.7.8. In case of nanostructured TiAlN coating (Fig.7.8.a); the X-ray mapping indicates presence of Al and Ti along with small amount of N in the coating. In case of nanostructured thin AlCrN coated superalloy; the X-ray mapping indicates the presence of Al and Cr along with some concentration of N in the coating (Fig.7.8.b). In case of conventional thick TiAlN coated superalloy, Fig.7.8 (c); Al and Ti rich coating along with negligible amount of N and O; has been observed. The splats in the coatings are visible. Figure.7.8 (e) depicts the BSEI and X-ray mapping in case of conventional AlCrN coated Superfer 800H superalloy. The coating is rich in Al and Cr with negligible presence of N and O. The X-ray mapping analysis indicates the presence of Fe in coating only for conventional AlCrN coated superalloy and for all the other coatings no sign of diffusion of substrate elements to the coating was observed.

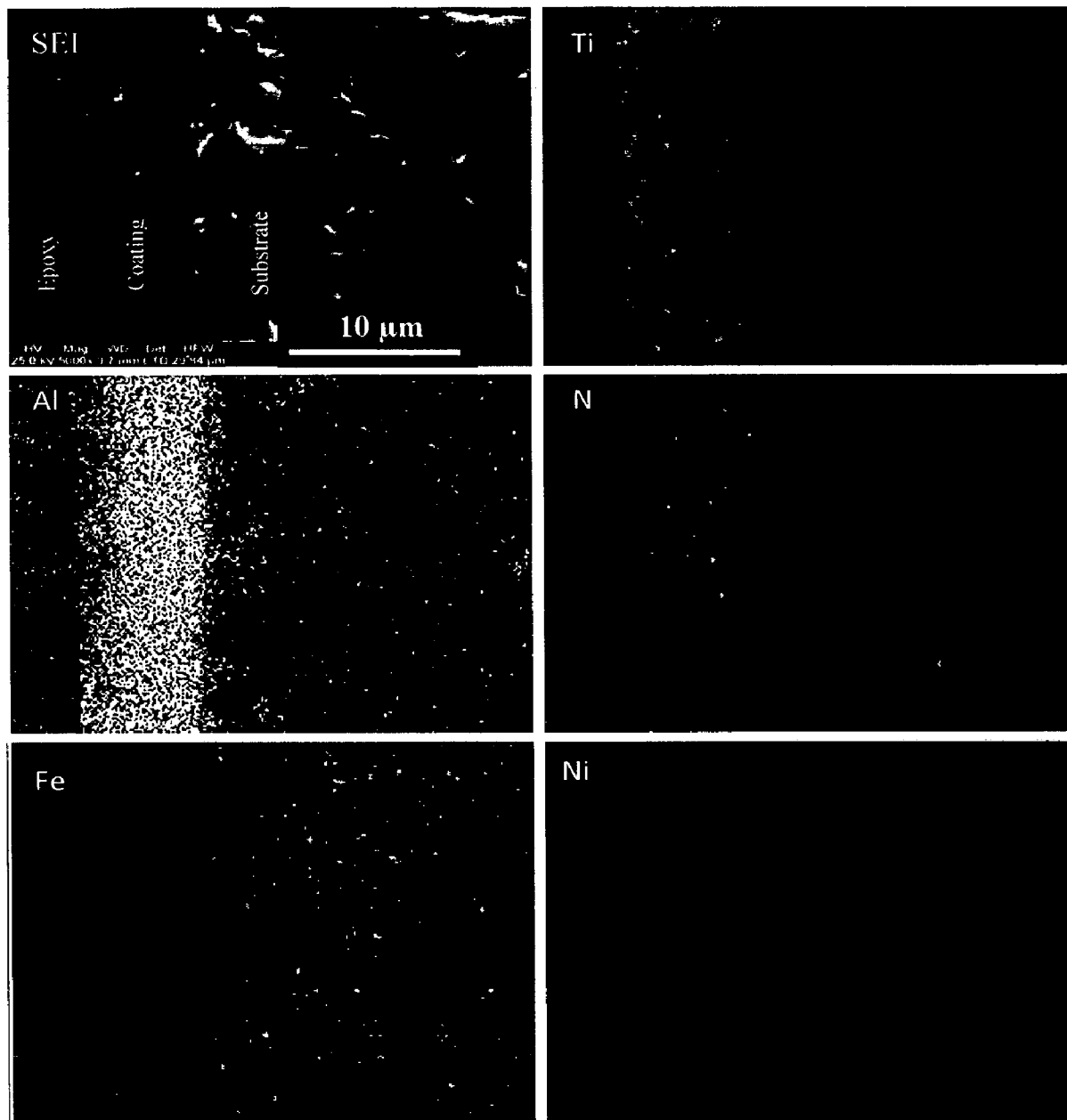


Fig. 7.8 (a) Composition image (SEI) and X-ray mapping of the cross-section of as-coated nanostructured TiAlN coating on Superfer800H superalloy

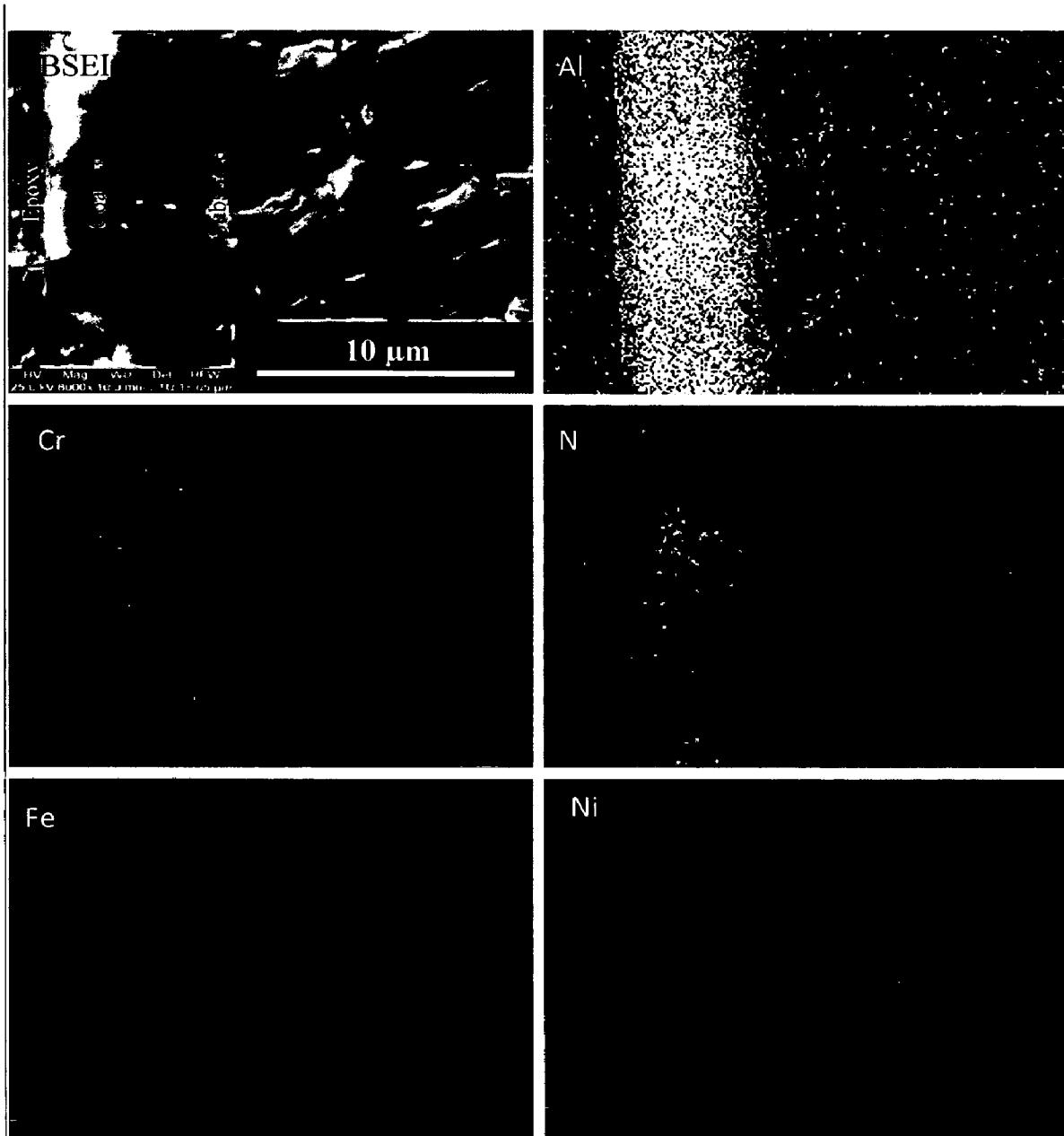


Fig. 7.8 (b) Composition image (BSEI) and X-ray mapping of the cross-section of as-coated nanostructured AlCrN coating on Superfer800H superalloy

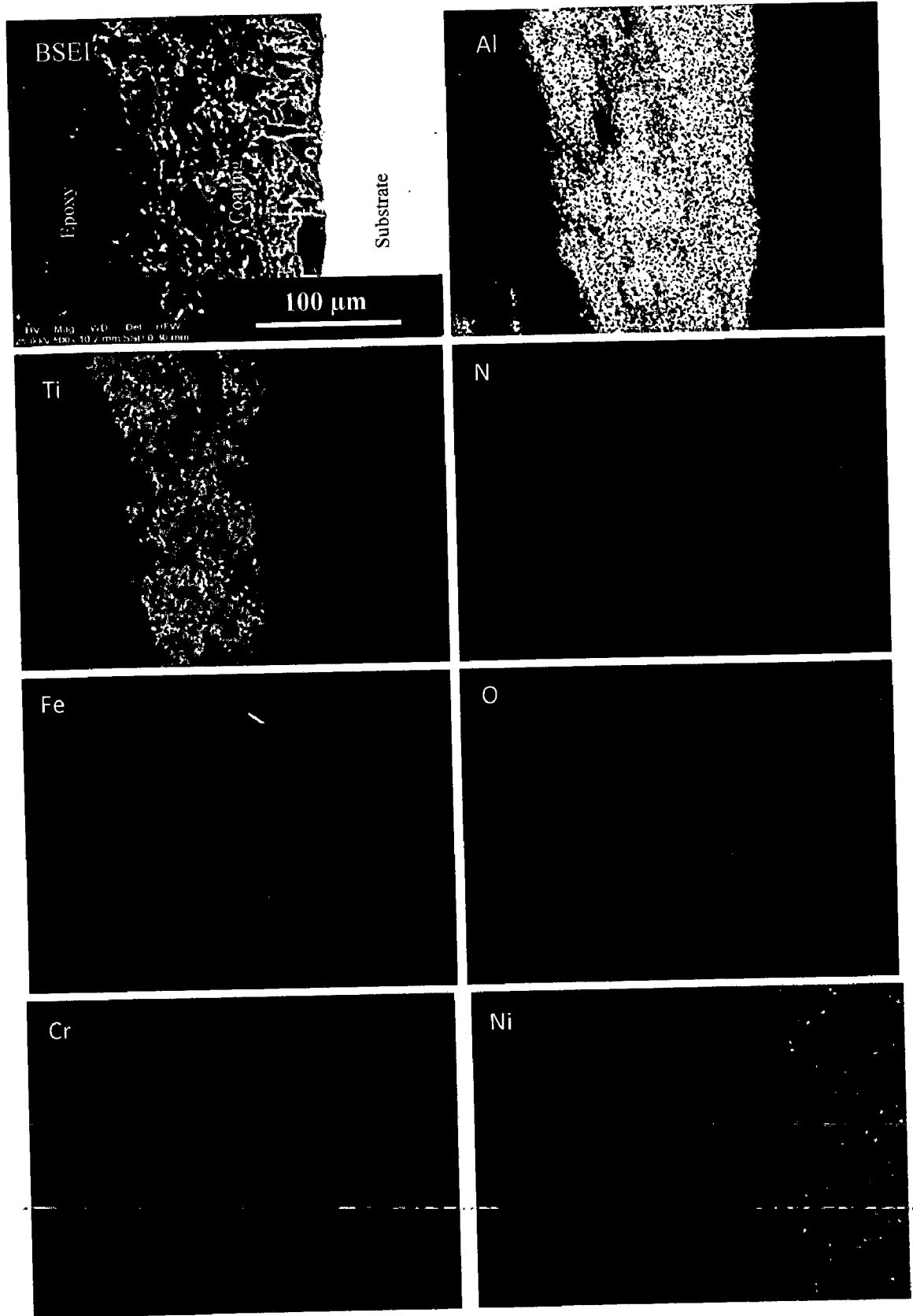


Fig. 7.8 (c) Composition image (BSEI) and X-ray mapping of the cross-section of as-coated conventional TiAlN coating on Superfer800H superalloy

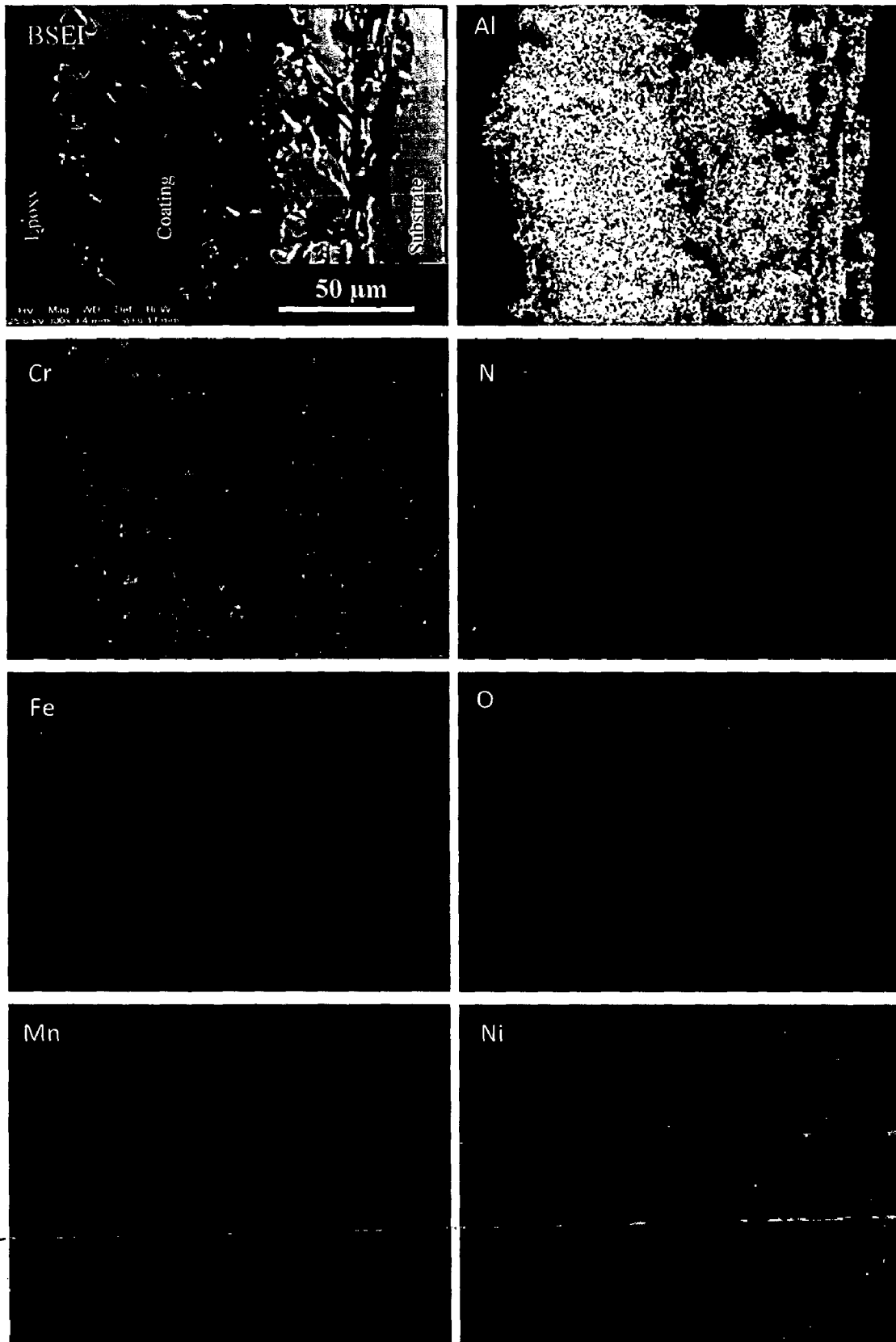


Fig. 7.8 (d) Composition image (BSEI) and X-ray mapping of the cross-section of as-coated conventional AlCrN coating on Superfer800H superalloy

7.1.2 Discussion

The nanostructured thin TiAlN and AlCrN coatings on Superfer800H superalloy were obtained using a front-loading Balzer's rapid coating system (RCS) machine at Oerlikon Balzers Ltd. Gurgaon (India). In case of conventional thick TiAlN and AlCrN coatings; the plasma spray coatings were obtained at Anod Plasma Ltd. Kanpur (India) using a 40 kW Miller Thermal Plasma Spray apparatus. The compositions of the targets used and the summary of the process parameters are presented in detail in chapter 3. The coating thickness was measured along the cross-section for some of the randomly selected samples and reported in Table 7.1 and 7.2. The coatings thickness was observed to be 6.3 and 4.4 μm in case of nanostructured TiAlN and AlCrN coatings respectively. The self-disintegration of thicker coatings usually restricts the thickness of the coatings (Sidhu et al., 2004). In case of conventional thick coatings; it was possible to obtain a thickness in range of 150-200 μm for Ti-Al and Al-Cr coatings. After coating deposition process; the gas nitriding was done in lab in order to obtain hard metal nitride coatings. The coating thickness was measured along the cross-section for some randomly selected samples and reported in Table 4.2. The coatings thickness was observed as 140 and 126 μm in case of conventional thick TiAlN and AlCrN coatings respectively.

The surface appearance of nanostructured TiAlN coating was violet grey in color and light grey in case of nanostructured AlCrN coating (Fig.7.1). In case of conventional thick coatings: the surface appearance of conventional TiAlN and AlCrN coatings was grey with some bluish shining (Fig.7.1). The surface of conventional thick coatings was rough. As inferred from optical micrographs (Fig.7.2 a & b) that the nanostructured coatings were dense with uniform microstructure. It is evident from the microstructure that the coatings contain some pores and inclusions. In case of conventional thick coatings (Fig.7.2.c & d); the massive microstructure could be observed with irregularly shaped grains.

The bond strength of the conventional thick TiAlN and AlCrN coatings was measured on three specimens as per ASTM standard C633-01. The coatings failed at the substrate-coating interface while remaining attached to the adhesive (Fig.7.6). Average bond strength of 68.74 MPa and 54.69 MPa was observed in case of conventional TiAlN and AlCrN coatings respectively. The bond strength in case of conventional TiAlN

coatings (68.74 MPa) is almost in good agreement with the results reported by Adachi and Nakata (2007).

The negligible porosity values for as coated nanostructured thin TiAlN and AlCrN coatings were observed; which were less than 0.5 % (Table 7.1). The measured porosity values of plasma sprayed and gas nitrided coatings are reported in Table 4.2. The measured values of porosity (1.90-4.10%) for as sprayed conventional Ti-Al and Al-Cr coatings are almost in close agreement with the findings of Chen et al. (1993), Erickson et al. (1998), Hidalgo et al. (1998 and 1999), Singh (2003) and Sidhu et al. (2004 and 2005) for thermal plasma sprayed coatings. Further, the porosity values found to be less than 0.6% after gas nitriding, which may be because of elimination of microstructural in-homogeneities by filling of pores and voids by nitrogen during gas nitriding.

The grain size (Table.7.1) of the nanostructured thin coatings was estimated from Scherrer formula. The calculated grain size for nanostructured thin TiAlN and AlCrN coatings was 09 and 22 nm respectively. The grain size in case of nanostructured coatings was further verified by AFM analysis and reported in Table 7.1. The particle size determined by AFM analysis is in good agreement with the results obtained from Scherrer formula.

The surface roughness was also measured with AFM analysis and reported in Table 7.1. As the axis scale indicates the overall roughness of the nanostructured TiAlN coating (Fig. 7.4.b) is less than that of AlCrN coating (Fig. 7.4.d). The surface roughness in case of nanostructured TiAlN coating was observed 2.62 nm and 5.99 nm in case of nanostructured AlCrN coating (Table.7.1). The coating surface was very rough in case of conventional thick TiAlN and AlCrN coatings due to the presence of unmelted/partially melted particles and the roughness was found to be in the range of 10.01-12.48 μm and 08.93-11.11 μm respectively.

The phases identified by XRD analysis (Fig.7.3) for nanostructured thin TiAlN coating are TiN and AlN. The phases analyzed are also in agreement with that reported by Yoo et al. (2008), Falub et al. (2007) and Man et al. (2004). The prominent phases in case of nanostructured AlCrN coating are CrN and AlN which are in agreement with the findings of Reiter et al. (2005) and Endrino et al. (2006). Further, the main phases identified for the conventional thick TiAlN coating are Al_2O_3 , TiN, Ti_3Al , AlN and small peaks of TiO_2 and Fe_2O_3 . The phases identified in case of conventional thick AlCrN coating are CrN,

AlN, and Al₂O₃ with minor peaks of Cr₂O₃. The presence of metal nitride phases indicates that the gas nitriding process has successfully produced the desired coatings. Further, the phases analyzed are also in agreement with that reported by Adachi and Nakata (2007).

Surface EDAX analysis supported the results obtained by XRD (Fig.7.3) and X-ray mapping analysis (Fig.7.8) in all the coatings. The XRD analysis indicates the presence of the oxide phases in the coatings i.e. Al₂O₃ and TiO₂ in case of conventional TiAlN coating and the presence of Al₂O₃ and Cr₂O₃ in case of conventional AlCrN coatings. The oxides may form due to the in-flight oxidation during spraying process and/or preexisting in the feed material (Bluni and Mardar, 1996). The latter reason for the oxides formation in the structure of coatings under study looks to be more relevant as the chances of in-flight oxidation are meager in case of the shrouded plasma spraying. Deshpande et al. (2006) proposed that, during in-flight oxidation, a layer of oxide is formed on the molten particle due to chemical reactions between the surface of the liquid phase and oxygen or due to diffusion of oxygen into the liquid. The turbulent mixing of the liquid part of the powder particle during its flight destroys the surface layer of oxides and causes the oxides to be distributed more uniformly through the bulk volume of the particle. However, when temperature of the particle starts dropping during later part of the flight, these oxides tend to solidify and a thin oxide shell would form around the droplet. The oxidation time during thermal spray coating is short typically less than 0.01 s, and can occur in either the solid or molten state. The oxidation of coatings is not always harmful, it is equally important to control and understand the different aspects of oxidation of coatings; therefore, it is important to find an optimum level for oxidation of coatings (Herman, 1988; Korpiola and Vuoristo, 1996; Nerz et al., 1992).

Hardness is the most frequently quoted mechanical property of the coatings (Tucker, 1994). The observed microhardness values (Fig.7.5) for the conventional coatings are within the range of microhardness values reported for plasma coatings by Adachi and Nakata (2007), Vuoristo et al. (1994), Chen and Hutchings (1998) and Westergard et al. (1998). Microhardness plots indicate some increase in the microhardness of substrate steel at the substrate coating interface. The hardening of the substrates as observed in the current study might have occurred due to the high speed impact of the coating particles during plasma spray deposition similar to the findings of Singh (2003), Hidalgo et al. (1997, 1998, 1999 and 2000) and Sidhu et al. (2004 and 2005). The observed

non-uniformity in the hardness values along the thickness of the coatings may be due to the microstructural changes along the cross section of the coatings (Staia et al., 2001). Moreover, the microhardness and other properties of the thermal spray coatings are anisotropic because of typical splat structure and directional solidification (Tucker, 1994).

7.1.3 Conclusions

The nanostructured thin TiAlN and AlCrN coatings (by physical vapour deposition process) and conventional thick TiAlN and AlCrN coatings (by plasma spraying followed by gas nitriding process) were successfully deposited on Superfer800H superalloy. The coatings were characterized for microstructural features and hardness in present work. The following observations were made based on the present study:

1. The nanostructured thin TiAlN and AlCrN coatings exhibited negligible porosity values for as coated; which were less than 0.5 %. The conventional TiAlN and AlCrN coatings showed; higher porosity values (1.90-4.20%) for as sprayed conventional Ti-Al and Al-Cr coatings which after gas nitriding were found to be less than 0.65 %.
2. The phases identified by XRD analysis for nanostructured thin TiAlN coating are TiN and AlN. Further, in case of nanostructured AlCrN coating, the prominent phases are CrN and AlN. The phases identified by XRD analysis in case of conventional thick AlCrN coating were CrN, AlN, and Al₂O₃ with minor peaks of Cr₂O₃.
3. The grain size (calculated by Scherrer formula from XRD plot) for nanostructured thin TiAlN and AlCrN coatings was 09 and 22 nm respectively. The particle size determined by AFM analysis is in good agreement with the results obtained from Scherrer formula.
4. The surface roughness in case of nanostructured TiAlN coating was observed 2.62 nm and 5.99 nm in case of nanostructured AlCrN coating. The coating surface was very rough in case of conventional thick TiAlN and AlCrN coatings.
5. Average bond strength of 68.74 MPa and 54.69 MPa Psi was observed in case of conventional TiAlN and AlCrN coatings respectively.

7.2 OXIDATION STUDIES IN AIR

The present work has been focused to compare the cyclic oxidation behavior of conventional thick (by plasma spraying and gas nitrided) and nanostructured thin (by physical vapor deposition process) TiAlN and AlCrN coatings on Superfer 800H superalloy in air environment at 900°C for 50 cycles. The kinetics of the cyclic oxidation of coated as well as uncoated specimens was determined using the weight change studies. After the oxidation studies, the exposed specimens were analyzed by XRD, SEM-EDAX analysis and elemental X-ray mapping. The detailed experimental procedure is explained in chapter 3.

7.2.1 Results

7.2.1.1 Visual observations

The macrographs for uncoated and coated Superfer800H (Fe-based superalloy) subjected to cyclic oxidation in air at 900°C for 50 cycles, are shown in Fig.7.9. For the uncoated superalloy, a dark grey colored scale appeared on the surface right from the 1st cycle, which turned to blackish green colored surface along with a light grey spot at the end of 50th cycle (Fig.7.9.a). The fragile porous corrosion products (NiO and Cr₂O₃) were formed on the surface for initial few cycles, there after sticky (adherent) oxide scale formed which lasted up to 50 cycles.

Color of the oxide scale at the end of the study was observed to be blackish green with some light grey areas on the surface, in case of nanostructured thin TiAlN coated Superfer800H superalloy (Fig.7.9.b). Golden shining on the surface with brown and white layer was seen after 1st cycle. The scale remains intact with the substrate and no spalling was observed. The oxide scale of nanostructured thin AlCrN coated Superfer800H superalloy showed no spalling and remained intact with the substrate. After 1st cycle, golden color shining was observed which turned to blackish green color along with light grey area at the end of 50th cycle (Fig.7.9.c).

A visual observation of conventional thick TiAlN coated Superfer800H superalloy (Fig.7.9.d), showed the formation of very light brownish grey color matrix with cream color spots after cyclic oxidation studies. Some amount of superficial spalling was noticed at the end of 3rd cycle, which may be due to the loosely bond particles on the

surface of the coating. In case of conventional thick AlCrN coated Superfer800H superalloy, the scale showed no signs of spalling and cracks. After 3rd cycle, light bluish grey color was seen which turns to whitish grey colored surface along with a light brown side layer. The scale remains intact with the substrate throughout the study.

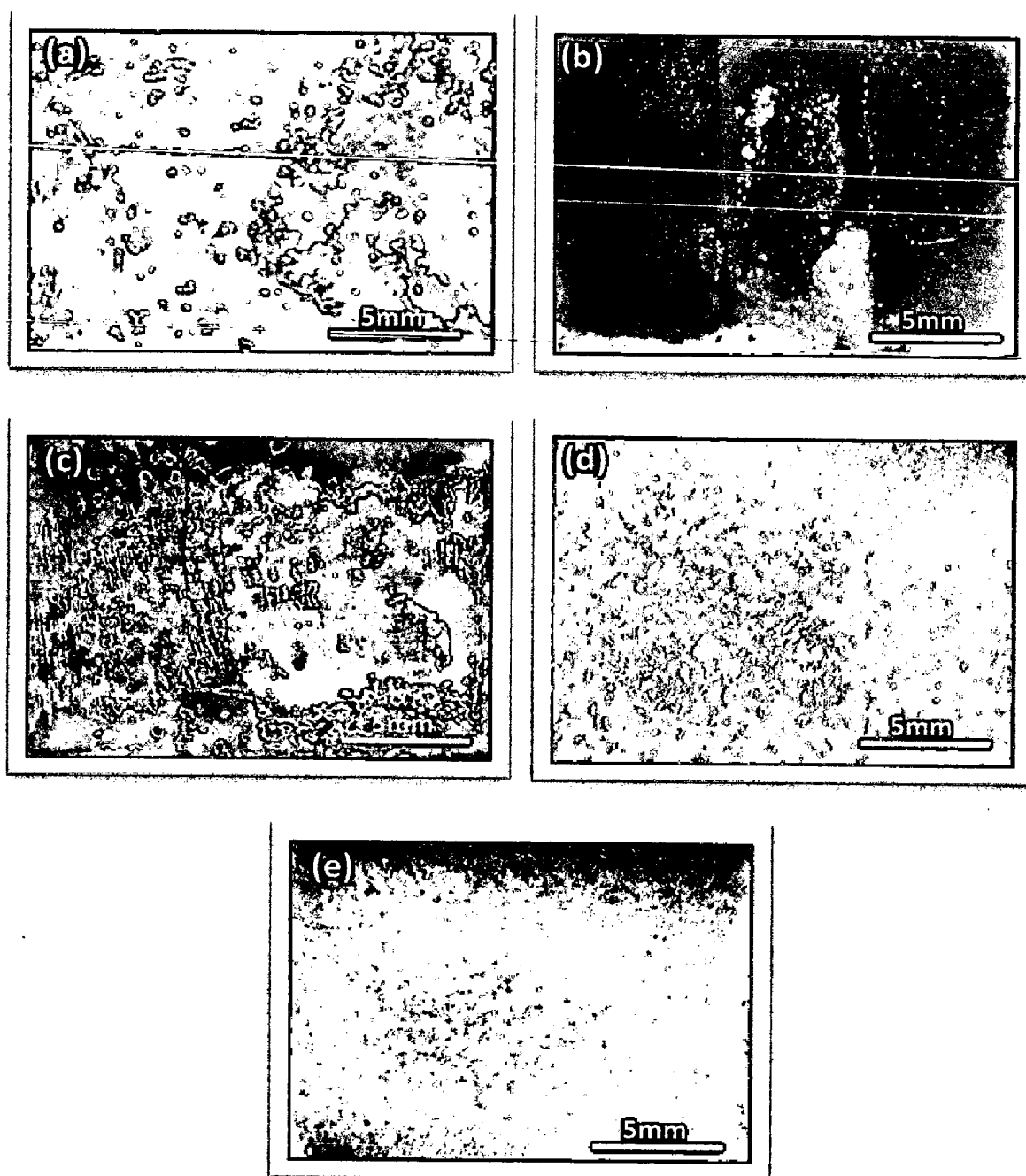


Fig. 7.9 Surface macrographs of uncoated and coated Superfer 800H superalloy after exposure to cyclic oxidation in air at 900°C for 50 cycles: (a) Uncoated Superfer 800H superalloy, (b) Nanostructured TiAlN coating, (c) Nanostructured AlCrN coating, (d) Conventional TiAlN coating, (e) Conventional AlCrN coating

7.2.1.2 Weight change measurements

Weight gain per unit area (mg/cm^2) versus time expressed in number of cycles plot for coated and bare Superfer800H superalloy subjected to cyclic oxidation in air at 900°C for 50 cycles, is presented in Fig. 7.10. The plots for all the samples show higher weight gain at initial cycles followed by gradual weight gain.

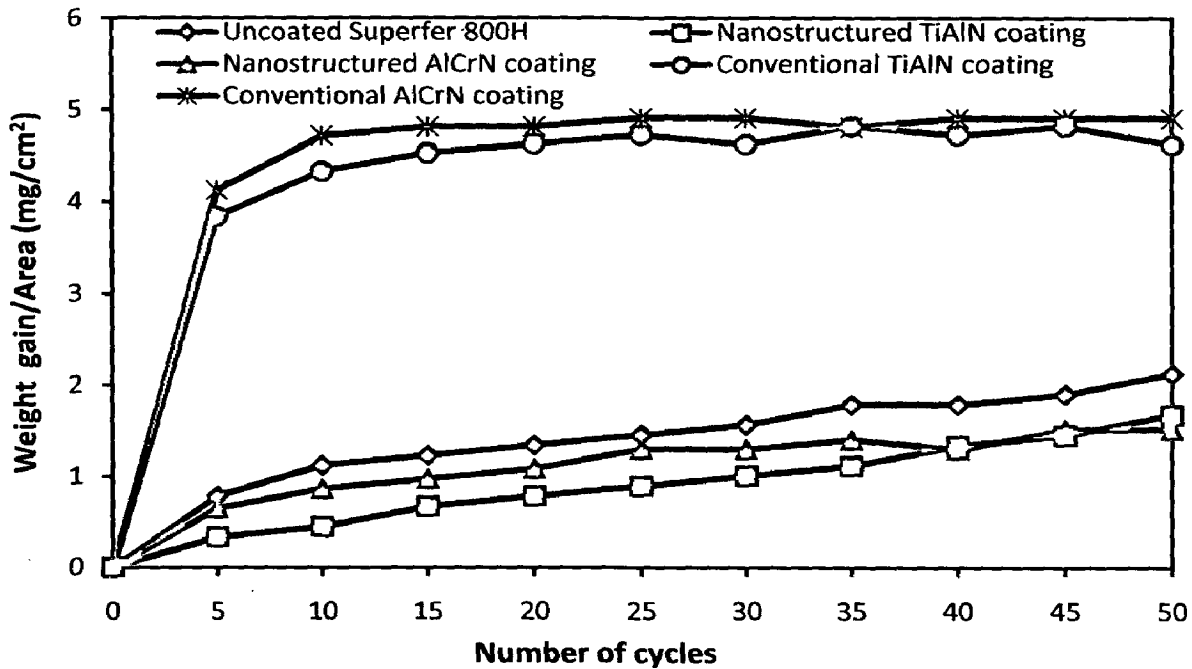


Fig. 7.10 Weight gain/area vs time (number of cycles) for the uncoated and coated Superfer 800H superalloy subjected to cyclic oxidation in air at 900°C for 50 cycles

The weight gain for conventional coatings is found to be slightly greater than that of the uncoated and nanostructured thin coated superalloy. All the coated and uncoated specimens have shown Initial rapid oxidation rate and weight gain have shown tendency to reach to steady state with the progress of exposure time with some minor deviations. The cumulative weight gain per unit area for the coated and uncoated Superfer800H superalloy subjected to cyclic oxidation in air at 900°C for 50 cycles is shown in Fig. 7.11. Further, the overall weight gain is highest in case of conventional AlCrN coating and is lowest in case of nanostructured AlCrN coating. In Fig. 7.12, the $(\text{weight gain}/\text{area})^2$ versus number of cycles plot are shown for all the cases to ascertain conformance with the parabolic rate law.

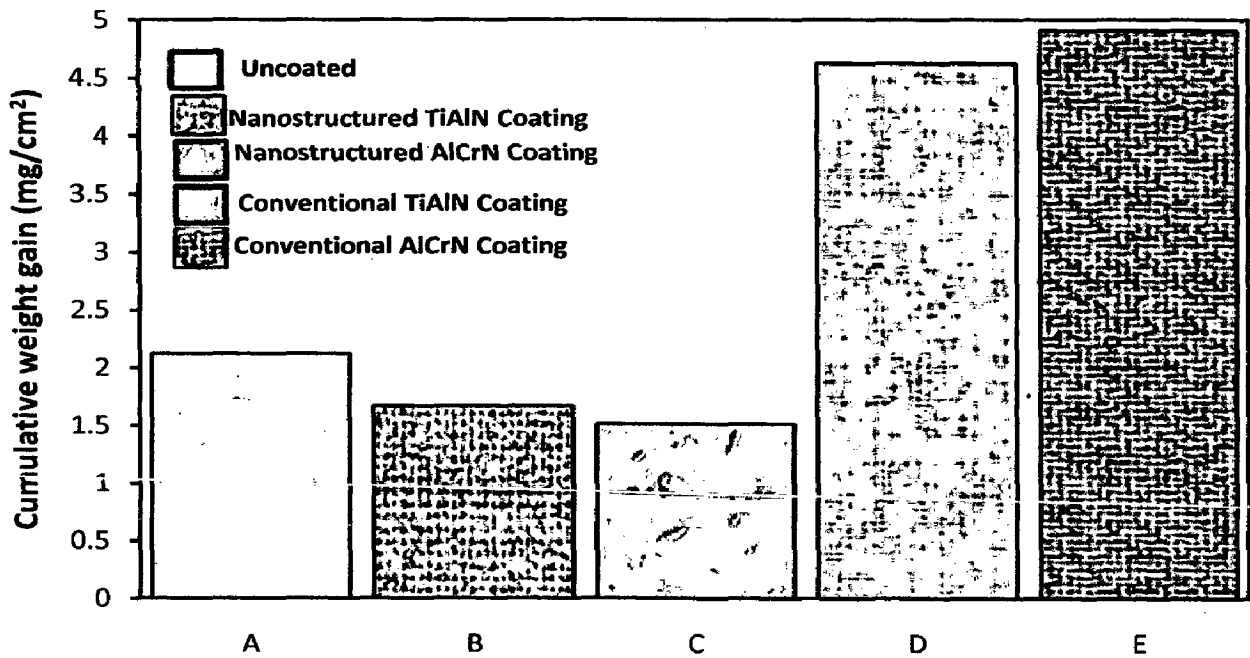


Fig. 7.11 Column chart showing cumulative weight gain per unit area for the uncoated and coated Superfer 800H superalloy subjected to cyclic oxidation in air at 900°C for 50 cycles: (A) Uncoated Superfer 800H superalloy, (B) Nanostructured TiAlN coating, (C) Nanostructured AlCrN coating, (D) Conventional TiAlN coating, (E) Conventional AlCrN coating

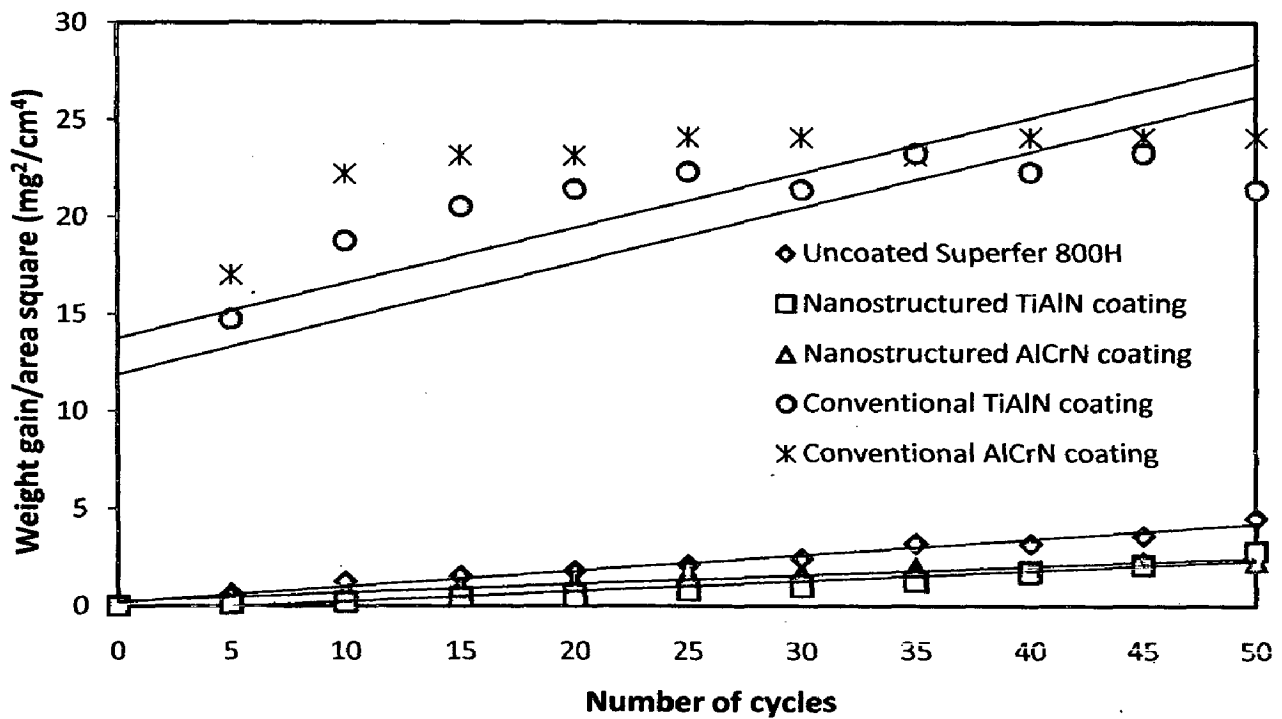


Fig. 7.12 Weight gain/area square vs time (number of cycles) for the uncoated and coated Superfer 800H superalloy subjected to cyclic oxidation in air at 900°C for 50 cycles

All the coated and uncoated Superfer800H superalloy followed the parabolic rate law as evident from the Fig.7.12. The parabolic rate constant K_p was calculated by a linear least-square algorithm to a function in the form of $(W/A)^2 = K_p t$, where W/A is the weight gain per unit surface area (mg/cm^2) and 't' indicates the number of cycles representing the time of exposure. The parabolic rate constants for the bare and coated Superfer 800H superalloy calculated on the basis of 50 cycle's exposure data are shown in Table.7.3.

Table 7.3 Parabolic rate constant ' K_p ' values of uncoated and coated Superfer800H superalloy subjected to cyclic oxidation in air at 900°C for 50 cycles

Boiler steel substrate	$K_p \times 10^{-12} \text{ gm}^2 \text{ cm}^{-4} \text{ s}^{-1}$
Uncoated Superfer800H superalloy	22.00
Nanostructured TiAlN coating	14.40
Nanostructured AlCrN coating	12.20
Conventional TiAlN coating	79.42
Conventional AlCrN coating	78.25

7.2.1.3 Surface scale analysis

7.2.1.3.1 X-ray diffraction analysis (XRD)

XRD diffractograms for coated and uncoated Superfer800H superalloy subjected to cyclic oxidation in air at 900°C for 50 cycles are depicted in Fig.7.13 (a and b) on reduced scale. As indicated by the diffractograms, in case of uncoated superfer800H superalloy the oxide phases found are Fe_2O_3 , Cr_2O_3 , NiO, NiCr_2O_4 and NiFe_2O_4 . The formation of Fe_2O_3 , Cr_2O_3 , NiO, TiO_2 and Al_2O_3 has been indicated in the scale of nanostructured thin TiAlN coated superfer800H superalloy. Fe_2O_3 , Cr_2O_3 and NiO are found to be present in the scale of nanostructured AlCrN coating. Further, the main phases identified for the conventional thick TiAlN coating are Al_2O_3 , Ti_2O_3 and NiO. The oxide phases found in case of conventional thick AlCrN coating are Al_2O_3 along with NiO.

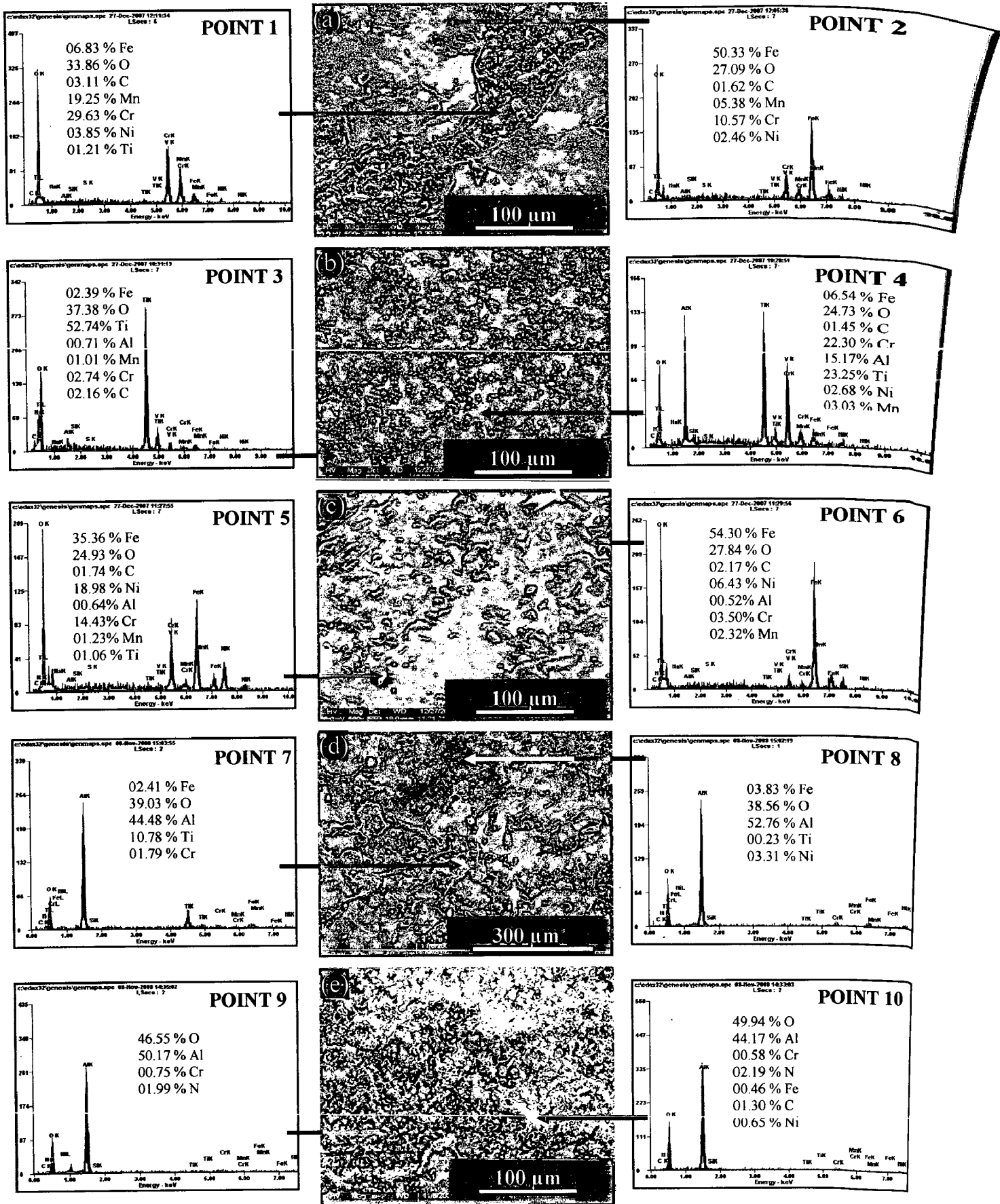


Fig. 7.14 Surface-scale morphology and EDAX patterns from different spots on uncoated and coated Superfer 800H superalloy after exposure to cyclic oxidation in air at 900°C for 50 cycles : (a) Uncoated Superfer 800H superalloy, (b) Nanostructured TiAlN coating, (c) Nanostructured AlCrN coating, (d) Conventional TiAlN coating, (e) Conventional AlCrN coating

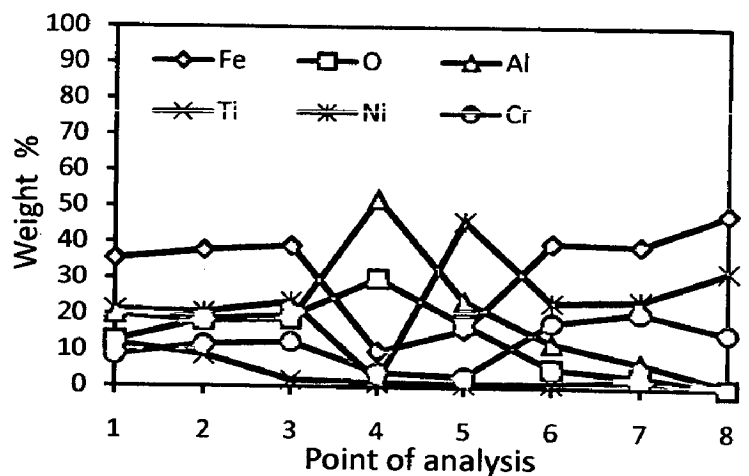
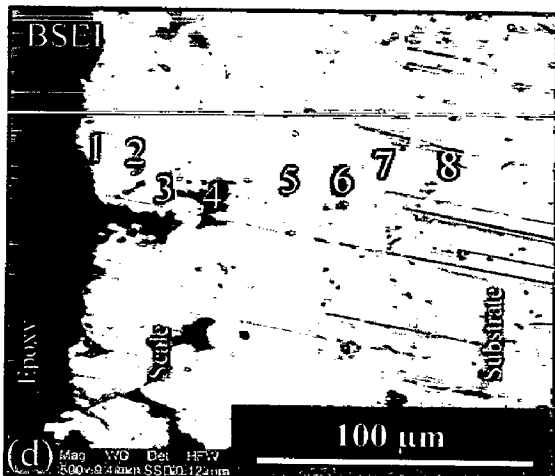
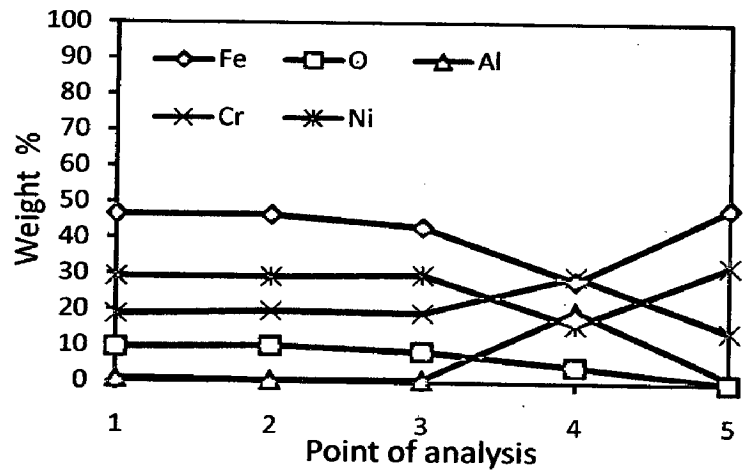
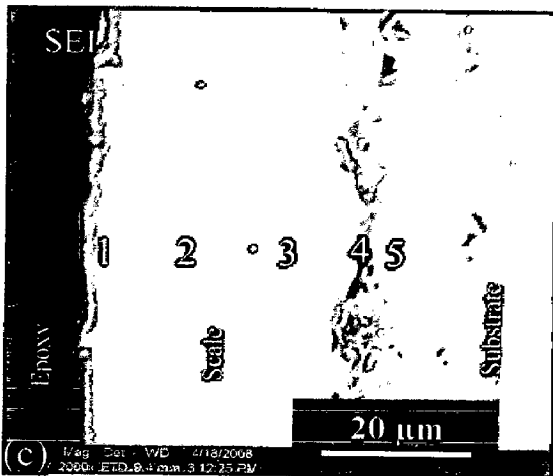
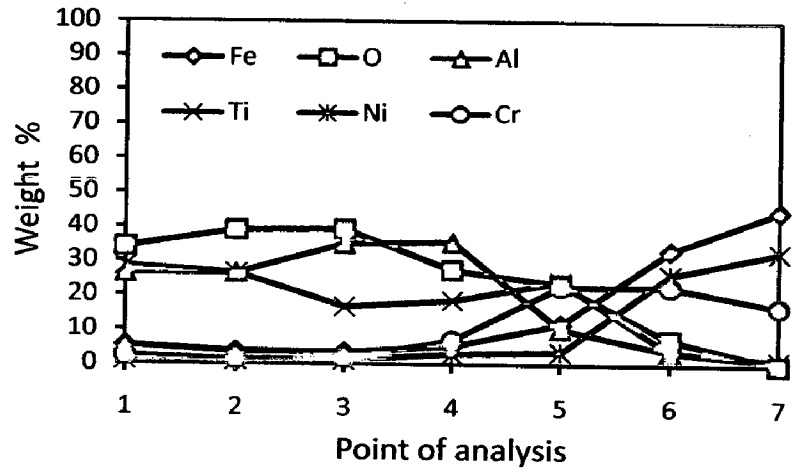
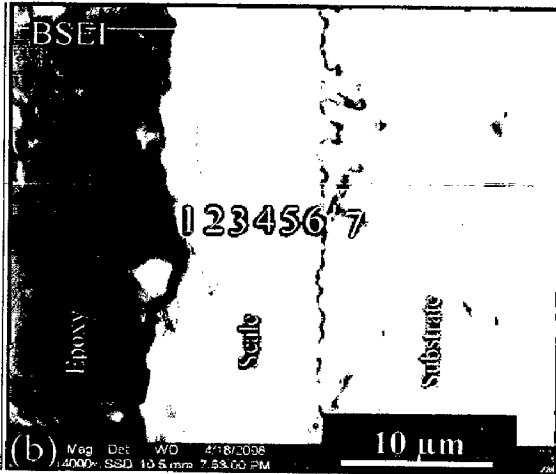
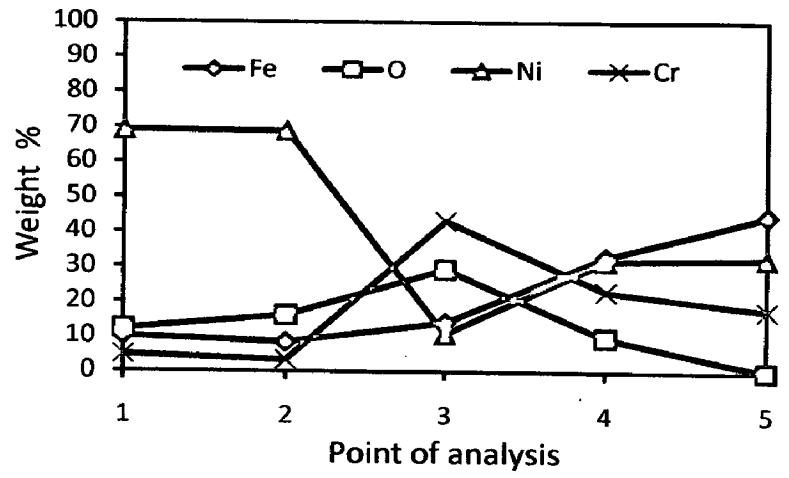
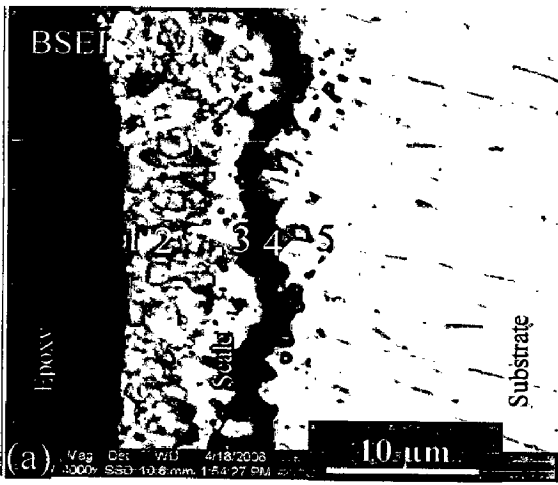
The scale thickness values were measured from SEM back scattered micrographs as shown in Fig.7.15. The measured average scale thickness values for Superfer800H superalloy, nanostructured thin TiAlN, nanostructured thin AlCrN, conventional thick TiAlN and conventional thick AlCrN coatings are 12, 09, 35, 100 and 120 μm respectively.

7.2.1.4.2 Cross-sectional scale morphology

Back Scattered Electron Image (BSEI) micrograph and elemental variation across the cross-section for coated and uncoated Superfer800H superalloy subjected to cyclic oxidation in air at 900°C for 50 cycles are shown in Fig.7.15. In case of uncoated superalloy, EDAX analysis reveals the presence of iron, oxygen, nickel and chromium throughout the scale. The scale is dense and nearly uniform in thickness. At point 3 (Fig. 7.15.a), the concentration of Cr and O is maximum, which points out the possibility of existence of Cr_2O_3 . The concentration of Fe is decreasing as one move away from the alloy-scale interface, whereas Ni has shown increase in the concentration along outward direction.

BSEI micrograph and elemental variation depicted in Fig.7.15 (b), for the exposed cross-section of nanostructured thin TiAlN coated Superfer800H superalloy shows the dense and continuous scale. The EDAX analysis reveals the presence of Ti, Al and O in the scale. The concentration of Fe, Ni and Cr is decreasing, as one move away from the alloy-scale interface. The outer scale is rich in Ti, Al and O. In case of nanostructured AlCrN coating (Fig.7.15.c), a continuous and adherent oxide scale can be seen. The scale mainly consists of Fe, Ni and Cr with oxygen. A location at Point 4 shows increase on the concentration of Al.

In case of conventional TiAlN coated Superfer800H superalloy, the scale is uniform and adherent as depicted in Fig.7.15 (d). The EDAX point analysis indicates the presence of Fe, Ni, Al, Ti and Cr in the scale with variable amounts. The concentration of oxygen is less except at certain oxygen rich pockets (Point 4) where the concentration of Al is also higher. The conventional thick AlCrN coated Superfer800H superalloy (Fig.7.15.e) indicates continuous, thick and adherent scale. EDAX point analysis shows the uniform presence of Fe, Al, Cr, O and Ni throughout the scale.



All the coated and uncoated Superfer800H superalloy followed the parabolic rate law as evident from the Fig.7.12. The parabolic rate constant K_p was calculated by a linear least-square algorithm to a function in the form of $(W/A)^2 = K_p t$, where W/A is the weight gain per unit surface area (mg/cm^2) and 't' indicates the number of cycles representing the time of exposure. The parabolic rate constants for the bare and coated Superfer 800H superalloy calculated on the basis of 50 cycle's exposure data are shown in Table.7.3.

Table 7.3 Parabolic rate constant ' K_p ' values of uncoated and coated Superfer800H superalloy subjected to cyclic oxidation in air at 900°C for 50 cycles

Boiler steel substrate	$K_p \times 10^{-12} \text{ gm}^2 \text{ cm}^{-4} \text{ s}^{-1}$
Uncoated Superfer800H superalloy	22.00
Nanostructured TiAlN coating	14.40
Nanostructured AlCrN coating	12.20
Conventional TiAlN coating	79.42
Conventional AlCrN coating	78.25

7.2.1.3 Surface scale analysis

7.2.1.3.1 X-ray diffraction analysis (XRD)

XRD diffractograms for coated and uncoated Superfer800H superalloy subjected to cyclic oxidation in air at 900°C for 50 cycles are depicted in Fig.7.13 (a and b) on reduced scale. As indicated by the diffractograms, in case of uncoated superfer800H superalloy the oxide phases found are Fe_2O_3 , Cr_2O_3 , NiO, NiCr_2O_4 and NiFe_2O_4 . The formation of Fe_2O_3 , Cr_2O_3 , NiO, TiO_2 and Al_2O_3 has been indicated in the scale of nanostructured thin TiAlN coated superfer800H superalloy. Fe_2O_3 , Cr_2O_3 and NiO are found to be present in the scale of nanostructured AlCrN coating. Further, the main phases identified for the conventional thick TiAlN coating are Al_2O_3 , Ti_2O_3 and NiO. The oxide phases found in case of conventional thick AlCrN coating are Al_2O_3 along with NiO.

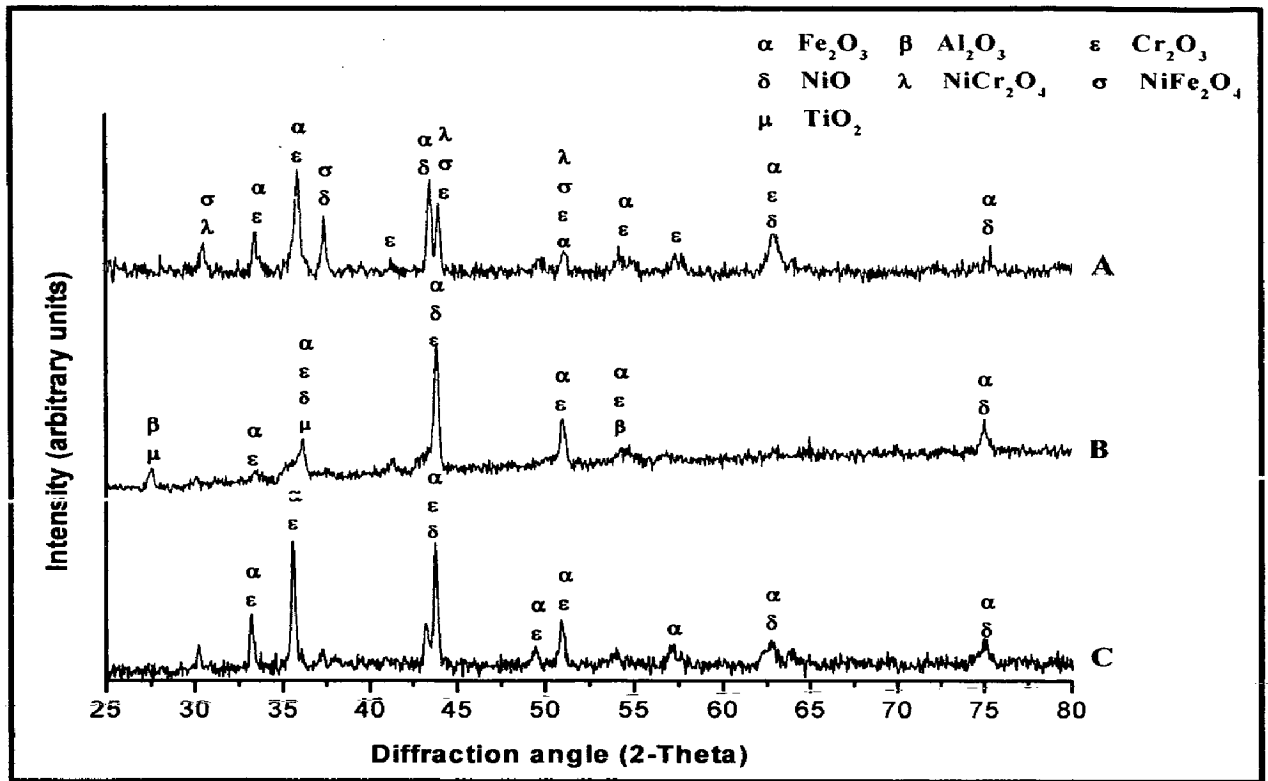


Fig. 7.13 (a) X-Ray Diffraction pattern of uncoated and coated Superfer 800H superalloy exposed to cyclic oxidation in air at 900°C for 50 cycles : (A) Uncoated superalloy, (B) Nanostructured TiAlN coating, (C) Nanostructured AlCrN coating

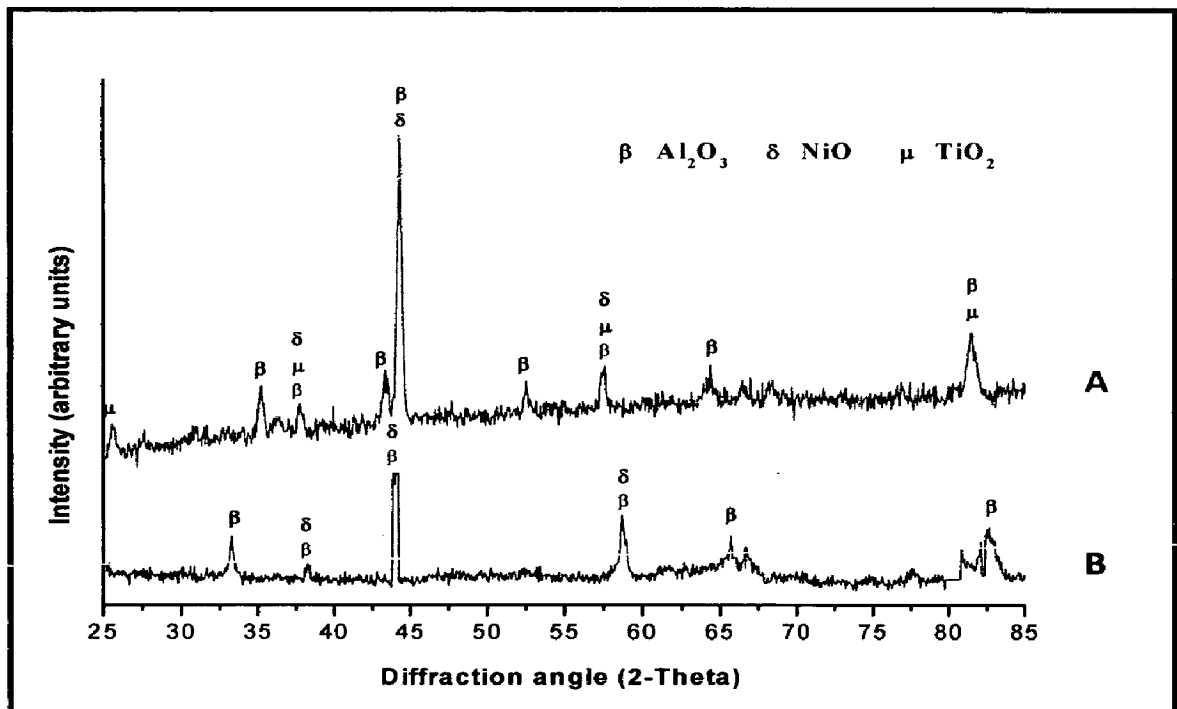


Fig. 7.13 (b) X-Ray Diffraction pattern of uncoated and coated Superfer 800H superalloy exposed to cyclic oxidation in air at 900°C for 50 cycles: (A) Conventional TiAlN coating, (B) Conventional AlCrN coating

7.2.1.3.2 Surface scale morphology

SEM micrographs along with EDAX point analysis reveals the surface morphology of the coated and uncoated superalloy subjected to cyclic oxidation in air at 900°C for 50 cycles are shown in Fig.7.14. The oxide scale for uncoated Superfer800H superalloy indicates the dominance of Fe and O along with some amount of Cr, Mn and Ni (Point 2). EDAX analysis at point 1 on Fig.7.14 i.e. at the portion of the matrix from which the upper layer has been removed during oxidation studies, shows the presence of Cr, Mn and O as the main elements along with small amount of Fe, Ni and Ti.

The SEM micrograph of oxidized nanostructured thin TiAlN coatings is shown in Fig.7.14 (b). The oxide scale is mainly consisting of grey colored matrix (Point 4) with white spots uniformly distributed on the entire surface (Point 3). The matrix is rich in Al (15.17%), Ti (23.25%), O (24.73%) and Cr (22.30%). A small amount of Ni, Fe and Mn are also present, as shown by EDAX point analysis. Ti (52.74%) and O (34.38%) are the main elements present in the region as shown by Point 3 i.e. the white spots region. In case of nanostructured thin AlCrN coating, the SEM micrograph indicates the grey and white regions (Fig. 7.14.c). The EDAX point analysis shows, the top scale rich in Fe, Ni, Cr and O. The small amount of Mn, Al, Ti and C are also present.

The surface scale developed on conventional thick TiAlN coating is with white contrast (Point 7) and black contrast regions (Point 8). The surface appearance is like eroded surface. EDAX analysis at point 7 indicates the presence of Ti, Al and O as the main phases along with very small amount of Fe, whereas the dark region (Point 8 on Fig.7.14) indicates maximum amount of Al (52.76%) and O (38.56%). A homogeneous and continuous surface scale is developed in case of conventional thick AlCrN coating, which has Al and O as main elements (Fig.7.14.e).

7.1.4 Cross-sectional analysis

7.1.4.1 Scale thickness

The oxidized samples were cut across the cross section using Buehler Isomet precision saw and mounted in transoptic mounting resin and subsequently mirrored to obtain scanning electron back scattered micrographs and X-ray mapping of element elements for coated and uncoated Superfer800H superalloy.

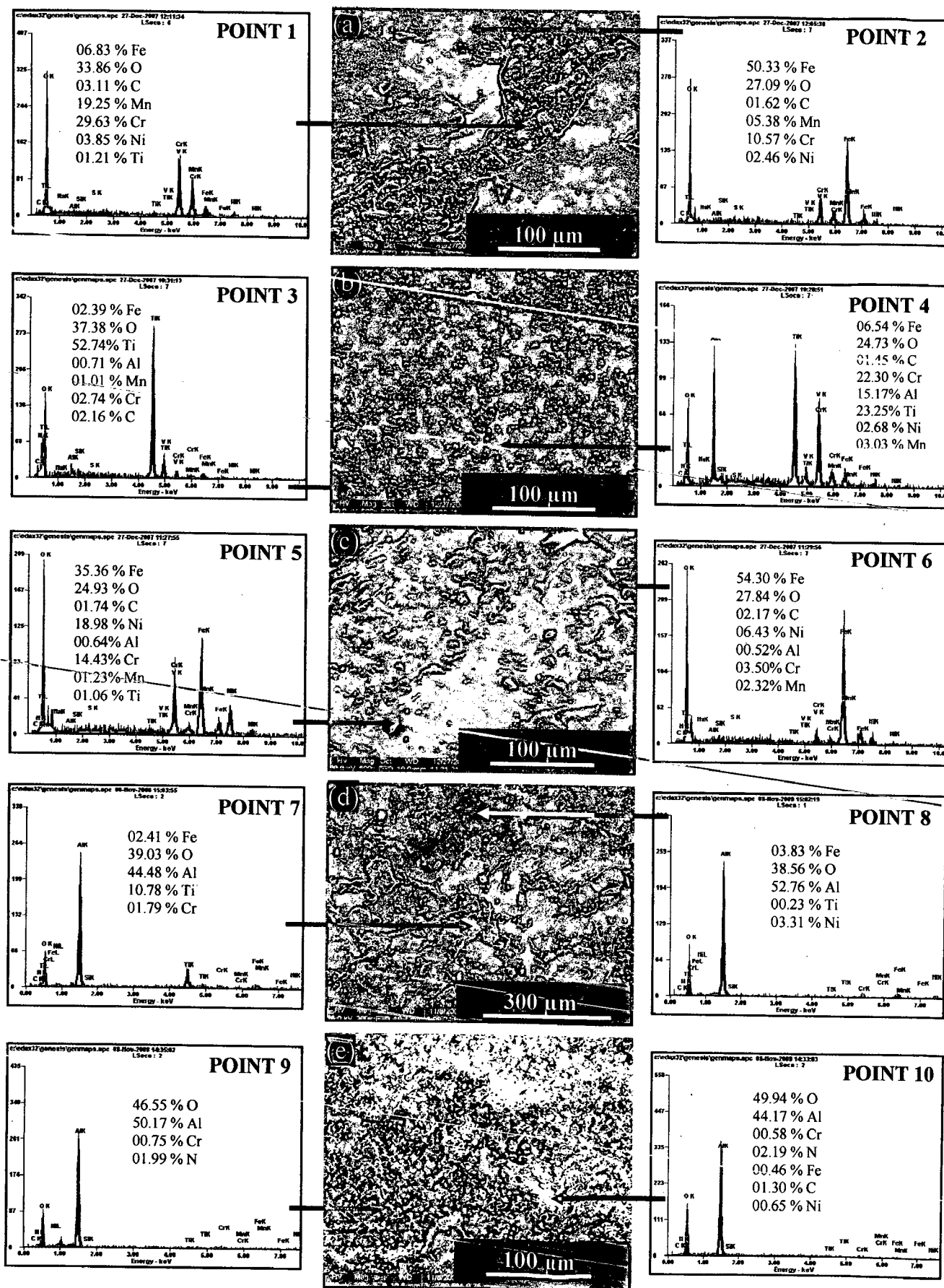


Fig. 7.14 Surface-scale morphology and EDAX patterns from different spots on uncoated and coated Superfer 800H superalloy after exposure to cyclic oxidation in air at 900°C for 50 cycles : (a) Uncoated Superfer 800H superalloy, (b) Nanostructured TiAlN coating, (c) Nanostructured AlCrN coating, (d) Conventional TiAlN coating, (e) Conventional AlCrN coating

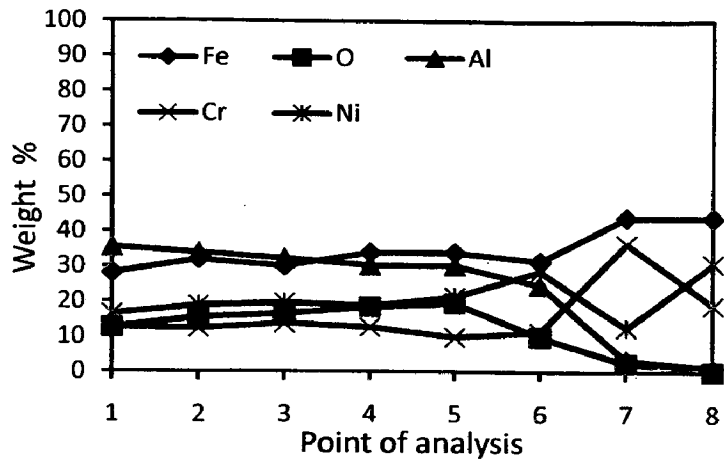
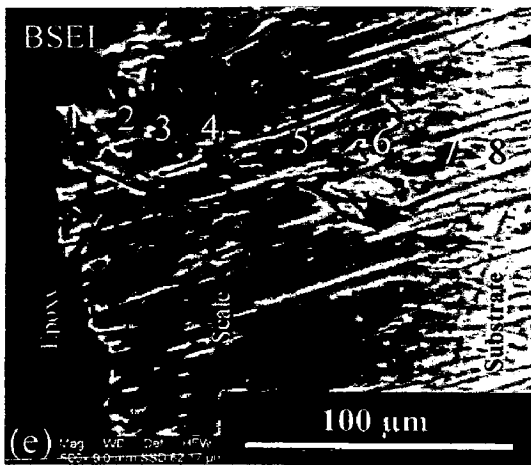


Fig. 7.15 Oxide scale morphology and variation of elemental composition across the cross-section of the uncoated and coated Superfer 800H superalloy after exposure to cyclic oxidation in air at 900°C for 50 cycles: (a) Uncoated Superfer 800H superalloy (4000 X), (b) Nanostructured TiAlN coating (4000 X), (c) Nanostructured AlCrN coating (2000 X), (d) Conventional TiAlN coating (500 X), (e) Conventional AlCrN coating (500 X)

7.2.1.4.3 X-Ray mapping

X-ray mappings for a part of oxide scale of uncoated and coated Superfer800H superalloy oxidized in air at 900°C for 50 cycles are shown in Fig. 7.16. BSEI and X-ray mapping for the oxidized uncoated Superfer 800H shows nickel dominating continuous scale, which contain substantial amounts of iron and oxygen (Fig.7.16.a). Chromium and oxygen have shown their co-presence in the form of a band at the scale-substrate interface. The BSEI image and X-ray mapping (Fig.7.16.b) in case of nanostructured TiAlN coating indicates the formation of a dense scale consisting mainly of aluminum, oxygen and titanium along with a thin regular band of Cr at scale-substrate interface. In case of nanostructured thin AlCrN coating, the X-ray mapping (Fig.7.16.c) indicates the presence of iron nickel and chromium throughout the scale. A thin band of Al, Cr and N is also indicated by X-ray mapping. In case of conventional thick TiAlN coated superalloy (Fig.7.16.d), Fe and O are present throughout the scale. Thick band of Ti is present in the top scale and of Ni is present at scale-substrate interface. Oxygen and aluminum rich pockets can be seen in the sub scale region. Figure 7.16 (e), depicts the BSEI and X-ray mapping in case of conventional AlCrN coating. Aluminum is uniformly distributed in the scale along with substantial amount of Cr, Ni and Fe. The other elements like O, Ti and N have shown negligible presence.

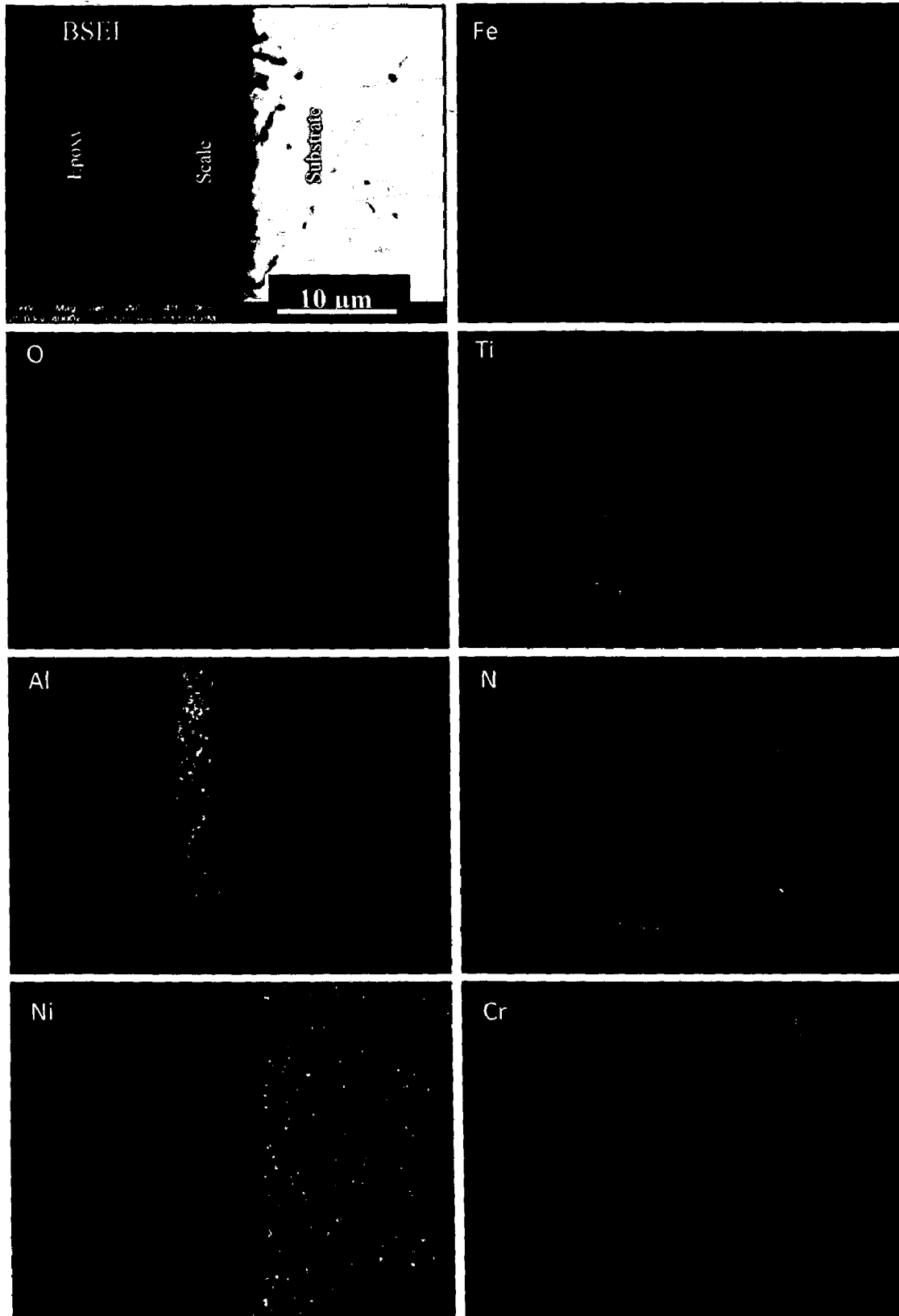


Fig. 7.16 (b) Composition image (BSEI) and X-ray mapping of the cross-section of Nanostructured TiAlN coated Superfer 800H superalloy subjected to cyclic oxidation in air at 900°C for 50 cycles

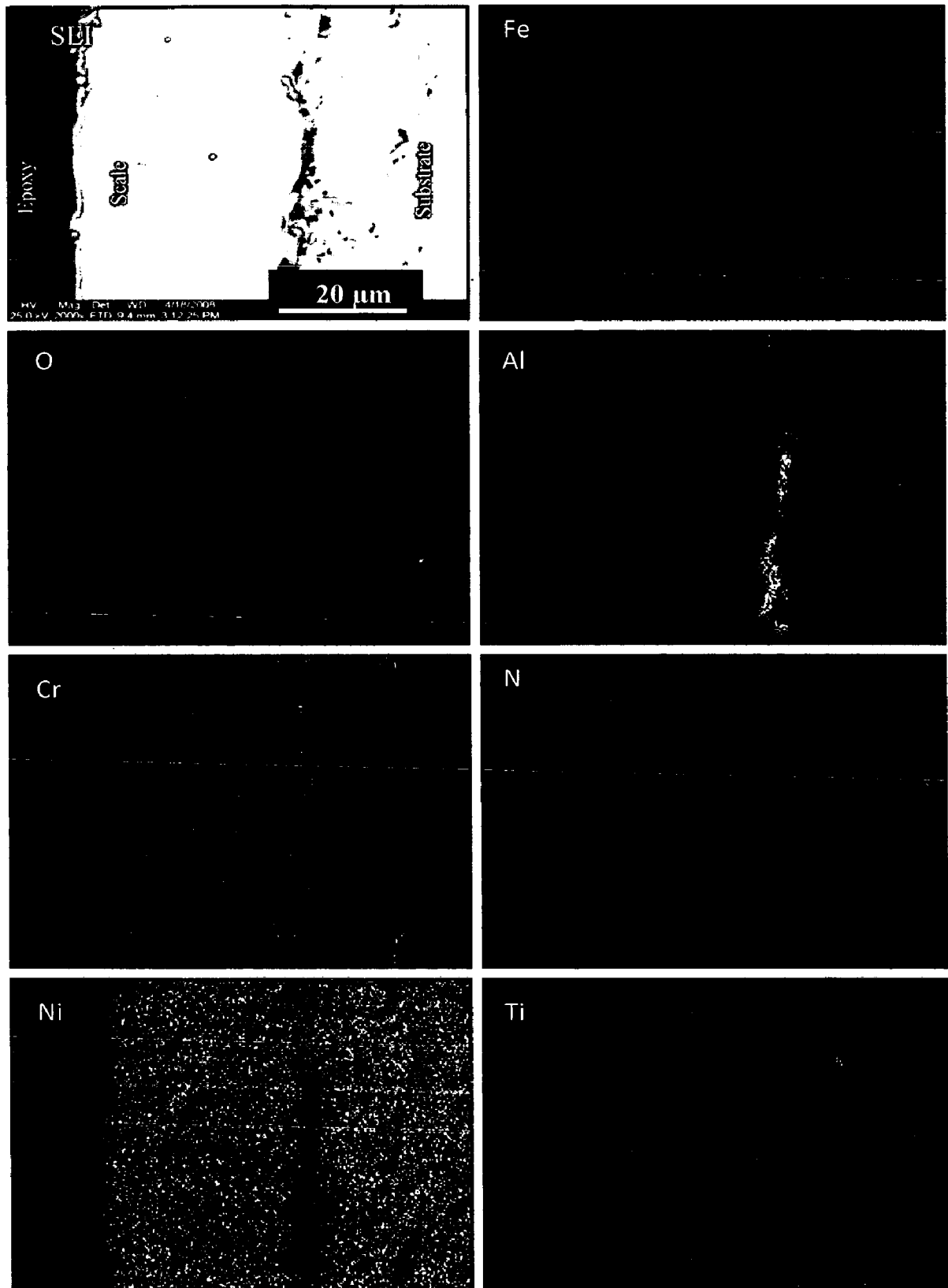


Fig. 7.16 (c) Composition image (BSEI) and X-ray mapping of the cross-section of Nanostructured AlCrN coated Superfer 800H superalloy subjected to cyclic oxidation in air at 900°C for 50 cycles

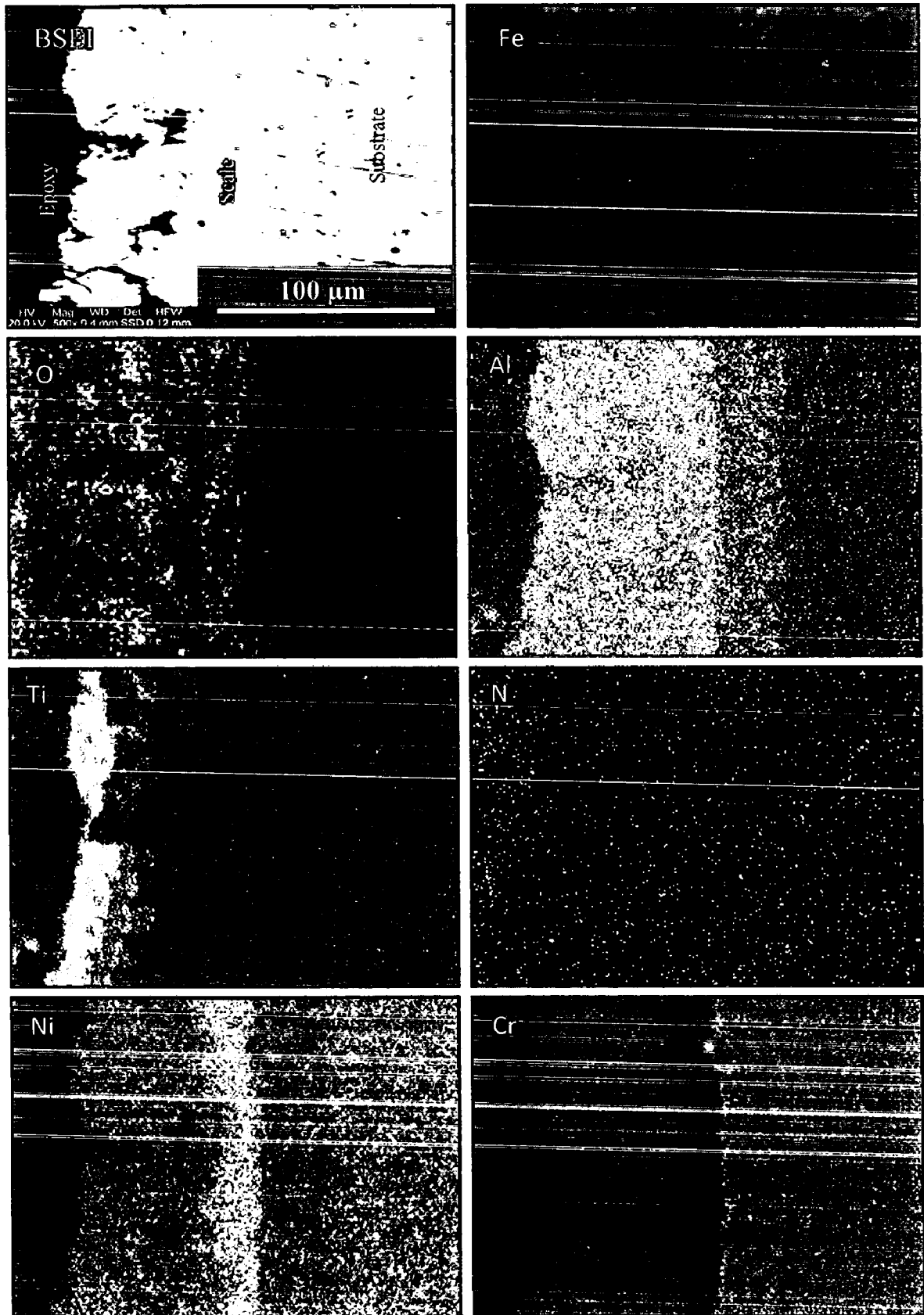


Fig. 7.16 (d) Composition image (BSEI) and X-ray mapping of the cross-section of conventional TiAlN coated Superfer 800H superalloy subjected to cyclic oxidation in air at 900°C for 50 cycles

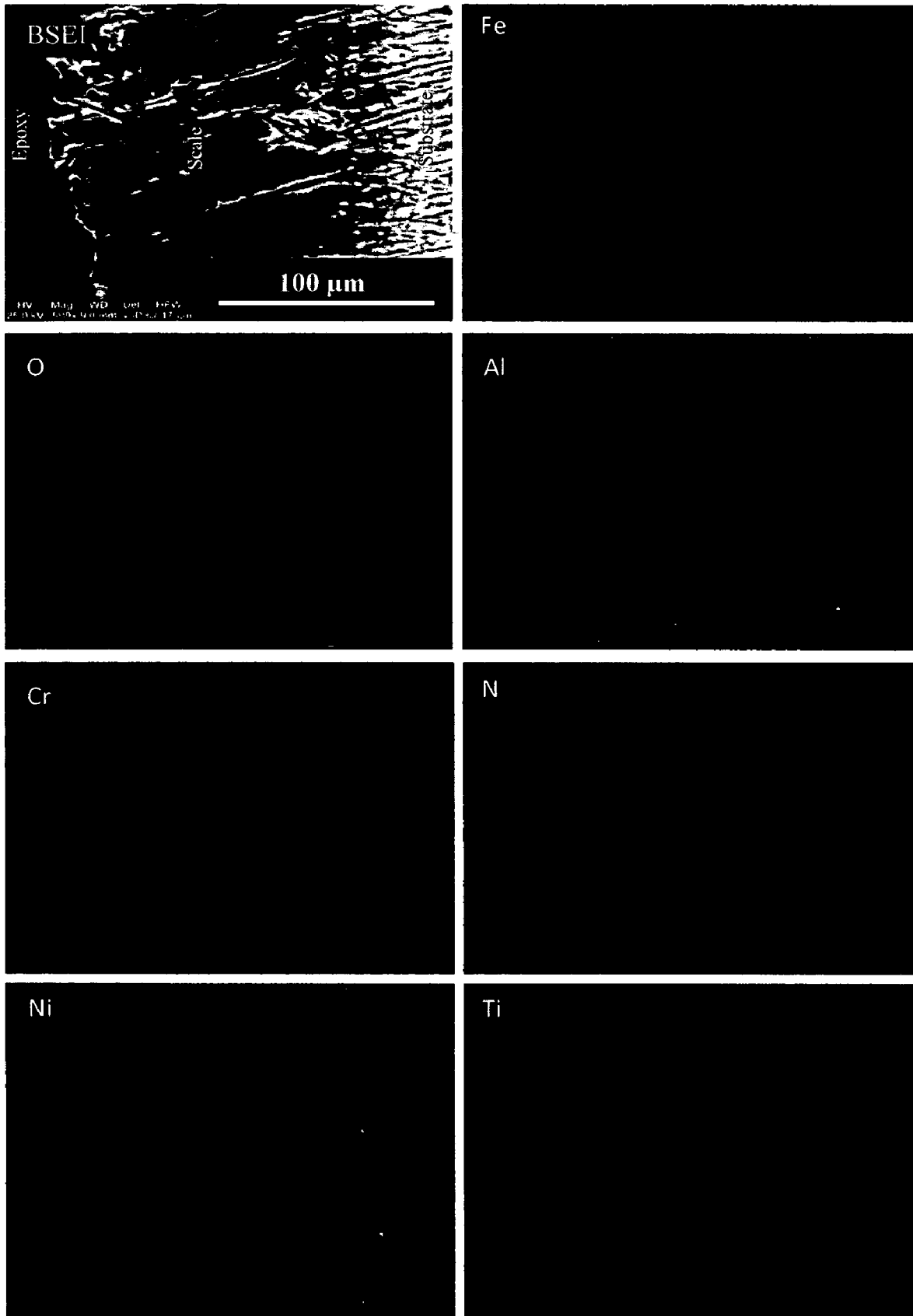


Fig. 7.16 (e) Composition image (BSEI) and X-ray mapping of the cross-section of conventional AlCrN coated Superfer 800H superalloy subjected to cyclic oxidation in air at 900°C for 50 cycles

7.2.2 Summary of Results

Results obtained after exposure of uncoated and coated Superfer 800H superalloy to cyclic oxidation in air at 900°C for 50 cycles are summarized in Table.7.4.

Table 7.4 Summary of the results obtained for uncoated and coated Superfer 800H superalloy subjected to cyclic oxidation in air at 900°C for 50 cycles

Coating	Cumulative Weight gain (mg/cm ²)	Parabolic rate constant ($K_p \times 10^{-12}$ gm ² cm ⁻⁴ s ⁻¹)	XRD phases	Remarks
Uncoated Superfer 800H superalloy	02.125	22.00	Fe ₂ O ₃ , Cr ₂ O ₃ , NiO, NiCr ₂ O ₄ and NiFe ₂ O ₄	A dark grey colored scale appeared on the surface right from the 1 st cycle, which turned to blackish green colored surface along with a light grey spot at the end of 50 th cycle
Nanostructured TiAlN coating	01.670	14.40	Fe ₂ O ₃ , Cr ₂ O ₃ , NiO, TiO ₂ and Al ₂ O ₃	Color of the oxide scale at the end of the study was observed to be blackish green with some light grey areas on the surface. The scale remains intact with the substrate and no spalling was observed.
Nanostructured AlCrN coating	01.513	12.20	Fe ₂ O ₃ , Cr ₂ O ₃ and NiO	The scale showed no spalling and remained intact with the substrate. After 1 st cycle, golden color shining was observed which turned to blackish green color along with light grey area at the end of 50 th cycle
Conventional TiAlN Coating	04.627	79.42	Al ₂ O ₃ , Ti ₂ O ₃ and NiO	The formation of very light brownish grey color matrix with cream color spots after cyclic oxidation studies was observed.
Conventional AlCrN coating	04.909	78.25	Al ₂ O ₃ along with NiO	The scale showed no signs of spalling and cracks. After 3 rd cycle, light bluish grey color was seen which turns to whitish grey colored surface along with a light brown side layer. The scale remains intact with the substrate throughout the study.

7.2.3 Discussion

The sequence of oxidation rates based on weight gain values for the coated and uncoated Superfer800H superalloy after 50 cycles of oxidation is:

Conven. AlCrN > Conven. TiAlN > Bare SF 800H > Nanostructured TiAlN > Nanostructured AlCrN

The plasma sprayed gas nitride conventional thick AlCrN and TiAlN coatings subjected to cyclic oxidation in air have shown relatively high weight gains (Fig.7.10) in the early cycles of the exposure. These initial high oxidation rates in general might partially be attributed to the rapid formation of oxides at the coating splat boundaries and within open pores due to the penetration of the oxidizing species along the splat boundaries/open pores in the early cycles of the study. Once the oxides are formed at places of porosity and splat boundaries, the coating becomes dense and the diffusion of oxidizing species to the internal portions of the coatings gets slowed down and the growth of the oxides becomes limited mainly to the surface of the specimens. This, in turn, will make the weight gain and hence the oxidation rate steady with the further progress of exposure time.

The surface scales for the coatings, have shown excellent spallation resistance against the cyclic oxidation in air, which indicates further effectiveness of the coatings under study as the cycle-oxidation behavior of an alloy is dictated mainly by scale spallation resistance as per the opinion of Stott (1992). Therefore, it can be inferred that the necessary protection has been provided by the coating to the substrate, in spite of the fact that the conventional thick coatings have shown high overall weight gains as compared to that shown by their uncoated and nanostructured coated counterparts.

These XRD results are well supported by the surface EDAX and X-Ray mapping analysis in the present study. In case of uncoated Superfer 800H superalloy, the oxide phases found are Fe_2O_3 , Cr_2O_3 , NiO, NiCr_2O_4 and NiFe_2O_4 . The X-ray mappings, Fig.7.16 (a) for the oxidised superalloy Superfer 800H are in good agreement with those reported by Polman et al. (1990) for a similar superalloy Incoloy 800H. The formation of Fe_2O_3 , Cr_2O_3 , NiO, TiO_2 and Al_2O_3 has been indicated in the scale of nanostructured thin TiAlN coating (Fig.8.b). The oxide phases in case of nanostructured AlCrN coating are Fe_2O_3 , Cr_2O_3 and NiO. The presence of Cr_2O_3 and NiO in the top scale of bare, nanostructured TiAlN and AlCrN coated superalloy is supported by the surface color of these samples

after oxidation studies, which is blackish green. Greenish color might be attributed to the presence of both Cr_2O_3 and NiO as reported by Khajavi and Shariat (2004). Further, the main phases identified for the conventional thick TiAlN coating are Al_2O_3 , Ti_2O_3 and NiO . The oxide phases found in case of conventional thick AlCrN coating are Al_2O_3 along with NiO .

Development of some superficial minor cracks near or along the edges of the coated specimens, and subsequent minor spalling may be attributed to the thermal shocks due to differences in the heat expansion coefficients of the oxides, coatings and the substrate (Rapp et al., 1981, Sidhu et al., 2003, Singh et al. 2004, Evans et al., 2001, Wang et al., 2002, Niranatlumpong et al., 2000 and Liu et al., 2001). Furthermore, the stress concentration factor at the sharp edges of the specimens might have also contributed to this minor cracking and spalling. It is pertinent to mention here that the edges of the specimens were kept sharp deliberately to add one more severe condition to the accelerated testing of the coatings. Otherwise in actual designs the sharp edges are always avoided to eliminate stress concentration.

The weight change plots (Fig.7.12) for the uncoated and coated Superfer 800H superalloy indicated that the oxidation behavior has shown conformance to parabolic rate law. The parabolic kinetic behavior is due to the diffusion controlled mechanism operating at 900°C under cyclic conditions (Mahesh et al., 2008). Small deviation from the parabolic rate law might be due to the cyclic scale growth. The higher weight gain during the first few cycles might be attributed to the rapid formation of oxides at the splat boundaries and within the open pores due to the penetration of the oxidizing species, further the subsequent increase in weight is gradual (Singh et al., 2007). Hussain et al. (1994) have also established the validity of parabolic rate law for a Fe-based superalloy Incoloy 800H.

A schematic diagram Fig.7.17 has been suggested to explain the oxidation phenomenon for the case of uncoated Superfer 800H in the light of explanations regarding oxidation put forward by Stott (1998) which is identical to the one reported by Singh, Harpreet (2003).. In the initial stage of oxidation process, when the alloy surface adsorb the oxygen molecules, small impinging nuclei of all the thermodynamically stable oxides such as those of Ni, Cr, Fe and Mn develop on the surface of the alloy.

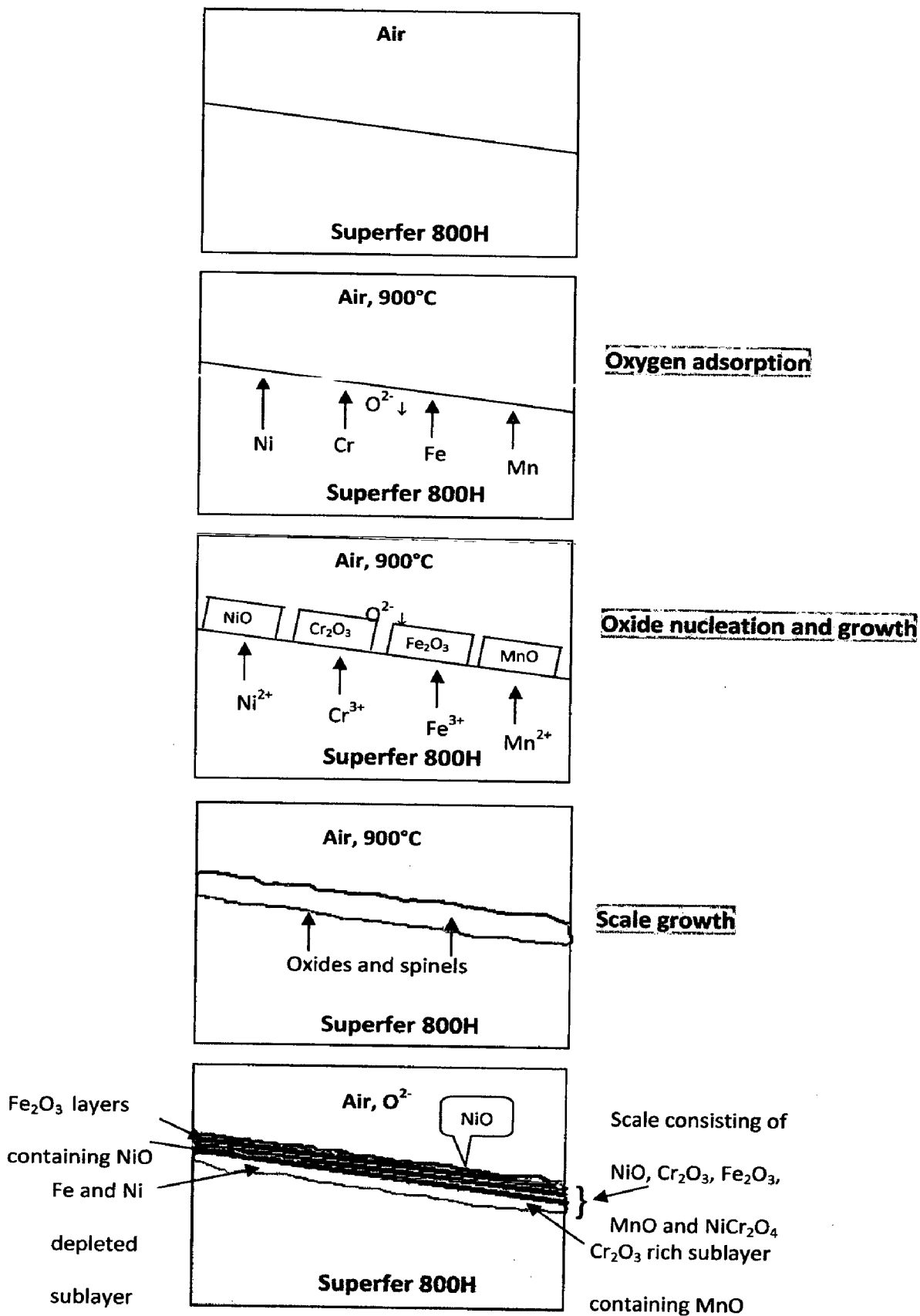


Fig. 7.17 Schematic diagram showing probable oxidation mechanism for the uncoated superalloy Superfer 800H exposed to air at 900°C for 50 cycles (Singh, Harpreet, 2005)

These nuclei then coalesce rapidly to give a transient layer of various oxides in a very short time as the temperature of study becomes very high. As the concentration of Fe and Ni is higher in the superalloy Superfer 800H, the amount of nickel and iron oxide in this layer will be the higher, whereas chromium oxide will be the second dominating phase, followed by oxides of Mn. In this transient layer, mixed type oxide such as NiCr_2O_4 may also form by reaction of oxides of Ni and Cr. As the oxidation progresses, this transient layer continues to grow with NiO at the top of the scale along with iron oxide, while the thermodynamically favored chromia attempt to establish a complete layer at the base of this transient layer along with MnO. With the progress of exposure, this transient layer continues to grow and sufficient nuclei of the various oxides develop to coalesce to form complete layers. Once a continuous layer Cr_2O_3 is formed at the alloy/scale interface, the rate of oxidation is then controlled by transport of reactants across this layer, which is much slower process than across the initially formed NiO-rich layer. Thereafter, oxidation process enters a steady state. The BSEI and X-ray mapping (Fig.7.16.a) support the above explained mechanism of oxidation in air for uncoated superfer 800H. It can be inferred based on the present investigation that conventional thick and nanostructured thin TiAlN and AlCrN coatings can provide a very good oxidation resistance at high temperature.

7.2.4 Conclusions

The high temperature oxidation behaviors of uncoated and coated Superfer 800H have been investigated in air at 900°C for 50 cycles. The behavior of nanostructured TiAlN and AlCrN coatings were compared with their conventional counterparts and the following conclusions are made:

1. The sequence of oxidation rates based on weight gain values for the coated and uncoated superalloy after 50 cycles of oxidation is:

Conventional AlCrN > Conventional TiAlN > Uncoated SF 800H > Nanostructured TiAlN > Nanostructured AlCrN

2. It can be inferred based on the present investigation that conventional thick and nanostructured thin TiAlN and AlCrN coatings can provide a very good oxidation resistance at high temperature.
3. The plasma sprayed gas nitride conventional thick AlCrN and TiAlN coatings subjected to cyclic oxidation in air have shown relatively high weight gains in the early cycles of the exposure. These initial high oxidation rates in general might partially be attributed to the rapid formation of oxides at the coating splat boundaries and within open pores due to the penetration of the oxidizing species along the splat boundaries/open pores in the early cycles of the study.
4. The plasma sprayed conventional thick coating AlCrN when subjected to cyclic oxidation at 900 °C for 50 cycles developed a protective scale mainly consisting on Al₂O₃.
5. The X-Ray mapping analysis for the conventional thick TiAlN and AlCrN coatings and nanostructured TiAlN coating shows that the oxygen has not penetrated into the substrate alloys.
6. The cracking and subsequent minor spalling may be attributed to the thermal shocks due to differences in the heat expansion coefficients of the oxides, coatings and the substrate.

7.3 HOT CORROSION STUDIES IN MOLTEN SALT ENVIRONMENT

Recent studies showed that the materials used for high temperature strength are highly susceptible to hot corrosion and the surface engineering plays a key role in effectively combating the hot corrosion problems (Gurrappa and Sambasiva Rao, 2006). Therefore, the present research work aims to evaluate and compare the hot corrosion behavior of conventional thick (by plasma spraying and gas nitrided) and nanostructured thin (by physical vapor deposition process) TiAlN and AlCrN coatings on Superfer 800H superalloy in an aggressive environment of Na_2SO_4 -60% V_2O_5 molten salt at 900°C under cyclic conditions. The cyclic conditions were chosen to create a very aggressive environment for corrosion attack. The cyclic conditions constitute a more realistic approach towards solving metal corrosion problems. X-ray diffraction (XRD), scanning electron microscopy/energy-dispersive analysis (SEM/EDAX) and X-ray mapping techniques have been used to characterize corrosion products after hot corrosion at 900°C.

7.3.1 Results

7.3.1.1 Visual observations

The macrographs for uncoated and coated Superfer800H (Fe-based superalloy) subjected to cyclic oxidation in Na_2SO_4 -60% V_2O_5 (molten salt) environment at 900°C for 50 cycles, are shown in Fig.7.18. For the uncoated superalloy, a dark grey colored scale appeared on the surface right from the 1st cycle, which turned to blackish green colored along with a small light grey spot at the end of 50th cycle (Fig.7.18.a). After 20th cycle some shining dots were also appeared in the scale

Color of the oxide scale at the end of the study was observed to be blackish green with some light grey spots on the surface, in case of nanostructured thin TiAlN coated superalloy (Fig.7.18 .b). The scale starts falling in the boat from 19th cycle and then after 26th cycle the weight starts decreasing as the scale starts falling outside the boat in the tube furnace. The nanostructured thin AlCrN coated superalloy showed no spalling and remained intact with the substrate during the initial cycles. After 30th cycle, the scale in the form of powder starts falling outside the boat in the tube furnace, which continued till 50th cycle. At the end of the study, the surface appearance of the oxidized

sample is blackish green with some light grey spots as shown in Fig.7.18 (c). A visual observation of conventional thick TiAlN coated superalloy (Fig.7.18.d), showed the formation of very light brownish grey color matrix with cream color spots after cyclic oxidation studies in $\text{Na}_2\text{SO}_4\text{-60\%V}_2\text{O}_5$ (molten salt) environment.

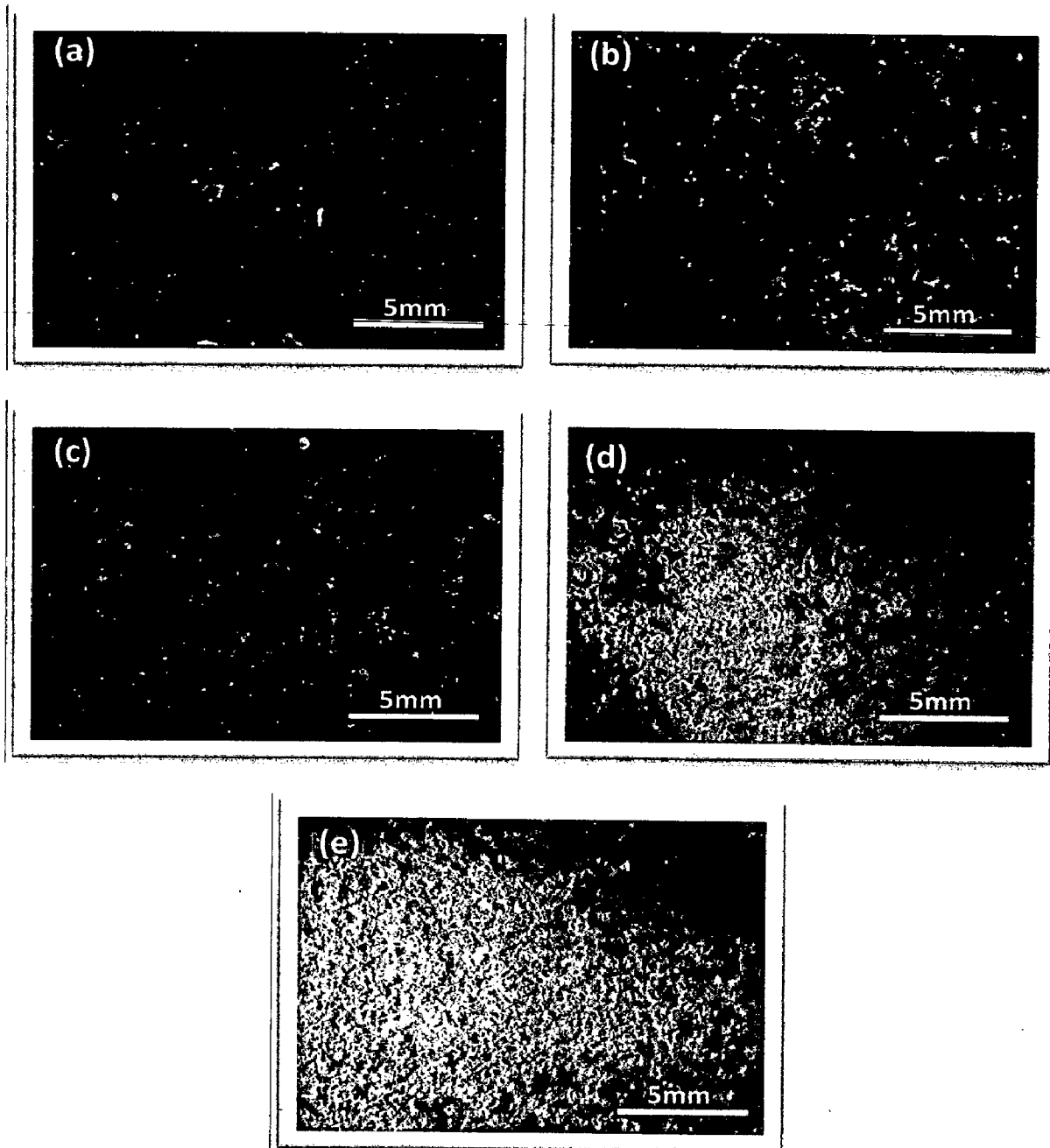


Fig. 7.18 Surface macrographs of uncoated and coated Superfer 800H superalloy exposed to molten salt ($\text{Na}_2\text{SO}_4\text{-60\%V}_2\text{O}_5$) environment at 900°C for 50 cycles: (a) Uncoated Superfer 800H superalloy, (b) Nanostructured TiAlN coating, (c) Nanostructured AlCrN coating, (d) Conventional TiAlN coating, (e) Conventional AlCrN coating

Some amount of superficial spalling was noticed at the end of 2nd cycle, which may be due to the loosely bond particles on the surface of the coating. In case of conventional thick AlCrN coated superalloy, the scale showed no signs of spalling and cracking (Fig.7.18.e). The scale remains intact with the substrate throughout the study and the color of the scale is light grey at the end of the study.

7.3.1.2 Weight change measurements

Weight gain per unit area (mg/cm^2) versus time expressed in number of cycles plot for coated and bare superalloy subjected to cyclic oxidation in $\text{Na}_2\text{SO}_4\text{-}60\%\text{V}_2\text{O}_5$ (molten salt) environment at 900°C for 50 cycles, is presented in Fig. 7.19. It can be inferred from the plots that the bare superalloy have shown high rate of oxidation as compared to coatings. The nanostructured thin coatings have shown weight gain in the initial cycles and then after 25th cycle (in case of nanostructured TiAlN) and 30th cycle (in case of nanostructured AlCrN coating) the weight gain rate suddenly drops as the scale starts falling outside the boat in the tube furnace during the course of study.

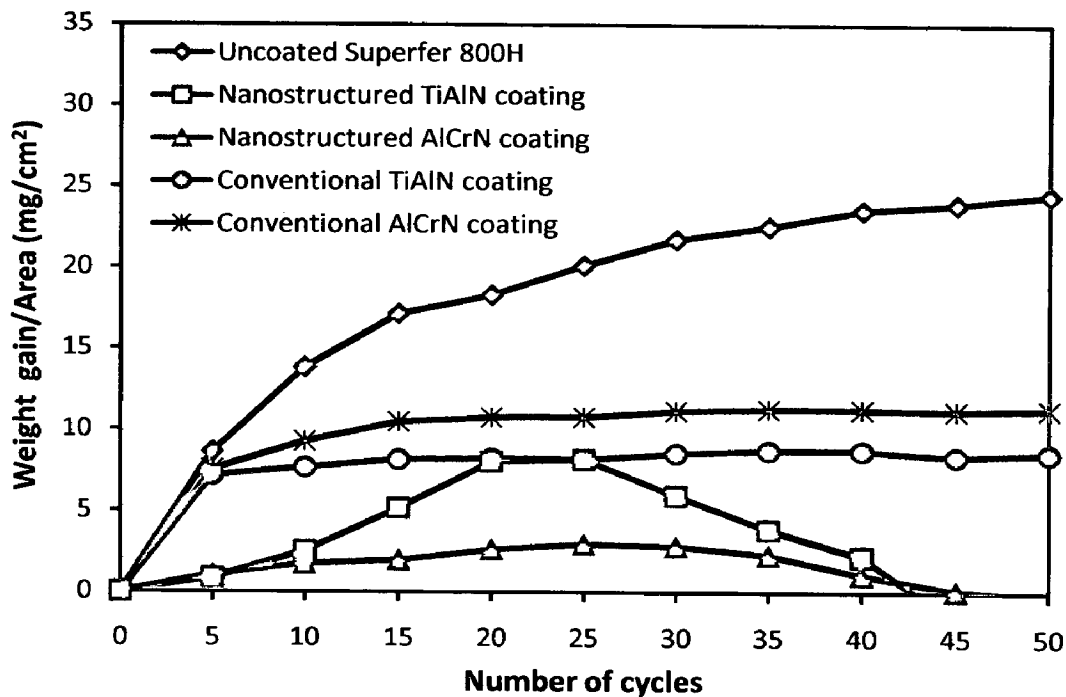


Fig. 7.19 Weight gain/area vs time (number of cycles) for the uncoated and coated Superfer 800H superalloy exposed to molten salt ($\text{Na}_2\text{SO}_4\text{-}60\%\text{V}_2\text{O}_5$) environment at 900°C for 50 cycles

The conventional thick coatings have shown relatively higher weight gain in the early cycles of study, followed by tendency to show gradual weight gain with further increase in number of cycles. The cumulative weight gain per unit area for the coated and uncoated superalloy subjected to cyclic oxidation in air at 900°C for 50 cycles is shown in Fig. 7.20. The overall weight gain is highest in case of uncoated superalloy (24.51 mg/cm²) and is lowest in case of nanostructured thin AlCrN coating (2.84 mg/cm² up to 30th cycle). The final weight gain in case of nanostructured TiAlN, Conventional TiAlN and AlCrN coatings is 8.15, 8.54 and 11.27 mg/cm² respectively.

The (weight gain/area)² versus number of cycles plot are shown in Fig. 7.21 for all the cases to ascertain conformance with the parabolic rate law. All the coated and uncoated superalloy followed the parabolic rate law as evident from the Fig.7.21. The parabolic rate constant K_p was calculated by a linear least-square algorithm to a function in the form of $(W/A)^2 = K_p t$, where W/A is the weight gain per unit surface area (mg/cm²) and 't' indicates the number of cycles representing the time of exposure. The parabolic rate constants for the bare and coated Superfer800H superalloy calculated on the basis of 50 cycle's exposure data are shown in Table.7.5.

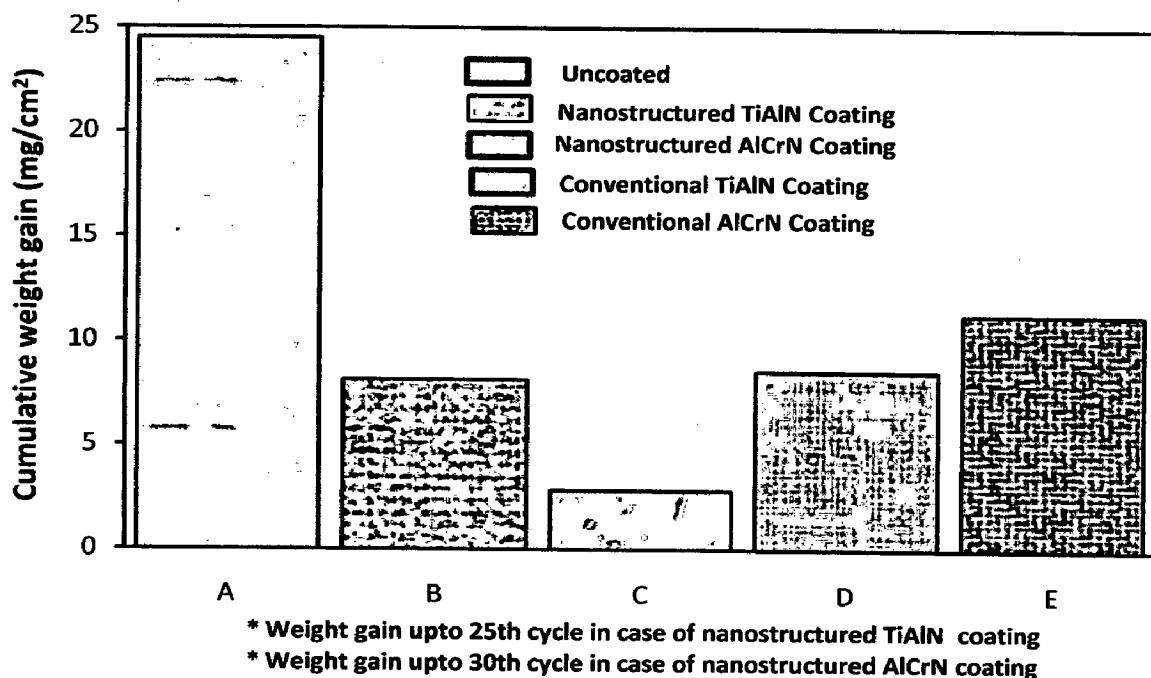


Fig. 7.20 Bar chart showing cumulative weight gain per unit area for the uncoated and coated Superfer 800H superalloy exposed to molten salt (Na₂SO₄-60%V₂O₅) environment at 900°C for 50 cycles: (A) Uncoated Superfer 800H superalloy, (B) Nanostructured TiAlN coating, (C) Nanostructured AlCrN coating, (D) Conventional TiAlN coating, (E) Conventional AlCrN coating

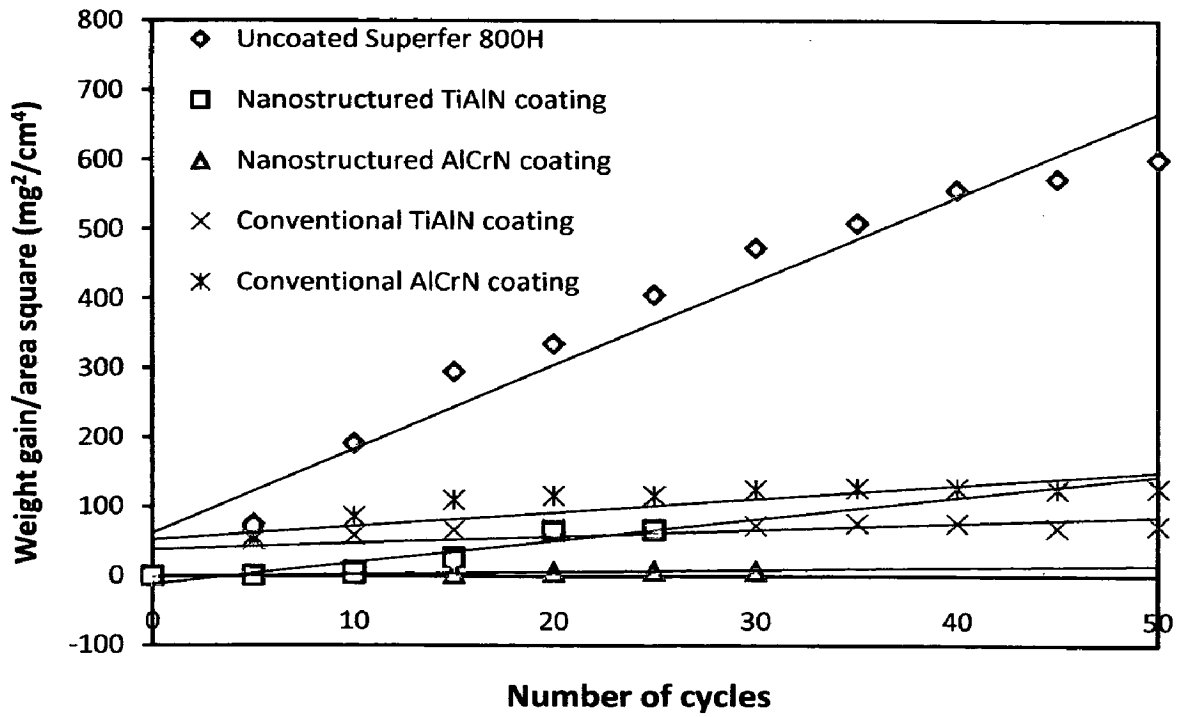


Fig. 7.21 Weight gain/area square vs time (number of cycles) for the uncoated and coated Superfer 800H superalloy exposed to molten salt ($\text{Na}_2\text{SO}_4\text{-60\%V}_2\text{O}_5$) environment at 900°C for 50 cycles

Table 7.5 Parabolic rate constant ' K_p ' values of uncoated and coated Superfer 800H superalloy subjected to cyclic oxidation in $\text{Na}_2\text{SO}_4\text{-60\%V}_2\text{O}_5$ molten salt at 900°C for 50 cycles

Substrate / Coating	$K_p \times 10^{-10} \text{ gm}^2\text{cm}^{-4}\text{s}^{-1}$
Uncoated Superfer800H superalloy	33.65
Nanostructured TiAlN coating	08.65
Nanostructured AlCrN coating	00.85
Conventional TiAlN coating	02.60
Conventional AlCrN coating	05.41

7.3.1.3 Surface scale analysis

7.3.1.3.1 X-ray diffraction analysis (XRD)

XRD diffractograms for coated and bare Superfer 800H superalloy subjected to cyclic oxidation in Na_2SO_4 -60% V_2O_5 (molten salt) environment at 900°C for 50 cycles are depicted in Fig. 7.22 (a and b) on reduced scale. As indicated by the diffractograms, in case of uncoated, nanostructured TiAlN and AlCrN coated Superfer 800H superalloy the oxide phases found are Fe_2O_3 , Cr_2O_3 , NiO, NiCr_2O_4 and NiFe_2O_4 . The formation of some weak peaks of Al_2O_3 has also been revealed in the scale of nanostructured thin coatings. Further, the main phases identified for the conventional thick TiAlN coating are Al_2O_3 , Ti_3Al and NiO. The oxide phases found in case of conventional thick AlCrN coating are Al_2O_3 , Fe_2O_3 , and Cr_2O_3 along with NiO.

7.3.1.3.2 Surface scale morphology

SEM micrographs along with EDAX point analysis reveals the surface morphology of the coated and uncoated Superfer 800H superalloy subjected to cyclic oxidation in Na_2SO_4 -60% V_2O_5 (molten salt) environment at 900 °C for 50 cycles are shown in Fig.7.23. The oxide scale for uncoated superalloy indicates the dominance of Fe, Cr and O along with some amount of Mn and Ni (Fig.7.23.a).

The SEM micrograph of oxidized nanostructured thin TiAlN coatings which appears like a structure of rock is shown in Fig.7.23 (b). The matrix is rich in Fe, Cr, O and Ni along with small amount of Mn, Al and Ti, as revealed by EDAX point analysis. In case of nanostructured thin AlCrN coating, the SEM micrograph indicates small needles (Point 5) like structures dispersed in matrix (Point 6 on Fig. 7.23.c). The top scale is rich in Fe, Ni, Cr and O. The small amount of Mn, Al, Ti and C are also present. The EDAX point analysis shows higher concentration of Ni (26.70%) and Cr (11.45%) in the needles comparable to matrix which shows lower concentration of Ni (6.43%) and Cr (3.50%). Further, the amount of Fe in the matrix is more than in needles.

The surface scale developed on conventional thick TiAlN coating is with black (Point 7) and white areas (Point 8 on Fig.7.23.d). The EDAX point analysis at point 7 indicates the presence of Al (42.29%) and O (39.12%) as the main phases along with small amount of Fe, Ni, Ti and Cr.

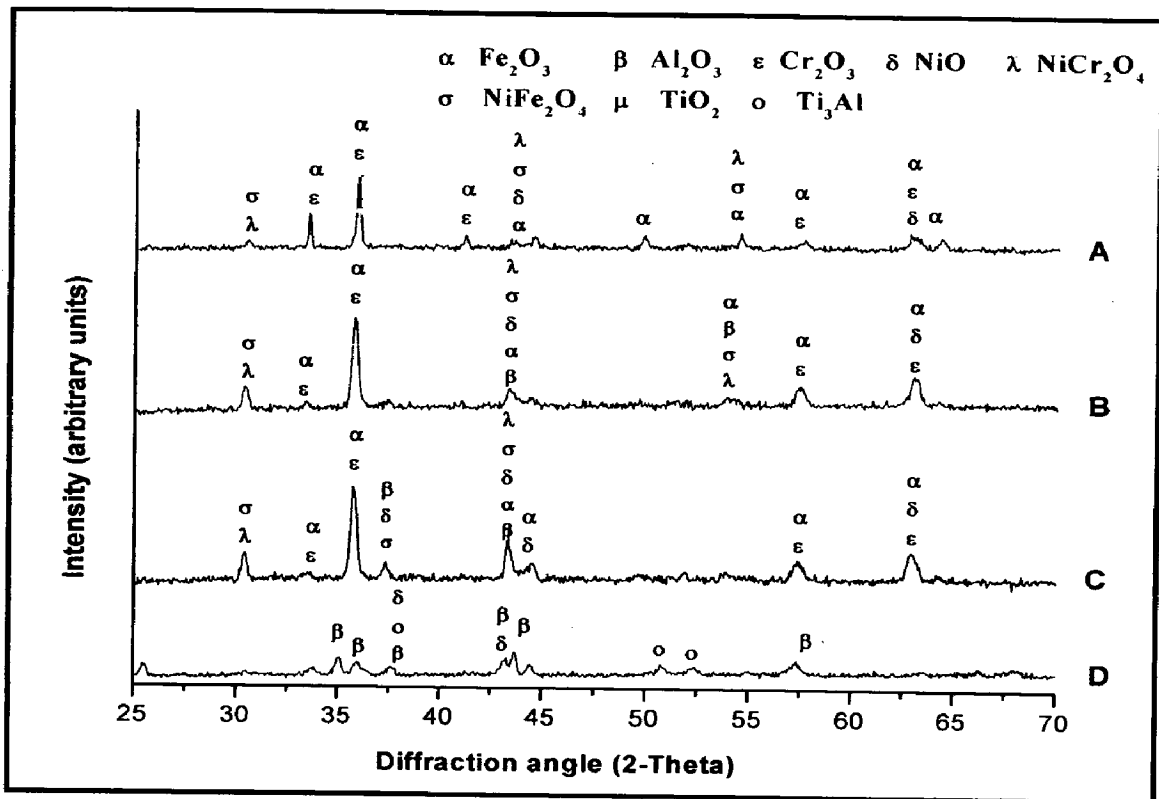


Fig. 7.22 (a) X-Ray Diffraction pattern of uncoated and coated Superfer 800H superalloy exposed to molten salt (Na_2SO_4 -60% V_2O_5) environment at 900°C for 50 cycles: (A) Uncoated superalloy, (B) Nanostructured TiAlN coating, (C) Nanostructured AlCrN coating, (D) Conventional TiAlN coating

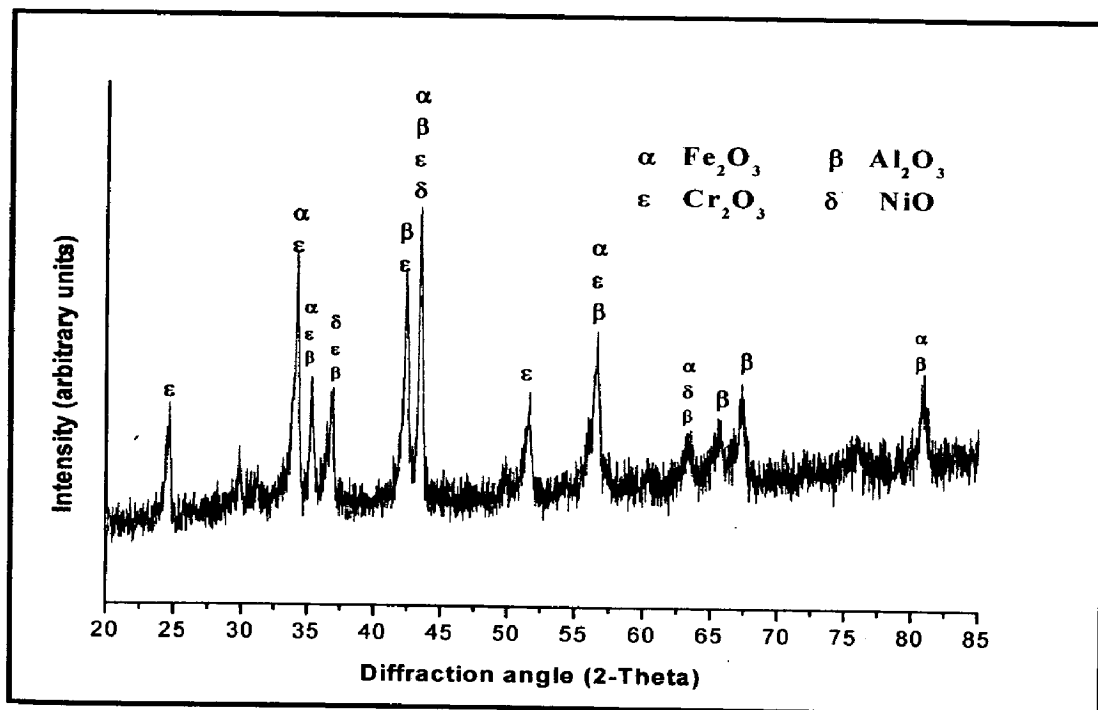


Fig. 7.22 (b) X-Ray Diffraction pattern of Conventional AlCrN coated Superfer 800H superalloy exposed to molten salt (Na_2SO_4 -60% V_2O_5) environment at 900°C for 50 cycles

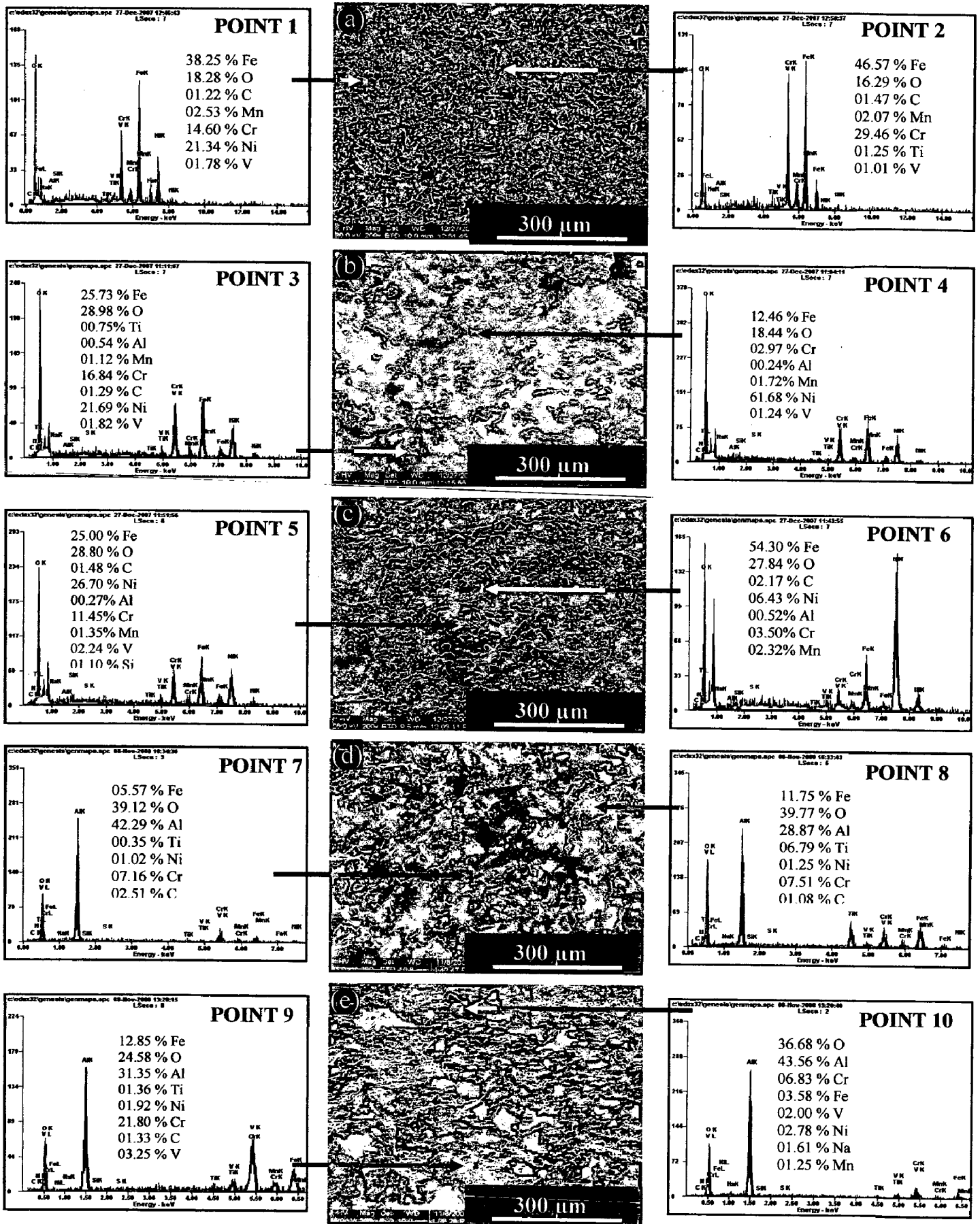


Fig. 7.23 Surface-scale morphology and EDAX patterns from different spots on uncoated and coated Superfer 800H superalloy exposed to molten salt ($\text{Na}_2\text{SO}_4\text{-60}\%\text{V}_2\text{O}_5$) environment at 900°C for 50 cycles : (a) Uncoated Superfer 800H superalloy, (b) Nanostructured TiAlN coating, (c) Nanostructured AlCrN coating, (d) Conventional TiAlN coating, (e) Conventional AlCrN coating

The white contrast region (Point 8 in Fig.7.23) shows the presence of Al (28.87%), Fe (11.75%), Ti (6.79%) and O (39.11%) along with Cr (7.51%). A homogeneous and continuous surface scale is developed in case of conventional thick AlCrN coating (Fig.7.23.e). The EDAX point analysis revealed more concentration of Cr and Fe in the white contrast region (Point 9) as compared to the dark grey region (Point 10), whereas the concentration of Al and O is less.

7.3.1.4 Cross-sectional analysis

7.3.1.4.1 Scale thickness

The oxidized samples were cut across the cross section using Buehler Isomet 1000 precision saw and mounted in transoptic mounting resin and subsequently mirror polished to obtain scanning electron back scattered micrographs and X-ray mapping of different elements for coated and uncoated Superfer 800H superalloy. The scale thickness values were measured from SEM back scattered micrographs as shown in Fig.7.24. The measured average scale thickness values for Superfer 800H superalloy, nanostructured thin TiAlN, nanostructured thin AlCrN, conventional thick TiAlN and conventional thick AlCrN coatings are 84, 81, 24, 108 and 106 μm respectively.

7.3.1.4.2 Cross-sectional scale morphology

Back Scattered Electron Image (BSEI) micrograph and elemental variation across the cross-section for coated and uncoated Superfer 800H superalloy subjected to cyclic oxidation in Na_2SO_4 -60% V_2O_5 (molten salt) environment at 900°C for 50 cycles are shown in Fig.7.24. In case of uncoated Superfer800H superalloy (Fig.7.24.a), EDAX analysis reveals the presence of iron, oxygen, nickel and chromium throughout the scale. The scale is dense and nearly uniform in thickness. At point 3 and 5 the concentration of Cr and O is higher, which points out the possibility of existence of Cr_2O_3 . The amount of Ni is higher at point 4. The concentration of O is varying throughout the scale and is almost zero at point 2 and 4. BSEI micrograph and elemental variation depicted in Fig.7.24 (b), for the exposed cross-section of nanostructured thin TiAlN coated Superfer 800H superalloy shows the dense and continuous scale.

7.3.1.4.3 X-Ray mapping

X-ray mappings for a part of oxide scale of uncoated and coated Superfer 800H superalloy oxidized in Na_2SO_4 -60% V_2O_5 (molten salt) environment at 900 °C for 50 cycles are shown in Fig.7.25. BSEI and X-ray mapping for the oxidized bare superalloy shows nickel dominating continuous scale, which contain substantial amounts of iron and oxygen (Fig.7.25.a). Chromium and oxygen have shown their co-presence in the form of some pockets in the scale and at the scale-substrate interface, where iron and nickel is completely missing. Figure 7.25 (b), shows X-ray mapping analysis of the scale formed on nanostructured TiAlN Superfer 800H superalloy. The BSEI image and X-ray mapping indicates the formation of a dense scale consisting mainly of iron, nickel, oxygen and chromium. Chromium and oxygen have shown their co-presence in the form of a band at the scale-substrate interface.

In case of nanostructured thin AlCrN coated superalloy, the BSEI and X-ray mapping are shown in Fig.7.25 (c). The X-ray mapping indicates the presence of iron oxygen nickel and chromium throughout the scale. A thin band of Cr and O is also indicated by X-ray mapping, where iron and nickel are completely absent. This band is followed by a thin band of Ni and O, where Fe and Cr are missing.

In case of conventional thick TiAlN coated superalloy (Fig.7.25.d), Fe and O are present throughout the scale. Thick band of Ti is present in the top scale whereas thin band of Ni is present at scale-substrate interface. The sub scale is rich in Al and Fe with substantial amount of O, Ni and Cr. Figure 7.25 (e), depicts the BSEI and X-ray mapping in case of conventional AlCrN coating. Aluminum is uniformly distributed in the scale along with substantial amount of Cr, Ni and Fe. The other elements like Ti and N have shown negligible presence.

7.3.2 Summary of Results

Results obtained after exposure of uncoated and coated Superfer 800H superalloy to cyclic oxidation in Na_2SO_4 -60% V_2O_5 molten salt environment at 900°C for 50 cycles are summarized in Table.7.6.

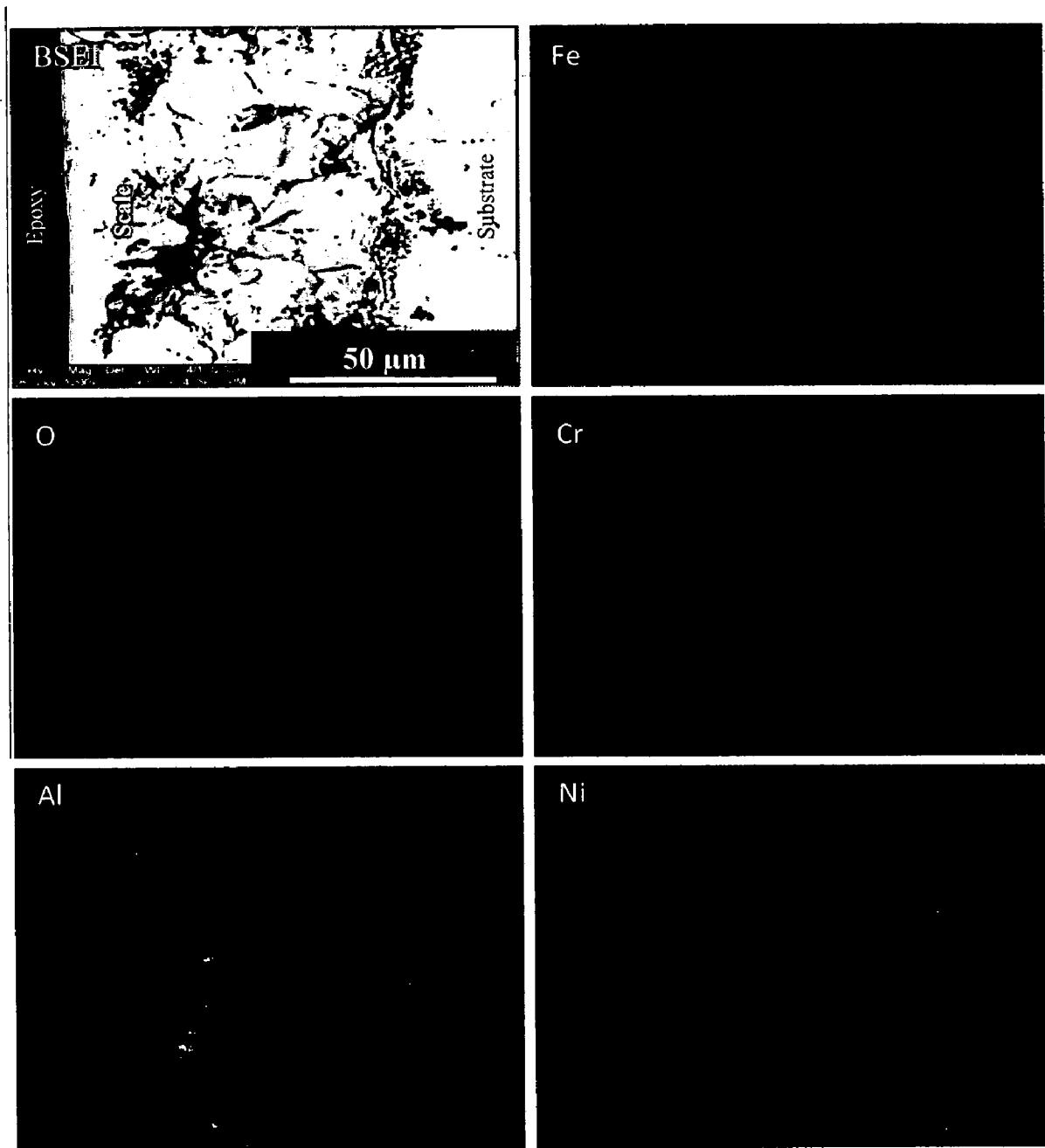


Fig. 7.25 (a) Composition image (BSEI) and X-ray mapping of the cross-section of uncoated Superfer 800H superalloy exposed to molten salt (Na_2SO_4 -60% V_2O_5) environment at 900°C for 50 cycles

The white contrast region (Point 8 in Fig.7.23) shows the presence of Al (28.87%), Fe (11.75%), Ti (6.79%) and O (39.11%) along with Cr (7.51%). A homogeneous and continuous surface scale is developed in case of conventional thick AlCrN coating (Fig.7.23.e). The EDAX point analysis revealed more concentration of Cr and Fe in the white contrast region (Point 9) as compared to the dark grey region (Point 10), whereas the concentration of Al and O is less.

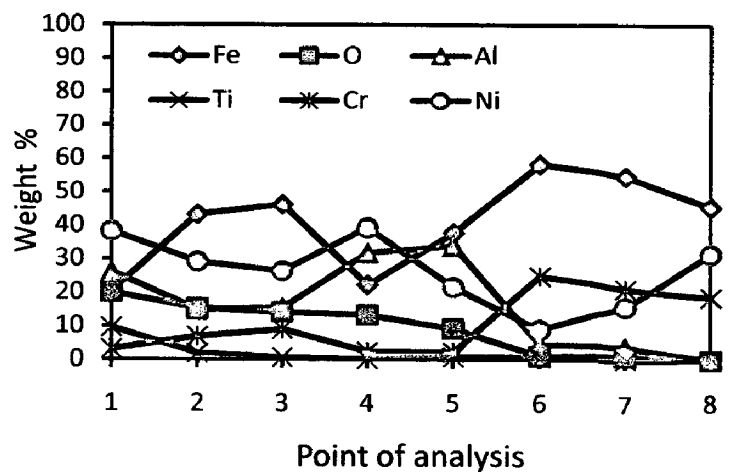
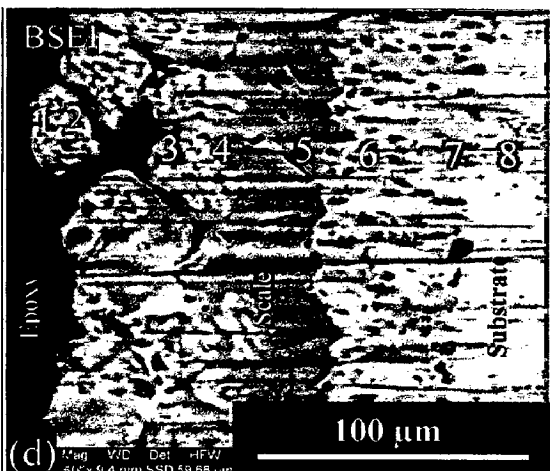
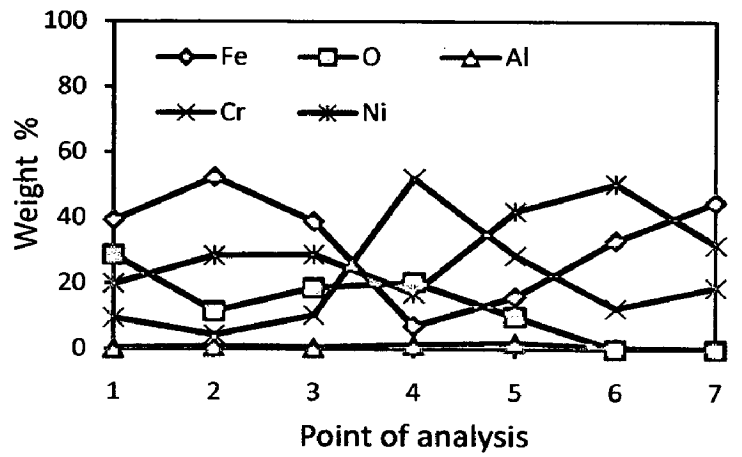
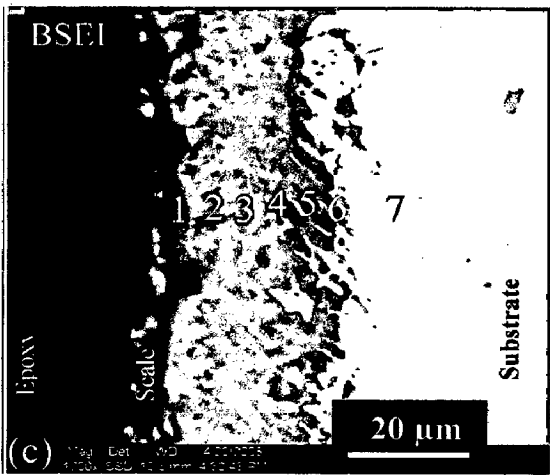
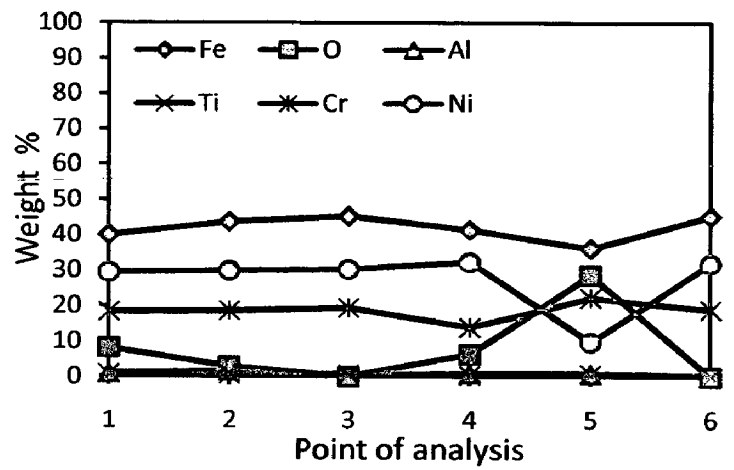
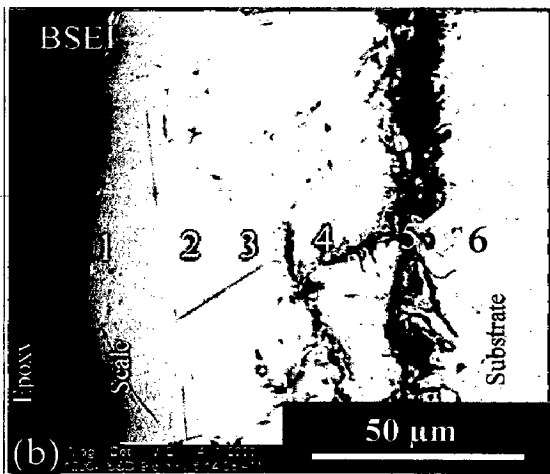
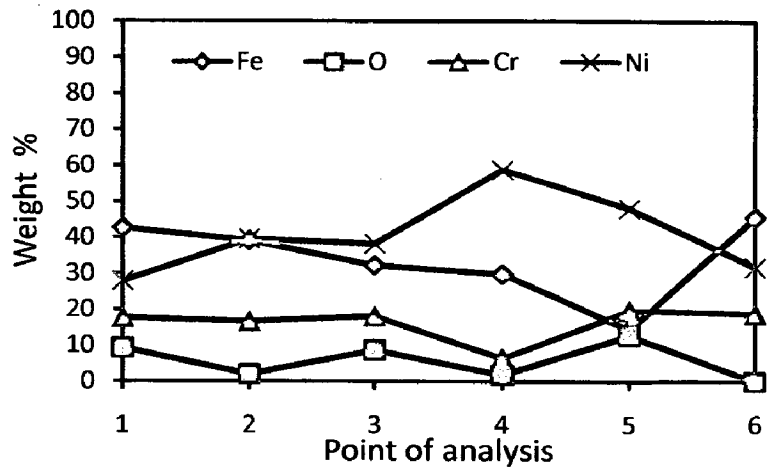
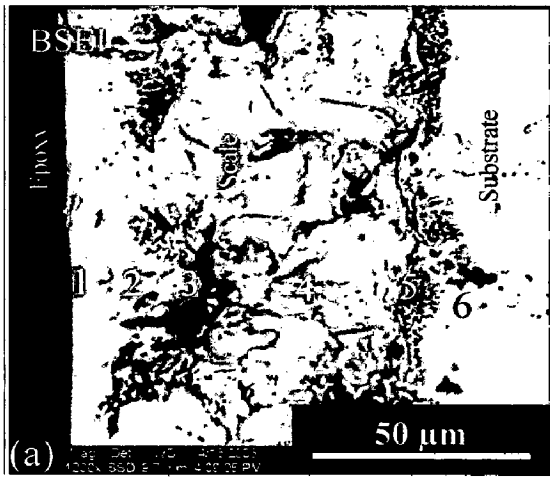
7.3.1.4 Cross-sectional analysis

7.3.1.4.1 Scale thickness

The oxidized samples were cut across the cross section using Buehler Isomet 1000 precision saw and mounted in transoptic mounting resin and subsequently mirror polished to obtain scanning electron back scattered micrographs and X-ray mapping of different elements for coated and uncoated Superfer 800H superalloy. The scale thickness values were measured from SEM back scattered micrographs as shown in Fig.7.24. The measured average scale thickness values for Superfer 800H superalloy, nanostructured thin TiAlN, nanostructured thin AlCrN, conventional thick TiAlN and conventional thick AlCrN coatings are 84, 81, 24, 108 and 106 μm respectively.

7.3.1.4.2 Cross-sectional scale morphology

Back Scattered Electron Image (BSEI) micrograph and elemental variation across the cross-section for coated and uncoated Superfer 800H superalloy subjected to cyclic oxidation in Na_2SO_4 -60% V_2O_5 (molten salt) environment at 900°C for 50 cycles are shown in Fig.7.24. In case of uncoated Superfer800H superalloy (Fig.7.24.a), EDAX analysis reveals the presence of iron, oxygen, nickel and chromium throughout the scale. The scale is dense and nearly uniform in thickness. At point 3 and 5 the concentration of Cr and O is higher, which points out the possibility of existence of Cr_2O_3 . The amount of Ni is higher at point 4. The concentration of O is varying throughout the scale and is almost zero at point 2 and 4. BSEI micrograph and elemental variation depicted in Fig.7.24 (b), for the exposed cross-section of nanostructured thin TiAlN coated Superfer 800H superalloy shows the dense and continuous scale.



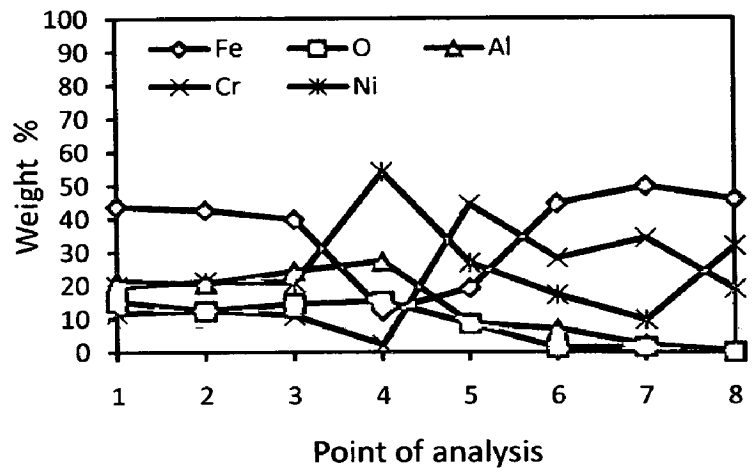
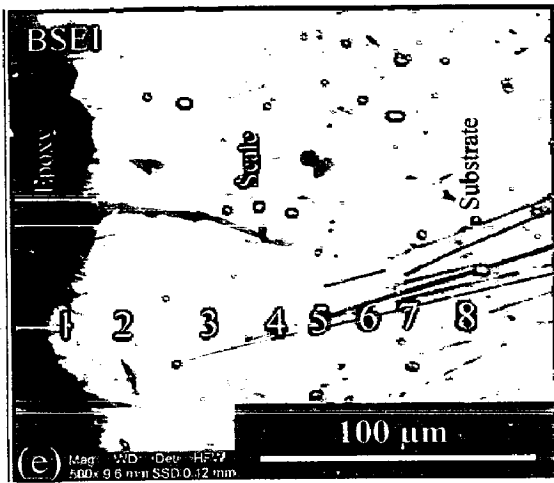


Fig. 7.24 Oxide scale morphology and variation of elemental composition across the cross-section of the uncoated and coated Superfer800H superalloy exposed to molten salt ($\text{Na}_2\text{SO}_4\text{-60}\%\text{V}_2\text{O}_5$) environment at 900°C for 50 cycles: (a) Uncoated Superfer800H superalloy (1200 X), (b) Nanostructured TiAlN coating (1200 X), (c) Nanostructured AlCrN coating (1700 X), (d) Conventional TiAlN coating (500 X), (e) Conventional AlCrN coating (500 X)

The EDAX analysis reveals the presence of Fe, Ni, Cr and O in the scale. The analysis at point 5 shows increase in the concentration of Cr and O, which points out the possibility of existence of Cr_2O_3 . In case of nanostructured AlCrN coating (Fig.7.24.c), a continuous and adherent oxide scale can be seen. The scale mainly consists of Fe, Ni and Cr with oxygen. A location at Point 4 shows increase in concentration of Cr and O with decreases in the concentration of Fe and Ni. In case of conventional TiAlN coated Superfer800H superalloy, the scale is uniform and adherent as depicted in Fig.7.24 (d). The EDAX point analysis indicates the presence of Fe, Ni, O, Al, Ti and Cr in the scale with variable amounts. The top scale is rich in Ti, Ni, Al, Fe and O. The concentration of Ti is almost zero in the subscale region. The analysis at point 4 shows increase in the amount of Al, Ni and O with less amount of Fe. The conventional thick AlCrN coated Superfer800H superalloy (Fig.7.24.e) indicates continuous, thick and adherent scale. EDAX point analysis shows the uniform presence of Fe, Al, Cr, O and Ni throughout the scale. The analysis at point 4 revealed higher concentration of Al, Ni and O with fewer amounts of Fe and Cr, whereas point 5 shows higher concentration of Cr.

7.3.1.4.3 X-Ray mapping

X-ray mappings for a part of oxide scale of uncoated and coated Superfer 800H superalloy oxidized in Na_2SO_4 -60% V_2O_5 (molten salt) environment at 900 °C for 50 cycles are shown in Fig.7.25. BSEI and X-ray mapping for the oxidized bare superalloy shows nickel dominating continuous scale, which contain substantial amounts of iron and oxygen (Fig.7.25.a). Chromium and oxygen have shown their co-presence in the form of some pockets in the scale and at the scale-substrate interface, where iron and nickel is completely missing. Figure 7.25 (b), shows X-ray mapping analysis of the scale formed on nanostructured TiAlN Superfer 800H superalloy. The BSEI image and X-ray mapping indicates the formation of a dense scale consisting mainly of iron, nickel, oxygen and chromium. Chromium and oxygen have shown their co-presence in the form of a band at the scale-substrate interface.

In case of nanostructured thin AlCrN coated superalloy, the BSEI and X-ray mapping are shown in Fig.7.25 (c). The X-ray mapping indicates the presence of iron oxygen nickel and chromium throughout the scale. A thin band of Cr and O is also indicated by X-ray mapping, where iron and nickel are completely absent. This band is followed by a thin band of Ni and O, where Fe and Cr are missing.

In case of conventional thick TiAlN coated superalloy (Fig.7.25.d), Fe and O are present throughout the scale. Thick band of Ti is present in the top scale whereas thin band of Ni is present at scale-substrate interface. The sub scale is rich in Al and Fe with substantial amount of O, Ni and Cr. Figure 7.25 (e), depicts the BSEI and X-ray mapping in case of conventional AlCrN coating. Aluminum is uniformly distributed in the scale along with substantial amount of Cr, Ni and Fe. The other elements like Ti and N have shown negligible presence.

7.3.2 Summary of Results

Results obtained after exposure of uncoated and coated Superfer 800H superalloy to cyclic oxidation in Na_2SO_4 -60% V_2O_5 molten salt environment at 900°C for 50 cycles are summarized in Table.7.6.

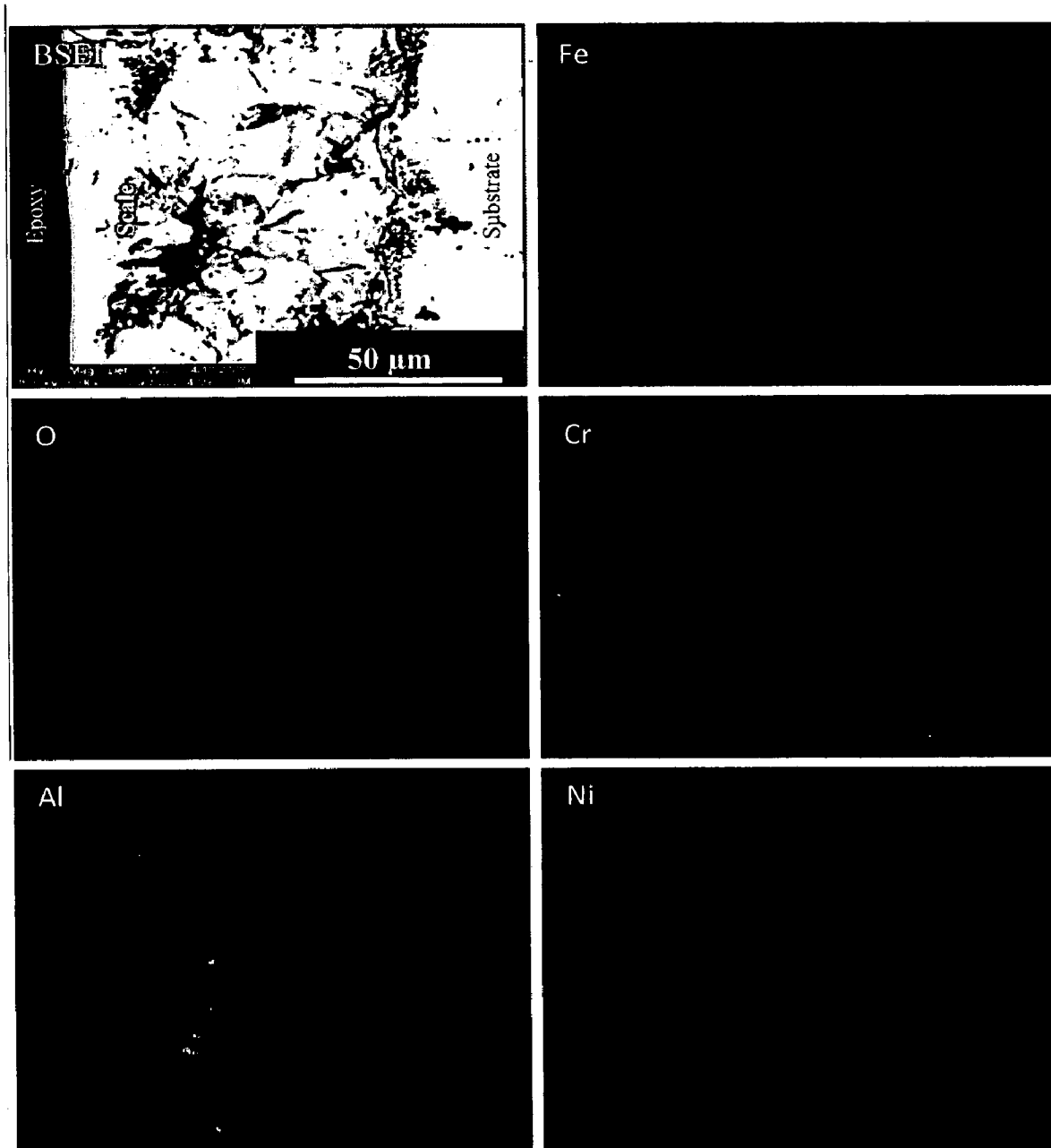


Fig. 7.25 (a) Composition image (BSEI) and X-ray mapping of the cross-section of uncoated Superfer 800H superalloy exposed to molten salt (Na_2SO_4 -60% V_2O_5) environment at 900°C for 50 cycles

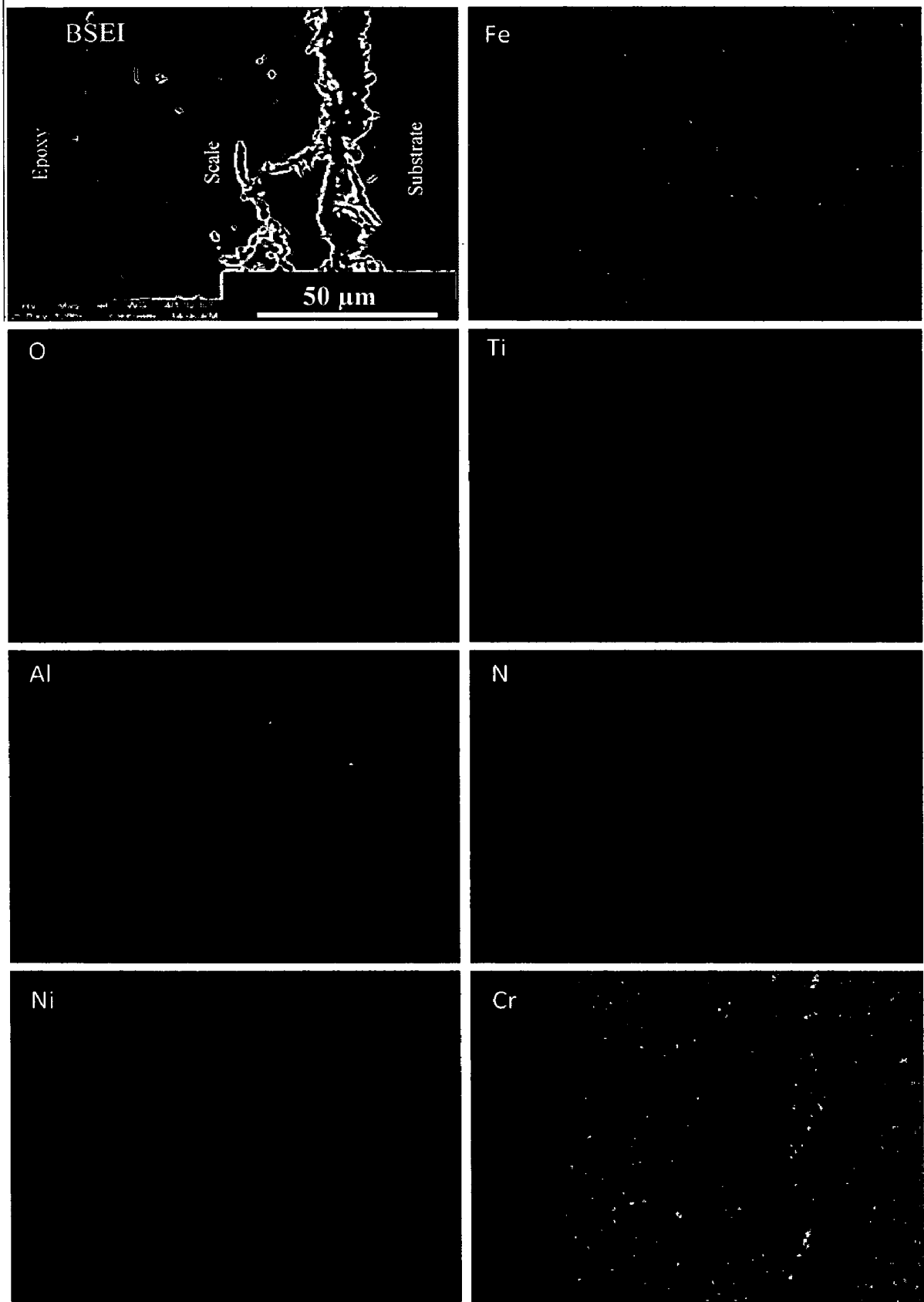


Fig. 7.25 (b) Composition image (BSEI) and X-ray mapping of the cross-section of Nanostructured TiAlN coated Superfer 800H superalloy exposed to molten salt ($\text{Na}_2\text{SO}_4\text{-60\%V}_2\text{O}_5$) environment at 900°C for 50 cycles

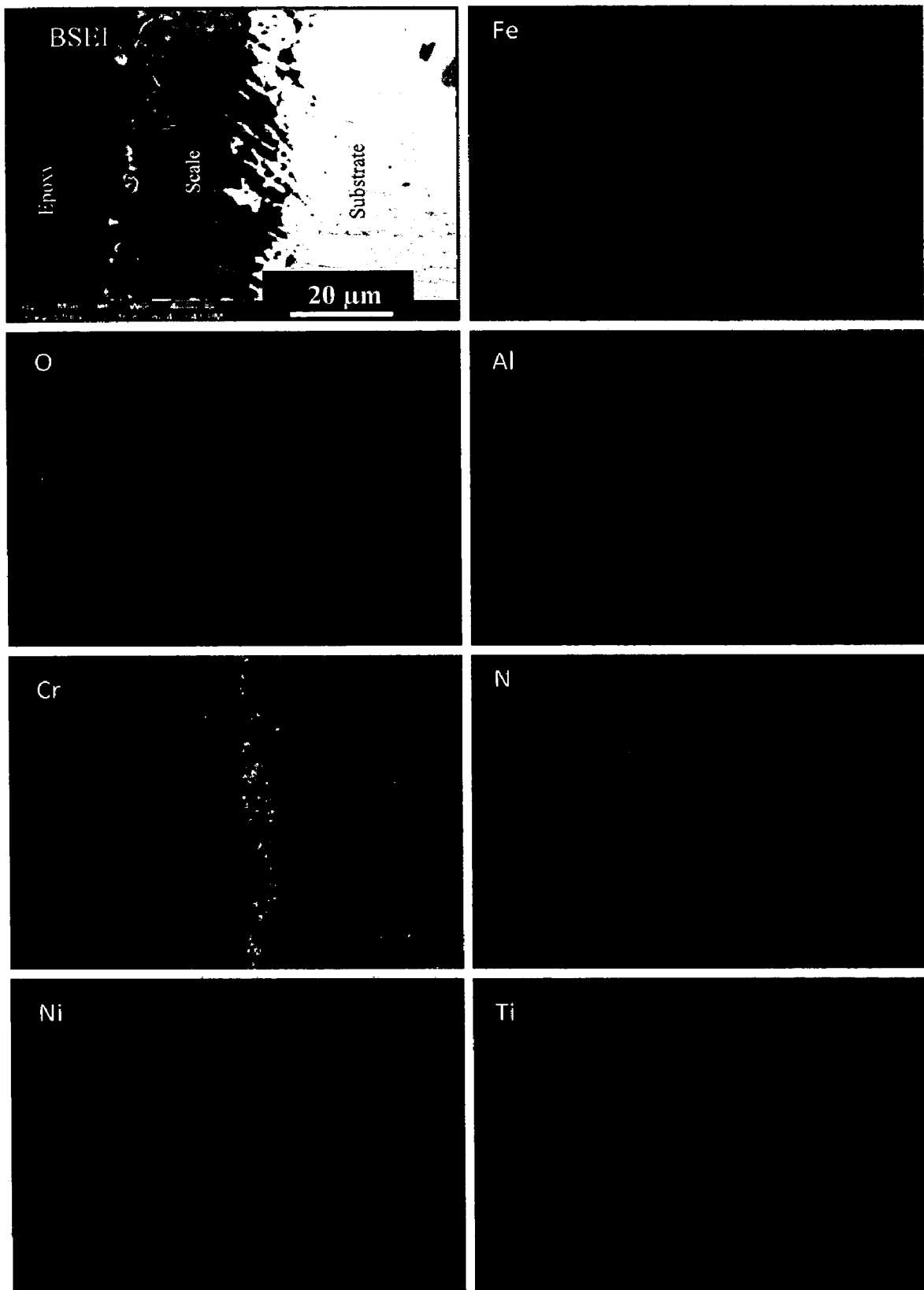


Fig. 7.25 (c) Composition image (BSEI) and X-ray mapping of the cross-section of Nanostructured AlCrN coated Superfer 800H superalloy exposed to molten salt ($\text{Na}_2\text{SO}_4\text{-60}\%\text{V}_2\text{O}_5$) environment at 900°C for 50 cycles

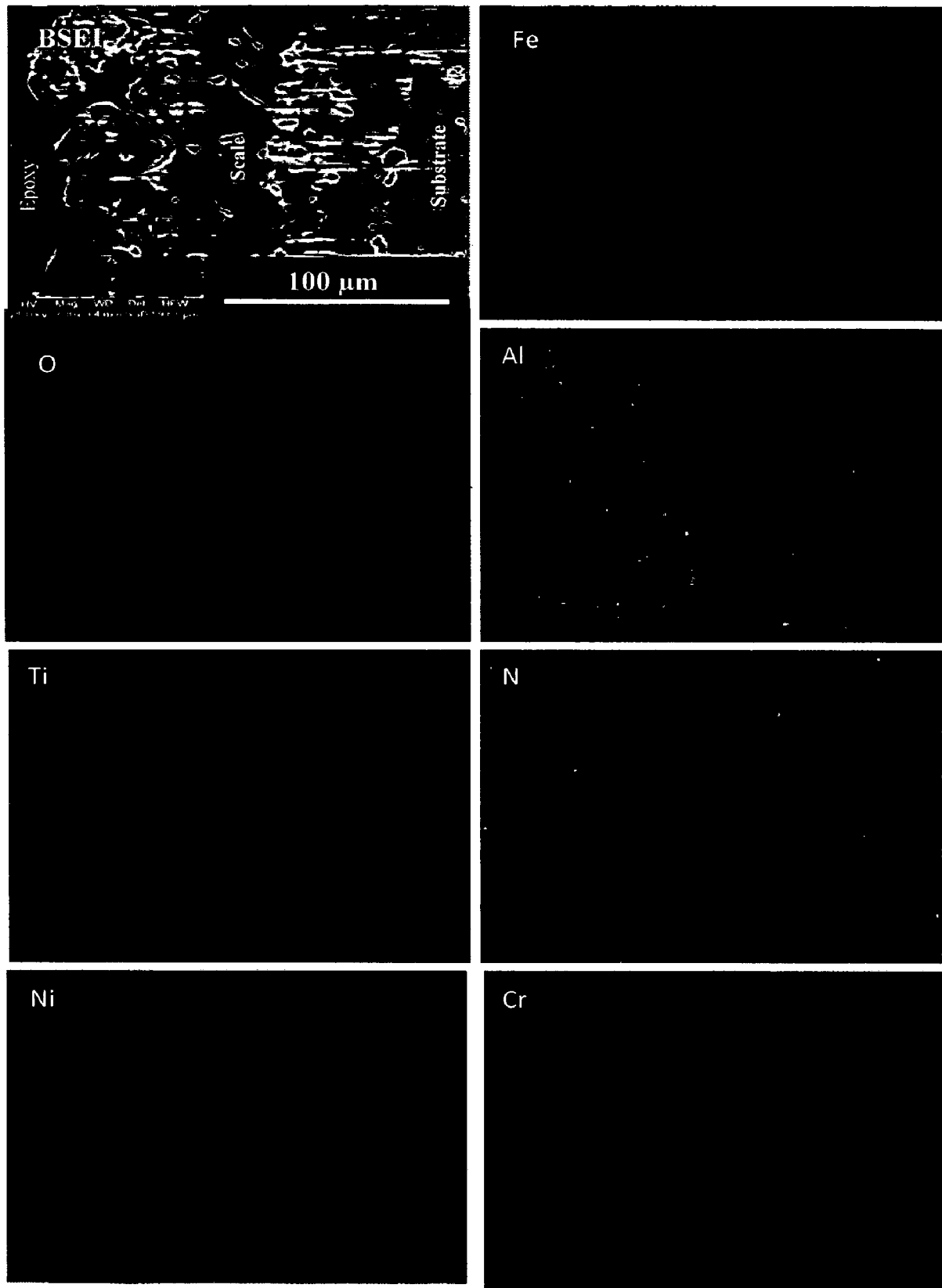


Fig. 7.25 (d) Composition image (BSEI) and X-ray mapping of the cross-section of conventional TiAlN coated Superfer 800H superalloy exposed to molten salt (Na_2SO_4 -60% V_2O_5) environment at 900°C for 50 cycles

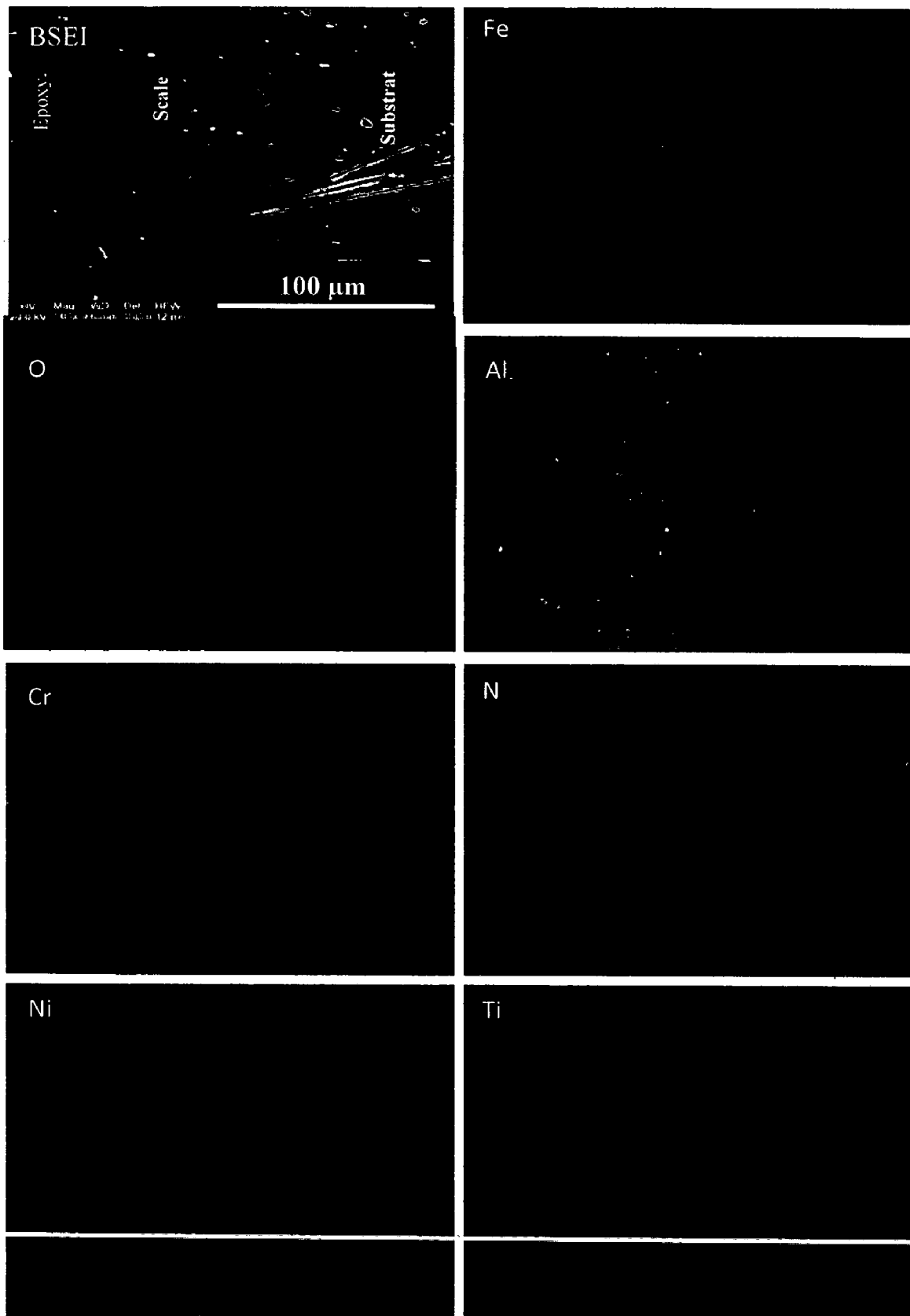


Fig. 7.25 (e) Composition image (BSEI) and X-ray mapping of the cross-section of conventional AlCrN coated Superfer 800H superalloy exposed to molten salt ($\text{Na}_2\text{SO}_4\text{-60\%V}_2\text{O}_5$) environment at 900°C for 50 cycles

Table 7.6 Summary of the results obtained for uncoated and coated Superfer 800H superalloy subjected to cyclic oxidation in molten salt (Na_2SO_4 -60% V_2O_5) environment at 900°C for 50 cycles

Coating	Cumulative Weight gain (mg/cm^2)	Parabolic rate constant ($K_p \times 10^{-10} \text{ gm}^2\text{cm}^{-4}\text{s}^{-1}$)	XRD phases	Remarks
Uncoated Superfer 800H superalloy	24.51	33.65	Fe_2O_3 , Cr_2O_3 , NiO, NiCr_2O_4 and NiFe_2O_4	A dark grey colored scale appeared on the surface right from the 1 st cycle, which turned to blackish green colored surface along with a small light grey spot at the end of 50 th cycle. After 20 th cycle some shining dots were also appeared.
Nanostructured TiAlN coating	08.15	08.65	Fe_2O_3 , Cr_2O_3 , NiO, NiCr_2O_4 and NiFe_2O_4 and Al_2O_3	Color of the oxide scale at the end of the study was observed to be blackish green with some light grey spots on the surface. The scale starts falling in the boat from 19 th cycle and then after 26 th cycle the weight starts decreasing as the scale starts falling outside the boat in the tube furnace.
Nanostructured AlCrN coating	02.84	00.85	Fe_2O_3 , Cr_2O_3 , NiO, NiCr_2O_4 , NiFe_2O_4 and Al_2O_3	After 30 th cycle, the scale in the form of powder starts falling outside the boat in the tube furnace, which continued till 50 th cycle. At the end of the study, the surface appearance of the oxidized sample is blackish green with some light grey spots
Conventional TiAlN Coating	08.54	02.60	Al_2O_3 , Ti_3Al and NiO	At the end of the study; very light brownish grey color matrix with cream color spots appeared on the surface. Some amount of superficial spalling was noticed at the end of 2 nd cycle.
Conventional AlCrN coating	11.27	05.41	Al_2O_3 , Fe_2O_3 , Cr_2O_3 and NiO	The scale showed no signs of spalling and cracks. The scale remains intact with the substrate throughout the study and the color of the scale is light grey at the end of the study.

7.3.3 Discussion

The weight gain plot, Fig.7.19, show that the weight gained by bare Superfer 800H super alloy increases continuously due to the accelerated oxidation in the molten salt environment, where as the coated superalloy in all cases showed better hot corrosion resistance. The rapid increase in the weight gain during the initial period of exposure to Na₂SO₄-60%V₂O₅ (molten salt environment) environment at 900°C can be attributed to the possible formation of NaVO₃. Kolta et al. (1972) proposed that in the temperature range of 900°C, the Na₂SO₄ and V₂O₅ will combine to form NaVO₃, as represented by eq.(7.1) having a melting point of 610°C.



This NaVO₃ acts as a catalyst and also serves as an oxygen carrier to the base alloy through the open pores present on the surface, which will lead to the rapid oxidation of the base elements of the substrate to form a protective oxide scale. There may be simultaneous dissolution of protective oxide Cr₂O₃ in the molten salt due to the reaction (Seiersten and Kofstad, 1987; Swaminathan et al., 1993):



The Na₂CrO₄ gets evaporated as a gas (Fryburg et al., 1984 and Guo et al., 2006). The rapid increase in the weight gain during the initial period was also reported by Sidhu et al. (2006), Harpreet Singh et al.(2005), Tiwari and Prakash (1997) and Ul-amid (2003) during hot corrosion studies. Also, the higher weight gain during the first few cycles can be attributed to the rapid formation of oxides at the splat boundaries and within the open pores due to the penetration of the oxidizing species. Once the oxides are formed at places of porosity and splat boundaries, the coating becomes dense and the diffusion of oxidizing species to the internal portions of the coatings gets slowed down and the growth of the oxides becomes limited mainly to the surface of the specimens. This, in turn, will make the weight gain and hence the oxidation rate steady with the further progress of exposure time (Singh et al., 2007 and Sidhu et al., 2006).

In case of conventional thick TiAlN and AlCrN coatings, after 5th cycle the weight gain rate becomes almost constant. Thus, these conventional coatings are providing full

protection to the substrate alloy in molten salt environment at 900°C. It can be inferred from the weight gain plots that the uncoated Superfer 800H superalloy have shown high rate of oxidation as compared to the coatings. Aluminum (Belzunce et al., 2001) and Chromium (Singh et al., 2005) exhibits higher affinity for oxygen to form Al_2O_3 and Cr_2O_3 during the earlier stages of hot corrosion. The formation of protective Al_2O_3 and Cr_2O_3 oxides in case of conventional thick TiAlN and AlCrN coated Superfer 800H superalloy has also been supported by EDAX analysis of surface (Fig.7.23.d and e) and cross-section (Fig. 7.24.d and e), XRD analysis (Fig.7.22) and X-ray mapping (Fig.7.25.d and e).

The nanostructured thin coatings have shown weight gain in the initial cycles and then after 25th cycle (in case of nanostructured TiAlN) and 30th cycle (in case of nanostructured AlCrN coating) the weight gain rate suddenly drops as the scale starts falling outside the boat in the tube furnace during the course of the study. So this weight gain or loss after 25th cycle (in case of nanostructured TiAlN) and 30th cycle (in case of nanostructured AlCrN coating) was not much relevant and thus not included in the study. Further, the overall weight gain is highest in case of uncoated superfer 800H superalloy (24.51 mg/cm^2) and is lowest in case of nanostructured thin AlCrN coating (2.84 mg/cm^2 up to 30th cycle). The sequence of oxidation rates based on weight gain values for the coated and uncoated superalloy after 50 cycles of oxidation is:

Bare SF > Conventional AlCrN > Conventional TiAlN > Nanostructured TiAlN > Nanostructured AlCrN

The surface scales for the coatings, have shown excellent spallation resistance against the cyclic oxidation in air, which indicates further effectiveness of the coatings under study as the cycle-oxidation behavior of an alloy is dictated mainly by scale spallation resistance as per the opinion of Stott (1992). These XRD results (Fig.7.22) are well supported by the surface EDAX and X-Ray mapping analysis in the present study. In case of uncoated, nanostructured thin TiAlN and nanostructured thin AlCrN coated Superfer 800H superalloy; the oxide phases found are Fe_2O_3 , Cr_2O_3 , NiO, NiCr_2O_4 and NiFe_2O_4 . Furthermore, the X-ray mappings, Fig.7.25 (a) for the oxidised bare superalloy Superfer 800H are in good agreement with those reported by Polman et al. (1990) for a similar superalloy Incoloy 800H. The presence of Cr_2O_3 and NiO in the top scale of bare, nanostructured TiAlN and AlCrN coated superalloy is supported by the surface color of these samples after oxidation studies, which is blackish green. Greenish color might be

attributed to the presence of both Cr_2O_3 and NiO as reported by Khajavi and Shariat (2004). Further, the main phases identified for the conventional thick TiAlN coating are Al_2O_3 , Ti_2O_3 and NiO . The oxide phases found in case of conventional thick AlCrN coating are Al_2O_3 , Fe_2O_3 and Cr_2O_3 along with NiO .

It could be seen from the respective X-Ray mapping (Fig.7.25) analysis that there is no sign of depletion of basic elements from the substrate alloys, except in case of nanostructured TiAlN coating. This indicates that the coatings have been successful in acting as a reservoir for the formation of protective oxides/spinels, consequently may increase the service life of the substrate alloy. Moreover, it is clear from the back scattered images (Fig.7.24) of cross-section for the coatings subjected to oxidation for 50 cycles that the coatings appear to be integral with the substrates. The X-Ray mapping analysis for the conventional thick TiAlN and AlCrN coatings coating shows that the oxygen has not penetrated into the substrate alloys. In case of uncoated superalloy; some pockets in the scale can be seen where Cr and O are present where Fe and Ni are completely missing (Fig.7.25.a). Also, the top scale is rich in Ni , Fe , Cr and O which is supported by XRD (Fig.7.22) and EDAX analysis of the surface (Fig.7.23.a) and cross-section (Fig.7.24.a). The presence of non protective NiO in the top scale of oxidized bare superalloy allows the penetration of corrosive species through the scale to the substrate. The identification of Fe_2O_3 in the scale (Fig.7.22) of uncoated superalloy after hot corrosion experiments indicated that non-protective conditions were established when Na_2SO_4 -60% V_2O_5 (molten salt) environment was present on the surface. This might be the reason of higher weight gain rate in case of uncoated Superfer 800H superalloy.

Some negligible cracking and minor spalling may be attributed to the thermal shocks due to differences in the heat expansion coefficients of the oxides, coatings and the substrate (Rapp et al, 1981, Sidhu et al. 2003, Singh H et al. 2004, Evans et al. 2001, Wang et al., 2002, Niranatlumpong et al., 2000 and Liu et al., 2001). The stress concentration factor at the sharp edges of the specimens might have also contributed to this minor cracking and spalling. It is pertinent to mention here that the edges of the specimens were kept sharp deliberately to add one more severe condition to the accelerated testing of the coatings. Otherwise in actual designs the sharp edges are always avoided to eliminate stress concentration. It can be inferred based on the

present investigation that conventional thick TiAlN, AlCrN, nanostructured thin TiAlN (up to 25th cycle) and nanostructured AlCrN (up to 30th cycle) coatings have provided a very good oxidation resistance in molten salt environment at high temperature.

7.3.4 Conclusions

The high temperature oxidation behaviors of uncoated and coated Superfer 800H superalloy have been investigated in Na₂SO₄-60%V₂O₅ (molten salt) environment at 900°C for 50 cycles. The behavior of nanostructured TiAlN and AlCrN coatings were compared with conventional counterparts and the following conclusions are made:

1. The oxidation rate (total weight gain values after 50 cycles) of the coated and uncoated Superfer 800H superalloy follows the sequence as given below:
Bare SF 800H > Conventional AlCrN > Conventional TiAlN > Nanostructured TiAlN > Nanostructured AlCrN
2. The plasma sprayed gas nitride conventional thick TiAlN and AlCrN coatings when subjected to cyclic oxidation in Na₂SO₄-60%V₂O₅ molten salt at 900°C for 50 cycles developed a protective scale mainly consisting on aluminum oxide.
3. The nanostructured thin coatings have shown weight gain in the initial cycles and then after 25th cycle (in case of nanostructured TiAlN) and 30th cycle (in case of nanostructured AlCrN coating) the weight gain rate suddenly drops as the scale starts falling outside the boat in the tube furnace during the course of the study.
4. The conventional thick coatings have shown relatively higher weight gain in the early cycles of study, followed by tendency to show gradual weight gain with further increase in number of cycles. In case of uncoated superalloy; the weight gain is highest.
5. It can be inferred based on the present investigation that conventional thick TiAlN, AlCrN, nanostructured thin TiAlN (up to 25th cycle) and nanostructured AlCrN (up to 30th cycle) coatings have provided a very good oxidation resistance in molten salt environment at high temperature.
6. The oxide scale formed is adherent to the substrate in all specimens after hot corrosion studies.

7.4 EROSION STUDIES IN SIMULATED COAL-FIRED BOILER ENVIRONMENT

The present work has been focused to compare the high temperature erosion behavior of conventional thick (by plasma spraying and gas nitrided) and nanostructured thin (by physical vapor deposition process) TiAlN and AlCrN coatings on Superfer800H superalloy. The erosion studies were carried out using a high temperature air-jet erosion test rig at a velocity of 35 ms^{-1} and impingement angles of 30° and 90° . The tests were carried out at high temperatures. The two temperatures were taken for the test, sample temperature 400°C and air/erodent temperature 900°C simulated to service conditions of boiler tubes in which sample temperature and flow gas temperature correspond to the inner and outer temperature of water wall pipes. The alumina particles of average size $50 \mu\text{m}$ were used as erodent. Erosion rates in terms of volumetric loss (mm^3/g) for different uncoated and coated alloys are compared. The eroded samples were analyzed with SEM/EDX and optical profilometer. The erosion rate data for each coated alloy has been plotted along with uncoated alloy in order to assess the coating performance. Efforts have been made to understand the mode of erosion.

7.4.1 Results

7.4.1.1 Visual observations

The macrographs for uncoated and coated Superfer 800H superalloy subjected to erosion studies in simulated coal-fired boiler environment are shown in Fig.7.26. The effect of corrosion along with the erosion was observed. The shape of the scar (developed by constant strike of erodent) is circular in case of normal impact (at 90°) and elliptical in case of oblique impact (at 30°) of erodent. The uncoated superalloy shows small scar with a thin scale after erosion. The erosion seems to clean the scale off the surface in the eroded/corroded region. The impact of erodent removes the scale. Away from this eroded region a thin layer of scale was observed on the surface and the eroded/corroded region showed dark grey colored scar (Fig.7.26.a). The nanostructured TiAlN coated Superfer 800H showed clear marks of erosion as shown in Fig.7.26 (b). The color of the coated specimen changed from violet-grey to whitish grey at scar and blackish blue ring around the scar.

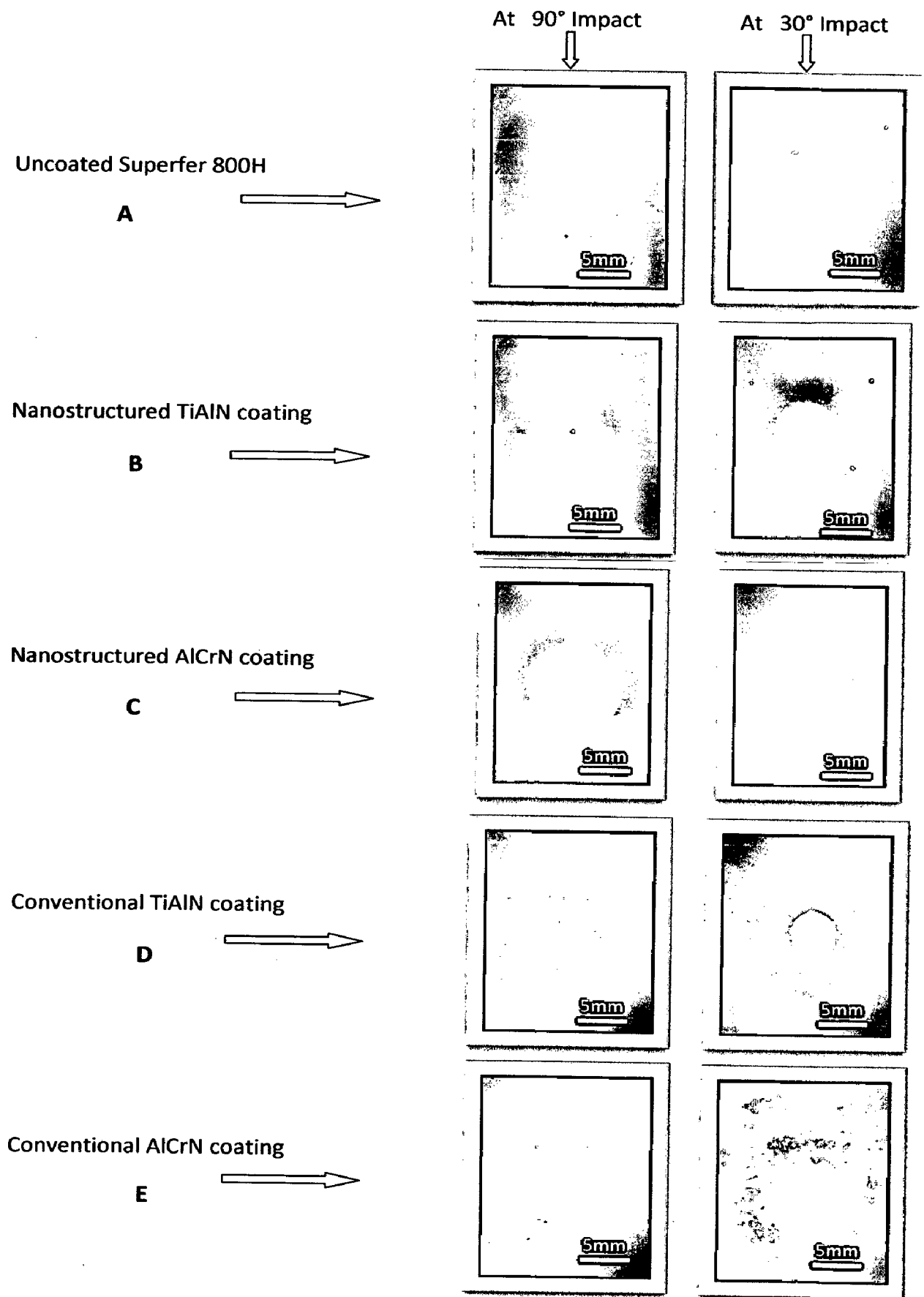


Fig. 7.26 Surface macrographs of eroded uncoated and coated Superfer 800 superalloy exposed to high temperature erosion studies in simulated coal-fired boiler environment

The macrograph in case of eroded nanostructured AlCrN coating are shown in Fig.7.26 (c). The color of the scars was observed as light grey surrounded by dark colored ring. A visual observation of conventional thick TiAlN and AlCrN coated Superfer 800H (Fig.7.26.d and e), showed the formation of dark grey colored scar surrounded by a light colored ring. Also, the un-eroded area around the scars appeared as rough surface.

7.4.1.2 Erosion rate

The erosion loss has been calculated by volume change method. The volume loss occurred after erosion testing was measured by using non contact optical profilometry as explained in chapter 3. The erosion depth was measured at six random locations to obtain the average erosion depth of an eroded scar. At each location (including eroded and un-eroded area) surface profiles were taken.

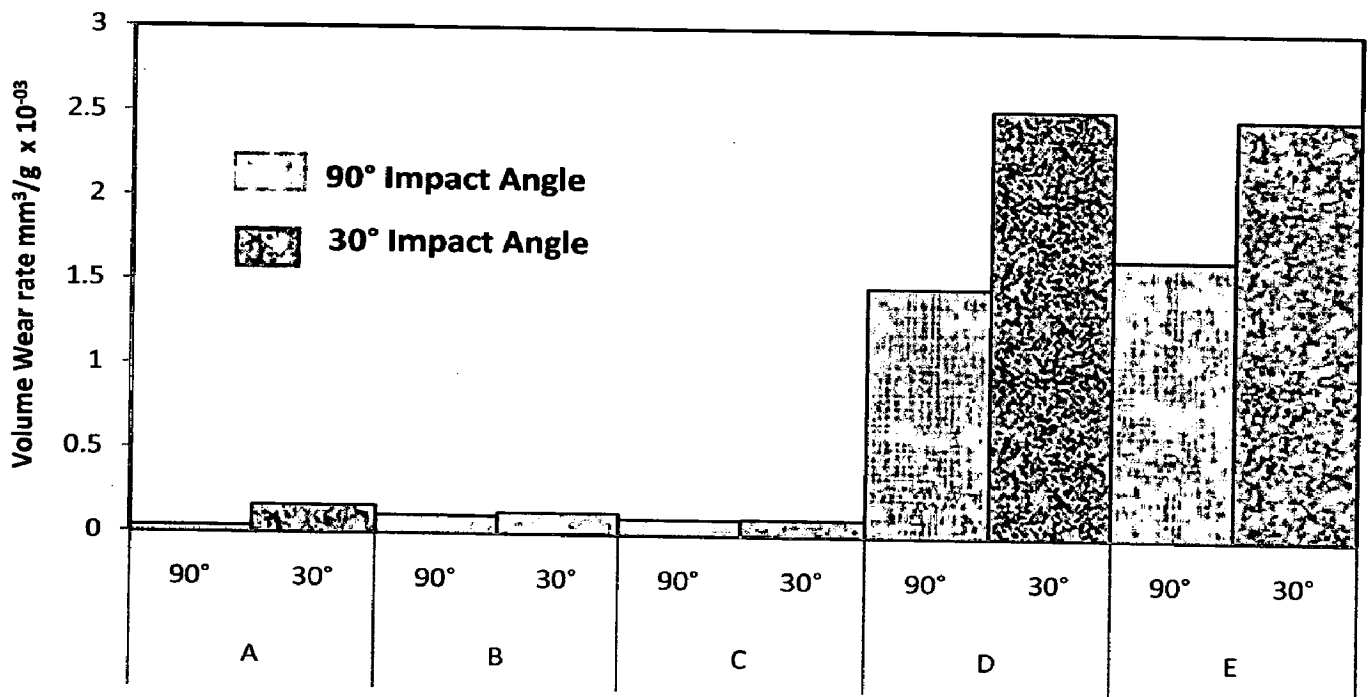


Fig.7.27 Column chart showing the Volume wear rate of uncoated and coated Superfer 800H superalloy eroded at normal and oblique impact: (A) Uncoated Superfer 800H, (B) Nanostructured TiAlN coating, (C) Nanostructured AlCrN coating, (D) Conventional TiAlN coating, (E) Conventional AlCrN coating

The erosion rate for uncoated and coated Superfer 800H superalloy at an impact velocity of 35 ms^{-1} and impingement angle of 30° and 90° when substrate temperature was 400°C and surrounding air at 900°C ; is shown in Fig. 7.27. The

volume erosion rate for uncoated Superfer 800H, nanostructured thin TiAlN, nanostructured thin AlCrN, conventional thick TiAlN and conventional thick AlCrN coatings; is 0.0384×10^{-3} , 0.1060×10^{-3} , 0.0935×10^{-3} , 1.475×10^{-3} and 1.653×10^{-3} mm^3/gm respectively at 90° impact angle. While at 30° impact, the volume erosion rate for uncoated superalloy, nanostructured thin TiAlN, nanostructured thin AlCrN, conventional thick TiAlN and conventional thick AlCrN coatings; is 0.1621×10^{-3} , 0.12586×10^{-3} , 0.099352×10^{-3} , 2.534×10^{-3} and 2.48996×10^{-3} mm^3/gm respectively.

From the graph, it can be inferred that the erosion rate of the uncoated Superfer 800H superalloy eroded at oblique impact i.e. at 30° impingement angle is more as compared to erosion rate at 90° impact thus showing the typical behavior of ductile materials. The similar behavior was observed in case of the nanostructured thin TiAlN and AlCrN hard coatings with negligible overall volume erosion loss (Fig.7.27). In case of the conventional thick TiAlN and AlCrN coated Superfer 800H; the erosion rate at oblique impact i.e. at 30° impingement angle is more as compared to erosion rate at 90° impact with higher volume erosion rate as compared to the uncoated and nanostructured coated Superfer 800H superalloy.

7.4.1.3 SEM/EDAX Analysis

SEM micrographs along with EDAX point analysis reveals the surface morphology of the uncoated and coated Superfer 800H superalloy subjected to erosion studies in simulated coal-fired boiler environment when substrate temperature was 400°C and surrounding air at 900°C ; are shown in Fig. 7.28 and 7.29. The SEM observations were made on the eroded surface of all the uncoated and coated superalloy specimens at both the impact angles i.e. at 90° and 30° . Scanning electron microscopy (SEM) revealed various erosion mechanisms like metal removal, oxide chipping, fracture and spalling within the oxide/coating layer and at the scale/metal interface etc. The micrographs have revealed fracture at the surfaces with impressions of formation of craters with crack network.

Micrographs (Fig.7.28) for the eroded surfaces of uncoated and coated Superfer 800H superalloy at 90° impact angle, clearly indicates the formation of crater, oxide fracture and removal, coating fracture and retained erodent.

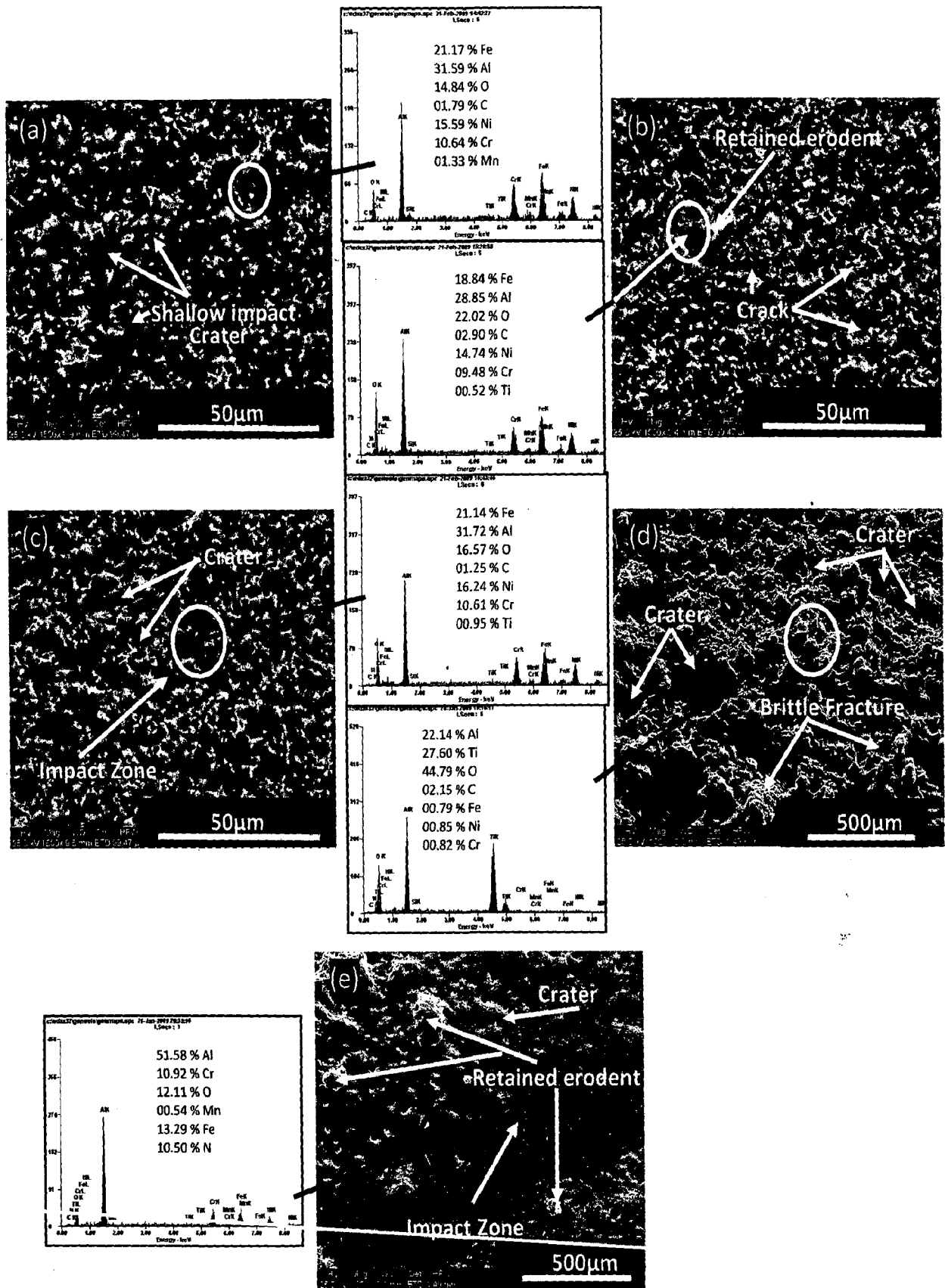


Fig. 7.28 Surface-scale morphology and EDAX patterns from different spots on eroded uncoated and coated Superfer 800H superalloy exposed to high temperature erosion studies in simulated coal-fired boiler environment at impact angle 90°: (a) Uncoated Superfer 800H, (b) Nanostructured TiAlN coating, (c) Nanostructured AlCrN coating, (d) Conventional TiAlN coating, (e) Conventional AlCrN coating

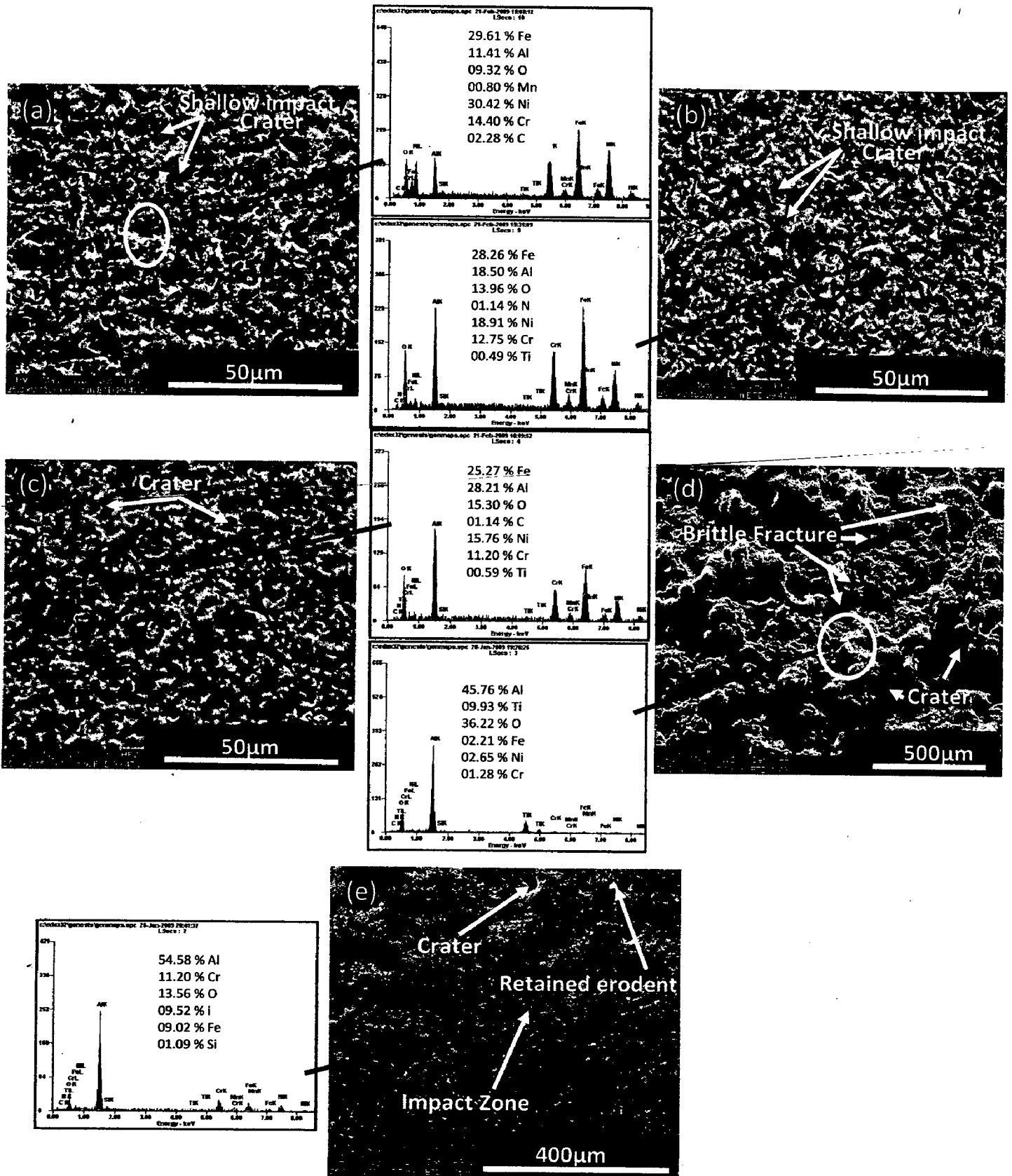


Fig. 7.29 Surface-scale morphology and EDAX patterns from different spots on eroded uncoated and coated Superfer 800H superalloy exposed to high temperature erosion studies in simulated coal-fired boiler environment at impact angle 30°: (a) Uncoated Superfer 800H, (b) Nanostructured TiAlN coating, (c) Nanostructured AlCrN coating, (d) Conventional TiAlN coating, (e) Conventional AlCrN coating

It can be observed from the micrographs of the eroded surface of the uncoated superalloy (Fig.7.28.a) that the erodent particles deform the exposed surface by ploughing and introducing the craters in the matrix by displacing material to the side. EDAX analysis revealed the presence of Fe, Al, Ni, Cr and O as the main elements on the eroded area, which indicates the presence of retained erodent i.e. alumina. In case of nanostructured TiAlN coating (Fig.7.28.b); the micrograph revealed cracks and retained erodent. EDAX analysis indicates the presence of Fe, Al, Ni, Cr and O as the main elements along with negligible amount of Ti and C. This is the indication that the nanostructured coating is severely damaged and fractured when the eroding particle strikes the surface of a coating at 90°; and hence failed to protect the substrate. Further, in case of nanostructured AlCrN coating; the signs of coating removal and wider impact crater have been observed (Fig. 7.28.c). EDAX analysis shows the presence of Al, Ni, Cr, Fe and O as the main elements along with some amount of chromium. The higher percentage of Fe indicates the substrate has been exposed and the erodent impacts causes cracking and fracture of the coating and thus removed the coating completely.

The micrograph of the conventional TiAlN coating (Fig.7.28.d) revealed the oxide fracture and removal at various locations. When the eroding particle strikes the surface of the coating at 90° the material is severely damaged and fractured as shown in Fig. 7.28 (d). EDAX analysis shows the presence of Al, Ti and O as the main elements along with very less amount of Ni, Cr, Fe and C. The coating has successfully protected the substrate. Further in case of conventional AlCrN coating, the erodent particle impacts have severely damaged the coating by causing cracking and fracture. The impact zone is wider (Fig.7.28.e) which may be caused by the continuous subsequent impacts of erodent particles. EDAX analysis revealed the presence of Al, Cr, N and O as the main elements with small amount of Fe and Mn. Thus, the conventional thick coatings have protected the substrate after three hours continuous erodent impacts at an impact velocity of 35 ms⁻¹ and impingement angle of 90° when substrate temperature was 400°C and surrounding air at 900°C.

In case of 30° impact, Micrographs (Fig.7.29) for the eroded surfaces of uncoated and coated Superfer 800H superalloy clearly indicates presence of retained erodent, the formation of wider and shallow crater, crack propagation, oxide fracture and removal and coating fracture. In case of uncoated superalloy; the micrographs (Fig.7.29.a)

revealed the severe deformation at the surface resulting in formation of craters. EDAX analysis revealed the presence of Fe, Al, Ni, Cr and O as the main elements on the eroded area, which indicates presence of retained erodent i.e. alumina. Micrograph in case of nanostructured TiAlN coating (Fig.7.29.b); revealed shallow impact craters. EDAX analysis indicates the presence of Fe, Al, Ni, Cr and O as the main elements along with some amount of Ti and N. It can be inferred that the nanostructured TiAlN coating gets severely damaged and fractured when the eroding particle strikes the surface of a coating at 30° and failed to protect substrate. Further, in case of nanostructured AlCrN coating; the signs of crater have been observed (Fig. 7.29.c). EDAX analysis shows the presence of Al, Ni, Cr, O and Fe along with some amount of C and Ti. The erodent impacts causes cracking and fracture of the coating, and removed the coating completely thus exposing the substrate which is supported by the EDAX analysis as the presence of Fe with higher amount (Fig.7.29.c).

The micrograph of the conventional TiAlN coating (Fig.7.29.d) revealed the oxide fracture and removal at various locations. When the eroding particle strikes the surface of the coating at 30° the material is severely damaged and fractured as shown in Fig. 7.29 (d). EDAX analysis shows the presence of Al, Ti and O as the main elements along with very less amount of Ni, Cr, Fe and C. The coating has successfully protected the substrate. Further in case of conventional AlCrN coating, the erodent particle impacts have severely damaged the coating by causing cracking and fracture. The impact zone is wider (Fig.7.29.e) which may be caused by the continuous subsequent impacts of erodent particles. EDAX analysis revealed the presence of Al, Cr, N and O as the main elements with small amount of Fe and Mn. Thus, the conventional thick coatings have protected the substrate when exposed to simulated coal-fired boiler environment.

7.4.2 Discussion

In erosion testing, the material is eroded by continuous impact of erodent particles; the erosion starts at the centre first, and then proceeds towards the edges of the samples. The shape of developed scar depends on the angle of impact. When erodent strikes the surface at an impact angle of 90°, material is eroded creating a circular depression; while at a 30° impact angle, material is eroded forming an elliptical shape depression. The erosion rate for uncoated and coated Superfer 800H superalloy

boiler steel at an impact velocity of 35 ms^{-1} and impingement angle of 30° and 90° when substrate temperature was 400°C and surrounding air at 900°C ; is shown in Fig. 7.27. The volume erosion rate for uncoated Superfer 800H, nanostructured thin TiAlN, nanostructured thin AlCrN, conventional thick TiAlN and conventional thick AlCrN coatings; is 0.0384×10^{-3} , 0.1060×10^{-3} , 0.0935×10^{-3} , 1.475×10^{-3} and $1.653 \times 10^{-3} \text{ mm}^3/\text{gm}$ respectively at 90° impact angle. Based on the present data the erosion rates for 90° impact angle can be arranged in the following order:

Conventional AlCrN > Conventional TiAlN > Nanostructured TiAlN > Nanostructured AlCrN > Bare alloy

It can be inferred from the above data that the relative erosion resistance of conventional thick AlCrN coating is least among the uncoated and coated Superfer 800H superalloy specimens. The SEM/EDAX analysis (Fig.7.28) indicates that in case of conventional TiAlN and AlCrN coated superalloy; the coating is still there after three hours continuous erodent impacts at an impact velocity of 35 ms^{-1} and impingement angle of 90° when substrate temperature was 400°C and surrounding air at 900°C . These coatings have successfully protected the substrate. The nanostructured coatings were removed by the continuous strikes of the eroding particles on the surface of the coating at 90° (Fig.7.28).

While at 30° impact, the volume erosion rate for uncoated superalloy, nanostructured thin TiAlN, nanostructured thin AlCrN, conventional thick TiAlN and conventional thick AlCrN coatings; is 0.1621×10^{-3} , 0.1258×10^{-3} , 0.0993×10^{-3} , 2.534×10^{-3} and $2.489 \times 10^{-3} \text{ mm}^3/\text{gm}$ respectively. Based on the present data the erosion rates for 30° impact angle can be arranged in the following order:

Conventional TiAlN > Conventional AlCrN > Bare alloy > Nanostructured TiAlN > Nanostructured AlCrN

it can be inferred from the above data that the relative erosion resistance of conventional thick TiAlN coating is least among the uncoated and coated superalloy specimens. Further, the SEM/EDAX analysis (Fig.7.29) indicates that in case of conventional TiAlN and AlCrN coated superalloy; the coating is still there after three hours continuous erodent impacts at an impact velocity of 35 ms^{-1} and impingement angle of 30° when substrate temperature was 400°C and surrounding air at 900°C . These coatings have successfully protected the substrate. The nanostructured

coatings were removed by the continuous strikes of the eroding particles on the surface of the coating at 30° (Fig.7.29).

The solid particle erosion rate of the uncoated and nanostructured thin TiAlN and AlCrN coated Superfer 800H superalloy as shown in Fig.7.27 indicated that maximum erosion took place at 30° impact angle, which indicate ductile behavior as proposed by Murthy et al. (2001). Authors suggested that the material subjected to erosion initially undergoes plastic deformation and is later removed by subsequent impacts of the erodent on the surface. The ploughing occurs by the impact of the erodent particles and lips or ridges are formed at the bank of the craters. These lips are fractured or removed with further erosion. At low erosion temperatures, at high impact velocities and feed rates, there is no oxide scale. Even if there is any oxide scale, it will be very thin and it will be able to deform in the same manner as that of the substrate target. The works of Shida and Fujikawa (1985), Singh and Sundararajan (1990) Levy et al., (1986) can be considered elevated temperature erosion of metals with minimum or negligible oxidation. Under such circumstances, erosion takes place from the metallic surface and this mechanism of erosion is called metal erosion. Most of the metallic materials, irrespective of temperature of erosion, exhibit a ductile behavior, i.e. a maximum erosion rate at oblique impact angles (Tabakoff and Vittal, 1983). The erosion behavior in this regime is similar to the ambient temperature erosion behavior of metallic materials. The erosion response in the metal erosion regime is ductile as described by Bellman and Lavy (1981). Authors suggested that the creation of platelet-like edges by impact extrusion protrude outward over adjacent material and the loss of these platelets appears to be responsible for the mass loss. Authors have further explained that repeated deformation of craters and forming of new craters is common and some platelets are extruded several times before getting knocked off.

Sundararajan and Roy (1997) proposed a model of metal erosion and oxide erosion. According to his model if steady state thickness of the oxide scale is smaller than the critical thickness of the oxide scale, three modes of interaction between erosion and oxidation are possible. In the first case, which applies either when there is no oxide scale or when the depth of deformation is much higher than the thickness of the oxide scale (as in the case of uncoated and nanostructured thin coated Superfer 800 superalloy in present case), metal erosion becomes important (presented in Figs 7.30.a

and b). In the second case, when the depth of deformation is smaller than the steady state thickness of the oxide scale, erosion of the oxide scale takes place as illustrated in Fig. 7.30 (c).

The solid particle erosion rate of the conventional thick TiAlN and AlCrN coated Superfer 800H superalloy as shown in Fig.7.27 indicated that maximum erosion took place at 30° impact angle, which indicate ductile behavior of the conventional coatings. The difference in erosion rates for shallow and normal impact angles can be attributed to the different material removal mechanisms in these two cases. At low angle impact, the kinetic energy of the erodent particles contributes mainly to the ploughing mechanism and very little to normal repeated impact.

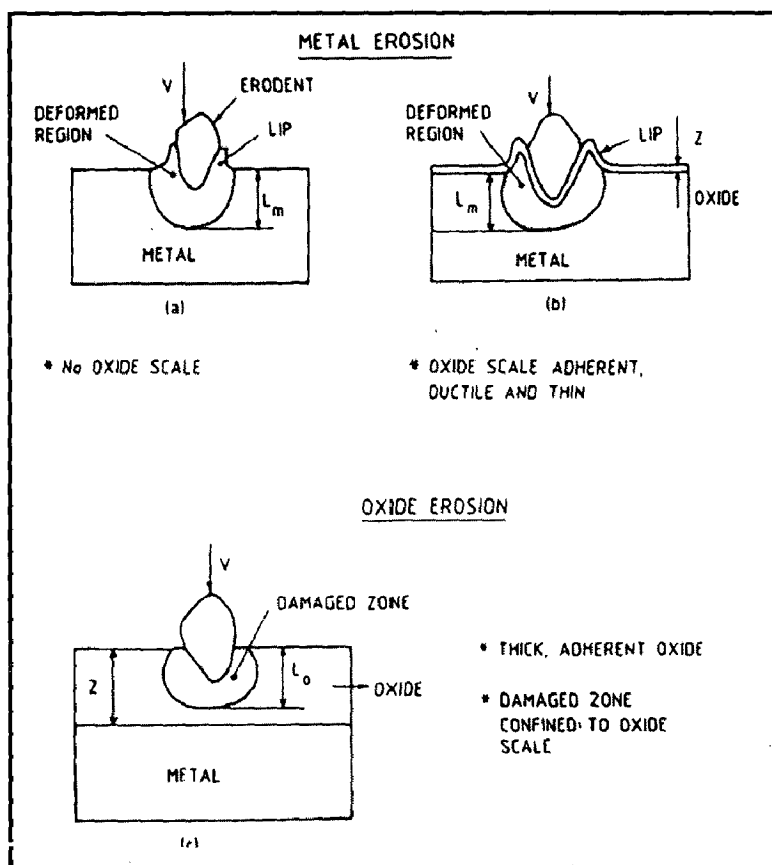


Fig. 7.30 Schematic representation of (a) & (b); metal erosion, and (c) oxide erosion illustrating the nature of interaction between the oxide scale and the substrate during erosion (Sundararajan and Roy, 1997)

The ploughing mechanism is associated with the plastic smearing and cutting of the materials, while the repeated impact mechanism is responsible for initiating and propagating the grain boundary microcracks. Brittle materials are not easily plastically deformed. Hence the material removal rate is low in case of brittle materials and higher in case of ductile materials. At high angle impact, the kinetic energy of the impinging particles contributes mainly to repeated impact. Brittle nature of the materials allows the cracks readily to propagate to form crack networks. The subsequent impacts will easily remove the surface material via the ejection of the upper layer grains. Hence the material removal rate is high in brittle materials and low in case of ductile materials. Figure 7.31 shows schematically the fracture of coatings dependent on impact angle. It is shown schematically how an impinging solid particle can damage coating surfaces.

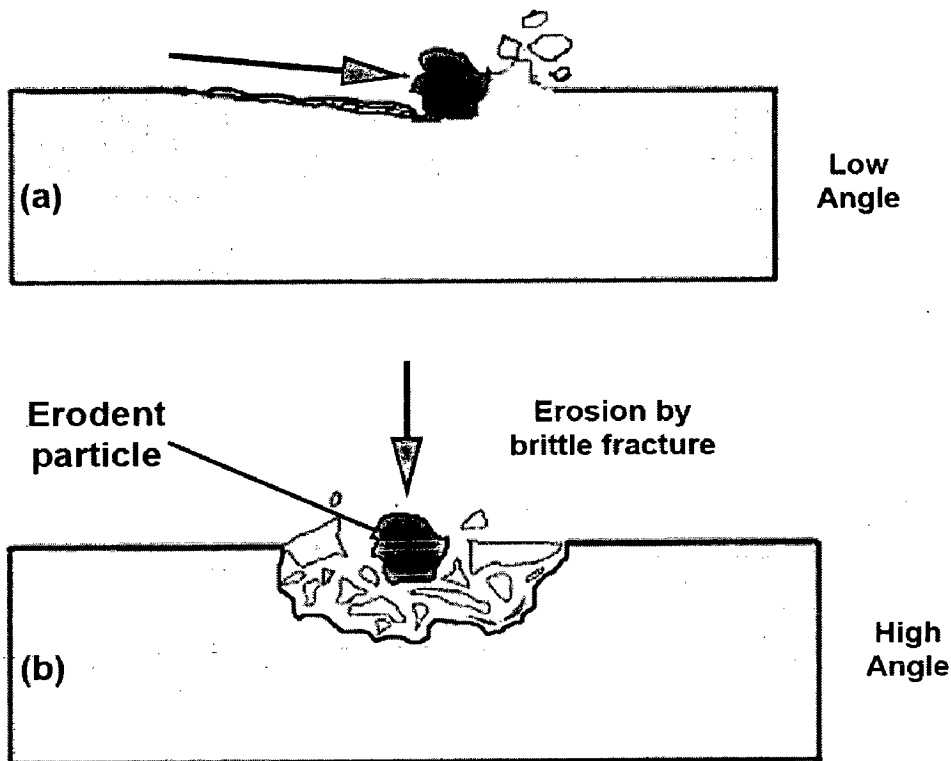


Fig. 7.31 Schematic representation of coating fracture dependent on impact angle; (a) Low angle, (b) High angle

7.4.3 Conclusions

The erosion behavior of conventional thick (by plasma spraying and gas nitrided) and nanostructured thin (by physical vapor deposition process) TiAlN and AlCrN coatings on Superfer 800H superalloy at an impact velocity of 35 ms^{-1} and impingement angle of 90° and 30° when substrate temperature was 400°C and surrounding air at 900°C ; has been analyzed. The following conclusions are made:

1. The erosion rates for 90° impact angle can be arranged in the following order:
Conventional AlCrN > Conventional TiAlN > Nanostructured TiAlN >
Nanostructured AlCrN > Uncoated alloy
2. The conventional TiAlN and AlCrN coatings have successfully protected the substrate at 30° and 90° impact. The nanostructured coatings were removed by the continuous strikes of the eroding particles on the surface of the coating.
3. At 30° impact, the volume erosion rate can be arranged in the following order:
Conventional TiAlN > Conventional AlCrN > Uncoated alloy > Nanostructured TiAlN > Nanostructured AlCrN
4. The erosion rate was more at 30° impact angle in case of uncoated, nanostructured and conventional coatings, which is the characteristic erosion behavior of ductile materials.

7.5 CORROSION STUDIES IN SIMULATED MARINE ENVIRONMENT

The present work has been focused to compare the corrosion behavior of conventional thick (by plasma spraying and gas nitrided) and nanostructured thin (by physical vapor deposition process) TiAlN and AlCrN coatings on Superfer 800H (INCOLOY 800 H) superalloy by electrochemical methods i.e. linear polarization resistance (LPR) and potentiodynamic polarization tests in an aerated 3.0 wt% NaCl solution at room temperature; and salt spray (Fog) tests. The detailed experimental procedure is explained in chapter 3.

7.5.1 Results and Discussion

7.5.1.1 Linear polarization resistance (LPR) and potentiodynamic polarization tests

Linear polarization resistance (LPR) and potentiodynamic polarization tests were conducted in an aerated 3 wt% NaCl solution at room temperature in order to evaluate the corrosion behavior of the substrate and coatings. The initial corrosion current density and LPR (R_p) was measured by LPR test. The linear polarization scans are conducted in very small potential range (-20mV to + 20mV vs Open Circuit Potential), which does not damage the surface of the sample. Whereas the potentiodynamic polarization scans require scanning over a longer potential range (Sahoo and Balasubramaniam, 2007).

The corrosion parameters obtained in LPR test are shown in Table 7.7. The corrosion current density of all the coatings was found much lower than that of the substrate except conventional thick TiAlN coating. The conventional thick TiAlN coated Superfer 800H superalloy has shown maximum current density i.e. 23.81 $\mu\text{A}/\text{cm}^2$. The nanostructured thin TiAlN, AlCrN and conventional AlCrN coatings have performed well and showed high corrosion resistance. The conventional thick TiAlN coating have shown highest corrosion current density as compared to the other coatings, which may be due to the open pores and voids in the coating. The corrosion protection is provided by nanostructured thin TiAlN, AlCrN and conventional AlCrN coatings at initial stage as indicated by the LPR test results in terms of corrosion current density and polarization resistance (Table.7.7).

Table 7.7 Results of Linear Polarization Resistance Test (LPR) of uncoated and coated Superfer 800H superalloy

Substrate / Coating	E_{corr} (mV)	i_{corr} ($\mu\text{A}/\text{cm}^2$)	β_a (V/decade)	β_c (V/decade)	R_p ($\text{k}\Omega\text{-cm}^2$)
Uncoated Superfer 800H	-204.2	05.37	0.1	0.1	04.04
Nanostructured TiAlN coating	-284.4	00.33	0.1	0.1	64.14
Nanostructured AlCrN coating	-416.9	00.47	0.1	0.1	45.73
Conventional TiAlN coating	-618.0	23.81	0.1	0.1	00.91
Conventional AlCrN coating	-482.7	00.37	0.1	0.1	58.10

Potentiodynamic polarization curves of the uncoated and coated Superfer 800H are shown in Fig.7.32 and the corrosion parameters in Table 7.8. The corrosion current density and the corrosion potential were obtained by the intersection of the extrapolation of anodic and cathodic Tafel curves. The corrosion current densities of the coatings were found lower than that of the substrate superalloy except in case of conventional TiAlN coating. The corrosion current densities of the substrate and the coatings were found lower as compared to the LPR test (at initial stage) results except for nanostructured TiAlN coating, which has shown slightly higher corrosion current density. With the duration of the experiment, a protective oxide layer may have formed which has blocked further corrosion as the substrate having composition with higher percentage of Cr (approx. 20%) and Ni (approx. 30%). The corrosion product formed may have reduced the passage of the electrolyte to attack the samples, and hence providing protection.

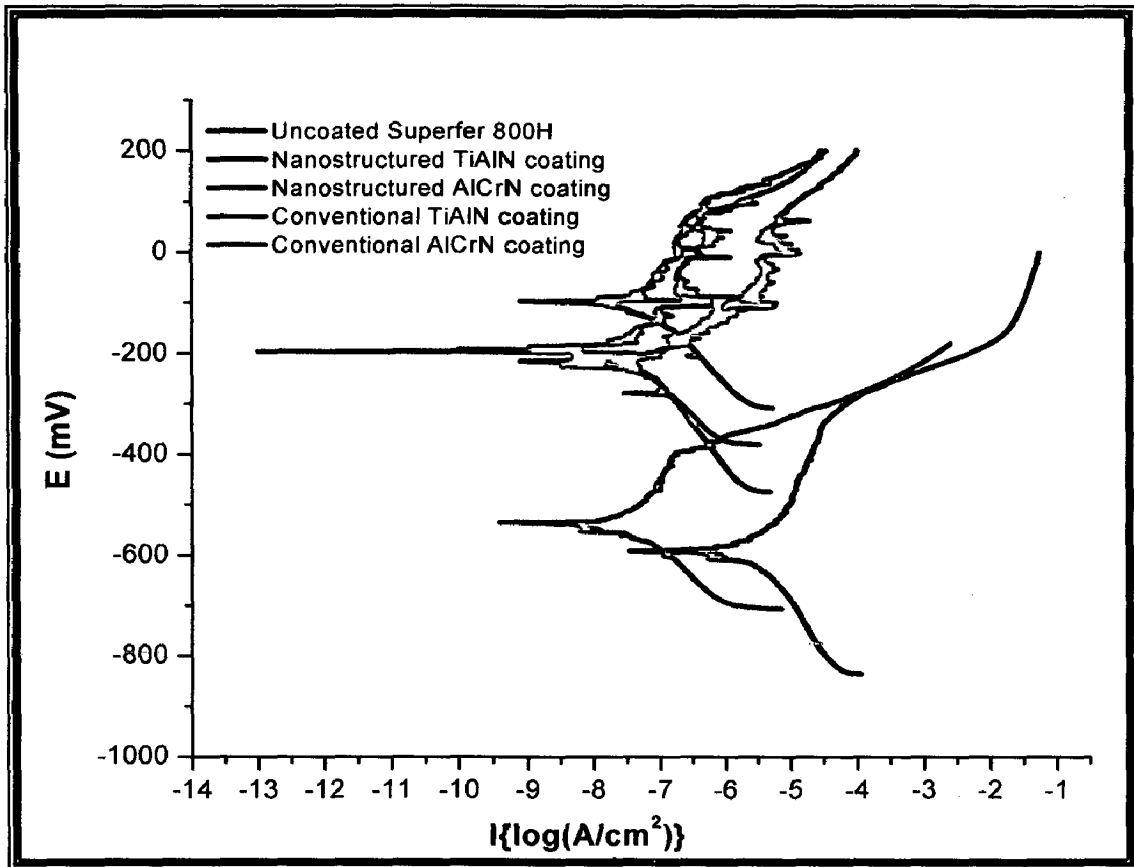


Fig. 7.32 Potentiodynamic Polarization Curves for uncoated and coated Superfer 800H superalloy

Table 7.8 Results of Potentiodynamic Polarization Tests of uncoated and coated Superfer 800H superalloy

Substrate / Coating	E_{corr} (mV)	i_{corr} ($\mu\text{A}/\text{cm}^2$)	β_a (V/decade)	β_c (V/decade)	R_p ($\text{k}\Omega\text{-cm}^2$)	P_i (%)
Uncoated Superfer800H	-097.3	0.058	0.2022	0.128	586.89	--
Nanostructured TiAlN	-220.9	0.068	0.0923	0.172	383.55	Not Protecting
Nanostructured AlCrN	-194.7	0.021	0.0971	0.109	1049.52	63.79
Conventional TiAlN	-591.3	5.368	0.315	0.260	011.52	Not Protecting
Conventional AlCrN	-484.8	0.0033	0.046	0.082	3812.81	94.21

The corrosion rate (i_{corr}) of the specimens was obtained using the Stern-Geary equation(Eq.7.3).

$$i_{corr} = \frac{1}{2.303} \times \frac{\beta_a \beta_c}{R_p \times (\beta_a + \beta_c)} = \frac{Z}{R_p} \quad (7.3)$$

Where β_a = anodic Tafel slope, β_c = cathodic Tafel slope, R_p = polarization resistance and, Z is a function of the Tafel slopes.

The conventional AlCrN coating has performed well and showed best corrosion resistance as evident from corrosion current density ($0.0033 \mu\text{A}/\text{cm}^2$) and polarization resistance ($3812.81 \text{ k}\Omega\text{-cm}^2$) reported in Table.7.8. All the coatings except conventional TiAlN coating have protected the substrate in 3 wt. % NaCl solution. The measured corrosion current density for uncoated Superfer 800H superalloy, nanostructured thin TiAlN, nanostructured thin AlCrN, conventional thick TiAlN and conventional thick AlCrN coatings is $0.058, 0.068, 0.021, 5.368$ and $0.0033 \mu\text{A}/\text{cm}^2$ respectively.

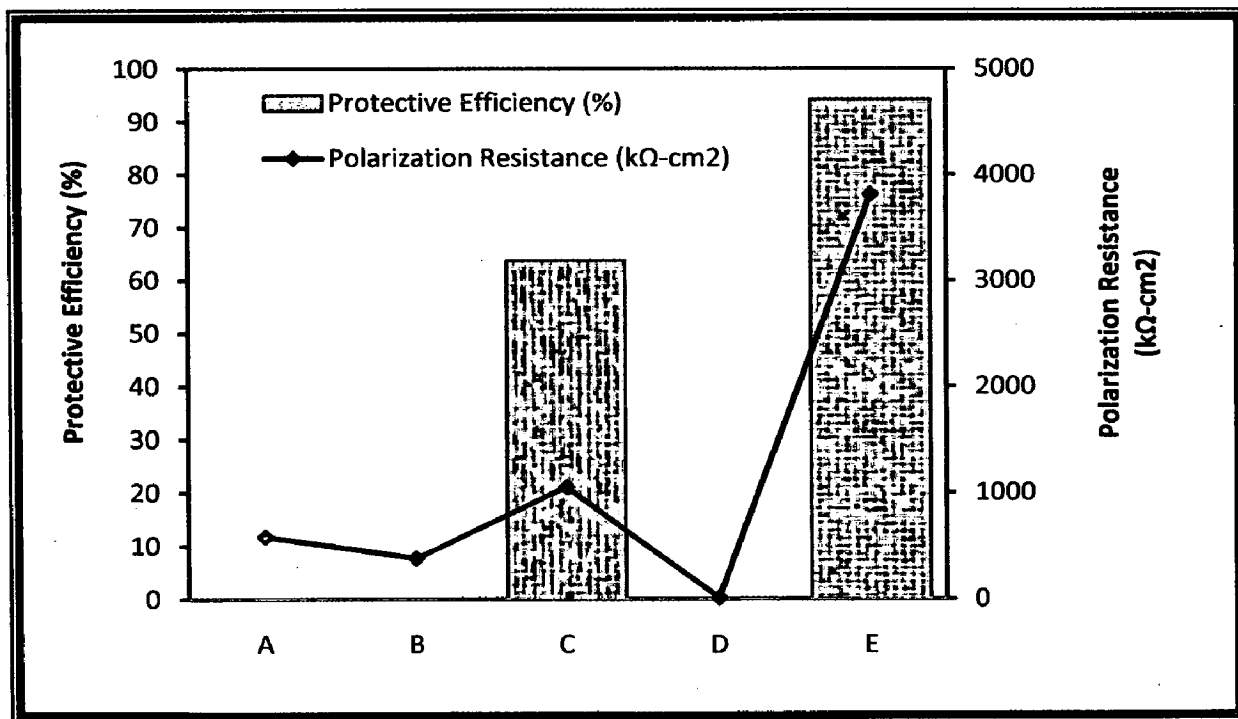


Fig. 7.33 Protective efficiency and Polarization resistance of uncoated and coated Superfer 800H superalloy: (A) Uncoated Superfer 800H, (B) Nanostructured TiAlN coating, (C) Nanostructured AlCrN coating, (D) Conventional TiAlN coating, (E) Conventional AlCrN coating

From polarization test results, the protective efficiency, P_i (%) of the coatings can be calculated by Eq. (7.4):

$$P_i (\%) = \left[1 - \left(\frac{i_{corr}}{i_{corr}^0} \right) \right] \times 100 \quad (7.4)$$

Where i_{corr} and i_{corr}^0 indicate the corrosion current density of the coating and substrate, respectively (Yoo et al., 2008). The variation in protective efficiency and polarization resistance of uncoated and coated Superfer 800H superalloy subjected to potentiodynamic polarization test is shown in Fig.7.33. The conventional thick AlCrN coating showed the highest protective efficiency of 94.21% with lowest corrosion current density ($0.0033 \mu\text{A}/\text{cm}^2$). The nanostructured AlCrN coating have shown protective efficiency of 63.79%. The conventional and nanostructured TiAlN coatings have failed to provide necessary protection to the Superfer 800H superalloy and have shown higher corrosion current densities (Table.7.8).

7.5.1.2 Salt spray (Fog) testing

The ASTM B117 Salt Fog test was used to evaluate the performance of the uncoated and nanostructured thin TiAlN and AlCrN coated Superfer 800H superalloy. The salt fog test is an accelerated corrosion test by which samples exposed to the same conditions can be compared. In the B117 test, the samples are exposed to a salt fog generated from a 5% sodium chloride solution with a pH between 6.5 and 7.2. All the samples were placed in the salt fog chamber for 24 Hrs, 48 Hrs and 72 Hrs. Photographs were taken before and subsequent to exposure to document the surface conditions. Initial weight and dimensions were measured. After exposure; samples were monitored and analyzed by using XRD and SEM/EDAX techniques. Then all the samples were cleaned in running water not warmer than 38°C to remove salt deposits from the surface and immediately dried with compressed air. The macro morphologies of the uncoated and nanostructured thin TiAlN and AlCrN coated superalloy exposed to salt fog test for 24 Hrs, 48 Hrs and 72 Hrs; are depicted in Fig.7.34. No signs of corrosion have been observed in case of uncoated and coated Superfer 800H superalloy subjected to salt fog tests for different durations.

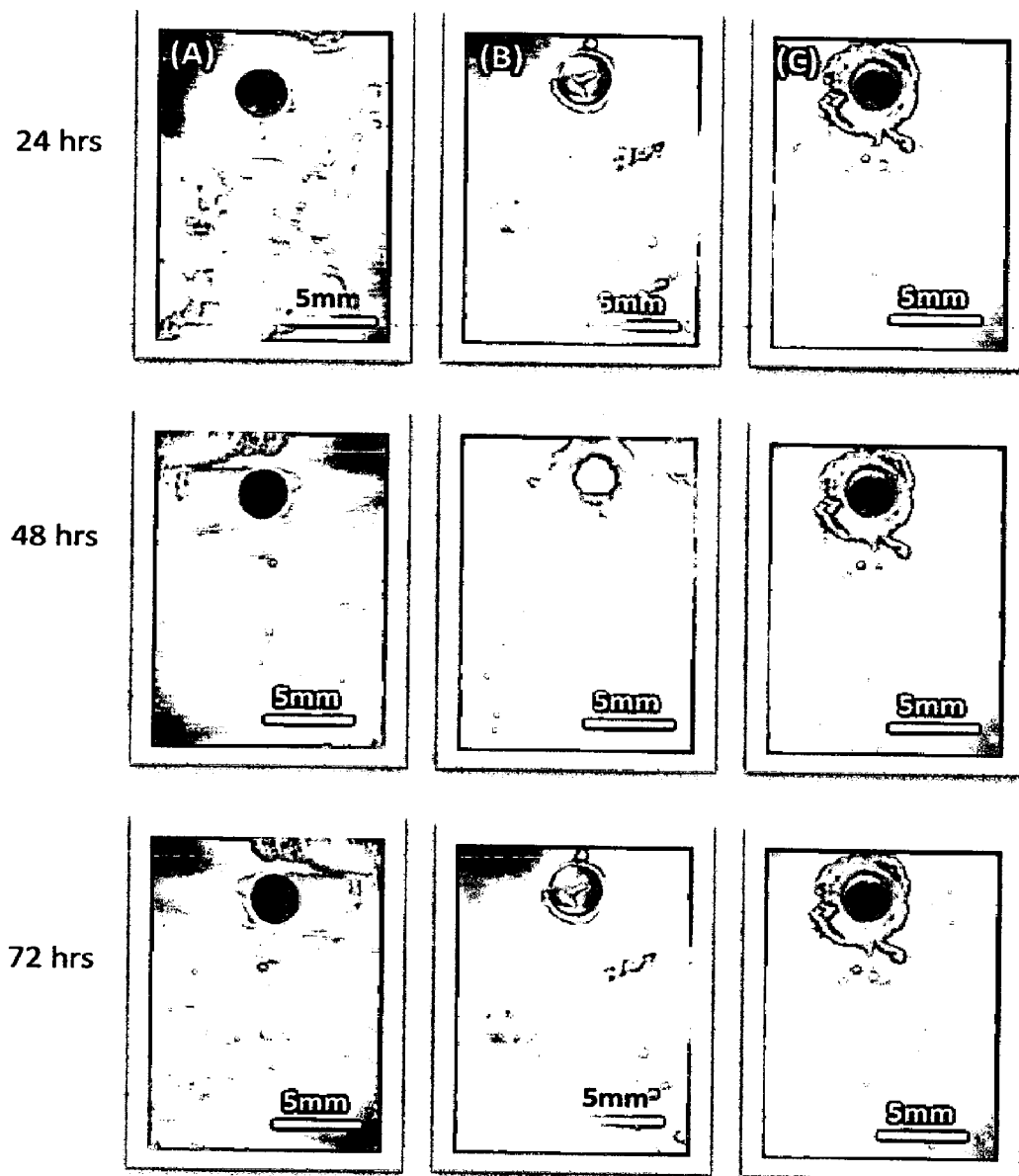


Fig. 7.34 Surface macrographs of uncoated and coated Superfer 800H superalloy subjected to salt-fog testing (5% NaCl) : (A) Uncoated T-22 boiler steel subjected to 24hrs, 48hrs and 72 hrs testing; (B) Nanostructured TiAlN coating subjected to 24hrs, 48hrs and 72 hrs testing; (C) Nanostructured AlCrN coating subjected to 24hrs, 48hrs and 72 hrs testing

Figure 7.35 shows the surface SEM images of uncoated and nanostructured TiAlN and AlCrN coated superalloy exposed to salt fog test for 72 Hrs. As the SEM/EDAX analysis of the samples exposed to 24 Hrs, 48 Hrs and 72 Hrs salt fog tests have shown similar results, therefore SEM/EDAX analysis in case of 72 Hrs (maximum duration of test in present investigation) test has been presented here. As can be seen in Fig.7.35, no corrosion product has been found on the surface of any sample.

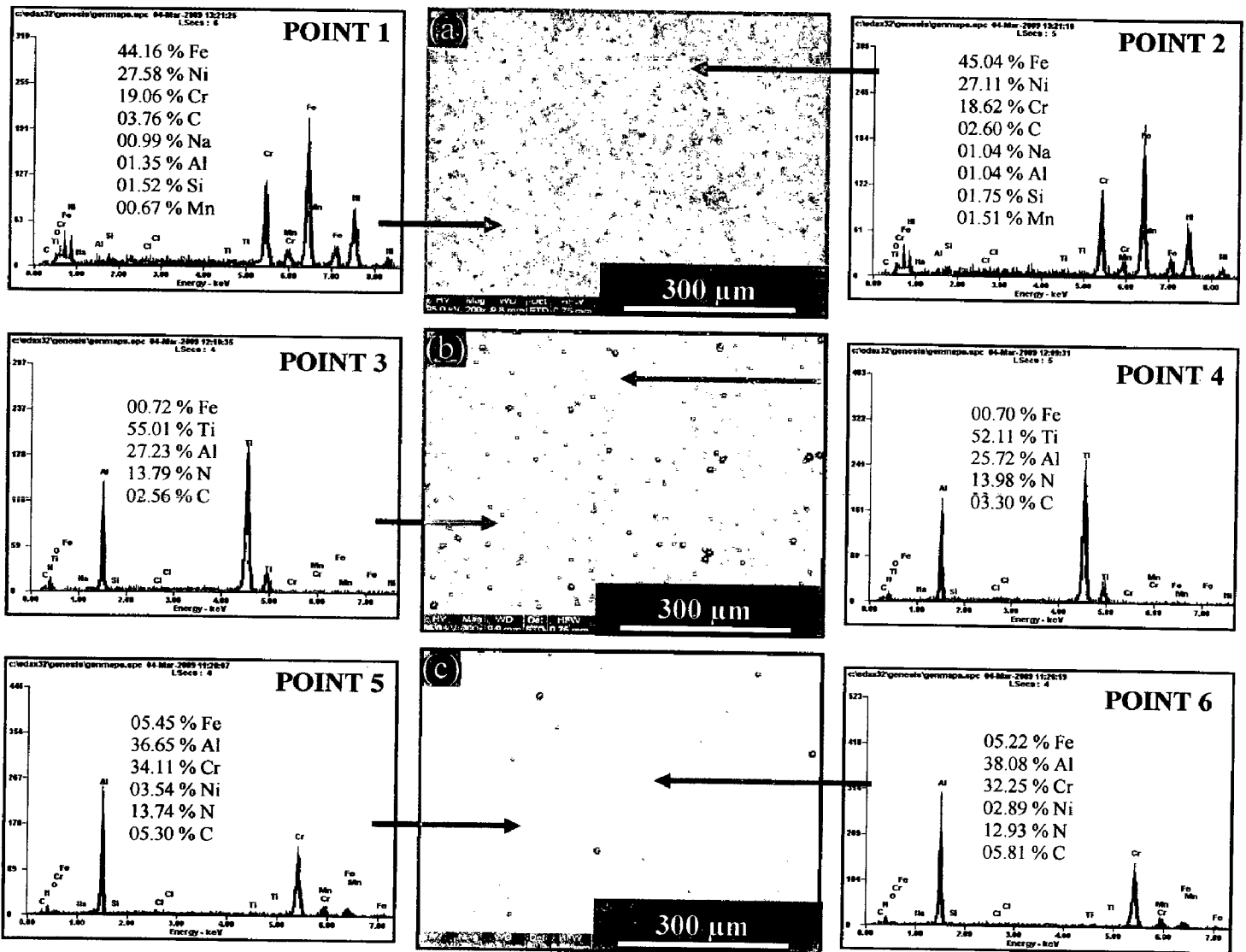


Fig. 7.35 Surface macrographs of uncoated and coated Superfer 800H superalloy subjected to salt-fog testing (5% NaCl) for 72 hrs: (a) Uncoated Superfer 800H superalloy (b) Nanostructured TiAlN coating (c) Nanostructured AlCrN coating

The EDAX point analysis indicates the presence of Fe, Ni and Cr in case of uncoated superalloy at point 1 and 2 on Fig.7.35. In case of nanostructured thin TiAlN and AlCrN coatings; no corrosion products were seen (Fig.7.35.b and c). The EDAX point analysis (Point 3 to 6 on Fig.7.35) revealed the presence of the coating elements only. The uncoated and nanostructured thin coated superalloy have performed well in salt fog tests 24, 48 and 72 Hrs duration. XRD diffractograms for coated and uncoated superalloy subjected to salt fog tests for 24 Hrs, 48 Hrs and 72 Hr; are depicted in Fig.7.36 on reduced scale.

As indicated by the diffractograms in Fig.7.36, Fe, Ni and Cr are the main phases present in case of uncoated superalloy. In nanostructured TiAlN coating, AlN and TiN are the main phases revealed by EDAX analysis. Further, the main phases identified for the nanostructured AlCrN coating are CrN and AlN.

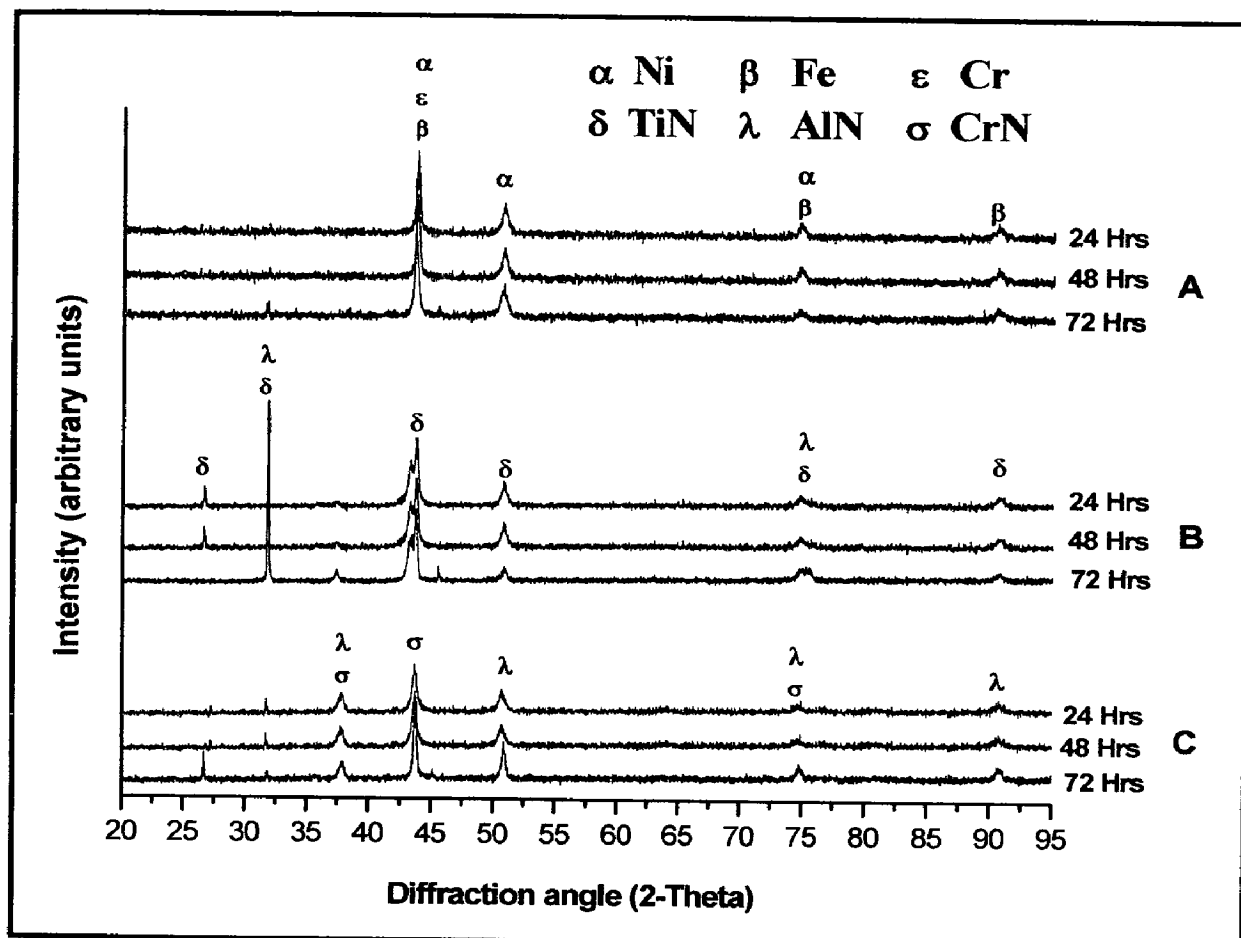


Fig. 7.36 X-Ray Diffraction pattern of uncoated and coated Superfer 800H superalloy subjected to salt-fog testing (5% NaCl): : (A) Uncoated Superfer 800H superalloy, (B) Nanostructured TiAlN coating, (C) Nanostructured AlCrN coating

The weight loss measurements were carried out for the uncoated and nanostructured thin TiAlN and AlCrN coated Superfer 800H superalloy exposed to the salt fog tests for 24 Hrs, 48 Hrs and 72 Hrs. No weight change was observed in any case. It can be mentioned based on the present investigation that uncoated Superfer 800H and nanostructured thin TiAlN and AlCrN coatings can provide a very good corrosion resistance when exposed to the simulated marine environment i.e. salt fog test.

7.5.2 Conclusions

The corrosion behavior of conventional thick (by plasma spraying and gas nitrided) and nanostructured thin (by physical vapor deposition process) TiAlN and AlCrN coatings on Superfer 800H superalloy, has been analyzed by electrochemical methods i.e. linear polarization resistance (LPR) and potentiodynamic polarization tests in an aerated 3.0 wt% NaCl solution at room temperature and salt spray (Fog) tests (5.0 wt% NaCl). The following conclusions are made:

1. In Linear polarization resistance (LPR) test, the corrosion current densities of all the coatings were found lower than that of the substrate except in the case of conventional TiAlN coating. The corrosion protection is provided by the coatings at the initial stage as indicated by the LPR test results in terms of corrosion current density and polarization resistance except conventional TiAlN coating. The corrosion resistance of the coatings and substrate followed the sequence:
Nanostructured TiAlN > Conventional AlCrN > Nanostructured AlCrN > Substrate > Conventional TiAlN
2. In Potentiodynamic Polarization test, the corrosion current densities of the coatings were found lower than that of the substrate except conventional TiAlN coating. The corrosion current densities of the substrate and the coatings in Potentiodynamic Polarization test were found much lower than the LPR test (at initial stage) results. The corrosion resistance of the coatings and substrate followed the sequence:
Conventional AlCrN > Nanostructured AlCrN > Substrate > Nanostructured TiAlN > Conventional TiAlN
3. The measured protective efficiency for nanostructured thin AlCrN and conventional thick AlCrN coatings is 63.79% and 94.21% respectively.
4. In salt spray tests; the uncoated as well as nanostructured TiAlN and AlCrN coated Superfer 800H superalloy have performed well and have shown no weight change during exposure for 24 Hrs, 48 Hrs and 72 Hrs to salt fog tests.

7.6 EROSION-CORROSION STUDIES IN INDUSTRIAL ENVIRONMENT

After conducting the various experiments on uncoated and coated Superfer 800H superalloy in lab; the present research work has been focused to investigate and compare the high temperature corrosion and erosion behavior of conventional thick (by plasma spraying and gas nitrided) and nanostructured thin (by physical vapor deposition process) TiAlN and AlCrN coatings on superalloy, in actual industrial environment of coal fired boiler. The uncoated and coated specimens were exposed to low temperature super-heater zone of the coal fired boiler of Guru Nanak Dev Thermal Power Plant, Bathinda, Punjab, India. The specimens were hanged in the platen super-heater of coal fired boiler where the gas temperature was around $900^{\circ}\text{C} \pm 10^{\circ}\text{C}$. Hot corrosion experiments were performed for 10 cycles, each cycle consisting of 100 hours exposure followed by 1 hour cooling

7.6.1 Results

7.6.1.1 Visual observations

The macrographs for uncoated and coated Superfer 800H superalloy exposed to super-heater of the coal fired boiler environment at 900°C for 1000 hours are shown in Fig.7.37. Light grey colored scale appeared on the surfaces of bare superfer 800H (Fig.7.37.a) after first cycle, which is lasted up to 3rd cycle, ash deposition has started after 4th cycle. Greenish and brownish spots appeared on the surface along with white spots of ash deposits, which further intensified towards the end and final scale was of dark brown color. No spalling and cracks were observed in the scale throughout the experimentation. After every cycle; the samples were washed with acetone in order to remove ash deposited before weight measurement.

In case of nanostructured thin TiAlN coated Superfer 800H superalloy, color of the oxide scale at the end of the study was observed to be blackish brown with some white spots of ash deposited, as shown in Fig.7.37 (b). The ash deposition was started after 4th cycle and no spalling and cracks were observed in the scale throughout the experimentation. Signs of erosion (in the form of small spots of striking particles on the surface) were observed during the study. The nanostructured thin AlCrN coated

superalloy has shown the formation of blackish brown scale with some white spots of ash deposited, as shown in Fig.7.37 (c). After 2nd cycle, golden spots were seen on the surface with ash deposition. No spalling and cracks were observed in the scale throughout the experimentation.

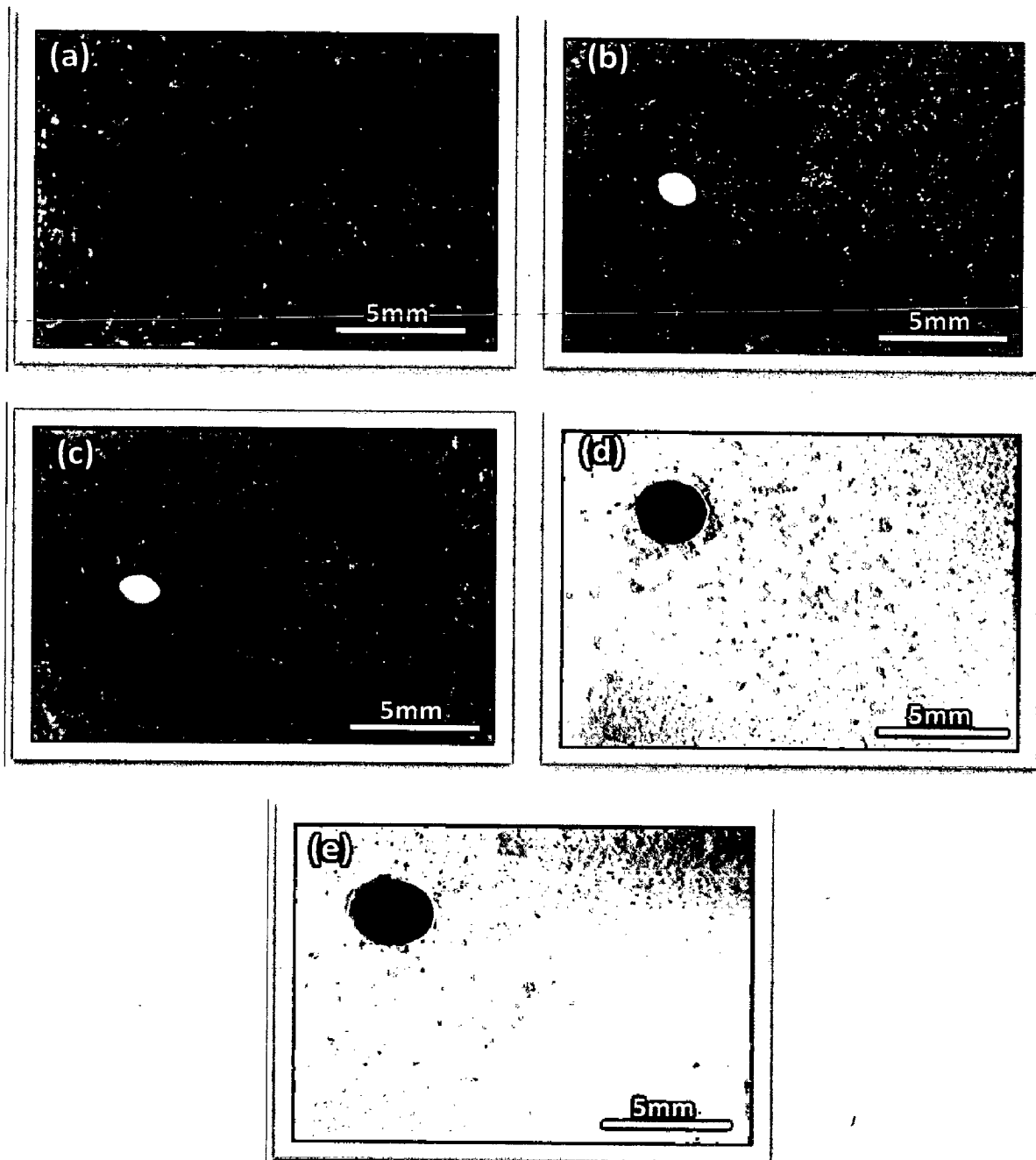


Fig. 7.37 Surface macrographs of uncoated and coated Superfer 800H superalloy exposed to super-heater of the coal fired boiler environment at 900°C for 1000 hours: (a) Uncoated Superfer 800H superalloy, (b) Nanostructured TiAlN coating, (c) Nanostructured AlCrN coating, (d) Conventional TiAlN coating, (e) Conventional AlCrN coating

A visual observation of conventional thick TiAlN coated superalloy (Fig.7.37.d) showed the formation of brownish cream colored ash deposited scale at the end of the study. No spalling and cracks were observed in the scale throughout the experimentation. Signs of erosion (in the form of small spots of striking particles on the surface) were observed after 3rd cycle which continued till the end of the study. The scale was very rough and adherent to the substrate. In case of conventional thick AlCrN coated superalloy, color of the oxide scale was dark brown with some whitish areas at the end of the study (Fig.7.37.e). The scale was found to be adherent. No spalling and cracks were observed in the scale throughout the experimentation.

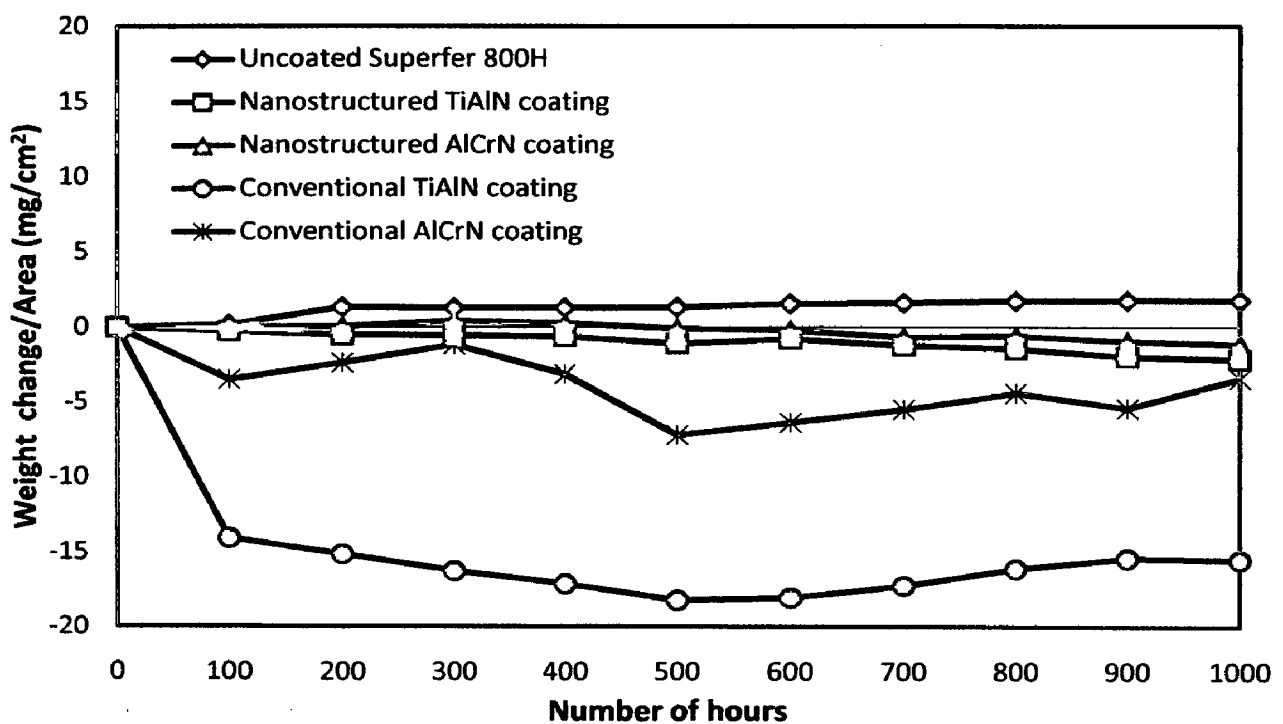


Fig. 7.38 Weight gain/area vs time for uncoated and coated Superfer 800H superalloy exposed to super-heater of the coal fired boiler environment at 900°C for 1000 hours

7.6.1.2 Weight change and sample thickness measurements

Weight gain per unit area (mg/cm²) versus time expressed in number of cycles plot for coated and bare Superfer 800H superalloy exposed to super-heater of the coal fired boiler environment at 900°C for 1000 hours; is presented in Fig. 7.38. However

weight change data could not be of much use for predicting the corrosion behavior because of suspected spalling and ash deposition on the specimens. Although the specimens were washed with acetone after every cycle before weight measurement in order to remove ash deposited yet it was difficult to remove the ash completely. Hence extent of corrosion could only be monitored by measuring the thickness of the unreacted sample after the total exposure of 1000 hrs i.e. measuring scale thickness in cross-sectional view. It can be inferred from the plots (Fig.7.38) that the uncoated superalloy has shown weight gain. All the coated specimens have shown weigh loss instead of weight gain. Conventional thick TiAlN coated Superfer 800H superalloy shows the highest weight loss.

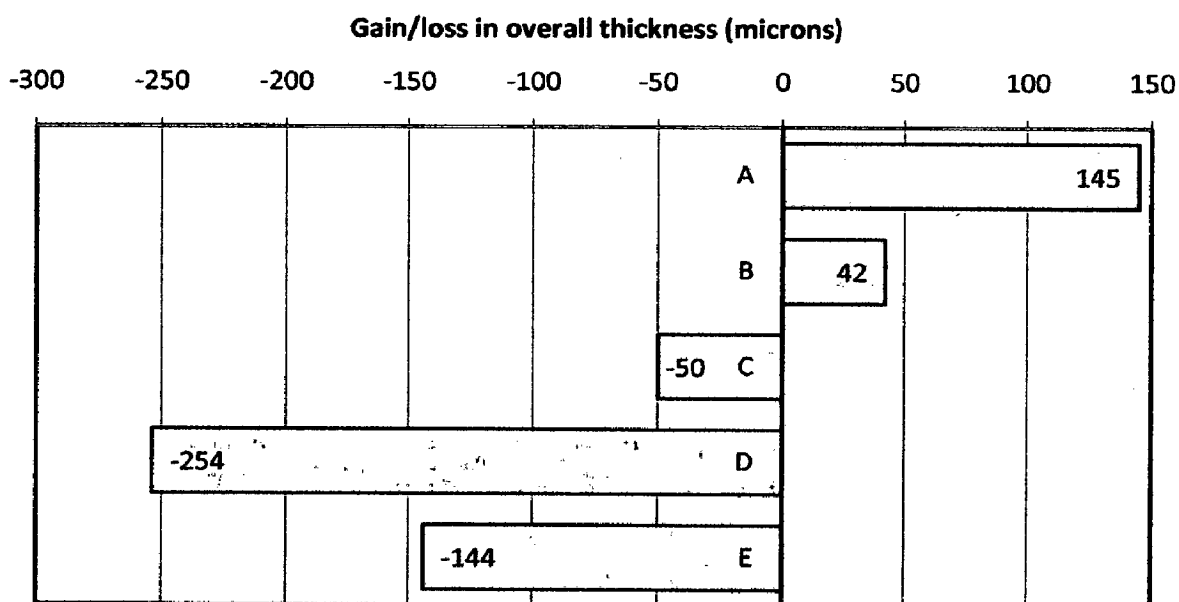


Fig. 7.39 Bar chart indicating overall gains/loss in thickness for uncoated and coated Superfer 800H superalloy specimens exposed to super-heater of the coal fired boiler environment at 900°C for 1000 hours: (a) Uncoated Superfer 800H superalloy, (b) Nanostructured TiAlN coating, (c) Nanostructured AlCrN coating, (d) Conventional TiAlN coating, (e) Conventional AlCrN coating

The weight gain in case of uncoated sample is consisting of the scale formation at the top surface by oxidation. Bar chart in Fig.7.39 indicates the overall gain/loss in the thickness (in mm) of the specimen. All the coatings have shown decrease in overall thickness after erosion-corrosion for 1000 hrs except nanostructured TiAlN coating. The thickness of the specimens was measured before and after the erosion-corrosion test

and average of ten values has been used to calculate the thickness gain/loss. The thickness of the specimens was measured before and after the erosion-corrosion test and average of ten values has been used to calculate the thickness gain/loss. The measured average gain/loss in overall specimen thickness values for uncoated superalloy, nanostructured thin TiAlN, nanostructured thin AlCrN, conventional thick TiAlN and conventional thick AlCrN coatings are +145, +42, -50, -254 and -144 μm respectively.

7.6.1.3 Surface scale analysis

7.6.1.3.1 X-ray diffraction analysis (XRD)

XRD diffractograms for coated and uncoated Suprefer 800H superalloy exposed to super-heater of the coal fired boiler environment at 900°C for 1000 hours; are depicted in Fig.7.40 (a and b) on reduced scale. As indicated by the diffractograms; in case of uncoated, Superfer 800H superalloy the oxide phases found are γ -Ni, Fe_2O_3 , Cr_2O_3 , α -Fe and SiO_2 . The formation of Al_2O_3 , Cr_2O_3 , SiO_2 , Fe_2O_3 , TiO_2 and NiO peaks has been revealed in the scale of nanostructured thin TiAlN coating. Further, the main phases identified for the nanostructured AlCrN coated Superfer 800H superalloy are Al_2O_3 , Cr_2O_3 , SiO_2 , Fe_2O_3 , and NiO. In case of conventional thick TiAlN coating; the peaks are Al_2O_3 , Cr_2O_3 , Fe_2O_3 , TiO_2 and Ti_3Al . The oxide phases found in case of conventional thick AlCrN coating are Al_2O_3 , Cr_2O_3 , SiO_2 , Fe_2O_3 , and NiO.

7.6.1.3.2 Surface scale morphology

SEM micrographs along with EDAX point analysis reveals the surface morphology of the coated and uncoated Suprefer 800H superalloy exposed to super-heater of the coal fired boiler environment at 900°C for 1000 hours are shown in Fig.7.41. Micrograph (Fig.7.41.a) for uncoated superalloy indicates a scale developed with dark grey and white regions. EDAX analysis at point 1 on Fig.7.41 (white region) indicates the presence of Al, O, Cr, Fe, Si with little amount of Ni and Ti, which shows the probability of SiO_2 , Al_2O_3 , Cr_2O_3 and Fe_2O_3 with little amounts of TiO_2 and NiO in the scale.

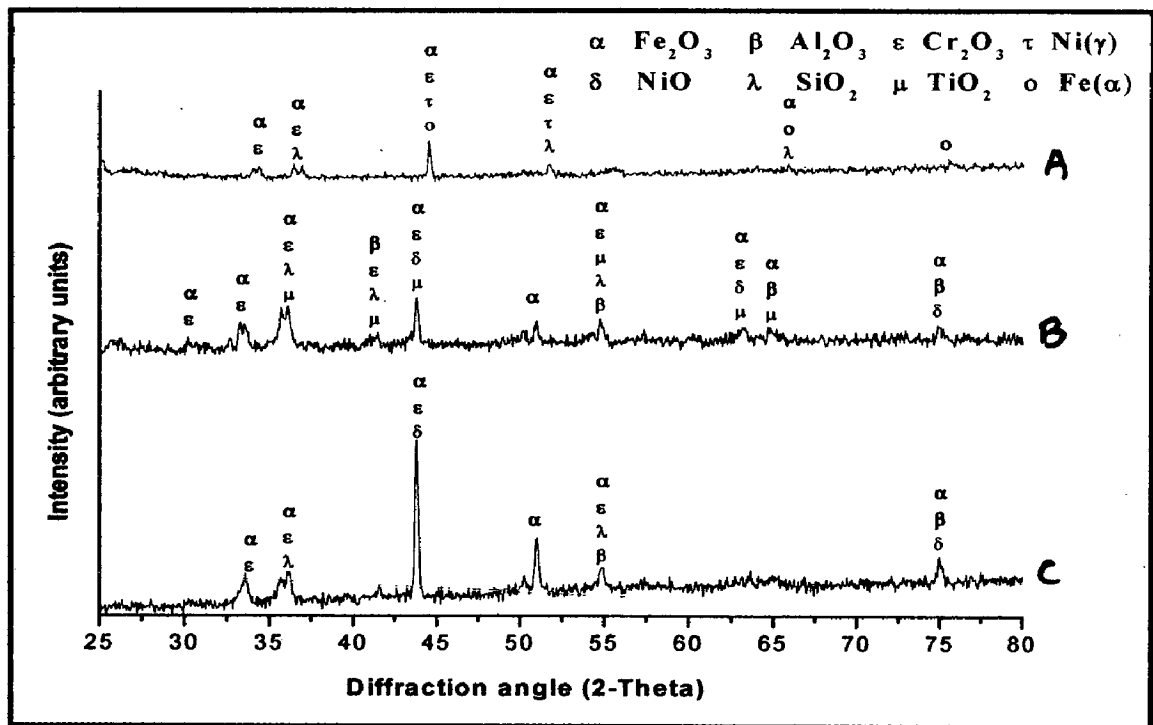


Fig. 7.40 (a) X-Ray Diffraction pattern of uncoated and coated Superfer 800H superalloy exposed to platen superheater of the coal fired boiler environment at 900°C for 1000 Hrs: (A) Uncoated Superfer 800H superalloy, (B) Nanostructured TiAlN coating, (C) Nanostructured AlCrN coating

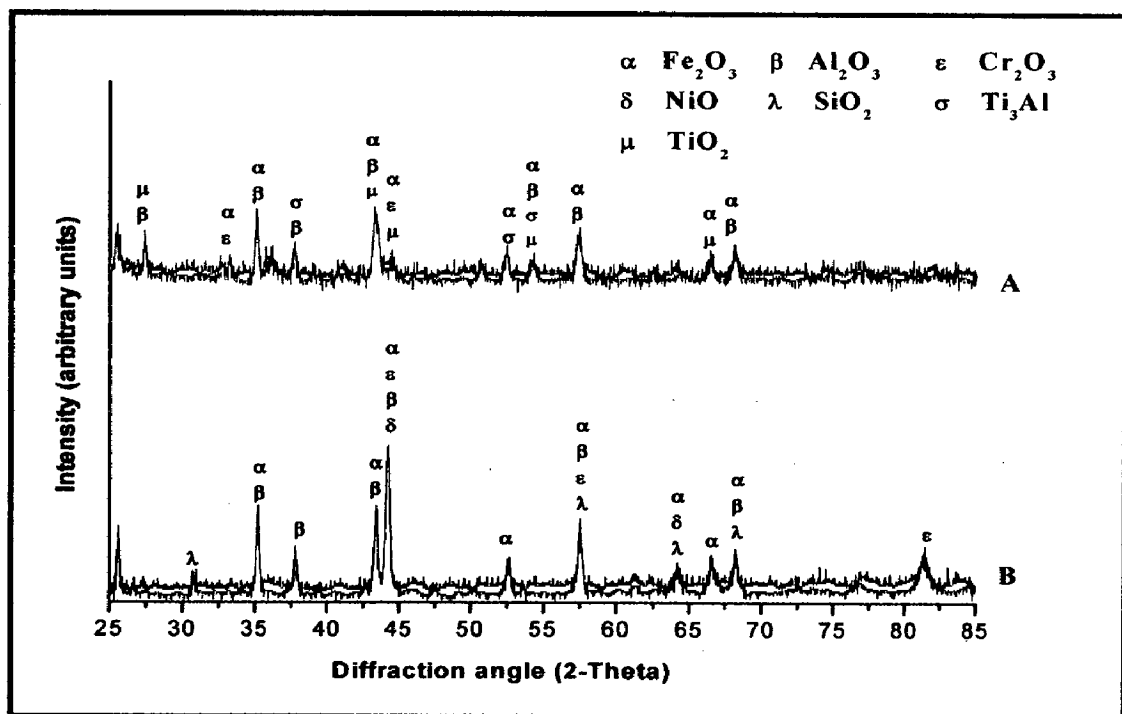


Fig. 7.40 (b) X-Ray Diffraction pattern of coated Superfer 800H superalloy exposed to platen superheater of the coal fired boiler environment at 900°C for 1000 Hrs: (A) Conventional TiAlN coating, (B) Conventional AlCrN coating

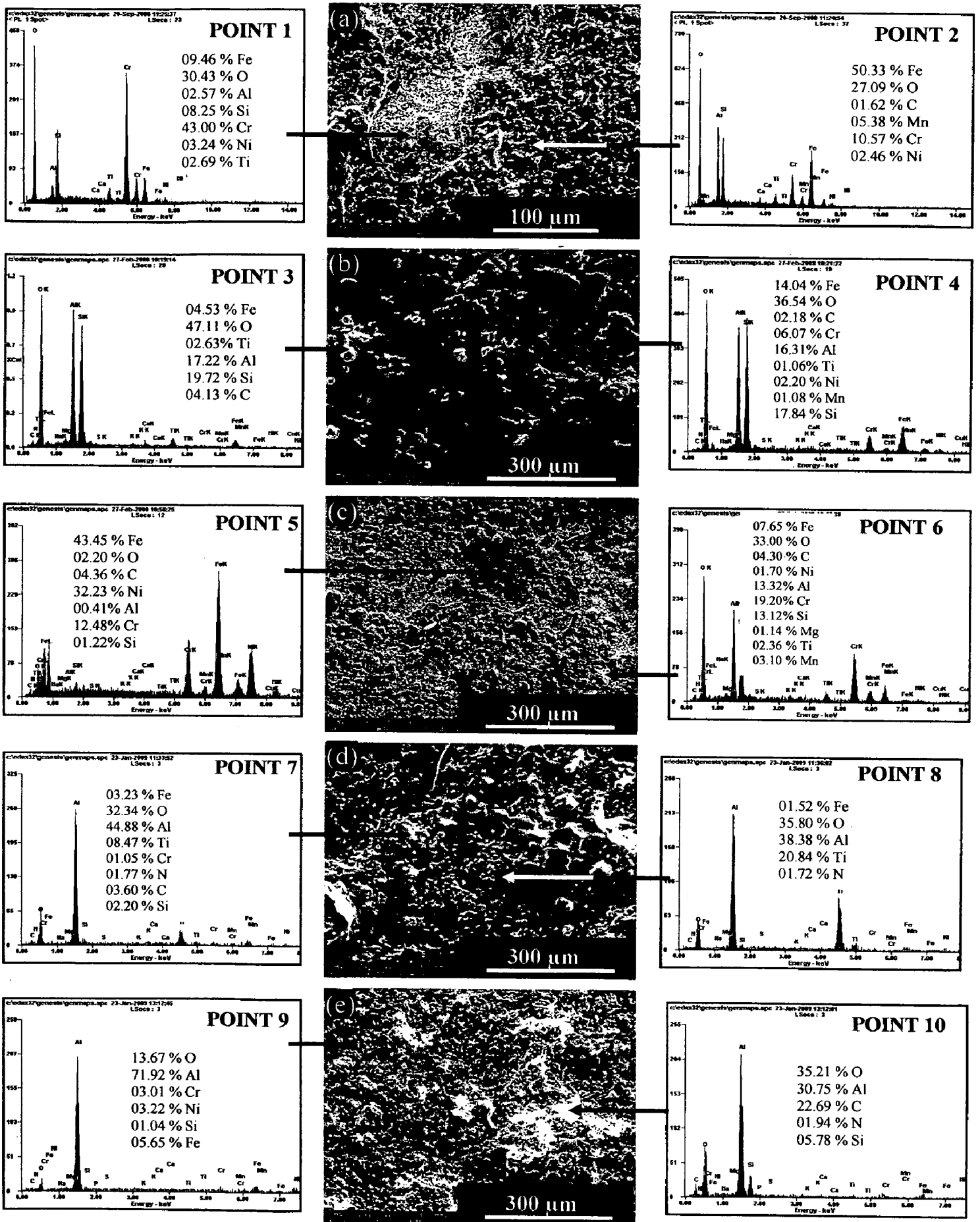


Fig. 7.41 Surface-scale morphology and EDAX patterns from different spots on uncoated and coated Superfer 800H superalloy exposed to platen superheater of the coal fired boiler environment at 900°C for 1000 Hrs : (a) Uncoated Superfer 800H superalloy, (b) Nanostructured TiAlN coating, (c) Nanostructured AlCrN coating, (d) Conventional TiAlN coating, (e) Conventional AlCrN coating

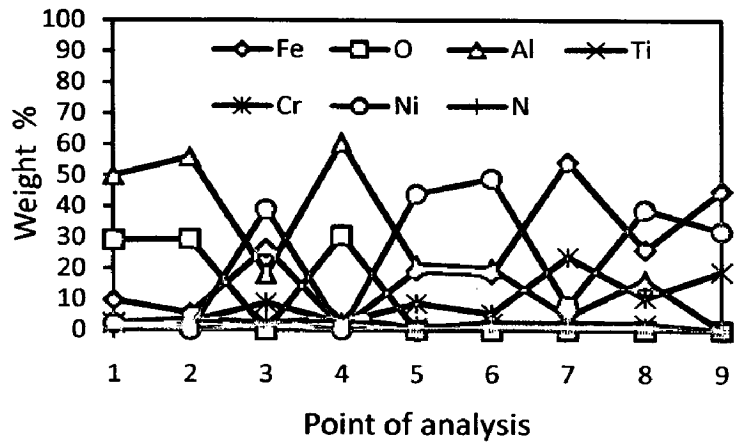
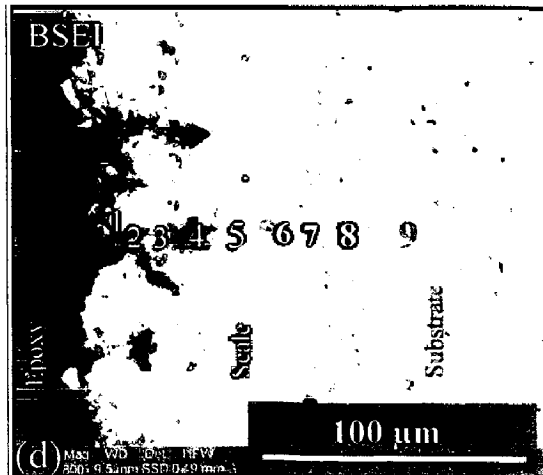
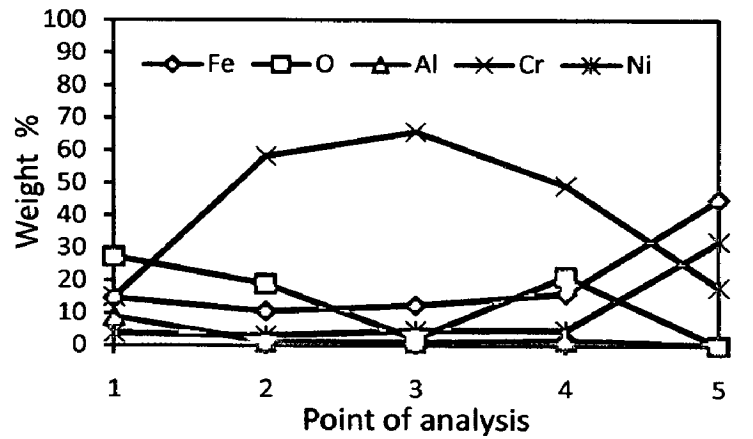
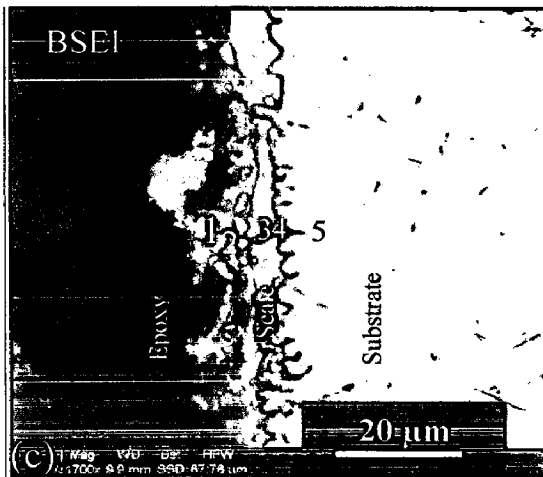
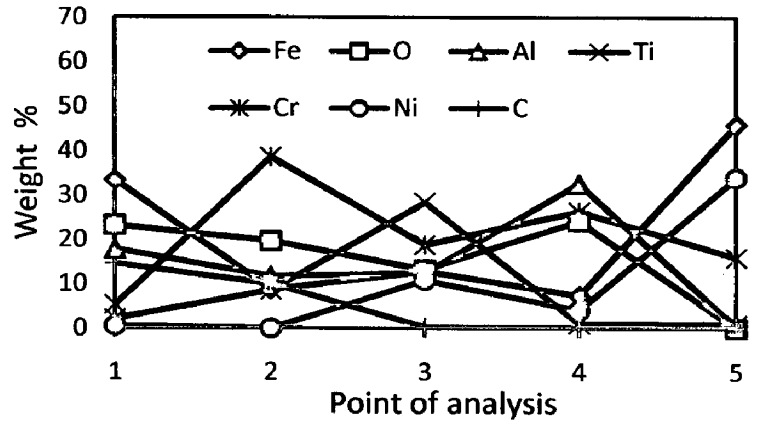
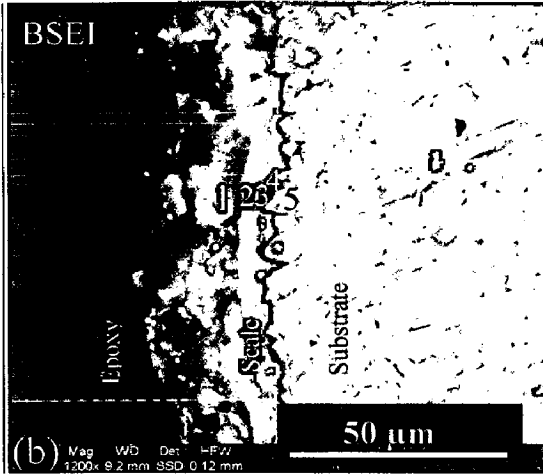
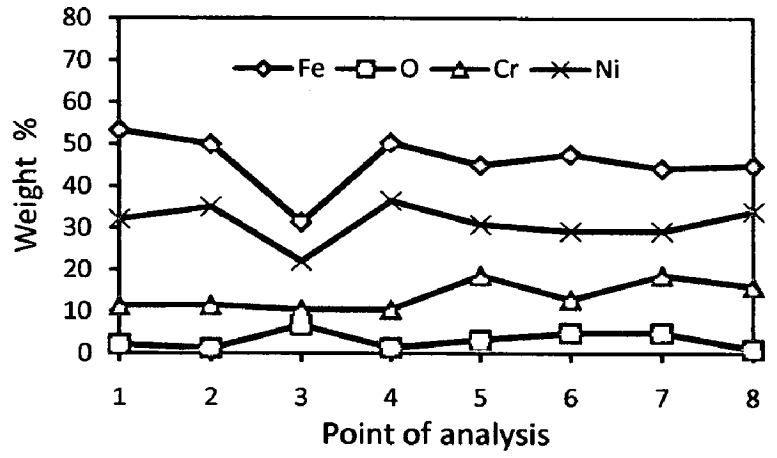
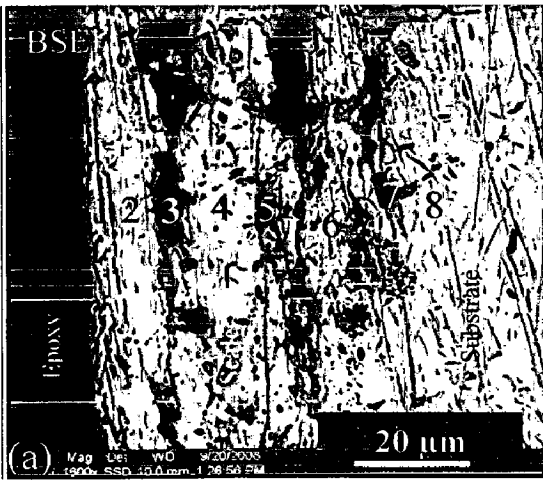
It can be inferred that the composition of the white phase is almost similar to ash composition along with some other oxides of the scale. The dark grey region (Point 2) mainly consists of Fe, Cr and O with minor amounts of Ni and Mn. The SEM micrograph of oxidized nanostructured thin TiAlN coatings is shown in Fig.7.41 (b). The surface scale consists of dark grey areas with some white regions. EDAX analysis (Point 3, white region) of the scale revealed the presence of Al, Si and O as the main elements along with very small amount of Fe, Ni and Cr. Whereas the dark grey areas have shown Al, O and Si as the main elements but with good amount of Fe, Cr, Ni and Ti. In case of nanostructured thin AlCrN coated superalloy, the scale consists of white and grey regions (Fig.7.41. c). EDAX point analysis at point 5 (grey region) shows the higher concentration of Fe and Ni with small amount of O, Cr, Al and Si; whereas the contrast region (Point 6) shows higher amount of Al, Cr, Si and O with very small amount of Fe, Ni, Ti and Mg.

The surface scale developed on conventional thick TiAlN coated superalloy consists of grey and white regions without any cracks. EDAX analysis of white contrast region (Point 7 on Fig.7.41.d) indicates the higher concentration of Al, Ti and O along with Fe, N, Cr and Si. The grey area shows the presence of Al, Ti and O as the main phases along with very small amount of Fe and Cr. Signs of erosion are visible on the surface. A massive surface scale is developed on conventional thick AlCrN coated superalloy. EDAX point analysis at point 10 (white region) shows Al (30.75%), Si (05.78%) and O (35.21%) as the main elements in the scale (Fig.7.41.e). whereas the grey matrix Point 9) shows more Al (71.92 %) and O (13.67 %) with negligible Fe, Ni, Cr and Si.

7.6.1.4 Cross-sectional analysis

7.6.1.4.1 Cross-sectional scale morphology

Back Scattered Electron Image (BSEI) micrograph and elemental variation across the cross-section for coated and uncoated Suprefer 800H superalloy exposed to superheater of the coal fired boiler environment at 900°C for 1000 hours are shown in Fig.7.42. The BSEI micrograph in case of uncoated superalloy is shown in Fig.7.42 (a). EDAX analysis reveals the presence of Fe, Cr and Ni throughout the scale.



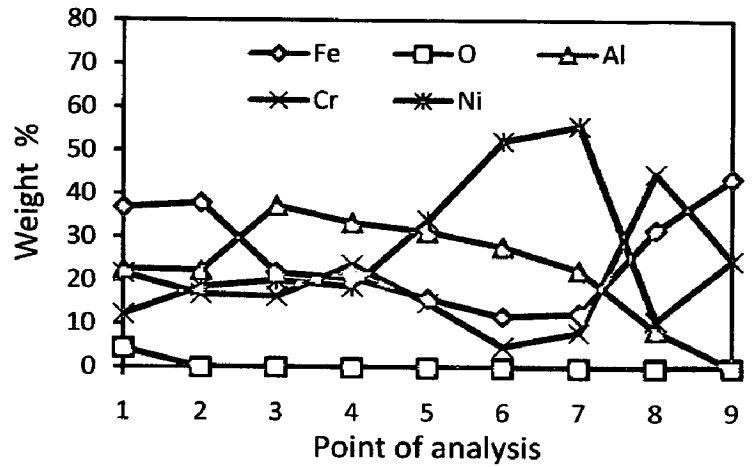
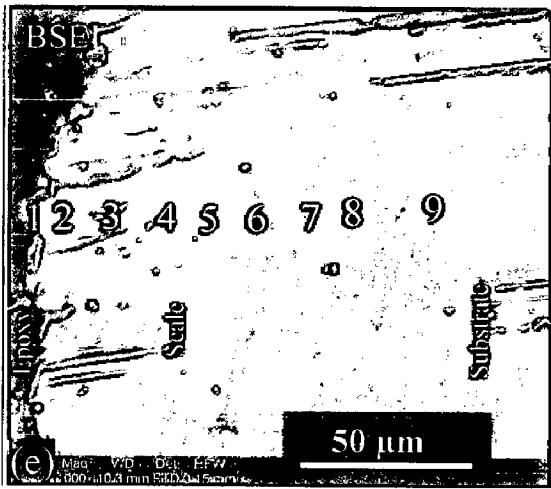


Fig. 7.42 Oxide scale morphology and variation of elemental composition across the cross-section of the uncoated and coated Superfer800H superalloy exposed to platen super-heater of the coal fired boiler environment at 900°C for 1000 Hrs: (a) Uncoated Superfer800H superalloy (1600 X), (b) Nanostructured TiAlN coating (1200 X), (c) Nanostructured AlCrN coating (1700 X), (d) Conventional TiAlN coating (800 X), (e) Conventional AlCrN coating (1000 X)

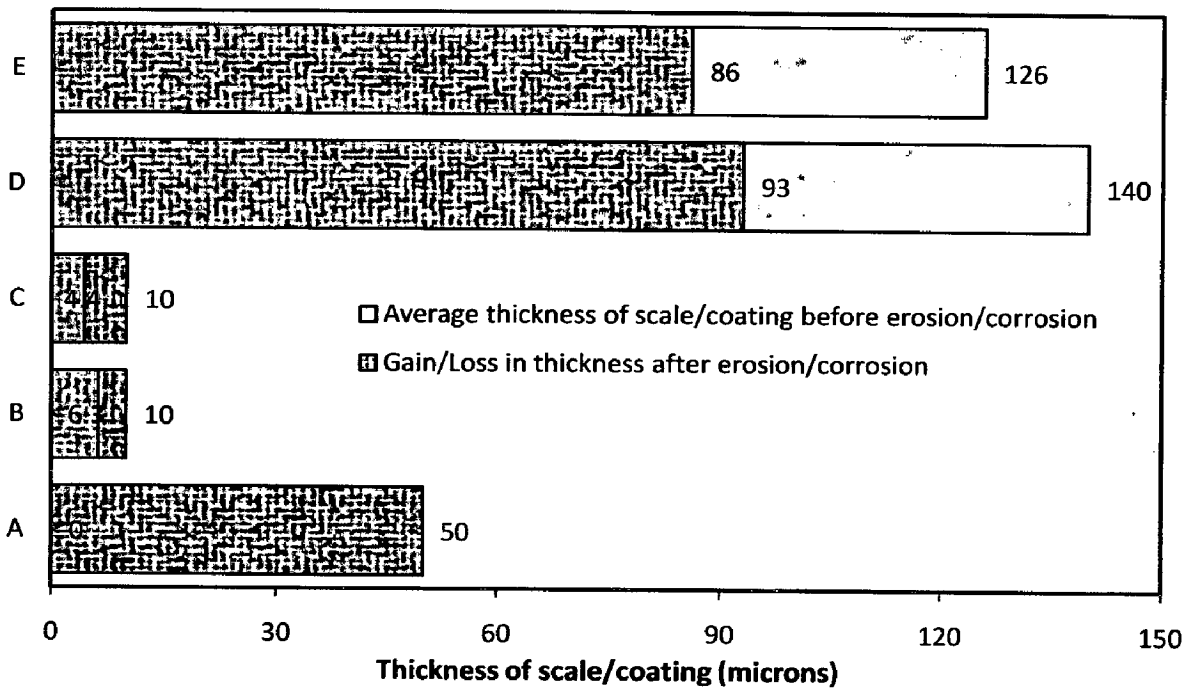


Fig. 7.43 Bar chart indicating the extent of erosion/corrosion for uncoated and coated Superfer 800H superalloy specimens exposed to super-heater of the coal fired boiler environment at 900°C for 1000 hours: (a) Uncoated Superfer 800H superalloy, (b) Nanostructured TiAlN coating, (c) Nanostructured AlCrN coating, (d) Conventional TiAlN coating, (e) Conventional AlCrN coating

Some Oxygen and Cr rich pockets can be seen in the oxide scale (Point 3, 5 and 7 in Fig.7.42.a) where concentration of Cr and O increases. BSEI micrograph and elemental variation depicted in Fig.7.42 (b), for the cross-section of nanostructured thin TiAlN coated superalloy. The EDAX analysis reveals the presence of Al, Ti, Cr and O throughout the scale with some amount of iron. A location at point 2 (Fig.7.42.b) in the micrograph depicts the good percentage of Cr, whereas point 4 indicates higher percentage of Al along with oxygen. A thin and adherent oxide scale can be seen in case of nanostructured AlCrN coated superalloy (Fig.7.42.c). The EDAX point analysis indicates the presence of Cr and O with some amount of Al, Ni and Fe throughout the scale.

In case of conventional TiAlN coated superalloy, the scale is non uniform, thin and adherent as depicted in Fig.7.42 (d). The EDAX point analysis indicates the presence of Al, Ni, Fe and Cr throughout the scale with variable amounts along with oxygen at some locations (Point 1, 2 and 4). The top scale is rich in Al and Ni along with some concentration of oxygen. The conventional thick AlCrN coated superalloy (Fig.7.42.e) indicates uniform, thin and adherent scale. EDAX point analysis shows the presence of Al, Cr, Ni and Fe throughout the scale with variable amount. The top scale shows higher percentage of Al, Cr and Fe (Point 1 and 2 on Fig.7.42.e).

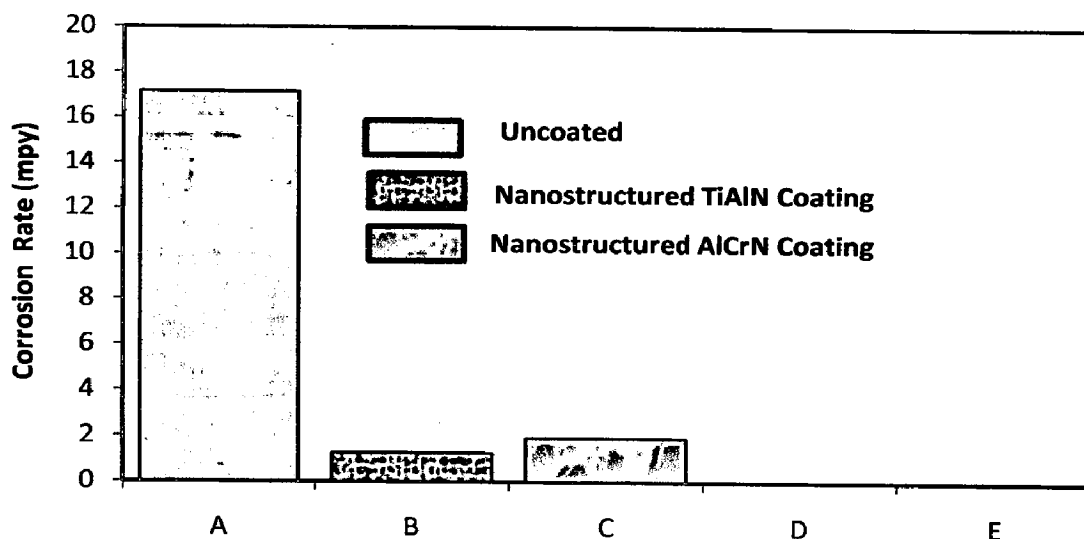


Fig. 7.44 Corrosion rate in mils per year (mpy) for uncoated and coated Superfer 800H superalloy exposed to super-heater of the coal fired boiler environment at 900°C for 1000 hours: (A) Uncoated SF 800H, (B) Nanostructured TiAlN coating, (C) Nanostructured AlCrN coating, (D) Conventional TiAlN coating, (E) Conventional AlCrN coating

7.6.1.4.2 Scale thickness

The oxidized samples were cut, mounted and polished to obtain scanning electron back scattered micrographs and X-ray mapping of different elements for coated and bare superalloy. The scale thickness values were measured from SEM back scattered micrographs as shown in Fig.7.42. The extent of erosion-corrosion in terms of scale/coating thickness (in microns) and corrosion rate in mils per year (mpy) for coated and bare superalloy is shown in Fig.7.43 and 7.44 respectively. The measured corrosion rate (mpy) for uncoated superalloy, nanostructured thin TiAlN and nanostructured thin AlCrN coatings is 17, 01, 01 mpy respectively. The coatings have shown good resistance to the corrosive environment in terms of corrosion rate (Fig.7.44). In case of conventional coatings there was no loss in substrate thickness as the environment was not able to reach substrate through the coating.

7.6.1.4.3 X-Ray mapping

X-ray mappings for a part of oxide scale of bare and coated superalloy exposed to super-heater of the coal fired boiler environment at 900°C for 1000 hours; are shown in Fig.7.45. In case of uncoated superalloy, the micrograph (Fig.7.45.a) indicates a dense scale, which mainly contains Fe, Cr and Ni with some amount of O, as indicated by X-ray mapping. In the sub-scale region; some oxygen and chromium rich pockets can be seen where Fe and Ni is absent. Also, presence of Si, Al and Ti can be observed in the sub-scale. The X-ray mapping analysis of the scale formed on nanostructured TiAlN coated superalloy is presented in Fig.7.45 (b). The X-ray mapping indicates presence of a thin layer of Al in the top scale which is having back up of a thin layer of Ti and then Cr along with the co-presence of oxygen. In case of nanostructured thin AlCrN coated superalloy; the BSEI and X-ray mappings are shown in Fig.7.45 (c). The X-ray mapping indicates the presence of a thin layer of Cr and oxygen along with some amount of Al, in the top scale. In case of conventional thick TiAlN coated superalloy, Fig.7.45 (d), Al rich thick band in the top scale is clearly seen along with some oxygen rich pockets. A thick band of Ni along with Al in the sub-scale region followed by a very thin band of chromium can be seen. A thick band of Al and Cr in the top scale is indicated by X-ray mapping (Fig. 7.45.e) in case of conventional thick AlCrN coated superalloy.

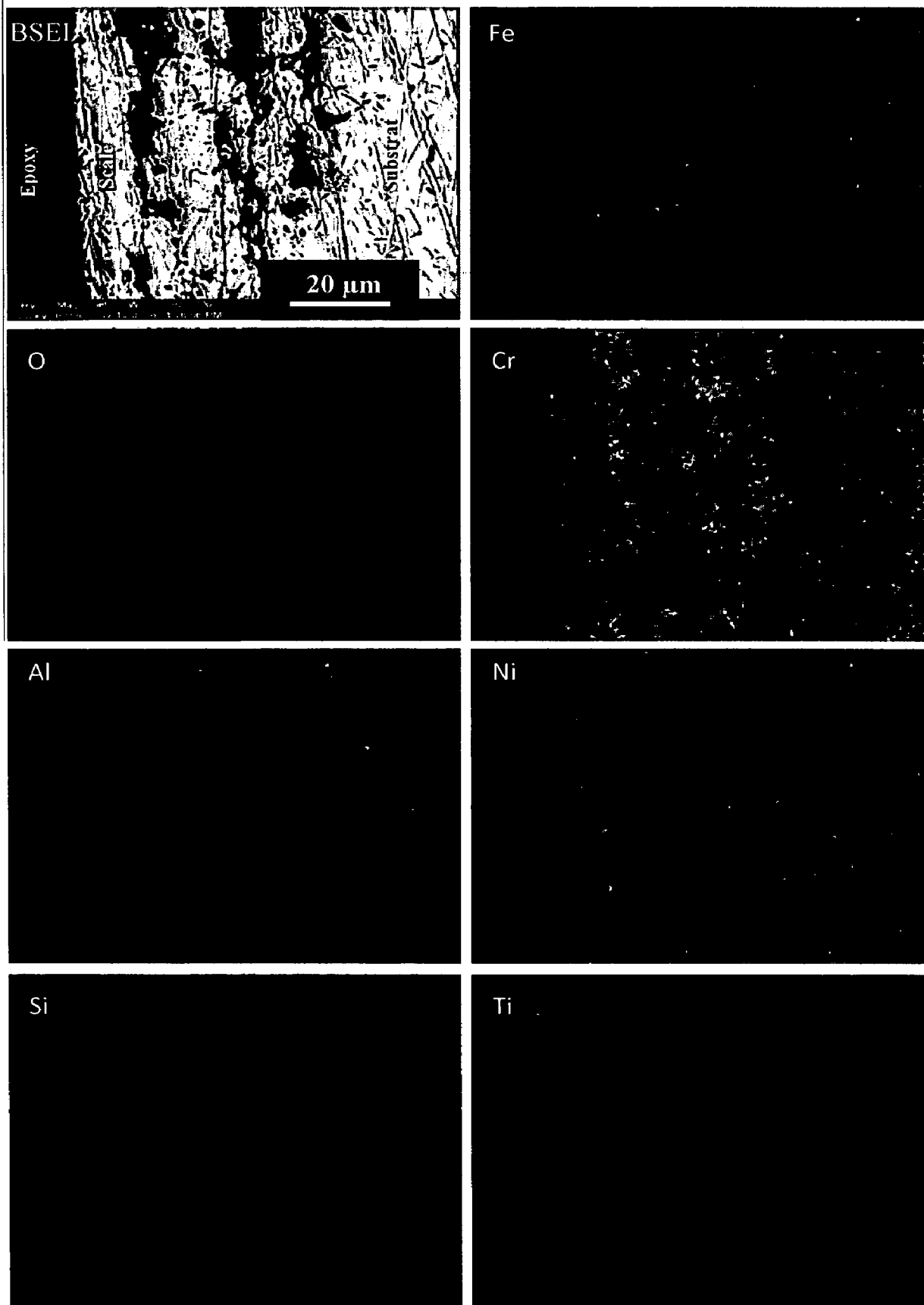


Fig. 7.45 (a) Composition image (BSEI) and X-ray mapping of the cross-section of uncoated Superfer 800H superalloy exposed to platen superheater of the coal fired boiler environment at 900°C for 1000 Hrs

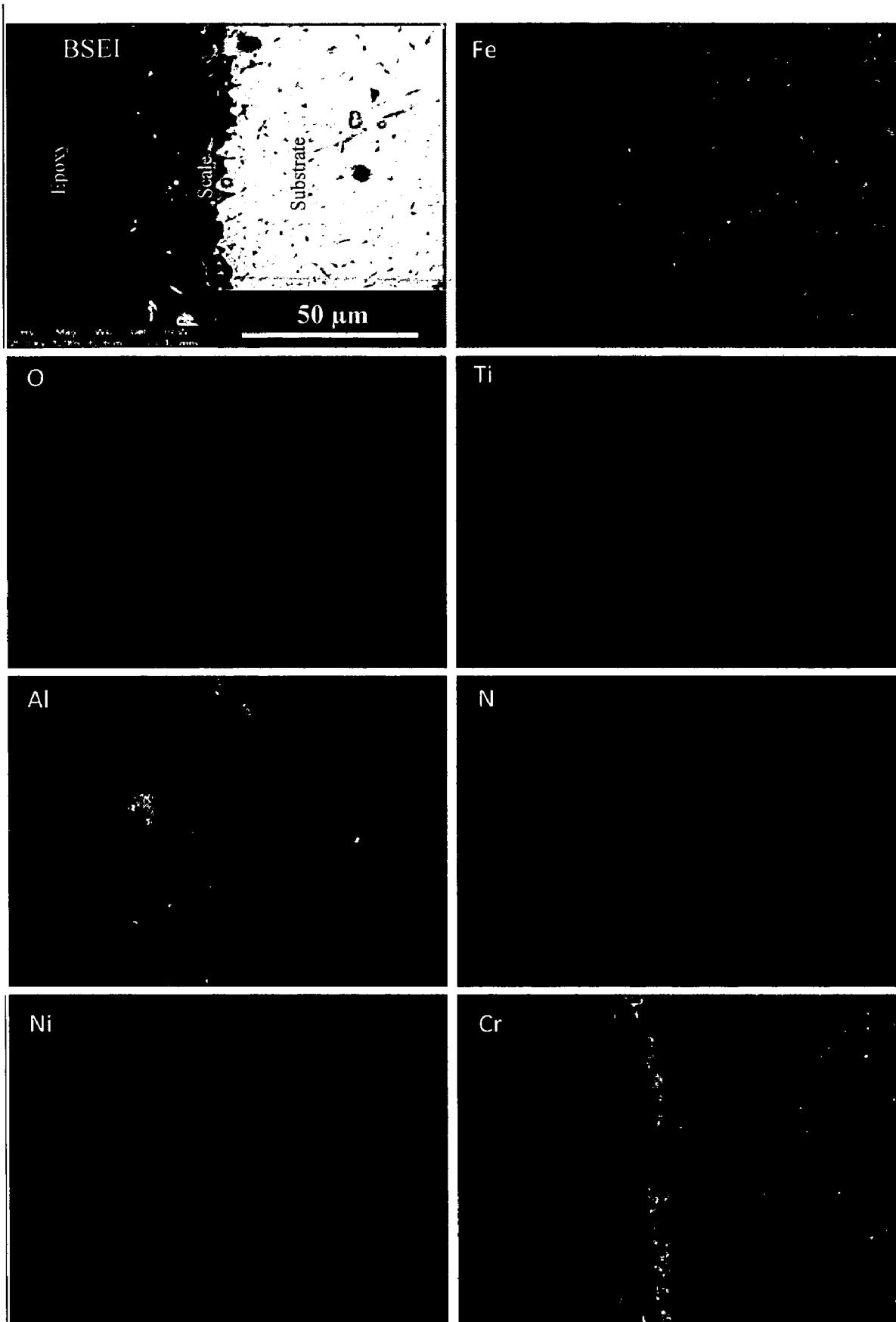


Fig. 7.45 (b) Composition image (BSEI) and X-ray mapping of the cross-section of Nanostructured TiAlN coated Superfer 800H superalloy exposed to platen superheater of the coal fired boiler environment at 900°C for 1000 Hrs

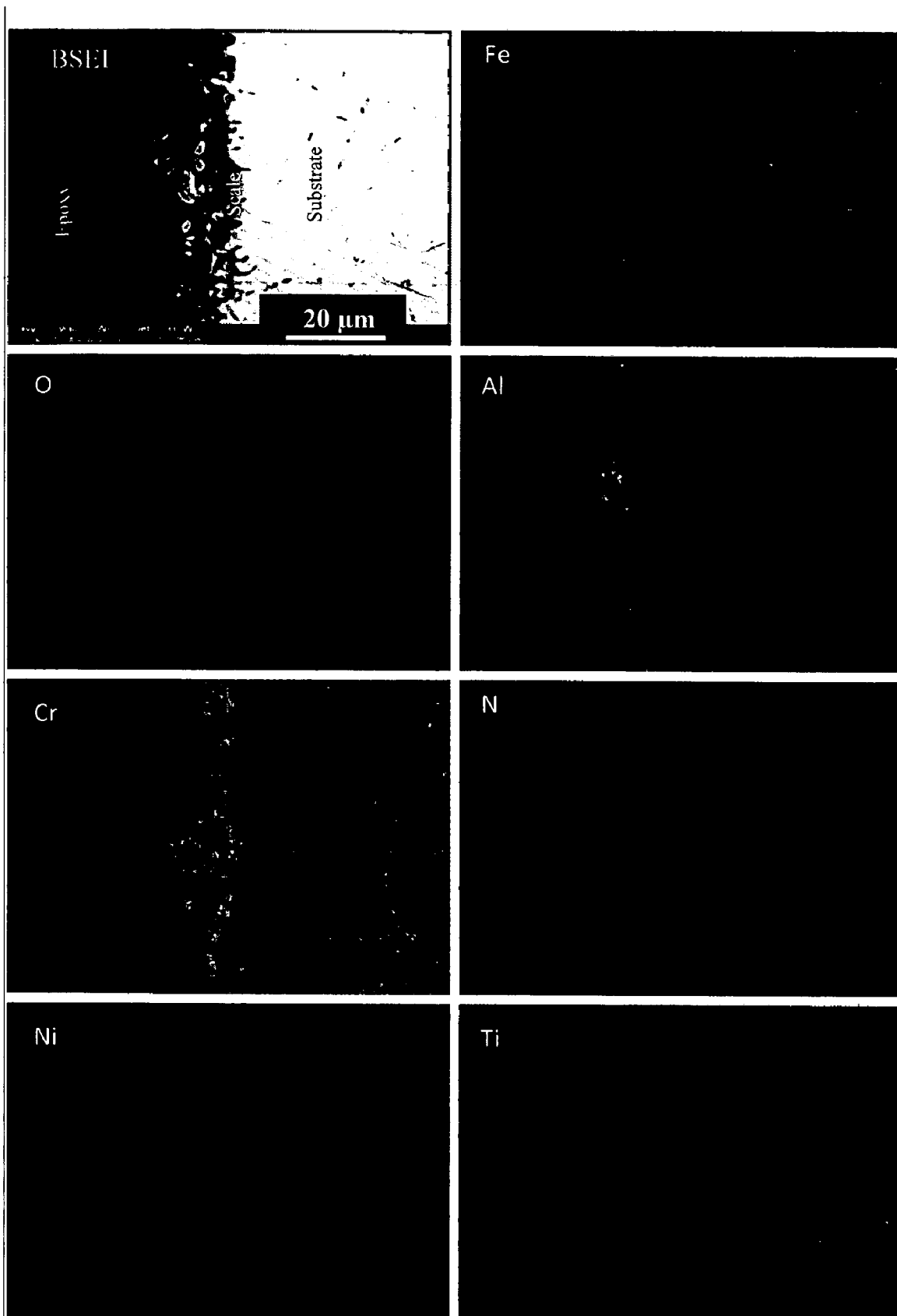


Fig. 7.45 (c) Composition image (BSEI) and X-ray mapping of the cross-section of Nanostructured AlCrN coated Superfer 800H superalloy exposed to platen superheater of the coal fired boiler environment at 900°C for 1000 Hrs

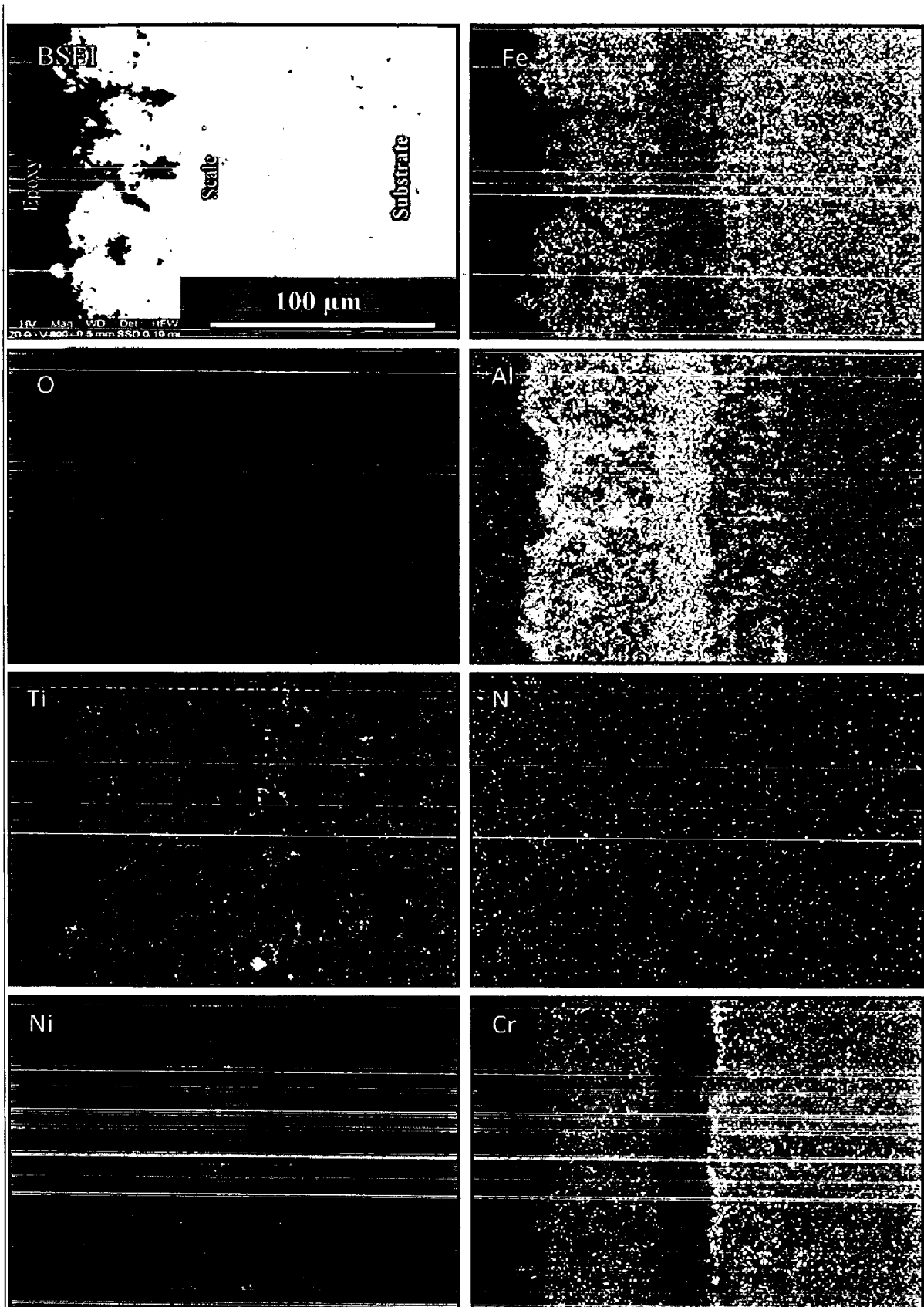


Fig. 7.45 (d) Composition image (BSEI) and X-ray mapping of the cross-section of conventional TiAlN coated Superfer 800H superalloy exposed to platen superheater of the coal fired boiler environment at 900°C for 1000 Hrs

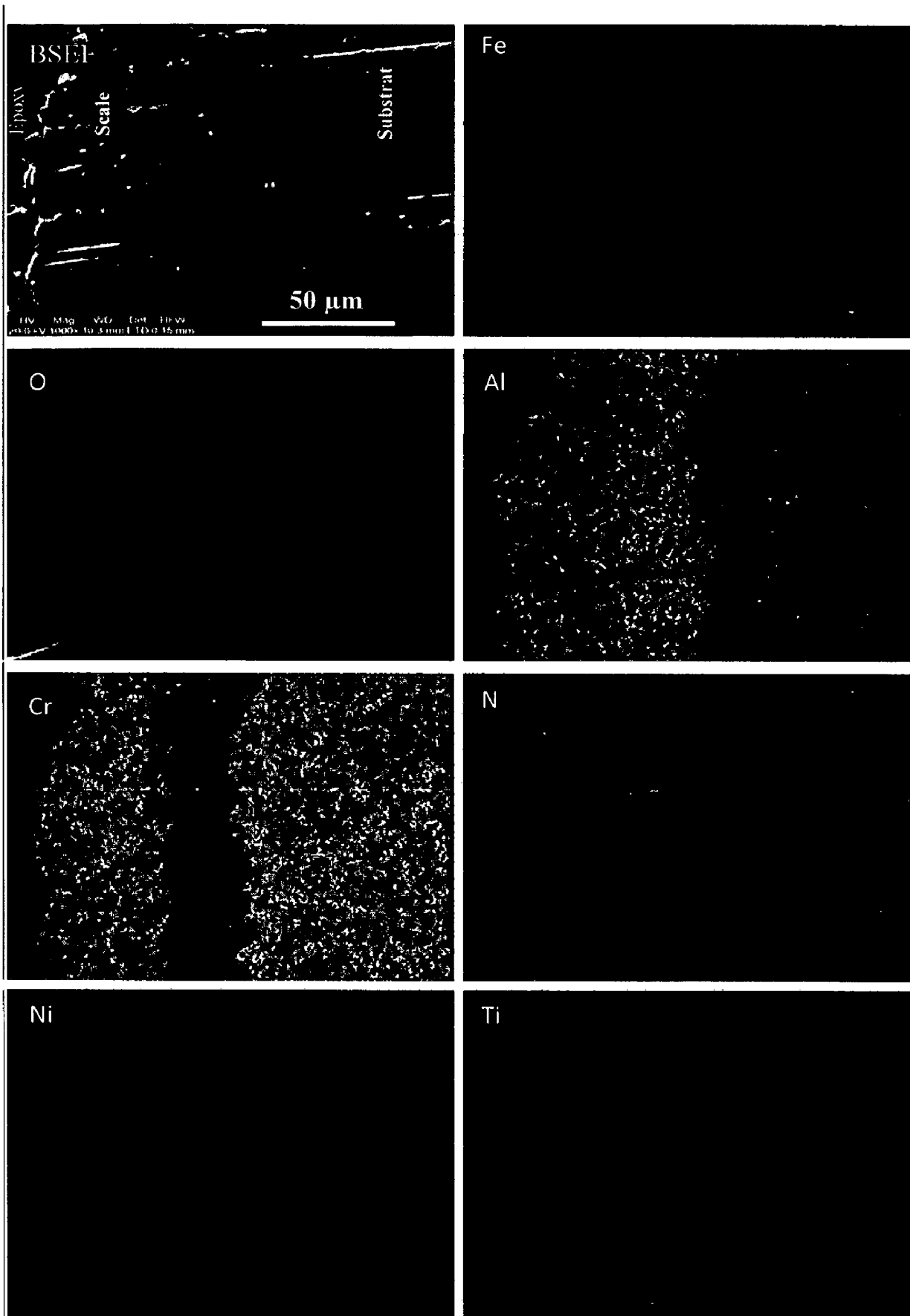


Fig. 7.45 (e) Composition image (BSEI) and X-ray mapping of the cross-section of conventional AlCrN coated Superfer 800H superalloy exposed to platen superheater of the coal fired boiler environment at 900°C for 1000 Hrs

7.6.2 Summary of Results

Results obtained after 1000 hrs of exposure of uncoated and coated Superfer 800H superalloy to super-heater of the coal fired boiler environment at 900°C are summarized in Table.7.9.

Table 7.9 Summary of the results obtained for uncoated and coated Superfer 800 superalloy exposed to super-heater of the coal fired boiler environment at 900°C for 1000 hours

Coating	Weight gain mg/cm ²	Extent of Corrosion (μm)	Corrosion Rate (mpy)	XRD phases	Remarks
Uncoated Superfer 800H superalloy	+01.71	50	17.16	γ-Ni, Cr ₂ O ₃ , α-Fe and SiO ₂	Greenish and brownish spots appeared on the surface along with white spots of ash deposits. No spalling and cracks were observed in the scale throughout the study.
Nanostructured TiAlN coating	-02.15	10	1.27	Al ₂ O ₃ , Cr ₂ O ₃ , SiO ₂ , Fe ₂ O ₃ , TiO ₂ and NiO	Color of the oxide scale at the end of the study was observed to be blackish brown with some white spots of ash deposited. Signs of erosion were observed during the study.
Nanostructured AlCrN coating	-01.16	10	1.92	Al ₂ O ₃ , Cr ₂ O ₃ , SiO ₂ , Fe ₂ O ₃ , and NiO	Blackish brown scale with some white spots of ash deposited. No spalling and cracks were observed in the scale throughout the experimentation.
Conventional TiAlN Coating	-15.54	93	00	Al ₂ O ₃ , Cr ₂ O ₃ , Fe ₂ O ₃ , TiO ₂ and Ti ₃ Al	Brownish cream colored ash deposited scale at the end of the study. Signs of erosion were observed after 3 rd cycle which continued till the end of the study.
Conventional AlCrN coating	-03.42	86	00	Al ₂ O ₃ , Cr ₂ O ₃ , SiO ₂ , Fe ₂ O ₃ , and NiO	Color of the ash deposited oxide scale was dark brown with some whitish areas at the end of the study. No spalling and cracks were observed in the scale throughout the study.

7.6.3 Discussion

The most common deposit found on boiler super heaters is sodium vanadyl vanadate, $\text{Na}_2\text{O} \cdot \text{V}_2\text{O}_4 \cdot 5\text{V}_2\text{O}_5$, which melts at a relatively low temperature, 550°C , above the melting point, this ash material corrodes metals by long-term contact (Sidhu and Prakash, 2006). The accumulation of low melting-point salts from flue-gas on the fire side surface of boiler tubes induces hot corrosion and is considered a root cause for the severe wastage of tube materials used for super heaters and reheaters in "advanced" steam-generating system (Sidhu et al., 2005). The interaction of ash (Na_2O , K_2O etc.) with the boiler gas (SO_2 , SO_3 , O_2 etc.) results in the formation of alkali sulphates (K_2SO_4 , Na_2SO_4). These alkali sulphates react with iron oxides (present in the scale or in the ash itself), in presence of SO_3 in the gas, to form alkali-ion trisulphates (Na , K) $_3\text{Fe}(\text{SO}_4)_3$, these alkali-iron trisulphates are molten at the operating temperature of the boiler due to their low melting temperatures: 624°C for $\text{Na}_3\text{Fe}(\text{SO}_4)_3$, 618°C for $\text{K}_3\text{Fe}(\text{SO}_4)_3$ and 552°C for the mixed compound (Na , K) $_3\text{Fe}(\text{SO}_4)_3$ (Srivastava et al., 1997; Weulersse-Mouturat et al., 2004). These molten compounds can flux the scale or react with the alloy to form internal sulphides. Therefore, the alkali-iron trisulphides are responsible for the degradation of super-heater in the coal-fired plants.

The weight gain (Fig.7.38) of bare superfer 800H and weight loss in case of coated superalloys might be attributed to oxidation and erosion affected corrosion respectively in the actual environment of the coal fired boiler. There is continuous formation of thin oxide scale with subsequent depletion by erosion under cyclic test conditions. As the coal used in Indian power stations has large amounts of ash (about 50%) which contain abrasive mineral species such as hard quartz (up to 15%) which increase the erosion propensity of coal (Krishnamoorthy and Seetharamu, 1989). As revealed by XRD (Fig. 7.40); the formation of Al_2O_3 and SiO_2 might be due to the deposition of ash on the surface. The higher amount of Al and Si is found in the ash. The presence of such phases in slag has also been reported by John (1986) during study on slag, gas and deposit thermochemistry in a coal gasifier and the possibility for formation of such phase in ash constituents during combustion has further been reported by Nelson et al. (1959). There is continuous formation of thin oxide scale with subsequent depletion by erosion under cyclic test conditions.

The top surface may contain inclusions, which leads to vertical cracks through which the corrosive species might have penetrated along the crack and between the metallic layers. An internal corrosion attack in case of uncoated superalloy has been revealed by X-ray mapping (Fig.7.45.a) and EDAX of the cross-section (Fig.7.42.a). There are some Cr and O rich pockets in the sub-scale region; in case of uncoated superalloy. The XRD analysis of the corroded bare superfer 800H did not indicate the presence of the sulphides in the oxide scale. This may be due to the formation of very thin oxide scale on the surface. Weulersse-Mouturat et al. (2004) reported that due to their low content, alkali-iron-trisulphates were not identified in the scale. Absence of sulphide formation as indicated by the XRD analysis is further supported by the findings of Crossley et al. (1948). They reported that the presence of fly ash particles rich in magnetite reduced the concentration of SO_3 in the boiler system fired by mechanical stokers.

The weight change plots (Fig.7.38) for the uncoated and coated Superfer 800H superalloy shows weight gain in case of uncoated and weight loss in case of all the coatings; when exposed to super-heater of the coal fired boiler environment at 900°C for 1000 hours. The conventional thick TiAlN coated superalloy has shown maximum weight loss. This may be attributed to the erosion due to ash particles. The weight loss in case of conventional coatings is supported by SEM/EDAX of cross-section (Fig.7.42) and X-ray mapping analysis (Fig.7.45). At the same time, the conventional thick coatings are showing full protection to the substrate against high temperature oxidation as the amount of oxygen present in the scale is very less as revealed by cross-section SEM/EDAX (Fig.7.42) and X-ray mapping analysis (Fig.7.45). Some Al and O rich pockets can be seen in case of conventional TiAlN coating. The XRD analysis (Fig.7.40) revealed the presence of Al_2O_3 , Cr_2O_3 , Fe_2O_3 , TiO_2 and Ti_3Al in case of conventional TiAlN coatings and Al_2O_3 , Cr_2O_3 , SiO_2 , Fe_2O_3 , and NiO peaks in case of conventional thick AlCrN coating. The formation of Al_2O_3 and SiO_2 might be due to the deposition of ash on the surface.

The extent of erosion-corrosion in terms of corrosion rate in mils per year (mpy) for coated and bare superalloy is shown in Fig.7.44. The measured corrosion rate (mpy) for uncoated superalloy, nanostructured thin TiAlN and nanostructured thin AlCrN coatings is 17, 01, 01 mpy respectively. The coatings have shown good resistance to the corrosive environment in terms of corrosion rate (Fig.7.44). In case of conventional coatings there was no loss in substrate thickness as the environment was not able to

reach substrate through the coating as revealed from cross-section SEM/EDAX (Fig. 7.42) and X-ray mapping analysis (Fig. 7.45). The nanostructured thin coatings have shown a little gain in scale thickness (Fig.6) and loss in weight due to erosion-corrosion. The formation of Al_2O_3 , Cr_2O_3 , SiO_2 , Fe_2O_3 and NiO peaks has been revealed in the scale of nanostructured thin coatings along with TiO_2 in case of nanostructured TiAlN coating. This is well supported by SEM/EDAX (Fig.7.42. b and c) and X-ray mapping analysis (Fig.7.45.b and c) of cross-section of the samples in case of nanostructured thin coatings. The X-ray mapping analysis in case of nanostructured thin TiAlN coating indicates the presence of a thin layer of Al in the top scale which is having back up of a thin layer of Ti and then Cr along with the co-presence of oxygen. In case of nanostructured thin AlCrN coated superalloy; the BSEI and X-ray mappings are shown in Fig.7.45 (c). The X-ray mapping indicates the presence of a thin layer of Cr and oxygen along with some amount of Al, in the top scale. So, the protective Al_2O_3 and Cr_2O_3 oxide bands formed in the top scale in case of nanostructured coatings are providing the full protection to the substrate.

7.6.4 Conclusions

The high temperature erosion-corrosion behaviors of uncoated and coated Suprefer 800H superalloy have been investigated in super-heater of the coal fired boiler environment at 900°C for 1000 hours (10 cycles) and the following conclusions are made:

1. The plasma sprayed gas nitride conventional thick coatings i.e. TiAlN and AlCrN have developed a protective scale mainly consisting on aluminum oxide.
2. The nanostructured thin coatings have protected the substrate by developing Al_2O_3 and Cr_2O_3 oxide bands in the top scale.
3. The oxide scale formed is adherent to the substrate in all coatings.
4. The bare superalloy has shown weight gain and all the coatings have shown weight loss.
5. The measured corrosion rate (mpy) for uncoated superalloy, nanostructured thin TiAlN and nanostructured thin AlCrN coatings is 17, 01, 01 mpy respectively. In case of conventional coatings there was no loss in substrate thickness as the environment was not able to reach substrate.

Chapter 8

COMPARATIVE DISCUSSION

This chapter presents the comparative performance of the uncoated and coated alloys when exposed to high temperature oxidation in air and in molten salt environments; at 900°C under cyclic conditions, erosion-corrosion in simulated coal-fired environment, corrosion in simulated marine environment as well as in the actual industrial environment of the coal-fired boiler at 900°C under cyclic conditions.

8.1 OXIDATION STUDIES IN AIR

The high temperature oxidation behaviors of conventional thick (by plasma spraying and gas nitrided) and nanostructured thin (by physical vapor deposition process) TiAlN and AlCrN coated and uncoated alloys have been investigated in air at 900°C for 50 cycles. The cumulative weight gain per unit area for the coated and uncoated alloys is shown in Fig. 8.1. From the column charts; it can be inferred that the coated and uncoated boiler steels have shown lower resistance to high temperature oxidation in air when compared with Superfer 800H superalloy. In case of uncoated Superfer 800H superalloy, the oxide phases found are Fe_2O_3 , Cr_2O_3 , NiO, NiCr_2O_4 and NiFe_2O_4 . According to Stott (1998) in the initial stage of oxidation process in case of Fe-based superalloy; the alloy surface adsorb the oxygen molecules, small impinging nuclei of all the thermodynamically stable oxides such as those of Ni, Cr, Fe and Mn develop on the surface of the alloy. As the concentration of Fe and Ni is higher in Superfer 800H, the amount of nickel and iron oxide in this layer will be the higher, whereas chromium oxide will be the second dominating phase, followed by oxides of Mn. Once a continuous layer Cr_2O_3 is formed at the alloy-scale interface, the rate of oxidation is then controlled by transport of reactants across this layer, which is much slower process than across the initially formed NiO-rich layer. Thereafter, oxidation process enters a steady state. So, due to higher percentage of Ni and Cr in the Superfer 800H; this superalloy has performed well in high temperature oxidation studies in air.

Among the uncoated boiler steels; Grade A-1 has shown lesser weight gain than T-11 and T-22 boiler steel. The higher weight gain and spalling as observed in case of T-11 and T-22 boiler steels may be attributed to the presence of molybdenum in the steels. Chatterjee et al. (2001) have suggested that during initial oxidation Fe is oxidized and the oxide scale is protective in nature. With progress of oxidation Mo becomes enriched at the alloy interface, leading to the formation of an inner layer of molten MoO_3 (m. p. 795°C) which penetrates along the alloy-scale interface. This liquid oxide disrupts and dissolves the protective oxide scale, causing the alloy to suffer catastrophic oxidation (Lai, 1990). In case of Grade A-1, T-11 boiler steel and Superfer 800H superalloy; all the coatings have shown protection to the substrate in terms of weight gain than respective uncoated alloys.

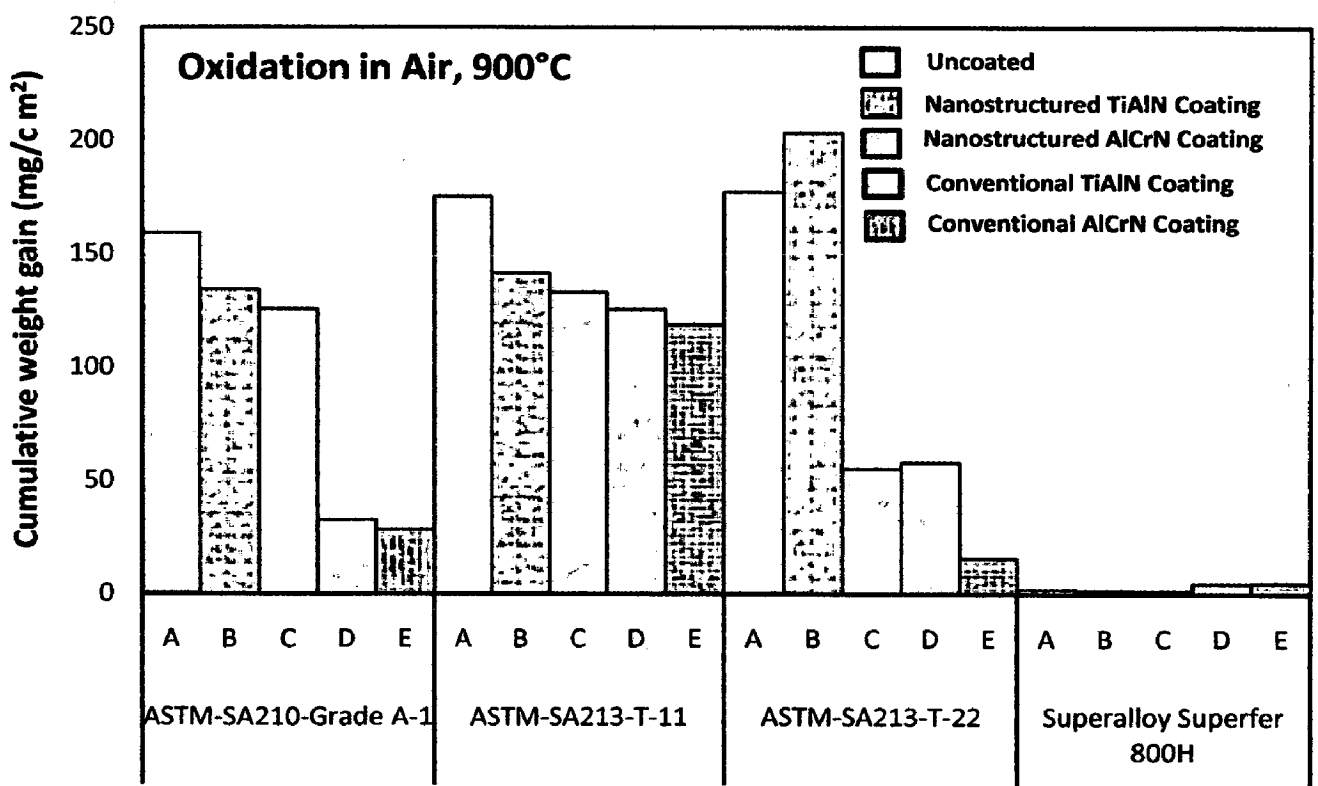


Fig. 8.1 Column chart showing cumulative weight gain per unit area (mg/cm^2) for the uncoated and coated alloys' specimens subjected to cyclic oxidation in air at 900°C for 50 cycles; (A) Uncoated alloy, (B) Nanostructured TiAlN coating, (C) Nanostructured AlCrN coating, (D) Conventional TiAlN coating, (E) Conventional AlCrN coating

The nanostructured TiAlN and AlCrN coatings has shown resistance to oxidation to some extent as the overall weight gain is less than uncoated alloys, but failed to sustain during the course of high temperature oxidation study in most of the cases in present investigation. The nanostructured AlCrN coating in case of T-22 boiler steel has provided excellent resistance to oxidation in air at 900°C for 50 cycles. Whereas the nanostructured thin TiAlN coating failed to sustain during the course of the study and has shown highest weight gain (Fig.8.1). This might be due to the formation of oxide scale which is composed of a porous oxide mixture of TiO₂ and Al₂O₃, with the domination of TiO₂.

The conventional thick AlCrN coating have successfully protected the respective substrate when subjected to cyclic oxidation at 900°C for 50 cycles due to the formation of a protective scale mainly consisting on Al₂O₃. The plasma sprayed gas nitride conventional thick TiAlN coating has successfully protected the substrate i.e. Grade A-1 boiler steel and Superfer 800H superalloy but failed to sustain during the course of the study in case of T-11 and T-22 boiler steel. Development of some minor cracks near or along the edges of the coated specimens, during oxidation experimentation in air, were observed for plasma sprayed gas nitrided coatings, which led to spalling of coatings. This cracking and subsequent spalling may be attributed to the thermal shocks due to differences in the heat expansion coefficients of the oxides, coatings and the substrate.

The plasma sprayed gas nitride conventional thick AlCrN and TiAlN coatings subjected to cyclic oxidation in air have shown relatively high weight gains in the early cycles of the exposure. These initial high oxidation rates in general might partially be attributed to the rapid formation of oxides at the coating splat boundaries and within open pores due to the penetration of the oxidizing species along the splat boundaries/open pores in the early cycles of the study. The weight change plots (as reported in chapters 4, 5, 6 and 7) for the uncoated and coated alloys indicated that the oxidation behavior has shown conformance to parabolic rate law. The parabolic kinetic behavior is due to the diffusion controlled mechanism operating at 900°C under cyclic conditions (Mahesh et al., 2008). Small deviation from the parabolic rate law might be due to the cyclic scale growth.

8.2 HOT CORROSION STUDIES IN MOLTEN SALT ENVIRONMENT

There is no reported study on cyclic high temperature corrosion behavior of nanostructured thin and conventional thick TiAlN and AlCrN hard coatings in molten salt environment. Therefore, the hot corrosion behavior of conventional thick (by plasma spraying and gas nitrided) and nanostructured thin (by physical vapor deposition process) TiAlN and AlCrN coatings on boiler steels (Grade A-1, T-11 and T-22) and a superalloy Superfer 800H, in an aggressive environment of Na_2SO_4 -60% V_2O_5 molten salt at 900°C under cyclic conditions has been investigated and compared. X-ray diffraction (XRD), scanning electron microscopy/energy-dispersive analysis (SEM/EDAX) and X-ray mapping techniques have been used to characterize corrosion products after hot corrosion at 900°C. The cumulative weight gain per unit area for the coated and uncoated alloys is shown in Fig. 8.2.

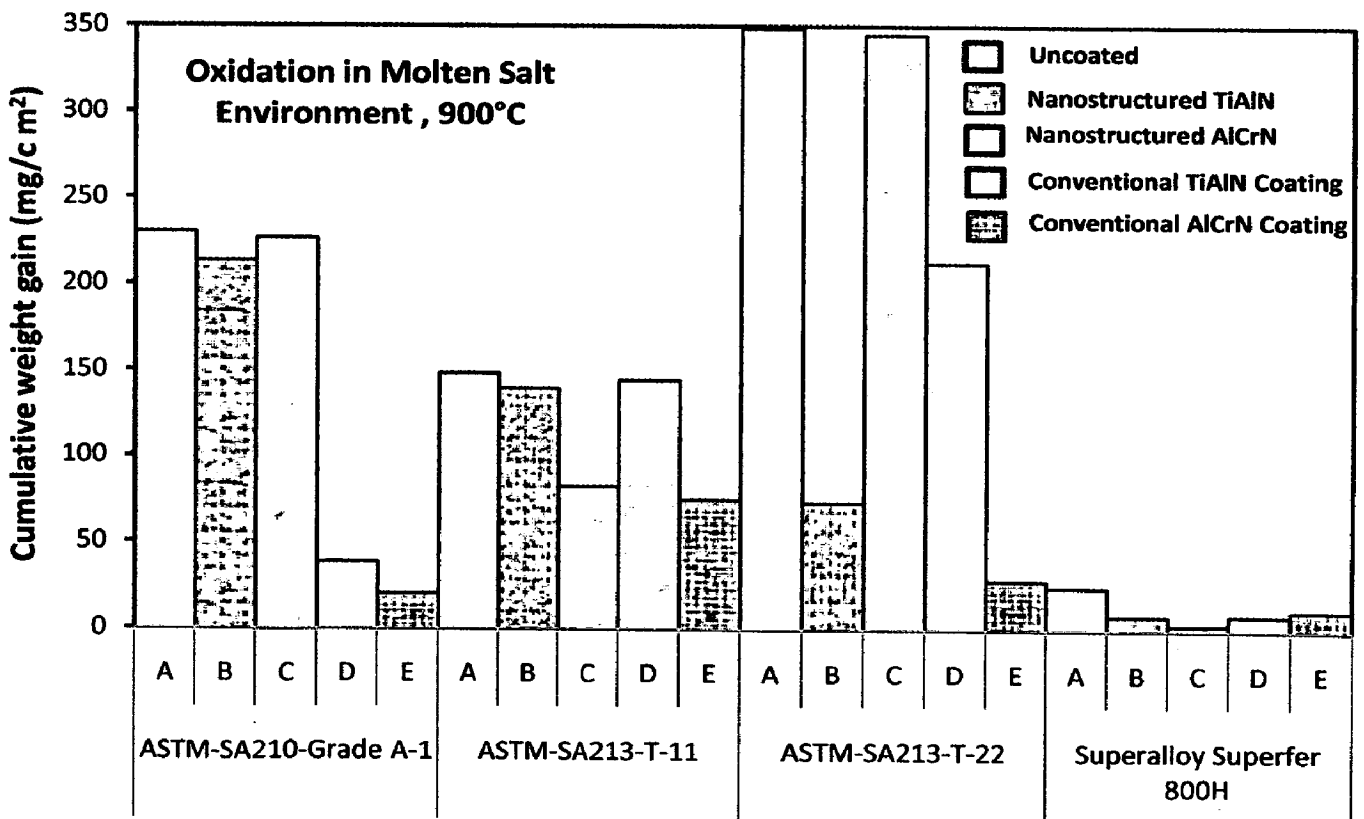


Fig. 8.2 Column chart showing cumulative weight gain per unit area (mg/cm^2) for the uncoated and coated alloys' specimens exposed to molten salt (Na_2SO_4 -60% V_2O_5) environment at 900°C for 50 cycles; (A) Uncoated alloy, (B) Nanostructured TiAlN coating, (C) Nanostructured AlCrN coating, (D) Conventional TiAlN coating, (E) Conventional AlCrN coating

From the column charts; it can be inferred that the uncoated alloys have shown lower resistance to high temperature oxidation in molten salt environment than coated alloys under cyclic conditions. Also, the coated and uncoated Superfer 800H has shown higher resistance to hot corrosion in molten salt environment at high temperature when compared with the coated as well as uncoated boiler steels. The conventional thick coatings have shown relatively higher weight gain in the early cycles of study, followed by tendency to show gradual weight gain with further increase in number of cycles. These initial high oxidation rates in general might partially be attributed to the rapid formation of oxides at the coating splat boundaries and within open pores due to the penetration of the oxidizing species along the splat boundaries/open pores in the early cycles of the study.

Based on the overall weight gain after 50 cycles in an aggressive Na_2SO_4 -60% V_2O_5 (molten salt) environment at 900°C temperature; the T-22 boiler steel has shown minimum resistance and Superfer 800H superalloy has shown maximum resistance to corrosion. As the concentration of Fe, Cr and Ni is higher in Superfer 800H, the amount of nickel and iron oxide in top oxide layer will be the higher, whereas chromium oxide will be the second dominating phase, followed by oxides of Mn. So, due to higher percentage of Ni and Cr in the Superfer 800H; this superalloy has performed well at high temperature oxidation in molten salt environment.

The plasma sprayed gas nitride conventional thick AlCrN coating when subjected to cyclic oxidation in Na_2SO_4 -60% V_2O_5 molten salt at 900°C for 50 cycles has developed a protective scale mainly consisting on aluminum oxide and chromium oxide, which are supported by XRD, EDAX and X-ray mapping analysis. This coating has successfully protected all the substrates. The oxide scale formed was found to be adherent to the substrate in all the specimens after hot corrosion studies. It has shown maximum weight gain in case of T-11 boiler steel (74 mg/cm² which is 50% of the weight gain in case of bare T-11 boiler steel) and lowest in case of Superfer 800H (11 mg/cm² which is 45% of the weight gain in case of bare superalloy).

The plasma sprayed gas nitride conventional thick TiAlN coating has shown full protection to the substrate i.e. Grade A-1 boiler steel and Superfer800H superalloy but failed to sustain during the course of the study in case of T-11 and T-22 boiler steel. It has shown maximum weight gain in case of T-22 boiler steel (212 mg/cm² which is 60%

of the weight gain in case of bare T-22 boiler steel) and lowest in case of Superfer 800H (0.08 mg/cm^2 which is 33% of the weight gain in case of the bare superalloy). The oxide scale formed was found to be adherent to the substrate in case of Grade A-1 boiler steel and Superfer 800H superalloy after hot corrosion studies. Whereas in case of T-11 and T-22 boiler steel the scale gets detached from the substrate after hot corrosion studies. The appearance of cracks/peeling off in the coatings during hot corrosion studies may be attributed to the different values of thermal expansion coefficients for the coating.

The nanostructured thin TiAlN and AlCrN coatings has shown resistance to oxidation to some extent as the overall weight gain is less than as compared to the uncoated alloys, but failed to sustain during the course of high temperature oxidation study in molten salt environment. The nanostructured AlCrN coated Superfer 800H has shown least weight gain (0.02 mg/cm^2 which is 08.3% of the weight gain in case of bare superalloy). This coating failed to provide protection to the substrate in case of Grade A-1 and T-22 boiler steel. Also, the scale is found to be detached from the substrate after hot corrosion studies. The nanostructured thin TiAlN coated T-22 boiler steel and Superfer 800H superalloy have shown resistance to oxidation as the overall weight gain is less than as compared to the uncoated counterparts, which may be due to the thick band of Cr along with O at the scale-substrate interface.

8.3 EROSION STUDIES IN SIMULATED COAL-FIRED BOILER ENVIRONMENT

The erosion studies were carried out using a high temperature air-jet erosion test rig. The erosion rate for uncoated and coated alloys; is shown in Fig. 8.3. The two temperatures were taken for the test, sample temperature 400°C and air/erodent temperature 900°C simulated to service conditions of boiler tubes in which sample temperature and flow gas temperature correspond to the inner and outer temperature of water wall pipes.

In case of uncoated alloys; at 90° impact angle the erosion rate was maximum ($0.38 \times 10^{-03} \text{ mm}^3/\text{gm}$) in case of T-22 boiler steel and minimum ($0.03 \times 10^{-03} \text{ mm}^3/\text{gm}$) in case of Superfer 800H superalloy and T-11 boiler steel. At 30° impact angle; the erosion rate was maximum ($0.49 \times 10^{-03} \text{ mm}^3/\text{gm}$) in case of Grade A-1 boiler steel and minimum ($0.16 \times 10^{-03} \text{ mm}^3/\text{gm}$) in case of Superfer 800H superalloy.

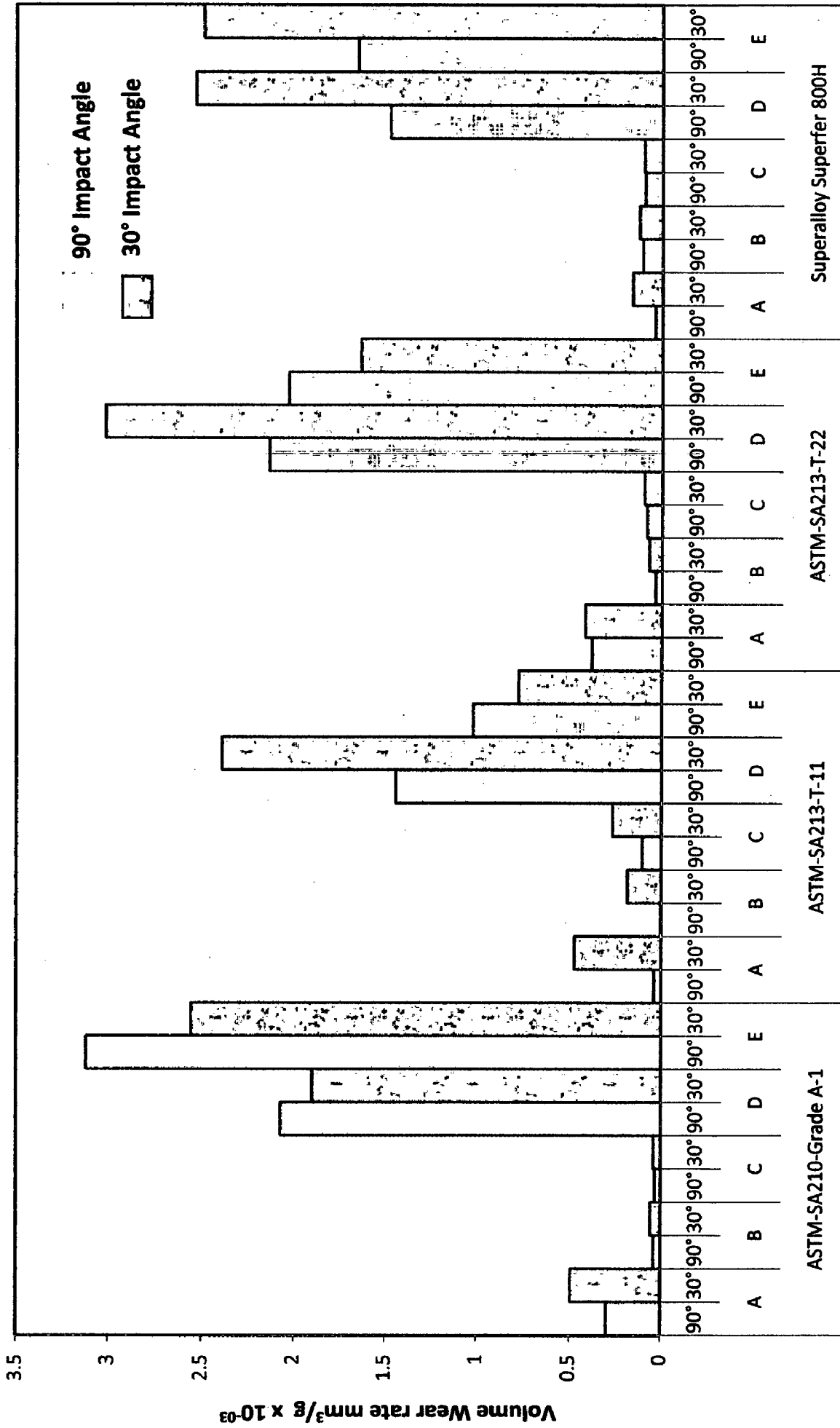


Fig. 8.3 Column chart showing the Volume wear rate of uncoated and coated alloys' specimens eroded at normal and oblique impact: (A) Uncoated Alloy, (B) Nanostructured TiAlN coating, (C) Nanostructured AlCrN coating, (D) Conventional TiAlN coating, (E) Conventional AlCrN coating

It can be inferred from Fig.8.3 that all the uncoated alloys have shown higher erosion rate at oblique impact (at 30°) than at normal impact (at 90°), which indicate ductile behavior as proposed by Murthy et al. (2001). Authors suggested that the material subjected to erosion initially undergoes plastic deformation and is later removed by subsequent impacts of the erodent on the surface. The ploughing occurs by the impact of the erodent particles and lips or ridges are formed at the bank of the craters. These lips are fractured or removed with further erosion. Most of the metallic materials, irrespective of temperature of erosion, exhibit a ductile behavior, i.e. maximum erosion rate at oblique impact angles (Tabakoff and Vittal, 1983, Bellman and Lavy, 1981).

In case of nanostructured thin TiAlN coated alloys; at 90° impact angle the erosion rate was maximum ($0.16 \times 10^{-03} \text{ mm}^3/\text{gm}$) in case of Superfer 800H superalloy and minimum ($0.004 \times 10^{-03} \text{ mm}^3/\text{gm}$) in case of T-11 boiler steel. At 30° impact angle; the erosion rate was maximum ($0.185 \times 10^{-03} \text{ mm}^3/\text{gm}$) in case of T-11 boiler steel and minimum ($0.05 \times 10^{-03} \text{ mm}^3/\text{gm}$) in case of Grade A-1 boiler steel. It can be inferred from Fig.8.3 that all the nanostructured thin TiAlN and AlCrN coated alloys have shown higher erosion rate at oblique impact (at 30°) than at normal impact (at 90°), which indicate ductile behavior as proposed by Murthy et al. (2001). In case of nanostructured thin AlCrN coated alloys; at 90° impact angle the erosion rate was maximum ($0.10 \times 10^{-03} \text{ mm}^3/\text{gm}$) in case of T-11 boiler steel and minimum ($0.03 \times 10^{-03} \text{ mm}^3/\text{gm}$) in case of Grade A-1 boiler steel. At 30° impact angle; the erosion rate was maximum ($0.26 \times 10^{-03} \text{ mm}^3/\text{gm}$) in case of T-11 boiler steel and minimum ($0.03 \times 10^{-03} \text{ mm}^3/\text{gm}$) in case of Grade A-1 boiler steel. The nanostructured thin TiAlN and AlCrN coatings were removed by the continuous strikes of the eroding particles on the surface of the coating at 30° impact in case of Superfer 800H superalloy.

The plasma sprayed conventional TiAlN and AlCrN coatings have successfully protected the substrates at both impact angles except in case of T-11 boiler steel. The conventional AlCrN coating gets removed by the continuous strikes of the eroding particles on the surface of the coating in case of T-11 boiler steel. In case of plasma sprayed gas nitride conventional thick TiAlN coated alloys; at 90° impact angle the erosion rate was maximum ($2.13 \times 10^{-03} \text{ mm}^3/\text{gm}$) in case of T-22 boiler steel and minimum ($1.44 \times 10^{-03} \text{ mm}^3/\text{gm}$) in case of T-11 boiler steel. At 30° impact angle; the erosion rate was maximum ($3.01 \times 10^{-03} \text{ mm}^3/\text{gm}$) in case of T-22 boiler steel and

minimum ($1.89 \times 10^{-03} \text{mm}^3/\text{gm}$) in case of Grade A-1 boiler steel. It can be inferred from Fig.8.3 that all the conventional thick TiAlN coated alloys have shown higher erosion rate at oblique impact (at 30°) than at normal impact (at 90°) except in case of Grade A-1 boiler steel.

In case of conventional thick AlCrN coated alloys; at 90° impact angle the erosion rate was maximum ($3.12 \times 10^{-03} \text{mm}^3/\text{gm}$) in case of Grade A-1 boiler steel and minimum ($1.023 \times 10^{-03} \text{mm}^3/\text{gm}$) in case of T-11 boiler steel. At 30° impact angle; the erosion rate was maximum ($2.55 \times 10^{-03} \text{mm}^3/\text{gm}$) in case of Grade A-1 boiler steel and minimum ($0.77 \times 10^{-03} \text{mm}^3/\text{gm}$) in case of T-11 boiler steel. It can be inferred from Fig.8.3 that all the conventional thick AlCrN coated alloys have shown higher erosion rate at normal impact (at 90°) than at oblique impact (at 30°) except in case of Superfer 800H superalloy.

8.4 CORROSION STUDIES IN SIMULATED MARINE ENVIRONMENT

The corrosion behavior of conventional thick (by plasma spraying and gas nitrided) and nanostructured thin (by physical vapor deposition process) TiAlN and AlCrN coatings on selected substrates has been compared with bare specimens by electrochemical methods i.e. linear polarization resistance (LPR) and potentiodynamic polarization tests in an aerated 3.0 wt% NaCl solution at room temperature; and salt spray (Fog) tests.

8.4.1 Linear polarization resistance and potentiodynamic polarization tests

Linear polarization resistance (LPR) and potentiodynamic polarization tests were conducted in an aerated 3 wt% NaCl solution at room temperature in order to evaluate the corrosion behavior of the substrate and coatings. The initial corrosion current density and LPR (R_p) was measured by LPR test. The linear polarization scans are conducted in very small potential range (-20mV to + 20mV vs Open Circuit Potential), which does not damage the surface of the sample. Whereas the potentiodynamic polarization scans require scanning over a longer potential range (Sahoo and Balasubramaniam, 2007).

The initial corrosion current density and LPR (R_p) was measured by LPR test. The corrosion parameters obtained in LPR test are shown in Table 8.1. The corrosion current

density of all the coatings was found much lower than that of the substrate except conventional coatings on T-11 boiler steel and conventional TiAlN coated Superfer 800H superalloy. In case of uncoated alloys; bare T-22 boiler steel has shown maximum corrosion current density ($108.60 \mu\text{A}/\text{cm}^2$) and Superfer 800H has shown best corrosion resistance at initial stage on the basis of corrosion current density ($05.37 \mu\text{A}/\text{cm}^2$) and polarization resistance values obtained in the test.

In case of nanostructured TiAlN coating; T-11 boiler steel has shown maximum current density ($03.99 \mu\text{A}/\text{cm}^2$) and Superfer 800H has shown least corrosion current density ($00.33 \mu\text{A}/\text{cm}^2$). These values are very less than corrosion current densities in case of respective bare alloys. Grade A-1 boiler steel has shown maximum corrosion current ($09.42 \mu\text{A}/\text{cm}^2$) and Superfer 800H with least corrosion current density ($00.47 \mu\text{A}/\text{cm}^2$) in case of nanostructured AlCrN coating. In case of conventional TiAlN coating; the T-11 boiler steel has shown least resistance to corrosion with higher corrosion current density ($43.63 \mu\text{A}/\text{cm}^2$) and Grade A-1 boiler steel has shown least current density ($12.87 \mu\text{A}/\text{cm}^2$). In case of conventional AlCrN coating; T-11 boiler steel has shown maximum current density ($51.89 \mu\text{A}/\text{cm}^2$) and Superfer 800H has shown least corrosion current density ($00.37 \mu\text{A}/\text{cm}^2$).

The corrosion parameters obtained in Potentiodynamic polarization test are shown in Table 8.2. The corrosion current density and the corrosion potential were obtained by the intersection of the extrapolation of anodic and cathodic Tafel curves, which are presented in Chapter 4, 5, 6 and 7 of the present study. The corrosion current densities of the coatings were found much lower than that of the substrate steel except for nanostructured and conventional TiAlN coated Superfer 800H superalloy. Also, the corrosion current densities of the substrate and the coatings were found much lower as compared to the LPR test (at initial stage) results. A protective oxide layer may have formed which has blocked further corrosion. The corrosion product formed may have reduced the passage of the electrolyte to attack the samples, and hence providing protection. In case of uncoated alloys; T-22 boiler steel has shown maximum current density ($17.02 \mu\text{A}/\text{cm}^2$) and Superfer 800H has shown best corrosion resistance with least corrosion current density ($0.058 \mu\text{A}/\text{cm}^2$).

Table 8.1 Results of Linear Polarization Resistance Test (LPR) of bare and coated alloys

Substrate Coatings	Grade A-1		T-11 Boiler steel		T-22 Boiler Steel		S.F 800H	
	i_{corr} ($\mu\text{A}/\text{cm}^2$)	R_p ($\text{k}\Omega\text{-cm}^2$)	i_{corr} ($\mu\text{A}/\text{cm}^2$)	R_p ($\text{k}\Omega\text{-cm}^2$)	i_{corr} ($\mu\text{A}/\text{cm}^2$)	R_p ($\text{k}\Omega\text{-cm}^2$)	i_{corr} ($\mu\text{A}/\text{cm}^2$)	R_p ($\text{k}\Omega\text{-cm}^2$)
A	22.40	0.969	12.54	01.73	108.60	00.20	05.37	04.04
B	01.92	11.27	03.99	05.43	03.467	06.26	00.33	64.14
C	09.42	02.30	08.99	02.44	06.692	03.24	00.47	45.73
D	12.87	01.68	43.63	00.49	19.330	01.12	23.81	00.91
E	03.77	05.75	51.89	00.41	43.750	00.49	00.37	58.10

Table 8.2 Results of Potentiodynamic Polarization Tests of bare and coated alloys

Substrate Coatings	Grade A-1			T-11 Boiler steel			T-22 Boiler Steel			S.F 800H		
	i_{corr} ($\mu\text{A}/\text{cm}^2$)	R_p ($\text{k}\Omega\text{-cm}^2$)	P_i (%)	i_{corr} ($\mu\text{A}/\text{cm}^2$)	R_p ($\text{k}\Omega\text{-cm}^2$)	P_i (%)	i_{corr} ($\mu\text{A}/\text{cm}^2$)	R_p ($\text{k}\Omega\text{-cm}^2$)	P_i (%)	i_{corr} ($\mu\text{A}/\text{cm}^2$)	R_p ($\text{k}\Omega\text{-cm}^2$)	P_i (%)
A	9.498	02.78	--	08.085	23.95	--	17.02	01.53	--	0.058	586.89	--
B	0.676	40.38	92.87	01.268	33.73	84.31	04.72	06.76	72.26	0.068	383.55	NP
C	5.982	04.46	37.01	00.315	64.77	96.10	00.87	27.39	94.88	0.021	1049.52	63.79
D	2.071	33.33	78.19	00.059	187.7	99.20	08.97	04.13	47.27	5.368	011.52	NP
E	1.308	31.43	86.22	06.641	02.80	17.86	3.93	06.42	76.87	0.0033	3812.81	94.21

A-Uncoated Alloy, B-Nanostructured TiAlN Coating, C-Nanostructured AlCrN Coating, D- Conventional TiAlN Coating, E- Conventional AlCrN Coating
 i_{corr} Corrosion Current, R_p Resistance, P_i Protective Efficiency

In case of nanostructured TiAlN coating; T-22 boiler steel has shown maximum current density ($04.72 \mu\text{A}/\text{cm}^2$) with protective efficiency (P_i) as 72.26 % and Supefer 800H has shown least corrosion current density ($0.068 \mu\text{A}/\text{cm}^2$) but more than that of bare Superfer 800H thus providing no protection to the superalloy. The protective efficiency in case of Grade A-1 and T-11 boiler steel was found 92.87 % and 84.31 % respectively. Grade A-1 boiler steel has shown maximum corrosion current ($05.98 \mu\text{A}/\text{cm}^2$) with protective efficiency 37.01 % and Supefer 800H with least corrosion current density ($0.021 \mu\text{A}/\text{cm}^2$) with protective efficiency 63.79 %; in case of nanostructured AlCrN coating. The protective efficiency in case of T-11 and T-22 boiler steel was found 96.10 % and 94.88 % respectively.

In case of conventional TiAlN coating; the T-22 boiler steel has shown least resistance to corrosion with higher corrosion current density ($08.97 \mu\text{A}/\text{cm}^2$) with protective efficiency 47.27 % and T-11 boiler steel has shown least current density ($0.059 \mu\text{A}/\text{cm}^2$) with protective efficiency 99.20 %. The protective efficiency in case of Grade A-1 boiler steel was found 78.19 %. The conventional TiAlN coating is not protecting the Superfer 800H superalloy. In case of conventional AlCrN coating; T-11 boiler steel has shown maximum current density ($6.64 \mu\text{A}/\text{cm}^2$) with protective efficiency 17.86 % and Supefer 800H has shown least corrosion current density ($0.0033 \mu\text{A}/\text{cm}^2$) with protective efficiency 94.21 %.

8.4.2 Salt spray (Fog) testing

The ASTM B117 Salt Fog test was used to evaluate the performance of the uncoated and nanostructured thin TiAlN and AlCrN coated alloys. The samples were exposed to a salt fog generated from a 5% sodium chloride solution with a pH between 6.5 and 7.2 for 24 Hrs, 48 Hrs and 72 Hrs. Photographs were taken before and subsequent to exposure to document the surface conditions. Initial weight and dimensions were measured. After exposure; samples were monitored and analyzed by using XRD and SEM/EDAX techniques. Then all the samples were cleaned in running water not warmer than 38°C to remove salt deposits from the surface and then immediately dried with compressed air.

Figure 8.4, depicts the column chart showing the weight loss per unit area for the uncoated and coated alloys. Salt spray corrosion is an electrochemical reaction process

(Bao et al., 2007). Generally, the corrosion resistance is influenced significantly by several factors, such as compositions, internal microstructure, and especially the surface condition. It can be inferred from the plots (Fig.8.4) that the uncoated boiler steels have shown higher weight loss per unit area in all three test conditions i.e. 24 Hrs, 48 Hrs and 72 Hrs tests; as compared to their coated counterparts. The uncoated as well as nanostructured TiAlN and AlCrN coated Superfer 800H superalloy have performed very well as these specimens have shown no weight change during exposure for 24 Hrs, 48 Hrs and 72 Hrs to salt fog tests. Both the coatings have shown good protection to the substrate in terms of weight loss per unit area.

The weight loss per unit area increases with the duration of the test in case of bare and coated boiler steels (Fig.8.4). In case of uncoated boiler steels; T-11 and T-22 have shown higher weight loss than Grade A-1 for 24 Hrs test duration. The bare Grade A-1 boiler steel undergoes higher weight loss during 48 Hrs and 72 Hrs test studies as compared to T-11 and T-22 boiler steels, which may be due to the formation of Cr_2O_3 in the oxide scale of T-11 and T-22 boiler steel as these boiler steel have good amount of Cr. The EDAX analysis at some locations of interest points out the presence of iron and oxygen on the corroded surface. XRD diffractograms for uncoated boiler steels have also indicated Fe_3O_4 is the main phases present in the oxide scale. The formation of Fe_3O_4 in the scale of corroded specimens in salt spray tests is found to be in agreement with those reported by Panda, Bijayani et al. (2008) and Vera et al (2009).

The weight loss per unit area in case of nanostructured thin TiAlN coating is less than the nanostructured AlCrN coating and uncoated boiler steels in all test durations. It can be mentioned based on the present investigation that nanostructured thin TiAlN and AlCrN coatings can provide good corrosion resistance when exposed to the simulated marine environment i.e. salt fog test. The proposed corrosion mechanism of the coated specimen is as explained by Bao et al., (2007). Authors reported that micro-cracks got initiated by residual stress during deposition of coatings. The micro-cracks would be corroded easily and the solution would infiltrate into loose corrosion products and reach crack tip to sustain the internal corrosion, followed by crack propagation. This process obeys the rules of crevice corrosion

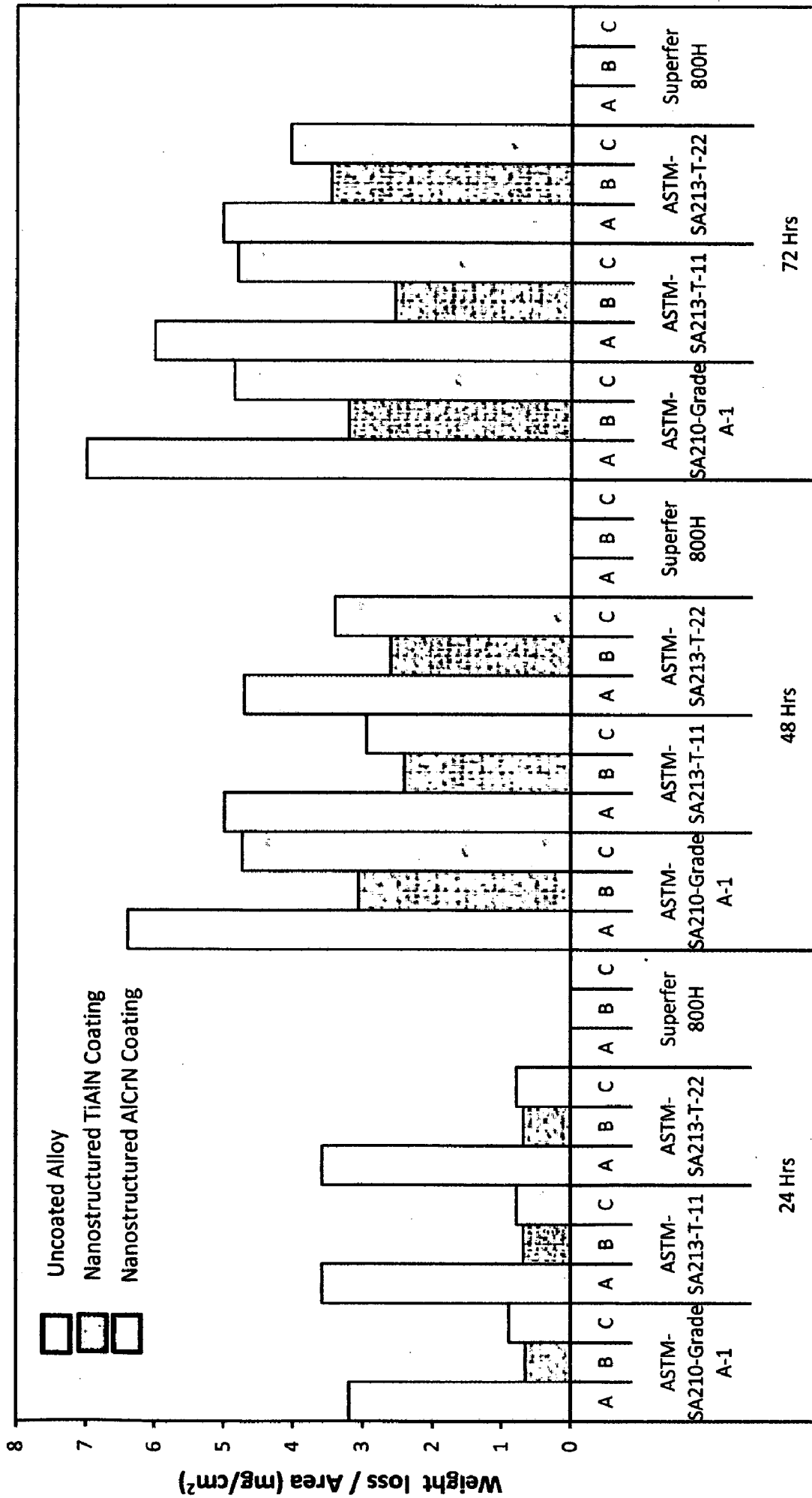


Fig. 8.4 Column chart showing weight loss per unit area for the uncoated and coated alloys subjected to salt-fog testing (5 % NaCl) : (A) Uncoated alloy; (B) Nanostructured TiAlN coating; (C) Nanostructured AlCrN coating

8.5 EROSION-CORROSION STUDIES IN INDUSTRIAL ENVIRONMENT

After conducting the various experiments on uncoated and coated alloys in lab, the specimens were exposed to low temperature super-heater zone of the coal fired boiler of Guru Nanak Dev Thermal Power Plant, Bathinda, Punjab, India. The specimens were hanged in the platen super-heater of coal fired boiler where the gas temperature was around $900^{\circ}\text{C} \pm 10^{\circ}\text{C}$ in order to investigate and compare the high temperature corrosion and erosion behavior of conventional thick (by plasma spraying and gas nitrided) and nanostructured thin (by physical vapor deposition process) TiAlN and AlCrN coatings with bare alloys. Hot corrosion experiments were performed for 10 cycles, each cycle consisting of 100 hours exposure followed by 1 hour cooling at ambient temperature.

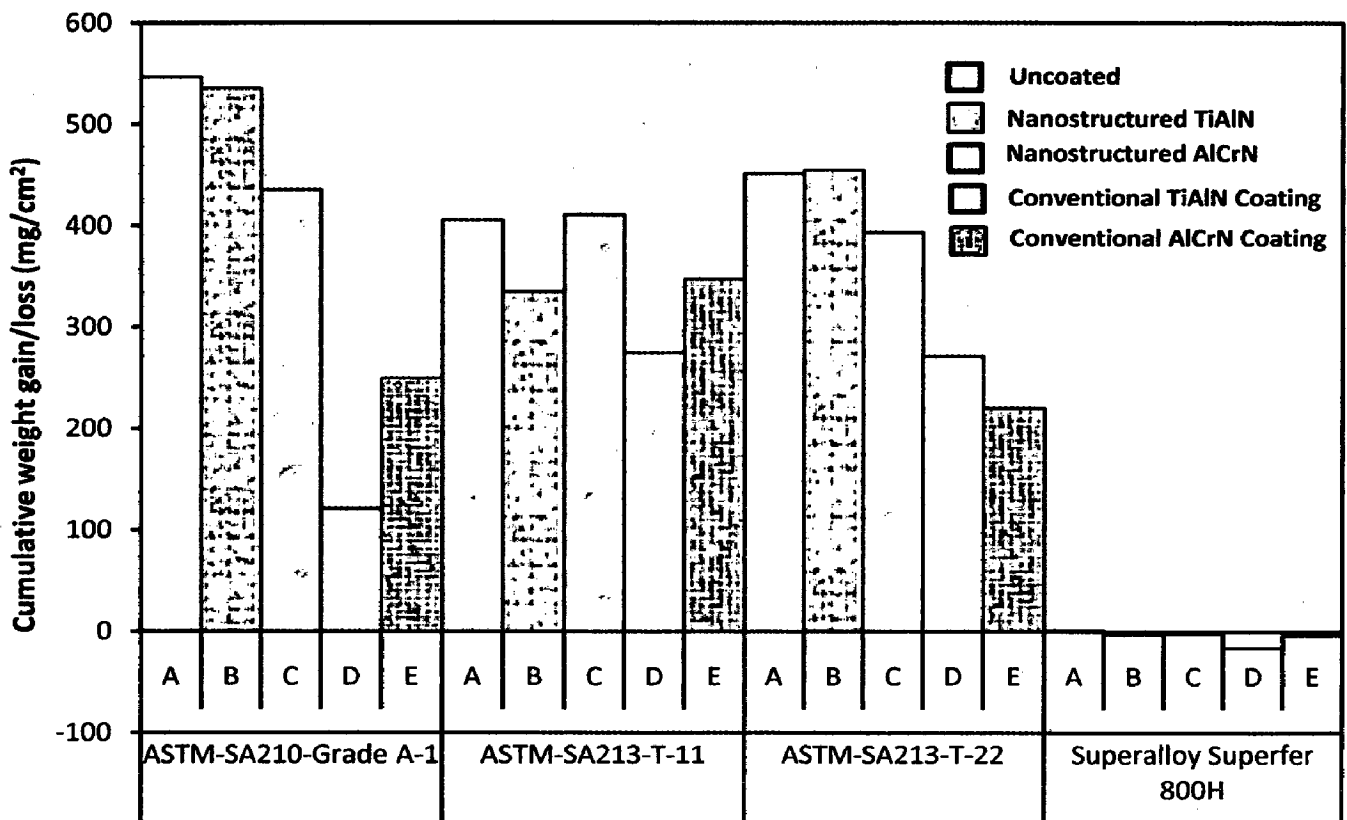


Fig. 8.5 Column chart indicating cumulative weight gain per unit area (mg/cm^2) for the uncoated and coated alloys' specimens exposed to super-heater of the coal fired boiler environment at 900°C for 1000 hours; (A) Uncoated alloy, (B) Nanostructured TiAlN coating, (C) Nanostructured AlCrN coating, (D) Conventional TiAlN coating, (E) Conventional AlCrN coating

The extent of corrosion has been evaluated by measuring weight change and thickness of the unreacted portion of the samples after the total exposure of 1000 hours and hence calculating corrosion rate in mils per year (mpy). Weight gain per unit area (mg/cm^2) versus time expressed in number of cycles plot for coated and bare alloys exposed to super-heater of the coal fired boiler environment at 900°C for 1000 hours; is presented in Fig. 8.5. It can be inferred from the plots (Fig.8.5) that in case of bare alloys; Grade A-1 boiler steels have shown highest weight gain and Superfer 800H with least weight gain. The weight gain in case of superalloy is almost negligible when compared with the weight gain in case of boiler steels. All the coated boiler steels have shown less weight gain as compared to the bare alloys except nanostructured AlCrN coated T-11 and nanostructured TiAlN coated T-22 boiler steel. All the coatings on Superfer 800H have shown decrease in weight due to erosion by ash (Fig.8.5). However weight change data could not be of much use for predicting the corrosion behavior because of suspected spalling and ash deposition on the specimens.

Although the specimens were washed with acetone after every cycle before weight measurement in order to remove ash deposited yet it was difficult to remove the ash completely. Hence extent of corrosion could only be monitored by measuring the thickness of the un-reacted sample after the total exposure of 1000 hrs i.e. measuring scale thickness in cross-sectional view. The oxidized samples were cut across the cross section and mounted in transoptic mounting resin and subsequently mirror polished to obtain scanning electron back scattered micrographs and X-ray mapping. The scale thickness values were measured from SEM back scattered micrographs of the cross-section of the eroded/corroded specimens as explain in Chapters 4, 5, 6 and 7. The extent of erosion-corrosion in terms of scale/coating thickness (in microns) for coated and uncoated alloys exposed to super-heater of the coal fired boiler environment at 900°C for 1000 hours; before and after erosion-corrosion studies are shown as bar chart in Fig.8.6. All the uncoated and coated boiler steels have shown increase in overall thickness after erosion-corrosion for 1000 hrs. In case of Superfer 800H superalloy; the uncoated and nanostructured thin coated superalloy has shown increase in scale thickness and the superalloy with conventional thick coatings have shown decrease in scale/coating thickness.

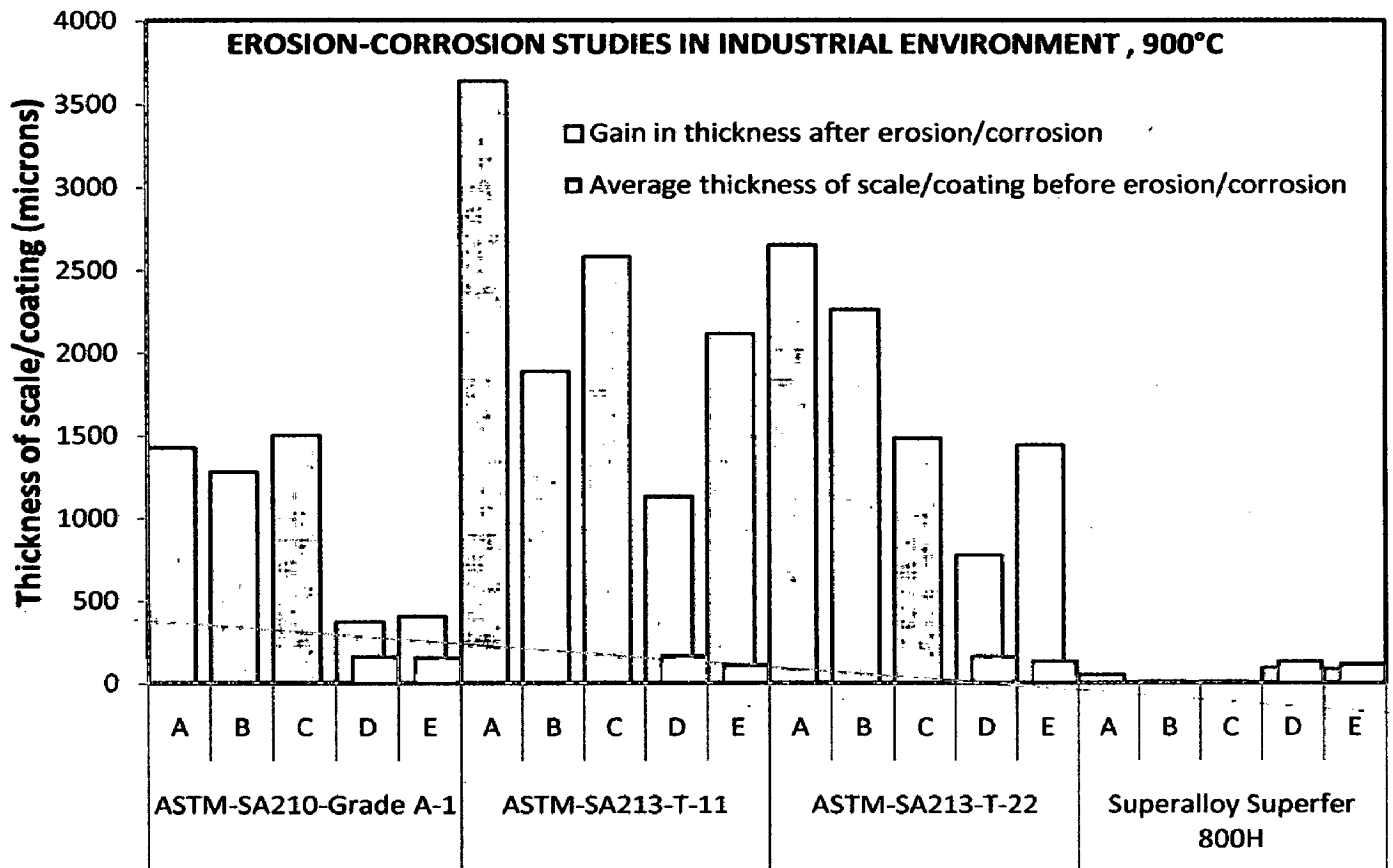


Fig. 8.6 Column chart indicating the extent of erosion/corrosion for uncoated and coated alloys' specimens exposed to super-heater of the coal fired boiler environment at 900°C for 1000 hours; (A) Uncoated alloy, (B) Nanostructured TiAlN coating, (C) Nanostructured AlCrN coating, (D) Conventional TiAlN coating, (E) Conventional AlCrN coating

A very thick scale was observed in case of uncoated and nanostructured coated boiler steels. The conventional coatings have shown good resistance to the corrosive environment as the oxygen penetration is limited to very less thickness as compared to the uncoated and nanostructured coated boiler steels. The uncoated T-11 boiler steel has shown maximum gain in scale thickness and all the coatings have shown protection to the substrate in terms of scale thickness except nanostructured thin AlCrN coated Grade A-1 boiler steel. After measuring the thickness of the un-reacted sample after the total exposure of 1000 hrs i.e. measuring scale thickness in cross-sectional view corrosion rate in mils per year (mpy) was calculated for all the coated and bare specimens. Figure 8.7 shows the corrosion rate for all the specimens.

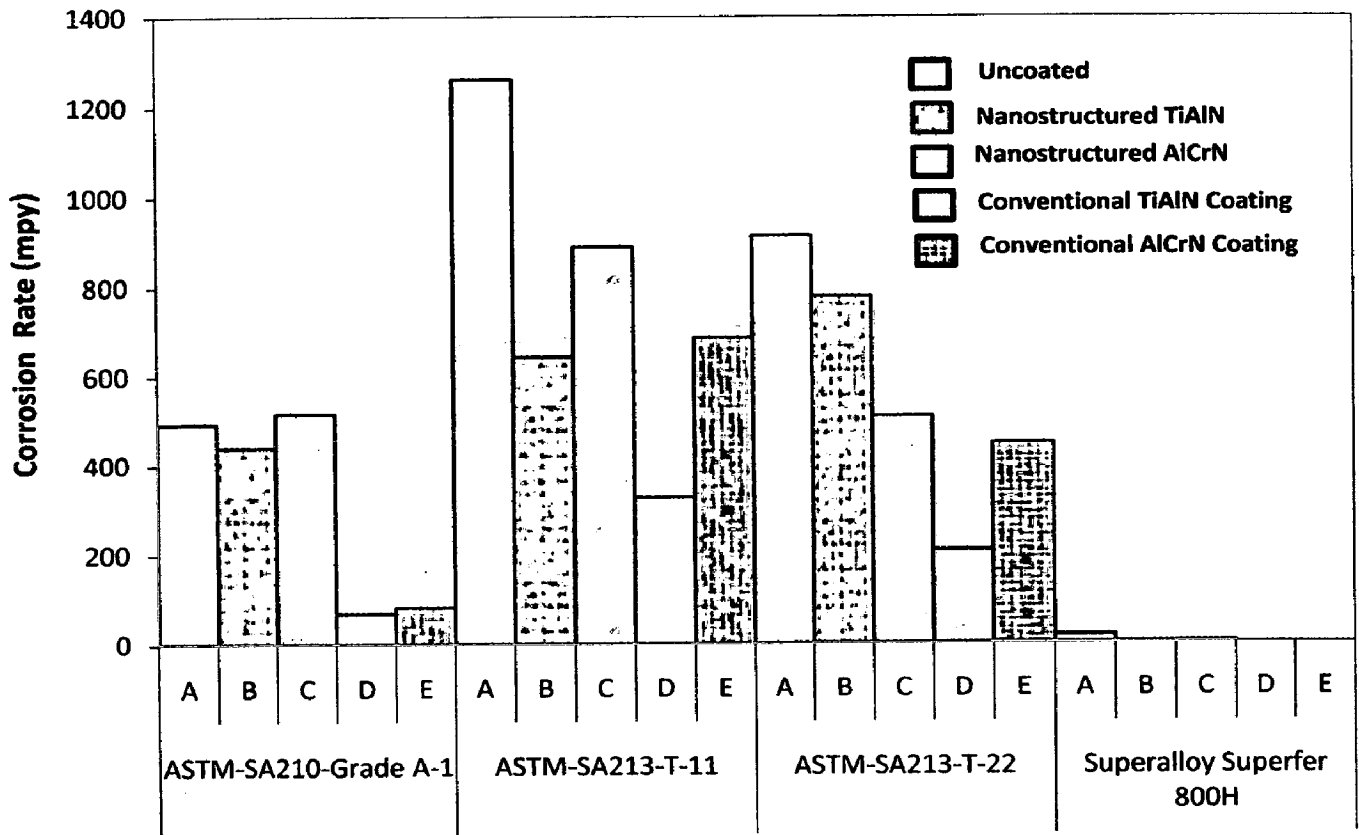


Fig. 8.7 Column chart indicating corrosion rate (mpy) for the uncoated and coated alloys' specimens exposed to super-heater of the coal fired boiler environment at 900°C for 1000 hours; (A) Uncoated alloy, (B) Nanostructured TiAlN coating, (C) Nanostructured AlCrN coating, (D) Conventional TiAlN coating, (E) Conventional AlCrN coating

It can be inferred from the column plots (Fig.8.7) that the coated as well as uncoated boiler steels have shown higher corrosion rate as compared with Superfer 800H superalloy. In case of boiler steels; maximum corrosion rate has been observed in bare T-11 and minimum in case of conventional TiAlN coated Grade A-1 boiler steel. All the coatings have shown less corrosion rate than bare boiler steels except nanostructured AlCrN coated Grade A-1. The conventional coatings have shown good resistance to the corrosive environment as the oxygen penetration is limited to very less thickness as compared to the uncoated and nanostructured coated boiler steels. In case of Superfer 800H superalloy; the coatings have shown protection to the substrate with very less corrosion rate as compared to the bare superalloy.

8.6 EVALUATION OF PERFORMANCE OF VARIOUS SUBSTRATE-COATING COMBINATIONS IN DIFFERENT ENVIRONMENT

This section deals with the evaluation of performance of various substrate-coating combinations in different environment. After conducting the various experiments on uncoated and coated alloys in lab and in actual industrial environment which includes the characterization of the nanostructured and conventional TiAlN and AlCrN coatings on selected Fe-based alloys and their behavior when exposed to high temperature oxidation studies in air, molten salt (Na_2SO_4 -60% V_2O_5) environment and in a coal fired boiler of a thermal plant, erosion studies in simulated coal-fired boiler environment and corrosion studies in simulated marine environment; the performance of different substrate-coating combinations have been evaluated in terms of excellent (E), moderate (M) and poor (P) as shown in Table 8.3. The behavior of all the selected bare alloys in different environments has been compared and grading is done accordingly. In case of coatings; the grading is done by comparing the behavior of the coating with the behavior of the respective substrate alloy in different environments.

Table 8.3(b) Performance* of various substrate-coating combinations in different environments

Substrate	Coating	High Temperature Oxidation in Air	High Temperature Oxidation in Molten Salt (Na ₂ SO ₄ -60%V ₂ O ₄) Environment	Erosion-Corrosion Studies in Simulated Coal-Fired Boiler Environment	Corrosion Studies in Simulated Marine Environment			Erosion-Corrosion Studies in Actual Industrial Environment
					Linear Resistance Polarisation Test (LPR)	Potentiodynamic Polarisation Test	Salt Fog Testing	
ASTM SA-213-T-22 Boiler steel	A	P	P	P	P	P	M	M
	B	P	E	E	E	E	E	M
	C	E	P	M	E	E	M	M
	D	E	M	E	E	M	-	E
	E	E	E	E	M	E	-	M
Superfer 800H superalloy	A	E	M	E	E	E	E	E
	B	E	M	M	E	M	E	E
	C	E	M	M	E	E	E	E
	D	E	E	E	P	P	-	E
	E	E	E	E	E	E	-	E

*(Excellent- E, Moderate- M, Poor-P)

A-Uncoated Alloy B-Nanostructured TiAlN Coating C-Nanostructured AlCrN Coating
D-Conventional TiAlN Coating E-Conventional AlCrN Coating

This chapter presents the conclusions from the present investigation regarding the behavior of the uncoated and conventional thick and nanostructured thin TiAlN and AlCrN coated Fe-based alloys namely Grade A-1, T-11 and T-22 boiler steels and Superfer 800H superalloy; when exposed to high temperature oxidation in air and in molten salt (Na_2SO_4 -60% V_2O_5) environments; at 900°C under cyclic conditions, erosion-corrosion in simulated coal-fired environment, corrosion in simulated marine environment in lab as well as in the actual industrial environment of the coal-fired boiler at 900°C under cyclic conditions at Guru Nanak Dev Thermal Plant, Bathinda, Punjab, INDIA. All the coatings were formulated by commercially available processes in INDIA. The salient conclusions from the present investigation are summarized as follows:

9.1 CHARACTERISATION OF COATINGS

- (1) The nanostructured thin TiAlN and AlCrN coatings (by physical vapour deposition process at Oerlikon Balzers Ltd. Gurgaon, India) and conventional thick TiAlN and AlCrN coatings (by plasma spraying process at Anod Plasma Ltd. Kanpur, India; followed by gas nitriding process) were successfully deposited on the selected Fe-based alloys. The coatings were characterized for their microstructural features, bond strength, surface roughness and hardness.
- (2) All the coatings were dense, uniform, continuous and adherent. The thickness of coating was in the range of 5.2-6.3 μm , 4.2-5.5 μm , 140-174 μm and 122-166 μm for the nanostructured TiAlN, nanostructured AlCrN, conventional TiAlN and conventional AlCrN coatings respectively.
- (3) The nanostructured thin TiAlN and AlCrN coatings exhibited negligible porosity values for as coated; which were less than 0.5 %. The conventional TiAlN and AlCrN coatings showed; higher porosity values (1.90-4.30%) for as sprayed conventional Ti-Al and Al-Cr coatings which after gas nitriding were found to be less than 0.65 %.

- (4) The grain size (calculated by Scherrer formula from XRD plot) for nanostructured thin TiAlN and AlCrN coatings was less than 22 and 28 nm respectively which was further verified by AFM analysis.
- (5) The surface roughness in case of nanostructured TiAlN and nanostructured AlCrN coating was found to be in the range of 2.62-4.52 nm and 5.18-6.19 nm respectively; as observed by AFM analysis. The coating surface was very rough in case of conventional thick TiAlN and AlCrN coatings and the roughness was found to be in the range of 7.36-16.12 μm and 11.84-15.60 μm respectively.
- (6) A good adhesion of the conventional thick TiAlN and AlCrN coatings was evident from bond test results. Average bond strength of 68.74 MPa and 54.69 MPa was observed in case of conventional TiAlN and AlCrN coatings respectively.

9.2 HOT CORROSION STUDIES IN AIR AND MOLTEN SALT ENVIRONMENT

- (7) Based on the overall weight gain after 50 cycles in air and in an aggressive Na_2SO_4 -60% V_2O_5 (molten salt) environment at 900°C temperature, the oxidation resistance of the bare Fe-based alloys studied in the present investigation has been found to be in the following order:

AIR ENVIRONMENT

S.F 800H superalloy > Grade A-1 boiler steel > T-11 boiler steel > T-22 boiler steel

Na_2SO_4 -60% V_2O_5 (MOLTEN SALT) ENVIRONMENT

S.F 800H superalloy > T-11 boiler steel > Grade A-1 boiler steel > T-22 boiler steel

- (i) The superior oxidation resistance of the Superfer 800H superalloy may be attributed to the development of homogeneous and continuous scale consisting of oxides of Ni and Cr due to higher percentage of Ni and Cr in the Superfer 800H.
- (ii) The higher weight gain and spalling as observed in case of T-11 and T-22 boiler steels may be attributed to the presence of molybdenum in the steels. Chatterjee et al. (2001) have suggested that during initial oxidation Fe is oxidized and the oxide scale is protective in nature. With progress of oxidation Mo becomes enriched at the alloy interface, leading to the formation of an inner layer of molten MoO_3 (m. p. 795°C) which penetrates along the alloy-

scale interface. This liquid oxide disrupts and dissolves the protective oxide scale, causing the alloy to suffer catastrophic oxidation (Lai, 1990).

- (8) Based on the overall weight gain after 50 cycles in air and in an aggressive Na_2SO_4 -60% V_2O_5 (molten salt) environment at 900°C temperature, the oxidation resistance of the coating on the Fe-based alloys studied in the present investigation has been found to be in the following order:

AIR ENVIRONMENT

Substrate ASTM-SA210-Grade A-1 Boiler Steel:

Conventional AlCrN > Conventional TiAlN > Nanost. AlCrN > Nanost. TiAlN > Bare Grade A-1

Substrate ASTM-SA213-T-11 Boiler Steel:

Conventional AlCrN > Conventional TiAlN > Nanost. AlCrN > Nanost. TiAlN > Bare T-11

Substrate ASTM-SA213-T-22 Boiler Steel:

Conventional AlCrN > Nanost. AlCrN > Conventional TiAlN > Bare T-22 > Nanost. TiAlN

Substrate Superfer 800H Superalloy:

Nanost. AlCrN > Nanost. TiAlN > Bare S.F 800H > Conventional TiAlN > Conventional AlCrN

Na_2SO_4 -60% V_2O_5 (MOLTEN SALT) ENVIRONMENT

Substrate ASTM-SA210-Grade A-1 Boiler Steel:

Conventional AlCrN > Conventional TiAlN > Nanost. TiAlN > Nanost. AlCrN > Bare Grade A-1

Substrate ASTM-SA213-T-11 Boiler Steel:

Conventional AlCrN > Nanost. AlCrN > Nanost. TiAlN > Conventional TiAlN > Bare T-11

Substrate ASTM-SA213-T-22 Boiler Steel:

Conventional AlCrN > Nanost. TiAlN > Conventional TiAlN > Nanost. AlCrN > Bare T-22

Substrate Superfer 800H Superalloy:

Nanost. AlCrN > Nanost. TiAlN > Conventional TiAlN > Conventional AlCrN > Bare S.F 800H

- (9) All the coatings have shown protection to the substrate based on the overall weight gain after 50 cycles in air environment at 900°C temperature except nanostructured TiAlN coated T-22 boiler steel.

- (10) The nanostructured TiAlN and AlCrN coatings has shown resistance to oxidation to some extent as the overall weight gain is less, but failed to sustain during the course of oxidation study. This might be due to the formation of oxide scale which is composed of a porous oxide mixture of TiO_2 and Al_2O_3 , with the domination of TiO_2 .
- (11) The plasma sprayed gas nitride conventional thick coatings i.e. TiAlN and AlCrN when subjected to cyclic oxidation studies at $900^\circ C$ for 50 cycles developed a protective scale mainly consisting on Al_2O_3 along with some amount of TiO_2 (in case of conventional TiAlN coating) and Cr_2O_3 (conventional AlCrN coating). In case of T-11 and T-22 boiler steels; the conventional TiAlN coating failed to sustain during the course of study.
- (12) The coated alloys subjected to cyclic oxidation in air have shown relatively high weight gains in the early cycles of the exposure specially in case of Superfer 800H superalloy. These initial high oxidation rates in general might partially be attributed to the rapid formation of oxides at the coating splat boundaries and within open pores due to the penetration of the oxidizing species along the splat boundaries/open pores in the early cycles of the study. In case of Superfer 800H superalloy although the conventional thick coatings have shown higher weight gain yet these have not allowed environment to penetrate into the substrate alloys.
- (13) The weight change plots for the uncoated and coated alloys indicated that the oxidation behavior has shown conformance to parabolic rate law. The parabolic kinetic behavior is due to the diffusion controlled mechanism operating at $900^\circ C$ under cyclic conditions (Mahesh et al., 2008). Small deviation from the parabolic rate law might be due to the cyclic scale growth.
- (14) Development of some minor cracks near or along the edges of the coated specimens during hot corrosion studies in air and molten salt environment were observed for coated and uncoated alloys. This cracking and subsequent spalling may be attributed to the thermal shocks due to differences in the heat expansion coefficients of the oxides, coatings and the substrate.

9.3 EROSION STUDIES IN SIMULATED COAL-FIRED BOILER ENVIRONMENT

- (15) All the uncoated and nanostructured TiAlN and AlCrN coated alloys have shown higher erosion rate at oblique impact (at 30°) than at normal impact (at 90°), which indicate ductile behavior as proposed by Murthy et al (2001). The nanostructured thin TiAlN and AlCrN coatings were removed by the continuous strikes of the eroding particles on the surface of the coatings in most of the cases.
- (16) The plasma sprayed conventional TiAlN coatings have successfully protected the substrates. All the conventional thick TiAlN coated alloys have shown higher erosion rate at oblique impact (at 30°) than at normal impact (at 90°) thus indicating ductile behavior except in case of Grade A-1 boiler steel.
- (17) The plasma sprayed conventional AlCrN coatings have successfully protected the substrates at both impact angles except in case of T-11 boiler steel. The conventional AlCrN coating gets removed by the continuous strikes of the eroding particles on the surface of the coating in case of T-11 boiler steel at both impact angles. All the conventional thick AlCrN coated alloys have shown higher erosion rate at normal impact (at 90°) than at oblique impact (at 30°) except in case of Superfer 800H superalloy.

9.4 CORROSION STUDIES IN SIMULATED MARINE ENVIRONMENT

9.4.1 Linear polarization resistance and potentiodynamic polarization tests

- (18) It can be inferred from the corrosion parameters i.e. corrosion current densities (i_{corr}) obtained in LPR test that all the coatings are protecting the substrates except conventional coatings on T-11 boiler steel and conventional TiAlN coated Superfer 800H superalloy. In case of uncoated alloys; bare T-22 boiler steel has shown maximum corrosion current density (108.60 $\mu\text{A}/\text{cm}^2$) and Superfer 800H has shown best corrosion resistance at initial stage on the basis of corrosion current density (05.37 $\mu\text{A}/\text{cm}^2$) and polarization resistance obtained in the test.
- (19) In Potentiodynamic polarization test; the corrosion current densities of the coatings were found much lower than that of the substrate steel except for nanostructured and conventional TiAlN coated Superfer 800H superalloy. Also,

the corrosion current densities of the substrate and the coatings were found much lower as compared to the LPR test (at initial stage) results. The corrosion product formed may have reduced the passage of the electrolyte to attack the samples, and hence providing protection.

- (20) In case of uncoated alloys; bare T-22 boiler steel has shown maximum current density ($17.02 \mu\text{A}/\text{cm}^2$) and Superalloy 800H has shown best corrosion resistance with least corrosion current density ($0.058 \mu\text{A}/\text{cm}^2$).
- (21) In case of nanostructured TiAlN coating; T-22 boiler steel has shown maximum current density ($04.72 \mu\text{A}/\text{cm}^2$) with protective efficiency (P_i) as 72.26 % and Superalloy 800H has shown least corrosion current density ($0.068 \mu\text{A}/\text{cm}^2$) but more than that of bare Superalloy 800H thus providing no protection to the superalloy. The protective efficiency in case of Grade A-1 and T-11 boiler steel was found 92.87 % and 84.31 % respectively.
- (22) Grade A-1 boiler steel has shown maximum corrosion current ($05.98 \mu\text{A}/\text{cm}^2$) with protective efficiency 37.01 % and Superalloy 800H with least corrosion current density ($0.021 \mu\text{A}/\text{cm}^2$) with protective efficiency 63.79 %; in case of nanostructured AlCrN coating.
- (23) In case of conventional TiAlN coating; the T-22 boiler steel has shown least resistance to corrosion with higher corrosion current density ($08.97 \mu\text{A}/\text{cm}^2$) with protective efficiency 47.27 % and T-11 boiler steel has shown least current density ($0.059 \mu\text{A}/\text{cm}^2$) with protective efficiency 99.20 %. The protective efficiency in case of Grade A-1 boiler steel was found 78.19 %. The conventional TiAlN coating is not protecting the Superalloy 800H superalloy.
- (24) In case of conventional AlCrN coating; T-11 boiler steel has shown maximum current density ($6.64 \mu\text{A}/\text{cm}^2$) with protective efficiency 17.86 % and Superalloy 800H has shown least corrosion current density ($0.0033 \mu\text{A}/\text{cm}^2$) with protective efficiency 94.21 %.

9.4.2 Salt spray (Fog) testing

- (25) The uncoated boiler steels have shown higher weight loss per unit area in all three test conditions i.e. 24 Hrs, 48 Hrs and 72 Hrs tests; as compared to their coated counterparts. The uncoated as well as nanostructured TiAlN and AlCrN

coated Superfer 800H superalloy have performed well as these specimens have shown no weight change during exposure for 24 Hrs, 48 Hrs and 72 Hrs to salt fog tests.

- (26) Both the coatings (nanostructured TiAlN and AlCrN) have shown good protection to the substrate in terms of weight loss per unit area. Also, the weight loss per unit area increases with the duration of the test in case of bare and coated boiler steels. In case of uncoated boiler steel; the T-11 and T-22 have shown higher weight loss than Grade A-1 for 24 Hrs test duration. The bare Grade A-1 boiler steel undergoes higher weight loss during 48 Hrs and 72 Hrs test studies as compared to T-11 and T-22 boiler steels.
- (27) XRD diffractograms for uncoated boiler steels have also indicated Fe_3O_4 is the main phases present in the oxide scale. The formation of Fe_3O_4 in the scale of corroded specimens in salt spray tests is found to be in agreement with those reported by Panda, Bijayani et al. (2008) and Vera et al (2009).

9.5 EROSION-CORROSION STUDIES IN INDUSTRIAL ENVIRONMENT

- (28) In case of bare alloys; Grade A-1 boiler steels have shown highest weight gain and Superfer 800H with least weight gain. The weight gain in case of superalloy is almost negligible when compared with boiler steels. All the coated boiler steels have shown resistance to corrosion in terms of weight gain as compared to the bare alloys except nanostructured AlCrN coated T-11 and nanostructured TiAlN coated T-22 boiler steel. All the coatings on Superfer 800H have shown decrease in weight due to erosion by ash.
- (29) Based on the materials depth effected by corrosion or corrosion rate in mils per year (mpy) after 1000 hours of exposure, the corrosion resistance of the bare Fe-based alloys studied in the present investigation has been found to be in the following order:

S.F 800H superalloy > Grade A-1 boiler steel > T-22 boiler steel > T-11 boiler steel

- (30) Based on the materials depth effected by corrosion or corrosion rate in mils per year (mpy) after 1000 hours of exposure, the corrosion resistance of the uncoated and coated Fe-based alloys studied in the present investigation has been found to be in the following order:

Substrate ASTM-SA210-Grade A-1 Boiler Steel:

Conventional TiAlN > Conventional AlCrN > Nanost. TiAlN > Bare Grade A-1 > Nanost. AlCrN

Substrate ASTM-SA213-T-11 Boiler Steel:

Conventional TiAlN > Conventional AlCrN > Nanost. TiAlN > Nanost. AlCrN > Bare T-11

Substrate ASTM-SA213-T-22 Boiler Steel:

Conventional TiAlN > Conventional AlCrN > Nanost. AlCrN > Conventional TiAlN > Bare T-22

Substrate Superfer 800H Superalloy:

Conventional TiAlN and AlCrN > Nanost. TiAlN > Nanost. AlCrN > Bare S.F 800H

- (31) The coated as well as uncoated boiler steels have shown higher corrosion rate as compare to Superfer 800H supeallloy. In case of boiler steels; maximum corrosion rate has been observed in bare T-11 and minimum in case of conventional TiAlN coated Grade A-1 boiler steel. All the coatings have shown resistance to corrosion in terms of corrosion rate when compared with respective bare alloy except nanostructured AlCrN coated Grade A-1.
- (32) The conventional coatings have shown good resistance to the corrosive environment as the oxygen penetration is limited to very less thickness as compare to the uncoated and nanostructured coated boiler steels. In case of Superfer 800H superalloy; the coatings have shown protection to the substrate with less corrosion rate as compare to the bare superalloy.
- (33) All the coated as well as uncoated boiler steels have shown ash deposition on the surface. Thus final thickness is contributed by scale formation, erosion and ash deposition.
- (34) The plasma sprayed gas nitride conventional thick TiAlN and AlCrN coatings can provide erosion-corrosion resistance when exposed to super-heater of the coal fired boiler environment at 900°C. These coatings can be used on all those surfaces which are facing the fire side corrosion such as in internal combustion engines, industrial waste incinerators, fluidized beds, gas turbine and steam turbines to provide protection against degradation in these environments.

SUGGESTIONS FOR FUTURE WORK

1. Studies can be made for the exposure of these coatings for different lengths of time so that progressive development of the scale can be studied and mechanism of transport of species and gradual development of the scale can be understood.
2. Hot stage microscopy can also be used to follow the development of the scale throughout the oxidation and hot corrosion runs.
3. Studies can be made to evaluate other types of coatings for providing resistant to hot corrosion. Role of coatings can also be studied for other types of boiler tube steels.
4. To have better insight into the behavior of coatings in aggressive environment, reactions between oxides and $\text{Na}_2\text{SO}_4\text{-V}_2\text{O}_5$ should be studied in more detail.
5. Cost effectiveness analysis should be done for different types of coatings.
6. The coatings behavior can be studied in the actual running boiler for longer duration may be for few years by providing these coatings on the actual boiler tubes.
7. The coatings behavior can be studied in the actual marine environments for longer durations.
8. Studies may be conducted to investigate the hot corrosion behavior of the thermal spray coatings developed by some other processes such as high-velocity oxy-fuel and detonation spray processes.
9. Attempts can be made to estimate the useful life of these coated alloys using mathematical modeling based on experimental data.
10. Some other coatings with different compositions should be formulated and evaluated especially by alloying the coating powders with rare earth elements.
11. Studies can be performed to calculate the thermal conductivity of the coatings and to develop the relation among the coatings thickness to the heat transfer rate through the coated boiler tubes.

Table A.1 Summary of oxidation of Fe, Ni & Co- base alloys in air

Material	Environment	Researchers	Brief Details
304 L stainless steel	In steam as well as in air, 1000-1375°C	Tamman, 1920, Pilling & Bedworth, 1923	As reported by Khanna (2002), the first paper which expressly addresses high temperature oxidation was that by G. Tamman, in 1920. However, the first paper which lays out the basics of the problem was by Pilling and Bedworth in 1923. Authors defined 'high temperature' as that at which the transport of the reactive components through the protective layer was the principal determinant of the reaction rate (as opposed to the situation in aqueous corrosion processes at close to ambient temperatures). Under these circumstances it could be expected that the rate of reaction would diminish as the protective scale thickened, leading to a 'parabolic rate law'. Authors also high-lighted the problems associated with forming an adherent crack-free protective oxide layer on the oxidizing surface because of the volume changes associated with the oxidation process.
Fe-15 wt %Cr-4% wt Al	Isothermal as well as cyclic oxidation, 1000-1300°C	Bittel et al., 1969 Pandey, 1983	The oxidation by steam was fast as compared to that by air. The diffusion through Fe-Ni-Cr-spinel layer was suggested as the parabolic rate controlling process in case of oxidation by steam. Whereas, in case of oxidation by air the formation of Cr ₂ O ₃ was reflected as a reason for slow oxidation. The effect of zirconium and yttrium alloying on the high temperature oxidation of Fe-15 wt %Cr-4% wt Al was investigated. It was observed that the yttrium addition decreased the oxidation rate appreciably at 1000°C in O ₂ -H ₂ O atmosphere where it did not affect oxidation rate in O ₂ . Whereas under similar conditions 1% Zr addition increased the weight gain both in O ₂ and air but in O ₂ -H ₂ O weight gain was much less as compared to that of the base alloy. At a temperature of 1200°C in air, the effect of Zr concentration on the oxidation of the alloy was to increase the oxidation rate. Further lower concentration of Zr i.e. 0.2% was found to be beneficial in improving the oxidation resistance under cyclic conditions with reduced spalling of the scale. Alloying with 1% Y was also observed to be equally effective in improving the oxidation resistance at 1200°C.
Iron	Gas mixtures containing Ar, O ₂ and Cl ₂ , 1100 and 1200K	Lee and McNellan, 1990	The rate of oxidation of iron was significantly inhibited by the presence of chlorine in the environment, which has been attributed to the formation of a dense layer of Fe ₂ O ₃ on the outside of the oxide scale formed in the presence of chlorine.
AISI 316 stainless steel	Under non-isothermal heating followed by isothermal holding at 1423 K	Kuiroy et al., 1994	The mechanically polished surfaces exhibited a shorter incubation period but better oxidation resistance during isothermal holding as compared to electro polished surfaces. This was attributed to enhanced outward diffusion of Cr favouring formation of continuous band of Cr-rich layers.
Plain carbon steel	In air, at 600, 800 and 1000°C for 10, 30 and 50 hours	Agarwal et al., 2000	The effect of long duration exposure at high temperature was investigated on Laser surface engineered composite boride coating on plain carbon steel. Thermogravimetric technique to study the kinetics of oxidation at elevated temperature was used. Oxidation rate for all the samples was observed to be parabolic in nature and oxidation kinetic rate constant was reported to increase with increasing temperature of exposure.

Thin films of Fe-20Cr-Al	Thermal-cycling conditions, 1150°C	Stott and Hiramatsu, 2000	The films were found to be very susceptible to breakdown oxidation after short periods of exposure to air, due to exhaustion of aluminium in the substrate arising from the large surface area to volume ratio. It was further observed that when the aluminium concentration in the alloy drops below a critical level, a layer of chromia was able to develop and grow at the alumina-alloy substrate interface. This eventually was suggested to cause breakaway oxidation and formation of iron-rich oxides on the specimen.
Grade A-1, T-11 and T-22 boiler steels	In air, at 900°C for 50 cycles	Sidhu et al., 2003	Studied the oxidation behaviour of boiler steels at 900°C under cyclic conditions (for 50 cycles, each cycle consists of 1Hr heating and 20min cooling). The resistance to oxidation in air at 900°C is slightly greater for T-11 and T-22 boiler steels than for Grade A-1, whereas the oxide scale for Grade A-1 steel is thick, porous and non-protective.
Ni-10Cr-5Al, Ni-20Cr-5Al and Ni-30Cr-5Al alloys	Isothermal oxidation in Air, 1000°C	Ul-Hamid, 2004	The oxide formed adjacent to the alloy was α -Al ₂ O ₃ such that the higher was the Cr content of the alloy the easier was its formation. The Ni-30Cr-5Al alloy formed a complete layer of α -Al ₂ O ₃ in the initial stages of oxidation through 'oxygen gettering' by Cr. Further a decrease in scale thickness and an increase in scale adherence were observed with an increase in Cr content from 10 to 30%
Superni 75 and Superni 600	At 900°C for 50 cycles in air	Singh et al., 2004	The two Ni-base superalloys Superni 75 and Superni 600 have shown very good oxidation resistance when exposed to cyclic oxidation for 50 cycles (each cycle consists of 1Hr heating and 20min cooling) at 900°C in air. A continuous chromia scale could be seen on the surface of the oxidised superalloy specimens, which is supposed to impart oxidation resistance to the superalloys by reducing oxygen activity.
Superfer 800H (Fe-based superalloy)	In air, at 900°C for 50 cycles	Singh et al., 2005	Authors used thermogravimetric technique to study the kinetics of oxidation at elevated temperature for 50 cycles (each cycle consists of 1Hr heating and 20min cooling). Oxidation rate was observed to be parabolic in nature. The formation of Cr ₂ O ₃ was reflected as a reason for constant oxidation rate after 4 th cycle.
Superni 75 and Superfer 800H	In air, at 800°C for 50 cycles	Sidhu et al., 2006	Studied the high temperature behaviour of Superni 75 (Ni-based superalloy) and Superfer 800H (Fe-based superalloy) in air at 800°C for 50 cycles (for 50 cycles, each cycle consists of 1Hr heating and 20min cooling). The nearly parabolic behaviour was observed. The parabolic rate constant (K_p , g ² cm ⁴ sec ⁻¹) was found 36×10^{-10} and 22.58×10^{-10} for Superfer 800H and Superni 75 respectively.
Superni 76, Superni 750 and Superfer 800	For 100 cycles at 900°C in air	Mahesh et al., 2008	The two Ni-base superalloys Superni 76 and Superni 750 and one Fe-base superalloy, Superfer 800 were studied for high temperature oxidation in air at 900°C temperature for 100 cycles. A nearly parabolic behaviour was observed for all the superalloys. Higher weight gain per unit area in case of Superni 750 was observed and least in case of Superfer 800. A continuous chromia scale could be seen on the surface of the oxidised superalloy specimens, which is supposed to impart oxidation resistance to the superalloys by reducing oxygen activity.

Table A.2 Summary of oxidation of Fe, Ni & Co- base alloys in Na₂SO₄, V₂O₅ and Na₂SO₄- 60% V₂O₅ environments

Na ₂ SO ₄ Induced Hot Corrosion			
Material	Environment	Researchers	Brief Details
Review	-	Simons et al., 1955	Outlined a reaction mechanism involving metal sulfidation by Na ₂ SO ₄ with emphasis on the accelerated oxidation of a sulphide-base eutectic.
Ni-base superalloys and seven binary Ni-base alloys	Pure O ₂ , 825-1000°C	Bornstein et al., 1973	Based upon the results, it was concluded that the reduction of the oxide ion content of Na ₂ SO ₄ was a necessity, but not sufficient condition for sulphidation inhibition. The addition of Mo or V to nickel imparted sulphidation resistance in it because their oxides reacted with and decreased the oxide ion content of Na ₂ SO ₄ . The disagreement in the literature regarding the effect of Molybdenum on hot corrosion was suggested to be largely due to differences in testing techniques and differences in whether the investigators have been more concerned with the initiation or with propagation modes of hot corrosion.
Pure iron & Fe-5Cr Alloy, and Fe-13Cr Alloy	1 atmosphere of oxygen, 900°C	Trafford & Whittle, 1980A	Pure iron did not undergo accelerated oxidation, which has been attributed to the thickening of the scale too rapidly for sulphur to penetrate the oxide and interact directly with the metal. Authors further reported an immediate acceleration in oxidation rate of Fe-5Cr alloy in the presence of Na ₂ SO ₄ deposits this was attributed to sulphide formation mechanism which initially restricted spinel formation.
Fe-13% Cr alloy	Na ₂ SO ₄	Trafford & Whittle, 1980 B	Study conducted on Fe-13% Cr alloy, Na ₂ SO ₄ coating markedly enhanced the oxidation rate and resulted in the formation of thick, compact and stratified scales. Authors postulated that formation of sulphides in the alloy substrate and mechanical failure of scale was responsible for the enhanced oxidation.
Ni-30Cr and Co-30Cr	600-900°C	Luthra and Shores, 1980	The rapid rate of attack was explained on the basis of sulphation of the transient surface oxides (Ni or Co oxides) and the dissolution of these transition metal sulphates into Na ₂ SO ₄ to yield a liquid phase.
Co-Cr, Co-Al and Co-Cr-Al Alloys.	In O ₂ -SO ₂ -SO ₃ , 600 to 750°C	Luthra, 1982	Co-Cr and Co-Cr-Al alloys reacted non-uniformly, usually in the form of pits and Co-Al alloys suffered broad frontal attack. Under all conditions, a thin sulphur-rich band containing sulphides was observed at the alloy/scale interface and cobalt dissolved near the interface and formed Co ₃ O ₄ /or CoSO ₄ (S).
Ni-base superalloys	1 atm O ₂ , 650-1000°C (Goebel et al), O ₂ , 750-950°C (Misra)	Goebel et al., 1973 and Misra, 1986	The accelerated oxidation occurred as a result of the formation of a liquid flux based on Na ₂ SO ₄ which dissolved the normally protective oxide scales. Catastrophic or self-sustaining rapid oxidation can occur in alloys which contain Mo, W or V because solution of oxides of these elements with Na ₂ SO ₄ decrease the oxide ion activity of the molten salts, producing melts which are acidic fluxes for oxide scales. The evaporation rate of MoO ₃ from Na ₂ Mo-MoO ₃ melts has been reported to decrease considerably by Misra (1986) when dissolved in Na ₂ MoO ₄ .

Fe-, Ni- and Co-base alloys	Atmospheres containing O ₂ , N ₂ and SO ₂ , 729-1076°C	Pehkonen et al., 1987	The corrosion rate was lowest when the chromium content of the alloy was highest. Further Mo and Cu were found to increase the corrosion rate. The main corrosion products formed in air were NiO and Cr ₂ O ₃ . In hot corrosion tests NiS and Cr ₅ S ₈ were found.
Pure Iron	Simulated combustion gas containing SO ₃ , 600-800°C	Gesmundo & Viani, 1988	The accelerated reaction observed in the presence of Na ₂ SO ₄ deposits was attributed to the formation of a liquid salt solution between Na ₂ SO ₄ and the sulphates of the corroded metal with the production of duplex scales consisting of a mixture of metal oxides and sulphides.
Inconel 600 and Incolloy 825	Ar +1% O ₂ , 940°C	Santorelli et al., 1989	Inconel 600 was able to form a protective layer of chromia in Ar +1% O ₂ with or without a thin layer of Na ₂ SO ₄ at a temperature of 940°C, whereas Incolloy 825 was not able to form chromia in the same environment. This was attributed to the formation of nickel and chromium molybdates due to 3.22% Mo present in the alloy. When O ₂ content was only 300ppm, sodium sulphate layer strongly enhanced the corrosion of Inconel 600 and Incolloy 825.
Pure Nickel	Under SO ₃ + SO ₂ + O ₂ gas mixture & SO ₂ and O ₂ atmospheres, 900°C	Hara et al., 1991	The corrosion loss in mixed atmosphere containing SO ₃ was reported to be larger than those observed in pure SO ₂ and O ₂ atmospheres. The corrosion loss was found to correspond to the thickness of the oxide layers. High corrosion losses were attributed to the fact that SO ₃ strongly acted as an oxidizing agent for the corrosion process.
Pure Ni and Al and Fe-Cr, Ni-Cr and Fe-Al alloys	In oxygen and air, 750°C	Shi, 1995	The researcher studied the possibility of Na ₂ SO ₄ -Na ₂ O eutectic melt formation on the metals deposited with Na ₂ SO ₄ . In case of Ni, Co, Al, Cr and their alloys he could not detect formation of Na ₂ SO ₄ -Na ₂ O. In case of iron base alloy with high Cr or Al content, where Cr ₂ O ₃ or Al ₂ O ₃ were formed, again Na ₂ SO ₄ -Na ₂ O eutectic was not observed. However, at lower Cr or Al content this eutectic melt was suggested to be the possible cause for accelerated rate of corrosion.
Pure Iron	Na ₂ SO ₄ , Na ₂ SO ₄ +NaCl, Na ₂ SO ₄ +V ₂ O ₅ , combustion gas, 600°C	Li et al., 1996	Iron suffered low temperature hot corrosion in the presence of salt deposits at 600°C. The additions of NaCl and V ₂ O ₅ to Na ₂ SO ₄ changed the corrosion kinetics significantly and modified the scale structure.
310 Stainless Steel	Various ratios of Na ₂ SO ₄ /NaCl deposit, in air at 750°C	Tsaur et al., 2005	The weight gain kinetics in simple oxidation was found to follow a steady state parabolic rate law after 3 hours, while the kinetics with the salt deposits displayed a multi-stage growth rates. The most severe corrosion took place with 75% NaCl mixtures. Uniform internal attack was the morphology of NaCl-induced hot corrosion, while the extent of intergranular attack was more pronounced as the content of Na ₂ SO ₄ in the mixture was increased.

V₂O₅ Induced Hot Corrosion

		Brief Details	
Material	Environment	Researchers	
Gas-turbine alloys	750°C and above	Harris et al., 1955	Vanadium pentaoxide coatings had a deleterious effect throughout the useful temperature range of all the alloys up to 1120 hrs in 70-hr cycles. The effect was reported to be more pronounced for iron base alloys at temperatures above 750°C.
Pure metals such as iron, cobalt, nickel, molybdenum, titanium, tungsten and 99.5% vanadium rods, and single crystals of chromium	Immersion in the melt, in O ₂	Pantony & Vasu, 1968	<p>A diffusion controlled corrosion process given by equation below hold good for the initial stages of vanadic corrosion of all metals under study except nickel and chromium.</p> $\Delta w = Kt$ <p>where Δw is the weight change per cm² at time t, and k is the velocity constant.</p> <p>Whereas nickel obeyed a logarithmic rate law. The velocity constant was found to be inversely proportional to the depth of melt. On the basis of comparison of activation energies of the various rate processes, a single mechanism underlying the corrosion processes of iron, cobalt, vanadium, titanium, tungsten and molybdenum was suggested, which involves an inward diffusion of oxygen (or other active species) and a sequential outward diffusion of the corrosion products. In case of nickel and chromium, the existence of a coherent corrosion layer separating the slag from nickel and chromium was revealed, which was named as protective barrier for these metals and was found to be absent for other metals under study.</p>
iron, nickel and several alloys containing iron, nickel, and chromium	Crucible and rotating disk testing	Kerby and Wilson, 1973	The stainless steels and particularly 440 stainless steel (25 wt% Cr) showed the best corrosion resistance to liquid V ₂ O ₅ . The rate of corrosion of Armco iron by liquid V ₂ O ₅ has been reported to be controlled initially by the diffusion of oxygen across the metal oxide-liquid vanadate interface. As the available oxygen ions got depleted from the melt, the rate controlling mechanism was observed to be changed to the sorption of oxygen at the liquid vanadate gas phase interface. Whereas in case of nickel, Inconel 600 and the iron alloys, the rates of corrosion were found to be affected by the formation and dissolution of the protective metal oxide layers. They concluded that the presence of Fe and Na in the vanadate melts did not alter the rate controlling process of oxygen diffusion and oxygen sorption, but it increased the non stoichiometry and hence increased the oxygen diffusion. The rate of corrosion was reported to be affected by temperature, oxygen partial pressure and rotational speed, volume of liquid vanadate, composition of the metal and composition of the liquid vanadates.
Superalloys	700°C	Hancock, 1987	The relationship of the high temperature corrosion of superalloys with contaminants has been reported by. It was proposed that to compare contaminant conditions the contaminant flux rate (CFR) rather than the contaminant level in the fuel or environment should be considered. He further suggested that at temperatures above 700°C where vanadates cause fluxing of the protective oxide scales, corrosion could be determined by the CFR and temperature rather than by material selection.

Na₂SO₄ – 60 % V₂O₅ Induced Hot Corrosion

Material	Environment	Researchers	Brief Details
Grade A-1, T-11 and T-22 boiler steels	In air and molten salt (Na ₂ SO ₄ – 60%V ₂ O ₅), at 900°C for 50 cycles	Sidhu et al., 2003	Studied the hot corrosion behaviour of boiler steels at 900°C under cyclic conditions (for 50 cycles, each cycle consists of 1Hr heating and 20min cooling) in molten salt (Na ₂ SO ₄ – 60 % V ₂ O ₅) environment. The maximum weight gain in case of T-22 steel is observed. The spalling and scale crack has been observed in all the specimens. In case of T-22 boiler steel, severe spalling and sputtering may be due to the presence of higher content of Mo, which results cracking of the scale.
Superfer 800H (Fe-based superalloy)	900°C for 50 cycles, air and molten salt (Na ₂ SO ₄ – 60%V ₂ O ₅)	Singh et al. 2005	Authors used thermogravimetric technique to study the kinetics of hot corrosion at 900°C for 50 cycles (each cycle consists of 1Hr heating and 20min cooling) in molten salt (Na ₂ SO ₄ – 60 % V ₂ O ₅) environment. The specimen showed intense spalling and sputtering and the weight gain was enormous. There was continuous increase in the weight, but the rate of increase was high during the initial period of exposure. This rapid increase in weight gain may be due to the rapid oxygen pick up by diffusion of oxygen through the molten salt layer.
ASTM-SA210 GrA1	In air and Na ₂ SO ₄ – 60%V ₂ O ₅ salt deposit, at 900°C for 50 cycles	Sidhu et al., 2005	The scale gets detached from the steel and gets cracked. The presence of Fe ₂ O ₃ in the spalled scale indicates the non-protective conditions on the surface. High rate of corrosion and weight gain per unit area has been observed.
Superni 75 (Ni-base superalloy)	In air and molten salt (Na ₂ SO ₄ – 60%V ₂ O ₅), at 900°C for 50 cycles	Sidhu et al., 2006	A fragile scale appeared on the surface of the superalloy after its exposure to Na ₂ SO ₄ – 60 % V ₂ O ₅ molten salt at 900°C for 50 cycles. Subsequently, cracks were developed in the scale and spalling of the scale was observed during the course of study. Some of the scale was seen to be detached from the surface of the superalloy. The colour of the scale, which was brownish grey during early cycles, turned to dark grey after some cycles.
Superni 76, Superni 750 and Superfer 800	900°C for 100 cycles, air and molten salt (Na ₂ SO ₄ – 60%V ₂ O ₅)	Mahesh et al., 2007	The mass gain of the alloys exposed to the molten salt environment, is gradual. In case of Superni 750, small pores are seen indicating possible escape of vaporised phases. These pores can help corroding species to easily penetrate into the substrate and cause the damage. Whereas, in the case of Superni 76 and Superfer 800 the mass gain was comparatively low.
Ti-6Al-5V (Ti-31) alloy	750°C, air and molten salt (Na ₂ SO ₄ – 60%V ₂ O ₅)	Anuwar et al. 2007	The corrosion rate of the Ti-31 alloy is relatively high in molten salt environment when compared to that in air. The degradation of Ti-31 occurs due to the chemical reactions between titania and sulphur and vanadium present in the environment.

Table A.3 Patent search results for U.S. Patent

Patent No.	Title
Results for	<p>1. Nitrided Ti-Al and Al-Cr based coatings high temperature applications</p> <p>2. Protective Ti-Al and Al-Cr based nitrided coatings</p>
<u>6,908,516</u>	Selected processing for non-equilibrium light alloys and products
<u>6,544,357</u>	Selected processing for non-equilibrium light alloys and products
Results for	<p>1. Development of hot corrosion oxidation resistant coatings</p>
7,422,793	Non-toxic corrosion-protection rinses and seals based on rare earth elements
7,316,899	Portable sensor array system
7,291,217	Non-toxic corrosion-protection pigments based on rare earth elements
7,235,142	Non-toxic corrosion-protection rinses and seals based on cobalt
7,220,398	Mixed-metal oxide particles by liquid feed flame spray pyrolysis of oxide precursors in oxygenated solvents
7,163,713	Method for making dense crack free thin films
7,128,850	Electrically conductive Si-Ti-C-N ceramics
7,040,397	Thermal processing of an oil shale formation to increase permeability of the formation
6,921,557	Process for making dense thin films
6,913,827	Nanocoated primary particles and method for their manufacture
6,887,578	Fluorocarbon-organosilicon copolymers and coatings prepared by hot-filament chemical vapor deposition
6,833,087	2,4,-Hexadienoic acid, its alkali salts and/or derivatives for preventing oxidative corrosion of metals
6,800,186	Method and apparatus for electrochemical processing
6,767,662	Electrochemical device and process of making
6,759,151	Multilayer article characterized by low coefficient of thermal expansion outer layer
6,733,908	Multilayer article having stabilized zirconia outer layer and chemical barrier layer
6,713,298	Method and apparatus for the delivery of samples to a chemical sensor array
6,713,177	Insulating and functionalizing fine metal-containing particles with conformal ultra-thin films
6,676,762	Method for cleaning a finished and polished surface of a metal automotive wheel
6,649,403	Method of preparing a sensor array

6,624,223	Internally plasticized and low VOC latex compositions and applications thereof
6,568,846	Pulsed laser heating simulation of thermal damage on coated surface
6,551,407	Method for treatment of surfaces to remove mold release agents with continuous ultraviolet cleaning light
6,517,802	Methods of synthesis for nanostructured oxides and hydroxides
6,451,485	Electrical energy devices
6,391,486	Fabrication of a membrane having catalyst for a fuel cell
6,217,725	Method and apparatus for anodizing
6,193,501	Microcombustor having submillimeter critical dimensions
6,162,530	Nanostructured oxides and hydroxides and methods of synthesis therefor
6,045,877	Pyrolytic chemical vapor deposition of silicone films
5,945,231	Direct liquid-feed fuel cell with membrane electrolyte and manufacturing thereof
5,834,840	Net-shape ceramic processing for electronic devices and packages
5,801,073	Net-shape ceramic processing for electronic devices and packages
5,454,999	Composite silicide/silicon carbide mechanical alloy
5,399,377	Borazine oligomers and composite materials including boron nitride and methods of making the same
5,374,318	Process for the deposition of diamond films using low energy, mass-selected ion beam deposition
5,370,171	Die-casting process and equipment
5,340,531	Refractory metal reinforced MoSi ₂ /SiC composite with matched thermal coefficients of expansion
5,275,670	High temperature, oxidation resistant noble metal-Al alloy thermocouple
5,246,055	Vacuum die-casting machine with apparatus and method for controlling pressure behind piston
5,242,563	Molten salt reactor for potentiostatic electroplating
5,076,344	Die-casting process and equipment
4,724,121	Powder treatment process
4,704,338	Steel bonded dense silicon nitride compositions and method for their fabrication
4,703,884	Steel bonded dense silicon nitride compositions and method for their fabrication
4,649,086	Low friction and galling resistant coatings and processes for coating
4,461,691	Organic conductive films for semiconductor electrodes
4,271,789	Energy conversion system
4,134,759	Light metal matrix composite materials reinforced with silicon carbide fibers
4,093,879	Magnetohydrodynamic electrode

Table A.4 Thermal expansion coefficients of substrate steels, coatings and oxides

Alloy or Oxide	Thermal Expansion coefficient (10^{-6} per °C)	Reference
T-11	13.9	Metal Hand book (1961)
T-22	14.2	
Al	23.10	Schutze et al., 2006
Ti	8.60	
Al ₂ O ₃	8.40	
Cr ₂ O ₃	8.06	
AlN	6.23	
TiN	7.76	
TiO ₂	10.53	
Ti ₃ Al	10.94	
Superfer 800H	18.29	

Annexure A.5



TO WHOM IT MAY CONCERN

This is to certify that we have provided the coating facility to Mr. Vikas Chawla, Dr. S. Prakash, Dr. D. Puri and Dr. Buta Singh Sidhu under the AICTE sponsored Nationally Co-ordinated Project (File No.8023/RID/BOIII/NCP/07/2-5-06). Further we want to state that we are interested in licensing the work titled, "Development of Ti-Al and Al-Cr based Nitrided Coatings for Boiler Applications".

For ANOD PLASMA SPRAY LTD

(R.K. TANDON)
MANAGING DIRECTOR

HEAD Office: E-20, Pankaj Industrial Area, Site -1, Kanpur - 208 022, UP, INDIA | ☎: +91 512 269 1857, 852, 552, 325 6518 | ☎: +91 512 269 1553 | ✉: info@anod.in | 🌐: www.anod.in

NCR Office

B-601, 6th Floor, Saheta Apartments,
Plot # 30, Sector - 4, Dwarka, New Delhi 110 075.
☎: +91 11 3296 7316 | ☎: +91 11 2508 5168

MUMBAI Office

A/301, Silver Oak, Beverly Park,
Opposite Mira Road Police Station,
Off. Mira Bhayandar Road, Mira Road (East)
District Thane, Mumbai - 401 107.
☎: +91 22 3256 1478 | ☎: +91 22 2810 0869

HYDERABAD Office


21-4-957, Near Charanmahal Gurudwara,
Patla Burz, Hyderabad 500 002.
☎: +91 40 3298 2631

Annexure A.6

PUNJAB STATE ELECTRICITY BOARD

TO WHOM IT MAY CONCERN

This is to certify that we have permitted Mr Vikas Chawla, Dr.S.Parkash, Dr D.Puri and Dr Buta Singh Sidhu to conduct the CYCLIC HOT CORROSION STUDIES of the Ti-Al and Al-Cr based nitrated coatings in boiler at temp.approx. 900 °C for 1000 hrs, under the AICTE sponsored nationally coordinated project (file no 8023/RID/BOIII/NCP/07/2-5-06).We recognise the work titled," **Protective Ti-Al and Al-Cr based nitriding coatings**" and its applications to thermal power plant.


(P.Singh),
Sr.Executive Engineer (Boiler),
Guru Nanak Dev Thermal Plant,
BATHINDA, PUNJAB (INDIA)

REFERENCES

1. **Adachi, S.** and Nakata, K., (2007), "Improvement of Adhesive Strength of Ti-Al Plasma -Sprayed Coatings," *Surf. Coat. Technol.*, Vol. 201, pp. 5617-5620.
2. **Agarwal, A.,** Katipelli, L. R. and Dahotre, N. B., (2000), "Elevated Temperature Oxidation of Laser Surface Engineered Composite Boride Coating on Steel," *Metall. Mater. Trans. A*, Vol. 31A, No. 2, pp. 461-473.
3. **Almeraya, C. F.,** Martinez, V. A. and Gonzalez, R. J. G., (1998B), "Electrochemical Studies of Hot Corrosion of Type 347H Stainless Steel," *Brit. Corros. J.*, Vol. 33, No. 4, pp. 288-291.
4. **Almeraya, C. F.,** Martinez, V. A., Gaona, C., Romero, M.A. and Malo, J.M., (1998A), "Hot Corrosion of the Steel SA213-T22 and SA213-TP347H in 80% V₂O₅-20% Na₂SO₄ Mixture," *Revista de Metalurgia*, Vol. 34, No. 1, pp. 11-17.
5. **Anand, K.,** Hovis, S.K. Conard, H. and Scattergood, R.O., (1987), "Flux Effects in Solid Particle Erosion," *Wear*, Vol. 118, No. 2, pp. 243-257.
6. **Ananthapadmanabhan, P.V.,** Sreekumar, K.P., Muraleedharan, K.V. and Venkatramani, N., (1991), "Plasma-sprayed Composite Coatings for High Temperature Applications", *Surf. Coat. Technol.*, Vol. 49, pp. 62-66.
7. **Anuwar, M.,** Jayaganthan, R., Tewari, V. K. and Arivazhagan, N., (2007), "A Study on the Hot Corrosion Behaviour of Ti-6Al-4V Alloy," *Materials Letter*, Vol. 61, pp. 1483-1488.
8. **Atkinson, A.,** (1988) "Wagner Theory and Short Circuit Diffusion," *Mater. Sci. Technol.*, Vol. 4, No. 12, pp. 1046-1051.
9. **Bao, Z. B.,** Wang, Q. M., Li, W. Z., Gong, J., Xiong, T. Y. and Sun, C., (2008), "Corrosion Behaviour of AIP NiCoCrAlYSiB Coatings in Salt Spray Tests," *Corr. Sci.*, Vol. 50, pp. 847-855.
10. **Barbooti, M.M.,** Al-Madfai, S.H. and Nassouri, H.J., (1988), "Thermochemical Studies on Hot Ash Corrosion of Stainless Steel 304 and Inhibition by Magnesium Sulphate," *Thermochim. Acta*, Vol. 126, pp. 43-49.

11. **Batchelor**, A.W., Lam, L.N. and Chandrasekaran, M, (2003), "Ch. 6: Discrete Coatings," in 'Materials Degradation and its Control by Surface Engineering,' 2nd Edition, Imperial College Press.
12. **Baxter**, D.J and Natesan, K., (1989), "Breakdown of Chromium Oxide Scales in Sulfur-Containing Environments at Elevated Temperatures," *Oxid. Met.*, Vol. 31, No. 3-4, pp. 305-323.
13. **Bellman**, R. Jr. and Levy, A., (1981), "Erosion Mechanism in Ductile Metals", *Wear*, Vol. 70, No. 1, pp. 1-27.
14. **Beltran**, A.M. and Shores, D.A., (1972), "Ch. 11: Hot Corrosion," in 'The Superalloys,' Eds. Sims, C.T. and Hagel, W.G., Wiley Publ., John Wiley and Sons, N. Y.
15. **Beltran**, A.M. and Shores, D.A., (1972), "Hot Corrosion," In: Sims CT, Hagel WC, editors. The superalloys. New York: Wiley, pp. 317-339.
16. **Belzunce**, F.J., Higuera, V. and Poveda, S., (2001), "High Temperature Oxidation of HFPD Thermal-Sprayed MCrAlY Coatings," *Mater. Sci. Engg. A*, Vol. 297, No. 1-2, pp. 162-167.
17. **Bertrand**, G., Mahdjoub, H. and Meunier, C., (2000), "A Study of the Corrosion Behaviour and Protective Quality of Sputtered Chromium Nitride Coatings," *Surf. & Coat. Technol.*, Vol. 126, pp. 199-209.
18. **Bhushan**, B. And Gupta, B.K., (1991), "Handbook of Tribology: Material Coatings and Surface Treatments," McGraw-Hill, New York.
19. **Bittel**, J.T., Sjudahl, L.H. and White, J.F., (1969), "Oxidation of 304L Stainless Steel by Steam and by Air," *Corros.*, Vol. 25, No. 1, pp. 7-14.
20. **Blum**, R., (1997), "Advanced (700°C) PF Power Plants," EC Contact No SF/1001/97/DK.
21. **Bluni**, S.T. and Mardar, A.R., (1996), "Effects of Thermal Spray Coating Composition and Microstructure on Coating Response and Substrate Protection at High Temperatures," *Corros.*, Vol. 52, No. 3, pp. 213-218.
22. **Branco**, J.R. T., Gansert, R., Sampath, S., Berndt, C. C. and Herman H., (2004), "Solid Particle Erosion of Plasma Sprayed Ceramic Coatings," *Materials Research*, Vol. 7, No.1, pp. 147-15

23. **Brandl, W., Marginean, G., Maghet, D. and Utu, D., (2004), "Effects of Specimen Treatment and Surface Preparation on the Isothermal Oxidation of MCrAlY Coatings," Surf. & Coat. Technol., Vol. 188–189, pp. 20–26.**
24. **Brown, R., Kosco, S. and Jun, E.J., (1983), "The Effect of Particle Shape and Size on Erosion of Aluminum Alloy 1100 at 90° Impact Angles," Wear, Vol. 88, No. 2, pp. 181-193.**
25. **Budinski, K. G., Budinski, M. K., (1979), "Ch.12: Corrosion" in 'Engineering Materials Properties and Selection', Prentice-Hall of India Private Limited, New Delhi, India.**
26. **Bunshah, Rointan F., (2001), "Ch: 3: Thermal Spraying and Detonation Gun Processes", in "Handbook of Hard Coatings, Deposition Technologies, Properties and Applications,' William Andrew Publishing, LLC, Newyork, U.S.A.**
27. **Burakowski, T. and Wierzchon, T., (1999), 'Surface Engineering of Metals, Principles, Equipment, Technology,' CRC Press, N. W., Boca Raton, Florida.**
28. **Calvarin, G., Molins, R. and Huntz, A. M., (2000), "Oxidation Mechanism of Ni-20Cr Foils and Its Relation to the Oxide-Scale Microstructure," Oxid. Met., Vol. 53, No. 1-2, pp. 25-48.**
29. **Chandler, P.E. and Quigley, M.B.C., (1986), "The Application of Plasma-Sprayed Coatings for the Protection of Boiler Tubing," Proc. Of the 11th International Thermal Spraying Conference, Montreal, Canada, 8-12 September, pp. 29-35.**
30. **Chatterjee, U. K., Bose, S. K. and Roy, S. K., (2001), "Environmental Degradation of Metals," Pub., Marcel Dekker, 270 Madison Avenue, New York.**
31. **Chawla, V., Prakash, S. and Singh, B., (2007A), "State of art: Applications of Mechanically Alloyed Nanomaterials: A Review", Materials & Manufacturing Processes, Taylor & Francis Group, Vol. 22, pp. 469-473.**
32. **Chawla, V., Prakash, S., and Singh, B., (2006A) "State of art: Applications of Mechanical Alloyed Nanomaterials-a review", Proc. of International Conference organized by Metallurgy Department, Indian Institute of Technology Kharagpur, 3-5th February.**
33. **Chawla, V., Prakash, S., Puri, D. and Singh, B., (2006B), "State of Art: Corrosion in Thermal Power Plants and Preventive Measures: a review", Proc. of National**

Conference on "Advancement & Futuristic Trends in Mechanical & Materials Engineering", organized by G.Z.S. College of Engineering & Technology, Bathinda, Punjab, 13-14th October.

34. **Chawla, V., Prakash, S., Puri, D. and Singh, B., (2006C)** "Plasma Sprayed Coatings for protection against Hot Corrosion-A Review", Proc. of International Conference on "Advances in Mechanical Engineering (AME 2006)", organized by Baba Banda Singh Bahadaur College of Engineering, Fatehgarh Sahib, Punjab, 1-3rd December.
35. **Chawla, V., Prakash, S., Puri, D. and Singh, B., (2007B)** "State of art: a survey of the studies on hard TiAlN and AlCrN coatings: a review", Proc. of National Conference on advances in materials and manufacturing technology (AMMT-2007), organized by mechanical engineering department, Panjab Engineering College, Chandigarh, on 21-22 September.
36. **Chawla, V., Prakash, S., Puri, D. and Singh, B., (2007C)**, "State of art: Hot Corrosion: A Review", Proc. of Global Conference on "Production & Industrial Engineering (CPIE-2007)", organized by Dr. B.R. Ambedkar National Institute of Technology, Jalandhar, Punjab, 22-24th March.
37. **Chawla, V., Prakash, S., Puri, D. and Singh, B., (2008)**, "Performance of plasma sprayed nanostructured and conventional coatings", J. Aus. Ceramic Soc., Vol. 44, No. 2, pp. 56-62.
38. **Chawla, V., Singh, T., (2005)**, "Hot Corrosion and prevention by surface treatment-a review", Proc. of National Conference on "Advances in Manufacturing Technology, organized by National Institute of Technical Teachers' Training & Research, Chandigarh, India, 9-11th November.
39. **Chen, H. and Hutchings, I. M., (1998)**, "Abrasive Wear Resistance of Plasma-Sprayed Tungsten Carbide-Cobalt Coatings," Surf. Coat. Technol., Vol. 107, pp. 106-14.
40. **Chen, H. C., Liu, Z. Y. and Chuang, Y. C., (1993)**, "Degradation of Plasma-Sprayed Alumina and Zirconia Coatings on Stainless Steel During Thermal Cycling and Hot Corrosion," Thin Solid Films, Vol. 223, No. 1, pp. 56-64.

41. **Chinnaduari, S. and Bahadur, S., (1995), "High-temperature Erosion of Haynes and Waspaloy: Effect of Temperature and Erosion Mechanisms", Wear, Vol. 186-187, pp. 299-305.**
42. **Colot, D., Petelot, D., Hoch, P. and Beranger, G., (1997), "Mechanism of Hot Corrosion in Coal Fired Boilers Gas T-91 and Em12 Steels," Mater. Sci. Forum, Vol. 251-54, pp. 641-648.**
43. **Conner, J.A. and Conner, W.B., (1994), "Ranking Protective Coatings: Laboratory Vs Field Experience," JOM, December, pp. 35-38.**
44. **Corvo, F., Betancourt N., and Mendoza A., (1995)," The Influence of Airborne Salinity on the Atmospheric Corrosion of Steel," Corros. Sci, Vol. 37, pp. 1889**
45. **Crossley, H. E., Poll, A. and Sweett, F., (1948), "The Reduction of Sulphur Trioxide by Constituents of Boiler Flue Dust," J. Inst. Fuel, Vol. 21, pp. 207-09.**
46. **Cuevas-Arteaga, C., Porcayo-Calderon, J., Izquierdo, G., Martinez-Villafane, A. and Gonzalez-Rodriguez, J.G., (2001), "Study of Hot Corrosion of Alloy 800 using Linear Polarization Resistance and Weight Loss Measurement," Mater. Sci. Technol., Vol.17, No. 7, pp. 880-885.**
47. **Cuevas-Arteaga, C., Uruchurtu-Chavarina, J., Porcayo-Calderonb, J., Izquierdo-Montalvob, G. and Gonzeleza, J., (2004), "Study of Molten Salt Corrosion of HK-40m Alloy Applying Linear Polarization Resistance and Conventional Weight Loss Techniques," Corros. Sci., Vol. 46, No. 11, pp. 2663-2679.**
48. **Cullity, B.D., (1970), "Elements of X-ray Diffraction," Addison-Wesley, U.S.A.**
49. **Cutler, A.J.B., (1971), "The Effect of Oxygen and SO₃ on Corrosion of Steels in Molten Sulphates," J. Appl. Electrochem., Vol. 1, pp. 19-26.**
50. **Davis, J.R and Hardbound, (1999), "Corrosion: Understanding the Basics (ASM)," ASM publisher, pages 563. ISBN 0-87170-641-5**
51. **DeMasi-Marcin, J. T. and Gupta, D. K., (1994), "Protective Coatings in the Gas Turbine Engine," Surf. Coat. Technol., Vol. 68-69, pp. 1-9.**
52. **Dent, A. H., Horlock, A.J., McCartney, D.G. and Harris, S.J., (1999), "The Corrosion Behaviour and Microstructure of High-Velocity Oxy-Fuel Sprayed Nickel-Based**

- Amorphous/Nanocrystalline Coatings," *J. Thermal Spray Technol.*, Vol. 8, pp. 399-404.
53. **Deshpande, S., Kulkarni, A., Sampath, S. and Herman, H., (2004), "Application of Image Analysis for Characterization of Porosity in Thermal Spray Coatings and Correlation with Small Angle Neutron Scattering,"** *Surf. Coat. Technol.*, Vol. 187, pp. 6-16.
54. **Deshpande, S., Sampath, S. and Zhang, H., (2006), "Mechanisms of Oxidation and its Role in Microstructural Evolution of Metallic Thermal Spray Coatings—Case Study For Ni–Al,"** *Surf. Coat. Technol.*, Vol.200, pp.5395–5406.
55. **Dexter, S. C., (1987), "Seawater,"** in "*ASM Handbook: Corrosion,*" Ed. Davis, J.R., ASM International Publishing, U.S.A, Ninth Edition, Vol. 13, pp. 893-902.
56. **Ding, X., Tan, A.L.K., Zeng, X.T., Wang, C., Yue, T. and Sun, C.Q., (2008), "Corrosion Resistance of CrAlN and TiAlN Coatings Deposited by Lateral Rotating Cathode Arc,"** *Thin Solid Films*, Vol. 516, No. 16, pp. 5716-5720.
57. **Dobrzanski, L. A., Brytan, Z., Grande, M. A. and Rosso, M., (2007), "Corrosion Resistance of Sintered Duplex Stainless Steels in the Salt Fog Test,"** *J. Mat. Proc. Technol.*, Vol. 192-193, pp. 443-448.
58. **Dooley, B., McNaughton, W., (1996), "Steam Touched Tubes,"** *SH/RH Fireside Corrosion/Coal-Fired Units*, Vol. 3, EPRI, Palo Alto, Chapter 33.
59. **Dooley, R. B. and Wilson, J. R., (1975), "The Corrosion of 50Cr-50Ni Alloy in Liquid Vanadate Systems in the Temperature Range 750-950°C,"** *Trans. ASME*, July, pp. 422-428.
60. **Doychak, J. (1995), "Ch: 43: Oxidation Behavior of High temperature intermettals,"** in "*Intermetallic Compounds, Principals and practice, Vol1-principals,*" Eds westbrook, J.H. and Fleischer, F.L., Pub. John Wiley & Sons Inc., U.S.A.
61. **Drivr, D., Hall, D.W. and Meetham, G.W., (1981), "The Gas Turbine Engine,"** In: G.W. Meetham, Editor, *the Development of Gas Turbine Materials*, Applied Science Publishers, London, pp. 1-30.

62. **Eliaz, N., Shemesh, G. and Latanision, R.M., (2002), "Hot Corrosion in Gas Turbine Components," Eng. Fail. Anal., Vol. 9, pp. 31-43.**
63. **Endrino, J. L., Fox-Rabinovich, G. S., and Gey, C., (2006), "Hard AlTiN, AlCrN PVD Coatings for Machining of Austenitic Stainless Steel," Surf. Coat. Technol., Vol. 200, pp. 6840-6845.**
64. **Endrino, J. L., Fox-Rabinovich, G. S., Reiter, A., Veldhuis, V., Galindo, R. E., Albella, J.M. and Marco, J.F., (2007), "Oxidation Tuning in AlCrN Coatings", Surf. Coat. Technol., Vol. 201, pp 4505-4511.**
65. **Erickson, L. C., Westergard, R., Wiklund, U., Axen, N., Hawthorne, H. M. and Hogmark, S., (1998), "Cohesion in Plasma-Sprayed Coatings: A Comparison between Evaluation Methods," Wear, Vol. 214, pp. 30-37.**
66. **Evans, H. E. and Taylor, M. P., (2001), "Diffusion Cells and Chemical Failure of MCrAlY Bond Coats in Thermal Barrier Coating Systems," Oxid. Met., Vol. 55, pp.17-34.**
67. **Evans, N.D., Mazizsz, P.J., Swindeman, R.W. and Smith, G.D., (2004), "Microstructure and Phase Stability in INCONEL alloy 740 During Creep," Scripta Materialia, Vol. 51, No. 6, pp. 503-507.**
68. **Falub, C. V., Karimi, A., Ante, M. and Kalss, W., (2007), "Interdependence between Stress and Texture in Arc Evaporated Ti-Al-N Thin Films," Surf. Coat. Technol., Vol. 201, No. 7, pp. 5891-5898.**
69. **Fauchais, P., (2004), "Topical Review: Understanding Plasma Spraying," J. Phys. D: Appl. Phys., Vol. 37, pp. R86-R108.**
70. **Fauchais, P., Coudert, J. F. and Vardelle, M., (1997), "Transient Phenomena in Plasma Torches and in Plasma Sprayed Coating Generation," J. De Physique IV, Vol. 7, pp. C4-187-198.**
71. **Fedrizzi, L., Rossi, S., Cristel, R. and Bonora, P. L., (2004), "Corrosion and Wear Behaviour of HVOF Cermet Coatings Used to eplace Hard Chromium," Electrochim. Acta, Vol. 49, pp. 2803-2814.**
72. **Fontana, M.G. and Greene, N.D. (1967), "Ch.3: The Eight Forms of Corrosion', McGraw-Hill Book Company, U.S.A.**

73. **Fryburg**, G. C., Kohl, F. J., Stearns, C. A. and Fielder, W. L., (1982), "Chemical Reactions Involved in the Initiation of Hot Corrosion of B-1900 and NASA-TRW VIA," J. Electrochem. Soc., Vol. 129, No. 3, pp. 571-85.
74. **Fujita**, K., (2005), "Research and Development of Oxidation, Wear and Corrosion Resistant Materials at High Temperature by Surface Modification using Ion Processing," Surf. Coat. Tech., Vol. 196, pp. 139-144.
75. **Gesmundo**, F. and Viani, F., (1988), "The Mechanism of Low-Temperature Corrosion of Pure Iron and Manganese at 600-800°C," Mater. Chem. Phys., Vol. 20, pp.513-528.
76. **Giggins**, C. S and Pettit, F.S. (1971), "The oxidation of TD NiC (Ni20Cr-2 Vol pct ThO₂) between 900 and 1200 °C," Meta. Trans., Vol.2, pp1071-1078
77. **Gitanjaly** and Prakash, S., (1999), "Review on Effect of Additives on the Hot Corrosion," 5th NACE Proc., New Delhi, India, 22-24th Nov., pp. 174-82.
78. **Gitanjaly**, (2003), 'Role of Inhibitors on Hot Corrosion of Superalloys in Na₂SO₄-V₂O₅ Environment,' Ph.D. Thesis, Met. Mat. Engg. Deptt., Indian Institute of Technology Roorkee, Roorkee, India.
79. **Gitanjaly**, Prakash, S. and Singh, S., (2002), "Effects of MgO and CaO on Hot Corrosion of Fe Base Superalloy Superfer 800H in Na₂SO₄-60%V₂O₅ Environment," Brit. Corros. J., Vol. 37, No. 1, pp. 56-62.
80. **Goebel**, J. A., Pettit, F. S. and Goward, G. W., (1973), "Mechanisms for the Hot Corrosion of Nickel-Base Alloys," Metall. Trans., Vol. 4, pp. 261-275.
81. **Goebel**, J.A. and Pettit, F.S., (1970A), "Mechanisms for the Hot Corrosion of Nickel-Base Alloys," Metall. Trans., Vol. 4, pp. 261-275.
82. **Goebel**, J.A. and Pettit, F.S., (1970C), "Na₂SO₄ – Induced Accelerated Oxidation (Hot Corrosion) of Nickel," Metall. Trans., Vol. 1, pp. 1943-1954.
83. **Goebel**, J.A. and Pettit, F.S., (1970B), "The Influence of Sulphides on the Oxidation Behavior of Nickel-Base Alloys," Metall. Trans., Vol. 1, pp. 3421-3429.
84. **Grainger**, S. and Blunt, J., (1989), "Ch.2: Mechanism of Wear and Corrosion", in 'Engineering Coatings-design and application', Abington Publishing, England.
85. **Griffin**, R. B., (1987), "Marine Atmospheres," in "ASM Handbook: Corrosion," Ed. Davis, J.R., ASM International Publishing, U.S.A, Ninth Edition, Vol. 13, pp. 902-906.

86. **Guessasma, S., Zhang, G., Liao, H., Coddet, C. And Bordes, J.M., (2006),** "Investigation of Friction and Wear Behavior of SiC-filled Peek Coatings Using Artificial Neural Network," *Surf. Coat. Technol.*, Vol. 200, No. 8, pp. 2610-2617.
87. **Gurrappa, I. and Sambasiva Rao, A., (2006),** "Thermal Barrier Coatings for Enhanced Efficiency as Turbine Engines," *Surf. Coat. Technol.*, Vol. 201, No. 6, pp 3016-3029.
88. **Habib, K.A., Saura, J.J., Ferrer, C., Damra, M.S., Giménez, E., Cabedo, L., (2006)** "Comparison of flame sprayed Al₂O₃/TiO₂ coatings: Their microstructure, mechanical properties and tribology behavior", *Surface & Coatings Technology* vol.201, pp.1436-1443.
89. **Hamner, N. E., (1977),** "Ch. 14: Coatings for Corrosion Protection," in 'NACE Basic Corros. Course,' Houston, Texas.
90. **Hancock, P., (1987),** "Vanadic and Chloride Attack of Superalloys," *Mater. Sci. Technol.*, Vol. 3, pp. 536-544.
91. **Hansen, J.S., (1979),** "Relative Erosion Resistance of Several Metals, Erosion: Prevention and Useful Applications", STP 664 ASTM, pp. 148-162.
92. **Hara, M., Hisaichi, T., Itoh, K. and Shinata, Y., (1991),** "Effects of SO₃, SO₂ and O₂ Gases on Hot Corrosion of Ni and Ni-Cr Alloys in Molten Na₂SO₄," *J. Jpn. I. Met.*, Vol. 55, No. 11, pp. 1207-1215.
93. **Harada, Y. and Kawamura, T., (1980),** "Control of Gas Side Corrosion in Oil Fired Boiler," *Mitsubishi Heavy Technical Review*, Vol. 17, pp. 139.
94. **Harada, Y., Naito, S., Tsuchiya, T. and Nakajima, Y., (1981),** "Problems of Low Grade Oil Firing Boilers and Their Solutions", *Mitsubishi Heavy Technical Review*, Vol. 18, No. 2, pp. 85-95.
95. **Harpreet Singh, Puri, D. and Prakash, S., (2005),** "Corrosion Behaviour of Plasma Sprayed Coatings on a Ni-base Superalloy in Na₂SO₄-60%V₂O₅ Environment at 900°C," *Metall. Mater. Trans. A*, Vol. 36, No. 4, pp. 1007-1015.
96. **Harris, G.T., Child, H.C. and Kerr, J.A., (1955),** "Effect of the Composition of Gas-Turbine Alloys on Resistance to Scaling and to Vanadium Pentaoxide Attack," *ISIJ Int.*, Vol. 179, pp. 342-347.

97. **He, J. L., Chen, K.C., Chen, C.C., Leyland, A. and Matthews, A., (2001), "Cyclic Oxidation Resistance of Ni-Al Alloy Coatings Deposited on Steel by a Cathodic Arc Plasma Process," Surf. Coat. Technol., Vol. 135, pp. 158-65.**
98. **Heath, G. R., Heimgartner, P., Irons, G., Miller, R. and Gustafsson, S., (1997), "An Assessment of Thermal Spray Coating Technologies for High Temperature Corrosion Protection," Mater. Sci. Forum, Vol. 251-54, pp. 809-16.**
99. **Heath, G. R., Heimgartner, P., Irons, G., Miller, R. and Gustafsson, S., (1997), "An Assessment of Thermal Spray Coating Technologies for High Temperature Corrosion Protection," Mater. Sci. Forum, Vol. 251-54, pp. 809-816.**
100. **Heidersbach, R. H., Baxter, R., Jöhn, S., Haroun, M., (1987), "Cathodic Protection," in "ASM Handbook: Corrosion," Ed. Davis, J.R., ASM International Publishing, U.S.A, Ninth Edition, Vol. 13, pp. 919-924.**
101. **Herman, h., "Plasma Sprayed Coatings," (1988), Scientific American, Vol. 259, No. 3, pp.78 -83.**
102. **Hidalgo, V. H., Varela, F. J. B. and Menendez, A. C., (1998), "Characterization and High Temperature Behaviour of Thermal Sprayed Coatings Used in Boilers," Proc. of the 15th Int. Thermal Spray Conf., 25-29th May, Nice, France, pp. 617-21.**
103. **Hidalgo, V. H., Varela, F. J. B. and Rico, E. F., (1997), "Erosion Wear and Mechanical Properties of Plasma-Sprayed Nickel- and Iron-Based Coatings Subjected to Service Conditions in Boilers," Trib. Int., Vol. 30, No. 9, pp. 641-49.**
104. **Hidalgo, V. H., Varela, F. J. B., Martinez, S.P. and Espana, S. G., (1999), "Characterization and High Temperature Behaviour of Cr₃C₂-NiCr Plasma Sprayed Coatings," Proc. of the United Thermal Spray Conf., Germany, pp. 683-86.**
105. **Hidalgo, V. H., Varela, J. B., Calle, J. M. de la and Menendez, A. C., (2000), "Characterisation of NiCr Flame and Plasma Sprayed Coatings for Use in High Temperature Regions of Boilers," Surface Engg., Vol. 16, No. 2, pp. 137-42.**
106. **Hidalgo, V.H., Varela, J.B., Menendez, A.C. and Martinez, S.P., (2001A), "High Temperature Erosion Wear of Flames and Plasma-sprayed Nickel-chromium Coatings under Coal-fired Boiler Atmospheres," Wear, Vol. 247, pp. 241-222.**

107. **Hidalgo**, V.H., Varela, J.B., Menendez, A.C. and Martinez, S.P., (2001B), "A comparative Study of High-temperature Erosion Wear of Plasma-sprayed NiCrBSiFe and WC-NiCrBSiFe Coatings under Simulated Coal-fired Boiler Conditions," *Tribology*, Vol. 34, pp. 161-169.
108. **Hocking**, M. G., (1993), "Coatings Resistant to Erosive/Corrosive and Severe Environments," *Surf. Coat. Technol.*, Vol. 62, pp. 460-66.
109. **Holt**, A. and Kofstad, P., (1989), "High Temperature Corrosion of Iron in O₂ + 4% SO₂/SO₃ at 500-800°C," *Mater. Sci. Engg. A*, Vol. A120, pp. 101-04.
110. **Hossain**, K. M. A., Easa, S. M. and Lachemi, M., (2009), "Evaluation of the Effect of Marine Salts on Urban Built Infrastructure," *Building and Environment*, Vol. 44, pp. 713-722.
111. **Hussain**, N., Shahid, K.A., Khan, I.H. and Rahman, S., (1994), "Oxidation of High-Temperature Alloys (Superalloys) at Elevated Temperatures in Air: I," *Oxid. Met.*, Vol. 41, No. 3-4, pp. 251-269.
112. **Hwang**, Y. S. and Rapp, R. A., (1989), "Thermochemistry and Solubilities of Oxides in Sodium Sulfate-Vanadate Solutions," *Corros.*, Vol. 45, No. 11, pp. 933-937.
113. **Jaffee**, R.I, (1987), "Corrosion in Fossil Fuel Power Systems," in "ASM Handbook: Corrosion," Ed. Davis, J.R., ASM International Publishing, U.S.A, Ninth Edition, Vol. 13, pp. 985-992.
114. **John**, R. C., (1986), "Slag, Gas and Deposit Thermochemistry in a Coal Gasifier," *J. of Electrochem. Soc.*, Vol. 133, No. 1, pp. 205-11.
115. **Kalss**, W., Reiter, A., Derflinger, V., Gey, C. and Endrino, J.L., (2006), "Modern Coatings in High Performance Cutting Applications," *Int. J. Ref. Met. Hard Mat.*, Vol. 24, No. 7, pp. 399-404.
116. **Kang**, C.T., Pettit, F.S. and Birks, N., (1987), "Mechanisms in the simultaneous erosion-oxidation attack of nickel and cobalt at high temperature," *Met. Trans. A.*, Vol. 18, pp. 1785.
117. **Kerby**, R. C. and Wilson J. R., (1973), "Corrosion of Metals by Liquid Vanadium Pentoxide and the Sodium Vanadates," *Trans. ASME*, January, pp. 36-44.

118. **Khajavi, M.R. and Shariat, M.H., (2004), "Failure of First Stage Gas Turbine Blades,"** Eng. Fail .Anal., Vol.11, pp.589–597.
119. **Khanna, A. S. and Jha, S. K., (1998), "Degradation of Materials Under Hot Corrosion Conditions,"** Trans. Indian Inst. Met., Vol. 51, No. 5, pp. 279-90.
120. **Khanna, A.S. (2002), "High Temperature Oxidation-Basics" in 'Introduction to High Temperature Oxidation and Corrosion',** ASM International, U.S.A.
121. **Knotek, O., (2001), "Chapter 3: Thermal Spraying and Detonation Spray Gun Processes,"** in "Handbook of Hard Coatings: Deposition Technologies, Properties and Applications," Ed. Bunshah, R.F., Noyes Pub. Park Ridge, New Jersey, U.S. A./ William Andrew Publishing, LLC, Norwich, New York. U.S.A., pp. 77-107.
122. **Koch, G. H., Brongers, M. P. H., Thompson, N. G., Virmani, Y. P. and Payer, J. H., (2002), "Historic Congressional Study: Corrosion Costs and Preventive Strategies in the United States,"** Supplement to Mater. Perfor., July, pp. 1-11.
123. **Kofstad, P. (1966), "Ch.1: General Introduction" in 'High Temperature Oxidation of Metals',** John Wiley & Sons Inc., U.S.A.
124. **Kofstad, P., (1990), "High Temperature Corrosion of Metals,"** Proc. of Conf. on Microscopy of Oxidation, London, pp. 1-9.
125. **Kolta, G. A., Hewaidy, L. F. and Felix, N. S., (1972), "Reactions Between Sodium Sulphate and Vanadium Pentoxide,"** Thermochim. Acta, Vol. 4, pp. 151-164.
126. **Korpiola, K. and Vuoristo, P., (1996), "Effect of HVOF Gas Velocity and Fuel to Oxygen Ratio on the Wear Properties of Tungsten Carbide Coating,"** In: Bernt, C. C. (ed.). Thermal Spray: Practical Solutions for Engineering Problems. Cincinnati. USA. 11 - 17 October. ASM.
127. **Kosel, T.H., (1992), "Friction, Lubrication and Wear Technology,"** ASM Handbook, Vol. 18, pp. 199-213.
128. **Krishnamoorthy, P.R. and Seetharamu, S., (1989), "The Wear Life of Pipe Bends and other Components under Pulverized Coal Erosion,"** Proc. of LIPREX-89, Hyderabad, India, January 1989.
129. **Krishnamoorthy, P.R., Seetharamu, S. and Sampathkumaran, P., (1993), "Influence of the Mass Flux and Impact Angle of the Abrasive on the Erosion Resistance of**

Materials used in Pulverized Fuel Bends and other Components in Thermal Power Stations”, *Wear*, Vol. 165, pp 151-157.

130. **Kuiry, C., Seal, S., Bose, S. K. and Roy, S. K., (1994), “Effect of Surface Preparation on the High-Temperature Oxidation Behaviour of AISI 316 Stainless Steel,”** *ISIJ Int.*, Vol. 34, No. 7, pp. 599-606.
131. **Lai, G. Y., (1990), ‘High Temperature Corrosion of Engineering Alloys,’** *ASM Inter. Book*, pp. 15-46.
132. **Landry, B.A., Hummel, J.D., Nelson, H.W., Krause, H.H., Ungar, E.W., Putnam, A.A., Slunder, C.J. and Miller, P.D. (1959), “A Review of Available Information on Corrosion and Deposition in Coal and Oil Fired Boilers and Gas Turbines”,** ASME research committee, Pergamon press, The American society of mechanical engineers, New York, 1959, pp 1-197.
133. **Lee, S.Y. and McNallan, M.J., (1990), “Inhibition of Oxidation of Iron in Environments Containing Chlorine at 1100 and 1200 K,”** *J. Electrochem. Soc.*, Vol. 137, No. 2, pp. 472-479.
134. **Levy, A. V., Slamovich, E. and Jee, N. (1986), “Elevated temperature combined erosion-corrosion of steels”,** *Wear*, Vol.110, pp117-149.
135. **Levy, A. V., Pauline, C., (1983), “The Effects of Erodent Composition and Shape on the Erosion of Steel,”** *Wear*, Vol. 89, Issue 2, pp. 151-162.
136. **Levy, A. V., Yong-Fa, M., (1989), “Effects of Particle Variables on the Erosion-corrosion of 9Cr1Mo Steel,”** *Wear*, Vol. 131, No. 1, pp. 53-69.
137. **Levy, A.V., (1988), “The Erosion Corrosion Behaviour of Protective Coatings,”** *Surf. Coat. Technol.*, Vol. 36, pp. 387-406.
138. **Levy, A.V., (1993), “The Erosion-corrosion of Tubing Steels in Combustion Boiler Environments,”** *Corros. Sci.*, Vol. 35, No. 5-8, pp. 1035-1043.
139. **Li, L., Zhu, R. and Gesmundo, F., (1996), “Hot Corrosion of Iron in the Presence of Salt Mixture Deposit containing NaCl and V₂O₅ at 600⁰C,”** *J. Mater. Sci. Technol.*, Vol. 12, No. 6, pp. 445-451.

140. Li, M. H., Zhang, Z. Y., Sun, X. F., Li, J. G., Yin, F. S., Hu, W. Y., Guan, H. R. and Hu, Z. Q., (2003), "Oxidation Behaviour of Sputter-Deposited NiCrAlY coating," *Surf. Coat. Technol.*, Vol. 165, No. 3, pp. 241-47.
141. Li, M.H., Sun, X.F., Li, J.G., Zhang, Z.Y., Jin, T., Guan, H.R. and Hu, Z.Q., (2003A), "Oxidation Behaviour of a Single-Crystal Ni-based Superalloy in Air-I: At 800 and 900°C," *Oxid. Met.*, Vol.59, No.5-6, pp 591-605.
142. Liang, M., (2008), "Theoretical Elucidation on the Corrosion Tube Growth Mechanism of Mild Steel in the Effect of pH on Oxygen Corrosion at Elevated Pressures," *J. Mar. Sci. Technol.*, Vol. 16, No. 4, pp. 265-270.
143. Link, R.J., Birks, N., Pettit, F.S. and Dethorey, F., (1998), "The Response of Alloys to Erosion-corrosion at High emperatures," *Oxidation of Metals*, Vol. 49, No. 314, pp. 1998.
144. Liscano, S., Gil, L., Leon, O.A., Cruz, M. and Staia, M. H., (2006), "Corrosion Performance of Duplex Treatments Based on Plasma Nitriding and PAPVD TiAlN Coating", *Surf. Coat. Technol.*, Vol. 201, pp. 4419-4423.
145. Liu, L., Li, Y. and Wang, F., (2007), "Influence of Nanocrystallization on Passive Behavior of Ni-based Superalloys in Acidic Solutions," *Electrochim. Acta*, Vol. 52, No. 7, pp. 2392-2400.
146. Liu, P.S., Liang, K.M. and Gu, S.R., (2001), "High-temperature Oxidation Behavior of Aluminide Coatings on a New Cobalt-bae Superalloy in Air," *Corros. Sci.*, Vol. 43, pp. 1217-1226.
147. Longa-Nava, Y., Zhang, Y. S., Takemoto, M. and Rapp, R. A., (1996), "Hot Corrosion of Nickel-Chromium and Nickel-Chromium-Aluminum Thermal-Spray Coatings by Sodium Sulfate-Sodium Metavanadate Salt," *Corrosion*, Vol. 52, No. 9. pp. 680-89.
148. Luthra, K. L. and Shores, D.A., (1980), "Mechanism of Na₂SO₄ Induced Corrosion at 600-900 °C," *J. Electrochem. Soc.*, Vol. 127, No. 10, pp. 2202-2210.
149. Luthra, K.L and Spacil, H.S., (1982), "Impurity Deposits in Gas Turbines from Fuels Containing Sodium and Vanadium," *J. Electrochem. Soc.*, Vol. 129, No. 3, pp. 649-656.

150. **Madhu Chittora**, Project Monitor, Economic Research India Ltd, January 28 - February 3, (2008).
151. **Mahesh**, R. A., Jayagandhan, R. and Prakash, S., (2008), "A Study on Hot Corrosion Behaviour of Ni-5Al Coatings on Ni- and Fe-based Superalloys in an Aggressive Environment at 900°C," *J. Alloy and Compounds*, Vol. 460, No. 1-2, pp. 220-231.
152. **Mahesh**, R. A., Jayaganthan, R. and Prakash, S., (2008A), "Oxidation Behavior of HVOF Sprayed Ni-5Al Coatings Deposited on Ni- and Fe-based Superalloys under Cyclic Condition," *Mater. Sci. Engg. A*, Vol. 475, pp. 327-335.
153. **Mahesh**, R.A., Jayaganthan R., Prakash S., (2009), "Microstructural Characteristics and Mechanical Properties of HVOF Sprayed NiCrAl Coating on Superalloys," *J Alloys and Compounds*, Vol. 468, pp. 392-405.
154. **Man**, B. Y., Guzman, L., Miotello, A. and Adami, M., (2004), "Microstructure, Oxidation and H₂-pemeation Resistance of TiAlN Films Deposited by DC Magnetron Sputtering Technique," *Surf. Coat. Technol.*, Vol. 180-181, pp. 9-14.
155. **Marek**, M. I., (1987), "Thermodynamics of Aqueous Corrosion," in "ASM Handbook: Corrosion," Ed. Davis, J.R., ASM International Publishing, U.S.A, Ninth Edition, Vol. 13, pp. 18-21.
156. **Marple**, B.R., Voyer, J., Bisson, J. F. and Moreau, C., (2001), "Thermal Spraying of Nanostructured Cermet Coatings," *J. Mater. Process. Technol.*, Vol. 117, pp. 418-423.
157. **Marriott**, J.B., (1990), "Future Materials Requirements for High Temperature Power Engineering Components," *Materials & Design*, Vol. 11, No. 3, pp. 122-128.
158. **Matthews** S. J., (2004) "Erosion-Corrosion of Cr₃C₂-NiCr High Velocity Thermal Spray Coatings," Ph.D. Thesis, The University of Auckland.
159. **Mattox**, D. M., (2000), "Ion Plating-Past, Present and Future," *Surf. Coat. Technol.*, Vol. 133-134, pp. 517-521.
160. **Meier**, G. H., (1989), "A Review of Advances in High-temperature Corrosion," *Mater. Sci. Eng. A*, Vol. 120, No. 1-3, pp. 1-11.
161. **Mishra**, S. B., Chandra, K. and Prakash, S. (2006B), "Studies on Erosion Behavior of Plasma Sprayed Coatings on a Ni-based Alloys," *Wear*, Vol. 260, pp. 422-432.
162. **Mishra**, S. B., Chandra, K., Prakash, S. and Venkataraman, B., (2006A), "Erosion

- Performance of Coatings Produced by Shrouded Plasma Spray Process on a Co-based Superalloy," Surf. Coat. Technol., Vol. 201, pp. 1477-1487.
163. **Misra, A. K.**, (1986), "Mechanism of Na₂SO₄-Induced Corrosion of Molybdenum Containing Nickel-Base Superalloys at High Temperatures," J. Electrochem. Soc., Vol. 133, No. 5, pp. 1029-37.
 164. **Mitra, S.K, Roy, S.K and Boset, S.K.**, (1993), "Influence of Superficial Coating of CeO₂ on the Oxidation Behavior of AISI 304 Stainless Steel," Oxid. Met, Vol. 39(3/4), pp.22-229.
 165. **Modi, M. D., Modi, S. C. and Mayuram, M. M.**, (1986), "A Case Study on the Use of Plasma Sprayed Oxide Ceramic Coatings in Hot Extrusion Dies for Non-Ferrous Metals," Proc. of the 11th Int. Thermal Spraying Conf., September 8-12, Montreal, Canada, pp.359-66.
 166. **Montemarano, J. A., Shaw, B. A.**, (1987), "Metallic Coatings," in "ASM Handbook: Corrosion," Ed. Davis, J.R., ASM International Publishing, U.S.A, Ninth Edition, Vol. 13, pp. 906-912.
 167. **Moujahid, S.E.**, (1987), "High Temperature Corrosion of Cast Iron Chains by Coal Ash," Proc. Of 10th ICMC, Madras, India, Vol. 1, pp. 2642-2652.
 168. **Murthy, J.K.N., Rao, D.S. and Venkataraman, B.**, (2001), "Effect of Grinding on The Erosion Behaviour of a WC-Co-Cr Coating Deposited by HVOF and Detonation Gun Spray Process," Wear, Vol. 249, pp. 592-600.
 169. **Nakagawa, P.M., Kawakami, F. and Kudoh, T.**, (1994), "Trends in Automotive Applications of Thermal Spray Technology in Japan," Proc. of the 7th National Therm. Spray Conf., Boston, pp. 1-6.
 170. **Natesan, K. and Liu, Y.Y.**, (1989), "Erosion-corrosion of Materials at Elevated Temperatures," Mater. Sci. Eng., Vol. 120-121, pp. 571-580.
 171. **Natesan, K.**, (1976), "Corrosion-Erosion Behavior of Materials in a Coal-Gasification Environment," Corrosion, Vol. 32, No. 9, pp. 364-70.
 172. **Natesan, K.**, (1985), "High-temperature Corrosion in Coal Gassification Systems," Corros., Vol. 41, No. 11, pp. 646-655.

173. **Natesan, K.**, (1997) "Corrosion Performance of Materials in Coal-fired Power Plants", Proc. International conference on corrosion (CONCORN 97), December 3-6, Mumbai, India, pp 24-35.
174. **National Materials Advisory Board**, (1996), "Coatings for High-Temperature Structural Materials: Trends and Opportunities," National Academy Press Washington D.C., <http://www.nap.edu/openbook/0309053811/html>, pp 1-85.
175. **Nelson, H. W.**, Krause, H. H., Ungar, E. W., Putnam, A. A., Slunder, C. J., Miller, P. D., Hummel, J. D. and Landry, B. A., (1959), "A Review of Available Information on, Corrosion and Deposits in Coal- and Oil-Fired Boilers and Gas Turbines," Report of ASME Research Committee on Corrosion and Deposits from Combustion Gases, Pub. Pergamon Press and ASME, New York.
176. **Nerz, J.E.**; Kushner B.A., Jr. Rotolico, A.J., (1992), "Microstructural Evaluation of Tungsten Carbide-Cobalt Coatings," ASM International (USA), pp.115-120.
177. **Nicholls, J. R.**, Simms, N. J., Chan, W. Y. and Evans, H. E., (2002), "Smart Overlay Coatings- Concept and Practice," Surf. Coat. Technol., Vol. 149, pp. 236-44.
178. **Nickel, H.**, Quadackers, W. J. and Singheiser, L., (2002), "Analysis of Corrosion Layers on Protective Coatings and High Temperature Materials in Simulated Service Environments of Modern Power Plants Using SNMS, SIMS, SEM, TEM, RBS and X-ray Diffraction Studies," Anal. Bioanal. Chem., Vol. 374, pp. 581-87.
179. **Nicoll, A. R.**, (1984), "Chapter 13: The Production and Performance Evaluation of High Temperature Coatings," in 'Coatings and Surface Treatment for Corrosion and Wear Resistance,' Eds. Strafford, K. N., Datta, P. K. and Googan, C. G., (1984), Institution of Corros. Sci. and Techol., Birmingham, Pub. Ellis Horwood Ltd., Chichester.
180. **Nicoll, A.R.**, (1994), "Production Plasma Spraying in the Automotive Industry: A European Viewpoint," Proc. Of the 7th National Therm. Spray. Conf., Boston, pp. 7-17.
181. **Niranatlumpong, P.**, Ponton, C. B. and Evans, H. E., (2000), "The Failure of Protective Oxides on Plasma-Sprayed NiCrAlY Overlay Coatings," Oxid. Met., Vol. 53, No. 3-4, pp. 241-256.

182. **Norling, R. and Olefjord, I.**, (2003), "Erosion-corrosion of Fe- and Ni-based Alloys at 550°C," *Wear*, Vol. 254, pp. 173-184.
183. **Otero, E., Merino, M. C., Pardo, A., Biezma, M. V. and Buitrago, G.**, (1987), "Study on Corrosion Products of IN657 Alloy in Molten Salts," *Proc. of 10th ICMC, Madras, India*, Vol. IV, pp. 3583-3591.
184. **Otsuka, N. and Rapp, R.A.**, (1990A), "Hot Corrosion of Preoxidized Ni by a Thin Fused Na₂SO₄ Film at 900°C", *J. Electrochem. Soc.*, Vol. 137, No. 1, pp. 46-52.
185. **Otsuka, N. and Rapp, R.A.**, (1990B), "Effects of Chromate and Vandate Anions on the Hot Corrosion of Peroxidised Ni by a Thin Fused Na₂SO₄ film at 900°C", *J. Electrochem. Soc.*, Vol. 137, No. 1, pp. 53-60.
186. **Panda, B., Balasubramaniam, R. and Dwivedi, G.**, (2008), "On the Corrosion Behaviour of Noval High Carbon Steel in Simulated Cyclic Wet-dry Salt Fog Conditions," *Corros. Sci.*, Vol. 50, pp. 1684-1692.
187. **Pandey, J. L.**, (1983), "Effect of Zirconium and Yttrium Alloying on High Temperature Oxidation of Fe-15wt%Cr-4wt%Al," University of Roorkee, Dept. of Chemistry, Roorkee, India.
188. **Pantony, D.A. and Vasu, K. I.**, (1968), "Studies in the Corrosion of Metals under Melts-1," *J. Inorg. Nucl. Chem.*, Vol. 10, pp. 423-432.
189. **Paul, L. D. and Seeley, R. R.**, (1991), "Oil Ash Corrosion- A Review of Utility Boiler Experience," *Corrosion*, Vol. 47, No. 2, pp. 152-59.
190. **Pawlowski, L.**, (1995), "The Science and Engineering of Thermal Spray Coatings," Wiley, New York, 1995.
191. **Pehkonen, A., Tikkanen, M. H., Ylasaari, S. and Forsen, O.**, (1987), "Behaviour of Some Super Alloys in Different High Temperature Atmospheres," *Proc. of 10th ICMC, Madras, India*, Vol. IV, pp. 3781-3787.
192. **Pei, Y.T., Galvan, D H., Cavaleiro, A.**,(2005), "Nanostructured TiC Coatings for Low Friction and Wear Resistant Application", *Surf. Coat. Technol.*, Vol. 198, pp. 44-50.
193. **Peters, K. R., Whittle, D. P. and Stringer, J.**, (1976), "Oxidation and Hot Corrosion of Nickel-Based Alloys Containing Molybdenum," *Corros. Sci.*, Vol. 16, pp. 791-804.

194. **Pettit, F. S. and Giggins, C. S., (1987), "Hot Corrosion, Ch. 12,"** in 'Superalloys II,' Eds. Sims, C. T., Stolof, N. S. and Hagel, W. C., Pub. Wiley Pub., N. Y.
195. **Pettit, F. S. and Meier, G. H., (1984), "Oxidation and Hot corrosion of Superalloys,"** Superalloys (1984), M. Gell, C. S. Kartovich, R. H. Bricknel, W. B. Kent, J. F. Radovich (Eds.), The Met. Soc. of AIME, Warrendale, Pennsylvania, pp. 651-687.
196. **Pettit, F. S. and Meier, G. H., (1985), "Oxidation and Hot corrosion of Superalloys,"** Superalloys 85, Eds. Gell, M., Kartovich, C. S., Bricknel, R. H., Kent W. B. and Radovich, J. F., Met. Soc. of AIME, Warrendale, Pennsylvania, pp. 651-687.
197. **Pfender, E., (1988), "Fundamental Studies Associated with the Plasma Spray Process,"** Surf. Coat. Technol., Vol. 34, pp. 1-14.
198. **Pierson, H. O., (1987), "CVD/PVD Coatngs,"** in "ASM Handbook: Corrosion," Ed. Davis, J.R., ASM International Publishing, U.S.A, Ninth Edition, Vol. 13, pp. 456-458.
199. **Polman, E.A., Fransen, T. and Gellings, P.J., (1990), "High-Temperature Corrosion and Mechanical Properties of Protective Scales on Incoloy 800H: The Influence of Preoxidation and Ion Implantation,"** Oxid. Met., Vol. 33, No. 1-2, pp. 135-155.
200. **Prakash, S., Singh, S., Sidhu, B. S. and Madeshia, A., (2001), "Tube Failures in Coal Fired Boilers,"** Proc. National Seminar on Advances in Material and Processing, 9-10th Nov., IIT, Roorkee, India, pp. 245-53.
201. **Prakash, S., Singh, S., Sidhu, B. S. and Madeshia, A., (2001), "Tube Failures in Coal Fired Boilers,"** Proc. National Seminar on Advances in Material and Processing, Nov., 9-10, IITR, Roorkee, India, pp. 245-253.
202. **Priyantha, N., Jayaweera, P., Sanjurjo, A., Lau, K. and Krish, K., (2003), "Corrosion-resistant Metallic Coatings for Applications in Highly Aggressive Environment",** Surf. Coat. Technol., Vol. 163-164, 31-36.
203. **Ramm ,D.A.J., Hutchings, I.M. and Clyne T.W., (1993), "Erosion resistance and adhesion of composite metauceramic coatings produced by plasma spraying" J. Phys. IV France 03 pp C7-913-C7-919**
204. **Randhawa, H., (1991), "Review of Plasma Assisted Deposition Processes,"** Thin Solid Films, Vol. 196, pp. 329-349.

205. **Rapp, R. A. and Goto, K. S., (1981), "The Hot Corrosion of Metals by Molten Salts,"** Sympos. Fused Salts, Eds. Braunstein, J. and Selman, J. R., The Electrochem. Soc., Pennington, N. J., pp.159.
206. **Rapp, R. A. and Zhang, Y. S., (1994), "Hot Corrosion of Materials: Fundamental Studies,"** JOM, Vol. 46, No. 12, pp. 47-55.
207. **Rapp, R. A. Devan, J. H., Douglass, D. L., Nordine, P. C., Pettit, F. S. and Whittle, D. P., (1981), "High temperature corrosion in energy systems,"** Mater. Sci. Eng., Vol. 50, No. 1, pp. 1-17.
208. **Rapp, R. A., (1986), "Chemistry and Electrochemistry of the Hot Corrosion of Metals,"** Corrosion, Vol. 42, No. 10, pp. 568-77.
209. **Rapp, R. A., (2002), "Hot Corrosion of Materials: A Fluxing Mechanism,"** Corros. Sci, Vol. 44, No. 2, pp. 209-221.
210. **Rapp, R.A., (1990), "Hot Corrosion of Materials,"** Pure and Appl. Chem., Vol. 62, No. 1, pp. 113-122.
211. **Reddy, A.V. and Sundararajan, G., (1986), "Erosion Behaviour of Ductile Materials with a Spherical Non-friable Eroder,"** Wear, Vol. 111, No. 3, pp. 313-323.
212. **Reiter, A. E., Derflinger, V. H., Hanselmann, B., Bachmann, T. and Sartory, B., (2005), "Investigation of the Properties of $Al_{1-x}Cr_xN$ Coatings Prepared by Cathodic Arc Evaporation,"** Surf. Coat. Technol., Vol. 200, pp. 2114-2122.
213. **Robert, H., (1987), "Marine Corrosion,"** in "ASM Handbook: Corrosion," Ed. Davis, J.R., ASM International Publishing, U.S.A, Ninth Edition, Vol. 13, pp. 893.
214. **Roy, Manish, Vishwanathan, B. and Sundararajan, G., (1994), "The solid Particle Erosion of Polymer Matrix Composites,"** Wear, Vol. 171, No. 1-2, pp. 149-161.
215. **Sadique, S. E., Mollah, A. H., Islam, M. S., Ali, M. M., Megat, M. H. H. and Basri, S., (2000), "High-Temperature Oxidation Behavior of Iron-Chromium-Aluminum Alloys,"** Oxid. Met., Vol. 54, Nos. 5-6, pp. 385-400.
216. **Sahoo, G. and Balasubramaniam, R. (2008), "Corrosion of Phosphoric Irons in Acidic Environments,"** J. ASTM Intern., Vol. 5, No. 5, pp. 1-7.
217. **Sahoo, G. and Balasubramaniam, R., (2008A), "On the Corrosion Behaviour of Phosphoric Irons in Simulated Concrete Pore Solutions,"** Corros. Sci., Vol. 50, pp.

131-143.

218. **Salmenoja, K., Makela, K., Hupa, M. and Backman, R. (1996), "Superheater Corrosion in Environments Containing Potassium and Chlorine," J. Inst. Energy, Vol.69, pp.155-162.**
219. **Samuel, A., (1987), "Fundamentals of Corrosion in Gases," in "ASM Handbook: Corrosion," Ed. Davis, J.R., ASM International Publishing, U.S.A, Ninth Edition, Vol. 13, pp. 61-75.**
220. **Santorelli, R., Sivieri, E. and Reggiani, R.C., (1989), "High-Temperature Corrosion of Several Commercial Fe-Cr-Ni Alloys Under a Molten Sodium Sulphate Deposit in Oxidizing Gaseous Environments," Mater. Sci. Eng. A-Struct., Vol. 120, pp. 283-291.**
221. **Schneider, J. M., Rohde, S., Sproul, W. D. and Matthews, A., (2000), "Recent Developments in Plasma Assisted Physical Vapour Deposition," J. Phy. D: Appl. Phy., Vol. 33, pp. R173-R186.**
222. **Schutze, M., Malessa, M., Rohr, V. and Weber, T., (2006), "Development of Coatings for Protection in Specific High Temperature Environments," Surf. Coat. Technol., Vol. 201, pp. 3872-3879.**
223. **Scully, J. R., (1987), "Electrochemical Methods of Corrosion Testing," in "ASM Handbook: Corrosion," Ed. Davis, J.R., ASM International Publishing, U.S.A, Ninth Edition, Vol. 13, pp. 212-220.**
224. **Seierdten, M and Kofstad, P., (1987), "Effect of SO₃ on Vanadate Induced Hot Corrosion," High Temp. Technol., Vol. 5, No. 3, pp. 115-122.**
225. **Seong, B.G., Hwang, S.Y. and Kim, K.Y., (2000), "High-temperature Corrosion of Remunerators Used In Steel Mills," Surf. Coat. Technol., Vol. 126, pp. 256-265.**
226. **Sharma, R. N., (1996), "Hot Corrosion Behaviour of Iron- and Nickel-Base Superalloys in Salt Environments at Elevated Temperatures," Ph. D. Thesis, Met. and Mat. Engg. Deptt., UOR, Roorkee, India.**
227. **Shi, L., (1995), "On the Possibility of a Na₂SO₄-Na₂O Eutectic Melt Developing on Metals Coated with Na₂SO₄ Deposit in Oxygen/Air at Intermediate Temperatures," Corros. Sci., Vol. 37, No. 8, pp. 1281-1287.**

228. **Shida**, Y. and Fujikawa, H. (1985), "Particle erosion behaviour of boiler tube materials at elevated temperature", *Wear*, Vol.103, pp 281-296.
229. **Sidhu**, B.S. and Prakash, S., (2003), "Evaluation of the Corrosion Behaviour of Plasma-Sprayed Ni₃Al Coatings on Steel in Oxidation and Molten Salt Environments at 900°C," *Surf. & Coat. Technol.*, Vol. 166, pp. 89-100.
230. **Sidhu**, B.S., Puri, D. and Prakash, S., (2004), "Characterisations of Plasma Sprayed and Laser Remelted NiCrAlY Bond Coats and Ni₃Al Coatings on Boiler Tube Steels," *Mater. Sci. Eng. A-Struct.*, Vol. 368, No. 1-2, pp. 149-158.
231. **Sidhu**, B.S., Puri, D. and Prakash, S., (2005), "Mechanical and Metallurgical Properties of Plasma Sprayed and Laser Remelted Ni-20Cr and Stellite-6 Coatings," *J. Mater. Process. Technol.*, Vol. 159, No. 3, pp. 347-355.
232. **Sidhu**, Buta Singh and Prakash, S., (2006), "Erosion-Corrosion of Plasma as Sprayed and Laser Remelted Stellite-6 Coatings in a Coal Fired Boiler," *Wear*, Vol. 260, pp. 1035-1044.
233. **Sidhu**, Buta Singh and Prakash, S., (2006A), "Performance of NiCrAlY, Ni-Cr, Stellite-6 and Ni₃Al coatings in Na₂SO₄-60% V₂O₅ environment at 900 °C under cyclic conditions," *Surf. Coat. Technol.*, Vol. 201, No. 3-4, pp. 1643-1654.
234. **Sidhu**, H. S., Singh, B.S. and Prakash, S., (2006B), "The role of HVOF coatings in improving hot corrosion resistance of ASTM-SA210 GrA1 steel in the presence of Na₂SO₄-V₂O₅ salt deposits," *Surf. Coat. Technol.*, Vol. 200, No. 18-19, pp. 5386-5394.
235. **Sidhu**, H. S., Singh, B.S. and Prakash, S., (2007), "Solid Particle Erosion of HVOF Sprayed NiCr and Stellite-6 Coatings," *Surf. Coat. Technol.*, Vol. 202, pp. 232-238.
236. **Sidhu**, T. S., Agarwal, R. D. and Prakash, S., (2005A), "Hot Corrosion of some Superalloy and Role of High-velocity Oxy Fuel Spray Coatings-a Review," *Surf. Coat. Technol.*, Vol. 198, pp. 441-446.
237. **Sidhu**, T. S., Agarwal, R. D. and Prakash, S., (2006C), "Evaluation of Hot Corrosion Resistance of HVOF Coatings on a Ni-based Superalloy in Molten Salt Environment," *Mater. Sci. Eng. A*, Vol. 430, pp. 64-78.
238. **Sidhu**, T. S., Agarwal, R. D. and Prakash, S., (2006D), "Hot Corrosion Studies of HVOF NiCrBSi and Stellite-6 Coatings on a Ni-based Superalloy in an Actual Industrial

- Environment of a Coal Fired Boiler," Surf. Coat. Technol., Vol. 201, pp. 1602-1612.
239. **Sidhu, T. S., Agarwal, R. D. and Prakash, S., (2006E), "Hot Corrosion of a NiCr Coated Ni-based Alloy," Scripta Materialia, Vol. 55, pp. 179-182.**
240. **Sidhu, T. S., Malik, A., Agarwal, R. D. and Prakash, S., (2006F), "Cyclic Oxidation Behaviour of Ni- and Fe-based Superalloys in Air and Na₂SO₄-25%NaCl Molten Salt Environment at 800°C," Inter. J. Physical Sci., Vol. 1, No.1, pp. 27-33.**
241. **Sidhu, T.S., Prakash, S. and Agrawal, R.D., (2005B), "Hot Corrosion Performance of a NiCr Coated Ni-based alloy," Scripta Materialia, Vol. 55, pp.179–182.**
242. **Sidhu, T.S., Prakash, S., Agrawal, R.D., (2006G), "Characterization of NiCr Wire Coatings on Ni- and Fe-based Superalloys by the HVOF Process," Surf. Coat. Technol., Vol. 200, pp. 5542-5549.**
243. **Sidhu, T.S., Prakash, S., Agrawal, R.D., (2007A), "Study of Molten Salt Corrosion of High Velocity Oxy-Fuel Sprayed Cermet and Nickel-based Coatings at 900°C," Metall. Mater. Trans. A, Vol. 38A, pp. 77-85.**
244. **Sidky, P.S., Hocking, M.G., (1999), "Review of Inorganic Coatings and Coating Processes For Reducing Wear and Corrosion," Brit. Corros. J., Vol. 34, No. 3, pp. 171-183.**
245. **Sims, C.T., Stoloff, N.S., Hagel, W.C., (1987), "The Superalloys," John Wiley and Sons, Inc, New York.**
246. **Singh, Buta, (2003), "Studies on the Role of Coatings in Improving Resistance to Hot Corrosion and Degradation," Ph.D. Thesis, Met. & Mat. Eng. Dept., Indian Institute of Technology Roorkee, Roorkee, India.**
247. **Singh, H., Prakash, S. and Puri, D., (2007), "Some Observations on the High Temperature Oxidation Behaviour of Plasma Sprayed Ni₃Al Coatings," Mater. Sci. Engg. A, 444 (2007) 242-250.**
248. **Singh, H., Puri, D. and Prakash, S., (2005), "Some Studies on Hot Corrosion Performance of Plasma Sprayed Coatings on a Fe-based Superalloy," Surf. Coat. Technol., Vol. 192, pp. 27-38.**

249. **Singh, Harpreet, (2005), "Hot Corrosion Studies of Plasma Sprayed Coatings Over Some Ni- and Fe-Based Superalloys," Ph.D. Thesis, Met. & Mat. Eng. Dept., Indian Institute of Technology Roorkee, Roorkee (2005).**
250. **Singh, Harpreet, Puri, D. and Prakash, S., (2004), "High Temperature Oxidation Behaviour of Plasma Sprayed NiCrAlY Coatings on Ni-based Superalloys in Air," Proc. of International Symposium of Research Students on Material Science and Engineering (ISRS), Department of Metallurgical and Materials Engineering, Indian Institute of Technology Madras, Chennai, India, December 20-22, pp. 1-17.**
251. **Singh, Harpreet, Puri, D. and Prakash, S., (2005), "Studies of Plasma Spray Coatings on a Fe-base Superalloy, their Structure and High Temperature Oxidation Behaviour," Anti-Corrosion Methods and Materials, Vol. 52, No. 2, pp. 84-95.**
252. **Singh, P. and Birks, N., (1979), "Attack of Co-Cr Alloys by Ar-So₂ Atmospheres," Oxid. Met., Vol. 13, pp. 457-474.**
253. **Singh, T. and Sundarajan, G., (1990), "Erosion Behaviour of 304 Stainless Steel at Elevated Temperatures," Metallurgical Transactions A, Vol. 21A, pp. 3187-3199.**
254. **Singh, Tejinder, (2006), "Studies on the Hot Corrosion Behaviour of HVOF Coatings on Some Ni- and Fe- Based Superalloys," Ph.D. Thesis, Met. & Mat. Eng. Dept., Indian Institute of Technology Roorke, Roorkee.**
255. **Smialek, J.L., (2001), "Advances in the Oxidation Resistance of High Temperature Turbine Materials," Surf. Interface Anal., Vol 31, pp 582-592.**
256. **Soessmith, D. W., (1987), "Kinetics of Aqueous Corrosion," in "ASM Handbook: Corrosion," Ed. Davis, J.R., ASM International Publishing, U.S.A, Ninth Edition, Vol. 13, pp. 29-36.**
257. **Spain, E., Batista, J.C., Letch, M., Housden, J. and Lerga, B., (2005), "Characterisation and Applications of Cr-Al-N Coatings," Surf. & Coat. Technol., Vol. 200, pp. 1507 – 1513.**
258. **Srikanth, S., Ravikumar, B., Das, S. K., Gopalakrishna, K., Nandakumar, K. and Vijayan, P., (2003), "Analysis of Failures in Boiler Tubes due to Fireside Corrosion in a Waste Heat Recovery Boiler," Engg. Failure Analysis, Vol. 10, pp. 59-66.**

259. **Srivastava, S.C., Godiwalla, K.M. and Banerjee, M.K., (1997), "Fuel ash Corrosion of Boiler and Superheater Tubes," Jour. Mater. Sci., Vol. 32, pp. 835-849.**
260. **Stack, M.M., Lekatos, S. and Stott, F.H., (1995), "Erosion-corrosion Regimes: Number, Nomenclature and Justification," Tribology International, Vol. 28, No. 7, pp. 445-451.**
261. **Stack, M.M., Stott, F.H. and Wood, G.C., (1993), "Review of Mechanisms of Erosion-corrosion of Alloys at Elevated Temperatures," Wear, Vol. 162-164, pp. 706-712.**
262. **Staia, M. H., Valente, T., Bartuli, C., Lewis, D.B. and Constable, C.P., (2001), "Part I: Characterization of Cr₃C₂-25% NiCr Reactive Plasma Sprayed Coatings Produced at Different Pressures," Surf. Coat. Technol., Vol. 146-147, pp. 553-562.**
263. **Stein, K. J., Schorr, B. S. and Marder, A. R., (1999), "Erosion of Thermal Spray MCr-Cr C Cermet Coatings", Wear, Vol. 224, pp 153-159.**
264. **Stott, F. H. and Hiramatsu, N., (2000), "Breakdown of Protective Scales during the Oxidation of Thin Foils of Fe-20Cr-5Al Alloys at High Temperature", Mater. High Temp., Vol. 17, No. 1, pp. 93-99.**
265. **Stott, F. H., (1992), "Developments in Understanding the Mechanisms of Growth of Protective Scales on High-Temperature Alloys," Mater. Charact., Vol. 28, No. 3, pp. 311-325.**
266. **Stott, F. H., (1998), "The Role of Oxidation in the Wear of Alloys," Trib. Int., Vol. 31, No. 1-3, pp. 61-71.**
267. **Stott, F. H., Wet, D. J. De and Taylor, R., (1994), "The Degradation Resistance of Thermal Barrier Coatings to Molten Deposits at Very High Temperatures," Trans. Mater. Res. Soc. Jpn., Vol. 14A, pp. 135-40.**
268. **Stott, F., (1998), "The Role of Oxidation in the Wear of Alloys," Tribology International, Vol. 31, No. 1-3, pp. 61-71.**
269. **Stott, F.H., Chong, F.M.F. and Stirling, C.A., (1984), International Congress on Metallic Corrosion, 9th Edition, pp. 1.**
270. **Stringer, J., (1987), "High Temperature Corrosion of Superalloys," Mater. Sci. Technol., Vol. 3, No. 7, pp. 482-493.**

271. **Stringer, J.**, (1997), "High Temperature Corrosion Problems in Coal Based Power Plant and Possible Solutions", Proc. of International conference on corrosion (CONCORN 97), December 3-6, Mumbai, India, pp 13-23.
272. **Stroosnijder, M. F., Mevrel, R. and Bennet, M. J.**, (1994), "The Interaction of Surface Engineering and High Temperature Corrosion Protection," Mater. High Temp., Vol. 12, No. 1, pp. 53-66.
273. **Suito, H. and Gaskell, D. R.**, (1971), "The Thermodynamics of Melts in the System VO_2 - V_2O_5 ," Metall. Trans., Vol. 2, pp. 3299-3303.
274. **Sundararajan, G. and Roy, Manish**, (1997), "Solid Particle Erosion Behaviour of Metallic Materials at Room and Elevated Temperatures," Tribology International, Vol. 30, No. 5 pp. 339-359.
275. **Sundararajan, G. and Shewmom, P.G.**, (1983), "A New Model for the Erosion of Metals at Normal Incidence," Wera, Vol. 84, No. 2 pp. 237-258.
276. **Sundararajan, G.**, (1991), "An analysis of the erosion-oxidation interaction mechanisms,"Wear,Vol. 145, No. 2, pp. 251-282.
277. **Sundararajan, G.**, (1993), "The differential effect of the hardness of metallic materials on their erosion and abrasion resistance," Wear, Vol. 162-164, No. 2, pp. 773-781.
278. **Sundararajan, T., Kuroda,S. and Abe, F.**, (2004), "Behaviour of Mn and Si in the Spray Powders During Steam Oxidation of Ni-Cr Thermal Spray Coatings," ISIJ Int., Vol. 44, pp. 139-144.
279. **Swadzba, L., Formanek, B., Gabriel, H. M., Liberski, P. and Podolski, P.**, (1993), "Erosion- and corrosion-resistant coatings for aircraft compressor blades," Surf. Coat. Technol., Vol. 10, No. 1-3, pp. 486-492.
280. **Swaminathan, J., Raghavan, S. and Iyer, S.R.**, (1993), "Studies on the Hot Corrosion of Some Nickel-base Superalloys by Vanadium Pentaoxide," T. Indian I. Metals, Vol. 46, No. 3, pp. 175-181.
281. **Tabakoff, W and Vittal, B V R**, (1983), "High temperature erosion study of INCO 600 metal", Wear, vol. 86, pp 89-99.

282. **Tabakoff, W.**, (1995), "High Temperature Erosion Resistance of Coatings for Use in Turbomachinery," *Wear*, Vol. 186-187, pp. 224-229.
283. **Tabakoff, W.**, (1999A), "Erosion Resistance of Superalloys and Different Coatings Exposed to Particulate Flows at High Temperature," *Surf. Coat. Technol.*, Vol. 120-121, pp. 542-547.
284. **Tabakoff, W.**, (1999B), "Protection of Coated Superalloys from Erosion in Turbomachinery and Other Systems Exposed to Particulate Flows," *Wear*, Vol. 233-235, pp. 200-208.
285. **Thilakan, H.R., Lahiri, A.K. and Banerjee, T.**, (1967), "Studies on the Resistance of Alloy Steels Against Oil-ash Corrosion-Part-I," *National Metallurgical Laboratory (NML) journal*, pp 20-25.
286. **Tiwari, S. N. and Prakash, S.**, (1996), "Hot Corrosion Behaviour of an Iron-Base Superalloy in Salt Environment at Elevated Temperatures," *Proc. of Sympos. Metals and Materials Research, Indian Institute of Technology Madras, Madras, 4-5th July*, pp. 107-117.
287. **Tiwari, S. N. and Prakash, S.**, (1997), "Studies on the Hot Corrosion Behaviour of Some Superalloys in $\text{Na}_2\text{SO}_4\text{-V}_2\text{O}_5$," *Proc. of SOLCEC, Kalpakkam, India, 22-24th Jan.*, Paper C33.
288. **Tiwari, S. N. and Prakash, S.**, (1998), "Literature Review-Magnesium Oxide as Inhibitor of Hot Oil Ash Corrosion," *Mater. Sci. Technol.*, Vol. 14, pp. 467-172.
289. **Tiwari, S. N.**, (1997), "Investigations on Hot Corrosion of Some Fe-, Ni- and Co-Base Superalloy in $\text{Na}_2\text{SO}_4\text{-V}_2\text{O}_5$ Environment under Cyclic Conditions," *Ph. D. Thesis, Met. Mat. Engg. Deptt., University of Roorkee, Roorkee, India.*
290. **Trafford, D. N. H. and Whittle, D. P.**, (1980), "The Salt Induced Corrosion Behaviour of Fe-Cr Alloys at Elevated Temperatures-II. Alloys Rich in Chromium," *Corros. Sci.*, Vol. 20, pp. 509-530.
291. **Trafford, D. N. H. and Whittle, D. P.**, (1980A), "The Salt Induced Corrosion Behaviour of Fe-Cr Alloys at Elevated Temperatures-I. Alloys Dilute in Chromium," *Corros. Sci.*, Vol. 20, pp. 497-507.

292. **Tsaur, C. C., Rock, J. C., Wang, C. J. and Su, Y. H., (2005), "The Hot Corrosion of 310 Stainless Steel with Pre-Coated NaCl/Na₂SO₄ Mixtures at 750°C," Mater. Chem. Phys., Vol. 89, No. 2-3, pp. 445-453.**
293. **Tucker, Jr., R. C., (1994), "Ch. 11: Advanced Thermal Spray Deposition Techniques," in 'Handbook of Deposition Technologies for Films & Coatings,' Eds. R.F. Bunshah, Noyes Pub. Park Ridge, New Jersey, U. S. A./William Andrew Publishing, LLC, Norwich, New York, U.S.A, pp. 591.**
294. **Ul-Hamid, A., (2004), "A TEM Study of the Oxide Scale Development in Ni-Cr-Al Alloys," Corros. Sci., Vol. 46, No. 1, pp. 27-36.**
295. **Unger, R. H., (1987), "Thermal Spray Coatings," in "ASM Handbook: Corrosion," Ed. Davis, J.R., ASM International Publishing, U.S.A, Ninth Edition, Vol. 13, pp. 459-462.**
296. **Uusitalo, M.A., Vuoristo, P.M.J. and Mantyla, T.A. (2003), "High Temperature Corrosion of Coatings and Boiler Steels in Oxidizing Chlorine-containing Atmosphere," Material Science and Engineering-Structures A, Vol. 346, No.1-2, pp. 168-77.**
297. **Uusitalo, M.A., Vuoristo, P.M.J. and Mantyla, T.A., (2003), "High Temperature Corrosion of Coatings and Boiler Steels in Oxidizing Chlorine-containing Atmosphere," Mater. Sci. Eng. A-Struct., Vol. 346, No. 1-2, pp. 168-177.**
298. **Vera, R., Villarroel, M., Carvajal, A. M., Vera, E. and Ortiz, C., (1009), "Corrosion Products of Reinforcement in Concrete in Marine and Industrial Environments," Mat.. Chem. Phy., Vol. 114, pp. 467-474.**
299. **Viswanathan, R., (1989), "Damage Mechanism and Life Assessment of High-temperature Components", ASM International, ISBN: 0-87170-358-0, pp 1-483.**
300. **Vuoristo, P., Niemi, K., Makela, A. and Mantyla, T., (1994), "Abrasion and Erosion Wear Resistance of Cr₃C₂-NiCr Coatings Prepared by Plasma, Detonation and High-Velocity Oxyfuel Spraying," Proc. of the 7th National Thermal Spray Conf., Boston, Massachusetts, pp. 121-26.**
301. **Wang, B. Q. and Luer, K., (1994), "The Relative Erosion-Corrosion Resistance of Commercial Thermal Sprayed Coatings in a Simulated Circulating Fluidized Bed**

- Combustor Environment," Proc. of the 7th National Spray Conf., 20-24th June, Boston, Massachusetts, pp. 115-20.
302. **Wang, B. Q., Ge ng, G. Q. and Levy, A.V. (1992), "Erosion and Erosion-corrosion Behavior of Chromized-siliconized Steel," Surf. Coat. Technol., Vol. 54-55, pp. 529-35.**
303. **Wang, B., Gong, J., Wang, A. Y., Sun, C., Huang, R. F., and Wen, L. S., (2002),"Corrosion Behavior of Plasma-sprayed NiCrAlY Coatings on Ni-based Superalloy," Surf. & Coat. Technol., Vol. 149, pp. 70-75.**
304. **Wang, B., Huang, R. F., Song, G. H., Gong, J., Sun, C., Wen, L. S. and Han, Y. F., (2001), "Interdiffusion Behavior of Ni-Cr-Al-Y Coatings Deposited by Arc-Ion Plating," Oxid. Met., Vol. 56, No. 1-2, pp. 1-12.**
305. **Wang, Bu-Qian, (1995), "Erosion-corrosion of Coatings by Bio-mass Fired Boiler Fly Ash," Wear, Vol. 188, pp. 40-48.**
306. **Wang, D., (1988), "Corrosion Behavior of Chromized and/or Aluminized 2¹/₄Cr-1Mo Steel in Medium-BTU Coal Gasifier Environments," Surf. Coat. Technol.,Vol. 36, pp. 49-60.**
307. **Wang, Y. and Chen, W., (2003), "Effect of Ceria on the Erosion Resistance of HVOF Thermal Sprayed NiAl Intermetallic Coatings," J. Mat. Sci. Lett., Vol. 22, pp. 845-848.**
308. **Wells, J. J., Wigley, F., Foster, D.J., Livingston, W.R., Gibb, W.H. and Williamson, J., (2005), "The nature of Mineral Matter in a Coal and the Effects on Erosive and Abrasive Behavior", Fuel Proc. Technol., Vol. 86, pp. 535-550.**
309. **Wensink, H. and Elwenspoek, M.C., (2002), "A Closer Look at the Ductile-Brittle Transition in Solid Particle Erosion", Wear, Vol. 253, pp. 1035-1043.**
310. **Westergard, R., Erickson, L. C., Axen, N., Hawthorne, H. M. and Hogmark, S., (1998), "The Erosion and Abrasion Characteristics of Alumina Coatings Plasma Sprayed Under Different Spraying Conditions," Trib. Int., Vol. 31, No. 5, pp. 271-79.**
311. **Weulersse, M. K., Moulin, G., Billard, P. and Pierotti, G., (2004), "High temperature corrosion of superheater tubes in waste incinerators and coal fired plants," Mat. Sci. Forum, Vol. 461-464, pp. 973-980.**

312. **Wielage, B., Hofmann, U., Steinhauser, S. and Zimmermann, G., (1998), "Improving Wear and Corrosion Resistance of Thermal Sprayed Coatings," Surface Engg., Vol. 14, No. 2, pp. 136-38.**
313. **Wong-Moreno, A. and Marchan Salsado, R.I., (1995), "Molten Salt Corrosion of Heat Resisting Alloys," In: Corrosion-95, NACE, Houston, TX (1995), pp. 465-1-465-16.**
314. **Wright, I. G., (1987), "High-temperature Corrosion," In: Metals Handbook, Vol. 13, 9th ed. Metals Park: ASM, pp. 97-103.**
315. **Wu, C. and Okuyama, M., (1996), "Evaluation of High Temperature Corrosion Resistance of Al Plasma Spray Coatings in Molten Sulfates at 1073 K by Electrochemical Measurements," Mater. Trans., JIM, Vol. 37, No. 5, pp. 991-97.**
316. **Yamada, K., Tomono, Y., Morimoto, J., Sasaki, Y. and Ohmori, A., (2002), "Hot Corrosion Behavior of Boiler Tube Materials in Refuse Incineration Environment," Vacuum, Vol. 65, No. 3-4, pp. 533-540.**
317. **Yang, G., Zhang, S., Wang, Y., Li, C. and Xian/CN, Li., (2008), "Comparing Study of High Temperature Erosion of HVOF Sprayed Cr₃C₂-NiCr Coatings on Mild Steel for Boiler Tubes," Proc. of International Thermal Spray Conference (ITSC 2008), Maastricht, The Netherlands, June 2-4.**
318. **Yoo, Y. H., Le, D. P., Kim, J. G., Kim, S. K. and Vinh, P. V., (2008), "Corrosion Behaviour of tiN, TiAlN, TiAlSiN thin Films Deposited on Tool Steel in the 3.5 wt. % NaCl Solution," Thin Solid Films, Vol. 516, NO. 11, pp. 3544-3548.**
319. **Yoshida, M., (1993), "Effect of Hot Corrosion on the Mechanical Performances of Superalloys and Coating Systems," Corros. Sci., Vol. 35, No. 5-8, pp. 1115-1124.**
320. **Zhang, J.S., Hu, Z.Q., Murata, Y., Morinaga, M. and Yukawa, N., (1993), "Design and Development of Hot Corrosion-Resistant Nickel-Base Single Crystal Superalloys by the d-Electron Alloy Design Theory; II: Effects of Refractory Metals Ti, Ta, and Nb on Microstructures and Properties," Metall. Trans. A, Vol. 24, No. 11, pp. 2451-2464.**
321. **Zhang, Y., Cheng, Y.B. and Lathabai, S., (2000), "Erosion of Aluminium Ceramics by Air- and Water – Suspended Gernet Particles," Wear, Vol. 240, pp. 40-51.**
322. **Zhou, J.R., Bahadur, S., (1989), "Effect of blending of silicon carbide particles in varying sizes on the erosion of Ti-6Al-4V," Wear, Vol. 132, No. 2, pp. 235-246.**